



Journal of the Turkish Chemical Society, Section A: Chemistry (JOTCSA)

e-ISSN: 2149-0120

Volume 5, issue 2, 2018

A triannual, open-access chemical journal, hosted by Dergipark
(Published, in English, in every January, May, and September)

Editorial Board (sorted by the last names)

Prof. Dr. Göktürk, Sinem (Physical Chemistry, Marmara University, Turkey)

Prof. Dr. Karagözler, A. Alev (Biochemistry, Adnan Menderes University, Turkey)

Prof. Dr. Karagözler, A. Ersin (Electrochemistry, Adnan Menderes University, Turkey)

Prof. Dr. Köse, Dursun Ali (Inorganic Chemistry, Hitit University, Turkey)

Prof. Dr. Küçükbay, F. Zehra (Analytical Chemistry, İnönü University, Turkey)

Prof. Dr. Küçükbay, Hasan (Organic Chemistry, İnönü University, Turkey) Editor-in-Chief

Assoc. Prof. Dr. Taşdelen, M. Atilla (Polymer Chemistry, Yalova University, Turkey)

Prof. Dr. Yalçın, Esin A. (Computational Chemistry, Ankara University, Turkey)

Address: Halaskargazi Str. Uzay Apt. No: 15/8, 34373 Harbiye, Istanbul/Turkey.

Fax: +90 212 231 70 37

E-mail: jotcsa@turchemsoc.org

Website: <http://turchemsoc.dergipark.gov.tr/jotcsa>.

N.B. JOTCSA is a peer-reviewed publication of the Turkish Chemical Society. Peer-reviewing process is performed with the Dergipark Journal System. The ideas outlined by the authors cannot be attributed to the journal management nor the editorial board.

Aim and Scope of the Journal

The journal will publish, after a peer-reviewing process, as provided by the Ulakbim Journal Systems (UJS), the following:

- a)** Research articles,
- b)** Review articles,
- c)** Letters to the editor.

The journal's scope will include, but not limited to, the following disciplines of chemistry:

- i)** Analytical chemistry,
- ii)** Biochemistry,
- iii)** Computational chemistry,
- iv)** Electrochemistry,
- v)** Inorganic chemistry,
- vi)** Organic chemistry
- vii)** Physical chemistry,
- viii)** Polymer chemistry.

ETHICAL GUIDELINES

Guidelines for the Editors

An editor (editors, associate editors, etc.) should provide impartial consideration to all manuscripts offered for publication, judging each on its particular feature without regard to race, religion, nationality, sex, seniority, or institutional affiliation of the author(s). An editor should review and treat a manuscript submitted for publication with all reasonable speed. An editor takes the sole responsibility for accepting or rejecting a manuscript for publication. An editor may seek assistance on a manuscript from specialists chosen for their expertise and fair judgment. An editor should not reveal any information about the manuscript under consideration to anyone other than the author and designated reviewers until after the evaluation process is complete. An editor should respect the intellectual independence of authors.

Authors

Our journal considers a person as an author who is responsible at least for a part of the work. Authors should be able to explain the problem in study in a deep manner. For our journal, all authors are responsible for the content they submitted. The corresponding author is responsible for the agreement of all the authors and to keep them informed about the submission process since first submission of their manuscript. He/she is responsible for providing the license to publish, in case of acceptance, on behalf of all the authors. Our journal assumes that submitting the paper implies in total agreement from all the authors. For manuscripts with more than 8 authors, all the authors should provide a declaration specifying what was their contribution to the manuscript. It is not acceptable for JOTCSA to consider for publication anything that was previously published, neither entirely nor partly in other journals. Anything sent to our journal must not be under analysis by anywhere else. Simultaneous submissions to JOTCSA and any other journal, is considered a major conduct flaw, and all the authors will be definitely banned, and all their previous publications in JOTCSA will be publicly retracted. Plagiarism and self-plagiarism will be treated in the same way. Multiple manuscripts, dealing with closely related subjects and/or variables are discouraged as long as they could figure in a single paper.

Reviewers

JOTCSA invites peers to review its submissions, relying on their expertise, curricula, and their will to review them as volunteers. By accepting to review a manuscript, the reviewer commits himself to do so in due time. Delays are extremely negative to the review process and makes it last much longer than it should. When a reviewer is requested, he/she is gently asked to answer the invitation e-mail, informing if he/she is willing or not willing to review the manuscript. It is a gesture of politeness, and it avoids delays too. By accepting to review a manuscript, the reviewer declares that no conflicts of interests do exist, and he/she is doing his/her revision for the wealth and progress of Science. Those reviewers who answer our requests, agreeing or not, and those who respect the deadlines, are scored positively, and eventual submissions they could send to JOTCSA will be treated with priority.

The online version of this declaration can be viewed on <http://dergipark.gov.tr/jotcsa/page/2796>.

Journal of the Turkish Chemical Society, Section A: Chemistry (JOTCSA)

e-ISSN: 2149-0120

A triannual, open-access chemical journal, hosted by Dergipark

(Published, in English, in every February, June, and October)

Editorial Advisory Board Members (sorted alphabetically by the last names)

Abo-dya, Nader Elmaghwry (Zagazig University, Egypt)

do Amaral, Marcos Serrou (Federal University of Mato Grosso do Sul, Instituto de Física, Campo Grande, Brazil)

Bachawala, Praveen (Sigma-Aldrich, OH, USA)

Beatriz, Adilson (Federal University of Mato Grosso do Sul, Brazil)

Carta, Fabrizio (Università degli Studi di Firenze, Italy)

Döndaş, Hacı Ali (Mersin University, Faculty of Pharmacy, Department of Basic Pharmaceutical Sciences, Mersin, Turkey)

El-Khatib, Mirna (under Professor Sergei Vinogradov (2015-present) University of Pennsylvania, USA)

Florio, Saverio (CINMPIS, Italy)

Isa, Seema Habib (G.M. Momin Women's College, Faculty of Organic Chemistry, Department of Chemistry, University of Mumbai, India)

Jishkariani, Davit (under Prof. Christopher B. Murray, University of Pennsylvania, USA)

Külcü, Nevzat (Emeritus professor of chemistry in Mersin University, Department of Chemistry, Mersin, Turkey)

Lebedeva, Iryna (Augusta University, Augusta, GA, USA)

Nájera, Carmen (Royal Spanish Academy of Sciences, Spain)

Orhan, Ersin (Düzce University, Faculty of Arts and Sciences, Department of Chemistry, Düzce, Turkey)

Öcal, Nüket (Yıldız Technical University Faculty of Arts and Sciences, İstanbul, Turkey) *Passed away on June 30, 2018*

Panda, Siva S. (Augusta University, Augusta, GA, USA)

Deepak Shankar Panmand (Mhaskewadi, Tal: Parner, Dist: Ahmadnagar, Pin: 414305, Maharashtra, India)

Pillai, Girinath G. (University of Tartu, Faculty of Science, Estonia)

Seçen, Hasan (Atatürk University, Faculty of Science, Erzurum, Turkey)

Souizi, Abdelaziz (University of Ibn Tofail, Morocco)

Stanovnik, Branko (University of Ljubljana, Ljubljana, Slovenia)

Supuran, Claudiu T. (University of Florence, Florence, Italy)

Sütay, Berkay (Istanbul Technical University, İstanbul, Turkey)

Tural, Bilsen (Dicle University Ziya Gökalp Education Faculty, Diyarbakır, Turkey)

Tüfekçi, Mehmet (Karadeniz Technical University, Faculty of Science, Trabzon, Turkey)

Yaman, Mehmet (Firat University, Faculty of Science, Elazığ, Turkey)

Yılmaz, İsmet (İnönü University, Faculty of Arts and Sciences, Malatya, Turkey)

Yılmaz, Ülkü (İnönü University, Battalgazi Vocational School, Malatya, Turkey)

Yus, Miguel (Ludwig-Maximilian-University of Munich, Department of Chemistry, München, Germany and Uppsala University, Uppsala, Sweden)

JOTCSA, Table of Contents, Volume 5, issue 2

No	Article type¹	Article name and authors	Pages
1	RA	Synthesis of 2,3-Dihydroxypropyl-Sulfanyl Derivative Nonionic Surfactants and Their Inhibition Activities Against Carbon Steel Corrosion in Acidic Media (S. Öztürk, S. Mudaber, A. Yıldırım)	333-346
2	RA	Isochamaejasmin and other Flavonoids Isolated from an Endemic Algerian Desert Species (L. Noman, F. Oke-Altuntas, A. Zellagui, I. Demirtas, R. Salah)	347-354
3	RA	A Green and Efficient Method for the Synthesis of 3,4-Dihydropyrano[c]chromene using Phosphate Fertilizers (MAP, DAP and TSP) as Heterogeneous Catalysts (S. Chehab, Y. Merroun, T. Ghailane, R. Ghailane, S. Boukhris, A. Souzi)	355-370
4	RA	Synthesis and Characterization of New Cyclic Aminobenzoquinones (A. F. Tuyen, M. Yıldız)	371-380
5	RA	Electrochemical Oxidation Pathway of the Anti-Cancer Agent Dasatinib Using Disposable Pencil Graphite Electrode and its Adsorptive Stripping Voltammetric Determination in Biological Samples (D. Eşiköy Bayraktepe, K. Polat, Z. Yazan)	381-392
6	RA	Synthesis of Thiazole Derivatives as Antimicrobial Agents by Green Chemistry Techniques (S. Demirci)	393-414
7	RA	PVA NANOCOMPOSITES OF ORGANOCCLAYS OBTAINED USING DIFFERENT CATIONIC SURFACTANTS (C. H. Ünlü, S. İşçi Turutoğlu, O. Galioglu Atıcı, Ö. I. Ece, N. Güngör)	415-432
8	RA	The Synthesis of New Aryl Boron-Dipyrromethene Compounds: Photophysical and pH Responsive Properties (G. Sevinç, M. Hayvalı)	433-444
9	RA	Investigation of Phenolic Compounds and Antioxidant Activity of <i>Mentha spicata</i> subsp. <i>spicata</i> and <i>M. longifolia</i> subsp. <i>typhoides</i> (Briq.) Harley Decoction and Infusion (Z. Özer)	445-456
10	RA	Optimization of synthetic route to PNA-T-OH monomers (O. Alptürk, Z. S. Yeşilbaş, G. Sarioğlu, A. Karaçaylı, A. Saylam, S. Özçubukcu)	457-468
11	RA	Photoinduced Synthesis of Block Copolymers by Combining Atom Transfer Radical Polymerization and Photoinduced Radical Oxidation/Addition/Deactivation (M. Ciftci)	469-478
12	RA	Spectrophotometric Determination of Sunset Yellow (E-110) in Powdered Beverages and Pharmaceutical Preparations after Cloud Point Extraction Method (T. Güray)	479-492
13	RA	Chemical Diversity and Biological Potential of <i>Tanacetum praeteritum</i> subsp. <i>praeteritum</i> Essential Oils (G. Özek)	493-510
14	RA	Sesquiterpene Lactones and Other Constituents from The Aerial Parts of <i>Tanacetum Abrotonifolium</i> Druce, Collected in East Turkey / (Z. Zerenler Çalışkan, N. Gören)	511-520

¹ RA: Research article, RE: Review article, LE: Letter to the editor.

No	Article type ¹	Article name and authors	Pages
15	RA	The Uranium Recovery from Aqueous Solutions Using Amidoxime Modified Cellulose Derivatives. II. Uranium Uptake Behavior of RA Amidoximated Ethyl Cellulose (S. Şener Başarır, N. Pekel Bayramgil)	521-538
16	RA	Synthesis of New Medium- and Large- Sized Racemic and Chiral Lactones (H.Yaşa, A. Sergüzel Yusufoglu)	539-550
17	RA	Microwave-Assisted Synthesis and Biological Evaluation of Some Coumarin Hydrazides (F. Yılmaz, Ö. Faiz)	551-568
18	RA	Quantitative Structure-Activity Relationship and Molecular Docking Study of Some Pyrrolones Antimalarial Agents against <i>Plasmodium Falciparum</i> (Z. Shehu, A. Uzairu, B. Sagagi)	569-584
19	RA	Preparation and Cytotoxicity Evaluation of Some Amino Acid Methyl Ester Schiff Bases (N. Akkuş Taş, A. Şenocak, A. Aydın)	585-606
20	RA	Synthesis and Characterization of A Novel Thermally Stable Schiff Base Oligomer: Investigation of Conductivity Properties (N. Yılmaz Baran)	607-620
21	RA	Syntheses and spectroscopic investigations of 2-pyridyl(N/N)spirocyclotriposphazenes (G. Elmas)	621-634
22	RA	Synthesis and Characterization of Novel Pd and Cu vic-dioxime Precursors for Their Supercritical Deposition on Multiwalled Carbon Nanotubes (F. Ulusal, B. Güzel)	635-652
23	RA	Hydrothermal Syntheses, Crystal Structures, and Properties of 1D Coordination Polymers Based on 5-Nitroisophthalic Acid and 1-Methylimidazole Linkers (M. Arıcı)	653-662
24	RA	EFFECT of IONIC LIQUID CONTENT on the MONOLITHIC STRUCTURE of AMINE-MEDIATED SILICA AEROGEL via AMBIENT PRESSURE DRYING (N. Gizli, S. Sert Çok, F. Koç)	663-678
25	RA	Quinaldinium Chlorochromate(VI), (QnCC) Catalyzed Oxidation of Alcohols with Periodic Acid Under Solvent-Free Conditions and Microwave Irradiation (M. Canbulat Özdemir)	679-690
26	RA	Removal of Zinc from an Aqueous Solution Using Micellar-Enhanced Ultrafiltration (MEUF) with Surfactants (D. Şahin Taş)	691-700
27	RA	Synthesis of Novel Chalcone Substituted Metallophthalocyanines: Electrochemistry, Spectroelectrochemistry, and Catalytic Oxidation of 2-mercaptoethanol (H. KARACA, Z. KURT, S. SEZER)	701-718
28	RA	Synthesis of Chlorotoxin by Native Chemical Ligation (U. Karaca, M. S. Kesici, S. Özçubukçu)	719-726
29	RA	Combination of Photoinduced ATRP and Click Processes for the Synthesis of Triblock Copolymers (G. Yılmaz)	727-736
30	RA	Enzyme-Catalyzed Trans-Benzoin Condensation (G. Bilir, A. S. Demir, S. Özçubukçu)	737-750
31	RA	Macro and Trace Element Contents of Some Wild Plants Consumed as Vegetable in Manisa District, Turkey (Ş. Targan, E. G. Yelboğa, M.	751-

No	Article type ¹	Article name and authors	Pages
		Cittan)	762
32	RA	A Facile HPLC-PDA Method for Simultaneous Determination of Paracetamol, Methyl Paraben, Sunset Yellow, and Carmosine in Oral Suspensions (Ş. Dinç Zor, Ö. A. Dönmez)	763-774
33	RA	Photophysics, pH Sensing, and Hydrolysis Study of a Novel 1,8-Naphthalimide Derivative (A. Atahan, E. Orhan)	775-784
34	RA	Synthesis and characterization of new homo and heteronuclear Schiff base copper(II) complexes (T. Topal, E. Karapınar)	785-802
35	RA	The Photochemical Degradation (PCD) of Nitrobenzene (NB) using UV Light and Fenton Reagent Under Various Conditions (Md. B. Ahmed, A. Kumer, M. N. Islam, T. S. A. Islam)	803-818
36	RA	Synthesis of Aromatic Structured Di-cationic Surfactants Used as Inhibitors Against Corrosion of Carbon Steel in Acidic Medium (S. Öztürk, A. Yıldırım)	819-834
37	RA	Decolorization of Reactive Yellow 17 in aqueous solution by ozonation in a semi-batch bubble column reactor (K. Turhan)	835-844
38	RA	Synthesis, spectral studies, XRD, thermal investigation and biological screening of metal complexes derived from (N-(3-methoxyphenyl)-2-[(2E)-3-phenylprop-2-enoyl] hydrazinecarboxamide (Yuvaraj TCM, Parameshwara Naik P, Venkatesh T. V, Krishnamurthy G, Manjuraj T)	845-856
39	RA	Determination of 12 heavy metals in hennas by microwave induced plasma optical emission spectrometry (N. Özbek)	857-868
40	RA	Stable Nano Calcite Synthesis (S. Kılıç)	869-880
41	RA	CrVMoO7: MICROWAVE SYNTHESIS AND STRUCTURAL CHARACTERIZATION (G. Ç. Gül)	881-884
42	RA	Synthesis and Characterization of Jeffamine Core PAMAM Dendrimer-Silver Nanocomposites (Ag JCPDNCs) and Their Evaluation in The Reduction of 4-Nitrophenol (M. U. Gürbüz, A. S. Ertürk)	885-894
43	RA	Palladium(II) Complexes of Monodentate Phosphine Ligands and Their Application as Catalyst in Suzuki-Miyaura C-C Coupling Reaction at Room Temperature (M. K. Yılmaz, S. İnce)	895-902
44	RA	Ferulic Acid Substituted Zn(II) Phthalocyanine: Synthesis, Characterization and Investigation of Photophysical and Photochemical Properties (S. Gördük)	903-918
45	RA	Synthesis, Characterization and Optimum Reaction Conditions of Oligo-N-Salicylidenephenylhydrazone via Oxidative Polymerization (F. Kolcu)	919-930
46	RA	Syntheses and characterization of new dithiophosphinato zinc complexes (E. G. Sağlam, N. Acar)	931-940
47	RA	Nicotinamide-Modified poly(HEMA-GMA)-Nic Cryogels for Removal of	941-

No	Article type¹	Article name and authors	Pages
		Pesticides (K. Köse, G. A. Akveran, K. Erol, D. A. Köse)	952
48	RA	Novel Coordination Compounds Based on 2-Methylimidazole and 2,2'-dimethylglutarate Containing Ligands: Synthesis and Characterization (P. K. Yaman, H. Erer)	953-962
49	RA	Synthesis of Some Mono-, Bis- NH-substituted-1,4-Benzoquinones (A. Kaçmaz)	963-970
50	RA	Synthesis of Some New Benzimidazole Derivatives Containing Chlorine and Investigation of Their Antioxidant and Anti-urease Activities (N. Karaali)	971-980



Editorial, Vol. 5, issue 2 (2018): Submissions between

May 2018-September 2018

We are very happy to present the volume 5, issue 2 of "Journal of the Turkish Chemical Society, Section A: Chemistry (JOTCSA)" which has already been indexed in TR-Dizin of TÜBİTAK (The Scientific and Technological Research Council of Turkey), Scopus, Sherpa/Romeo, DOAJ (Directory of Open Access Journals), Index Copernicus, JournalSeek, Google Scholar, CrossRef, Bielefeld Academic Search Engine (BASE), and Chemical Abstracts Service Source Index (CASSI). More information can be found at <http://dergipark.gov.tr/jotcsa>.

This issue includes 50 papers, 5 by authors of various nationalities and 45 by Turkish authors.

We wish to thank all the authors and reviewers of the manuscripts, and to the editorial team of "Journal of the Turkish Chemical Society, Section A: Chemistry" for their contributions over the last four years to making a success of JOTCSA.

Please visit to the website of our journal at <http://dergipark.gov.tr/jotcsa> and send your manuscript using our website. In case of any queries please do not hesitate to contact our managing editor, Dr. Barbaros AKKURT, at jotcsa@turchemsoc.org or myself at hasan.kucukbay@inonu.edu.tr.

There is not any publication, processing or subscription charges for our journal.

Best regards,

Prof. Dr. Hasan KÜÇÜKBAY, PhD

Editor-in-chief, JOTCSA



Synthesis of 2,3-Dihydroxypropyl-Sulfanyl Derivative Nonionic Surfactants and Their Inhibition Activities Against Carbon Steel Corrosion in Acidic Media

Serkan Öztürk*, Sebghatullah Mudaber, Ayhan Yıldırım

Uludağ University, 16059, Bursa, Turkey

Abstract: In the present study, various amide-based, sulfur-containing nonionic surfactants were synthesized and characterized by spectroscopic methods. The corrosion inhibition properties of these synthesized compounds were investigated. For this purpose, mild steel coupons were immersed for 24 hours at room temperature in 1 M HCl containing different concentrations of inhibitor according to the standard method. As a result of these corrosion tests, the synthesized compounds exhibited excellent inhibitory properties (76.58-93.74 *IE%*). Surface characterization studies were also performed for the metal coupons to support the obtained corrosion inhibition efficiency results.

Keywords: Metal corrosion, non-ionic surfactant, acidic medium, SEM.

Submitted: April 27, 2017. **Accepted:** February 05, 2018.

Cite this: Öztürk S, Mudaber S, Yıldırım A. Synthesis of 2,3-Dihydroxypropyl-Sulfanyl Derivative Nonionic Surfactants and Their Inhibition Activities Against Carbon Steel Corrosion in Acidic Media. JOTCSA. 2018;5(2):333-46.

DOI: <http://dx.doi.org/10.18596/jotcsa.309423>.

***Corresponding author. E-mail:** serkanozturk@uludag.edu.tr.

INTRODUCTION

Corrosion is the change of physical, chemical and mechanical properties of materials as a result of chemical and electrochemical reactions with the influence of environment (1). If the content consists of metals and alloys, then it can be used as metal corrosion and can be defined as corrosion of metal or metal alloys by oxidation or other chemical effects. Metallic corrosion is one of the most critical problems in various industrial fields. It is an undesirable phenomenon, causing economic loss for every country. As a result of corrosion, a significant portion of iron and steel is lost annually or becomes unusable. The metal, which is lost after the corrosion, causes economic losses at much higher cost than its value. On the other hand, corrosion losses affect not only the iron and steel industry but also the efficiency of all the investments being made by utilizing this sector, and it is a topic that interests the country's economy. Corrosion is also a cause of damage to human life and health and environmental pollution as well as material losses.

The corrosion phenomenon in the metals consists of two electrochemical reactions that proceed in the same way as oxidation in the anode and reduction in the cathode. Elements inducing to corrosion (metal, anodic reaction, cathodic reaction, and electrolyte) must be in one piece for the formation of metallic corrosion at the electrode/electrolyte interface, which is called the electrical interface.

Acid cleaning (pickling), which is a useful surface cleaning method, is frequently used in the industry to clean the rust and foreign materials on the metal surface. The most commonly used acids in this cleaning process are HCl and H₂SO₄ solutions (2). During the cleaning process with acid, metal corrosion occurs on the metal surface over time. In the cathode reaction of the metal corrosion in the acidic medium, hydrogen ions from the acid are reduced to form the H₂ gas. One of the most effective methods to deal with metallic corrosion in the acidic environment is to design and use appropriate organic corrosion inhibitors. A corrosion inhibitor is a substance that significantly reduces corrosion rate when added at low concentrations.

Investigations made in recent years have discovered that surfactants can be used as inhibitors against metal corrosion. High corrosion inhibition efficiency at low concentrations, lower toxicity, easy and economical price production are being the advantages of using a surfactant as corrosion inhibitor (3). In particular, it has been proven in scientific studies that non-ionic surfactants, where the polar head group is without charge, that known to have many applications throughout industry, including cosmetics, detergents, are useful inhibitors against metal corrosion in acidic environments (4-10). It is understood that non-ionic surfactants can adsorb onto the metal surface and therefore reduces anodic dissolution, and retards the hydrogen evolution reaction (9). The nonionic surfactants can also be mixed with other types of surfactants, *e.g.*, anionic or

cationic, to enhance their properties and increase their inhibition activities against metal corrosion (9, 10). In the literature, it is also reported that nonionic surfactant increases the inhibitory activity of the amino acid derivative by synergistic effect (11).

In this study, (2,3-dihydroxypropyl) sulfanyl derivatized three nonionic surfactants containing high carbon chained amide functional group were synthesized, and their corrosion inhibition efficiencies against metallic corrosion in the acidic medium were investigated.

MATERIALS AND METHODS

Materials and Instrumentation

Reagents and solvents were purchased from Merck (Germany). Thermo Nicolet 6700 FT-IR spectrometer was used for acquisition of the FT-IR spectra. ^1H NMR and ^{13}C NMR spectra were measured using Agilent 600 MHz Premium Compact NMR spectrometer in DMSO using TMS as the internal standard.

Synthesis of Compounds

Synthesis of 2-chloro-*N*-alkylacetamides (1a-c): Octylamine, decylamine, dodecylamine and chloroacetyl chloride compounds used as starting materials in the syntheses were purchased from Merck (Germany). Synthesis of the 2-chloro-*N*-octyl, -decyl and dodecylacetamide compounds was carried out as previously reported in the literature (12, 13).

Synthesis of 2-[(2,3-dihydroxypropyl)sulfanyl]-*N*-octylacetamide (2a): The procedure used to synthesize this compound was performed in some minor variations, similar to previously reported procedures (14, 15). In a round-bottom reaction flask, 0.27 g (4.76 mmol) of KOH was dissolved in absolute ethanol, and 0.52 g (4.76 mmol) of 3-mercapto-1,2-propanediol was added gradually to the reaction flask. The mixture was stirred for about 10 minutes, and then 0.98 g (4.76 mmol) of 2-chloro-*N*-octylacetamide (**1a**) was added slowly to the flask. The reaction mixture was stirred overnight at room temperature. At the end of the reaction, ethanol was evaporated, and the residue was dissolved in dichloromethane and extracted with water. The organic phase was dried over sodium sulfate, and the solvent was removed with a rotary evaporator. The residue was crystallized from petroleum ether/ethyl acetate to give a solid white product. Yield (0.69 g, 52 %); mp 64-65 °C.

Synthesis of 2-[(2,3-dihydroxypropyl)sulfanyl]-*N*-decylacetamide (2b): 0.32 g (5.69 mmol) of KOH, 0.62 g (5.69 mmol) of 3-mercapto-1,2-propanediol and 1.33 g (5.69 mmol) of 2-chloro-*N*-decylacetamide (**1b**) were used for the synthesis. The same experimental procedure as used in the synthesis of compound **2a** was carried out. Yield (0.97 g, 56 %); mp 66-67 °C.

Synthesis of 2-[(2,3-dihydroxypropyl)sulfanyl]-*N*-dodecylacetamide (2c): 0.43 g (7.66 mmol) of KOH, 0.83 g (7.66 mmol) of 3-mercapto-1,2-propanediol and 2.0 g (7.66 mmol) of 2-chloro-*N*-dodecylacetamide (**1c**) were used for the synthesis. The same experimental procedure as used in the synthesis of compound **2a** was carried out. Yield (2.0 g, 79 %); mp 79-79 °C.

Corrosion Tests Performed in Acidic Media

Preparations of Coupons and Acidic Solutions

Gravimetric measurements were performed using the coupons made from cold-rolled low-carbon steel, possessing DIN EN 10130 special conditions (16). Their composition was 0.07% C, 0.35% Mn, 0.015% P, and 0.015% S. The coupons were cut into rectangular shapes of 0.1 x 2.2 x 5.0 cm in thickness, width, and length, respectively. Before the immersion test, the coupons were immersed in 15 % HCl, polished lightly with a paper tissue, washed with deionized water and soaked in acetone. 1.0 M HCl solution was prepared from the concentrated HCl (37 %) (Merck grade).

Weight Loss Measurements

The synthesized cationic surfactants with the concentration of 25, 50, 100, 150 and 250 ppm were tested to determine the inhibition efficiency in 100 mL of 1.0 M HCl solution. All the corrosion inhibitors were directly dissolved in the acidic solution. The treatment solutions were poured into 150-mL sealed glass bottles, and the coupons were suspended in these solutions without stirring for 24 h at room temperature. Control tests were performed in the same way without the inhibitors. After the corrosion test, the coupons were removed, rinsed with water and wiped with paper tissues. Then, they were washed with acetone and dried to a constant weight in an oven (17, 18).

SEM

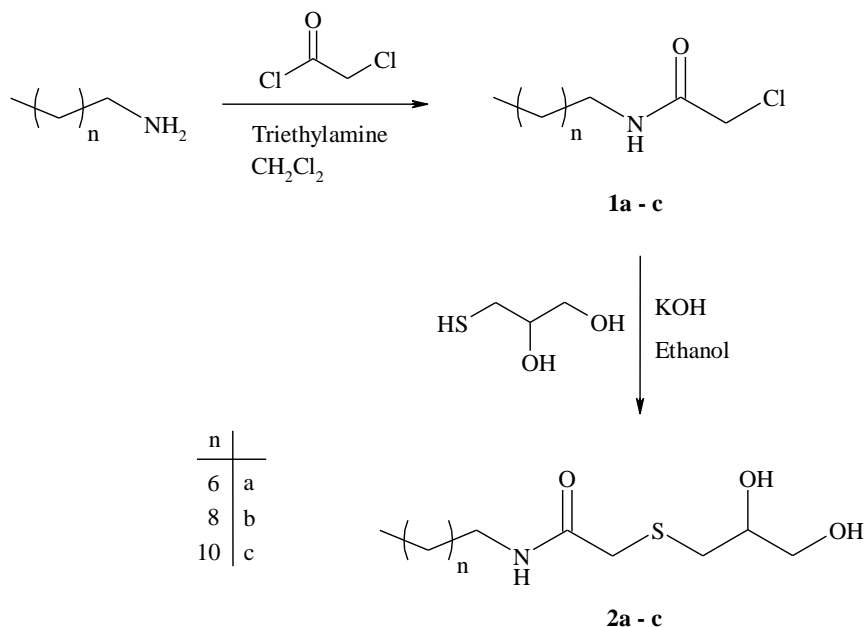
The carbon steel specimens (of a size of 0.1 cm x 2.0 cm x 2.0 cm) were abraded with emery paper and then were washed with distilled water and acetone. They were then immersed in 1.0 M HCl solutions containing no inhibitor and containing 250 ppm of the corresponding inhibitor for 24 h at room temperature. After the immersion time, the steel specimens were cleaned with distilled water and dried in a vacuum desiccator. Finally, the surface images of the steel specimens were obtained from a Carl Zeiss EVO 40 (SEM) device.

RESULTS AND DISCUSSION

Synthesis of nonionic surfactants

The synthesis scheme of the designed and synthesized organic nonionic surfactants to test corrosion inhibition in acidic media is given in Scheme 1. As seen in Scheme 1, the synthesis of organic surfactants was carried out in two steps. In the first step, the long-chained amine

compound was reacted with chloroacetyl chloride in the presence of triethylamine to synthesize 2-chloro-N-alkylacetamides (**1a-c**). In the second stage, 2-chloro-N-alkyl acetamides (**1a-c**) were reacted under basic medium with 3-mercapto-1,2-propanediol in alcohol to obtain the nonionic surfactants (**2a-c**).



Scheme 1. Synthetic pathways for the preparation of the compounds (**2a-c**).

The structures of the nonionic were confirmed by FT-IR, ^1H NMR, and ^{13}C NMR spectroscopic methods. The spectral data of **2a**, **2b**, and **2c** compounds are shown in Table 1. FT-IR, ^1H NMR and ^{13}C NMR spectra of compound **2b** as spectrum samples are given in Figure 1. The FT-IR spectra of (**2b**) showed absorption bands at 3332 cm^{-1} , due to the -OH groups, at 3266 cm^{-1} , due to the amide N-H group, at 1638 cm^{-1} , due to the amide C=O group, and at 698 cm^{-1} , due to the $\text{CH}_2\text{-S-CH}_2$ group. The ^1H NMR spectrum of (**2b**) showed a triplet peak at $\delta = 6.83\text{ ppm}$ for the amide-NH (HN-CO) proton, a sextet peak at $\delta = 3.85\text{ ppm}$ for the $\text{S-CH}_2\text{-CH-OH}$ proton. Moreover, and a doublet peak at $\delta = 3.70\text{ ppm}$ is observed for the $\text{S-CH}_2\text{-CH-OH}$ proton. Also, a doublet peak at $\delta = 3.68\text{ ppm}$ for the $\text{HO-CH}_2\text{-CH-OH}$ proton, a singlet peak at $\delta = 3.26\text{ ppm}$ for the $\text{HN-CO-CH}_2\text{-S}$ protons and a quartet peak at $\delta = 3.24\text{ ppm}$ for the $\text{CH}_2\text{-HN-CO}$ protons were observed. The peak attributed to the $\text{HN-CO-CH}_2\text{-S}$ protons at 3.26 ppm is the evidence that the nucleophilic substitution reaction between **1b** and 3-mercapto-1,2-propanediol was successfully actualized. The formation of the compound **2b** has been proved by the peak showed at 36.24 ppm for the carbon atom in the ^{13}C NMR spectrum.

Table 1. Spectral data of compound **2a**, **2b** and **2c**.

Compound	Spectral Data
2a	<p>FT-IR (KBr), ν/cm^{-1}: 3336 (-OH), 3268 (amide N-H), 2919 and 2852 (aliphatic C-H), 1639 (amide C=O), 1548 (secondary amide band, N-H bending), 697 ($\text{CH}_2\text{-S-CH}_2$)</p> <p>$^1\text{H}$ NMR (600 MHz, CDCl_3): δ (ppm) = 6.87 (t, 1H, HN-CO), 3.84 (quin., 1H, $\text{S-CH}_2\text{-CH-OH}$), 3.68 (d, 1H, $\text{S-CH}_2\text{-CH-OH}$), 3.66 (d, 1H, $\text{HO-CH}_2\text{-CH-OH}$), 3.56 (dd, 2H, $\text{HO-CH}_2\text{-CH-OH}$), 3.26 (s, 2H, $\text{HN-CO-CH}_2\text{-S}$), 3.24 (quartet, 2H, $\text{CH}_2\text{-HN-CO}$), 2.69 (d, 2H, $\text{CO-CH}_2\text{-S-CH}_2\text{-CH-OH}$), 1.50 (quin., 2H, $\text{CH}_2\text{-CH}_2\text{-HN-CO}$), 1.32-1.22 (m, 10H, $-(\text{CH}_2)_5-$), 0.86 (t, 3H, CH_3)</p> <p>^{13}C NMR (150 MHz, CDCl_3): δ (ppm) = 169.65 ($\text{HN-CO-CH}_2\text{-S}$), 71.24 ($\text{S-CH}_2\text{-CH-OH}$), 65.29 ($\text{HO-CH}_2\text{-CH-OH}$), 40.04 ($\text{CH}_2\text{-HN-CO}$), 36.35 ($\text{HN-CO-CH}_2\text{-S}$), 36.19 ($\text{CO-CH}_2\text{-S-CH}_2$), 31.74 ($\text{CH}_3\text{-CH}_2\text{-CH}_2-$), 29.37 ($\text{CH}_3\text{-(CH}_2)_2\text{-CH}_2-$), 29.20 ($\text{CH}_3\text{-(CH}_2)_3\text{-CH}_2-$), 29.16 ($\text{CH}_3\text{-(CH}_2)_5\text{-CH}_2\text{-CH}_2\text{-HN-CO}$), 26.90 ($\text{CH}_3\text{-(CH}_2)_4\text{-CH}_2\text{-(CH}_2)_2\text{-HN-CO}$), 22.59 ($\text{CH}_3\text{-CH}_2-$), 14.04 ($\text{CH}_3\text{-CH}_2-$)</p>
2b	<p>FT-IR (KBr), ν/cm^{-1}: 3332 (-OH), 3266 (amide N-H), 2917 and 2851 (aliphatic C-H), 1638 (amide C=O), 1551 (secondary amide band, N-H bending), 698 ($\text{CH}_2\text{-S-CH}_2$)</p> <p>$^1\text{H}$ NMR (600 MHz, CDCl_3): δ (ppm) = 6.83 (t, 1H, HN-CO), 3.85 (sextet, 1H, $\text{S-CH}_2\text{-CH-OH}$), 3.70 (d, 1H, $\text{S-CH}_2\text{-CH-OH}$), 3.68 (d, 1H, $\text{HO-CH}_2\text{-CH-OH}$), 3.56 (dd, 2H, $\text{HO-CH}_2\text{-CH-OH}$), 3.26 (s, 2H, $\text{HN-CO-CH}_2\text{-S}$), 3.24 (quartet, 2H, $\text{CH}_2\text{-HN-CO}$), 2.70 (d, 2H, $\text{CO-CH}_2\text{-S-CH}_2\text{-CH-OH}$), 1.51 (quin., 2H, $\text{CH}_2\text{-CH}_2\text{-HN-CO}$), 1.32-1.22 (m, 14H, $-(\text{CH}_2)_7-$), 0.87 (t, 3H, CH_3)</p> <p>^{13}C NMR (150 MHz, CDCl_3): δ (ppm) = 169.61 ($\text{HN-CO-CH}_2\text{-S}$), 71.17 ($\text{S-CH}_2\text{-CH-OH}$), 65.25 ($\text{HO-CH}_2\text{-CH-OH}$), 40.04 ($\text{CH}_2\text{-HN-CO}$), 36.34 ($\text{HN-CO-CH}_2\text{-S}$), 36.18 ($\text{CO-CH}_2\text{-S-CH}_2$), 31.85 ($\text{CH}_3\text{-CH}_2\text{-CH}_2-$), 29.52 ($\text{CH}_3\text{-(CH}_2)_2\text{-CH}_2-$), 29.39 ($\text{CH}_3\text{-(CH}_2)_5\text{-CH}_2-$), 29.26 ($\text{CH}_3\text{-(CH}_2)_7\text{-CH}_2\text{-CH}_2\text{-HN-CO}$), 26.91 ($\text{CH}_3\text{-(CH}_2)_6\text{-CH}_2\text{-(CH}_2)_2\text{-HN-CO}$), 22.63 ($\text{CH}_3\text{-CH}_2-$), 14.06 ($\text{CH}_3\text{-CH}_2-$)</p>
2c	<p>FT-IR (KBr), ν/cm^{-1}: 3332 (-OH), 3265 (amide N-H), 2917 and 2850 (aliphatic C-H), 1638 (amide C=O), 1551 (secondary amide band, N-H bending), 698 ($\text{CH}_2\text{-S-CH}_2$)</p> <p>$^1\text{H}$ NMR (600 MHz, CDCl_3): δ (ppm) = 6.74 (t, 1H, HN-CO), 3.85 (sextet., 1H, $\text{S-CH}_2\text{-CH-OH}$), 3.70 (d, 1H, $\text{S-CH}_2\text{-CH-OH}$), 3.68 (d, 1H, $\text{HO-CH}_2\text{-CH-OH}$), 3.57 (dd, 2H, $\text{HO-CH}_2\text{-CH-OH}$), 3.26 (s, 2H, $\text{HN-CO-CH}_2\text{-S}$), 3.25 (quartet, 2H, $\text{CH}_2\text{-HN-CO}$), 2.71 (d, 2H, $\text{CO-CH}_2\text{-S-CH}_2\text{-CH-OH}$), 1.51 (quin., 2H, $\text{CH}_2\text{-CH}_2\text{-HN-CO}$), 1.32-1.24 (m, 18H, $-(\text{CH}_2)_9-$), 0.87 (t, 3H, CH_3)</p> <p>^{13}C NMR (150 MHz, CDCl_3): δ (ppm) = 169.52 ($\text{HN-CO-CH}_2\text{-S}$), 71.12 ($\text{S-CH}_2\text{-CH-OH}$), 65.27 ($\text{HO-CH}_2\text{-CH-OH}$), 40.04 ($\text{CH}_2\text{-HN-CO}$), 36.34 ($\text{HN-CO-CH}_2\text{-S}$), 36.27 ($\text{CO-CH}_2\text{-S-CH}_2$), 31.85 ($\text{CH}_3\text{-CH}_2\text{-CH}_2-$), 29.51 ($\text{CH}_3\text{-(CH}_2)_2\text{-CH}_2-$), 29.40 ($\text{CH}_3\text{-(CH}_2)_7\text{-CH}_2-$), 29.26 ($\text{CH}_3\text{-(CH}_2)_9\text{-CH}_2\text{-CH}_2\text{-HN-CO}$), 29.25 ($\text{CH}_3\text{-(CH}_2)_3\text{-(CH}_2)_4\text{-(CH}_2)_4\text{-HN-CO}$), 26.90 ($\text{CH}_3\text{-(CH}_2)_8\text{-CH}_2\text{-(CH}_2)_2\text{-HN-CO}$), 22.63 ($\text{CH}_3\text{-CH}_2-$), 14.06 ($\text{CH}_3\text{-CH}_2-$)</p>

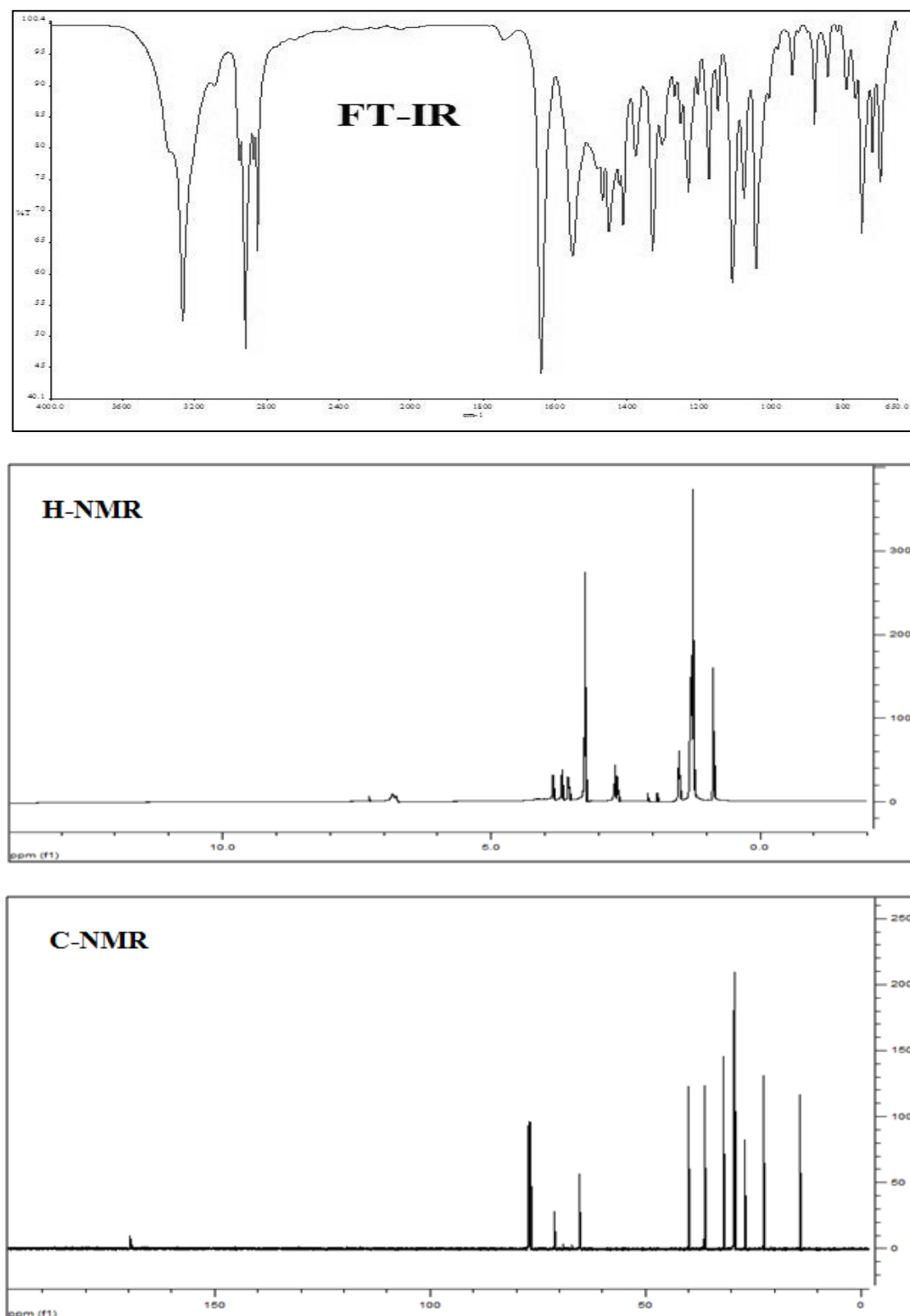


Figure 1. FT-IR, ¹H NMR and ¹³C NMR spectra of (2b).

Corrosion tests in acidic media

Corrosion tests in acidic media (1.0 M HCl) were performed using weight loss measurements according to the ASTM NACE / ASTM G31-12a standard method (19). The corrosion test results of the synthesized **2a-c** surfactants in 1.0 M HCl corrosive media are shown in Table 2. In the

corrosion tests, corrosion inhibitors were directly dissolved in the acid solution. Corrosion inhibition capabilities of the synthesized compounds tested in 1.0 M HCl are given as percentage inhibition efficiencies (IE %). Percentage inhibition efficiencies were calculated using the following Eq. 1:

$$IE \% = \frac{W_0 - W}{W_0} \times 100 \quad (\text{Eq. 1})$$

Where (IE %) is the percentage inhibition efficiency, W_0 is the weight loss of the coupon in the absence of an inhibitor and W is the weight loss of the coupon in the same environment in the presence of an inhibitor. The corrosion rate (CR) values that are given in Table 2, are derived from Eq. 2 (20-22):

$$CR = \frac{\Delta W}{A t} \quad (\text{Eq. 2})$$

where ΔW is the weight loss (mg); A is the area of the coupon (cm^2), and t is the immersion time (h).

Table 2 Weight loss, corrosion rate and corrosion inhibition efficiencies (IE %) for varying concentrations of compounds **2a-c** in 1.0 M HCl medium for 24 h at room temperature.

Concentration (ppm)	Weight loss (mg cm^{-2}) *			Corrosion Rate ($\text{mg cm}^{-2} \text{hr}^{-1}$) $\times 10^{-2}$			Inhibition Efficiency (IE %)		
	2a	2b	2c	2a	2b	2c	2a	2b	2c
0	12.50	12.50	12.50	52.08	52.08	52.08	—	—	—
25	2.93	1.12	1.25	12.20	4.66	5.19	76.58	91.05	90.04
50	2.32	1.04	0.90	9.66	4.32	3.75	81.45	91.71	92.80
100	1.42	0.93	1.07	5.91	3.86	4.47	88.65	92.58	91.42
150	1.35	0.91	1.24	5.61	3.79	5.15	89.24	92.73	90.11
250	0.78	0.85	0.83	3.26	3.52	3.45	93.74	93.24	93.38

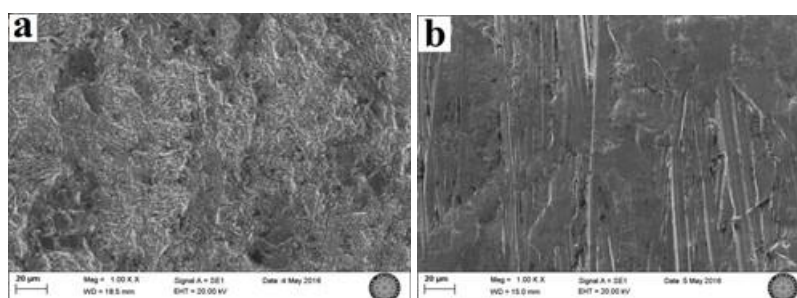
* Mean of the two measured values

When Table 2 is examined, it can be seen that at high concentrations, the three surfactants exhibit perfect inhibition activity. The corrosion resistance of the three compounds at 250 ppm inhibitor concentration was almost the same. However, it has been found that the inhibitory actions of compounds **2b** and **2c** are close to each other in all studied inhibitor concentrations. Furthermore, compound **2a** showed lower corrosion inhibition activity at lower levels than compounds **2b** and **2c**. The order of inhibition efficiency of these compounds is related to the molecular size of surfactant molecules. The long carbon chain of compound **2a** is shorter than the other two compounds. Higher molecular size tends to increase the adsorption on the metal

surface and hence to result in more surface coverage (23). With this more surface coverage, more effective protection against corrosion is achieved, especially at low concentrations. However, as the inhibitor concentration increases, the increase in inhibition activity is an expected result. It is proven that the inhibition efficiency increases with the increasing of inhibitor concentration. On the other hand, as seen in Table 2, the weight loss and corrosion rates in the inhibitor medium are considerably lower than in the uninhibited environment. The decrease in weight loss in the presence of inhibitors is due to the adsorption of the nonionic surfactants onto the carbon steel surface, forming a protecting layer, which leads to the increase in the coverage metal area. This adsorption of inhibitors decreases the contact between the metal surface and the aggressive medium. Therefore, this fall the corrosive effect of aggressive medium on the metal surface (24). All these results demonstrate that the synthesized nonionic surfactants are effective against metal corrosion.

SEM

Surface analysis with scanning electron microscopy is essential concerning the interaction of organic molecules with the metal surface and the observation of the morphological changes occurring on the surface of the metal. As for this purpose, scanning electron microscopic images were recorded to verify the interaction of the synthesized nonionic surfactants with the metal surface (Figure 2). The SEM image of Figure 2a, which was taken from the 1,000 x magnified surface, shows the feature of the steel surface after immersion in 1.0 M HCl at room temperature for 24 h in the absence of inhibitor. Figures 2b, 2c and 2d show the properties of the steel surface after immersion in 1.0 M HCl containing 250 ppm of inhibitor. As seen in Figure 2a, wear was observed on the entire surface of the metal exposed to the acid environment without the inhibitor. It is clear that corrosion products are accumulated on the metal surface due to corrosion, and therefore the surface becomes rough. On the other hand, there is no wear or roughness on the metal surfaces exposed to the inhibitor-containing acid environment. The scratch marks on the metal surfaces are due to the sanding process made before the test. This proves that the inhibitor molecules are adsorbed to the metal surface and protect the surface against corrosion in HCl media. As a result, the metal surface images obtained from the SEM device support the high inhibition activity results given in Table 2.



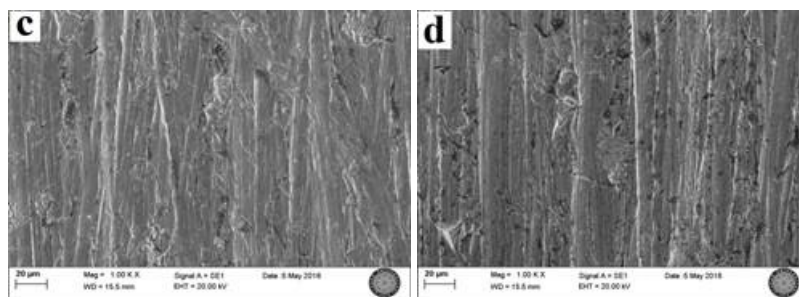


Figure 2. SEM images of the metal coupon surfaces immersed in 1.0 M HCl for 24 h. **a** without inhibitor 1,000x, **b** 250 ppm (**2a**) 1,000x, **c** 250 ppm (**2b**) 1,000x, **d** 250 ppm (**2c**) 1,000x

Corrosion inhibition mechanism

The first step in the mechanism of action of surfactant molecules as corrosion inhibitors is the adsorption onto the metal surface. The adsorption process is influenced by the nature and the surface charge of the metal, the chemical structure of the surfactant, the type of surfactant and the kind of the corrosive medium. The inhibition efficiency of nonionic surfactant molecules is related to the surfactant's ability to associate with one another at interfaces and in solution to aggregate to form micelles (23). In the nonionic surfactants, the driving force of micellization is the hydrophobic force and van der Waals attractions. The strong interaction between water molecules repels the hydrocarbon chain from the water bulk phase. It causes the non-polar hydrophobic groups to be directed away from the water molecule with the aid of polar hydrophilic groups in the molecule. Thus, at lower concentrations, it is expected that micelle formation will occur for extended chain surfactants (9). As can be seen in Table 2, the close inhibitory activity of compounds **2b** and **2c** in each studied concentration can be explained by this micellar formation and critical micelle concentration (CMC). It is known that nonionic surfactants may form micelles at lower levels than ionic surfactants and have lower CMCs (3, 25). The gathering of surfactants as micelles at low concentrations causes to more adsorption on the metal surface and hence a more efficient inhibition at lower levels (23). When surfactants form micelles and reach the CMC, the inhibition efficiency of these compounds, which are very similar to each other, is very close to each other and does not change much with increasing concentrations. The inhibition efficiencies obtained for compounds **2b** and **2c** are a result of this phenomenon.

Apart from micelle formation, the mechanism of adsorption of nonionic surfactant molecules at metal/solution interfaces can also be governed by the following factors (23):

- The interaction between the lone pair of electrons located in p-orbitals in the inhibitor molecules and the vacant metal orbitals.
- The interaction between uncharged moieties in the inhibitor molecules and the metal surface.

When the structures of the synthesized nonionic surfactants are examined, the following points were observed:

- There are two hydroxyl groups to facilitate dissolution in water.
- There are N, O and S heteroatoms in their structure. Through these heteroatoms, they adsorb onto the metal surface by chemical adsorption and reduce the adverse effect of the acidic corrosive environment on the metal surface by closing the active centers on the surface.
- They contain a hydrophobic group (long carbon chain) which prevents the contact of the corrosive environment with the metal surface. The long carbon chain pushes water molecules and prevents the acidic aqueous solution from approaching the surface. However, the long alkyl chains enter a non-polar interaction with each other due to the van der Waals attraction forces, and as a result of this interaction, they provide more effective protection on the metal surface against the corrosive medium.

The orientations of the inhibitor molecules at the metal-acidic solution interface and the possible inhibition mechanism are shown in Figure 3. As seen, molecules are found in an upright position in the metal surface which provides maximum protection. Primarily, to form bilayer or multimolecular layers, the hydrophobic tail of the surfactant molecule is oriented perpendicularly to the metal surface. The van der Waals interactions (non-polar physical interaction) occurring between the long alkyl chains in this perpendicular position are shown in Figure 3. These layers, designated as protective layers, behave as a barrier between the metal and the corrosive medium (18).

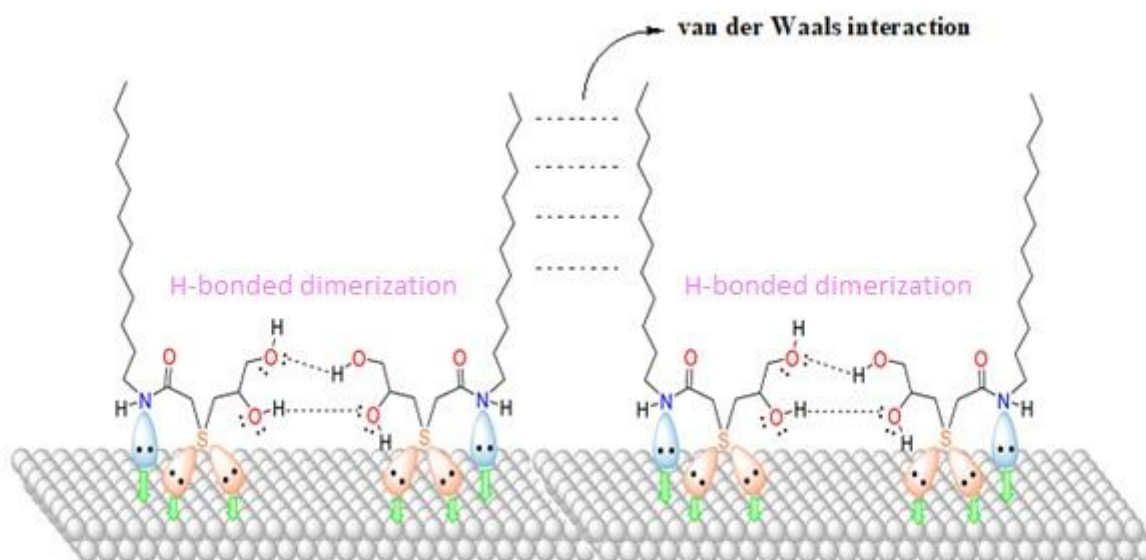


Figure 3. A possible orientation of non-ionic surfactant molecules between the metal-acidic solution interfaces.

In Figure 3, it can also be seen that nonionic surfactant molecules are adsorbed onto the metal surface via N and S heteroatoms by chemical adsorption. The chemical adsorption occurs from

the donor-acceptor interaction between p electrons of donor atoms (N and S) of the inhibitors and the vacant d-orbitals of iron surface atoms. Through this chemical adsorption, coordination bonds occur between the heteroatom and iron (26, 27). Sulfur and nitrogen atoms can form a protective layer (through coordination bonds between these heteroatoms and metal atoms), which covers the entire surface quickly and blocks the access to the active site of corrosion on the surface (9). Besides, intermolecular H-bonds are formed via hydroxyl groups, which increase the stability of the protective layer. It has been reported that the pH can influence this intermolecular interaction between hydroxyl groups of nonionic surfactants. At neutral pH, these intermolecular interactions and hence the adsorption to the metal surface of the synthesized nonionic surfactants are low, but it is increased at lower pH values (28). Furthermore, the formation of the hydrogen bond and the van der Waals interactions between the hydrophobic groups increase with an increase of the inhibitor concentration. It, therefore, leads to better protection of the metal surface and increased the inhibition efficiency of the nonionic surfactants (29, 30).

CONCLUSIONS

2,3-dihydroxypropyl-sulfanyl derivatized three nonionic surfactants containing high carbon chained amide functional group were synthesized as potential corrosion inhibitors for mild steel in 1.0 M HCl acidic media. From the results, we can conclude the following:

- All the nonionic surfactants exhibited good corrosion inhibition at high inhibitory concentrations.
- The corrosion inhibition efficiencies of the synthesized compounds increased with the increase in the inhibitory concentration.
- In the corrosion inhibition mechanism, the adsorption of the synthesized nonionic surfactants to the metal surface was performed with the help of micellar formation, chemical adsorption and physical adsorptions (intermolecular H-Bonds between hydroxyl groups and van der Waals interaction between the hydrophobic groups of the nonionic surfactants).
- The SEM images supported the inhibition results obtained by weight loss measurements.

CONFLICT OF INTEREST

The authors declare no conflict of interest.

REFERENCES

1. Görenler A. Al-Si Matrisli Kompozit Malzemelerin Korozyon Davranışlarının İncelenmesi. Yıldız Teknik Üniversitesi, Fen Bilimleri Entüsü, Yüksek Lisans Tezi, 2007 İstanbul.
2. Bereket G, Pinarbasi A. Inhibition effect of some heterocyclic compounds on pure aluminium in 0.1 M hydrochloric acid solution. Corrosion. 2008 16: 17-22.

3. Shaban S M, Abd-Elaal A A, Tawfik S M. Gravimetric and electrochemical evaluation of three nonionic dithiol surfactants as corrosion inhibitors for mild steel in 1 M HCl solution. J. Mol. Liq. 2010 Apr; 216:392-400.
4. Yıldırım A, Çetin M. Synthesis and evaluation of new long alkyl side chain acetamide, isoxazolidine and isoxazoline derivatives as corrosion inhibitors. Corros Sci. 2008 Jan; 50:155-65
5. Negm N A, Kandile N G, Badr E A, Mohammed M A. Gravimetric and electrochemical evaluation of environmentally friendly nonionic corrosion inhibitors for carbon steel in 1 M HCl. Corros. Sci. 2012 Dec; 65:94-103.
6. Hegazy M A, El-Tabei A S, Ahmed H M. Synthesis of nonionic surfactants and their inhibitive action on carbon steel in hydrochloric acid. Corros.Sci. 2012 Nov; 64:115-25
7. El-Tabei A S, Hegazy M A. A corrosion inhibition study of a novel synthesized gemini nonionic surfactant for carbon steel in 1 M HCl solution. J. Surfact. Deterg. 2013 Sep;16:757-66.
8. Sobhi M, El-Sayed R, Abdallah M. Synthesis, surface properties, and inhibiting action of novel nonionic surfactants on carbon steel corrosion in 1M hydrochloric acid solution. Chem. Eng. Commun. 2016; 203:758-68.
9. Fuchs-Godec R. Inhibitory effect of non-ionic surfactants of the Triton-X series on the corrosion of carbon steel in sulphuric acid. Electrochim. Acta 2007 Apr; 52:4974-81.
10. Hegazy M A, Zaky M F. Inhibition effect of novel nonionic surfactants on the corrosion of carbon steel in acidic medium. Corros. Sci. 2010 Apr; 52:1333-41.
11. Mobin M, Zehra S, Parveen M. L-Cysteine as corrosion inhibitor for mild steel in 1MHCl and synergistic effect of anionic, cationic and non-ionic surfactants, J. Mol. Liq. 2016 Apr; 216:598-607.
12. Van Esch J H, Hoffmann M M, Nolte R J M. Reduction of nicotinamides, flavins, and manganese porphyrins by formate, catalyzed by membrane-bound rhodium complexes. J. Org. Chem. 1995 Mar; 60:1599-1610.
13. Maksoud SAAE (2004) The effect of hexadecyl pyridinium bromide and hexadecyl trimethyl ammonium bromide on the behaviour of iron and copper in acidic solutions. J. Electroanal. Chem. 2004 Apr; 565:321-8.
14. Morris-Natschke S L, Gumus F, Marasco C J, Meyer K L, Marx M, Piantadosi C, Layne M D, Modest E J. Synthesis of phosphocholine and quaternary amine ether lipids and evaluation of *in vitro* antineoplastic activity. J. Med. Chem. 1993 Jul; 36:2018-25.
15. Alexander R L, Morris-Natschke S L, Ishaq K S, Fleming R A, Kucera G L. Synthesis and cytotoxic activity of two novel 1-dodecylthio-2-decyloxypropyl-3-phosphatidic acid conjugates with gemcitabine and cytosine arabinoside. J. Med. Chem. 2003 Sep; 46:4205-8.
16. Anonim. Cold rolled low carbon steel flat products for cold forming - Technical delivery conditions; German version EN 10130:2006, DIN Deutsches Institut für Normung e. V., 14s., 2007, Berlin, Germany.
17. Öztürk S, Yıldırım A, Çetin M, Tavaslı M. Synthesis of quaternary, long-chain N-alkyl amides and their corrosion inhibition in acidic media. J. Surfact. Deterg. 2014 May; 17: 471-81.
18. Yıldırım A, Öztürk S, Çetin M. Novel amide-based cationic surfactants as efficient corrosion inhibitors for carbon steel in HCl and H₂SO₄ media. J. Surf. Deterg. 2013 Jan; 16:13-23.
19. ASTM NACE / ASTM G31-12a, Standard Guide for Laboratory Immersion Corrosion Testing of Metals, ASTM International, West Conshohocken, PA, 2012 Oct; p.10.
20. Okoronkwo A E, Olusegun S J, Oluwasina O O. The inhibitive action of chitosan extracted from *Archachatina marginata* shells on the corrosion of plain carbon steel in acid media. Anti. Corros. Method M. 2015; 62:13-8.
21. Mohamed H A, Rehim, M H A. Surface active hyperbranched polyamide-ester as a corrosion inhibitor for carbon steel in both neutral and acidic media. Anti. Corros. Method M. 2015; 62:95-102.

22. Lashgari M, Arshadi M R, Biglar M. Comparative studies of some heterocyclic compounds as corrosion inhibitors of copper in phosphoric acid media. *Chem. Eng. Commun.* 2010; 197:1303-14.
23. Sobhi M, El-sayed R, Abdallah M. The effect of non ionic surfactants containing triazole, thiadiazole and oxadiazole as inhibitors of the corrosion of carbon steel in 1M hydrochloric acid. *J. Surfact. Deterg.* 2013 Nov; 16:937-46.
24. Shaban SM, Aiad I, El-Sukkary MM, Soliman EA, El-Awady MY. Inhibition of mild steel corrosion in acidic medium by vanillin cationic surfactants. *J. Mol. Liq.* 2015 Mar; 203:20-8.
25. Fuchs-Godec R, Pavlovic MG. Synergistic effect between non-ionic surfactant and halide ions in the forms of inorganic or organic salts for the corrosion inhibition of stainless-steel X4Cr13 in sulphuric acid, *Corros. Sci.* 2012 May; 58:192-201.
26. Athareh D, Fatemeh B. A new synthesized corrosion inhibitor for mild steel in 0.5 M H₂SO₄. *Gazi University Journal of Science (GU J Sci)*. 2011; 24:219-26.
27. Tawfik SM, Negm NA. Vanillin-derived non-ionic surfactants as green corrosion inhibitors for carbon steel in acidic environments. *Res. Chem. Intermed.* 2016 Apr; 42:3579-607.
28. Paria S, Khilar KC. A review on experimental studies of surfactant adsorption at the hydrophilic solid-water interface. *Adv. Colloid Interface Sci.* 2004 Aug; 110:75- 95.
29. Ramachandran S, Jovancicevic V. Molecular modeling of the inhibition of mild steel carbon dioxide corrosion by imidazolines. *Corrosion.* 1999 Jun; 55:259-67.
30. Mahmoud S S, Ahmed M M, Marie A H, El-Kasaby R A. Pitting Corrosion Inhibition of Some Copper Alloys in Neutral Solutions by Straight Chain Carboxylates. *Portugaliae Electrochim. Acta.* 2007; 25:453-70.



Isochamaejasmin and other Flavonoids Isolated from an Endemic Algerian Desert Species

Labib Noman^{1,4}  , Feyza Oke-Altuntas^{2*}  , Amar Zellagui^{1,3}  , Ibrahim Demirtas⁴  , Rhouati Salah¹  

¹University of Mentouri Brothers–Constantine I, Faculty of Science, Department of Chemistry, Constantine, Algeria

²Gazi University, Faculty of Science, Department of Biology, Ankara, Turkey

³University of Larbi Ben Mhidi Oum El Bouaghi, Department of Life Science and Nature, Oum El Bouaghi, Algeria

⁴Cankiri Karatekin University, Faculty of Science, Department of Chemistry, Cankiri, Turkey

Abstract: *Thymelaea microphylla* Coss. et Dur is an endemic desert species from Algeria belonging to Thymelaeaceae family. The dichloromethane-methanolic extract from aerial parts of *T. microphylla* was subjected to a silica gel column. Three flavonoids were isolated from the extract; isochamaejasmin (**1**), *cis*-tiliroside (**2**) and *trans*-tiliroside (**3**). The structures of the compounds were determined on the basis of the HPLC-TOF/MS, 1D and 2D NMR spectroscopic analysis. To the best of our knowledge, compound (**1**) was isolated from *T. microphylla* for the first time and there is no report in the literature. Moreover, in this study, antioxidant activity of the compound (**3**) was also evaluated.

Keywords: *Thymelaea microphylla*, flavonoids, antioxidant.

Submitted: November 13, 2017. **Accepted:** February 05, 2018.

Cite this: Noman L, Oke-Altuntas F, Zellagui A, Demirtas I, Salah R. Isochamaejasmin and other Flavonoids Isolated from an Endemic Algerian Desert Species. JOTCSA. 2018;5(2):347–54.

DOI: <http://dx.doi.org/10.18596/jotcsa.351651>.

***Corresponding author. E-mail:** feyzaoke@gazi.edu.tr.

INTRODUCTION

Thymelaeaceae family consists of approximately 67 genera and 1200 species. It is widespread in the tropics and temperate climate of the Earth, particularly in Africa (1). Although this family is a small taxon, it has very varied uses, giving them a significant economic importance in the regions where they grow (2, 3). *Thymelaea* is one of the genus of this family, which contains about 30 species in the world (4). Some species of this genus have been used in the traditional medicine and reported have some biological activities such as antidiabetic, antihypertensive (5), anti-inflammatory (6) as well as antimicrobial and antioxidant activity (7).

Thymelaea microphylla called "Al Methnan" is a small shrub and its length does not exceed a meter. It has been used in folk medicine for the treatment of wounds, erysipelas, skin cancer, pimples, and abscess (8). Several studies have shown that this species had remarkable antibacterial, antioxidant (9, 10), antiinflammatory (6), and antiproliferative (11) activities. Phytochemical studies on this species were indicated the presence of bicoumarin and their glycoside derivatives, linear-type furanocoumarin glucosides and simple coumarin glucosides (12). Daphnoretine (bicoumarin), umbelliferone (simple coumarin) and prestegeane B (lignans) have been isolated from the aerial parts of *Thymelaea microphylla* (11). The report related to the chemical analysis of *Thymelaea microphylla* essential oil in the literature showed the major components were D-menthone (41.86 %), 2-undecanone (23.74 %), pulegone (11.94 %) and perillal (9.34 %) (13).

Recently, we have reported the new benzimidazole and six known compounds with their antiproliferative and antioxidant activities from *T. microphylla* (11). We herein report the isolation and structural elucidation of three flavonoids from the chloromethanolic extract of *T. microphylla*. Also, in this study, we investigated the antioxidant activity of the compound (**3**).

EXPERIMENTAL SECTION

Extraction and isolation

Dried aerial parts of *Thymelaea microphylla* (2200 g) were crushed and extracted with CH₂Cl₂: MeOH (1:1, v:v) at room temperature. The extract was concentrated *in vacuo* to obtain the crude extract (F; 103.7 g), which was fractionated by column chromatography eluted with n-hexane, followed by a gradient of n-hexane and CH₂Cl₂ up to 100% CH₂Cl₂ and CH₂Cl₂-MeOH up to 100% MeOH to obtain 9 fractions. The fraction 6 (F6; 5.5 g) was subjected to flash column chromatography eluted with n-hexane, followed by a gradient of n-hexane-CH₂Cl₂ up to 100% CH₂Cl₂ and CH₂Cl₂-EtOAc up to 100% EtOAc and EtOAc-ethanol up to 100% ethanol to obtain 25 fractions from collective tubes and 51 fractions from waste tubes. The fraction F6-C4 from collective tubes was purified by TLC eluted with n-hexane: CH₂Cl₂: MeOH (1: 2: 0.5, v:v:v) to

afford compound **1** (isochamaejasmin; 11.35 mg). The fraction 7 (F7; 6.3 g) was applied on column chromatography eluted with n-hexane: CH₂Cl₂: MeOH (0,5: 2 :1) to obtain 12 sub-fractions, the precipitate from sub-fraction 7 purified by TLC eluted with the same system to afford compounds (**2**) (*cis*-tiliroside; 5.14 mg) and (**3**) (*trans*-tiliroside; 6.43 mg).

General experimental procedure

¹H (400 MHz) and ¹³C NMR (100 MHz) spectra were recorded on Bruker Avence III spectrometer (in DMSO-d₆ with tetramethylsilane (TMS) as internal standard). HPLC-TOF/MS spectra were recorded in the negative ion mode on an Agilent 6210 spectrometer. Column chromatography and thin-layer chromatography were performed over silica gel (Merck, Germany), 60A and 60F₂₅₄, respectively.

Antioxidant activity

Radical scavenging activity of the compound (**3**) was determined according to the method of Blois (14). BHT was used as a positive control. Scavenging of DPPH radical was calculated according to the formula: Radical scavenging % = [(A_{control} - A_{sample})/ A_{control}] × 100.

Metal chelating activity of the compound (**3**) was determined according to the method of Decker and Welch (15), with some modifications. EDTA was used as a positive control.

RESULTS AND DISCUSSION

Compound (**1**) was obtained as an amorphous powder. The mass experiment was carried out using HPLC-TOF/MS in a negative mode, which presented an ion whose quasi-molecular at m/z 541 corresponding to the molecular formula C₃₀H₂₂O₁₀. The ¹H NMR spectrum of **1** showed pair signals of doublets at δ 5.8 and 5.7 (each 2H, J = 2.0 Hz) were assigned to 6, 6'', and 8, 8'' protons, respectively. Four signals of ortho-coupled doublets (J = 8.5 Hz) at δ 7.0, 6.9, 6.8 and 6.7 integrating for two protons each, were assigned to (6', 6'''), (2', 2'''), (5', 5''') and (3', 3''') protons, respectively, along with two signals of doublets with coupling constant (J = 12.0 Hz) at δ 5.71 and 2.7 for two protons each, assigned to 2, 2'' and 3, 3'' protons, respectively, characteristic for the biflavanone structure. ¹³C NMR spectral data of **1** (see Table I), displayed that C-3 was linked with C-3'' according to the resonance of C-3 and C-3'' (49.3 ppm), and compared with carbon resonance of naringenin (43.7 ppm)(16). The stereochemistry at the C-2/C-3 and C-2''/C-3'' positions were determined as *trans-trans* geometry based on the values of the coupling constants (J = 12.0 Hz) of the protons (H-2/H-3 and H-2''/H-3''), All these NMR data together with the mass spectrum suggested the structure of compound **1** was elucidated as isochamaejasmin (17). Compound **2** was obtained as a yellow powder and had a molecular formula C₃₀H₂₆O₁₃ established by HPLC-TOF/MS (m/z 593 [M-H]⁻). Compound **3** was obtained as a yellow powder, the molecular formula of which was determined to be C₃₀H₂₆O₁₃ from the

molecular ion peak at m/z 593.0701 $[M-H]^-$ (Calcd for 593.1295) in the HR-EI-MS. Compounds 2 and 3 were identified as *cis*-tiliroside and *trans*-tiliroside, respectively, by comparing their EI-MS, 1H NMR and spectra with published data ^{13}C NMR(18, 19) (Table 1, Table 2, Figure 1.).

Table 1: ^{13}C NMR spectral data of compounds (Cmp) (1), (2), and (3).

Position	Cmp (1)	Position	Cmp (2)	Position	Cmp (3)
2/2''	83.4	2	157.4	2	156.5
3/3''	49.3	3	133	3	132.4
4/4''	195.5	4	177.3	4	177
10/10''	101.2	10	113.2	10	113
5/5''	164	5	160.2	5	159.4
6/6''	97	6	100.6	6	99.3
7/7''	170	7	159.3	7	158.3
8/8''	96	8	95	8	94.2
9/9''	162.7	9	161.2	9	160.2
1'/1'''	127	1'	121.4	1'	121
2'/2'''	131.4	2'/6'	131	2'/6'	130
3'/3'''	116	3'/5'	115.5	3'/5'	114.3
4'/4'''	158	4'	160.1	4'	160
5'/5'''	116	1''	103.3	1''	102.5
6'/6'''	130	2''	74.4	2''	74.4
		3''	73.34	3''	72.4
		4''	70.24	4''	69.42
		5''	74.3	5''	73.18
		6''	63	6''	62.13
		1'''	126	1'''	124.2
		2'''/6'''	130	2'''/6'''	129
		3'''/5'''	116	3'''/5'''	114.3
		4'''	160	4'''	159.2
		7'''	145.2	7'''	144.5
		8'''	114.5	8'''	114
		9'''	167.4	9'''	166.4

Table 2: 1H NMR spectral data of compounds (Cmp) (1), (2), and (3).

Position	Compound 1	Position	Compound 2	Position	Compound 3
6/6''	5.78 (<i>d</i> , <i>J</i> = 2.01)	6	6.0 (<i>d</i> , <i>J</i> = 2.2)	6	6.2 (<i>d</i> , <i>J</i> = 2.3)
8/8'	5.70 (<i>d</i> , <i>J</i> = 2.01)	8	6.2 (<i>d</i> , <i>J</i> = 2.2)	8	6.3 (<i>d</i> , <i>J</i> = 2.3)
2'/2'''	6.86 (<i>d</i> , <i>J</i> = 8.53)	2'/6'	8.0 (<i>d</i> , <i>J</i> = 9.0)	2'/6'	8.0 (<i>d</i> , <i>J</i> = 9.0)
6'/6'''	6.98 (<i>d</i> , <i>J</i> = 8.53)	3'/5'	6.8 (<i>d</i> , <i>J</i> = 8.8)	3'/5'	6.9 (<i>d</i> , <i>J</i> = 8.8)
3'/3'''	6.73 (<i>d</i> , <i>J</i> = 8.53)	1''	5.15 (<i>d</i> , <i>J</i> = 7.28)	1''	5.2 (<i>d</i> , <i>J</i> = 7.3)
5'/5'''	6.78 (<i>d</i> , <i>J</i> = 8.53)	2''	3.37 (<i>m</i>)	2''	3.4 (<i>m</i>)
2/2''	5.71 (<i>d</i> , <i>J</i> = 12.30)	3''	3.5 (<i>m</i>)	3''	3.5 (<i>m</i>)
3/3''	2.69 (<i>d</i> , <i>J</i> = 12.30)	4''	3.4 (<i>m</i>)	4''	3.3 (<i>m</i>)
		5''	3.4 (<i>m</i>)	5''	3.47 (<i>m</i>)
		6''a	4.32 (<i>dd</i> , <i>J</i> = 11.8-6.5)	6''a	4.3 (<i>dd</i> , <i>J</i> = 11.9-6.5)
		6''b	4.18 (<i>dd</i> , <i>J</i> = 11.8- 2.0)	6''b	4.2 (<i>dd</i> , <i>J</i> = 11.9- 2.0)
		2'''/6'''	7.3 (<i>d</i> , <i>J</i> = 8.8)	2'''/6'''	7.4 (<i>d</i> , <i>J</i> = 8.9)
		3'''/5'''	6.8 (<i>d</i> , <i>J</i> = 9.0)	3'''/5'''	6.8 (<i>d</i> , <i>J</i> = 9.3)
		7'''	7.4 (<i>d</i> , <i>J</i> = 12.3)	7'''	7.5 (<i>d</i> , <i>J</i> = 15.8)
		8'''	6.16 (<i>d</i> , <i>J</i> = 12.3)	8'''	6.18 (<i>d</i> , <i>J</i> = 15.8)

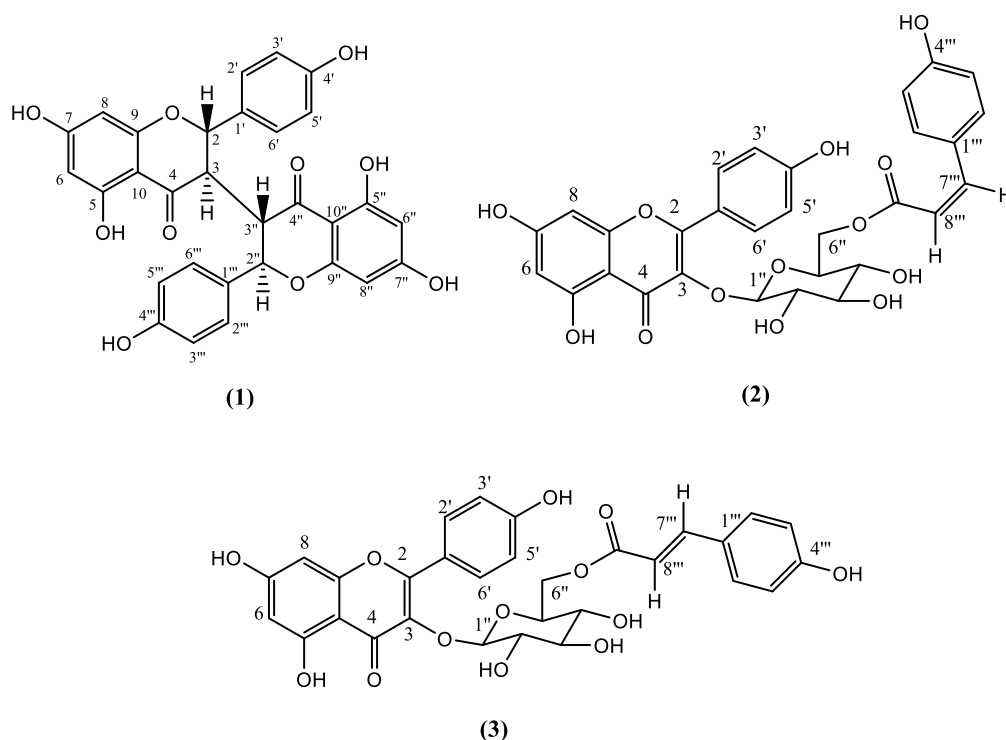


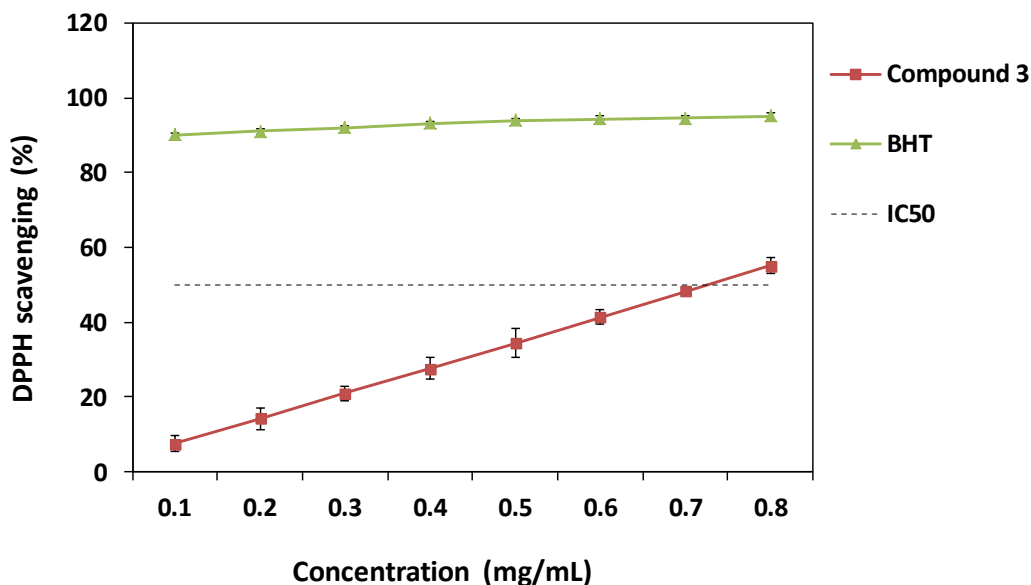
Figure 1: The structure of compounds **1**, **2**, and **3**.

Trans-tiliroside compound (**3**) isolated from *T. microphylla* was studied *in vitro* for its metal chelating and scavenger properties. As can be seen Table 3, this compound ($IC_{50} = 0.726 \pm 0.043$ mg/mL) exhibited lower DPPH scavenging effect than BHT ($IC_{50} = 0.023 \pm 0.001$ mg/mL) (Figure 2). On the other hand, compound (**3**) was not an active metal chelator at the concentration of 1 mg/mL. According to the literature, several researchers reported that tiliroside compound has antioxidant activity (20-23). Sala, Recio (21) determined that the tiliroside has a high antioxidant activity measured by the DPPH test and reported the IC_{50} value of the this compound was about 6 μ M, in the same range as that of the flavonol quercetin-3-O-glucoside. Ding (23) studied DPPH radical scavenging activity of the tiliroside compound which isolated from the fruits of *Rubus chingii* and reported as 13.7 μ M. On the other hand, Mekhelfi (24) reported that the radical scavenging effect of *trans*-tiliroside compound isolated from *T. microphylla* (% 21.82 at 10 mg/mL). Li, Tian (22) presented that Astragalín (kaempferol-3-O- β -D-glucopyranoside) and tiliroside (kaempferol-3-O- β -D-(6''-O-*p*-coumaroyl)-glucopyranoside) both efficiently scavenged DPPH radicals; however, tiliroside showed higher DPPH radical scavenging ability than astragalín. They explained the reason of this situation as follows; *p*-coumaroyl moiety in tiliroside enhanced the efficiency of the hydrogen atom transfer-based pathways.

Table 3: Antioxidant of compound 3 (*trans*-tiliroside)*.

	DPPH IC ₅₀ (mg/mL)	Metal chelating (%, at 1 mg/mL)
Compound (3)	0.726 ± 0.043 ^a	NA
BHT	0.023 ± 0.001 ^b	NS
EDTA	NS	93.1 ± 0.2

*Values represent averages ± standard deviations for triplicate experiments. Values in the same column with different superscripts (a and b) are significantly ($p < 0.01$) different. NA: not active at tested concentration, NS: not studied.

**Figure 2:** DPPH radical scavenging activity of compound (3).

CONCLUSION

In this study, three flavonoids; isochamaejasmin, *cis*-tiliroside, and *trans*-tiliroside were isolated from *Thymelaea microphylla*. The structures of the compounds were determined on the basis of the HPLC-TOF/MS, 1D and 2D NMR spectroscopic analysis. This is the first report on the isolation and structure elucidation of isochamaejasmin compound from this plant. Also, in this study, *trans*-tiliroside compound isolated from *T. microphylla* was evaluated for its antioxidant activity and found as a potent radical scavenger. These results suggest that *trans*-tiliroside compound may be used as a natural antioxidant in cosmetic, food, and pharmaceutical industries.

ACKNOWLEDGMENT

The authors are grateful for the partial financial support of the Ministère de l'Enseignement Supérieur et de la Recherche Scientifique (MESRES - Alger, Algeria); Turkish State Planning Organization [grant number DPT2010K120720]; and Cankiri Karatekin University.

REFERENCES

1. Borris RP, Blaskó G, Cordell GA. Ethnopharmacologic and phytochemical studies of the Thymelaeaceae. *Journal of Ethnopharmacology*. 1988;24(1):41-91.
2. Takeuchi W, Golman M. The identity of eaglewood (*Gyrinops*, Thymelaeaceae), a new economic resource for Papua New Guinea. *SIDA, Contributions to Botany*. 2002;20(1):261-7.
3. Bredenkamp CL, van Wyk AE. Taxonomy of the genus *Passerina* (Thymelaeaceae). *Bothalia: African Biodiversity & Conservation*. 2003;33:53-7.
4. Vincent MA, Thieret JW. *Thymelaea passerina* (Thymelaeaceae) in Ohio. *SIDA, Contributions to Botany*. 1987;12(1):75-8.
5. Bnouham M, Benalla W, Bellahcen S, Hakkou Z, Ziyat A, Mekhfi H, et al. Antidiabetic and antihypertensive effect of a polyphenol-rich fraction of *Thymelaea hirsuta* L. in a model of neonatal streptozotocin-diabetic and NG-nitro-L-arginine methyl ester-hypertensive rats. *Journal of Diabetes*. 2012;4(3):307-13.
6. Dehimi K, Speciale A, Saija A, Dahamna S, Raciti R, Cimino F, et al. Antioxidant and anti-inflammatory properties of Algerian *Thymelaea microphylla* Coss. and Dur. extracts. *Pharmacognosy Magazine*. 2016;12(47):203-10.
7. Trigui M, Hsouna AB, Tounsi S, Jaoua S. Chemical composition and evaluation of antioxidant and antimicrobial activities of Tunisian *Thymelaea hirsuta* with special reference to its mode of action. *Industrial Crops and Products*. 2013;41:150-7.
8. Ghanem H, Haba H, Marcourt L, Benkhaled M, Wolfender JL. Microphynolides A and B, new spiro-gamma-lactone glycosides from *Thymelaea microphylla*. *Natural Product Research*. 2014;28(20):1732-8.
9. Noman L, Zellagui A, Hallis Y, Yaglioglu AS, Demirtas I, Gherraf N, et al. Antioxidant and antimicrobial activities of an endemic desert species *Thymelaea microphylla* Coss. et Dur. *Der Pharmacia Lettre*. 2015; 7(1):118-21.
10. Kerbab K, Mekhelfi T, Zaiter L, Benayache S, Benayache F, Picerno P, et al. Chemical composition and antioxidant activity of a polar extract of *Thymelaea microphylla* Coss. et Dur. *Natural Product Research*. 2015;29(7):671-5.
11. Noman L, Oke-Altuntas F, Zellagui A, Sahin Yaglioglu A, Demirtas I, M Cardoso S, et al. A novel benzimidazole and other constituents with antiproliferative and antioxidant properties from *Thymelaea microphylla* Coss. et Dur. *Natural Product Research*. 2017;31:2032-41.
12. Rizk A, Hammouda F, Ismail S. Phytochemical investigation of *Thymelaea hirsuta*. 3. Coumarins. *Acta Chimica Academiae Scientiarum Hungaricae*. 1975;85(1):107-15.
13. Labib SN, Zellagui A, Mesbah K, Gherraf N, Lahouel Mand Rhouati S. Essential oil Composition of *Thymelaea microphylla* Coss et Dur. *Der Pharmacia Lettre*. 2010;2(5):428-31.
14. Blois MS. Antioxidant determinations by the use of a stable free radical. *Nature*. 1958;181:1199-200.
15. Decker EA, Welch B. Role of ferritin as a lipid oxidation catalyst in muscle food. *Journal of Agricultural and Food Chemistry*. 1990;38(3):674-7.
16. Agrawal PK. Flavonoid glycosides. Carbon-13 NMR of flavonoids. Amsterdam, Elsevier, 1989, pp. 102-103.
17. Niwa M, Otsuji S, Tatematsu H, Liu G-Q, Chen X-F, Hirata Y. Stereostructures of two biflavanones from *Stellera chamaejasme* L. *Chemical and Pharmaceutical Bulletin*. 1986;34(8):3249-51.
18. Trendafilova A, Todorova M, Gavrilova A, Vitkova A. Flavonoid glycosides from Bulgarian endemic *Alchemilla achtarowii* Pawl. *Biochemical Systematics and Ecology*. 2012;43:156-8.

19. Liao C-R, Kuo Y-H, Ho Y-L, Wang C-Y, Yang C-S, Lin C-W, et al. Studies on cytotoxic constituents from the leaves of *Elaeagnus oldhamii* Maxim. in non-small cell lung cancer A549 cells. *Molecules*. 2014;19(7):9515-34.
20. Qiao W, Zhao C, Qin N, Zhai HY, Duan HQ. Identification of trans-tiliroside as active principle with anti-hyperglycemic, anti-hyperlipidemic and antioxidant effects from *Potentilla chinensis*. *Journal of Ethnopharmacology*. 2011;135(2):515-21.
21. Sala A, Recio MC, Schinella GR, Máñez S, Giner RM, Cerdá-Nicolás M, et al. Assessment of the anti-inflammatory activity and free radical scavenger activity of tiliroside. *European Journal of Pharmacology*. 2003;461(1):53-61.
22. Li X, Tian Y, Wang T, Lin Q, Feng X, Jiang Q, et al. Role of the p-Coumaroyl Moiety in the Antioxidant and Cytoprotective Effects of Flavonoid Glycosides: Comparison of Astragalin and Tiliroside. *Molecules*. 2017;22(7):1165.
23. Ding H-Y. Extracts and constituents of *Rubus chingii* with 1, 1-diphenyl-2-picrylhydrazyl (DPPH) free radical scavenging activity. *International journal of molecular sciences*. 2011;12(6):3941-9.
24. Mekhelfi T, Adouni K, Zaiter L, Guella G, Benayache S, Benayache F, Venskutonis PR. Antioxidant activity of extracts, *cis* and *trans* tilirosides, and other compounds from *Thymelaea microphylla* Coss. et Dur. *Der Pharmacia Lettre*. 2016;8:233-9.



A Green and Efficient Method for the Synthesis of 3,4-Dihydropyrano[c]chromene using Phosphate Fertilizers (MAP, DAP and TSP) as Heterogeneous Catalysts

Soukaina CHEHAB¹  , Youssef MERROUN¹  , Touriya GHAILANE¹  ,
Rachida GHAILANE¹  , Said BOUKHRIS¹   and Abdelaziz SOUIZI*  

Laboratory of Organic, Organometallic and Theoretical Chemistry, University of Ibn Tofail, Faculty of Science, B.P. 133, 14000 Kenitra, Morocco

Abstract: This article presents a simple and green method for the synthesis of 3,4-dihydropyrano[c]chromenes, they have been obtained by the condensation of an aromatic aldehyde, malononitrile and 4-hydroxycoumarin in presence of phosphate fertilizers (Monoammonium phosphate MAP, Diammonium phosphate DAP and Triple superphosphate TSP) as heterogeneous catalysts and ethanol as an ecological solvent. This method has remarkable advantages, such as excellent catalytic performance of the catalysts used in the ethanol and the facility of preparation of the desired products with high to excellent yields (>92%) in short reaction times varying from 30 to 45 min, the long-term durability and easy recovery of catalysts, constitute a good heterogeneous system. All these advantages added to the low cost of these catalysts and their ecological profile have allowed them to be an alternative to the other synthetic and toxic catalysts used previously.

Keywords: Heterogeneous catalysts, MAP, DAP, TSP, 3,4-dihydropyrano[c]chromene, phosphate fertilizers.

Submitted: November 28, 2018. **Accepted:** January 23, 2018

Cite this: Chehab S, Merroun Y, Ghailane T, Ghailane R, Boukhris S, Souzi A. A Green and Efficient Method for the Synthesis of 3,4-Dihydropyrano[c]chromene using Phosphate Fertilizers (MAP, DAP and TSP) as Heterogeneous Catalysts. JOTCSA. 2018;5(2):355–70.

DOI: <http://dx.doi.org/10.18596/jotcsa.358609>.

***Corresponding author. E-mail:** souzi@yahoo.com

INTRODUCTION

Awareness of the harmful effects of certain practices used in chemical synthesis and the need to protect the environment was the reason why research in the chemical area was directed for developing some synthesis strategies that are environmentally friendly (1-2). Consequently, the main aim of chemists is to find the procedures of synthesis using different kinds of catalysts to reduce the cost and time of reaction with good yields of desired products (3). Indeed, the use of heterogeneous phosphate-based catalysts takes great importance in chemical synthesis due to their availability essentially in Morocco which is considered as the most known country in the production of natural phosphate (4-9). Other heterogeneous catalysts as hydroxyapatite (10-13) and fluoroapatite (14-16) are also used in organic synthesis. In particular our work is aimed to 3,4-dihydropyrano[c]chromene synthesis, which gains a lot of attention due to their various biological activities (17-22), they are well known as spasmolytic, diuretic, anticoagulant, anti-cancer and anti-anaphylactic, they can also be used as cognitive enhancers, for the treatment of neurodegenerative diseases, including Alzheimer's disease, amyotrophic lateral sclerosis, Huntington's disease, Parkinson's disease, AIDS-associated dementia and Down syndrome as well as for the treatment of schizophrenia and myoclonus (23). Following the importance and usefulness of dihydropyrano[c]chromene derivatives, numerous synthetic pathways have been described, including electrolysis (24) microwave and ultrasonic irradiation (25-26) by piperidine/pyridine in ethanol (27), $H_6P_2W_{18}O_{62} \cdot 18H_2O$, tetrabutylammonium bromide, copper oxide nanoparticles, sodium dodecyl sulfate (SDS), trisodium citrate, selectfluor chloride triethylbenzylammonium DABCO in aqueous media (28-35). Tetramethylguanidinium trifluoroacetate (TMGT) (36), rare earth perfluorooctanoates (37), Na_2SeO_4 (38), SiO_2 -Pr- SO_3 (39), functionalized sulfonic acid silica (40), hexamethylenetetramine (41), Fe_2O_3 nanoparticles (42), the complexes of silica gel (43), Ru (II)(44), Urea (45), NH_4VO_3 (46), starch solution (47), grindstone chemistry (48), SBPPSP (49), MgO nanoparticle (50), ammonium acetate (51), 4-(dimethylamino)pyridine (DMAP) (52). Some synthetic catalysts of phosphate have also been reported in the literature for 3,4-dihydropyrano[c]chromenes synthesis; one found the Disodium hydrogen phosphate (53) and DHAP which has been described once as a homogeneous catalyst in the presence of ethanol-water (54). The majority of these methods use the expensive or homogenous catalysts that present certain disadvantages such as deactivation of the catalyst, difficult work and toxic effluents, not forgetting in some cases the low yields of the desired product, the long reaction time, and the most of them are synthetic and they require special efforts in their preparation. For these reasons, the development of a new and mild method that overcomes the drawbacks of previous procedures. In this context, this is the first time that phosphate fertilizers (MAP, DAP and

TSP) are used directly as heterogeneous catalysts in their granule form for the synthesis of 3,4-dihydropyrano [c] chromene, in order to valorize one of the important natural resources in Morocco that is considered among the first countries producer of the natural phosphate.

The present work is oriented in particular on the direct application of phosphate monoammonium phosphate (MAP), di-ammonium phosphate (DAP) and triple super phosphate (TSP) as heterogeneous catalysts that they are already used in some researchers developed in our laboratory focused on synthesis in organic chemistry (55). Thus, we projected to the synthesis of 3,4-dihydropyrano[c]chromene in the presence of these heterogeneous catalysts, It was shown that they could be easily recovered and reused, as a consequence they can be considered among the most efficient catalysts in organic synthesis from the multicomponent reactions (MCRs) (56-57). The novelty of this study is the use of new catalysts, available in large quantities and inexpensive because Morocco is considered as a leader in the phosphate production. For this reason, this work is focused on the valorization of the fertilizer phosphate in the catalytic area. It is well known as reported before that these catalysts led to the desired products with excellent yields in short reaction times. The contribution of this work in the development of Moroccan natural resources for participating to economize of the cost of manipulation and energy of the reaction as well as to the development of green chemistry. In addition, the besides one of the strong point of these catalysts is that they are used as a heterogeneous catalyst in their natural shape without further preparation.

MATERIALS AND METHODS

The chemicals used in this work were purchased from Sigma-Aldrich Chemical Companies. The known products were identified by comparison of their melting points and their spectral data with those reported in the literature. Monitoring of the evolution of the reactions was carried out by TLC on silica gel SILG / UV 254 plates. The melting points were taken on a hot Kofler and are not corrected. ¹H NMR and ¹³C NMR spectra were recorded on a 300 MHz Bruker spectrometer in DMSO-d₆.

General procedure for the synthesis of 3,4-dihydropyrano [c] chromene

A mixture of malononitrile (1 mmol), aromatic aldehyde (1 mmol) and 4-hydroxycoumarin (1 mmol) in ethanol (1 mL), in the presence of 0.01 g of catalyst, was brought to reflux, the reaction was monitored by TLC. After completion of the reaction, the reaction mixture was cooled to room temperature, the solid thus formed was collected by filtration, washed with ethanol and purified by recrystallization from hot ethanol to give pure products **4a-**

4f. The product obtained was characterized on the basis of their melting points reported in Table 5 and spectroscopic data that are given below and their comparison with the ones given in the literature show a good agreement.

2-Amino-4-phenyl-4,5-dihydro-5-oxopyrano[3,2-c]chromene-3-carbonitrile 4a:

¹H NMR (300 MHz, DMSO-d₆, delta, ppm): 7.91 (1H, d, Ar-H), 7.70 (1H, t, Ar-H), 7.49 (1H, t, Ar-H), 7.45 (1H, d, Ar-H), 7.42 (2H, s, NH₂), 7.35 -7.24 (5H, m, Ar-H), 4.45 (1H, s, CH). ¹³C NMR (75 MHz, DMSO-d₆): δ 160, 158.46, 153.89, 152.61, 143.80, 133.38, 128.99, 128.10, 127.59, 125.13, 122.94, 119.70, 117.03, 113.43, 104.48, 58.48.

2-Amino-4-p-tolyl-4,5-dihydro-5-oxopyrano[3,2-c]chromene-3-carbonitrile 4b:

¹H NMR (300 MHz, DMSO-d₆, delta, ppm): 7.91 (1H, d, Ar-H), 7.72 (1H, t, Ar-H), 7.50-7.42 (2H, m, Ar-H), 7.38 (2H, s, NH₂), 7.17-7.10 (4H, m, Ar-H), 4.40 (1H, s, CH), 2.26 (3H, s, CH₃). ¹³C NMR (75 MHz, DMSO-d₆): δ 159.97, 158.41, 153.72, 152.57, 140.87, 136.75, 133.32, 129.53, 127.99, 125.10, 122.91, 119.72, 117, 113.43, 104.61, 58.60, 21.09.

2-Amino-4-(4-diméthylaminophenyl)-4,5-dihydro-5-oxopyrano[3,2-c]chromene-3-

carbonitrile 4c: ¹H NMR (300 MHz, DMSO-d₆, delta, ppm): 7.83 (1H, d, Ar-H), 7.72 (1H, t, ArH), 7.50 -7.42 (2H, m, Ar-H), 7.19 (2H, s, NH₂), 7.08-6.65 (4H, m, Ar-H), 4.33 (1H, s, CH), 2.86 (6H, s, N (CH₃)₂). ¹³C NMR (75 MHz, DMSO-d₆): δ 159.97, 158.44, 154.88, 152.54, 134.04, 131.41, 128.63, 125.05, 122.89, 119.73, 116.96, 113.56, 105.22, 59.27.

2-Amino-4-(4-nitrophenyl)-4,5-dihydro-5-oxopyrano[3,2-c]chromene-3-carbonitrile 4d:

¹H NMR (300 MHz, DMSO-d₆, delta, ppm): 8.17 (1H, d, Ar-H), 7.91 (1H, d, Ar-H), 7.77 (1H, t, Ar-H), 7.74 (1H, t, Ar-H), 7.57 (2H, s, NH₂), 7.55-7.46 (4H, m, Ar-H), 4.68 (1H, s, CH). ¹³C NMR (75 MHz, DMSO-d₆): δ 160.05, 158.52, 154.43, 152.75, 151.23, 147.09, 133.66, 129.65, 125.23, 124.20, 123.06, 119.35, 117.11, 113.38, 103.28, 57.24.

2-Amino-4-(4-bromophenyl)-4,5-dihydro-5-oxopyrano[3,2-c]chromene-3-carbonitrile 4e:

¹H NMR (300 MHz, DMSO-d₆, delta, ppm): 7.93(1H,d, ArH), 7.73 (1H, t, Ar-H), 7.68 (1H, t, Ar-H), 7.52-7.48 (3H, m, Ar-H), 7.45(2H, s, NH₂), 7.26 (2H, d, Ar-H), 4.48 (1H, s, CH). ¹³C NMR (75 MHz, DMSO-d₆): δ 159.95, 158.53, 154.07, 152.70, 143.17, 133.43, 131.82, 130.42, 125.09, 123.02, 120.70, 119.39, 117, 113.43, 103.97, 58.22.

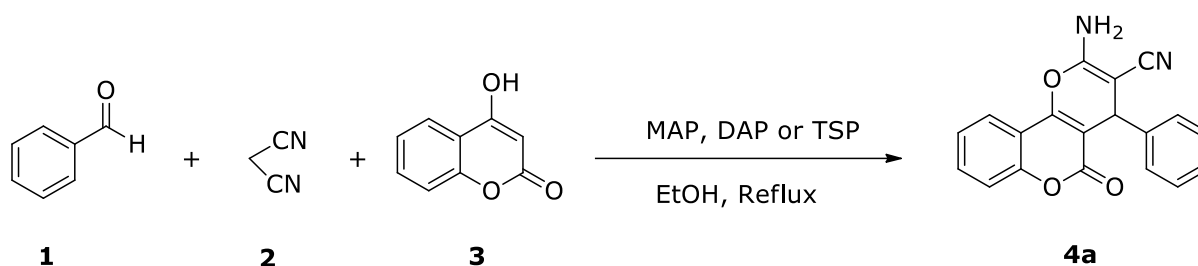
2-Amino-4-(4-chlorophenyl)-4,5-dihydro-5-oxopyrano[3,2-c]chromene-3-carbonitrile 4f:

¹H NMR (300 MHz, DMSO-d₆, delta, ppm): 7.92 (1H, d, Ar-H), 7.71 (1H, t, Ar-H), 7.48 (1H, t, Ar-H), 7.43 (1H, d, Ar-H), 7.40 (2H, s, NH₂), 7.37-7.30 (4H, m, Ar-H), 4.50 (1H,

s, CH). ^{13}C NMR (75 MHz, DMSO- d_6): δ 159.94, 158.54, 154.05, 152.69, 142.73, 133.39, 132.25, 130.05, 129.14, 125.06, 123, 119.40, 116.97, 113.43, 104.04, 58.31.

RESULTS AND DISCUSSION

In order to test the catalytic activity of the phosphate heterogeneous catalysts MAP, DAP, and TSP used herein, we have chosen the synthesis of 3,4-dihydropyrano[c]chromene, which is a condensation between an aromatic aldehyde, malononitrile, and 4-hydroxycoumarin (MCR) (Scheme 1).



Scheme 1. Synthesis of 3,4-dihydropyrano[c]chromene.

Table 1. Catalytic Test for the Synthesis of the 3,4-Dihydropyrano[c]Chromene^a.

Entry	Catalyst	Amount of catalyst (g)	Time	Yield (%) ^b
1	-	0	24 h	25
2	MAP	0.01	30 min	86
3	DAP	0.01	45 min	82
4	TSP	0.01	35 min	82

^aReaction conditions: Benzaldehyde (1 mmol), malononitrile (1 mmol), 4-hydroxycoumarin (1 mmol), EtOH (3 mL), 0.01 g of MAP, DAP and TSP, Reflux.

^bIsolated yield.

First, the reaction was tested in the absence of the catalyst, when the experiment had started no product was observed, but after prolonged reaction time (24 h), the desired product was obtained with a yield of 25%, while the reaction in the presence of the catalysts MAP, DAP and TSP improve the reactivity and provide products with reasonable yields which were respectively 86, 82 and 82%. The reaction times are short as 30 min for the MAP, 45 min for the DAP and 35 min for the TSP. These results confirm that the used catalysts possess catalytic activity efficient for the synthesis of the 3,4-dihydropyrano[c]chromene (Table 1).

In order to optimize the reaction conditions of the 3,4-dihydropyrano[c]chromene synthesis catalyzed by MAP, DAP, and TSP, it seems interesting for us to examine the effect

of different parameters namely the of the reaction time, the amount of catalyst as well as the nature and volume of the solvent.

We have opted to examine the influence of the reaction time which is the fundamental parameter providing a straight effect on of the reaction yield. The yield of the desired product **4a** was determined in function of the reaction time that was varied by a step of 5 min starting from 30, 45 and 35 min, respectively for the MAP, DAP and TSP catalysts, these times are those obtained under the same conditions described previously ((a) given after Table 1). The results of this study are presented in Figure 1.

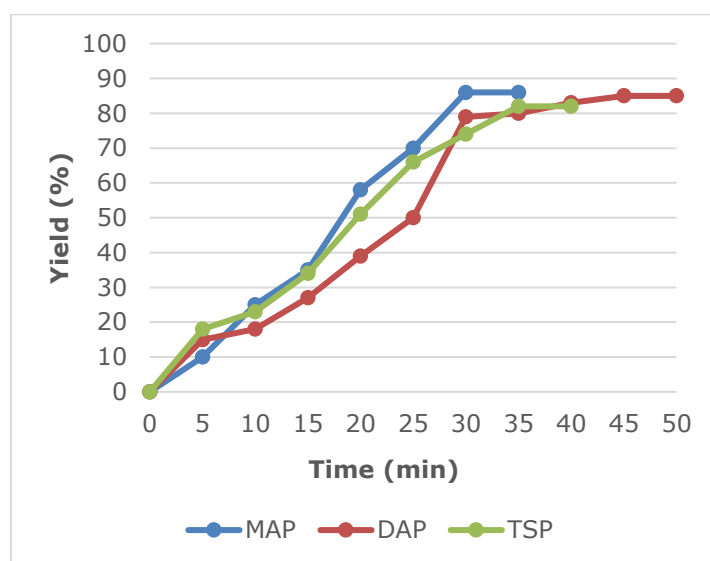


Figure 1. Time reaction optimization of the synthesis of 3,4-dihydropyran[c]chromene.

Figure 1 shows that the yield increases when the reaction time increases until the platform where the yield remains constant in function of time, indeed the yield of synthesis product reaches 86% after 30 min for the MAP. Whereas, both DAP and TSP catalysts give the same yield by 82% with 45 and 35 min as reaction times respectively.

After having optimized the reaction time, we consider useful to study the amount effect of the catalysts MAP, DAP and TSP used herein. For that, the amount of each catalyst has been varied from 0.002 g to 0.01 g. The obtained yields are collected in Table 2.

Table 2. The catalysts mass optimization for the synthesis of 3,4-dihydropyrano[c]chromene^a.

Entry	Amount of catalyst (g)	Time (min)			Yield (%) ^b		
		MAP	DAP	TSP	MAP	DAP	TSP
1	0.002	30	45	35	80	86	87
2	0.004	30	45	35	85	90	92
3	0.006	30	45	35	93	87	88
4	0.008	30	45	35	89	83	85
5	0.01	30	45	35	86	82	82

^aReaction conditions: benzaldehyde (1 mmol), malononitrile (1 mmol), 4-hydroxycoumarin (1 mmol), EtOH (3 mL), (xg) mass of MAP, DAP and TSP, Reflux.

^bIsolated yield.

From the table above, it is noticeable that the amount of 0.006 g for the MAP and 0.004 g for both DAP and TSP catalysts are sufficient to provide excellent yields in case of the reaction leading to product **4a**. The obtained yields are 93, 90 and 92% for MAP, DAP and TSP, respectively. Beyond these amounts, the observation of a remarkable decrease in yields, parallel to the increase in the quantity of the catalyst, is justified by the dispersive effect of the reagent on the surface of the catalysts.

The influence of the solvent nature on the catalytic activity of MAP, DAP, and TSP was studied in case of the model reaction while maintaining the same optimized parameters, namely reaction time and catalyst amount, described previously. For this, solvents of different nature, protic polar (EtOH, MeOH), aprotic (CH₃CN, THF), as well as solvents of apolar nature (toluene, dioxane), were used, the reaction was also performed in absence of the solvent. Table 3 summarizes all the results obtained in this study.

Table 3. Reaction yield of the synthesis of 3,4-dihydropyrano[c]chromene^a in presence of a different kind of solvent.

Entry	Solvent	Time (min)			Yield (%) ^b		
		MAP	DAP	TSP	MAP	DAP	TSP
1	Solvent-free	30	45	35	78	74	74
2	EtOH	30	45	35	93	90	92
3	MeOH	30	45	35	75	77	83
4	CH ₃ CN	30	45	35	74	77	79
5	THF	30	45	35	61	75	80
6	Dioxane	30	45	35	63	60	77
7	Toluene	30	45	35	59	55	70

^a Reaction conditions: Benzaldehyde (1 mmol), malononitrile (1 mmol), 4-hydroxycoumarin (1 mmol), (3 mL) of solvent, 0.006 g of MAP, 0.004 g of DAP and TSP, Reflux.

^bIsolated yield.

The results given in Table 3 show that the reaction is clearly favored in protic polar solvents and more specifically in ethanol, this is available for the model reaction where the MAP,

DAP, and TSP catalysts were applied, the product **4a** is obtained with yields which are 93, 90 and 92% respectively. However, in the case of methanol it is noted that it allows obtaining the product with a lower yield than ethanol even though its dielectric constant is greater compared to the ethanol one, which may be explained by the fact that the methanol is more acidic than the ethanol, thus the O-H bond is more polar in methanol than in ethanol. Therefore, the methanol tends to liberate the proton more easily, unlike to the ethanol which just allows the polarization of the reagents leading to the formation of the desired product **4a** with a good yield. Moreover, the appropriate solvent for each organic synthesis depends on the nature of the reaction mixture. Therefore, the use of ethanol as a solvent facilitates the formation and the separation of the charges on the active sites of the reagents, indeed this process is caused by the electrostatic interaction involved between the atomic charge on the atom forming polar bond of the solvent with the active atomic center which possesses the opposite sign of charge, in the reagent, this interaction makes easy the formation of the final product **4a**.

As regards on the aprotic polar solvents (CH₃CN, THF) and nonpolar (toluene, dioxane), used in this part of our study, one can notice that the yield obtained in presence of each solvent is lower than that obtained in ethanol. One can deduce that the ethanol is the appropriate solvent allowing to obtain the desired product with excellent yields.

The volume of the solvent can also be a determining factor that can influence the yield of the 3,4-dihydropyrano[c]chromene synthesis, for this reason, it would be interesting to study the volume effect that was carried out by taking into account of the optimized parameters obtained previously, for this, the volume of ethanol was decreased from 3 to 1 ml, and Table 4 summarizes the obtained results.

Table 4. Optimization of the ethanol volume on the synthesis of 3,4-dihydropyrano[c]chromene ^a.

Entry	Volume of ethanol	Time (min)			Yield (%) ^b		
		MAP	DAP	TSP	MAP	DAP	TSP
1	Solvent-free	30	45	35	78	74	74
2	1mL	30	45	35	95	92	93
3	2mL	30	45	35	94	91	93
4	3mL	30	45	35	93	90	92

^a Reaction conditions: benzaldehyde (1 mmol), malononitrile (1 mmol), 4-hydroxycoumarine (1 mmol), (x mL) of EtOH, 0.006 g of MAP, 0.004 g of DAP and TSP, reflux.

^bIsolated yield.

From Table 4, it can be shown that 1 mL of ethanol appears to be the sufficient volume to achieve a yield of 95, 92 and 93% for the model reaction catalyzed by the MAP, DAP and

TSP respectively, whereas beyond 1 mL a decrease in yield has been observed, this is due the dispersion phenomenon of the reagents on the catalyst surface.

One of the most important factors that determine the efficiency of the catalytic activity of the catalyst is its ability to be reused for several times and its reliability to give a good reaction yield for each reuse, this allows to ensure sustainable chemistry. In this context the recovery and study of the reuse of MAP, DAP and TSP catalysts were carried out under the optimum reaction conditions already determined, the catalysts recovered by simple filtration and reused in a second reaction involving the same reagents and under the same operating conditions. This operation was repeated for four times, Figure 2 presents the results obtained.

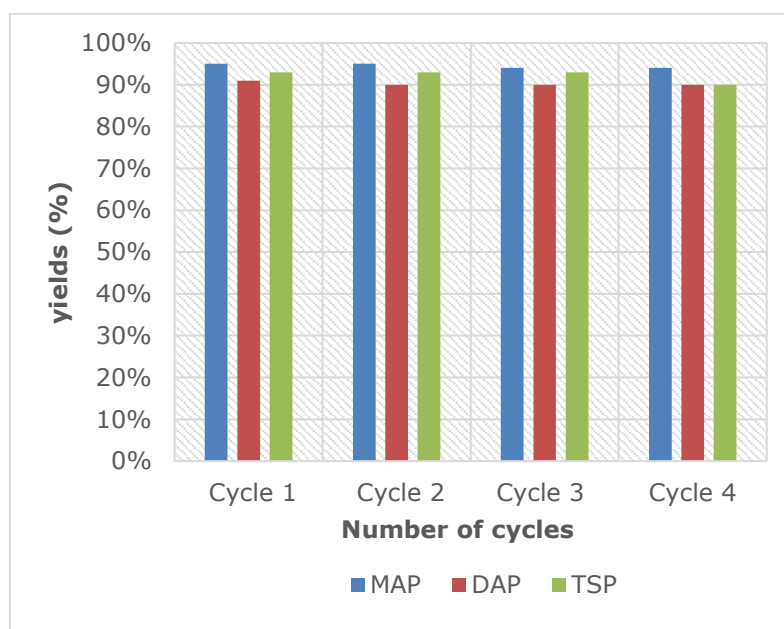
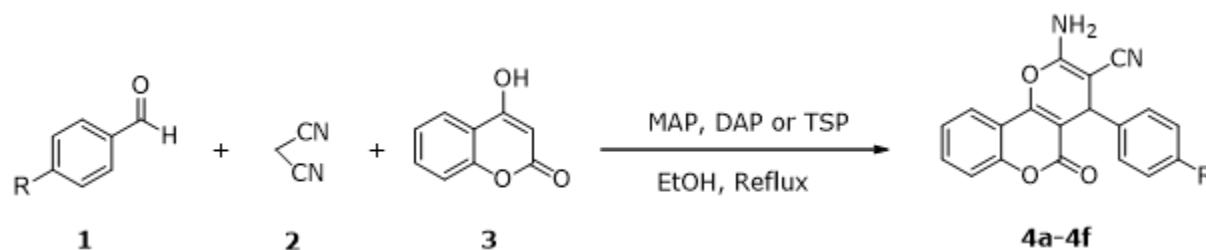


Figure 2. Reusability of the MAP, DAP, and TSP catalysts in case of the synthesis of 3,4-dihydropyrano [c] chromene.

The results clearly show that MAP, DAP and TSP catalysts can be reused several times without significant loss of their catalytic activities even after 4 cycles of application. After optimization of the reactional conditions for the synthesis of a product (**4a** 3,4-dihydropyrano[c]chromene), a generalization study of the reaction was carried out in order to synthesize other derivatives belonging to the same family of 3,4-dihydropyrano [c] chromene. These derivatives have been synthesized from various aromatic aldehydes, malononitrile and 4-hydroxycoumarin under the optimum operating conditions already determined, the obtained yields are given in Table 5.



Scheme 2. Synthesis of 3,4-dihydropyrano[c]chromene derivatives.

Table 5. Reaction times and yields of the synthesis reactions of 3,4-dihydropyrano[c]chromene^a

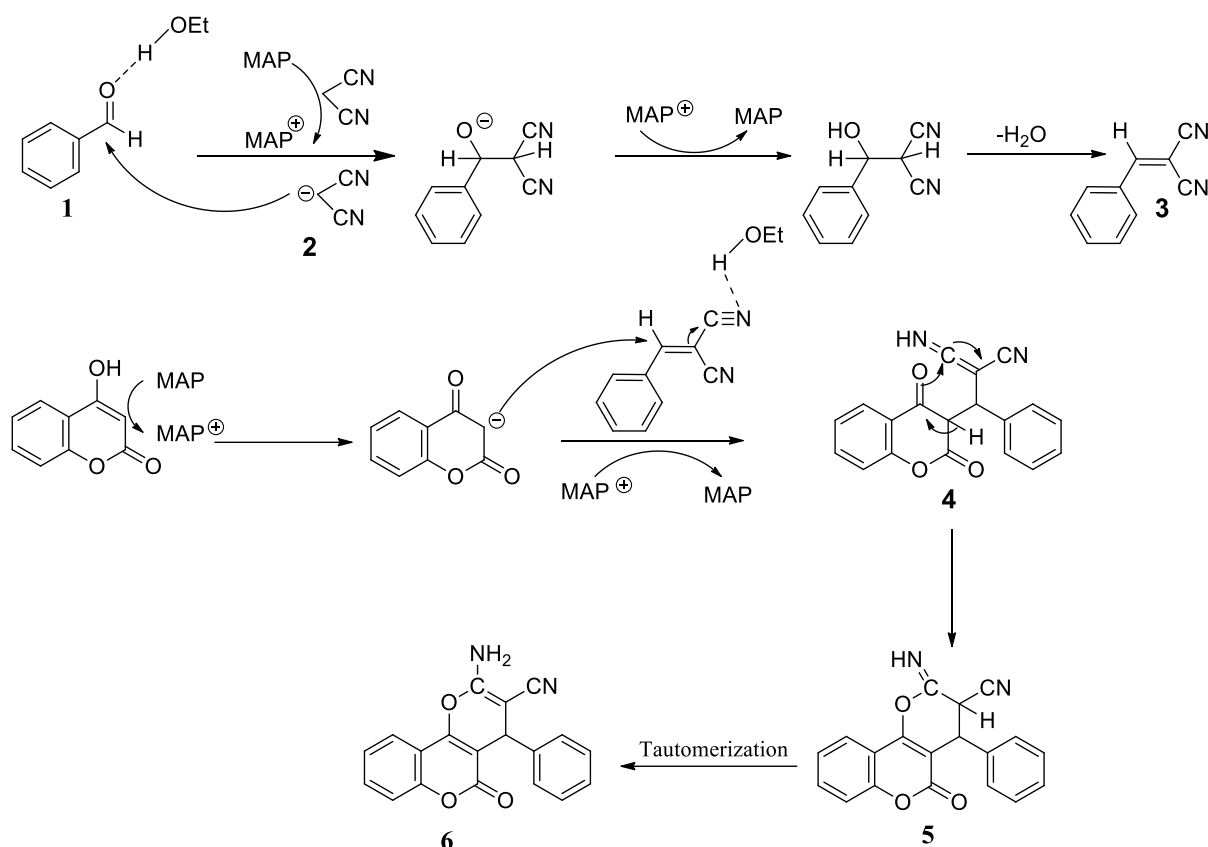
Entry	R	Time (min)			Yield (%) ^b			Mp (°C)	
		MAP	DAP	TSP	MAP	DAP	TSP	Found	Reported
4a	H	30	45	35	95	92	93	256-258	256-258(58)
4b	CH ₃	30	30	35	88	80	81	251-253	250-252 (32)
4c	(CH ₃)N	45	45	45	97	87	94	>260	266-268 (32)
4d	NO ₂	15	15	15	98	85	84	258-260	258-260(58)
4e	Br	15	15	15	84	83	87	248-250	247-249 (58)
4f	Cl	15	15	15	77	79	85	256-258	258-260 (32)

^aReaction conditions: aromatic aldehyde (1 mmol), malononitrile (1 mmol), 4-hydroxycoumarin (1 mmol), (1 mL) ethanol, 0.006 g of MAP, 0.004 g of DAP and TSP, reflux.

^bIsolated yield.

The yields of desired products presented in Table 5 remains better regardless of the nature of the group, used as a substituent on the aromatic aldehyde, that is electron attractor in case of NO₂ or electron donor in cases of CH₃, N(CH₃)₂, Br and Cl groups. The best-obtained yield is 98% for the entry **4d** when the MAP catalyst is used while it is by 92% for entry **4a** using DAP catalyst and it is 94% for entry **4c** using TSP as a catalyst. Whereas the reaction times vary between 15 min and 45 min for the six synthesis reactions in presence of MAP, DAP and TSP catalysts used in this study.

To understand the interaction involved, between the catalyst and the reagents as well as between the solvent and the reagents, during the reaction process, the following mechanism is proposed to describe the condensation of an aromatic aldehyde, malononitrile and 4-hydroxycoumarin, using MAP catalyst and EtOH as solvent, for the synthesis of 2,3-dihydroquinazolin-4 (1H)-One (Scheme 3).



Scheme 3. A plausible mechanism (catalyst and solvent) for the formation of 3,4-Dihydropyrano[c]Chromene.

Scheme 3 shows the proposed mechanism for the synthesis of 3,4 Dihydropyrano [c] chromene, firstly the condensation of Knoevenagel between benzaldehyde **1** and malononitrile **2** in the presence of MAP (proposed as an ampholyte catalyst, in this mechanism plays the role of a base), which removes the proton from the malononitrile, and the ethanol which allows activation of the carbonyl group, followed by dehydration to produce the 2-benzylidenemalononitrile **3**. And then, the nucleophilic addition of 4-hydroxycoumarin at intermediate **3**, followed by intramolecular cyclization **4** and tautomerization for formation of corresponding product **6**.

In order to conclude about the effectiveness of MAP, DAP and TSP catalysts used herein, Table 6 collect the results of this work and some data from the literature concerning the same synthesis reaction and using another type of catalysts.

Table 6. Comparative table of the reaction conditions for the synthesis of 3, 4-dihydropyrano[c]chromene

Entry	Catalyst	Catalyst amount	Solvent	T (°C)	time	Yield (%)	Ref
1	Al ₂ O ₃	10 mol%	Ethanol	Reflux	2 h	71	(39)
2	SDS	20 mol%	Water	Reflux	2.5 h	88	(32)
3	RuBr ₂ (PPh ₃) ₄	5 mol%	Water	Reflux	60 min	Trace	(44)
4	RuBr ₂ (PPh ₃) ₄	5 mol%	Ethanol	Reflux	45 min	45	(44)
5	Silica gel	300 wt%	Ethanol	25	4 h	95	(43)
6	TEBA	0.15 g	Water	Reflux	10 h	96	(35)
7	DBSA	25 mol%	Water	90	4 h	90	(59)
8	Na ₂ HPO ₄	10 mol%	H ₂ O:EtOH	Reflux	10 min	93	(53)
9	Piperidine	10 mol%	Ethanol	25	30 min	90	(60)
10	OBS	50 mol%	Solvent-free	120	50 min	85	(61)
11	NH ₄ OAc	15 mol%	Ethanol	Reflux	3 min	94	(51)
12	EDTA-4Na	2mol%	H ₂ O:EtOH	50	20 min	91	(62)
13	SBS	10 mol%	H ₂ O:EtOH	Reflux	23 min	89	(63)
14	MAP	0.006 g/ 2.5 mol%	Ethanol	Reflux	30 min	95	this work
15	DAP	0.004 g/ 3.1 mol%	Ethanol	Reflux	45 min	92	this work
16	TSP	0.004 g/1.7 mol%	Ethanol	Reflux	35 min	93	this work

Recently several works have been developed concerning the use of different kinds of catalyst for the synthesis studied herein. From the table 6, it can be seen that the catalysts MAP, DAP and TSP show interesting catalytic activities for the 3,4-dihydropyrano[c]chromene synthesis, they lead high yields of the desired products in short reaction times even with smaller amounts of the catalyst compared to the that given in the literature. Nevertheless, some of these catalysts have a shorter reaction time and good yields compared to the results obtained in this work but have certain drawbacks as NH₄OAc which is a homogeneous catalyst, piperidine which is a corrosive product and EDTA-4Na is a synthetic catalyst. To sum up, the catalysts used herein present several advantages, they resent interesting catalytic activities and they can be reused for at least 4 times.

CONCLUSION

To sum up, six 3, 4-dihydropyrano[c]chromenes have been successfully synthesized, using MAP, DAP and TSP phosphate fertilizers as heterogeneous catalysts which are available, inexpensive, non-toxic, and recyclable. The reactional conditions optimized in this work, namely, reaction time, catalyst amount, solvent nature and its volume, show that method has been characterized by simplicity of operation by reducing the cost of handling for organic synthesis, soft working conditions, short reaction times, excellent yields, and respect to the environment.

REFERENCES

1. Anastas PT, Kirchhoff MM. Origins, Current Status, and Future Challenges of Green Chemistry †. *Acc Chem Res.* 2002;35(9):686-94.

2. Clark JH. Green chemistry: challenges and opportunities. *Green Chem.* 1999;1(1):1-8.
3. R S. Catalysis and Pollution Prevention. *Chemistry & Industry.* 1997; 1:12-15.
4. Abba MO, Gonzalez-DelaCruz VM, Colón G, Sebti S, Caballero A. In situ XAS study of an improved natural phosphate catalyst for hydrogen production by reforming of methane. *Appl Catal B Environ.* 2014 ; 150-151 :459-65.
5. Hassine A, Sebti S, Solhy A, Zahouily M, Len C, Hedhili MN, et al. Palladium supported on natural phosphate: Catalyst for Suzuki coupling reactions in water. *Appl Catal Gen.* 2013 ; 450 :13-8.
6. Dakkach M, Atlamsani A, Sebti S. Le phosphate naturel modifié au vanadium : un nouveau catalyseur pour l'oxydation des cycloalcanones et des α -cétols en présence de l'oxygène moléculaire. *Comptes Rendus Chim.* 2012;15(6):482-92.
7. Zahouily M, Salah M, Bahlaouane B, Rayadh A, Houmam A, Hamed EA, et al. Solid catalysts for the production of fine chemicals: the use of natural phosphate alone and doped base catalysts for the synthesis of unsaturated arylsulfones. *Tetrahedron.* 2004;60(7):1631-5.
8. Zahouily M, Bahlaouan B, Rayadh A, Sebti S. Natural phosphate and potassium fluoride doped natural phosphate: efficient catalysts for the construction of a carbon–nitrogen bond. *Tetrahedron Lett.* 2004;45(21):4135-8.
9. Alahiane A, Rochdi A, Taourirte M, Redwane N, Sebti S, Lazrek H. Natural phosphate as Lewis acid catalyst: a simple and convenient method for acyclonucleoside synthesis. *Tetrahedron Lett.* 2001;42(21):3579-81.
10. Wen C, Cui Y, Chen X, Zong B, Dai W-L. Reaction temperature controlled selective hydrogenation of dimethyl oxalate to methyl glycolate and ethylene glycol over copper-hydroxyapatite catalysts. *Appl Catal B Environ.* 2015; 162:483-93.
11. Maleki B, Barat Nam Chalaki S, Sedigh Ashrafi S, Rezaee Seresht E, Moeinpour F, Khojastehnezhad A, et al. Caesium carbonate supported on hydroxyapatite-encapsulated Ni 0.5 Zn 0.5 Fe 2 O 4 nanocrystallites as a novel magnetically basic catalyst for the one-pot synthesis of pyrazolo[1,2-b] phthalazine-5,10-diones: Nanocatalyst for synthesis of pyrazolo[1,2-b] phthalazine-5,10-diones. *Appl Organomet Chem.* 2015;29(5):290-5.
12. Peeters A, Claes L, Geukens I, Stassen I, De Vos D. Alcohol amination with heterogeneous ruthenium hydroxyapatite catalysts. *Appl Catal Gen.* 2014; 469:191-7.
13. Razavi N, Akhlaghinia B. Hydroxyapatite nanoparticles (HAP NPs): a green and efficient heterogeneous catalyst for three-component one-pot synthesis of 2,3-dihydroquinazolin-4(1H)-one derivatives in aqueous media. *New J Chem.* 2016;40(1):447-57.
14. El Badaoui H, Bazi F, Tahir R, Lazrek HB, Sebti S. Synthesis of 3,4-dihydropyrimidin-2-ones catalysed by fluorapatite doped with metal halides. *Catal Commun.* 2005;6(7):455-8.
15. Mulla SAR, Chavan SS, Pathan MY, Inamdar SM, Shaikh TMY. Ligand-, base-, co-catalyst-free copper fluorapatite (CuFAP) as a versatile, ecofriendly, heterogeneous and reusable catalyst for an efficient homocoupling of arylboronic acid at ambient reaction conditions. *RSC Adv.* 2015;5(31):24675-80.
16. Mulla SAR, Inamdar SM, Pathan MY, Chavan SS. Ligand free, highly efficient synthesis of diaryl ether over copper fluorapatite as heterogeneous reusable catalyst. *Tetrahedron Lett.* 2012;53(14):1826-9.
17. Geen G, Evans J, Vong A. Pyrans and Their Benzo Derivatives Synthesis: In *Comprehensive Heterocyclic Chemistry II*; Oxford, UK: Pergamon Press; 1995.
18. Jain S, Rajguru D, Keshwal BS, Acharya AD. Solvent-Free Green and Efficient One-Pot Synthesis of Dihydropyrano[3,2-c]chromene Derivatives. *ISRN Org Chem.* 2013; 2013:1-5.

19. Bonsignore L, Loy G, Secci D, Calignano A. Synthesis and pharmacological activity of 2-oxo-(2H) 1-benzopyran-3-carboxamide derivatives. *Eur J Med Chem.* 1993;28(6):517-20.
20. Kostova I. New lanthanide complexes of 4-methyl-7-hydroxycoumarin and their pharmacological activity. *Eur J Med Chem.* 2001;36(4):339-47.
21. Chohan ZH, Shaikh AU, Rauf A, Supuran CT. Antibacterial, antifungal and cytotoxic properties of novel N-substituted sulfonamides from 4-hydroxycoumarin. *J Enzyme Inhib Med Chem.* 2006;21(6):741-8.
22. Zhao H, Neamati N, Hong H, Mazumder A, Wang S, Sunder S, et al. Coumarin-Based Inhibitors of HIV Integrase 1. *J Med Chem.* 1997;40(2):242-9.
23. Khoobi M, Ma'mani L, Rezazadeh F, Zareie Z, Foroumadi A, Ramazani A, et al. One-pot synthesis of 4H-benzo[b]pyrans and dihydropyrano[c]chromenes using inorganic-organic hybrid magnetic nanocatalyst in water. *J Mol Catal Chem.* 2012; 359:74-80.
24. Fotouhi L, Heravi MM, Fatehi A, Bakhtiari K. Electrogenated base-promoted synthesis of tetrahydrobenzo[b]pyran derivatives. *Tetrahedron Lett.* juill 2007;48(31):5379-81.
25. Kidwai M, Saxena S. Convenient Preparation of Pyrano Benzopyranes in Aqueous Media. *Synth Commun.* 2006;36(18):2737-42.
26. Tu S-J, Jiang H, Zhuang Q-Y, Miao C-B, Shi D, Wang X-S, et al. One-pot synthesis of 2-amino-3-cyano-4-aryl-7,7-dimethyl-5-oxo-5,6,7,8-tetrahydro-4H-benzo[b]pyran under ultrasonic irradiation without catalyst. *Chin J Org Chem.* 2003; 23:488-90.
27. Shaker RM. Synthesis and reactions of some new 4H-pyrano[3,2-c] benzopyran-5-one derivatives and their potential biological activities. *Pharm.* 1996;51(3):148-51.
28. Heravi MM, Jani BA, Derikvand F, Bamoharram FF, Oskooie HA. Three components, one-pot synthesis of dihydropyrano[3,2-c] chromene derivatives in the presence of H₆P₂W₁₈O₆₂·18H₂O as a green and recyclable catalyst. *Catal Commun.* 2008;10(3):272-5.
29. Khurana JM, Kumar S. Tetrabutylammonium bromide (TBAB): a neutral and efficient catalyst for the synthesis of biscoumarin and 3,4-dihydropyrano[c]chromene derivatives in water and solvent-free conditions. *Tetrahedron Lett.* 2009;50(28):4125-7.
30. Mehrabi H, Kazemi-Mireki M. CuO nanoparticles: An efficient and recyclable nanocatalyst for the rapid and green synthesis of 3,4-dihydropyrano[c]chromenes. *Chin Chem Lett.* 2011;22(12):1419-22.
31. Zheng J, Li Y-Q. One-pot synthesis of tetrahydrobenzo[b]pyran and dihydropyrano[c]chromene derivatives in aqueous media by using trisodium citrate as a green catalyst. *Arch Appl Sci Res.* 2011;3.
32. Mehrabi H, Abusaidi H. Synthesis of biscoumarin and 3,4-dihydropyrano[c]chromene derivatives catalysed by sodium dodecyl sulfate (SDS) in neat water. *J Iran Chem Soc.* 2010;7(4):890-4.
33. Heravi MM, Zakeri M, Mohammadi N. Morpholine Catalyzed One-pot Multicomponent Synthesis of Compounds Containing Chromene Core in Water. *Chin J Chem.* 2011;29(6):1163-6.
34. Ranjbar-Karimi R, Hashemi-Uderji S, Mousavi M. Selectfluor promoted environmental-friendly synthesis of 2H-chromen-2-one derivatives under various reaction conditions. *Journal of the Iranian Chemical Society.* 2011;8(1):193-197.
35. Shi D, Wang J, Zhuang Q-Y, Wang X-S. Three-component one-pot synthesis of 1,6-dioxo-5-oxo-1,4,5,6-tetrahydrophenanthrene derivatives in aqueous media. *Chin J Org Chem.* 2006; 26:643-7.
36. Shaabani A, Samadi S, Badri Z, Rahmati A. Ionic Liquid Promoted Efficient and Rapid One-pot Synthesis of Pyran Annulated Heterocyclic Systems. *Catal Lett.* 2005;104(1-2):39-43.

37. Wang L-M, Shao J-H, Tian H, Wang Y-H, Liu B. Rare earth perfluorooctanoate [RE(PFO)₃] catalyzed one-pot synthesis of benzopyran derivatives. *J Fluor Chem.* 2006;127(1):97-100.
38. Hekmatshoar R, Majedi S, Bakhtiari K. Sodium selenate catalyzed simple and efficient synthesis of tetrahydro benzo[b]pyran derivatives. *Catal Commun.* 2008;9(2):307-10.
39. Mohammadi Ziarani G, Badieli A, Azizi M, Zarabadi P. Synthesis of 3,4-Dihydropyrano[c]Chromene Derivatives Using Sulfonic Acid Functionalized Silica (SiO₂PrSO₃H). *Iran J Chem Chem Eng IJCCE.* 2011;30(2):59-65.
40. Ziarani GM, Abbasi A, Badieli A, Aslani Z. An Efficient Synthesis of Tetrahydrobenzo[b]pyran Derivatives Using Sulfonic Acid Functionalized Silica as an Efficient Catalyst. *E-J Chem.* 2011;8(1):293-9.
41. Wang H-J, Lu J, Zhang Z-H. Highly efficient three-component, one-pot synthesis of dihydropyrano[3,2-c] chromene derivatives. *Monatshefte Für Chem - Chem Mon.* 2010;141(10):1107-12.
42. Nagabhushana H, Sandeep Saundalkar S, Muralidhar L, Nagabhushana BM, Giriya CR, Nagaraja D, et al. α -Fe₂O₃ nanoparticles: An efficient, inexpensive catalyst for the one-pot preparation of 3,4-dihydropyrano[c]chromenes. *Chin Chem Lett.* 2011;22(2):143-6.
43. Prasanna TSR, Raju KM. Silica Gel Promoted Mild, Efficient and Inexpensive Protocol for the Preparation of 3,4-dihydropyrano[c]chromenes. *J Korean Chem Soc.* 20 août 2011;55(4):662-5.
44. Tabatabaeian K, Heidari H, Mamaghani M, Mahmoodi NO. Ru(II) complexes bearing tertiary phosphine ligands: a novel and efficient homogeneous catalyst for one-pot synthesis of dihydropyrano[3,2-c] chromene and tetrahydrobenzo[b]pyran derivatives: Ru(II)-catalyzed synthesis of dihydropyrano[c]chromene derivatives. *Appl Organomet Chem.* 2012;26(2):56-61.
45. Brahmachari G, Banerjee B. Facile and One-Pot Access to Diverse and Densely Functionalized 2-Amino-3-cyano-4 H -pyrans and Pyran-Annulated Heterocyclic Scaffolds via an Eco-Friendly Multicomponent Reaction at Room Temperature Using Urea as a Novel Organo-Catalyst. *ACS Sustain Chem Eng.* 3 mars 2014;2(3):411-22.
46. Shitole BV, Shitole NV, Shingare MS, Kakde GK. An efficient one pot three-component synthesis of dihydropyrano[3,2-c] chromenes using ammonium metavanadate as catalyst. *Curr Chem Lett.* 2016;137-44.
47. Hazeri N, Maghsoodlou MT, Mir F, Kangani M, Saravani H, Molashahi E. An efficient one-pot three-component synthesis of tetrahydrobenzo[b]pyran and 3,4-dihydropyrano[c]chromene derivatives using starch solution as catalyst. *Chin J Catal.* 2014;35(3):391-5.
48. Patel DS, Avalani JR, Raval DK. One-pot solvent-free rapid and green synthesis of 3,4-dihydropyrano[c]chromenes using grindstone chemistry. *J Saudi Chem Soc.* 2016;20:S401-5.
49. Niknam K, Jamali A. Silica-Bonded N-Propylpiperazine Sodium n-Propionate as Recyclable Basic Catalyst for Synthesis of 3,4-Dihydropyrano[c]chromene Derivatives and Biscoumarins. *Chin J Catal.* 2012;33(11-12):1840-9.
50. Safaei-Ghomi J, Eshteghal F, Ghasemzadeh MA. Solvent-free synthesis of dihydropyrano [3,2-c]chromene and biscoumarin derivatives using magnesium oxide nanoparticles as a recyclable catalyst. *Acta Chim Slov.* 2014;61(4):703-8.
51. Kanakaraju S, Prasanna B, Basavoju S, Chandramouli GVP. Ammonium acetate catalyzed an efficient one-pot three component synthesis of pyrano[3,2- c]chromene derivatives. *Arab J Chem.* 2017;10:S2705-13.
52. Khan AT, Lal M, Ali S, Khan MM. One-pot three-component reaction for the synthesis of pyran annulated heterocyclic compounds using DMAP as a catalyst. *Tetrahedron Lett.* 2011;52(41):5327-32.

53. Shitole NV, Shitole BV, Kakde GK. Disodium Phosphate: A Highly Efficient Catalyst for One-Pot Synthesis of Substituted 3,4-Dihydropyrano[3,2-C]Chromenes. *Orbital - Electron J Chem.* 2017;9(3):131-4.
54. Abdolmohammadi S, Balalaie S. Novel and efficient catalysts for the one-pot synthesis of 3,4-dihydropyrano[c]chromene derivatives in aqueous media. *Tetrahedron Lett.* 2007;48(18):3299-303.
55. Bahammou I, Esaady A, Boukhris S, Ghailane R, Habbadi N, Hassikou A, et al. Direct use of mineral fertilizers MAP, DAP, and TSP as heterogeneous catalysts in organic reactions. *Mediterr J Chem.* 2016;5(6):615-23.
56. Sibous S, Ghailane T, Houda S, Ghailane R, Boukhris S, Souizi A. Green and efficient method for the synthesis of 1,5-benzodiazepines using phosphate fertilizers as catalysts under free solvent. *Mediterr J Chem.* 2017;6(3):53-9.
57. Sibous S, Boukhris S, Ghailane R, Habbadi N, Hassikou A, Souizi A. Easy synthesis of 3,4-dihydropyrimidin -2-(1H)-ones using phosphate fertilizers MAP, DAP AND TSP as efficient catalysts. *J Turk Chem Soc Sect Chem.* 2017; 4(2): 477-88.
58. Sheikhhosseini E, Sattaei Mokhtari T, Faryabi M, Rafiepour A, Soltaninejad S. Iron Ore Pellet, A Natural and Reusable Catalyst for Synthesis of Pyrano[2,3-d] pyrimidine and Dihydropyrano[c]chromene Derivatives in Aqueous Media. *Iran J Chem Chem Eng IJCCE.* 2016;35(1):43-50.
59. Sheikhhosseini E, Ghazanfari D, Nezamabadi V. A new method for synthesis of tetrahydrobenzo[b]pyrans and dihydropyrano[c]chromenes using p-dodecylbenzenesulfonic acid as catalyst in water. *Iran J Catal.* 2013;3(4):197-201.
60. Irani, S, Maghsoodlou, MT, Hazeri, Nourallah. Piperidine, an efficient base catalyst for the one-pot synthesis of 3,4-dihydropyrano[3,2-c]chromene derivatives. *NISCAIR-CSIR.* 2017;649-55.
61. Maleki B. Green Synthesis of *bis* -Coumarin and Dihydropyrano[3,2-c]chromene Derivatives Catalyzed by *o*-Benzenedisulfonimide. *Org Prep Proced Int.* 2016;48(3):303-18.
62. Chen L, Lin J, Chen B, Zhao L. Sodium ethylene diamine tetraacetate catalyzed synthesis of chromene derivatives via multi-component reactions at low catalyst loading. *Res Chem Intermed.* 2017;43(11):6691-700.
63. Abaszadeh M, Seifi M. Three-Component Synthesis of Mono and Bis 4,5-Dihydropyrano[3,2-C]Chromenes and 4,5- Dihydropyran[4,3-B]Pyrans Catalyzed by Sodium Benzenesulfonates as a Green Organocatalyst. *Acta Chem Iasi.* 2017; 25(1):38 -50



Synthesis and Characterization of New Cyclic Aminobenzoquinones

Amaç Fatih Tuyun¹, * and Mahmut Yıldız²

¹Istanbul University, Engineering Faculty, Engineering Sciences Department, 34320 Avcılar, Istanbul, Turkey

²Gebze Technical University, Chemistry Department, Gebze, 41400, Kocaeli, Turkey

Abstract: The aim of this research is to synthesize and characterize new members of cyclic aminobenzoquinones. Mono amino substituted products, namely 2-chloro-5,6-dimethyl-3-(pyrrolidin-1-yl)-1,4-benzoquinone (**2**), 2-chloro-5,6-dimethyl-3-(piperidin-1-yl)-1,4-benzoquinone (**3**), 2-chloro-5,6-dimethyl-3-morpholino-1,4-benzoquinone (**4**), and 2-chloro-5,6-dimethyl-3-thiomorpholino-1,4-benzoquinone (**5**) have been synthesized by the nucleophilic substitution reactions between 2,3-dichloro-5,6-dimethyl-1,4-benzoquinone (**1**) and cyclic secondary amines with a green methodology using water as solvent. Structure determination of the new products (**2-5**) was established on the basis of FTIR, ¹H NMR, ¹³C NMR, and mass spectrometry.

Keywords: Benzoquinones, secondary amine, aminoquinones.

Submitted: November 2, 2017. **Accepted:** February 06, 2018.

Cite This: Tuyun AF, Yıldız M. Synthesis and Characterization of New Cyclic Aminobenzoquinones. JOTCSA. 2018;5(2):371-80.

DOI: <http://dx.doi.org/10.18596/jotcsa.348606>.

*Corresponding author. E-mail:aftuyun@gmail.com

INTRODUCTION

Compounds containing quinone core exist widely in nature (plants, microorganisms, animals, etc.) and have been utilized by mankind during many years (1, 2). These structures could be either isolated from natural products or synthesized in the laboratories by applying various experimental methods (3-8). Plenty of molecules which belong to quinone family are particularly biologically active compounds and possess antitumor, cytotoxic, anticancer, antimalarial, and antifungal properties (9-13). These type of compounds can also find potential application as the electron-deficient compounds in heterocyclic synthesis, a generator of reactive oxygen species in photodynamic therapies, the organic electrode materials in lithium-ion batteries, a chemosensor in metal detection analyses, and the quinone oligomers in the field of DNA sensors (2, 14-21).

The reactions of quinones with a variety of amines give aminoquinone compounds (22-24). Particularly, aminoquinone structures draw interest in the literature because of the similar biological characteristics to quinone moieties (5, 23, 25-36). Although they have numerous beneficial biological activities, quinone structures including pharmacophore groups could sometimes cause possible toxic effects in *in vivo* implementations. However, Zakharova *et al.* have investigated also the cytotoxicity of new polyfluorinated 1,4-naphthoquinones and indicated that a number of synthesized structures exhibited a substantial cytotoxic effect against cancer cells compared to normal mammalian cells (36). Moreover, Khodade *et al.* have suggested that there is a good correlation between reactive oxygen species production of 2-aryl-3-amino-1,4-naphthoquinones and their DNA damage inducing ability (37). Besides that, Sharma *et al.* showed a new synthesis of 2-aryl-3-amino-1,4-naphthoquinones by using an eco-friendly, non-toxic, efficient, inexpensive, and reusable $\text{HClO}_4\text{-SiO}_2$ heterogeneous catalyst which is applied to different organic reactions (29). In a study reported by Verma *et al.* in 2015, some metal complexes of 2-chloro-3-amino-1,4-naphthoquinone derivatives with Mn, Co, Ni, Cu, and Zn metals were synthesized and characterized. The complex compounds exhibited a promising antimicrobial activity and fluorescence emission behavior and they were also found as electro active compounds (35). Nitrogen and sulfur containing quinones known also sulfanyl aminoquinones in the literature are of great importance in drug exploration researches due to their bioactive properties (13, 38-43). Recently, new sulfanyl and arylamine substituted 1,4-naphthoquinones have been synthesized and characterized (44, 45).

Encouraged by the previous studies and taking into account the well-documented quinone chemistry associated with the 1,4-benzoquinone pharmacophoric unit, it was attempted to synthesize several new cyclic aminobenzoquinone compounds. Thus, as a part of our research, aiming at the discovery of novel biologically active molecules based on 1,4-benzoquinone moiety, we have recently reported

the synthesis and characterization of cyclic aminobenzoquinones which contain a heterocyclic fragment as a key structural element.

MATERIALS AND METHODS

All reagents used were purchased from the various commercial supplier. Reactions were monitored by TLC performed on silica gel plate purchased from Merck KGaA (silica gel 60 F₂₅₄) based on Merck DC-plates (aluminum-based) and visualization was achieved by UV light (254 nm). Column chromatography was performed with silica gel 60 (Merck, 63–200 μm particle size, 60–230 mesh). ¹H NMR and ¹³C NMR spectra (VarianUNITY INOVA spectrometers 500 MHz frequency for ¹H and 125 MHz frequency for ¹³C NMR) and Fourier transform infrared (FT-IR) spectra as ATR (Thermo Scientific Nicolet 6700 spectrometer) were used to elucidate the structures of the products. Chemical shifts are expressed in parts per million (δ in ppm) and coupling constants are expressed in Hz. ¹H NMR spectroscopic data are used as follows: s (singlet), d (doublet), t (triplet), q (quartet), and m (multiplet). Mass spectra were recorded with either a Thermo Finnigan LCQ Advantage MAX MS/MS spectrometer equipped with ESI (electrospray ionization) sources or a BRUKER Microflex LT by MALDI (Matrix Assisted Laser Desorption Ionization)-TOF (Time of Flight) technique via addition of 1,8,9-anthracenetriol (DIT, dithranol) as matrix. The 2,3-dichloro-5,6-dimethyl-1,4-benzoquinone (**1**) was prepared according to the literature reported previously and the reference cited therein (46).

General Procedure for Synthesis of the Cyclic Aminobenzoquinone Derivatives (2-5)

The mixture of 2,3-dichloro-5,6-dimethyl-1,4-benzoquinone (**1**, 0.5 mmol) in water (10 mL) and cyclic secondary amines (1.1 mmol) was stirred at 50-60 °C for 6 to 18 h as stated in the literature (42). The resulting solution was extracted with 100 mL chloroform, and then was washed with water (4 x 25 mL) and dried over calcium chloride. The solvent was removed *in vacuo*. The residue was subjected to column chromatography on silica gel using suitable solvents to give the products (**2-5**).

2-Chloro-5,6-dimethyl-3-(pyrrolidin-1-yl)-1,4-benzoquinone (2). Following general procedure by applying pyrrolidine (0.076 g, 1.07 mmol), the crude residue was purified by column chromatography to furnish **2** as purple oil. Yield: 71%. FTIR (ATR) ν (cm^{-1}): 2919, 2850 ($\text{CH}_{\text{aliphatic}}$), 1661 ($>\text{C}=\text{O}$). ¹H NMR (CDCl_3) δ (ppm): 1.80-1.82 (m, 4H, H10 and H10'), 1.89 (dd, $J = 1.13$ and 2.33 Hz, 3H, H8), 1.99 (dd, $J = 1.17$ and 2.37 Hz, 3H, H7), 3.78-3.81 (m, 4H, H9 and H9'). ¹³C NMR (CDCl_3) δ (ppm): 11.4, 12.2 (C7 and C8), 24.7 (C10 and C10'), 52.7 (C9 and C9'), 107.6, 135.8, 140.8, 146.0 (C2, C3, C5, and C6), 178.2, 184.2 (C1 and C4). MS (+ESI) m/z (%): 240 (27, $[\text{M}+\text{H}]^+$), 238 (10, $[\text{M}-\text{H}]^+$). Calcd. for $\text{C}_{12}\text{H}_{14}\text{ClNO}_2$ (239.70).

2-Chloro-5,6-dimethyl-3-(piperidin-1-yl)-1,4-benzoquinone (3). Following general procedure by applying piperidine (0.091 g, 1.07 mmol), the crude residue was purified by column chromatography to furnish **3** as purple oil. Yield: 57%. FTIR (ATR) ν (cm^{-1}): 2934, 2853 ($\text{CH}_{\text{aliphatic}}$), 1657 ($>\text{C}=\text{O}$). ^1H NMR (CDCl_3) δ (ppm): 1.60-1.64 (m, 6H, H10, H10', and H11), 1.92 (m, 3H, H8), 1.98 (m, 3H, H7), 3.33-3.35 (m, 4H, H9 and H9'). ^{13}C NMR (CDCl_3) δ (ppm): 11.6, 12.1 (C7 and C8), 23.1, 25.8 (C10, C10', and C11), 51.6 (C9 and C9'), 117.6, 137.5, 140.2, 147.9 (C2, C3, C5, and C6), 179.1, 183.1 (C1 and C4). MS (MALDI TOF) m/z : 252 $[\text{M}-\text{H}]^+$. Calcd. for $\text{C}_{13}\text{H}_{16}\text{ClNO}_2$ (253.72).

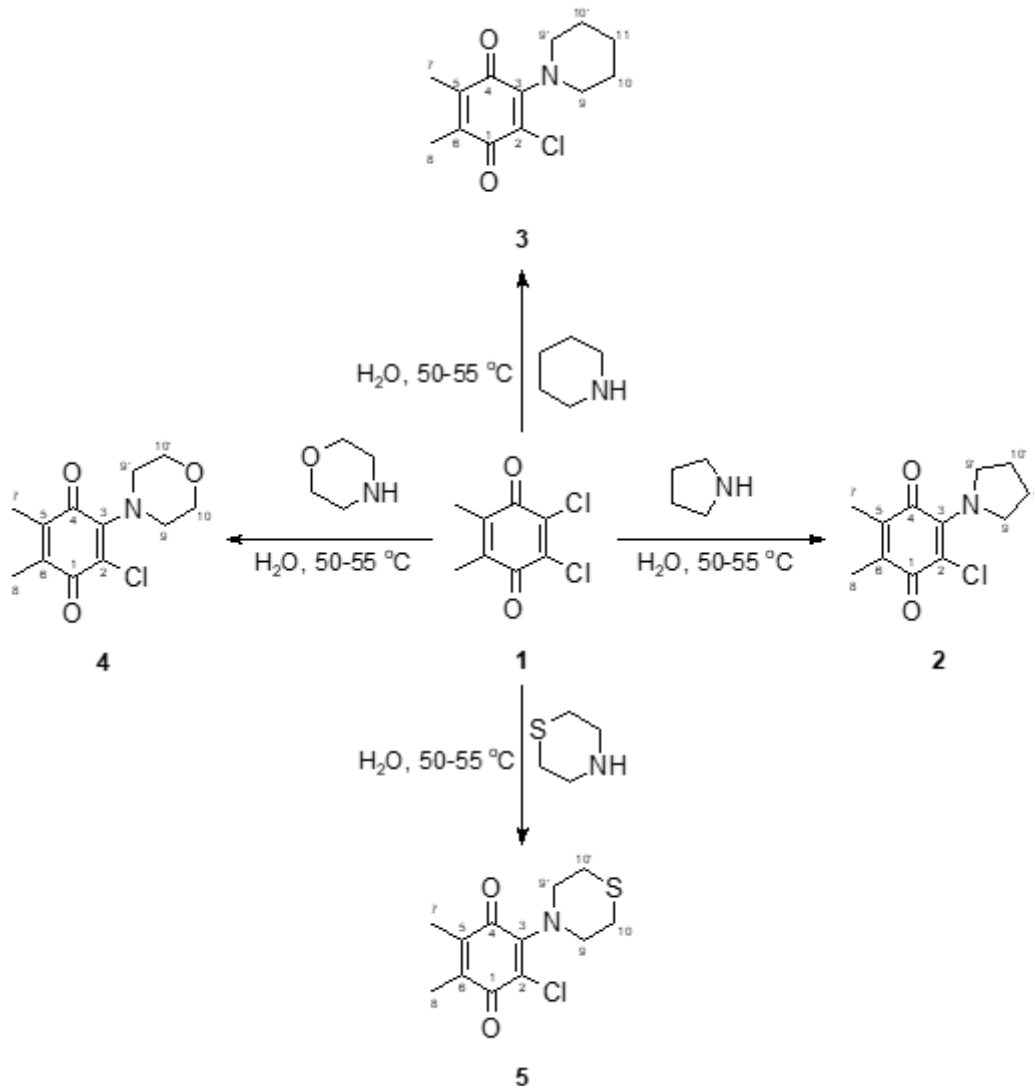
2-Chloro-5,6-dimethyl-3-morpholino-1,4-benzoquinone (4). Following general procedure by applying morpholine (0.093 g, 1.07 mmol), the crude residue was purified by column chromatography to furnish **4** as dark red oil. Yield: 29%. FTIR (ATR) ν (cm^{-1}): 2966, 2916, 2854 ($\text{CH}_{\text{aliphatic}}$), 1656 ($>\text{C}=\text{O}$). ^1H NMR (CDCl_3) δ (ppm): 1.93 (dd, $J = 1.11$ and 2.31 Hz, 3H, H8), 1.99 (dd, $J = 1.10$ and 2.30 Hz, 3H, H7), 3.43 (t, $J = 4.40$ Hz, 4H, H9 and H9'), 3.57 (t, $J = 4.39$ Hz, 4H, H10 and H10'). ^{13}C NMR (CDCl_3) δ (ppm): 11.5, 12.1 (C7 and C8), 50.5 (C9 and C9'), 66.5 (C10 and C10'), 118.8, 137.8, 140.3, 146.7 (C2, C3, C5, and C6), 179.1, 182.8 (C1 and C4). MS (MALDI TOF) m/z : 256 $[\text{M}+\text{H}]^+$. Calcd. for $\text{C}_{12}\text{H}_{14}\text{ClNO}_3$ (255.70).

2-Chloro-5,6-dimethyl-3-thiomorpholino-1,4-benzoquinone (5). Following general procedure by applying thiomorpholine (0.110 g, 1.07 mmol), the crude residue was purified by column chromatography to furnish **5** as a dark red oil. Yield: 61%. FTIR (ATR) ν (cm^{-1}): 2957, 2910, 2846 ($\text{CH}_{\text{aliphatic}}$), 1654 ($>\text{C}=\text{O}$). ^1H NMR (CDCl_3) δ (ppm): 1.93 (s, 3H, H8), 1.98 (s, 3H, H7), 2.68-2.70 (m, 4H, H10 and H10'), 3.57 (t, $J = 4.88$ Hz, 4H, H9 and H9'). ^{13}C NMR (CDCl_3) δ (ppm): 11.6, 12.1 (C7 and C8), 27.2 (C10 and C10'), 52.5 (C9 and C9'), 120.6, 138.0, 140.1, 147.9 (C2, C3, C5, and C6), 179.2, 182.9 (C1 and C4). MS (+ESI) m/z (%): 273 (13, $[\text{M}+2\text{H}]^+$), 272 (100, $[\text{M}+\text{H}]^+$). Calcd. for $\text{C}_{12}\text{H}_{14}\text{ClNO}_2\text{S}$ (271.76).

RESULTS AND DISCUSSION

It is well known the reactions of 1,4-quinones containing chlorine atoms with amine, sulfur, or oxygen nucleophiles proceed by nucleophilic substitution. Herein, when 2,3-dichloro-5,6-dimethyl-1,4-benzoquinone (**1**) was stirred with different cyclic secondary amines (pyrrolidine, piperidine, morpholine, and thiomorpholine) according to the literature (42) at 50-60 °C in the absence of a base using water as solvent, mono substituted products; 2-chloro-5,6-dimethyl-3-(pyrrolidin-1-yl)-1,4-benzoquinone (**2**), 2-chloro-5,6-dimethyl-3-(piperidin-1-yl)-1,4-benzoquinone (**3**), 2-chloro-5,6-dimethyl-3-morpholino-1,4-benzoquinone (**4**), and 2-chloro-5,6-dimethyl-3-thiomorpholino-

1,4-benzoquinone (**5**) were obtained in 29-71% yield, respectively. The newly synthesized products (**2-5**) were characterized on the basis of FTIR, ^1H NMR, ^{13}C NMR, and mass spectrometry.



Scheme 1. Synthesis of cyclic aminobenzoquinones (**2-5**) from the reactions of 2,3-dichloro-5,6-dimethyl-1,4-benzoquinone (**1**) with different cyclic secondary amines.

The FT-IR spectra of aminobenzoquinones (**2-5**) have showed characteristic carbonyl ($>\text{C}=\text{O}$) band at around 1650 cm^{-1} . The ^1H NMR spectra of aminobenzoquinone (**5**) exhibited two singlets at 1.93 and 1.98 ppm for the aliphatic methyl groups attached to the quinone moiety. On the other hand, aliphatic methyl protons in aminobenzoquinones (**2** and **4**) have resonated in doublet of doublets at around 1.90 and 1.99 ppm because of the interaction of the protons in the methyl groups. In the ^1H NMR spectra of **4**, protons of methylene group which are adjacent to the oxygen atom have appeared as triplet at 3.57 ppm while protons of methylene group which are adjacent to the nitrogen atom have appeared as triplet at 3.43 ppm. In the ^1H NMR spectra of **5**, protons of methylene group

next to the sulfur atom have appeared as multiplet at between 2.68-2.70 ppm while protons in methylene group which are adjacent to the nitrogen atom have appeared as triplet at 3.57 ppm. In the ^{13}C NMR spectra of all compounds, the presence of methyl carbons could be seen as two peaks at around 11 and 12 ppm. In the ^{13}C NMR spectra of all the cyclic aminobenzoquinones (**2-5**), there are signals corresponding to the $>\text{C}=\text{O}$ carbons at around 178 and 182 ppm as two peaks. In the mass spectrum of compounds (**2-5**), the accurate mass measurements of the molecular ion peaks were noticed at m/z 240 $[\text{M}+\text{H}]^+$, 252 $[\text{M}-\text{H}]^+$, 256 $[\text{M}+\text{H}]^+$, and 272 $[\text{M}+\text{H}]^+$, respectively.

CONCLUSION

In conclusion, the present study describes the synthesis and characterization of new cyclic aminobenzoquinones (**2-5**) by a green methodology using water as solvent according to the literature reported previously by Tandon (42). The conditions are mild and good yields are obtained in the absence of any additives. We believe that these new cyclic aminobenzoquinone compounds (**2-5**) could be biologically important because of the fact that the compounds containing quinone skeleton with heteroatoms usually have anticancer and antimicrobial activities. Since the multifaceted biologically character of the quinone moiety provides significant potential in medicinal chemistry, further extension of our research is now ongoing in our laboratory.

ACKNOWLEDGMENTS

This work was financially supported by the Scientific Research Projects Coordination Unit of Istanbul University (Project number: FYD-2016-22584) in the supply of the equipment and materials.

REFERENCES

1. Thomson RH. Distribution of Naturally-Occurring Quinones. *Pharm Weekblad*. 1991;13(2):70-73.
2. Aly AA, Hassan AA. Heterocycles from Donor-Acceptor Interactions. *Adv Heterocycl Chem*. 2014;112:145-181.
3. Mbaveng AT, Kuete V, Efferth T. Potential of Central, Eastern and Western Africa Medicinal Plants for Cancer Therapy: Spotlight on Resistant Cells and Molecular Targets. *Front Pharmacol*. 2017;8.
4. Duraipandiyan V, Al-Dhabi NA, Balachandran C, Raj MK, Arasu MV, Ignacimuthu S. Novel 1,5,7-Trihydroxy-3-Hydroxy Methyl Anthraquinone Isolated from Terrestrial *Streptomyces* sp. (eri-26) with Antimicrobial and Molecular Docking Studies. *Appl Biochem Biotech*. 2014;174(5):1784-1794.
5. Jordao AK, Novais J, Leal B, Escobar AC, dos Santos HM, Castro HC, et al. Synthesis using microwave irradiation and antibacterial evaluation of new N,O-acetals and N,S-acetals derived from 2-amino-1,4-naphthoquinones. *Eur J Med Chem*. 2013;63:196-201.

6. Claessens S, Verniest G, Jacobs J, Van Hende E, Habonimana P, Van TN, et al. A survey of synthetic routes towards the pyranonaphthoquinone antibiotic pentalongin and syntheses of the corresponding nitrogen derivatives. *Synlett*. 2007(6):829-850.
7. Bulbule VJ, Koranne PS, Munot YS, Borate HB, Deshpande VH. Simple synthesis of two naphthoquinone antibiotics psychorubrin and pentalongin. *Synthetic Commun*. 2003;33(4):587-94.
8. Hosamani B, Ribeiro MF, da Silva EN, Namboothiri INN. Catalytic asymmetric reactions and synthesis of quinones. *Org Biomol Chem*. 2016;14(29):6913-6931.
9. Kim JS, Rhee HK, Park HJ, Lee IK, Lee SK, Suh ME, et al. Synthesis of 6-chloroisoquinoline-5,8-diones and pyrido[3,4-b]-phenazine-5,12-diones and evaluation of their cytotoxicity and DNA topoisomerase II inhibitory activity. *Bioorgan Med Chem*. 2007;15(1):451-457.
10. Gellis A, Kovacic H, Boufatah N, Vanelle P. Synthesis and cytotoxicity evaluation of some benzimidazole-4,7-diones as bioreductive anticancer agents. *Eur J Med Chem*. 2008;43(9):1858-1864.
11. Belorgey D, Lanfranchi DA, Davioud-Charvet E. 1,4-Naphthoquinones and Other NADPH-Dependent Glutathione Reductase-Catalyzed Redox Cyclers as Antimalarial Agents. *Curr Pharm Design*. 2013;19(14):2512-2528.
12. Yildirim H, Bayrak N, Tuyun AF, Kara EM, Celik BO, Gupta GK. 2,3-Disubstituted-1,4-naphthoquinones containing an arylamine with trifluoromethyl group: synthesis, biological evaluation, and computational study. *RSC Adv*. 2017;7(41):25753-25764.
13. Tandon VK, Maurya HK, Yadav DB, Tripathi A, Kumar M, Shukla PK. Naphtho[2,3-b][1,4]-thiazine-5,10-diones and 3-substituted-1,4-dioxo-1,4-dihydronaphthalen-2-yl-thioalkanoate derivatives: Synthesis and biological evaluation as potential antibacterial and antifungal agents. *Bioorg Med Chem Lett*. 2006;16(22):5883-5887.
14. Batenko N, Kricka A, Belyakov S, Turovska B, Valters R. A novel method for the synthesis of benzimidazole-based 1,4-quinone derivatives. *Tetrahedron Lett*. 2016;57(3):292-295.
15. Rajendran M. Quinones as photosensitizer for photodynamic therapy: ROS generation, mechanism and detection methods. *Photodiagn Photodyn*. 2016;13:175-187.
16. Kim KC, Liu TY, Lee SW, Jang SS. First-Principles Density Functional Theory Modeling of Li Binding: Thermodynamics and Redox Properties of Quinone Derivatives for Lithium-Ion Batteries. *J Am Chem Soc*. 2016;138(7):2374-2382.
17. Lee J, Kim H, Park MJ. Long-Life, High-Rate Lithium-Organic Batteries Based on Naphthoquinone Derivatives. *Chem Mater*. 2016;28(7):2408-2416.
18. Hamdan AJ. Sn (II) selective 2-Amino-1,4-Naphthoquinone Derived poly(vinyl chloride) Membrane Sensors. *Int J Electrochem Sc*. 2010;5(2):215-231.
19. Hamdan AJ. Yttrium Selective Poly(Vinyl) Chloride Sensor Based on Derivative of 2-Amino-1,4-Naphthoquinone. *Int J Electrochem Sc*. 2013;8(4):5838-5850.
20. Wu SP, Huang RY, Du KJ. Colorimetric sensing of Cu(II) by 2-methyl-3-[(pyridin-2-ylmethyl)-amino]-1,4-naphthoquinone: Cu(II) induced deprotonation of NH responsible for color changes. *Dalton T*. 2009(24):4735-4740.
21. Zhang QD, Piro B, Noel V, Reisberg S, Serradji N, Dong CZ, et al. An electroactive conjugated oligomer for a direct electrochemical DNA sensor. *Synthetic Met*. 2012;162(17-18):1496-1502.
22. Bayrak N, Tuyun AF, Yildirim H, Onul N. Spectroscopic and structural aspects of the reactions of 1,4-quinones with sulfur and nitrogen nucleophiles. *Cr Chim*. 2014;17(6):563-569.

23. Tuyun AF, Bayrak N, Yildirim H, Onul N, Kara EM, Celik BO. Synthesis and In Vitro Biological Evaluation of Aminonaphthoquinones and Benzo[b]phenazine-6,11-dione Derivatives as Potential Antibacterial and Antifungal Compounds. *J Chem*. 2015.
24. Valderrama JA, Ibacache JA, Theoduloz C. Synthesis and antiproliferative evaluation of new isomeric ellipticine quinones. *B Latinoam Caribe Pl*. 2014;13(6):566-574.
25. Van Aeken S, Deblander J, De Houwer J, Mosselmans T, Tehrani KA. Unexpected reaction of 2-amino-1,4-naphthoquinone with aldehydes: new synthesis of naphtho[2,1-d]oxazole compounds. *Tetrahedron*. 2011;67(2):512-517.
26. Bala BD, Muthusaravanan S, Choon TS, Ali MA, Perumal S. Sequential synthesis of amino-1,4-naphthoquinone-appended triazoles and triazole-chromene hybrids and their antimycobacterial evaluation. *Eur J Med Chem*. 2014;85:737-746.
27. Li J, Zhang XF, Xiang HY, Tong LJ, Feng F, Xie H, et al. C-H Trifluoromethylation of 2-Substituted/Unsubstituted Aminonaphthoquinones at Room Temperature with Bench-Stable (CF₃SO₂)(2)Zn: Synthesis and Antiproliferative Evaluation. *J Org Chem*. 2017;82(13):6795-6800.
28. Lisboa CD, Santos VG, Vaz BG, de Lucas NC, Eberlin MN, Garden SJ. C-H Functionalization of 1,4-Naphthoquinone by Oxidative Coupling with Anilines in the Presence of a Catalytic Quantity of Copper(II) Acetate. *J Org Chem*. 2011;76(13):5264-5273.
29. Sharma U, Katoch D, Sood S, Kumar N, Singh B, Thakur A, et al. Synthesis, antibacterial and antifungal activity of 2-amino-1,4-naphthoquinones using silica-supported perchloric acid (HClO₄-SiO₂) as a mild, recyclable and highly efficient heterogeneous catalyst. *Indian J Chem B*. 2013;52(11):1431-1440.
30. Sharma A, Santos IO, Gaur P, Ferreira VE, Garcia CRS, da Rocha DR. Addition of thiols to o-quinone methide: New 2-hydroxy-3-phenylsulfanylmethyl [1,4]naphthoquinones and their activity against the human malaria parasite *Plasmodium falciparum* (3D7). *Eur J Med Chem*. 2013;59:48-53.
31. Shvartsberg MS, Kolodina EA, Lebedeva NI, Fedenok LG. Vicinal acetylenic derivatives of 2-amino-1,4-naphthoquinone as key precursors of heterocyclic quinones. *Russ Chem B+*. 2012;61(3):582-588.
32. Singh MW, Karmakar A, Barooah N, Baruah JB. Variations in product in reactions of naphthoquinone with primary amines. *Beilstein J Org Chem*. 2007;3.
33. Tapia RA, Venegas J, Cantuarias LB. Copper Bromide-Catalyzed C-Alkylation of 2-Amino-1,4-Naphthoquinone: New Synthesis of 1-Azaanthraquinones. *Synthetic Commun*. 2010;40(1):151-156.
34. Tseng CC, Wu YL, Chuang CP. Cerium salts in the oxidative free radical reactions between 2-amino-1,4-naphthoquinones and beta-dicarbonyl compounds. *Tetrahedron*. 2002;58(38):7625-7633.
35. Verma SK, Singh VK. Synthesis, electrochemical, fluorescence and antimicrobial studies of 2-chloro-3-amino-1,4-naphthoquinone bearing mononuclear transition metal dithiocarbamate complexes [M{ κ -S-2,S-S2C-piperazine-C₂H₄N(H)CINQ}(n)]. *RSC Adv*. 2015;5(65):53036-53046.
36. Zakharova OD, Ovchinnikova LP, Goryunov LI, Troshkova NM, Shteingarts VD, Nevinsky GA. Cytotoxicity of new alkylamino- and phenylamino-containing polyfluorinated derivatives of 1,4-naphthoquinone. *Eur J Med Chem*. 2010;45(6):2321-2326.
37. Khodade VS, Dharmaraja AT, Chakrapani H. Synthesis, reactive oxygen species generation and copper-mediated nuclease activity profiles of 2-aryl-3-amino-1,4-naphthoquinones. *Bioorg Med Chem Lett*. 2012;22(11):3766-3769.
38. Ryu CK, Choi JA, Kim SH. Synthesis and antifungal evaluation of 6-(N-Arylamino)-7-methylthio-5,8-quinolinediones. *Arch Pharm Res*. 1998;21(4):440-444.
39. Tandon VK, Yadav DB, Maurya HK, Chaturvedi AK, Shukla PK. Design, synthesis, and biological evaluation of 1,2,3-trisubstituted-1,4-dihydrobenzo[g]quinoxaline-5,10-diones and related compounds as antifungal and antibacterial agents. *Bioorgan Med Chem*. 2006;14(17):6120-6126.

40. Tandon VK, Maurya HK, Mishra NN, Shukia PK. Design, synthesis and biological evaluation of novel nitrogen and sulfur containing hetero-1,4-naphthoquinones as potent antifungal and antibacterial agents. *Eur J Med Chem.* 2009;44(8):3130-3137.
41. Tandon VK, Maurya HK, Tripathi A, ShivaKeshava GB, Shukla PK, Srivastava P, et al. 2,3-Disubstituted-1,4-naphthoquinones, 12H-benzo[b]phenothiazine-6, 11-diones and related compounds: Synthesis and Biological evaluation as potential antiproliferative and antifungal agents. *Eur J Med Chem.* 2009;44(3):1086-1092.
42. Tandon VK, Maurya HK, Verma MK, Kumar R, Shukla PK. 'On water' assisted synthesis and biological evaluation of nitrogen and sulfur containing hetero-1,4-naphthoquinones as potent antifungal and antibacterial agents. *Eur J Med Chem.* 2010;45(6):2418-2426.
43. Bayrak N, Yildirim H, Tuyun AF, Kara EM, Celik BO, Gupta GK. Synthesis, Biological, and Computational Study of Naphthoquinone Derivatives Containing Heteroatoms. *J Chem Soc Pakistan.* 2016;38(6):1211-1221.
44. Bayrak N. Novel Straight-chained Sulfanyl Members of Arylamino-1,4-naphthoquinones: Synthesis and Characterization. *JOTCSA.* 2017; 4(2):597-606.
45. Yıldırım H. Synthesis and Structural Analysis of Some New Sulfanyl Amino 1,4- Naphthoquinone Derivatives. *JOTCSA.* 2017; 5(1):149-158.
46. Ryu CK, Song AL, Lee JY, Hong JA, Yoon JH, Kim A. Synthesis and antifungal activity of benzofuran-5-ols. *Bioorg Med Chem Lett.* 2010;20(22):6777-6780.

Electrochemical Oxidation Pathway of the Anti-Cancer Agent Dasatinib Using Disposable Pencil Graphite Electrode and its Adsorptive Stripping Voltammetric Determination in Biological Samples

Dilek ESKİKÖY BAYRAKTEPE  , Kamran POLAT  , and Zehra YAZAN*  

Ankara University, Faculty of Science, Department of Chemistry, Ankara, TURKEY, 06560

Abstract: The present study describes the use of pencil graphite electrode (PGE) so as to investigate the electro-oxidation mechanism and voltammetric stripping determination of dasatinib (DST) in Britton-Robinson buffer solution (BR). Relating to cyclic voltammetric studies, an irreversible oxidation signal was obtained at about 1.0 V. The oxidation electrode process is adsorption-controlled and pH-dependent. For quantitative determination of DST, square wave adsorptive stripping voltammetry (AdsSWV) was employed in BR of pH 3.0. The oxidation signal varies linearly with the DST concentration in the range of 0.0092 – 1.0 μM . Detection and quantification (LOD and LOQ) values are founded as 0.0028 μM and 0.0092 μM , respectively. The developed AdsSWV method based on disposable and cheap PGE was applied successfully to the real human urine samples and the recovery results are given in the range of 97.94% to 100.82%.

Keywords: Dasatinib, pencil graphite electrode, voltammetry, urine.

Submitted: October 19, 2017. **Accepted:** February 17, 2018.

Cite this: Eskiköy Bayraktepe D, Polat K, Yazan Z. Electrochemical Oxidation Pathway of the Anti-Cancer Agent Dasatinib Using Disposable Pencil Graphite Electrode and its Adsorptive Stripping Voltammetric Determination in Biological Samples. JOTCSA. 2018;5(2):381-92.

DOI: <http://dx.doi.org/10.18596/jotcsa.345238>.

***Corresponding author.** e-mail: zehrayazan67@gmail.com

INTRODUCTION

Dasatinib (DST), N-(2-chloro-6-methylphenyl)-2-[[6-[4-(2-hydroxyethyl)-1-piperazinyl]-2-methyl-4-pyrimidinyl]amino]-5-thiazole, inset in Fig. 1, is a multiple target tyrosine kinase inhibitor, forceful against the proliferation of cells expressing mutant kinases. DST is synthesized from a 2-aminothiazole that is taken in consideration the atypical Src family kinase inhibitor template (1). DST is displayed for the treatment of different myeloid leukaemia types (2-5). Also, DST used for treatment of nonHodgkin's lymphoma, prostate cancer and metastatic breast cancer.

Up to now, there are a few methods described for the determination of DST only including chromatography (6-10), spectroscopy (11,12) and voltammetry (16,17). However, chromatographic and spectroscopic methods have some disadvantages like that they are time-consuming procedures, using expensive equipment and sample pre-treatments. In this context, electroanalytical methods are very good alternatives and more in particular, stripping techniques provide immense properties for determination of metal ions and some organic substances with excellent detection limits (13,14). Also, voltammetric techniques are relatively of low cost, sensitive and selective. Due to these advantages, voltammetric techniques has been used widely in the investigation of redox reactions and analysis of organic and inorganic substances using various electrodes. Nowadays carbon-based electrodes are available for electroanalytical applications by the reason of their lower background current, extensive potential window, low price, and inertness. In particular, pencil graphite electrode has been used as working electrode because of high electrochemical reactivity, low cost and ease of modification, ease of miniaturization, no need to time consuming processes (15).

There are few studies on the voltammetric analysis of DST. Jesus *et al.* and Karimi-Maleh *et al.* reported that DST was electrochemically analyzed at glassy carbon electrode and modified carbon paste electrode by square wave voltammetry. The values of LOD were found to be 0.13 and 1.0 μM in the other works (16, 17). However, a survey of literature reveals that not much work has been performed on electrochemical oxidation mechanism and adsorptive stripping voltammetric analysis of DST in the low limit of detection at the disposable pencil graphite electrode.

Thus, the goal of current study was to investigate the voltammetric oxidation mechanism of dasatinib by using disposable pencil graphite electrode and to develop a new sensitive voltammetric stripping method for the rapid, cheap and sensitive analysis in human urine samples.

EXPERIMENTAL

Chemicals and Apparatus

Standard DST powder was taken from Nobel© and all other solvents purchased from Sigma Company 1.0 mM stock solution of DST was prepared by dissolving a known amount of DST in a mixture of 40% DMSO and 60% double distilled water and kept in the fridge at +4 °C until assay. 0.02 M Britton- Robinson buffer solution was used as supporting electrolyte and 0.1 M NaOH solution was used to adjust the pH of medium.

Cyclic voltammetric (CV), square wave adsorptive stripping voltammetric (AdsSWV) and Electrochemical Impedance Spectroscopic (EIS) measurements were carried out on a CHI 760B (USA) Workstation with BAS C3 cell stand. A traditional three electrode system was used and pencil graphite electrode (PGE) was used as working electrode, Ag/AgCl (in 3.0 mol L⁻¹ NaCl, BAS MW-1032) was used as reference and platinum wire was used as an auxiliary electrode (BAS MF-2052). A pencil lead with 0.5 mm diameter (2B) and 60 mm a total length (Tombow, Japan). A pencil of Rotring from Germany was used as a holder for the pencil lead and all of them were taken from a local bookstore. Electrical contact was provided by wrapping a metallic wire to the metallic part of the holder. 12 mm of lead was measured with a ruler and then immersed into the solution before each measurement. pH measurements were carried out with a HANNA Instruments HI2211 pH/ORP meter.

Analytical procedure

All electrochemical measurements (CV, AdsSWV, EIS) were made in a 10 mL-voltammetric cell. A known volume of stock solution was mixed with the required volume of BR buffer with the determined pH. Before all measurements, the solution inside the cell was purged with ultra-pure nitrogen (99.99 %) for a period of 60 s to expel the dissolved oxygen. The voltammograms were recorded after a 2- second quiet time, in the potential range, (+0.4)– (+1.40) V.

Calibration solutions

By using the stock 1.0 mM DST solution, calibration solutions at the concentrations of 0.010, 0.050, 0.10, 0.30, 0.50, 0.80, and 1.0 μM were prepared in the volumetric cell, then the current of each solution were measured by AdsSWV method.

The calibration of the pH electrode were done by commercial buffer solutions at the pH values of 4.0, 7.0, and 10. Double-distilled water was supplied from a Human Power I+, Ultra-Pure Water System. All measurements were performed at room temperature.

Biological sample preparation

Human urine samples were taken from healthy volunteers. As soon as the urine sample was taken, calculated amount of supporting electrolyte was mixed with 20 μL of urine in the voltammetric cell. To this mixture, a sufficient volume of DST stock solution was added to make the final volume exactly to 10.0 mL.

RESULT and DISCUSSION

Electrochemical behavior of DST on PGE

Electrochemical redox behavior, adsorption, and diffusion properties of DST on PGE were studied by using CV. As can be understood in Figure 1, DST has one irreversible oxidation peak at about 1.0 V at pH 3.0 (vs. Ag/AgCl) and there is no reduction peak on the reverse scan. Also, there is no oxidation or reduction signal when only BR solution was scanned under the same circumstances.

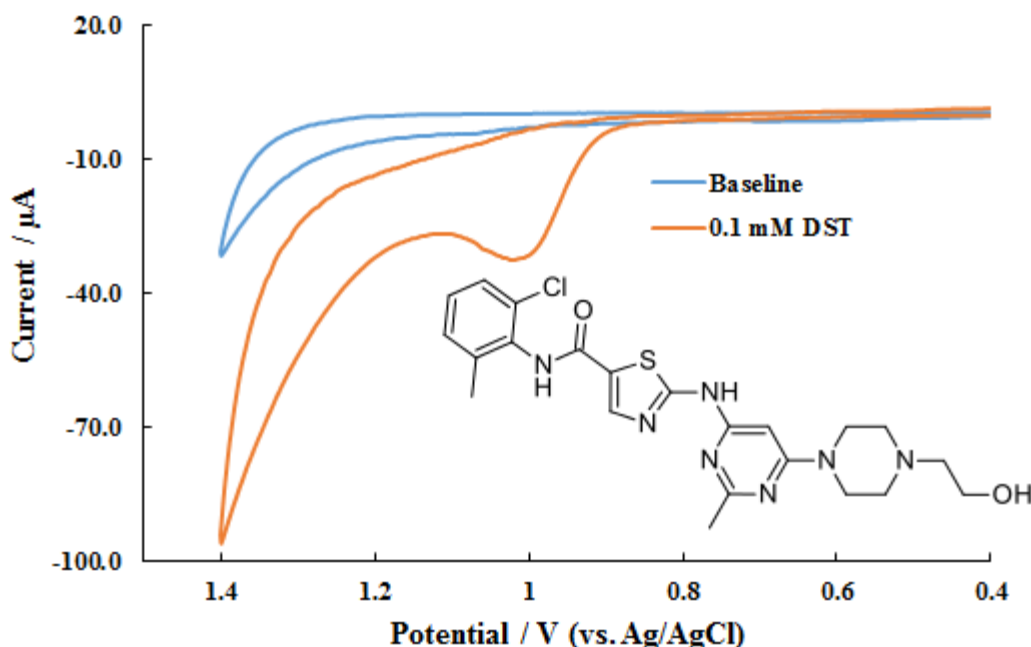


Figure 1. Cyclic voltammograms of blank BR and 0.1 mM DST on PGE (BR buffer solution, pH: 3.0) **inset:** Chemical structure of DST, scan rate: 0.1Vs^{-1} .

Influence of pH

The pH dependence of DST's peak potential and peak current was examined by using CV in BR buffer solution at different pH values (2.0-6.0; with pH increment of 1.0). The oxidation peak was seen in the pH interval of 2.0 to 6.0 then at pH values of ≥ 7.0 , the peak was disappeared. As can

be understood in Fig. 2, the relevant peak was reached maximum current value at pH 3.0. Thereby, pH 3.0 was chosen as optimum pH for analysis of DST.

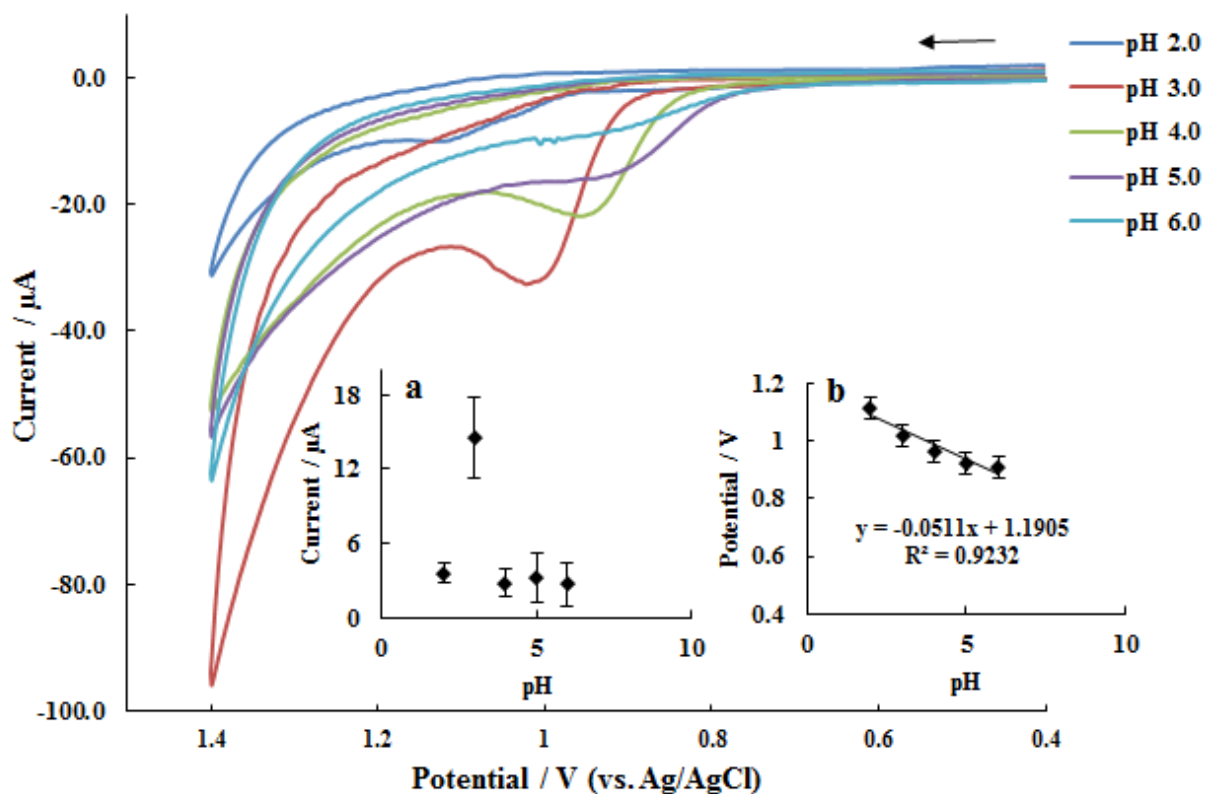


Figure 2. Cyclic voltammograms of 0.1 mM DST on different pH values in BR buffer solution.

Inset a. pH- i_p graph, **inset b.** pH- E_p graph of DST (scan rate:0.1 Vs⁻¹).

The peak potential of DST moves more negative potential values with increasing pHs (Fig. 2b). This behavior indicates that, the oxidation mechanism of DST includes proton transfer as well as electron transfer. The peak potential of the linear relation relates (E_p) to the pH value:

$$E_p = -0.0511\text{pH} + 1.1905 \quad (R^2=0.9232).$$

Slope of this equation (0.0511 V/pH) is nearly the same with the theoretical value of 0.059 V/pH and this result shows that, in the electrode reaction mechanism, transferred electron and proton numbers are equal (18).

Influence of scan rate

The voltammograms obtained by using CV were recorded at various scan rates to see the differences in the peak potential and current in 0.02 M BR buffer solution at pH 3.0 (0.1 mmolL⁻¹ DST, Fig.3). The scan rates were changed in the interval $\nu=0.05-0.50$ Vs⁻¹. The voltammograms show that, with increasing scan rate, the peak current permanently increases and the peak potential moves in values that are more positive. As can be seen in the inset of Figure 3, the equation between the peak current and the scan rate for oxidation peak is given below:

$$i_p = 122.26\nu + 3.48 \quad (R^2 = 0.9893)$$

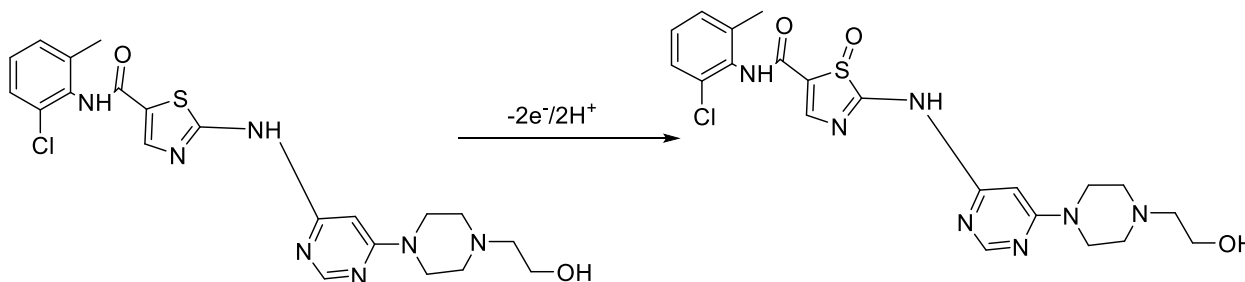
The linearity of i_p^a vs. ν graphs specified that the reaction is adsorption-controlled process (19). The $\log i_p^a$ vs. $\log \nu$ is presented in Fig.3 for DST. The slope of the graph is 0.82. This result indicates that the adsorption phenomenon is dominant (18).

To find out the transferred electron numbers of oxidation mechanism, the following equation for irreversible reactions is used (19):

$$|E_p - E_{p/2}| = \frac{48}{\alpha_c n \alpha} \text{ mV} \quad (1)$$

According to this equation, n is the transferred electron numbers, E_p represents the peak potential, $E_{p/2}$ represents the half peak potential, and α represents the electron transfer coefficient. By using corresponding equation, the number of electrons (n) transferred in the oxidation of DST occurring at the potential value of about 1.0 V is 1.99 ± 0.18 .

According to all these results, in oxidation mechanism of DST, $2e^-$ and $2H^+$ are transferred. This may be attributed to the fact that the sulfur group of the thiazole ring is oxidized to sulfonyl group (16) and tentative reaction mechanism is suggested as follows:



Scheme 1. Electro-oxidation mechanism of DST on PGE.

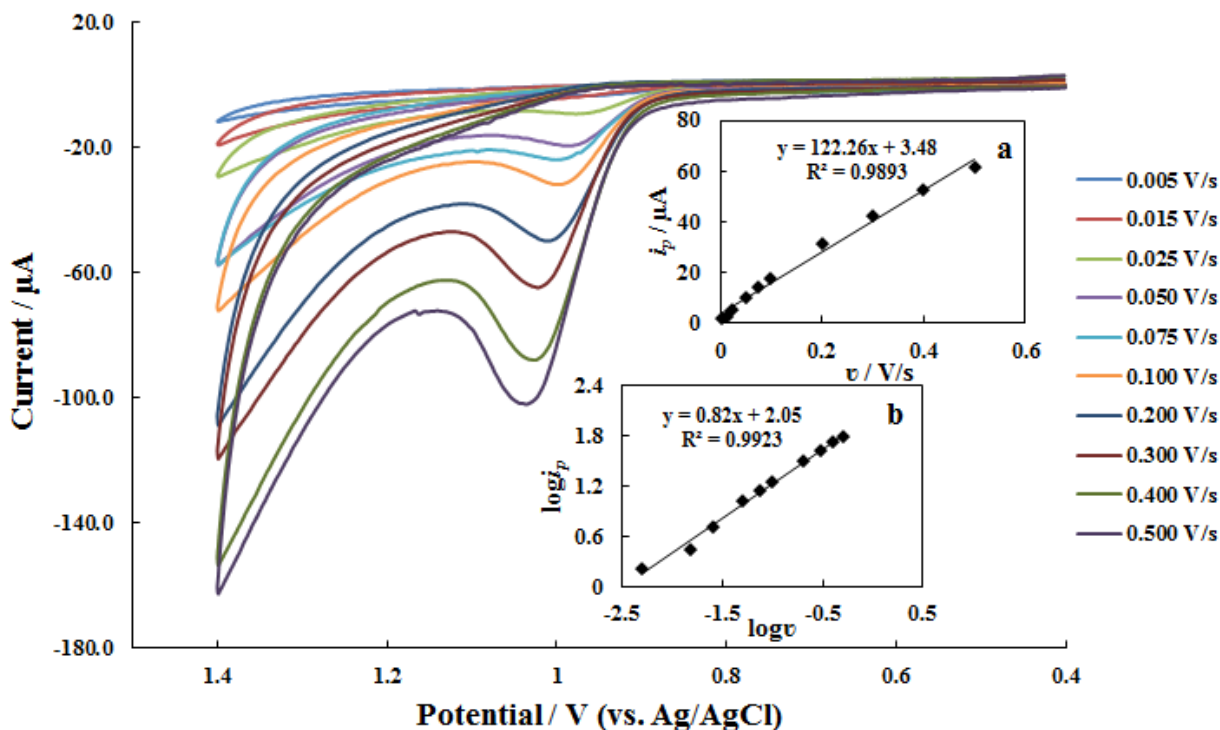


Figure 3. Cyclic voltammograms of 0.1 mmol L^{-1} DST at different scan rate values in BR buffer solution pH 3.0 **Insets a.** $i_p - v$ and **Insets b.** $\log v - \log i_p$ plots.

Analytical procedure

The AdsSWV method with the PGE indicates some prospects for the quantitative determination of DST in real human urine samples. The circumstances of the determination studies are given below.

Optimization of experimental conditions

The applicability of adsorptive stripping square wave voltammetry (AdsSWV) procedure as analytical methods for the analysis of DST was examined by measuring the anodic peak current as a function of the concentration of DST. The linear concentration range, LOD and LOQ were determined from the calibration graph obtained by measuring the anodic peak current as a function of concentration. For this reason, the effects of accumulation time and accumulation potentials on the peak currents obtained with $1.0 \times 10^{-6} \text{ mol L}^{-1}$ DST were investigated by using AdsSWV. Accumulation potentials were changed in the range (0.0) – (+1.0 V) with 0.1 V increments. Accumulation times were in the range 0 – 90.0 s (15s increments). The results are summarized in Figure 4. The graphs show that the optimum accumulation potential and accumulation time values are 0.2 V and 30.0 s, respectively.

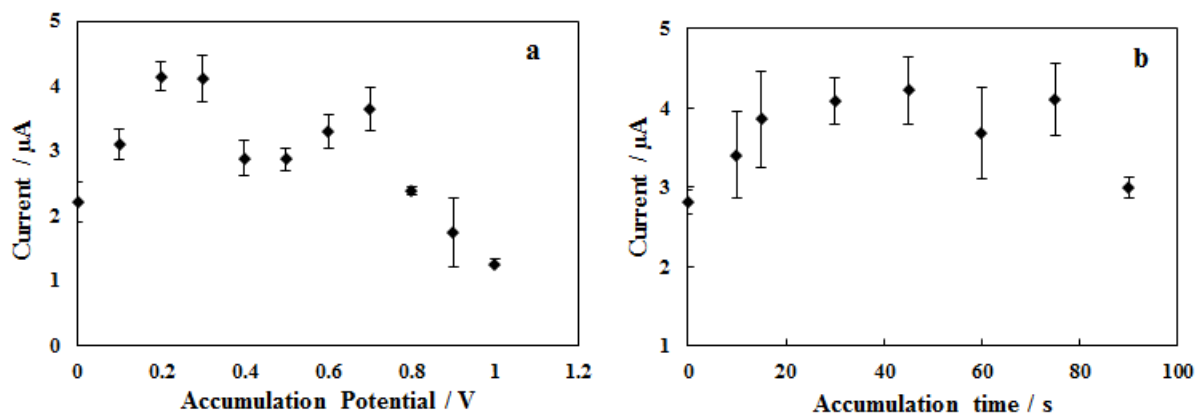


Figure 4. The effect of accumulation potential (a) and accumulation time (b) on AdsSW voltammograms of DST (C_{DST} : $1.0 \mu\text{molL}^{-1}$, pH 3.0).

Calibration studies

Under optimum experimental conditions, the calibration graph is established. As it can be seen in Figure 5, DST's oxidation peak current linear with DST concentration in the concentration range of $0.01 - 1.0 \mu\text{M}$. The regression equation of calibration graph is given below:

$$i_p (\mu\text{A}) = 6.68C_{\text{DST}} (\mu\text{M}) + 1.20 \quad (R^2 = 0.9973).$$

The values of LOD and LOQ were calculated using the equations are mentioned below (19-21); LOD and LOQ values were calculated using the following Equation;

$$\text{LOD} = 3s/m; \text{LOQ} = 10s/m$$

where s is the standard deviation for the peak currents of lowest DST concentration studied and m is the slope of the calibration graph.

By using corresponding equations, LOD and LOQ values were calculated as $0.0028 \mu\text{molL}^{-1}$ and $0.0092 \mu\text{molL}^{-1}$, respectively. According to our literature knowledge, the obtained limits are the lowest results notch up to now (16, 17). A comparison of our study with literature reports is shown in Table 1 and validation parameters of proposed method are shown in Table 2.

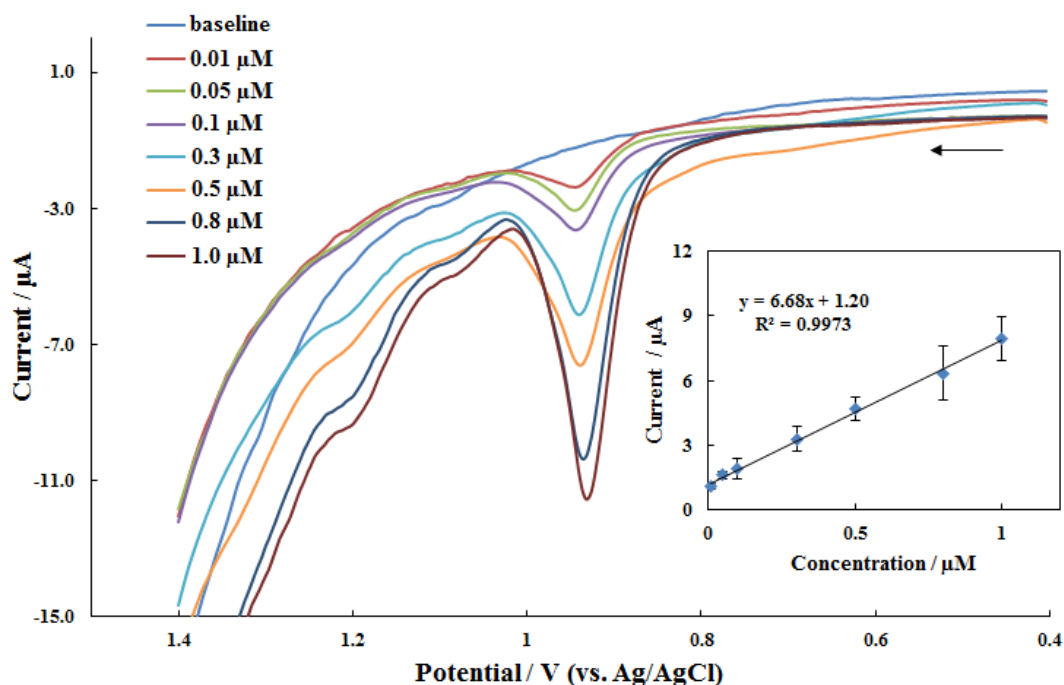


Figure 5. AdsSW voltammograms of DST for solutions with various concentrations (0.01 μM -1.0 μM). **Inset:** Calibration curve of AdsSWV.

Table 1. Regression data of the calibration curve for the analysis of DST by AdsSWV.

Method	AdsSWV
Peak potential, V	0.936
Slope, ($\mu\text{A}/\mu\text{M}$)	6.68
Regression coefficient, R^2	0.9973
Working range, μmolL^{-1}	0.0092-1.0
LOD, μmolL^{-1} *	0.0028
LOQ, μmolL^{-1} *	0.0092
Reproducibility of peak current, RSD % (n=3)	5.80
Reproducibility of peak potential, RSD % (n=3)	0.43

*In the confidence limit of 95 %, $t = 2.57$ for $N = 4$ for all experiments
RSD is the relative standard deviation of **four** replications.

Table 2. Comparison of the successes of different voltammetric methods for the analysis of DST.

Technique	Electrode	Working range ($\mu\text{mol L}^{-1}$)	LOD ($\mu\text{mol L}^{-1}$)	Sample	Reference
AdsSWV	PGE	0.0092 – 1.0	0.0028	Urine	This work
DPV	GCE	0.43-2.0	0.13	Serum	(16)
SWV	Pt/MWCNTs-BMIHFP-CPE	5.0 - 500	1.0	Urine and tablets	(17)

DPV: Differential pulse voltammetry, SWV: Square wave voltammetry, PGE: pencil graphite electrode, GCE: glassy carbon electrode, Pt/MWCNTs-BMIHFP-CPE: platinum/multiwalled carbon nanotubes-1-butyl-3-methylimidazolium hexafluorophosphate-modified carbon paste electrode.

Real sample application

In order to demonstrate the applicability of developed method, DST was analyzed in human urine by using AdsSWV. The analysis procedure was given in Experimental part (in Real sample preparation section). According to the calculated recovery results, DST can be analyzed in urine samples with high accuracy. The results of recovery are given in Table 3.

Table 3. Recovery results for DST in urine samples.

Added, μM	Found, μM	Recovery, %	%RSD
0.300	0.302	100.82 \pm 7.01	2.80
0.500	0.494	98.71 \pm 10.03	4.09
0.800	0.783	97.94 \pm 6.67	4.37

Interferences

The impact of interferents that can be present in human urine samples were examined. In this context, 0.3 μmolL^{-1} DST sample was mixed with known amounts of uric acid, ascorbic acid, glucose, L-glutamic acid and L-cysteine for the purpose of adjust their concentrations to 30 μmolL^{-1} (100 times higher than DST). Present responses obtained from only DST and samples blended with DST and components were compared. Calculated differences between the peak currents were found to be less than 10% of the signal obtained with DST solution.

CONCLUSION

This work has demonstrated that DST has only one oxidation peak at about +1.0 V at PG electrode in Britton Robinson buffer solution, pH 3.0. The electrochemical oxidation occurs through step by two electrons and two protons. For the quantification analysis of DST with AdsSWV method was optimized to voltammetric parameters. The oxidation signal is linearly

related to DST in the concentrations range of 0.0092–1.0 μmolL^{-1} , with a LOD of 0.0028 μmolL^{-1} and a LOQ of 0.0092 μmolL^{-1} . To the best of our literature knowledge, these values are the lowest detection limits ever. Moreover, the method was applied successfully to real human urine sample.

ACKNOWLEDGMENTS

Our research group is grateful to Ankara University Research Fund (Project numbers of 13L4240009 and 15L0430006) for financial support.

REFERENCES

1. Das J, Chen P, Norris D, Padmanabha R, Lin J, Moquin RV and Pang S. 2-Aminothiazole as a novel kinase inhibitor template. Structure– activity relationship studies toward the discovery of N-(2-chloro-6-methylphenyl)-2-[[6-[4-(2-hydroxyethyl)-1-piperazinyl]]-2-methyl-4-pyrimidinyl] amino)-1, 3-thiazole-5-carboxamide (dasatinib, BMS-354825) as a potent pan-Src kinase inhibitor. *Journal of medicinal chemistry* 2006; 49(23):6819-6832.
2. Montero JC, Seoane S, Ocaña A and Pandiella A. Inhibition of SRC family kinases and receptor tyrosine kinases by dasatinib: possible combinations in solid tumors. *Clinical cancer research*, 2011; 17(17):5546-5552.
3. Steinberg, M. Dasatinib: A tyrosine kinase inhibitor for the treatment of chronic myelogenous leukemia and philadelphia chromosome–positive acute lymphoblastic leukemia. *Clinical therapeutics* 2007; 29(11):2289-2308.
4. Tokarski JS, Newitt JA, Chang CYJ, Cheng JD, Wittekind M, Kiefer SE and Xie D. The structure of Dasatinib (BMS-354825) bound to activated ABL kinase domain elucidates its inhibitory activity against imatinib-resistant ABL mutants. *Cancer research* 2006; 66(11):5790-5797.
5. Vandyke K, Fitter S and Zannettino ACW. The tyrosine kinase inhibitor dasatinib (SPRYCEL) inhibits chondrocyte activity and proliferation. *Blood cancer journal* 2011; 1(2), e2.
6. Lankheet NA, Hillebrand MJ, Rosing H, Schellens JH, Beijnen JH and Huitema AD. Method development and validation for the quantification of dasatinib, erlotinib, gefitinib, imatinib, lapatinib, nilotinib, sorafenib and sunitinib in human plasma by liquid chromatography coupled with tandem mass spectrometry. *Biomedical Chromatography* 2013; 27(4):466-476.
7. Kralj E, Trontelj J, Pajič T and Kristl A. Simultaneous measurement of imatinib, nilotinib and dasatinib in dried blood spot by ultra high performance liquid chromatography tandem mass spectrometry. *Journal of Chromatography B* 2012; 903:150-156.
8. De Francia S, D'Avolio A, De Martino F, Pirro E, Baietto L, Siccardi M and Di Perri G. New HPLC–MS method for the simultaneous quantification of the antileukemia drugs imatinib, dasatinib, and nilotinib in human plasma. *Journal of Chromatography B* 2009; 877(18), 1721-1726.
9. Hsieh Y, Galviz G, Zhou Q and Duncan C. Hydrophilic interaction liquid chromatography/tandem mass spectrometry for the simultaneous determination of dasatinib, imatinib and nilotinib in mouse plasma. *Rapid Communications in Mass Spectrometry* 2009; 23(9); 1364-1370.
10. Roche S, McMahon G, Clynes M and O'Connor R. Development of a high-performance liquid chromatographic–mass spectrometric method for the determination of cellular levels of the tyrosine kinase inhibitors lapatinib and dasatinib. *Journal of Chromatography B* 2009; 877(31):3982-3990.

11. Vadia N and Rajput S. Development of colorimetric method for determination of dasatinib in bulk and in tablet formulation. *International Journal of Pharmacy and Pharmaceutical Sciences* 2011; 3(2):188-190.
12. Sankar, DG, Rajeswari A, Babu AN and Krishna MV. UV-spectrophotometric determination of dasatinib in pharmaceutical dosage forms. *Asian Journal of Chemistry* 2009; 21(7): 5777 – 5779.
13. Tiğ GA, Günendi G and Pekyardımcı Ş. A selective sensor based on Au nanoparticles-graphene oxide-poly (2, 6-pyridinedicarboxylic acid) composite for simultaneous electrochemical determination of ascorbic acid, dopamine, and uric acid. *Journal of Applied Electrochemistry* 2017; 47(5):607-618.
14. Pekin M, Bayraktepe DE and Yazan Z. Electrochemical sensor based on a sepiolite clay nanoparticle-based electrochemical sensor for ascorbic acid detection in real-life samples. *Ionics* 2017; 1-9.
15. Gao W, Song J and Wu N. Voltammetric behavior and square-wave voltammetric determination of trepibutone at a pencil graphite electrode. *Journal of Electroanalytical Chemistry* 2005; 576(1):1-7.
16. Jesus CS and Diculescu VC. Redox mechanism, spectrophotometrical characterisation and voltammetric determination in serum samples of kinases inhibitor and anticancer drug dasatinib. *Journal of Electroanalytical Chemistry* 2015; 752:47-53.
17. Karimi-Maleh H, Shojaei AF, Tabatabaieian K, Karimi F. Shakeri S and Moradi R. Simultaneous determination of 6-mercaptopruine, 6-thioguanine and dasatinib as three important anticancer drugs using nanostructure voltammetric sensor employing Pt/MWCNTs and 1-butyl-3-methylimidazolium hexafluoro phosphate. *Biosensors and Bioelectronics* 2016; 86:879-884.
18. Zare HR, Rajabzadeh N, Nasirizadeh N and Ardakani MM. Voltammetric studies of an oracet blue modified glassy carbon electrode and its application for the simultaneous determination of dopamine, ascorbic acid and uric acid. *Journal of Electroanalytical Chemistry* 2006; 589(1):60-69.
19. Bayraktepe DE, Yazan Z and Polat K. Sensitive and selective voltammetric determination of anti- cancer agent shikonin on sepiolite clay/TiO₂ nanoparticle/MWCNTs composite carbon paste sensor and investigation of its electro- oxidation mechanism. *Journal of Electroanalytical Chemistry* 2016; 780:38-45.
20. Tiğ GA. Development of electrochemical sensor for detection of ascorbic acid, dopamine, uric acid and l-tryptophan based on Ag nanoparticles and poly (l-arginine)-graphene oxide composite. *Journal of Electroanalytical Chemistry* 2017; 807:19-28.
21. Guzmán A, Agüí L, Pedrero M, Yáñez-Sedeño P and Pingarron JM. Voltammetric Determination of Antibacterial Nitro-Compounds at Activated Carbon Fibre Microelectrodes. *Electroanalysis* 2004; 16(21):1763-1770.



Synthesis of Thiazole Derivatives as Antimicrobial Agents by Green Chemistry Techniques

Serpil Demirci¹  

1 Giresun University, Vocational High School of Health Services Department of Medical Services and Techniques, 28100, Giresun, Turkey.

Abstract: Amines (**2**) and (**26**) were obtained from the condensation of the corresponding amines with 3,4-difluoronitrobenzene. The reduction of nitro group produced the corresponding amines (**3** and **27**). The synthesis of esters (**7**, **12**, **19**, **28**) was carried out from the treatment of the amines, (**1**, **3**, **18**, **27**) with ethyl bromoacetate, then these compounds were converted to the corresponding hydrazides (**8**, **13**, **29**) by the treatment with hydrazine hydrate. The triazole was obtained from the intramolecular cyclisation of the corresponding carbothioamide in basic media and this compound was then converted to the morpholine-triazole-penicillin hybrid by a mannich reaction. The cyclocondensation of hydrazine carbothioamides (**9b**, **14**, **21**) or urea (**4**) with 2-bromo-1-(4-chlorophenyl)ethenone generated the thiazole derivatives. On the other hand, the treatment of **4**, **9b**, and **14** with ethyl bromoacetate yielded 4-oxo-1,3-thiazolidines (**6**, **11**, **16**). Three methods containing conventional, microwave, and ultrasound-mediated techniques were applied. Best results were assessed using microwave- and ultrasound-promoted procedures. The structures of the newly synthesised compounds were elucidated by spectroscopic techniques, and the antimicrobial activity screening studies were also performed. Some of them exhibited good to moderate activity on the test bacteria.

Keywords: Antimicrobial activity, microwave, imidazole, morpholine, green chemistry.

Submitted: January 06, 2018. **Accepted:** February 16, 2018.

Cite this: Demirci S. Synthesis of Thiazole Derivatives as Antimicrobial Agents by Green Chemistry Techniques. JOTCSA. 2018;5(2):393-414.

DOI: <http://dx.doi.org/10.18596/jotcsa.375716>.

***Corresponding author. E-mail:** demirciserpil17@gmail.com. **Tel/Fax:** ++90-507-923-4321, +90-454-310-2932.

INTRODUCTION

Although humans are accustomed to fighting with the invasion of such pathogens with both inherent defenses as well as medical protections, many bacteria succeed to get rid of our immunities and are resistant to most of synthetic or natural antibiotics caused by the excessive and prolonged use of currently available antibiotics, and this made microbial infections one of the foremost health crises worldwide.

Literature survey reveals that bacterial infections cause to hundreds of thousands of deaths annually and billions of dollars in healthcare expenses emphasizing the urgent need to constant push to discover and improve strategies to counter these threats (1–5). Molecular hybridization is one of the mostly referenced strategy aiming to overcome bacterial resistance involving the integration of two or more pharmacophoric subunits from molecular structure of previously reported bioactive molecules in one framework. The expected features from the newly designed architecture are having improved activity and efficacy than the parent compounds with less tendency to resistance, reduced side effects with maintaining the desired properties of the original version (6). In the studies aiming the discovery of new drug candidates, the combination of bioactive structural motifs in a single skeleton improving the overall biological efficacy has become the widely applied strategy (7).

Azoles are accepted as immensely important members of heterocyclic class of organic compounds since their existence in a number of synthetic or natural products with biological activity as privileged pharmacophores (8). Among these, imidazole scaffold constitutes a major pharmacophoric group responsible antifungal activity. Imidazole containing antifungal drugs such as econazole, miconazole, clotrimazole, ketoconazole, oxiconazole, sulconazole, *etc* control fungal infections by blocking ergosterol biosynthesis which is an essential component of fungal cell wall (8–11). Imidazole core constitutes also a part some of other the clinically used drugs such as acetomidate, cimetidine, omeprazole, lansoprazole, azomycine, flumazenil, thyroliberin, methimazole, acting as a pharmacophoric group or a substituent. Furthermore, the existence of imidazole nucleus in the structure of a bioactive agent may be preferable for increasing solubility in water. Due to this reason, the introduction of imidazole unit to a synthetic or natural product has become a frequently referenced methodology aiming to improve bioactivity (11,12). Moreover, imidazoles constitute a main structural unit of some biomolecules in human organisms including histidine, vitamin B12, histamine, and biotin. Another biomolecule Ribotide possessing 4(5)-aminoimidazole-5(4)-carboxamide structure acts as a key compound in the biosynthesis of natural purine component of RNA and DNA (11).

Another azole nucleus, thiazolidinone unit constitutes the core structure of a number of natural biomolecules, drugs and synthetic bioactive compounds possessing antimicrobial, antifungal, anticancer, and antidiabetic activity and is of considerable attention (7).

In the recent years, the literature has been enriched with progressive studies on the preparation and biological activities of morpholine derivatives (13). The morpholine unit has been extensively used in the drug design studies since its presence in the structure of a bioactive compound can supply some improvements in the pharmacokinetics. It constitutes functional unit of nearly 19 drugs approved by FDA. Linezolid, which is an oxazolidinone class antibacterial drug, contains a morpholine subunit in its structure. Moreover, The World Drug Index contains well over 100 drugs including a morpholine unit as a core scaffold, a capping fragment or a component in a hybrid system (14). Furthermore, some morpholine derivatives have been reported as anticancer, antifungal, antibacterial and antihypertensive agents. Some representative examples of bioactive morpholines are presented. The major structural feature doing morpholine ring so popular is the inclusion an oxygen, which forms a strong complex with its target participating in donor-acceptor type interactions with the substrate. Furthermore, oxygen displays a pharmacophoric feature by decreasing the basicity of nitrogen. In addition, if the nucleus is linked to a lipophilic skeleton, it improves the bioavailability of bioactive compound in oral administration by enhancing its solubility in water (15–19).

In recent years, the application of green methodologies has aroused as more efficient techniques environmentally. Compared with conventional methods, eco-friendly procedures have some advantages including decreased reaction time, improved yields, ease of work-up and isolation of products. Furthermore, polar and aprotic solvents which are often expensive, toxic and difficult to remove, are environmental pollutants.

Since these reasons, the focus has now shifted to eliminate or minimise the use of organic solvents with solvent-free methodologies yielding pure products with high yields. The application of microwave mediated procedures for the synthesis of organic compounds has supplied an efficient, safe, and ecofriendly technique with shorter reaction time (20, 21).

Sonication technique constitutes another methodology which supply clean and environmentally harmless procedure leading to the formation of bioactive compounds. In most of cases, the application of this method has led to take place organic reactions with higher yields and shorter reaction times (22,23).

It is accepted that both two methods have their own advantages. Although microwaves supply fast and appropriate heating for synthetic procedures, it has some limitations in mass transfer. On the other hand, ultrasonic irradiation provides strong physical mixing by cavitation but lacks

the ability to provide or induce high thermal energy leading to reaction (24). Even so, sonication has been applied successfully in many of organic reactions providing enhancement of reactions rates and yield as well as modification of the reaction pathway, greater selectivity, simplicity of operation, and energy-saving protocols. (25). Moreover, this way has led to develop a simple purification process suitable with the concept of green chemistry (26,27).

Continuing our efforts on the synthesis of novel antibacterial compounds, here we designed novel hybrid molecules including several heterocyclic units with biological activity. The *in vitro* antibacterial activity screening studies were carried towards some selected Gram (+) and Gram (-) bacteria and yeast like fungi. The effect of microwave and ultrasonic irradiations on the synthetic procedures was investigated as well.

MATERIALS AND METHODS

All chemicals were purchased from Fluka Chemie AG Buchs (Switzerland) and used without further purification. Melting points of the synthesised compounds were determined in open capillaries on a Büchi B-540 melting point apparatus and are uncorrected. Reactions were monitored by thin-layer chromatography (TLC) on silica gel 60 F254 aluminium sheets. The mobile phase was ethyl acetate: diethyl ether (1:1, v:v), and detection was made using UV light. FT-IR spectra were recorded using a Perkin Elmer 1600 series FTIR spectrometer. ¹H NMR and ¹³C NMR spectra were recorded in DMSO-d₆ on a BRUKER AVENE II 400 MHz NMR Spectrometer (400.13 MHz for ¹H and 100.62 MHz for ¹³C). The chemical shifts are given in ppm relative to Me₄Si as an internal reference, *J* values are given in Hz. Microwave and ultrasound-mediated syntheses were carried out using monomode CEM-Discover microwave apparatus and Bandelin Sonorex Super RK102H ultrasonic bath, respectively. The elemental analysis was performed on a Costech Elemental Combustion System CHNS-O elemental analyzer. All the compounds gave C, H and N analysis within ±0.4% of the theoretical values. The Mass spectra were obtained on a Quattro LC-MS (70 eV) Instrument.

General method for the preparation of compounds **2**, **26**

Method 1. To a solution of 3-(1*H*-imidazol-1-yl)propan-1-amine (for **2**) or 2-morpholino ethanamine (for **26**) (10 mmol) in dry acetonitrile, 3,4-difluoronitrobenzene (10 mmol) were added dropwise at 0-5 °C, temperature was then allowed to reach to room temperature and the reactions were maintained for 10 h until TLC showed completion. The solvent was evaporated under reduced pressure and the obtained solid was recrystallised from an appropriate solvent to give the target product. **Method 2.** The mixture of 3-(1*H*-imidazol-1-yl)propan-1-amine (10 mmol) and 3,4-difluoronitrobenzene (10 mmol) were irradiated in monomode microwave reactor in closed vessel with pressure control at 100 W (for **2**) or 100 W (for **26**), for 8-10 min. **Method 3.** The mixture of 3-(1*H*-imidazol-1-yl)propan-1-amine (for **2**) or 2-morpholinoethanamine (for

26) (10 mmol) and 3,4-difluoronitrobenzene (10 mmol) was sonicated at 45-70 kHz, 25 °C for 5-30 min.

General method for the preparation of compounds **3** and **27**

Method 1. Hydrazine hydrate (25 mmol) was added to a solution of compound **2** (for **3**) or **26** (for **27**) (10 mmol) in 1-butanol containing Pd/C (1 mmol) and the mixture was allowed to reflux in an oil bath for 12 h. catalyst was removed by filtration on celite, the solvent was removed under reduced pressure, and the obtained crude product was purified by thin layer chromatography (20x20 cm. normal phase silica-coated glass plate 60 F254, ethyl acetate:chloroform (3:1), 100 mL). **Method 2.** The mixture of hydrazine hydrate (25 mmol), Pd/C (1 mmol) and compound **2** (for **3**) or **26** (for **27**) (10 mmol) in 1-butanol was irradiated in a monomode microwave reactor with pressure control in closed vessel at 200 W, 150 °C for 8-30 min. Catalyst was removed by filtration on celite and the solvent was removed under reduced pressure and the obtained crude product was purified by thin layer chromatography (20x20 cm. normal phase silica-coated glass plate 60 F254, ethyl acetate-chloroform (3:1), 100 mL). **Method 3.** The mixture of hydrazine hydrate (25 mmol), Pd/C (1 mmol) and compound **2** (for **3**) or **26** (for **27**) (10 mmol) in 1-butanol was sonicated at 70 kHz, 25 °C for 5-35 min. the catalyst was removed by filtration on celite, the solvent was removed under reduced pressure, and the obtained crude product was purified by thin layer chromatography (20x20 cm. normal phase silica-coated glass plate 60 F254, ethyl acetate-chloroform (3:1), 100 mL).

General method for the preparation of compounds **4**, **9a**, **9b**, **14**, **21**

Method 1. The solution of the corresponding compounds **3**, **8**, **13** or **20** (10 mmol) in dry dichloromethane was stirred with benzyl- or phenylisothiocyanate at room temperature for 12-20 h. The solvent was evaporated under reduced pressure and the obtained solid was recrystallised from an appropriate solvent to give the target product. **Method 2.** The mixture of the corresponding compound **3**, **8**, **13** or **20** (10 mmol) and benzyl- or phenylisothiocyanate was irradiated in a monomode microwave reactor in closed vessel with the pressure control at 150 W, 100 °C for 15 min. The obtained solid was purified by crystallization from an appropriate solvent to give the target product. **Method 3.** The mixture of the corresponding compound **3**, **8**, **13** or **20** (10 mmol) and benzyl- or phenylisothiocyanate was sonicated at 60-70 kHz, 35 °C for 15 min. The obtained solid was purified by crystallization from an appropriate solvent to give the target product.

General method for the synthesis of compounds **6**, **11** and **16**

Method 1. Ethyl bromoacetate (10 mmol) was added to a solution of the corresponding carbothioamide (**4**, **9b** and **14**) (10 mmol) in absolute ethanol and the mixture was refluxed in the presence of dried sodium acetate (20 mmol) for 16-18 h. The mixture was then cooled to room temperature, poured into ice-cold water while stirring, and left overnight in cold. The solid

formed was filtered off, washed with water 3 times, and recrystallised from an appropriate solvent to afford the desired compound. **Method 2.** The mixture of ethyl bromoacetate (10 mmol), the corresponding carbothioamide (10 mmol) and dried sodium acetate (20 mmol) was irradiated in a monomode microwave reactor with pressure control at 100 W, 100 °C for 12 min. The mixture was then poured into ice-cold water while stirring, and left overnight in cold. The formed solid was filtered off, washed with water 3 times, and recrystallised from an appropriate solvent to afford the desired compound. **Method 3.** The mixture of ethyl bromoacetate (10 mmol), the corresponding carbothioamide (10 mmol) and dried sodium acetate (20 mmol) was sonicated at 50 kHz, 30 °C for 15 min. The mixture was then poured into ice-cold water while stirring, and left overnight in cold. The formed solid was filtered off, washed with water 3 times, and recrystallised from an appropriate solvent to afford the desired compound.

General Method for the Synthesis of Compounds 5, 10, 15 and 22

Method 1. 2-Bromo-1-(4-chlorophenyl)ethanone (10 mmol) and dried sodium acetate (20 mmol) were added to a solution of the corresponding carbothioamine (**4, 9b, 14, 21**) in absolute ethanol, and the mixture was refluxed for 16-18 h. Then, the reaction content was poured into ice-cold water while stirring, and left overnight in the cold. The formed solid was filtered off, washed with water 3 times, and recrystallised from acetone to afford the desired compound.

Method 2. 2-Bromo-1-(4-chlorophenyl)ethanone (10 mmol) and dried sodium acetate (20 mmol) were added to a solution of the corresponding carbothioamine (**4, 9b, 14, 21**) in absolute ethanol, and the mixture was irradiated in a monomode microwave reactor with pressure control in closed vessel at 150 W, 80 °C for 15 min. Then, the reaction content was poured into ice-cold water while stirring, and left overnight in the cold. The formed solid was filtered off, washed with water 3 times, and recrystallised from acetone to afford the desired compound. **Method 3.** 2-Bromo-1-(4-chlorophenyl)ethanone (10 mmol) and dried sodium acetate (20 mmol) were added to a solution of the corresponding carbothioamine (**4, 9b, 14, 21**) in absolute ethanol, and the mixture was sonicated at 60 kHz, 25 °C for 18 min. Then, the reaction content was poured into ice-cold water while stirring, and left overnight in the cold. The formed solid was filtered off, washed with water 3 times, and recrystallised from acetone to afford the desired compound.

General Method for the Synthesis of Compounds 7, 12, 19 and 28

Method 1. Ethyl bromoacetate (10 mmol) was added to a mixture of the corresponding compound **1, 3, 18** or **27** (10 mmol) in dry tetrahydrofuran dropwise at 0-5 °C. Then, the reaction mixture was allowed to reach room temperature and stirred for 16-24 h in the presence of triethylamine (10 mmol). The precipitated triethylammonium salt was removed by filtration and the resulting solution was evaporated under reduced pressure to dryness. Then the acetonitrile was removed using a rotary evaporator and the obtained crude product was purified by thin layer chromatography (20x20 cm. normal phase silica-coated glass plate 60 F254, ethyl acetate-chloroform (3:1), 100 mL). **Method 2.** Ethyl bromoacetate (10 mmol) was added to the

mixture of the corresponding compounds **1**, **3**, **18** or **27** (10 mmol) in dry tetrahydrofuran dropwise at 0-5 °C. Then, the reaction mixture was irradiated in a monomode microwave reactor with pressure control in closed vessel corresponding to 80 W, 50 °C for 18 min. The precipitated triethylammonium salt was removed by filtration and the resulting solution was evaporated under reduced pressure and the obtained crude product was purified by thin layer chromatography (20x20 cm. normal phase silica-coated glass plate 60 F254, ethyl acetate-chloroform (3:1, v:v), 100 mL). **Method 3.** Ethyl bromoacetate (10 mmol) was added to the mixture of the corresponding compound **1**, **3**, **18** or **27** (10 mmol) in dry tetrahydrofuran dropwise at 0-5 °C. Then, the reaction mixture was sonicated at 40 kHz, 25 °C for 20 min. The precipitated triethylammonium salt was removed by filtration and the resulting solution was evaporated under reduced pressure and the obtained crude product was purified by thin layer chromatography (20x20 cm. normal phase silica-coated glass plate 60 F254, ethyl acetate-chloroform (3:1, v:v), 100 mL).

General method for the synthesis of compounds **8**, **13**, **20** and **29**

Method 1. Hydrazine hydrate (25 mmol) was added to the solution of the corresponding ester (**7**, **12**, **19**, and **28**) (10 mmol) in 1-butanol, and the mixture was heated under reflux for 5 h. On cooling, the reaction mixture to room temperature, a white solid appeared. The crude product was filtered off and recrystallised from ethyl acetate to afford the desired compound. **Method 2.** The mixture of hydrazine hydrate (25 mmol) and the corresponding ester (**7**, **12**, **19**, and **28**) (10 mmol) in *n*-butanol, and the mixture was irradiated in a monomode microwave reactor with pressure control at 200 W 150 °C for 14 min. On cooling, the reaction mixture to room temperature, a white solid appeared. The product obtained was filtered off and used without further purification. **Method 3.** The mixture of hydrazine hydrate (25 mmol) and the corresponding ester (**7**, **12**, **19**, and **28**) (10 mmol) in *n*-butanol, and the mixture was sonicated at 40-70 kHz, 50 °C for 15-20 min. On cooling the reaction mixture to room temperature, a white solid appeared. The product obtained was filtered off and used without further purification.

General method for the synthesis of compounds **17a-d** and **25a-b**

Method 1. A solution of the corresponding compounds **3** or **20** (10 mmol) in absolute ethanol was refluxed with the suitable aldehyde for 3 h. Then, the reaction content was allowed to reach room temperature, and a solid appeared. This crude product was filtered off and recrystallised from acetone to give the desired compound. **Method 2.** A mixture of the corresponding compound **3** or **20** (10 mmol) and the suitable aldehyde in absolute ethanol was irradiated in a monomode microwave reactor with pressure control in closed vessel at 100 W, 80 °C for 8 min. Then, the reaction content was allowed to reach room temperature, and a solid appeared. This crude product was filtered off and recrystallised from acetone to give the desired compound. **Method 3.** A mixture of the corresponding compound **3** or **20** (10 mmol) and the suitable aldehyde in absolute ethanol was sonicated at 70 kHz, 30 °C for 5 min. Then, the reaction

content was allowed to reach room temperature, and a solid appeared. This crude product was filtered off and recrystallised from acetone to give the desired compound.

3-[[[(2-Morpholinoethyl)amino]methyl]-4-phenyl-1H-1,2,4-triazole-5(4H)-thione (23).

Method 1. A solution of compound **21** (10 mmol) in ethanol:water (1:1, v:v) was refluxed in the presence of 2 M NaOH for 3 h, and then the resulting solution was cooled to room temperature and acidified to pH 7 with 37% HCl. The precipitate formed was filtered off, washed with water, and recrystallised from ethanol:water (1:1, v:v) to afford the desired compound.

Method 2. The mixture of 2 M NaOH (2,5 mL) and compound **21** (1 mmol) in water was irradiated in monomode microwave reactor in closed vessel with pressure control at 200 W for 12 min. (hold time). Upon acidification of reaction content to pH 7 with 37% HCl, a white solid appeared. This crude product was filtered off, washed with water, and recrystallised from ethanol:water (1:1, v:v) to afford the desired compound. **Method 3.** A solution of compound **21** (10 mmol) in ethanol:water (1:1 v:v) and 2 M NaOH was sonicated at 70 kHz, 30 °C for 15 min. Then, the reaction content was allowed to reach room temperature, and acidified to pH 7 with 37% HCl. The precipitate formed was filtered off, washed with water, and recrystallised from ethanol:water (1:1) to afford the desired compound. Recrystallised from butyl acetate:diethyl ether (2:1, v:v)

3,3-Dimethyl-6-[[[(3-[[[(2-morpholinoethyl)amino]methyl]-4-phenyl-5-thioxo-4,5-dihydro-1H-1,2,4-triazol-1-yl)methyl]amino]-7-oxo-4-thia-1-azabicyclo[3.2.0]heptane-2-carboxylic acid (24).

Method 1. 6-Aminopenicillanic acid (10 mmol) was added into a solution of compound **23** (10 mmol) dry tetrahydrofuran containing HCl (50 % mmol) and the mixture was stirred at room temperature in the presence of formaldehyde (%37, 30 mmol) for 3 h. Then, the solvent was evaporated under reduced pressure and a solid appeared. The crude product was recrystallised from DMF:H₂O (1:3, v:v) solvent to give the desired compound. **Method 2.** The mixture of appropriate secondary amine (6-aminopenicillanic acid) (1 mmol), compound **23** (1 mmol) HCl (50 % mmol) and formaldehyde (%37, 3 mmol) was irradiated in monomode microwave reactor in closed vessel with pressure control at 100 W for 5 min. The solid obtained was purified by recrystallisation from DMF:H₂O (1:3, v:v) to give the desired compound. **Method 3.** 6-aminopenicillanic acid (10 mmol) was added into a solution of compound **23** (10 mmol) dry tetrahydrofuran containing HCl (50 % mmol) was sonicated at 40 kHz, 30 °C for 10 min. Then, the reaction content was allowed to reach room temperature. The solvent was then evaporated under reduced pressure and a solid appeared. The crude product was recrystallised from DMF:H₂O (1:3) solvent to give the desired compound.

Antimicrobial activity

The test microorganisms were obtained from the Refik Saydam Hifzissihha Institute (Ankara, Turkey) and were as follows: *Escherichia coli* (E. coli) ATCC35218, *Yersinia pseudotuberculosis* (Y. pseudotuberculosis) ATCC911, *Pseudomonas aeruginosa* (P. aeruginosa) ATCC43288, *Enterococcus faecalis* (E. faecalis) ATCC29212, *Staphylococcus aureus* (S. aureus) ATCC25923, *Bacillus cereus* (B. cereus) 709 Roma, *Mycobacterium smegmatis* (M. smegmatis) ATCC607, *Candida albicans* (C. albicans) ATCC60193 and *Saccharomyces cerevisiae* (S. cerevisia) RSKK 251 which are laboratory strains. All the newly synthesised compounds were weighed and dissolved in DMSO to prepare extract stock solution of 20.000 µg/mL.

The antimicrobial effects of the substances were tested quantitatively in respective broth media by using double microdilution and the minimal inhibition concentration (MIC) values (µg/mL) were determined. The antibacterial and antifungal assays were performed in Mueller-Hinton broth (MH) (Difco, Detroit, MI) at pH 7.3 and buffered Yeast Nitrogen Base (Difco, Detroit, MI) at pH 7.0, respectively. The micro dilution test plates were incubated for 18-24 h at 35 °C. Brain Heart Infusion broth (BHI) (Difco, Detroit, MI) was used for *M. smegmatis*, and incubated for 48-72 h at 35 °C (31). Ampicillin (10 µg), streptomycin, and fluconazole (5 µg) were used as standard antibacterial, antimycobacterial, and antifungal drugs, respectively. Dimethylsulfoxide with dilution of 1:10 (v:v) was used as solvent control. The results obtained were submitted in Table 2.

Antimicrobial activity

All compounds were screened for their antimicrobial activities, and the results are presented in Table 2. Compounds with low activity (**3**, **14**, **22**) were not included. Most of the newly synthesised compounds exhibited good to slight activity on some of the test microorganisms. No clear structure-activity relationships could be detected, showing that the antibacterial activity is significantly affected by the structure of the compound.

It is evident from Table 2 that compounds **17c**, **24** and **25** exhibited excellent activity on *Mycobacterium smegmatis* (Ms), a non-typical tuberculosis factor leading to morbidity and mortality with the mic values between 0.24-1.87 µg/µL. Further, these compounds are more active than standard drug streptomycin with the mic of 4 µg/µL. Other compounds **2**, **9b**, **13**, **20** and **21** displayed good-moderate activity on Ms with the mic values varying between 7.13-31.3 µg/µL. The imine derivatives **17a-c** demonstrated quite good activity towards the test bacteria with the mic values of 0.24-15.63 µg/µL. On the other hand, the remaining imine compound **17d**, showed moderate activity on *Staphylococcus aureus* (Sa) with the mic 31.25 µg/µL. Five compounds, **8**, **13**, **20**, **25b** and **29** were found to be more active than ampicillin against *Pseudomonas aeruginosa* (Pa). Among these, compound **20** also displayed activity towards *Yersinia pseudotuberculosis* (Yp), and compound **25b** towards *Yersinia*

pseudotuberculosis (Yp) and *Escherichia coli* (Ec). In addition to imines **17a-c** and **25b**, compounds **13**, **20**, **23** and **28** showed activity on *Bacillus cereus* (Bc). In fact, the activity of **28** on Bc was better than ampicillin. Compound **24** demonstrated good activity towards *Enterococcus faecalis* (Ef) with the mic of 30 µg/µL. No significant inhibition was observed on yeast like fungi *Candida albicans* (Ca) and *Saccharomyces cerevisiae* (Sc).

RESULTS AND DISCUSSION

In the present study, the conventional and ecofriendly synthesis and antimicrobial activity screening studies of new thiomorpholine derivatives containing different substituents has been intended. The synthetic strategy of the title compounds was outlined in Schemes 1-6. The condensation of both 3-(1*H*-imidazol-1-yl)propan-1-amine (tryptamine, **1**) and 2-morpholinoethanamine (**18**) with 3,4-difluoronitrobenzene under thermal heating and also microwave and ultrasonic irradiation led to the formation of compounds **2** and **26** respectively, which were then subjected to catalytic hydrogenation to yield the corresponding substituted anilines (**3** and **27**). The reaction was performed under reflux conditions as well as under microwave (MW) and ultrasonic (US) irradiation with a view to maximizing the yield and minimizing the reaction time. Therefore, the yield of the reaction was increased to 83% however, more substantially, the entire consumption time of starting compounds was reduced from 10 h with thermal heating to a remarkable 25 min using MW irradiation and 30 min with sonication. The best MW power in terms of yields and product stability was defined as 80 W and 50 °C in closed vessel in solvent free media. On the other hand, the maximum power of ultrasonic irradiation was determined as 45 kHz (Table 1).

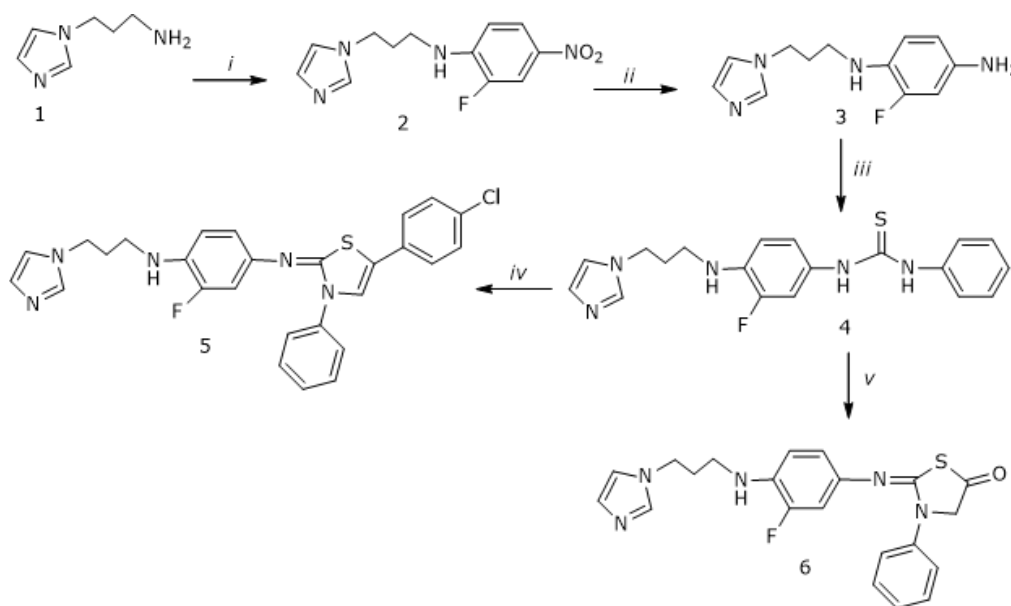
Table 1: Microorganisms and their minimum inhibitory concentrations.

Comp No	Microorganisms and Minimal Inhibitory Concentration($\mu\text{g}/\mu\text{L}$).								
	Ec	Yp	Pa	Sa	Ef	Bc	Ms	Ca	Sc
2	-	-	500	250	500	-	31.3	250	250
4	-	-	-	78,8	-	-	-	-	39,4
5	-	62.5	-	250	-	500	-	-	-
6	125	125	-	-	-	-	-	500	250
7	-	125	-	62,5	62,5	-	500	500	-
8	32.5	62.5	62.5	-	250	62.5	125	-	-
9a	-	-	-	-	-	-	62,5	62,5	62,5
9b	-	-	-	-	-	-	15,6	62,5	62,5
10	-	-	-	-	-	-	500	62,5	31,3
11	-	-	-	-	-	-	225	225	225
12	-	-	-	28,7	-	57,0	<7,13	-	456
13	15,6	7,8	62,5	31,3	62,5	31,3	31,3	125	125
15	-	-	-	-	-	-	250	125	125
16	-	-	-	-	-	-	525	131	131
17a	1.95	15.63	7.81	7.81	3.91	15.63	125	-	-
17b	0.98	15.65	-	1.95	1.95	3.91	62.5	-	-
17c	0.24	1.95	1.95	0.49	0.98	0.98	<0.24	-	-
17d	250	250	-	31.25	250	125	-	-	-
19	-	-	-	-	250	-	-	-	-
20	31.3	15.6	31.3	31.3	62.5	31.3	15.6	125	125
21	-	-	-	500	250	500	31.3	62.5	62.5
23	-	-	-	15.6	62.5	31.3	7.8	125	125
24	120	120	120	60	30	60	1,87	120	60
25a	-	-	-	-	125	-	-	31.3	-
25b	15.6	31.3	15.6	31.3	31.3	31.3	0.97	125	500
26	-	-	-	-	-	250	-	-	-
27	-	500	-	62.5	62.5	62.5	62.5	500	500
28	125	-	-	62.5	-	4.0	62,5	250	500
29	62.5	62.5	62.5	125	250	62.5	125	-	-
Amp.	10	18	>128	10	35	15			
Strep.							4		
Flu								<8	<8

Ec: *Escherichia coli* ATCC 25922, Yp: *Yersinia pseudotuberculosis* ATCC 911, Pa: *Pseudomonas aeruginosa* ATCC 27853, Sa: *Staphylococcus aureus* ATCC 25923, Ef: *Enterococcus faecalis* ATCC 29212, Bc: *Bacillus cereus* 702 Roma, Ms: *Mycobacterium smegmatis* ATCC607, Ca: *Candida albicans* ATCC 60193, *Saccharomyces cerevisiae* RSKK 251, Amp.: Ampicillin, Str.: Streptomycin, Flu.: Fluconazole, (—): no activity

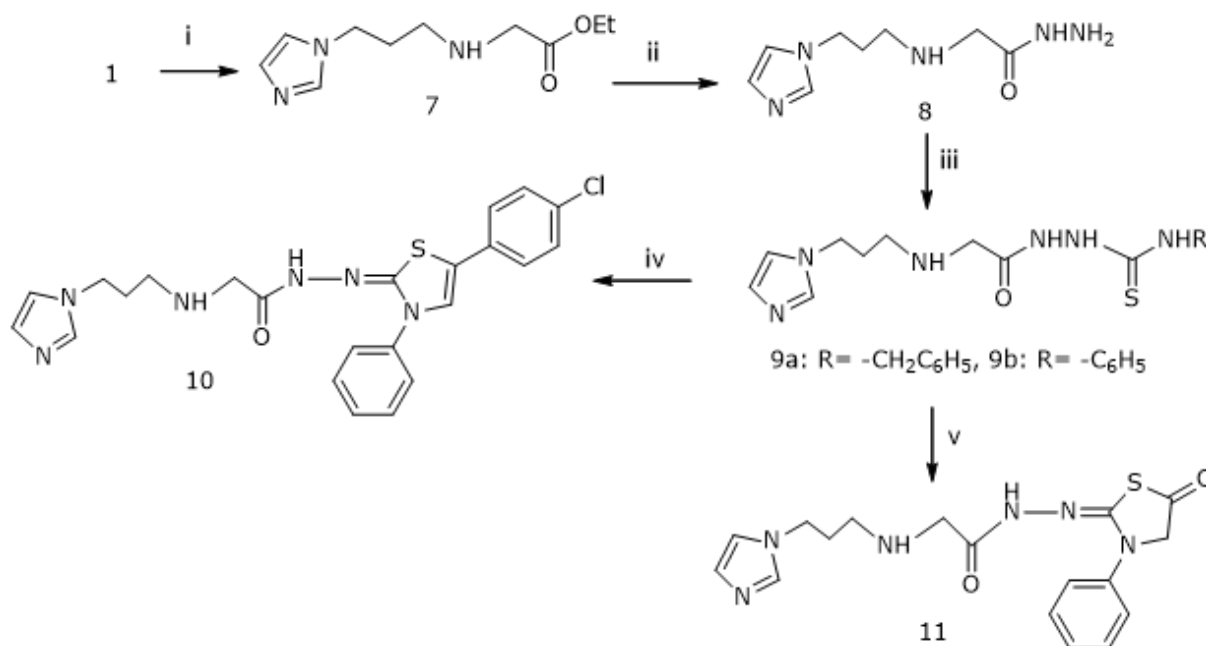
Further, the latter two techniques did not require the use of a toxic solvent such as acetonitrile, which was used as reaction solvent in the conventional method. In order to compare the advantages of all three methods namely ultrasound sonication, microwave irradiation, and conventional method, the reduction of nitro group on compound **2** and **26** was performed applying all three techniques. Compared with conventional method, ultrasonic irradiation reduced the reaction time from 600 min to 5–30 min and rise the yields from 62–60% to 83–90. The comparison of the microwave and ultrasonic irradiation showed that the yields were too close to each other and they requested nearly the same reaction time. Therefore, sonication and microwave irradiation allowed a fast, eco-friendly, and effective synthetic procedure. The formation of compounds **2** and **26** was confirmed by recording their FT-IR, ^1H NMR, ^{13}C NMR, LC-MS spectra and elemental analysis results. Two sharp peaks at 1483, 1330 (for **2**) and 15313, 1329 (for **26**) confirmed the presence of nitro group. The shifting of these peaks to 3330, 3215 (for **3**) and 3336, 3223 (for **27**) supported the reduction of nitro group to primary amine. ^1H NMR spectra of compounds **3** and **27** showed a new D_2O exchangeable singlet at 4.49 (for **3**) and 4.54 (for **27**) ppm which was attributed to amine function in addition to the expected ones from compounds **3** and **27**. The molecular ion peak of $[\text{M}]$ and/or $[\text{M}+1]$ ($[\text{M}+1]=265.28$, $[\text{M}+1]=235.17$, $[\text{M}+1]=270.12$, $[\text{M}]=239.21$) corresponded to the molecular masses of the compounds **2**, **3**, **26** and **27**.

Compounds **3**, **8**, **13**, **20** were further treated with benzyl- and/or phenyl isothiocyanate to afford the corresponding urea or carbothioamides (**4**, **9a**, **9b**, **14**, **21**). With the intent the optimisation of reaction conditions, MW and US mediated techniques were performed as well and the reaction yielding compound **4** was selected as model reaction. Diverse reaction factors were tested on the model reaction and was monitored by TLC (Table 1).



Scheme 1: i: 3,4-difluoronitrobenzene, ii: NH_2NH_2 , Pd/C, iii: phenylisothiocyanate, iv: 2-bromo-1-(4-chlorophenyl)ethanone, NaOAc, v: ethylbromoacetate, NaOAc.

In order to get further improvement for these synthetic procedures, the model reaction was also implemented in different solvents such as EtOH, THF, H₂O, and DCM. The results of these analyses indicated that the experiments in solvent led to relatively lower the reaction yield and prolonged reaction time compared with solvent free media in the MW- and US-mediated methods, while dichloromethane was the best solvent in the conventional method at room temperature. Therefore, we next carried out the above model reaction under MW and US irradiation, and the targeted product was obtained in nearly quantitative yield within 5 min. The remaining compounds **4**, **9a**, **9b**, **14**, and **21** were obtained under the above optimised conditions. The most prominent peak in ¹³C NMR spectra of these compounds at 172-183 ppm confirmed the presence of thioamide carbon. The stretching peak derived from this group appeared at 1241-1287 cm⁻¹ in the FT-IR spectra of carbothioamides (**4**, **9a**, **9b**, **14**, and **21**). Further, the carbothiamides except **9a** were cyclised to 1,3-thiazoles (**5**, **10**, **15**, and **22**) by the condensation with 2-bromo-1-(4-chlorophenyl)ethanone under reflux, microwave and ultrasound mediated conditions. Literature findings demonstrated that the synthesis of 1,3-thiazole and 1,3-thiazolidinone derivatives require the harsh reaction conditions with long reaction times and relatively lower yields and difficult product isolation (28–30).



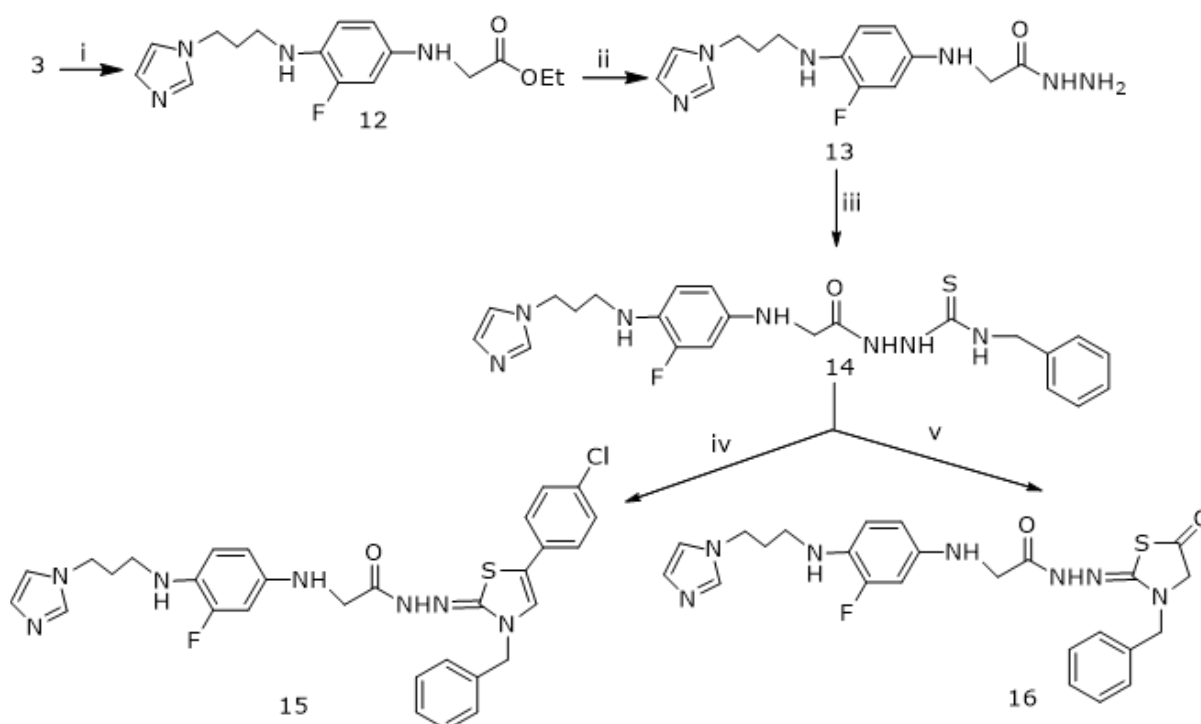
Scheme 2: i: Ethylbromoacetate, triethylamine, ii: NH₂NH₂, iii: benzylisothiocyanate, iv: 2-Bromo-1-(4-chlorophenyl)ethanone, NaOAc, v: ethylbromoacetate, NaOAc.

The optimisation analyses indicated that 5 min was the optimal reaction total time at 150 W maximum MW irradiation with the maximum product formation varying between 89-97% in ethanol. On the other hand, in the US irradiated method, sonication time was established to be 5-15 min with high yield (96%) at 60 kHz, 25 °C. The formation of 1,3-thiazoles (**5**, **10**, **15**, and **22**) was confirmed from the corresponding spectra. With the conversion of thioamides (**4**, **9b**, **14**, and **21**) to 1,3-thiazoles (**5**, **10**, **15**, and **22**), the signal belonging to C=S absorption

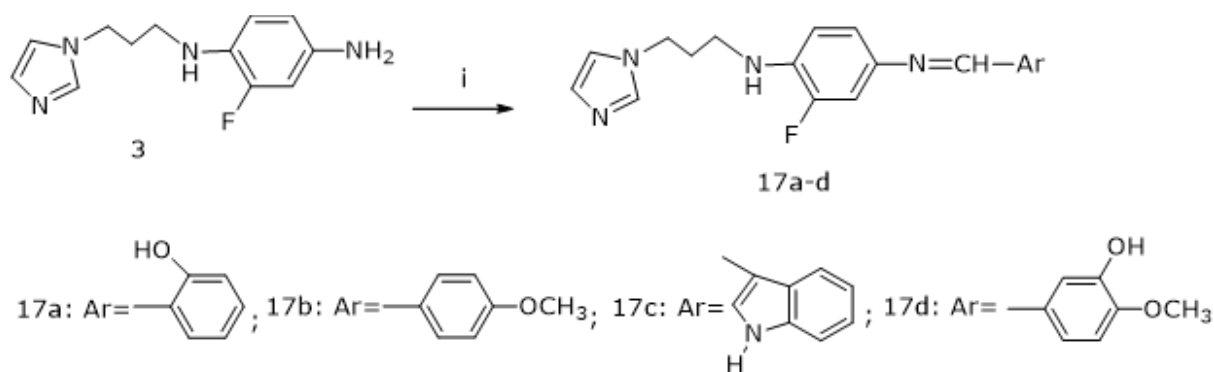
disappeared in the FT-IR spectrum, while additional signals derived from C-4 proton of 1,4-thiazole ring and 4-chlorophenyl substituent were observed at the related chemical shift values in the ^1H NMR spectra.

The ^{13}C NMR spectra of these compounds displayed signals originated from C-4 and C-5 carbons of 1,3-thiazole ring between 117.33-126.18 and 118.26-130.41 ppm as expected. Moreover, the presence of $[\text{M}]^+$ and/or $[\text{M}+1]^+$ ion peak in the mass spectrum was in accordance with their molecular weights, and these compounds exhibited reasonable elemental analysis data. The cyclisation of **4**, **9b** and **14** with ethyl bromoacetate generated the corresponding 1,3-thiazolidinones (**6**, **11** and **16**).

To optimise MW and US irradiation conditions, compound **6** was selected as the model product, MW and US were implemented at different power values of 100 and 150 W and ultrasound frequencies of 40 and 50 kHz, respectively. The complete consumption of the corresponding compound **4** with best yield was monitored upon microwave irradiation at 80 °C for 12 min at 100 W maximum power, while the optimum reaction parameters for sonication were 50 kHz, 30 °C and 15 min (Table 1).



Scheme 3.i: Ethylbromoacetate, triethyl amine, ii: NH_2NH_2 , iii: benzylisothiocyanate, iv: 2-Bromo-1-(4-chlorophenyl)ethanone, v: ethyl bromoacetate, NaOAc.

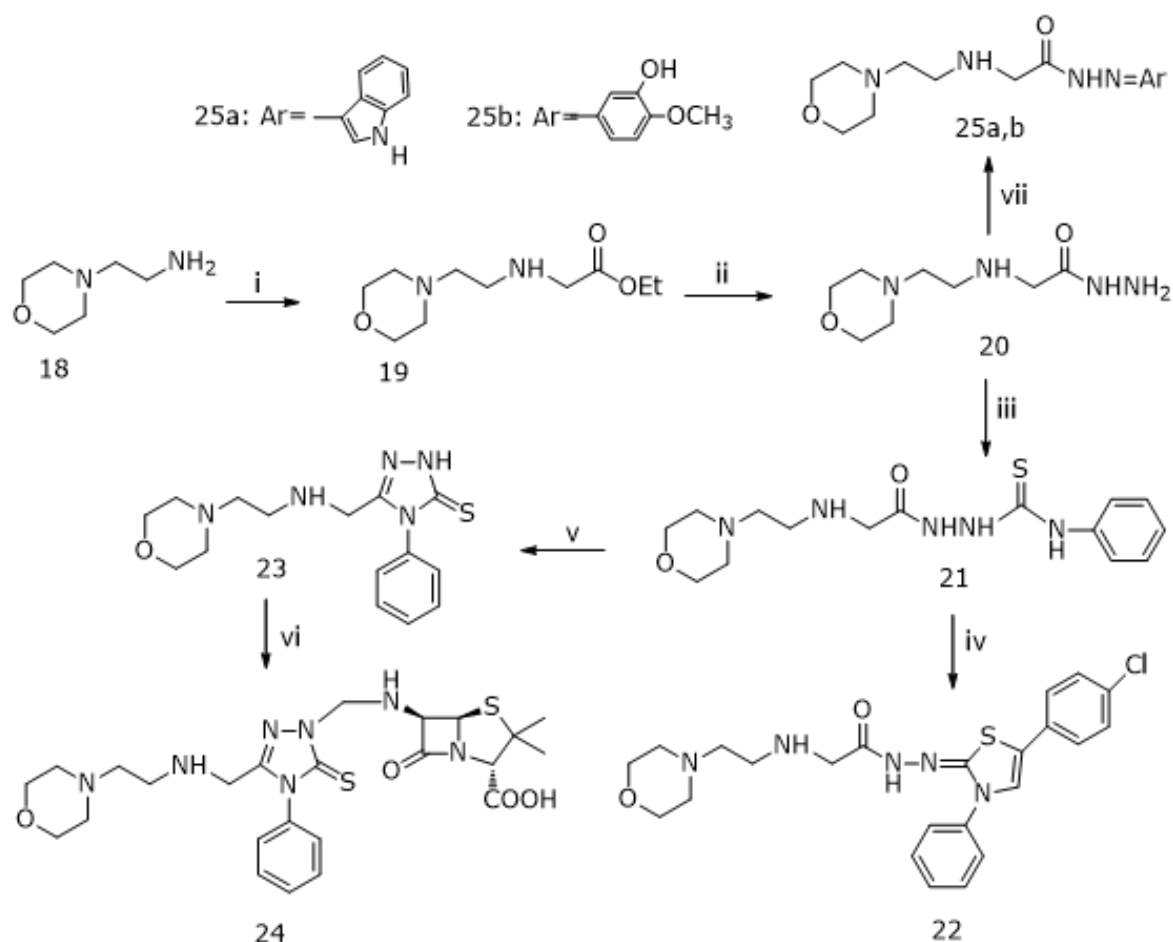


Scheme 4. i: suitable aldehyde, ethanol, reflux, 3 h.

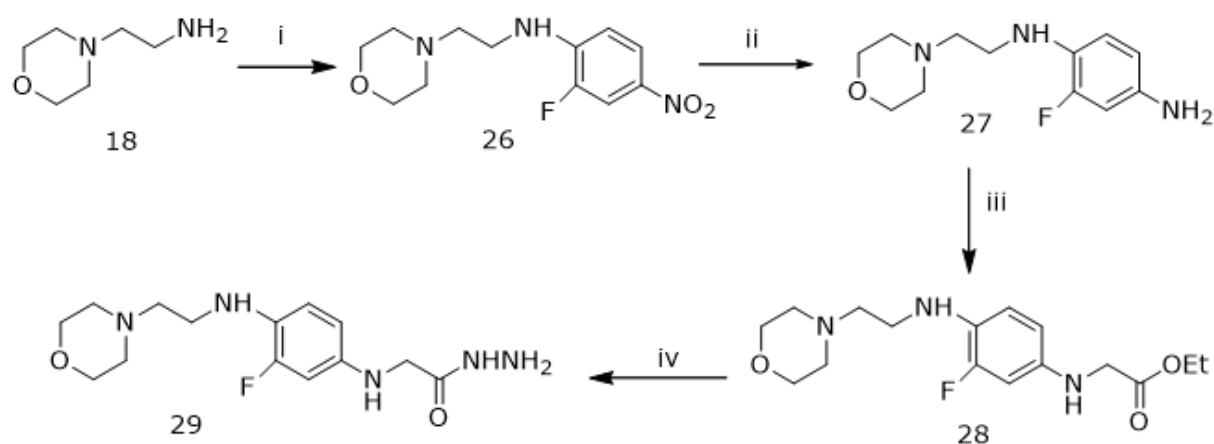
The FT-IR spectra of 1,3-thiazolidinones displayed a peak in the wavenumber value of the thiocarbonyl absorption from 1227-1287 cm^{-1} to 1701-1731 cm^{-1} which represents characteristic carbonyl band at the position 5 of 1,3-thiazolidinone ring. The disappearances of two NH signals and the appearance of CH_2 protons of 1,3-thiazolidin-5-one ring at 4.06-4.79 ppm in the ^1H NMR spectra supported the formation of 1,3-thiazolidinones **6**, **11**, and **16**.

These products gave mass spectral and elemental analysis data corresponding to the proposed structures. ^{13}C NMR spectra of these compounds (**6**, **11**, and **16**) exhibited peaks for C-4 and C-5 carbons at 32.02-33.23 ppm and 167.41-181.75 ppm, respectively which is consistent with formation of 1,3-thiazolidinone ring. The synthesis of esters (**7**, **12**, **19**, and **28**) was achieved by the condensation of **1**, **3**, **18**, and **27** with ethylbromoacetate in the presence of triethyl amine in THF under conventional, MW and ultrasonic conditions. Under MW irradiation, maximum yield and minimum reaction time was specified as 50 $^\circ\text{C}$, 80 W with the yields varying between 94-100%. On the other hand, sonication of the reaction mixtures resulted in a bit better yields, while reaction times of both methods (MW and US) were nearly the same.

In the ^1H NMR spectra, the shift in the peak of NH_2 from 4.49-4.54 ppm to 8.05-9.11 ppm attributed to NH proton and the presence additional signals due to ester function at the appropriate chemical shift values verified the condensation. The treatment of **7**, **12**, and **19** and **28** with hydrazine hydrate afforded the corresponding acetohydrazides (**8**, **13**, **20** and **29**) which was established by the appearance of NHNH_2 stretching bands of hydrazide function in the FT-IR spectrum. In ^1H NMR, the appearance of NH_2 and NH protons and disappearance of signals for CH_3 and two CH_2 protons confirmed the formation of the target products (**8**, **13**, **20**, and **29**).



Scheme 5. i: Ethylbromoacetate, triethylamine, ii: NH_2NH_2 , iii: phenylisothiocyanate, iv: 2-Bromo-1-(4-chlorophenyl)ethanone, NaOAc, v: NaOH (aq), vi: 6-aminopenicillanic acid, formaldehyde, HCl, vii: suitable aldehyde, r.t, 3 h.



Scheme 6. i: 3,4-difluoronitrobenzene, ii: NH_2NH_2 , Pd/C, iii: ethyl bromoacetate, triethylamine, iv: NH_2NH_2 .

The synthesis of 1,2,4-triazole (**23**) was carried out from the intramolecular cyclisation of thioamide **21** in the basic media. The reaction was carried out in water as a non-toxic solvent under thermal, microwave and ultrasonic conditions. MW and US mediated techniques led to higher yields; however, the virtual effect of MW assistance and sonication was on reaction times

changing from 3 h to 5-15 min with increased yields from 79% to 89% (for MW)–80% (for US). Among the latter two methods, the microwave irradiation resulted in a bit better reaction yield for this condensation. The supplemental support verifying the structures of these compounds was obtained by LC-MS spectrum, and these compounds gave elemental analysis data confirming the proposed structures.

The 1,2,4-triazole **23** was then subjected to a one pot three component condensation with R(+)-6-aminopenicillanic acid to yield compound **24**, the structure of which was verified by using spectroscopic techniques. The synthesis of imine compounds, **17a-d** and **25a,b** was performed from the reaction of hydrazides **3** and **20** with the corresponding aldehydes namely, salicylaldehyde, anisaldehyde, vanillin and indol-3-carbaldehyde which were clearly evident with the disappearance of NH₂ signals in the ¹H NMR spectra. Instead, new signal due to azomethine proton was recorded at 8.35-8.52 ppm. The imine-carbon resonated at 153.29-141.22 ppm in the ¹³C NMR spectra.

Other signals originated arylidene moiety were recorded at the expected chemical shift values. Furthermore, the mass spectral data and elemental analysis results are in accordance with their structures. The proton NMR observations revealed that, two singlets belonging to two NH protons were disappeared with the formation of the triazole.

Table 1: Physical parameters for the synthesis of new compounds by conventional, microwave and ultrasound mediated methods.

Comp No	Conventional Method			Microwave Irradiated Method			Ultrasound Irradiated Method		
	Time(h)	Temp(°C)	Yield(%)	Time (min)	Pow.(W)	Yield(%)	Time(min)	Pow.(kHz)	Yield(%)
2	10	rt	62	10	100	81	30	45	83
3	12	118	84	30	150	94	35	70	98
4	12	rt	81	15	150	97	15	60	94
5	16	reflux	85	15	150	97	18	60	95
6	18	reflux	60	12	100	88	15	50	30
7	24	rt	80	18	80	100	20	40	100
8	5	reflux	96	14	200	100	16	40	100
9a	12	rt	46	15	150	79	15	60	77
9b	16	rt	83	15	150	96	15	60	96
10	18	reflux	86	15	150	99	18	60	99
11	16	reflux	75	12	100	85	15	50	30
12	16	rt	89	18	80	94	20	40	100
13	5	rt	95	14	200	100	18	70	100
14	20	rt	60	15	150	92	15	65	89
15	17	reflux	84	15	150	94	18	60	98
16	18	reflux	69	12	100	97	15	50	96
17a	3	reflux	73	8	100	98	5	70	100
17b	3	reflux	55	8	100	76	5	70	99
17c	3	reflux	99.5	8	100	100	5	70	100
17d	3	reflux	58	8	100	90	5	70	100
19	24	rt	65	18	80	100	20	40	100
20	5	rt	99.5	14	200	100	15	70	100
21	12	rt	46	15	150	89	15	70	87
22	18	reflux	65	15	150	89	18	60	88
23	3	rt	79	12	200	89	15	70	80
24	3	rt	65	5	100	80	10	40	82
25a	3	reflux	75	8	100	90	5	70	100
25b	3	reflux	98	8	100	90	5	70	100
26	10	rt	60	8	100	92	5	70	90
27	12	reflux	75	8	150	95	5	70	98
28	24	rt	79	18	80	97	20	40	100
29	5	reflux	79	14	200	100	18	70	100

CONCLUSIONS

In this study, we reported the synthesis of some new hybrid molecules containing several heterocyclic units with conventional, microwave irradiated and ultrasound-promoted procedures. Four imidazole derivatives and, two morpholine-derived Schiff bases were synthesised. Antimicrobial activities screening studies were also performed. Most of the newly synthesised compounds exhibited good to moderate activities on some of the test microorganisms. Of these, the compounds containing a fluoroquinolone unit linked to the **1-7** and **12-17** scaffold via a methylene linkage exhibited excellent activity on the test bacteria. Compounds **17c**, **24** and **25** which are hybrid compounds with a β -lactam unit, were found to exhibit microbial activity on the *Mycobacterium smegmatis* (Ms) respectively.

ACKNOWLEDGMENTS

Thanks are expressed to Prof. Dr. Sengul Alpay Karaoglu for antimicrobial studies. The support provided by Giresun University, BAP, Turkey (Ref. No. Fen-Bap-A-200515-88 and Fen-Bap-A-140316-24) are gratefully acknowledged.

REFERENCES

1. Minbiole KPC, Jennings MC, Ator LE, Black JW, Grenier MC, LaDow JE, et al. From antimicrobial activity to mechanism of resistance: the multifaceted role of simple quaternary ammonium compounds in bacterial eradication. *Tetrahedron* 2016;72:3559–66.
2. Yang H, Wang H-W, Zhu T-W, Yu L-M, Chen J-W, Wang L-X, et al. Syntheses and antibacterial activity of soluble 9-bromo substituted indolizinoquinoline-5,12-dione derivatives. *Eur J Med Chem* 2017;127:166–73.
3. Kawai T, Kazuhiko I, Takaya N, Yamaguchi Y, Kishii R, Kohno Y, et al. Sulfonamide-based non-alkyne LpxC inhibitors as Gram-negative antibacterial agents. *Bioorg Med Chem Lett* 2017;27:1045–9.
4. Yan S, Song L, Luan S, Xin Z, Du S, Shi H, et al. A hierarchical polymer brush coating with dual-function antibacterial capability. *Colloids Surfaces B Biointerfaces* 2017;150:250–60.
5. Alagumuthu M, Arumugam S. Molecular docking, discovery, synthesis, and pharmacological properties of new 6-substituted-2-3-phenoxyphenyl. -4-phenyl quinoline derivatives; an approach to developing potent DNA gyrase inhibitors/antibacterial agents. *Bioorg Med Chem* 2017;25:1448–55.

6. Jeankumar VU, Renuka J, Santosh P, Soni V, Sridevi JP, Suryadevara P, et al. Thiazole-aminopiperidine hybrid analogues: Design and synthesis of novel Mycobacterium tuberculosis GyrB inhibitors. *Eur J Med Chem* 2013;70:143–53.
7. War JA, Srivastava SK, Srivastava SD. Design, synthesis and DNA-binding study of some novel morpholine linked thiazolidinone derivatives. *SpectrochimActa Part A MolBiomolSpectrosc* 2017;173:270–8.
8. Padmavathi V, PremaKumari C, Venkatesh BC, Padmaja A. Synthesis and antimicrobial activity of amido linked pyrrolyl and pyrazolyl-oxazoles, thiazoles and imidazoles. *Eur J Med Chem* 2011;46:5317–26.
9. Chen W, Deng X-Y, Li Y, Yang L-J, Wan W-C, Wang X-Q, et al. Synthesis and cytotoxic activities of novel hybrid 2-phenyl-3-alkylbenzofuran and imidazole/triazole compounds. *Bioorg Med Chem Lett* 2013;23:4297–302.
10. Wang K, Xu W, Liu Y, Zhang W, Wang W, Shen J, et al. Design and synthesis of imidazole and triazole derivatives as Lp-PLA2 inhibitors and the unexpected discovery of highly potent quaternary ammonium salts. *Bioorg Med Chem Lett* 2013;23:1187–92.
11. Yurttas L, Duran M, Demirayak S, Gençer HK, Tunalı Y. Synthesis and initial biological evaluation of substituted 1-phenylamino-2-thio-4,5-dimethyl-1H-imidazole derivatives. *Bioorg Med Chem Lett* 2013;23:6764–8.
12. Wen S-Q, Jeyakkumar P, Avula SR, Zhang L, Zhou C-H. Discovery of novel berberineimidazoles as safe antimicrobial agents by down regulating ROS generation. *Bioorg Med Chem Lett* 2016;26:2768–73.
13. Rathore A, Sudhakar R, Ahsan MJ, Ali A, Subbarao N, Jadav SS, et al. In vivo anti-inflammatory activity and docking study of newly synthesized benzimidazole derivatives bearing oxadiazole and morpholine rings. *BioorgChem* 2017;70:107–17.
14. Tereshchenko AD, Myronchuk JS, Leitchenko LD, Knysh I V., Tokmakova GO, Litsis OO, et al. Synthesis of 3-oxadiazolyl/triazolyl morpholines: Novel scaffolds for drug discovery. *Tetrahedron* 2017;73:750–7.
15. Surendra Kumar R, Moydeen M, Al-Deyab SS, Manilal A, Idhayadhulla A. Synthesis of new morpholine-connected pyrazolidine derivatives and their antimicrobial, antioxidant, and cytotoxic activities. *Bioorg Med Chem Lett* 2017;27:66–71.

16. Doan P, Karjalainen A, Chandraseelan JG, Sandberg O, Yli-Harja O, Rosholm T, et al. Synthesis and biological screening for cytotoxic activity of N-substituted indolines and morpholines. *Eur J Med Chem* 2016;120:296–303.
17. Gadekar PK, Roychowdhury A, Kharkar PS, Khedkar VM, Arkile M, Manek H, et al. Design, synthesis and biological evaluation of novel azaspiro analogs of linezolid as antibacterial and antitubercular agents. *Eur J Med Chem* 2016;122:475–87.
18. Micheli F, Cremonesi S, Semeraro T, Tarsi L, Tomelleri S, Cavanni P, et al. Novel morpholine scaffolds as selective dopamine DA₂ D₃ receptor antagonists. *Bioorganic Med Chem Lett* 2016;26:1329–32.
19. Zhao Z, Pissarnitski DA, Josien HB, Bara TA, Clader JW, Li H, et al. Substituted 4-morpholine N-arylsulfonamides as ??-secretase inhibitors. *Eur J Med Chem* 2016;124:36–48.
20. Desai NC, Rajpara KM, Joshi V V. Microwave induced synthesis of fluorobenzamides containing thiazole and thiazolidine as promising antimicrobial analogs. *J Fluor Chem* 2013;145:102–11.
21. Zhao Z, Shi Z, Liu M, Liu X. Microwave-assisted synthesis and in vitro antibacterial activity of novel steroidal thiosemicarbazone derivatives. *Bioorg Med Chem Lett* 2012;22:7730–4.
22. Mamaghani M, Loghmanifar A, Taati MR. An efficient one-pot synthesis of new 2-imino-1,3-thiazolidin-4-ones under ultrasonic conditions. *UltrasonSonochem* 2011;18:45–8.
23. Hossein Nia R, Mamaghani M, Tabatabaeian K, Shirini F, Rassa M. An expeditious regioselective synthesis of novel bioactive indole-substituted chromene derivatives via one-pot three-component reaction. *Bioorganic Med Chem Lett* 2012;22:5956–60.
24. Martinez-Guerra E, Gude VG. Synergistic effect of simultaneous microwave and ultrasound irradiations on transesterification of waste vegetable oil. *Fuel* 2014;137:100–8.
25. Mahmoodi NO, Shoja S, Tabatabaeian K, Sharifzadeh B. Ultrasound-promoted one-pot five-components synthesis of biologically active novel bis(6-alkyl or phenyl)-2-phenylpyrimidine-4-yl-oxo-alkane or methyl benzene derivatives. *UltrasonSonochem* 2015;23:31–6.
26. Chen B-H, Li J-T, Chen G-F. Efficient synthesis of 2,3-disubstituted-2,3-dihydroquinazolin-4(1H)-ones catalyzed by dodecylbenzenesulfonic acid in aqueous media under ultrasound irradiation. *UltrasonSonochem* 2015;23:59–65.
27. Nyborg WL. Biological effects of ultrasound: Development of safety guidelines. Part II: General review. *Ultrasound Med Biol* 2001;27:301–33.

28. Mentese MY, Bayrak H, Uygun Y, Mermer A, Ulker S, Karaoglu SA, et al. Microwave assisted synthesis of some hybrid molecules derived from norfloxacin and investigation of their biological activities. *Eur J Med Chem* 2013;67:230–42.
29. Ceylan S, Bektas H, Bayrak H, Demirbas N, Alpay-Karaoglu S, Ülker S. Syntheses and biological activities of new hybrid molecules containing different heterocyclic moieties. *Arch Pharm Weinheim*. 2013;346:743–56.
30. Mentese M, Demirci S, Ozdemir SB, Demirbas A, Ulker S, Demirbas N. Microwave assisted synthesis and antimicrobial activity evaluation of new heterofunctionalized norfloxacin derivatives. *Lett Drug Des Discov* 2016;13:1076–90.
31. Weatherburn MW. Phenol-hypochlorite reaction for determination of ammonia. *Anal Chem* 1967;39:971–4.



PVA NANOCOMPOSITES OF ORGANOCCLAYS OBTAINED USING DIFFERENT CATIONIC SURFACTANTS

Cüneyt H. Ünlü¹, Sevim İşçi Turutoğlu², Oya Galioğlu Atıcı¹, Ö. Işık Ece³, Nurfer Güngör²

¹Istanbul Technical University, Science & Letters Faculty, Chemistry Department, Maslak 34469, Istanbul, TURKEY. ²Istanbul Technical University, Science & Letters Faculty, Physics Department, Maslak 34469, Istanbul, TURKEY. ³Istanbul Technical University, Faculty of Mines, Department of Geology, Maslak 34469, Istanbul, TURKEY

Abstract: This study is about the preparation of two different organoclays with cationic surfactants and their poly(vinyl alcohol) nanocomposites with increased thermal and mechanical behavior. Organoclays were prepared to modify clay mineral with solution intercalation method using aqueous solutions of cationic surfactants dodecyltrimethylammonium bromide (DTABr) and cetylpyridinium bromide (CPBr). Obtained organoclays (D-MMT and C-MMT for DTABr/MMT and CPBr/MMT, respectively) were characterized using different methods including zeta potential and XRD. Results indicated an absolute decrease in zeta potential about 20 mV for C-MMT and 14 mV for D-MMT indicating flocculation and coating of the surface. Moreover, measurements indicated that interlayer distance increased based on basal spacing peak shift whose value was 1.27 nm for NaMMT, whereas 1.40 nm for D-MMT, and 1.75 nm for C-MMT. The organoclays were used in the preparation of PVA/clay nanocomposites; thermal stability of the nanocomposites was determined using TGA, while mechanical strength measurements were done using DMA. The maximum thermal decomposition temperature of the pristine PVA and nanocomposites were compared, and an average increase of 4°C was observed. Also, the activation energy of the decomposition was observed ca. 40 kJ.mol⁻¹ higher than pristine PVA.

Keywords: Polymer/clay nanocomposites, Organoclay, Poly(vinyl alcohol) (PVA), Thermal stability, Cationic surfactants, Principal components analysis.

Submitted: April 22, 2017 . **Accepted:** February 20, 2018.

Cite this: Ünlü C, Turutoğlu S, Galioğlu Atıcı O, Ece Ö, Güngör N. PVA NANOCOMPOSITES OF ORGANOCCLAYS OBTAINED USING DIFFERENT CATIONIC SURFACTANTS. JOTCSA. 2018;5(2):415-32.

DOI: <http://dx.doi.org/10.18596/jotcsa.307602>.

***Corresponding author. E-mail:** unlucu@itu.edu.tr, fax: +90-212-285 6386.

INTRODUCTION

One of the popular research topics is polymer/clay nanocomposites and has been studied extensively in recent years.(1–5) Research in this field has been started with Toyota R&D department's work on nylon in the early nineties in order to produce materials with enhanced physical and chemical properties. Later, other applications of polymer/clay nanocomposites in different industrial fields are also developed such as food packaging, automobile parts, microelectronic packaging, and medical tubing.(5–7) Montmorillonite, which is a member of the smectite group clay minerals, is the most popular material used in polymer/clay nanocomposites. Smectites are composed of approximately 1 nm thick layers with high aspect ratios; each layer consists of one alumina sheet between two silica sheets. Due to naturally occurring network defects, large surfaces of the layers (faces) bear negative charges, and these faces can interact electrostatically with inorganic (exchangeable) cations such as sodium, potassium, calcium which reside among interlayer galleries of the clay mineral. When clay mineral swells in water interlayer galleries expand and the exchangeable cations substitute with organic (i.e., surface active agents or polymeric materials) compounds to form intercalated compounds resulting in an increase in basal spacing of the clay. In some cases, the polymeric matrix may separate the clay layers forming an exfoliated nanocomposite.(8) As the clay surfaces have hydrophilic nature, modifying them to obtain organophilic surfaces with the use of cationic surfactants for exchangeable cations may help penetration of the polymeric material into the galleries finally producing a better and uniformly dispersed clay mineral in the polymeric matrix. Alkylammonium salts are the most used cationic surfactant for production of organoclays.(9)

Poly(vinyl alcohol), PVA, is a cheap, water soluble, and non-toxic polymeric material and has many applications in different industrial areas including textiles, and coating.(10,11) In polymer/clay nanocomposites prepared with PVA polymer matrix may be solely PVA or along with other polymeric materials (such as cellulose, chitosan) in order to enhance material properties. (11–15) Addition of clay into PVA matrix causes an increase in mechanical and thermal properties as expected as well as enhancements in film formation capability and chemical resistance. Recent studies with PVA indicate that organically modified montmorillonite layers more easily disperse into the PVA matrix uniformly producing an exfoliated nanostructures.

The aim of this study can be divided into two subsections; the first part is the synthesis of organoclays by modification with use of two different cationic surfactants; then the

second part is the formation of PVA/organoclay nanocomposites using organoclays via the solution intercalation method. The results are evaluated using different characterizations methods such as spectroscopy (FTIR, X-ray diffraction), dynamic mechanical analysis (DMA), and thermogravimetric analysis (TGA).

EXPERIMENTAL SECTION

Materials and Methods

Poly(vinyl alcohol) (PVA, molecular weight 145 kg/mol), dodecyltrimethylammonium bromide (DTABr, $C_{12}H_{25}N(CH_3)_3Br$) and cetylpyridinium bromide (CPBr, $C_{5}H_5NCH_2(CH_2)_{14}CH_3$) were Fluka brand; they were used as received.

The clay mineral was Na-montmorillonite (NaMMT) collected locally from Enez-Turkey. The dominant clay mineral was found to be dioctahedral montmorillonite with minor amounts of illite and kaolinite. The chemical composition of NaMMT was determined by atomic adsorption spectroscopy (Perkin Elmer 3030 model), and the silica content was determined gravimetrically. The chemical composition of clay sample was (wt.%): SiO_2 58.8, Al_2O_3 18.73, Fe_2O_3 3.71, CaO 3.34, MnO 0.09, Na_2O 3.36, MgO 2.62, K_2O 2.70 and TiO_2 0.49.

Cation exchange capacity (CEC) of clay mineral was determined using methylene blue method.(16) Methylene blue solution was prepared and added to clay dispersion in small amounts. Then a droplet of the dispersion was placed on a filter paper. When a blue circle around the blot was observed this meant that the clay was saturated with the dye thus releasing an excess of it. CEC for NaMMT was determined as 89 milliequivalents per 100 g clay.

Characterization Methods

The zeta potential measurements were carried out using Malvern Instruments Zetasizer 2000 with an optical unit which had 5 mW He-Ne (638 nm) laser. All dispersions were centrifuged at 6000 rpm for 30 minutes before the measurements then supernatant fraction was used for the measurements.

X-ray diffraction (XRD) analyses of solvent-cast films were performed on Philips PW 1040 at room temperature using Ni-filtered $Cu-K\alpha$ radiation. The diffractograms were obtained by scanning in 2θ ranges from 2 to 10° at a rate of 2 degrees per minute.

FTIR analyses were done on Perkin Elmer Spectrum One FTIR spectrophotometer in 4000–400 cm^{-1} range as either 1% KBr pellet or solvent-cast film; results were recorded in absorbance mode.

Principal component analysis (PCA) of the FTIR data was performed using R (version 3.4.3) software. First, the data were processed to obtain derivative spectra (first and second order) within a selected range (1800-400 cm^{-1}) using Savitzky-Golay procedure. Then PCA was applied to the data in order to see clustering.

Dynamic mechanical analyses (DMA) were performed on Perkin Elmer Diamond DMA under tension film mode in a temperature range 20–200°C at a frequency of 1 Hz and a heating rate of 5 °C/min. Samples were prepared by the solvent casting method.

The thermal properties were analyzed by thermogravimetric analysis (TGA) on TA Instruments Q50 with a heating rate of 20 °C/min under N₂ atmosphere in a range of 25-600 °C. Kinetic parameters were calculated using Broido method(17) with Python interpreter NumPy and SciPy modules.

Preparation of Organoclay

The organoclay as prepared by using cationic surfactants as intercalating agents. NaMMT (10 g) was dispersed in 500 ml 50% aqueous ethanol at 65 °C. Then the surfactant (0.01 M, DTABr or CPBr) was added; pH of the dispersion was adjusted to 3.5 with aqueous HCl. The dispersion was stirred at 65°C for 1 hour then samples were centrifuged; obtained organoclay (D-MMT or C-MMT) was washed two times with water at 70°C and dried at 40°C.

Preparation of PVA/Organoclay Nanocomposites

Aqueous organoclay dispersion (1% by weight) was shaken for 2 days in order to obtain uniformly and well-swelled organoclay. Then an appropriate amount of the dispersion was blended with 5 g PVA in 200 ml distilled water during 100 minutes at 75(\pm 5) °C. Obtained PVA/organoclay nanocomposites had organoclay contents of at 1, 2, and 3% by weight with respect to PVA. The products dried at room temperature and named as D-PVA or C-PVA denoting the surfactant used was D-MMT or C-MMT, respectively.

RESULTS AND DISCUSSION

Characterization of Clay and Organoclay Dispersions

Zeta potential characterization techniques rely on the determination of total surface charge of the colloidal particles. The instrument uses a laser beam to count the number of the charged particles moving between oppositely charged electrodes under a potential difference. Surface charge (or zeta potential) may differ if coagulation or flocculation occurs because the size of the particle grows while charges on the surface may decrease or increase as a result of the interactions. Clay particles carry a net surface charge due to the structure of the clay; larger siloxane surfaces (face, Si-O-Si groups) are negatively charged due to substitutional point defects in the lattice while smaller side surfaces (edges, aluminol, Al-OH and silanol, Si-OH groups) have positive charges. Electrostatic interactions among oppositely charged clay surfaces cause screening of the charges and lead to flocculation. This occurrence results in a net decrease of the surface charge (regardless of the sign) of the large clay particles. Interactions may take place among edges and faces at different aspects (edge-face, edge-edge, and face-face) resulting in variations in shapes and sizes of the particles.(18)

The zeta potential of NaMMT dispersion was measured as -41.20 mV indicating the dispersion had deflocculated structure. However, zeta potential values belonging to organoclays were found as -27.6 for D-MMT and -22.23 mV for C-MMT. The absolute decrease in zeta potentials of the organoclay dispersions was the indicator of clay-surfactant interactions; surfactant molecules covered surfaces of the clay particles leading to flocculation. According to the results, especially C-MMT had a more flocculated structure in the dispersion compared to D-MMT.

Basal spacing (d_{001}), another key feature directly related to the structure, was measured using XRD. Diffractograms of NaMMT, C-MMT, and D-MMT were shown in Figure 1. The values indicated some intercalation for both organoclays. NaMMT had a d_{001} value of 1.271 nm. After modification of NaMMT, this value increased to 1.401 nm for D-MMT and 1.748 nm for C-MMT. These increases displayed that clay layers were separated slightly as a result of intercalation by cationic surfactants, but in different amounts. This occurrence might be related to the orientation of the surfactants into the interlayer galleries. The basal spacing increase was found greater for C-MMT (0.48 nm) than D-MMT (0.13 nm) probably due to bilayer type arrangement of the CPBr molecules parallel to the silicate layer.(19)

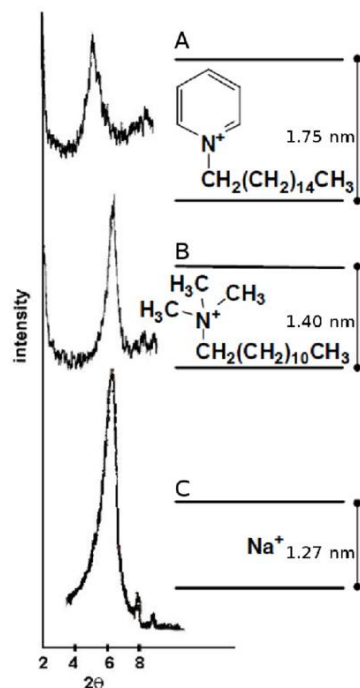


Figure 1. XRD diffractograms of C-MMT (a), D-MMT (b), and NaMMT (c).

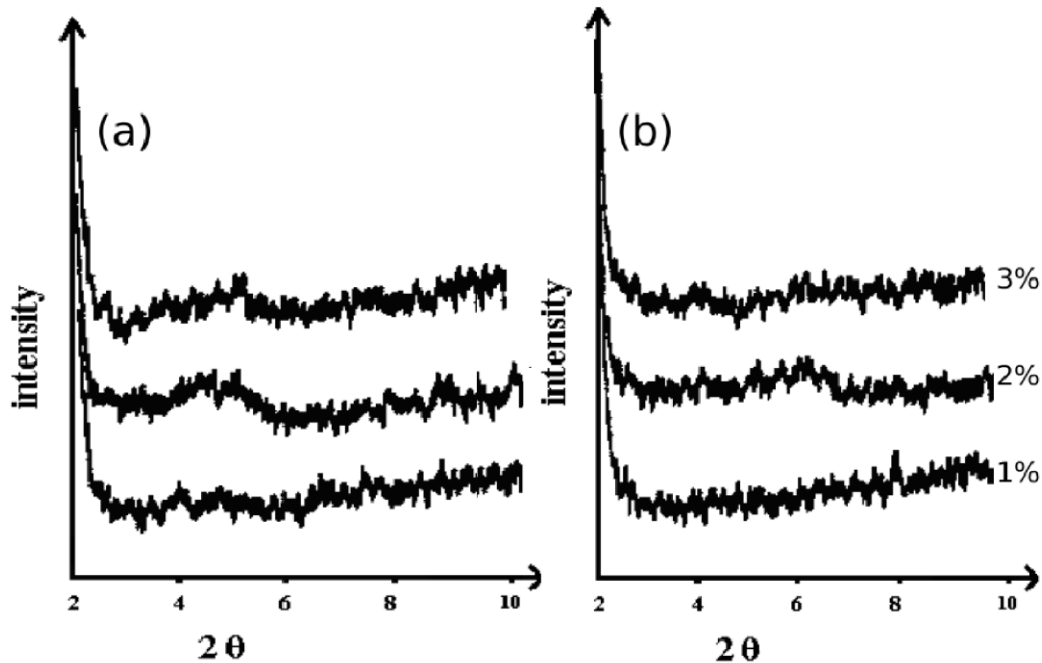
Better intercalation of NaMMT by CPBr was also attributed to alkyl chain length of cationic surfactants, which had a positive effect on adsorption by clays; longer chain caused an increase in adsorption by clay surface via Van der Waals forces.(20–22) The mentioned interactions among surfactant and clay were stronger for CPBr compared to DTABr under same conditions. Finally, another plausible cause for this result was related with aqueous solubilities of the surfactants; DTABr was more soluble in water compared with CPBr; thus desorption of DTABr from clay surfaces to aqueous phase would be higher than CPBr. Once CP⁺ cation was adsorbed by the clay surface, it hardly detached and went back to the aqueous phase, unlike DTA⁺ cation.

Evaluation of the results obtained from XRD and electrokinetic measurements indicated that (a) surfactant molecules were adsorbed by both inner and outer surfaces of the clay, and (b) CPBr intercalated NaMMT more efficiently compared to DTABr.

Characterization of PVA/Organoclay Nanocomposites

The PVA/organoclay nanocomposites (C-PVA and D-PVA) were identified using several spectroscopic techniques. XRD measurements of both nanocomposites with different clay concentrations were done to observe intercalation of PVA into interlayer galleries of the organoclay. Basal spacing peak (d_{001}) of NaMMT was absent in all diffractograms of PVA nanocomposites (Figure 2). The disappearance of the d_{001} peak might be attributed to the shift of this peak under 2° diffraction angle due to highly intercalated or completely

exfoliated organoclay platelets. As literature survey about PVA/(organo)clay nanocomposites indicated that this occurrence was highly plausible.(14) Thus



intercalated platelets possibly dispersed within PVA matrix forming nanostructures.

Figure 2. XRD diffractograms of D-PVA (a), and C-PVA (b).

The structure of the PVA nanocomposites was also analyzed using FTIR spectroscopy. FTIR spectra of PVA, NaMMT, and nanocomposites were first evaluated separately then compared with each other. Characteristic vibrations and attributed vibration modes for pristine PVA were observed as 3339 cm^{-1} (O-H stretching), $2942, 2912\text{ cm}^{-1}$ (alkyl C-H stretching), $1436, 1424\text{ cm}^{-1}$ (C-H bending), 1093 cm^{-1} (C-O stretching). Signals related to residual acetate groups in the polymer were observed at 1707 cm^{-1} (C=O stretching with intramolecular H-bond), 1377 cm^{-1} (CH_3 group) and 1238 cm^{-1} (C-O bending).(23)

Characteristic absorption bands of NaMMT were determined as structural (3627 cm^{-1}) and intra/intermolecular hydrogen bonded O-H stretching (3453 cm^{-1}), H-O-H deformation vibration due to adsorbed water (1635 cm^{-1}), Si-O stretching vibration at 1033 cm^{-1} with a shoulder at 1087 cm^{-1} , Al-OH (917 and 622 cm^{-1}) and (Al, Mg)-O (848 and 793 cm^{-1}) vibrations modes, Si-O bending vibration at 521 and 467 cm^{-1} .(24,25)

Structural O-H vibration of MMT at 3627 cm^{-1} was absent in the spectra of organoclays; it possibly overlapped with O-H stretching of PVA. The strongest signal of organoclay spectrum was Si-O stretching at 1033 cm^{-1} and it also overlapped with C-O stretching of PVA at 1093 cm^{-1} and could not be observed in the spectra of PVA/organoclay

nanocomposites; however, its presence was slightly distinguishable by a widening towards 1050 cm^{-1} in C-O signal (Figure 3).

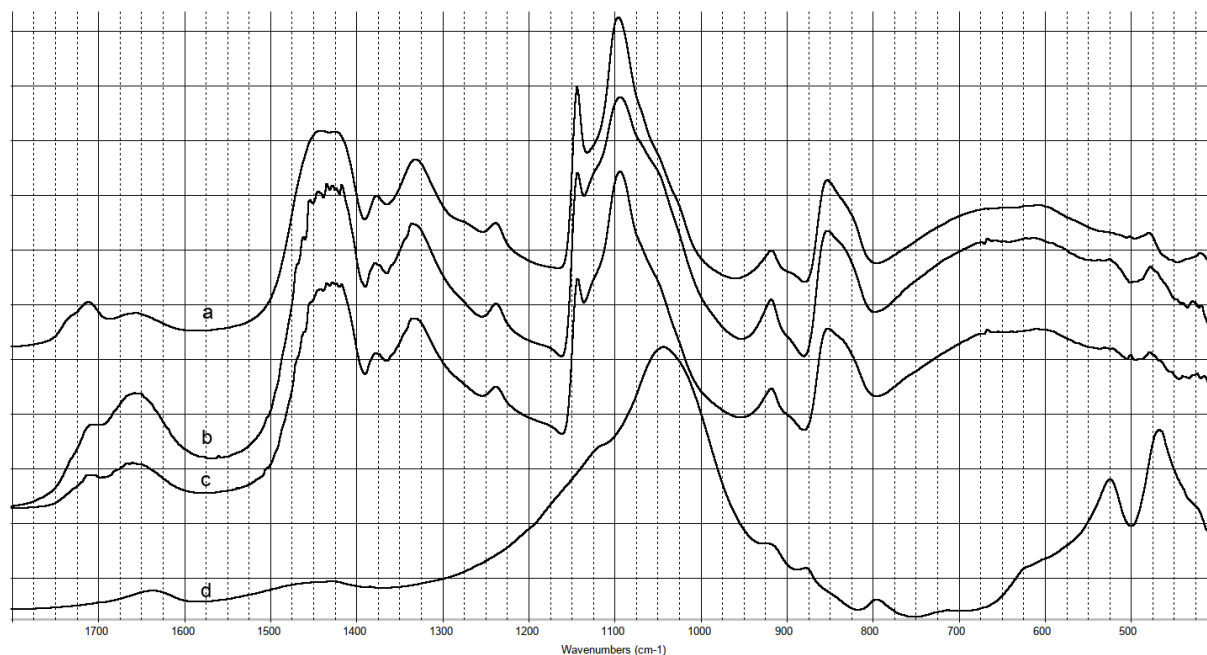


Figure 3. FTIR spectra of nanocomposites PVA (a), D-PVA (b), C-PVA (c) with 2% clay and pristine NaMMT (d).

The magnitude of the signal widening was directly proportional to the amount of organoclay in the PVA/organoclay system; the shoulder at 1054 cm^{-1} became more distinct as the amount of organoclay increased. Another factor affecting signal shape in this region was the type of the surfactant used in organoclay. The shape of the signal observed more distorted for D-PVA compared to C-PVA under same conditions indicating a difference in the interaction between organoclay and PVA. Another indicator of organoclay presence in PVA matrix was slightly increasing the intensity of signals belonging to Si-O bending vibrations at 521 and 467 cm^{-1} . Peak positions of these signals were slightly shifted according to organoclay type and amount in the PVA matrix. These results proposed that a change in crystal structure of the organoclay as a result of the interaction with PVA matrix.

As the difference is very hard to detect among the spectra, a statistical method called as principal component analysis (PCA) was used to emphasize the differences among the data. Differences among the spectra were observed mainly in range $1800\text{-}400$ where characteristic absorption bands of PVA and MMT were located. As the signals of C-O stretching and bending signals of PVA were overlapping with Si-O stretchings of MMT, it was very hard to distinguish the interaction. Thus the first-order derivative of each sample was calculated using Savitzky-Golay algorithm. Then PCA was applied to these

derivative data in R software with centering. Analysis of total the variance change yielded that the first three principal components (PCs) were responsible for 99.05% of the total change. Further analysis of the PCs indicated that PC1 was responsible for 92.48% of the total change, while PC2 and PC3 were 4.05% and 2.49%, respectively. Thus plotting PC1 versus PC2 gave a meaningful comparison for the classification of the samples. Scores plot was shown in Figure 4a. As seen in the scores plot PVA and NaMMT located at opposite sides of the PC1. This occurrence was examined using loadings plot (Figure 4b). In the figure PC1, PC2 and derivatives of PVA and NaMMT were plotted with raw spectra at the bottom. PC1 and derivative PVA had the same signals at the same positions with the exception of the sign; thus PVA was located at the left-hand side of the PC1. However, derivative NaMMT and PC1 had an in-phase correlation placing the NaMMT on the positive side of the PC1.

As a result of the PCA analyses, PVA, NaMMT, and composites located in different parts of the scores plot indicating they had spectral features concerning derivative FTIR spectra. It could be concluded that the appearance of the samples at different portions of the scores plot was attributed to the change in the FTIR signals and it was related with the amount and type of the organoclay used.

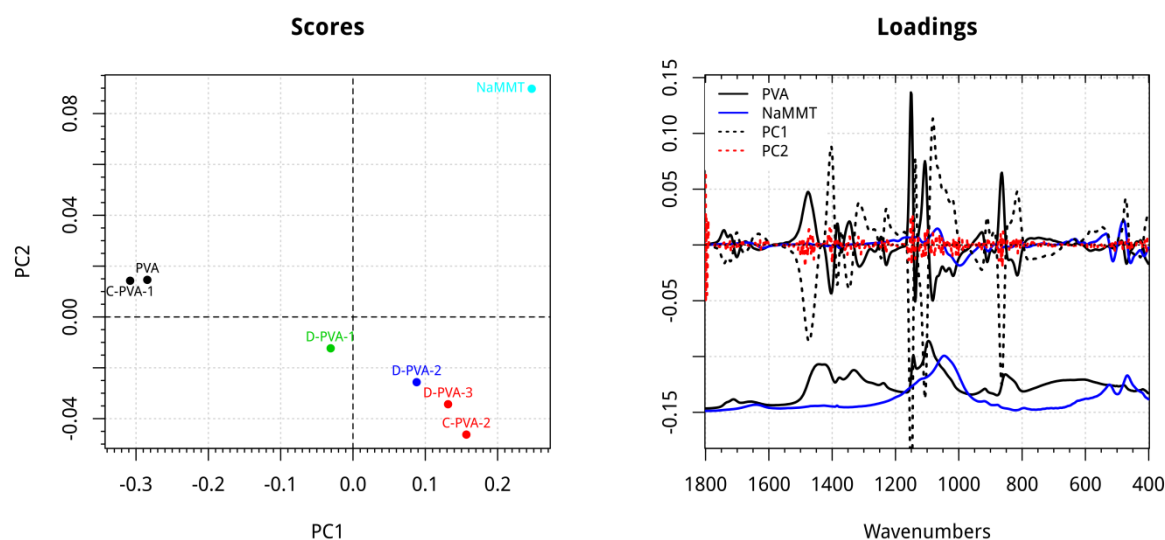


Figure 4. Scores plot of derivative FTIR spectra and loadings plot for PC1, PC2, PVA and NaMMT samples (lower part raw spectra of PVA and NaMMT).

Evaluation of XRD, FTIR and PCA analyses with literature data altogether lead to two results: (a) organoclays and PVA interacted possibly giving intercalated nanocomposites, and (b) type of the surfactant used played an important role on interaction efficiency, C-MMT better than D-MMT regarding signal shifts.

Thermal and Dynamic Mechanical Characterization of PVA Nanocomposites

Thermogravimetric analyses (TGA) were done to determine the contribution of organoclay to the thermal stability of the PVA; results of thermal analyses were summarized in Table 1. TGA thermograms, regardless pristine or organoclay containing PVA, showed about 7% weight loss starting from 80 to 200 °C which was attributed to water loss adsorbed by the sample (Figure 5). Char amount at the end was about 4.8% for PVA and D-PVA samples. However, C-PVA samples displayed lower char amount (2%) compared with other samples.

Table 1. Results of TGA measurements and activation energy estimations regarding Broido method with correlation coefficients higher than 0.995.

Sample	Clay %, (w/w)	Max. weight loss		Activation energy ^a			
		At 380 °C	At 440 °C	I	II	III	IV
PVA	0	377.5	440.7	86	133	51	84
C-PVA	1	382.6	444.4	117	177	69	120
	2	381.6	447.2	121	174	60	96
	3	381.8	449.9	126	176	61	98
D-PVA	1	380.1	440.8	127	162	62	103
	2	380.3	441.1	141	167	58	101
	3	378.4	441.3	130	170	63	111

^a300–350 °C, II 350–400 °C, III 400–440 °C, IV 440–470 °C

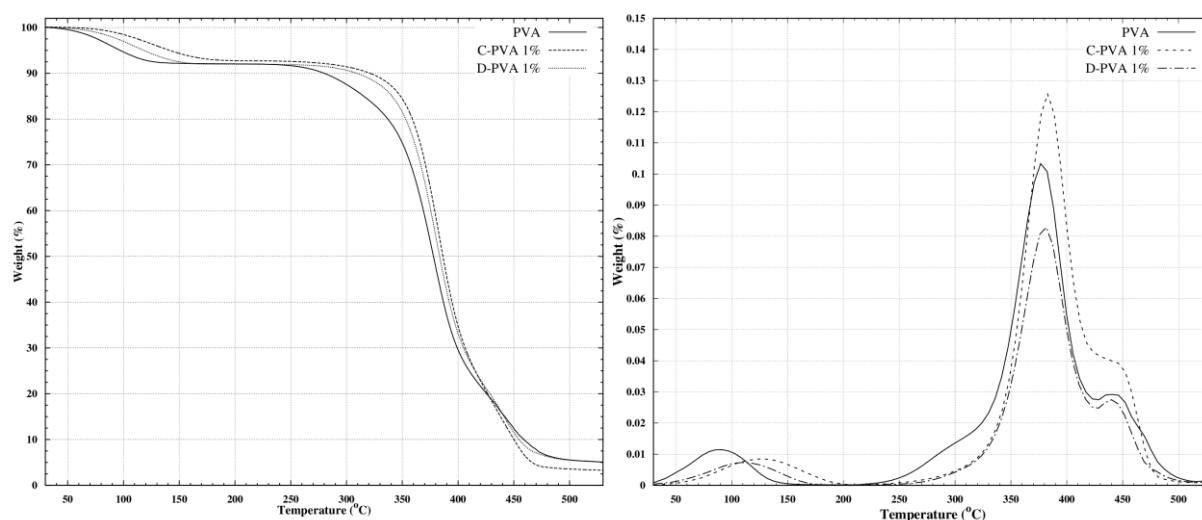


Figure 5. TGA (a) and derivative TGA (b) thermograms of PVA, 1% C-PVA, and D-PVA nanocomposites.

Maximum degradation temperature of the samples was determined using the first-order derivative of weight loss-temperature plot. In terms of degradation temperature pristine PVA displayed two maxima; a major signal (T_1) at 378 °C as a peak, and a minor distinguishable signal (T_2) at 441 °C as a shoulder. Thus thermal degradation kinetics of

PVA could be separated into two main parts; the first part was mainly related to dehydration and decarboxylation and the second part covered more complex reactions and chain scissions. (26–29) The first part of the decomposition started around 300 °C which was observed as a shoulder in derivative TG plot (Figure 5b). This data was consistent with the literature cited.

Organoclay addition caused an increase in both degradation maxima of the PVA as an indicator of enhanced thermal stability. The degree of improvement was related to the organoclay used. In the case of C-PVA samples T_1 position was observed at 382°C, approximately 5°C higher compared to pristine PVA regardless of C-MMT content. In a similar manner T_2 values were observed at higher temperatures; however, this time clay proportion caused some variations. T_2 peak was at 444°C for C-PVA with 1% C-MMT content, 3 °C higher compared with pristine PVA; each 1% clay increase in C-MMT content caused an approximate increase of 3 °C. In the case of D-PVA a small increase in T_1 was observed compared to pristine PVA with an approximate value of 2.5 °C for 1 and 2% D-MMT content and ca. 1.0°C for 3% C-MMT; however, T_2 values were comparatively same regardless of clay content.

The detailed examination of the thermograms was done to find out decomposition activation energy values as a measure of thermal stability using Broido's method with Python SciPy and NumPy modules with a single run TGA measurement to evaluate the data. After the data acquisition some necessary manipulations were done to create the plot of the $\ln(\ln 1/y)$ as a function of reciprocal temperature whose slope was the activation energy over universal gas constant where y was the fraction at temperature t regarding the remaining and starting weights of the decomposition (W_t , W_∞ , W_0).

$$\ln \ln \frac{1}{y} = \left(\frac{E_a}{R} \right) \frac{1}{T} ; \quad y = \frac{W_t - W_\infty}{W_0 - W_\infty}$$

Having multiple regions with different slopes, the plots indicated that degradation followed different reaction routes at various orders. The whole degradation region was divided into subdivisions whose boundaries were determined using correlation coefficient values; boundary value was changed until the highest correlation coefficient ($r^2 > 0.995$) was obtained for the region under examination. In this way 4 subdivisions were obtained and labeled as I, II, III, and IV for 300-350, 350-400, 400-440, and 440-470°C; then activation energy estimations were done for each region simultaneously.

Estimated activation energy values for PVA were found as 86, 133, 51, and 84 kJ mol⁻¹ for each corresponding section. These values were consistent with the literature cited with small deviations arising from the used method. All samples with an amount of clay content displayed higher values compared to pristine PVA as an indicator of enhanced thermal stability. However, improvement degree was varying with the type of the organoclay used. C-PVA samples displayed a gradual increase related to C-MMT content; activation energy of samples containing 1, 2, 3% C-MMT by weight in I were calculated as 117, 121, 126 kJ mol⁻¹, while D-PVA samples displayed a better performance compared with C-PVA; the estimated activation energy values were 127, 141, 130 kJ mol⁻¹ for the same range. The second subdivision, II, where T₁ peak located, also showed increased thermal resistance regarding activation energy rise. In this section C-PVA samples granted faintly better results than D-PVA by 7 kJ mol⁻¹. The third subdivision, III, displayed similar results for both nanocomposites, an approximate increase of 10 kJ mol⁻¹ resulted in activation energy estimations of 60–63 kJ mol⁻¹. Range IV showed that the highest enhancement was obtained for C-PVA with 1% C-MMT content with an activation energy estimate of 120 kJ mol⁻¹, it was followed by D-PVA with 3% D-MMT content with a value of 111 kJ mol⁻¹; remaining samples displayed approximately same result approximately 100 kJ mol⁻¹.

These results indicated that interactions among PVA chains and organoclay particles were different in C-PVA and D-PVA nanocomposites. The obtained results were consistent with the literature of PVA with inorganic additive(15,29). It could be deduced that distribution and intercalation of PVA into interlayer spaces of organoclay particles were better for C-PVA than D-PVA; because first sections of the thermal decomposition were related to dehydration and decarboxylation reactions. Thermal degradation was retarded a result of the interactions among organoclay surface and hydroxyl/carbonyl groups of PVA; intercalation degree might affect the magnitude of the retardation because PVA would contain more uniformly dispersed an amount of organoclay to absorb the heat retarding the degradation. In the case of D-PVA, organoclay particles probably dispersed in PVA matrix partly dispersed causing only some parts interacted with PVA; however, organoclay particles were intercalated better for C-PVA resulting in better thermal stability than D-PVA.

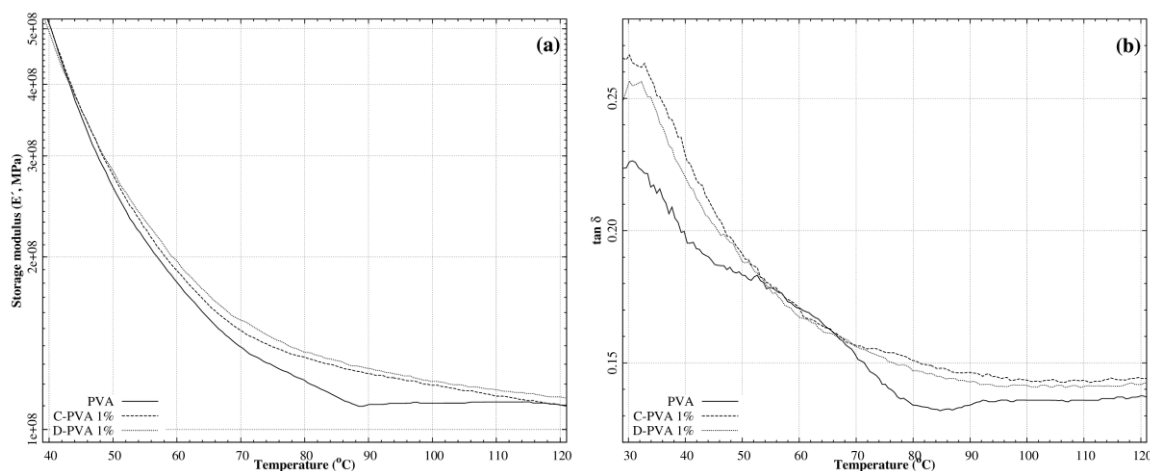


Figure 6. Storage (E') moduli (a) and $\tan \delta$ (b) as a function of temperature for PVA, 1% C-PVA and D-PVA nanocomposites.

The storage modulus, E' , could be used as a measure of the energy stored elastically in the system. Results of dynamic mechanical analyses (DMA) were summarized in Table 2. Introduction of organoclay into PVA matrix also enhanced mechanical strength due to increase in storage moduli of nanocomposites resulting in an increase in elongation regarding organoclay amount (Figure 6a). Each increase in organoclay component of the nanocomposites caused an approximate increase of 15% elongation of the material. Glass transition temperatures (T_g) were found from peak positions of $\tan \delta$ versus temperature plot of each sample; increasing T_g values affirmed increase in thermal stability of nanocomposites (Figure 6b).

Table 2. Results of mechanical properties of PVA and its organoclay nanocomposites

Sample	Clay %, (w/w)	Tensile strength (Mpa, ± 5) ^a	Elongation ^b (%, ± 2)	T_g (°C)
PVA	0	110	-	30.3
C-PVA	1	125	13	31.0
	2	140	27	32.8
	3	153	38	33.1
D-PVA	1	127	15	30.9
	2	136	23	32.7
	3	154	40	33.0

^aStorage modulus at 90°C and 1 Hz. ^bWith respect to storage modulus of pristine PVA. ^cFound from the peak position of $\tan \delta$.

Evaluation of thermal and mechanical analyses indicated that both thermal and mechanical stability of PVA nanocomposites were better than raw PVA polymer even in addition to the smallest amount of clay at 1% by weight.

CONCLUSIONS

Two different types of organoclay were synthesized using cationic surfactants DTABr and CPBr. Spectral and electrokinetic measurements indicated that interactions among clay particles and surfactant mainly occurred at surfaces resulting in surfactant covered clay particles and these interactions also caused an increase along interlayer spacing of clay structure. These organoclays were used to obtain PVA nanocomposites at different proportions of 1, 2, and 3% by weight. Dispersing C-MMT in PVA matrix with different proportions gave C-PVA nanocomposites while using D-MMT produced D-PVA. Spectral characterizations showed that PVA nanocomposites were obtained with the organoclays. Thermal and mechanical analyses proposed that properties of nanocomposites were enhanced in thermal and mechanical aspects for both nanocomposites concerning pristine PVA. When C-PVA and D-PVA nanocomposites were compared, it was deduced that interactions among PVA chains and organoclays were fairly different.

ACKNOWLEDGMENTS

This paper is supported by Research Fund of Istanbul Technical University (Project No: 30451) and The Scientific and Technological Research Council of Turkey (TUBITAK) (Project No: 105M088 (MAG-HD-18)).

REFERENCES

1. Sinha Ray S, Okamoto M. Polymer/layered silicate nanocomposites: a review from preparation to processing. *Prog Polym Sci.* 2003;28(11):1539–641.
2. Fahmy TYA, Mobarak F. Nanocomposites from natural cellulose fibers filled with kaolin in presence of sucrose. *Carbohydr Polym.* 2008;72(4):751–5.
3. Bordes P, Pollet E, Averous L. Nano-biocomposites: Biodegradable polyester/nanoclay systems. *Prog Polym Sci.* 2009;34:125–55.
4. Pavlidou S, Papaspyrides CD. A review on polymer-layered silicate nanocomposites. *Prog Polym Sci.* 2008;33(12):1119–98.
5. Mallakpour S, Rashidimoghadam S. 8 - Recent developments in the synthesis of hybrid polymer/clay nanocomposites: Properties and applications. In: *Hybrid*

- Polymer Composite Materials [Internet]. Woodhead Publishing; 2017 [cited 2017 Dec 26]. p. 227–65. Available from: <https://www.sciencedirect.com/science/article/pii/B9780081007853000085>
6. Utracki LA. Clay-containing polymeric nanocomposites. Shrewsbury: Rapra Technology Ltd; 2004. 2 p.
 7. Rhim J-W, Park H-M, Ha C-S. Bio-nanocomposites for food packaging applications. *Prog Polym Sci.* 2013 Ekim;38(10–11):1629–52.
 8. Mermut AR, Lagaly G. Baseline Studies of the Clay Minerals Society Source Clays: Layer-Charge Determination and Characteristics of Those Minerals Containing 2:1 Layers. *Clays Clay Miner.* 2001;49(5):393–7.
 9. Lagaly G, Reese M, Abend S. Smectites as colloidal stabilizers of emulsions I. Preparation and properties of emulsions with smectites and nonionic surfactants. *Appl Clay Sci.* 1999;14(1–3):83–103.
 10. Kokabi M, Sirousazar M, Hassan ZM. PVA–clay nanocomposite hydrogels for wound dressing. *Eur Polym J.* 2007 Mar;43(3):773–81.
 11. Turhan Y, Alp ZG, Alkan M, Doğan M. Preparation and characterization of poly(vinylalcohol)/modified bentonite nanocomposites. *Microporous Mesoporous Mater.* 2013;174:144–53.
 12. Nistor M-T, Vasile C. Influence of the nanoparticle type on the thermal decomposition of the green starch/poly(vinyl alcohol)/montmorillonite nanocomposites. *J Therm Anal Calorim.* 2013 Mar 1;111(3):1903–19.
 13. Mehta HR, Murthy ZVP. Preparation of Sodium Montmorillonite Clay Loaded Poly(Vinyl Alcohol)-Chitosan Composite Mixed Matrix Membranes and Their Application in Pervaporation Dehydration of Isopropanol. *J Polym Mater New Delhi.* 2016 Jun;33(2):319–31.
 14. Mallakpour S, Dinari M. Novel bionanocomposites of poly(vinyl alcohol) and modified chiral layered double hydroxides: Synthesis, properties and a morphological study. *Prog Org Coat.* 2014 Mar;77(3):583–9.

15. Mallakpour S, Dinari M. Synthesis and Properties of Biodegradable Poly(vinyl alcohol)/Organo-nanoclay Bionanocomposites. *J Polym Environ.* 2012 Apr 18;20(3):732–40.
16. Worrall WE. *Clays and ceramic raw materials.* London: Elsevier; 1986.
17. Broido A. A simple, sensitive graphical method of treating thermogravimetric analysis data. *J Polym Sci Part -2 Polym Phys.* 1969;7(10):1761–73.
18. Ünlü CH, Günister E, Atıcı O. Effect of acidity on xylan–montmorillonite bionanocomposites. *Mater Chem Phys.* 2012;136(2–3):653–60.
19. Vaia RA, Teukolsky RK, Giannelis EP. Interlayer Structure and Molecular Environment of Alkylammonium Layered Silicates. *Chem Mater.* 1994;6(7):1017–22.
20. Pan J, Yang G, Han B, Yan H. Studies on Interaction of Dodecyltrimethylammonium Bromide with Na- and Al-Montmorillonite. *J Colloid Interface Sci.* 1997 Ekim;194(2):276–80.
21. Chen G, Han B, Yan H. Interaction of Cationic Surfactants with Iron and Sodium Montmorillonite Suspensions. *J Colloid Interface Sci.* 1998;201(2):158–63.
22. İşçi S, Ece ÖI, Güngör N. Characterization of Rheology, Electrokinetic Properties, and Surface Micromorphology of DTABr-MMT and CPBr-MMT Organoclays. *J Compos Mater.* 2006;40(12):1105–15.
23. Jayasekara R, Harding I, Bowater I, Christie GBY, Lonergan GT. Preparation, surface modification and characterisation of solution cast starch PVA blended films. *Polym Test.* 2004;23(1):17–27.
24. Alemdar A, Güngör N, Ece ÖI, Atıcı O. The rheological properties and characterization of bentonite dispersions in the presence of non-ionic polymer PEG. *J Mater Sci.* 2005;40(1):171–7.

25. Marel HW van der, Beutelspacher H. Atlas of infrared spectroscopy of clay minerals and their admixtures. Amsterdam: Elsevier Scientific Pub. Co.; 1976.
26. Lai JC-H, Rahman MR, Hamdan S, Liew FK, Rahman MM, Hossen MF. Impact of nanoclay on physicommechanical and thermal analysis of polyvinyl alcohol/fumed silica/clay nanocomposites. J Appl Polym Sci [Internet]. 2015 Nisan [cited 2016 Apr 25];132(15). Available from: <http://onlinelibrary.wiley.com/doi/10.1002/app.41843/abstract>
27. Peng Z, Kong LX. A thermal degradation mechanism of polyvinyl alcohol/silica nanocomposites. Polym Degrad Stab. 2007;92(6):1061–71.
28. Gilman JW, VanderHart DL, Kashiwagi T. Thermal Decomposition Chemistry of Poly(vinylalcohol). In: Nelson GL, editor. Fire and Polymers II: Materials and Test for Hazard Prevention. Washington, DC: American Chemical Society; 1994. p. 161–85.
29. Goiti E, Salinas MM, Arias G, Puglia D, Kenny JM, Mijangos C. Effect of magnetic nanoparticles on the thermal properties of some hydrogels. Polym Degrad Stab. 2007;92(12):2198–205.



The Synthesis of New Aryl Boron-Dipyrrromethene Compounds: Photophysical and pH Responsive Properties

Gökhan Sevinç¹  , Mustafa Hayvalı^{2*}  

¹Bilecik Şeyh Edebali University, Science and Literature Faculty, Department of Chemistry, 11230, Bilecik, Turkey.

²University of Ankara, Faculty of Science, Department of Chemistry, 06100, Ankara, Turkey.

Abstract: In this work, a convenient protocol enabled the synthesis of novel Arylated Borondipyrrromethene (BODIPY) compounds was applied that synthesis yields found to be higher than classical alkyl substituted analogues. Arylated chromophores exhibited the broader red-shifted absorption and fluorescence bands with higher stokes shifts with regard to reference Borondipyrrromethene compound (4,4'-difluoro-8-phenyl-1,3,5,7-tetramethyl-4-bora-3a,4a-diaza-s-indacene). We were interested in the electron transfer mechanism of compound BDPNH₂ which has amine subunit to alkyl substituted reference. The fluorescence enhancement of this compound in acidic media was associated with the inactivation of the acceptor type photoinduced electron transfer mechanism by fluorimetric measurements. Our results are helpful for designing new photosensitizers and for applications in the study of the molecular photochemistry.

Keywords: Aryl Borondipyrrromethene, Pentaaryldipyrin, BODIPY, pH Sensor

Submitted: December 28, 2017. **Accepted:** February 22, 2018.

Cite this: Sevinç G, Hayvalı M. The Synthesis of New Aryl Boron-Dipyrrromethene Compounds: Photophysical and pH Responsive Properties. JOTCSA. 2018;5(2):433-44.

DOI: <http://dx.doi.org/10.18596/jotcsa.372452>.

*Corresponding author. E-mail: hayvali@science.ankara.edu.tr.

INTRODUCTION

Investigating the photophysical properties of molecules provides convenient methods in various applications such as the determination of chemically or biologically important species (1-9), photodynamic therapy (10-14), TPA imaging microscopy (15-17), and organic photovoltaics (18-21). There are many studies in the literature about designing and synthesizing new molecules for these applications.

Dipyrrin based boron complexes known as BODIPY dyes have appeared as a fascinating class of luminescent molecules since their relative ease of preparation and modification over the past two decades. Actually, the widespread interest stems from their large molar absorption coefficients in the visible region, chemical robustness, solubility, high fluorescence quantum yields and photostability. Furthermore, photophysical properties of BODIPYs can be tailored and tuned by different substitution patterns on pyrrole rings and organic side, depending on application. Thus, many efforts have been devoted to engineer new BODIPY dyes and remarkable spectroscopic properties.

Alkyl substituted pyrrole derivatives such as 2,4-dimethylpyrrole and 2,4-dimethyl-3-ethylpyrrole are used as starting materials to obtain 4,4'-difluoro-8-phenyl-1,3,5,7-tetramethyl-4-bora-3a,4a-diaza-s-indacene derivatives known as BODIPY dyes. Although there are many studies for the photophysical properties of these types of dyes in the literature, only a few examples of arylated BODIPY derivatives on the 1,7,3,5 positions of the indacene core were reported (22-24).

We note that, investigation of photophysical properties of arylated BODIPYs in terms of substitution patterns of aryl groups are lacking. The enhancement of the conjugation by direct linking and free rotation of aryl groups on the BODIPY core could change the photophysical absorption and fluorescence properties lead to fluorescence enhancement or quenching.

With these considerations, we designed and synthesized novel arylated BODIPY compounds by introducing 4-nitrophenyl and 4-aminophenyl moieties to investigate the pH sensor capability. We also synthesized 1,3,5,7-tetramethyl substituted BODIPY (TMB) to be able to compare the results and reveal the effect of substitution in terms of photophysical properties. The target compounds were isolated in higher yields compared to alkyl substituted analogue (TMB). In this work we showed the use of arylated BODIPYs as pH probe by explaining the fluorescence enhancement mechanism of the compound BDPNH₂ with an amine substituted by using fluorescence spectroscopy technique as well as steady state UV-vis measurements.

EXPERIMENTAL SECTION

Materials and measurement

All reagents were purchased from Sigma-Aldrich and Merck Chemical Companies and used as received without further purification. 2,4-diphenylpyrrole was prepared according to the literature procedure (2). Reactions were monitored by thin layer chromatography using Silica gel plates (Merck, Kieselgel 60, 0.25 mm thickness) with F₂₅₄ indicator. Column chromatography was carried out on silica (230-400 mesh). Melting points were determined on a Barnstead Electrothermal IA9100 platform. UV-Visible spectra were recorded on a SHIMADZU UV-1800 UV-Vis spectrophotometer. Fluorescence spectra were recorded on a Perkin Elmer LS55 Fluorescence Spectrometer. Mass spectral analyses were performed on an Agilent 6224 TOF LC/MS spectrometer. ¹H-NMR spectra were recorded on a VARIAN Mercury 400 MHz spectrometer. ¹H-NMR chemical shifts (δ) are given in ppm downfield from Me₄Si, determined by chloroform (δ = 7.26 ppm) and DMSO (δ = 2.48 ppm). ¹³C-NMR spectra were recorded on a VARIAN Mercury 100 MHz spectrometer. ¹³C-NMR chemical shifts (δ) are reported in ppm with the internal CDCl₃ δ =77.0 ppm as standard.

Titration studies

Compound BDPNH₂ was dissolved in 2:1 CH₃CN-H₂O mixture and solution with 1×10⁻⁵ M concentration was prepared. Then 0.1 M solution of HCl were used to adjust the pH of the solutions by gradually adding a microliter of H⁺ to the dye solution. Then fluorimetric titration was applied as a function of pH using the emission spectra. The recorded steady-state fluorescence data (F) was fitted to the following equation (Eq. 1) as a function of [H⁺] yield value of K_a.

$$F = \frac{F_{max} H^{+n} + F_{min} K_a}{K_a + H^{+n}} \quad (\text{Eq. 1})$$

Here, F_{min} and F_{max} denote fluorescence signals at minimal and maximal [H⁺], respectively, and n denotes the number of protons bounded per fluorescent pH probe. n was kept fixed at 1 in the final curve fitting. Predicted an apparent pK_a value was obtained as 2.45 from the sigmoidal plot of pH versus fluorescence intensity.

Determination of fluorescence Quantum yields (Φ_F)

In order to determine the fluorescence quantum yields of the compounds BDPNO₂, BDPNH₂ and TMB, comparative method (Eq. 2) was applied.

$$\phi_F = \phi_F(\text{Std}) \frac{F \times A_{\text{Std}} \times n^2}{F_{\text{Std}} \times A \times n_{\text{Std}}^2} \quad (\text{Eq. 2})$$

Where ϕ_F (Std) is the fluorescence quantum yield of Rhodamine B. F and F_{Std} denote the areas under the fluorescence emission curves of samples and the standard, respectively. A and A_{Std} are the respective absorbance of the samples and standard compound at the excitation wavelengths. n^2 and n_{Std}^2 are the refractive indices of the solvents used for the sample and standard, respectively. Rhodamine B in ethanol ($\Phi_f = 0.65$) was used as the fluorescence standard for fluorescence quantum yield calculations. The concentration of the dilute solutions at the excitation wavelengths fixed at 1×10^{-6} M in dichloromethane. All spectra were recorded at 25 °C.

The synthesis of 4-difluoro-8-[4-nitrophenyl]-1,3,5,7-tetraphenyl-4-bora-3a,4a-diaza-s-indacene (BDPNO₂)

2,4-diphenylpyrrole (600 mg, 2.73 mmol) and 4-nitrobenzaldehyde (195 mg, 1.29 mmol) were dissolved in absolute CH₂Cl₂ (125 mL) under Ar atmosphere. Then one drop of trifluoroacetic acid (TFA) and tetrachloro-1,4-benzoquinone (0.48 g, 1.95 mmol) was added to the solution. The solution was stirred at room temperature for 6 h. The reaction mixture was condensed to 30 mL and filtered to provide a green solid. Without purification, the green solid and Hünig's base (1.50 mL, 9.12 mmol) were dissolved in 60 mL of CH₂Cl₂, the mixture was stirred at room temperature for 10 min; BF₃.OEt₂ (1.80 mL, 14.34 mmol) were then added and stirring was continued overnight. The resulting solution was washed with water and dried over anhydrous Na₂SO₄, filtered, and evaporated. The residue was chromatographed on silica gel (elution: benzene) to afford 291 mg (yield: 36%) Compound **BDPNO₂** in the form of purple powder. Mp = 315-318 °C. ¹H NMR (400 MHz, CDCl₃, δ, ppm): 7.92-7.90 (4H, m, Ar-H), 7.46-7.44 (6H, m, Ar-H), 7.30 (2H, d, *J*=8.8 Hz, Ar-H), 6.99 (2H, d, *J*=8.8 Hz, Ar-H), 6.95-6.92 (2H, m, Ar-H), 6.86-6.83 (4H, m, Ar-H), 6.73-6.72 (4H, m, Ar-H), 6.56 (2H, s, Ar-H), ¹³C NMR (100 MHz, CDCl₃): 157.9, 147.5, 147.4, 142.4, 138.2, 135.0, 132.7, 132.2, 129.9, 129.5, 129.5, 128.8, 128.3, 127.4, 126.9, 123.6, 121.40 HRMS/TOF-ESI: Calculated as 617.20862, found: 640.20210 [M+Na]⁺, Δ=5.79 ppm.

The synthesis of 4,4-difluoro-8-[4-aminophenyl]-1,3,5,7-tetraphenyl-4-bora-3a,4a-diaza-s-indacene (BDPNH₂)

BDPNO₂ (225 mg, 0.36 mmol) was dissolved in THF (15 mL) and EtOH (80 mL) under nitrogen, 5% Pd/C (15 mg), and hydrazine monohydrate (0.54 mL, 80% v/v) were added. The resulting solution was refluxed for 3 h. TLC analysis showed complete consumption of the starting material and then cooled to room temperature. The catalyst was removed by filtration

and the solvent was removed by rotary evaporation. The target product was obtained by a column chromatography on silica gel using CH_2Cl_2 :toluene (95:5 v/v) to afford the corresponding product **BDPNH₂**. Yield: 87 mg (41 %). Decomp. >300 °C. ¹H-NMR (400 MHz, DMSO, δ , ppm): 7.80-7.78 (4H, m, Ar-H), 7.43-7.41 (6H, m, Ar-H), 6.98-6.92 (6H, m, Ar-H), 6.86-6.84 (4H, m, Ar-H), 6.71 (2H, s, Ar-H), 6.55 (2H, d, $J=8.4$ Hz, Ar-H), 5.65 (2H, d, $J=8.4$ Hz, Ar-H), 5.27 (2H, s, -NH₂), ¹³C-NMR (100 MHz, DMSO): 157.9, 147.5, 147.4, 142.4, 138.2, 135.0, 132.7, 132.2, 129.9, 129.5, 128.8, 128.3, 127.4, 126.9, 123.7, 123.6, 121.4. HRMS/TOF-ESI: Calculated as 587.23443, found: 588.24820 [M+H]⁺, $\Delta=3.93$ ppm

RESULTS AND DISCUSSION

The compound BDPNO₂ was obtained by a standard procedure starting from the 2,4-diphenylpyrrole and 4-nitrobenzaldehyde in the presence of trifluoroacetic acid catalyst as shown in Figure 1. In the first step, *p*-chloranil was used for the oxidation of dipyrromethanes. Then the treatment with hunig's base and boron trifluoride diethyl etherate gave the desired product.

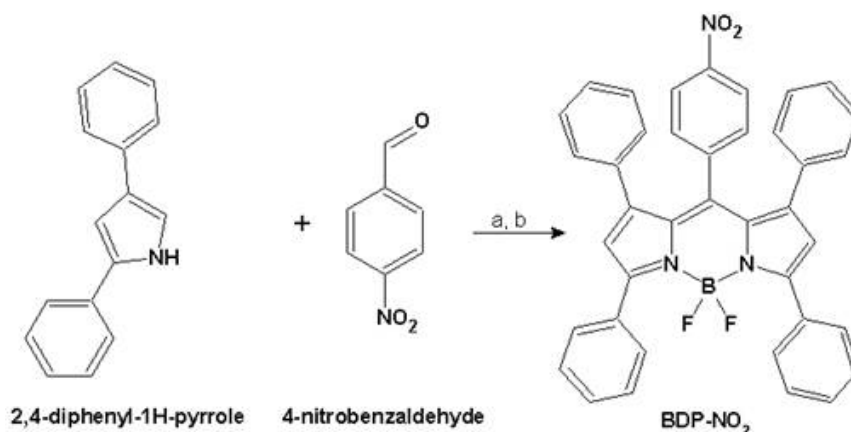


Figure 1: The synthesis of compound BDPNO₂ a) Tetrachloro-1,4-benzoquinone, Trifluoroacetic acid (cat.), CH_2Cl_2 , 25 °C, a) 8-12 h. b) DIPEA, $\text{BF}_3 \cdot \text{OEt}_2$, 12 h.

In the first step of the reaction, oxidizing agent *p*-chloranil was added immediately after mixing pyrrole and aldehyde derivative. After adding the catalyst, the color of the reaction mixture turned to deep green. After the complexation with boron difluoride and isolation, yield for the synthesis was found to be as 36%. The compound BDPNH₂ was obtained by reducing of compound BDPNO₂ with hydrazine and palladium/carbon catalyst and reduction afforded in 41% yield (Figure 2).

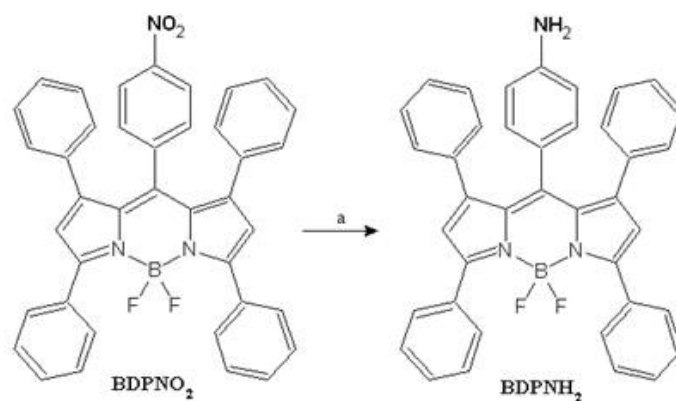


Figure 2: The synthesis of compound BDPNH₂ a) (NH₂)₂, Pd/C, THF:EtOH, reflux, 3h, Yield 41%

The identification of compounds was established by NMR spectroscopy. The most significant difference in the ¹H-NMR spectrum is the chemical shift of aromatic pyrrole protons. While the signal at 5.98 ppm is assigned to pyrrole protons of reference alkyl substituted compound TMB for the aryl substituted compounds BDPNO₂ and BDPNH₂ the chemical shifts observed in the higher values. For the comparison the chemical shifts of compounds TMB and BDPNO₂ were indicated in Figure. 3.

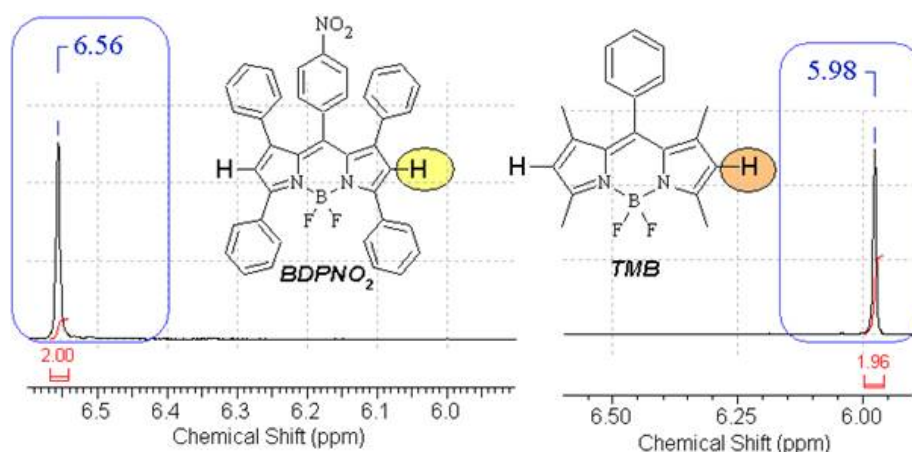


Figure 3: The scale of chemical shifts for compounds BDPNO₂ and TMB for pyrrolic protons in ¹H-NMR.

The downfield shifts of the aromatic pyrrole protons caused by the effect of aryl groups. In the series of compounds BDPNO₂ and BDPNH₂, there was a minor changes in chemical shifts of pyrrole protons when the meso substituents were changed from 4-nitrophenyl to 4-aminophenyl. Although these moieties have different donor or acceptor properties, no remarkable differences were observed in ¹H-NMR spectra. This is because the orthogonal geometry of meso (8) position of the indacene core.

The photophysical parameters of the dyes in dichloromethane are presented in Table 1. In general, the absorption spectra of synthesized BODIPY compounds show a similar shape as meso-substituted borondipyrromethene chromophores (Figure 4). UV-Vis absorption spectra of the compounds in DCM displayed an intense band between 553-565 nm assigned to the $S_0 \rightarrow S_1$ transitions along with high molar absorption coefficients. The broader absorption band localized between 350-400 nm is ascribed to the $S_0 \rightarrow S_2$ transitions of BODIPY moiety. Introducing aryl groups at the 1, 3, 5, 7 positions of the BODIPY core showed significant bathochromic shifts compared to alkyl substituted analogue due to the extended conjugation. Additionally, the absorption bands of the compounds are relatively broader and the Stokes shifts are larger compared to those of alkyl substituted counterpart. However, the molar absorption coefficients and fluorescence quantum yields were decreased.

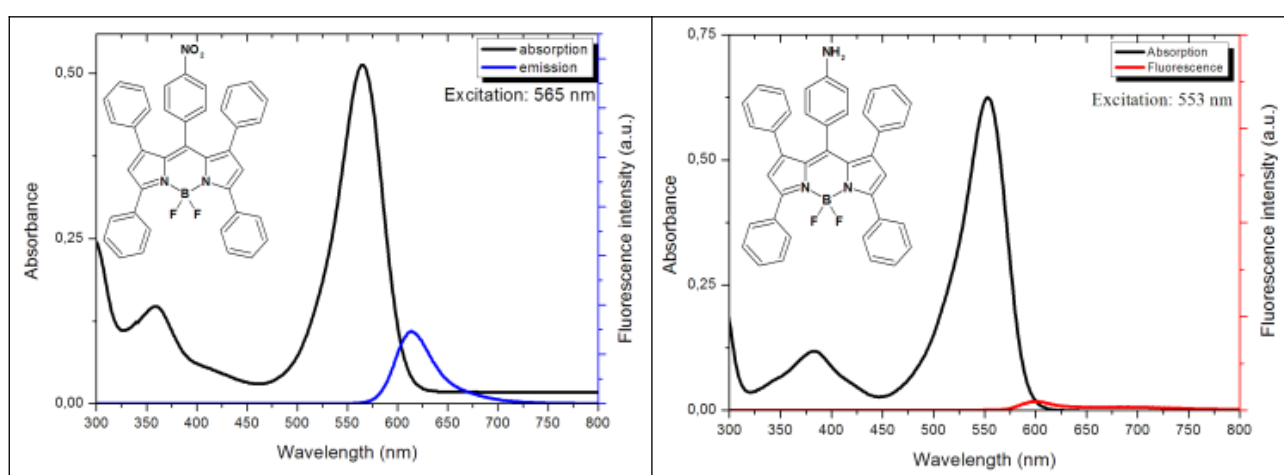


Figure 4: UV and Fluorescence spectrum of BDPNO₂ (left) and BDPNH₂ (right) in DCM.

Compounds with 4-nitrophenyl group on the 8 position of the BODIPY core showed a clear bathochromic shift in their absorption maxima, as compared to 4-aminophenyl substituted analogue BDPNH₂. For aryl substituted compounds, absorption bandwidths (FWHM) are 2-3 times broader than TMB counterpart. Furthermore, the fluorescence emission spectra display a Stokes-shifted (ca. 49 nm) for BDPNO₂, mirror-symmetrical bands relative to the absorption of BODIPY units. The Stokes shift (expressed in nm) was measured as 49 nm.

Table 1. Photophysical data of synthesized compounds in DCM (1×10^{-6} M)

Compound	λ_{Abs} max (nm)	λ_{Ems} max (nm)	ϵ ($\text{M}^{-1}\text{cm}^{-1}$)	FWHM (nm)	Stokes' shift (nm)	Φ_f
TMB	501	515	71400	21	14	0.36
BDPNO ₂	565	614	51300	54	49	0.09
BDPNH ₂	553	-	62500	51	-	-

A Stokes-shifted band of perfect mirror image shape with minimum energy loss that shows the main absorption band corresponds to the $S_0 \rightarrow S_1$ transition. The diminishing fluorescence intensity for the compound BDPNH₂ can be attributed to the lone-pair electrons on the nitrogen atom that enables the photoinduced electron transfer. The decreasing fluorescence quantum yield of the compound BDPNO₂ is related with the same mechanism. It is obvious that extended π conjugation and free rotation of aryl groups around Ar-Ar bonds have responsible the both absorption and fluorescence properties of the compounds (23).

4-aminophenyl moiety of compound BDPNH₂ is sensitive to the pH and -NH₂ group can be protonated in acidic environments. The effect of pH was assessed by altering the solution pH from neutral to acidic environment through the addition of aq. HCl in CH₃CN:H₂O (2:1). The pH dependent absorption and fluorescence graphs were given in Figure 5.

The spectroscopic data revealed that the main absorption band was nearly unchanged with a slight shift to longer wavelengths. This insignificant bathochromic shift in acidic solution may be caused by transpacer electronic interactions between the protonated -NH₂ subunit and the fluorophore that in agreement with the meso substitution. Besides, there is a bathochromic shift of band with higher energy in the range of 300-450 nm with decreasing pH indicate the formation of anilinium cation.

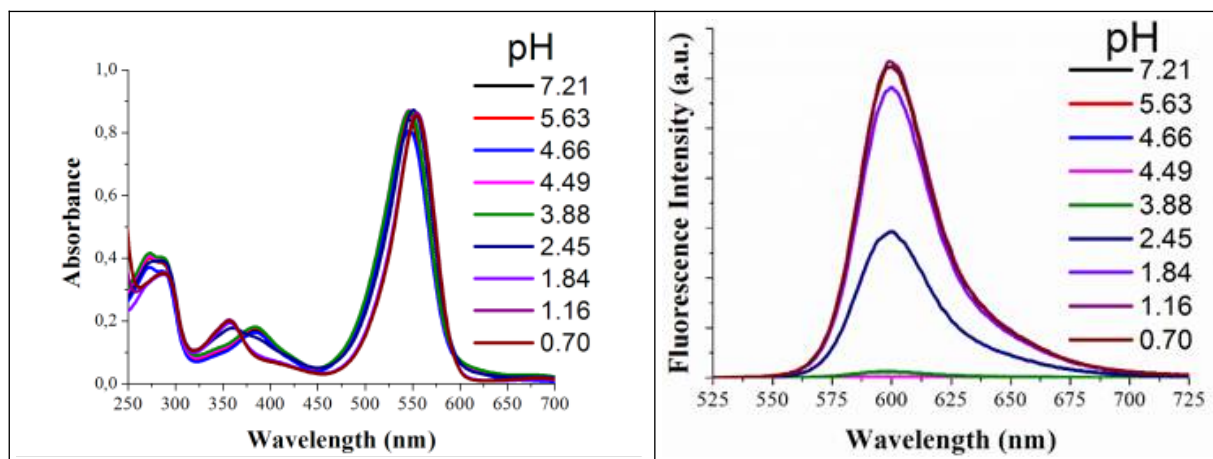


Figure 5. Dependence of the absorption (top) and fluorescence (bottom) of compound BDPNH_2 on a change in pH upon addition of aq. HCl solution (excitation: 553 nm, dye concentration: 1×10^{-5} M)

The corresponding emission features have also been investigated upon altering the pH. Although BDPNH_2 is not a fluorescent molecule in a neutral environment, upon protonation fluorescence signal showed drastic enhancement at a maximum emission wavelength at 600 nm. The studies were The nonlinear sigmoidal fitting of titration data was given in Figure 6. The reversibility experiments have been carried out and it was found that all changes are found to be fully reversible. The addition of pyridine to the acidic solution of compound BDPNH_2 resulted the fluorescence quenching as observed in the neutral solution.

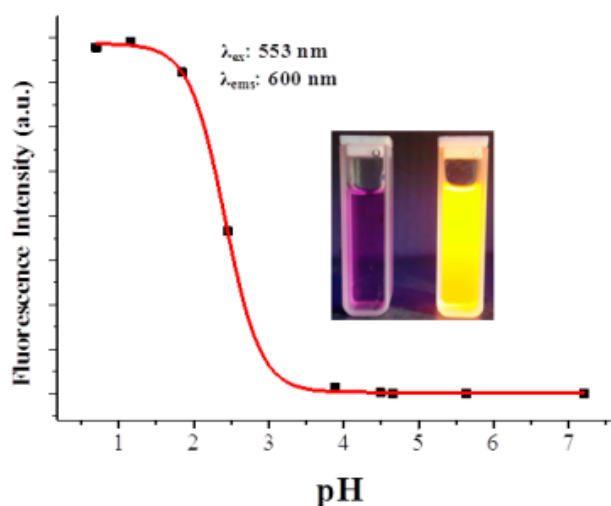


Figure 6: Nonlinear fitting of fluorescence intensity depends on decreasing pH for BDPNH_2 , Figure inset shows Compound BDPNH_2 at neutral (left) and acidic (right) environment under UV irradiation.

these observations can be explained by the inactivation of the acceptor type photoinduced electron transfer (PET) process between BODIPY core and the substituted group. The

intramolecular PET process strongly quenches the fluorescence of the compound BDPNH₂ in neutral media. The enhancement of fluorescence intensity shows that the inactivation of the PET process altered the energy level of the side group binding to the BODIPY core. This situation was depicted schematically in Figure. 7.

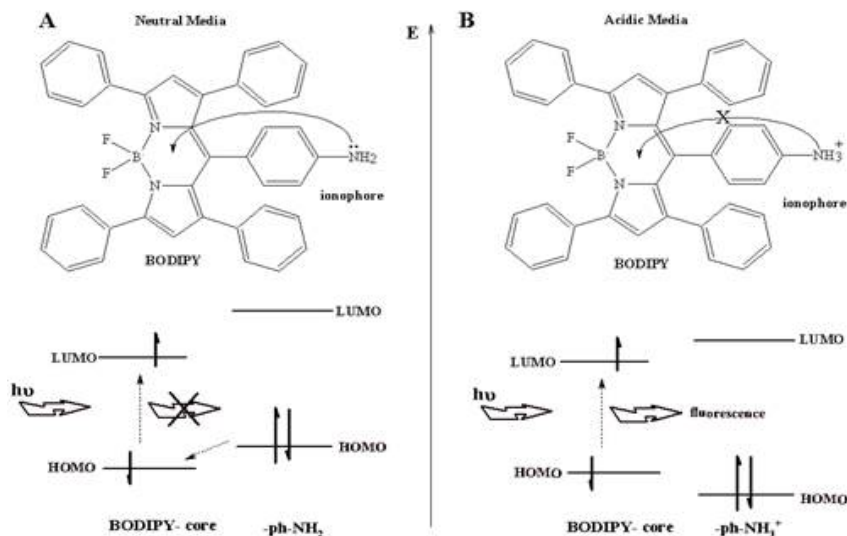


Figure 7: Proposed mechanism for fluorescence enhancement of BDPNH₂ in acidic media attributed by a-PET (a) quenching mechanism (b) fluorescence mechanism.

Coordination of the H⁺ ion makes the ionophore electron poor and lowers the HOMO of the ionophore, so that PET from the excited BODIPY fluorophore to the ionophore becomes infeasible, leading to fluorescence enhancement.

CONCLUSION

In summary, we have synthesized new arylated BODIPY chromophores which show broadband absorption in visible spectral region. The photophysical studies exhibited that arylatedboron-dipyrromethenecompounds have the red-shifted absorption bands and 2-3 times higher stokes shifts and full width at half media (FWHM) values compared to alkyl substituted analogue (TMB). We performed the pH probe application of aminophenyl substituted BDPNH₂ compound which has showed drastic fluorescence enhancement upon increasing protonation. Coordination of the H⁺ ion lowers the HOMO level of the ionophore. Therefore, electron transfer from ionophore to the excited BODIPY fluorophore becomes possible. This electron transfer leads to fluorescence enhancement. Our results are helpful for designing new photosensitizers and for applications in photodynamic therapy and for study of the molecular photochemistry.

ACKNOWLEDGEMENT

This article was produced from a part of PhD thesis entitled "Sevinç, G., The Synthesis of Pentaaryldipyrrin BF₂ complexes and the Investigation of their photophysical Properties, Ankara University, Graduate School of Natural and Applied Sciences, Chemistry Department, Ankara"

REFERENCES

1. Chen YT, Wang HL, Wan L, Bian YZ, Jiang JZ. 8-Hydroxyquinoline-Substituted Boron-Dipyrrromethene Compounds: Synthesis, Structure, and OFF-ON-OFF Type of pH-Sensing Properties. *J Org Chem*. 2011 May 20;76(10):3774-81.
2. Gawley RE, Mao H, Haque MM, Thorne JB, Pharr JS. Visible fluorescence chemosensor for saxitoxin. *J Org Chem*. 2007 Mar 16;72(6):2187-91.
3. Gee KR, Rukavishnikov A, Rothe A. New Ca²⁺ fluoroionophores based on the BODIPY fluorophore. *Comb Chem High T Scr*. 2003 Jun;6(4):363-6.
4. Guo HM, Jing YY, Yuan XL, Ji SM, Zhao JZ, Li XH, et al. Highly selective fluorescent OFF-ON thiol probes based on dyads of BODIPY and potent intramolecular electron sink 2,4-dinitrobenzenesulfonyl subunits. *Org Biomol Chem*. 2011;9(10):3844-53.
5. Han JY, Burgess K. Fluorescent Indicators for Intracellular pH. *Chem Rev*. 2010 May;110(5):2709-28.
6. Namkung W, Padmawar P, Mills AD, Verkman AS. Cell-based fluorescence screen for K(+) channels and transporters using an extracellular triazacryptand-based K(+) sensor. *J Am Chem Soc*. 2008 Jun 25;130(25):7794-+.
7. Sevinç G, Kucukoz B, Yilmaz H, Sirikci G, Yaglioglu HG, Hayvalı M, et al. Explanation of pH probe mechanism in borondipyrrromethene-benzimidazole compound using ultrafast spectroscopy technique. *Sensor Actuat B-Chem*. 2014 Mar;193:737-44.
8. Son H, Lee HY, Lim JM, Kang D, Han WS, Lee SS, et al. A Highly Sensitive and Selective Turn-On Fluorogenic and Chromogenic Sensor Based on BODIPY-Functionalized Magnetic Nanoparticles for Detecting Lead in Living Cells. *Chem-Eur J*. 2010;16(38):11549-53.
9. Teknikel E, Unaleroglu C. Colorimetric and fluorometric pH sensor based on bis(methoxycarbonyl)ethenyl functionalized BODIPY. *Dyes Pigments*. 2015 Sep;120:239-44.
10. Awuah SG, You Y. Boron dipyrromethene (BODIPY)-based photosensitizers for photodynamic therapy. *Rsc Adv*. 2012;2(30):11169-83.
11. Kamkaew A, Lim SH, Lee HB, Kiew LV, Chung LY, Burgess K. BODIPY dyes in photodynamic therapy. *Chem Soc Rev*. 2013;42(1):77-88.
12. Turan IS, Yildiz D, Turksoy A, Gunaydin G, Akkaya EU. A Bifunctional Photosensitizer for Enhanced Fractional Photodynamic Therapy: Singlet Oxygen Generation in the Presence and Absence of Light. *Angew Chem Int Edit*. 2016 Feb 18;55(8):2875-8.
13. Wang WQ, Wang L, Li ZS, Xie ZG. BODIPY-containing nanoscale metal-organic frameworks for photodynamic therapy. *Chem Commun*. 2016;52(31):5402-5.
14. Zhang T, Lan RF, Gong LL, Wu BY, Wang YZ, Kwong DWJ, et al. An Amphiphilic BODIPY-Porphyrin Conjugate: Intense Two-Photon Absorption and Rapid Cellular Uptake for Two-Photon-Induced Imaging and Photodynamic Therapy. *Chembiochem*. 2015 Nov 2;16(16):2357-64.

15. Didier P, Ulrich G, Mely Y, Ziessel R. Improved push-pull-push E-Bodipy fluorophores for two-photon cell-imaging. *Org Biomol Chem*. 2009;7(18):3639-42.
16. Kasischke KA, Vishwasrao HD, Fisher PJ, Zipfel WR, Webb WW. Neural activity triggers neuronal oxidative metabolism followed by astrocytic glycolysis. *Science*. 2004 Jul 2;305(5680):99-103.
17. Kim B, Yue XL, Sui BL, Zhang XF, Xiao Y, Bondar MV, et al. Near-Infrared Fluorescent 4,4-Difluoro-4-bora-3a,4a-diaza-s-indacene Probes for One- and Two-Photon Fluorescence Bioimaging. *Eur J Org Chem*. 2015 Sep(25):5563-71.
18. Chen JJ, Conron SM, Erwin P, Dimitriou M, McAlahney K, Thompson ME. High-Efficiency BODIPY-Based Organic Photovoltaics. *Acs Appl Mater Inter*. 2015 Jan 14;7(1):662-9.
19. Economopoulos SP, Chochos CL, Ioannidou HA, Neophytou M, Charilaou C, Zissimou GA, et al. Novel BODIPY-based conjugated polymers donors for organic photovoltaic applications. *Rsc Adv*. 2013;3(26):10221-9.
20. Poe AM, Della Pelle AM, Subrahmanyam AV, White W, Wantz G, Thayumanavan S. Small molecule BODIPY dyes as non-fullerene acceptors in bulk heterojunction organic photovoltaics. *Chem Commun*. 2014;50(22):2913-5.
21. Squeo BM, Gasparini N, Ameri T, Palma-Cando A, Allard S, Gregoriou VG, et al. Ultra low band gap alpha,beta-unsubstituted BODIPY-based copolymer synthesized by palladium catalyzed cross-coupling polymerization for near infrared organic photovoltaics. *J Mater Chem A*. 2015;3(31):16279-86.
22. Duan X, Li PM, Li P, Xie T, Yu FBA, Tang B. The synthesis of polarity-sensitive fluorescent dyes based on the BODIPY chromophore. *Dyes Pigments*. 2011 Jun;89(3):217-22.
23. Kucukoz B, Sevinc G, Yildiz E, Karatay A, Zhong F, Yilmaz H, et al. Enhancement of two photon absorption properties and intersystem crossing by charge transfer in pentaaryl boron-dipyrromethene (BODIPY) derivatives. *Phys Chem Chem Phys*. 2016 May 21;18(19):13546-53.
24. Wakamiya A, Sugita N, Yamaguchi S. Red-emissive Polyphenylated BODIPY Derivatives: Effect of Peripheral Phenyl Groups on the Photophysical and Electrochemical Properties. *Chem Lett*. 2008 Oct 5;37(10):1094-5.



Investigation of Phenolic Compounds and Antioxidant Activity of *Mentha spicata* subsp. *spicata* and *M. longifolia* subsp. *typhoides* (Briq.) Harley Decoction and Infusion

Züleyha Özer^{1,*}  

¹University of Balıkesir, Altınoluk Vocational School, Medicinal and Aromatical Plants Programme, 10870, Altınoluk, Edremit-Balıkesir, Turkey

Abstract: In the present study, phenolic compounds and antioxidant activity of decoction and infusion of aerial parts of *Mentha spicata* subsp. *spicata* and *M. longifolia* subsp. *typhoides* (Briq.) Harley were investigated. Phenolic contents of the decoction and infusion were analyzed using LC-MS/MS. Also, the antioxidant activity of the species was determined by three methods: 2,2-diphenyl-1-picrylhydrazyl (DPPH) free radical scavenging, β -carotene linoleic acid assays, and CUPRAC assays. Flavonoids and derivatives were the most abundant components of the *M. spicata* subsp. *spicata* decoction and *M. longifolia* subsp. *typhoides* decoction and infusion, whereas coumaric acids and derivatives were found to be the most abundant components of *M. spicata* subsp. *spicata* infusion. Particularly, the main compounds were determined as follow for *M. spicata* subsp. *spicata* decoction and infusion; caffeic acid and fumaric acid. Rosmarinic acid was detected in high amounts in *M. longifolia* subsp. *typhoides* decoction and infusion. For all the activity assays, infusion and decoction of the samples showed good activity.

Keywords: *Mentha spicata* subsp. *spicata*, *Mentha longifolia* subsp. *typhoides*, antioxidant activity, phenolic compound.

Submitted: Aug 11, 2017. **Accepted:** Feb 22, 2018.

Cite this: Ozer Z. Investigation of Phenolic Compounds and Antioxidant Activity of *Mentha spicata* subsp. *spicata* and *M. longifolia* subsp. *typhoides* (Briq.) Harley Decoction and Infusion. JOTCSA. 2018;5(2):445-456.

DOI: <http://dx.doi.org/10.18596/jotcsa.350089>.

***Corresponding author.** E-mail: zuleyhaozer@balikesir.edu.tr.

INTRODUCTION

Lamiaceae (Labiatae) family consisting of about 236 genera and 6,900 to 7,200 species distributed all over the world (1). This family has strong antioxidant properties due to their rich source of polyphenolic compounds (2, 3). The genus *Mentha* (Lamiaceae) is represented in Turkey by 6 species, 4 hybrids and 13 taxa (4). *Mentha* species are used as herbal tea and folk medicine for treatment of several disorders (5, 6). *M. spicata* (eşek nanesi) is a medicinally important plant and commonly known as spearmint. Infusion and hydrolate of the aerial parts of *M. spicata* used for treatment of colds and flu, respiratory tract problems, gastralgia, hemorrhoids, and stomachache (7). Also, *M. longifolia* is generally known under the name "dere nanesi" and widely used for sore throat, hemorrhoids, shortness of breath, stomachache, sunstroke, headache, cough, and menstrual pain (8).

Many studies have been conducted to investigate the chemical content and biological activities of *Mentha* species (3-6). The studies especially related to essential oil composition and biological activities (9-12). Previous studies have been reported that the extracts of different species possess phenolic content, antioxidant, anti-inflammatory and antimicrobial activities (13-15). Also, there are some reports on total phenolic content and antioxidant activity of infusion of *M. spicata* and *M. longifolia* from different regions of the world and the main phenolic compounds were determined as mainly eriocitrin, luteolin-7-*O*-glucoside, rosmarinic acid, luteolin, and caffeic acid (15-23). The results showed that, since locality, climatic and seasonal conditions affect the chemical constituents of the plants, biological activity results differ. Also, previous studies have demonstrated that the phenolic content of herbal infusion is strongly correlated with their antioxidant activity (17-21). The antioxidant activity of phenolic compounds is widely due to their free radical scavenger, singlet and triplet oxygen quencher, metal chelation potential, and hydrogen donor properties (13-16). Therefore, the present study aimed to investigate comparative antioxidant activities as well as phenolic compounds of decoction and infusion of aerial parts of *M. spicata* subsp. *spicata* and *M. longifolia* subsp. *typhoides* Turkey.

EXPERIMENTAL SECTION

Plant materials

The aerial parts of *M. longifolia* subsp. *typhoides* (Briq.) Harley;

Balıkesir: On the road of Çamlık-Turnacı, forest bottoms, 1310 m, 10.9.2015, (herbarium number SS 6809).

The aerial parts of *M. spicata* subsp. *spicata*;

Balıkesir: Sındırgı, Ulus Peak, 1768 m, 21.8.2015, (herbarium number SS 6701).

The species were identified by Dr. Selami Selvi at Balıkesir University. The voucher specimens were deposited at the Herbarium of the Altınoluk Vocational School, Balıkesir University, Balıkesir, Turkey.

Preparation of decoction and infusion samples

4 g of aerial parts of the plant, dried in the shade and chopped into small pieces. For infusion; 2 g of the plant were added to 98 mL of distilled boiling water and allowed to stay for 15 minute. For decoction; 2 g of the plant were added to 98 mL of distilled water and heated together in a steel kettle and allowed to stay for 15 minute after it boiled. The teas were filtered with an ashless filter paper. The filtrates were diluted with 25 mL of distilled water.

Phenolic compounds were determined by LC-MS/MS.

Chemicals

Standard compounds used for LC-MS/MS analysis were as follows: fumaric acid (99%, Sigma-Aldrich), pyrogallol (98%, Sigma-Aldrich), rutin (94%, Sigma-Aldrich), chlorogenic acid (95%, Sigma-Aldrich), gallic acid (99%, Merck), syringic acid (95%, Sigma-Aldrich), t-ferulic acid (99%, Sigma-Aldrich), caffeic acid (98%, Sigma-Aldrich), pelargonin chloride (98%, Sigma-Aldrich), quercitrin (97%, Sigma-Aldrich), salicylic acid (99%, Sigma-Aldrich), *p*-coumaric acid (98%, Sigma-Aldrich), luteolin-7-*O*-glu (99%, AppliChem), rosmarinic acid (96%, Sigma-Aldrich), apigenin (95%, Sigma-Aldrich), kaempferol (96%, Sigma-Aldrich) and isorhamnetin (98%, ExtraSynthese, Genay-France). Stock solutions were prepared as 10 mg/L in methanol. HPLC grade methanol was purchased from Merck (Darmstadt, Germany). Calibration solutions were prepared in methanol in a linear range. Dilutions were performed using automatic pipettes and glass volumetric flasks (A class). 0 mg/L curcumin solution was freshly prepared, from which 50 μ L was used as an Internal Standard (IS) in all experiments.

Liquid chromatography-mass spectrometry

LC-MS/MS experiments were performed by a Zivak® HPLC and Zivak® Tandem Gold Triple quadrupole (Istanbul, Turkey) mass spectrometry equipped with a Synergy Max C18 column (250 x 2 mm i.d., 5mm particle size). The mobile phase was composed of water (A, 0.1 % formic acid) in methanol (B, 0.1 % formic acid), the gradient programme of which was 0-1.00 minute 55 % A and 45 % B, 1.01-20.00 minutes 100 % B and finally 20.01-23.00 55 % A and 45 % B. The flow rate of the mobile phase was 0.25 mL/min, and the column temperature was set to 30 °C. The injection volume was 10 µL.

The detailed information on preparation of test solution and evaluation of uncertainty has been reported in the literature (24, 25).

Biological activity

The antioxidant activities were measured based on 2,2-diphenyl-1-picrylhydrazyl (DPPH) free radical scavenging activity (24-30), β -carotene linoleic acid assays (24, 26, 30) and cupric (Cu²⁺) ion reducing power assay (CUPRAC) (24, 26, 30-32).

RESULTS AND DISCUSSION

Phenolic contents

The results of the studied phenolic compounds of decoction and infusion of *M. spicata* subsp. *spicata* and *M. longifolia* subsp. *typhoides* by LC-MS/MS are shown in Table 1. All the phenolic compounds of *M. spicata* subsp. *spicata* and *M. longifolia* subsp. *typhoides* decoction and infusion were classified into three groups as flavonoids and derivatives, coumaric acids and derivatives, and simple phenolics and others. Total 20 compounds, composed of 12 flavonoids and 8 phenolic acids were determined in the decoction and infusion of *M. spicata* subsp. *spicata* and *M. longifolia* subsp. *typhoides*. Caffeic acid (4126.6 mg), quercetagenin-3,6-dimethylether (2141.5 mg) and penduletin (1472.7 mg) were found to be the main phenolic compounds in *M. spicata* subsp. *spicata* decoction, whereas fumaric acid (4220.1 mg), *t*-ferulic acid (1148.7 mg), and caffeic acid (1064.1 mg) were found to be the main phenolic compounds in infusion. In *M. longifolia* subsp. *typhoides*, the main phenolic compounds for decoction were rosmarinic acid (1570.7 mg), luteolin (460.9 mg), and quercetagenin-3,6-dimethylether (420.2 mg). Rosmarinic acid, luteolin and fumaric acid (620.9; 518.2; 489.8 mg, respectively) were found to be the main compounds of *M. longifolia* subsp. *typhoides* infusion.

Flavonoids and derivatives were the dominant group (6303.8 mg) in the decoction of *M. spicata* subsp. *spicata* with quercetagenin-3,6-dimethylether, penduletin, and kaempferol. Coumaric acids and derivatives were represented with 4434.8 mg and caffeic acid (4126.6 mg)

was found to be the dominant compound in decoction *M. spicata* subsp. *spicata*. While simple phenolics and others were detected in scarce amounts (187.4 mg).

On the contrary, phenolic compounds of *M. spicata* subsp. *spicata* infusion were characterized by the presence of simple phenolics and others (4280.0 mg) and fumaric acid was found to be the major compound (4220.1 mg). Flavonoids and derivatives of infusion of *M. spicata* subsp. *spicata* were detected in scarce amounts (548.2 mg).

Flavonoids and coumaric acids derivatives were presented almost in equal amount (1771.2 and 1838.8 mg, respectively) in decoction of *M. longifolia* subsp. *typhoides* with rosmarinic acid (1570.7 mg), luteolin (460.9 mg) and quercetageitin-3,6-dimethylether (420.2 mg) were found to be the main components. In the infusion of *M. longifolia* subsp. *typhoides*, flavonoids and coumaric acids derivatives were detected in equal amount (884.3 and 937.6 mg, respectively). Rosmarinic acid (620.9 mg) was detected as main coumaric acid derivative and luteolin (518.2 mg) was detected as main flavonoid.

As a result the amount of phenolic compounds extracted in decoction of *M. spicata* subsp. *spicata* is very high comparison with other extracts. Especially amount of flavonoids were found to be higher than the other extracts. Also, the decoction extracts of both plants were found to contain more phenolic compounds than the infusions.

In the previous studies, aqueous extract of *M. spicata* var. *crispa* characterized by a high content of phenolic compounds such as eriocitrin, naringenin-gluc and rosmarinic acid and antioxidant properties were analyzed by iron reduction and chelation, 1,1-diphenyl-2-picrylhydrazyl radical and iron-ascorbate generated hydroxyl radical scavenging (15). Also, antioxidant activity and phenolic content of aqueous extracts were investigated of *M. spicata* L. from Bulgaria (21). In another study, chemical characterization such as chlorogenic acid, rosmarinic acid, salvianolic acid B and salicylic acid of aqueous extracts were investigated of *M. spicata* from Italy (9). Additionally, total phenolic and antioxidant activity of methanolic extract of different *M. spicata* and *M. longifolia* five Iranian mint accessions were investigated (19). *Dinis et.al.* (23) reported the chemical compounds (eriocitrin, eriodictyol) and acetylcholinesterase inhibitory activity of infusion of *M. spicata* from Portugal. Also, *Sytar et. al.* (20) reported the phenolic compounds and antioxidant activity of methanolic extracts of *M. spicata* L. from Slovakia. Previous studies showed that aqueous extracts of the species had a variety of phenolic contents. The variation might be concerned local, climatic and seasonal differences.

Table 1: Phenolic contents of *M. spicata* subsp. *spicata* and *M. longifolia* subsp. *typhoides* decoction and infusion.

	Parent ion	Daughter ion	Collision energy (V)	<i>M. spicata</i>		<i>M. longifolia</i>	
				Decoction	Infusion	Decoction	Infusion
Flavonoids and derivatives							
pelargonin	271.2	121	34	441.7±449.0	147.4±7.5	73.9±7.5	152.9±7.8
penduletin	345.2	311	25	1472.7±149.3	90.1±9.1	55.5±5.6	-
luteolin	285	132	30	-	-	460.9±118.4	518.2±66.5
apigenin	269	151	22	218.9±17.6	57.9±4.7	51.8±4.2	85.4±6.9
isorhamnetin	315	300	15	36.4±3.2	-	6.2±0.6	-
quercetagenin-3,6-dimethylether	345.1	329.5	16	2141.5±400.9	-	420.2±78.7	43.3±8.1
luteolin-7- <i>O</i> -glucoside	447	284.5	14	206.6±21.0	41.9±2.1	77.9±7.9	32.1±1.6
luteolin-5- <i>O</i> -glucoside	447	289.5	20	283.9±18.3	13.8±0.9	244.3±15.7	13.9±0.9
kaempferol	287	152.3	30	1364.8±96.3	-	363.3±25.6	-
rutin	609	301	16	137.3±8.9	159.5±10.4	-	35.3±2.3
salvigenin	329	295.8	15	-	37.6±2.6	17.2±1.2	-
isoquercetin	463.3	300	25	-	-	-	3.2±0.9
Total (mg/kg dried herb)				6303.8	548.2	1771.2	884.3
Coumaric acids and derivatives							
caffeic acid	179	135	10	4126.6±816.6	1064.1±210.6	215.4±42.6	113.1±22.4
t-ferulic acid	193	133	15	-	1148.7±80.3	10.9±0.8	162.7±11.4
chlorogenic acid	353	191	14	308.2±42.7	102.4±14.2	27.4±3.8	26.3±3.6
rosmarinic acid	359.2	160.5	15	-	-	1570.7±120.4	620.9±47.6
<i>p</i> -coumaric acid	163.2	118.7	14	-	63.1±9.7	14.4±2.2	14.6±2.2
Total (mg/kg dried herb)				4434.8	2378.3	1838.8	937.6
Simple phenolics and others							
gallic acid	168.6	124	13	11.3±0.8	5.6±0.4	4.4±0.3	4.6±0.3
syringic acid	196.7	181.4	12	176.1±11.9	54.3±3.7	55.5±3.7	18.7±1.3
fumaric acid	115	71	8	-	4220.1±292.7	-	489.8±33.9
Total (mg/kg dried herb)				187.4	4280.0	59.9	513.1
curcumin*	369.3	176.9	20				
				10926.0	7206.5	3669.9	2335.0

* Used as internal standard

Antioxidant activity

The antioxidant activities were determined applying DPPH free radical scavenging activity, β -carotene linoleic acid assays and CUPRAC assays. Inhibition of lipid peroxidation and DPPH free radical scavenging effect were determined at 2, 5, 10, and 20 μ L. The results were given in Tables 2 and 3 and Figures 1 and 2. Butylated hydroxyanisole (BHA) and butylated hydroxytoluene (BHT) were used as standard compounds in DPPH and β -carotene linoleic acid assays. In DPPH-free radical scavenging activity assay, decoction and infusion samples of *M. spicata* subsp. *spicata* and *M. longifolia* subsp. *typhoides* at all concentrations showed good activity. In the same way β -carotene linoleic acid assay had good activity results. For the CUPRAC method, decoction and infusion samples of *M. spicata* subsp. *spicata* and *M. longifolia* subsp. *typhoides* had better activity than curcumin, which was used as a standard compound. *M. spicata* subsp. *spicata* samples having 2, 5, 10, 20 μ L concentrations, DPPH and β -carotene methods showed higher activities. For especially the decoction of *M. spicata* subsp. *spicata*, CUPRAC method had better activity. The results are given in the Figure 2.

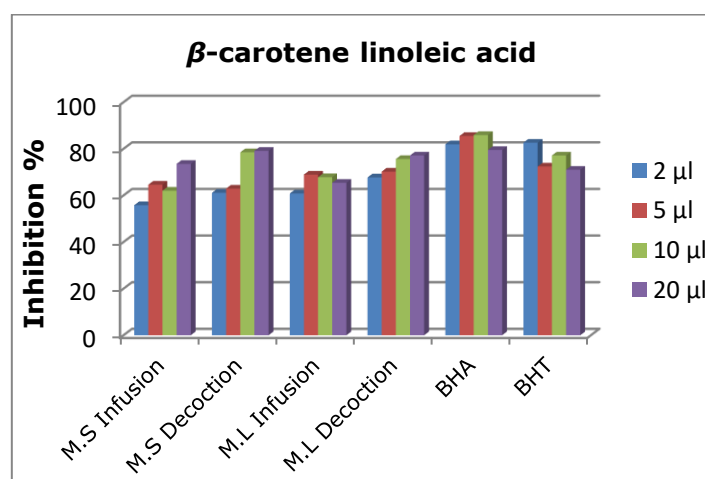
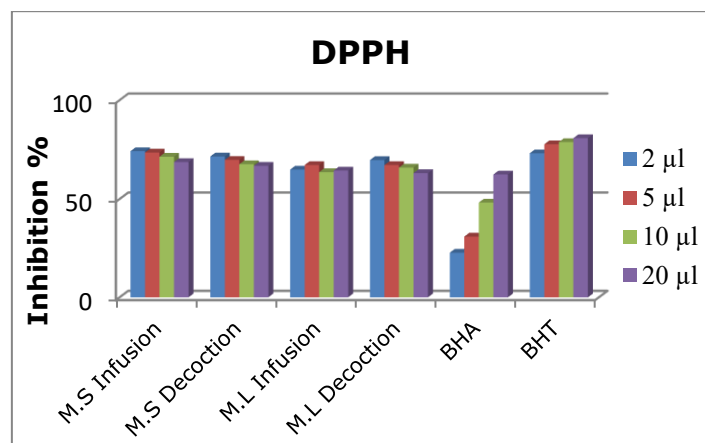
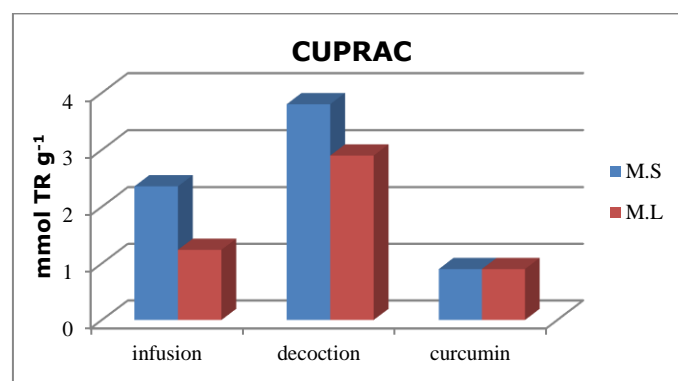
In the literature, the antioxidant activity of 50% aqueous methanol extract of *M. aquatica* L., *M. longifolia* (L.) Huds. subsp. *longifolia*, *M. longifolia* L. subsp. *typhoides* (Briq.) Harley var. *typhoides*, *M. pulegium* L., *M. spicata* L. subsp. *spicata*, *M. spicata* L. subsp. *tomentosa* (Briq.) Harley, was measured by free radical scavenging, hydrogen peroxide (H₂O₂) scavenging and metal (Fe²⁺) chelating assays (17). Also, antioxidant properties were analyzed in mint (*M. spicata*) from Malaysia (18). Our results are compatible with other studies in the literature (15, 18-22).

Table 2: Inhibition (%) of DPPH and lipid peroxidation of *M. spicata* subsp. *spicata* and *M. longifolia* subsp. *typhoides*, BHA and BHT

			2 μ L	5 μ L	10 μ L	20 μ L
DPPH	<i>M. spicata</i>	Infusion	74.2±0.2	73.5±0.5	71.4±1.2	68.7±1.6
		Decoction	71.5±1.1	69.8±2.2	67.6±2.0	66.8±2.4
	<i>M. longifolia</i>	Infusion	64.9±12.7	67.2±4.0	63.6±7.4	64.4±0.8
		Decoction	69.7±0.8	67.2±1.4	65.9±0.6	63.1±0.8
β -carotene linoleic	<i>M. spicata</i>	BHA	22.7±2.1	30.9±4.1	48.2±3.9	62.4±2.9
		BHT	73.1±2.6	77.7±0.7	78.8±0.8	80.8±1.6
		Infusion	55.8±9.9	64.6±2.4	62.0±8.6	73.5±1.4
		Decoction	61.1±5.8	62.9±4.4	78.5±4.2	79.1±2.4
	<i>M. longifolia</i>	Infusion	60.8±6.5	68.9±4.2	67.8±4.5	65.4±6.3
		Decoction	67.7±8.5	70.2±1.7	75.6±4.1	77.1±4.3
		BHA	81.9±1.9	85.5±1.7	85.9±2.4	79.5±4.1
		BHT	82.6±5.0	72.4±11.8	77.1±2.9	71.0±1.0

Table 3: Antioxidant activity of *M. spicata* subsp. *spicata* and *M. longifolia* subsp. *typhoides* extracts (CUPRAC)

CUPRAC (mmol TR g ⁻¹)	<i>M. spicata</i>	<i>M. longifolia</i>
Infusion	2.36±0.09	1.24±0.13
Decoction	3.8±0.00	2.9±0.04
Curcumin	0.9	0.9

**Figure 1:** Antioxidant activities of decoction and infusion *M. spicata* subsp. *spicata* (M.S) and *M. longifolia* subsp. *typhoides* (M.L), BHA and BHT (DPPH and β-carotene linoleic acid assays).**Figure 2:** Cu²⁺ reducing power (CUPRAC) assay of the extracts and curcumin.

CONCLUSION

In conclusion, we examined and reported the main phenolic components and antioxidant activity of decoction and infusion of *M. spicata* subsp. *spicata* and *M. longifolia* subsp. *typhoides* in Turkey. *M. spicata* subsp. *spicata* was found to be the richest species in terms of phenolic compounds. Especially caffeic acid was found to be major compound in decoction and infusion of this species. The results indicated that of phenolic contents of decoction and infusion of the samples are an important factor for the antioxidant capacities. In addition, when the results compared with the literature, the content of phenolics can vary greatly, depending on the locality, climatic, and seasonal conditions. Thus, *Mentha* species is very important species which are commonly used in folk medicine, food industry, and herbal tea throughout the world.

REFERENCES

1. Raja RR. Medicinally Potential Plants of Labiatae (Lamiaceae) Family: An Overview. Vol. 3, Research Journal of Medicinal Plant. 2012. p. 203–13.
2. Bimakr M, Rahman RA, Taip FS, Ganjloo A, Salleh LM, Selamat J, et al. Comparison of different extraction methods for the extraction of major bioactive flavonoid compounds from spearmint (*Mentha spicata* L.) leaves. Food Bioprod Process. Institution of Chemical Engineers; 2011;89(1):67–72.
3. Atoui AK, Mansouri A, Boskou G, Kefalas P. Tea and herbal infusions: Their antioxidant activity and phenolic profile. Food Chem. 2005; 89(1): 27–36.
4. Güner, A. (Ed.). Türkiye bitkileri listesi:(darmarlı bitkiler). ANG Vakfı; 2012.
5. Riahi L, Elferchichi M, Ghazghazi H, Jebali J, Ziadi S, Aouadhi C, et al. Phytochemistry, antioxidant and antimicrobial activities of the essential oils of *Mentha rotundifolia* L. in Tunisia. Ind Crops Prod. Elsevier B.V.; 2013; 49: 883–9.
6. Desam NR, Al-Rajab AJ, Sharma M, Mylabathula MM, Gowkanapalli RR, Albratty M. Chemical constituents, in vitro antibacterial and antifungal activity of *Mentha × Piperita* L. (peppermint) essential oils. J King Saud Univ - Sci. 2017; in press.
7. Costa DC, Costa HS, Albuquerque TG, Ramos F, Castilho MC, Sanches-Silva A. Advances in phenolic compounds analysis of aromatic plants and their potential applications. Trends Food Sci Technol. Elsevier Ltd; 2015; 45(2):336–54.
8. Yeşil Y, Akalin E. Folk medicinal plants in kürecik area (Akçadağ/Malatya-Turkey). Turkish J Pharm Sci. 2009; 6(3):207–20.
9. Caboni P, Saba M, Tocco G, Murgia A, Maxia A, Menkissoglu-Spiroudi U, Ntalli N. Nematicidal activity of mint aqueous extracts against the Root-Knot nematode *meloidogyne incognita*. J Agric Food Chem. 2013; 61: 9784–88.
10. Aksit, H., Demirtas, I., Telci, I., & Tarimcilar, G. Chemical diversity in essential oil composition of *Mentha longifolia* (L.) Hudson subsp. *typhoides* (Briq.) Harley var. *typhoides* from Turkey. Journal of essential oil research, 2013; 25(5): 430-437.
11. Kızıl, S., Hasimi, N., Tolan, V., Kilinc, E., & Yuksel, U. Mineral content, essential oil components and biological activity of two mentha species (*M. piperita* L., *M. spicata* L.). Turkish Journal of Field Crops, 2010; 15(2): 148-153.
12. Busatta, C., Barbosa, J., Cardoso, R. I., Paroul, N., Rodrigues, M., Oliveira, D. D., ... & Cansian, R. L. Chemical profiles of essential oils of marjoram (*Origanum majorana*) and oregano (*Origanum vulgare*)

- obtained by hydrodistillation and supercritical CO₂. Journal of Essential Oil Research, 2017; 29(5): 367-374.
13. Ilemona AJ, Gbekele-oluwa AYOR, Ojo OA. Chemical investigation and antioxidant activity of fractions of *Lannea humilis* (Oliv.) Engl. JOTCSA. 2017; 4(2): 563-72.
14. Hasdemir B, Yaşa H, Onar HÇ, Yusufoglu AS. Investigation of essential oil composition, polyphenol content and antioxidant activity of *Myrtus communis* L. from Turkey. JOTCSA. 2016; 3(3): 427-38.
15. Dorman HJD, Koşar M, Kahlos K, Holm Y, Hiltunen R. Antioxidant properties and composition of aqueous extracts from *Mentha* species, hybrids, varieties, and cultivars. J Agric Food Chem. 2003; 51(16): 4563-9.
16. Riachi LG, De Maria CAB. Peppermint antioxidants revisited. Food Chem. Elsevier Ltd; 2015; 176: 72-81.
17. Serteser A, Kargioğlu M, Gök V, Bağcı Y, Özcan MM, Arslan D. Antioxidant properties of some plants growing wild in Turkey. Grasas Aceites. 2009; 60(2): 147-54.
18. Chan EWC, Lim YY, Chong KL, Tan JBL, Wong SK. Antioxidant properties of tropical and temperate herbal teas. J Food Compos Anal. 2010; 23(2): 185-9.
19. Abootalebian M, Keramat J, Kadivar M, Ahmadi F, Abdinian M. Comparison of total phenolic and antioxidant activity of different *Mentha spicata* and *M. longifolia* accessions. Ann Agric Sci [Internet]. 2016; 61(2): 175-9. Available from: <http://dx.doi.org/10.1016/j.aos.2016.10.002>
20. Sytar O, Hemmerich I, Zivcak M, Rauh C, Brestic M. Comparative analysis of bioactive phenolic compounds composition from 26 medicinal plants. Saudi J Biol Sci. King Saud University; 2016; Available from: <http://www.sciencedirect.com/science/article/pii/S1319562X16000383>
21. Kiselova Y, Ivanova D, Chervenkov T, Gerova D, Galunska B, Yankova T. Correlation between the in vitro antioxidant activity and polyphenol content of aqueous extracts from Bulgarian herbs. Phyther Res. 2006; 20: 961-5.
22. Mata AT, Proença C, Ferreira AR, Serralheiro MLM, Nogueira JMF, Araújo MEM. Antioxidant and antiacetylcholinesterase activities of five plants used as Portuguese food spices. Food Chem. 2007; 103(3): 778-86.
23. Dinis PC, Falé PL, Madeira PJA, Florêncio MH, Serralheiro ML. Acetylcholinesterase inhibitory activity after in vitro gastrointestinal digestion of infusions of *Mentha* species. European J Med Plants. 2013; 3(3): 381-93.
24. Sağır ZO, Çarıkçı S, Kılıç T, Gören AC. Metabolic profile and biological activity of *Sideritis brevibracteata* P. H. Davis endemic to Turkey. Int J Food Prop. Taylor & Francis; 2017; 20(12): 2994-3005. Available from: <http://dx.doi.org/10.1080/10942912.2016.1265981>
25. Köksal E, Bursal E, Gülçin İ, Korkmaz M, Çağlayan C, Gören AC, et al. Antioxidant activity and polyphenol content of Turkish thyme (*Thymus vulgaris*) monitored by liquid chromatography and tandem mass spectrometry. Int J Food Prop. 2017; 20(3): 514-25. Available from: <https://www.tandfonline.com/doi/full/10.1080/10942912.2016.1168438>.
26. Özer Z, Kılıç T, Çarıkçı S, Yılmaz, H. Investigation of phenolic compounds and antioxidant activity of *Teucrium polium* L. decoction and infusion, J. BAUN Inst. Sci. Technol. 2018; DOI: 10.25092/baunfbed.370594.
27. Ertaş A, Gören AC, Haşimi N, Tolan V, Kolak U. Evaluation of antioxidant, cholinesterase inhibitory and antimicrobial properties of *Mentha longifolia* subsp. *noeana* and Its secondary metabolites. Rec Nat Prod. 2015; 9(1): 105-15.
28. Miller HE. A simplified method for the evaluation of antioxidants. J Am Oil Chem Soc. 1971; 48(2): 91.
29. Blois MS. Antioxidant determinations by the use of a stable free radical. Nature. 1958; 181: 1199-200.

30. Yılmaz H, Çarıkcı S, Kılıç T, Dirmenci T, Arabacı T, Gören AC. Screening of chemical composition, antioxidant and anticholinesterase activity of section Brevifilamentum of *Origanum* (L.) species. *Rec Nat Prod.* 2017; 11(5): 439-55.
31. Bener M, Özyürek M, Güçlü K, Apak R. Optimization of microwave-assisted extraction of curcumin from *Curcuma longa* L. (Turmeric) and evaluation of antioxidant activity in multi-test systems. *Rec Nat Prod.* 2016; 10(5): 542-54.
32. Bener M, Shen Y, Xu Z, Apak R. Changes of the anthocyanins and antioxidant properties of concord grape (*Vitis labrusca*) pomace after acid hydrolysis. *Rec Nat Prod.* 2016; 10(6): 794-9.



Optimization of synthetic route to PNA-T-OH monomers

Onur Alptürk^{1*}  , Z. Sevcan Yeşilbaş¹  , Gözde Sarıoğlu¹  , Aslı Karaçaylı¹  , Aytül Saylam²  , Salih Özçubukcu²  .

¹Istanbul Technical University, Department of Chemistry, 34469, Istanbul, Turkey

²Middle East Technical University, Department of Chemistry, 06531, Ankara, Turkey

Abstract: Peptide nucleic acids are synthetic molecules crafted to mimic natural nucleic acids, and thus, they are widely utilized in many chemical, and, biomedical applications. Although there exist many approaches to synthesize monomers to date, there is still room to improve these methodologies. With this motivation, we compared some widely utilized synthetic routes to obtain *N*-Boc-PNA-T-OH, and *N*-Fmoc-PNA-T-OH. Our results indicate that *N*-Boc-ethylenediamine is the most pivotal intermediate in the chemistry of PNA, and synthetic route commencing with this material affords these two PNA monomers in relatively high yield, and purity, while being very reproducible.

Keywords: Peptide nucleic acid, monomer synthesis, optimization.

Submitted: January 17, 2018. **Accepted:** February 26, 2018.

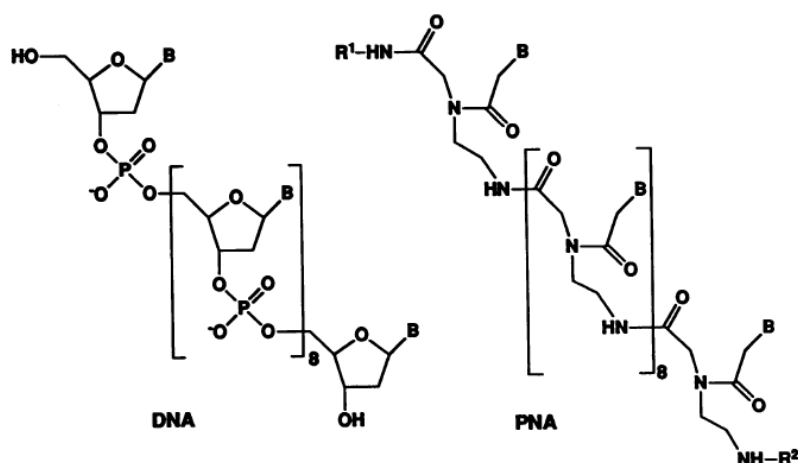
Cite this: Alptürk O *et al.*, Optimization of synthetic route to PNA-T-OH monomers. JOTCSA. 2018;5(2):457-468.

DOI: <http://dx.doi.org/10.18596/jotcsa.380410>.

***Corresponding author.** E-mail: onur.alpturk@itu.edu.tr, Tel: +90(212) 285 3249

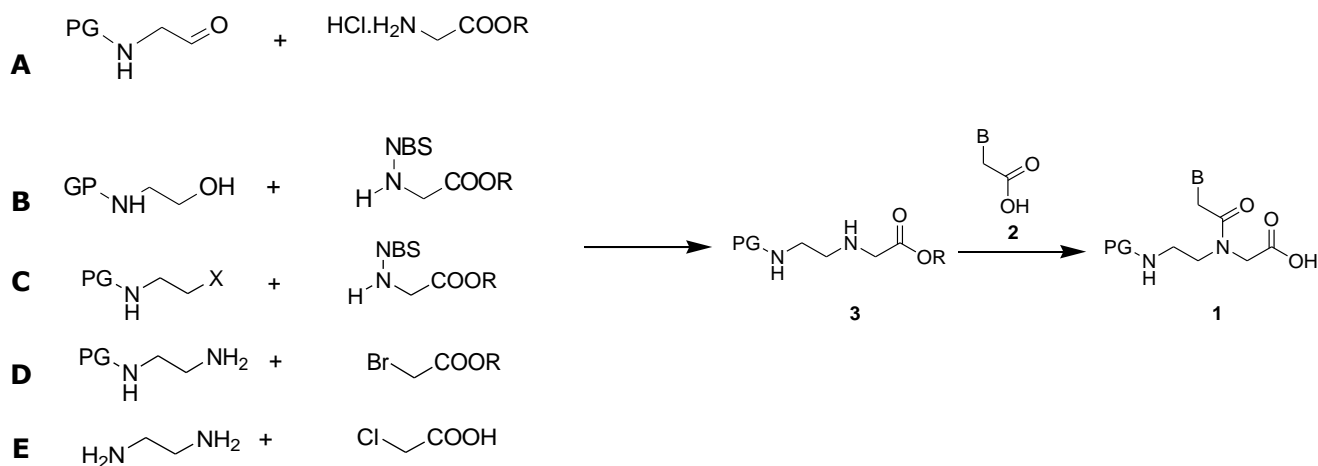
INTRODUCTION

First reported in 1991, peptide nucleic acids (PNA, for short) are single-stranded molecules designed to recognize nucleic acids in sequence-selective manner. By design, these synthetic compounds are composed of *N*-(2-aminoethyl) glycine moiety harboring a nucleobase in such a way that intact PNA monomer corresponds to an entire nucleoside of natural nucleic acids. Notwithstanding its being inspired from nature, PNA strands indeed diverges structurally from DNA, and RNA; its backbone is constructed through conventional peptide bonds amongst building blocks, in lieu of phosphodiester bonds encountered in nucleic acids (1) (**Scheme 1**). Unsurprisingly, absence of phosphate group grants a neutral charge to PNA structure and more remarkably, it accounts for superior hybridization propensity of these synthetic oligomers whereby eliminating infamous electrostatic interactions amongst DNA or RNA chains (2). In short, these synthetic oligomers presently emerge as an ideal tool to probe natural nucleic acids and thus, they are extensively utilized in biomedical applications including (but not limited to) antigene and antisense therapies (3), microarrays (4), biosensors (5), and fluorescent *in situ* hybridization (FISH) assays (6).



Scheme 1. Structures of DNA and PNA (adapted from reference 1 with permission).

Retro-synthetically, all customary synthetic routes to PNA monomer (**1**) rely on the coupling of *N*-(2-aminoethyl) glycine backbone (**3**) with nucleobase-acetic acid moiety (**2** where B = adenine, cytosine, guanine, or thymine) (**Scheme 2**). Undoubtedly, this reaction demands protecting groups on both N-terminal (such as Fmoc, Boc and so on), and C-terminal (such as ethyl or tertiary-butyl group and so on) of backbone prior to conjugation of nucleobase harboring moiety. Whereas some routes utilize the coupling of glycine or its derivatives to an electrophile (see routes A-C in **Scheme 2**) to prepare the backbone (7-9), the others switch the position of the nucleophile whereupon ethylene diamine or its derivatives attack to a glycine-derived electrophile (see routes D, and E in **Scheme 2**) (10).



Scheme 2. A summary of synthetic routes to N-protected PNA monomer **1** (PG, and NBS stand for protecting group, and 2-nitrobenzenesulfonyl moiety, respectively).

As effortless as it may seem on paper, the synthesis of PNA backbone could in reality be troublesome, which obliged the scientific community to devise a diverse repertoire of synthetic methodologies. Of them, a small fraction, such as the coupling of chloroacetic acid and ethylenediamine (as in route E), suffer from poor reproducibility (11). Yet, the chief complication regarding the synthesis of monomers revolves around the observation of how some key reactions (like coupling of nucleobases to the PNA backbone) afford moderate yields, which ultimately demands a chromatographic purification with highly polar solvents (12,13). Naturally, this complication appears tolerable to some extent but it becomes labor-demanding, especially in large scale synthesis where the yields of reactions and difficulties in purification becomes a major concern. As we experienced similar problems in an attempt to synthesize *N*-Boc-PNA-T-OH, and *N*-Fmoc-PNA-T-OH, we felt compelled to optimize synthetic route leading to these monomers, in conjunction with purification procedures. With this motivation, we have crafted this manuscript to provide a concise comparison of certain methodologies, and key reactions to better the synthesis of these monomers.

MATERIALS AND METHODS

Ethyl acetate, hexanes, dichloromethane (DCM), tetrahydrofuran (THF), and acetonitrile were purchased from Merck, and were used without any purification. Anhydrous *N,N*-dimethylformamide (DMF), trifluoroacetic acid (TFA), triisopropylsilane (TIPS), and *N*-Boc-ethanol amine were purchased from Sigma-Aldrich. *N,N*-diisopropylethyl amine (DIPEA), ethyl bromoacetate, O-(1H-benzotriazol-1-yl)-*N,N,N',N'*-tetramethyl uronium (HBTU), and 12-molybdophosphoric acid were purchased from Alfa Aesar. Lithium hydroxide, 9-fluorenylmethyl-*N*-succinimidyl carbonate (Fmoc-OSu), and *N*-Boc-ethylenediamine were obtained from EMD Millipore, ChemImpex, and Ench Industry Co. (Shanghai, China),

respectively. TLC was performed on analytical Merck silica plates with F254 indicator. TLCs were viewed either under 254 nm UV or by staining with ninhydrin, where indicated.

^1H NMR and ^{13}C NMR were acquired on an Agilent VNMRS Spectrometer at 500 MHz, and 125 MHz, respectively. Coupling constant values were given in Hertz and chemical shifts were reported in δ (ppm) with respect to the internal standard TMS. Splitting patterns were described as follows: s (singlet), d (doublet), t (triplet), q (quartet), m (multiplet), and br (broad signal).

EXPERIMENTAL SECTION

Methyl glycinate hydrochloride **4** (14): To a suspension of glycine (3.67 g, 48.99 mmol) in methanol (100 mL) chilled with an ice bath, SOCl_2 (10.7 mL) was added dropwise over 15 minutes. Then, the ice-bath was removed and the reaction was refluxed for three hours. Excess of thionyl chloride and methanol were evaporated and the product was obtained as white powder (yield 85%). ^1H NMR (DMSO-d_6): 3.7 (3H, s); 3.85 (2H, s), 8.7 (2H, s). ^{13}C NMR (DMSO-d_6): 52.9, 168.2.

Methyl *N*-(2-nitrophenylsulfonyl)-glycinate (*N*-(NBS-Gly-OMe)) **5** (15): Triethyl amine (2.32 mL, 16.71 mmol) and methyl glycinate hydrochloride (1 g, 7.96 mmol) were dissolved in dichloromethane (20 mL) at 0 °C. 2-nitrophenylsulfonyl chloride (1.94 g, 8.75 mmol) dissolved in dichloromethane (15 mL) was added dropwise over 30 minutes. Upon the completion of addition, ice bath was removed and the reaction mixture is further stirred overnight at room temperature. Dichloromethane was evaporated under reduced pressure and the crude material was portioned between ethyl acetate (50 mL), and distilled water (60 mL). The organic phase was separated and washed with distilled water (1x25 mL), 1 M HCl (2x25 mL), brine (2x25 mL), 5% NaHCO_3 (2x25 mL), and brine (2x25 mL), respectively. Organic phase was dried over Na_2SO_4 and concentrated under reduced pressure and the title compound was obtained as white solid (yield 60%). ^1H NMR (CDCl_3): 3.64 (3H, s), 4.05 (2H, d, $J = 5$ Hz); 6.16 (1H, t, $J = 5$ Hz), 7.67-8.35 (4H, m). ^{13}C NMR (125 MHz): 44.7, 52.5, 125.6, 130.6, 132.9, 133.7, 133.9, 147.7, 169.

2-(Boc-amino) ethyl mesylate **6** (16): Tert-butyl (2-hydroxyethyl) carbamate (1.34 g, 8.33 mmol) and trimethylamine (1.15 mL, 8.33 mmol) were dissolved in DCM (15 mL) under inert atmosphere and the reaction mixture was cooled with ice. Afterwards, methanesulfonyl chloride (0.95 g, 8.33 mmol) dissolved in dry DCM (3 mL) was added over 15 minutes and the reaction mixture was stirred at room temperature for 4 hours. The reaction mixture was diluted with DCM (15 mL), and was washed with cold water (2x20 mL). Organic phase was dried over sodium sulfate and concentrated under reduced pressure to afford the title

compound as a viscous oil (yield 96%). ¹H NMR (CDCl₃): 4.93 (bs, 1H), 4.29 (t, *J* = 5 Hz, 2H), 3.48 (q, *J* = 5 Hz, 2H), 3.04 (s, 3H), 1.45 (s, 9H).

Boc-GlyΨ[CH₂N(NBS)]Gly-OMe **7 (Method A)** (15): *N*-(NBS)-Gly-OMe (0.19g, 1.43 mmol), *N*-Boc-ethanolamine (0.17 g, 2.14 mmol), and triphenylphosphine (0.28 g, 2.14 mmol) were dissolved in dry THF (15 ml) under inert atmosphere. The resulting mixture is cooled to 0 °C with ice-salt bath and diethyl azodicarboxylate (0.37 g, 2.14 mmol) dissolved in dry THF (3 mL) was added over 10 minutes in three portions. The reaction was warmed to room temperature, and was further stirred overnight. After the solvent was evaporated *in vacuo*, oily crude material was re-dissolved in ether and chilled to 0°C with ice-salt bath. Precipitated materials were filtered off and crude material was purified with flash column chromatography on silica gel (ethyl acetate/petroleum ether, 1:6-1:3, v:v).

Boc-GlyΨ[CH₂N(NBS)]Gly-OMe **7 (Method B)** (17): To a solution of *N*-(NBS)glycinate methyl ester (0.5 g, 4 mmol) in DMF (15 mL), Cs₂CO₃ (2.67 g, 8.4 mmol) was suspended in DMF (15 mL) and the reaction was stirred for one hour at room temperature. Then, 2-(Boc-amino) ethyl mesylate (0.96 g, 4 mmol) dissolved in DMF (5 ml) was added dropwise for 10 minutes. The reaction mixture was stirred at room temperature for 16 hours. Inorganic salts were filtered and the solvent was evaporated under reduced pressure.

Tert-butyl 2-((ethoxycarbonyl)methylamino)ethylcarbamate **8** (10): To a solution of *N*-(Boc)-ethylenediamine (1.5 mL, 9.47 mmol) dissolved in a mixture of acetonitrile (10 mL) and chloroform (10 mL), K₂CO₃ (1.35 g, 9.84 mmol) was added. Ethyl bromoacetate (1 mL, 9.47 mmol) dissolved in acetonitrile (10 mL) was added dropwise over six hours under nitrogen atmosphere. After the completion of addition, the reaction mixture was stirred for another 30 minutes. Insoluble materials were filtered off and the solvents were evaporated under reduced pressure. The crude product was purified with flash column chromatography (*vide infra*) and the title compound is obtained as a yellow liquid (yield 84%). TLC R_f (MeOH) 0.6 (ninhydrin). ¹H NMR (CDCl₃): 5.05 (s br, 1H), 4.20 (q, *J* = 5, 2H), 3.42 (s, 2H), 3.22 (t, *J* = 5.8 Hz, 2H), 2.75 (t, *J* = 5.8 Hz, 2H), 1.66 (s, 1H), 1.44 (s, 9H), 1.26 (t, *J* = 5 Hz, 3H).

N-(*N*-Boc-2-aminoethyl)-*N*-[(1-thyminy)acetyl] glycine ethyl ester **9**: The coupling of thymine-1-acetic acid to the intermediate **8** was as reported with a minor modification as such neat DMF was utilized as solvent rather than DCM:DMF mixture, as reported by Albrecht *et al* (18). To a suspension of thymine-1-acetic acid (2.04 g, 11.05 mmol) in anhydrous DMF (20 mL), a solution of HBTU (5.03 g, 13.26 mmol) in anhydrous DMF (20 mL) was added. Then, DIPEA (2.12 mL, 12.16 mmol) was added to the reaction mixture which is stirred for 1 hour at room temperature. Afterwards, compound **8** (2.72 g, 11.05 mmol) dissolved in DMF (15 mL) was added and the reaction mixture was further stirred at room temperature overnight. Upon the

completion of reaction, the solvent was evaporated under reduced pressure. The crude material was dissolved in ethyl acetate (100 mL) and was washed with saturated solutions of NH₄Cl (2x50 mL), NaHCO₃ (2x50 mL), NaCl (2x50 mL), respectively. The organic phase was dried over Na₂SO₄ and concentrated under reduced pressure. The title compound was obtained as a yellow oil (yield 95%) and was used in the next step without any purification. R_f (EtOAc/MeOH, 1:9, v:v) 0.37 (UV).

N-(*N*-Boc-2-aminoethyl)-*N*-[(1-thyminy)acetyl] glycine **10**: The intermediate **10** was prepared according to conventional procedures, as exemplified in reference 19. To a solution of compound **9** (1.90 g, 4.61 mmol) dissolved in THF (50 mL), 2 M LiOH (50 mL) solution was added dropwise over 15 minutes. The reaction was stirred at room temperature until complete conversion of starting material. Afterwards, the work-up procedures that were utilized independently are as tabulated:

Work-up method A (19): The reaction mixture was extracted with ethyl acetate (2x25 mL) and remaining aqueous phase is acidified with 1 M HCl to pH=4 at 0 °C. Aqueous phase was extracted with ethyl acetate (2x25 mL). Combined organic phases were dried over Na₂SO₄ and were concentrated under reduced pressure to afford an oily material (yield 93%).

Work-up method B (20): The reaction mixture was acidified with 1 M HCl to pH=4 at 0 °C, and the product was extracted with excess amount of ethyl acetate. Combined organic phases were dried over Na₂SO₄ and the solvent was removed under reduced pressure to afford an oily material (yield 45%). In both cases, ¹H NMR analysis of the product revealed that the final compound was pure enough to be used in the subsequent step. TLC R_f (EtOAc/MeOH, 1:9, v:v) 0.61 (UV). ¹H NMR (DMSO-d₆): 12.54 (s br, 1H), 11.30 (s, 1H, mj), 11.28 (s, 1H, mi), 7.31 (s, 1H, mj), 7.27 (s, 1H, mi), 6.94 (t, 1H, mj), 6.75 (t, 1H, mi), 4.64 (s, 2H, mj), 4.47 (s, 2H, mi), 4.19 (s, 2H, mj), 3.97 (s, 2H, mj), 3.60 (m, 2H, mi), 1.38 (s, 9H).

N-[2-(Aminoethyl)]-*N*-(thymine-1-ylacetyl) glycine **11** (21): Compound **10** (625 mg, 1.51 mmol) was dissolved in 17.9 mL of TFA/DCM/TIPS (47:50:3). The reaction was stirred at room temperature until TLC indicates complete conversion of compound **10** and then, volatile materials were evaporated under reduced pressure. The title compound was precipitated from cold ether and was used in the following step as it is, with no characterization, and further purification. TLC R_f (MeOH) 0.14 (UV).

N-Fmoc-PNA-T-OH **12** (22): To a solution of compound **11** (2.2 g, 7.99 mmol) dissolved in THF (40 mL), DIPEA (3.06 mL, 17.5 mmol) was added. Fmoc-OSu (2.69 g, 8.69 mmol) dissolved in dry DMF (9 mL) was added to the reaction mixture and the flask was sonicated for about five minutes. Reaction mixture was stirred at room temperature until TLC (ethyl

acetate/hexanes, 1:4) analysis indicated complete conversion of starting material. Afterwards, volatile materials were evaporated under reduced pressure. The crude material is re-dissolved in ethyl acetate (270 mL) and washed with KHSO₄ (1x90 mL), water (3x90 mL), respectively. The organic phase was dried over MgSO₄ and the solvent is concentrated under reduced pressure. Two procedures were employed independently to optimize the purification of the title compound.

Purification method A: Crude material was simply washed with hexanes to remove trace amount of unreacted Fmoc-OSu and the title compound was obtained as white foam (yield 91%).

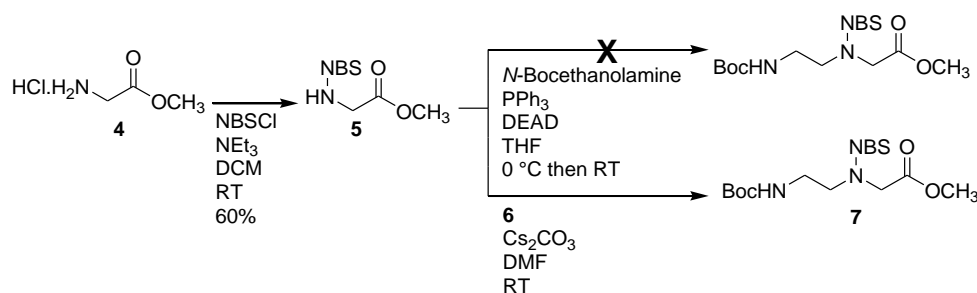
Purification method B: Crude material was purified with flash column chromatography with ethyl acetate/methanol/acetic acid (95:3:2). Combined fractions were poured into chilled water and *N*-Fmoc-PNA-T-OH was collected by filtration. TLC R_f (EtOAc/Hexane, 1:4) 0.81, 0.94 UV (two structural isomers are observed upon this reaction) (yield 71%). ¹H NMR (DMSO-d₆): 12.72 (s, br, 1H), 11.33 (s, 1H, mj), 11.31 (s, 1H, mi), 7.86 (d, *J*=7.5 Hz, 2H), 7.69 (d, *J*=7.2 Hz, 2H), 7.42 (m, 3H), 7.34 (m, 3H), 4.65 (s, 2H, mj), 4.47 (s, 2H, mi), 4.37-4.18 (m, 4H), 3.98 (s, 2H, mj), 3.26 (m, 1H), 3.10 (m, 1H), 1.73 (s, 3H).

RESULTS AND DISCUSSION

As precedented heavily by Berg (23), and Buchardt (24), early reports on synthesis of PNA monomers, as well its oligomers, centred primarily on Boc-chemistry. With Fmoc-chemistry being the current method of choice, numerous research groups endeavored latter on to prepare Fmoc-protected PNA monomers. Assuredly, obviation of hydrogen fluoride synthesis renders the latter prominent for one thing, but more importantly, Fmoc-chemistry is recognized to offer better coupling yields, improved solubility in reaction milieu (25). Yet, this chemistry may be challenging, especially through the synthesis of PNA monomers only because some Fmoc-protected intermediates do not always exhibit comparable reactivity to their Boc-protected counterparts (for a short comparison on this matter, see reference 26). One further drawback regarding this protecting group is the sensitivity of Fmoc moiety to reducing agents (such as LiAlH₄) or basic reagents (such as LiOH or NaOH). Thus, it appears that a plausible approach to access both *N*-Boc-PNA-T-OH and *N*-Fmoc-PNA-T-OH is to synthesize the former at first, whereupon it is converted to *N*-Fmoc-PNA-T-OH.

With this paradigm, we initially sought to prepare Boc-protected backbone of PNA through Mitsunobu reaction because of its prevalence in the synthesis of PNA chemistry (see pathway B in **Scheme 2**) (27). Although mostly favoured in the attachment of nucleobases to the backbone (28), Mitsunobu reaction is also conformed to the synthesis of PNA backbone (15).

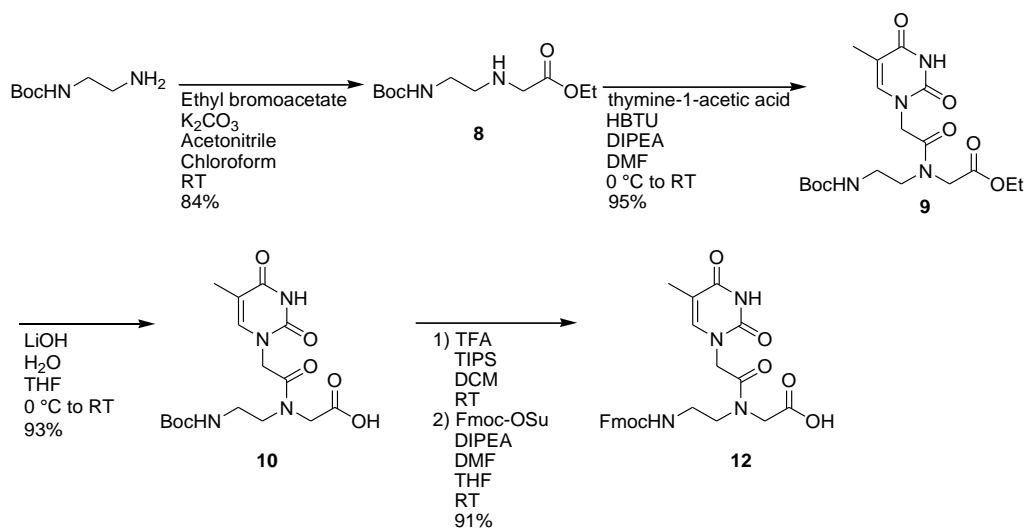
In keeping with the report by Wiśniewski, this synthetic route commences with esterification of glycine amino acid via methanolic solution of SOCl_2 (**Scheme 3**). Subsequently, methyl glycinate hydrochloride **4** is converted to methyl *N*-(NBS)-glycinate **5** in good yield. However, we came to notice that we genuinely failed to reproduce Mitsunobu reaction between **4** and **5** to afford Boc-Gly Ψ [CH₂N(NBS)]Gly-OMe **7** backbone. This finding is supported by ¹³C NMR of the isolated product that reveals the lack of ethylene bridge on the backbone that should have appeared in the region between 40 ppm and 50 ppm. With methyl *N*-(NBS)-glycinate in our hand, we next explored the synthesis of **7** through conventional alkylation of **5**. In that regard, methyl *N*-(NBS)-glycinate reacted with 2-(Boc-amino) ethyl mesylate **6** under basic condition. Unlike Mitsunobu reaction, this reaction afforded the peptidic backbone in moderate yield based on TLC. However, *r_f* of **7** being similar to that of *N*-(NBS)-glycinate rendered the chromatographic purification rather time-consuming.



Scheme 3. The synthesis of PNA backbone through *N*-(NBS)-Gly-OMe intermediate (pathways B and C of **Scheme 2**).

In light of these results, we turned our attention to synthetic pathways D and E (*vide supra*), wherein the positions of nucleophile and electrophile are switched. With the latter being reported to be irreproducible, synthetic pathway D, wherein *N*-Boc-ethylenediamine reacts with methyl bromoacetate, was investigated to synthesize PNA backbone **3** (**Scheme 4**) (10). In contrast to previously depicted ones, the synthetic route was free-of-trouble and proceeded very smoothly. As reported by many groups, the sole problem we have also encountered was unmanageable di-alkylation of *N*-Boc-ethylenediamine, which necessitated one further step of purification. Taking the basic character of product into consideration, we firstly attempted to isolate intermediate **8** (**Scheme 4**) through neutral alumina, in lieu of conventional silica gel (ethyl acetate/hexanes, 1:2, v:v). Nonetheless, we have managed to isolate only 43% of crude material, presumably because the title compound tended to stick even to neutral alumina. Oddly enough, the use of basic alumina did not alter this profile either, which ultimately compelled us to opt for more aggressive solvent systems. With a solvent of system of DCM/methanol/NH₄OH (95:5:0.8, v:v), and silica gel, the isolated yield eventually neared to 84%, which was very much in concert with the relevant literature (10). In short, it is safe to conclude that the intermediate **8** could be prepared the most conveniently from *N*-Boc-

ethylenediamine, and ethyl bromoacetate in high yield, and purity, based on our personal experience.



Scheme 4. The sequential synthesis of *N*-Boc-PNA-T-OH, and *N*-Fmoc-PNA-T-OH from *N*-(Boc)-ethylenediamine.

The coupling of thymine-1-acetic acid to **8** are conventionally achieved with reagents such as *N,N'*-dicyclohexylcarbodiimide (DCC) coupled with 3-hydroxy-1,2,3-benzotriazin-4-one (DhbtOH) (28) or HBTU (29). Not only these reactions reportedly afforded **9** in moderate-to-good yield, but also the latter reportedly obligated a purification step, which accounts for a slight disadvantage. In respect to this complication, we recognized that the reaction could only be improved by altering the order in the addition of compounds. Rather than reacting **8**, thymine-1-acetic acid, and HBTU at once – as stated in references 28, and 29, we pre-activated thymine-1-acetic acid with HBTU for one hour at first, and then added the backbone **8** to the reaction mixture. In this manner, we obtained the title compound in 95% yield, and in sufficient purity after overnight reaction, and standard work-up procedure detailed in experimental part (*vide supra*).

Surprisingly, the perplexing part of this synthetic route was de-esterification of **9**, as we have experienced that work-up procedure drastically impacted the yield. Therein, work-up procedure following the reaction involved acidification with 1 M HCl, followed by the extraction of title compound with ethyl acetate (20). However, we have observed that with this procedure, the yield was no more than 45%, and more interestingly, a UV-active by-product was formed in aqueous phase, while acidification. At this point, our failure to retrieve this by-product with extraction led us speculate that the process of acidification may have essentially conducted towards a side-reaction whereupon a highly polar compound is formed. On the contrary, we found out that washing the reaction with ethyl acetate prior to acidification raised the yield to 90%, with no sign of this by-product (19). Considering well-documented stability of Boc group and PNA monomer under slightly acidic conditions, what might have triggered

this side-reaction remained predominantly vague to this point. On the verge of these observations, we should remark that work-up procedure by Tsantrizos appear to be the most suited one to achieve high yield in this step.

The procedures to cleave Boc moiety, and subsequently to introduce Fmoc group were in compliance with references 21, and 22, respectively. Boc group was removed from **10** with TFA/DCM/TIPS (47:50:3), and Fmoc group was subsequently introduced through Fmoc-OSu in the presence of DIPEA. In these two steps, the sole complication we faced was the purification of final compound *N*-Fmoc-PNA-T-OH. In this context, we have initially attempted to purify the crude material via flash column chromatography with ethyl acetate/methanol/acetic acid (95:3:2). However, inability to remove solvents afterwards coerced us to pour combined organic fractions on ice and water, and to obtain **12** through filtration. Because this approach, however, caused loss of material to some extent, we considered simply to wash the crude material with hexanes, instead. Frequently utilized after reaction involving Fmoc-OSu, this method indeed removed impurities without any substantial loss of product, and is seemingly applicable to the synthesis of *N*-Fmoc-PNA-T-OH, as well.

CONCLUSION

As outlined in **Scheme 2**, *N*-Boc-PNA-T-OH, and *N*-Fmoc-PNA-T-OH could be synthesized through many synthetic routes and methodologies. Despite all the efforts in this field, we came to realize that certain reaction and synthetic routes still need some improvements, and modifications, which encouraged us to conduct this study. Of them, we have experienced that the best approach to attain these two monomers is through *N*-Boc-ethylenediamine, where yields of reactions are *ca.* 90%, in addition to each reaction being fully reproducible.

ACKNOWLEDGMENT

This research was supported by Research Fund of Istanbul Technical University (Project Number: 38056 and 38866).

REFERENCES

1. Nielsen PE, Egholm M, Berg RH, Buchardt O. Sequence-selective recognition of DNA by strand displacement with a thymine-substituted polyamide. *Science* 1991; 254:1497–1500.
2. Jensen KK, Örum H, Nielsen PE, Nordén B. Kinetics for hybridization of peptide nucleic acids (PNA) with DNA and RNA studied with the BIAcore technique. *Biochemistry* 1997; 36(16):5072–5077.
3. Ray A, Nordén B. Peptide nucleic acid (PNA): its medical and biotechnical applications and promise for the future. *FASEB J.* 2000; 14(9):1041–1060.
4. Brandt O, Feldner J, Stephan A, Schröder M, Schnölzer M, Arlinghaus HF, Hoheisel JD, Jacob A. PNA microarrays for hybridization of unlabelled DNA samples. *Nucleic Acids Res.* 2003; 31(19):e119.

5. Tian K, He Z, Wang Y, Chen S-J, Gu L-Q. Designing a Polycationic Probe for Simultaneous Enrichment and Detection of MicroRNAs in a Nanopore. *ACS Nano* 2013; 7(5):3962–3969.
6. Stender H, Williams B, Coull J. PNA fluorescent in situ hybridization (FISH) for rapid microbiology and cytogenic analysis. *Methods Mol. Biol.* 2014; 1050:167-178.
7. Manna A, Rapireddy S, Sureshkumar G, Ly DH. Synthesis of optically pure γ PNA monomers: a comparative study. *Tetrahedron* 2015; 71(21):3507-3514.
8. Falkiewicz B, Kozyra A, Kolodziejczyk AS, Liberek B, Wisniewski K. New procedure of the Mitsunobu reaction as the key step in peptide nucleic acid (PNA) monomers synthesis. *Nucleic Acids Symp. Ser.* 1999; 42:9-10.
9. Bonnard V, Azoulay S, Di Giorgio A, Patino N. "Polyamide Amino Acids": a new class of RNA Ligands. *Chem. Commun.* 2009; 17:2302–2304.
10. Aldrian-Herrada G, Rabié A, Wintersteiger R, Brudiou J. Solid-phase synthesis of peptide nucleic acid (PNA) monomers and their oligomerization using disulphide anchoring linkers. *J. Pept. Sci.* 1998; 4(4):266-281.
11. Feagin TA, Shah NI, Heemstra JM. Convenient and Scalable Synthesis of Fmoc-Protected Peptide Nucleic Acid Backbone. *J. Nucleic Acids* 2012; 354549.
12. Debaene F, Da Silva JA, Pianowski Z, Duran FJ, Winssinger N. Expanding the scope of PNA-encoded libraries: divergent synthesis of libraries targeting cysteine, serine and metalloproteases as well as tyrosine phosphatases. *Tetrahedron* 2007; 63(28):6577–6586.
13. Altenbrunn F, Seitz O. O-Allyl protection in the Fmoc based synthesis of difficult PNA. *Org. Biomol. Chem.* 2008; 6(14):2493–2498.
14. Coban G, Kose FA, Kirmizibayrak PB, Pabuccuoglu V. Synthesis, biological activity screening and molecular modeling study of acylaminoacetamide derivatives. *Med. Chem. Res.* 2015; 24(10):3710-3729.
15. Falkiewicz B, Kolodziejczyk AS, Liberek B, Wiśniewski K. Synthesis of achiral and chiral peptide nucleic acid (PNA) monomer using Mitsunobu reaction. *Tetrahedron*, 2001; 57(37):7909-7917.
16. Fox BM, Beck HP, Roveto PM, Kayser F, Cheng Q, Dou H, Williamson T, Treanor J, Liu H, Jin L, Xu G, Ma J, Wang S, Olson SH. A Selective Prostaglandin E₂ Receptor Subtype 2 (EP2) Antagonist Increases the Macrophage-Mediated Clearance of Amyloid-Beta Plaques. *J. Med. Chem.* 2015; 58(13):5256–5273.
17. Patino N, Di Giorgio C, Dan-Covalciuc C, Peytou V, Terreux R, Cabrol-Bass D, Bailly C, Condom R. Modelling, synthesis and biological evaluation of an ethidium–arginine conjugate linked to a ribonuclease mimic directed against TAR RNA of HIV-1. *Eur. J. Med. Chem.* 2002; 37:573–584.
18. Albrecht M, Zauner J, Eisele T, Weis P. The Synthesis of Catechol and 8-Hydroxyquinoline Derivatives with Short Peptide-Type Side Chains: Metal Complex Ligands with Additional Receptor Properties. *Synthesis* 2003; 7:1105-1111.
19. Fader LD, Boyd M, Tsantrizos YS. Backbone Modifications of Aromatic Peptide Nucleic Acid (APNA) Monomers and Their Hybridization Properties with DNA and RNA. *J. Org. Chem.* 2001; 66(10):3372-3379.
20. Sahu B, Sacui I, Rapireddy S, Zanolli KJ, Bahal R, Armitage BA, Ly DH. Synthesis and Characterization of Conformationally Preorganized, (R)-Diethylene Glycol-Containing γ -Peptide Nucleic Acids with Superior Hybridization Properties and Water Solubility. *J. Org. Chem.* 2011; 76(14):5614–5627.
21. Pensato S, Saviano M, Bianchi N, Borgatti M, Fabbri E. α -Hydroxymethyl PNAs: Synthesis, interaction with DNA and inhibition of protein/DNA interactions. *Bioorg. Chem.* 2010; 38(5):196–201.
22. Slaitas A, Yeheskiely E. A Novel N-(Pyrrolidinyl-2-methyl) glycine-Based PNA with a Strong Preference for RNA over DNA. *Eur. J. Org. Chem.* 2002; 14:2391-2399.
23. Egholm M, Buchardt O, Nielsen PE, Berg RH. Peptide Nucleic Acids (PNA) Oligonucleotide Analogues with an Achiral Peptide Backbone. *J. Am. Chem. Soc.* 1992; 114(5):1895-1897.

24. Dueholm KL, Egholm M, Behrens C, Christensen L, Hansen HF, Vulpius T, Petersen KH, Berg RH, Nielsen PE, Buchardt O. Synthesis of Peptide Nucleic Acid Monomers Containing the Four Natural Nucleobases: Thymine, Cytosine, Adenine, and Guanine and Their Oligomerization. *J. Org. Chem.* 1994; 59(19):5767-5773.
25. Thomson SA, Josey JA, Cadilla R, Gaul MD, Hassman CF, Luzzio MJ, Pipe AJ, Reed KL, Ricca DJ, Wiethe RW, Noble SA. Fmoc mediated synthesis of Peptide Nucleic Acids. *Tetrahedron* 1995; 51(22):6179-6194.
26. Feagin TA, Shah NI, Heemstra JM. Convenient and Scalable Synthesis of Fmoc-Protected Peptide Nucleic Acid Backbone. *J. Nucleic Acids* 2012; 354549.
27. Wisniewski K, Joswig S, Falkiewicz B, Kolodziejczyk A. A New Method of the Synthesis of Gly-Aaa Type Reduced Peptide Bond. *Pol. J. Chem.* 1997; 71(10):1506-1509.
28. For instance, see: Li P, Zhan C, Zhang S, Ding X, Guo F, He S, Yao J. Alkali metal cations control over nucleophilic substitutions on aromatic fused pyrimidine-2,4-[1H,3H]-diones: towards new PNA monomers. *Tetrahedron* 2012; 68(43):8908-8915.
29. For instance, see: Ellipilli, S.; Palvai, S.; Ganesh, K. N. Fluorinated Peptide Nucleic Acids with Fluoroacetyl Side Chain Bearing 5-(F/CF₃)-Uracil: Synthesis and Cell Uptake Studies. *J. Org. Chem.* 2016; 81:6364–6373.



Photoinduced Synthesis of Block Copolymers by Combining Atom Transfer Radical Polymerization and Photoinduced Radical Oxidation/Addition/Deactivation

Mustafa Ciftci^{1, 2}  

¹ Bursa Technical University, Faculty of Natural Science, Architecture and Engineering, Department of Chemistry, 16310, Bursa, Turkey.

² Istanbul Technical University, Faculty of Science and Letters, Department of Chemistry, 34469, Istanbul, Turkey.

Abstract: A new polymerization mechanistic transformation strategy, combining two different techniques of controlled polymerization modes, namely atom transfer radical polymerization (ATRP) and photoinduced radical oxidation/addition/deactivation (PROAD), is effectively used for the block copolymers' formation. Thus, mono- or bi- bromide functional polystyrenes (PS-Br or Br-PS-Br) synthesized by light-induced ATRP were used as a macroinitiator on isobutyl vinyl ether in the living cationic polymerization via PROAD process to give the corresponding block copolymers. Thus, depending upon the macroinitiator's surface, AB/ABA type block copolymers (PS-*b*-PIBVE or PIBVE-*b*-PS-*b*-PIBVE) were formed. The final polymers and precursor polymers were characterized by spectral and chromatographic analyses.

Keywords: Mechanistic transformation, block copolymer, ATRP, PROAD.

Submitted: February 19, 2018. **Accepted:** March 1, 2018.

Cite this: Çiftçi M. Photoinduced Synthesis of Block Copolymers by Combining Atom Transfer Radical Polymerization and Photoinduced Radical Oxidation/Addition/Deactivation. Journal of the Turkish Chemical Society, Section A: Chemistry. 5(2):469-478.

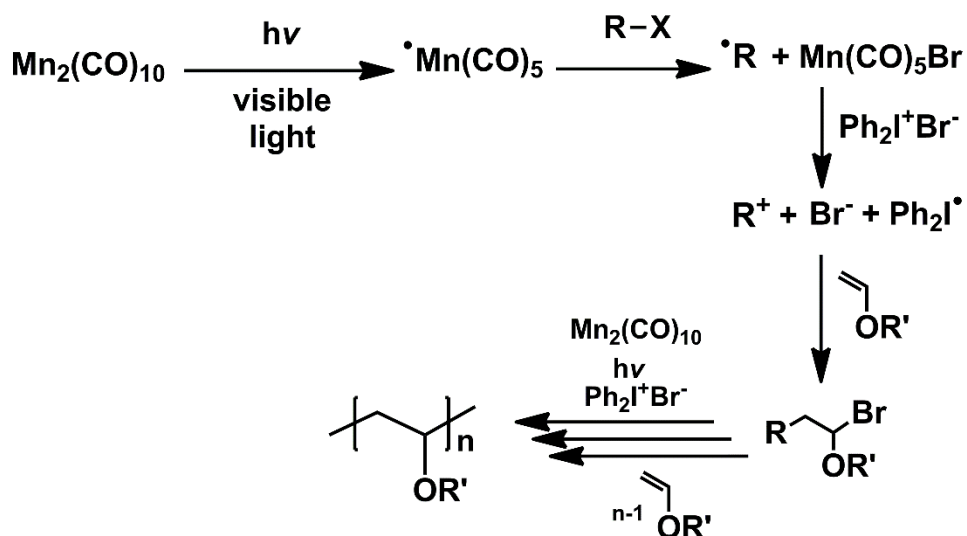
DOI: <http://dx.doi.org/10.18596/jotcsa.396618>.

Corresponding author. E-mail: mustafaciftcis@gmail.com.

INTRODUCTION

There are limitations for the synthesis of segmented copolymers by one polymerization mode owing to the structure and comparative reactivity of the monomeric species and the others involved. Although there are various synthetic approaches to obtain such copolymers, mechanistic transformation methodology that combines different polymerization techniques appears as one of the most commonly applied techniques due to the immediacy and operational simplicity (1). In recent years, many block and graft copolymers were synthesized via different transformation approaches involving different polymerization techniques (2-5). With the recent notable evolution in controlled/living polymerizations, the concept is further extended to ionic, controlled free radical, metathesis, Ziegler–Natta, activated monomer, and group transfer reactions (6-11). In some other studies, it was also proved that transformations could be achieved in the same polymerization mode using different initiating systems. For instance, two differing controlled radical polymerization methods, namely nitroxide-mediated radical polymerization (NMRP) and atom transfer radical polymerization (ATRP), were used in combination for this purpose (2, 12). In another study, Yagci and co-workers represented successful block copolymerization by the combination ATRP and light induced free radical polymerization (13).

Photoinduced polymerizations involving cationic and free radical modes are also often used in such mechanistic transformations (14, 15). Numerous photoinitiators with different absorption features have been employed for the both modes (16-18). Such light-induced systems represent several advantages over conventional thermal techniques regarding the level of control since they can be accurately moderated in terms of wavelength, polarization direction, and intensity, allowing spatial and temporal control of the reactions. With the recent significant progress made in controlled polymerization techniques, the use of light has been implanted to such systems (19). Thus, common controlled polymerization methods were triggered by light as adapted from thermal counterparts including reversible addition–fragmentation chain transfer polymerization, also known as RAFT (20), NMRP mentioned above (21), ATRP (22-25), and some cationic polymerization techniques (26). Very recently, we have reported a new light-induced system of initiation (27) for isobutyl vinyl ether's living/controlled cationic polymerization by dimanganese decacarbonyl [$\text{Mn}_2(\text{CO})_{10}$] (28). Scheme 1 shows the process of visible light irradiation of $\text{Mn}_2(\text{CO})_{10}$, which then decomposes into $\cdot\text{Mn}(\text{CO})_5$ radicals to abstract the halide from the alkyl bromide compound which results with the formation of radicals at carbon center. Then, diphenyliodonium ions oxidize these radicals to the related cations. The formed carbocations add IBVE, and bromide anions rapidly deactivate them to form a-halide functional end group. In a controlled manner, poly(vinyl ether) chains were then grown through successive photoinduced radical oxidation/addition/deactivation (PROAD) scheme.



Scheme 1: Photoinduced living cationic polymerization of vinyl ethers by PROAD.

In the current study, we present a novel protocol to prepare block copolymers through a mechanistic transformation which combines ATRP and PROAD. Depending on the macroinitiator used, AB or ABA type block copolymers were formed. Additionally, the segment lengths could be adjusted by varying polymerization conditions. Block copolymers formed by the described chemistry had low molecular weight distribution due to the controlled nature of both modes.

EXPERIMENTAL SECTION

Materials

Styrene (St; 99%, Aldrich) was passed through a basic alumina column to remove the inhibitor prior to use. Isobutyl vinyl ether (IBVE, 99%, Aldrich) was distilled from CaH₂ in vacuum. Dimanganese decacarbonyl (Mn₂(CO)₁₀, 99%, Aldrich) was purified by sublimation and stored in a refrigerator in the dark. N,N,N',N'',N'''-Pentamethyldiethylenetriamine (PMDETA; 99%, Aldrich) was distilled prior to use. Copper(II) bromide (Cu^{II}Br₂, 99%; Acros), Copper(I) bromide (CuBr, 98%, Aldrich), ethyl-2-bromopropionate (>99%, Aldrich), diphenyliodonium bromide (Ph₂I⁺Br⁻, 97%, Aldrich), dimethylformamide (DMF, 99.8%, Aldrich), tetrahydrofuran (THF, ≥99%, Merck) and methanol (99.9%, Aldrich) were used as received.

Characterization

¹H NMR spectra were recorded on an Agilent VNMRS 500 (500 MHz). Fourier transform infrared (FT-IR) spectra were recorded on a Perkin-Elmer FTIR Spectrum One spectrometer. Gel-permeation chromatography (GPC) measurements were obtained from a ViscotekGPC max Autosampler system consisting of a pump module (GPCmax, Viscotek Corp., Houston, TX, U.S.A.), a combined light

scattering (Model 270 Dual Detector, Viscotek Corp.), and a refractive index (RI) detector (VE 3580, Viscotek Corp.). The light scattering detector ($\lambda_0 = 670$ nm) included two scattering angles: 7° and 90° . The RI-detector was calibrated vs polystyrene standards having narrow molecular weight distribution, and so, the quoted molecular weights of the polymers are expressed in terms of polystyrene equivalents. Two columns, that is, a $7,8 \times 300$ mm LT5000L, Mixed, Medium Org and a $7,8 \times 300$ mm LT3000L, Mixed, Ultra-Low Org column equipped with a guard column 4.6×10 mm (Viscotek, TGuard), were used for the chloroform eluent at 35°C (flow rate: 1 mL min^{-1}). Data were analyzed using ViscotekOmniSEC Omni-01 software.

Synthesis of PS-Br

First, PS-Br was synthesized as described previously.(23) In a typical reaction, St (4 mL, 34.8 mmol), PMDETA (8 mL, 3.5×10^{-2} mmol), $\text{Cu}^{\text{II}}\text{Br}_2$ (8.4 mg, 3.5×10^{-2} mmol), EtBP (24.4 mL, 18.8×10^{-2} mmol), $\text{Mn}_2(\text{CO})_{10}$ (3.9 mg, 9.4×10^{-3} mmol) and methanol (0.2 mL, 5 mmol) were charged into a Schlenk tube (i.d = 10 mm) equipped with a magnetic stirring bar and the reaction mixture was degassed by three freeze-pump-thaw cycles and left in a vacuum. The mixture was irradiated by a Ker-Vis blue photoreactor equipped with six lamps (Philips TL-D 18 W) emitting light nominally at 400–500 nm at room temperature. The light intensity was 45 mW cm^{-2} as measured by a Delta Ohm model HD-9021 radiometer. After the given time, the mixture was diluted with THF and precipitated in a tenfold excess of methanol. The polymer was dried under vacuum at room temperature.

Synthesis of Br-PS-Br

Bifunctional polystyrenes were prepared essentially as described elsewhere.(29)

Synthesis of PS-*b*-PIBVE

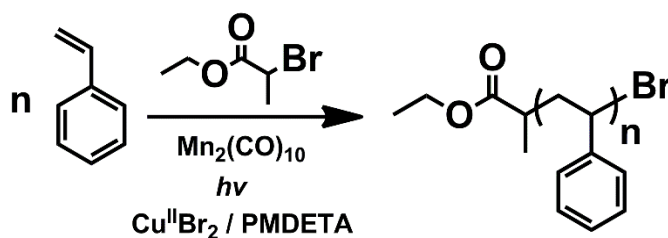
A representative block copolymerization process was as follows; obtained PS-Br (80 mg, 3×10^{-5} mol), IBVE (1 mL, 7.7×10^{-3} mol), propylene carbonate (2 mL), $\text{Ph}_2\text{I}^+\text{Br}^-$ (7 mg, 2×10^{-5} mol) and $\text{Mn}_2(\text{CO})_{10}$ (7.5 mg, 2×10^{-5} mol) were added to the Pyrex tube which was previously heated with a heat gun under vacuum and flushed with dry nitrogen. The solution was also flushed with nitrogen for 4–5 min and sealed. The formulation was stirred and exposed to light continuously at ambient temperature. At the end of the irradiation, the resultant polymer was precipitated in excess methanol and dried under reduced pressure.

RESULTS AND DISCUSSION

It is possible to create any cation from radicals generated by various techniques via electron transfer reactions. In various studies, not only low-molar-mass free radicals, but also polymeric radicals

could be oxidized to the corresponding cations (30). Although corresponding block or graft copolymers are formed by described methods, cationic polymerization steps of the approaches were suffering from the uncontrolled polymerization mechanism. The possibility of using a recently developed photoredox catalytic system for living cationic polymerization let us employ the same redox process for the block copolymerization.

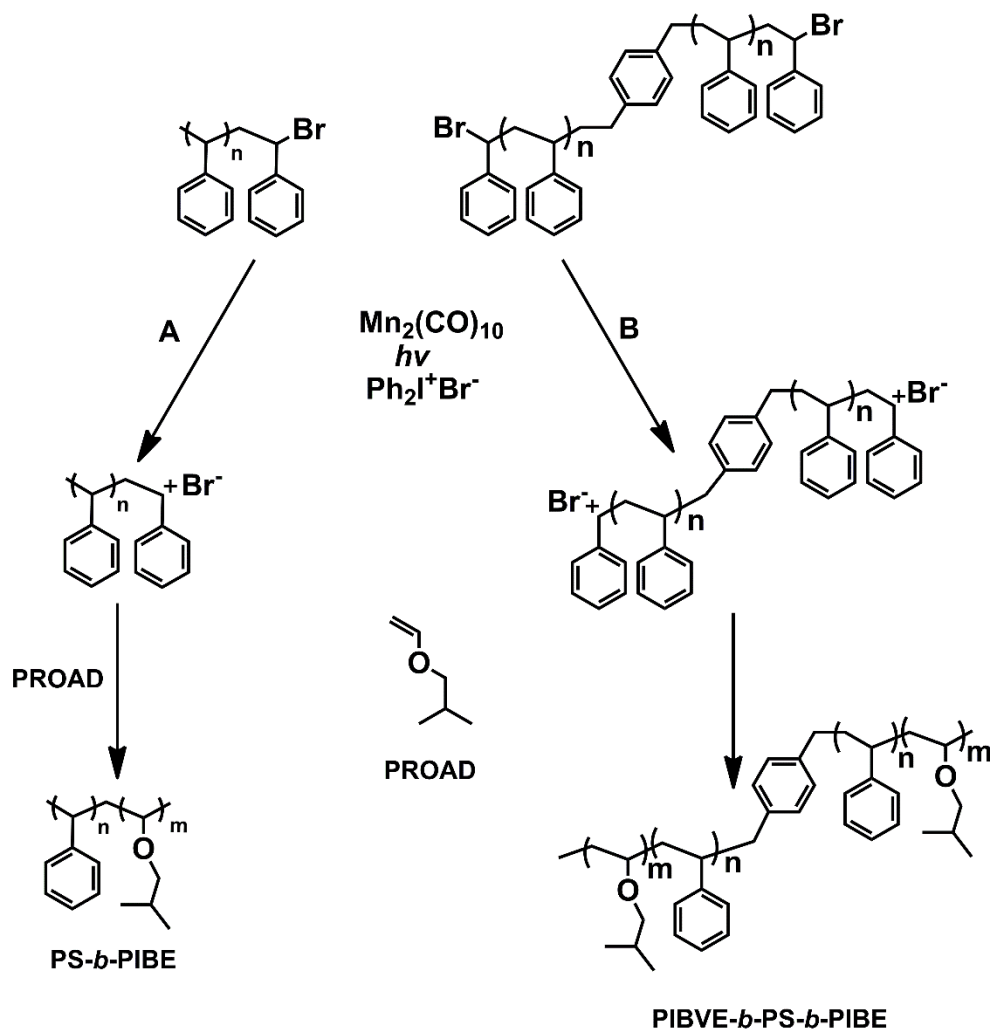
In the described approach, block copolymers were obtained in two distinct steps. The overall process for the example of monofunctional macroinitiator is as follows. In the first step, a bromide functional PS was synthesized by ATRP of St under visible light irradiation using ethyl-2-bromopropionate, $\text{Mn}_2(\text{CO})_{10}$ and $\text{Cu}^{\text{II}}\text{Br}_2/\text{PMDETA}$ initiator, photosensitive compound, catalyst and ligand, respectively (Scheme 2).



Scheme 2: Synthesis of PS-Br via ATRP.

In the second step, the photolysis of $\text{Mn}_2(\text{CO})_{10}$ in the presence of the obtained macro co-initiators initiated the PROAD of IBVE initiated resulting in the formation of the block copolymers, PS-*b*-PIBVE (Scheme 3-A). Since only $\text{Mn}_2(\text{CO})_{10}$ absorbs the light in the irradiation region, upon irradiation, $\text{Mn}(\text{CO})_5$ radicals were formed from the decomposition of the of $\text{Mn}_2(\text{CO})_{10}$ and they abstracted bromine atom from the macroinitiator. Then the generated polymeric radicals were oxidized by diphenyliodonium ions to the related initiating cations. Due to the living/controlled nature of the both steps, block copolymers with narrow molecular weight distributions were obtained.

Additionally, to represent the high adaptability of the described process, ABA block copolymers were also formed by similar strategy. Thus, by using bifunctional PS as macroinitiator PIBVE-*b*-PS-*b*-PIBVE block copolymers were also obtained (Scheme 3-B).



Scheme 3: Synthesis of block copolymers by sequential ATRP and PROAD.

As can be seen from results are collected in Table 1, depending on the polymerization conditions polymers with different segment length were readily formed. Prolonged irradiation time of the PROAD process results into higher PIBVE chain length Table 1.

Table 1: Block copolymerization of IBVE by PROAD.

Polymer	Macroinitiator	Time (min.)	$M_{n,GPC}$ ($\text{g}\cdot\text{mol}^{-1}$)	PDI
PS- <i>b</i> -PIBVE-1	PS-Br ^a	45	3950	1.20
PS- <i>b</i> -PIBVE-2	PS-Br ^a	90	4680	1.24
PS- <i>b</i> -PIBVE-3	PS-Br ^a	135	5200	1.28
PIBVE- <i>b</i> -PS- <i>b</i> -PIBVE	Br-PS-Br ^b	90	6400	1.29

^a $M_n = 2300 \text{ g mol}^{-1}$, PDI = 1.20, ^b $M_n = 2800 \text{ g mol}^{-1}$, PDI = 1.21.

The successful block copolymerization was confirmed by ¹H NMR analysis of the precursor polymer and the resulting block copolymers. As can be seen from Figure 2, the appearance of new signals

between 3–3.7 ppm corresponding to the $-OCH_2$ protons of isobutyl vinyl ether clearly indicates the presence of PIBVE segments.

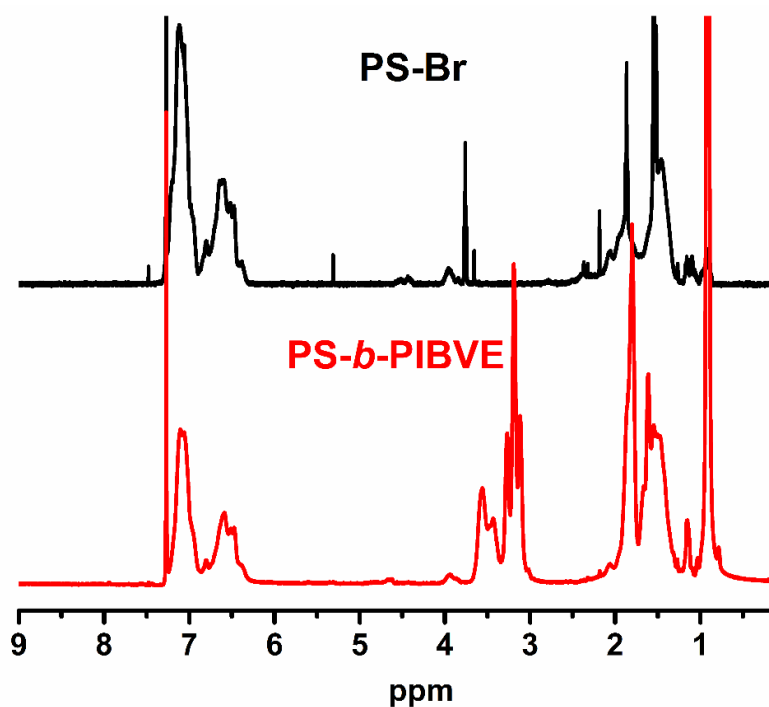


Figure 1: ^1H NMR spectra of PS and PS-*b*-PIBVE.

Figure 2 shows GPC traces of the precursor polymer and the final block copolymers. The clear shift of the GPC trace to higher elution volumes indicates an increase in the molecular weight after the block copolymerization process. Furthermore, any residuals from the remaining unreacted precursor polymer or from free PIBVE were not observed. The higher molecular weights were observed when Br-PS-Br was used as initiator under the identical experimental conditions that of PS-Br.

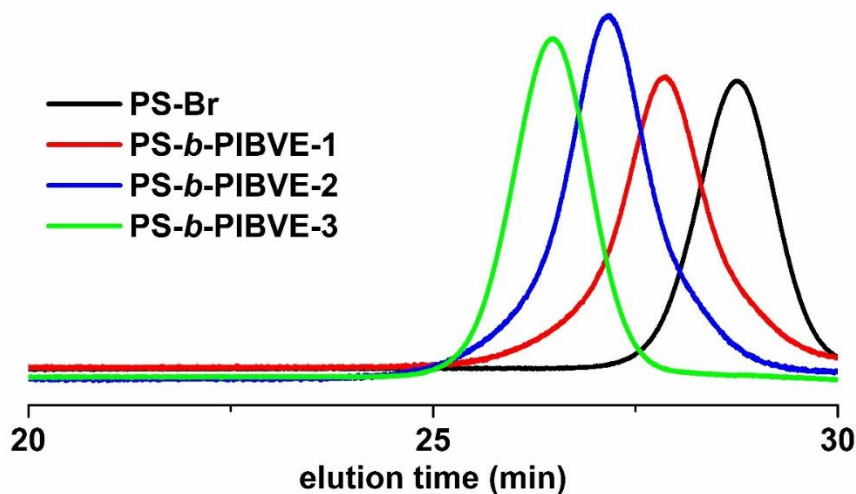
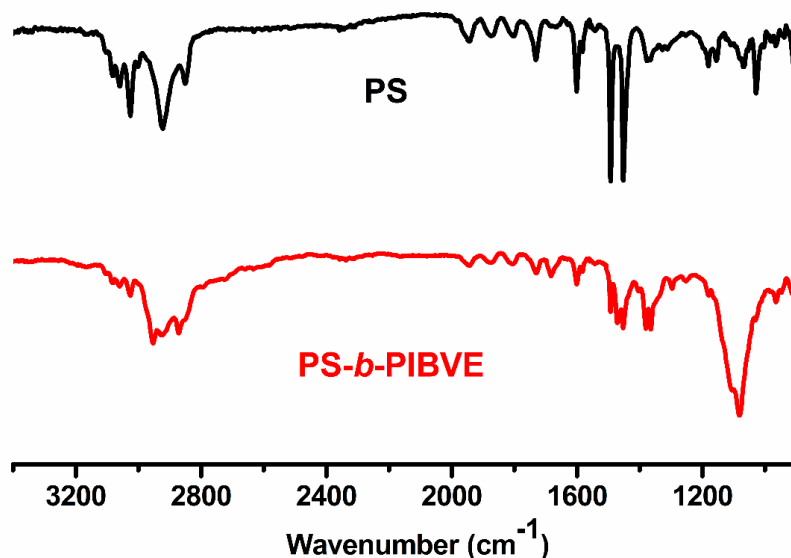


Figure 2: GPC traces for PS-Br and PS-*b*-PIBVE at different time intervals.

The IR spectra of the block copolymers demonstrate the characteristic bands for both the PS and PIBVE chains (Figure 3). Thus, in addition to the typical aromatic bands, the spectrum shows the characteristic etheric bands of the IBVE around 1100 cm^{-1} .

**Figure 3:** FT-IR spectra of PS and PS-*b*-PIBVE.

In conclusion, a simple transformation approach for the synthesis of block copolymers in a controlled manner by combination of ATRP and PROAD processes has been shown. The method lets us directly use of halide functional polymers gained by atom transfer radical polymerization, in the subsequent visible light-induced living/controlled cationic polymerization of a second monomer to give block copolymers. Both steps, ATRP and PROAD, require relatively mild conditions compared to conventional thermal systems as they are triggered by light. Moreover, the growth of the segments can be adjusted by varying experimental conditions.

REFERENCES

1. Yagci Y, Atilla Tasdelen M. Mechanistic transformations involving living and controlled/living polymerization methods. *Progress in Polymer Science*. 2006;31(12):1133-70.
2. Ciftci M, Arslan M, Buchmeiser M, Yagci Y. Polyethylene-*g*-Polystyrene Copolymers by Combination of ROMP, Mn₂(CO)₁₀-Assisted TEMPO Substitution and NMRP. *ACS Macro Letters*. 2016;5(8):946-9.
3. Ciftci M, Norsic S, Boisson C, D'Agosto F, Yagci Y. Synthesis of Block Copolymers Based on Polyethylene by Thermally Induced Controlled Radical Polymerization Using Mn₂(CO)₁₀. *Macromolecular Chemistry and Physics*. 2015;216(9):958-63.

4. Ciftci M, Kork S, Xu GJ, Buchmeiser MR, Yagci Y. Polyethylene-g-poly(cyclohexene oxide) by Mechanistic Transformation from ROMP to Visible Light-Induced Free Radical Promoted Cationic Polymerization. *Macromolecules*. 2015;48(6):1658-63.
5. Ciftci M, Kork S, Xu G, Buchmeiser MR, Yagci Y. Polyethylene-g-poly(cyclohexene oxide) by Mechanistic Transformation from ROMP to Visible Light-Induced Free Radical Promoted Cationic Polymerization. *Macromolecules*. 2015;48(6):1658-63.
6. Castle TC, Hutchings LR, Khosravi E. Synthesis of Block Copolymers by Changing Living Anionic Polymerization into Living Ring Opening Metathesis Polymerization. *Macromolecules*. 2004;37(6):2035-40.
7. Yagci Y, Serhatli IE, Kubisa P, Biedron T. SYNTHESIS OF BLOCK COPOLYMERS BY COMBINATION OF AN ACTIVATED MONOMER AND FREE-RADICAL POLYMERIZATION MECHANISM. *Macromolecules*. 1993;26(10):2397-9.
8. Hizal G, Yagci Y, Schnabel W. N-ALKOXY PYRIDINIUM ION TERMINATED POLYTETRAHYDROFURANS - SYNTHESIS AND THEIR USE IN PHOTOINITIATED BLOCK COPOLYMERIZATION. *Polymer*. 1994;35(20):4443-8.
9. Yagci Y, Onen A, Schnabel W. BLOCK COPOLYMERS BY COMBINATION OF RADICAL AND PROMOTED CATIONIC POLYMERIZATION ROUTES. *Macromolecules*. 1991;24(16):4620-3.
10. Hizal G, Sarman A, Yagci Y. SYNTHESIS OF HYDROXY-TERMINATED POLYTETRAHYDROFURAN BY PHOTOINDUCED PROCESS. *Polym Bull*. 1995;35(5):567-73.
11. Kahveci MU, Acik G, Yagci Y. Synthesis of Block Copolymers by Combination of Atom Transfer Radical Polymerization and Visible Light-Induced Free Radical Promoted Cationic Polymerization. *Macromol Rapid Commun*. 2012;33(4):309-13.
12. Studer A, Schulte T. Nitroxide-mediated radical processes. *Chemical Record*. 2005;5(1):27-35.
13. Acik G, Kahveci MU, Yagci Y. Synthesis of Block Copolymers by Combination of Atom Transfer Radical Polymerization and Visible Light Radical Photopolymerization Methods. *Macromolecules*. 2010;43(21):9198-201.
14. Degirmenci M, Toprak A. Synthesis of block copolymers by transformation of free radical promoted cationic polymerization to atom transfer radical polymerization C. *Polym J*. 2005;37(9):700-6.
15. Yagci Y, Schnabel W. LIGHT-INDUCED SYNTHESIS OF BLOCK AND GRAFT-COPOLYMERS. *Prog Polym Sci*. 1990;15(4):551-601.
16. Murtezi E, Ciftci M, Yagci Y. Synthesis of clickable hydrogels and linear polymers by type II photoinitiation. *Polymer International*. 2015;64(5):588-94.
17. Aydogan C, Ciftci M, Yagci Y. Hyperbranched Polymers by Type II Photoinitiated Self-Condensing Vinyl Polymerization. *Macromol Rapid Commun*. 2016;37(7):650-4.
18. Aydogan C, Ciftci M, Kumbaraci V, Talinli N, Yagci Y. Hyperbranched Polymers by Photoinduced Self-Condensing Vinyl Polymerization Using Bisbenzodioxinone. *Macromolecular Chemistry and Physics*. 2017;218(10):6.
19. Pan X, Tasdelen MA, Laun J, Junkers T, Yagci Y, Matyjaszewski K. Photomediated controlled radical polymerization. *Progress in Polymer Science*. 2016;62:73-125.
20. Liu G, Shi H, Cui Y, Tong J, Zhao Y, Wang D, et al. Toward rapid aqueous RAFT polymerization of primary amine functional monomer under visible light irradiation at 25 [degree]C. *Polymer Chemistry*. 2013;4(4):1176-82.
21. Guillaneuf Y, Bertin D, Gimes D, Versace D-L, Lalevée J, Fouassier J-P. Toward Nitroxide-Mediated Photopolymerization. *Macromolecules*. 2010;43(5):2204-12.

22. Tasdelen MA, Ciftci M, Yagci Y. Visible Light-Induced Atom Transfer Radical Polymerization. *Macromolecular Chemistry and Physics*. 2012;213(13):1391-6.
23. Ciftci M, Tasdelen MA, Yagci Y. Sunlight induced atom transfer radical polymerization by using dimanganese decacarbonyl. *Polym Chem*. 2014;5(2):600-6.
24. Matyjaszewski K. Atom Transfer Radical Polymerization (ATRP): Current Status and Future Perspectives. *Macromolecules*. 2012;45(10):4015-39.
25. Kork S, Ciftci M, Tasdelen MA, Yagci Y. Photoinduced Cu(0)-Mediated Atom Transfer Radical Polymerization. *Macromolecular Chemistry and Physics*. 2016;217(6):812-7.
26. Crivello JV. Radical-Promoted Visible Light Photoinitiated Cationic Polymerization of Epoxides. *J Macromol Sci Part A-Pure Appl Chem*. 2009;46(5):474-83.
27. Ciftci M, Yoshikawa Y, Yagci Y. Living Cationic Polymerization of Vinyl Ethers through a Photoinduced Radical Oxidation/Addition/Deactivation Sequence. *Angewandte Chemie International Edition*. 2017;56(2):519-23.
28. Ciftci M, Tasdelen MA, Yagci Y. Macromolecular design and application using Mn₂(CO)₁₀-based visible light photoinitiating systems. *Polymer International*. 2016;65(9):1001-14.
29. Iskin B, Yilmaz G, Yagci Y. Telechelic Polymers by Visible-Light-Induced Radical Coupling. *Macromolecular Chemistry and Physics*. 2013;214(1):94-8.
30. Dadashi-Silab S, Doran S, Yagci Y. Photoinduced Electron Transfer Reactions for Macromolecular Syntheses. *Chemical Reviews*. 2016;116(17):10212-75.



Spectrophotometric Determination of Sunset Yellow (E-110) in Powdered Beverages and Pharmaceutical Preparations after Cloud Point Extraction Method

Tufan GÜRAY^{1*}  

¹Eskisehir Osmangazi University, Faculty of Arts and Science, Department of Chemistry, 26480, Eskisehir, Turkey.

Abstract: In this study, Brij 58 was used for the spectrophotometric determination of sunset yellow (SY) (E-110) in pharmaceutical preparations and powdered beverages after cloud point extraction (CPE). Certain parameters such as pH, surfactant concentration, extraction time and temperature, speed of centrifugation, and salt concentration were optimized. Linear range in the optimum conditions was 0.01 – 4.00 $\mu\text{g mL}^{-1}$ and the correlation coefficient was 0.9995. The limit of detection (LOD) and the limit of quantification (LOQ) of this method were 0.0078 $\mu\text{g mL}^{-1}$ and 0.0261 $\mu\text{g mL}^{-1}$, respectively.

Keywords: Brij 58; Sunset Yellow (E-110); Cloud Point Extraction (CPE); Spectrophotometric Determination; Surfactant

Submitted: November 05, 2017. **Accepted:** March 04, 2018.

Cite this: Güray T. Spectrophotometric Determination of Sunset Yellow (E-110) in Powdered Beverages and Pharmaceutical Preparations after Cloud Point Extraction Method. JOTCSA. 2018;5(2):479–92.

DOI: <http://dx.doi.org/10.18596/jotcsa.349382>.

***Corresponding author. E-mail:** tguray@ogu.edu.tr; tufanguray@gmail.com

INTRODUCTION

Food dyes are used to provide more attractive, appetizing appearances to enhance the taste, flavor, and color of foods (1). Food coloring Sunset Yellow (6-hydroxy-5- [(4-sulfophenyl) azo] -2-naphthalenesulfonic acid disodium salt) (SY) (E-110) is a food additive commonly used in foods, pharmaceuticals, and cosmetics. Nevertheless, it is vital that SY is one of the synthetic dyes most likely present in widespread food products that may lead to allergies, diarrhea, anxiety migraines and also could harm to the kidney and the liver if it is consumed to the extreme (2-4). It is also known as Orange Yellow S, INS No.110 and CI Food Yellow 3. Acceptable daily dose of SY, an azo dye, is 2.5 mg kg^{-1} (5). Nowadays, the use of such additives is taking much attention owing to a series of health risks induced by food dyes, since it plays an indispensable part in human public health (6). For this reason, it is imperative to make and monitor the identification of SY and similar azo dyes in various samples.

Several methods such as high performance liquid chromatography (HPLC) (7), capillary electrophoresis (CE) (8), thin layer chromatography (TLC) (9), voltammetry (10), and spectrophotometry (11) have been given in the literature for the determination of SY. These analytical methods require the use of harmful solvents especially for laboratory workers and the environment (12).

The cloud point extraction (CPE) method is also an alternative to other enrichment and separation methods as simple, sensitive, inexpensive, non-polluting, and environmentally sensitive (13). The aqueous solutions of nonionic surfactant materials become cloudy when their temperature reaches the cloud point temperature and analyte collapses with a small volume by a surfactant. The CPE procedure can also be termed as temperature induced phase separation or micelle-mediated extraction (14-16). Thus, CPE can lead to high recovery efficiency and a large preconcentration factor due to a very small volume of micellar phase binding the analyte that has been dispersed in the original matrix (17). CPE is not only preconcentration procedure but also a separation method.

Non-ionic surfactants such as Triton X-100 (18), Triton X-114 and Brij 56 (19) have been used for the determination of SY. To the best of our knowledge, there is no enrichment of the SY with CPE method using Brij 58, another non-ionic surfactant, in the literature.

In this study, it was aimed to develop a new method of CPE using Brij (polyethylene glycol hexadecyl ether) 58 for the first time the spectrophotometric determination of SY.

EXPERIMENTAL

Instrumentation

Absorption spectra and absorbance measurements have been made by an Agilent (Stevens Creek Boulevard, Santa Clara, CA, USA) Transport 60 UV spectrophotometer. 1.00 cm light-beam quartz cells have been used in these measurements. To measure the pH of the solutions, a ThermoOrion 720A model pH / ion counter (Beverly, MA, USA) with Orion 71-03 brand glass electrode has been used. Centrifugations were performed using a Sigma 1-6P (Osterode am Harz, Germany) centrifuge.

Chemicals

All the reagents are of analytical grade. Brij 58 (polyethylene glycol hexadecyl ether), Sunset Yellow (6-hydroxy-5- [(4-sulfophenyl) azo] -2-naphthalenesulfonic acid disodium salt) (SY), CH₃COOH, H₃PO₄, NaOH, HCl, NaCl, Na₂CO₃, NaH₂PO₄, Na₂HPO₄, and anhydrous Na₂SO₄ were purchased from Sigma-Aldrich. All reagents were diluted using deionized water.

For the routine calibration and monitoring of our pH instruments, a ready-to-use buffer solutions with exact pH reference values (pH 4.01= citric acid/sodium hydroxide/hydrogen chloride, pH 7.00= di-sodium hydrogen phosphate/potassium dihydrogen phosphate, pH 10.04= boric acid/potassium chloride/sodium hydroxide in 20 °C, Merck) have been used. Buffer solutions (pH 2-11) were prepared by using 0.04 M H₃PO₄, 0.04 M CH₃COOH, 0.2 M NaH₂PO₄, 0.2 M Na₂HPO₄, and 0.04 M boric acid and the pH was adjusted with 0.2 mol L⁻¹ NaOH solution. The pH 2 solution was prepared with 0.1 mol L⁻¹ HCl.

Pharmaceutical preparations (Bemiks® tablets, *Zentiva Health Products Industry and Trade Co., Kırklareli, Turkey*; Magnorm® tablets, *NEUTEC Ilac Sanayi ve Ticaret A.Ş., Istanbul, Turkey*) and powdered beverage drinks have been purchased by pharmacies and local grocery stores.

Preparation of Standard and Sample Solutions

To prepare 100 µg mL⁻¹ stock solution of SY, 0.1 g of the dye was dissolved in deionized water and diluted to 1000 mL. with deionize water. The working standard solutions are prepared daily by diluting the desired concentrations from the stock solution. These solutions were stored in the dark at 4 °C. To prepare Brij 58 solution of 20% (w/v), twenty grams of the Brij 58 is weighed and dissolved in 100 mL of deionized water in an ultrasonic bath.

Bemiks® tablet contains vitamin B1, vitamin B2, vitamin B6, vitamin B12, folic acid, niacinamide, Ca-pantothenate and certain inactive ingredients, such as quinoline sarcine (E104), sunset yellow FCF (E110), titanium dioxide (E171), Ponceau 4R (E124). Ten Bemiks® tablets have been weighed and powdered. Accurately weighed 0.9496 ± 0.0005 g (amount of 5 tablets) has been transferred to a 100 mL volumetric flask. The required volume with deionized water has been

completed. Subsequently, an appropriate amount of this solution has been taken by filtration and used for the analysis.

Magnorm® tablet contains magnesium oxide and certain inactive ingredients, such as citric acid anhydrides, citric acid anhydrides, sodium hydrogen carbonate, povidone K30, sodium saccharin, sorbitol (E420), polyethylene glycol, aerosil 200, sunset yellow (E110), orange flavor, and apricot flavor. Ten Magnorm® tablets were powdered and mixed. An amount of 3.7885 g (1 tablet) was powdered and taken into a 500 mL volumetric flask. Then, the solution was diluted to 500 mL with deionized water. The 5 mL of this solution was taken and filtered, then the solution was diluted to 100 mL with deionized water.

The powdered beverage drink of 5.0000 ± 0.0005 g has been weighed and taken into a 250 mL volumetric flask and the required volume was diluted with deionized water. Subsequently, appropriate amounts of this solution have been taken by filtration and they have been used for the analysis.

Proposed CPE Method

The method has applied to the standard solution of SY: A solution containing 8 mL of the buffered SY in NaH_2PO_4 and Na_2HPO_4 (pH 6) has been transferred to a 15 mL screw-capped centrifuge tube (Figure 1a). 1 mL of 20% (w/v) Brij 58, 2.0050 ± 0.0005 g Na_2SO_4 were added and the solution has been diluted 10 mL with deionized water (Figure 1b). This mixture was immediately stirred until it was dissolved. The mixture left at 70 °C for 15 minutes until a cloudy phenomenon occurred. Then it has been cooled down to the room temperature (Figure 1c). The mixture has been centrifuged at 4000 rpm for 5 minutes for phase separation (Figure 1d). The surfactant-rich phase has been separated and it has been collected on the top of the tube (Figure 1 e). Finally, the aqueous phase has been removed by means of a syringe and the surfactant-rich phase has been diluted with 1 mL of water and the absorbance of the solution was measured by UV-Vis. against blank at 482 nm.

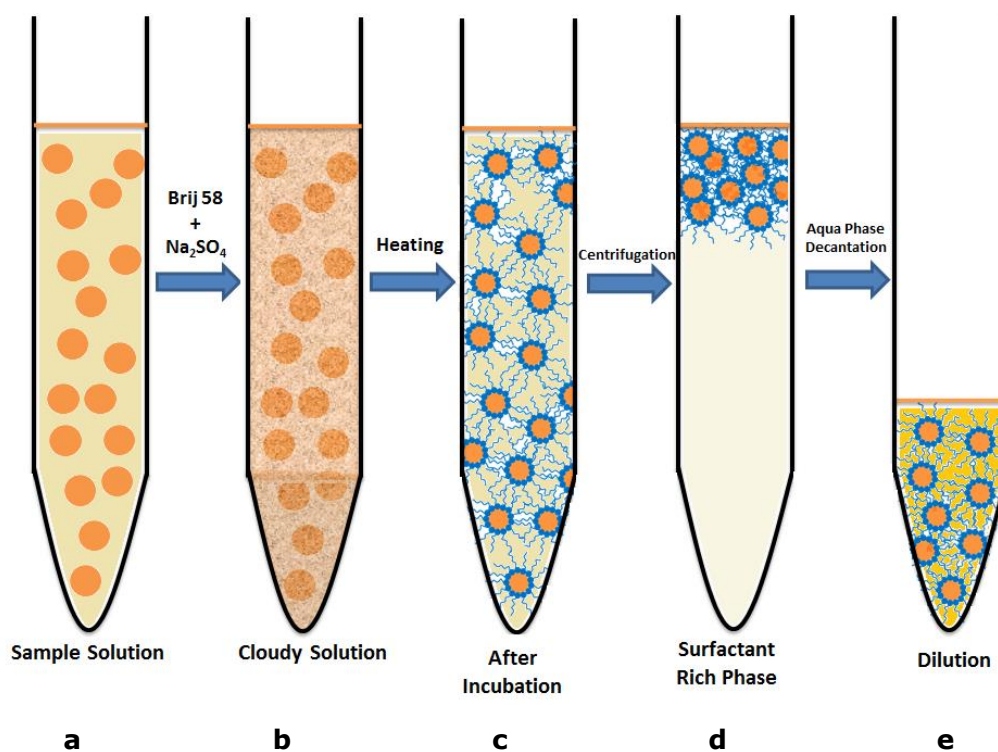


Figure 1: **a-** Sample solution, **b-** Mixture after Brij 58 + Na₂SO₄ added, **c-** After incubation, **d-** After centrifugation, **e-** After decantation of 1 mL of water-soluble surfactant-rich phase.

The developed method has applied to two drugs and two powdered beverages as detailed in 'The preparation of standard and sample solutions' section in a preceding page.

RESULT AND DISCUSSION

The maximum absorbance of 0.01-4.00 $\mu\text{g mL}^{-1}$ the SY standard solution is 482 nm (Figure 2a). The surfactant (Brij 58) has been added to the medium. It did not make a significant change in the maximum wavelength of the dye by comparing the SY solution (Figure 2b). For this reason, all absorbance measurements have been made at this wavelength. The effects of the main variables in the CPE method such as the medium pH value, surfactant concentration, salt concentration, temperature, and time, have been optimized to achieve maximum sensitivity and recovery.

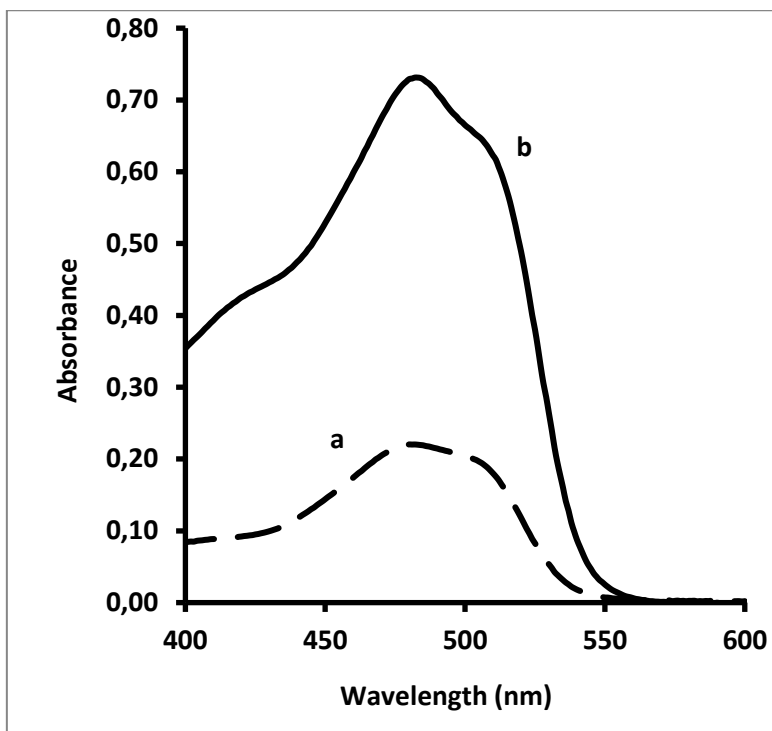


Figure 2: Absorption spectra for $4 \mu\text{g mL}^{-1}$ SY, **a-** without extraction, **b-** after CPE.

The Effect of pH

In the CPE procedure, the pH is an important parameter that increases the coefficient of dispersion of the analyte between the aqueous phase and the surfactant-rich phase. For this reason, the pH effecting on SY extraction efficiency has been examined between pH 2 and 11. The pH of the solution was adjusted to the desired value by the addition of hydrochloric acid and sodium hydroxide and using a pH meter. The SY solution was prepared in detail in the section of '*Proposed CPE Method*'. The absorbance of the SY has been measured at 482 nm (Figure 3). The increase has been observed in absorbance up to pH 6 and, then the absorbance did not change too much up to pH 8. The results indicate the range of pH 6-8 is most suitable for dye in the viewpoint of CPE efficiency and the pH range was selected as an optimum pH. All the studies have been carried out at pH 6-8.

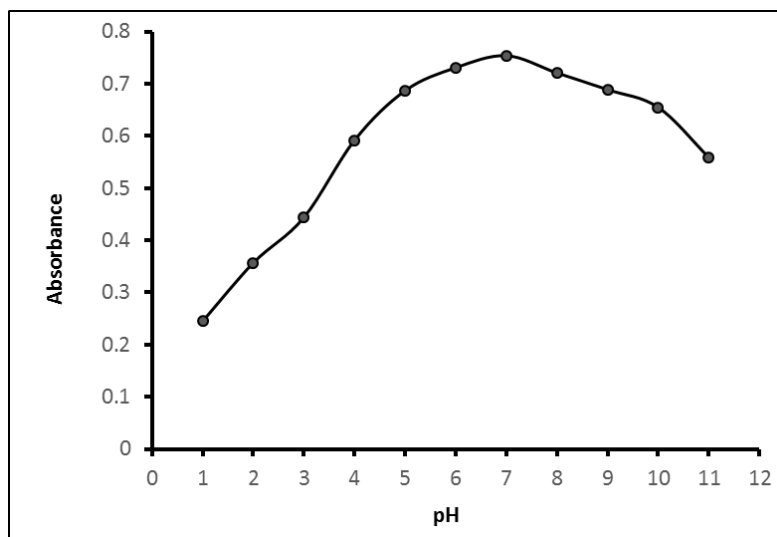


Figure 3: Effect of pH on CPE efficiency. $4 \mu\text{g mL}^{-1}$ SY, 2% Brij 58, 2.00 g Na_2SO_4 , incubation at 70°C for 15 minutes.

The Effect of Surfactant Concentration

Optimizing the concentration of the surfactant is one of the important parameters to increase extraction efficiency. Thus, the effect of concentration of Brij 58 on the absorbance of the SY has been studied. The results are given in Figure 4. As can be seen, the absorbance does not change at concentrations greater than 2% (w/v) of Brij 58. For this reason, 2% (w/v) Brij 58 has been used throughout the study.

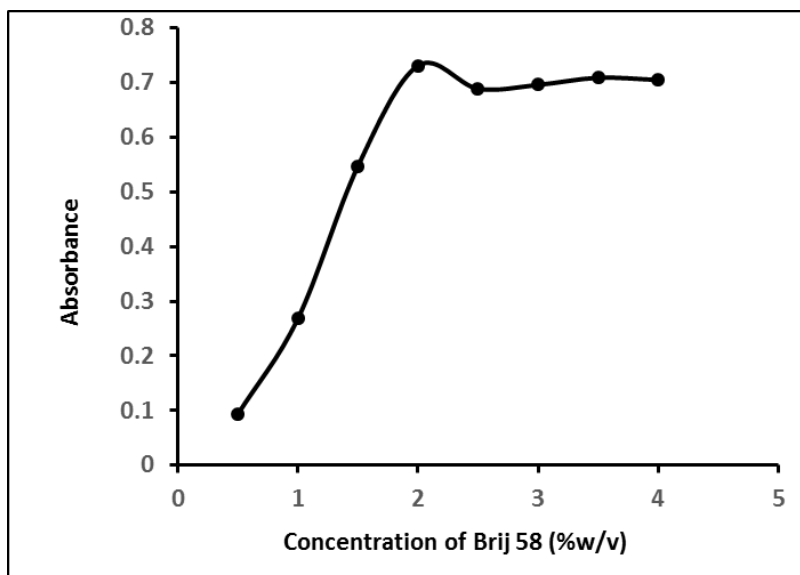


Figure 4: The effect of Brij 58 concentration on the CPE efficiency of SY. $4 \mu\text{g mL}^{-1}$ SY, pH 6, 2.00 g Na_2SO_4 , 15 minutes of incubation time at 70°C .

The Effect of Salt

A salt concentration is important in the CPE procedure because it helps the phase separation, to increase the mass transfer of the analyte from the aqueous phase to the surfactant-rich phase and to reduce the cloud point temperature. For these reasons, the commonly used salts such as NaCl, Na_2SO_4 and Na_2CO_3 have been tried and their effects on the extraction process have been

investigated. The surfactant-rich phase has not been separated or the surfactant-rich phase was too poor to be separated when other salts were used. So, a 20% (w/v) concentration of Na_2SO_4 , which maximizes the absorption of SY, has been selected as the optimum salt concentration. The results are given in Figure 5.

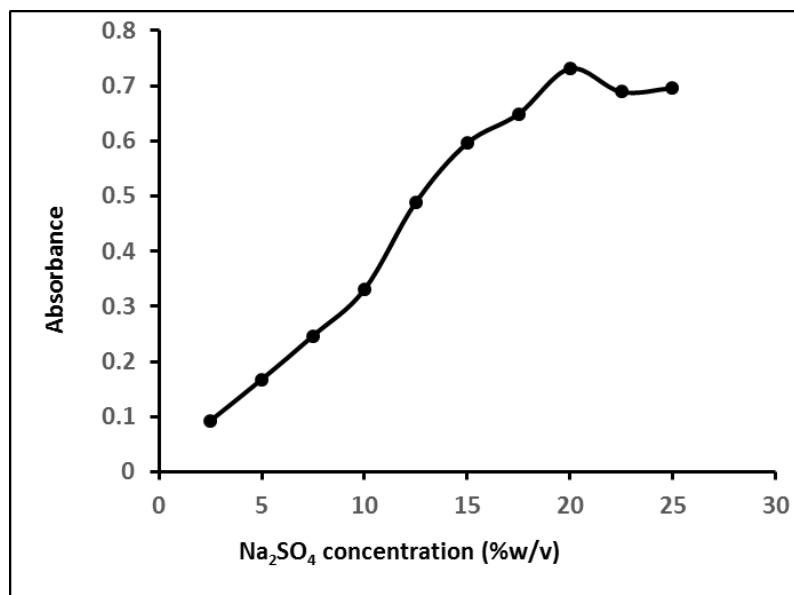


Figure 5: The effect of Na_2SO_4 concentration on the CPE efficiency of SY. $4 \mu\text{g mL}^{-1}$ SY, pH=6, 2% (w/v) Brij 58, 15 minutes of incubation time at 70°C .

Effect of Equilibrium Temperature and Incubation Time

Two other important parameters examined in the CPE procedure are the equilibrium temperature and incubation time. The studied temperature ranges were $50\text{-}90^\circ\text{C}$ and the highest extraction efficiency was observed at 70°C . The incubation time in the range of $10\text{-}40$ min has been studied. The maximum absorbance has been obtained for 15 min. In further studies, these optimum conditions have been carried out.

The Effect of Interference Ions

In this study, the effect of different anions and cations on the determination of 5 ppm SY has been studied by the proposed method. The tolerance limit has been examined taking into account the amount of foreign species causing the absorbance change of less than $\pm 5\%$. The results are given in Table 1.

Table 1: Comparison of the effect of interfering species on the determination of SY in the optimum conditions, $C_{SY} = 4 \text{ mg L}^{-1}$.

Interfering species (I)	Limiting mass ratio (SY: I)
K^+, Mg^{2+}, Na^+	1:2000
$Hg^{2+}, Mn^{2+}, Pb^{2+}, Be^{2+}, Fe^{3+}, Al^{3+}, Sr^{2+}, Sn^{2+}$	1:100
$Co^{2+}, Zn^{2+}, Ni^{2+}, Cd^{2+}, Si^{2+}$	
$F^-, Cl^-, Br^-, I^-, NO_3^-, SO_4^{2-}$	1:4000
$AsO_4^{3-}, B_4O_7^{2-}, HPO_4^{2-}, SCN^-$	1:200

Analytical Performance

Correlation graphs with the proposed method have been obtained in the optimal conditions between increasing concentrations of SY versus the measured absorbance.

Absorbance of the SY obeys Beer's law between $0.01 \mu\text{g mL}^{-1}$ and $4.00 \mu\text{g mL}^{-1}$ in the optimum conditions. The correlation coefficient for the SY is 0.9995. The value of slope is 0.2105 and the intercept is + 0.0237. Thus, the calibration equation was $A = 0.2105 C (\mu\text{g mL}^{-1}) + 0.0237$.

The accuracy of this method was determined by performing five repetitions of $0.80 \mu\text{g mL}^{-1}$ SY. The RSD value is 1.44%. The limit of detection (LOD) of the method is $0.0078 \mu\text{g mL}^{-1}$ depending on the standard deviation of blank with repetition number of 3.

Sample Application of the Proposed CPE Method

This method has been applied to the spectrophotometric determination of SY in two different drug samples and two different powdered beverages. The analysis of the SY in the samples was realized as stated in the experimental section of '*Proposed CPE Method*'. Recovery experiments were performed by spiking the samples prior to the CPE with the addition of known amounts of SY. The recovery values obtained from the results in Table 2 are between 96.88% and 103.75%. According to these values, it can be said that the materials present in the samples do not interfere with the developed method. The acceptable Daily Intake for SY has been given as 0.0-2.5 mg/kg body weight by World Health Organization (WHO) (2). The results show that the developed CPE method can be used for the accurately determination of SY in these samples.

Table 2: The spectrophotometric determination of SY in powdered beverages and pharmaceutical preparations after the developed CPE.

Sample	Added, SY ($\mu\text{g mL}^{-1}$)	Found, SY \pm CL ^a ($\mu\text{g mL}^{-1}$)	Recovery ^b , %
Powdered beverage 1	-	0.95 \pm 0.11	-
	0.80	1.74 \pm 0.15	98.75
	1.60	2.51 \pm 0.15	98.13
Powdered beverage 2	-	2.16 \pm 0.01	-
	0.80	2.95 \pm 0.07	99.24
	1.60	3.78 \pm 0.06	100.99
Magnorm® (Pharmaceutical preparation)	-	1.46 \pm 0.06	-
	0.80	2.26 \pm 0.07	101.25
	1.60	3.06 \pm 0.16	96.88
Bemiks® (Pharmaceutical preparation)	-	0.78 \pm 0.07	-
	0.80	1.61 \pm 0.10	103.75
	1.60	2.30 \pm 0.07	98.13

^aCL is confidence limits, ($\frac{ts}{\sqrt{n}}$); n=5

^bRecovery = $\frac{(C_2 - C_1)}{C_3} \times 100$

C₁ = Measured sample concentration (blank)

C₂ = The measured "spiked sample" concentration (blank + spike)

C₃ = Spike concentration

Comparison of the Proposed Method with Literature

An comparison of some apparent features of the developed method with other reported methods for the simultaneous determination of SY in various samples is shown in Table 3. All existing methods for SY are based on CPE. The LOD value obtained for SY in the present work is superior compared to some of these methods (12, 20). While the method is slightly less sensitive compared to the other two methods (18, 19), these methods have certain disadvantages. El-Shahawi MS, *et al.* used an extra chemical such as trioctylamine to increase the efficiency of their work (18) and the repeatability of study of Heydari R. *et al.* is low (19). Among the values in Table 3, our method has the widest linear range and almost the lowest LOD with a high recovery.

Table 3: Comparison of certain CPE methods for spectrophotometric determination of SY reported in the literature.

Surfactant	Salt	pH	Inc. ^a Temp. (°C)	Inc. ^a Time (min)	Centr. ^b Time (min.)	Solvent of Dilution	Linear Range $\mu\text{g mL}^{-1}$	LOD $\mu\text{g mL}^{-1}$	RSD %	Recovery %	Remarks	Ref.
Triton X-100 0.03 M, 4 mL	Na ₂ SO ₄ 1 M, 1 mL	HCl 0.01 M	70	10	10	MeOH 0.1 mL	0.020- 0.452	5.0 x 10 ⁻³	1.49	96.79	Triocetylamine was used to increase efficiency	(18)
Triton X-100 200 g/L, 3 mL	Na ₂ SO ₄ 1 M, 5 mL	-	40	10	10	Water 5 mL	20-120	5.0	1.97	94.75	LOD is high	(12)
Triton X-114 200 g/L, 2 mL	Na ₂ SO ₄ 1 M, 5 mL	-	40	10	10	Water 5 mL	20-120	10.4	1.13	91.72	LOD is high	(12)
Brij 56 200 g/L, 3 mL	Na ₂ SO ₄ 1 M, 5 mL	-	60	15	10	Water 5 mL	20-120	2.8	1.06	89.13	LOD is high	(12)
Triton X-100 % 40, 1.5 mL	NaCl 1.5 g	6	55	15	5	Water 1 mL	0.025- 1.300	6.0 x 10 ⁻³	3.35	98.64	Repeatability is low	(19)
Triton X-100 0.5 M, 4.5 mL	KCl 1 M, 5 mL	4	80	40	-	Water 5 mL	0.020- 4.000	9.0 x 10 ⁻³	3.50	99.80	Repeatability is low	(20)
Brij 58 % 20, 1 mL	Na ₂ SO ₄ 2 g	6	70	15	5	Water 1 mL	0.010- 4.000	7.8 x 10 ⁻³	1.44	99.64 ^c		This work

^aInc.: Incubation, ^bCentr.: Centrifugation, ^c \bar{x} : Recovery (%) average in Table 2.

CONCLUSION

The developed CPE technique has advantages such as low cost, sensitiveness, selectiveness, high extraction efficiency, and environmentally friendliness. Brij 58 was used, for the first time, as a surfactant for the determination of SY after CPE method. This new CPE spectrophotometric method can be used for the sensitive, selective and reproducible determination of SY in short time in routine analysis.

ACKNOWLEDGEMENT

The author is grateful to Prof. Dr. Ülkü Dilek UYSAL for her help.

REFERENCES

1. Pourreza N, Elhami S. Cloud point extraction and spectrophotometric determination of amaranth in food samples using nonionic surfactant triton X-100 and tetrabutylammonium hydrogen sulfat. *Journal of The Iranian Chemical Society*. 2009;6(4): 784-788.
2. Miao X, Wang W, Xiong B, Zhou X, Hu J. A separation-free method for simultaneous determination of sucrose and sunset yellow in different abundance by integrating RBI and TL detectors *Analytical Methods*. 2011; 3(3):514-518.
3. Minioti KS, Sakellariou CF, Thomaidis NS. Determination of 13 synthetic food colorants in water-soluble foods by reversed-phase high-performance liquid chromatography coupled with diode-array detector. *Analytica Chimica Acta*.2007; 583(1): 103-110.
4. Yadav A, Kumar A, Dwivedi PD, Tripathi A, Das M. In vitro studies on immunotoxic potential of Orange II in splenocytes. *Toxicology Letters*. 2008; 208(3): 239-245.
5. Joint FAO/WHO Expert Committee on Food Additives, Compendium of Food Additive Specifications. FAO JECFA Monographs 5, 2008; 69th 79–82.
6. Zhu J, Liu S, Liu Z, Li Y, Tian J, Hu X. A highly sensitive and selective assay of doxycycline by dualwavelength overlapping resonance Rayleigh scattering. *Spectrochimica Acta Part A: Molecular and Biomolecular Spectroscopy*. 2014; 124: 237-248.
7. Gosetti F, Gianotti V, Polati S, Gennaro MC. HPLC-MS degradation study of E110 Sunset Yellow FCF in a commercial beverage. *Journal of Chromatography A*. 2005;1090: 107-115.
8. Del Giovine L, Bocca AP. Determination of synthetic dyes in ice-cream by capillary electrophoresis. *Food Control*. 2003;14: 131-135.
9. Soponar F, Mot AC, Sarbu C. Quantitative determination of some food dyes using digital processing of images obtained by thin-layer chromatography. *Journal of Chromatography A*. 2008;1188: 295-300.
10. Ni YN, Bai JL, Simultaneous determination of Amaranth and Sunset Yellow by ratio derivative voltammetry. *Talanta*. 1997;44; 105-109.
11. Dinc E, Baydan E, Kanbur M, Onur F. Spectrophotometric multicomponent determination of sunset yellow, tartrazine and allura red in soft drink powder by double divisor-ratio spectra derivative, inverse least-squares and principal component regression methods. *Talanta*. 2002;58: 579-594.
12. Wang Y, Zhang Z, Xiao Y, Li N. Spectrophotometric determination of Sunset Yellow in beverage after preconcentration by the cloud point extraction method. *Analytical Methods*. 2014;6: 8901-8905.
13. Kaur A, Gupta U. The review on spectrophotometric determination of synthetic food dyes and lakes. *Gazi University Journal of Sciences*. 2012;25(3): 579-588.

14. Saitoh T, Tan H, Watanabe H, Kamidate T. Phase separation in aqueous micellar solutions of nonionic surfactants for protein separation. *Trends in Analytical Chemistry*. 1995; 14(5): 213-217.
15. Hinze WL, Pramauro E. A Critical Review of Surfactant-Mediated Phase Separations (Cloud-Point Extractions): Theory and Applications *Journal C R C Critical Reviews in Analytical Chemistry* 1993; 24(2): 133-177.
16. Tani H, Kamidate T, Watanabe H. Micelle-mediated extraction. *Journal of Chromatography A*. 1997; 780(1-2): 229-241.
17. Escalera LA, Santelli RE, Oliveira EP, de Fátima M, de Carvalho B, Bezerra MA. Preconcentration procedure for determining trace amounts of Ni, Cd, Pb and Cu in high-salinity waters after cloud-point extraction. *International Journal of Environmental Analytical Chemistry*. 2009; 89(7): 515-527.
18. El-Shahawi MS, Hamza A, Al-Sibaai AA, Bashammakh AS, Al-Saidi HM. A new method for analysis of sunset yellow in food samples based on cloud point extraction prior to spectrophotometric determination. *Journal Industrial and Engineering Chemistry*. 2013;19: 529-535.
19. Heydari R, Hosseini M, Alimoradi M, Zarabi S. A simple method for simultaneous spectrophotometric determination of brilliant blue FCF and sunset yellow FCF in food samples after cloud point extraction. *Journal of Chemical Society Pakistan*. 2016;38: 438-445.
20. Heidarizadi E, Tabaraki R. Simultaneous spectrophotometric determination of synthetic dyes in food samples after cloud point extraction using multiple response optimizations. *Talanta*. 2016;148: 237-246.



Chemical Diversity and Biological Potential of *Tanacetum praeteritum* subsp. *praeteritum* Essential Oils

Gülmira Özek*  

¹Anadolu University, Faculty of Pharmacy, Department of Pharmacognosy, 26470, Eskişehir, Turkey

Abstract: Two samples of *Tanacetum praeteritum* (Horwood) Heywood subsp. *praeteritum* (Horwood) were collected in flowering period and subjected separately to hydrodistillation to yield the essential oils (A and B). The oils were investigated for chemical composition with GC-FID and GC/MS techniques and evaluated against acetylcholinesterase and α -amylase enzymes and free radicals (DPPH^{*} and ABTS⁺⁺) using microtiter plate assays. Both oils were characterized with high abundance of oxygenated monoterpenes. The oils were distinguished by the main constituents, namely, camphor (37.6%), 1,8-cineole (19.5%) and terpinen-4-ol (9.3%) were found as the major constituents in the oil A, while α -thujone (79.4%) and β -thujone (8.5%) were detected in the oil B. The oils demonstrated significant inhibitory (80% and 60.0%) potentials on acetylcholinesterase (an IC₅₀ of 0.74 mg/mL and an IC₅₀ of 1.78 mg/mL, respectively) which is involved in Alzheimer's disease. With respect to antidiabetic activity, the oils demonstrated significant inhibiting potential on porcine pancreatic α -amylase (an IC₅₀ of 1.02 mg/mL and an IC₅₀ of 0.89 mg/mL) in I₂/KI assay. The oils demonstrated weak free radical scavenging activity against DPPH radicals and moderate activity (0.23 mM and 0.15 mM) against ABTS⁺⁺ in TEAC assay.

Keywords: *Tanacetum*; essential oil; chemical composition; GC/MS; activity.

Submitted: February 02, 2018. **Accepted:** March 05, 2018.

Cite this: Özek G. Chemical Diversity and Biological Potential of *Tanacetum praeteritum* subsp. *praeteritum* Essential Oils. JOTCSA. 2018;5(2):493-510.

DOI: <http://dx.doi.org/10.18596/jotcsa.389075>.

***Corresponding author.** Tel.: +90 222 335 05 80 /3716; Fax: +90 222 330 07 50.

INTRODUCTION

The genus *Tanacetum* is one of large genera of Asteraceae family. The genus is represented by nearly 200 species around the world. In Turkey, the genus *Tanacetum* encompasses 60 taxa (1).

Different type extracts (solvent extracts, essential oils and fractions) and pure compounds isolated from *Tanacetum* species have been reported for a range of biological activities. Namely, antibacterial, antioxidant (2), anthelmintic (3), repellent, insecticidal (4), cytotoxic and acetylcholinesterase inhibitory (5), and antidiabetic (6). Flavonoids, mono-, di- and sesquiterpenes, and sesquiterpene lactones have been found to be responsible for biological activities of *Tanacetum* species (7-11).

Nowadays, there is increasing demand for effective and safe natural products with antioxidant, antiacetylcholinesterase and hypoglycemic properties. The efficacy of known synthetic antioxidants (12), antiacetylcholinesterase agents (13), and hypoglycemic products (14, 15) is debatable. The plants reputed for their neurodegenerative healing and antidiabetic effects should be verified either experimentally or clinically. However, evidenced-based therapeutic usage of many plants is scarce.

T. praeteritum subsp. *praeteritum* has earlier been reported for flavonoids (16), sesquiterpene lactones (17), eudesmane-type sesquiterpenes (18) essential oil (19). However, there is no information about its biological activity. The present work is the first investigation of *T. praeteritum* subsp. *praeteritum* essential oil for antioxidant, antiacetylcholinesterase and antidiabetic potential.

MATERIALS AND METHODS

Chemicals

Hydrochloric acid, *n*-hexane, dimethyl sulfoxide (DMSO) (Sigma-Aldrich, Germany), anhydrous sodium sulfate (Fluka, Germany), iodine (ACS reagent), potassium iodide (Saint Louis, USA), methanol (Sigma-Aldrich, Poland), potassium persulfate (Sigma-Aldrich, Saint Louis, USA), sodium phosphate, and disodium phosphate were of analytical grade. A C₈-C₄₀ *n*-alkane standard solution was purchased from Fluka (Buchs, Switzerland). Gallic acid (GA), (±)-6-hydroxy-2,5,7,8-tetramethylchromane-2-carboxylic acid (Trolox), 2,2-diphenyl-1-picrylhydrazyl (DPPH), 2,2'-azino-bis(3-ethylbenzothiazoline-6-sulfonic acid) diammonium salt (ABTS), soluble starch, acarbose, α -amylase from porcine pancreas (Type VI-B, EC 3.2.1.1), tris(hydroxymethyl) aminomethane (ACS reagent), acetylcholinesterase (AChE) from *Electrophorus electricus* (Type VI-S), bovine serum albumin (BSA), acetylthiocholine iodide (ATCI), 5,5'-dithiobis(2-

nitrobenzoic acid) (DTNB), galanthamine from *Lycoris* sp. were purchased from Sigma-Aldrich (St. Louis, MO, USA).

Instrumentation

Agilent 5975 GC-MSD system (Agilent, USA; SEM Ltd., Istanbul, Turkey) was equipped with the HP-Innowax FSC column (60 m × 0.25 mm id with 0.25 µm film thickness, Agilent, USA). The GC-FID analysis was carried out with capillary GC using an Agilent 6890N GC system (SEM Ltd., Istanbul, Turkey). Microtiter plate assays were performed with Biotek Powerwave XS microplate reader. Ultrapure water (0.05 µS/cm) was obtained from a Direct-Q® Water Purification System (Germany).

Plant Material

Plant materials were two samples (A and B) of *T. praeteritum* subsp. *praeteritum* collected in period of flowering in Karçukuru Yaylasi in Antalya province of Turkey, on June, 2015. The plant material was dried under the shade. Botanical identification was performed by Dr. M. Arslan. Voucher specimens are deposited at the Herbarium of the Forest Regional Department.

Hydrodistillation of Essential Oil

Aerial parts of two *T. praeteritum* ssp. *praeteritum* samples (A and B) were separately subjected to hydrodistillation (3 h) in a Clevenger type apparatus (Eu.Ph.) to yield essential oils (20).

Gas-Chromatography - Mass Spectrometry (GC/MS)

The GC/MS analysis was carried out with an Agilent 5975 GC-MSD system (Agilent, USA; SEM Ltd., Istanbul, Turkey). HP-Innowax FSC column (60 m × 0.25 mm, 0.25 µm film thickness, Agilent, USA) was used with a helium carrier gas at 0.8 mL/min. GC's oven temperature was kept at 60 °C for 10 min and programmed to 220 °C at a rate of 4 °C/min, kept constant for 10 min at 220 °C, and then programmed to increase at a rate of 1 °C/min to 240 °C. The oils were analyzed with a split ratio of 40:1. The injector temperature was 250 °C. Mass spectra were taken at 70 eV and the mass range was from m/z 35 to 450.

Gas Chromatography – Flame Ionization Detection (GC-FID)

The GC-FID analysis was carried out with capillary GC using an Agilent 6890N GC system (SEM Ltd., Istanbul, Turkey). Flame ionization detector (FID) temperature was set at 300 °C in order to obtain the same elution order with GC/MS. Simultaneous injection was performed using the same column and appropriate operational conditions.

Identification and Quantification of Compounds

Identification of the volatile constituents was achieved as reported previously (21). Briefly, identification of the individual compounds was based on the following: (i) comparison of the

GC/MS Relative Retention Indices (RRI) of the compounds on polar column determined relative to the retention times of a series of *n*-alkanes (C₈-C₄₀), with those of authentic compounds or literature data; (ii) computer matching with commercial mass spectral libraries: MassFinder software 4.0 (22), Adams Library (23), Wiley GC/MS Library (Wiley, New York, USA) and NIST Library, and comparison of the recorded spectra with literature data Confirmation was also achieved using the in-house "Başer's Library of Essential Oil Constituents" database, obtained from chromatographic runs of pure compounds performed with the same equipment and conditions (24).

Determination of Anti-Acetylcholinesterase Activity (Ellman's Assay)

The essential oils were tested for inhibition of acetylcholinesterase (AChE) using Ellman's method as previously reported (25) with slight modification. Three buffers were used: (A) 50 mM Tris-HCl (pH=8.0, in ultrapure water); (B) 0.1% BSA in buffer A; (C) 0.1 M NaCl and 0.02 M MgCl₂·6H₂O in buffer A. The oils were previously dissolved in DMSO (20% in buffer). In the 96-well flat bottom plates, 25 µL of the sample (EO or standard), 50 µL of buffer B and 25 µL of AChE (0.22 U/mL in buffer A) solution were pipetted with 8-channel automatic pipette (Eppendorf Research® plus, Germany) and incubated for 15 min at 25 °C. Then, 125 µL of Ellman's reagent DTNB (3.0 mM in buffer C) and 25 µL substrate ATCI (15 mM, in ultrapure water) were added. Hydrolysis of ATCI was monitored by the formation of the yellow 5-thio-2-nitrobenzoate anion as a result of the reaction of DTNB with thiocholines, catalyzed by enzymes at 412 nm utilizing a 96-well microplate reader (Biotek Powerwave XS, USA). The mixture allowed to stand 15 min at 25 °C and the absorbance was recorded at 412 nm. Similarly, a blank (for eliminating the colors of the samples) was prepared by adding sample solution to all reaction reagents and 25 µL buffer instead of enzyme. The control wells contained all the reagents without the sample (the solvents of the samples instead were added). Galanthamine hydrobromide (0.1 mg/mL) was used as positive control. The percentage inhibition was calculated according to Equation 1:

$$\%Inh = \left[\frac{(Abs_{control} - Abs_{control\ blank}) - (Abs_{sample} - Abs_{sample\ blank})}{Abs_{control} - Abs_{control\ blank}} \right] \times 100 \quad (\text{Eq. 1})$$

where Abs_{control} and Abs_{control blank} are the absorbance of the control and its blank, Abs_{sample} and Abs_{sample blank} are the absorbance of the sample and its blank.

Determination of Anti-α-Amylase Activity

The activity of α-amylase under effect of *T. praeteritum* ssp. *praeteritum* essential oils was measured using Caraway-Somogyi iodine/potassium iodide (I₂/KI) method (26) with slight modifications. The substrate solution (0.05%) was prepared by dissolving of soluble potato starch (10 mg) in 20 mL ultrapure water then boiling for 10 min and cooling to room temperature before use. As a positive control experiment, acarbose (0.01-0.1 mg/mL in buffer) was used. In the experiment, 20 mM sodium phosphate buffer (pH 6.9) was pipetted in the 96-well flat bottom plates with multichannel automatic pipette (Eppendorf Research® plus, Germany), then 25 µL

of sample solution and 50 μL of α -amylase (0.8 U/mL in buffer) were added and incubated for 10 min at 37 °C. After incubation, 50 μL of substrate solution was added to the mixture. The mixture was subjected to a second incubation for 10 min at 37 °C. The reaction was stopped by addition of 25 μL of HCl solution (1 M). Finally, 100 μL of I_2/KI reagent was added to the wells. The sample blanks contained all reaction reagents and 50 μL of buffer instead of enzyme. The control wells contained all reaction reagents and 25 μL of solvent (instead of the sample solution). The absorbance values were recorded for the sample and blank at 630 nm. The percentage inhibition of the α -amylase activity (Inh%) was calculated according to Equation 1.

Antioxidant Activity

Free radical scavenging activity (DPPH assay)

The hydrogen atoms or electrons donation ability of the oils were evaluated according to bleaching of purple-colored DPPH stable radicals. The effect of *T. praeteritum* ssp. *praeteritum* essential oils on DPPH free radicals was determined using a method of Brand-Williams (27) with slight modifications. The DPPH solution (0.08 mg/mL, in methanol) was freshly prepared daily, kept in the dark at 4 °C between the measurements. The solutions of the essential oils (30 mg/mL) and gallic acid (0.1 mg/mL) were prepared in methanol. 100 μL of the sample (oil or standard) solution and 100 μL of DPPH solution were pipetted by multichannel automatic pipette (Eppendorf Research® plus, Germany) into 96-flat bottom well plate cells and allowed to stand in the dark for 30 min. The control well contained 100 μL methanol (instead of the sample) mixed with 100 μL of DPPH. The decrease in the absorbance was recorded at 517 nm. Gallic acid (standard) was used as positive control. Experiments were performed in triplicate. The free radical scavenging activity of the samples was expressed as percentage of inhibition calculated according to Equation 2:

$$\% \text{ Inh} = \left(\frac{\text{Abs}_{\text{control}} - \text{Abs}_{\text{sample}}}{\text{Abs}_{\text{control}}} \right) \times 100 \quad (\text{Eq. 2})$$

where, $\text{Abs}_{\text{control}}$ is the absorbance of the control (containing all reagents except the test compound), $\text{Abs}_{\text{sample}}$ is the absorbance of the sample with added DPPH. The IC_{50} values were obtained by plotting the DPPH scavenging percentage of each sample against the sample concentration.

Trolox-equivalent antioxidant capacity (TEAC assay)

ABTS^{•+} free radical cation scavenging activity of the samples were tested according to the procedure described by Re *et al.* (28) with slight modifications. 7 mM ABTS and 2.5 mM $\text{K}_2\text{S}_2\text{O}_8$ dissolved in 10 mL of ultrapure water were allowed to stand in dark for 16 h at room temperature to create ABTS^{•+} free radical cation. Prior to the assay, ABTS^{•+} solution was diluted with absolute ethanol to an absorbance between 0.7-0.8 at 734 nm. The solutions of the essential oils (5 mg/mL), and Trolox (standard, 3.0; 2.0; 1.0; 0.5; 0.25; 0.125 mM) were prepared in MeOH. 10 μL of the sample solution was mixed with 990 μL of ABTS^{•+} solution. 10 μL of MeOH instead of sample or standard mixed with ABTS^{•+} solution was used as control. Gallic acid (0.1 mg/mL)

was used as the positive control. Decrease in the absorbance after 30 minutes of incubation was recorded at 734 nm to get a linear Trolox equation. ABTS^{•+} scavenging activity of the samples was expressed as Trolox equivalent antioxidant capacity and calculated using linear equation obtained for Trolox ($y = 23,224x - 1,7141$, $r^2 = 0.9989$) (Figure 1).

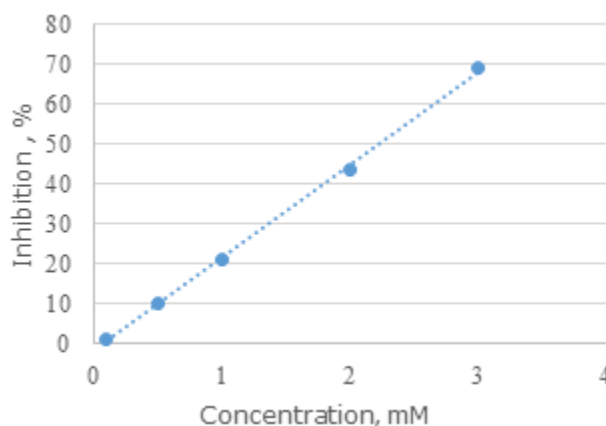


Figure 1. Calibration curve obtained for Trolox.

Statistical Analysis of Data

Data obtained from antioxidant and enzyme inhibition experiments were expressed as mean standard error (\pm SEM). IC_{50} values were estimated using a nonlinear regression algorithm. Data were analyzed using the *SigmaPlot* software (Version 12.0).

RESULTS AND DISCUSSION

In course of our ongoing studies on biodiversity of Turkish essential oil bearing plants, the composition of *Tanacetum praeteritum* ssp. *praeteritum* essential oils (A and B) from two localities and their biological activities were comparatively studied. The oils were hydrodistilled from aerial parts of the plants and phytochemically investigated with GC-FID and GC/MS techniques. The essential oils of *T. praeteritum* ssp. *praeteritum* obtained by hydrodistillation method were yellow with a distinct odor. The oils yields obtained after 3 h were 0.18% and 0.24% (w/w) for the oils A and B, respectively.

GC-FID and GC/MS analyses of the oils A and B resulted with 60 and 53 compounds respectively which belong to monoterpene hydrocarbons, oxygenated monoterpenes, sesquiterpene hydrocarbons, and oxygenated sesquiterpenes. Distribution of the major compound groups detected in the oils A and B of *T. praeteritum* ssp. *praeteritum* is presented on Figure 2. The list of detected compounds with their relative retention indices, relative percentages and method of identification is given in Table 1 in order of their elution on the HP-Innowax FSC column. Gas-chromatographic profiles of *T. praeteritum* ssp. *praeteritum* oils is presented on Figure 3. Gas chromatographic study revealed distinguish difference between the oils A and B. The oils A and

B were characterized by predominance of the oxygenated monoterpenes (79.5% and 95.8%, respectively). However, the main constituents were different. Namely, camphor (37.6%), 1,8-cineole (19.5%) and terpinen-4-ol (9.3%) were found as the major constituents in the oil A, while α -thujone (79.4%) and β -thujone (8.5%) were detected in the oil B. The monoterpene hydrocarbons constituted 17.1% in the oil A with *p*-cymene (8.6%) and camphene (6.2%) as the main representatives. However, the oil B was characterized by scarce amount (2.1%) of this group. The sesquiterpenes were detected in low amounts in both of the oils (1.5% and 0.7%).

Table 1. Chemical compositions of *Tanacetum praeteritum* ssp. *praeteritum* essential oils.

No	RRI ^{a)}	RRI ^{b)}	Compound	% ^{b)}		ID
				A	B	Method
1.	1014	1017(29)	Tricyclene	0.3	-	c),d),e)
2.	1032	1029(29)	α -Pinene	0.6	0.3	c),d),e)
3.	1034	1029(29)	α -Thujene	0.8	0.2	c),d),e)
4.	1076	1074(29)	Camphene	6.2	0.1	c),d),e)
5.	1118	1116(29)	β -Pinene	0.3	0.2	c),d),e)
6.	1132	1132(30)	Sabinene	0.2	0.1	c),d),e)
7.	1174	1161(29)	Myrcene	-	t	c),d),e)
8.	1188	1180(29)	α -Terpinene	-	0.2	c),d),e)
9.	1195	1193(31)	Dehydro-1,8-cineole	0.1	t	c),d),e)
10.	1203	1204(29)	Limonene	-	t	c),d),e)
11.	1213	1211(29)	1,8-Cineole	19.5	4.3	c),d),e)
12.	1244		2-Pentyl furan	t	-	c),d),e)
13.	1255	1255(32)	γ -Terpinene	0.1	0.4	c),d),e)
14.	1280	1280(32)	<i>p</i> -Cymene	8.6	0.5	c),d),e)
15.	1285	1304(33)	Isoamyl isovalerate	t	-	c),d),e)
16.	1290	1290(32)	Terpinolene	t	0.1	c),d),e)
17.	1296	1283(34)	Octanal	t	-	c),d),e)
18.	1437	1428(35)	α -Thujone	-	79.4	c),d),e)
19.	1451	1446(35)	β -Thujone	-	8.5	c),d),e)
20.	1474	1474(32)	<i>trans</i> -Sabinene hydrate	2.4	0.3	c),d),e)
21.	1478		Norbornyl acetate	t	-	d),e)
22.	1482		(<i>Z</i>)-3-Hexenyl-2-methyl butyrate	-	t	d),e)
23.	1532	1532(30)	Camphor	37.6	0.7	c),d),e)
24.	1542	1564(36)	<i>cis</i> -Sabinene hydrate acetate	1.6	-	c),d),e)
25.	1553	1553(30)	Linalool	-	t	c),d),e)
26.	1556	1555(30)	<i>cis</i> -Sabinene hydrate	-	0.2	c),d),e)
27.	1558	1548(36)	Linalyl acetate	-	t	c),d),e)
28.	1568		1-Methyl-4-acetylcyclohex-1-ene*	0.4	0.4	e)

No	RRI ^{a)}	RRI ^{b)}	Compound	% ^{b)}		ID
				A	B	Method
29.	1575	1578(33)	<i>trans-p</i> -Menth-2-en-1-ol	0.9	0.1	c),d),e)
30.	1582	1561(30)	<i>cis</i> -Chrysanthenyl acetate	0.6	-	c),d),e)
31.	1586	1587(37)	Pinocarvone	t	t	c),d),e)
32.	1590	1597(32)	Bornyl acetate	0.1	-	c),d),e)
33.	1611	1611(32)	Terpinen-4-ol	9.3	1.0	c),d),e)
34.	1612	1612(37)	β -Caryophyllene	t	t	c),d),e)
35.	1630		Terpinen-4-yl acetate	0.3	-	d),e)
36.	1640	1645(33)	<i>cis-p</i> -Menth-2-en-1-ol	0.6	-	c),d),e)
37.	1670	1671(33)	<i>trans</i> -Pinocarveol	0.1	-	c),d),e)
38.	1682	1687(33)	δ -Terpineol	0.2	0.1	c),d),e)
39.	1683	1685(30)	<i>trans</i> -Verbenol	-	0.1	c),d),e)
40.	1685	1675(36)	<i>trans</i> -Piperitol	0.3	t	c),d),e)
41.	1694		Drima-7,9(11)-diene	-	0.1	d),e)
42.	1702		Selina-4(14),7-diene	-	t	d),e)
43.	1706	1706(37)	α -Terpineol	1.7	0.5	c),d),e)
44.	1719	1719(37)	Borneol	0.9	0.2	c),d),e)
45.	1720	1720(38)	<i>trans</i> -Sabinol	-	0.3	d),e)
46.	1726	1722(32)	Germacrene D	-	t	c),d),e)
47.	1729	1729(39)	<i>cis</i> -1,2-Epoxy-terpin-4-ol	0.3	-	d),e)
48.	1742	1741(30)	β -Selinene	-	t	c),d),e)
49.	1744	1735(33)	α -Selinene	-	t	c),d),e)
50.	1748	1744(33)	Piperitone	t	-	c),d),e)
51.	1751	1750(33)	Carvone	0.1	-	c),d),e)
52.	1755	1747(33)	Bicyclogermacrene	-	0.1	c),d),e)
53.	1758	1757(33)	<i>cis</i> -Piperitol	0.3	t	c),d),e)
54.	1764	1764(40)	<i>cis</i> -Chrysanthenol	1.7	-	c),d),e)
55.	1782	1772(41)	<i>cis</i> -Carvyl acetate	0.1	-	c),d),e)
56.	1802	1800(33)	Cumin aldehyde	0.1	-	c),d),e)
57.	1804	1807(33)	Myrtenol	t	-	c),d),e)
58.	1805	1793(40)	α -Campholene alcohol	t	t	c),d),e)
59.	1845	1845(30)	<i>trans</i> -Carveol	0.1	-	c),d),e)
60.	1864	1856(30)	<i>p</i> -Cymen-8-ol	0.2	-	c),d),e)
61.	1882	1880(37)	<i>cis</i> -Carveol	0.3	-	c),d),e)
62.	1969	1959(30)	<i>cis</i> -Jasmone	-	t	d),e)
63.	1985	1965(42)	2-Phenylethyl-2-methylbutyrate	-	t	c),d),e)
64.	2008	2008(32)	Caryophyllene oxide	0.2	0.2	c),d),e)
65.	2037	2037(32)	Salvial-4(14)-en-1-one	t	-	c),d),e)
66.	2050	2042(43)	(<i>E</i>)-Nerolidol	0.3	-	c),d),e)
67.	2056		13-Tetradecanolide	0.1	t	d),e)

No	RRI ^{a)}	RRI ^{b)}	Compound	% ^{b)}		ID
				A	B	Method
68.	2063	2041(44)	<i>p</i> -Mentha-1,4-dien-7-ol	-	t	d),e)
69.	2084	2084(45)	Octanoic acid	t	-	c),d),e)
70.	2113	2114(46)	Cumin alcohol	t	t	c),d),e)
71.	2144	2136(33)	Spathulenol	0.5	0.3	c),d),e)
72.	2184	2184(47)	<i>cis-p</i> -Menth-3-en-1,2-diol	0.1	-	c),d),e)
73.	2192	2173(48)	Nonanoic acid	0.1	-	c),d),e)
74.	2198	2187(35)	Thymol	0.1	-	c),d),e)
75.	2232	2236(37)	α -Bisabolol	t	t	c),d),e)
76.	2239	2239(37)	Carvacrol	-	0.1	c),d),e)
77.	2247	2247(32)	<i>trans</i> - α -Bergamotol	-	t	c),d),e)
78.	2260	2260(40)	15-Hexadecanolide	0.3	0.2	d),e)
79.	2273	2273(49)	Selin-11-en-4 α -ol	0.3	-	c),d),e)
80.	2324	2324(50)	Caryophylla-2(12),6(13)-dien-5 α -ol	0.1	-	c),d),e)
81.	2365	2349(51)	(<i>Z</i>)-Methyl jasmonate	t	t	c),d),e)
82.	2931	2931(32)	Hexadecanoic acid	t	t	c),d),e)
Total				99.0	99.2	

^{a)} Relative Retention Indices calculated against *n*-alkanes (C₈-C₄₀) on HP-Innowax column; ^{b)}% calculated from FID data; ^{c)} Identification based on retention index of genuine compounds on the HP-Innowax column; ^{d)} Identification on the basis of computer matching of the mass spectra from Başer; ^{e)} Tentative identified on the basis of computer matching of the mass spectra from Adams, MassFinder, Wiley, and NIST libraries; t Trace (< 0.1%).

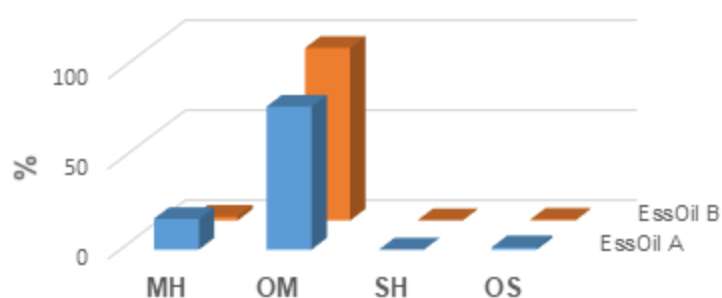


Figure 2. Distribution of the major compound groups in the oils A and B of *Tanacetum praeteritum* ssp. *praeteritum*. MH, monoterpene hydrocarbons; OM, oxygenated monoterpenes; SH, sesquiterpene hydrocarbons; OS, oxygenated sesquiterpenes.

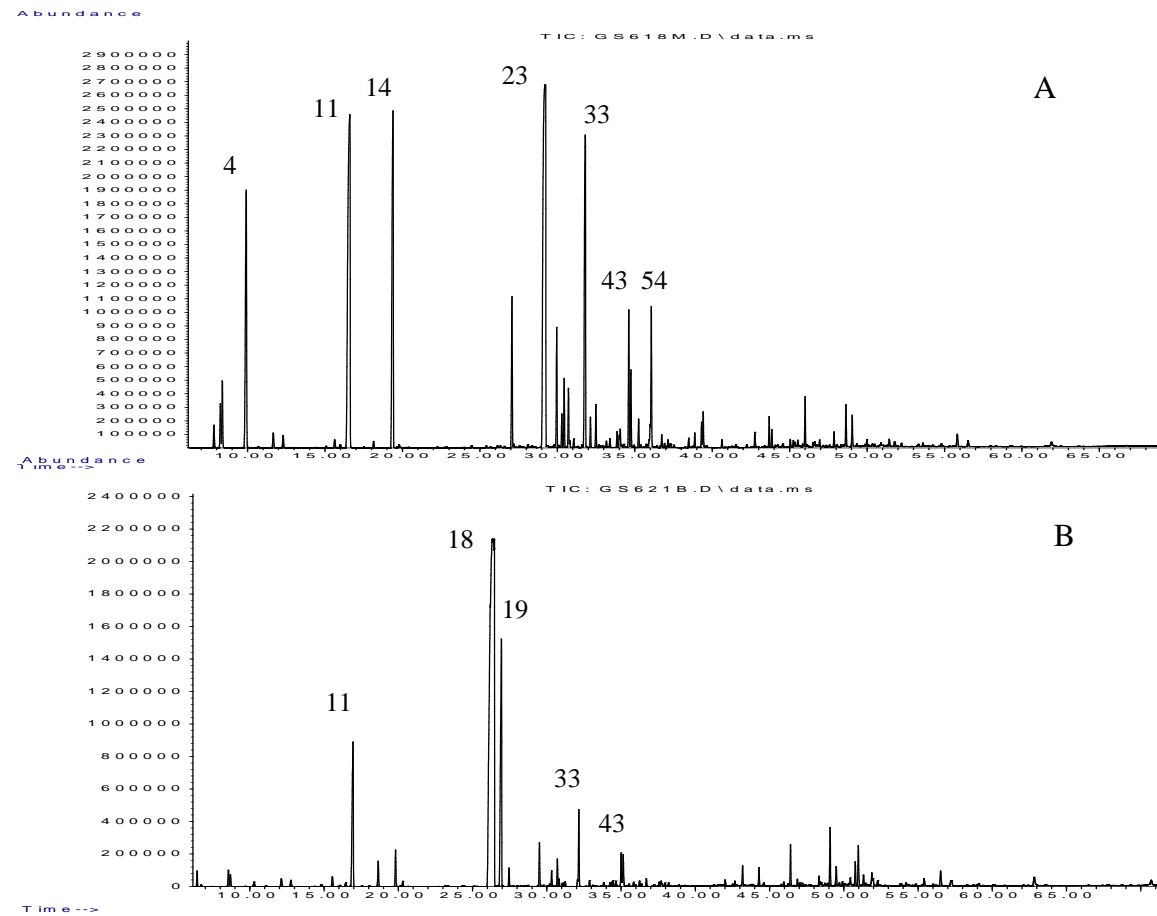


Figure 3. Chromatographic profile of the essential oils (A) and (B) of *Tanacetum praeteritum* ssp. *praeteritum*. Numeration of the peaks is depicted according to the list (Table 1) of detected compounds.

Results of the gas-chromatographic analyses of *T. praeteritum* ssp. *praeteritum* oils were compared with previously reported for this species actually and for *Tanacetum* species in general. Earlier, two subspecies, *T. praeteritum* ssp. *praeteritum* and *T. praeteritum* (Horwood) Heywood ssp. *massicyticum* Heywood collected in Muğla and Antalya provinces, respectively, have been investigated for the oils' chemical profiles. Noteworthy differences on the major compounds of the oils were detected. Namely, borneol (28.1%), 1,8-cineole (12.3%), bornyl acetate (10.0%), terpinen-4-ol (7.1%), β -pinene (5.7%) were reported for *T. praeteritum* ssp. *praeteritum*. The oil of *T. praeteritum* ssp. *massicyticum* was characterized with 1,8-cineole (4.0%), α - and β -thujone (51.1% and 10.0%, respectively) (19). It seems to be that the oils A and B investigated in the present work have different compositions than the previously reported ones. Borneol and bornyl acetate were detected in our samples in very scarce amounts. In our work, high abundance of camphor (>37%) was detected, while scarce amount of camphor was detected by Gönen et al. (19).

Although, oxygenated monoterpenes as major constituents have earlier been detected in different representatives of *Tanacetum* genus. The literature search revealed that α -thujone was found to be the major constituent in *T. argyrophyllum* var. *argyrophyllum* leaf (52%) and flower (63%) oils; in *T. argenteum* subsp. *canum* var. *canum* (12%) and *T. praeteritum* subsp. *massicyticum* (51%) oils (19). Table 2 summarizes *Tanacetum* species in which similar major constituents have earlier been detected. As can be seen from Table 2, the oxygenated monoterpenes such as camphor, 1,8-cineole, α - and β -thujone and borneol belong to common volatile constituents detected in *Tanacetum* oils.

Table 2. *Tanacetum* species with oxygenated monoterpenes as major volatile constituents (literature survey).

Tanacetum species	Main compounds (%)	Ref.
<i>T. argyrophyllum</i> (C. Koch) Tvel. var. <i>argyrophyllum</i> (C. Koch) Tvel.	Camphor (26.6-29.7), 1,8-cineole (8.4-17.5), borneol (12.0-15.0)	(52)
	α -Thujone (52.0, 69.0)	(19, 53)
<i>T. balsamita</i> L. subsp. <i>balsamita</i> L.	β -Thujone (20.8)	(54)
<i>T. chiliophyllum</i> (Fisch. Et Mey.) Schultz Bip. var. <i>chiliophyllum</i> (Fisch. Et Mey.) Schultz	Camphor (19.7), 1,8-cineole (16.6), borneol (15.4)	(55)
<i>T. chiliophyllum</i> (Fisch. et Mey.) Schultz Bip. var. <i>monocephalum</i> Grierson	Camphor (17.0)	(56)
<i>T. chiliophyllum</i> (Fisch. et Mey.) Schultz Bip. var. <i>monocephalum</i> Grierson	1,8-Cineole (8.3), camphor (17.3)	(57)
<i>T. densum</i> (Lab.) Schultz Bip. subsp. <i>eginense</i> Heywood	Camphor (25.7-30.9)	(58)
<i>T. densum</i> (Lab.) Schultz Bip. subsp. <i>sivasicum</i> Hub.-Mor. et Grierson	1,8-Cineole (21.1, 28.3), camphor (19.2, 16.4), borneol (5.8, 6.4)	(59)
<i>T. mucroniferum</i> Hub. – Mor. et Grierson	1,8-Cineole (21.9), camphor (6.4)	(60)
<i>T. parthenium</i> (L.) Schultz Bip. varieties	Camphor (28-61)	(53, 61, 62)
<i>T. tabrisianum</i> (Boiss.) Sosn. et Takht	1,8-Cineole (17.6, 22.5)	(63)
<i>T. vulgare</i> L.	1,8-Cineole (10.8), camphor (30.5), borneol (14.8)	(9)

Biological activities of the oils

In the present work we evaluated the biological properties of *T. praeteritum* subsp. *praeteritum* essential oils, including antioxidant, antineurodegenerative, and antidiabetic effects *in vitro* using microplate titer assays. Antioxidant activity assessments were performed *in vitro* by using non-enzymatic systems employing different model substrates: Stable free radical DPPH[•] and cation radical ABTS^{•+}. Our results for antioxidant activities showed that the *T. praeteritum* subsp. *praeteritum* essential oils A and B had moderate (0.23 mM and 0.15 mM, respectively) Trolox equivalent antioxidant capacities. The oils demonstrated weak (3% and 8% inhibition) scavenging activities towards DPPH free radicals (Table 3).

Evaluation of *T. praeteritum* subsp. *praeteritum* oils for anti-neurodegenerative activity *via* inhibition of acetylcholinesterase revealed that the oil A showed higher inhibitory effect with an IC₅₀ of 0.74 mg/mL than the oil B (IC₅₀ of 1.78 mg/mL). Anti-cholinesterase effects

of 1,8-cineole, camphor and terpinen-4-ol which were the main constituents of the oil A have earlier been reported in a number of papers (34, 64-66).

A previous literature search revealed information about antidiabetic and enzyme inhibition properties of thujone (6, 67, 68). The use of thujone for the treatment of diabetes mellitus has recently been suggested by Baddar (6). Moreover, it was reported that the application of thujone appeared to have an effect similar to metformin; four-weeks treatment with thujone produced a pronounced hypoglycemic effect in alloxan diabetic rats (69). This information led us to the empirical search of the *T. praeteritum* subsp. *praeteritum* oils A and B to find additional therapeutic resources for diabetes treatment. The oils of *T. praeteritum* subsp. *praeteritum* were *in vitro* evaluated for hypoglycemic activity via inhibition of the porcine pancreatic α -amylase. So, previous testing showed that both the oils have noteworthy inhibitory activity (> 80%). Further serial dilution on microtiter plate allowed us to detect an IC_{50} values of the oils. As can be seen in Table 3, the oil B demonstrated higher inhibitory activity (IC_{50} of 0.89 ± 0.13 mg/mL) than the oil A (IC_{50} of 1.02 ± 0.24).

Table 3. Biological activities of *Tanacetum praeteritum* subsp. *praeteritum* essential oils.

Test sample	Antioxidant activity		Enzyme Inhibition	
	DPPH, Inh%	TEAC, mM \pm SED	AChE, $IC_{50} \pm$ SED	α -Amylase, $IC_{50} \pm$ SED
Essential oil A	8	0.23 \pm 0.008	0.74 \pm 0.07	1.02 \pm 0.24
Essential oil B	3	0.152 \pm 0.035	1.78 \pm 0.16	0.89 \pm 0.13
Gallic acid	85	2.4	-	-
Galanthamine	-	-	0.01	-
Acarbose	-	-	-	0.08

CONCLUSION

Analysis of the chemical composition of *T. praeteritum* subsp. *praeteritum* essential oils demonstrated that they were mainly comprised of oxygenated monoterpenes such as camphor, borneol, 1,8-cineole, α - and β -thujone. In the present study, the essential oils were found to provide promising and effective alternative in the field of antineurodegenerative and antidiabetic applications. The oils demonstrated significant inhibitory potential on acetylcholinesterase and α -amylase enzymes, which involved into Alzheimer's disease and carbohydrate metabolism disorders. Finally, the essential oils inhibited ABTS cation radicals.

ACKNOWLEDGMENTS

The author is grateful to Dr. M. Arslan for help with collection and botanical identification of the plant material and to Biol. S. Yur for assistance in biological activity experiments.

REFERENCES

1. Grierson AJC. *Tanacetum* L. (emend. Briq.). In: Davis PH, editor. Flora of Turkey and The East Aegean Islands. 5. Edinburgh: Edinburgh University Press; 1975. p. 256-92
2. Bączek KB, Kosakowska O, Przybył JL, Pióro-Jabrucka E, Costa R, Mondello L, et al. Antibacterial and antioxidant activity of essential oils and extracts from costmary (*Tanacetum balsamita* L.) and tansy (*Tanacetum vulgare* L.). Ind. Crops Prod. 2017;102:154-63.
3. Godinho LS, Aleixo de Carvalho LS, Barbosa de Castro CC, Dias MM, Pinto PdF, Crotti AEM, et al. Anthelmintic activity of crude extract and essential oil of *Tanacetum vulgare* (Asteraceae) against adult worms of *Schistosoma mansoni*. Scientific World J. 2014;2014.
4. Haider SZ, Mohan M, Pandey AK, Singh P. Use of *Tanacetum tomentosum* and *Ta. dolichophyllum* essential oils as botanical repellents and insecticidal agents against storage pest *Tribolium castaneum* (Coleoptera: Tenebrionidae). Entomol. Res. 2017;47(5):318-27.
5. Polatoğlu K, Servi H, Yücel YY, Nalbantsoy A. Cytotoxicity and acetylcholinesterase inhibitory and PRAP activities of the essential oils of selected *Tanacetum* L. species. Nat. Volatiles Essent. Oils. 2015;2(4):11-6.
6. Baddar NWA-H, Aburjai TA, Taha MO, Disi AM. Thujone corrects cholesterol and triglyceride profiles in diabetic rat model. Nat. Prod. Res. 2011;25(12):1180-4.
7. de Almeida LMS, Carvalho LSAd, Gazolla MC, Silva Pinto PL, Silva MPNd, de Moraes J, et al. Flavonoids and sesquiterpene lactones from *Artemisia absinthium* and *Tanacetum parthenium* against *Schistosoma mansoni* worms. Evidence-Based Comp. Alterna. Medicine. 2016;2016:1-9.
8. Pålsson K, Jaenson TG, Bäckström P, Borg-Karlson A-K. Tick repellent substances in the essential oil of *Tanacetum vulgare*. J. Med. Entomol. 2008;45(1):88-93.
9. Coté H, Boucher M-A, Pichette A, Legault J. Anti-inflammatory, antioxidant, antibiotic, and cytotoxic activities of *Tanacetum vulgare* L. essential oil and its constituents. Medicines. 2017;4(2):34.
10. Ozbilgin S, Akkol EK, Ergene Oz B, Ilhan M, Saltan G, Bahadir Acikara O, et al. In vivo activity assessment of some *Tanacetum* species used as traditional wound healer along with identification of the phytochemical profile by a new validated HPLC method. Ir. J. Basic Med. Sci. 2018;21(2):145-52.
11. Adekenov S. Sesquiterpene lactones with unusual structure. Their biogenesis and biological activity. Fitoterapia. 2017;121:16-30.
12. Carochio M, Ferreira IC. A review on antioxidants, prooxidants and related controversy: natural and synthetic compounds, screening and analysis methodologies and future perspectives. Food Chem. Toxicol. 2013;51:15-25.
13. Pope C, Karanth S, Liu J. Pharmacology and toxicology of cholinesterase inhibitors: uses and misuses of a common mechanism of action. Environment. Tox. Pharmacol. 2005;19(3):433-46.

14. Pan H-J, Lin Y, Chen YE, Vance DE, Leiter EH. Adverse hepatic and cardiac responses to rosiglitazone in a new mouse model of type 2 diabetes: Relation to dysregulated phosphatidylcholine metabolism. *Vasc. Pharmacol.* 2006;45(1):65-71.
15. White JA, Hirsch IB. Nonhypoglycemic drug reactions of agents used to treat diabetes. *Endocrin. Metabol. Clinics North Am.* 2000;29(4):803-11.
16. Gören N. Flavonoids of *Tanacetum praeteritum* subsp. *praeteritum*. *Journal of Faculty Pharmacy of Istanbul University.* 1994;30:25-30.
17. Gören N. Sesquiterpene lactones from *Tanacetum praeteritum*. *Phytochemistry.* 1995;38(5):1261-4.
18. Gören N. Eudesmane-type sesquiterpenes from *Tanacetum praeteritum* subsp. *praeteritum*. *Phytochemistry.* 1996;42(3):747-9.
19. Gören N, Demirci B, Başer KHC. Composition of the essential oils of *Tanacetum* spp. from Turkey. *Flavour and Fragrance Journal.* 2001;16(3):191-4.
20. EDQM. Determination of Essential Oils in Herbal Drugs 9th ed. Europe Co, editor. Strasbourg: European Directorate for the Quality of Medicines and Healthcare; 2017. 285-6 p.
21. Özek G, Ishmuratova M, Tabanca N, Radwan MM, Göger F, Özek T, et al. One-step multiple component isolation from the oil of *Crinitaria tatarica* (Less.) Sojak by preparative capillary gas chromatography with characterization by spectroscopic and spectrometric techniques and evaluation of biological activity. *J. Sep. Sci.* 2012;35(5-6):650-60.
22. Joulain D, König WA, Hochmuth DH. Library of MassFinder-4. In: Hochmuth DH, editor. *Terpenoids and Related Constituents of Essential oils.* Hamburg, Germany: Hochmuth Scientific Consulting; 2001.
23. Adams RP. Identification of Essential Oil Components by Gas Chromatography / Mass Spectrometry. 4th ed. Adams RP, editor: Allured Pub. Corp.; 2007. 804 p.
24. Baser KHC, Demirci F. Flavours and Fragrances. Chemistry of Essential Oils. In: Berger RG, editor. *Flavours and Fragrances: Chemistry, Bioprocessing and Sustainability.* Springer-Verlag Berlin Heidelberg; 2007. p. 648.
25. Ellman GL, Courtney KD, Andres V, Featherstone RM. A new and rapid colorimetric determination of acetylcholinesterase activity. *Biochem. Pharmacol.* 1961;7(2):881N191-9095.
26. Yang XW, Huang MZ, Jin YS, Sun LN, Song Y, Chen HS. Phenolics from *Bidens bipinnata* and their amylase inhibitory properties. *Fitoterapia.* 2012;83(7):1169-75.
27. Brand-Williams W, Cuvelier ME, Berset CLWT. Use of a free radical method to evaluate antioxidant activity. *LWT-Food Sci. Technol.* 1995;28(1):25-30.
28. Re R, Pellegrini N, Proteggente A, Pannala A, Yang M, Rice-Evans C. Antioxidant activity applying an improved ABTS radical cation decolorization assay. *Free Rad. Biol. Med.* 1999;26(9):1231-7.
29. Orav A. Identification of terpenes by gas chromatography-mass spectrometry. In: Niessen WMA, editor. *Current Practice of Gas-Chromatography Mass-Spectrometry Chromatographic Science Series.* 86. Basel, Switzerland: Marcel Dekker AG; 2001. p. 483-94.
30. Maggio A, Rosselli S, Bruno M, Spadaro V, Raimondo FM, Senatore F. Chemical composition of essential oil from Italian populations of *Artemisia alba* Turra (Asteraceae). *Molecules.* 2012;17(9):10232-41.
31. Cha J-D, Jeong M-R, Jeong S-I, Moon S-E, Kim J-Y, Kil B-S, et al. Chemical composition and antimicrobial activity of the essential oils of *Artemisia scoparia* and *A. capillaris*. *Planta Med.* 2005;71(02):186-90.

32. Noorizadeh H, Farmany A, Noorizadeh M. Application of GA-PLS and GA-KPLS calculations for the prediction of the retention indices of essential oils. *Química Nova*. 2011;34(8):1398-404.
33. Bignell C, Dunlop P, Brophy J. Volatile leaf oils of some south-western and southern Australian species of the genus *Eucalyptus* (series 1). Part XIX. *Flavour Fragr. J.* 1998;13(2):131-9.
34. López MD, Campoy FJ, Pascual-Villalobos MJ, Muñoz-Delgado E, Vidal CJ. Acetylcholinesterase activity of electric eel is increased or decreased by selected monoterpenoids and phenylpropanoids in a concentration-dependent manner. *Chem. Biol. Interact.* 2015;229:36-43.
35. Bader A, Panizzi L, Cioni PL, Flamini G. *Achillea ligustica*: composition and antimicrobial activity of essential oils from the leaves, flowers and some pure constituents. *Central Eur. J. Biol.* 2007;2(2):206-12.
36. Chéraif I, Jannet HB, Hammami M, Khouja M, Mighri Z. Chemical composition and antimicrobial activity of essential oils of *Cupressus arizonica* Greene. *Biochem. Syst. Ecol.* 2007;35(12):813-20.
37. Noorizadeh H, Farmany A. Exploration of linear and nonlinear modeling techniques to predict of retention index of essential oils. *J. Chinese Chem. Soc.* 2010;57(6):1268-77.
38. Tan N, Yazici-Tutunis S, Yesil Y, Demirci B, Tan E. Antibacterial activities and composition of the essential oils of *Salvia sericeo-tomentosa* varieties. *Rec. Nat. Prod.* 2017;11:456-61.
39. Baser K, Demirci B, Ozek T, Viljoen A, Victor J. Composition of the essential oils of five *Coleonema* species from South Africa. *J. Essent. Oil Res.* 2006;18:26-9.
40. Demirci F, Demirci B, Gürbüz I, Yesilada E, Baser KHC. Characterization and biological activity of *Achillea teretifolia* Willd. and *A. nobilis* L. subsp. *neilreichii* (Kerner) Formanek essential oils. *Turk. J. Biol.* 2009;33(2):129-36.
41. Arze JBL, Collin G, Garneau F-X, Jean F-I, Gagnon H. Essential Oils from Bolivia. VI. Lamiaceae: *Lepechinia graveolens* (Reg.) Epling *L. floribunda* (Benth.) Epling, and *L. meyeri* (Walp.) Epling. *J. Essent. Oil Res.* 2009;21(1):36-40.
42. Nam AM, Tomi F, Gibernau M, Casanova J, Bighelli A. Composition and chemical variability of the needle oil from *Pinus halepensis* growing in Corsica. *Chem. Biodivers.* 2016;13(4):380-6.
43. Lopes-Lutz D, Alviano DS, Alviano CS, Kolodziejczyk PP. Screening of chemical composition, antimicrobial and antioxidant activities of Artemisia essential oils. *Phytochemistry*. 2008;69(8):1732-8.
44. Collin G. Aromas from Quebec. IV. Chemical composition of the essential oil of *Ledum groenlandicum*: A review. *Am. J. Essent. Oils Nat. Prod.* 2015;2(3):06-11.
45. Fang Y, Qian M. Aroma compounds in Oregon Pinot Noir wine determined by aroma extract dilution analysis (AEDA). *Flavour Fragr. J.* 2005;20(1):22-9.
46. Kurose K, Okamura D, Yatagai M. Composition of the essential oils from the leaves of nine Pinus species and the cones of three of Pinus species. *Flavour Fragr. J.* 2007;22(1):10-20.
47. Tabanca N, Avonto C, Wang M, Parcher JF, Ali A, Demirci B, et al. Comparative investigation of *Umbellularia californica* and *Laurus nobilis* leaf essential oils and identification of constituents active against *Aedes aegypti*. *J. Agric. Food Chem.* 2013;61(50):12283-91.
48. Perry PL, Wang Y, Lin J. Analysis of honeydew melon (*Cucumis melo* var. *inodorus*) flavour and GC-MS/MS identification of (E, Z)-2, 6-nonadienyl acetate. *Flavour Fragr. J.* 2009;24(6):341-7.

49. Baser KHC, Demirci B, Iscan G, Hashimoto T, Demirci F, Noma Y, et al. The essential oil constituents and antimicrobial activity of *Anthemis aciphylla* Boiss. var. *discoidea* Boiss. Chem. Pharm. Bull. 2006;54(2):222-5.
50. Öztürk B, Özek G, Özek T, Baser KHC. Chemical diversity in volatiles of *Helichrysum plicatum* DC. subspecies in Turkey. Rec. Nat. Prod. 2014;8(4):373.
51. Bousbia N, Vian MA, Ferhat MA, Petitcolas E, Meklati BY, Chemat F. Comparison of two isolation methods for essential oil from rosemary leaves: Hydrodistillation and microwave hydrodiffusion and gravity. Food Chem. 2009;114(1):355-62.
52. Polatoglu K, Demirci F, Demirci B, Gören N, Baser KHC. Antimicrobial activity and essential oil composition of a new *T. argyrophyllum* (C. Koch) Tvetz var. *argyrophyllum* chemotype. J. Oleo Sci. 2010;59(6):307-13.
53. Akpulat HA, Tepe B, Sokmen A, Daferera D, Polissiou M. Composition of the essential oils of *Tanacetum argyrophyllum* (C. Koch) Tvetz var. *argyrophyllum* and *Tanacetum parthenium* (L.) Schultz Bip. (Asteraceae) from Turkey. Biochem. Syst. Ecol. 2005;33(5):511-6.
54. Yousefzadi M, Ebrahimi SN, Sonboli A, Miraghasi F, Ghiasi S, Arman M, et al. Cytotoxicity, antimicrobial activity and composition of essential oil from *Tanacetum balsamita* L. subsp. *balsamita*. Nat. Prod. Comm. 2009;4(1):119-22.
55. Salamci E, Kordali S, Kotan R, Cakir A, Kaya Y. Chemical compositions, antimicrobial and herbicidal effects of essential oils isolated from Turkish *Tanacetum aucheranum* and *Tanacetum chiliophyllum* var. *chiliophyllum*. Biochem. Syst. Ecol. 2007;35(9):569-81.
56. Başer K, Demirci B, Tabanca N, Özek T, Gören N. Composition of the essential oils of *Tanacetum armenum* (DC.) Schultz Bip., *T. balsamita* L., *T. chiliophyllum* (Fisch. & Mey.) Schultz Bip. var. *chiliophyllum* and *T. haradjani* (Rech. fil.) Grierson and the enantiomeric distribution of camphor and carvone. Flavour Fragr. J. 2001;16(3):195-200.
57. Polatoğlu K, Demirci B, Demirci F, Gören N, Başer KHC. Biological activity and essential oil composition of two new *Tanacetum chiliophyllum* (Fisch. & Mey.) Schultz Bip. var. *chiliophyllum* chemotypes from Turkey. Ind. Crops Prod. 2012;39:97-105.
58. Polatoglu K, Demirci B, Demirci F, Gören N, Baser KHC. The essential oil composition of *Tanacetum densum* (Labill.) Heywood ssp. *eginense* Heywood from Turkey. Rec. Nat. Prod. 2012;6(4):402.
59. Polatoğlu K, Gören N, Başer KHC, Demirci B. The essential oil composition of *Tanacetum densum* (Labill.) Heywood ssp. *sivasicum* Hub.-Mor. & Grierson from Turkey. J. Essent. Oil Res. 2009;21(3):200-2.
60. Polatoglu K, Sen A, Kandemir A, Gören N. Essential oil composition and DPPH scavenging activity of endemic *Tanacetum mucroniferum* Hub.-Mor. & Grierson from Turkey. J. Essent. Oil Bearing Plants. 2012;15(1):66-74.
61. Hendriks H, Bos R, Woerdenbag H. The Essential Oil of *Tanacetum parthenium* (L.) Schultz-Bip. Flavour Fragr. J. 1996;11(6):367-71.
62. Polatoglu K, Demirci F, Demirci B, Gören N, Baser KHC. Antibacterial activity and the variation of *Tanacetum parthenium* (L.) Schultz Bip. essential oils from Turkey. J. Oleo Sci. 2010;59(4):177-84.
63. Polatoğlu K, Demirci B, Gören N, Başer KHC. Essential oil composition of endemic *Tanacetum zahlbruckneri* (Náb.) and *Tanacetum tabrisianum* (Boiss.) Sosn. and Takht. from Turkey. Nat. Prod. Res. 2011;25(6):576-84.
64. Dohi S, Terasaki M, Makino M. Acetylcholinesterase inhibitory activity and chemical composition of commercial essential oils. J Agric Food Chem. 2009;57(10):4313-8.
65. Kaufmann D, Dogra AK, Wink M. Myrtenal inhibits acetylcholinesterase, a known Alzheimer target. J Pharm Pharmacol. 2011;63(10):1368-71.

66. Awasthi M, Upadhyay AK, Singh S, Pandey VP, Dwivedi UN. Terpenoids as promising therapeutic molecules against Alzheimer's disease: amyloid beta- and acetylcholinesterase-directed pharmacokinetic and molecular docking analyses. *Molecular Simulation*. 2017;1-11.
67. Daradka HM, Abas MM, Mohammad MA, Jaffar MM. Antidiabetic effect of *Artemisia absinthium* extracts on alloxan-induced diabetic rats. *Comparative Clinical Pathology*. 2014;23(6):1733-42.
68. Lachenmeier DW, Walch SG. The choice of thujone as drug for diabetes: Reply to: Al-Haj Baddar et al. (2011). *Natural Product Research*. 2011;25(20):1890-2.
69. Al-Omari SM. The effect of thujone and myrcene on diabetes mellitus in albino rats. Faculty of Graduate Studies University of Jordan. 2007; Master's Degree of Science in Biological Sciences.



Sesquiterpene Lactones and Other Constituents from The Aerial Parts of *Tanacetum Abrotonifolium* Druce, Collected in East Turkey

Zerrin ZERENLER ÇALIŞKAN¹  , Nezhun GÖREN¹  

¹ Yıldız Technical University, Faculty of Science and Arts, Department of Molecular Biology and Genetics, Davutpaşa Campus, Davutpaşa str. No:127, Esenler 34210, İstanbul-TURKEY

Abstract: In these notable study successful by chemical composition of the aerial parts of *Tanacetum abrotonifolium* Druce, collected in eastern region of Anatolia in Turkey and was study for the first time. Eight known sesquiterpene lactones, namely tanachin (**1**), tavulin (**2**), tamirin (**3**), spiciformin (**4**), isospiciformin (**5**), 1 β -hydroxy-6 α -angeloxy-oxygermacra-4(5),10(14),11(13)-trien-8,12-olide (**6**), dentatin A (**7**), 1- β -hydroxy-6 α -angeloyloxyeudesm-4(15), 11(13)-dien-8,12-olide (**8**) as well as α -amyrin (**9**) and β -sitosterol (**10**) were isolated by using ethyl acetate and MeOH extracts from the aerial parts of *Tanacetum abrotonifolium* Druce. The structures were isolated and identified by comparing their physical and spectroscopic data with those given in the literature.

Keywords: *Tanacetum abrotonifolium*, Asteraceae, Compositae, sesquiterpene lactones, eudesmanolides

Submitted: November 16, 2017. **Accepted:** March 09, 2018.

Cite this: Zerenler Çalışkan Z, Gören N. Sesquiterpene Lactones and Other Constituents from The Aerial Parts of *Tanacetum Abrotonifolium* Druce, Collected in East Turkey. JOTCSA. 2018;5(2):511–20.

DOI: <http://dx.doi.org/10.18596/jotcsa.354568>.

*Corresponding author. Zerrin Zerenler Çalışkan. E-mail: zcalis@yildiz.edu.tr

INTRODUCTION

The genus *Tanacetum* is distributed in Europe and in Western part of Asia throughout the northern temperate regions. *Tanacetum* genus has about 200 (1, 2) species and is represented by 44 species altogether 59 taxa in Turkey, 17 of them being endemic (3). Since some *Tanacetum* species which belong to the family of Asteraceae have been used as folk remedies for centuries in all over the world, it seemed to be important to investigate the genus being one of the richest genera in the flora of Turkey (4). Although many species of the genus *Tanacetum*, such as *T. annuum*, *T. balsamita*, *T. indicum*, *T. nubigenum*, *T. santolinoides*, *T. microphyllum*, *T. artemisioides*, *T. vulgare* and *T. parthenium* are used therapeutically around the world the last two are the most studied and the best characterized (5-8).

Tanacetum abrotanifolium Druce. (Asteraceae) is a tall (60–100 cm), perennial herb that finds a natural habitat on rocky slopes or in Quercus woods at 1630–2300 m altitude. This species intrinsically grows in eastern and northeastern Asia Minor (1).

Previous investigations on the essential oils of *T. abrotanifolium* were documented comprehensively in the literature (9, 10). Aerial part of *T. abrotanifolium* was also documented in the literature for biological activity tests (11). Flavonoids and essential oils are also pointed out as active substance in *T. abrotanifolium* (9, 10).

However, to the best of our knowledge, there is no report on constituents of the aerial parts of *T. abrotanifolium*. In the course of our studies on *Tanacetum* species growing in Turkey, we investigated the chemical composition of *Tanacetum abrotanifolium* which afforded eight sesquiterpene lactones as well as α -amyrin and β -sitosterol.

MATERIAL AND METHODS

General

CC was carried out on Kieselgel 60 (0.063-0.200 mm, Merck), TLC was performed on precoated silica gel 60 F₂₅₄, 0.2 mm plates (Merck), spots were detected under UV light and spraying acidified ceric sulfate followed by heating. FTIR spectra were recorded on a Mattson 1000 on NaCl cells at Yıldız Technical University; ¹H NMR spectra were recorded at 400 MHz on a Bruker-Spectrospin Avance DPx400 Ultrashield NMR instrument at Middle East Technical University (Ankara).

List of abbreviations: Thin Layer Chromatography (TLC); Ultraviolet (UV); Fourier-transform infrared spectroscopy (FTIR); Nuclear magnetic resonance spectroscopy (NMR); Column Chromatography (CC).

Plant Material

T. abrotanifolium was collected from Muradiye – Van at 2494 m altitude in its flowering period. Voucher specimen has been deposited in the Herbarium of the Faculty of Pharmacy, Istanbul University, Turkey (Voucher no. ISTE 83755). Plant materials were identified by Dr.Kerim Alpinar.

Extraction and Isolation

The extraction of 2800 gr dried and powdered aerial parts of *T. abrotanifolium* collected from Muradiye – Van at 2494 m altitude in its flowering period. Voucher specimen has been deposited in the Herbarium of the Faculty of Pharmacy, Istanbul University, Turkey (Voucher no. ISTE 83755). Plant materials were identified by Dr.Kerim Alpinar. 2800 g of viscous mass which subjected to column chromatography on silica gel with n-hexane, ethyl acetate, and MeOH. The ethyl acetate and MeOH extracts (93.80 g) were combined and treated with MeOH in order to remove the long-chain saturated hydrocarbons.

The residue was applied on a silica gel column to afford 8 fractions and eluted successively with the following solvent systems in increasing polarity: Fraction 1) n-hexane (1500 mL), Fraction 2) dichloromethane-hexane (750:750 mL), Fraction 3) dichloromethane (1500 mL), Fraction 4) dichloromethane-ethyl acetate (750:750 mL), Fraction 5) ethyl acetate (1500 mL), Fraction 6) ethyl acetate-methanol (750:750 mL), 77) methanol (1500 mL) and 8) methanol-dist. H₂O (750-750 mL).

The fractions from CC were controlled by TLC and similar fractions were combined and further separated on silica gel columns and by prep. TLC. Thus Fraction 2 by elution with dichloromethane-hexane (%50:% 50) yielded 1 β -hydroxy-6 α -angeloxy-oxylgermacra-4(5),10(14),11(13)-trien-8,12-olide (**6**) (3 mg), dentatin A (**7**) (27.10 mg), 1- β -hydroxy-6 α -angeloyloxyeudesm-4(15), 11(13)-dien-8,12-olide (**8**) (4.50 mg). Fraction 3 gave α -amyrin (**9**) (50.80 mg) by column chromatography on silica gel using % 100 dichloromethane; Fraction 4 by elution with by CC on silica gel using dichloromethane-ethyl acetate (%50:%50) yielded β -sitosterol (**10**) (383.20 mg) ; Fraction 5 gave tanachin (**1**) (359.52 mg) and tavulin (**2**) (301.32 mg) by column chromatography on silica gel using % 100 ethyl acetate, Finally from the fraction 6 that was submitted to CC with ethyl acetate-methanol (%50:%50 mL) tamirin (**3**) (14 mg), spiciformin (**4**) (355.61 mg), isospiciformin (**5**) (449.88 mg) was obtained. (Fig. 1).

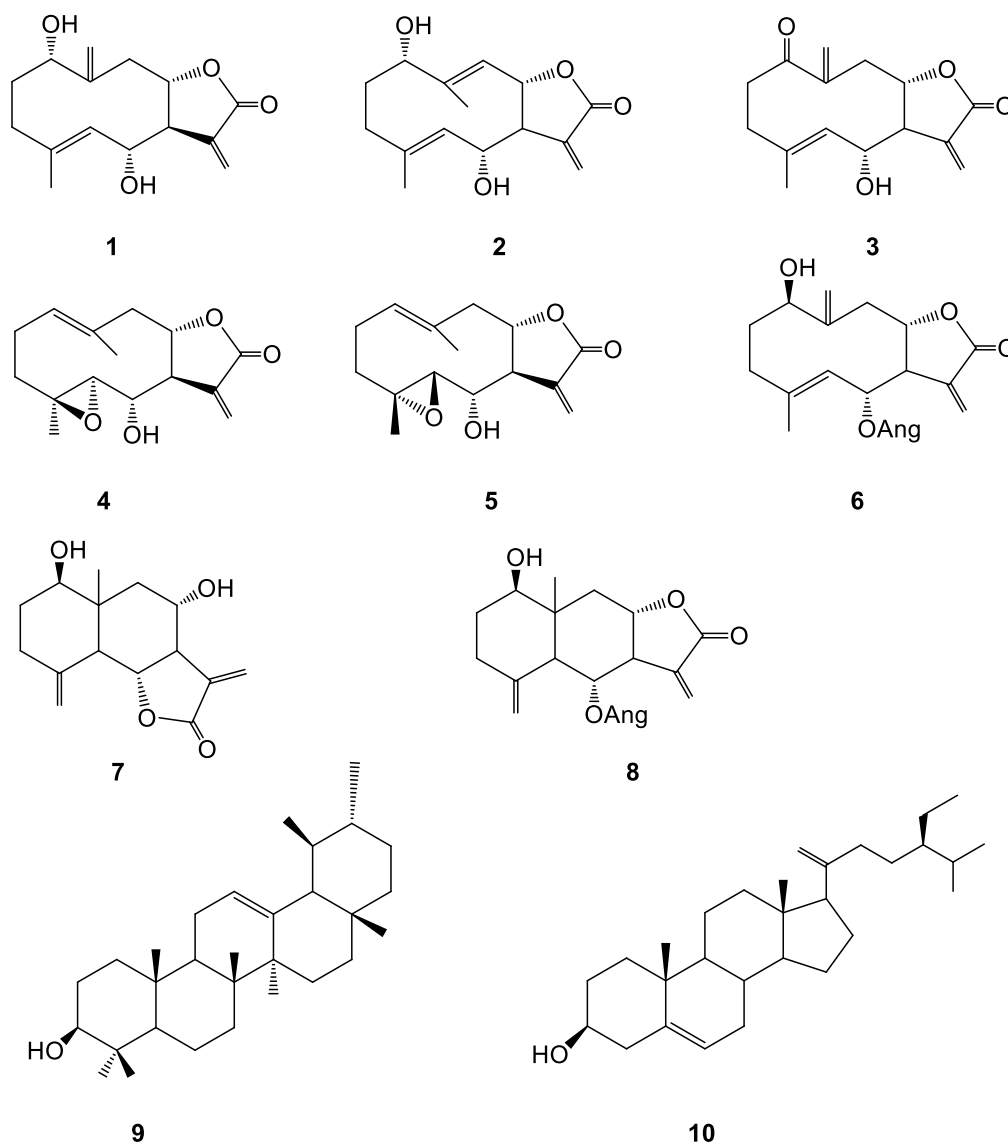


Figure 1: Compounds isolated from *T. Abrotonifolium*.

RESULTS AND DISCUSSION

In this study, the chemical compositions of the aerial parts of *T. abrotonifolium* collected from Eastern Turkey is reported for the first time.

The genus *Tanacetum* belongs to family Asteraceae or Compositae. Interest is increasing in species of *Tanacetum* due to constituents and the presence of sesquiterpene lactones, which exhibited biological activities like cytotoxicity, antimicrobial activity, and growth regulation.(7). *Tanacetum* species have been used for centuries as folk remedies due to their diverse biological activities. Sesquiterpenoids which are the main components of the genus, supposed to be active principles of the plants. The lactone ring of sesquiterpene lactones, having exocyclic methylene group, has been suggested to be responsible for biological activities of sesquiterpenoids (7) Biological activities of the sesquiterpene lactones from *Tanacetum* genus were reported extensively. Tavulin, isospiciformin, tanachin, and dentatin A were isolated from *T.*

argyrophyllum var. *argyrophyllum*, exhibited bactericidal effects against *Staphylococcus aureus*, and *Escherichia coli* (12). Tavulin, spiciformin, dentatin A isolated from *T. densum* ssp. *sivasicum*, were found to be active activity against human epidermoid (KB) cells, with the IC₅₀ values of 3.2, 2.9 and 2.4 µgm⁻¹, respectively (13). The sesquiterpene lactones tavulin, tanachin and tamirin isolated from *Tanacetum praeteritum* ssp. *praeteritum* showed cytotoxic activity against the human pulmonary carcinoma cell line GLC₄ and the colorectal cancer cell line COLO 320 as well as antibacterial activities against the bacteria *Bacillus subtilis*, *Staphylococcus aureus*, *Proteus mirabilis*, *Escherichia coli*, *Klebsiella pneumoniae*, *Pseudomonas aeruginosa*, *Enterococcus*, beta-hemolytic *Streptococcus*, and the yeast *Candida albicans* (14).

In Table 1 shows that, biological activities and active principles in *Tanacetum* species which also analyzed in chemical structure of *T. abrotonifolium*.

Table 1. Biological active principles in *T. abrotonifolium*

Sources	Name	Activity	References
T. argyrophyllum var. argyrophyllum T. densum ssp Sivasicum	Tanachin	Antimicrobial activity	(12, 13)
T. argyrophyllum var. argyrophyllum T. densum ssp Sivasicum	Tavulin	Antimicrobial activity Cytotoxic activity	(12, 13)
T. argyrophyllum var. argyrophyllum	Spiciformin	Cytotoxic activity	(13)
T. argyrophyllum var. argyrophyllum	Isospiciformin	Antimicrobial activity	(12)
T. densum ssp Sivasicum	Dentatin A	Cytotoxic activity	(13)
T. praeteritum ssp. Praeteritum	Tamirin	Antimicrobial activity Cytotoxic activity	(14)

Polatoglu *et al.* investigated on the phytochemistry and the essential oils composition of *T. abrotonifolium* and they reported that insecticidal and biological activity of this species. (9)

Gecibesler *et al.* reported of the essential oils components of *T. abrotonifolium* by using HS-SPME-GC-MS method. (10) Gecisler also investigated biological activity studies of aerial parts this species. According to this report aireal parts of *T. abrotonifolium* were shown that anti-cancer, anti-microbial anti-oxidant activity (11).

However, the chemical constituents of aireal parts of *T. abrotonifolium* species have not been investigated. It is important to know the chemical structures of the air parts of *T. abrotonifolium* for scientific studies and future drug investigations.

Therefore, the aim of the study presented here was to examine the chemical compositions of the aerial parts of *T. abrotonifolium*.

The aerial parts of *T. abrotonifolium* yielded the known compounds tanachin (**1**) (15), tavulin (**2**) (16), tamirin (**3**) (16, 17), spiciformin (**4**) (18, 13), isospiciformin (**5**) (13, 12), 1 β -hydroxy-6 α -angeloxy-oxygermacra-4(5),10(14),11(13)-trien-8,12-olide (**6**) (19), dentatin A (**7**) (20), 1- β -hydroxy-6 α -angeloyloxyeudesm-4(15), 11(13)-dien-8,12-olide (**8**) (19). β -sitosterol (**10**) (21) which is the common steroids in the genus and α -amyrin (**9**) (22) which is only few common triterpenes were also isolated from *T. abrotonifolium*.

The $^1\text{H-NMR}$ spectrum of some compounds which belongs to *T. abrotonifolium* and $^{13}\text{C-NMR}$ spectrum of compounds were given in Table 2 and Table 3 respectively.

Table 2. The $^1\text{H-NMR}$ spectrum of some compounds which belongs to *T. abrotonifolium* (400 MHz; a. CDCl_3 b. $\text{CDCl}_3 + \text{CD}_3\text{OD}$)

H	1 ^a (15)	2 ^a (16)	3 ^a (16, 17)	7 ^b (20)
1	4.02 brd	4.38 brd.d		3.54 d.d
2		2.05-1.85 m	3.27 m	1.85 d.d.d
2'		2.05-1.85 m	3.27 m	1.55d.d.d
3	2.30-1.90 m	2.29 brd.d	2.30-2.60 m	
3'		1.78 m	2.30-1.60 m	
5	5.25 brd	4.99brd	5.07 brd	2.19 brd
5'				
6	4.41 d.d	4.50 d.d.d	4.15 d.d	4.04 d.d
7	2.88 d.d.d.d	2.80 d.d.d.d	2.73 d.d.d.d.d	2.62 d.d.d.d
8	3.94 d.d.d	4.54 d.d	3.95 d.d.d	4.10 d.d.d
8'				
9	3.05 d.d.d.d	5.32 brd	3.40 d.d.d.d.d	2.38 d.d
9'	2.41 d.d		2.15 d.d	1.33 d.d
13	6.30 d.d	6.30 d.d	6.37 d.d	6.18 d.d
13'	6.18 d.d	6.21 d.d	6.17 d.d	5.99 d.d
14		1.83 d	5.83 d	0.82 s
14'	5.16 d		5.78 d	
15	1.70 d	1.78 brs	1.65 d	5.0 brs
15'				4.87 brs

Table 3. The $^{13}\text{C-NMR}$ and the $^1\text{H-NMR}$ data of the compounds isolated from *T. abrotonifolium* (50-50.75 MHz; a. CDCl_3 b. $\text{CDCl}_3 + \text{CD}_3\text{OD}$)

C	1 ^a (15)	2 ^a (16)	3 ^a (16, 17)	7 ^b (20)
1	76.6	66.9	203.1	67.7

2	36.3	27.2	36.4	31.4
3	36.5	35.3	35.6	46.3
4	138.2	135.3	136.5	141.8
5	127.9	129.9	131.5	52.0
6	71.4	71.1	70.2	78.0
7	58.1	52.3	50.5	55.2
8	83.5	74.2	76.8	67.7
9	41.9	126.8	40.2	33.6
10	152.9	142.5	146.6	42.2
11	137.3	137.6	136.3	136.6
12	170.1	169.9	169.6	170.6
13	124.5	123.7	124.2	119.8
14	113.0	16.8	126.0	12.8
15	17.8	15.7	17.3	110.8

CONCLUSIONS

Tanacetum species have been used for centuries as folk remedy since their various biological activity. *T. abrotanifolium* is used by the people for cure purposes, even sold by herbalists, in Turkey. Phytochemical investigation on the essential oil composition of *T. abrotanifolium* and biological activity studies of this species is reported but the chemical constituents of aerial parts of *T. abrotanifolium* species have not been reported so far. Therefore, the main goal of this study of the chemical constituents of aerial parts of *T. abrotanifolium*. It is important to know the chemical structures of the aerial parts of *T. abrotanifolium* for scientific studies and future drug investigations. Further study should be carried out to the active compounds for pharmaceutical and industrial purposes.

ACKNOWLEDGEMENT

This work was supported by Yıldız Technical University, Grant No. 23-01-07-01.

REFERENCES

1. Davis P. Flora of Turkey and the East Aegean Islands. Vol. 5. Edinburgh: Edinburgh University Press. 1975; 256-292.
2. Duke J. CRC Handbook of Medicinal Herbs. England: CRC Press. 1987; 474-475.
3. Abad M, Bermejo P, Villar A. An approach to the genus *Tanacetum* L.(Compositae): phytochemical and pharmacological review. *Phytotherapy Research*. 1995; 9(2):79-92.
4. Davis P, Mill R, Tan K, editors. Flora of Turkey and the East Aegean Islands (supplement). Edinburgh: Edinburgh University Press; 1998. 5.5. Lahlou S, Tahraoui A, Israili Z, Lyoussi B. Diuretic activity of the aqueous extracts of *Carum carvi* and *Tanacetum vulgare* in normal rats. *J. Ethnopharmacol*. 2007; 110: 458-463.

6. Akpulat H.A, Tepe B, Sokmen A, Daferera D, Polissiou M. Composition of the essential oils of *Tanacetum argyrophyllum* (C. Koch) var. *argyrophyllum* and *Tanacetum parthenium* (L.) Schultz Bip. (Asteraceae) from Turkey. *Biochem. Syst. Ecol.* 2005; 33: 511-516.
7. Gören N, Arda N, Çalışkan Z. Chemical Characterization and Biological Activities of the genus *Tanacetum* (Compositae). *Studies in Natural Products Chemistry* 2002; 27: (Bioactive Natural Products (Part H)): 547-658. Publisher: (Elsevier Science B.V.,) CODEN:SNPCE2
8. Brown A.M.G, Love K.C, Davey M.R, Power J.B. *Plant Science.* 1996; 116: 223.
9. Polatoglu K, Karakoc O.C, Yucel Y, Betul Demirci B, Goren N, Baser K.H.C. Composition, insecticidal activity and other biological activities of *Tanacetum abrotanifolium* Druce. essential oil. *Industrial Crops and Products.* 2015; 71: 7–14.
10. Geçibesler I.H, Demirtas I, Koçak A. Based on the Quantity, Temperature and Time, The Examination of Variability in Odorous Components of *Tanacetum abrotanifolium* from Turkey: An Exclusive Gradient Work. *Journal of Essential Oil Bearing Plants.* 2015; 18 (4): 840–843.
11. Geçibesler I.H. *In vitro* biological activity studies on *Tanacetum abrotanifolium* (L.) Druce (Asteraceae). *Anadolu Univ. J. of Sci. and Technology A-Appl. Sci. and Eng.* 2017; 18(2).
12. Gören N, Jakupovic J, Topal Ş. Sesquiterpene lactones with antibacterial activity from *Tanacetum argyrophyllum* var. *argyrophyllum*. *Phytochemistry.* 1990 Jan; 29(5):1467–1469.
13. Gören N, Bozok-Johansson C, Jakupovic J, Lee-Juian L, Hui-Ling S, Cordell GA, et al. Sesquiterpene lactones with antibacterial activity from *Tanacetum densum* subsp.*sivasicum*. *Phytochemistry.* 1992 Jan; 31(1):101–104.
14. Gören N, Woerdenbag H, Bozok-Johansson C. Cytotoxic and Antibacterial Activities of Sesquiterpene Lactones Isolated from *Tanacetum praeteritum* subsp. *praeteritum*. *Planta Medica.* 1996 Oct; 62(05):419–422.
15. Yunusov A, Kasymov S.Z, Sidyakin G. Lactones of *Tanacetum pseudoachillea*. *Chemistry of natural compounds.* 1973; 9(2):267–167.
16. Nano G, Appendino G, Bicchi C, Frattini C. Wild Piedmontese Plant. Part III. On a chemotype of *Tanacetum vulgare* L. containing sesquiterpene lactones with germacrene skeleton. 1980.
17. Mnatsakanyan V, Revazova L. Phytochemical analysis of plant *tanacetum myriophyllum* willd. 1. sesquiterpenic lactones-tamirin. *Armyanskii Khimicheskii Zhurnal.* 1973; 26(11):914–919.
18. Gören N, Arda N, Çalışkan Z. Chemical characterization and biological activities of the genus *Tanacetum* (Compositae). In: *Studies in Natural Products Chemistry* [Internet]. Elsevier; 2002

19. Gören N, Tahtasakal E. Sesquiterpenoids from *Tanacetum argenteum* subsp. *canum* var. *canum*. *Phytochemistry*. 1997; 45(1):107–109.
20. Yunusov A, Abduazimov B.K, Sidyakin G. Dentatin A from *Tanacetum vulgare*. *Khim Prir. Soedin*. 1980; 4:573.
21. Gören N, Tahtasakal E, Pezzuto J.M, Cordell G.A, Shwarz B, Prokscht P. Sesquiterpene lactones from *Tanacetum argenteum*. *Phytochemistry*. 1994 May; 36(2):389–392.
22. Gören N, Tahtasakal E. Constituents of *Tanacetum densum* subsp. *eginense*. *Phytochemistry*. 1994 Aug;36(5):1281–1282.



The Uranium Recovery from Aqueous Solutions Using Amidoxime Modified Cellulose Derivatives. II. Uranium Uptake Behavior of Amidoximated Ethyl Cellulose

Seyhan Şener Başarır, Nursel Pekel Bayramgil  *

Hacettepe University, Faculty of Science, Chemistry Department, 06800, Beytepe, Ankara, Turkey

Abstract: Amidoxime modified ethyl cellulose (EC-*g*-AO) was utilized to recover uranyl ions from aqueous solutions through a process of complexation. Adsorption trials were carried out at varying UO_2^{2+} concentrations ranging from 100 to 1000 mg/L and at temperatures ranging from 25 to 50°C. Thermodynamics and kinetics of the adsorption of uranyl ions (UO_2^{2+}) by EC-*g*-AO were examined. The findings suggested an adsorption capacity of 240 mg UO_2^{2+} /g dry copolymer. Thermodynamic parameters applicable to the interaction of UO_2^{2+} with EC-*g*-AO were calculated from thermodynamic relations. Calculations indicated that adsorption took place through powerful electrostatic interactions with an enthalpy of -23.6 kJ/mol. UO_2^{2+} desorption was investigated by desorption agents like EDTA, HCl, $NaHCO_3$, and NaOH. The desorption yield found for $NaHCO_3$ was 52%.

Keywords: Ethyl cellulose, uranium, $NaHCO_3$, adsorption enthalpy, EDX.

Submitted: May 08, 2017. **Accepted:** March 13, 2018.

Cite this: Şener Başarır S, Pekel Bayramgil N. The Uranium Recovery from Aqueous Solutions Using Amidoxime Modified Cellulose Derivatives. II. Uranium Uptake Behavior of Amidoximated Ethyl Cellulose. JOTCSA. 2018;5(2):521-38.

DOI: <http://dx.doi.org/10.18596/jotcsa.310947>.

***Corresponding author. E-mail:** nursel@hacettepe.edu.tr. Phone & Fax: 90 (312) 297 7965.

INTRODUCTION

Seawater contains abundant dissolved alkali and rare earth alkali metal ions, alongside a lesser amount of some valuable metals like lithium and uranium (1). The relevant literature (2-5) features numerous studies related to the removal of heavy metal ions from seawater and wastewater, especially for the selective recovery and the enrichment of uranyl ions.

Being toxic and radioactive, uranium poses a risk for both surface and underground waters. On the other hand, uranium is utilized as a raw material for nuclear power plants and has had a tremendous commercial significance. Nevertheless, as the uranium reserves are anticipated to be depleted in the near future, studies have focused on the recovery of uranium from natural water sources (0.1–10 mg U/m³), especially from sea water (2.8–3.3 mg U/m³). Various organic adsorbents containing different functional groups or organic chelates that are more or less selective towards uranium were synthesized and used to recover uranium from seawater or mining wastewaters (6-9). The desired properties of these chelates are high capacity, high selectivity, fast kinetics, high mechanical strength, and a fast equilibrium established with metal ion solution. Notably, amidoxime containing synthetic and natural polymers are the most promising systems for the uranium recovery (10). From past to present, a number of studies were published on the adsorption of uranyl ions by polymers and copolymers containing amidoxime functional groups (11-14).

Neti *et al.* (15) reported their effort to induce hydrophilicity in the support polymer through the grafting of a hydrophilic monomer onto PE prior to ATRP polymerization of acrylonitrile and 2-hydroxyethyl acrylate. The prepared adsorbents demonstrated promise (159.9 g U/kg of adsorbent) in laboratory screening tests using a high uranium concentration brine and 1.24 g U/kg of adsorbent in the filtered natural seawater in 21 days. Abney *et al.* (16) published a review of inorganic and organic materials used in the recovery of uranium from seawater and their detailed synthesis methods. He mentioned that amidoxime-functionalized polymers are the most technologically ripe adsorbent for the uranium recovery and have indicated impressive performance following protracted contact with seawater in screening studies, as well as in long-term desorption at the pilot scale in the open ocean. In another study (17), uranyl ion uptake from sulfuric acid solutions has been evaluated as a function of pH and sulfate concentration, with comparison to a commercially available weak base anion exchange resin. Maximum uranyl loading capacity was found as 269.50 mg/g for weak base anion exchange resin.

It is well known that currently available adsorbents require security measures and a sophisticated installation process, and they are more expensive than water treatment. Due to such constraints and environmental issues, there is a growing interest in the use of biomass for the removal of dissolved metals. For this purpose, numerous low-cost biomasses have been developed and commercially utilized to control pollution (18-21). Examples to low-cost

adsorbents include activated carbon, clay, agricultural waste, tea leaves, cellulose, fly ash, wool fiber, animal bones, immobilized fungal biomass, peanut shell pellets, and pineapple shells. Among them, cellulose has attractive properties; it is biodegradable, biocompatible, highly abundant, cheap, and it has been obtained from renewable resources. Cellulose interacts with soil microorganisms, transforms into eco-friendly end products, CO₂ and H₂O, and does not cause secondary pollution; thus, it is superior to synthetic polymers (22,23).

In our previous study, we synthesized graft copolymers consisting of ethyl cellulose (EC) and acrylonitrile (AN) through high-energy radiation. Details concerning the characterization and yield of grafting and amidoxime conversion were provided in this previous study (24). This study aimed to investigate how UO₂²⁺- and amidoxime-modified ethyl cellulose interacted within a certain temperature range, and it also revealed some conclusions about the physicochemical quantities that are effective in the specific adsorption process. These interactions were investigated as a function of temperature based on adsorption isotherms. The enthalpy, entropy, activation energy, and Gibbs free energy parameters of UO₂²⁺ adsorption were calculated from basic thermodynamic equations. Different releasing agents including HCl, EDTA, NaHCO₃ and NaOH were tested for desorption studies. Morphological, structural, and thermal changes were monitored through SEM-EDX, FTIR/ATR, and TGA, respectively.

MATERIALS AND METHODS

Materials

Ethyl cellulose (Sigma-Aldrich Chemie GmbH, Germany) and acrylonitrile (Aldrich, Germany) were used as received. Hydroxylamine hydrochloride and sodium hydroxide were supplied from Riedel de Haën and Merck, respectively.

Uranyl nitrate, UO₂(NO₃)₂.6H₂O (purity ≥ 98%) (BDH Chemicals Ltd., Poole, U.K.) was utilized as the source of uranyl ions. Sodium salicylate, HOC₆H₄COONa (analytical grade), which forms a complex with UO₂²⁺ for UV spectrophotometric measurements, was obtained from Fischer Scientific, U.K.

Synthesis of ethyl cellulose and acrylonitrile graft copolymers

Ethyl cellulose (EC) and acrylonitrile (AN) graft copolymers (EC-*g*-AN) were synthesized by irradiating various initial feed compositions of EC and AN through ⁶⁰Co- γ irradiator at room temperature. The conversion of initial mixtures into crosslinked, insoluble structures was determined gravimetrically after the copolymers kept in dimethyl formamide for a period of one week in order to extract the unreacted monomers and uncrosslinked soluble fractions. With 100% success, nitrile groups were converted into amidoxime groups in a neutralized NH₂OH.HCl solution at 50 °C. The details concerning the characterization, radiation synthesis, and amidoximation of EC-*g*-AN copolymers were reported in our previous study (24).

Adsorption of UO_2^{2+} onto amidoxime (AO) modified ethyl cellulose (EC-g-AO)

Approximately 0.25 g of EC-g-AO copolymers in cylindrical form (~0.5 cm in length) were immersed into 25 mL UO_2^{2+} solutions at concentrations varying from 100 to 1000 mg/L (pH 4.1). In a thermostatically controlled water bath, the solutions were shaken in closed flasks at $25 \text{ }^\circ\text{C} \pm 0.5 \text{ }^\circ\text{C}$. 0.5 mL aliquot was taken and sodium salicylate was added to form a complex during the shaking process. Then, the absorbance of this solution was recorded at 429 nm using a Jasco V-530 model UV-vis spectrophotometer and concentration changes were read from a previously obtained calibration curve. The adsorption equilibrium was achieved in 7-10 days. We repeated the adsorption trials following the same experimental route at other temperatures (30°C , 40°C , and 50°C). The adsorbed amount of UO_2^{2+} was calculated with the equation (1):

$$q_e = \frac{V}{m} \times (C_0 - C) \quad (\text{Eq. 1})$$

Where q_e is the amount of adsorbed UO_2^{2+} (mg UO_2^{2+} / g dry EC-g-AO), V is the volume of the UO_2^{2+} solution (L), m is the dry weight of EC-g-AO (g), and C_0 and C are the initial and equilibrium concentrations of UO_2^{2+} (mg/L), respectively.

The kinetics and thermodynamic quantities as activation energy (E_a), adsorption enthalpy ($\Delta H^{\circ}_{\text{ads}}$), Gibbs free energy of adsorption ($\Delta G^{\circ}_{\text{ads}}$), and entropy of adsorption ($\Delta S^{\circ}_{\text{ads}}$) were calculated based on the below-given classical equations, respectively:

$$k = A \cdot e^{-\frac{E_a}{RT}} \quad \text{Arrhenius equation} \quad (\text{Eq. 2})$$

$$\Delta G^{\circ}_{\text{ads}} = -RT \ln K_L \quad \text{Gibbs free energy} \quad (\text{Eq. 3})$$

$$\ln K_L = -\Delta H^{\circ}/RT + \Delta S^{\circ}/R \quad \text{Gibbs-Helmholtz equation} \quad (\text{Eq. 4})$$

Desorption of UO_2^{2+} from EC-g-AO copolymers using different agents

Solutions each of which having the concentration of 0.1 M EDTA, NaOH, HCl, and $NaHCO_3$ functioned as desorption agents in order to release adsorbed UO_2^{2+} from EC-g-AO copolymers. EDTA was provided by BDH; and the other three were obtained from Merck, Darmstadt, Germany. Also, desorption was carried out at pH 4.1. UO_2^{2+} adsorbed EC-g-AO copolymers were placed, separately and in predetermined amounts, into the aforementioned solutions, and the concentration of released UO_2^{2+} was measured in regular intervals with the UV-Vis spectrophotometer at 429 nm. Desorption (%) values were calculated in the following manner:

$$\text{Desorption (\%)} = \frac{\text{amount of released } UO_2^{2+}}{\text{total amount of adsorbed } UO_2^{2+}} \times 100 \quad (\text{Eq. 5})$$

Thermal, spectroscopic, and morphological analyses of UO_2^{2+} adsorbed EC-g-AO

We directly recorded the FTIR/ATR spectra of EC-g-AO copolymers with and without UO_2^{2+} in a $4000\text{-}400 \text{ cm}^{-1}$ range and took a total of 10 scans at 4 cm^{-1} resolution. A Nicolet IS10 Model FTIR/ATR spectrometer was used for this operation. We examined UO_2^{2+} adsorbed EC-g-AO's

thermal behavior with a DTG-60H Shimadzu (Simultaneous DTA-TG Apparatus) thermogravimetric analyzer in N₂ atmosphere; the temperature range was 0-700 °C and the heating rate was 10°C/min. The flow rate of N₂ gas was 60 mL/min. SEM images of UO₂²⁺ adsorbed EC-*g*-AO copolymers were obtained with Quanta 200 FEG SEM-FEI Model Scanning Electron Microscope, which enabled an observation of morphological changes at an accelerating voltage ranging from 10.00 kV to 15.00 kV. We ensured the conductivity of polymer samples by gold-coating. A simultaneous analysis of SEM and EDX (Energy Dispersive X-Ray Spectroscopy) with Bruker Electron Microscope enabled the elemental analysis of UO₂²⁺ adsorbed EC-*g*-AO copolymers.

RESULTS AND DISCUSSION

Detailed information regarding the amidoxime conversion, radiation synthesis, and characterization of EC-*g*-AO copolymers were presented as another study (24). EC-*g*-AO copolymers were subjected to adsorption experiments in order to determine their UO₂²⁺ uptake capacity, which is explained in the experimental section. For the adsorption kinetics studies, copolymer samples were removed from UO₂²⁺ solutions at regular intervals and complexed with sodium salicylate. Then, using a UV-Vis spectrophotometer, the absorbance of orange-colored complexes was recorded at 429 nm.

The ion-exchange mechanism for UO₂²⁺, which binds to the polymer, is complicated by the hydrolyzation of UO₂²⁺ in an aqueous solution within the pH range of the examined adsorption system, and different types of hydrolyzed UO₂²⁺ species are formed. UO₂²⁺ species are dominant in pH 1-4 range. At pH 4, the presence of UO₂(OH)⁺ within the solution remains around 2.2%; the maximum value of which rises to 18.6% at pH 6. The presence of UO₂(OH)₂ within the solution – maintained at pH 4 – is approximately 1.5%. UO₂²⁺ and H₃O⁺ compete in the solution within the range of pH 1-4. As the aqueous solution's pH value rises from 1 to 4, UO₂²⁺ adsorption increases, whereas the adsorption of H₃O⁺ decreases. Above pH 4, the hydrolysis of UO₂²⁺ triggers the formation of UO₂(OH)₂, UO₂(OH)⁺, and UO₂(OH)₃⁺ species (25). Based on these evaluations, we kept the pH value at constant 4.1 (own value of UO₂²⁺ solution). Below this value, we observed some distortions in the geometry of amidoximated copolymer, and even better UO₂²⁺ adsorption values were obtained. Some hydroxyl species formed above this limit pH value. During the whole adsorption experiments, this pH value was not affected with the presence of neutral ethyl cellulose copolymers although very few fluctuations occurred within pH 4-4.5.

Figure 1 shows the decrease in UO₂²⁺ concentrations in time for constant composition of EC-*g*-AO (the initial composition of 0.6 g EC in 6 mL acrylonitrile (AN) were used in our previous paper) copolymers for different initial UO₂²⁺ concentrations at 25°C (at pH 4.1). Using first order kinetic model, the initial rates ($-d[\text{UO}_2^{2+}]/dt = r_i$), calculated based on the initial slope of those

curves shown in Figure 1, are presented in Table 1, for each temperature, as a function of the initial UO_2^{2+} concentration. Table 1 demonstrates that the r_i of interaction between UO_2^{2+} and amidoxime groups increases with increasing concentration of UO_2^{2+} at a given temperature. In addition, contrary to what we know about the physical and chemical adsorption, the UO_2^{2+} adsorption increases with rising temperatures. This is because the structure of ethyl cellulose contains plenty of OH groups that link the glucose units layered. Rising temperature may cause some of these bonds to be broken and the rigidity of ethyl cellulose is decomposed to a certain extent. The adsorption rate of UO_2^{2+} on copolymers increases, enabling access to amidoxime groups.

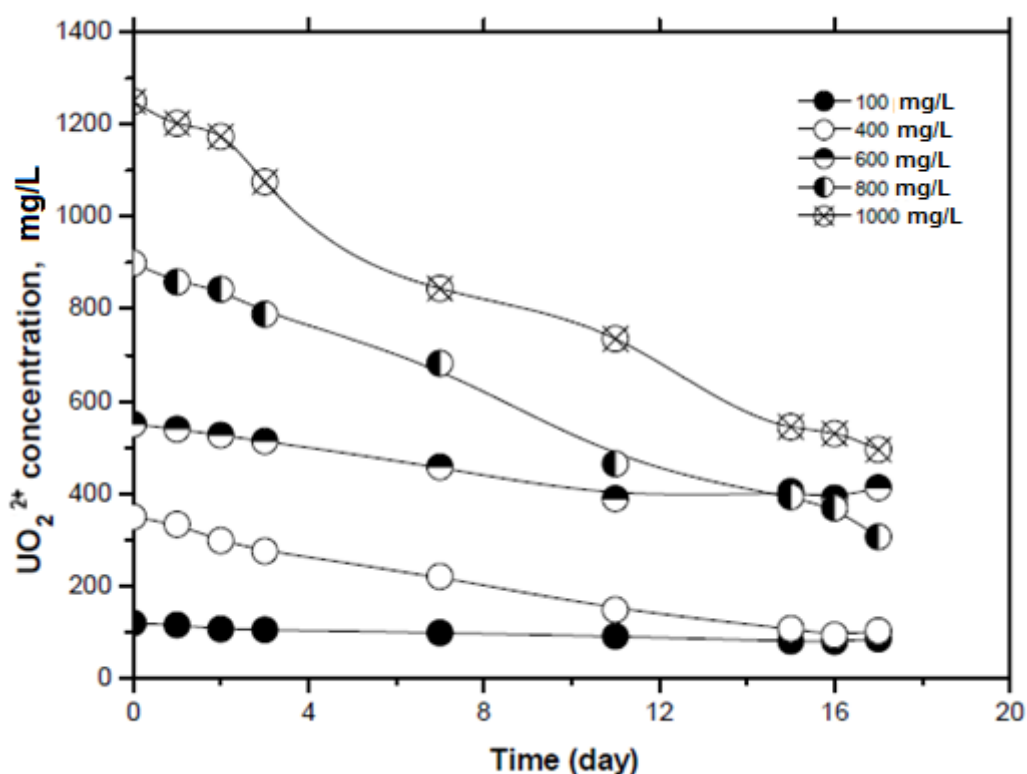


Figure 1. Kinetics of UO_2^{2+} adsorption at different UO_2^{2+} concentrations (0.6 g EC dissolved in 6 mL of AN; 25°C; pH 4.1)

Table 1. Initial rates and rate constants calculated from kinetic data.

Temperature	Initial conc. of UO ₂ ²⁺ (mg/L)	initial conc. of UO ₂ ²⁺ (x10 ⁴ mol/L)	Initial rate, r _i (x10 ⁶ mol/L.h)	rate constant, k (x10 ⁴ 1/h)
25 °C	400	14.80	2.34	5.1
	600	22.22	3.76	
	800	29.62	4.43	
	1000	37.03	4.96	
40 °C	400	14.80	4.32	6.6
	600	22.22	4.96	
	800	29.62	7.13	
	1000	37.03	8.63	
50 °C	400	14.80	4.87	7.3
	600	22.22	6.39	
	800	29.62	8.24	
	1000	37.03	9.79	

Calculated **E_a** value from Arrhenius equation = **43.04 kJ/mol**

Certain amounts of EC-*g*-AO copolymers were added to varying concentrations of UO₂²⁺ solutions at known volume and shaken for a predetermined period (around 10 days). This process continued until the adsorption equilibrium was reached. The equilibrium amounts of adsorbed UO₂²⁺ were calculated based on Equation 1. The adsorption capacity values of UO₂²⁺ mg/g dry copolymer were plotted versus equilibrium concentrations (**C_e**) of UO₂²⁺ to obtain adsorption isotherms for each temperature studied. From Figure 2, the adsorption isotherms demonstrate a high-affinity type (26) behavior due to the strong interaction between UO₂²⁺ and amidoxime groups for all temperatures. The shape of the isotherms shows that the same amount of UO₂²⁺ adsorption takes place in all active regions of EC-*g*-AO copolymers. In other words, adsorption takes place when the specifically adsorbed amount of ionic species on solid polymer exceeds that of ionic species found in the solution (27). To put it another way, copolymer gives a specific and strong significance to uranium; adsorption takes place very fast initially, then slows down as the sites available for adsorption decrease. This is the usual case for Langmuir isotherm. The linearized Langmuir equation (28) enables one to determine a significant parameter representing a measurement of the chelating resin-binding capacity for a given species [**K_L**, the equilibrium-binding constant (**k_{ads}/k_{des}**)]. The linearized form of Langmuir equation is presented in Equation (6):

$$\frac{C_e}{q_e} = \frac{1}{K_L q_s} + \frac{C_e}{q_s} \quad (\text{Eq. 6})$$

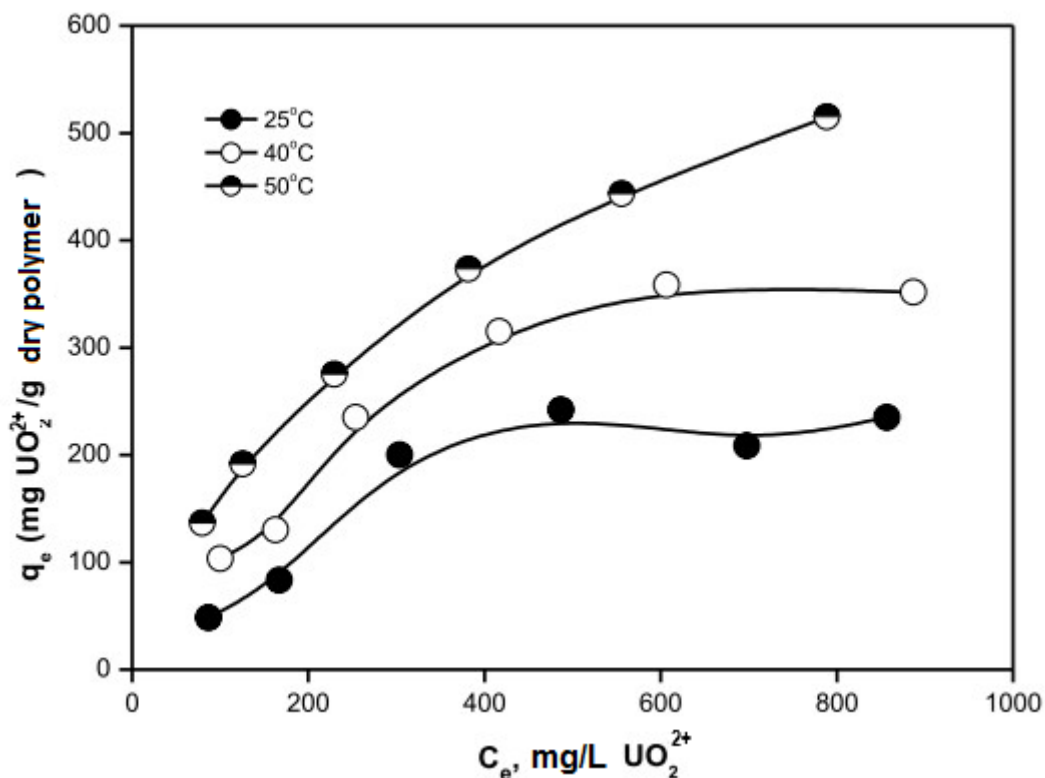


Figure 2. Adsorption isotherms obtained at different temperatures.

The K_L values obtained for Ec-g-AO copolymers are listed in Table 2 with q_e values. Despite the fact that UO_2^{2+} adsorption rose at higher temperatures, K_L values indicated the genuine results: The desorption rate remained high at high temperatures for K_L values from 25 to 50°C. Equations 2-4 and 6 are interpreted together in order to calculate the thermodynamic parameters of UO_2^{2+} adsorption. Activation energy, entropy, enthalpy, and Gibbs free energy values applicable to the UO_2^{2+} adsorption onto EC-g-AO copolymers were demonstrated in Tables 1 and 2. Calculated from Equation 2, E_a (43.04 kJ/mol) indicates that the adsorption of UO_2^{2+} by EC-g-AO copolymers has taken place through an internal diffusion-controlled process for chemical adsorption (30-120 kJ/mol) (29). Moreover, the other thermodynamic parameters calculated using Eq. 2-4 confirmed the powerful interaction between amidoxime groups and UO_2^{2+} , and such interactions have been demonstrated for exothermic favorability. In our study, the most important parameter that determines the tendency of a spontaneous event, Gibbs free energy, ΔG_{ads} , has a negative value. In addition, ΔH_{ads} value has been found as -23.61 kJ/mol. This is very close to the threshold of the enthalpy of chemical adsorption and that of the physical adsorption. Adsorption happens physically at $\Delta H_{ads} < -40$ kJ/mol and chemically at $\Delta H_{ads} > -40$ kJ/mol. Although the interaction between UO_2^{2+} and amidoxime groups takes place with the aim of physical forces, binding between the two is quite strong. Desorption studies support our findings in this context.

Table 2. Thermodynamic parameters of UO_2^{2+} adsorption onto EC-*g*-AO copolymers

Temperature (°C)	q_e (mg/g)	K_L (Langmuir eqn.)	$-\Delta G_{\text{ads}}$ (kJ/mol, Gibbs eqn.)	ΔS_{ads} (J/K mol, Gibbs-Helmholtz eqn.)
25	24	523	15.51	27.18
40	35	292	14.07	30.48
50	51	255	13.73	30.60

$\Delta H_{\text{ads}} = -23.61 \text{ kJ/mol}$ (Gibbs-Helmholtz eqn.)

The relevant literature (12-14,30,31) contains many studies conducted on both amidoximated resin and unmodified biomass, separately, for the uranium recovery. But none of them included the uranium recovery by amidoximated biomass. In some studies, the modification was achieved by some acid groups (13), and in others, those heavy metal ions other than uranium (10) were used, or they presented only the synthesis and characterization. Therefore, direct study was not present for the uranium recovery by amidoximated cellulose. Only in one study performed by Badawy et al. (7) the authors showed that acrylonitrile/methacrylic acid grafted cotton cloths can be used to recover uranium from aqueous systems with an adsorption capacity of 662 $\mu\text{g/g}$. This value is a rather small value from the value obtained in our study (240 mg/g).

To be able to explain the mechanism by which UO_2^{2+} binds to amidoxime groups, FTIR/ATR spectra of UO_2^{2+} adsorbed EC-*g*-AO copolymers were obtained, which are shown in Figure 3. Because of interactions with UO_2^{2+} , there are some shifts on some characteristic bands. The band for C=N belonging to amidoxime group at 1660 cm^{-1} shifts by approximately 15 cm^{-1} , and also there is an 8 cm^{-1} shift for N-O stretching vibrations at 912 cm^{-1} . The band intensity at 1550 cm^{-1} , attributed to C-N group of amidoxime, increased, and it got clearer after UO_2^{2+} adsorption. Other band shifts occur at 3200 cm^{-1} for the interaction of both =N-OH and $-\text{NH}_2$ (of amidoxime) groups with UO_2^{2+} . This suggests that UO_2^{2+} on EC-*g*-AO copolymers is absorbed through both $-\text{C}-\text{NH}_2$ and $-\text{C}=\text{N}-\text{O}-\text{H}$ segments of amidoxime, and the mechanism is proposed as in scheme 1:

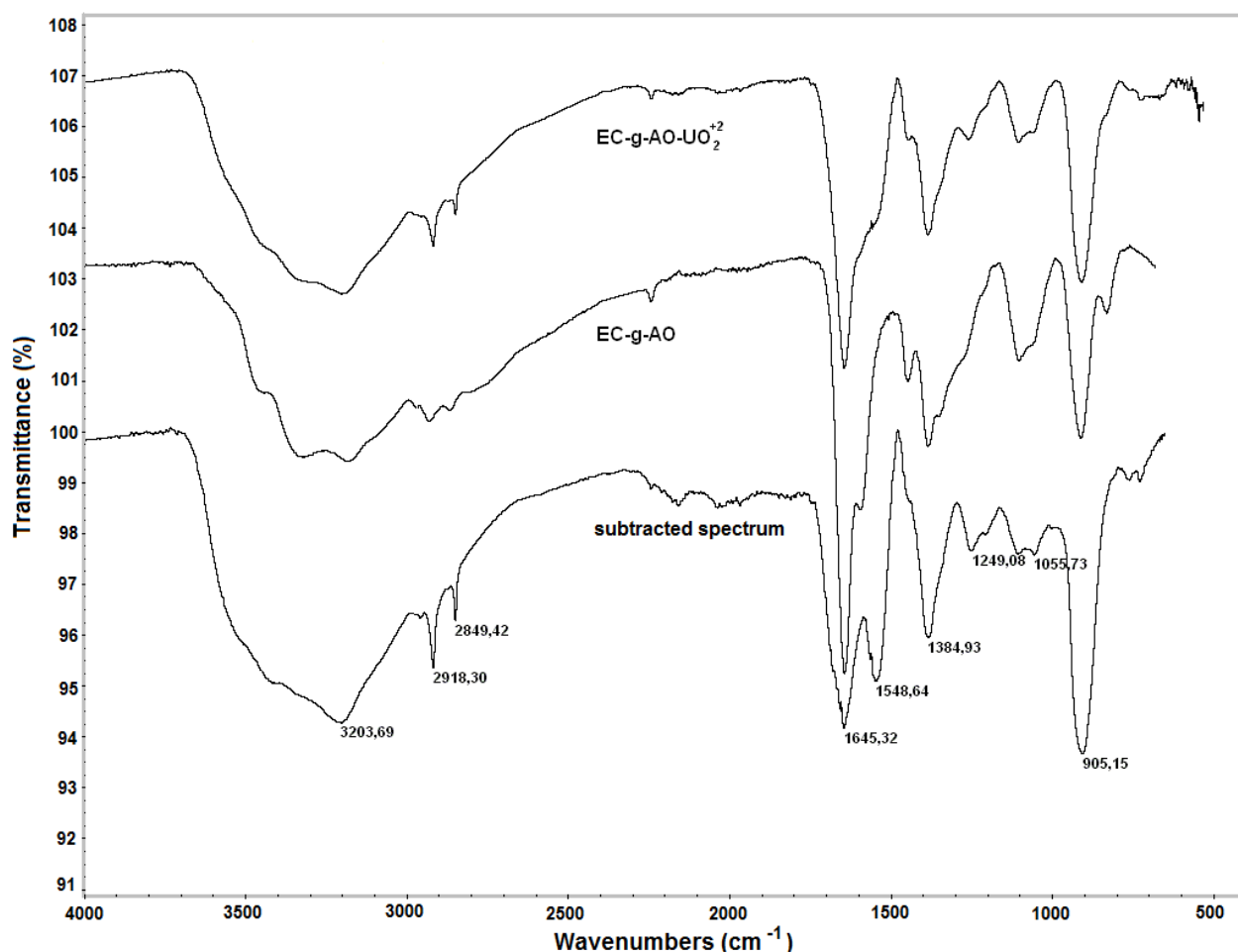
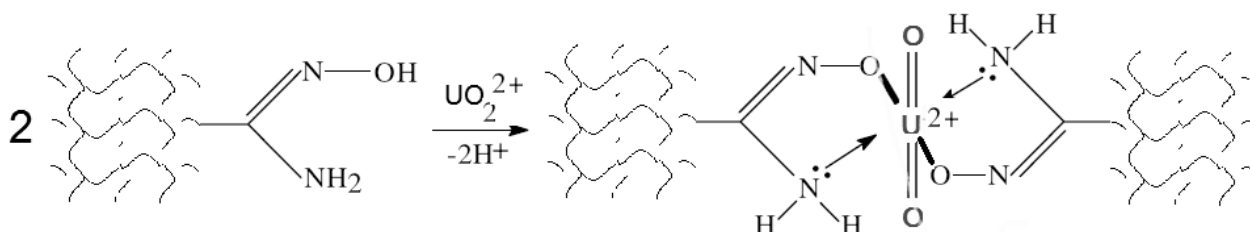


Figure 3. FTIR/ATR spectra of EC-g-AO copolymers before and after UO_2^{2+} adsorption



Scheme 1. Coordination of amidoxime group to uranyl cation.

Another similar mechanism was observed as part of the study of adsorption of metal ions by amidoxime-modified synthetic resins (32). Given the bidentate character of amidoxime groups, two amidoxime groups hold an UO_2^{2+} as a clamp and ensure 6-coordination.

Thermal analyses were performed to account for the thermal behavior of EC-g-AO after UO_2^{2+} adsorption. Evaluations of EC-g-AN copolymers in terms of TGA and derivative TGA before and after amidoxime conversion were reported in another study of ours (24). Figure 4 presents TGA,

der.TGA, and DTA thermograms for UO_2^{2+} adsorbed EC-*g*-AO copolymer. As can be seen in the figure, there are different steps of decomposition upon the adsorption of UO_2^{2+} . Due to the interaction between the amidoxime group and UO_2^{2+} , the level of decomposition observed at 275 °C corresponded to the amidoxime groups and the decomposition at 433 °C corresponded to cellulosic structures. The addition of $\text{C}\equiv\text{N}$ (nitrile) groups affected it, leading a slight increase in the cellulose's stability. The decompositions observed at 462°C, 508°C and 621°C probably show the decompositions of some groups which interacted with UO_2^{2+} . The last three decompositions were not observed in the TGA thermogram of EC-*g*-AO copolymer itself (24). The EC-*g*-AO copolymer lost approximately 90% of its weight throughout the heating process that continued up to 700°C. Since the UO_2^{2+} did not diffuse thoroughly into the crystalline cellulose by defeating strong H-bonds, it would not access to all adsorption sites, and the adsorption amounts of UO_2^{2+} is lesser compared to the other studies in the literature (33-35). As a result, such a high weight loss arose from carbonization of cellulosic units. When the residue of TGA was analyzed, it was shown that the structure belongs to U_3O_8 (36).

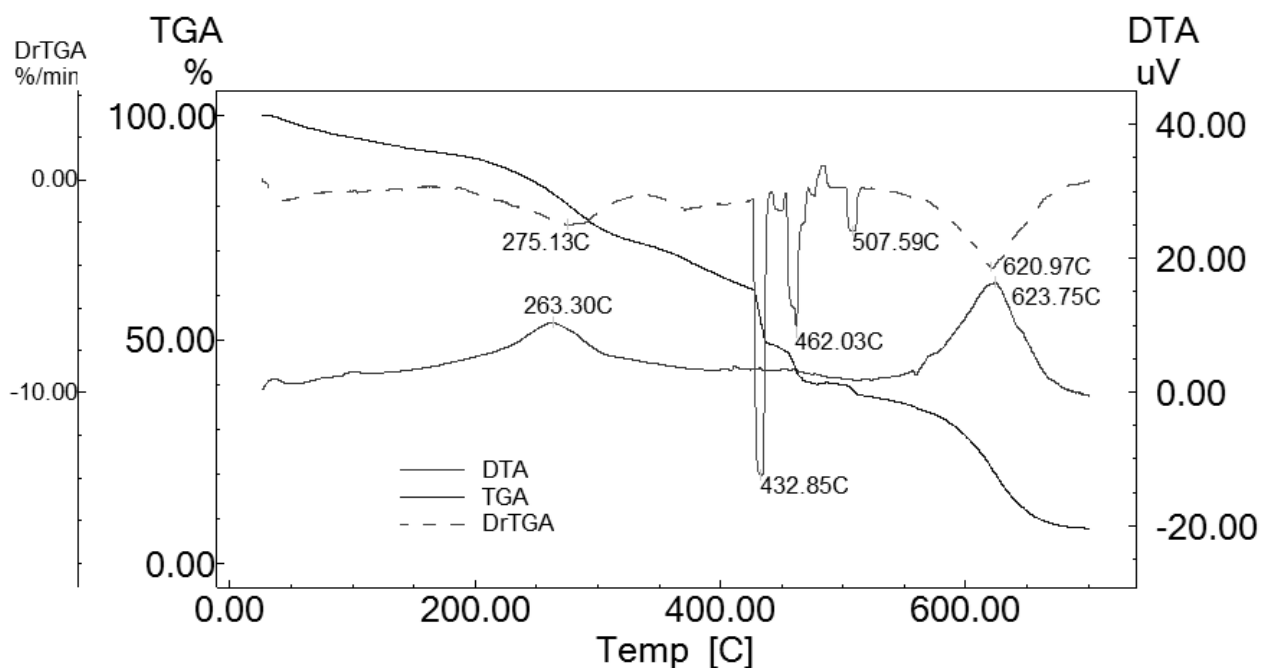
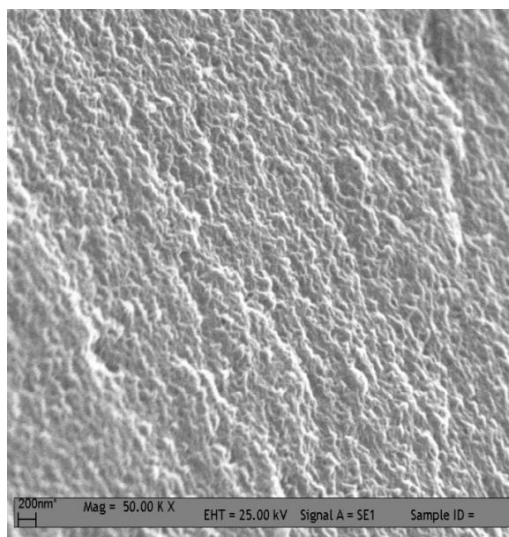


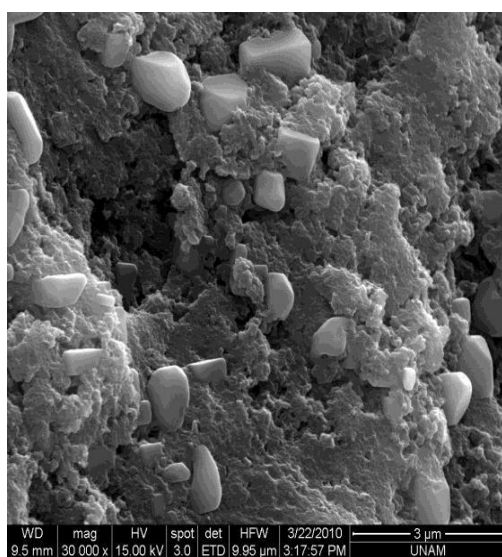
Figure 4. TGA thermogram of EC-*g*-AO copolymers after UO_2^{2+} adsorption.

SEM and SEM-EDX images were obtained to analyze the surface morphology of EC-*g*-AO copolymers following UO_2^{2+} adsorption. The Scanning Electron Microscopy (SEM) enables an observation of the materials' topographic features as 3-D images, whereas the Energy Dispersive X-Ray Spectroscopy (EDX) allows performance of an elemental analysis on the materials' microscopic sections. The SEM images of EC-*g*-AO copolymers, before and after UO_2^{2+} adsorption, are provided in Figure 5. As shown in the figure (b,c), there are highly visible orthorhombic bipyramidal crystal structures of UO_2^{2+} . In the colored figure, bright regions observed around crystals indicates that radioactive heavy metal ion is attached to the structure.

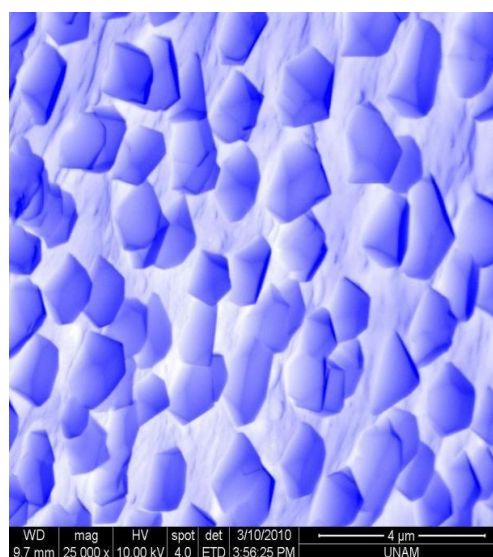
SEM images were taken to analyze if the UO_2^{2+} is connected to EC-*g*-AN copolymer before amidoxime conversion (Figure 5(a)). As can be clearly seen, the absence of UO_2^{2+} crystals on the topological image of EC-*g*-AN copolymer confirmed that the unamidoximated copolymer did not adsorb UO_2^{2+} . This draws attention to similar crystal occurrences on the surface, reported by Allen and Tempest (37). The orthorhombic bipyramidal crystal structure of UO_2^{2+} , which is seen on the copolymer surface, is presented in Scheme 2:



(a)

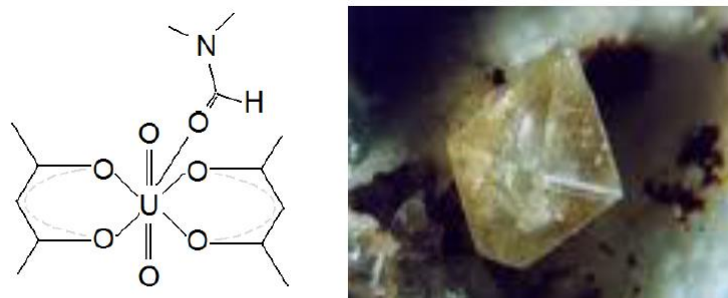


(b)



(c)

Figure 5. SEM images of (a) EC-*g*-AN- UO_2^{2+} , (b), and (c) EC-*g*-AO- UO_2^{2+} systems



Scheme 2. The orthorhombic bipyramidal crystal structure of UO₂²⁺.

Using EDX as a non-destructive determination method, it is possible to perform a quantitative analysis of uranium in the organic or inorganic compounds. To this aim, EDX spectrum of UO₂²⁺ adsorbed EC-*g*-AO was taken simultaneously based on the SEM image. The surface was coated with gold (Au) for conductivity during the analysis. As indicated in Figure 6, the UO₂²⁺ attached sites are marked in red, and the copolymer surface is almost entirely covered by UO₂²⁺. Starting from the low energy region, the bands observed for 0.4 keV and 0.5 keV were attributed to N K_α and O K_α X-ray lines, respectively. Due to the copolymer surface coated with Au, bands observed at 2.120 keV, and 9.712 keV belong to Au M_α, and Au L_α X-ray lines, respectively. The EDX spectrum revealed two different lines depending on UO₂²⁺ adsorption: one is at 3.17 keV, which corresponds to U M_α, and the other is at 3.34 keV, belonging to U M_β. It is normal that the band intensities corresponding to the energy values are different because the UO₂²⁺ adsorption values obtained at different initial concentrations are different.



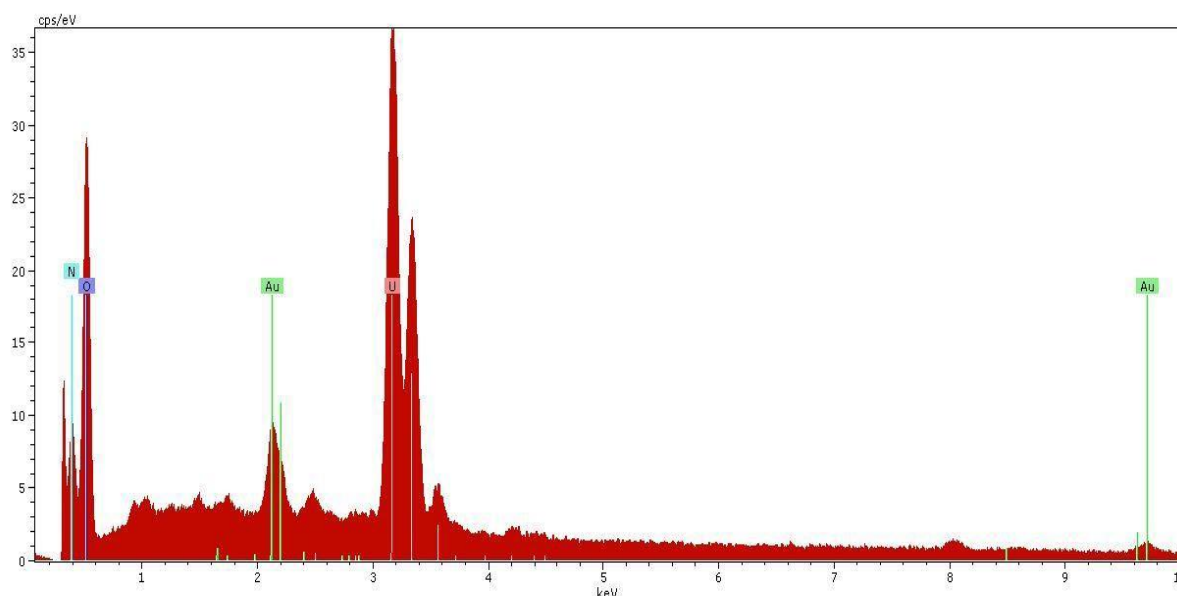


Figure 6. SEM-EDX spectrum of UO_2^{2+} adsorbed EC-*g*-AO copolymer (adsorption conditions: 800 mg/L UO_2^{2+} , 25°C, pH 4.1)

The final part of our study featured desorption experiments to determine the release of UO_2^{2+} from EC-*g*-AO copolymers. Certain amounts of UO_2^{2+} adsorbed EC-*g*-AO copolymers were separately added to 10 mL of EDTA, HCl, NaOH, and NaHCO_3 solutions (0.1 M each), and we measured, in regular intervals, the concentration of released UO_2^{2+} with UV-Vis spectrophotometer at 429 nm. The values of desorption (%) were calculated based on Equation 5. Table 3 indicates the total amounts of UO_2^{2+} (%) released from different desorption agent solutions. As can be seen in the table, NaHCO_3 is the most effective agent for desorption. Desorption of UO_2^{2+} from EC-*g*-AO copolymer in 0.1 M NaHCO_3 was found to be 52 %. A similar result was observed in the study conducted by Das *et al.* (13). In their study, amidoximated electron-beam-grafted polypropylene membranes were used for the uranium recovery; desorption of uranium from membrane was realized with 1.0 M NaHCO_3 with 85 % yield. Table 3 reveals another interesting point: We found that the desorption yield remained only at 52%. In our view, the low desorption yield might be due to the strong interaction between amidoxime groups close to the chemical adsorption boundary.

Table 3. Total release amounts (%) of UO_2^{2+} from EC-*g*-AO copolymers using different desorption agents.

mg UO_2^{2+} / g copolymer	Total UO_2^{2+} release (%)			
	0.1 M HCl	0.1 M EDTA	0.1 M NaHCO_3	0.1 M NaOH
240	17	12	52	13

CONCLUSIONS

The EC-*g*-AO copolymers are prepared by gamma irradiating binary mixtures of ethyl cellulose and acrylonitrile and subsequent amidoximation of the grafting chains. The adsorption behavior

of the uranyl ions in initial concentrations over a range of 100 – 1000 mg/L on the EC-*g*-AO copolymers is studied by the batch technique at a pH value of 4.1 at different temperatures. Interaction between UO_2^{2+} and amidoxime groups increases with increasing concentration of UO_2^{2+} at a given temperature. It can be found that the temperature induces a positive effect on the adsorption process and the adsorption capacity increases with an increase of UO_2^{2+} initial concentration. The findings suggested an adsorption capacity of 240 mg UO_2^{2+} /g dry copolymer. Desorption of adsorbed UO_2^{2+} ions from EC-*g*-AO copolymers was performed using different agents and it was found that NaHCO_3 is the most effective agent for desorption.

ACKNOWLEDGMENTS

This study was conducted as part of the Chemistry Department, Hacettepe University. The authors gratefully acknowledge the support provided by the HU Scientific Research Foundation through the project no. HU-BAB-010D08601006.

REFERENCES

1. David Talbot: Uranium and lithium demand powers stocks. Available at <http://www.theenergyreport.com/pub/na/10323>.
2. Egawa H, Kabay N, Jyo A, Hirono M, Shuto T. Recovery of uranium from seawater.15. Development of amidoxime resins with high sedimentation velocity for passively driver fluidized bed adsorbers. *Ind Eng Chem Res.* 1994; 33:657-61.
3. Atia AA, Donia AM, Abou-El-Enein SA, Yousif AM. Studies on uptake behaviour of copper(II) and lead(II) by amine chelating resins with different textural properties. 2003; *Sep Purif Technol.* 33:295-301.
4. Nilchi A, Babalou AA, Rafiee R, Sid Kalal H. Adsorption properties of amidoxime resins for separation of metal ions from aqueous systems. *Reac Func Polym.* 2008; 68:1665-70.
5. Liu X, Chen H, Wang C, Qu R et al. Adsorption properties of amidoximated porous acrylonitrile/methyl acrylate copolymer beads for Ag (I). *Polym Adv Technol.* 2011; 22:2032-8.
6. Tagami K, Uchida S. Use of TEVA resin for the determination of U isotopes in water samples by Q-ICP-MS. *Appl Radiat Isotopes.* 2004; 61:255-9.
7. Badawy SM, Sokker HH, Othman SH, Hashem A. Cloth filter for recovery of uranium from radioactive waste. *Radiat Phys Chem.* 2005; 73:125-130.
8. D'Souzaa SF, Sarb P, Kazyc SK, Kubala BS. Uranium sorption by Pseudomonas biomass immobilized in radiation polymerized polyacrylamide bio-beads. *J Environ Sci Health, Part A.* 2006; 41:487-500.
9. Chauhan GS, Kumar A. A study in the uranyl ions uptake on acrylic acid and acrylamide copolymeric hydrogels. *J Appl Polym Sci.* 2008; 110:3795-803.
10. O'Connell DW, Birkinshaw C, Dwyer TF. Heavy metal adsorbents prepared from the modification of cellulose: A review. *Biores Technol.* 2008; 99:6709-24.
11. Egawa H, Harada H. Recovery of uranium from seawater by using chelating resins containing amidoxime groups. *Nippon Kagaku Kaishi.* 1979; 958-9.
12. Rivas BL, Maturana HA, Villegas S. Adsorption behavior of metal ions by amidoxime chelating resin. *J Appl Polym Sci.* 2000; 77:1994-9.

13. Choi SH, Nho YC. Adsorption of UO_2^{+2} by polyethylene adsorbents with amidoxime, carboxyl, and amidoxime/carboxyl group. *Radiat Phys Chem.* 2000; 57:187-93.
14. Das S, Pandey AK, Athawale A, Kumar V, Bhardwaj YK, Sabharwal S, Manchanda VK. Chemical aspects of uranium recovery from seawater by amidoximated electron-beam-grafted polypropylene membranes. *Desalination.* 2008; 232:243-53.
15. Neti VS, Das S, Brown S, Janke CJ, Kuo L, Gill GA, Dai S, Mayes RT. Efficient functionalization of polyethylene fibers for the uranium extraction from seawater through atom transfer radical polymerization. *Ind Eng Chem Res.* 2017; 56:10826-32.
16. Abney CW, Mayes RT, Saito T, Dai S. Materials for the recovery of uranium from seawater. *Chem Rev.* 2017; 117:13935-14013.
17. Amphlett JTM, Ogden MD, Foster RI, Syna N, Soldenhoff K, Sharrad CA. Polyamine functionalised ion exchange resins: Synthesis, characterization and uranyl uptake. *Chem Eng J.* 2018; 334:1361-70.
18. Chau H, Yu P. Production of biodegradable plastics from chemical wastewater – A novel method to resolve excess activated sludge generated from industrial wastewater treatment. *Water Sci Technol.* 1999; 39:273-80.
19. Gupta KC and Sahoo S. Graft copolymerization of acrylonitrile and ethyl methacrylate comonomers on cellulose using ceric ions. *Biomacromol.* 2001; 2:239-47.
20. Gurgel LVA, Karnitz Jr O, de Freitas Gil RP, Gil LF. Adsorption of Cu(II), Cd(II), and Pb(II) from aqueous single metal solutions by cellulose and mercerized cellulose chemically modified with succinic anhydride. *Biores Technol.* 2008; 99:3077-83.
21. Akhtar K, Khalid AM, Akhtar MW, Ghauri MA. Removal and recovery of uranium from aqueous solutions by Ca-alginate immobilized *Trichoderma harzianum*. *Biores Technol.* 2009; 100:4551-8.
22. Zhou D, Zhang L, Zhou J, Guo S. Cellulose/chitin beads for adsorption of heavy metals in aqueous solution. *Water Res.* 2004; 38:2643-50.
23. Wang L, Dong W, Xu Y. Synthesis and characterization of hydroxy propylmethyl cellulose and ethyl acrylate graft copolymers. *Carbohydr Polym.* 2007; 68:626-36.
24. Başarır SŞ and Bayramgil NP. The uranium recovery from aqueous solutions using amidoxime modified cellulose derivatives. I. Preparation, characterization and amidoxime conversion of radiation grafted ethyl cellulose-acrylonitrile copolymers. *Radiochim Acta.* 2012; 100:893-9.
25. Qadeer R, Hanif J, Saleem M, Afzal M. Effect of alkali metals, alkaline earth metals and lanthanides on the adsorption of uranium on activated charcoal from aqueous solutions. *J Radioanal Nucl Chem.* 1992; 165:243-53.
26. Giles CH, MacEwan TH, Nakhwa SN, Smith D. Studies in adsorption. Part XI. A system of classification of solution adsorption isotherms, and its use in diagnosis of adsorption mechanisms and in measurements of specific surface areas of solids. *J Chem Soc.* 1960; 10:3973-93.
27. IUPAC Compendium Chem Terminology (1986) IUPAC. 58:448.
28. Bolster CH, Hornberger GM. On the use of linearized Langmuir equations. *Soil Sci Soc Am J.* 2007; 71:1796-1806, <http://agris.fao.org/agris-search/search.do?recordID=US201300814267>.
29. Saeed MM, Rusheed A, Ahmed N. Kinetics and thermodynamic aspect of the adsorption of Fe (III) on HTTA-embedded polyurethane foam. *J Radioanal Nucl Chem.* 1996; 211:293-303.
30. Cou WH, Chao L, Zhu L. Efficient uranium(VI) biosorption on grapefruit peel: Kinetic study and thermodynamic parameters. *J Radioanal Nucl Chem.* 2012; 292:1303-15.
31. Li F, Tang Y, Wang HL, Yang JJ, Li SJ, Liu J, Tu H, Liao JL, Yang YY, Liu N. Functionalized hydrothermal carbon derived from waste pomelo peel as solid-phase extractant for the removal of uranyl from aqueous solution. *Environmental Sci Poll Res.* 2017; 24:22321-31.

32. Zohuriaan-Mehr MJ. Advances in chitin and chitosan modification through graft copolymerization: A comprehensive review. *Iran Polym J.* 2005; 14:235-65.
33. Nakajima A, Horikoshi T and Sakaguchi T. Recovery of uranium by immobilized microorganisms. *Eur J Appl Microbiol Biotechnol.* 1982; 16:88-91.
34. Gerente C, Andres Y and Le Cloirec P. Uranium removal onto chitosan: Competition with organic substances. *Environ Technol.* 1999; 20:515-21.
35. Na C, Park H, Kim B. Optimal amidoximation conditions of acrylonitrile grafted onto polypropylene by photoirradiation-induced graft polymerization. *J Appl Polym Chem.* 2012; 125:776-85.
36. Nyquist RA, Kagel RO. *Infrared Spectra of Inorganic Compounds.* Academic: New York, 1971; p 232.
37. Allen GC, Tempest PA. Ordered defects in the oxides of uranium. *Proceedings of the Royal Society of London Series A.* 1986; 406:325-44.



Synthesis of New Medium- and Large- Sized Racemic and Chiral Lactones

Hasniye Yaşa^{1*} and Ayşe Sergüzel Yusufoglu¹

¹ Istanbul University, Faculty of Engineering, Department of Chemistry, 34320 Avcılar, İstanbul, Turkey

Abstract: Successive reaction of long chain ω -1, ω -2, ω -4 and ω -5 hydroxycarboxylic acids **1a-1e** with a cyanuric chloride (CC) and triethylamine afforded the corresponding racemic lactones **2a-2e** in high yields. Optically pure *R* lactones **4a-4e** were synthesized stereoselectively by porcine pancreas lipase-catalyzed resolution of racemic **2a-2e**. The resolution conditions were investigated, determined and optical rotations were measured. The mentioned chiral lactones were synthesized by this method for the first time. The obtained racemic and chiral lactones were analyzed by NMR, IR, Mass, optical rotation, and elemental analysis.

Keywords: Synthesis, medium and large ring, lactone, enzymatic resolution

Submitted: December 29, 2017. **Accepted:** March 16, 2018.

Cite this: Yasa H., Yusufoglu S. Synthesis of New Medium- and Large- Sized Racemic and Chiral Lactones. JOTCSA. 2018;5(2): 539-50.

DOI: <http://dx.doi.org/10.18596/jotcsa.372628>.

* **Corresponding author. E-mail:** hasniye@istanbul.edu.tr

INTRODUCTION

Racemic and chiral lactones are commonly found in natural products as a series of pheromones and medical compounds (1-9). They are used also as intermediates for the synthesis of biological substances and natural products (10) due to their biological activities. There are many types of lactones and among them alkyl substituted lactones have gained a lot of interest from the synthetic and medicinal chemists (11, 12). Short chain alkyl lactones are essential and significant aromatic compounds in beverages and food.

Enzymes as biocatalysts find significant usage for preparing enantiomerically pure compounds (13). Lipases (triacylglycerol hydrolases, EC 3.1.1.3) are the most commonly used enzymes. They are not only cheap and easy to deliver but also are highly stable and have high enantioselectivity in synthesis.

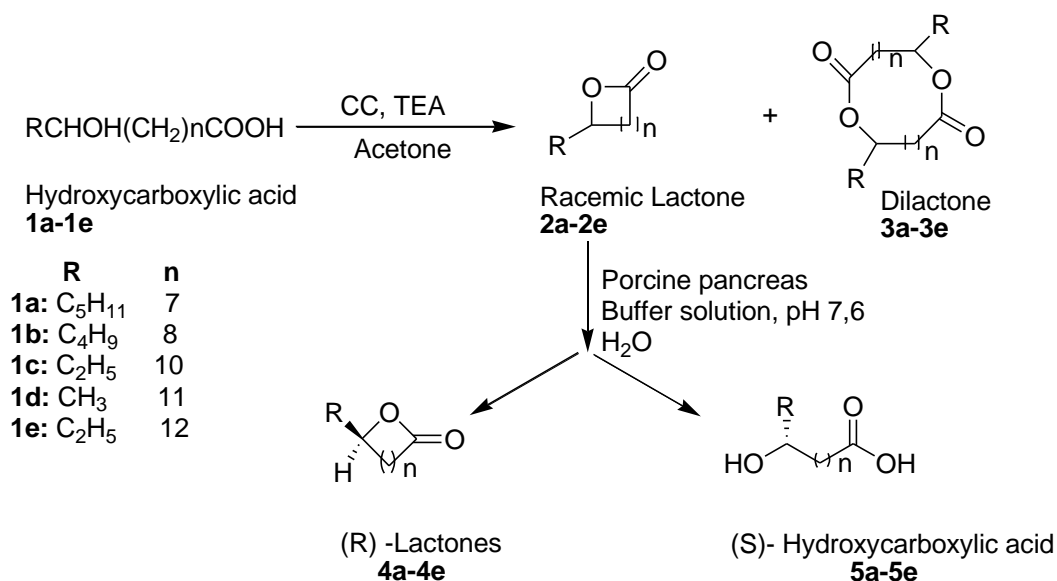
Various synthetic procedures have been declared in the literature for the preparation of racemic and enantiomerically pure medium and large- ring sized lactones. Several methods using reagents like DCC (14), 2,4,6-trichlorobenzoyl chloride (15), 2,2'-dipyridyl disulfide /Ph₃P (16), 1-methyl-2-chloropyridinium iodide / Et₃N (17), 2-Me-6-NO₂-benzoic anhydride (18,19) and cyanuric chloride (20) have been known for the preparation of the lactones from their corresponding hydroxy acids.

Cyanuric chloride method was chosen in this study, because it is an economical and commercially available reagent. This method has been applied for the synthesis of isoambrettolide (20), exaltolide (21), phorocantholide (21,22), pentadecanolide (22) and patutolide (23). According to the literature survey, the synthesized racemic lactones **2a-2e** have not yet been synthesized by cyanuric chloride method. The obtained *R*- lactones **4a-4e** were synthesized by hydrolysis of porcine pancreatic lipase by the first time in this work.

Racemic forms of 12-tetradecanolide (**2c**) and 14-hexadecanolide (**2e**) were obtained before differently from the used method in this study (24). There is no record available about their enantiomeric forms **4c** and **4e**. Information on racemic and chiral 9-tetradecanolide (**2a**) and 13-tetradecanolide (**2d**) is accessible (25-29), but the procedures are not the same. Racemic forms of **2a**, **2c**, **2d** and **2e** were found in the literature but the methods are dissimilar. Chiral **4a**, **4c**, **4d** and **4e** were known compounds but their preparation methods are not similar. Racemic 10 tetradecanolide (**2b**) and chiral (**4b**) are original compounds in this study.

These synthesized racemic and chiral lactones can be used in perfumery, medicine, and chemistry as ionic liquids and chromatographic separators due to their ring size. In previous studies, lactones and their derivatives were used as elastase inhibitors (30, 31), but this

inhibition was carried out there only with small ring lactones. In the future, these mentioned racemic and chiral lactones **2a-2e**, **4a-4e** will be examined for their inhibition of different enzymes especially for their elastase activity, which plays an important and protective role against diseases of lung, arteries, skin, and ligaments.



Scheme 1. Synthesis of medium and large sized racemic and enantiomeric lactones.

EXPERIMENTAL SECTION

General

All reagents were purchased from commercial products and were used without further purification. Acetone and triethylamine were dried with CaCl₂. The reactions were followed up with TLC plate (Merck 60 F-254). Column chromatography was performed on silica gel 60 (70-230 mesh). ¹H-NMR and ¹³C-NMR spectra were moderated in CDCl₃ and booked on a Varian (400 MHz). Mass spectra (ESI) were recorded on a Thermo Finnigan Spectrometer. Infrared (IR) spectra were booked on a Mattson 1000 series spectrometer as thin films between NaCl plates. Optical rotations were measured on an Optical Activity AA-55 digital polarimeter.

General method for the synthesis of chiral lactones

Enzymatic hydrolysis of substrate / PPL of varying the weight ratio and reaction time (entries 1-4) were applied by the conditions described in Table 3. Several suspension amounts of the racemic lactones (2a-e, 100 mg) were incubated at pH 7.6 (citric acid/Na₂HPO₄ buffer solution 0.02 M) and 36 °C in water. The obtained suspension was stirred in an ultrasonic bath. Then, the reaction was finished with the supplementation of CH₂Cl₂ (32) at the time shown in the Table III. The organic layer was separated, washed with distilled water and dried with Na₂SO₄. The solvent was removed *in vacuo*. To offer a mixture (R)-4a-e and (S)-5a-e that was separated with column chromatography (silica gel, hexane/ethyl acetate= 4/1 v:v) to give

lactones in good yield. The obtained lactones that are not UV-active can be seen by the TLC plate dipped into a 5% H₂SO₄ solution and then heated.

(9*R*)-(-)-9-tetradecanolide (**4a**). 58% yield (58 mg) as a colorless oil, hexane/ethyl acetate=4/1 R_f: 0.44. $[\alpha]_D^{20} = -28^\circ$ (c 0.45, CHCl₃). FTFTIR (neat): $\nu_{\max} = 2946, 2865, 1727, 1188 \text{ cm}^{-1}$. ¹H-NMR (400 MHz, CDCl₃): $\delta = 0.84$ (t, *J* = 7.3 Hz, 3H), 0.98-1.1 (m, 2H), 1.2-1.33 (m, 14H), 1.46-1.7 (m, 4H), 2.27 (ddd, *J* = 14.16, 7.8 and 5.3 Hz, 2H), 4.82 (m, 1H) ppm. ¹³C-NMR (125 MHz, CDCl₃): $\delta = 9.9, 22.2, 24.6, 26.4, 28.1, 28.4, 28.6, 28.7, 28.9, 32.6, 34.00, 40.2, 74.00, 172.75$ ppm. MS (EI): *m/e* 227 [M+1]⁺. Anal. Calc. for C₁₄H₂₆O₂: C, 74.29; H, 11.58. Found: C, 74.20; H, 11.52.

(10*R*)-(-)-10-tetradecanolide (**4b**). 54% yield (54 mg) as a colorless oil, hexane/ethyl acetate=4/1 R_f: 0.41 $[\alpha]_D^{20} = -25^\circ$ (c 0.45, CHCl₃). FTIR (neat): $\nu_{\max} = 2919, 2865, 1730, 1212 \text{ cm}^{-1}$. ¹H-NMR (400 MHz, CDCl₃): $\delta = 0.89$ (t, *J* = 6.8 Hz, 3H), 1.18-1.32 (m, 14H), 1.42-1.7 (m, 6H), 2.25 (m, 2H), 4.88 (dddd, *J* = 7.8, 6.8, 6.35 and 3.9 Hz, 1H) ppm. ¹³C-NMR (125 MHz, CDCl₃): $\delta = 12.95, 21.59, 24.12, 24.28, 26.53, 27.66, 27.97, 28.11, 28.30, 32.85, 33.69, 34.12, 76.11, 175.26$ ppm. MS (EI): *m/e* 227 [M+1]⁺. Anal. Calc. for C₁₄H₂₆O₂: C, 74.29; H, 11.58. Found: C, 74.25; H, 11.52.

(12*R*)-(-)-12-tetradecanolide (**4c**). 50% yield (50 mg) as a colorless oil, hexane/ethyl acetate=4/1 R_f: 0.32. $[\alpha]_D^{20} = -26^\circ$ (c 0.45, CHCl₃). FTFTIR (neat): $\nu_{\max} = 2920, 2865, 1728, 1202 \text{ cm}^{-1}$. ¹H-NMR (400 MHz, CDCl₃): $\delta = 0.84$ (t, *J* = 7.3 Hz, 3H), 0.98-1.1 (m, 2H), 1.2-1.33 (m, 14H), 1.46-1.7 (m, 4H), 2.27 (ddd, *J* = 14.16, 7.8 and 5.3 Hz, 2H), 4.82 (m, 1H) ppm. ¹³C-NMR (125 MHz, CDCl₃): $\delta = 9.99, 24.2, 24.6, 26.4, 28.1, 28.4, 28.6, 28.7, 28.9, 32.6, 34.00, 40.2, 74.00, 172.75$ ppm. MS (EI): *m/e* 227 [M+1]⁺. Anal. Calc. for C₁₆H₂₆O₂: C, 74.29; H, 11.58. Found: C, 74.27; H, 11.56.

(13*R*)-(-)-13-tetradecanolide (**4d**). 60% yield (60 mg) as a colorless oil, hexane/ethyl acetate=4/1 R_f: 0.27. $[\alpha]_D^{20} = -33^\circ$ (c 0.45, CHCl₃). FTIR (neat): $\nu_{\max} = 2919, 2865, 1728, 1266, 1104 \text{ cm}^{-1}$. ¹H-NMR (400 MHz, CDCl₃): $\delta = 1.19$ (d, *J* = 6.25 Hz, 3H), 1.22-1.51 (m, 16H), 1.54-1.64 (m, 2H), 1.66-1.72 (m, 1H), 1.94-2.05 (m, 1H), 2.26 (ddd, *J* = 15.09, 7.5 and 4.3 Hz, 1H), 2.34 (ddd, *J* = 15.09, 7.4 and 4.3 Hz, 1H), 4.9 (qdd, *J* = 6.76, 12.25 and 6.25 Hz, 1H) ppm. ¹³C-NMR (125 MHz, CDCl₃): $\delta = 14.49, 23.73, 25.23, 25.99, 29.38, 29.49, 29.78, 29.87, 34.65, 39.63, 39.65, 60.39, 68.44, 174.17$ ppm. MS (EI): *m/e* 227 [M+1]⁺. Anal. Calc. for C₁₄H₂₆O₂: C, 74.29; H, 11.58. Found: C, 74.26; H, 11.52.

(14*R*)-(-)-14-hexadecanolide (**4e**). 56% yield (56 mg) as a colorless oil, hexane/ethyl acetate=4/1 R_f: 0.25. $[\alpha]_D^{20} = -44^\circ$ (c 0.45, CHCl₃). FTIR (neat): $\nu_{\max} = 2919, 2865, 1732, 1185 \text{ cm}^{-1}$. ¹H-NMR (400 MHz, CDCl₃): $\delta = 0.86$ (t, *J* = 7.3 Hz, 3H), 1.1 (m, 2H), 1.2-1.34 (m, 16H),

1.48-1.62 (m, 6H), 2.28 (ddd, $J= 14.65, 7.8$ and 4.3 Hz, 2H), 4.8 (m, 1H) ppm. ^{13}C -NMR (125 MHz, CDCl_3): $\delta= 8.7, 24.34, 24.42, 25.26, 25.95, 26.24, 26.76, 27.95, 28.12, 28.54, 30.48, 32.62, 33.74, 37.10, 74.15, 175.26$ ppm. MS (EI): m/e 254 $[\text{M}]^+$. Anal. Calc. for $\text{C}_{16}\text{H}_{30}\text{O}_2$: C, 75.53; H, 11.89. Found: C, 75.48; H, 11.85.

General method for the synthesis of racemic lactones

0.01 mole of hydroxy acid was placed in a two-necked reaction flask equipped with a magnetic stirrer. It was dissolved in 100 mL of acetone with heating (if necessary) and cooled to room temperature. 0.01 mole of cyanuric chloride and 0.02 mole of triethylamine was added until a clear solution was obtained. After about 20 minutes, a precipitate comes out and gradually increases. The obtained precipitate was filtered. The filtrate was diluted with water and extracted with chloroform. The organic phase was washed with 10% Na_2CO_3 and water, dried by Na_2SO_4 , and evaporated. The colorless oil was purified by flash chromatography to give lactones in excellent yield (20).

9-tetradecanolide (**2a**). This compound is a colorless oil and has 64% yield. The spectroscopic data were identical to that of enantiomeric **4a**.

10-tetradecanolide (**2b**). This compound is a colorless oil and has 73% yield. The spectroscopic data were identical to that of enantiomeric **4b**.

12-tetradecanolide (**2c**). This compound is a colorless oil and has 75% yield. The spectroscopic data were identical to that of enantiomeric **4c**.

13-tetradecanolide (**2d**). This compound is a colorless oil and has 78% yield. The spectroscopic data were identical to that of enantiomeric **4d**.

14-hexadecanolide (**2e**). This compound is a colorless oil and has 54% yield. The spectroscopic data were identical to that of enantiomeric **4e**.

RESULTS AND DISCUSSION

The starting substances 9-, 10-, 12- hydroxytetradecanoic acids and 14-hydroxyhexadecanoic acid (**1a-1e**) were synthesized by NaBH_4 reduction and hydrolysis of their corresponding keto esters, which were prepared by Blaise condensation method (33) and 13-hydroxytetradecanoic acid was obtained according to the acetoacetic ester method with good yields (Table 1) (34, 35).

Table 1: The results of synthesized racemic hydroxy acids (RHOHC(CH₂)_nCOOH (**1a-1e**)).

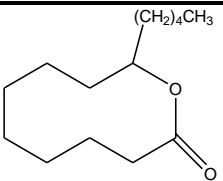
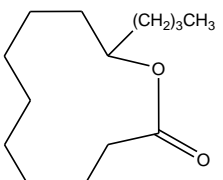
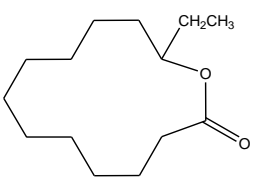
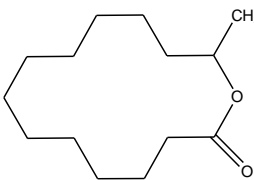
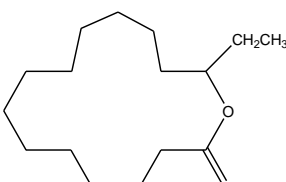
Entry	R	n	Hydroxy Acids	mp (°C)	n_D^{80}	Yield %	*
1	C ₅ H ₁₁	7	1a	69-70	1.4432	80	
2	C ₄ H ₉	8	1b	57-58	1.4410	85	
3	C ₂ H ₅	10	1c	58-59	1.4390	90	
4	CH ₃	11	1d	58-59	1.4405	90	
5	C ₂ H ₅	12	1e	59-60	1.4420	95	

* Isolated yield.

The synthesized hydroxycarboxylic acids were converted to their corresponding racemic lactones by cyanuric chloride method (Scheme 1, Table 2).

The best lactonization yield was found for the molar fraction of hydroxy acid:CC:TEA as 1:1:2. Increased ring size is reduced the efficiency of lactonization yield (Table 2, entries 13-15). The size of alkyl substitution has not played an important role in the lactonization yield. Various acetone amounts were tried to increase of the lactonization reaction yield, the optimal amount was found to be 10 mL (Table 2). The lactonization was carried out at room temperature until the disappearance of hydroxy acid. The reaction was also examined at refluxing temperature for the reduced reaction time, but dilactone was obtained as a by-product in this reaction. Therefore, lactonization was preferred at room temperature. (Table 2).

Table 2: Synthesis of medium- and large-sized racemic lactones.

Entry	R	n	Lactone	Acetone (mL)	Yield (%) ^[b]
1		7	2a	10	65 (19 ^[c])
2				20	64 (20 ^[c])
3				30	63 (18 ^[c])
4		8	2b	10	74.5 (10 ^[c])
5				20	73 (11 ^[c])
6				30	72 (12 ^[c])
7		10	2c	10	76 (17 ^[c])
8				20	75 (18 ^[c])
9				30	74 (19 ^[c])
10		11	2d	10	80 (21 ^[c])
11				20	78 (20 ^[c])
12				30	78.5 (19 ^[c])
13		12	2e	10	56 (9 ^[c])
14				20	54 (10 ^[c])
15				30	53 (11 ^[c])

[a] Conditions, hydroxycarboxylic acids 1 mmol, cyanuric chloride (CC) 1 mmol, triethylamine (TEA) 2 mmol, t= room temperature, reaction time: 24 h. [b] Isolated yield. [c] Dilactone yield.

Choice of lipase enzyme to be used

According to the literature survey made, porcine pancreas lipase was considered to be proper in the enzymes for enzymatic hydrolysis. Moreover, it is advantageous that this enzyme is much more economical than other enzymes. It hydrolyzed the *S* enantiomers making the formations of (*R*)-**4a-4e** by enzyme PPL chosen in this study. The best conditions for synthesis of (*R*)-**4a-4e** in good yields are given in Table 4.

Table 3: Enantioselective resolution of **2a-2e** by PPL.

Entry	<i>(R)</i> - 4a		<i>(R)</i> - 4b		<i>(R)</i> - 4c		<i>(R)</i> - 4d		<i>(R)</i> - 4e	
	$[\alpha]_D^{20}$	Yield ^a	$[\alpha]_D^{20}$	Yield ^a	$[\alpha]_D^{20}$	Yield ^a	$[\alpha]_D^{20}$	Yield ^a	$[\alpha]_D^{20}$	Yield ^a
		%		%		%		%		%
1	-27°	45	-22°	35	-25°	38	-30°	42	-39°	41
2	-28°	58	-25°	54	-26°	50	-33°	60	-44°	56
3	-20°	20	-21°	25	-23°	30	-29°	34	-36°	36
4	-19°	10	-20°	20	-24°	25	-28°	30	-31°	32

^a isolated yields

Table 4: PPL-catalyzed hydrolysis of racemic **2a-2e** with different ratios of substrate/PPL.

Entry	Substrate ^a (mg)/ Suspension ^b (cm ³)	PPL (mg)/ Suspension(cm ³)	Substrate/PPL	Reaction time(h)
1	1,000:56	1,000/56	1:1	7
2	1,000:28	500/28	2:1	7
3	1,000:18.67	333:18.67	3:1	7
4	1,000:9.33	166.6:9.33	6:1	7

^a Racemic 2a-e (1.000 mg) was taken in these procedures.

^b 1 cm³ of suspension, produced from 1 g of lipase and 15 cm³ of water, hydrolyzed 50 mg of trimyristine (36)

The best resolution for **2a-2e** was entry 3. *(R)*-**4a-4e** were synthesized with good yields after 7 h incubation with a substrate/PPL weight ratio 2:1 (Entry 2, Table 4). There are a lot of studies mentioned about chiral lactones that clearly refined by R configuration due to negative optical rotation. Therefore, the synthesized chiral lactones were attributed to be of R configuration according to the measured optical rotations. The configurations of the chiral lactones with negative sign were defined in the literature as *(R)* (25-29).

Therefore, enantioseparation studies were also tried in this work and the enantiospecificity of the resolution was determined after purification of the *(R)*-**4a-4e** by column chromatography. For determination of enantiomeric enrichment (% ee), Cyclodex β-25 m column chiral capillary GC column was used for gas chromatographic separation. Different GC separation conditions were tried, but resolution of *(R)* and *(S)* enantiomers of the obtained lactones were not succeeded. Configuration of the synthesized lactones were assigned due to the optical rotation degrees in the literature (24-28), where lactones with negative optical rotations were defined as *(R)*. Therefore the synthesized lactones in this study were attributed to be of R configuration (Table 3). Synthesized racemic and chiral lactones were obtained for the first time by the method used in this study.

CONCLUSION

In this work, medium- and large-ring racemic **2a-2e** and chiral lactones **4a-4e** were synthesized in good yields. The enzymatic resolution of the synthesized racemic lactones was carried out under mild conditions. The described processes in this study are cheap and environmentally friendly. The purification of the lactones were achieved by column chromatography. The synthesized racemic and chiral lactones **2a-2e** and **4a-4e** mentioned were analyzed by FTIR, ¹H-NMR, ¹³C-NMR, Mass spectra, optical rotation, and C,H analysis. The synthesized racemic and chiral lactones will be examined in the future for their usefulness in food, pharmacy and cosmetic industries. They will be investigated for their inhibition effect of several enzyme types.

ACKNOWLEDGEMENTS

This work was supported by Scientific Research Projects Coordination Unit of Istanbul University. Project number: T-1132/18062001 and YADOP-5161.

REFERENCES

1. Siegel SM. Inhibitory activity of the phenolic glucoside psilotin and its several by gibberellic acid and thiols. *Phytochem.* 1976; 15: 566-7.
2. Ohloff G. Recent developments in the field of naturally occurring aroma components. *Prog. Chem. Org. Nat. Prod.* 1978; 35: 431-527.
3. Davies-Coleman MT, Rivett DEA. Naturally occurring 6-substituted 5,6-dihydro- α -pyrones. *Chem. Org. Nat.* 1989; 55: 1-35.
4. Fukusaki E, Senda S, Nakazono Y, Omata T. Lipase-catalyzed kinetic resolution of methyl 4-hydroxy-5-tetradecynoate and its application to a facile synthesis of Japanese beetle pheromone. *Tetrahedron* 1991; 47: 6223-30.
5. Mori K. Synthesis of optically active pheromones. *Tetrahedron* 1989; 45: 3233-98.
6. Fujita T, Nishimura H, Kaburagi K, Mizutani J. Plant-growth-inhibiting α -pyrones from *Alpina spiciosa*. *Phytochem.* 1994; 36: 23-7.
7. Nyandat E, Rwekika E, Galeffi C, Palazzino G, Nicoletti M. Olinioside, 5-(4'-O- β -D-glucopyranosyl)-caffeoyloxy-5,6-dihydro-4-methyl-(2H)-pyran-2-one from *Olinia usambarensis*. *Phytochem.* 1993; 33: 1493-6.
8. Adrianaivoravelona JO, Sahpaz S, Terreaux C, Hostettmann K, Stoeckli-Evans H, Rasolondramanitra H. Two 6-substituted 5,6-dihydro- α -pyrones from *Ravensara anisata*. *Phytochem.* 1999; 52: 265-9.
9. Pereda-Miranda R, Garcia M, Delgado G. Structure and stereochemistry of four α -pyrones from *Hyptis oblongifolia*. *Phytochem.*, 1990; 29: 2971-4.

10. Nicolaou KC, Rodrigues RM, Mitchell HJ, Suzuki H, Fylaktakidou KC, Baudoin O, van Delft FL. Total synthesis of evernimicin 13,384-1, part 1: Retrosynthetic analysis of the A1B(A)C fragment. *Chem. Eur. J.* 2000; 6: 3095-115.
11. Jodynis-Liebert J, Murias M, Bloszyk E. Effect of sesquiterpene lactones and antioxidant enzymes and some drug-metabolizing enzymes in rat liver and kidney. *Planta Med.* 2009; 66: 199-205.
12. Drewes SE, Schlapelo BM, Horn MM, Scott-Shaw V, Sandor O. 5,6-Dihydro- α -pyrones and two bicyclic tetrahydro- α -pyrone derivatives from *Cryptocarya latifolia*. *Phytochem.* 1995; 38: 1427-30.
13. (a) Drauz K, Waldmann H. *Enzyme Catalysis in Organic Synthesis*. VCH: Weinheim, 1995.
(b) Bornscheuer UT, Kazlauskas RJ. *Hydrolases in Organic Synthesis*, Wiley- VCH: Weinheim, 1999.
14. Boden EP, Keck GE. Proton-transfer steps in Steglich esterification: a very practical new method for macrolactonization, *J.Org.Chem.* 1985; 50: 2394.
15. Inanaga J, Hirata K, Saeki L, Katsuki T, Yamaguchi M. A rapid esterification by mixed anhydride and its application to large-ring lactonization. *Bull. Chem. Soc. Jpn.* 1979; 52: 1989.
16. Corey EJ, Nicolaou KC. Efficient and mild lactonization method for the synthesis of macrolides. *J.Am.Chem.Soc.* 1974; 96: 5614-6.
17. Mukaiyama T, Usui M, Saigo K. The facile synthesis of lactones. *Chem. Lett.* 1976; 5: 49-50.
18. Shiina I, Kubota M, Ibuka R. A novel and efficient macrolactonization of ω -hydroxycarboxylic acids using 2-methyl-6-nitrobenzoic anhydride (MNBA). *Tetrahedron Lett.* 2002; 43: 7535-9.
19. Shiina I, Kubota M, Oshiumi H, Hashizume M. An Effective Use of Benzoic Anhydride and Its Derivatives for the Synthesis of Carboxylic Esters and Lactones: A Powerful and Convenient Mixed Anhydride Method Promoted by Basic Catalysts. *J.Org.Chem.* 2004; 69: 1822-30.
20. Venkataraman K, Wagle DR. Cyanuric chloride, a useful reagent for macrocyclic lactonization. *Tetrahedron Lett.* 1980; 21: 1893-6.
21. Cossy J, Peten JP. A three step synthesis of exaltolide and phoracantholide I. *Tetrahedron Lett.* 1986; 27: 2369-70.
22. Cossy J, Pete JP. Synthesis of medium-ring lactones: Application to the synthesis of 15-pentadecanolide and phoracantholide I. *Bull. Soc. Chim.Fr.* 1988; 6: 989-94. CODEN: BSCFAS; ISSN: 0037-8968; French
23. Ayyangar NR, Chanda B, Wakharkar RD, Kasar RA. A short convergent synthesis of Patulolide A. *Synth.Commun.* 1988; 18: 2103-19.
24. Hinkamp L, Schaefer H, Wippich B, Luftmann H. Regioselective conversion of nonactivated carbon-hydrogen bonds. VI. Selective ω - to (ω -2)-chlorination of fatty acids via adsorption on alumina. *Liebigs Annalen der Chemie* 1992; 6: 559-63.
25. Noda Y, Kashin H. Synthesis of Both Enantiomers of Four Different Macrocyclic Lactones. *Heterocycles* 1998; 48: 5-10.

26. Stanchev S, Hesse M. Synthesis of the enantiomerically enriched macrocyclic lactones (+)-(S)- and (-)-(R)-phorocantholide I and (+)-(S)-tetradecan-13-olide. *Helv. Chim. Acta* 1990; 73: 460-7.
27. Bestmann H.J, Kellermann W. Synthese der natürlichen R-(-)Enantiomere dreier Galbanum-Harz Macrolide. *Synthesis* 1994; 12: 1257-61.
28. Kaiser R, Lamparsky D. Neue Macrolide und einige sesquiterpen-derivative aus dem Galbanum-Harz. *Helv.Chim.Acta.* 1978; 61: 2671-80.
29. Bollbuck B, Kraft P, Tochtermann W. Nature-like odorants by stereoselective ring enlargement of cyclohexanone and cyclododecanone. *Tetrahedron* 1996; 52: 4581-92.
30. Siedle B, Gustavsson L, Johansson S, Murillo R, Castro V, Bohlin V, Merfat I. The effect of sesquiterpene lactones on the release of human neutrophil elastase. *Biochem. Pharmacol.* 2003; 65: 897-903.
31. Dou D, He G, Li Y, Lai Z, Wei L, Alliston KR, Lushington GH, Eichhorn DM, Groutas WC. Utilization of the 1,2,3,5-thiatriazolidin-3-one 1,1-dioxide scaffold in the design of potential inhibitors of human neutrophil proteinase 3. *Bioorg. Med. Chem.* 2010; 18: 1093-102.
32. Baspinar Küçük H, Yusufoglu A. Enantioselective synthesis of 3-hydroxytetradecanoic acid and its methyl ester enantiomers as new antioxidants and enzyme inhibitors. *Monatsh Chem.* 2013; 144: 1087-91.
33. Blaise EE. Blaise Reactions. *C.R.Hebd. Seacens Acad. Sci.* 1913; 157: 1440
34. Stenhagen SS, Stenhagen E. Synthesis of higher beta keto acids with 9 to 24 carbon atoms. *Arkiv Kemi Mineral Geol. A* 1945; A20: No:19.
35. Çelik H. Synthesis of monoketo and monohydroxy eicosanoic acids and esters with substituents at odd-numbered (3-13) carbons. *J. Serb. Chem. Soc.* 2002; 67: 473-80.
36. Yanardağ R, Bapçum A. *Chim Acta Turc.* 1996; 24: 15.



Microwave-Assisted Synthesis and Biological Evaluation of Some Coumarin Hydrazides

Fatih Yılmaz¹  , Özlem Faiz²  

¹Recep Tayyip Erdogan University, Vocational School of Technical Studies, Department of Chemistry and Chemical Processing Technology, 53100, Rize, Turkey

²Recep Tayyip Erdogan University, Faculty of Art and Sciences, Department of Chemistry, 53100, Rize, Turkey

Abstract: In this work, 15 different coumarin hydrazides were successfully synthesized and screened for their antioxidant and antilipase activities. To do this, firstly, salicylaldehyde derivatives and Meldrum's Acid were reacted in absolute ethanol with catalytic amount of pyridine to obtain coumarin-3-carboxylic acid derivatives (**1a-e**). Then, these compounds were treated with 1H-benzotriazole in dichloromethane by using thionyl chloride to synthesize benzotriazole derivatives (**2a-e**). Then, compounds **2a-e** were reacted with three commercial hydrazides (nicotinic hydrazide, benzhydrazide, and phenyl acetichydrazide) in ethanol by using microwave irradiation and conventional heating procedures to obtain final products (**3-5a-e**). Finally, these compounds were tested for their anti-oxidant and anti-lipase activities. The structure of newly synthesized compounds was identified by IR, ¹H NMR, ¹³C NMR, and elemental analysis data.

Keywords: Coumarin, Hydrazide, Porcine pancreatic lipase, Antioxidant.

Submitted: February 06, 2018. **Accepted:** March 16, 2018.

Cite this: Yılmaz F, Faiz Ö. Microwave-Assisted Synthesis and Biological Evaluation of Some Coumarin Hydrazides. JOTCSA. 2018;5(2):551-68.

DOI: <http://dx.doi.org/10.18596/jotcsa.390928>.

***Corresponding author:** Fatih YILMAZ , **E-mail:** fyilmaz@erdogan.edu.tr (telephone: +90 (464) 228 00 22, fax: +90 (464) 228 00 25)

INTRODUCTION

Since the first publication on microwave synthesis in 1986, the use of microwave heating in organic synthesis has become so popular that it has been termed as the Bunsen burner of the 21st century. In many respects, this technique is superior to classical heating because it reduces the reaction time and provides higher yields and purity (1-5).

Coumarins (known as benzopyran-2-ones) are a family of lactones and they are the most abundant secondary metabolite. They show important biological activities such as antibacterial (6, 7), antifungal (8, 9), anti-tubercular (10, 11), antitumor (12), antioxidant (13), and [anti-HIV](#) (14). Also, coumarins are used as food additive and cosmetics industry (15). The general commercial application of coumarins is the use of dispersed fluorescent brightening agents and as dyes for tuning lasers (16-18). A few coumarin-based derivatives acenocoumarol, dicoumarolum, and hymecromone which are approved for therapeutic purposes in the clinic are given below ([Figure 1.](#)) (10). This broad spectrum of biological activities and successful usage of coumarin derivatives in medicinal and industrial chemistry have further inspired more research on coumarin derivatives. In addition to numerous activities of coumarin derivatives, some enzyme inhibitors were reported such as α -glucosidase, anti-lipase, carbonic anhydrase, urease and acetylcholinesterase (19-27).

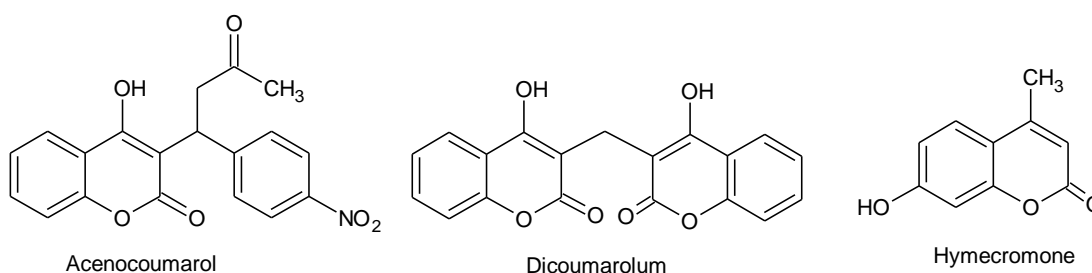


Figure 1. Acenocoumarol, Dicoumarolum, and Hymecromone.

Recent researches have proved that coumarin hydrazones have pharmacologically powerful properties. Nasr *et al.* reported *in vitro* anticancer activity of some coumarin hydrazide-hydrazone derivatives and found that one of the compounds could be a potent anticancer drug to overcome drug resistance in cancer (26, 28, 29). Also, Karatas *et al.* have showed that coumarins bind to the active pocket of the enzyme in a similar carbonic anhydrase enzyme study of coumarin by molecular docking study (19).

In our previous works, we have already synthesized coumarin-triazole and coumarin-quinazolinone hybrid molecules and investigated their biological activities. Some of the compounds showed potent antitumor, antilipase and α -glucosidase activities (26, 27). In these works, we have found that coumarin has a positive effect on antitumor, antilipase and α -

glucosidase activities. In the present study, we focused on the synthesis of coumarin hydrazides and investigation of their antioxidant and lipase inhibition activities (27, 30).

MATERIALS AND METHODS

Chemistry

All reaction progress was monitored by TLC on silica gel plates (Merck 60, F₂₅₄, 0.2 mm). The melting points were determined on capillary tubes on Stuart SMP30 melting point apparatus and are uncorrected. The FTIR spectra were recorded on a Perkin-Elmer 100 FTIR spectrometer as KBr pellets. ¹H and ¹³C NMR spectra (400 and 100 MHz, respectively) were obtained using a Varian-Mercury (tetramethylsilane as the internal standard) and the chemical shifts are expressed in δ values (ppm). The experiments were carried out in microwave process vials (30 mL) with control of the temperature by infrared detection temperature sensor. It was monitored by a computer and maintained at a constant value by a discrete modulation of delivered microwave power. After the completion of the reaction, the vial was cooled to 60 °C via air jet cooling.

EXPERIMENTAL SECTION

General procedure for the synthesis of compounds 1a-e

A solution of corresponding salicylaldehyde derivative (0.01 mol) and 2,2-dimethyl-1,3-dioxane-4,6-dione (Meldrum's acid) (1.58 g, 0.011 mol) in absolute ethanol (50 mL) and pyridine (0.5 mL) was refluxed in a round-bottomed flask for 6 h. After the reaction was completed (monitored by TLC, eluent ethyl acetate–hexane, 4:1 v:v), the solvent was evaporated under reduced pressure. The obtained solid was washed with H₂O and recrystallized from a mixture of EtOH–H₂O, 3:2.

2-Oxo-2H-chromene-3-carboxylic acid (1a). Yield: 1.39 g (73%). M.P.: 189–190°C (M.P.: 188°C (31)).

6-Chloro-2-oxo-2H-chromene-3-carboxylic acid (1b). Yield: 1.57 g (70%). M.P.: 200-201 °C (M.P.: 198-199 °C (32)).

6-Bromo-2-oxo-2H-chromene-3-carboxylic acid (1c). Yield: 1.80 g (67%). M.P.: 195–196°C (M.P.: 194–196°C (33)).

6,8-Dichloro-2-oxo-2H-chromene-3-carboxylic acid (1d). Yield: 1.80 g (67%).M.P.: 225-226 °C (M.P.: 220-224 °C (34)).

7-diethylamino-2-oxo-2H-chromene-3-carboxylic acid (1e). Yield: 1.88 g (67%). M.P.: 225-226 °C (M.P.: 224-225 °C (35)).

General procedure for the synthesis of compounds 2a-e

Thionyl chloride (1.78 g, 0.015 mol) was added to a solution of 1H-benzotriazole (5.95 g, 0.05 mol) in CH₂Cl₂ (75 mL). The mixture was stirred for 30 min at room temperature. Then the corresponding coumarin-3-carboxylic acid **1a-e** (0.01 mol) was added and the reaction mixture was stirred for 12 hours at room temperature. The precipitate was removed by filtration, and the filtrate was evaporated under reduced pressure. The residue was diluted with CH₂Cl₂ (100 mL), and the solution was washed with 10% Na₂CO₃ solution (50 mL) and 4 N HCl (50 mL) and dried over MgSO₄. Removal of the solvent under reduced pressure gave compounds **2a-e**, which were recrystallized from CH₂Cl₂-hexane, 1:1.

3-(1H-Benzotriazol-1-ylcarbonyl)-2H-chromen-2-one (2a). Yield: 2.12 g (73%). M.P.: 179-180°C (M.P.: 176-177 °C (36)).

3-(1H-Benzotriazol-1-ylcarbonyl)-6-chloro-2H-chromen-2-on (2b) Yield: 2.20 g (63%). M.P.: 248-249 °C.

3-(1H-Benzotriazol-1-ylcarbonyl)-6-bromo-2H-chromen-2-one (2c). Yield 2.52 g (68%). M.P.: 250-251 °C.

3-(1H-Benzotriazol-1-ylcarbonyl)-6,8-dichloro-2H-chromen-2-on (2d). Yield: 2.34 g (65%). M.P.: 263-264 °C.

3-(1H-Benzotriazol-1-ylcarbonyl)-7-diethylamino-2H-chromen-2-on (2e). Yield: 2.46 g (68%). M.P.: 210-211°C (M.P.: 212-214 °C (37)).

General procedure for the synthesis of compounds 3-5a-e

Conventional method: A solution of compounds **2a-e** (0.01 mol) in absolute ethanol (15 mL) and corresponding hydrazide derivative (0.011 mol) was taken in a round-bottomed flask. The mixture was refluxed for 4h. After the completion of the reaction, the mixture was cooled to room temperature and the product appeared as a white solid. It was filtered and washed with ethanol to obtain the pure product.

Microwave method: Compounds **2a-e** (0.01 mol) and corresponding hydrazide derivative (0.011 mol) were taken in a microwave process vial (30 mL) and dry ethanol (5 mL) was added. Then, the mixture was irradiated in microwave at 135 °C for 15 min at 200 W maximum power. After the completion of the reaction, the mixture was taken in the beaker with hot ethanol, and

a product appeared as a white solid. It was filtered and washed with ethanol to obtain the pure product.

***N'*-(2-Oxo-2*H*-1-benzopyran-3-ylcarbonyl)pyridine-3-carbohydrazide (3a):** M.P.: 269–270 °C (38), FTIR (KBr): 3365, 3232 (NH), 1709, 1681, 1640 (C=O), 1190 (C-O) cm⁻¹. ¹H NMR (400 MHz, DMSO-d₆): 7.43 (s, 1H, Ar-H), 7.52 (d, J=6.4 Hz, 1H, Ar-H), 8.00 (d, J=6.8 Hz, 1H, Ar-H), 8.27 (d, J=9.2 Hz, 1H, Ar-H), 8.75 (d, J=7.6 Hz, 2H, Ar-H), 8.90 (d, J=8.4 Hz, 2H, Ar-H), 9.05 (s, 1H, coumarin C-4H), 10.61 (s, 1H, NH), 11.20 (s, 1H, NH). ¹³C NMR (100MHz, DMSO-d₆): 116.72, 118.74, 118.82, 124.11, 128.36, 130.86, 134.92, 135.81, 148.51, 149.03, 153.00 (coumarin C-3), 154.47 (coumarin C-4), 160.17 (C=O), 160.57 (C=O), 163.79 (C=O). Elemental Analysis: Calculated C₁₆H₁₁N₃O₄: C, 62.14; H, 3.58; N, 13.59. Found: C, 62.10; H, 3.51; N, 13.50.

***N'*-(6-Chloro-2-oxo-2*H*-1-benzopyran-3-ylcarbonyl)pyridine-3-carbohydrazide (3b):** M.P.: 284–285 °C, FTIR (KBr): 3201, 3039 (NH), 1706, 1683 (C=O), 1192 (C-O) cm⁻¹. ¹H NMR (400 MHz, DMSO-d₆): 7.39 (s, 1H, Ar-H), 7.62 (d, J=6.0 Hz, 1H, Ar-H), 8.00 (d, J=6.0 Hz, 1H, Ar-H), 8.28 (d, J=9.2 Hz, 1H, Ar-H), 8.69 (d, J=7.6 Hz, 1H, Ar-H), 8.96 (d, J=8.0 Hz, 2H, Ar-H), 9.03 (s, 1H, coumarin C-4H), 10.55 (s, 1H, NH), 11.24 (s, 1H, NH). ¹³C NMR (100 MHz, DMSO-d₆): 121.07, 121.18, 121.37, 124.11, 128.31, 128.75, 129.21, 133.48, 135.82, 146.84, 149.02, 153.0 (coumarin C-4), 158.76 (coumarin C-3), 160.11 (C=O), 163.94 (C=O), 165.79 (C=O). Elemental analysis: Calculated for C₁₆H₁₀ClN₃O₄: C, 55.91; H, 2.93; N, 12.23. Found: C, 55.93; H, 2.95; N, 12.27.

***N'*-(6-Bromo-2-oxo-2*H*-1-benzopyran-3-ylcarbonyl)pyridine-3-carbohydrazide (3c):** M.P.: 289–290 °C, FTIR (KBr): 3363, 3282 (NH), 1739, 1694, 1662 (C=O), 1240 (C-O) cm⁻¹. ¹H NMR (400 MHz, DMSO-d₆): 7.35 (s, 1H, Ar-H), 7.80 (d, J=6.4 Hz, 1H, Ar-H), 8.03 (d, J=6.8 Hz, 1H, Ar-H), 8.20 (d, J=9.0 Hz, 1H, Ar-H), 8.73 (d, J=7.6 Hz, 1H, Ar-H), 8.80 (d, J=8.0 Hz, 2H, Ar-H), 9.05 (s, 1H, coumarin C-4H), 10.50 (s, 1H, NH), 11.20 (s, 1H, NH). ¹³C NMR (100 MHz, DMSO-d₆): 117.17, 119.01, 120.63, 124.11, 128.34, 132.66, 135.82, 137.02, 147.68, 148.20, 149.02 (coumarin C-4), 155.64 (coumarin C-3), 156.31 (C=O), 160.35 (C=O), 163.90 (C=O). Elemental analysis: Calculated for C₁₆H₁₀BrN₃O₄: C, 49.51; H, 2.60; N, 10.83. Found: C, 49.55; H, 2.57; N, 10.76.

***N'*-(6,8-Dichloro-2-oxo-2*H*-1-benzopyran-3-ylcarbonyl)pyridine-3-carbohydrazide (3d):** M.P.: 292–293 °C, FTIR (KBr): 3199, 3040 (NH), 1706, 1684 (C=O), 1192 (C-O) cm⁻¹. ¹H NMR (400 MHz, DMSO-d₆): 7.54 (s, 1H, Ar-H), 8.09–8.15 (m, 2H, Ar-H), 8.25 (s, 1H, Ar-H), 8.56–8.76 (m, 2H, Ar-H), 9.04 (s, 1H, coumarin C-4H), 10.60 (s, 1H, NH), 11.10 (s, 1H, NH). ¹³C NMR (100 MHz, DMSO-d₆): 121.20, 121.37, 124.12, 128.12, 128.32, 128.75, 129.20, 133.49, 135.83, 146.82, 148.92, 149.02 (coumarin C-3), 153.04 (coumarin C-4), 158.75 (C=O), 160.14 (C=O), 163.95 (C=O). Elemental analysis: Calculated for C₁₆H₉Cl₂N₃O₄: C, 50.82; H, 2.40; N, 10.78.

11.11. Found: C, 50.79; H, 2.37;N,11.11.

***N'*-[7-(diethylamino)-2-oxo-2*H*-1-benzopyran-3-carbonyl]pyridine-3-carbohydrazide (3e):** M.P.: 266–267 °C (266–267 °C (16)), FTIR (KBr): 3268 (NH), 1685,1644 (C=O), 1190 (C-O) cm⁻¹. ¹H NMR (400 MHz, DMSO-d₆): 1.13 (t, J=6.8 Hz, 6H, CH₃), 3.90 (q, J=6.8 Hz, 4H, CH₂), 6.63 (s, 1H,Ar-H), 6.82 (d, J=6.4 Hz, 1H, Ar-H), 7.55 (d, J=6.8Hz, 1H, Ar-H), 7.73(d, J=9.2 Hz,1H,Ar-H),8.24(d, J=7.6 Hz, 1H, Ar-H), 8.74(d, J=8.4 Hz, 2H, Ar-H), 9.03 (s, 1H, coumarin C-4H), 10.47 (s, 1H, NH), 11.12 (s, 1H,NH).¹³C NMR (100 MHz,DMSO-d₆):12.77 (2CH₃), 44.87 (2CH₂), 96.38, 108.13, 108.29, 110.81, 124.06, 128.45, 132.33, 135.79, 148.94, 149.01 (coumarinC-4), 152.90, 153.31 (coumarin C-3), 157.94 (C=O), 161.65 (C=O), 161.84 (C=O), 163.79 (C=O). Elemental analysis: Calculated for C₂₀H₂₀N₄O₄: C, 63.15; H, 5.30; N, 14.73. Found: C, 63.08; H, 5.25; N, 14.68.

***N'*-Benzoyl-2-oxo-2*H*-1-benzopyran-3-ylcarbohidrazide (4a):** M.P.: 239-240°C (38), FTIR (KBr): 3266, 3112 (NH), 1706, 1681 (C=O), 1188 (C-O) cm⁻¹. ¹H NMR (400 MHz, DMSO-d₆): 7.42 (s, 1H, Ar-H), 7.54 (t, J=6.8 Hz, 1H, Ar-H), 7.61 (d, J=9.2 Hz, 2H, Ar-H), 7.73 (t, J=7.6 Hz, 2H, Ar-H), 8.00(d, J=8.4 Hz, 2H, Ar-H), 8.03 (s, 1H, Ar-H), 8.89 (s, 1H, coumarin C-4H), 10.57 (s, 1H, NH), 10.93 (s, 1H, NH). ¹³C NMR (100 MHz, DMSO-d₆): 116.70, 118.73, 118.87, 125.68, 128.06 (2C), 128.94 (2C), 130.83, 132.42, 134.88, 148.53 (coumarin C-4), 154.43 (coumarin C-3), 160.21 (C=O), 160.62 (C=O), 165.32 (C=O). Elemental analysis: Calculated for C₁₇H₁₂N₂O₄: C, 66.23; H, 3.92; N, 9.09. Found: C,66.29;H,3.82;N,9.00.

***N'*-Benzoyl-6-chloro-2-oxo-2*H*-1-benzopyran-3-ylcarbohydrazide (4b):** M.P.:266–267 °C, FTIR (KBr): 3326, 3184 (NH), 1688, 1648 (C=O), 1135 (C-O) cm⁻¹. ¹H NMR (400 MHz, DMSO-d₆): 7.49 (s, 2H,Ar-H), 7.55 (d, J=6.6Hz, 2H, Ar-H), 7.90 (d, J=9.2 Hz, 2H, Ar-H), 8.74 (d, J=8.4 Hz,2H, Ar-H), 8.82 (s, 1H, coumarin C-4H), 10.47 (s, 1H, NH), 10.96 (s,1H,NH).¹³C NMR (100 MHz, DMSO-d₆): 121.20, 121.36, 128.06, 128.73 (2C), 128.95 (2C), 129.19, 132.45, 133.45, 146.73, 148.90 (coumarin C-4) (coumarin C-3), 158.76 (C=O), 160.17 (C=O), 165.34 (C=O). Elemental analysis: Calculated for C₁₇H₁₁ClN₂O₄: C, 59.57; H, 3.23; N, 8.17. Found: C, 59.65; H, 3.29; N, 8.11.

***N'*-Benzoyl-6-bromo-2-oxo-2*H*-1-benzopyran-3-ylcarbohydrazide (4c):** M.P.: 258–259 °C (Cas No: 322414-14-2), FTIR (KBr): 3320, 3085 (NH), 1715, 1654 (C=O), 1190 (C-O) cm⁻¹. ¹H NMR (400 MHz, DMSO-d₆):7.47 (d, J=6.6 Hz, 2H, Ar-H), 7.21 (d, J=6.0 Hz ,2H, Ar-H), 7.70 (d, J=9.2Hz, 1H, Ar-H), 8.10 (d, J=7.6 Hz, 1H, Ar-H), 8.76 (d, J=8.4 Hz, 2H, Ar-H), 8.82 (s, 1H, coumarin C-4H), 10.48 (s, 1H, NH), 10.95 (s, 1H, NH). ¹³C NMR (100 MHz, DMSO-d₆): 117.18, 118.98, 120.98, 121.14, 121.60, 128.05 (2C), 128.93 (2C), 132.44, 132.63, 136.97, 147.11 (coumarin C-4), 153.48 (coumarin C-3), 159.68 (C=O), 160.37 (C=O), 165.31 (C=O). Elemental analysis: Calculated for C₁₇H₁₁BrN₂O₄: C, 52.74; H, 2.86; N, 7.24. Found: C, 52.70;

H, 2.80; N, 7.21.

***N'*-Benzoyl-6,8-dichloro-2-oxo-2*H*-1-benzopyran-3-ylcarbohydrazide (4d):** M.P.: 269–271 °C, FTIR (KBr): 3156, 3030 (NH), 1723, 1645 (C=O), 1190 (C-O) cm⁻¹. ¹H NMR (400 MHz, DMSO-d₆): 7.54 (s, 1H, Ar-H), 8.11 (d, J=6.0 Hz, 2H, Ar-H), 8.25 (d, J=9.2 Hz, 1H, Ar-H), 8.74–8.82 (m, 3H, Ar-H), 9.05 (s, 1H, coumarin C-4H), 10.15 (s, 1H, NH), 11.11 (s, 1H, NH). ¹³C NMR (100 MHz, DMSO-d₆): 121.18, 121.36, 124.11 (2C), 128.31 (2C), 128.73, 129.18, 133.47, 135.81, 146.80, 148.90, 148.99 (coumarin C-4), 153.02 (coumarin-C-3), 158.73 (C=O), 160.12 (C=O), 163.93 (C=O). Elemental analysis: Calculated for C₁₇H₁₀Cl₂N₂O₄: C, 54.13; H, 2.67; N, 7.43. Found: C, 54.10; H, 2.61; N, 7.39.

***N'*-Benzoyl-7-(diethylamino)-2-oxo-2*H*-chromen-3-ylcarbohydrazide (4e):** M.P.: 263–264 °C, (263–264 °C (16)), FTIR (KBr): 3326, 3264 (NH), 1688, 1648 (C=O), 1191 (C-O) cm⁻¹. ¹H NMR (400 MHz, DMSO-d₆): 1.12 (t, J=6.8 Hz, 6H, CH₃), 3.48 (q, J=6.8 Hz, 4H, CH₂), 6.62 (s, 1H, Ar-H), 6.81 (d, J=6.8 Hz, 1H, Ar-H), 7.49 (t, J=7.2 Hz, 2H, ArH), 7.57 (d, J=7.2 Hz, 1H, Ar-H), 7.72 (d, J=6.8 Hz, 1H, ArH), 7.92 (d, J=6.8 Hz, 2H, Ar-H), 8.70 (s, 1H, coumarin C-4H), 10.40 (s, 1H, NH), 10.85 (s, 1H, NH). ¹³C NMR (100 MHz, DMSO-d₆): 12.75 (2CH₃), 44.87 (2CH₂), 96.36, 108.11, 108.41, 110.79, 128.01 (2C), 128.91 (2C), 132.31, 132.66, 148.89 (coumarin C-4), 153.28 (coumarin C-3), 157.91 (C=O), 161.76 (C=O), 165.27 (C=O). Elemental analysis: Calculated for C₂₁H₂₁N₃O₄: C, 66.48; H, 5.58; N, 11.08. Found: C, 66.39; H, 5.50; N, 11.01.

2-Oxo-*N'*-(phenylacetyl)-2*H*-1-benzopyran-3-ylcarbohydrazide (5a): M.P.: 253–254 °C (Cas No: 505065-35-0), FTIR (KBr): 3231, 3048 (NH), 1703, 1664 (C=O), 1206 (C-O) cm⁻¹. ¹H NMR (400 MHz, DMSO-d₆): 3.58 (s, 2H, CH₂), 7.22 (s, 1H, Ar-H), 7.39 (s, 2H, Ar-H), 7.72 (d, J=9.2 Hz, 2H, Ar-H), 7.80 (d, J=7.6 Hz, 2H, Ar-H), 8.00 (d, J=8.4 Hz, 2H, Ar-H), 8.87 (s, 1H, coumarin C-4H), 10.68 (s, 1H, NH), 11.04 (s, 1H, NH). ¹³C NMR (100 MHz, DMSO-d₆): 40.23 (CH₂), 116.68, 118.43, 125.67, 127.02, 128.66 (2C), 128.96 (2C), 129.44, 129.52, 130.78, 134.85, 136.00, 148.36 (coumarin C-4), 154.36 (coumarin C-3), 158.83 (C=O), 160.34 (C=O), 167.88 (C=O). Elemental analysis: Calculated for C₁₈H₁₄N₂O₄: C, 67.07; H, 4.38; N, 8.69. Found: C, 67.01; H, 4.33; N, 8.62.

6-Chloro-2-oxo-*N'*-(phenylacetyl)-2*H*-1-benzopyran-3-ylcarbohydrazide (5b): M.P.: 253–254 °C, FTIR (KBr): 3238, 3054 (NH), 1702, 1681 (C=O), 1189 (C-O) cm⁻¹. ¹H NMR (400 MHz, DMSO-d₆): 3.56 (s, 2H, CH₂), 7.22–7.31 (m, 5H, Ar-H), 8.10 (m, 2H, Ar-H), 8.81 (s, 1H, coumarin C-4H), 10.59 (s, 1H, NH), 11.03 (s, 1H, NH). ¹³C NMR (100 MHz, DMSO-d₆): 39.32 (CH₂), 120.71, 121.18, 121.35, 127.02, 128.68, 128.72, 129.22 (2C), 129.52 (2C), 133.43, 135.94, 146.61 (coumarin C-4), 148.79 (coumarin C-3), 158.41 (C=O), 158.92 (C=O), 168.01 (C=O). Elemental analysis: Calculated for C₁₈H₁₃ClN₂O₄: C, 60.60; H, 3.67; N, 7.85. Found: C, 60.53; H, 3.60; N, 7.76.

6-Bromo-2-oxo-N'-(phenylacetyl)-2H-1-benzopyran-3-ylcarbohydrazide (5c): M.P.: 250–252 °C (Cas No: 353473-63-9), FTIR (KBr): 3274, 3100 (NH), 1715, 1680 (C=O), 1187 (C-O) cm^{-1} . ^1H NMR (400 MHz, DMSO- d_6): 3.33 (s, 2H, CH_2), 7.22-7.33(m, 4H, Ar H), 7.48 (s, 1H, Ar-H), 7.88 (d, $J=9.2$ Hz, 1H, Ar-H), 8.23 (d, $J=7.6$ Hz, 2H, Ar-H), 8.82 (s, 1H, coumarin C-4H), 10.59 (s, 1H, NH), 11.17 (s, 1H, NH). ^{13}C NMR (100 MHz, DMSO- d_6): 39.33 (CH_2), 117.18, 119.72, 120.61, 127.02, 128.72 (2C), 129.51 (2C), 132.59, 135.98, 136.94, 146.95 (coumarin C-4), 153.40 (coumarin C-3), 158.62 (C=O), 159.81 (C=O), 167.93(C=O). Elemental analysis: Calculated for $\text{C}_{18}\text{H}_{13}\text{BrN}_2\text{O}_4$: C, 53.89; H, 3.27; N, 6.98. Found: C, 53.81; H, 3.20; N, 6.91.

6,8-Dichloro-2-oxo-N'-(phenylacetyl)-2H-1-benzopyran-3-ylcarbohydrazide (5d): M.P.: 250–252 °C, FTIR (KBr): 3187, 3056 (NH), 1700, 1685 (C=O), 1190 (C-O) cm^{-1} . ^1H NMR (400 MHz, DMSO- d_6): 3.56 (s, 2H, CH_2), 7.22-7.33 (m, 5H, Ar-H), 7.46 (d, $J=6.8$ Hz, 1H, Ar-H), 7.89 (d, $J=9.6$ Hz, 1H, Ar-H), 8.82 (s, 1H, coumarin C-4H), 10.64 (s, 1H, NH), 11.03 (s, 1H, NH). ^{13}C NMR (100 MHz, DMSO- d_6): 40.36 (CH_2), 116.67, 118.41, 118.73, 125.66, 127.00, 128.70, 129.51 (2C), 130.77 (2C), 134.83, 135.99, 148.35 (coumarin C-4), 154.34 (coumarin C-3), 158.82 (C=O), 160.32 (C=O), 167.87 (C=O). Elemental analysis: Calculated for $\text{C}_{18}\text{H}_{12}\text{Cl}_2\text{N}_2\text{O}_4$: C, 55.26; H, 3.09; N, 7.16. Found: C, 55.20; H, 3.03; N, 7.11.

7-(Diethylamino)-2-oxo-N'-(phenylacetyl)-2H-1-benzopyran-3-ylcarbohydrazide (5e): M.P.: 263–264 °C, FTIR (KBr): 3362, 3300 (NH), 1697, 1672 (C=O), 1199 (C-O) cm^{-1} . ^1H NMR (400 MHz, DMSO- d_6): 1.11 (t, $J=6.8$ Hz, 6H, CH_3), 3.43 (q, $J=6.8$ Hz, 4H, CH_2), 3.56 (s, 2H, CH_2), 6.59 (s, 1H, Ar-H), 6.78 (d, $J=8.8$ Hz, 1H, Ar-H), 7.23-7.31 (m, 4H, ArH), 7.66 (s, 1H, Ar-H), 7.89 (d, $J=6.8$ Hz, 1H, ArH), 8.66 (s, 1H, coumarin C-4H), 10.55 (s, 1H, NH), 10.95 (s, 1H, NH). ^{13}C NMR (100 MHz, DMSO- d_6): 12.74 (CH_3), 39.32 (CH_2), 44.85 (CH_2), 96.34, 108.11, 108.13, 110.75, 126.97, 128.69 (2C), 129.49 (2C), 132.21, 136.11, 148.60 (coumarin C-4), 153.19, 157.80 (coumarin-C-3), 159.99 (C=O), 161.82 (C=O), 167.66 (C=O). Elemental analysis: Calculated for $\text{C}_{22}\text{H}_{23}\text{N}_3\text{O}_4$: C, 67.16; H, 5.89; N, 10.68. Found: C, 67.11; H, 5.80 N, 10.62.

Anti-lipase activity

Lipase inhibition potential of synthesized compounds was investigated according to the method described previously (39, 40) against porcine pancreatic lipase using 4-nitrophenylpalmitate as the substrate. Enzyme and compounds (10 μM) were preincubated for 20 minutes at 37 °C in 50 mM pH 7.5 phosphate buffer containing 5mM sodium deoxycholate and 1 mg/mL gum arabic. Then, substrate (0.1 mM) was added to the reaction mixture and after 15-minute incubation, the amount of *p*-nitrophenol released was measured at 410 nm. Orlistat was used as positive control

and ethanol was used as the negative control. %lipase inhibition was calculated using the following equation:

$$\text{Lipase inhibition (\%)} = 100 (A - B) - (C - D) / (A - B)$$

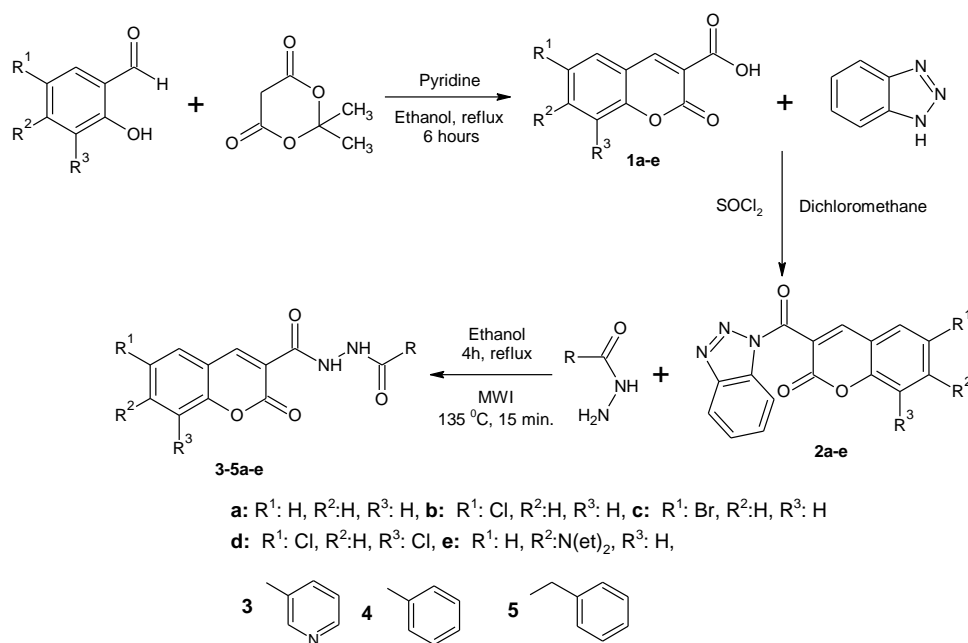
where A is the activity in the absence of inhibitor, B is the negative control in the presence of inhibitor, C is the activity in the presence of inhibitor, and D is the negative control in the presence of inhibitor.

Cupric ion reducing antioxidant capacity (CUPRAC)

1 mL of 10 mM Cu (II) Cl₂, 1 mL of 7.5 mM neocuproine, 1 mL of 1 M NH₃COOCH₃ pH 7 buffer and 20 µL of compounds solution were mixed in test tubes. The final volume in the test tubes was adjusted to 4.1 mL by adding distilled water. After 45 min incubation period at room temperature, the absorbances were recorded at 450 nm against a blank containing no compound (41) used as a standard. The CUPRAC of compounds was expressed as milligrams of Trolox per 1 mg synthesized compound. Trolox® (Sigma Chemical Co, USA) was also tested under the same conditions as a standard antioxidant compound. The standard curve was linear between 8 mg/mL and 0.125 mg/mL trolox ($r^2 = 0.998$). CUPRAC values were expressed as mg Trolox equivalent of 1 mg synthesized compound.

RESULTS AND DISCUSSION

In this study, a convenient method has been used for the synthesis of coumarin hydrazides (**3-5a-e**). The synthesis of the target compounds (**3-5a-e**) was performed by the reaction of 3-(1*H*-benzotriazol-1-ylcarbonyl)-2*H*-chromen-2-ones (**2a-e**) and corresponding hydrazide derivatives. Coumarin-3-carboxylic acid derivatives **1a-e** were obtained from the treatment of corresponding salicylic aldehydes and Meldrum's acid in absolute ethanol with catalytic amount of pyridine. Then, compounds **1a-e** were treated with 1*H*-benzotriazole in the presence of SOCl₂ to synthesize compounds **2a-e** (Scheme 1.).



Scheme 1. Synthetic route of target compounds.

In the literature, it is found that benzotriazole group offers some advantages in organic synthesis. Moreover, we have seen that compound **2a** has been used for the preparation of some biologically active compounds in literature. Especially, this compound was reacted with some type of molecules like amino acids, thioles and peptides to synthesize some coumarin-hybrid compounds. However, many of these reactions have required long reaction time, hard purification technique, and expensive catalyst requirement. Therefore, microwave heating was used for a short reaction time and a catalyst-free synthesis of compounds (**3-5a-e**). By this time, these compounds were synthesized with conventional heating for comparison with microwave heating (Table 1.).

Table 1. Comparison of yield and reaction times of compounds **3-5a-e**.

Compound	Conventional Heating		Microwave Irradiation	
	Time (h)	Yield (%)	Time (min.)	Yield (%)
3a	4	70	15	74
3b	4	67	15	70
3c	4	71	15	69
3d	4	74	15	75
3e	4	67	15	70
4a	4	69	15	70
4b	4	71	15	72
4c	4	72	15	75
4d	4	59	15	65
4e	4	72	15	77
5a	4	76	15	80
5b	4	74	15	82
5c	4	75	15	78
5d	4	76	15	82
5e	4	68	15	75

In literature, some of the obtained compounds were previously synthesized from the reaction of coumarin-3-acylchloride and hydrazide derivatives (42-45). However, these reactions were not performed under microwave irradiation. Also, the microwave irradiation technique was not suitable for this type of reaction because, in this type of reactions, the discharge of HCl gas causes the increase of reaction pressure and that is very dangerous. Therefore, we have chosen to synthesize coumarin-benzotriazole derivative instead of acyl chloride derivative because benzotriazole derivatives are more stable and benzotriazole is an easy leaving group (26, 30, 37).

Spectral investigations of compounds **3-5a-e** are suitable with the proposed structures. FTIR spectra of each compounds have two NH signals 3300-3200 cm^{-1} and three C=O signals at about 1700-1600 cm^{-1} . In ^1H NMR spectra of compounds **3-5a-e**, two NH signals were obtained at about 11.50 and 10.00 ppm. In ^{13}C NMR spectra of compounds **3-5a-e**, three C=O were found at about 164.00 (hydrazide), 159.00 (hydrazide) and 158.00 ppm (coumarin C-2), while coumarin C-3 and coumarin C-4 were shown at about 155.00 and 148.00 ppm. The FTIR, ^1H NMR and ^{13}C NMR (APT) spectra of compounds **5e** are given in Figure 1,2, and 3. Also, in ^{13}C NMR spectra the number of aromatic carbons was suitable with the structure.

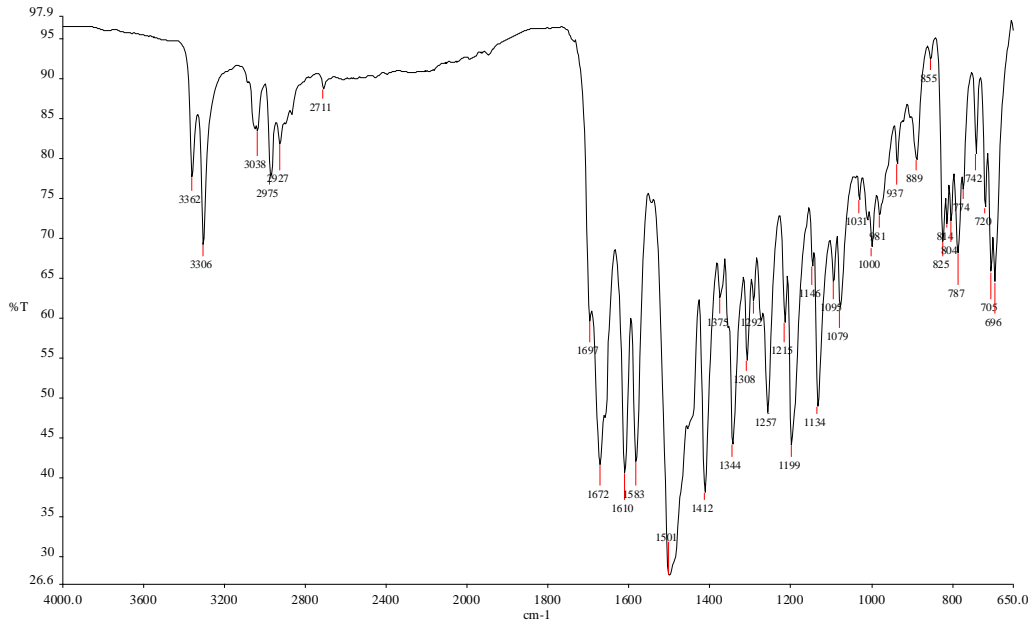


Figure 1. FTIR spectra of compound 5e.

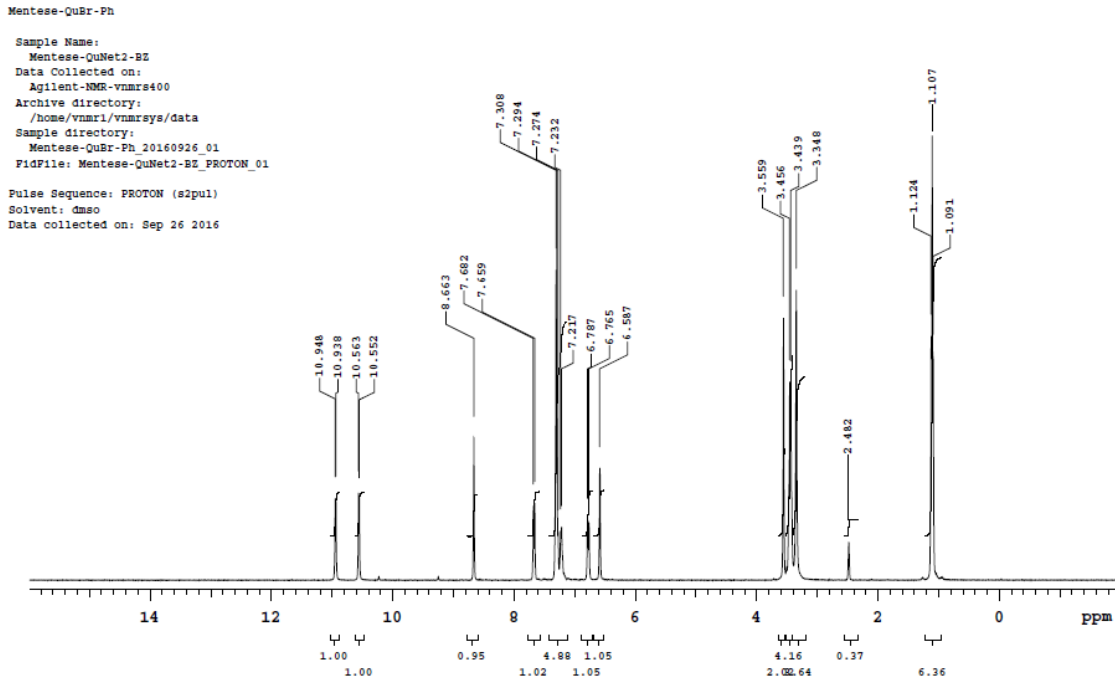


Figure 2. ¹H NMR spectra of compound 5e.

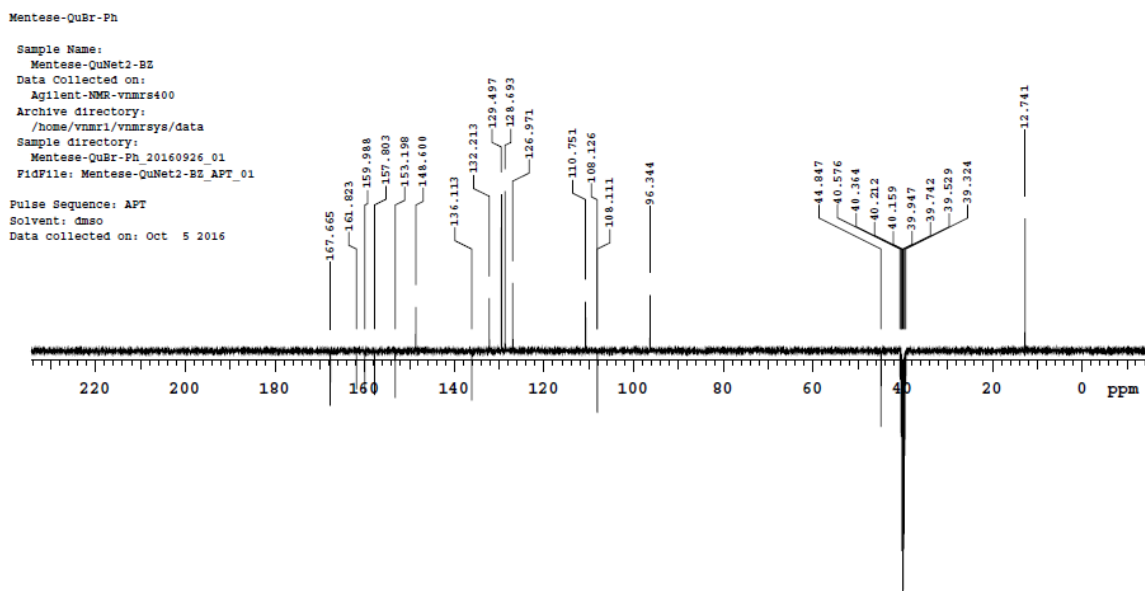


Figure 3. ^{13}C NMR (APT) spectra of compound **5e**.

Lipase Inhibition

Compounds **3-5a-e** were evaluated for their lipase inhibitory potential against porcine pancreatic lipase. All compounds except **3d**, **3e**, **4d** and **4e** inhibited porcine pancreatic lipase at different ratios. Compounds **5d**, **5e** and **3b** presented greatest lipase inhibitory activity by 46.31 ± 3.55 , 42.96 ± 3.75 and 42.50 ± 3.62 , respectively. Compound **5d** was determined to be the most effective lipase inhibitor among studied compounds. There is no inhibitory effect for the compounds **4a** and **4b**. Orlistat, a known anti-obesity drug approved by European Medical Association (46), showed 97.97 ± 0.15 inhibition at 300 nM (Tablo 2.).

Table 2. Lipase inhibitory activities of the synthesized compounds **3-5a-e** at 10 μM final concentration against porcine pancreatic lipase.

Compound (10 μM)	% Pancreatic lipase inhibition
3a	35.00 ± 2.41
3b	42.50 ± 3.62
3c	27.50 ± 1.25
4a	11.25 ± 1.66
4b	8.08 ± 1.08
4c	26.67 ± 1.98
5a	20.61 ± 2.00
5d	46.31 ± 3.55
5e	42.96 ± 3.75
Orlistat (300 nM)	97.97 ± 0.15

Cupric ion reducing antioxidant capacity (CUPRAC)

In CUPRAC method bis (2,9-dimethyl-1,10-phenanthroline: neocuproine) Cu(II) chelate cation is used as the chromogenic oxidant. Antioxidants reduce neocuproine to the cuprous neocuproine

chelate [Cu(I)-Nc] which shows maximum absorption at 450 nm (41). All studied compounds reduced cupric ions at different ratios (Table 3.). The highest cupric ion reducing activity was observed for compound **4e**. When compared with other studied compounds, compound **3c** showed the least antioxidant power.

Table 3.Antioxidant capacities of the synthesized compounds **3-5a-e**.

Compounds	CUPRAC method (mg TEAC/mg compound)
3a	1.23±0.02
3b	1.51±0.08
3c	0.80±0.01
3d	1.09±0.02
3e	1.34±0.03
4a	1.23±0.02
4b	1.57±0.04
4c	1.38±0.03
4d	1.65±0.05
4e	1.82±0.08
5a	1.46±0.05
5b	1.51±0.06
5c	1.48±0.02
5d	1.68±0.05
5e	1.38±0.03

CONCLUSION

This study reports the synthesis of novel coumarin hydrazone derivatives from 3-(1*H*-benzotriazol-1-ylcarbonyl)-2*H*-chromen-2-ones **2a-e** and hydrazone derivatives by using microwave heating and conventional heating procedures. Microwave heating procedure has shown some advantages on classical heating with short reaction times, easy work-up, and the less quantity of organic solvent. In anti-lipase inhibition study, compound **5d** showed the highest activity among the synthesized compounds with 46.31±3.55% pancreatic lipase inhibition. In antioxidant activity study, all compounds showed the activity, while compound **4e** showed the best antioxidant capacity.

ACKNOWLEDGMENTS

This work was supported by Recep Tayyip Erdogan University Scientific Research Project Unit (FBA-2016-662). We thank to Recep Tayyip Erdogan University and all the colleagues in the project unit for their support.

REFERENCES

1. Kahveci B, Yilmaz F, Mentese E, Beris FS. Effect of microwave irradiation on the synthesis of 1,2,4-triazol-3-one derivatives and their antimicrobial activities. *J Chem Res.* 2012(8):484-8.
2. Kahveci B, Mentese E. Microwave-Assisted Synthesis of Benzimidazoles and Their Derivatives From 1994 to 2016-A Review. *Curr Microwav Chem.* 2017;4(1):73-101.
3. Frecentese F, Saccone I, Caliendo G, Corvino A, Fiorino F, Magli E, et al. Microwave Assisted Organic Synthesis of Heterocycles in Aqueous Media: Recent Advances in Medicinal Chemistry. *Med Chem.* 2016;12(8):720-32.
4. Kappe CO, Dallinger D. Controlled microwave heating in modern organic synthesis: highlights from the 2004-2008 literature. *Mol Divers.* 2009;13(2):71-193.
5. Kappe CO, Stadler A, Dallinger D, Strohmeier G, Perez R, Zbruyev OI, et al. Adventures in microwave-assisted organic synthesis: Contributions from the Kappe laboratory 2000-2005. *Nato Sci Ser II-Math.* 2008;246:225-51.
6. de Souza SM, Delle Monache F, Smania A. Antibacterial activity of coumarins. *Z Naturforsch C.* 2005;60(9-10):693-700.
7. Srinivas B, Suryachandram J, Devi YK, Rao KP. Synthesis and Antibacterial Activity Studies of 8,9-Dihydro [7h] Benzo 1,2,4-Oxadiazoles and its Coumarin Derivatives. *J Heterocyclic Chem.* 2017;54(6):3730-4.
8. Zhang RR, Liu J, Zhang Y, Hou MQ, Zhang MZ, Zhou FE, et al. Microwave-assisted synthesis and antifungal activity of novel coumarin derivatives: Pyrano[3,2-c]chromene-2,5-diones. *Eur J Med Chem.* 2016;116:76-83.
9. Khan KM, Saify ZS, Khan MZ, Zia-Ullah, Choudhary MI, Atta-ur-Rahman, et al. Synthesis of coumarin derivatives with cytotoxic, antibacterial and antifungal activity. *J Enzym Inhib Med Ch.* 2004;19(4):373-9.
10. Hu YQ, Xu Z, Zhang S, Wu X, Ding JW, Lv ZS, et al. Recent developments of coumarin-containing derivatives and their anti-tubercular activity. *Eur J Med Chem.* 2017;136:122-30.
11. Liu MM, Chen XY, Huang YQ, Feng P, Guo YL, Yang G, et al. Hybrids of Phenylsulfonylfuroxan and Coumarin as Potent Antitumor Agents. *J Med Chem.* 2014;57(22):9343-56.
12. Kumbhare RM, Kosurkar UB, Ramaiah MJ, Dadmal TL, Pushpavalli SNCVL, Pal-Bhadra M. Synthesis and biological evaluation of novel triazoles and isoxazoles linked 2-phenyl benzothiazole as potential anticancer agents. *Bioorg Med Chem Lett.* 2012;22(17):5424-7.
13. Musad EA, Mohamed R, Saeed BA, Vishwanath BS, Rai KML. Synthesis and evaluation of antioxidant and antibacterial activities of new substituted bis(1,3,4-oxadiazoles), 3,5-bis(substituted) pyrazoles and isoxazoles. *Bioorg Med Chem Lett.* 2011;21(12):3536-40.
14. Kamiyama H, Kubo Y, Sato H, Yamamoto N, Fukuda T, Ishibashi F, et al. Synthesis, structure-activity relationships, and mechanism of action of anti-HIV-1 lamellarin alpha 20-sulfate analogues. *Bioorgan Med Chem.* 2011;19(24):7541-50.
15. Carochi M, Morales P, Ferreira ICFR. Natural food additives: Quo vadis? *Trends Food Sci Tech.* 2015;45(2):284-95.
16. Karaoglu K, Yilmaz F, Mentese E. A New Fluorescent "Turn-Off" Coumarin-Based Chemosensor: Synthesis, Structure and Cu-Selective Fluorescent Sensing in Water Samples. *J Fluoresc.* 2017;27(4):1293-8.
17. Acar M, Bozkurt E, Meral K, Ank M, Onganer Y. The fluorescence quenching mechanism of coumarin 120 with CdS nanoparticles in aqueous suspension. *J Lumin.* 2015;157:10-5.
18. Raghav SK, Gupta B, Shrivastava A, Das HR. Inhibition of lipopolysaccharide-inducible nitric oxide synthase and IL-1 beta through suppression of NF-kappa B activation by 3-(1'-1'-dimethyl-

- allyl)-6-hydroxy-7-methoxy-coumarin isolated from *Ruta graveolens* L. *Eur J Pharmacol.* 2007;560(1):69-80.
19. Karatas MO, Uslu H, Sari S, Alagoz MA, Karakurt A, Alici B, et al. Coumarin or benzoxazinone based novel carbonic anhydrase inhibitors: synthesis, molecular docking and anticonvulsant studies. *J Enzym Inhib Med Ch.* 2016;31(5):760-72.
 20. Maresca A, Temperini C, Vu H, Pham NB, Poulsen SA, Scozzafava A, et al. Non-Zinc Mediated Inhibition of Carbonic Anhydrases: Coumarins Are a New Class of Suicide Inhibitors. *J Am Chem Soc.* 2009;131(8):3057-62.
 21. Anand P, Singh B, Singh N. A review on coumarins as acetylcholinesterase inhibitors for Alzheimer's disease. *Bioorgan Med Chem.* 2012;20(3):1175-80.
 22. Aziz-ur-Rehman, Magsi S, Abbasi MA, Rasool S, Malik A, Hussain G, et al. Synthesis, characterization and enzyme inhibition study of O-substituted derivatives of chlorinated coumarin. *Pak J Pharm Sci.* 2014;27(2):271-8.
 23. Ali MY, Jannat S, Jung HA, Choi RJ, Roy A, Choi JS. Anti-Alzheimer's disease potential of coumarins from *Angelica decursiva* and *Artemisia capillaris* and structure-activity analysis. *Asian Pac J Trop Med.* 2016;9(2):101-8.
 24. Mentese E, Yilmaz F, Emirik M, Ulker S, Kahveci B. Synthesis, molecular docking and biological evaluation of some benzimidazole derivatives as potent pancreatic lipase inhibitors. *Bioorg Chem.* 2018;76:478-86.
 25. Mentese E, Bektas H, Sokmen BB, Emirik M, Cakir D, Kahveci B. Synthesis and molecular docking study of some 5,6-dichloro-2-cyclopropyl-1H-benzimidazole derivatives bearing triazole, oxadiazole, and imine functionalities as potent inhibitors of urease. *Bioorg Med Chem Lett.* 2017;27(13):3014-8.
 26. Kahveci B, Yilmaz F, Mentese E, Ulker S. Design, Synthesis, and Biological Evaluation of Coumarin-Triazole Hybrid Molecules as Potential Antitumor and Pancreatic Lipase Agents. *Arch Pharm.* 2017;350(8).
 27. Mentese E, Karaali N, Akyuz G, Yilmaz F, Ulker S, Kahveci B. Synthesis and evaluation of alpha-glucosidase and pancreatic lipase inhibition by quinazolinone-coumarin hybrids. *Chem Heterocycl Com+.* 2016;52(12):1017-24.
 28. Nagamallu R, Srinivasan B, Ningappa MB, Kariyappa AK. Synthesis of novel coumarin appended bis(formylpyrazole) derivatives: Studies on their antimicrobial and antioxidant activities. *Bioorg Med Chem Lett.* 2016;26(2):690-4.
 29. Wen F, Jin H, Tao K, Hou TP. Design, synthesis and antifungal activity of novel furancarboxamide derivatives. *Eur J Med Chem.* 2016;120:244-51.
 30. Kahveci B, Yilmaz F, Mentese E, Ulker S. Microwave-assisted synthesis of some new coumarin derivatives including 1,2,4-triazol-3-one and investigation of their biological activities. *Chem Heterocycl Com+.* 2015;51(5):447-56.
 31. Garino C, Tomita T, Pietrancosta N, Laras Y, Rosas R, Herbette G, et al. Naphthyl and coumarinyl biaryl piperazine derivatives as highly potent human beta-secretase inhibitors. Design, synthesis, and enzymatic BACE-1 and cell assays. *J Med Chem.* 2006;49(14):4275-85.
 32. Tang J, Huang X. An efficient solid-phase synthesis of 3-carboxycoumarins based on a scaffold-polymer-bound cyclic malonic ester. *J Chem Res-S.* 2003(6):354-5.
 33. Hekmatshoar R, Rezaei A, Beheshtiha SYS. Silica Sulfuric Acid: A Versatile and Reusable Catalyst for Synthesis of Coumarin-3-carboxylic Acids in a Solventless System. *Phosphorus Sulfur.* 2009;184(9):2491-6.
 34. Creaven BS, Egan DA, Kavanagh K, McCann M, Noble A, Thati B, et al. Synthesis, characterization and antimicrobial activity of a series of substituted coumarin-3-carboxylatosilver(I) complexes. *Inorg Chim Acta.* 2006;359(12):3976-84.

35. Bardajee GR, Jafarpour F, Afsari HS. ZrOCl₂ center dot 8H₂O: An efficient catalyst for rapid one-pot synthesis of 3-carboxycoumarins under ultrasound irradiation in water. *Cent Eur J Chem.* 2010;8(2):370-4.
36. Katritzky AR, Cusido J, Narindoshvili T. Monosaccharide-based water-soluble fluorescent tags. *Bioconjugate Chem.* 2008;19(7):1471-5.
37. Katritzky AR, Abdelmajeid A, Tala SR, Amine MS, Steel PJ. Novel Fluorescent Aminoxy Acids and Aminoxy Hybrid Peptides. *Synthesis-Stuttgart.* 2011(1):83-90.
38. Badran MM, El-Gendy AA, Soliman LN, El-Assi HR. Synthesis of certain novel 3-substituted coumarins. *Bulletin of the Faculty of Pharmacy (Cairo University).* 1990;28(2):39-42.
39. Winkler UK, Stuckmann M. Glycogen, hyaluronate, and some other polysaccharides greatly enhance the formation of exolipase by *Serratia marcescens*. *Journal of Bacteriology.* 1979;138(3):663-70.
40. Kantar GK, Faiz O, Sahin O, Sasmaz S. Phthalocyanine and azaphthalocyanines containing eugenol: synthesis, DNA interaction and comparison of lipase inhibition properties. *J Chem Sci.* 2017;129(8):1247-56.
41. Apak R, Guclu K, Ozyurek M, Celik SE. Mechanism of antioxidant capacity assays and the CUPRAC (cupric ion reducing antioxidant capacity) assay. *Microchim Acta.* 2008;160(4):413-9.
42. Badran MM, Elansari AK, Elmeligie S. Novel Substituted-Aminocoumarins as Potential Antimicrobial Agents. *Rev Roum Chim.* 1990;35(6):777-83.
43. Mohareb RM, Ho JZ, Alfarouk FO. Synthesis of thiophenes, azoles and azines with potential biological activity by employing the versatile heterocyclic precursor N-benzoylcyanooacetylhydrazine. *J Chin Chem Soc-Taip.* 2007;54(4):1053-66.
44. Ma L, Xu YX, Wang KN, Zhou CJ, Cao DX, Shan YY, et al. Synthesis and recognition properties for copper ions and cyanide anions of two coumarin hydrazide compounds. *Inorg Chem Commun.* 2015;58:24-6.
45. Long LL, Zhang DD, Li XF, Zhang JF, Zhang C, Zhou LP. A fluorescence ratiometric sensor for hypochlorite based on a novel dual-fluorophore response approach. *Anal Chim Acta.* 2013;775:100-5.
46. Heck AM, Yanovski JA, Calis KA. Orlistat, a new lipase inhibitor for the management of obesity. *Pharmacotherapy.* 2000;20(3):270-9.



Quantitative Structure-Activity Relationship and Molecular Docking Study of Some Pyrrolones Antimalarial Agents against *Plasmodium Falciparum*

Zaharaddeen Shehu^{1*}, Adamu Uzairu², Balarabe Sagagi³

¹ Department of Science Laboratory Technology, Jigawa State Polytechnic Dutse, Jigawa State, Nigeria

² Department of Chemistry, Ahmadu Bello University Zaria, Kaduna State, Nigeria

³ Department of Chemistry, Kano University of Science and Technology Wudil, Kano State, Nigeria

Abstract: The growing increase in multidrug resistance malaria cases necessitates the need to search for new cost-effective drugs. Quantitative Structure-Activity Relationship (QSAR) and molecular docking studies were performed on a data set of forty-nine Pyrrolones antimalarial agents against *Plasmodium falciparum* (*P. falciparum*). Forty-two molecules were used as a training set and seven as the test set. The molecular descriptors were obtained by Density Functional Theory (DFT) using Becke's three-parameter Lee-Yang-Parr hybrid functional (B3LYP) in combination with the 6-31G* basis set. The QSAR model was built using Genetic Function Algorithm (GFA) method. The model with the best statistical significance ($N = 42$, $R^2_{\text{ext}} = 0.700$, $R^2 = 0.933$, $R^2_a = 0.916$, $Q^2_{\text{cv}} = 0.894$, $\text{LOF} = 0.417$, Minimum experimental error for non-significant LOF (95%) = 0.250) was selected. The docking experiment was carried out using AutoDock Vina of PyRx and Discovery Studio Visualizer. Docking analysis revealed that three of the studied compounds with binding affinity values of -10.7 kcal/mol, -10.9 kcal/mol and -11.1 kcal/mol possess higher potency than standard antimalarial drugs with binding affinity values of -8.8 kcal/mol, -9.5 kcal/mol and -9.0 kcal/mol. It is envisioned that the wealth of information provided by the QSAR and molecular docking results in this study will offer important structural insights for further laboratory experiments in the future design of novel and highly potent antimalarial from the pyrrolones.

Keywords: Antimalarial Agents, Density Functional Theory, Genetic Function Algorithm, Discovery Studio Visualizer, Hydrophobic Interaction.

Submitted: October 26, 2017. **Accepted:** January 15, 2018.

Cite this: Shehu Z, Uzairu A, Sagagi B. Quantitative Structure-Activity Relationship and Molecular Docking Study of Some Pyrrolones Antimalarial Agents against *Plasmodium Falciparum*. JOTCSA. 2018;5(2):569-84.

DOI: <http://dx.doi.org/10.18596/jotcsa.346661>.

***Corresponding author. E-mail:** zahru2006@yahoo.com, zshehu@jigpoly.edu.ng & zahru1069@gmail.com. Tel.: +2348061547455.

INTRODUCTION

Approximately half of the world's population is at risk of malaria. In 2015, there were roughly 212 million malaria cases and an estimated 429 000 malarial deaths. Increased prevention and control measures have led to a 29% reduction in malaria mortality rates globally since 2010. Sub-Saharan Africa continues to carry a disproportionately high share of the global malarial burden. In 2015, the region was home to 90% of malaria cases and 92% of malaria deaths (1). Among the *Plasmodium* species responsible for this disease, most commonly encountered and deadliest is *Plasmodium falciparum* (*P. falciparum*) (2). In addition to its fatal effects, it has been reported to also have a huge economic impact in countries where it is prevalent. Malaria disease have a huge tendency of spreading to other regions of the world due to increasing globalization and global warming (3). The increasing resistance of *P. falciparum* to clinically used chemotherapeutic agents coupled with the unavailability of vaccines (3,4,5). Though many drugs are abounded for the treatment of this disease, the increasing instances of resistance against antimalarial drugs in recent years are becoming worrisome (6). This underscores the need to discover novel and highly potent drugs in the drug development pipeline to combat the scourge of this disease. In the pursuant of this effort, several molecular drug targets have been identified to develop new drug candidates. Very prominent among these targets are cysteine proteases. This target protein plays an essential role in malaria parasites; therefore, an obvious area of investigation is the inhibition of these enzymes to treat malaria. Studies with cysteine protease inhibitors have revealed its role in hemoglobin hydrolysis. The best characterized Plasmodium cysteine proteases are falcipains, which are papain family enzymes. Falcipain-2 and falcipain-3 are major hemoglobinas of *P. falciparum* (7). In-silico techniques such as QSAR and molecular docking have been proving valuable tools in recent years for rapid discovery of novel drug candidates, e.g. the discovery of o-acetyl-L-serine sulfhydrylase of *Entamoeba histolytica* inhibitors, acetylcholinesterase inhibitors, and antagonists acetophenazine, fluphenazine and periciazine against human androgen receptor (8,9,10).

QSAR plays a crucial role in drug development as it analyzes the properties of the drug. It is mathematical model that links the structural features of compounds (*i.e.* molecular descriptors) to their quantity showing specific biological or chemical activity (11). It gives description of how biological activity can vary as a function of molecular descriptors derived from the chemical structure of a set of molecules using regression models. Hence, a model containing those calculated descriptors can be used to predict responses of new compounds (12). The molecular descriptors for the compounds are calculated and used to build QSAR Model (13).

Molecular docking, on the other hand, is a computational method used to determine the binding compatibility of the active site residues to specific groups and to reveal the strength of interaction.

The results of docking procedure are analyzed by a statistical scoring function which converts interacting energy into numerical values known as the docking score. The 3D pose of the bound ligand can be visualized using different visualizing tools like Pymol, Rasmol, and Discovery Studio, which could help in the inference of the best fit of ligand. Predicting the mode of protein-ligand interaction can assume the active site of the protein molecule and further help in protein annotation. Moreover, molecular docking has major application in drug discovery and designing (14).

The main aim of the present study was to develop various QSAR models using Genetic Function Algorithm (GFA) method for pyrrolones for their antimalarial activities and to relate antimalarial activity to its physicochemical properties. Also to docked falcipain-2 protein (2GHU) with bound ligands (pyrrolone analogues).

MATERIALS AND METHODS

Dataset of Experimental Falcipain-2 Inhibitors

A dataset of 49 pyrrolone compounds known as inhibitors of *P. falciparum* was obtained from reference (3) and used in this study. The inhibitory bioactivities of the compounds expressed as half maximal effective concentration (EC_{50}) were converted to the logarithmic scale ($pEC_{50} = \text{Log } EC_{50}$) to reduce data dispersion and obtain a more linear response in the process of building the QSAR model. EC_{50} is the concentration of the drug which induces a response halfway between the baseline and maximum after a specified exposure time (15). It is a commonly used index for assessing the drug's potency. The IUPAC name and biological activities of antimalarial used in this study are presented in Table 1 (See Supplementary Information).

Computational and Statistical Techniques

The molecular structure of each compound was optimized using the molecular modeling program, Spartan'14 V1.1.0 on Speedstar computer system (4.00 GB RAM, 2.66 GHz processor) on Microsoft windows 10 Ultimate using Density Functional Theory (DFT) level using Becke's three-parameter Lee-Yang-Parr hybrid functional (B3LYP) in combination with the 6-31G* basis set. Our choice of B3LYP/6-311G* basis set is anchored on the fact that it gives a far more accurate result. Optimization of the molecules is necessary to get the lowest energy geometries (most stable geometries). The molecular descriptors of the optimized compounds were calculated using the Spartan'14 V.1.1.0 quantum chemistry package and paDEL descriptor toolkit. The data sets of the molecules were split into the training set (42 molecules) for model development and test set (7 molecules) for external validation of the models using Euclidian Distance Based model and the distance between cluster was set at 5. Subsequently, the QSAR models were built by means of Genetic Function Approximation (GFA) techniques embedded in Material Studio, a modeling and

simulation software using the experimentally obtained biological activities as the dependent variable the computed molecular descriptors as independent variables. Five QSAR models were generated but the best set was selected based on the model with the lowest Lack of Fit (LOF) score, a parameter used for assessing the robustness of GFA derived QSAR model. As a form of quality assurance evaluation of the built QSAR model, the external predictive ability and extrapolation of the best model evaluated using the test set molecules with the aid of Equation 1.

$$R^2_{pred} = 1 - \frac{\sum(Pred.Y_{te} - Act.Y_{te})^2}{\sum(Act.Y_{te} - Y_m)^2} \quad (\text{Eq 1})$$

Where R^2_{pred} is termed the predictive R^2 of a development model and is an important parameter that is used to test the external predictive ability of a QSAR model, $Pred.Y_{te}$ and $Act.Y_{te}$ indicate predicted and observed activity values of the test set compounds respectively and Y_m indicates mean activity value of the training set (17).

Applicability Domain of the Model

Applicability domain (AD) is the physicochemical, structural or biological space, knowledge or information on which the training set of the model has been developed (18). The resulting model can be reliably applicable for only those compounds which are inside this domain since it cannot be applied to the entire universe of anti-*P.falciparum* compounds. The AD of the model was calculated by the leverage approach (19).

The leverage values of all compounds were calculated and plotted against the standardized residuals (William plot) (20). This method offers a graphical assessment of the leverage values (h_{ii}) as a function of the standardized cross-validated residuals. It is suitable not only for detection of the structurally-influential outliers, but also for determination of the response outliers. The leverage is defined as a compound's distance from the centroid of X . Mathematically, the leverage (h_{ii}) of a given compound in the multidimensional descriptor space, can be calculated as in the following equation:

$$h_{ii} = x_i^T (X^T X)^{-1} x_i \quad (\text{Eq 2})$$

Where x_i the descriptor row matrix of the compound under consideration and X is the multidimensional matrix carrying the structural information (calculated molecular descriptors) for each training set compound.

Molecular docking studies

In order to have an in-depth knowledge of the nature of the described interaction of inhibitors (3) with the falcipain-2 receptor, molecular docking was performed using AutoDock Vina of PyRx virtual

screening software. The energy grid calculations and visual analysis of the docking site performed using AutoDock Vina of PyRx and Discovery Studio visualization software, respectively. The crystal structure of falcipain-2 was obtained from protein data bank (PDB CODE: 2GHU). The removal of native ligands present in the protein was confirmed by calculating the root mean square deviation (RMSD) value of the original structure and the structure with ligand deletion (21,22).

All heteroatomic molecules were excluded from the three-dimensional structure of falcipain-2 receptor (Figure 1) and its structure was minimized, protonated and saved in PDBQT file format in all polar residues. Likewise, the 3D structures of the optimized 49 different pyrrolone compounds (Figure 2) were also converted to PDBQT format with the aid of AutoDock 4.2 software. The protein-ligand interaction was analyzed using AutoDock Vina of PyRx Virtual Screening software. (23)

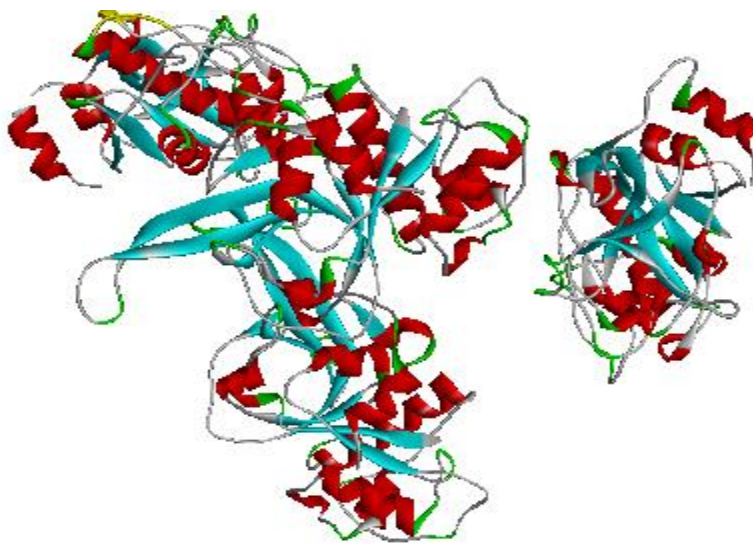


Figure 1: Structure of falcipain-2 (2GHU)

Source: (<http://www.pdb.org>) (24).

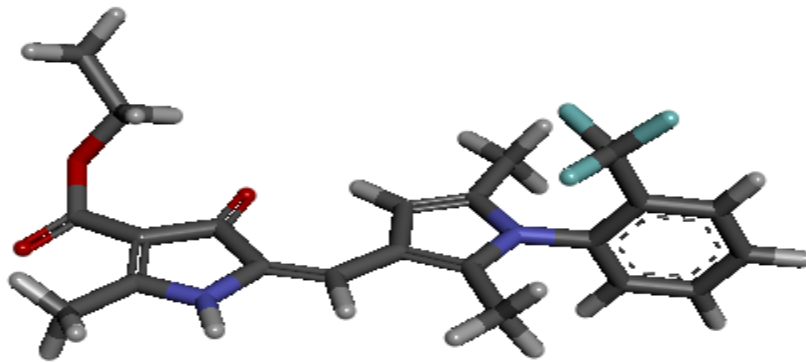


Figure 2: 3D structure of the prepared ligand.

RESULTS AND DISCUSSION

The five models constructed are detailed as follows:

Model 1

$$pEC_{50} = -3.441 (GATS2m) + 1.934 (minsssN) + 1.314 (MDEO - 22) + 3.251 (RDF95u) - 5.776 (RDF130u) + 3.038 (RDF30v) + 2.324 (RDF155v) - 1.739 (RDF15s) + 7.131$$

Model 2

$$pEC_{50} = -4.943 (GATS2m) - 1.663 (SpMax6Bhs) + 1.799 (minsssN) + 1.196 (MDEO - 22) + 2.707 (RDF95u) - 5.842 (RDF130u) + 2.774 (RDF30v) + 2.375 (RDF155v) + 7.982$$

Model 3

$$pEC_{50} = -4.585 (GATS2m) + 1.959 (maxsssN) - 1.735 (TIC0) + 1.261 (MDEO - 22) + 3.278 (RDF95u) - 5.290 (RDF130u) + 3.123 (RDF30v) + 2.609 (RDF155v) + 7.276416456$$

Model 4

$$pEC_{50} = -4.242 (GATS2m) + 1.783 (maxsssN) + 1.659 (MDEO - 22) + 2.908 (RDF95u) - 5.612 (RDF130u) - 1.076 (RDF20m) + 2.999 (RDF30v) + 2.136 (RDF155v) + 7.216$$

Model 5

$$pEC_{50} = -3.544 (GATS2m) - 1.983 (VP) - 7 + 2.459 (minsssN) + 1.218 (MDEO - 22) + 3.482 (RDF95u) - 6.363 (RDF130u) + 3.007 (RDF30v) + 2.708 (RDF155v) + 7.0614$$

The validation parameters for the QSAR models are presented in Table 2 and the detailed definition of the descriptors in the model 1 are presented in Table 3. Out of the five models generated, Model 1 shows the best GFA derived QSAR models for inhibitory activity of the studied pyrrolones against *P. falciparum*. Table 4 gives the comparison of observed pEC_{50} and predicted pEC_{50} of the model 1.

Table 2: Validation Metrics for Models

Parameter	Model 1	Model 2	Model 3	Model 4	Model 5	Recommended
R^2	0.933	0.929	0.928	0.928	0.928	≥ 0.6
R^2_a	0.916	0.911	0.911	0.911	0.911	Very close to R^2
Q_{cv}^2	0.844	0.887	0.891	0.887	0.882	< 0.5
LOF	0.417	0.441	0.443	0.444	0.444	Very low
R^2_{ext}	0.700	-	-	-	-	≥ 0.6
Error	0.490	0.257	0.257	0.257	0.257	Very minimal
F-value	56.993	53.676	53.427	53.323	53.312	High

Source: Ravinchandran, (2011) (25)

Table 3: Definition of descriptors in Model 1.

S/n	Descriptor	Definition
1	GATS2m	Geary autocorrelation - lag 2 / weighted by mass
2	MinsssN	Minimum atom-type E-State: >N-
3	MDEO-22	Molecular distance edge between all secondary oxygens
4	RDF95u	Radial distribution function - 095 / unweighted
5	RDF130u	Radial distribution function - 130 / unweighted
6	RDF30v	Radial distribution function - 030 / weighted by relative van der Waals volumes
7	RDF155v	Radial distribution function - 155 / weighted by relative van der Waals volumes
8	RDF15s	Radial distribution function - 015 / weighted by relative I-state
9	RDF20m	Radial Distribution Function-020 / weighted by mass
10	MaxsssN	Maximum atom-type E-State: >N-
11	spMax6Bhs	largest eigenvalue n. 6 of Burden matrix weighted by I-state
12	TICO	Total Information Content index (neighborhood symmetry of 0-order)
13	Vp	Valance path order

Source: Descriptor Manual (2012) (26,27)

Table 4: Comparison of observed pEC₅₀ and predicted pEC₅₀ of Model 1

Cpd	Act. pEC ₅₀	Pred. pEC ₅₀	Cpd	Act. pEC ₅₀	Pred. pEC ₅₀
1^a	7.85	7.78	26^a	6.96	7.05
2^a	7.46	7.27	27^a	5.85	6.34
3^a	4.92	5.00	28^a	8.39	8.23
4^a	5.85	5.59	29^b	9.39	9.13
5^a	5.62	5.49	30^a	6.82	6.75
6^a	6.72	6.39	31^a	5.92	6.51
7^a	5.96	5.61	32^b	7.00	8.91
8^a	7.23	7.36	33^a	7.74	7.81
9^a	6.42	6.77	34^b	6.00	7.11
10^a	6.33	6.49	35^a	7.92	7.43
11^b	7.62	6.98	36^a	9.00	8.94
12^a	7.64	7.62	37^a	5.82	6.21
13^a	8.69	8.78	38^a	8.12	7.94
14^a	9.30	9.41	39^a	5.59	7.71
15^b	7.62	8.18	40^a	7.21	7.24
16^a	6.49	7.02	41^a	7.33	7.21
17^a	7.08	6.78	42^a	7.85	7.85
18^a	6.89	6.97	43^a	7.68	7.64
19^b	7.02	6.47	44^a	6.82	7.30
20^a	8.15	8.21	45^a	6.64	6.16
21^a	9.00	8.91	46^a	6.60	6.86
22^b	5.28	6.39	47^a	6.64	6.75
23^a	5.62	-0.03	48^a	7.34	7.36
24^a	5.46	5.61	49^a	7.11	6.99
25^a	7.79	7.51			

a: training set, b: test set Cpd: compounds, Act: Actual, Pred: Predicted

Figures 3a and 3b give the plot of predicted pEC₅₀ against actual pEC₅₀ of the compounds for the test set and training set, respectively. The William's plot is depicted in Figure 4.

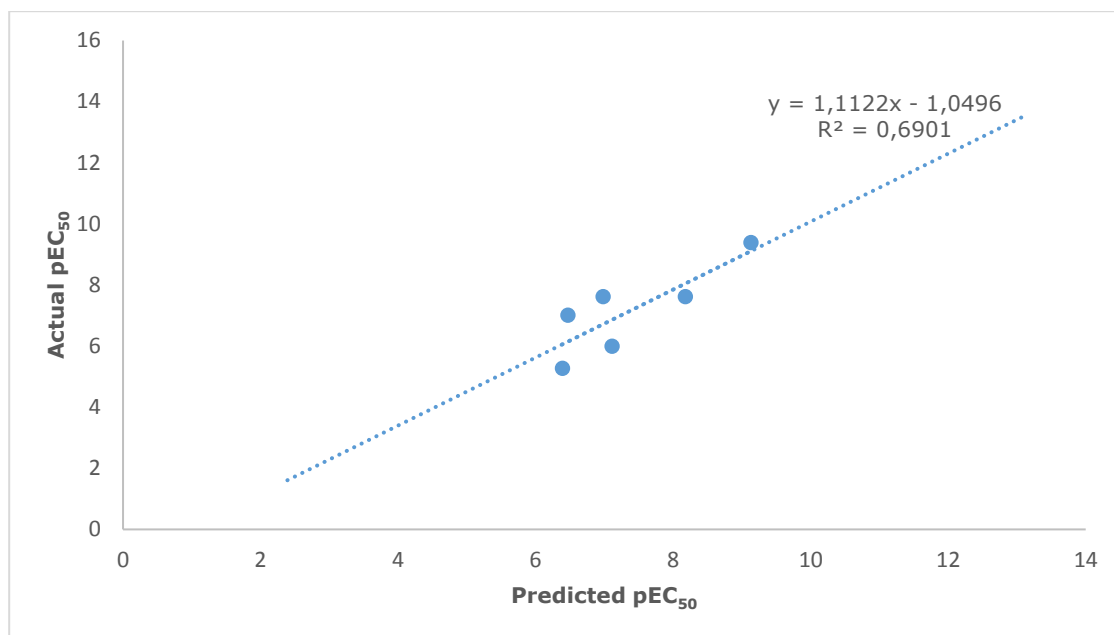


Figure 3a: Plot of predicted versus the observed pEC₅₀ values for the test set compounds.

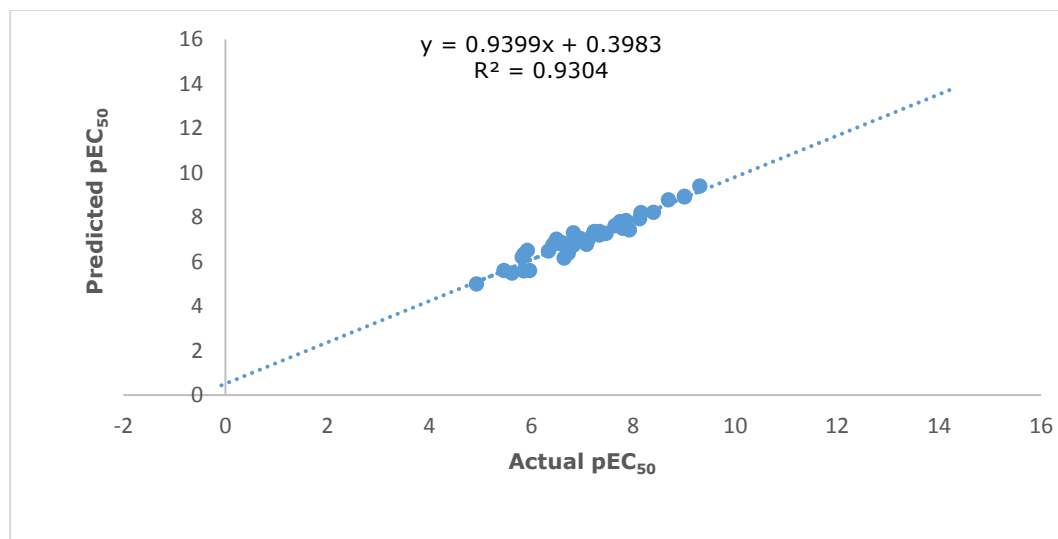


Figure 3b: Plot of predicted versus the observed pEC₅₀ values for the training set compounds

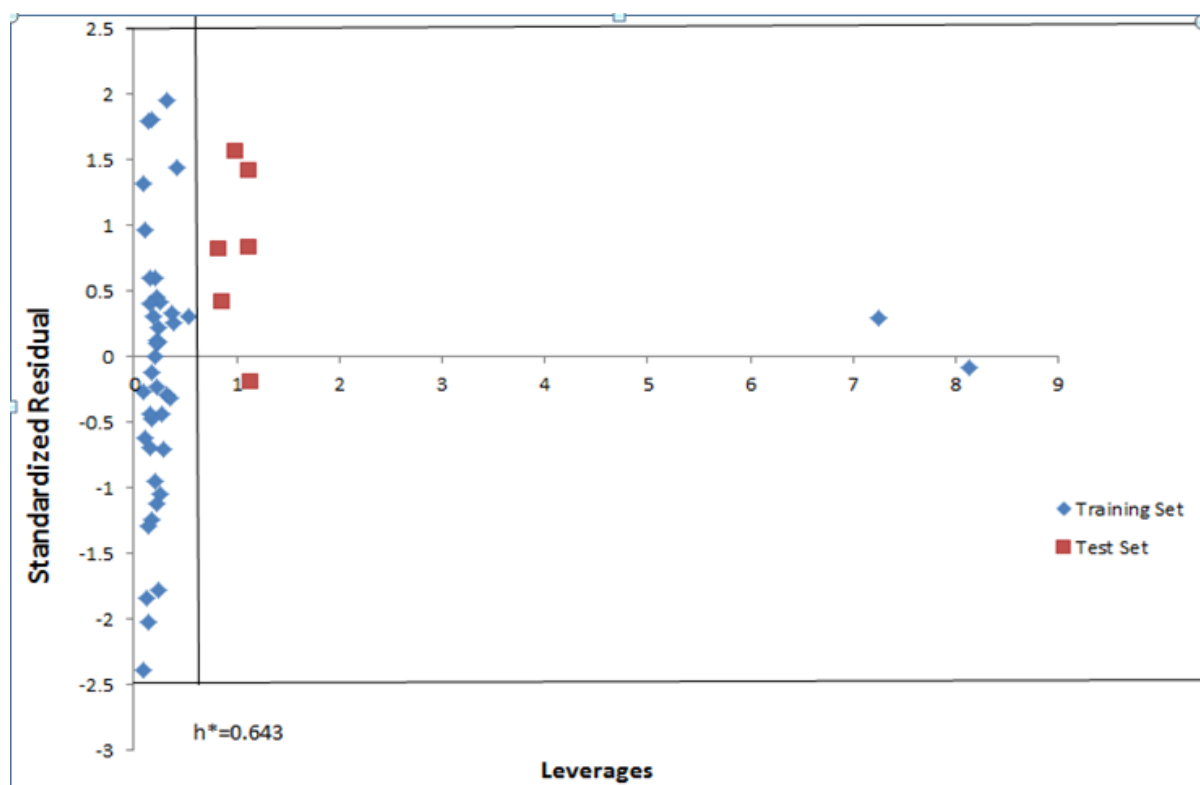
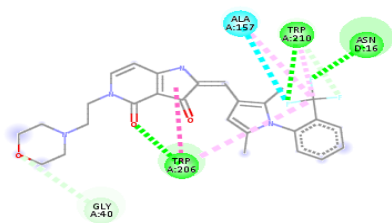
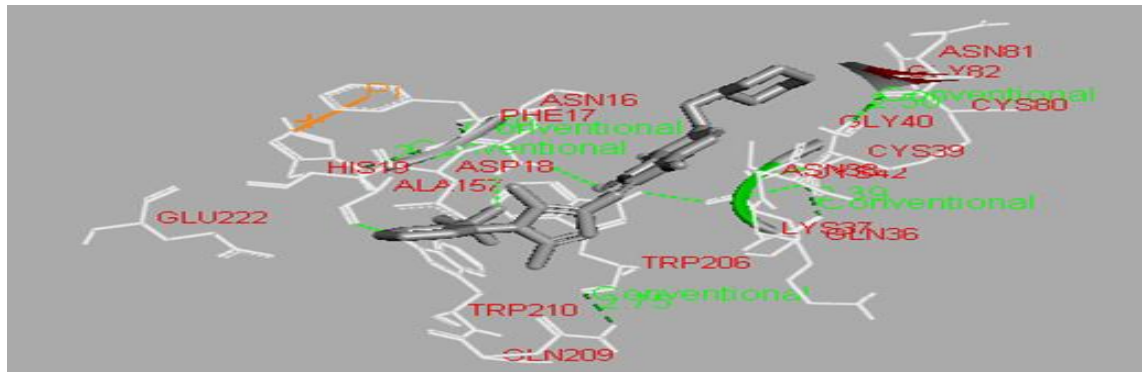


Figure 4. William's plot, the plot of the standardized residuals versus the activity leverage value of model 1.

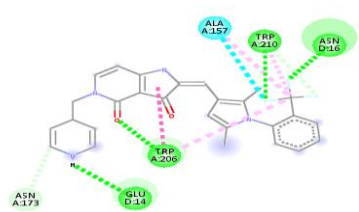
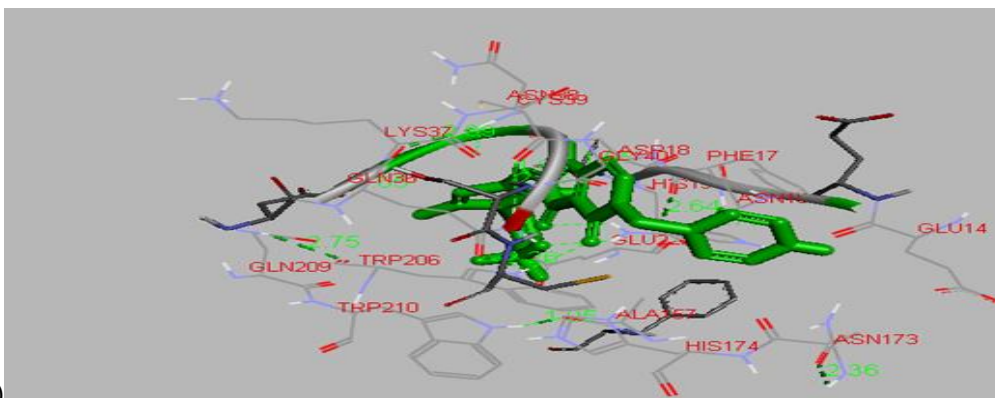
Table 5 (supplementary files) shows the docking scores, hydrogen bonding length (in Angström) and interacting residues involved in the docking of inhibitors (ligands) at the active site of Falcipain-2.

Figures 5a-c show the best three docking results obtained.

(5a)



(5b)



(5c)

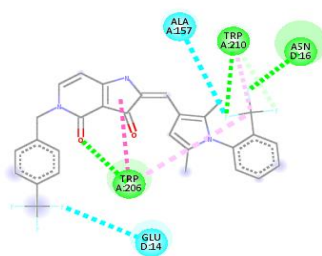
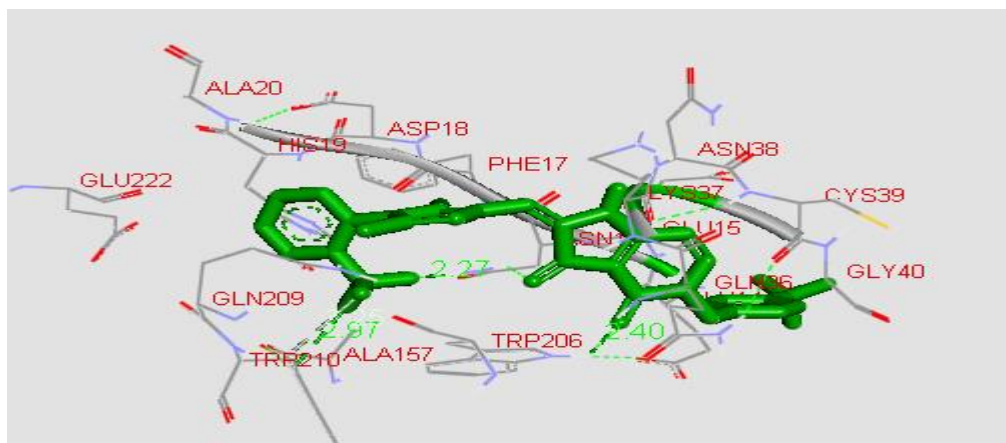


Figure 5: Three-dimensional docked Falcipain-2-Ligands Complex: (5a) Interactions between Falcipain-2 and Ligand 45^a, (5b) interactions between Falcipain-2 and Ligand 49^a and (5c) interactions between Falcipain-2 and Ligand 48^a Green dashed lines represent the H-bond interactions, and red dashed lines represent the hydrophobic interactions.

The statistical parameters of the Genetic Function Algorithm derived QSAR model is in compliance with the standard QSAR validation metrics shown in Table 2. The high predictability of the model is evidenced by the low residual values observed in Table 4 which gives the comparison of observed and predicted anti-*P. falciparum* activities of the Pyrrolones. Also, the high linearity of the plot of predicted pEC₅₀ against observed pEC₅₀ depicted in Figures 3a and 3b for test set and training set molecules, respectively confirms the robustness of the model.

William's plot (Figure 4) obtained to ascertain the inclusiveness of the studied pyrrolones in model's applicability domain reveals that all the compounds of the training set have leverage values lower than the warning h_i value ($h_i = 0.64$) except two compounds with leverage values higher than h_i . This implies that the models can be successfully applied to this series of pyrrolone antimalarial

compounds. The two compounds with higher leverage than h_i value are most likely to be structural outliers.

Molecular docking studies were carried out between the targets (falcipain-2) and the inhibitors reveal that all the compounds were found to strongly inhibit the growth of *P. falciparum* by completely occupying the active sites of the target protein (falcipain-2). Most of the inhibitors were found to be involved in both hydrophobic interactions and hydrogen bonding with the receptor (falcipain-2).

The best three docking results are shown in Figure 5. Ligand 45^a with a binding energy of -10.7 kcal/mol shows hydrophobic interactions Trp210, Trp206, Gln209, Gln36, Lys37, Asn38, Cys39, Cys42, Cys80, Gly82, Asn81, Glu222, Ala157, Asp18, His19, Asn16 and Phe17 with the target in addition to three hydrogen bonding (2.57 Å, 2.91 Å, and 2.21 Å) with Trp206, Trp210 and Asn16. Ligand 49^a with binding score of -10.9 kcal/mol forms four hydrogen bonding (2.26 Å, 2.92 Å, 2.22 Å and 2.69 Å) with Trp206, Trp210, Asn16 and Glu14 respectively, and hydrophobic interaction with Trp210, Trp206, Gln209, Gln36, Lys37, Asn38, Cys39, Gly40, Asn16, Asp18, Ala157, His19, Glu222, Phe17, Asn173, Glu14. Similarly, compound 48^a with binding score of -11.1 kcal/mol forms hydrogen bonds (2.40 Å, 2.97 Å, and 2.27 Å) with Trp206, Trp210 and Asn16 respectively, and hydrophobic interactions with Trp210, Trp206, Gln209, Gln36, Lys37, Asn38, Cys39, Gly40, Asn16, Asp18, Ala157, His19, Glu222, Phe17, Glu14, and Glu15.

CONCLUSIONS

The present study aimed to generate a highly predictive GFAQSAR model capable of revealing the structural requirements for the observed antimalarial inhibitory activities of Pyrrolones against the Plasmodium, *P. falciparum*. In addition to that, it also investigates the Pyrrolones with best binding affinity to falcipain-2 of the parasite. Falcipain-2 is an essential and validated drug target involved in performing various enzymatic functions such as hemoglobin digestion, erythrocyte invasion, and parasite growth in the host cell. The robustness and applicability of QSAR equation have been established by internal and external validation techniques. The best three docking score is seen in compounds 45^a, 49^a and 48^a, due to their low binding affinity (-10.7, -10.9 and -11.1 kcal/mol) which is higher compared to the standard antimalarial drugs binding affinity value of (-8.8, -9.5 and -9.0 kcal/mol) (28). These compounds may be considered for further studies in view of their high potency and binding affinity to the target protein of *P. falciparum*.

It is envisioned that the wealth of information provided by the QSAR and Molecular docking results in this study will offer important structural insight for further laboratory experiments in the future design of novel and highly potent antimalarial.

In view of the high potency and binding affinity of the compounds to falcipain-2, it is recommended that these compounds be subjected to further laboratory studies. Also, our study advocates the use of combined approaches of QSAR and molecular docking to search for novel potential inhibitors unique to falcipain-2 of *P. falciparum*.

REFERENCES

1. WHO. 10 facts on malaria [Internet]. World Health Organization; 2016 [cited 2018 Jan 10]. Available from: <http://www.who.int/features/factfiles/malaria/en/>
2. Newton C. Severe Falciparum Malaria in Children Current Understanding of Pathophysiology and Supportive Treatment. *Pharmacology & Therapeutics*. 1998 Jul;79(1):1-53.
3. Kumari M, Chandra S, Tiwari N, Subbarao N. 3D QSAR, pharmacophore and molecular docking studies of known inhibitors and designing of novel inhibitors for M18 aspartyl aminopeptidase of Plasmodium falciparum. *BMC Structural Biology* [Internet]. 2016 Dec [cited 2018 Jan 13];16(1). Available from: <http://bmcstructbiol.biomedcentral.com/articles/10.1186/s12900-016-0063-7>
4. Basco LK, Bras JL. In Vitro Activity of Artemisinin Derivatives Against African Isolates and Clones of Plasmodium falciparum. *The American Journal of Tropical Medicine and Hygiene*. 1993 Sep 1;49(3):301-7.
5. Pandey KC, Dixit R. Structure-Function of Falcipains: Malarial Cysteine Proteases. *Journal of Tropical Medicine*. 2012;2012:1-11.
6. Bisson WH, Cheltsov AV, Bruey-Sedano N, Lin B, Chen J, Goldberger N, et al. Discovery of antiandrogen activity of nonsteroidal scaffolds of marketed drugs. *Proceedings of the National Academy of Sciences*. 2007 Jul 17;104(29):11927-32.
7. Mizutani MY, Itai A. Efficient Method for High-Throughput Virtual Screening Based on Flexible Docking: Discovery of Novel Acetylcholinesterase Inhibitors. *Journal of Medicinal Chemistry*. 2004 Sep;47(20):4818-28.
8. Nagpal I, Raj I, Subbarao N, Gourinath S. Virtual Screening, Identification and In Vitro Testing of Novel Inhibitors of O-Acetyl-L-Serine Sulphydrylase of Entamoeba histolytica. Bogyo M, editor. *PLoS ONE*. 2012 Feb 15;7(2):e30305.
9. Esposito EX, Hopfinger AJ, Madura JD. Methods for Applying the Quantitative Structure-Activity Relationship Paradigm. In: Bajorath J, editor. *Chemoinformatics* [Internet]. Totowa, NJ: Humana Press; 2004 [cited 2018 Jan 13]. p. 131-213. Available from: <http://link.springer.com/10.1385/1-59259-802-1:131>
10. Xue L, Bajorath J. Molecular Descriptors in Chemoinformatics, Computational Combinatorial Chemistry, and Virtual Screening. *Combinatorial Chemistry & High Throughput Screening*. 2000 Oct 1;3(5):363-72.
11. Barril X, Morley SD. Unveiling the Full Potential of Flexible Receptor Docking Using Multiple Crystallographic Structures. *Journal of Medicinal Chemistry*. 2005 Jun;48(13):4432-43.
12. Anonymous. EC50 [Internet]. *revolv.com*; [cited 2018 Oct 1]. Available from: <https://www.revolv.com/main/index.php?s=EC50&uid=1575>

13. Anonymous. Stardrop. Optibrium;
14. Veeresamy R, Rajak H, Jain A, Sivadasan S, Varghese C, Agrawal R. Validation of QSAR Models - Strategies and Importance. *Int J Drug Des Dis.* 2011;2(3):511-9.
15. Eriksson L, Jaworska J, Worth A, Cronin M, McDowell R, Gramatica P. Methods for reliability and uncertainty assessment and for applicability evaluations of classification- and regression-based QSARs. *Environ Health Perspect.* 2003;111(10):1361-75.
16. Gramatica P. Principles of QSAR models validation: internal and external. *QSAR & Combinatorial Science.* 2007 May;26(5):694-701.
17. Madheswaran A, Umamaheswari M, Asokkumar K, Sivashanmugam T, Subhadradevi V, Jagannath P. Computational drug discovery of potential phosphodiesterase inhibitors using in silico studies. *Asian Pacific Journal of Tropical Disease.* 2012 Jan;2:S822-6.
18. Daisy P, Nivedha R, Bakiya RH. In silico drug designing approach for biotin protein Ligase of *Mycobacterium tuberculosis*. *Asian J Pharm Clin Res.* 2013;6(11):103-107.
19. Monika JK, Singh K. Virtual screening using the ligand ZINC database for novel lipoxigenase-3 inhibitors. *Bioinformation.* 2013;9(11):583.
20. Hogg T, Nagarajan K, Schmidt CL, Hilgenfeld R. Crystal structure of falcipain-2 from *Plasmodium falciparum*. 2006 Jun 6;
21. Veerasamy R, Rajak H, Jain A, Sivadasan S, Varghese CP, Agrawal RK. Validation of QSAR models- strategies and importance. *International Journal of Drug Design & Discovery.* 2011;3:511-519.
22. Anonymous. List of molecular descriptors calculated by Dragon [Internet]. Talete; Available from: http://www.taletе.mi.it/products/dragon_molecular_descriptor_list.pdf
23. Adejoro I, Waheed S, Adeboye O. Molecular Docking Studies of *Lonchocarpus cyanescens* Triterpenoids as Inhibitors for Malaria. *Journal of Physical Chemistry & Biophysics.* 2016;6:213.



Preparation and Cytotoxicity Evaluation of Some Amino Acid Methyl Ester Schiff Bases

Nilay Akkuş Taş, Ayşegül Şenocak*, Ali Aydın

Gaziosmanpaşa University, College of Art and Science, Department of Chemistry, 60240, Tokat/TURKEY

Abstract: In this study, we prepared nine Schiff bases by condensation of amino acid methyl esters (isoleucine, phenylalanine, and methionine) with salicylaldehyde derivatives (2,4-dihydroxybenzaldehyde, 2-hydroxy-3-methoxybenzaldehyde, and 5-bromo-2-hydroxybenzaldehyde) and characterized by various spectroscopic methods (FT-IR, UV-Vis, and NMR techniques). FT-IR and UV-Vis spectra exhibited characteristic peaks for all imine compounds. NMR spectra pointed out the imine bond which is the indicator of the formation of Schiff bases. Besides, antiproliferative and cytotoxic features of the Schiff bases were examined by using MTT cell proliferation and LDH cytotoxicity assays, respectively. Amongst the synthesized Schiff bases, compound **3d** exhibited a very strong antiproliferative effect against all cells except A549. The experimental studies revealed that the Schiff bases synthesized in this study, especially **3d**, have an important potential to enter drug developmental studies.

Keywords: Amino acid Schiff bases, salicylaldehyde, antiproliferative activity, cytotoxicity, NMR spectra.

Submitted: January 03, 2018. **Accepted:** March 27, 2018.

Cite this: Taş NA., Şenocak A., Aydın A. Preparation and Cytotoxicity Evaluation of Some Amino Acid Methyl Ester Schiff Bases. JOTCSA. 2018;5(2):585–606.

DOI: <http://dx.doi.org/10.18596/jotcsa.373904>.

***Corresponding author.** E-mail: aysegul.senocak@gop.edu.tr, Tel: +90 356 252 1616/3051, Fax: +90 356 252 1585.

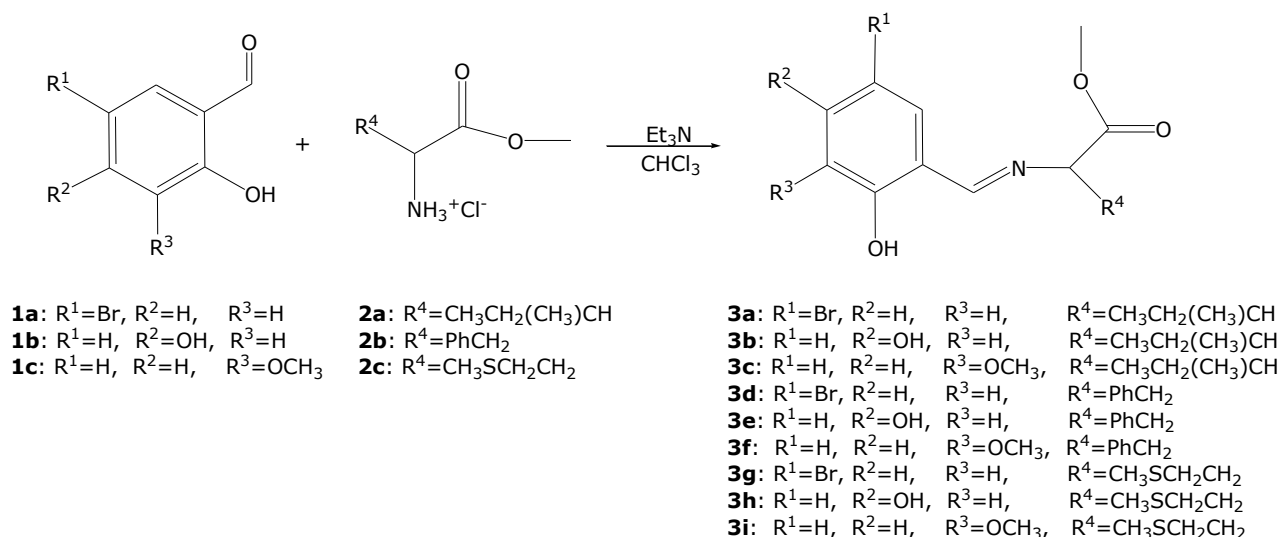
INTRODUCTION

The nitrogen atom in an amine compound can attack to an electrophilic carbon atom of a carbonyl compound under certain conditions like acidic or basic media or with heating. This nucleophilic attack results in a compound known as Schiff base named after Hugo Schiff, who synthesized first this compound group in 1864 (1).

Schiff bases are regarded as very significant compounds because of their potential uses ranging from pharmacology and industry to biology and chemistry. According to the literature survey, Schiff bases have wide applications containing antibacterial (2-6), antifungal (7-11), anticancer (12-17), antimalarial (18-22), and antioxidant (23-28). Besides, they are convenient pioneers of a great number of compounds, such as α -branched amines (29,30), tetramic acids (31), α - and β -amino acids (32,33), bicyclic lactams (34,35), and oxaziridines (36,37).

Amino acid-derived Schiff bases have attracted more attention because of incorporating amino acid component to the structure, taking important parts in chemical processes in living organisms. There are so many studies about the synthesis and the biological activities of amino acid Schiff bases and metal complexes. One of them focused on the effect of two amino acid Schiff bases on certain enzyme activities (38). The results showed that the Schiff bases acted as the activator or inhibitor on total, prostatic and non prostatic acid phosphatase enzymes depending upon their concentration. In another study, Zhang *et al.* synthesized chiral gossypol derivative Schiff bases (39). Some of the Schiff bases exhibited high anticancer activity, even higher than cisplatin anticancer drug. A series of benzaldehyde Schiff bases were prepared and their structure-microbicidal activity correlation was studied by Xia *et al.* (40). They expressed that the Schiff bases exhibited unique antibacterial activity and might be used for therapeutic purposes for bacterial infections. Another Schiff base series with aloin, a bioactive compound obtained from Aloe Vera, and amino acids was examined for anticancer and antioxidant properties (41). The results emphasized the enhanced antioxidant activity of aloin by the Schiff bases. The amino acid Schiff bases with a pyrazole derivative synthesized by Joksovic *et al.* were studied for anticancer activity (42). According to the results, the phenylalanine Schiff base was the most active compound against leukemic cell lines.

The purpose of this work was to synthesize nine Schiff bases (**3a-i**), from which the reduced form of **3a** was known (43), from amino acid methyl esters and salicylaldehyde derivatives (Scheme 1). Structures of the obtained Schiff base compounds were elucidated by FT-IR and UV-Vis spectrometry, elemental analysis, $^1\text{H-NMR}$ and $^{13}\text{C-NMR}$ techniques. Besides, cytotoxic activities of aforesaid compounds were investigated.



Scheme 1: The Schiff bases synthesized in this study.

MATERIALS AND METHODS

Chemistry

¹H-NMR and ¹³C-NMR spectra of all imine compounds were measured using AC Bruker 400 MHz NMR spectrometer in DMSO-d₆ at ambient temperature. FT-IR spectra were recorded on a Jasco FT-IR 430 spectrometer in the range of 400-4000 cm⁻¹ by using KBr pellets. UV-Vis absorption spectra were measured using a Perkin-Elmer Lambda 35 Spectrophotometer in a 10 mm quartz cell. The concentration of the Schiff base solutions prepared in methanol was about 10⁻⁴ M. Elemental analyses were recorded on a Elementar Vario Micro Cube elemental analyzer. Isoleucine, phenylalanine and methionine were used without purification and these amino acids were converted to corresponding methyl esters according to the literature (44). Solvents were used as received from commercial sources.

Experimental Procedure For the Preparation of the Amino Acid Schiff Bases

A round-bottomed flask containing amino acid methyl ester (**2a-c**) (1 mmol), N(Et)₃ (0.7 mmol) and CHCl₃ (20 mL) was fitted with a reflux condenser. This mixture was refluxed until all amino acid was dissolved. When all content was dissolved, salicylaldehyde derivative (**1a-c**) (0.7 mmol) was added to the clear solution. The reaction mixture was refluxed a couple of days long. During this time the color of the solution has changed to yellow. The completion of the reaction was followed by TLC. After completion of the reaction, the reaction mixture was extracted with CHCl₃ and 1 M HCl. The extract was dried using Na₂SO₄ and evaporated under vacuum.

3a: Yield 65%; FT-IR (KBr, cm⁻¹): 3458 (O-H), 2963,2935,2876 (aliphatic C-H), 1737 (C=O), 1630 (azomethine, C=N), 1256 (C-O phenolic); ¹H-NMR (DMSO-d₆, δ, ppm): 0.84 (3H, d, ³J_{HH}=1.5, CH₃), 0.86 (3H, t, ³J_{HH}=7.3, CH₃), 1.14 (H₁, m, CH₂), 1.43 (H₂, m, CH₂), 2.00 (1H, m, CH), 3.67 (3H, s, OCH₃), 4.02 (1H, d, ³J_{HH}=5.5, CH), 6.86 (1H, d, ³J_{HH}=8.8, Ph), 7.48 (1H, dd,

$^3J_{HH}=8.8$, $^4J_{HH}=2.5$, Ph), 7.68 (1H, d, $^4J_{HH}=2.5$, Ph), 8.53 (1H, s, azomethine), 13.39 (1H, s, OH). $^{13}\text{C-NMR}$ (DMSO- d_6 , δ , ppm): 11.16, 15.56, 24.54, 37.98, 51.94 (OCH₃), 74.84, 109.38 (PhBr), 119.01, 120.19, 133.63, 135.17, 159.68 (PhOH), 166.38 (azomethine), 170.99 (C=O). Anal. calcd. for C₁₄H₁₈BrNO₃ (328.2 g/mol): C, 51.23; H, 5.53; N, 4.27. Found: C, 51.68; H, 6.27; N, 4.96%.

3b: Yield 94%; FT-IR (KBr, cm^{-1}): 3371 (O-H), 2960,2932,2876 (aliphatic C-H), 1737 (C=O), 1638 (azomethine, C=N), 1227 (C-O phenolic); $^1\text{H-NMR}$ (DMSO- d_6 , δ , ppm): 0.83 (3H, d, $^3J_{HH}=6.7$, CH₃), 0.86 (3H, t, $^3J_{HH}=7.7$, CH₃), 1.12 (H₁, m, CH₂), 1.42 (H₂, m, CH₂), 1.96 (1H, m, CH), 3.65 (3H, s, OCH₃), 3.91 (1H, d, $^3J_{HH}=5.6$, CH), 6.20 (1H, d, $^4J_{HH}=2.5$, Ph), 6.30 (1H, dd, $^3J_{HH}=8.5$, $^4J_{HH}=2.5$, Ph), 7.21 (1H, d, $^3J_{HH}=8.5$, Ph), 8.37 (1H, s, azomethine), 13.64 (1H, s, OH). $^{13}\text{C-NMR}$ (DMSO- d_6 , δ , ppm): 11.16, 15.63, 24.54, 37.91, 51.83 (OCH₃), 74.43, 102.40, 107.22, 111.19, 133.57, 161.97 (azomethine), 163.44 (PhOH), 166.77 (PhOH), 171.48 (C=O). Anal. calcd. for C₁₄H₁₉NO₄ (265.3 g/mol): C, 63.38; H, 7.22; N, 5.28. Found: C, 63.51; H, 7.26; N, 4.87%.

3c: Yield 73%; FT-IR (KBr, cm^{-1}): 3424 (O-H), 2963,2935,2876 (aliphatic C-H), 1739 (C=O), 1630 (azomethine, C=N), 1226 (C-O phenolic); $^1\text{H-NMR}$ (DMSO- d_6 , δ , ppm): 0.84 (3H, d, $^3J_{HH}=7.7$, CH₃), 0.87 (3H, t, $^3J_{HH}=6.8$, CH₃), 1.15 (H₁, m, CH₂), 1.43 (H₂, m, CH₂), 2.03 (1H, m, CH), 3.67 (3H, s, OCH₃), 3.77 (3H, s, OCH₃), 4.03 (1H, d, $^3J_{HH}=5.4$, CH), 6.82 (1H, t, $^3J_{HH}=7.9$, Ph), 7.03 (1H, d, $^3J_{HH}=7.9$, Ph), 7.05 (1H, d, $^3J_{HH}=7.9$, Ph), 8.53 (1H, s, azomethine), 13.51 (1H, s, OH). $^{13}\text{C-NMR}$ (DMSO- d_6 , δ , ppm): 11.20, 15.62, 24.56, 37.94, 51.91 (OCH₃), 55.81 (OCH₃), 74.65, 115.25, 118.11, 118.28, 123.34, 147.95 (Ph-OCH₃), 151.04 (PhOH), 167.93 (azomethine), 171.19 (C=O). Anal. calcd. for C₁₅H₂₁NO₄ (279.3 g/mol): C, 64.50; H, 7.58; N, 5.01. Found: C, 64.86; H, 8.01; N, 5.52%.

3d: Yield 78%; FT-IR (KBr, cm^{-1}): 3382 (O-H), 3087,3061,3028 (aromatic C-H), 2950,2901 (aliphatic C-H), 1744 (C=O), 1630 (azomethine, C=N), 1276 (C-O phenolic); $^1\text{H-NMR}$ (DMSO- d_6 , δ , ppm): 3.09 (1H, dd, $^2J_{HH}=13.6$, $^3J_{HH}=8.2$, CH₂), 3.25 (1H, dd, $^2J_{HH}=13.6$, $^4J_{HH}=5.3$, CH₂), 3.65 (3H, s, OCH₃), 4.43 (1H, dd, $^3J_{HH}=8.2$, $^4J_{HH}=5.3$, CH), 6.85 (1H, d, $^3J_{HH}=8.8$, Ph), 7.18 (3H, m, Ph), 7.26 (2H, m, Ph), 7.45 (1H, dd, $^3J_{HH}=8.8$, $^4J_{HH}=2.5$, Ph), 7.57 (1H, d, $^4J_{HH}=2.5$, Ph), 8.32 (1H, s, azomethine), 13.01 (1H, s, OH). $^{13}\text{C-NMR}$ (DMSO- d_6 , δ , ppm): 51.39, 52.15 (OCH₃), 71.13, 118.98 (PhBr), 120.24, 126.31, 126.60, 128.27, 129.35, 133.39, 135.19, 136.68, 159.35 (PhOH), 166.17 (azomethine), 170.82 (C=O). Anal. calcd. for C₁₇H₁₆BrNO₃ (362.2 g/mol): C, 56.37; H, 4.45; N, 3.87. Found: C, 56.97; H, 4.63; N, 3.51%.

3e: Yield 63%; FT-IR (KBr, cm^{-1}): 3390 (O-H), 3059,3028 (aromatic C-H), 2950,2926 (aliphatic C-H), 1741 (C=O), 1626 (azomethine, C=N), 1221 (C-O phenolic); $^1\text{H-NMR}$ (DMSO- d_6 , δ , ppm): 3.04 (1H, dd, $^2J_{HH}=13.6$, $^3J_{HH}=8.2$, CH₂), 3.21 (1H, dd, $^3J_{HH}=13.6$, $^4J_{HH}=5.4$, CH₂), 3.64 (3H, s,

OCH₃), 4.33 (1H, dd, ³J_{HH}=8.2, ⁴J_{HH}=5.4, CH), 6.19 (1H, d, ⁴J_{HH}=2.2, Ph), 6.27 (1H, dd, ³J_{HH}=8.4, ⁴J_{HH}=2.2, Ph), 7.09 (1H, d, ³J_{HH}=8.4, Ph), 7.18 (3H, m, Ph), 7.25 (2H, m, Ph), 8.15 (1H, s, azomethine), 13.29 (1H, s, OH). ¹³C-NMR (DMSO-d₆, δ, ppm): 52.03, 70.74 (OCH₃), 79.16, 102.34, 107.26, 111.15, 126.50, 128.23, 129.35, 133.53, 136.97, 161.90 (azomethine), 162.96 (PhOH), 166.88 (PhOH), 171.27 (C=O). Anal. calcd. for C₁₇H₁₇NO₄ (299.3 g/mol): C, 68.21; H, 5.72; N, 4.68. Found: C, 68.16; H, 5.91; N, 4.44%.

3f: Yield 88%; FT-IR (KBr, cm⁻¹): 3412 (O-H), 3061,3028,3003 (aromatic C-H), 2950,2938 (aliphatic C-H), 1741 (C=O), 1632 (azomethine, C=N), 1224 (C-O phenolic); ¹H-NMR (DMSO-d₆, δ, ppm): 3.08 (1H, dd, ²J_{HH}=13.5, ³J_{HH}=8.3, CH₂), 3.25 (1H, dd, ²J_{HH}=13.5, ⁴J_{HH}=5.3, CH₂), 3.66 (3H, s, OCH₃), 3.76 (3H, s, OCH₃), 4.44 (1H, dd, ³J_{HH}=8.3, ⁴J_{HH}=5.3, CH), 6.78 (1H, t, ³J_{HH}=7.9, Ph), 6.90 (1H, d, ³J_{HH}=7.9, Ph), 7.03 (1H, d, ³J_{HH}=7.9, Ph), 7.19 (3H, m, Ph), 7.26 (2H, m, Ph), 8.32 (1H, s, azomethine). ¹³C-NMR (DMSO-d₆, δ, ppm): 51.29, 52.11 (OCH₃), 55.73 (OCH₃), 70.97, 115.16, 118.19, 123.20, 126.24, 126.56, 128.08, 128.26, 129.16, 129.37, 137.91, 147.83 (Ph-OCH₃), 150.58 (PhOH), 167.94 (azomethine), 170.99 (C=O). Anal. calcd. for C₁₈H₁₉NO₄ (313.4 g/mol): C, 68.99; H, 6.11; N, 4.47. Found: C, 69.71; H, 6.82 N, 4.64%.

3g: Yield 86%; FT-IR (KBr, cm⁻¹): 3436 (O-H), 2953,2916,2840 (aliphatic C-H), 1741 (C=O), 1632 (azomethine, C=N), 1276 (C-O phenolic); ¹H-NMR (DMSO-d₆, δ, ppm): 2.03 (3H, s, SCH₃), 2.08 (H₁, m, CH₂), 2.18 (H₂, m, CH₂), 2.42 (H₁, m, CH₂), 2.49 (H₂, m, CH₂), 3.68 (3H, s, OCH₃), 4.30 (1H, dd, ³J_{HH}=7.9, ⁴J_{HH}=5.0, CH), 6.87 (1H, d, ³J_{HH}=8.8, Ph), 7.48 (1H, dd, ³J_{HH}=8.8, ⁴J_{HH}=2.5, Ph), 7.71 (1H, d, ⁴J_{HH}=2.5, Ph), 8.57 (1H, s, azomethine). ¹³C-NMR (DMSO-d₆, δ, ppm): 14.46 (SCH₃), 29.20 (SCH₂), 32.15, 52.25 (OCH₃), 68.52, 109.55 (PhBr), 118.97, 120.40, 133.55, 135.23, 159.36 (PhOH), 166.55 (azomethine), 171.05 (C=O). Anal. calcd. for C₁₃H₁₆BrNO₃S (346.2 g/mol): C, 45.10; H, 4.66; N, 4.05. Found: C, 45.38; H, 5.54; N, 4.73%.

3h: Yield 69%; FT-IR (KBr, cm⁻¹): 3412 (O-H), 2953,2916,2837 (aliphatic C-H), 1740 (C=O), 1630 (azomethine, C=N), 1226 (C-O phenolic); ¹H-NMR (DMSO-d₆, δ, ppm): 2.02 (3H, s, SCH₃), 2.06 (2H, m, CH₂), 2.47 (2H, m, CH₂), 3.66 (3H, s, OCH₃), 4.19 (1H, s, CH), 6.21 (1H, s, Ph), 6.32 (1H, d, ³J_{HH}=8.0, Ph), 7.24 (1H, d, ³J_{HH}=8.0, Ph), 8.40 (1H, s, azomethine), 13.20 (1H, s, OH). ¹³C-NMR (DMSO-d₆, δ, ppm): 14.50 (SCH₃), 29.30 (SCH₂), 32.33, 52.14 (OCH₃), 68.08, 102.35, 107.37, 111.20, 133.66, 162.04 (azomethine), 162.96 (PhOH), 167.28 (PhOH), 171.49 (C=O). Anal. calcd. for C₁₃H₁₇NO₄S (283.3 g/mol): C, 55.11; H, 6.05; N, 4.94. Found: C, 55.80; H, 6.63; N, 5.71%.

3i: Yield 78%; FT-IR (KBr, cm⁻¹): 3435 (O-H), 2950,2913,2837 (aliphatic C-H), 1740 (C=O), 1630 (azomethine, C=N), 1227 (C-O phenolic); ¹H-NMR (DMSO-d₆, δ, ppm): 2.02 (3H, s, SCH₃), 2.10 (H₁, m, CH₂), 2.18 (H₂, m, CH₂), 2.43 (H₁, m, CH₂), 2.50 (H₂, m, CH₂), 3.67 (3H, s, OCH₃), 3.78 (3H, s, OCH₃), 4.30 (1H, dd, ³J_{HH}=7.9, ⁴J_{HH}=5.0, CH), 6.83 (1H, t, ³J_{HH}=7.9, Ph), 7.05 (1H,

d, $^3J_{HH}=7.9$, Ph), 7.06 (1H, d, $^3J_{HH}=7.9$, Ph), 8.58 (1H, s, azomethine), 13.12 (1H, s, OH). ^{13}C -NMR (DMSO- d_6 , δ , ppm): 14.48 (SCH₃), 29.25 (SCH₂), 32.23, 52.21 (OCH₃), 55.82 (OCH₃), 68.36, 115.33, 118.27, 118.41, 123.36, 147.89 (Ph-OCH₃), 150.63 (Ph-OH), 168.31 (azomethine), 171.19 (C=O). Anal. calcd. for C₁₄H₁₉NO₄S (297.4 g/mol): C, 56.55; H, 6.44; N, 4.71. Found: C, 57.28; H, 6.89; N, 5.00%.

BIOLOGICAL ACTIVITY

MTT Cell Proliferation Assay

HT29 (Human colorectal adenocarcinoma, ATCC® HTB-38™), HeLa (Human cervix adenocarcinoma, ATCC® CCL-2™), MCF7 (Human breast adenocarcinoma, ATCC® HTB22™), A549 (Human lung carcinoma, ATCC® CCL185™), C6 (Rat brain glioma, ATCC® CCL-107™), and Hep3B (Human hepatocellular carcinoma, ATCC® HB8064™) cancer cells and, FL (Human amnion cells, ATCC® CCL62™) and Vero (African green monkey kidney normal epithelial, ATCC® CCL-81™) normal cells were kept in a suitable medium involving fetal bovine serum and antibiotic solution. The cell suspension was adjusted to 1×10^6 cells in 10 mL and transferred 100 μL into the each well in culture plates. The compounds dissolved in sterile DMSO at 10-200 $\mu\text{g}/\text{mL}$ final concentration were transferred to the cells and incubated at 37 °C under 5% CO₂ atmosphere overnight. The cytotoxic activity of the Schiff bases was examined using MTT cell proliferation assay noted as percent inhibition. The percent inhibition calculated as shown below:

$$\% \text{inhibition} = [1 - (\text{Absorbance of Treatments} / \text{Absorbance of DMSO}) \times 100].$$

The half maximal inhibitory concentration (IC₅₀) of the compounds was noted in $\mu\text{g}/\text{mL}$ at 95 % confidence intervals. GI₅₀ values were calculated by following:

$$[(\text{Ti}-\text{Tz})/(\text{C}-\text{Tz})] \times 100 = 50,$$

which is the drug concentration bringing about a 50% reduction in the net growth in control cells in the course of the drug incubation.

Total growth inhibition (TGI) was calculated by $\text{Ti} = \text{Tz}$. The LC₅₀ indicating a net loss of cells following treatment was calculated according to the formula below:

$$[(\text{Ti}-\text{Tz})/\text{Tz}] \times 100 = -50.$$

Cytotoxicity Assay

The cytotoxicity of the Schiff bases was determined by using the cytosolic LDH measurement kit. Into each well, 5×10^3 cells were conveyed as triplicates in order to expose to IC₅₀

concentrations of the test compounds and incubated at 37 °C under 5% CO₂ atmosphere overnight. The percentage cytotoxicity was obtained by the following equation:

$$(\text{experimental value} - \text{low control} / \text{high control} - \text{low control}) \times 100,$$

in which experimental value is the test-compound treated cells, high control (maximum LDH release) is Triton X-100 treated cells, low control (spontaneous LDH release) is the untreated cells.

Cell imaging

HeLa and C6 cells were plated in 96-well plates at a density of 5.000 cells per well and awaited for 24 h. The compound **3d** in a concentration dependent manner was added and morphological changes of the cells were screened by phase contrast microscopy in every 6 h for 24 h. Images of the treated and untreated cells were photographed after the completion of the process by an inverted microscope equipped with a digital camera.

Statistical Analysis

The statistical significance of the variations was determined by the one-way analyses of variance (one-way ANOVA) followed by Tukey's test. SPSS for Windows was used for statistical analyses.

RESULTS AND DISCUSSION

The Schiff bases were obtained by refluxing amino acid esters with salicylaldehyde derivatives in a chloroform medium under basic conditions. The condensation products were obtained in a couple of days with moderate to high yields. Azomethines were yellow oily compounds which did not need further purification. The compounds were soluble in common organic solvents (methanol, ethanol, CHCl₃, CH₂Cl₂, etc.) Their structures were proved by elemental analysis and, UV-Vis, FT-IR, ¹H- and ¹³C-NMR spectroscopic methods.

FT-IR and UV-Vis Spectra

The positions of the important IR bands were shown in the experimental part and the FT-IR spectra of **3a** was depicted in Figure 1. Sharp absorption bands between 1638-1626 cm⁻¹ were ascribed to the CH=N stretching bands for all of the Schiff bases. Aromatic hydroxy substituent participating in intramolecular hydrogen bonding with azomethine nitrogen atom was observed as a broad band about 3400 cm⁻¹. The sharp absorption bands near 1740 cm⁻¹ were related to the asymmetric carboxylate stretches (COO). The Ph-O vibrations were observed around 1276-1221 cm⁻¹. Symmetric and asymmetric aliphatic C-H stretching bands were assigned to 2953-2837 cm⁻¹ range. As it comes to aromatic C-H protons, they could not be observed in **3a-c** and **3g-i** Schiff bases, however the FT-IR spectra of **3d-f** Schiff bases exhibited aromatic proton

stretching vibration peaks because of existence of aromatic protons of phenylalanine in addition to those of aldehyde part.

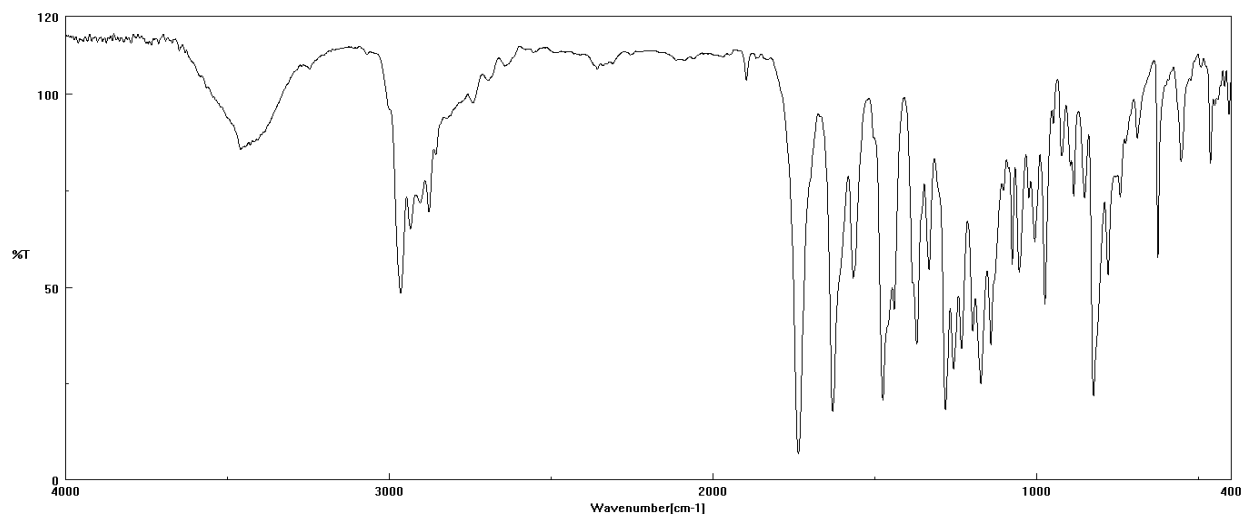


Figure 1: FT-IR spectrum of **3a**.

UV-Vis studies were also performed for all of the Schiff bases by dissolving in methanol. UV-Vis spectra exhibited three bands for all compounds as listed in Table 1.

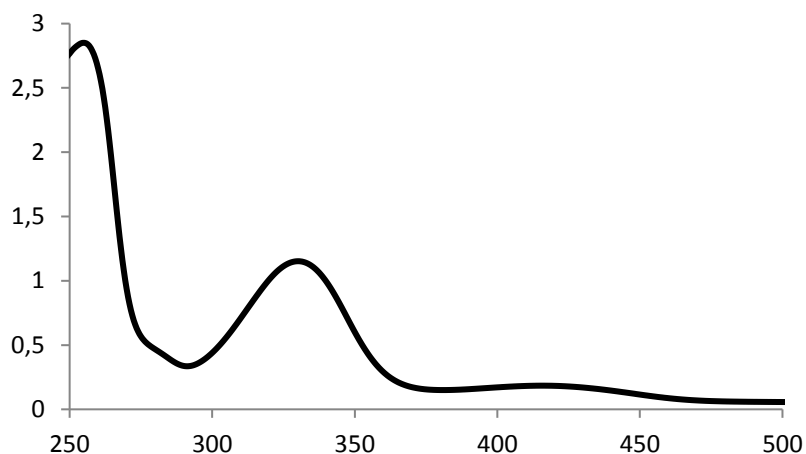


Figure 2: UV-Vis spectrum of **3a**.

A high energy band observed below 300 nm can be assigned to $\pi \rightarrow \pi^*$ transitions carried out in aromatic rings. The band at 376 and 379 nm in phenylalanine Schiff bases **3b**, **3e** and **3h** can be sprung from charge transfer within the whole Schiff base molecule. That kind of band is caused by the strong intramolecular hydrogen bond between the hydroxyl and the azomethine group of o-hydroxyl Schiff bases (45). As it comes to the bands observed in the range of 327-424 nm, they can be assigned to the $n \rightarrow \pi^*$ transitions for the isoleucine and methionine Schiff bases.

¹H- and ¹³C-NMR Spectra

The ¹H- and ¹³C-NMR spectra of all of the Schiff bases were consistent with the suggested structures. The ¹H- and ¹³C-NMR spectra for **3a** were demonstrated in Figure 3. A singlet peak about 13.5 ppm was attributed to the hydroxyl group of all imine compounds. The azomethine peak, an evidence for the Schiff base formation, was observed as a singlet in the range of 8.15-8.58 ppm. Methoxy group belonging to the amino acid ester induced to a singlet about 3.65 ppm. Aromatic ring protons were observed at 6.20-7.71 ppm as doublets and triplets for isoleucine (**3a-c**) and methionine (**3g-i**) Schiff bases. Same protons appeared in the similar region, but as overlapped with aromatic protons of phenylalanine for the Schiff bases **3d-f**. As it comes to aliphatic protons, they were observed in characteristic methyl, methylene and methyne region as shown in the experimental.

BIOLOGICAL ACTIVITY

Antiproliferative Actions of the Compounds

The antiproliferative activities of the Schiff bases and positive control against cell lines were screened according to a cell proliferation assay performed by using the 3-(4,5-dimethylthiazol-2-yl)-2,5-diphenyltetrazolium bromide (MTT). The antiproliferative actions and selectivity of the Schiff bases were evaluated through tumor cells and normal cells (Vero and FL). Also, statistically significant differences ($P < 0.05$) attracted the attention among cancer cell lines compared to normal cell lines for the different concentrations. According to TGI and IC₅₀ values in Table 2, **3d** displayed very strong cytotoxic activity than the control drugs, 5-fluorouracil and cisplatin, on all cancer cell lines (TGI 5.81-52.36 µg/mL, IC₅₀ 5.72-46.35), except for A549. Compounds **3c**, **3e**, **3h** and **3i** were effective on HeLa (TGI 44.24 µg/mL, IC₅₀ 41.99±2.9 µg/mL), HT29 (TGI 28.19 µg/mL, IC₅₀ 18.58±3.4 µg/mL), and C6 (TGI 38.70 µg/mL, IC₅₀ 36.33±3.8 for **3h** and TGI 3.75 µg/mL, IC₅₀ 3.69±2.7 µg/mL for **3i**) cell lines, respectively (Table 2-4) (Figure 4). For HeLa and HT29 cell lines, compounds **3a**, **3b**, **3f**, and **3g** had remarkable TGI values (Table 3-4). The IC₅₀ values of the **3a**, **3b**, **3f**, and **3g** (2.79-23.31, 12.49-64.17, 21.98-26.59, and 6.27-89.89 µg/mL, respectively) for these two cancer lines were similar to the TGI parameters. **3a** and **3b** also had potent cytotoxic activity on C6 cells (TGI 5.63, IC₅₀ 5.42 and TGI 7.59, IC₅₀ 7.49 µg/mL, respectively) (Table 3-4) (Figure 4). For C6 cells, compounds **3b**, **3d** and **3i** had remarkable LC₅₀ values (37.21, 26.76 and 17.39 µg/mL, respectively) (Figure 4). However, the LC₅₀ values of compounds **3a** and **3g** were only meaningful for HeLa cell line (11.09 and 29.73 µg/mL, respectively) (Tables 2-4) (Figure 4). Compound **3a** had the best GI₅₀ values (1.55, 1.93, and 1.78 µg/mL, respectively) when it came to the HeLa, MCF7, and C6 cell lines. In addition, compound **3d** and **3e** had remarkable GI₅₀ values (1.68 and 1.84 µg/mL, respectively) for MCF7 cell line. Compound **3i** exhibited significant GI₅₀ value (1.84 µg/mL) for C6 cell line.

Table 1: UV-Vis spectral data for the Schiff bases in methanol.

Compound	λ (nm)
3a	255
	330
3b	282
	307
3c	265
	327
3d	255
	330
3e	282
	310
3f	264
	328
3g	255
	330
3h	282
	310
3i	265
	330

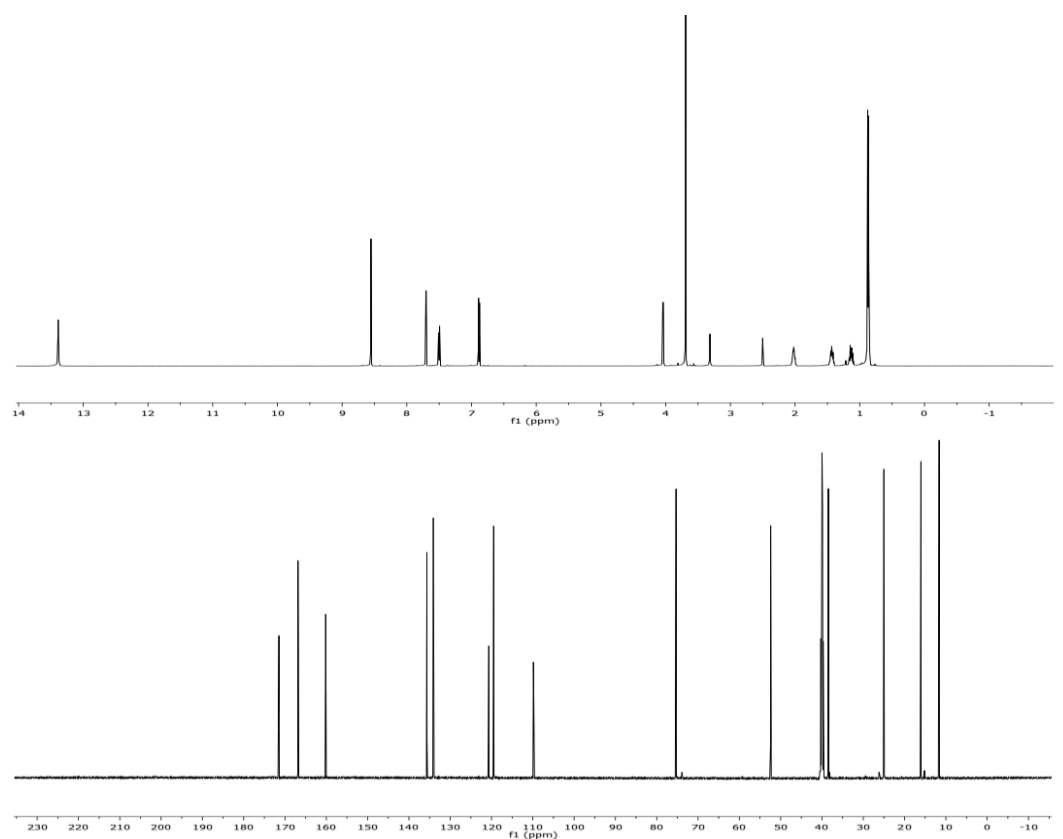
**Figure 3:** ^1H - and ^{13}C -NMR spectra of **3a**.

Table 2: GI50, TGI, LC50 and IC50 values for **3a**, **3b**, and **3c**.

$\mu\text{g/mL}$	3a				3b				3c			
	GI50	TGI	LC50	IC50	GI50	TGI	LC50	IC50	GI50	TGI	LC50	IC50
A549	68.49 ± 8.34	>10000	>10000	>10000	104.53 ± 8.4	>10000	>10000	>10000	18.89 ± 1.0	>10000	>10000	>10000
HeLa	1.55 \pm 0.08	2.80 \pm 0. 08	11.09 \pm 0 .77	2.79 \pm 0. 07	2.92 \pm 0 .21	12.70 \pm 0 .64	416.42 \pm 15.3	12.49 \pm 0 .71	2.64 \pm 0.12	44.24 \pm 3 .7	>10000	41.99 \pm 3 .1
HT29	4.18 \pm 0.17	28.39 \pm 1 .3	2504.05 ± 51.9	23.31 \pm 0 .89	3.79 \pm 0 .25	115.02 \pm 7.9	>10000	64.17 \pm 4 .3	3.60 \pm 0.17	3613.74 ± 54.6	>10000	702.60 \pm 28.3
Hep3B	3.81 \pm 0.11	1316.12 ± 47.5	>10000	1133.57 ± 33.9	6.53 \pm 0 .37	>10000	>10000	>10000	5.11 \pm 0.43	>10000	>10000	>10000
MCF7	1.93 \pm 0.09	1296.89 ± 42.8	>10000	904.30 \pm 28.4	2.68 \pm 0 .29	4169.61 ± 61.7	>10000	2833.66 ± 59.2	1.68 \pm 0.08	2099.80 ± 72.3	>10000	1347.86 ± 54.8
C6	1.78 \pm 0.09	5.63 \pm 0. 46	176.18 \pm 14.5	5.42 \pm 0. 18	3.11 \pm 0 .20	7.59 \pm 0. 76	37.21 \pm 2 .1	7.49 \pm 0. 33	5.32 \pm 0.51	5675.32 ± 71.4	>10000	3796,80 ± 65.4
Vero	3.50 \pm 0.21	10.55 \pm 0 .98	83.99 \pm 1 1.0	10.26 \pm 0 .34	2.43 \pm 0 .19	115.33 \pm 5.6	>10000	92.31 \pm 5 .32	4.03 \pm 0.36	248.67 \pm 17.9	>10000	195.66 \pm 15.8
FL	4.21 \pm 0.27	31.57 \pm 1 .4	3977.09 ± 71.4	30.91 \pm 1 .5	3.63 \pm 0 .27	19.90 \pm 2 .7	1020.77 ± 22.6	19.54 \pm 1 .4	4.14 \pm 0.37	2736.46 ± 65.1	>10000	2394.84 ± 69.1

Values are given as the mean \pm SD of three experiments and $r^2=0.86$ to 0.97 . Significant at $P < 0.05$

Table 3: GI50, TGI, LC50 and IC50 values for **3d**, **3e**, and **3f**.

$\mu\text{g/mL}$	3d				3e				3f			
	GI50	TGI	LC50	IC50	GI50	TGI	LC50	IC50	GI50	TGI	LC50	IC50
A549	74.49 ± 4.3	>10000	>10000	>10000	152.22 ± 9.7	>10000	>10000	>10000	32.98 ± 1.2	>10000	>10000	>10000
HeLa	3.06 \pm 0.41	13.63 \pm 0.49	442.07 \pm 21.0	13.39 \pm 0.77	3.59 \pm 0 .63	108.90 ± 9.1	>10000	102.28 \pm 5.7	3.28 \pm 0.54	22.56 \pm 0.87	3513.62 ± 71.6	21.98 \pm 0 .88
HT29	2.63 \pm 0.22	14.97 \pm 0.41	1933.71 ± 59.7	12.01 \pm 0.63	2.48 \pm 0 .57	28.19 \pm 0.93	>10000	18.58 \pm 1 .1	3.29 \pm 0.21	36.87 \pm 0.93	>10000	26.59 \pm 0 .87
Hep3B	3.07 \pm 0.37	30.62 \pm 0.97	>10000	29.55 \pm 1.5	4.67 \pm 0 .45	>10000	>10000	>10000	7.13 \pm 0.48	>10000	>10000	>10000
MCF7	2.19 \pm 0.33	52.36 \pm 1.4	>10000	46.35 \pm 1.7	1.84 \pm 0 .24	814.18 ± 19.2	>10000	581.23 \pm 17.8	3.96 \pm 0.27	>10000	>10000	>10000
C6	2.56 \pm 0.31	5.81 \pm 0. 37	26.76 \pm 1 .0	5.72 \pm 0. 19	9.61 \pm 0 .61	>10000	>10000	7380.55 ± 51.0	4.13 \pm 0.18	2897.4 ± 62.7	>10000	1962.94 ± 21.3
Vero	2.34 \pm 0.34	12.43 \pm 0.42	1740.98 ± 44.0	11.61 \pm 0.23	4.64 \pm 0 .42	100.54 ± 8.7	>10000	86.56 \pm 5 .9	3.76 \pm 0.19	36.31 \pm 0.99	>10000	32.89 \pm 1 .1
FL	3.58 \pm 0.33	20.70 \pm 0.88	1327.85 ± 42.5	20.31 \pm 0.41	4.20 \pm 0 .39	66.21 \pm 4.3	>10000	63.61 \pm 5 .3	5.53 \pm 0.34	265.96 ± 8.6	>10000	250.97 \pm 7.4

Values are given as the mean \pm SD of three experiments and $r^2=0.86$ to 0.97 . Significant at $P < 0.05$

Table 4: GI50, TGI, LC50 and IC50 values for **3g**, **3h**, and **3i**.

<i>µg/mL</i>	3g				3h				3i			
	GI50	TGI	LC50	IC50	GI50	TGI	LC50	IC50	GI50	TGI	LC50	IC50
A549	145.66± 14.7	>10000	>10000	>10000	27.42± 1.2	>10000	>10000	>10000	26.43 ±0.97	>10000	>10000	>10000
HeLa	2.72± 0.09	6.31±0 .30	29.73 ±1.7	6.27± 0.43	5.36± 0.52	3123.2 ±57.8	>10000	2708.12 ±59.2	3.75± 0.44	116.36 ±5.4	>10000	108.75± 9.8
HT29	3.71± 0.13	160.88± 15.2	>10000	89.89± 11.4	2.56± 0.43	>10000	>10000	>10000	2.86± 0.11	1193.61 ±14.9	>10000	268.47± 10.1
Hep3B	4.42± 0.22	996.31± 37.8	>10000	874.91 ±32.1	2.74± 0.37	>10000	>10000	>10000	7.23± 0.28	>10000	>10000	>10000
MCF7	2.15± 0.14	374.11± 24.7	>10000	293.37 ±17.4	3.09± 0.39	2657.17 ±54.6	>10000	1903.43 ±51.3	2.43± 0.14	>10000	>10000	>10000
C6	4.79± 0.25	>10000	>10000	>10000	4.98± 0.40	38.70± 1.6	4110.5 ±67.4	36.33± 1.1	1.84± 0.07	3.75± 0.19	17.39± 2.2	3.69± 0.55
Vero	4.06± 0.31	17.57± 1.7	349.06± 27.6	16.84± 0.49	3.00± 0.35	>10000	>10000	>10000	3.35± 0.34	647.63± 13.5	>10000	452.61± 12.7
FL	3.43± 0.27	26.20± 1.8	5663.91 ±77.3	25.60± 1.0	5.06± 0.46	>10000	>10000	9447.3 ±71.4	6.82± 0.95	1625.41 ±37.2	>10000	1475.11 ±47.6

Values are given as the mean ± SD of three experiments and $r^2=0.86$ to 0.97 . Significant at $P < 0.05$

Some cancer cells were more sensitive to the tested Schiff bases than FL and Vero normal cells. A comparison of the activities of these compounds in regard to the IC₅₀ values as against normal cells (FL and Vero) revealed the following: **3d**, **3e**, **3h** for HT29, **3a**, **3b**, **3c**, **3d**, **3e**, **3f**, **3g** for HeLa and **3a**, **3b**, **3d**, **3h**, **3i** for C6 were more selective than others. Hence, the findings significantly highlight some compounds as possible selective antiproliferative agents for some cancer types. The pharmacological activities of these compounds are probably due to the major bioactive substituents such as hydroxy, methoxy, phenyl, methylthio, and bromine. Especially, bromine group may be responsible for cytotoxic activities of **3a**, **3d** and **3g** having the highest pharmacological activity against cancer cells. The higher antiproliferative activity of compound **3d** than **3a** points out the importance of the phenyl substituent on cytotoxic activity. Overall, the high cytotoxic effects of these compounds may be related to their unique three-dimensional structures arising from the substituents. It was noted that three parameters (GI₅₀, TGI, LC₅₀) of these compounds met NCI-60 criteria enough to pass into further pharmacological investigations.

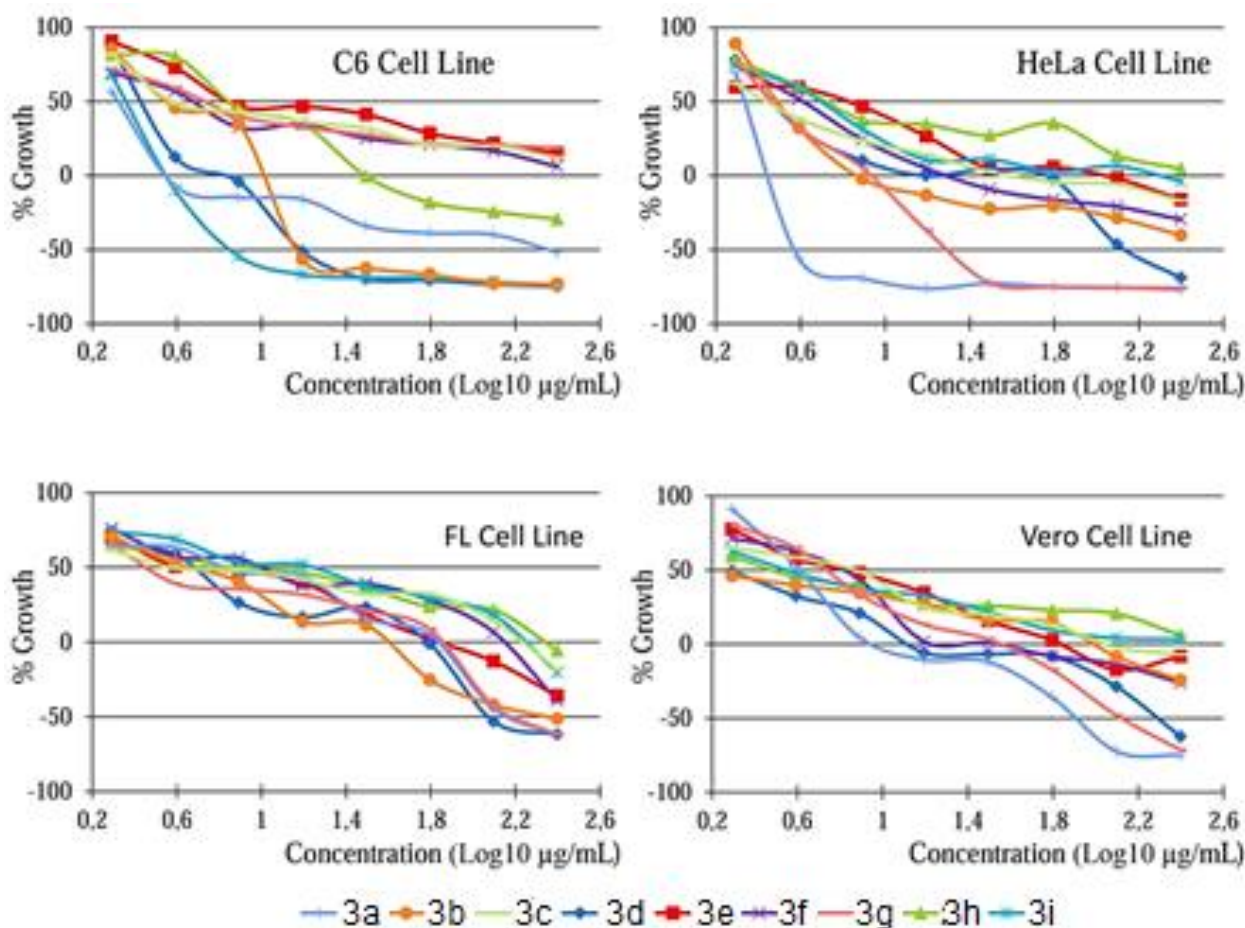


Figure 4: Effects of the compounds on the proliferation of C6, HeLa, FL, and Vero cells. Exponentially growing cells were incubated with the Schiff bases for 24 hours.

Table 5: IC₅₀ (µg/mL) of positive controls in cell lines.

	HeLa	HT29	A549	MCF7	C6	Hep3B	FL	Vero
Cisplatin	50.29±	40.39±	60.49±	63.79±	33.08±	48.69±	52.79±	56.20±
	8.3	5.6	8.5	7.4	4.8	5.3	6.0	5.3
5FU	61.59±	65.19±	69.79±	74.19±	54.30±	62.89±	59.09±	65.35±
	7.1	5.3	8.1	8.0	7.3	6.8	6.4	5.9

Values are given as the mean ± SD of three experiments and $r^2=0.94$ to 0.99 . Significant at $P < 0.05$

Cytotoxic Mode of the Compounds

Cytotoxic activities of the Schiff bases (25, 50, 75, and 100 µg/mL) on cell lines were monitored by the LDH cytotoxicity kit. The %cytotoxicity values of these compounds at concentration of 25 µg/mL were in the range of 6.21%-34.74% against all cell lines. Compound **3b** caused the most powerful cytotoxic effect (34.71%, $p < 0.05$) against C6 cell when compared to the other compounds and cell lines (Table 7). Compound **3e** had the lowest percentage cytotoxicity with the values of 10.45% (A549) and 23.31% (C6) (Tables 6 and 7) (Figure 5). Compound **3c** also exhibited the smallest percentage cytotoxicity for HeLa (8.11%) and FL (14.88%) cells. Compound **3i**, the condensation product of methionine methyl ester and o-vanilin, was interestingly highly toxic for A549 and HT29 cells (22.80% and 32.68%, respectively), whereas less toxic for Hep3B and Vero cells (8.36% and 11.91%, respectively) (Tables 6-8) (Figure 5). Similarly, **3b**, composed of isoleucine methyl ester and 2,4-dihydroxybenzaldehyde, was very toxic for C6 (34.71%) and less toxic for HT29 (16.34%). However, **3i** and **3b** may cause cytotoxic effect via the same mechanisms of action. It is noteworthy that the compound **3f**, containing phenylalanine methyl ester and o-vanilin, had slightly high toxicity against MCF7, Vero, and FL cells (11.91%, 23.69%, and 29.32%, respectively) than the other compounds which had similar potent cytotoxic activity. Compound **3h** exhibited the lowest percentage cytotoxicity for MCF7 cell lines. The rest of the compounds (**3a** and **3d**) had the highest cytotoxic effect towards HeLa and Hep3B cells (31.22% and 19.57, respectively). One of the most important conditions for being an anticancer agent is the minimal toxicity against normal cells. Therefore, cytotoxic features were compared in order to find out the advanced pharmacological capacities of these compounds. Compounds **3c** (for HeLa, 8.11%), **3e** (for A549, 10.45%), **3h** (for MCF7, 6.21%), and **3i** (for Hep3B and Vero, 8.36% and 11.91%, respectively) exhibited equal cytotoxicity with controls, indicating their significant antiproliferative potential as well as low cytotoxicity (Tables 6-9).

Table 6: % Cytotoxicity of the compounds against A549, HeLa, and HT29.

%Cytotoxicity	A549				HeLa				HT29			
	25µg/mL	50µg/mL	75µg/mL	100µg/mL	25µg/mL	50µg/mL	75µg/mL	100µg/mL	25µg/mL	50µg/mL	75µg/mL	100µg/mL
3a	17,73± 1.3	26,85± 1.9	50,73± 3.7	60,67± 4.3	31,22± 1.6	68,90± 1.7	77,71± 2.7	103,86± 5.1	23,12± 1.4	52,44± 2.9	70,17± 3.5	89,74± 3.9
3b	17,54± 1.4	24,07± 2.1	43,64± 3.1	53,45± 3.9	18,94± 1.4	34,96± 1.5	53,07± 2.1	58,45± 2.4	16,34± 1.1	54,34± 2.5	80,24± 3.7	100,63± 4.9
3c	15,64± 1.4	27,61± 1.8	47,44± 2.9	71,56± 4.4	8,11± 0.8	18,43± 1.2	36,10± 1.8	44,52± 2.4	22,55± 1.1	28,37± 1.8	54,97± 2.8	79,16± 4.0
3d	10,64± 1.2	20,27± 1.5	27,99± 1.8	46,87± 3.1	18,62± 1.4	31,92± 1.8	52,06± 2.2	81,06± 3.1	25,21± 1.6	53,70± 2.3	80,11± 4.0	102,47± 5.0
3e	10,45± 1.1	20,01± 1.5	42,37± 2.7	51,11± 3.8	17,16± 1.4	26,60± 1.5	35,02± 1.7	50,28± 1.9	25,97± 1.5	48,01± 1.9	72,70± 3.8	85,18± 4.1
3f	18,43± 1.5	39,01± 2.1	60,73± 3.6	66,56± 4.1	21,72± 1.5	36,16± 1.6	49,40± 2.0	93,79± 4.7	32,17± 1.5	34,71± 1.8	60,67± 3.1	76,12± 3.7
3g	14,12± 1.4	34,77± 2.0	60,92± 3.4	76,50± 4.5	22,23± 1.5	72,70± 2.3	82,77± 3.4	93,98± 5.0	20,39± 1.4	49,27± 2.7	72,70± 3.5	100,13± 4.3
3h	21,15± 1.7	28,56± 1.7	50,03± 3.3	58,71± 4.0	14,00± 1.1	22,42± 1.3	31,86± 1.9	50,73± 2.4	24,89± 1.4	43,57± 2.0	69,54± 3.4	85,81± 3.9
3i	22,80± 1.5	48,20± 3.7	54,53± 3.5	58,96± 4.0	18,05± 1.1	24,70± 1.4	43,64± 1.9	45,60± 2.3	32,68± 1.6	44,84± 1.9	72,70± 3.4	90,63± 4.6

Values are given as the mean ± SD of three experiments and $r^2=0.88$ to 0.99 . Significant at $P < 0.05$

Table 7: % Cytotoxicity of the compounds against Hep3B, MCF7, and C6.

%Cytotoxicity	<i>Hep3B</i>				<i>MCF7</i>				<i>C6</i>			
	25µg/mL	50µg/mL	75µg/mL	100µg/mL	25µg/mL	50µg/mL	75µg/mL	100µg/mL	25µg/mL	50µg/mL	75µg/mL	100µg/mL
3a	10,01± 0.8	25,46± 2.2	38,38± 2.7	51,04± 3.0	10,64± 0.8	18,49± 1.5	29,51± 1.9	43,89± 3.0	30,27± 1.5	66,37± 3.4	78,97± 4.0	99,94± 5.1
3b	14,00± 1.0	23,81± 2.1	41,61± 2.8	55,29± 3.0	6,84± 0.7	14,31± 1.0	32,74± 2.1	50,66± 3.6	34,71± 1.4	64,47± 3.5	82,08± 4.5	96,20± 5.2
3c	11,91± 1.1	21,22± 1.7	32,55± 2.3	49,91± 3.1	9,37± 0.8	18,49± 1.5	26,47± 1.9	54,21± 3.7	30,91± 1.8	67,00± 3.9	82,96± 4.7	99,11± 5.3
3d	19,57± 1.5	28,88± 2.0	48,01± 2.5	60,99± 3.8	10,01± 0.9	20,14± 1.1	27,04± 1.8	45,35± 2.1	27,68± 1.5	63,84± 2.9	79,42± 4.0	104,75± 5.4
3e	18,56± 1.4	26,35± 1.6	45,41± 2.3	51,23± 3.4	9,37± 0.9	19,19± 1.3	30,53± 1.9	40,28± 2.0	23,31± 1.4	62,57± 3.1	78,28± 4.2	85,18± 4.9
3f	14,63± 1.2	32,68± 2.5	57,82± 3.4	70,80± 4.1	11,91± 0.9	15,96± 1.0	29,26± 1.5	47,31± 2.2	31,54± 1.8	55,60± 3.1	80,56± 4.9	96,45± 5.0
3g	14,31± 1.1	26,98± 2.0	35,66± 2.7	48,51± 2.9	11,27± 0.9	19,13± 1.4	27,68± 1.8	57,88± 3.4	25,84± 1.1	63,84± 3.5	82,46± 4.8	97,21± 5.4
3h	14,25± 1.4	25,40± 2.1	39,65± 2.9	51,68± 3.2	6,21± 0.8	16,02± 1.2	32,11± 1.9	47,18± 2.3	29,64± 1.4	56,87± 3.0	78,72± 4.6	93,60± 5.0
3i	8,36± 0.78	25,90± 2.0	33,82± 2.4	51,99± 3.1	8,11± 0.7	23,75± 1.1	38,51± 2.3	50,35± 3.4	33,44± 1.9	63,20± 3.7	81,13± 4.2	101,01± 5.3

Values are given as the mean ± SD of three experiments and $r^2=0.88$ to 0.99 . Significant at $P < 0.05$

Table 8: % Cytotoxicity of the compounds against Vero and FL.

%Cytotoxicity	Vero				FL			
	25µg/mL	50µg/mL	75µg/mL	100µg/mL	25µg/mL	50µg/mL	75µg/mL	100µg/mL
3a	19,76± 1.5	32,93± 2.1	44,97± 2.8	73,46± 3.9	20,08± 1.5	29,39± 1.9	57,76± 3.5	72,96± 4.0
3b	16,85± 1.5	29,32± 1.9	56,87± 3.2	81,63± 4.2	15,64± 1.1	29,83± 1.7	48,77± 3.0	70,87± 4.1
3c	17,23± 1.3	36,67± 2.2	51,61± 2.9	60,99± 3.7	14,88± 1.2	32,74± 2.1	44,59± 2.9	68,14± 3.7
3d	17,99± 1.2	33,38± 1.9	52,56± 3.1	74,48± 3.9	25,40± 1.6	65,10± 2.9	70,93± 4.1	77,33± 4.4
3e	14,95± 1.0	30,91± 1.8	63,77± 3.4	79,16± 4.0	18,94± 1.4	33,38± 1.7	46,55± 2.4	66,75± 2.9
3f	23,69± 1.5	34,33± 1.8	54,65± 2.7	87,71± 5.0	29,32± 1.4	54,34± 2.0	82,08± 4.3	93,35± 5.1
3g	18,11± 1.4	30,40± 2.0	59,66± 3.5	83,09± 4.5	16,21± 1.2	37,75± 2.4	46,61± 2.8	70,74± 4.0
3h	19,25± 1.4	32,74± 1.7	64,28± 3.0	80,30± 4.4	19,19± 1.5	46,42± 1.8	59,91± 3.6	72,32± 4.0
3i	11,91± 0.9	24,13± 1.5	43,19± 2.9	54,02± 3.5	28,37± 1.6	43,57± 1.9	63,84± 3.8	73,46± 4.2

Values are given as the mean ± SD of three experiments and r²=0.88 to 0.99. Significant at P < 0.05

Table 9: % Cytotoxicity of positive controls at IC50 concentrations.

	HeLa	HT29	A549	MCF7	C6	ep3B	FL	Vero
Cisplatin	9.85± 0.8	11.23± 0.9	8.63± 0.8	10.71± 0.9	9.04± 0.8	8.46± 0.8	8.33± 0.7	9.41± 0.9
5FU	8.83± 0.7	7.91± 0.7	9.19± 0.8	7.69± 0.7	10.01± 0.9	9.67± 0.8	8.44± 0.8	8.81± 0.9

Values are given as the mean ± SD of three experiments and r²=0.95 to 0.98. Significant at P < 0.05

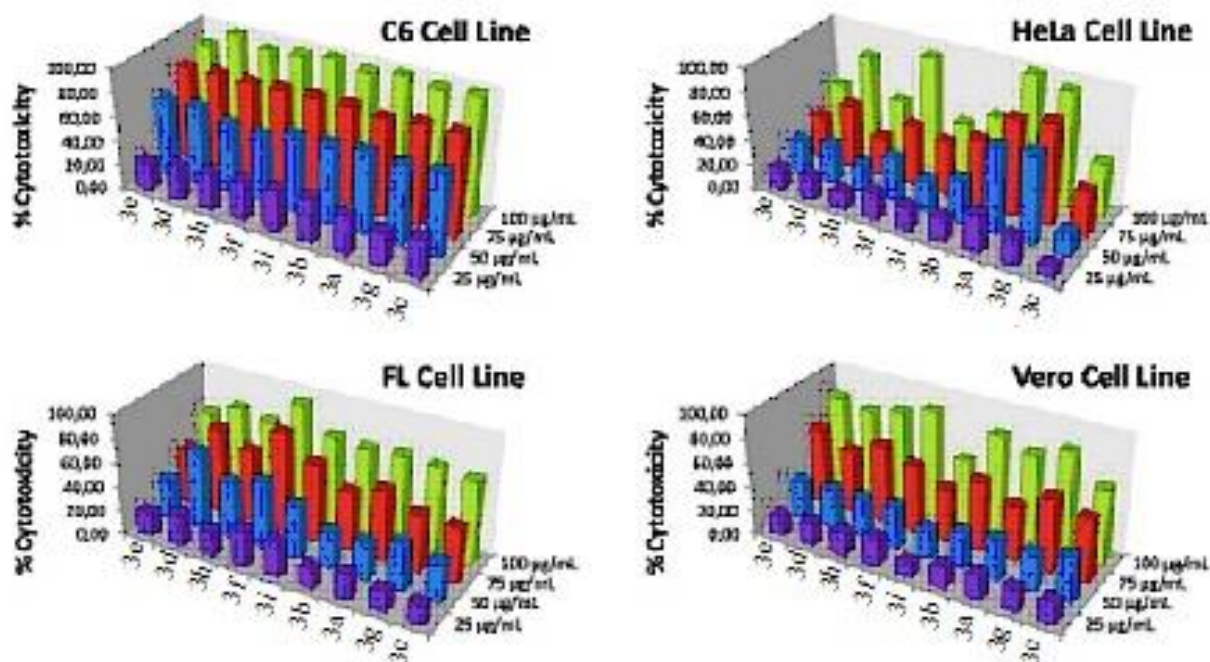


Figure 5. The cytotoxic activity of the compounds on C6, HeLa, FL, and Vero cells. Exponentially growing cells were incubated with various concentrations of the Schiff bases and cytotoxicity was measured by LDH Cytotoxicity Assay.

The Effect of the 3d on the Morphology of the Cells

The morphology alters of treated and untreated (control) cells were monitored by using the inverted phase-contrast microscopy techniques. As shown in Figures 6 and 7, visible morphology alters such as cytoplasmic blebs, anomalous globular structure and reduction in cell quality and cell count in the flask monolayer were recorded.

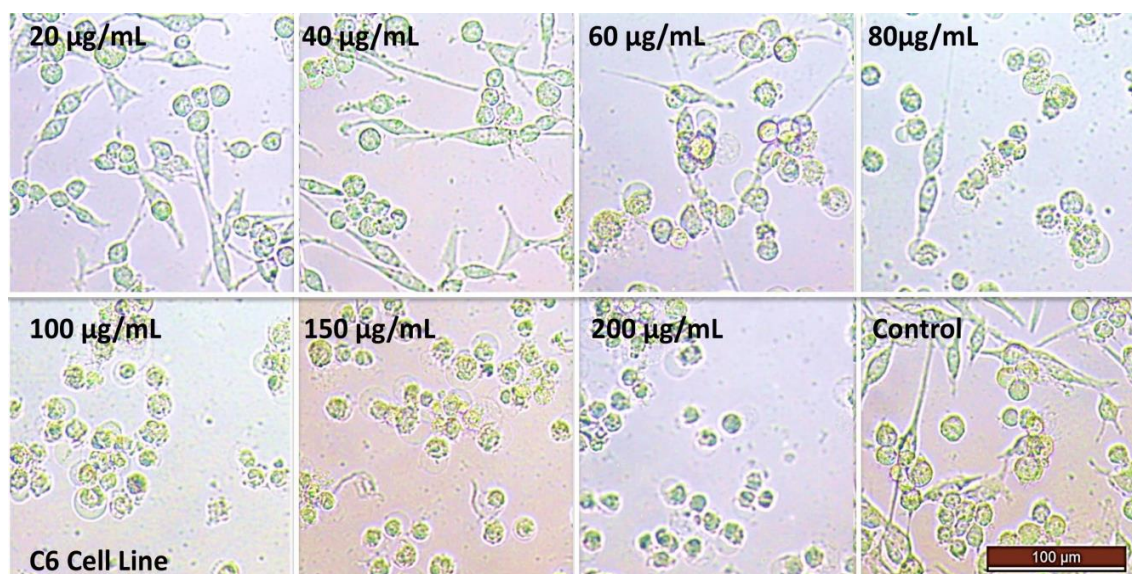


Figure 6: The effect of **3d** on the morphology of C6 cell line. Exponentially growing cells were incubated by adding various concentrations of **3d** at 37 °C overnight. Control cells were treated with only DMSO.

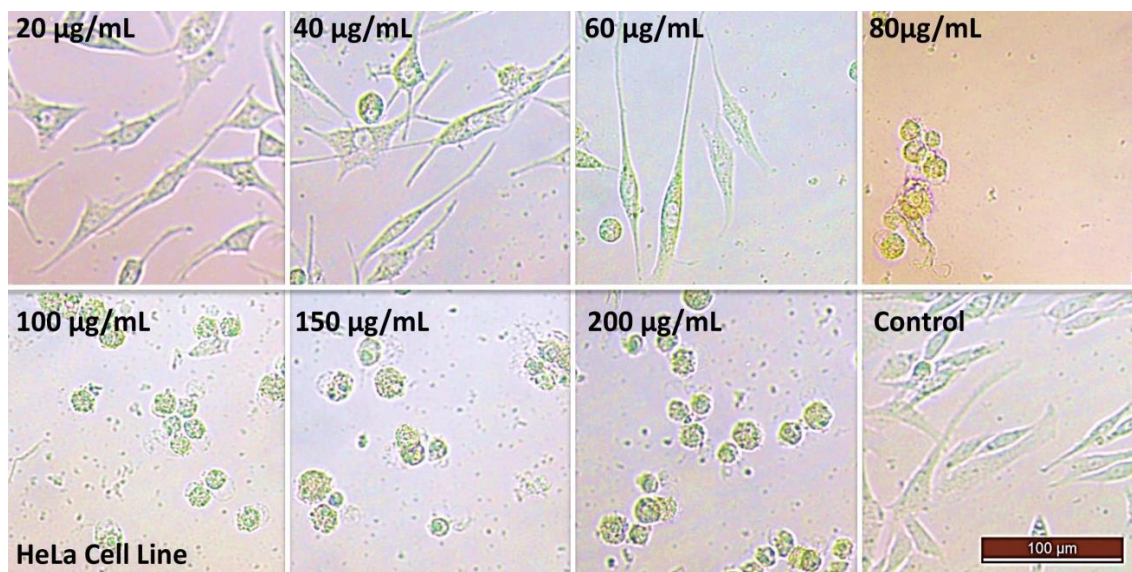


Figure 7: The effect of **3d** on the morphology of HeLa cell line. Exponentially growing cells were incubated by adding various concentrations of **3d** at 37 °C overnight. Control cells were treated with only DMSO.

CONCLUSIONS

In brief, a new series of amino acid methyl ester Schiff bases (**3a-i**) was prepared and characterized by spectroscopic methods (FT-IR, UV-Vis, ^1H - and ^{13}C -NMR). Schiff bases were synthesized by condensation reactions of salicylaldehyde derivatives and amino acid methyl esters in alkaline chloroform media. All analysis results were in accordance with suggested Schiff base structures. All Schiff bases were validated against A549, HeLa, HT29, Hep3B, MCF7 and C6 cell lines by the MTT assay. According to the results, all of the imine compounds exhibited selectivity for aforementioned carcinoma cell lines. Especially, compound **3d** was the most active compound against all tested cell lines with good TGI and IC50 values of 5.81-52.36 µg/mL and 5.72-46.35 µg/mL, respectively. GI50, TGI and LC50 values of the Schiff bases **3a-i** emphasized that they satisfied the NCI-60 criteria to pass into further pharmacological investigations. Although full mechanism underlying the cytotoxic activity could not be explained, it is known that some organic substituents like phenyl, halogens, hydroxy and methoxy enhance cytotoxic activity. It can be concluded that the existence of two phenyl rings and bromo substituent and the position of bromo group highlight compound **3d** as a strong anticancer agent.

REFERENCES

1. Tidwell TT. Hugo (Ugo) Schiff, Schiff Bases and a Century of β -Lactam Synthesis. *Angewandte Chemie International Edition*. 2008; 47(6): 1016-20.
2. Malladi S, Isloor AM, Isloor S, Akhila DS, Fun H-K, Synthesis, characterization and antibacterial activity of some new pyrazole based Schiff bases. *Arabian Journal of Chemistry*. 2013; 6(3): 335-40.

3. Wang J, Lian Z, Wang H, Jin X, Liu Y. Synthesis and antimicrobial activity of Schiff base of chitosan and acylated chitosan. *Journal of Applied Polymer Science*. 2012; 123(6): 3242-7.
4. Goszczyńska A, Kwiecień H, Fijałkowski K. Synthesis and antibacterial activity of Schiff bases and amines derived from alkyl 2-(2-formyl-4-nitrophenoxy)alkanoates. *Medicinal Chemistry Research*. 2015; 24(9): 3561-77.
5. Sikarwar P, Tomar S, Singh AP. Synthesis, Spectral Characterization and Antimicrobial Activity of Schiff Bases and Their Mixed Ligand Metal Complexes of Co(II), Ni(II), Cu(II) and Zn(II). *American Journal of Chemistry*. 2016; 6(5): 119-25.
6. Chigurupati S. Designing New Vanillin Schiff Bases and their Antibacterial Studies. *Journal of Medical and Bioengineering*. 2015; 4(5): 363-6.
7. Yang Q, Sun X, Liu Y, Chen B, Shen S. Synthesis and Antifungal Activity of Schiff Bases of 5-Ethoxycarbonylmethylsulfanyl-1,2,4-triazole. *Chinese Journal of Applied Chemistry*. 2014; 31(07): 788-92.
8. Rehman W, Baloch MK, Muhammad B, Badshah A, Khan KM. Characteristic spectral studies and in vitro antifungal activity of some Schiff bases and their organotin (IV) complexes. *Chinese Science Bulletin*. 2004; 49(2): 119-22.
9. Guo Z, Xing R, Liu S, Zhong Z, Ji X, Wang L, Pengcheng L. Antifungal properties of Schiff bases of chitosan, N -substituted chitosan and quaternized chitosan. *Carbohydrate Research*. 2007; 342(10): 1329-32.
10. Karthikeyan MS, Prasad DJ, Poojary B, Bhat KS, Holla BS, Kumari NS. Synthesis and biological activity of Schiff and Mannich bases bearing 2,4-dichloro-5-fluorophenyl moiety. *Bioorganic & Medicinal Chemistry*. 2006; 14(22): 7482-9.
11. Panneerselvam P, Nair RR, Vijayalakshmi G, Subramanian EH, Sridhar SK. Synthesis of Schiff bases of 4-(4-aminophenyl)-morpholine as potential antimicrobial agents. *European Journal of Medicinal Chemistry*. 2005; 40(2): 225-9.
12. Abd-Elzaher MM, Labib AA, Mousa HA, Moustafa SA, Ali MM, El-Rashedy AA. Synthesis, anticancer activity and molecular docking study of Schiff base complexes containing thiazole moiety. *Beni-Suef University Journal of Basic and Applied Sciences*. 2016; 5(1): 85-96.
13. Poonia K, Siddiqui S, Arshad M, Kumar D. In vitro anticancer activities of Schiff base and its lanthanum complex. *Spectrochimica Acta Part A: Molecular and Biomolecular Spectroscopy*. 2016; 155: 146-54.
14. Shukla S, Srivastava RS, Shrivastava SK, Sodhi A, Kumar P. Synthesis, characterization, in vitro anticancer activity, and docking of Schiff bases of 4-amino-1,2-naphthoquinone. *Medicinal Chemistry Research*. 2013; 22(4): 1604-17.
15. Emam SM, El Sayed IET, Ayad MI, Hathout HMR. Synthesis, characterization and anticancer activity of new Schiff bases bearing neocryptolepine. *Journal of Molecular Structure*. 2017; 1146: 600-19.
16. Kuzmin VE, Artemenko AG, Lozytska RN, Fedtchouk AS, Lozitsky VP, Muratov EN, Mescheriakov AK. Investigation of anticancer activity of macrocyclic Schiff bases by means of 4D-QSAR based on simplex representation of molecular structure. *SAR and QSAR in Environmental Research*. 2005; 16(3): 219-30.
17. Luo H, Sui Y, Lin W-H, Wu H-Q. Study on the antiproliferative activity of four Schiff bases derived from natural biomass dehydroabiethylamine. *Indian Journal of Chemistry*. 2016; 55B(2): 248-51.
18. Harpstrite SE, Collins SD, Oksman A, Goldberg DE, Sharma V. Synthesis, characterization, and antimalarial activity of novel schiff-base-phenol and naphthalene-amine ligands. *Medicinal Chemistry*. 2008; 4(4): 392-5.
19. Sharma R, Goswami A, Rudrapal M, Sharma D, Kumar Sharma H, Chetia D. In vitro evaluation of the antimalarial activity of a designed novel quinuclidine derivative. *Current Science*. 2016; 111(12): 2028-30.

20. Sharma M, Chauhan K, Srivastava RK, Singh SV, Srivastava K, Saxena JK, Puri SK, Chauhan PMS. Design and Synthesis of a New Class of 4-Aminoquinolinyl- and 9-Anilinoacridinyl Schiff Base Hydrazones as Potent Antimalarial Agents. *Chemical Biology & Drug Design*. 2014; 84(2): 175-81.
21. Bringmann G, Dreyer M, Faber JH, Dalsgaard PW, Staerk D, Jaroszewski JW, Ndangalasi H, Mbago F, Brun R, Christensen SB. Ancistrotanzanine C and related 5,1'- and 7,3'-coupled naphthylisoquinoline alkaloids from *Ancistrocladus tanzaniensis*. *Journal of Natural Products*. 2004; 67(5): 743-8.
22. Rathelot P, Vanelle P, Gasquet M, Delmas F, Crozet MP, Timon-David P, Maldonado J. Synthesis of novel functionalized 5-nitroisoquinolines and evaluation of in vitro antimalarial activity. *European Journal of Medicinal Chemistry*. 1995; 30(6): 503-8.
23. Tadele KT. Antioxidant Activity of Schiff Bases and Their Metal Complexes: A Recent Review. *Journal of Pharmaceutical and Medicinal Research*. 2017; 3(1): 73-7.
24. Anouar EH, Raweh S, Bayach I, Taha M, Baharudin MS, Di Meo F, Hasan MH, Adam A, Ismail NH, Weber JF, Trouillas P. Antioxidant properties of phenolic Schiff bases: structure-activity relationship and mechanism of action. *Journal of Computer-Aided Molecular Design*. 2013; 27(11): 951-64.
25. Guo Z, Xing R, Liu S, Yu H, Wang P, Li C, Li P. The synthesis and antioxidant activity of the Schiff bases of chitosan and carboxymethyl chitosan. *Bioorganic & Medicinal Chemistry Letters*. 2005; 15(20): 4600-3.
26. Brodowska K, Sykuła A, Garribba E, Łodyga-Chruścińska E, Sójka M. Naringenin Schiff base: antioxidant activity, acid-base profile, and interactions with DNA. *Transition Metal Chemistry*. 2016; 41(2): 179-89.
27. Ozdemir M, Sonmez M. Antioxidant Activity, Synthesis and Characterization of Schiff Base Ligand 'asasp' and Metal Complexes. *Asian Journal of Chemistry*. 2014; 26(20): 7009-15.
28. Turan N, Bursal E, Çolak N, Buldurun K. Investigation of Synthesis, Structural Characterization, Antioxidant Activities and Thermal Properties of Zn(II), Fe(II) and Mn(II) Complexes with Thiophene-Carboxylate Ligand. *Journal of Chemistry and Biochemistry*. 2015; 3(2): 13-29.
29. Liu G, Cogan D, Ellman JA. Catalytic asymmetric synthesis of tert-butanesulfinamide. Application to the asymmetric synthesis of amines. *Journal of the American Chemical Society*. 1997; 119(41): 9913-4.
30. Cimarelli C, Palmieri G. Asymmetric reduction of enantiopure imines with zinc borohydride: stereoselective synthesis of chiral amines. *Tetrahedron: Asymmetry*. 2000; 11(12): 2555-63.
31. Yendapally R, Hurdle JG, Carson EI, Lee RB, Lee RE. N-Substituted 3-Acetyltetramic Acid Derivatives as Antibacterial Agents. *Journal of Medicinal Chemistry*. 2008; 51(5): 1487-91.
32. Barreau M, Commercon A, Mignani S, Mouysset D, Perfetti P, Stella L. Stereoselective synthesis of racemic α -amino-acid derivatives with a β -lactam skeleton: Application of the Staudinger reaction to chiral imines of methyl glyoxylate. *Tetrahedron*. 1998; 54(38): 11501-16.
33. Hasegawa M, Taniyama D, Tomioka K. Facile Asymmetric Synthesis of α -Amino Acids Employing Chiral Ligand-Mediated Asymmetric Addition Reactions of Phenyllithium with Imines. *Tetrahedron*. 2000; 56(52): 10153-8.
34. Blaney P, Grigg R, Rankovic Z, Thornton-Petta M, Xu J. Fused and bridged bi- and tri-cyclic lactams via sequential metallo-azomethine ylide cycloaddition-lactamisation. *Tetrahedron*. 2002; 58(9): 1719-37.
35. Grigg R, Sridharan V, Suganthan S, Bridge AW. Sequential and Cascade 1,3-Dipolar Cycloaddition-Palladium Catalysed Carbonylation-Cyclisation Reactions. Diastereospecific and Homochiral Processes. *Tetrahedron*. 1995; 51(1): 295-306.
36. Davis FA, Sheppard AC. Applications of oxaziridines in organic synthesis. *Tetrahedron*. 1989; 45(18): 5703-42.
37. Petrov VA, Resnati G. Polyfluorinated Oxaziridines: Synthesis and Reactivity. *Chemical Reviews*. 1996; 96(5): 1809-23.

38. Al-Garawi ZSM, Tomi IHR, Al-Daraji AHR. Synthesis and Characterization of New Amino Acid-Schiff Bases and Studies their Effects on the Activity of ACP, PAP and NPA Enzymes (In Vitro). *E-Journal of Chemistry*. 2012; 9(2): 962-9.
39. Zhang L, Jiang H, Cao X, Zhao H, Wang F, Cui Y, Jiang B. Chiral gossypol derivatives: Evaluation of their anticancer activity and molecular modeling. *European Journal of Medicinal Chemistry*. 2009; 44(10): 3961-72.
40. Xia L, Xia Y-F, Huang L-R, Xiao X, Lou H-Y, Liu T-J, Pan W-D, Luo H. Benzaldehyde Schiff bases regulation to the metabolism, hemolysis, and virulence genes expression in vitro and their structure microbicidal activity relationship. *European Journal of Medicinal Chemistry*. 2015; 97: 83-93.
41. Kumar S, Priya Matharasi D, Gopi S, Sivakumar S, Narasimhan S. Synthesis of cytotoxic and antioxidant Schiff's base analogs of aloin. *Journal of Asian Natural Products Research*. 2010; 12(5): 360-70.
42. Joksovic MD, Bogdanovic G, Kojic V, Szecsenyi KM, Leovac VM, Jakimov D, Trifunovic S, Markovic V, Joksovic L. Synthesis, Cytotoxic Activity, and Thermal Studies of Novel N-[(1,3-Diphenylpyrazol-4-yl)methyl] α -Amino Acids. *Journal of Heterocyclic Chemistry*. 2010; 47(4): 850-6.
43. Li L-J, Fu B, Qiao Y, Wang C, Huang Y-Y, Liu C-C, Tian C, Du J-L. Synthesis, characterization and cytotoxicity studies of platinum(II) complexes with reduced amino acid ester Schiff-bases as ligands. *Inorganica Chimica Acta*. 2014; 419: 135-40.
44. Zhoua Y, Zhao M, Wub Y, Li C, Wub J, Zheng M, Peng L, Peng S. A class of novel Schiff's bases: Synthesis, therapeutic action for chronic pain, anti-inflammation and 3D QSAR analysis. *Bioorganic & Medicinal Chemistry*. 2010; 18(6): 2165-72.
45. Abdel-Rahman LH, Abu-Dief, AM, Ismael M, Mohamed MAA, Hashem NA. Synthesis, structure elucidation, biological screening, molecular modeling and DNA binding of some Cu(II) chelates incorporating imines derived from amino acids. *Journal of Molecular Structure*. 2016; 1103(5): 232-44.



Synthesis and Characterization of A Novel Thermally Stable Schiff Base Oligomer: Investigation of Conductivity Properties

Nuray Yılmaz Baran*

Aksaray University, Technical Vocational School, Department of Chemistry Technology, 68100, Aksaray, TURKEY

Abstract: This paper presents the design of a novel Schiff base, 2,2'-{[1,2-di(pyridin-2-yl)ethane-1,2-diylidene]bis(azanylylidene)}diphenol (2,2'-DBD), and its oligophenol, Oligo-(2,2'-{[1,2-di(pyridin-2-yl)ethane-1,2-diylidene]bis(azanylylidene)}diphenol) O(2,2'-DBD), synthesized with NaOCl and O₂ oxidants by oxidative polycondensation reaction in aqueous alkaline media. The effects of oxidant type, polymerization temperature, and time on oligomer yield were determined. Characterization of the structures of the synthesized (2,2'-DBD) and O(2,2'-DBD) were done by UV-Vis, FTIR and ¹HNMR techniques. Also, thermal degradations of the monomer and oligomer were investigated TG-DTG analysis and it was determined that the oligomer thermally stable up to 1200 °C. Additionally, electrical conductivity of the oligomer was improved by doping with iodine at 20 °C and the conductivity of the oligomer reached to 9x10⁻⁴ S/cm by increasing 10⁷ at the end of the 48 h doping time fold according to its undoped form.

Keywords: Conductivity, oxidative polycondensation, oligophenols, Schiff base polymers.

Submitted: November 22, 2017. **Accepted:** March 27 2018.

Cite this: .Yılmaz Baran N. Synthesis and Characterization of A Novel Thermally Stable Schiff Base Oligomer: Investigation of Conductivity Properties. JOTCSA. 2018;5(2):607–20.

DOI: <http://dx.doi.org/10.18596/jotcsa.351460>.

***Corresponding author.** E-mail: nybaran@aksaray.edu.tr. Tel.: +90 382 2882028; Fax: +90 382 2882125.

INTRODUCTION

Schiff base polymers, also known as polyazomethines, have drawn attention of researchers to design thermally resistant (1) and semiconductive (2) materials. They are promising materials for several applications such as photorefractive holographic materials (PRHMs) (3), solar cells (4) (SCs), organic light emitting diodes (OLEDs) (5), and organic field effect transistors (OFETs) (6).

Researchers have enhanced superior properties of the Schiff base polymers by adding different functional groups to their structures (7-11). One of these polymers are Schiff base polymers containing phenol groups. These polymers have excellent properties such as high thermal stability (12), bonding ability to metals (13), electrochemical (14, 15), antimicrobial (11, 16), semiconductive (11, 15), and superior optical (14) properties. Although several methods have been used (17, 18) to synthesize Schiff base polymers containing phenol groups, oxidative polycondensation method have been frequently preferred due to its superior advantages such as cheapness of the used oxidants (NaOCl, H₂O₂, O₂), to synthesize polymers with high solubility, moderate reaction conditions and release of eco-friendly by products (NaCl and H₂O) (12, 19).

In this study, a novel Schiff base oligomer, O(2,2'-DBD), was produced with NaOCl, and O₂ oxidants by oxidative polycondensation of 2,2'-DBD monomer in an aqueous alkaline media. The effects of oxidant types, polymerization temperature, and time on oligomer yield were investigated. UV-Vis, FTIR, ¹H-NMR techniques were used for verifying of structures of 2,2'-DBD and O(2,2'-DBD). Additionally, thermal degradations of monomer and oligomer were determined by TG-DTG. Also, the changing of electrical conductivity of O(2,2'-DBD) were monitored by doping with iodine at 20 °C with increasing doping time.

EXPERIMENTAL

Materials

2-Aminophenol, 2,2'-pyridil, potassium hydroxide (KOH), hydrochloric acid (HCl, 37%), iodine, acetone, dimethylformamide (DMF), dimethyl sulfoxide (DMSO), methanol, ethyl acetate, ethanol, *n*-methylpyrrolidone, 1,4-dioxane, *n*-heptane and tetrahydrofuran were purchased from Merck Chem. Co. (Germany). Also, sodium hypochlorite (NaOCl, 15% aqu.) was supplied from Birpa Co. (Turkey).

Method

Synthesis of 2,2'-DBD

Production of 2,2'-DBD monomer was carried out by condensation of 2-aminophenol and 2,2'-pyridil (Scheme 1). Solution of 2,2'-pyridil (0,01 mol, 2.12 g) prepared in 40 mL of methanol

was added on the solution of 2-aminophenol (0.02 mol, 2.18 g) in 15 mL methanol. The prepared mixture was continuously stirred at 40 °C for 24 h. After the reaction was completed, ice water-salt mixture was added on the obtained brown solution and the yellow product precipitated. Then it was filtered out and rinsed with cold methanol. The product was recrystallized from n-heptane for purification. (Yield: 86%; melting point: 147 °C.)

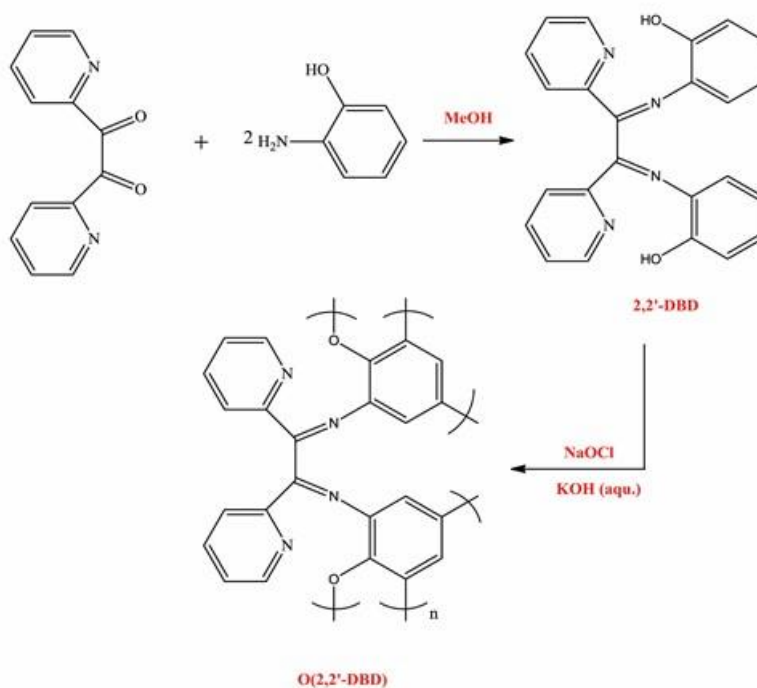
Synthesis of O(2,2'-DBD)

O(2,2'-DBD) was synthesized using NaOCl (15%), and air O₂ oxidants by oxidative polycondensation reaction of 2,2'-DBD in aqueous alkaline media. Firstly, 2,2'-DBD (1 mmol, 0,394 g) was dissolved in aqueous solution of KOH (10%, 1 mmol) under nitrogen atmosphere at the temperature which the polymerization reaction would be carried out. Then, 1 mmol NaOCl was added drop by drop. Nitrogen was passed during the reaction. When aerial O₂ was used to be an oxidant, after the dissolution of monomer was completed, nitrogen gas was discontinued. At the end of the desired polymerization time, the cooled polymerization solution to room temperature was precipitated by neutralizing with HCl (37%). The product was filtered, washed with hot water and methanol, and then dried in oven.

Oligomer yield was determined using Equation 1:

$$\text{Yield (\%)} = \frac{W_p}{W_m} \times 100 \quad (1)$$

Where W_p and W_m show the oligomer and initial monomer weights, respectively.



Scheme 1. Synthesis of 2,2'-DBD and O(2,2'-DBD).

Characterization

UV-Vis spectra of 2,2'-DBD and O(2,2'-DBD) were got in DMSO in a 260-700 nm wavelength range using Shimadzu UV-1700 PharmaSpec UV-Visible Spectrophotometer. FTIR spectra of the products were obtained by Perkin Elmer FTIR Spectrometer in the frequency range of 4000-650 cm^{-1} . To clarify the molecular structures of the 2,2'-DBD and O(2,2'-DBD), $^1\text{H-NMR}$ spectra were acquired from their solutions in DMSO by Bruker Avance 500 MHz NMR. Thermal degradations of the products were determined by TG/DTG techniques recorded in the temperature range of 30-1200 $^{\circ}\text{C}$ with a heating rate of 10 $^{\circ}\text{C}/\text{min}$ using EXSTAR S11 7300 thermal analyzer under nitrogen atmosphere with a platinum crucible. To determine molecular weight values of the oligomer, Shimadzu Prominence Gel Permeation Chromatography which was fitted out a Nucleogel GPC 103-5 VA300/7.7 column was employed (eluent: DMF, flow rate: 0.5 mL/min, temperature: 40 $^{\circ}\text{C}$).

Surface resistivity values of the oligomer were measured from the prepared sample pellets 2 mm thick and 1.3 cm in diameter under a hydraulic pressure (1687.2 kg/cm^2) by two probe technique. The electrical conductivity values of the O(2,2'-DBD) were calculated using the measured surface resistivity values according to Equation 2:

$$\sigma = \frac{l}{Ra} \quad (2)$$

Where σ (S/cm) corresponds the conductivity of the oligomer, R (ohm cm^{-2}) is the monitored surface resistivity. a (cm^2) and l (cm) are the area and thickness of the prepared sample pellet, respectively.

Solubility test

To determine qualitative solubility of 2,2'-DBD and O(2,2'-DBD) 1 mg sample was dissolved in 1 mL of solvent (Table 1). It was observed that 2,2'-DBD dissolved in all of the tested solvents at room temperature. However, O(2,2'-DBD) was only dissolved in DMF and DMSO. The solubility of the oligomer will facilitate the characterization and processability of the oligomer.

Table 1. The solubility of 2,2'-DBD and O(2,2'-DBD) in several solvents.

	Ethanol	Methanol	Acetone	1,4-Dioxane	DMF	DMSO	NMP	Ethyl Acetate	n-Heptane	THF
2,2'-DBD	+	+	+	+	+	+	+	+	+	+
O(2,2'-DBD)	-	-	-	-	+	+	-	-	-	-
	+ : soluble							- : insoluble		

RESULTS AND DISCUSSION

Effect of Synthesis Conditions on the Yield of O(2,2'-DBD)

Oxidant type and concentration

O(2,2'-DBD) was synthesized in aqueous alkaline media with NaOCl and O₂ (aerial) oxidants. Yields and molecular weight values of oligomers which obtained 80 °C for 6 h (11) were determined. While yield and M_w, M_n and PDI values of the oligomer synthesized with NaOCl oxidant were 76% and 5435, 4216 g/mol and 1.28, the same values, which were obtained using air O₂ as oxidant, were 8% and 1321,992 g/mol 1.33, respectively. Thus, since higher yield and molecular weight values were obtained with NaOCl oxidant, the next experiments were carried out using NaOCl (11, 20, 21). Also, 0.1 mol/L NaOCl concentration at which the highest polymer yields were obtained in the literature was used in the experiments.

Polymerization temperature and time

The effect of polymerization temperature and time on oligomer yield were investigated and the data were given in Figures 1 and 2, respectively.

As seen from Figure 1, the oligomer yield increased with increasing polymerization temperature (11, 12). Thus, the following experiments were performed at 90 °C which the highest oligomer yield was obtained.

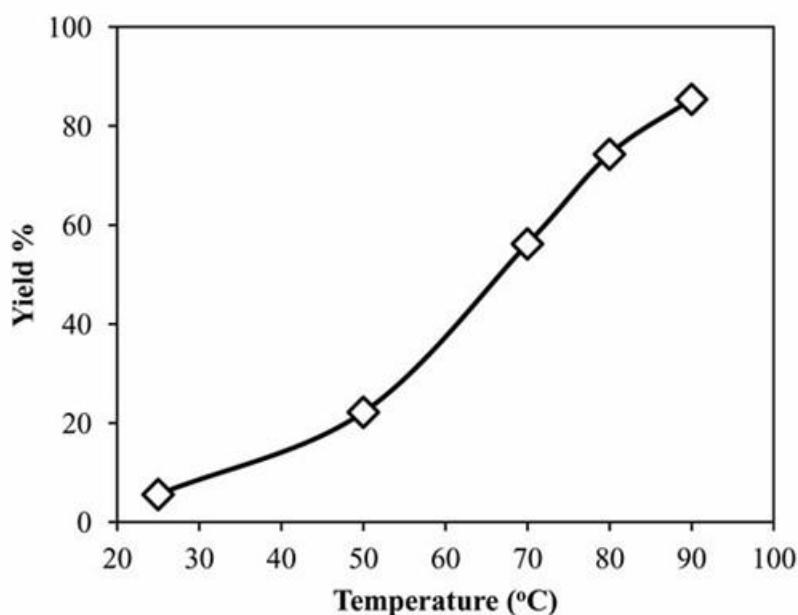


Figure 1. The effect of polymerization temperature on % yield of O(2,2'-DBD) ([2,2'-DBD]₀=[NaOCl]₀=[KOH]₀=0.1 mol/L, polymerization time: 6 h).

When Figure 2, showing the change of the oligomer yield with polymerization time, was examined, it was seen that the yield increased with increasing time up to 4h. A significant

increase in yield was not seen after 4 h. Also, the highest oligomer yield (85.4 %) was obtained at the end of 6 h.

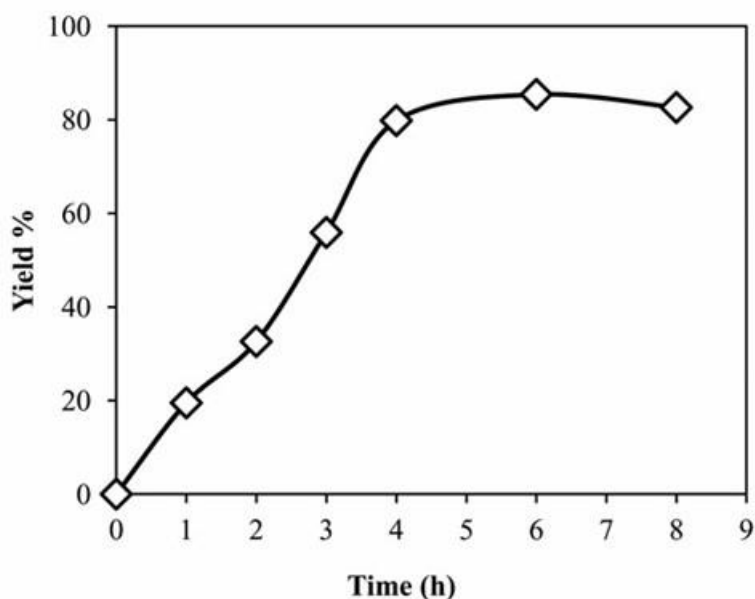


Figure 2. The effect of polymerization time on % yield of O(2,2'-DBD) ($[2,2'\text{-DBD}]_0 = [\text{NaOCl}]_0 = [\text{KOH}]_0 = 0.1$, polymerization temperature: 90 °C).

Structures of 2,2'-DBD and O(2,2'-DBD)

UV-Vis Spectra

UV-Vis spectra of 2,2'-DBD and O(2,2'-DBD) acquired from their solutions in DMSO in the range of 250-700 nm wavelength are presented in Figure 3. While it is seen a sharp band at 302 nm wavelength and a shoulder at 341 nm in the spectrum of 2,2'-DBD, the same bands are observed at wavelengths of 270 and 305 nm as shoulders in the spectrum of oligomer. These bands can be ascribed to $n\text{-}\pi^*$ transitions of -C=C- , $n\text{-}\pi^*$ transitions of the imine functional groups and the $n\text{-}\pi^*$ transitions of OH functional groups, respectively. When the spectra of monomer and oligomer were compared to each other, it was determined that the O(2,2'-DBD) spectrum broadened to 700 nm while the spectrum of 2,2'-DBD finished at 500 nm, and the bands of oligomer broadened and shifted to blue wavelengths. These changes originate from increasing of conjugation during polymerization and verify that polymerization was achieved (11, 13, 21, 22).

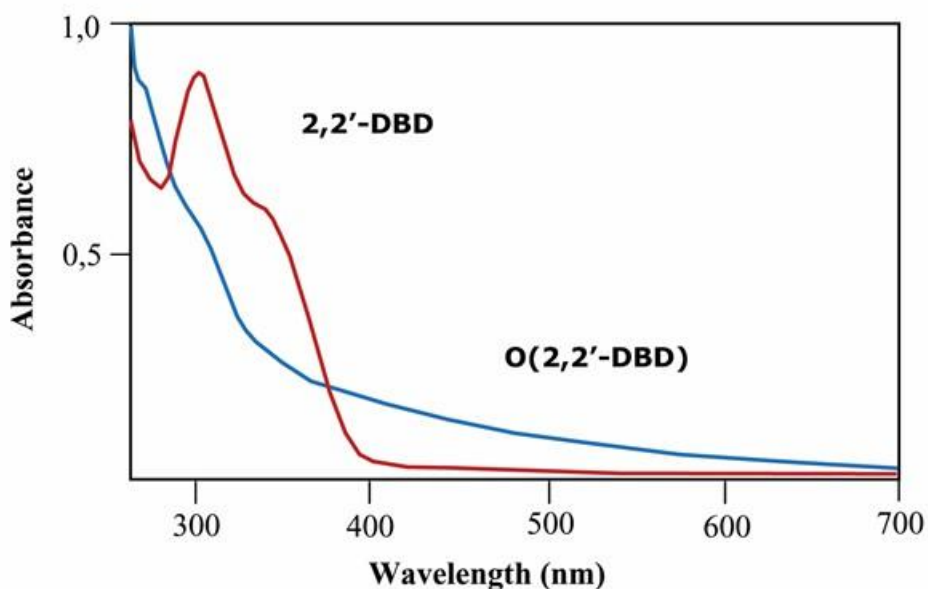


Figure 3. UV-Vis spectra of 2,2'-DBD and O(2,2'-DBD).

FTIR Spectra

FTIR spectra recorded to support the structures of 2,2'-DBD and O(2,2'-DBD) and emphasize the changes in the structure after polymerization are given in Figure 4.

In the spectrum of 2,2'-DBD, while the peak seen at 3056 cm^{-1} is arisen from phenolic OH groups, the same peak is determined at 3364 cm^{-1} in the O(2,2'-DBD) spectrum. While the -C=N- vibration, which is characteristic for Schiff bases, is appeared to be sharp peak at 1620 cm^{-1} in the monomer spectrum, in the oligomer spectrum this vibration shifted to 1606 cm^{-1} . The presence of the -C=N- peak in the oligomer spectrum also indicates that the imine groups characteristic for polyazomethines are preserved without decomposition during polymerization (11). Additionally, the peaks at 1587 , 1468 , 1435 cm^{-1} in the monomer spectrum and at 1582 and 1562 cm^{-1} in the oligomer spectrum are due to -C=C- vibrations. While the peaks belonging to -C-O- and C-N stretching vibrations are seen at 1235 and 1137 cm^{-1} for monomer, these same peaks are recorded at 1232 and 1098 cm^{-1} for oligomer, respectively. When the FTIR spectra of monomer and oligomer are compared to each other, the changes (i) broadening of the peaks, (ii) decrease in the peak number and (iii) shifting in the characteristic -C=N- vibration to lower wavenumber are seen in the oligomer spectrum. All of these changes are originated from increasing in conjugation length and support that the polymeric structure was achieved (11, 13, 21, 22).

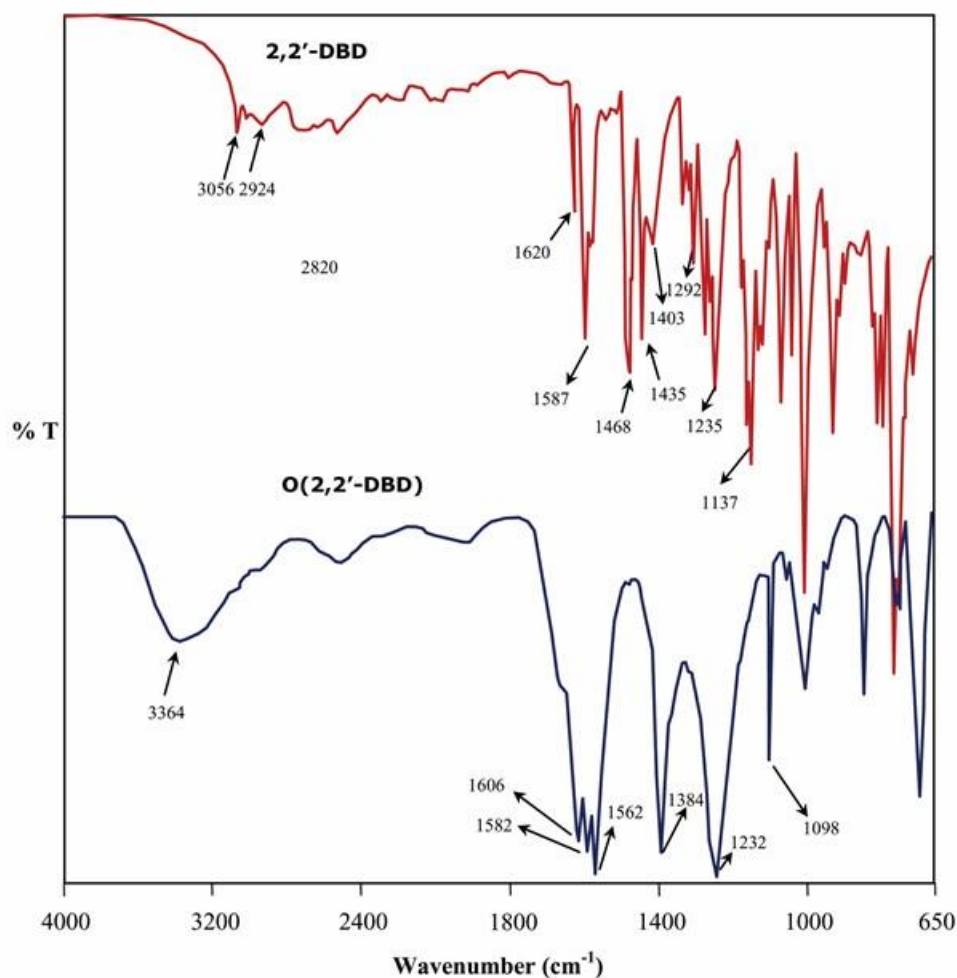


Figure 4. FTIR spectra of 2,2'-DBD and O(2,2'-DBD).

¹H-NMR Spectra

To prove that the synthesis of 2,2'-DBD and O(2,2'-DBD) was successfully performed, ¹H-NMR spectra of the samples were recorded and they are presented in Figure 5 and 6, respectively. In the ¹H-NMR spectrum of Schiff base monomer, the signal of protons –OH functional groups is seen at 10.55 (s, 2H). The other signals indicating the aromatic structure of 2,2'-DBD were determined at δ = 7.90 (d, 2H, Ar-H_a); 7.82 (t, 2H, Ar-H_b); 7.78 (t, 2H, Ar-H_c); 7.57 (d, 2H, Ar-H_d); 7.27 (t, 2H, Ar-H_f); 7.21 (d, 2H, Ar-H_h); 7.09 (d, 2H, Ar-H_e); 6.96 (t, 2H, Ar-H_g) ppm. Also the signals confirming the aromatic structure of O(2,2'-DBD) were recorded at δ = 8.53 (s, 2H, Ar-H_f); 8.40 (s, 2H, Ar-H_e); 7.80 (d, 2H, Ar-H_a); 7.78 (t, 2H, Ar-H_b); 7.66 (t, 2H, Ar-H_c); 7.20 (d, 2H, Ar-H_d) ppm. When the ¹H-NMR spectrum of oligomer is compared to monomer spectrum, (I) absence of the signals of H_e (doublet) and H_g (triplet) protons of monomer, in the polymer spectrum, (II) while H_f and H_h protons of monomer seen as triplet and doublet, respectively in the monomer spectrum, observation of the same protons as singlets in the polymer spectrum, emphasizing that the oligomerization continues from the C-C couplings which occur on the ortho and para positions of the OH groups. Moreover, absence of the signal of OH groups in the polymer

spectrum states that the oligomerization also progresses from C-O-C couplings which form from OH groups in addition to C-C couplings (11, 15, 21).

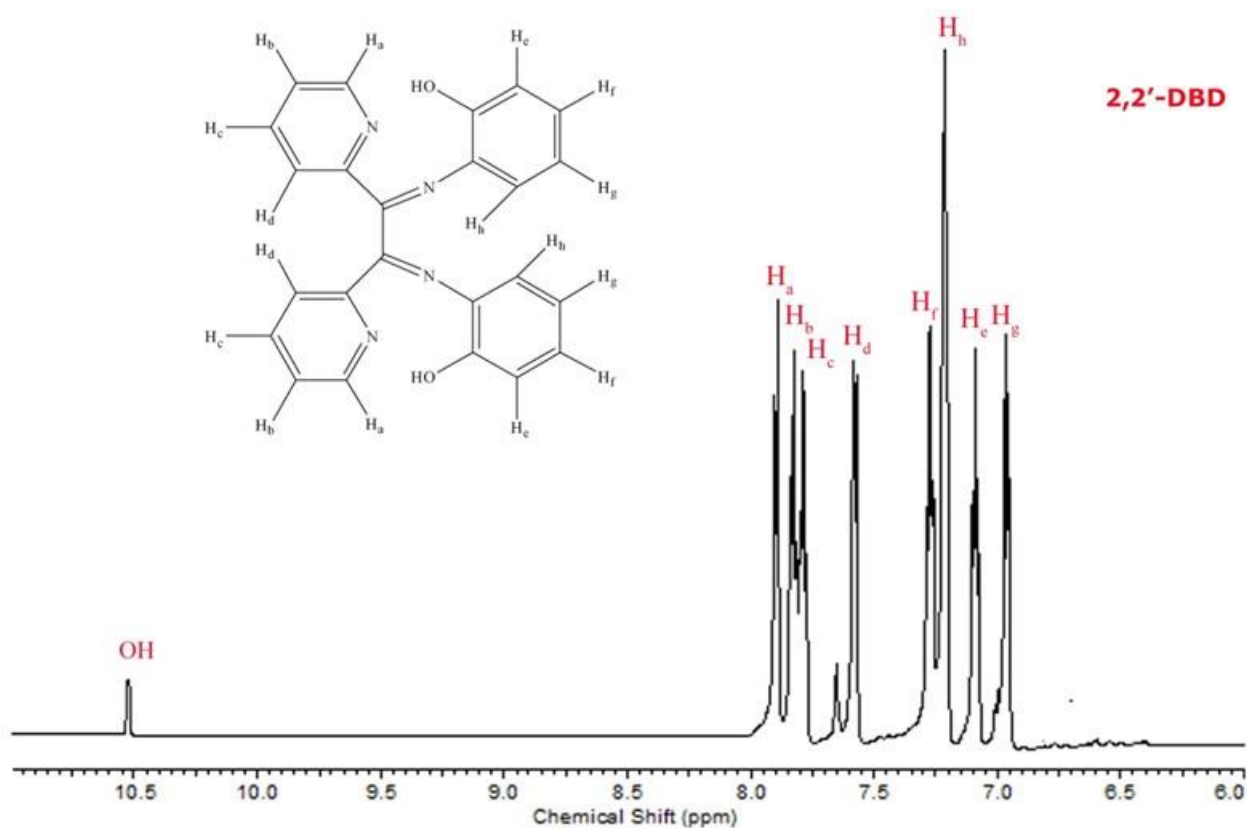


Figure 5. ^1H NMR spectrum of 2,2'-DBD.

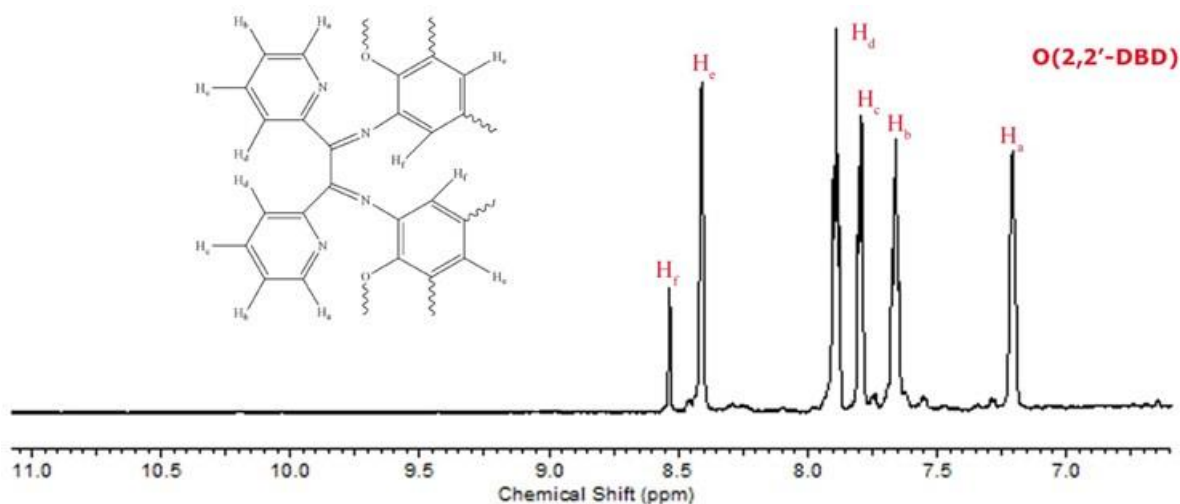


Figure 6. ^1H NMR spectrum of O(2,2'-DBD).

Thermal Degradation Process of O(2,2'-DBD)

To determine the thermal stability of 2,2'-DBD and O(2,2'-DBD), their TG and DTG curves were acquired up to 600 and 1200 °C, respectively (Figure 7). It was determined from TG curve of 2,2'-DBD that 2,2'-DBD decomposed in two steps which are in the temperature range of 166-282 °C and 282-560 °C. The monomer which started to degrade at 166 °C finished the process at 78.25% up to 282 °C. Also the weight loss in the second degradation step was 21.75% in the temperature range of 282-560 °C. The maximum degradation temperature (T_{max}) were determined from DTG curve as 243 °C.

From the TG curve, which was recorded up to 1200 °C, belonging to O(2,2'-DBD), it was seen that the oligomer degraded in three steps. Firstly, the weight loss of 4.25 % in the temperature range of 30-180 °C can be ascribed to removal of water of crystallization (23). The other weight losses of the oligomer were determined as 8.5% in the temperature range of 180-339 °C for the first step, 20.25% in the temperature range of 339-555 °C for the second step and 67.0% in the temperature range of 555-1200 °C for the third step. The maximum degradation temperatures (T_{max}) found from DTG curve corresponded to 136 °C, 264 °C, 442 °C, and 867 °C for each degradation steps, respectively.

When the thermal degradations of the monomer and oligomer were compared to each other, while the temperatures at which the 30% weight loss formed were 234 °C and 464 °C, these temperatures for 50% weight loss were 251 °C and 784 °C for monomer and oligomer, respectively. Moreover, while the monomer completely decomposed up to 560 °C without any carbon residue, the oligomer completely degraded up to 1200 °C without any carbon residue. These data verify that the thermal stability of oligomer is much higher than its monomer. The case is also due to the increasing conjugation of the oligomer according to monomer (11, 13, 21).

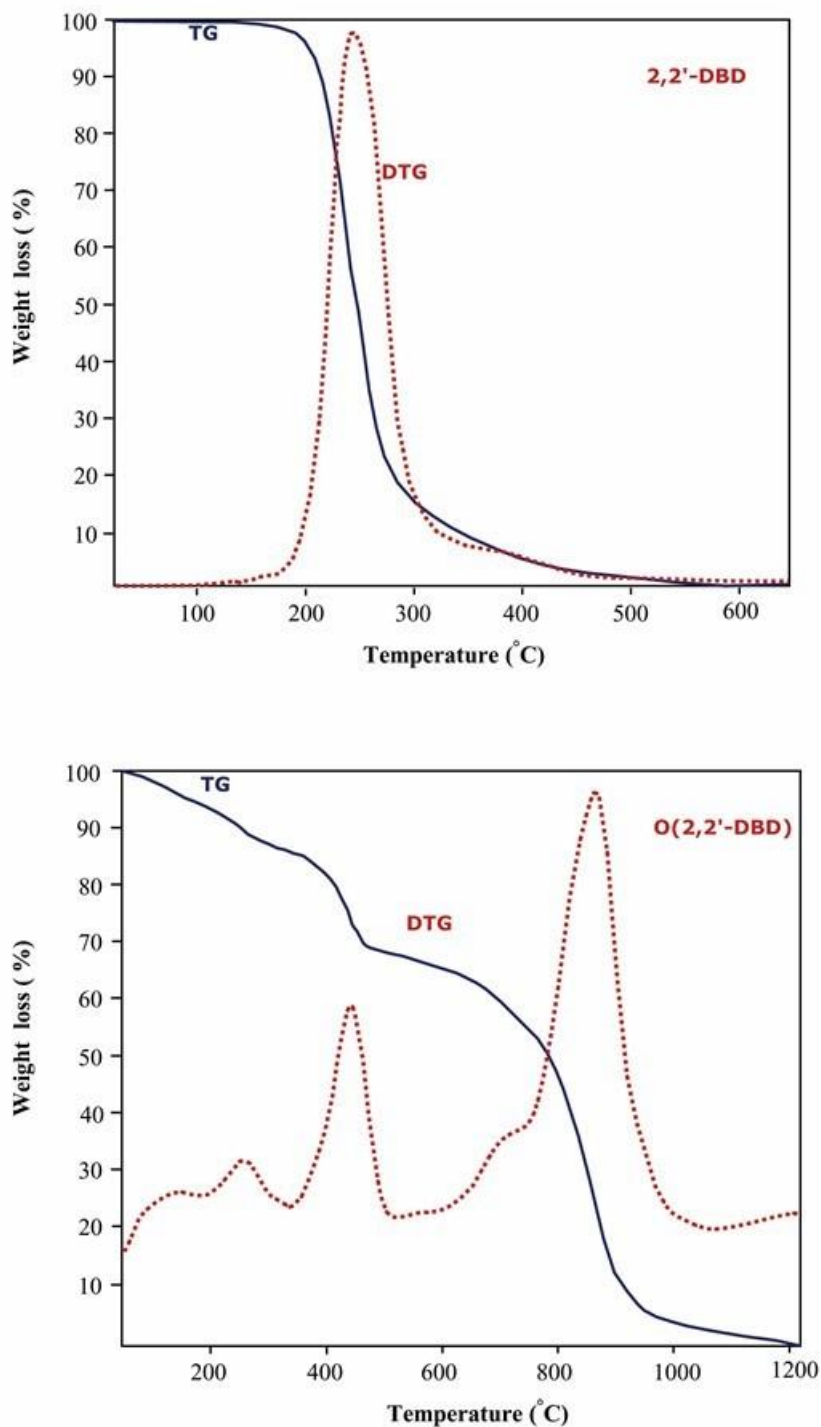


Figure 7. TG and DTG curves of 2,2'-DBD and O(2,2'-DBD).

Doping with Iodine

The effects of doping time were monitored on conductivity of oligomer which was doped with iodine vapor at 20 °C up to 120 h and the obtained data are presented in Figure 8. The initial conductivity value of the oligomer was measured as 6.5×10^{-11} S/cm before doping. By starting of doping, the conductivity value of the oligomer increased fastly and the conductivity value was measured as 8×10^{-5} S/cm by increasing 10^6 fold after doping 1 h. The increase of the conductivity

value continued to 48 h with increasing doping time and at the end of the 48 h doping time, the values was reached to 9×10^{-4} S/cm by increasing 10^7 fold according to initial conductivity value. After 48 h doping time, it was not observed a significant increase in the conductivity.

This doping process occurring between iodine and the Schiff base oligomer can be explained by the coordination between iodine molecules and the highly electronegative N atoms of the oligomer (24, 25).

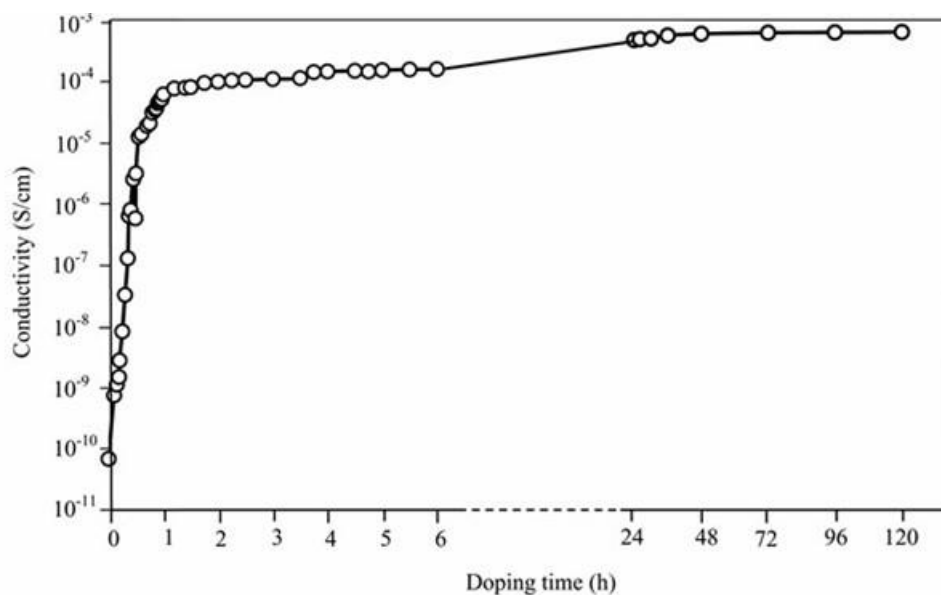


Figure 8. The effect of doping time with iodine on conductivity of O(2,2'-DBD) at 25 °C.

CONCLUSIONS

Within the scope of this study, synthesis of O(2,2'-DBD) was achieved by oxidative polycondensation reaction of 2,2'-DBD in an aqueous alkaline media using NaOCl and O_2 oxidants. To be soluble oligomer in DMF, DMSO, which were the most widely used organic solvents, enables us to investigate different analytical, environmental usages and its properties such as fluorescence and phosphorescence, catalysis and antimicrobial activity. From the thermal analysis results, it was determined that the oligomer is thermally stable up to 1200 °C and it facilitates that the oligomer may be used in materials which requires high thermal resistance. The studies carried out to increase the conductivity of the oligomer showed that the conductivity value of the oligomer increased 10^7 fold according to initial conductivity value and it was measured 9×10^{-4} S/cm at 20 °C after doping 48 h. Thus, it can be said that the oligomer could be used in applications which require semiconductive properties.

REFERENCES

1. Spiliopoulos IK, Mikroyannidis JA. Soluble, Rigid-Rod Polyamide, Polyimides, and Polyazomethine with Phenyl Pendent Groups Derived from 4,4''-Diamino-3,5,3'',5''-tetraphenyl-p-terphenyl. *Macromolecules*. 1996;29(16):5313-9.
2. Aly KI, Khalaf AA. New polymer syntheses. IX. Synthesis and properties of new conducting polyazomethine polymers containing main chain cycloalkanone and pyridine moieties. *Journal of Applied Polymer Science*. 2000;77(6):1218-29.
3. Jae-Wook K, Jang-Joo K, Jinkyu K, Xiangdan L, Myong-Hoon L. Low-loss and thermally stable TE-mode selective polymer waveguide using photosensitive fluorinated polyimide. *IEEE Photonics Technology Letters*. 2002;14(9):1297-9.
4. Iwan A, Boharewicz B, Tazbir I, Malinowski M, Filapek M, Kłab T, et al. New environmentally friendly polyazomethines with thiophene rings for polymer solar cells. *Solar Energy*. 2015;117:246-59.
5. Niu H, Huang Y, Bai X, Li X, Zhang G. Study on crystallization, thermal stability and hole transport properties of conjugated polyazomethine materials containing 4,4'-bisamine-triphenylamine. *Materials Chemistry and Physics*. 2004;86(1):33-7.
6. Iwan A, Palewicz M, Chuchmala A, Sikora A, Gorecki L, Sek D. Opto(electrical) properties of triphenylamine-based polyazomethine and its blend with 6,6 -phenyl C-61 butyric acid methyl ester. *High Perform Polym*. 2013;25(7):832-42.
7. Kamacı M, Kaya İ. 2,4-Diamino-6-Hydroxypyrimidine Based Poly(azomethine-Urethane): Synthesis and Application as a Fluorescent Probe for Detection of Cu²⁺ in Aqueous Solution. *Journal of Fluorescence*. 2015;25(5):1339-49.
8. Marin L, Cozan V, Bruma M, Grigoras VC. Synthesis and thermal behaviour of new poly(azomethine-ether). *European Polymer Journal*. 2006;42(5):1173-82.
9. Şek D. Liquid crystalline properties of new poly(azomethine esters). *European Polymer Journal*. 1984;20(9):923-6.
10. Cozan V, Butuc E, Stoleriu A, Rusa M, Rusu M, Ni Y, et al. Poly(Azomethine Sulfones) with Thermotropic Liquid Crystalline Behavior. *Journal of Macromolecular Science, Part A*. 1995;32(7):1243-62.
11. Yılmaz Baran N, Demir HÖ, Kostekçi S, Sacak M. Poly-2-[(4-methylbenzylidene)amino]phenol: Investigation of thermal degradation and antimicrobial properties. *Journal of Applied Polymer Science*. 2015;132(14):n/a-n/a.
12. Demir HÖ. Ketimine substituted polyphenol: Synthesis, characterization and investigation of its thermal and electrochemical properties. *Journal of Applied Polymer Science*. 2013;127(6):5037-44.
13. Demetgül C, Delikanlı A, Sarıbiyık OY, Karakaplan M, Serin S. Schiff Base Polymers Obtained by Oxidative Polycondensation and Their Co(II), Mn(II) and Ru(III) Complexes: Synthesis, Characterization and Catalytic Activity in Epoxidation of Styrene. *Designed Monomers and Polymers*. 2012;15(1):75-91.
14. Kaya İ, Yıldırım M, Avcı A. Synthesis and characterization of fluorescent polyphenol species derived from methyl substituted aminopyridine based Schiff bases: The effect of substituent position on optical, electrical, electrochemical, and fluorescence properties. *Synthetic Metals*. 2010;160(9-10):911-20.
15. Yıldırım M, Kaya İ. Synthesis and characterizations of poly(ether)/poly(phenol)s including azomethine coupled benzothiazole side chains: the effect of reaction conditions on the structure, optical, electrochemical, electrical and thermal properties. *Polymer Bulletin*. 2014;71(12):3067-84.
16. Kaya, Emdi D, Saçak M. Synthesis, Characterization and Antimicrobial Properties of Oligomer and Monomer/Oligomer-Metal Complexes of 2-[(Pyridine-3-yl-methylene)amino]phenol. *J Inorg Organomet Polym*. 2009;19(3):286-97. DOI: 10.1007/s10904-009-9270-z.

17. Kaya İ, Aydın A. A new approach for synthesis of electroactive phenol based polymer: 4-(2,5-Di(thiophen-2-yl)-1H-pyrrol-1-yl)phenol and its oxidative polymer. *Progress in Organic Coatings*. 2012;73(2):239-49.
18. Eker B, Zagorevski D, Zhu G, Linhardt RJ, Dordick JS. Enzymatic polymerization of phenols in room-temperature ionic liquids. *Journal of Molecular Catalysis B: Enzymatic*. 2009;59(1):177-84.
19. Mart H. Oxidative polycondensation reaction. *Designed Monomers and Polymers*. 2006;9(6):551-88.
20. Yılmaz Baran N, Saçak M. Synthesis, characterization and molecular weight monitoring of a novel Schiff base polymer containing phenol group: Thermal stability, conductivity and antimicrobial properties. *Journal of Molecular Structure*. 2017;1146(Supplement C):104-12.
21. Yılmaz Baran N, Karakışla M, Demir HÖ, Saçak M. Synthesis, characterization, conductivity and antimicrobial study of a novel thermally stable polyphenol containing azomethine group. *Journal of Molecular Structure*. 2016;1123:153-61.
22. Özbülbül A, Mart H, Tunçel M, Serin S. A new soluble Schiff base polymer with a double azomethine group synthesized by oxidative polycondensation. *Designed Monomers and Polymers*. 2006;9(2):169-79.
23. Cazacu M, Marcu M, Vlad A, Rusu GI, Avadanei M. Chelate polymers. VI. New copolymers of the some siloxane containing bis(2,4-dihydroxybenzaldehyd-imine)Me₂+ with bis(p-carboxyphenyl)diphenylsilane. *Journal of Organometallic Chemistry*. 2004;689(19):3005-11.
24. Diaz FR, Moreno J, Tagle LH, East GA, Radic D. Synthesis, characterization and electrical properties of polyimines derived from selenophene. *Synthetic Metals*. 1999;100(2):187-93.
25. Kaya I, Bilici A, Sacak M. New conjugated azomethine oligomers obtained from bis-(hydroxyphenyl)methylenediamine via oxidative polycondensation and their complexes with metals. *Synthetic Metals*. 2009;159(14):1414-21.



Syntheses and spectroscopic investigations of 2-pyridyl(N/N)spirocyclotriphosphazenes

Gamze Elmas  

Ankara University, 06100, Ankara, Turkey

Abstract: The Cl substitution reaction of $N_3P_3Cl_6$ (**1**) with *N*-(2-pyridyl)-methyl-*N'*-methylpropane-1,3-diamine (**2**) afforded the partly substituted 2-pyridyl(N/N)spirocyclotriphosphazene (**3**) (with a yield of 57%) in dry THF. When the Cl replacement reactions of **2** carried out with excess pyrrolidine, morpholine, and 1,4-dioxo-8-azaspiro[4,5]decane (DASD), the corresponding 2-pyridyl(N/N)spirotetrapyrrolidino (**3a**), tetramorpholino (**3b**) and tetra(1,4-dioxo-8-azaspiro[4,5]decano) (**3c**) cyclotriphosphazenes were prepared in moderate yields. The structures of four cyclotriphosphazene derivatives were elucidated by the elemental analyses, Fourier transform infrared (FTIR), heteronuclear mass spectrometry (ESI-MS), heteronuclear multiple-bond correlation (HMBC), single quantum coherence (HSQC), 1H , ^{13}C , and ^{31}P NMR techniques.

Keywords: 2-Pyridyl(N/N)spirocyclotriphosphazenes, Replacement reactions, Spectroscopy

Submitted: January 17 ,2018. **Accepted:** March 29, 2018.

Cite This: Elmas G. Syntheses and spectroscopic investigations of 2-pyridyl(N/N)spirocyclotriphosphazenes. JOTCSA. 2018;5(2):621–34.

DOI: <http://dx.doi.org/10.18596/jotcsa.379971>.

***Corresponding author. E-mail:** gegemen@ankara.edu.tr

Tel: +90 0312 2126720/1195.

INTRODUCTION

Cyclophosphazenes are inorganic heterocyclic ring systems consisting of a backbone that contains the repeating unit $[N=PX_2]_n$ ($n=3,4,5,\dots$) with nitrogen and phosphorus atoms and two organic, inorganic and/or organometallic side groups (X), linked covalently to each phosphorus atom (1,2). Hexachlorocyclotriphosphazene, $N_3P_3Cl_6$, is the best-known starting compound used for the preparation of the new phosphazene derivatives in the field of phosphazene chemistry (3). Hence, its Cl substitution reactions with monodentate (4,5) and bidentate reagents (6,7) have been thoroughly examined for years on account of the formation of various structural isomers and stereoisomers. The replacement reactions of $N_3P_3Cl_6$ with monoamines and diamines led to the formation of partly and fully substituted aminocyclotriphosphazenes (8). For instance, in the literature, there are many studies on the reactions of $N_3P_3Cl_6$ with various N/N donor typed difunctional ligands, *e.g.* containing 4-fluorobenzyl, ferrocenyl, and 4-nitrobenzyl pendant arms for the formation of the partly substituted (N/N)spirocyclotriphosphazenes (9-11). The fully substituted cyclophosphazenes are also obtained with the reactions of these products with excess monoamines (9-11).

On the other hand, the prepared cyclotriphosphazenes are used as liquid crystalline materials (12), ionic liquids (13), organic light emitting diodes (OLEDs) (14), photosensitizers (15), fluorescence chemosensors (16) and Langmuir–Blodgett thin films (17).

Besides, aziridino, pyrrolidino, morpholino and tetra(1,4-dioxa-8-azaspiro[4,5]decano) phosphazenes have revealed significant antibacterial, antifungal, and anticancer activities, and they were determined to be efficient in changing the mobility of the DNA (18-21). In such a manner, that some of the cyclophosphazenes were also found to be active in the different tumor cells; *e.g.* Hep2, HT-29, Hela, C6, Vero, DLD1 and A549 cells (22-24).

In addition, the pyridine derivatives are quite essential compounds with the incredible biological applications (25,26). The new compounds, which contain a trimeric phosphazene ring with 2-pyridyl pendant arm, may be considered to have possibly antimicrobial, anticancer, antituberculosis, and antiproliferative activities.

Consequently, this paper reports herein the salient features of the synthetic and spectroscopic properties of the partly (**3**) and fully heterocyclic amine substituted *spiro*-phosphazene derivatives (**3a-3c**).

EXPERIMENTAL PART

Materials and Methods

The starting compound, $N_3P_3Cl_6$ (Aldrich) was recrystallized from n-hexane. The solvents and reagents were purified using the standard methods before use. N-methylpropane-1,3-diamine, pyridine-2-carboxaldehyde, pyrrolidine, morpholine and 1,4-dioxo-8-azaspiro[4,5]decane (DASD) were supplied by Merck. The reactions were performed under Ar and monitored by TLC on Merck DC Alufolien Kiesegel 60 B254 sheets using various solvents. The melting points of the phosphazenes were designated on a Gallenkamp apparatus by capillary tubes. The elemental analyses of the compounds were carried out using a Leco CHNS-932 instrument in microanalytical service of Ankara University. The FTIR spectra were obtained from Jasco FT/IR-430 spectrometer in KBr disks and reported in cm^{-1} units. Mass spectra (ESI-MS) of the products were recorded on the Waters 2695 Alliance Micromass ZQ spectrometer. The 1D (1H and ^{13}C NMR) and 2D (HSQC and HMBC) spectra were monitored on a Varian Mercury FT-NMR (400 MHz) spectrometer using $SiMe_4$ as an internal standard operating at 400.13 and 100.62 MHz (at Ankara University). ^{31}P $\{^1H\}$ NMR spectra were saved on a Bruker Avance III HD (600 MHz) spectrometer using 85% H_3PO_4 as an external standard operating at 242.94 MHz (at İnönü University). The spectrometer was fitted with a 5 mm PABBO BB inverse-gradient probe, and standard Bruker pulse programs (27) were used.

Synthesis of 2-pyridyldiamine (2). *N*-(2-Pyridyl)-methyl-*N'*-methylpropane-1,3-diamine (**2**) was obtained from the reaction of pyridine-2-carboxaldehyde with *N*-methylpropane-1,3-diamine in ethanol at -10 °C concerning to the published procedure (28).

Synthesis of 2-pyridyl(N/N)spirocyclophosphazene (3). A solution of **2** (2.20 g, 12.30 mmol) in THF (100 mL) and triethylamine (5.70 mL, 40.00 mmol) was added to a solution of $N_3P_3Cl_6$ (3.56 g, 10.00 mmol) in THF (50 mL) at -10 °C under Ar. The mixture was stirred for three days at room temperature, and then it was refluxed for two days. The precipitated triethylamine hydrochloride was filtered off, and the solvent was evaporated at reduced pressure. The product was purified by column chromatography using toluene:THF (2:1) as eluent, and an off-white powder of **3** crystallized from toluene. Yield: 2.59 g (57%). mp: 120 °C. Anal. Calcd. for $P_3N_6Cl_4C_{10}H_{15}$: C, 26.46; H, 3.33; N, 18.51. Found: C, 25.98; H, 3.67; N, 18.41. ESI-MS (fragments are based on ^{35}Cl , Ir %, Ir designates the fragment abundance percentage): m/z 455 ($[M+H]^+$, 100). FTIR (KBr, cm^{-1}): ν 2924, 2855 (C-H aliph.), 1220 (asymm.), 1169 (symm.) (P=N), 579 (asymm.), 510

(symm.) (PCI). ^1H NMR (400 MHz, CDCl_3 , ppm, numberings of protons are given in Figure 1): δ 8.59 (d, H, $^3J_{\text{HH}}=5.2$ Hz, H_5), 7.89 (dd, H, $^3J_{\text{HH}}=7.6$ Hz, $^3J_{\text{HH}}=8.0$ Hz, H_3), 7.73 (d, H, $^3J_{\text{HH}}=8.0$ Hz, H_2), 7.38 (dd, H, $^3J_{\text{HH}}=5.2$ Hz, $^3J_{\text{HH}}=7.6$ Hz, H_4), 4.31 (d, 2H, $^3J_{\text{PH}}=11.2$ Hz, Py- CH_2 -N), 3.20 (t, 2H, $^3J_{\text{PH}}=12.0$ Hz, $^2J_{\text{HH}}=6.0$ Hz, Py- CH_2 -N- CH_2), 3.15 (t, 2H, $^3J_{\text{PH}}=11.6$ Hz, $^2J_{\text{HH}}=5.6$ Hz, CH_3 -N- CH_2), 2.63 (d, 3H, $^3J_{\text{PH}}=14.0$ Hz, N- CH_3), 1.92 (m, 2H, $^3J_{\text{HH}}=6.0$ Hz, $^3J_{\text{HH}}=5.2$ Hz, N- CH_2 - CH_2). ^{13}C NMR (100 MHz, CDCl_3 , ppm, numberings of carbons are given in Figure 1): δ 156.79 (d, $^3J_{\text{PC}}=8.5$ Hz, C_1), 147.02 (s, C_5), 138.96 (s, C_3), 123.18 (s, C_2), 122.94 (s, C_4), 51.44 (d, $^2J_{\text{PC}}=3.8$ Hz, Py- CH_2 -N), 50.03 (s, Py- CH_2 -N- CH_2), 47.16 (s, CH_3 -N- CH_2), 34.98 (d, $^2J_{\text{PC}}=1.5$ Hz, N- CH_3), 25.09 (d, $^3J_{\text{PC}}=3.0$ Hz, N- CH_2 - CH_2).

Synthesis of 2-pyridyl(N/N)spirotetrapyrrolidino-cyclotriphosphazene (3a).

A solution of **3** (0.80 g, 1.80 mmol) and triethylamine (1.00 mL, 7.20 mmol) in dry THF (100 mL) was added slowly to a solution of pyrrolidine (1.19 mL, 14.40 mmol) in dry THF (50 mL) under Ar. The mixture was stirred for two days at ambient temperature, and then it was refluxed for two days. The crude product was purified by column chromatography using toluene-THF (2:1) as eluent, and an off-white powder of **3a** was crystallized from toluene. Yield: 0.68 g (64%). mp: 169 °C. Anal. Calcd. for $\text{P}_3\text{N}_{10}\text{C}_{26}\text{H}_{47}$. 0.5 C_7H_8 : C, 55.50; H, 8.05; N, 21.94. Found: C 55.66; H, 8.28; N, 21.48. ESI-MS (Ir %): m/z 593 ($[\text{M}+\text{H}]^+$, 100). FTIR (KBr, cm^{-1}): ν 2958, 2851 (C-H aliph.), 1225 (asymm.), 1172 (symm.) (P=N). ^1H NMR (400 MHz, CDCl_3 , ppm): δ 8.48 (d, H, $^3J_{\text{HH}}=4.2$ Hz, H_5), 7.72 (d, H, $^3J_{\text{HH}}=8.0$ Hz, H_2), 7.63 (dd, H, $^3J_{\text{HH}}=7.6$ Hz, $^3J_{\text{HH}}=8.0$ Hz, H_3), 7.12 (dd, H, $^3J_{\text{HH}}=6.0$ Hz, $^3J_{\text{HH}}=7.6$ Hz, H_4), 4.20 (d, 2H, $^3J_{\text{PH}}=7.6$ Hz, Py- CH_2 -N), 3.16 (m, 2H, CH_3 -N- CH_2), 3.08 [m, 16H, N- CH_2 (pyrr)], 3.07 (m, 2H, Py- CH_2 -N- CH_2), 2.60 (d, 3H, $^3J_{\text{PH}}=13.6$ Hz, N- CH_3), 1.79 (m, 2H, $^3J_{\text{HH}}=5.2$ Hz, N- CH_2 - CH_2), 1.78 [m, 8H, N- CH_2 - CH_2 (pyrr)], 1.64 [m, 8H, N- CH_2 - CH_2 (pyrr)]. ^{13}C NMR (100 MHz, CDCl_3 , ppm): δ 161.16 (d, $^3J_{\text{PC}}=11.6$ Hz, C_1), 148.68 (s, C_5), 136.45 (s, C_3), 121.72 (s, C_2), 121.61 (s, C_4), 52.78 (d, $^2J_{\text{PC}}=2.9$ Hz, Py- CH_2 -N), 50.99 (s, Py- CH_2 -N- CH_2), 47.09 (s, CH_3 -N- CH_2), 46.20 and 46.18 [s, N- CH_2 (pyrr)], 36.36 (m, N- CH_3), 26.29 [(d, $^3J_{\text{PC}}=6.9$ Hz, N- CH_2 - CH_2 (pyrr)], 26.22 [(d, $^3J_{\text{PC}}=6.1$ Hz, N- CH_2 - CH_2 (pyrr)], 25.01 (d, $^3J_{\text{PC}}=2.9$ Hz, N- CH_2 - CH_2).

Synthesis of 2-pyridyl(N/N)spirotetramorpholino-cyclotriphosphazene (3b).

The experimental procedure was carried out as in **3a**, using **3** (0.80 g, 1.80 mmol), triethylamine (1.00 mL, 7.20 mmol) and morpholine (1.25 mL, 14.40 mmol). The mixture was stirred for two days at ambient temperature, and then it was refluxed for three days. The crude product was purified by column chromatography using toluene-THF (2:1) as eluent, and an off-white powder of **3b** crystallized from toluene. Yield: 0.66 g (56%). mp: 145 °C. Anal. Calcd. for $\text{P}_3\text{N}_{10}\text{O}_4\text{C}_{26}\text{H}_{47}$. 0.5 C_7H_8 : C, 50.45; H, 7.32; N, 19.94. Found: C, 50.93; H, 7.38; N, 20.05. ESI-MS (Ir %): m/z 657 ($[\text{M}+\text{H}]^+$, 100). FTIR (KBr, cm^{-1}): ν

2918, 2851 (C-H aliph.), 1248 (asymm.), 1159 (symm.) (P=N). ^1H NMR (400 MHz, CDCl_3 , ppm): δ 8.55 (d, H, $^3J_{\text{HH}}=4.8$ Hz, H_5), 7.45 (d, H, $^3J_{\text{HH}}=8.0$ Hz, H_2), 7.30 (dd, H, $^3J_{\text{HH}}=8.0$ Hz, $^3J_{\text{HH}}=8.0$ Hz, H_3), 7.18 (dd, H, $^3J_{\text{HH}}=4.4$ Hz, $^3J_{\text{HH}}=8.0$ Hz, H_4), 4.32 (d, 2H, $^3J_{\text{PH}}=9.6$ Hz, Py- $\text{CH}_2\text{-N}$), 3.69 [m, 8H, O- CH_2 (morp)], 3.65 [m, 8H, O- CH_2 (morp)], 3.21 (t, 2H, $^3J_{\text{PH}}=12.0$ Hz, $^2J_{\text{HH}}=6.0$ Hz, Py- $\text{CH}_2\text{-N-CH}_2$), 3.16 [m, 16H, N- CH_2 (morp)], 3.12 (t, 2H, $^3J_{\text{PH}}=11.2$ Hz, $^2J_{\text{HH}}=5.6$ Hz, $\text{CH}_3\text{-N-CH}_2$), 2.69 (d, 3H, $^3J_{\text{PH}}=11.6$ Hz, N- CH_3), 1.97 (m, 2H, $^3J_{\text{HH}}=7.2$ Hz, $^3J_{\text{HH}}=7.2$ Hz, N- $\text{CH}_2\text{-CH}_2$). ^{13}C NMR (100 MHz, CDCl_3 , ppm): δ 157.45 (d, $^3J_{\text{PC}}=6.1$ Hz, C_1), 149.45 (s, C_5), 137.17 (s, C_3), 122.77 (s, C_2), 121.66 (s, C_4), 67.10 [(d, $^3J_{\text{PC}}=7.7$ Hz, O- CH_2 (morp)], 66.87 [(s, O- CH_2 (morp)], 52.18 (d, $^2J_{\text{PC}}=2.8$ Hz, Py- $\text{CH}_2\text{-N}$), 50.49 (s, Py- $\text{CH}_2\text{-N-CH}_2$), 46.99 (s, $\text{CH}_3\text{-N-CH}_2$), 44.96 and 44.70 [s, N- CH_2 (morp)], 35.61 (d, $^2J_{\text{PC}}=3.1$ Hz, N- CH_3), 25.07 (d, $^3J_{\text{PC}}=3.1$ Hz, N- $\text{CH}_2\text{-CH}_2$).

Synthesis of 2-pyridyl(N/N)spirotetra-DASD-cyclotriphosphazene (3c). The experimental procedure was carried out as in **3a**, using **3** (0.80 g, 1.80 mmol), triethylamine (1.00 mL, 7.20 mmol) and DASD (1.85 mL, 14.40 mmol). The mixture was stirred for two days at ambient temperature, and then it was refluxed for two days. The crude product was purified by column chromatography using toluene-THF (2:1) as eluent, and an off-white powder of **3c** crystallized from toluene. Yield: 0.95 g (60%). mp: 177 °C. Anal. Calcd. for $\text{P}_3\text{N}_{10}\text{O}_8\text{C}_{38}\text{H}_{63}$: C, 51.84; H, 7.21; N, 15.91. Found: C, 51.49; H, 7.33; N, 15.46. ESI-MS (Ir %): m/z 881 ($[\text{M}+\text{H}]^+$, 100). FTIR (KBr, cm^{-1}): ν 2918, 2851 (C-H aliph.), 1216 (asymm.), 1152 (symm.) (P=N). ^1H NMR (400 MHz, CDCl_3 , ppm): δ 8.49 (d, H, $^3J_{\text{HH}}=4.8$ Hz, H_5), 7.68 (dd, H, $^3J_{\text{HH}}=6.0$ Hz, $^3J_{\text{HH}}=7.6$ Hz, H_3), 7.65 (d, H, $^3J_{\text{HH}}=7.6$ Hz, H_2), 7.13 (dd, H, $^3J_{\text{HH}}=6.0$ Hz, $^3J_{\text{HH}}=7.6$ Hz, H_4), 4.11 (d, 2H, $^3J_{\text{PH}}=7.6$ Hz, Py- $\text{CH}_2\text{-N}$), 3.95 [s, 8H, O- CH_2 (DASD)], 3.89 [s, 8H, O- CH_2 (DASD)], 3.22 [m, 16H, N- CH_2 (DASD)], 3.14 (m, 2H, Py- $\text{CH}_2\text{-N-CH}_2$), 3.05 (m, 2H, $\text{CH}_3\text{-N-CH}_2$), 2.54 (d, 3H, $^3J_{\text{PH}}=13.6$ Hz, N- CH_3), 1.81 (m, 2H, N- $\text{CH}_2\text{-CH}_2$), 1.65 [m, 8H, N- $\text{CH}_2\text{-CH}_2$ (DASD)], 1.52 [m, 8H, N- $\text{CH}_2\text{-CH}_2$ (DASD)]. ^{13}C NMR (100 MHz, CDCl_3 , ppm): δ 160.16 (d, $^3J_{\text{PC}}=7.5$ Hz, C_1), 148.64 (s, C_5), 136.57 (s, C_3), 125.45 (s, C_2), 121.74 (s, C_4), 107.79 and 107.52 [s, O-C-O (DASD)], 64.16 and 64.07 [s, O- CH_2 (DASD)], 52.63 (d, $^2J_{\text{PC}}=3.0$ Hz, Py- $\text{CH}_2\text{-N}$), 50.83 (s, Py- $\text{CH}_2\text{-N-CH}_2$), 47.16 (s, $\text{CH}_3\text{-N-CH}_2$), 42.77 and 42.68 [s, N- CH_2 (DASD)], 36.31 (m, N- CH_3), 35.65 and 35.44 [m, N- $\text{CH}_2\text{-CH}_2$ (DASD)], 25.16 (d, $^3J_{\text{PC}}=3.0$ Hz, N- $\text{CH}_2\text{-CH}_2$).

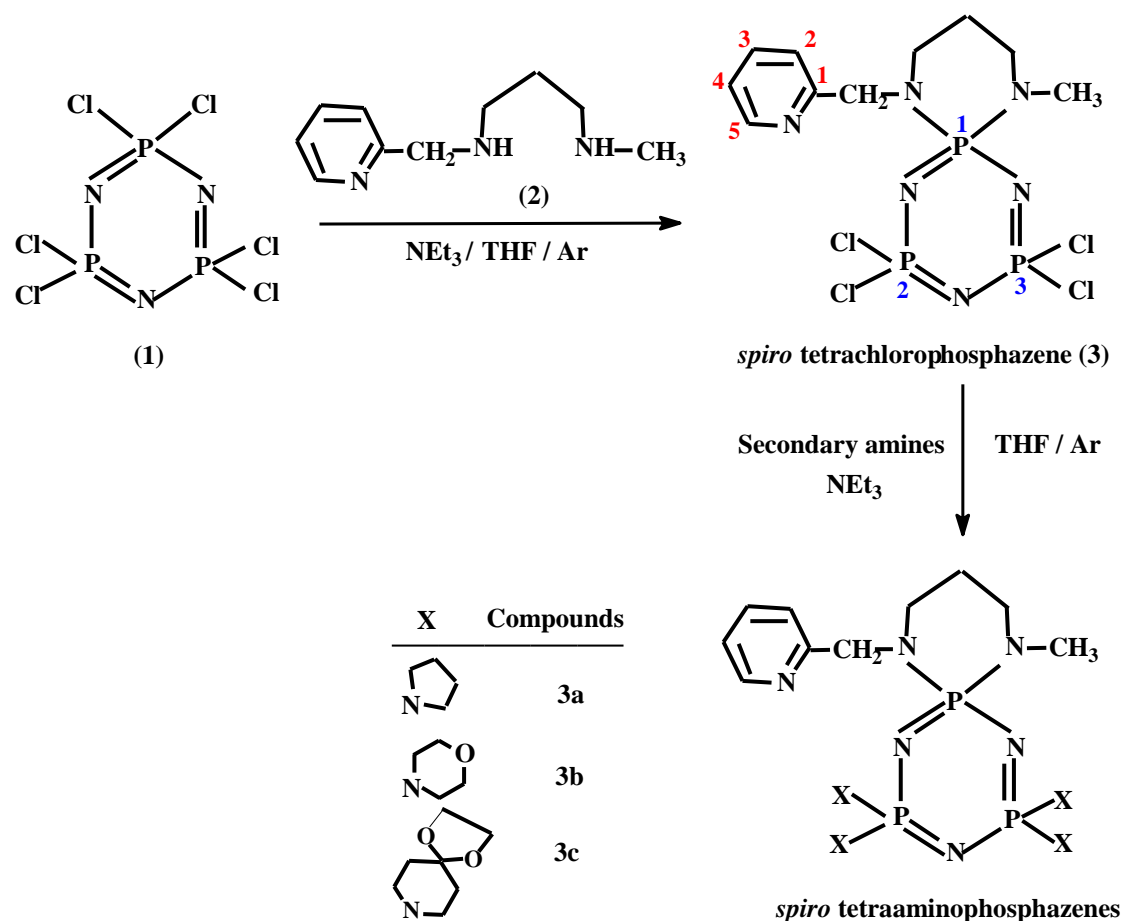


Figure 1. The synthesis of 2-pyridylspiro(N/N)cyclotriphosphazene (**3**) and its tetraamino derivatives (**3a-3c**).

RESULTS AND DISCUSSION

Syntheses

The reaction of pyridine-2-carboxyaldehyde with *N*-methylpropane-1,3-diamine led to the formation of the intermediate Schiff base. This product was reduced with NaBH_4 in ethanol to produce the difunctional ligand, *N*-(2-pyridyl)-methyl-*N'*-methylpropane-1,3-diamine (**2**), in accordance with the literature (28). The preliminary spiro cyclotriphosphazene; 2-pyridyl(N/N)spiro cyclotriphosphazene (**3**), was prepared from the reaction of $\text{N}_3\text{P}_3\text{Cl}_6$ with one equimolar amount of the 2-pyridyldiamine (**2**) with a yield of 57% in dry THF. The condensation reactions of **3** with excess pyrrolidine, morpholine and 1,4-dioxaspiro[4,5]decane (DASD) afforded the fully amino substituted cyclotriphosphazenes (**3a-3c**). The estimating yields of these products were found to be 64, 56 and 60%, respectively (Figure 1).

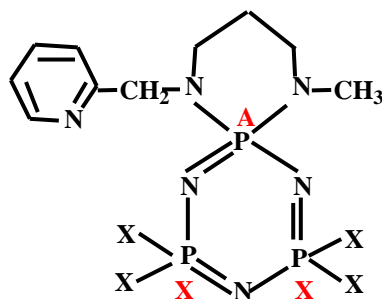
The structures of the 2-pyridylspiro(N/N)cyclotriphosphazenes with a half mole of toluene for **3a** and **3b**, were characterized by the elemental analyses, ESI-MS, FTIR, HSQC, HMBC, ^1H , ^{13}C and ^{31}P NMR techniques. The analytical and NMR results are given in the "Experimental Part". The ESI-MS spectra of all the trimeric phosphazenes exhibit the protonated molecular $[\text{MH}]^+$ ion peaks. The first leaving group in the ESI-MS spectra of the fully substituted compounds (**3a-3c**) was determined as 2-pyridyl-methyl $[\text{M}-\text{C}_5\text{H}_4\text{N}-\text{CH}_2$, 92].

NMR and IR Spectroscopy

The ^{31}P $\{^1\text{H}\}$ NMR chemical shifts and the coupling constants of 2-pyridylspiro(N/N)cyclotriphosphazenes (**3** and **3a-3c**) are tabulated in Table 1. The ^{31}P spectra of all the compounds display AX_2 type spectra on account of two different phosphorus environments within the structures, and they appear as one doublet (P_X) and one triplet (P_spiro , P_A). It is determined that the δ P_spiro chemical shifts of all the tetraamino-2-pyridylspiro(N/N)cyclotriphosphazenes (**3a-3c**) are higher than the compound **3**. As known, in compound **3**, the Cl atoms are withdrawing the electrons of the phosphazene ring. Hence, electrons are releasing from the nitrogen atoms of the spiro ring to the phosphazene skeleton and negative hyperconjugation occurs on the spiro phosphorus atom (29). This is reversed for the amino phosphazenes (**3a-3c**). On the contrary, the coupling constants of all the phosphazenes are nearly the same.

As examples, ^{31}P $\{^1\text{H}\}$ NMR spectra of the beginning spiro compound (**3**) and its morpholine substituted derivative (**3b**) are depicted in Figure 2. In the spectra of **3** and **3b**, the δ P_A of spiro (P_NN) and δ P_X (P_{Cl_2} or P_NN) are 11.66 and 23.25 ppm, and 22.02 and 20.14 ppm, respectively. The $^2J_{\text{PP}}$ values of both are calculated as 38.9 Hz.

X: Cl, Pyrrolidine, Morpholine, DASD



AX_2 (**3**, **3a**, **3b** and **3c**)

Compound d	Spin Systems	P _A (P _{NN})	P _X (P _{NN})	P _X (P _{Cl2})	² J _{PP} (Hz)
3	AX ₂	11.66 (t)	-	22.02 (d)	² J _{AX} 38.9
3a	AX ₂	23.79 (t)	17.39 (d)	-	² J _{AX} 38.9
3b	AX ₂	23.25 (t)	20.14 (d)	-	² J _{AX} 38.9
3c	AX ₂	23.00 (t)	20.33 (d)	-	² J _{AX} 36.4

Table 1. ³¹P {¹H} NMR data of 2-pyridyl(N/N)spirocyclo-triphosphazenes.^a

^a242.925 MHz ³¹P NMR measurements in CDCl₃ solutions at 298 K, and the chemical shifts referenced to external standard H₃PO₄.

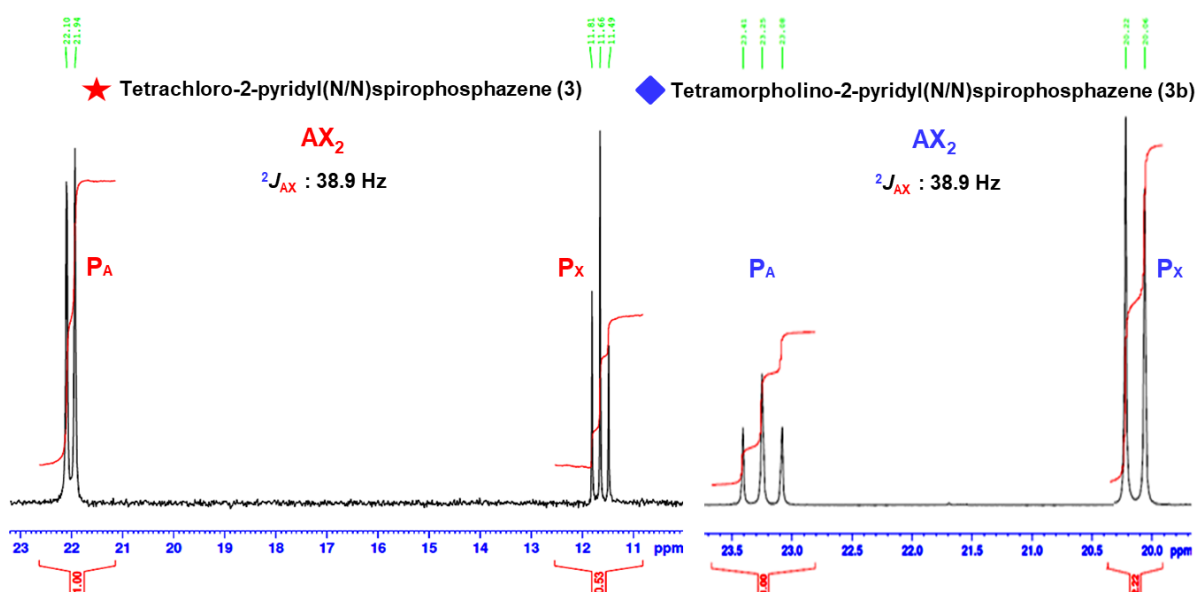


Figure 2. ³¹P {¹H} NMR spectra of the compounds **3** and **3b**.

The interpretations of the δ chemical shifts, multiplicities, and J coupling constants are elucidated from the ¹³C and ¹H NMR spectra of the new 2-pyridyl(N/N)spirocyclo-triphosphazenes (**3** and **3a-3c**), and presented in "Experimental Part". The HSQC [using values corresponding to ¹J_{CH}] and HMBC [using values corresponding to ²J_{CH}, ³J_{CH} and ⁴J_{CH} between the protons and carbons] are also quite useful for the assignments of the signals. The HMBC and HSQC spectra of **3a** are given in Figures 3a and 3b, respectively, as examples.

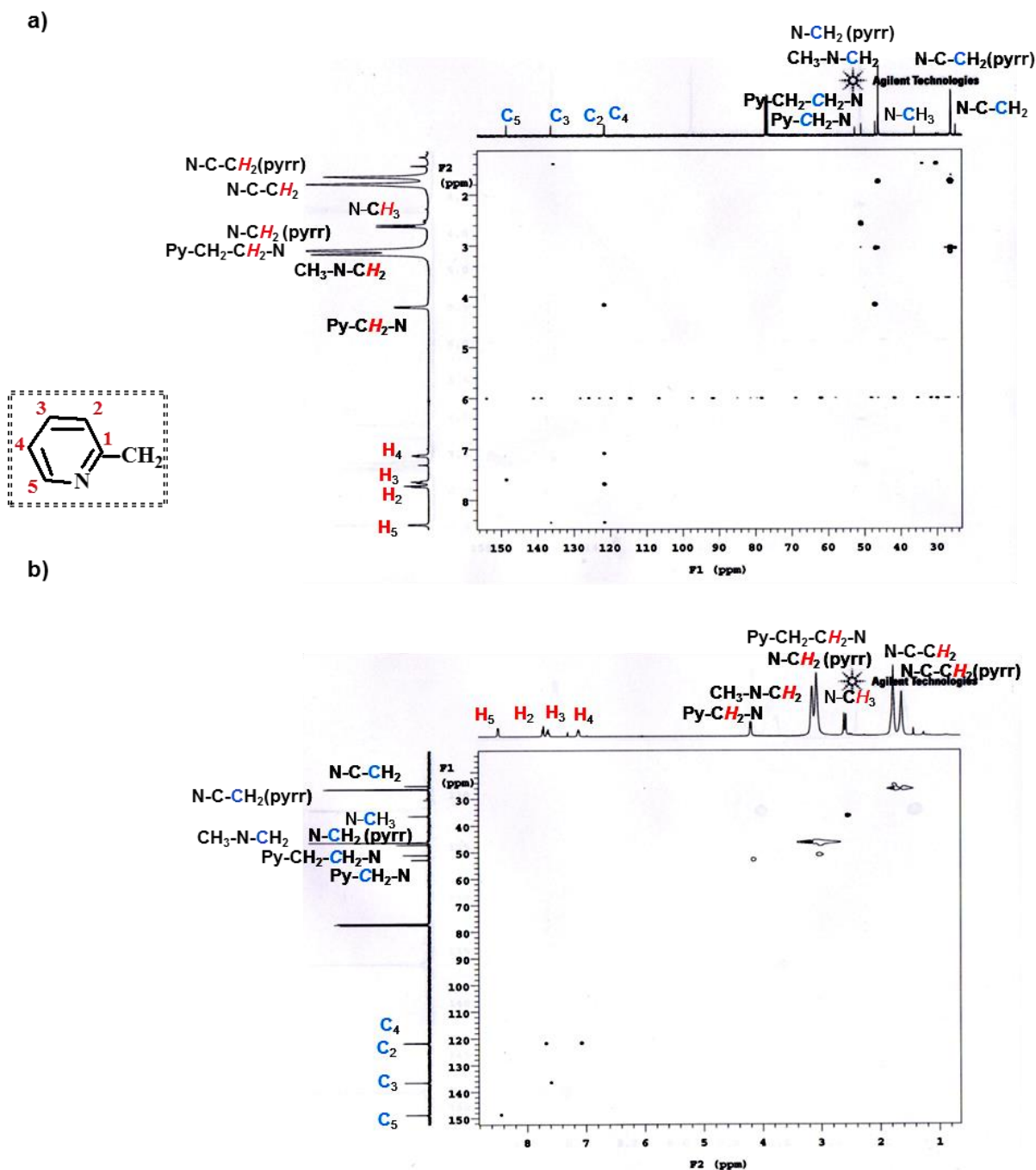


Figure 3. The (a) HMBC and (b) HSQC spectra of **3a**.

The signals of all the carbons of the 2-pyridyl(N/N)spirocyclotriphosphazenes are interpreted in the ^{13}C NMR spectra. The $\text{N}-\underline{\text{C}}\text{H}_3$ carbons of the phosphazenes are observed in the range of 34.98-36.36 ppm, and the average value is 35.88 ppm. The average values of $^3J_{\text{PNC}}$, for the $\text{N}-\underline{\text{C}}\text{H}_2-\underline{\text{C}}\text{H}_2$ carbons of the cyclotriphosphazene derivatives are 6.5 Hz (for pyrrolidine rings), 7.7 Hz (for morpholine) and 3.0 Hz (for six-membered NN spiro rings). In contrast with, the $^2J_{\text{PNC}}$, for the $\text{Py}-\underline{\text{C}}\text{H}_2-\text{N}-\underline{\text{C}}\text{H}_2$ and $\text{CH}_3-\text{N}-\underline{\text{C}}\text{H}_2$ carbons of the compounds are not observed. As expected, the *geminal* amine substituents in the ^{13}C spectra of the tetraaminocyclotriphosphazenes (**3a-3c**) displayed two small separated peaks for $\text{N}-\underline{\text{C}}\text{H}_2$,

N-CH₂-CH₂, O-CH₂ and O-C-O groups, because two *geminal* groups were not equivalent to each other. The O-C-O and C-O-CH₂ carbon signals of **3c** are very characteristic, and they are observed at *ca.* 107 and 64 ppm as four separate singlets. The O-CH₂ carbons of tetramorpholino-2-pyridyl(N/N)spirocyclophosphazene (**3b**) also appear at *ca.* 67 ppm as two separate singlets. On the other hand, the expected carbon peaks (C₁-C₅) of the pyridyl ring are assigned from the ¹³C NMR spectra of all the compounds, and the obtained results are consistent with the literature findings of 2-pyridyl substituted derivatives (28).

The ³J_{PNCC} values of the tetrapyrrolidino-2-pyridyl(N/N)spirocyclophosphazenes (**3a**) reveal to triplets of the N-CH₂-CH₂ carbons on account of the second-order effects that have also been observed previously for some of the cyclophosphazenes (30,31) (Figure 4). The ³J_{PNCC} values were estimated using the external transitions of the triplet peaks.

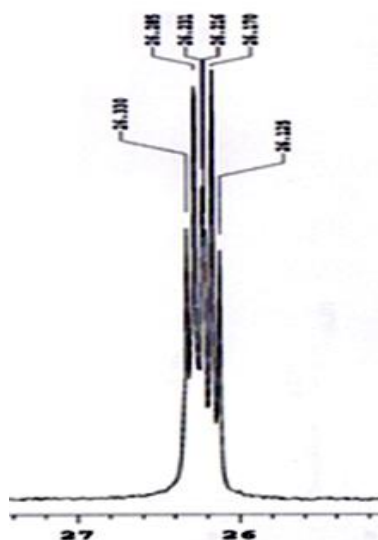


Figure 4. The second order effect in ¹³C {¹H} NMR spectrum of **3a**.

The signals of the protons of the 2-pyridyl(N/N)spirocyclophosphazenes are evaluated in the ¹H NMR spectra. The ¹H NMR spectra of the fully substituted phosphazenes (**3a-3c**) show that four secondary monoamines (pyrrolidine, morpholine and DASD) were bonded to the P2 and P3 atoms (see numbering of trimer in Figure 1). The average values of N-CH₂-CH₂, Py-CH₂-N-CH₂ and CH₃-N-CH₂ spiro protons of the phosphazenes (**3a-3c**) were found to be at 1.86 ppm, 3.14 ppm and 3.12 ppm, respectively, in comparison to the values (1.92 ppm, 3.20 ppm and 3.15 ppm) of the starting phosphazene (**3**). Furthermore, the δ_H shift of the protons of Py-CH₂-N of the compounds was observed in the range of 4.11-4.32 ppm, and the average ³J_{PH} value is 9.0 Hz. On the other hand, the expected proton peaks (H₂-H₅) of the pyridyl ring were determined from the ¹H NMR spectra of all the compounds, and the finding data are in accordance with the literature (28). The N-CH₃

protons of the cyclotriphosphazenes were observed in the range of 2.54-2.69 ppm, and the average $^3J_{\text{PH}}$ value, 13.2 Hz, was very large.

The characteristic FTIR bands of the 2-pyridyl(N/N)spirocyclotriphosphazenes are given in "Experimental Part". The compounds exhibited intense asymmetric and symmetric stretching vibrations between 1216-1248 cm^{-1} and 1152-1172 cm^{-1} , ascribed to the P=N bonds of the P_3N_3 skeletons (32). As expected, the asymmetric and symmetric vibrations of ν_{PCl_2} for the partly substituted phosphazene (3) emerged at 579 cm^{-1} and 510 cm^{-1} , respectively (33). In other compounds (3a-3c), these peaks disappeared.

CONCLUSIONS

The reactions of $\text{N}_3\text{P}_3\text{Cl}_6$ (1) with one equimolar amount of the 2-pyridyl substituted N/N donor-type bidentate ligand (2) produced 2-pyridyl(N/N)spirocyclotriphosphazene (3) regioselectively in dry THF. The partly substituted spiro compound (3) reacted with excess secondary amines in THF to afford the fully substituted cyclotriphosphazenes (3a-3c). The obtained 2-pyridyl(N/N)spirocyclotriphosphazenes (3 and 3a-3c) are the first examples of the pyridyl pendant armed cyclotriphosphazenes. The spectroscopic features of the cyclophosphazenes were scrutinized using one and two dimensional NMR techniques in CDCl_3 solution. The synthetic and spectroscopic properties of the compounds were compared to each other. As known, the aminospicyclotriphosphazenes are strong bases. Thus, the tetraamino-2-pyridyl(N/N)spirocyclotriphosphazenes synthesized in this paper ought to be used as heterocyclic ligands for the transition metal cations, and they may be produced phosphazanium salts with biologically active bulky organic acids. Moreover, 2-pyridyl-diamine (2), which is a pyridine derivative, is very essential chemical with great biological applications. Hence, the obtained new phosphazene derivatives (3 and 3a-3c), which contain a trimeric phosphazene ring with 2-pyridyl pendant arm, are considered to have probably anticancer, antituberculosis, antimicrobial, antiviral and antiproliferative activities.

ACKNOWLEDGMENTS

The work was supported by the "Scientific and Technical Research Council of Turkey" (Grant No. 216Z105). The author thanks to Professor Zeynel Kılıç for his helpful discussions in spectroscopy.

REFERENCES

1. Chandrasekhar V, Narayanan RS. Phosphazenes. *Organophosphorus Chem.* 2017 Mar; 46: 342-417, Royal Society of Chemistry (RSC Publishing).
2. Stewart FF. Phosphazenes. *Organophosphorus Chem.* 2015 Apr; 44: 397-430, Royal Society of Chemistry (RSC Publishing).
3. Chandrasekhar V, Narayanan RS. Phosphazenes. *Organophosphorus Chem.* 2016 Mar; 45: 375-437, Royal Society of Chemistry (RSC Publishing).
4. Medjdoub L, Mohammed B. New method for nucleophilic substitution on hexachlorocyclotriphosphazene by allyamine using an algerian proton exchanged montmorillonite clay (magnite-H⁺) as a green solid catalyst. *Bull. Chem. React. Eng.&Catal.* 2016 Aug; 11: 151-160.
5. Egemen G, Hayvalı M, Kılıç Z, Solak AO, Üstündağ Z. Phosphorus-Nitrogen Compounds. Part 17. The Synthesis, Spectral and Electrochemical Investigations of Porphyrinophosphazenes. J. Porphyrins Phthalocyanines. 2010 Mar; 14: 227-234.
6. Okumuş A, Elmas G, Kılıç Z, Ramazanoğlu N, Açık L, Türk M, Akça G. The reactions of N₃P₃Cl₆ with monodentate and bidentate ligands: The syntheses and structural characterizations, in vitro antimicrobial activities and DNA interactions of 4-fluorobenzyl(N/O)spirocyclophosphazenes. *Turk. J. Chem.* 2017 Mar; 41: 525-547.
7. Tümer Y, Asmafiliz N, Zeyrek CT, Kılıç Z, Açık L, Çelik SP, Türk M, Tunalı BÇ, Ünver H, Hökelek T, Syntheses, spectroscopic and crystallographic characterizations of *cis*- and *trans*-dispirocyclic ferrocenylphosphazenes: molecular dockings, cytotoxic and antimicrobial activities. *New J. Chem.* 2018 Jan; 42: 1740-1756.
8. Kılıç Z, Okumuş A, Demiriz Ş, Bilge S, Öztürk A, Çaylak N, Hökelek T. Phosphorus-nitrogen compounds: Part 16. Synthesis, stereogenism, anisochronism and the relationship between ³¹P NMR spectral and crystallographic data of monotopic *spiro*-crypta phosphazene derivatives. *J. Incl. Phenom. Macrocycl. Chem.* 2009 Dec; 65: 269-286.
9. Okumuş A, Kılıç Z, Hökelek T, Dal H, Açık L, Öner Y, Koç L.Y. Phosphorus-nitrogen compounds part 22. syntheses, structural investigations, biological activities and DNA interactions of new mono and bis (4-fluorobenzyl)spirocyclophosphazenes. *Polyhedron.* 2011 Nov; 30: 2896-2907.
10. Tümer Y, Koç LY, Asmafiliz N, Kılıç Z, Hökelek T, Soltanzade H, Açık L, Yola ML, Solak AO. Phosphorus-nitrogen compounds: part 30. syntheses and structural investigations, antimicrobial and cytotoxic activities and DNA interactions of vanillinato-substituted NN or NO spirocyclic monoferrocenyl cyclotriphosphazenes. *J. Biol. Inorg. Chem.* 2015 Dec; 20: 165-178.
11. Okumuş A, Akbaş H, Kılıç Z, Koç LY, Açık L, Aydın B, Türk M, Hökelek T, Dal H. Phosphorus-nitrogen compounds: part 33: in vitro cytotoxic and antimicrobial activities, DNA interactions, syntheses and structural investigations of new mono(nitrobenzyl)cyclotriphosphazenes. *Res. Chem. Intermed.* 2016; 42: 4221-4251.
12. Jimenez J, Laguna A, Gascon E, Sanz JA, Serrano JL, Barbera J, Oriol L. New liquid crystalline materials based on two generations of dendronised cyclophosphazenes. *Chem. Eur. J.* 2012 Nov; 18: 16801-16814.
13. Omotowa BA, Phillips BS, Zabinski JS, Shreeve JM. Phosphazene- based ionic liquids: synthesis, temperature-dependent viscosity, and effect as additives in water lubrication of silicon nitride ceramics. *Inorg. Chem.* 2004 July; 43: 5466-5471.
14. Nishimoto T, Yasuda T, Lee S.Y, Kondo R, Adachi C. A six-carbazole-decorated cyclophosphazene as a host with high triplet energy to realize efficient delayed-fluorescence OLEDs. *Mater. Horiz.* 2014 Sep; 1: 264-269.

15. Şenkuytu E, Eçik ET. Novel fully-BODIPY functionalized cyclotetraphosphazene photosensitizers having high singlet oxygen quantum yields. Spectrochim. Acta Part A, 2017 July; 182: 26-31.
16. Coşut B. Highly efficient energy transfer in BODIPY-pyrene decorated cyclotriphosphazene. Dyes and Pigments, 2014 Jan; 100: 11-16.
17. Asmafiliz N, Kılıç Z, Civan M, Avcı O, Gönder LY, Açık L, Aydın B, Türk M, Hökelek T. Phosphorus-nitrogen compounds. Part 36. Syntheses, Langmuir-Blodgett thin films and biological activities of spiro-bino-spiro trimeric phosphazenes. New J. Chem. 2016 Nov; 40: 9609-9626.
18. Elmas G, Okumuş A, Sevinç P, Kılıç Z, Açık L, Atalan M, Türk M, Deniz G, Hökelek T. Phosphorus-nitrogen compounds. Part 37. Syntheses and structural characterizations, biological activities of mono and bis(4-fluorobenzyl)spirocyclotetraphosphazenes. New J. Chem. 2017 May; 41: 5818-5835.
19. Labarre JF, Faucher JP, Levy G, Sournies F, Cros S, François G. Antitumour activity of some cyclophosphazenes. Eur. J. Cancer, 1979 May; 15: 637-643.
20. Elmas G, Okumuş A, Kılıç Z, Çam M, Açık L, Hökelek T. Phosphorus-nitrogen compounds. Part 40. The syntheses of (4-fluorobenzyl) pendant armed cyclotetraphosphazene derivatives: Spectroscopic, crystallographic and stereogenic properties, DNA interactions and antimicrobial activities. Inorg. Chim. Acta. 2018 Jan; 476: 110-122.
21. Elmas G, Okumuş A, Kılıç Z, Çelik SP, Açık L. The spectroscopic and thermal properties, antibacterial and antifungal activity and DNA interactions of 4-(fluorobenzyl)spiro(N/O) cyclotriphosphazanium salts, J. Turk. Chem. Soc. Sect. A: Chem. 2017 Sep; 4 (3): 993-1016.
22. Mutlu G, Elmas G, Kılıç Z, Hökelek T, Koç LY, Türk M, Açık L, Aydın B, Dal H. Phosphorus-nitrogen compounds: part 31. syntheses, structural and stereogenic properties, *in vitro* cytotoxic and antimicrobial activities, DNA interactions of novel bicyclotetraphosphazenes containing bulky side group. Inorg. Chim. Acta. 2015 July; 436: 69-81.
23. Akbaş H, Karadağ A, Aydın A, Destegül A, Kılıç Z. Synthesis, structural and thermal properties of hexapyrrolidinocyclotriphosphazenes-based protic molten salts: antiproliferative effects against HT29, HeLa, and C6 cancer cell lines. J. Mol. Liq. 2017 Jan; 230: 482-495.
24. Okumuş A, Elmas G, Cemaloğlu R, Aydın B, Binici A, Şimşek H, Açık L, Türk M, Güzel R, Kılıç Z, Hökelek T. Phosphorus-nitrogen compounds. part 35. syntheses, spectroscopic and electrochemical properties, antituberculosis, antimicrobial and cytotoxic activities of mono-ferrocenyl-spirocyclotetraphosphazenes. New J. Chem. 2016 Apr; 40: 5588-5603.
25. Sangshetti JN, Zambare AS, Kalam Khan FA, Gonjari I, Zaheer Z. Synthesis and biological activity of substituted 4,5,6,7-tetrahydrothieno pyridines: a review. Mini Rev. Med. Chem. 2014; 14 (12): 988-1020.
26. Das RN, Chevret E, Desplat V, Rubio S, Mergny JL, Guillon J. Design, synthesis and biological evaluation of new substituted diquinoliny-pyridine ligands as anticancer agents by targeting g-quadruplex. Molecules, 2018 Dec; 23 (1): 81-95.
27. Bruker program 1D WIN-NMR (release 6.0) and 2D WIN-NMR (release 6.1).
28. Hongyan L, Lo JM, Fanwick PE, Stowell JG, Green MA. Monoprotic tetradentate N3O-donor ligands and their Cu(II) and Ni(II) complexes. Inorg. Chem. 1999 Apr; 38: 2071-2078.
29. Davidson RJ, Ainscough EW, Brodie AM, Harrison JA, Waterland MR. The Nature of the Phosphazene Nitrogen-Metal Bond: DFT Calculations on 2-(Pyridyloxy)cyclophosphazene Complexes. Eur. J. Inorg. Chem. 2010 March; 11: 1619-1625.
30. Elmas G, Okumuş A, Kılıç Z, Gönder LY, Açık L, Hökelek T. The Syntheses and Structural Characterizations, Antimicrobial Activity and *in vitro* DNA Binding of 4-Fluorobenzylspiro(N/O)cyclotriphosphazenes and their Phosphazanium Salts. J. Turk. Chem. Soc. Sect. A: Chem. 2016 Aug; 3 (3): 25-46.

31. Koçak SB, Koçođlu S, Okumuş A, Kılıç Z, Öztürk A, Hökelek T, Öner Y, Açık L. Syntheses, spectroscopic properties, crystal structures, biological activities, and dna interactions of heterocyclic amine substituted spiro-ansa-spiro- and spiro-bino-spiro-phosphazenes. Inorg. Chim. Acta. 2013 Sep; 406: 160-70.
32. Elmas, G. The reactions of 2-*trans*-6-bis(4-fluorobenzyl)spirocyclotetraphosphazene with primary amines: spectroscopic and crystallographic characterizations. Phosphorus Sulfur Silicon Relat. Elem. 2017 Sep; 192 (11): 1224-1232.
33. Elmas G, Okumuş A, Cemalođlu R, Kılıç Z, Çelik SP, Açık L, Tunalı BÇ, Türk M, Çerçi NA, Güzel R, Hökelek T. Phosphorus-nitrogen compounds. part 38. Syntheses, characterizations, cytotoxic, antituberculosis and antimicrobial activities and DNA interactions of spirocyclotetraphosphazenes with bis-ferrocenyl pendant arms. J. Organometallic Chem. 2017 Dec; 853: 93-106.



Synthesis and Characterization of Novel Pd and Cu vic-dioxime Precursors for Their Supercritical Deposition on Multiwalled Carbon Nanotubes

Fatma Ulusal¹, *, Bilgehan Güzel¹

¹ Chemistry Department, Art and Science Faculty, University of Çukurova, 01330, Adana, Turkey

Abstract: Novel precursors were developed for deposition of Cu and Pd nanoparticles on multiwalled carbon nanotubes for supercritical carbon dioxide deposition technique. 3-(heptadecafluorooctyl)aniline-vic-dioxime and phenanthrenequinone dioxime were used as ligands in synthesis of the palladium and copper precursors. All synthesized ligands and complexes were characterized with elemental analysis, ¹H and ¹⁹F NMR, FT-IR and magnetic susceptibility technique. Deposition of these precursors in supercritical carbon dioxide was performed at 363 K in the pressure 0.69 MPa H₂ and 27.6 MPa CO₂. Surface morphology of metal deposited multiwalled carbon nanotubes has been investigated with X-ray diffraction, high-resolution transmission electron microscopy and scanning electron microscopy with EDX. TEM micrographs showed homogenous distributions of Cu and Pd nanoparticles on the multiwalled carbon nanotubes. The nature and crystallinity of the nanoparticles were confirmed using XRD. This study showed that these novel vic-dioxime complexes are suitable precursors for the preparation of supported metal nanoparticles in supercritical carbon dioxide.

Keywords: Vic-dioxime, precursor, multi-walled carbon nanotubes, supercritical deposition.

Submitted: December 12, 2017. **Accepted:** March 29, 2018.

Cite this: Ulusal F, Güzel B. Synthesis and Characterization of Novel Pd and Cu vic-dioxime Precursors for Their Supercritical Deposition on Multiwalled Carbon Nanotubes. JOTCSA. 2018;5(2):635-52.

DOI: <http://dx.doi.org/10.18596/jotcsa.363662>.

***Corresponding author. E-mail:** fatma_ulusal@hotmail.com, GSM: (0539)886 81 10.

INTRODUCTION

The green chemistry techniques gain importance day by day due to their use as an alternative solvent. Especially, supercritical fluids (SCF) have been used in various techniques such as organic synthesis, extraction, cosmetics, energy, food, materials, pharmaceuticals, chemistry, sterilization, formulation, impregnation, cleaning, waste treatment and deposition of metals on the solid materials (1, 2). For the past two decades, the deposition process in the $scCO_2$ environment has become a focus of interest for scientists and has made an important contribution to the preparation of catalysts, especially with green chemistry. The method of preparing these nano-catalysts in supercritical fluids (SCF) follows a three-step deposition process. The first step involves dissolving a metallic precursor and treating the support material in the SCF. In the second step, the precursor is adsorbed onto the support surface. The last step requires the thermal or chemical reduction of the precursors to their metallic form.

The deposition of transition metals such as Ni, Pd, Cu, Pt, and Rh on a solid support is an important research area because of the extensive applications of these supported nanoparticles in a wide variety of disciplines (3-6). Metal nanoparticles on supporting materials are commonly used as catalysts for hydrogenation, oxidation, synthesis, Heck and Suzuki-Miyaura C-C bond forming reactions. (5-8). Among various supports, carbon materials are desired for a wide variety of applications (9). Common substrates used as supports in deposition are carbon black, activated carbon, carbon aerogel and carbon nanotubes (CNTs). Carbon-supported nanoparticle metals are used widely as catalysts for a variety of reactions; palladium catalysts deposited on multi-walled carbon nanotubes (MWCNTs) are often used in hydrogenation and oxidation reactions (10). This catalyst also shows a high electro-catalytic activity in oxygen reduction for potential fuel cell application (11, 12).

The metal precursor plays an important role in the control of the morphology of the metal nanoparticles (8). The metallic precursors used so far include complexes containing cyclooctadiene, dithiocarbamate, hexamethylene glycol dimethyl ether, hexamethyl triethylene, acetylacetonate, and tetramethyl heptanedionate ligands (13-18). However, these precursors have proven to be inadequate for some metals due to the formation of large clusters on the surface as well as the wide size distribution of the nanoparticles (18). By synthesizing new precursors, it is expected that better alternatives allowing for adequately small sizes and uniform distribution of nickel nanoparticles on the substrate will be discovered. An oxime is defined as a compound with a C=N-OH functional group; a molecule with two of these functional groups on adjacent carbons is known as a vic-dioxime. Another advantage of vic-dioxime type precursors is their inexpensive and easy synthesis with a wide variety of metals, such as Ni, Pd, Cu, Co, and Fe (17, 19).

Our group has been working on developing new precursors used in the scCO₂ deposition due to the limited alternatives in the literature. So far, we have been able to synthesize Pd(II) complexes of phenanthrenequinone dioxime and dimethylglyoxime ligands and carried out depositions on alumina in the scCO₂ medium and used the nanocatalysts for Suzuki-Miyaura coupling reactions (1). In addition to this, we also synthesized bipyridyl-derived Pd(II) complexes and deposited Pd on SBA-15 supports in the scCO₂ medium (20). In this paper, 3-(heptadecafluorooctyl)aniline-vic-dioxime and phenanthrene quinonedioxime were synthesized, used as a ligands for preparing Cu and Pd precursors. The preparation of the M/MWCNT composites was done by adsorbing the dissolved precursors in scCO₂ followed by a subsequent chemical reduction by introduction of a mixture of H₂ and CO₂ gas into the system to produce the metal nanoparticles. The resulting MWCNT supported metal nanocatalysts were characterized with XRD, HR-TEM and TEM. A comparative analysis of their solubility in supercritical carbon dioxide, the size and distribution of the resulting nanoparticles is reported.

MATERIALS AND METHODS

All chemicals were obtained from Sigma Aldrich and used without further purification. It was characterized by general spectroscopic techniques. Multiwalled carbon nanotubes (MWCNT), obtained from Sigma Aldrich, were used and had the following average dimensions: O.D. xL (6-9nm x 5µm), diameter (mode, 5.5 nm; median, 6.6 nm). Elemental analysis was performed with Thermo Scientific Flash 2000 CHN. The ¹H NMR spectra of ligands were recorded on a Bruker AVANCE- 500 (in DMSO). The FT-IR spectra of compounds were obtained on a Thermo FT-IR spectrometer; Smart ITR diamond attenuated total reflection (ATR). The magnetic susceptibilities of metal complexes were determined on a Sherwood Scientific Magnetic Susceptibility balance (Model MK1) using CuSO₄.5H₂O as a calibration standard at room temperature; diamagnetic corrections were calculated from Pascal's constants. The separation and washing of the MWCNTs by precipitation were performed with a Serico 80-2 centrifuge machine. The XRD spectra were recorded on Rigaku Miniflex CuKα, λ=0.154 nm. High-resolution transmission electron microscope (HR-TEM) and high-angle annular dark-field scanning TEM (HAADF-TEM) were recorded on Jem Jeol 2100F 200kV HR-TEM. Scanning Electron Microscopy (SEM) images were recorded on Zeiss Supra 55. The resolution of this microscope is a working distance of 10 mm at an accelerating voltage of 10 kV. The metal/MWCNTs nanoparticles were mounted on platinum pins with double-sided carbon tape and their corresponding SEM images were recorded. Elemental analysis of metals was obtained from EDAX Genesis EDS system. We described the effect of a dioxime derivative on Pd loading yield by inductively coupled plasma-optical emission spectrometry (ICP-OES) (Perkin Elmer 2100 DV).

Synthesis of phenanthrenequinone dioxime [PTQD]: PTQD was synthesized to be used as ligand according to the methodology given in (21). A nitrogen-flushed mixture of 9,10-phenanthrenequinone (2.1331 g, 10.2 mmol), hydroxylamine hydrochloride (2.7 g, 35.6 mmol),

and BaCO_3 (2.91 g, 15.3 mmol) in 150 mL of anhydrous ethanol was refluxed for 24 hours. Then, the mixture was cooled to room temperature, after which the ethanol was evaporated using a rotary evaporator. The residue was treated with 250 mL of 0.25 M HCl. This mixture was stirred for 1.5 hours and filtered. The filtered solid was washed with water, ethanol, and anhydrous diethyl ether respectively; then, it was dried in a vacuum desiccator to afford 2.4 g (98%) of phenanthrenequinone dioxime as a yellowish solid: m.p.: 214.2 °C ; Elemental analysis for $[\text{C}_{14}\text{H}_{10}\text{O}_2\text{N}_2]$, calculated: C, 70.58; N, 11.76; H, 4.23, found: C, 68.92; N, 11.30; H, 4.14; IR 3140 cm^{-1} (O-H), 3029 cm^{-1} (C-H Ph), 1647 cm^{-1} (C=N), 1598 cm^{-1} (C=C Ph), $1297\text{-}1341\text{ cm}^{-1}$ (N-O), $910\text{-}1021\text{ cm}^{-1}$ (N-O) ; $^1\text{H NMR}$ (CDCl_3), δ ppm: 12.45-12.10 (m, 2H, -OH), 8.4-7.4 (m, 4H, Ph). The ligand was found to be soluble in some organic solvents like THF, DMSO, ethanol and acetone; and insoluble in chloroform, n-hexane and water. (Figure 1.)

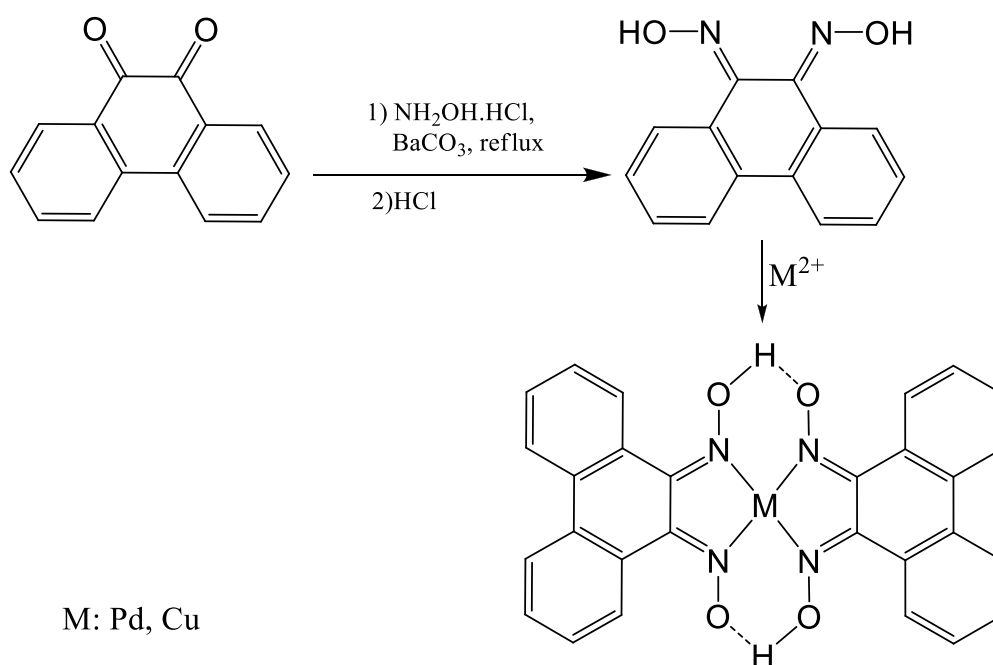


Figure 1. Synthesis of phenanthrenequinone dioxime and metal complexes.

Synthesis of 3-perfluoro-vic-dioxime [3PFVD]: The ligand was synthesized to be used as ligand according to the methodology given in (19). A solution of 3-(heptadecafluorooctyl) aniline (1 mmol) in 20 mL of absolute ethanol at $-10\text{ }^\circ\text{C}$ was added to a solution of anti-monochloroglyoxime (1 mmol) in 10 mL of ethanol at $-10\text{ }^\circ\text{C}$ (22, 23). Then the mixture was stirred for 4.5 hours, keeping its temperature under $-10\text{ }^\circ\text{C}$. When the solution turned yellow, the pH was brought to 6 by adding 0.1 M NaOH, in a drop wise manner. As a result, its color turned to yellowish-orange. 30 mL of water was added to the mixture and left for 20 days. After this time, yellow crystals formed. These were filtered and then dried in a vacuum desiccator. Yield: %66. m.p.: 205.32 °C. Elemental analysis $[\text{C}_{16}\text{H}_8\text{F}_{17}\text{N}_3\text{O}_2]$; Found C, 32.28; H, 1.07; N, 6.20%, calculated C, 32.18; H, 1.35; N, 7.04%; FT-IR (ATR, mmax/cm^{-1}); 3383 (N-H), 3244 (O-H), 1611 (C=N), 1608-1527(C=C), 1310 (N-O), 1202 (C-F), 950 (N-O); $^1\text{H NMR}$ (CDCl_3), δ

ppm: 11.5 (d, 2H, -OH), 8.0 (s, 1H, -NH), 7.26-6.8 (m, 4H, Ph), 3.8 (s, 1H, =CH); ^{19}F NMR (CDCl_3), δ ppm: -80.73, -80.75, -80.77, -80.81 (CF_2CF_3), -110.92, -110.85, -110.78, -121, -122, -123 ($\text{CF}_2\text{-CF}_2\text{-CF}_2$). The yellowish-orange ligand proved soluble in some organic solvents like THF, DMSO, ethanol and acetone; and insoluble in chloroform, n-hexane and water. (Figure 2.).

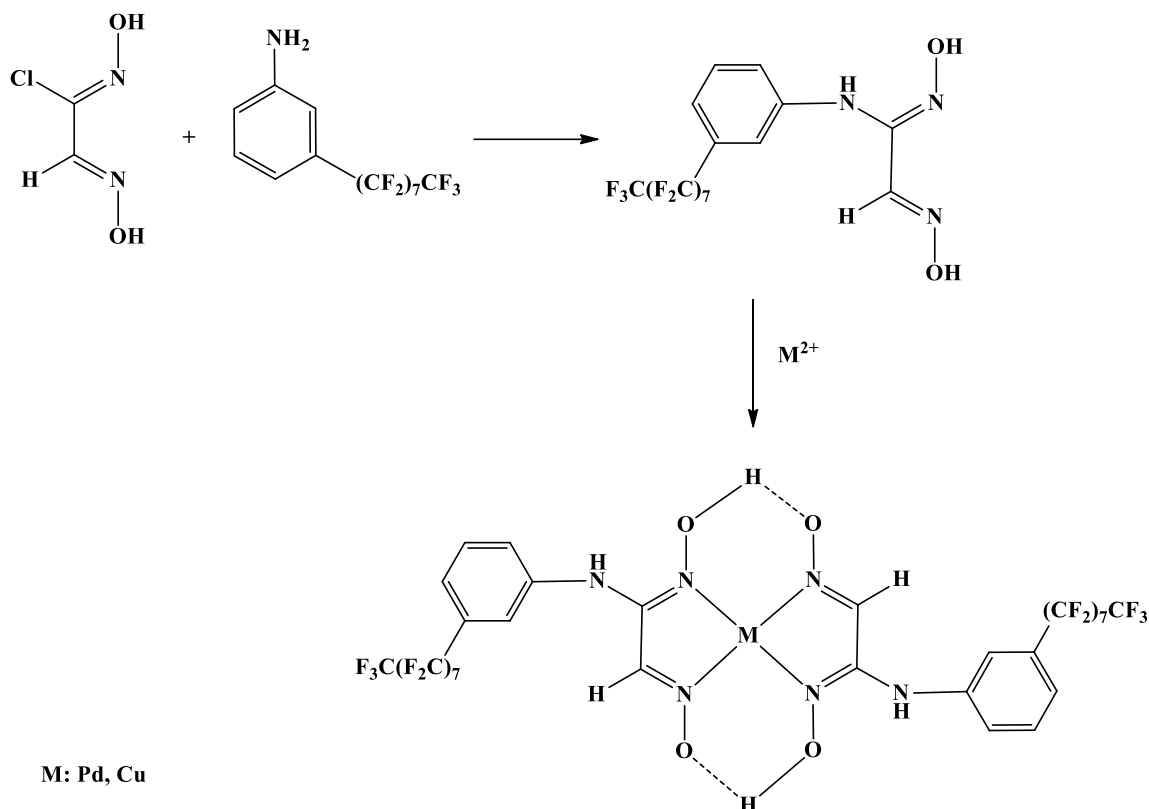


Figure 2. Reaction of 3PFVD and its metal complexes.

Synthesis of bis(3-perfluoro-*vic*-dioxime)copper(II) [Cu(3PFVD)₂]: The complex was synthesized to be used as metalloorganic precursor according to the methodology given in (19). A solution of *vic*-dioxime (2 mmol) in 15 mL of absolute ethanol was added to a solution of copper(II) acetate monohydrate (1mmol) in 10 mL of absolute ethanol. The mixture was refluxed at 65 °C for 4.5 hours and then it was allowed to cool to room temperature. The precipitate was filtered and dried in desiccator by vacuum to furnish the pure Cu oxime. Yield: 80% m.p.>330 °C. Elemental Analysis [$\text{C}_{32}\text{H}_{14}\text{F}_{34}\text{N}_6\text{O}_4\text{Cu}$]; Found C, 31.20; H, 1.39; N, 6.49%; calculated, C, 30.60; H, 1.12; N, 6.69%; FT-IR (ATR) ($\text{mmax}/\text{cm}^{-1}$); 3400(N-H), 1673 (O•••H-O)(w), 1597(C=N), 1304(N-O), 1197-1140(C-F), 968(N-O). The green complex was soluble in some organic solvents like THF, DMSO, ethanol and acetone; and insoluble in chloroform, n-hexane and water.

Synthesis of bis(phenanthrenequinone dioxime)copper(II) [Cu(PTQD)₂]: Synthesis was done by following the same procedure as described above for [Cu(PTQD)₂]. Yield: 98% m.p.>330 °C. Elemental Analysis [$\text{C}_{28}\text{H}_{18}\text{O}_4\text{N}_4\text{Cu}$]; Found C, 61.57; H, 3.29; N, 10.03%; calculated, C, 62.51; H, 3.37; N, 10.41%; IR(ATR)($\text{mmax}/\text{cm}^{-1}$); 3063(C-H (ar)), 1594 (C=N),

1525 (C=C), 1240-1289 (N-O) 1095-957 (N-O). The green complex was soluble in some organic solvents like THF, DMSO, ethanol and acetone and insoluble in chloroform, n-hexane and water.

Synthesis of bis(3-perfluoro-*vic*-dioxime)palladium(II) [Pd(3PFVD)₂]: The Pd complex was synthesized to be used as metalloorganic precursor according to the methodology given in (24,25). A solution of oxime (2 mmol) in 20 mL of absolute ethanol was put in a solution of palladium(II) chloride (1 mmol) in 10 mL of absolute ethanol. Sodium acetate (0.5 g) was added to the solution. Then the mixture was refluxed at 75°C for 4.5 hours. It was allowed to cool to room temperature. The mixture was filtered and dried in a vacuum desiccator to furnish the pure Pd oxime complex. Yield: 70.0% m.p.:258 °C. Elemental Analysis [C₃₂H₁₄F₃₄N₆O₄Pd]; Found C, 29.19; H, 1.05; N, 6.12%; calculated, C, 29.59; H, 1.09 ;N, 6.47%; FT-IR(ATR) (mmax/cm⁻¹); 3302 (N-H), 3058 (C-H (ar)), 1667 (O•••H-O)(w), 1617 (C=N), 1568 (C=C), 1131 (N-O), 1194-1144 (C-F), 958 (N-O); ¹H NMR (DMSO-d₆) δ ppm: 3.8 (s, 2H, H-C=NOH), 8.0 (s, 2H, Ph-N-H), 6.8-7.5 (m, 8H, Ar-H). The yellowish-orange complex was soluble in some organic solvents like THF, DMSO, ethanol and acetone and insoluble in chloroform, n-hexane and water.

Synthesis of bis(phenanthrenequinone dioxime)palladium(II) [Pd(PTQD)₂]: Synthesis was done by following the same method as described above for [Pd(PTQD)₂]. Yield: %90. m.p.>330 °C. Elemental Analysis [C₂₈H₁₈O₄N₄Pd]; Found C, 56.19; H, 2.73; N, 7.77%; calculated, C, 57.89; H, 3.12; N, 9.65%; FT-IR(ATR) (mmax/cm⁻¹); 3065 (C-H(ar)), 1595 (C=N), 1510 (C=C), 1256-1293 (N-O), 1010 (N-O). The yellow complex was soluble in some organic solvents like THF, DMSO, ethanol, and acetone and insoluble in chloroform, n-hexane and water.

Determination of Solubility in Supercritical Carbon Dioxide: The solubility of the precursors was measured in a stainless steel reactor with an inner volume of 54 mL and equipped with two sapphire windows. In a typical experiment held in scCO₂, the reactor was cleaned with CO₂ and ethanol at a pressure of 4.8 MPa. A determined amount (45-50 mg) of precursor were weighed and placed inside the reactor. The solubility tests were performed three times at a temperature of 363 K and pressure (13.8, 20.7 and 27.6 MPa) for 4 hours by stirring. At the end of this time, the solubility of each complex in scCO₂ was determined quantitatively by releasing CO₂ gas from the reactor into a receptacle with an inner volume of 5 mL. The CO₂ gas in the receptacle was run through 5 mL ethanol. The receptacle was washed with approximately 15 mL ethanol and added to first solution. The standard solutions of complexes among 10⁻⁷-10⁻³ M were prepared. These solutions were measured by UV-Vis spectrophotometer at the wavelength of maximum absorption and concentration-absorption graph was drawn according to these data. Molar absorption coefficients were calculated from this graph. The ethanolic solutions of dissolved complexes in scCO₂ were measured at the wavelength of maximum absorption. The amount of precursors dissolved in scCO₂ was calculated from Beer law.

Deposition of Precursors on MWCNT: A stainless steel reactor with a 100 mL inner volume was used for the deposition of the metals onto MWCNTs. The precursor was first adsorbed onto a MWCNT and then converted to metal nanoparticles (Figure 3). The reactor was firstly cleaned using chemical solvents and then with flowing CO₂ under a pressure of 5 MPa. 50 mg precursor and 50 mg MWCNT (precursor/MWCNT:1/1 mass ratio) were placed in the reactor. The reactor was heated to 363 K and charged to 0.69 MPa with H₂ gas and to 27.6 MPa with CO₂. It was stirred for 4 hours and then the reactor was allowed to cool to room temperature. Then the pressure in the reactor was released. The MWCNTs were then washed by centrifuging with THF until the impurity had been removed. The M/MWCNT nanoparticles were dried in an oven at 75 °C. XRD was used to confirm the presence of the metal, the size of its particles. SEM-EDX was used to confirm of the distribution of the metals on the MWCNT and the percent of metals present. HR-TEM was used to confirm of the metals' distribution on the MWCNT and the particle size range.

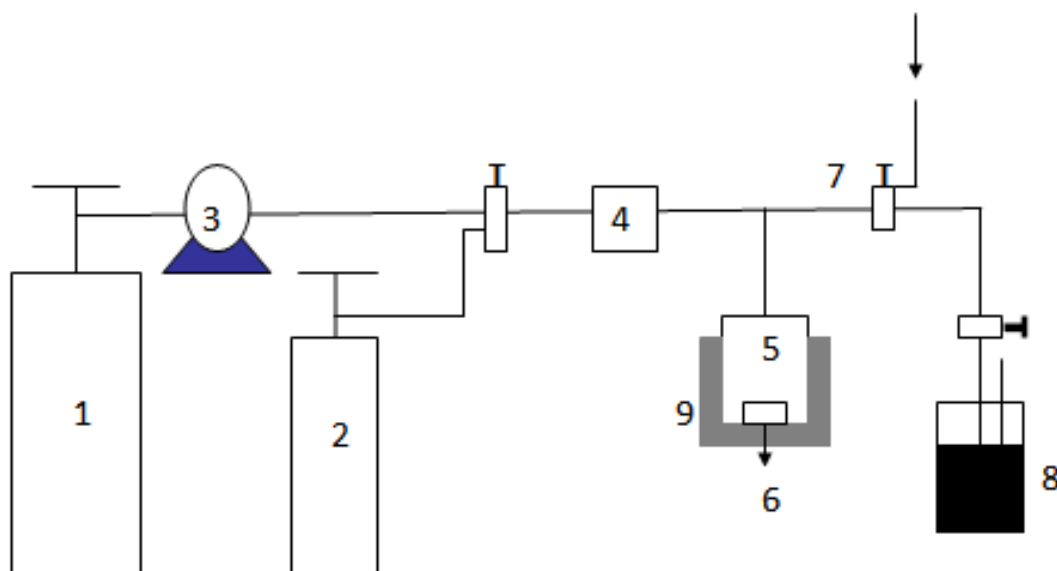


Figure 3. Schematic diagram of deposition system (1: CO₂, 2: H₂, 3: Syringe pump, 5: High pressure reactor, 6: Support and precursor 7: Vent, 8: Receiving vessel, 9: Mantle heater).

RESULTS AND DISCUSSION

Structure characterization of ligands and metal complexes (precursors)

3-Perfluoro *vic*-dioxime [3PFVD]: The elemental analysis of the [3PFVD] agreed with the calculated values, confirming the successful synthesis of the desired compounds. The FTIR spectra showed characteristic peaks at 3383 cm⁻¹ (N-H), 3244-3000 cm⁻¹ (O-H), 1680 cm⁻¹ (C=N), 1310 cm⁻¹ (N-O), 1202 cm⁻¹ (C-F) and 950 cm⁻¹ (N-O). New bands, which were not present in the starting material, appeared between 1100 cm⁻¹ and 1250 cm⁻¹ in the FTIR spectra of 3PFVD which correspond to the new C-F bond. The presence of these as well as the peaks corresponding to O-H, C=N and N-O bonds confirm that the desired ligand was synthesized. The ¹H NMR spectra showed two overlapping singlet peaks at 11.5 ppm (19). This is due the presence of two different =N-OH groups in the ligand. The rest of the peaks observed in the ¹H NMR and ¹⁹F NMR spectra were consistent with what was expected. The expected number of peaks was present in the ¹⁹F NMR spectrum.

Phenanthrenequinone dioxime [PTQD]: The IR spectra of [PTQD] showed peaks at 3140-3050 cm⁻¹ (O-H), 3029 cm⁻¹ (C-H (aromatic)), 1647 cm⁻¹ (C=N), 1598 cm⁻¹ (C=C), 1297-1341 cm⁻¹ (N-O), 910-1021 cm⁻¹ (N-O). The presence of the N-O, O-H and C=N bands confirm that the desired ligand was procured. The ¹H NMR spectra of [PTQD] demonstrated a very sharp singlet peak at 12.45-12.10 ppm, arising from the two identical =N-OH groups present (19). The other peaks observed in the ¹H NMR spectra were as expected. All of the spectral data agree with what would be expected for this ligand, so it was determined that the desired ligand was synthesized.

Bis(3-perfluoro-*vic*-dioxime)palladium(II) [Pd(3PFVD)₂]: The elemental analysis data for this complex was in agreement with the calculated values. The analytical and physical data (elemental analysis, magnetic susceptibility) indicated a metal to ligand ratio of 1:2 (26). This showed that reactions of [3PFVD] with PdCl₂ yielded complexes with the overall formula [Pd(3PFVD)₂]. The FTIR spectra of the palladium complex showed that the peaks assigned to the ν(C=N) frequency shifted downfield from those the free ligand. This is due to coordination of the metal to the nitrogen atom, which in turn weakened the C=N bond. For the [3PFVD] ligand, the C=N peak was observed at 1680 cm⁻¹. The same peak was shifted downfield to 1667 cm⁻¹ in [Pd(3PFVD)₂]. In the free ligand, bands arising from the O-H bond were observed. These were lost after complexation (27, 28). The magnetic susceptibility of the Pd(II) complex 3PFVD indicated that the complex is diamagnetic.

Bis(3-perfluoro-*vic*-dioxime)copper (II) [Cu(3PFVD)₂]: The elemental analysis of the complex is in agreement with calculated values. The analytical and physical data (FTIR and magnetic susceptibility) indicated a metal to ligand ratio of 1:2. This showed that reactions of

[3PFVD] with $\text{Cu}(\text{CH}_3\text{COO})_2 \cdot \text{H}_2\text{O}$ yielded complexes with the overall formula $[\text{Cu}(\text{3PFVD})_2]$. The FTIR spectra of the complex showed that the peaks assigned to the $\nu(\text{C}=\text{N})$ frequency shifted downfield from those of the free ligand. This is due to coordination of the metal to the nitrogen atom, which in turn weakened the $\text{C}=\text{N}$ bond. For the [3PFVD] ligand, the $\text{C}=\text{N}$ peak was observed at 1680 cm^{-1} . The same peak was shifted downfield to 1673 cm^{-1} for $[\text{Cu}(\text{3PFVD})_2]$. In the free ligand, bands arising from the $\text{O}-\text{H}$ bond were observed. These were lost after complexation. The $\text{Cu}(\text{II})$ complexes are paramagnetic as expected and the magnetic susceptibility value of the copper complex is $1.42 \mu\text{B}$.

Bis(phenanthrenequinonedioxime)palladium(II) [Pd(PTQD)₂]: The elemental analysis of the complex is in agreement with calculated values. The analytical and physical data (elemental analysis, magnetic susceptibility) indicated a metal to ligand ratio of 1:2. This showed that reactions of [PTQD] with PdCl_2 yielded complexes with the overall formula $[\text{Pd}(\text{PTQD})_2]$. The FTIR spectra of the complex showed that the peaks assigned to the $\nu(\text{C}=\text{N})$ frequency shifted downfield from those the free ligand. This is due to coordination of the metal to the nitrogen atom, which in turn weakened the $\text{C}=\text{N}$ bond. For the [3PFVD] ligand, the $\text{C}=\text{N}$ peak was observed at 1680 cm^{-1} . The same peak was shifted downfield to 1595 cm^{-1} for $[\text{Pd}(\text{3PFVD})_2]$. In the free ligand, bands arising from the $\text{O}-\text{H}$ bond were observed. These were lost after complexation. Magnetic susceptibility measurements supplied sufficient data to characterize the geometry of the metal complexes. The magnetic susceptibility of the $\text{Pd}(\text{II})$ complex PTQD indicated that the complex is diamagnetic.

Bis(phenanthrenequinone dioxime)copper(II) [Cu(PTQD)₂]: The elemental analysis of the complex is in agreement with calculated expectations. The analytical and physical data (FTIR and magnetic susceptibility) indicated a metal to ligand ratio of 1:2. This showed that reactions of [3PFVD] with $\text{Cu}(\text{CH}_3\text{COO})_2 \cdot \text{H}_2\text{O}$ yielded complexes with the overall formula $[\text{Cu}(\text{3PFVD})_2]$. The FTIR spectra of the complex showed that the peaks assigned to the $\nu(\text{C}=\text{N})$ frequency shifted downfield from those the free ligand. This is due to coordination of the metal to the nitrogen atom, which in turn weakened the $\text{C}=\text{N}$ bond. For the [3PFVD] ligand, the $\text{C}=\text{N}$ peak was observed at 1680 cm^{-1} . The same peak was shifted downfield to 1594 cm^{-1} for $[\text{Cu}(\text{3PFVD})_2]$. In the free ligand, bands arising from the $\text{O}-\text{H}$ bond were observed. These were lost after complexation. The $\text{Cu}(\text{II})$ complexes are paramagnetic as expected and the magnetic susceptibility value of the copper complex is $2.12 \mu\text{B}$.

Solubility of Precursors

The solubility of all four complexes was performed, to indicate the suitability of these oxime complexes for using precursor in scCO_2 deposition method. The solubility of all synthesized *vic*-dioxime precursors were in agreement with commonly known precursors reported in literature (29, 30). The solubility data are shown in Table 1. Precursors in comparison, the solubility of Pd

complexes are better than Cu complexes. Distance between ligand and center atom is the bigger in palladium complexes because of palladium diameter is bigger than copper's. The distance between ligand and center atom is inversely proportional to the shielding of the center palladium atom by the ligands. The solubility of Pd complex of 3PFVD was 6.7 times, PTQD was 2 times better than Cu complexes.

Table1. The solubility data of precursor in scCO₂ at different pressures.

	Solubility (molar fraction)			molar absorptivity coefficient (ϵ)	Wavelength (nm)
	2000 (PSI)	3000 (PSI)	4000 (PSI)		
[Pd(PTQD) ₂]	1.59 x10 ⁻³	1.89 x10 ⁻³	2.74 x10 ⁻³	14883	235
[Cu(PTQD) ₂]	1.06 x10 ⁻³	1.64 x10 ⁻³	2.55 x10 ⁻³	19407	236
[Pd(3PFVD) ₂]	3.26 x10 ⁻³	5.22 x10 ⁻³	8.27 x10 ⁻³	6006	234
[Cu(3PFVD) ₂]	1.78 x10 ⁻⁴	3.96 x10 ⁻⁴	9.12 x10 ⁻⁴	9761	316

Characterization of MW-CNT supported metal nanoparticles

The following *vic*-dioxime metal complexes were used as precursors in the deposition process.

The deposition was performed in three steps:

- (1) Dissolving of the precursor in supercritical carbon dioxide,
- (2) Adsorbing of metal complex on the MWCNTs
- (3) Supercritical reduction.

A chemical reduction method utilizing H₂ gas was employed to deposit Cu(0) and Pd(0) form nanoparticles onto MWCNTs. After this step, precursors were converted to metallic Cu and Pd. However, Cu nanoparticles were found to convert to Cu(OH)₂, CuO and Cu₂O form by contact with oxygen in air after the synthesis.

HR-TEM results

High resolution TEM image that was taken from the composite obtained from the [Pd(PTQD)₂] precursor, after its deposition using a 1:1 ratio of precursor: MWCNT indicates that palladium nanoparticles were distributed homogeneously on the MWCNTs. HR-TEM image is shown in Figure 4. The HR-TEM results indicated a size range between 2-5 nm, which is as good as nanoparticles obtained from available precursors (6,13,14). Aggregate of palladium was not observed on MWCNT. The HR-TEM images of Cu/MWCNT composite obtained from [Cu(3PFVD)₂] precursor is shown in Figure 5. These images indicate that the copper nanoparticles are distributed homogeneously on the MWCNTs and there is no aggregate on the substrate. The HR-TEM results indicated a size range between 2-5 nm.

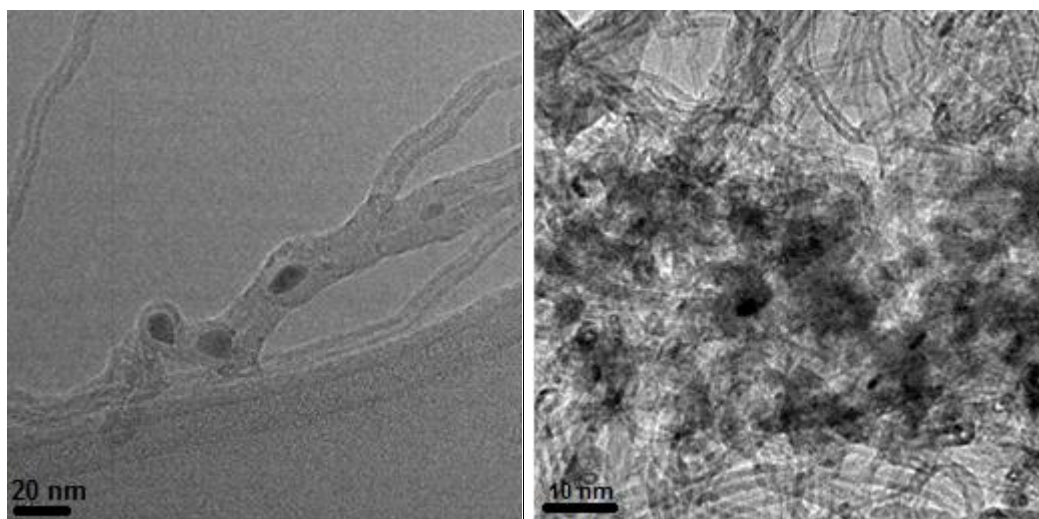


Figure 4. High-resolution TEM images of Pd/MWCNT obtained from $[\text{Pd}(\text{PTQD})_2]$.

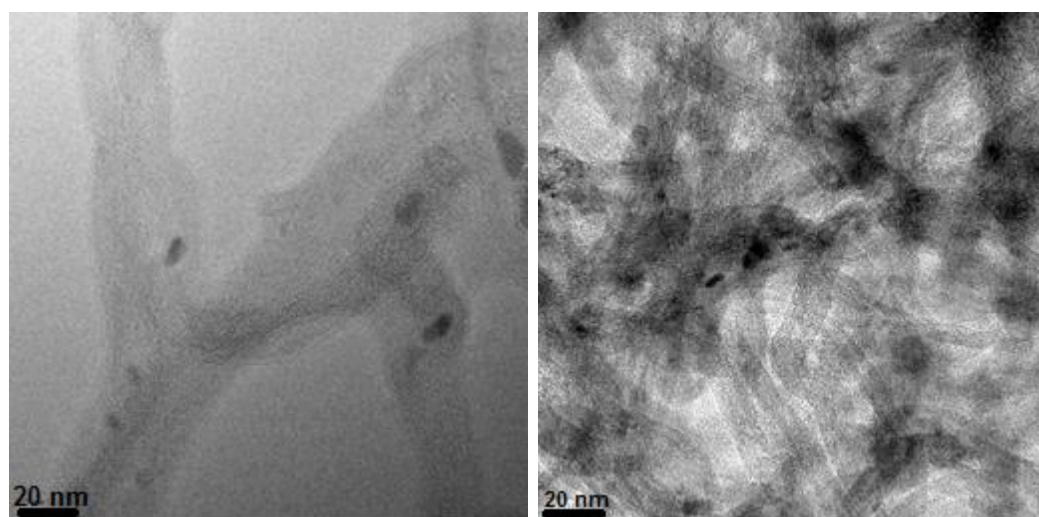


Figure 5. High resolution TEM images of Cu/MWCNT obtained from $[\text{Cu}(3\text{PFVD})_2]$.

SEM-EDX Results

The percentages of the metals on the MWCNTs were obtained from SEM-EDX images. SEM-EDX data provided the chemical properties of these particles.

The SEM-EDX micrographs of Pd/MWCNT obtained from $[\text{Pd}(\text{PTQD})_2]$ is shown in Figure 6(a) and $[\text{Pd}(3\text{PFVD})_2]$ is shown in Figure 6(b). These EDX spectra showed that Pd and C atoms are the main elements in these composites. While a high intensity carbon peak was observed, the palladium peak had a relatively low intensity. This is because MWCNTs are the main components in these samples. Metal content was calculated from the EDX data. From the SEM-EDX micrograph of Pd/MW-CNTs composites indicated that the palladium nanoparticles were distributed homogeneously on the MWCNTs. The ICP-OES and EDX data results showed that the percentage of Pd on the MWCNTs is 5.6 % wt. (68 % of the total Pd in the system) for $[\text{Pd}(3\text{PFVD})_2]$ and 10 % wt. (54.4 % of the total Pd in the system) for $[\text{Pd}(\text{PTQD})_2]$.

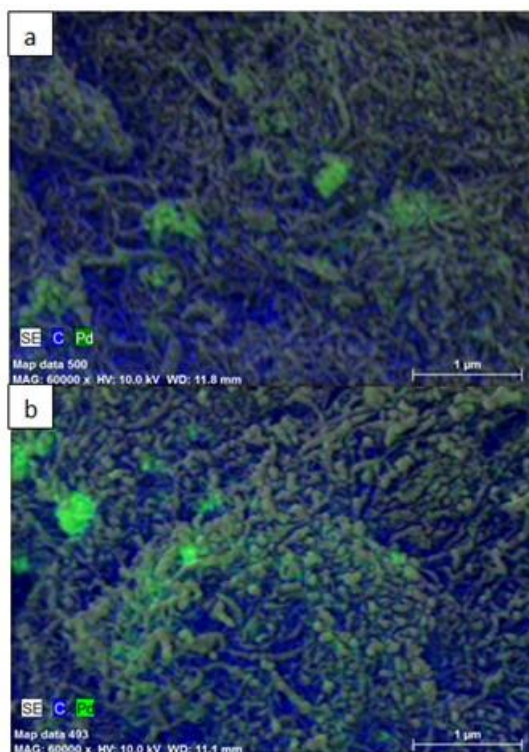


Figure 6. SEM-EDX images of Pd/MWCNT obtained from [Pd(PTQD)₂] (a) and [Pd(3PFVD)₂] (b).

The SEM-EDX micrographs of Cu/MWCNT obtained from [Cu(PTQD)₂] is shown in Figure 7(a) and [Cu(3PFVD)₂] is shown in Figure 7(b). The Cu and C atoms are the main elements in these composites according to EDX spectra. Carbon peaks were observed to have a high intensity and the copper peaks had relatively low intensity. This is because MWCNTs are the main components in these samples and MWCNT is composed from only carbon atoms (31). EDX figures were used for calculation of metal content. SEM images show that a large fraction of Cu nanoparticles had very small size. Differently from Pd/MWCNT, there were no Cu agglomerates on MWCNTs. From the SEM-EDX micrograph of Cu/MWCNTs composites clearly show that the copper is distributed on the MWCNTs. The ICP-OES and EDX data results showed that the percentage of Pd on the MWCNTs is 7.19 % wt. (59.3 % of the total Cu in the system) for [Cu(3PFVD)₂] and 2.3 % wt. (46.5% of the total Cu in the system) for [Cu(PTQD)₂].

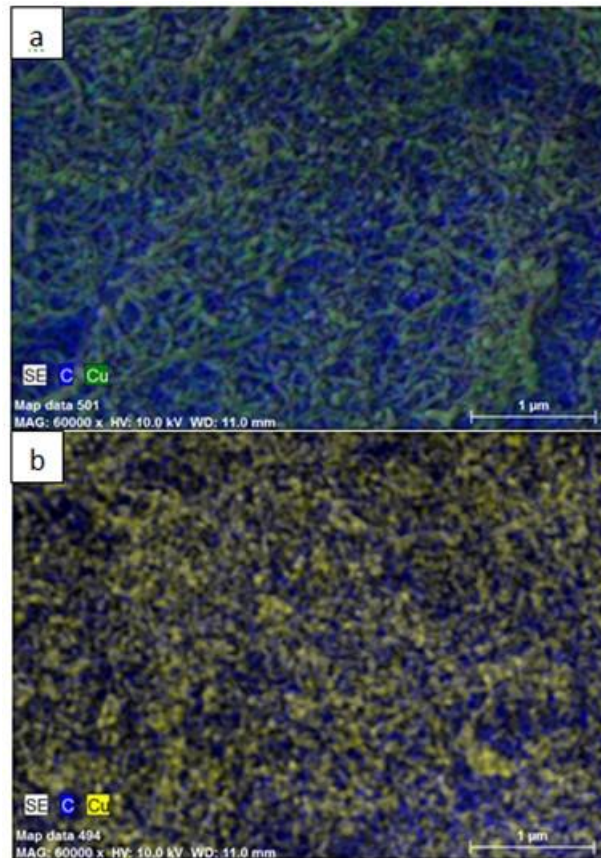


Figure 7. SEM-EDX images of Cu/MWCNT obtained from $[\text{Cu}(\text{PTQD})_2]$ (a) and $[\text{Cu}(\text{3PFVD})_2]$ (b).

XRD Results

The XRD patterns of the Pd/MWCNT composites obtained from the $[\text{Pd}(\text{PTQD})_2]$ and $[\text{Pd}(\text{3PFVD})_2]$ precursors are given in Figure 8 and show that the metals on the MW-CNT surface were polycrystalline. The observed main diffraction peaks of the Pd nanoparticles on the MW-CNTs were as expected. Three very sharp diffraction peaks were observed at 40.0, Pd(111); 46.5, Pd(200); and 68.1, Pd(220) (Reference was made to the surface-centered cubic system with JCPDS card number; 46-1043) [7-9, 32]. All these peaks indicate that the Pd metal particles are arranged in a cubic crystallite structure on the MW-CNTs. The average particle size of the Pd metal nanoparticles were calculated according to the Scherrer's equation taking Pd(111) as the main peak. The mean metal particle size was calculated to be 6.4 nm for the composite obtained from $[\text{Pd}(\text{PTQD})_2]$ and 3.1 nm for the one obtained from $[\text{Pd}(\text{3PFVD})_2]$. The mean particle size obtained from the TEM images was slightly different than that obtained from the XRD data. (Figure 8)

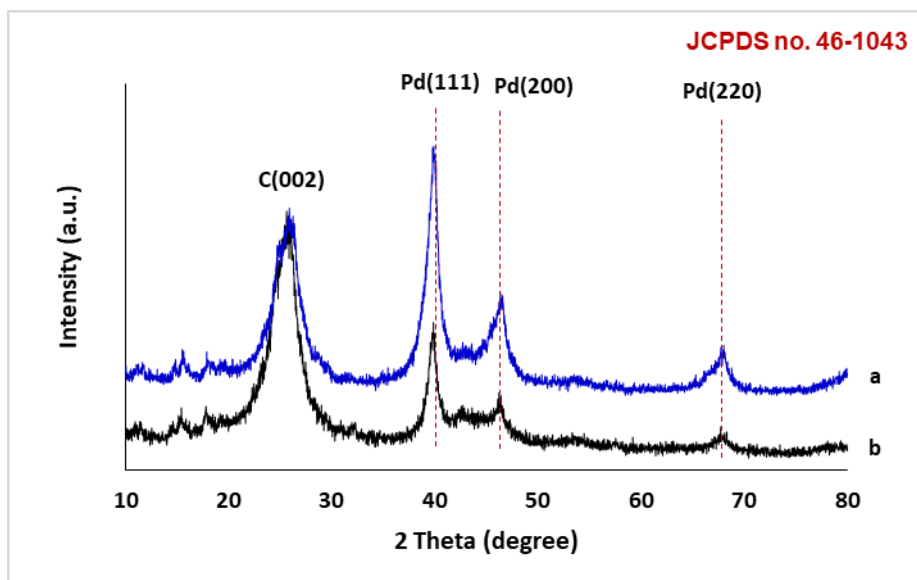


Figure 8. XRD pattern of MWCNT deposited with Pd by $[\text{Pd}(\text{PTQD})_2]$ (a) and $[\text{Pd}(\text{3PFVD})_2]$ (b) mechanism of PTQD and its metal complexes.

The XRD patterns of the Cu/MW-CNT composites obtained from the $[\text{Cu}(\text{PTQD})_2]$ and $[\text{Cu}(\text{3PFVD})_2]$ precursors are given in Figure 9 and show that the metals on the MW-CNT surface were polycrystalline. The Cu nanoparticles seem to have been converted to CuO and Cu₂O form by contact with air after removing from the reactor. The observed main diffraction peaks of the Cu nanoparticles on the MW-CNTs were as expected. Three diffraction peaks were observed at 17.0, Cu(OH)₂ (020) (JCPDS 13-420); 33.1, CuO(110) (JCPDS 48-1548) and 42.3, Cu(111) (JCPDS 04-0836) (13,21,30-31). The main diffraction peak was observed at 17.0, Cu(OH)₂ for $[\text{Cu}(\text{PTQD})_2]$ and at 33.1, Cu(111) for $[\text{Cu}(\text{3PFVD})_2]$. Cu and Cu(OH)₂ peaks for $[\text{Cu}(\text{3PFVD})_2]$ and Cu peak for $[\text{Cu}(\text{PTQD})_2]$ appear to be amorphous. The average particle size of the Cu metal nanoparticles were calculated according to the Scherrer's equation taking Cu(OH)₂ for $[\text{Cu}(\text{PTQD})_2]$ and CuO for $[\text{Cu}(\text{3PFVD})_2]$ as the main peak. The mean metal particle size was calculated to be 2.0 nm for obtained from $[\text{Cu}(\text{PTQD})_2]$ and 2.1 nm for obtained from $[\text{Cu}(\text{3PFVD})_2]$. The mean particle size obtained from the TEM images was slightly different than that obtained from the XRD data (Fig.9).

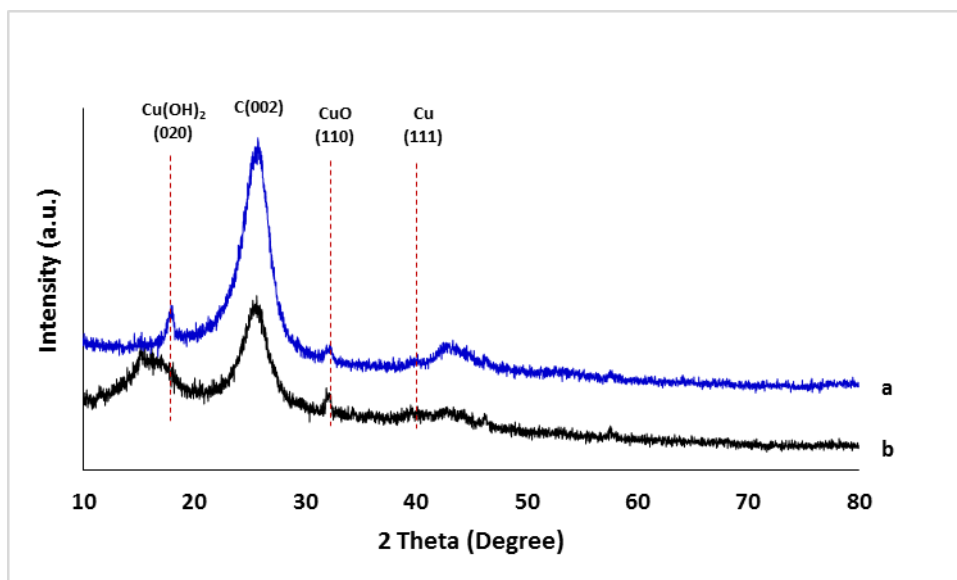


Figure 9. XRD pattern of MWCNT deposited with Pd by [Cu(PTQD)₂] (a) and [Cu(3PFVD)₂] (b).

CONCLUSION

Vic-dioxime metal complexes were synthesized, characterized, and used as precursors for the deposition of Pd and Cu nanoparticles on MWCNTs. The resulting composites were analyzed by TEM, SEM-EDX, and XRD. The metal nanoparticles formed were evenly dispersed over the substrate with particle sizes as small as 2 nm. These results clearly show that vic-dioxime metal precursors have been used as a precursor on SCF deposition technique. Further research on the different isomers of *vic*-dioximes, such as the *syn* form, could provide insight. This research is hoped to be expanded by studying the deposition of other oxime derivatives on various supports as well as testing the effects of different temperature and pressures during the deposition process.

ACKNOWLEDGMENTS

The authors acknowledge Prof. Dr. Ramazan Esen from Ç.U. Physics Department for XRD measurements. This study was supported by Scientific and Technological Research Council of Turkey (TUBITAK project number 111T153). These are gratefully acknowledged.

REFERENCES

1. Ulusal H, Fındıkkıran G, Demirkol O, Akbaşlar D, Giray ES. Supercritical diethylether: A novel solvent for the synthesis of aryl-3,4,5,6,7,9-hexahydroxanthene-1,8-diones. *The Journal of Supercritical Fluids*. 2015;105;146–50.
2. Ulusal F, Darendeli B, Erünel E, Eğitimci A, Güzel B. Supercritical carbondioxide deposition of γ -Alumina supported Pd nanocatalysts with new precursors and using on Suzuki-Miyaura coupling reactions. *The Journal of Supercritical Fluids*. 2017;127;111–20.

3. Daoush WM, Lim BK, Mo CB, Nam DH, Hong SH. Electrical and mechanical properties of carbon nanotube reinforced copper nanocomposites fabricated by electroless deposition process. *Materials Science and Engineering: A*. 2009;513-514;247-53.
4. Park PW, Ledford JS. The influence of surface structure on the catalytic activity of alumina supported copper oxide catalysts. Oxidation of carbon monoxide and methane. *Applied Catalysis B: Environmental*. 1998;15;221-31.
5. Rather S, Zacharia R, Hwang SW, Naik M, Nahm KS. Hydrogen uptake of palladium-embedded MWCNTs produced by impregnation and condensed phase reduction method. *Chemical Physics Letters*. 2007;441;261-7.
6. Cangul B, Zhang LC, Aindow M, Erkey C. Preparation of carbon black supported Pd, Pt and Pd-Pt nanoparticles using supercritical CO₂ deposition. *The Journal of Supercritical Fluids*. 2009; 50; 82-90.
7. Parker HL, Rylott EL, Hunt AJ, Dodson JR, Taylor AF, Bruce NC, Clark JH. Supported Palladium Nanoparticles Synthesized by Living Plants as a Catalyst for Suzuki-Miyaura Reactions. *Plos one*. 2014; 9; 1-6.
8. Du H, Li B, Kang F, Fu R, Zeng Y. Carbon aerogel supported Pt-Ru catalysts for using as the anode of direct methanol fuel cells. *Carbon*. 2007; 45; 429-35.
9. Zhang Y, Erkey C. Preparation of supported metallic nanoparticles using supercritical fluids: A review. *The Journal of Supercritical Fluids*. 2006;38;252-67.
10. Dobrovolna Z, Kacer P, Cervený L. Competitive hydrogenation in alkene-alkyne-diene systems with palladium and platinum catalysts. *Journal of Molecular Catalysis A: Chemical*. 1998;130;279-84.
11. Ye XR, Lin Y, Whang C, Engelhard MH, Wang Y, Wai CM. Supercritical fluid synthesis and characterization of catalytic metal nanoparticles on carbon nanotubes. *Journal of Materials Chemistry*. 2004;14;908-13.
12. Lin Y, Cui X, Ye X. Electrocatalytic reactivity for oxygen reduction of palladium-modified carbon nanotubes synthesized in supercritical fluid. *Electrochemistry Communications*. 2005;7;267-74.
13. Cabanas A, Blackburn J, Watkins J. Deposition of Cu films from supercritical fluids using Cu(I) β -diketonate precursors. *Microelectronic Engineering*. 2002;64;53-61.
14. Erkey C. Preparation of metallic supported nanoparticles and films using supercritical fluid deposition. *The Journal of Supercritical Fluids*. 2009;3;517-22.
15. Teoh WH, Mammucari R, Foster NR. Solubility of organometallic complexes in supercritical carbon dioxide: A review. *Journal of Organometallic Chemistry*. 2013;724;102-16.
16. Guzel B, Avşar G, Çinkır H. Supercritical Carbon Dioxide-Soluble Fluorous vic-Dioxime Ligands and their Ni(II) Complexes: Synthesis, Characterization and Solubility Properties. *Synthesis and Reactivity in Inorganic, Metal-Organic, and Nano-Metal Chemistry*. 2007;37;801-4.
17. Smart NG, Carleson T, Kast T, Clifford AA, Burford MD, Wai CM. Solubility of chelating agents and metal-containing compounds in supercritical fluid carbon dioxide. *Talanta*. 1997; 44; 137-50.
18. Peng Q, Hojo D, Park KJ, Parsons GN. Low temperature metal oxide film deposition and reaction kinetics in supercritical carbon dioxide. *Thin Solid Films*. 2008;516;4997-5003.
19. Yildirim B, Özcan E, Devenci P. New glyoxime derivatives and their transition metal complexes. *Russian Journal of Coordination Chemistry*. 2007;33;417-21.
20. Ulusal F, Güzel B. Deposition of palladium by the hydrogen assisted on SBA-15 with a new precursor using supercritical carbon dioxide. *The Journal of Supercritical Fluids*. 2018; 133; 233-8.
21. Chandima A, Arthur DB. Efficient Synthesis of 1,4,5,12-Tetraazatriphenylene and Derivatives. *Journal of American Chemical Society*. 2004;69;7741-4.
22. Lam F, Hu X. A new system design for the preparation of copper/activated carbon catalyst by metal-organic chemical vapor deposition method. *Chemical Engineering Science*. 2003;58;687 - 95.

23. Dervishi E, Li Z, Shyaka J, Watanabe F, Biswas A, Umwungeri JL, Courte A, Biris AB, Kebdani O, Biris AS. The role of hydrocarbon concentration on the synthesis of large area few to multi-layer graphene structures. *Chemical Physics Letters*. 2011;501;390-5.
24. Yüksel F, Gümüş G, Gürol İ, Ahsen V, Chumakov Y, Jeanneaub E, Luneau D. Channel architecture via self assembly of oxamide oximes complexes. *Dalton Transactions*. 2008;0; 241-52.
25. Gürol İ, Ahsen V, Bekaroğlu Ö. Synthesis of soluble complexes from a tetradentate dithioglyoxime ligand. *Journal of the Chemical Society, Dalton Transactions*. 1992; 0; 2283-6.
26. Singh MS, Singh AK. Heterocyclization of vicinal dioximes to seven membered N, P and O heterocycles. *Indian Journal of Chemistry –B*. 2000; 32; 551-3.
27. Burakevi JV, Lore AM, Volpp GP. Phenylglyoxime. Separation, characterization, and structure of three isomers. *The Journal of Organic Chemistry*. 1971; 36; 1-4.
28. Özcan E, Karapınar E, Demirtas B. Synthesis of four new *vic*-dioximes and their nickel(II), cobalt(II), copper(II) and cadmium(II) complexes. *Transition Metal Chemistry*. 2002; 27; 557-61.
29. Rajkumar K, Aravindan S. Tribological studies on microwave sintered copper-carbon nanotube composites. *Wear*. 2011;270;613-21.
30. Wu HX, Zhang CX, Jin L, Yang H, Yang SP. Preparation and magnetic properties of cobalt nanoparticles with dendrimers as templates. *Materials Chemistry and Physics*. 2010;121;342-8.
31. Brintzinger H, Titzmann R. Notiz über einige halogenierte aliphatische Oxime. *Chemische Berichte*.1952;85;344-5.
32. Erünal E, Ulusal F, Aslan MY, Güzel B, Üner D. Enhancement of hydrogen storage capacity of multi-walled carbon nanotubes with palladium doping prepared through supercritical CO₂ deposition method. *International Journal of Hydrogen Energy*. 2017; <https://doi.org/10.1016/j.ijhydene.2017.12.058>, in press.



Hydrothermal Syntheses, Crystal Structures, and Properties of 1D Coordination Polymers Based on 5-Nitroisophthalic Acid and 1-Methylimidazole Linkers

Mürsel Arıcı^{1*}

¹Eskişehir Osmangazi University, Faculty of Science and Arts, Department of Chemistry, 26480, Eskişehir, Turkey.

Abstract: Two new coordination polymers, namely $[\text{Mn}(\mu_3\text{-5-nip})(1\text{-meim})_2(\text{H}_2\text{O})]_n$ (**1**) and $\{[\text{Co}(\mu\text{-5-nip})(1\text{-meim})_3]\cdot\text{H}_2\text{O}\}_n$ (**2**) (5-nip: 5-nitroisophthalate, 1-meim: 1-methylimidazole), were hydrothermally synthesized and characterized by FTIR spectroscopy, elemental analysis, single crystal X-ray diffraction, and simultaneous thermal analysis techniques. The 5-nip ligand exhibited two different coordination modes in its structures. In **1** and **2**, 1D chains were generated by 5-nip ligands and metal(II) ions. In **1** and **2**, 5-nip ligand coordinated to three Mn(II) and two Co(II) ions as bis(monodentate) bridging mode and a monodentate and bidentate chelating modes, respectively. For **1** and **2**, 2D supramolecular layers were formed by hydrogen bonds which were extend into 3D supramolecular structures via $\pi\cdots\pi$ stacking interactions between two symmetry-related imidazole rings of neighboring molecules. Furthermore, optical and thermal properties of the complexes were also studied.

Keywords: 5-nitroisophthalate, coordination polymer, optical properties.

Submitted: September 25, 2017. **Accepted:** March 29, 2018.

Cite this: Arıcı M. Hydrothermal Syntheses, Crystal Structures, and Properties of 1D Coordination Polymers Based on 5-Nitroisophthalic Acid and 1-Methylimidazole Linkers. JOTCSA. 2018;5(2):653-64.

DOI: <http://dx.doi.org/10.18596/jotcsa.339915>.

***Corresponding author.** E-mail: marici@ogu.edu.tr, Tel: +902222393750, Fax: +902222393578).

INTRODUCTION

In recent years, the field of crystal engineering of coordination polymers has received considerable interest due to their interesting architectures and their application areas such as gas adsorption/separation, magnetism, sensor, luminescence, and catalysis, *etc.* (1-6). For the above-mentioned applications, the selections of organic building blocks and metal ions are crucial factors in the construction of coordination polymers with desired architecture (7, 8). Moreover, several factors as *e.g.* metal-ligand ratio, temperature, and pH have influence on the final structure (9). In the synthesis of coordination polymers, aromatic multi-carboxylic acids, especially dicarboxylic acid as an anionic ligand have been extensively preferred owing to their diverse coordination modes and structural stabilities in their complexes (10). Hence, in this study, 5-nitroisophthalic acid was selected as an anionic ligand in the construction of coordination polymers. It can connect to metal ions with four potential oxygen donor atoms from two carboxylate groups with the bending angle of 120° and its 5-substituted nitro group has electron withdrawing ability and steric effect (11-14) (Scheme 1). Moreover, mixed-ligand coordination polymers (with dicarboxylic acid and N- donor neutral ligand) have been widely synthesized to improve the structural diversity and dimensionality in the assembly process (7, 15). 1-methylimidazole ligand was used as a secondary neutral ligand to provide geometric need of metal centers. In this work, two 1D mixed-ligand Mn(II) and Co(II) coordination polymers, $[\text{Mn}(\mu_3\text{-5-nip})(1\text{-meim})_2(\text{H}_2\text{O})]_n$ (**1**) and $\{[\text{Co}(\mu\text{-5-nip})(1\text{-meim})_3]\cdot\text{H}_2\text{O}\}_n$ (**2**) were hydrothermally synthesized with 5-nipH₂ and 1-meim ligands and characterized by using FTIR spectroscopy, single crystal X-ray diffraction, elemental analysis, and thermal analysis techniques (TG/DTA). Moreover, diffuse reflectance spectra of the compounds were recorded and band-gaps of the complexes were calculated by using Kubelka-Munk function (16).

EXPERIMENTAL SECTION

Materials and measurements

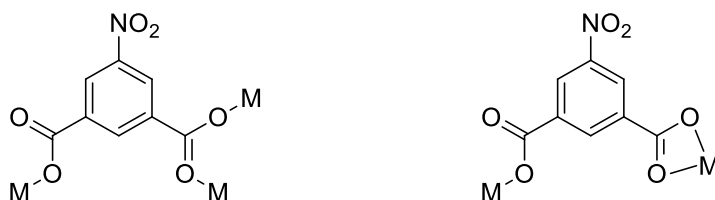
All reagents were of analytical grade and used without further purification. Perkin-Elmer 2400C elemental analyzer was used for elemental analyses (CHN). FTIR spectra using KBr pellets were acquired with a Bruker Tensor 27 spectrometer device in the range of 4000–400 cm⁻¹. The diffuse reflectance spectra (DRS) were obtained with Shimadzu UV-2600 spectrophotometer using BaSO₄ as a reference in the wavelength range 200–800 nm. TG/DTA analyses were measured on a Perkin Elmer Diamond TG/DTA Thermal Analyzer from 30 to 700 °C under static air. A Bruker Smart Apex II CCD with a D8-QUEST diffractometer equipped with a graphite-monochromatic Mo-K α radiation ($\lambda = 0.71073 \text{ \AA}$) was used for single crystal data collections at 296 K. The structure solutions and refinements were performed with direct methods using SHELXT and full-matrix least-squares on all F² data using SHELXL in connection with the OLEX2 software (17). Refinements of all non-hydrogen atoms were carried out with anisotropic

parameters. Molecular graphics were drawn with Mercury software (18). Crystallographic information files are deposited with the CCDC 1576332 and 1576333.

Syntheses

$[Mn(\mu_3-5-nip)(1-meim)_2(H_2O)]_n$ (**1**): $Mn(CH_3COO)_2 \cdot 4H_2O$ (1 mmol, 0.245 g) and 5-nitroisophthalic acid (5-nipH₂) (1 mmol, 0.22 g) were mixed in water (20 mL) and stirred at 70 °C for an hour and then 1-methylimidazole (1-meim) (3 mmol, 0.246 g) was added into the mixture. The final mixture was placed in a 25 mL closed capped-glass bottle and heated at 120 °C for four days to obtain colorless crystals of **1**. (Yield: 0.112 g, 25.11 % based on $Mn(CH_3COO)_2 \cdot 4H_2O$). Anal. Calcd. for $C_{16}H_{17}MnN_5O_7$: C, 43.06; H, 3.84; N, 15.69 %. Found: C, 43.56; H, 3.38; N, 15.13 %. FTIR (KBr, cm^{-1}): 3356, 3288, 3129, 3316, 3089, 2967, 1629, 1612, 1562, 1535, 1453, 1373, 1346, 1106, 942, 840, 762, 738 cm^{-1} .

$\{[Co(\mu-5-nip)(1-meim)_3] \cdot H_2O\}_n$ (**2**): The procedure for preparation of complex **2** was similar to that used for **1**, except that the $Co(CH_3COO)_2 \cdot 4H_2O$ (1 mmol, 0.249 g) was used instead of $Mn(CH_3COO)_2 \cdot 4H_2O$. After hydrothermal conditions, the resulting mixture was filtered and evaporated at room temperature. The purple-colored crystals of **2** were obtained (Yield: 0.168 g, 31.58% based on $Co(CH_3COO)_2 \cdot 4H_2O$). Anal. Calcd. for $C_{20}H_{23}CoN_7O_7$: C, 45.12; H, 4.35; N, 18.42 %. Found: C, 44.97; H, 4.41; N, 18.02 %. FTIR (KBr, cm^{-1}): 3509, 3373, 3146, 3112, 3051, 2963, 1629, 1615, 1564, 1534, 1368, 1344, 1104, 944, 840, 731 cm^{-1} .



Scheme 1: Coordination modes of 5-nip ligand in its compounds

RESULTS AND DISCUSSION

Synthesis and characterization

The complexes were hydrothermally synthesized by using $M(CH_3COO)_2 \cdot 4H_2O$ (M: Mn(II) and Co(II)), 5-nipH₂ and 1-meim ligands. The complexes were characterized with various techniques. In the FTIR spectra of the complexes, the broad bands appearing in the range of 3556–3509 cm^{-1} are assigned to $\nu(O-H)$ stretching vibrations of coordinated and uncoordinated water molecules. For **1** and **2**, the bands observed between 3146 and 3051 cm^{-1} are due to aromatic $\nu(C-H)$ stretchings. For **1** and **2**, aliphatic $\nu(C-H)$ stretching vibrations of 1-meim ligand appeared at 2967 and 2963 cm^{-1} , respectively. For both complexes, the bands observing between at 1629 and 1612 cm^{-1} and between at 1373 and 1368 cm^{-1} are due to the asymmetric ($\nu_{asym}(COO)$) and symmetric ($\nu_{sym}(COO)$) stretching vibrations of 5-nip, respectively.

Description of crystal structure

Table 1 indicates the crystal data and structural refinement parameters.

Table 1: Crystal data and structural refinement parameters for **1** and **2**.

	1	2
Empirical formula	C ₁₆ H ₁₇ MnN ₅ O ₇	C ₂₀ H ₂₃ CoN ₇ O ₇
Formula weight	446.28	532.38
Crystal system	Triclinic	Monoclinic
Space group	<i>P</i> -1	<i>C</i> 2/ <i>c</i>
<i>a</i> (Å)	8.836	20.570
<i>b</i> (Å)	10.162	16.679
<i>c</i> (Å)	11.960	15.327
α (°)	105.12	90
β (°)	105.87	115.99
γ (°)	105.30	90
<i>V</i> (Å³)	930	4726.8
<i>Z</i>	2	8
<i>D</i>_c (g cm⁻³)	1.594	1.496
μ (mm⁻¹)	0.76	0.78
Measured refls.	44930	58988
Independent refls.	4621	5796
<i>R</i>_{int}	0.046	0.042
<i>S</i>	1.18	1.21
<i>R</i>1/<i>wR</i>2	0.043/0.110	0.057/0.123
$\Delta\rho_{\max}/\Delta\rho_{\min}$ (eÅ⁻³)	0.42/-0.78	0.61/-0.55

[Mn(μ_3 -5-nip)(1-meim)₂(H₂O)]_n (1**).** The crystal structure of **1** is given in Figure 1 and selected bond distances, angles and hydrogen bond geometries are given in Table 2. X-ray result shows that **1** crystallizes in triclinic system and *P*-1 space group. The asymmetric unit has one Mn(II) ion, one 5-nip, two 1-meim ligands, and a coordinated water molecule. As seen in Figure 1, each Mn(II) ion is coordinated by three oxygen atoms from different 5-nip ligands, two nitrogen atoms from two different 1-meim ligands, and one oxygen atom from one aqua ligand to form a distorted octahedral geometry. Each nip ligand acts as a μ_3 -bridging ligand to connect three Mn(II) ions. Two Mn(II) ions are bridged by two carboxylate groups from two different 5-nip ligands with Mn...Mn distance of 5.017 Å to generate [Mn₂(CO₂)₂] secondary building unit (SBU). SBUs are linked by carboxylate oxygen atoms (O9) of 5-nip to generate 1D chain with 16-membered rings (Figure 2). 1D chains are extended to 2D supramolecular layer with hydrogen bonds between carboxylate oxygen atom (O4ⁱⁱ) of 5-nip and coordinated water molecule (O7) and [O7...O4ⁱⁱ = 2.964 Å; O7-H7...O4ⁱⁱ = 155.31°] (ii: 1-x, -y, 1-z) (Figure 3). Moreover, adjacent 2D layers are further connected by *n*...*n* stacking interactions between two symmetry-related

imidazole rings of neighboring molecules forming a 3D supramolecular network ($Cg1 \cdots Cg1^{iii} = 3.719 \text{ \AA}$, $Cg1$: N1-C9-N2-C11-C10, iii : 2-x, 2-y, 2-z) (Figure 3).

Table 2: Selected bond distances (\AA), angles ($^\circ$) and hydrogen-bond geometry data for **1***

Bond Lengths (\AA)				
Mn1-O2 ⁱ	2.1656 (1)	Mn1-N3	2.2292 (2)	
Mn1-O1	2.1649 (1)	Mn1-N1	2.2271 (2)	
Mn1-O7	2.2985 (1)	Mn1-O3 ⁱⁱ	2.1947 (1)	
Angles ($^\circ$)				
O2 ⁱ -Mn1-O3 ⁱⁱ	93.74 (5)	O1-Mn1-O2 ⁱ	94.36 (5)	
O2 ⁱ -Mn1-N3	90.50 (6)	O1-Mn1-O7	91.31 (5)	
O2 ⁱ -Mn1-N1	89.30 (6)	N3-Mn1-O7	91.57 (6)	
O1-Mn1-N1	93.07 (6)	N1-Mn1-O7	88.33 (6)	
O3 ⁱⁱ -Mn1-O7	80.63 (5)	N1-Mn1-N3	176.98 (6)	
O3 ⁱⁱ -Mn1-N3	89.11 (6)	O2 ⁱ -Mn1-O7	173.97 (5)	
Hydrogen bond geometry (\AA , $^\circ$)				
<i>D</i> -H \cdots <i>A</i>	<i>D</i> -H	H \cdots <i>A</i>	<i>D</i> \cdots <i>A</i>	<i>D</i> -H \cdots <i>A</i>
O7-H7B \cdots O4 ⁱⁱ	0.88	1.85	2.722(2)	167 (3)
O7-H7A \cdots O4 ^{iv}	0.80	2.22	2.964(2)	155 (3)

*Symmetry codes: (i) $-x+1, -y+1, -z+2$; (ii) $x, y+1, z$; (iii) $x, y-1, z$, (iv) $-x+1, -y, -z+1$.

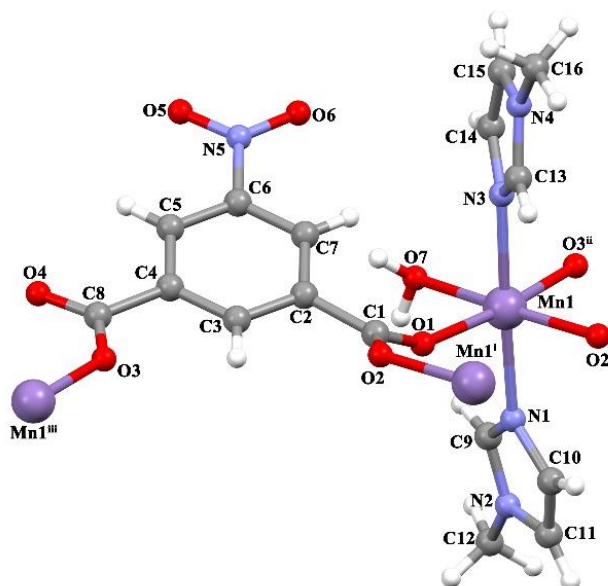


Figure 1: The molecular structure of **1**

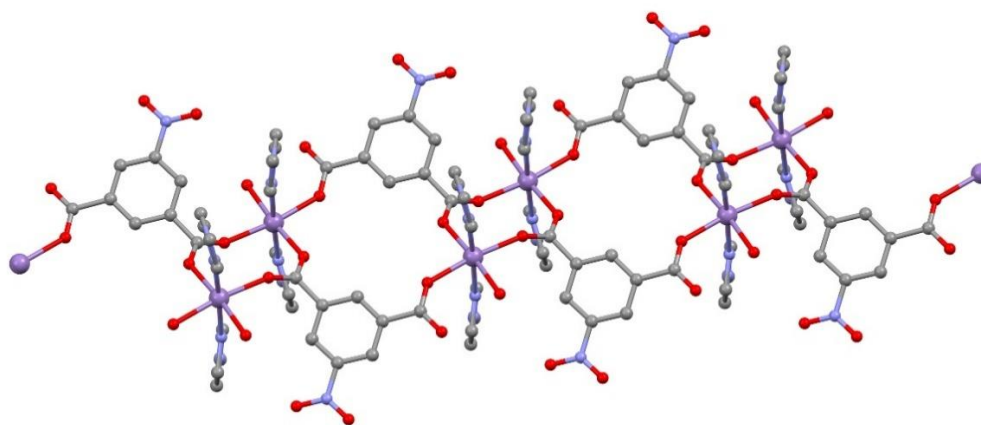


Figure 2: 1D chain structure of complex **1**.

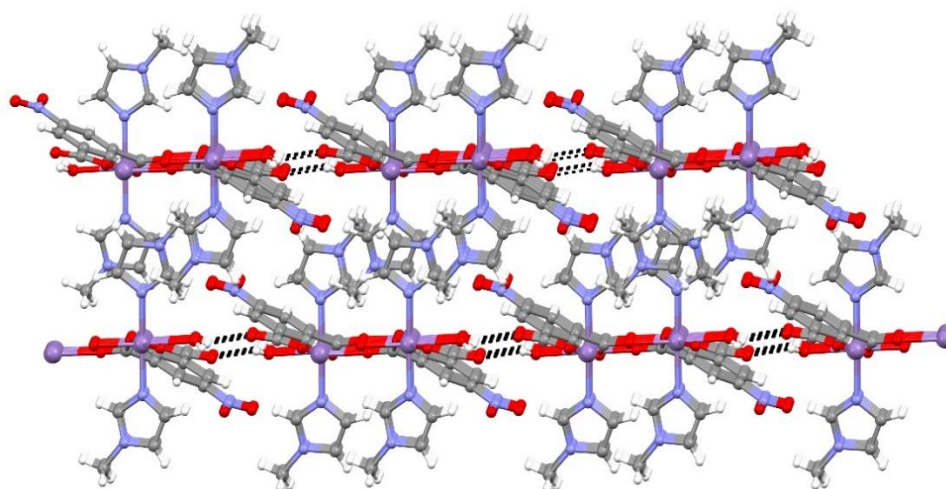


Figure 3: 3D supramolecular structure of complex **1** generated by hydrogen bonds and $\pi \cdots \pi$ stacking interactions.

$\{[\text{Co}(\mu\text{-}5\text{-nip})(1\text{-meim})_3]\cdot\text{H}_2\text{O}\}_n$ (2**).** Table 3 shows the selected bond distances and angles. X-ray result demonstrates that complex **2** crystallizes in monoclinic $C2/c$ space group. There are one Co(II) ion, one 5-nip, three 1-meim ligands, and one uncoordinated water molecule in the asymmetric unit (Figure 4). Each Co(II) ion is six-coordinated by three carboxylate oxygen atoms from two different 5-nip ligands and three nitrogen atoms from three different 1-meim ligands.

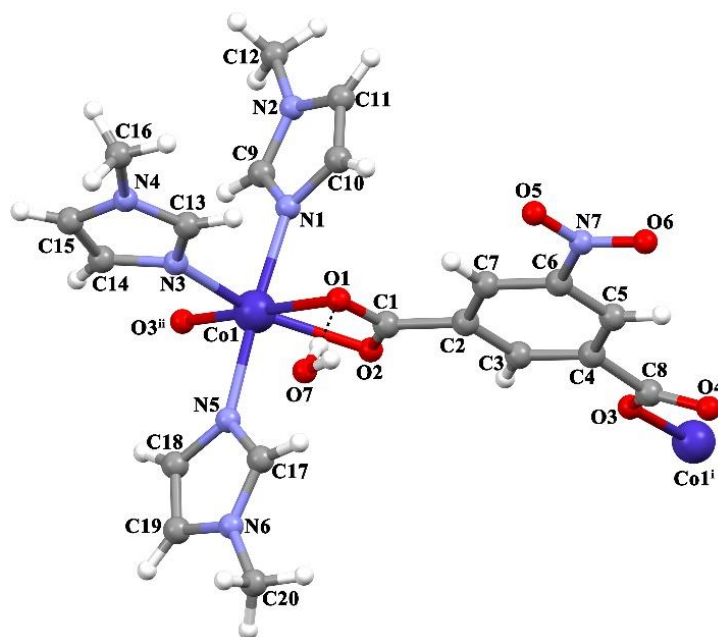


Figure 4: The molecular structure of **2**

In **2**, 5-nip ligand coordinates to two Co(II) ions in monodentate and bidentate chelating modes to form 1D zig-zag chain (Figure 5).

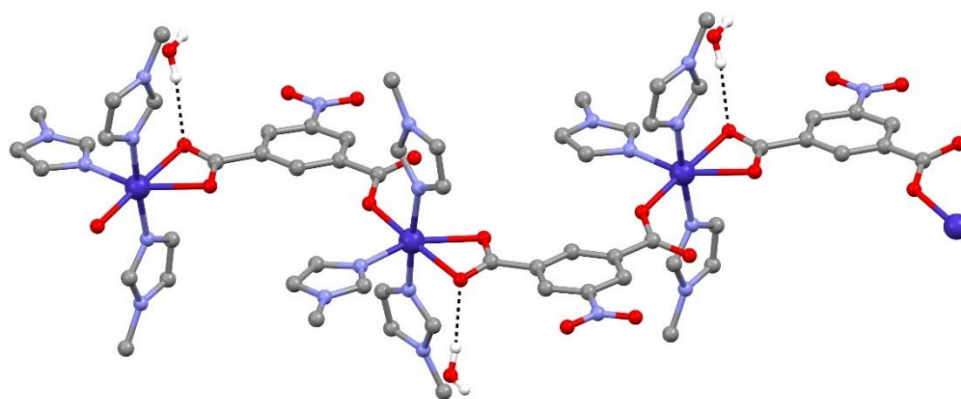


Figure 5: 1D chain structure of complex **2**.

Adjacent 1D chains expand into 2D supramolecular layer with hydrogen bonding between carboxylate oxygen atom (O2) of 5-nip and uncoordinated water molecule (O7) [$O2 \cdots O7 = 2.76 \text{ \AA}$, $O2 \cdots H7B-O7 = 176.16^\circ$] and between uncoordinated carboxylate oxygen atom ($O4^{iii}$) of adjacent 5-nip ligand and water molecule (O7) [$O7 \cdots O4^{iii} = 2.931 \text{ \AA}$, $O7-H7A \cdots O4^{iii} = 168.27^\circ$] (Figure 6a). Furthermore, 2D layers are further connected by $n \cdots n$ stacking interactions between two symmetry-related imidazole rings of neighboring molecules forming a 3D supramolecular network ($Cg3 \cdots Cg3^{iv} = 3.719 \text{ \AA}$, Cg1: N1-C9-N2-C11-C10, iv: $1/2-x, 1/2-y, 1-z$) (Figure 6b).

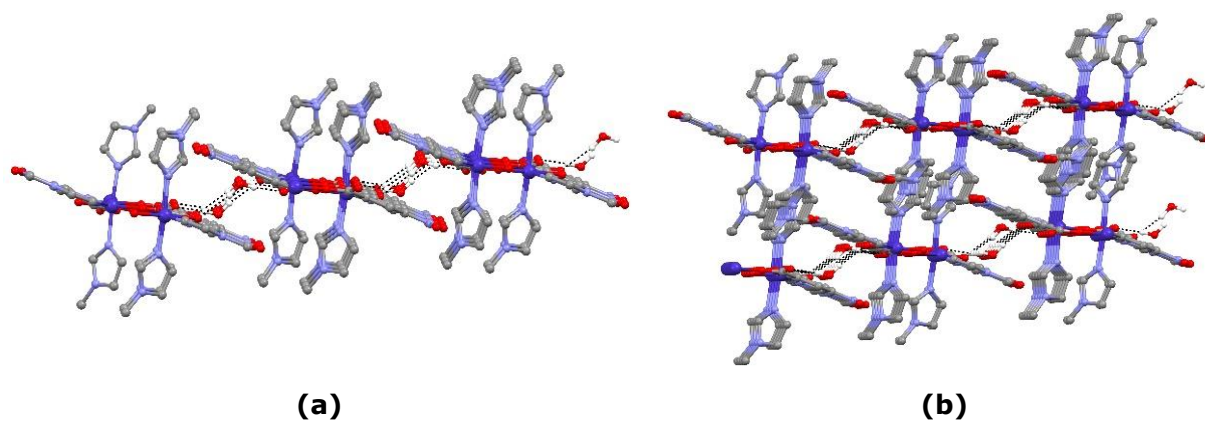


Figure 6: (a) 2D supramolecular layer of complex **2** generated by hydrogen bondings (b) 3D supramolecular structure of complex **2** generated by $\pi \cdots \pi$ stacking interactions

Table 3: Selected bond distances (\AA), angles ($^\circ$) and hydrogen-bond geometry data for **2**^{*}.

Bond Lengths (\AA)				
Co1–O4 ⁱ	2.293 (2)	Co1–N1	2.115 (2)	
Co1–O3 ⁱ	2.241 (2)	Co1–N5	2.122 (2)	
Co1–O1	2.0714 (2)	Co1–N3	2.088 (2)	
Angles ($^\circ$)				
O3 ⁱ –Co1–O4 ⁱ	57.98 (7)	N1–Co1–O3 ⁱ	87.17 (8)	
O1–Co1–O4 ⁱ	177.88 (8)	N1–Co1–N5	174.50 (9)	
O1–Co1–O3 ⁱ	120.34 (8)	N5–Co1–O4 ⁱ	88.06 (9)	
O1–Co1–N1	88.10 (9)	N5–Co1–O3 ⁱ	88.86 (9)	
O1–Co1–N5	90.63 (9)	N3–Co1–O4 ⁱ	89.77 (8)	
O1–Co1–N3	91.90 (8)	N3–Co1–O3 ⁱ	147.75 (8)	
N1–Co1–O4 ⁱ	93.05 (9)	N3–Co1–N1	95.31 (9)	
N3–Co1–N5	90.08 (9)			
Hydrogen bond geometry (\AA, $^\circ$)				
<i>D</i> –H \cdots <i>A</i>	<i>D</i> –H	H \cdots <i>A</i>	<i>D</i> \cdots <i>A</i>	<i>D</i> –H \cdots <i>A</i>
O7–H7A \cdots O4 ⁱⁱⁱ	0.85	2.09	2.931(4)	168
O7–H7B \cdots O2	0.85	1.91	2.760(3)	176

*Symmetry codes: (i) $-x+1/2, y+1/2, -z+3/2$; (ii) $-x+1/2, y-1/2, -z+3/2$, (iii) $-x+1, -y, -z+2$.

Optical absorption and thermal properties

Solid state UV-Vis diffuse reflectance spectra of the compounds were acquired at room temperature to determine optical absorption properties and evaluate semiconductor properties. Solid state UV-Vis absorption spectra and curves of Kubelka–Munk function of free ligand 5-nipH₂ and the complexes as a function of energy are given in Figure 7. The optical band gap (E_g) was determined by extrapolation from the linear portion of absorption edges based on Kubelka–Munk function (the curve of $(h\nu F(R))^{1/2}$ versus photon energy ($h\nu$): where, $h\nu$ is the photon energy, $F(R)$ is Kubelka–Munk function ($F(R) = (1-R)^2/2R$). The E_g values of 5-nipH₂ and complexes **1** and **2** are 2.93, 2.85 and 2.874 eV, respectively. These results show the semiconductive properties of complexes **1** and **2** and complex **1** displays higher conductivity than complex **2**.

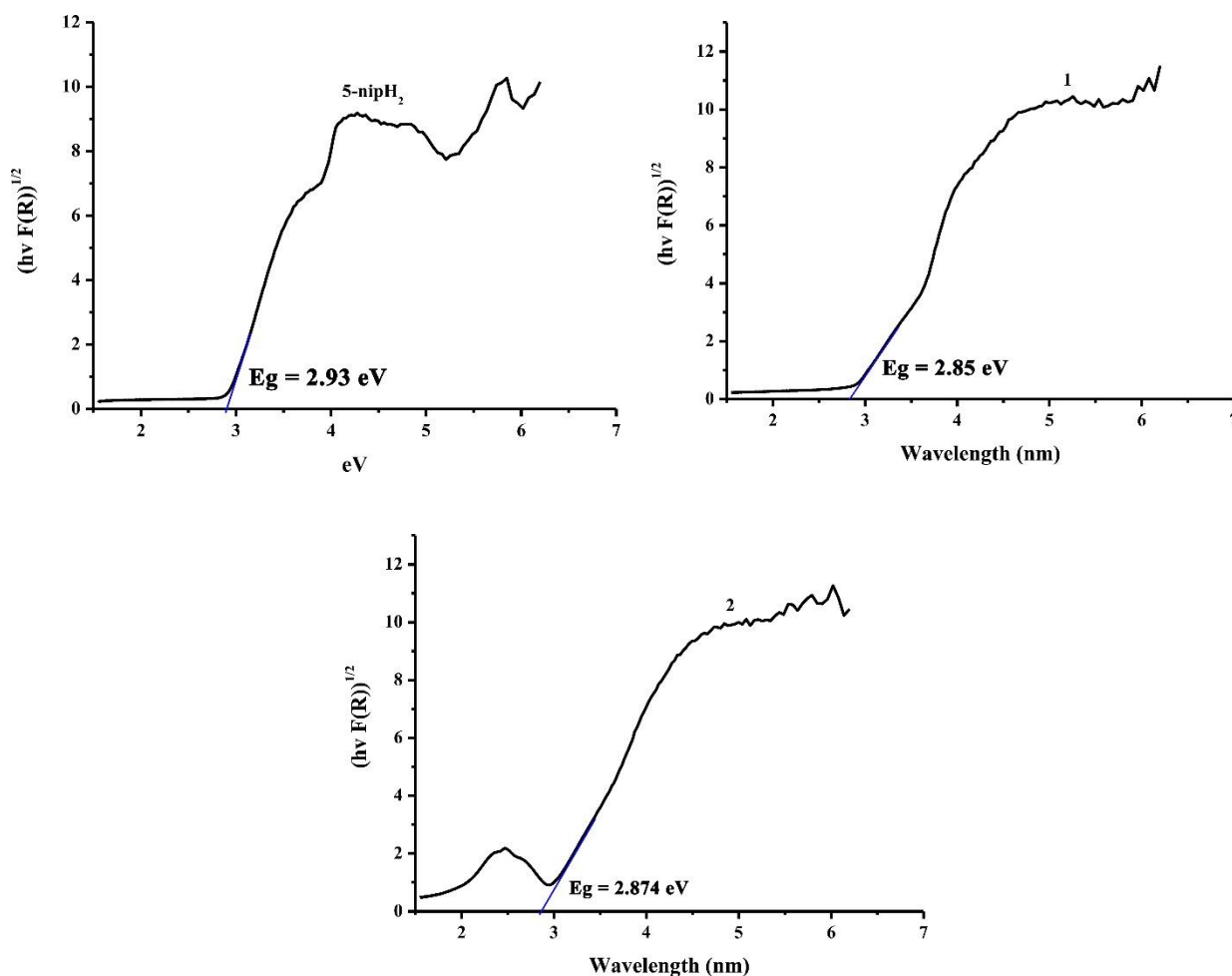


Figure 7: Plots of Kubelka-Munk as a function of energy for free ligand 5-nipH₂ and complexes **1** and **2**.

In order to determine thermal behaviors and stabilities of title complexes, simultaneous TG/DTA analyses were carried out (Figures 8 and 9). For complexes **1** and **2**, the first weight losses in the temperature range 40-125 °C are related to elimination of coordinated and uncoordinated water molecules (found: 4.80 %, calcd.: 4.033 % for **1**; found: 3.50 %, calcd.: 3.40 % for **2**). After these steps, the weight losses of 35.34% in the temperature range 160-368 °C for **1** and 45.5 % in the temperature range 118-365 °C for **2** correspond to the removal of 1-meim ligands. On further heating, the complexes were completely decomposed with exothermic picks and remaining products are possibly MnO and CoO (found: 15.62 %, calcd.: 15.90 % for **1**; found: 14.13 %, calcd.: 14.08 % for **2**).

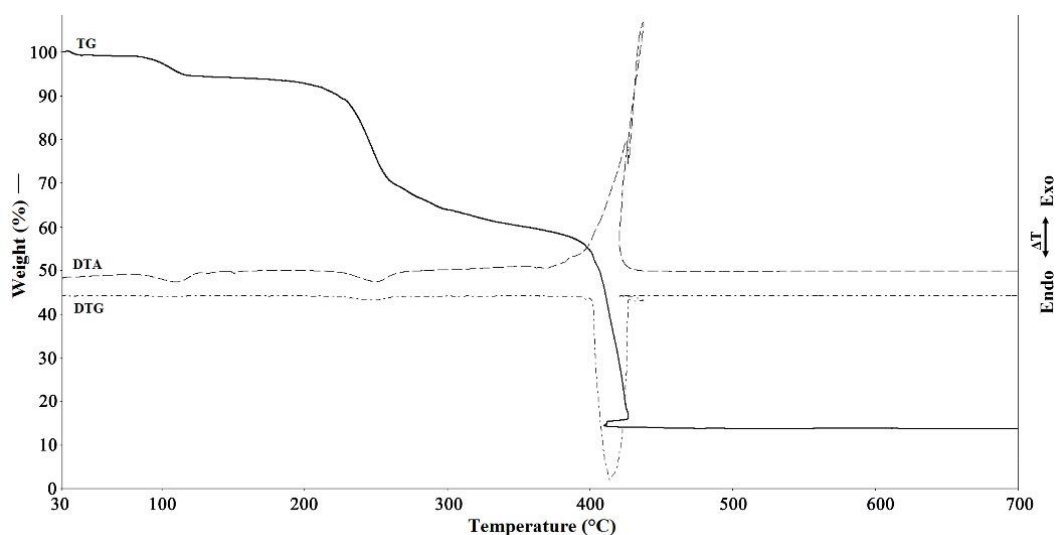


Figure 8: TG, DTG, and DTA curves of complex **1**.

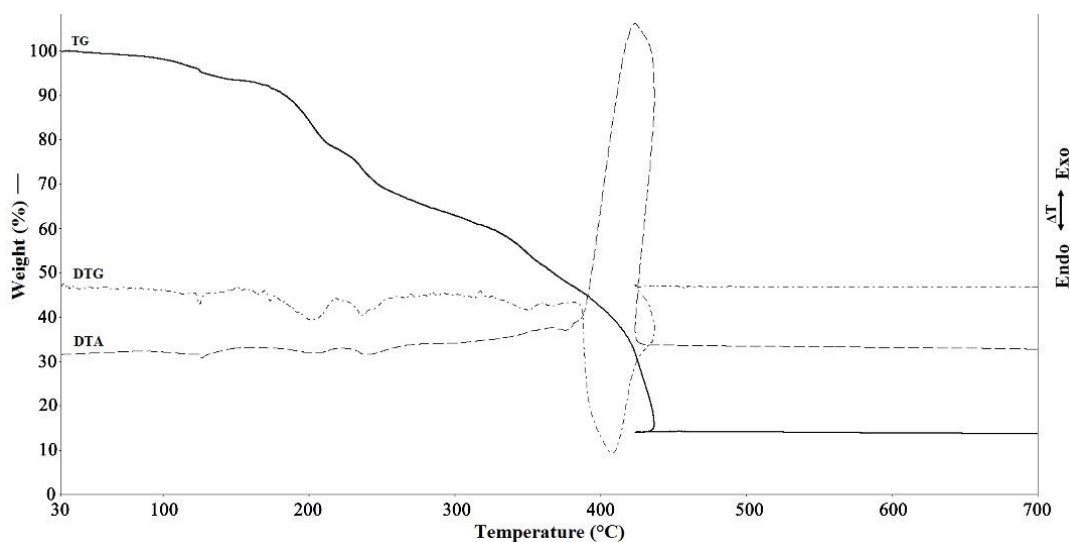


Figure 9: TG, DTG and DTA curves of complex **2**.

CONCLUSION

In this study, two new Mn(II) and Co(II)-coordination polymers were synthesized and characterized. 5-nip ligand displayed different coordination modes in two structures. 5-nip ligand acted as a bridging ligand between metal(II) centers to form 1D. 2D and 3D supramolecular structures are generated through hydrogen bondings and $\pi \cdots \pi$ stacking interactions. Optical band gap results of the complexes showed that complex **1** had higher conductivity than free ligand 5-nipH₂ and complex **2**.

REFERENCES

1. He Y, Zhou W, Qian G, Chen B. Methane storage in metal–organic frameworks. *Chemical Society Reviews*. 2014;43(16):5657-78.
2. Noro S-i, Ochi R, Inubushi Y, Kubo K, Nakamura T. CH₄/CO₂ and CH₄/C₂H₆ gas separation using a flexible one-dimensional copper (II) porous coordination polymer. *Microporous and Mesoporous Materials*. 2015;216:92-6.
3. Gu J-Z, Liang X-X, Cui Y-H, Wu J, Shi Z-F, Kirillov AM. Introducing 2-(2-carboxyphenoxy) terephthalic acid as a new versatile building block for design of diverse coordination polymers: synthesis, structural features, luminescence sensing, and magnetism. *CrystEngComm*. 2017;19(18):2570-88.
4. Arici M, Yeşilel OZ, Taş M, Demiral H. CO₂ and iodine uptake properties of Co (II)-coordination polymer constructed from tetracarboxylic acid and flexible bis (imidazole) linker. *Crystal Growth & Design*. 2017;17(5):2654-9.
5. Arıcı M, Yeşilel OZ, Büyükgüngör O. Four coordination polymers based on 5-tert-butyl isophthalic acid and rigid bis (imidazol-1yl) benzene linkers: Synthesis, luminescence detection of acetone and optical properties. *Journal of Solid State Chemistry*. 2017;249:141-8.
6. Wezendonk TA, Santos VP, Nasalevich MA, Warringa QS, Dugulan AI, Chojecki A, et al. Elucidating the Nature of Fe Species during Pyrolysis of the Fe-BTC MOF into Highly Active and Stable Fischer–Tropsch Catalysts. *ACS Catalysis*. 2016;6(5):3236-47.
7. Zhu X, Sun P-P, Ding J-G, Li B-L, Li H-Y. Tuning cobalt coordination architectures by bis (1, 2, 4-triazol-1-ylmethyl) benzene position isomers and 5-nitroisophthalate. *Crystal Growth & Design*. 2012;12(8):3992-7.
8. Guo F, Zhu B, Xu G, Zhang M, Zhang X, Zhang J. Tuning structural topologies of five photoluminescent Cd (II) coordination polymers through modifying the substitute group of organic ligand. *Journal of Solid State Chemistry*. 2013;199:42-8.
9. Zhao F-H, Che Y-X, Zheng J-M. Syntheses, structures and magnetic properties of two new complexes constructed from mixed rigid ligands. *Inorganic Chemistry Communications*. 2012;16:55-60.
10. Lin J-D, Lin M-Z, Tian C-B, Lin P, Du S-W. Syntheses, topological structures and physical properties of two 2D lanthanide–organic frameworks constructed from 5-nitroisophthalic acid. *Journal of Molecular Structure*. 2009;938(1):111-6.
11. Huang Y, Yan B, Shao M. Synthesis, crystal structure and photoluminescent properties of four lanthanide 5-nitroisophthalate coordination polymers. *Journal of solid state chemistry*. 2009;182(4):657-68.
12. Ye J, Wang J, Wu Y, Ye L, Zhang P. Supramolecular coordination networks constructed from infinite one-dimensional chains with 5-nitroisophthalate as bridge. *Journal of Molecular Structure*. 2008;873(1):35-40.
13. Wang X-L, Xia Z-Q, Wei W, Xie G, Chen S-P, Gao S-L. Synthesis, structure, and thermodynamics of a lanthanide coordination compound incorporating 5-nitroisophthalic acid. *The Journal of Chemical Thermodynamics*. 2012;55:124-9.
14. Chen Q, Zhu X, Ding J-G, Li B-L, Li H-Y. Syntheses, structures and properties of three cobalt coordination polymers based on flexible bis (triazole) and 5-nitroisophthalate coligands. *Journal of Molecular Structure*. 2013;1038:194-9.
15. Semerci F. Syntheses and photoluminescence properties of new Zn (II) and Cd (II) coordination polymers prepared from 5-sulfoisophthalate ligand. *Turkish Journal of Chemistry*. 2017;41(2):243-55.
16. López R, Gómez R. Band-gap energy estimation from diffuse reflectance measurements on sol–gel and commercial TiO₂: a comparative study. *Journal of Sol-Gel Science and Technology*. 2012;61(1):1-7.
17. Dolomanov OV, Bourhis LJ, Gildea RJ, Howard JA, Puschmann H. OLEX2: a complete structure solution, refinement and analysis program. *Journal of Applied Crystallography*. 2009;42(2):339-41.

18. Macrae CF, Edgington PR, McCabe P, Pidcock E, Shields GP, Taylor R, et al. Mercury: visualization and analysis of crystal structures. *Journal of Applied Crystallography*. 2006;39(3):453-7.



EFFECT of IONIC LIQUID CONTENT on the MONOLITHIC STRUCTURE of AMINE-MEDIATED SILICA AEROGEL via AMBIENT PRESSURE DRYING

Nilay GİZLİ*, Selay SERT ÇOK, Fatoş KOÇ

Ege University, Faculty of Engineering, Department of Chemical Engineering, 35100, İzmir, Turkey.

Abstract: In this study, amine-mediated silica aerogels dried under the ambient conditions in monolithic form were prepared by following sol-gel method. 3-aminopropyltriethoxysilane (APTES) was involved in the synthesis as a silica co-precursor. Imidazolium-based short-chain ionic liquids (ILs) were incorporated into the silica gel structure to control the gel shrinkage within the pores, as well as to eliminate the capillary effect during the solvent evaporation. A production procedure was developed to explore the synergistic effect of ionic liquids and amine-functionalized silica precursor on the textural and chemical properties of the final silica gels. Surface modifications of the samples were performed by using 3-Methacryloxypropyltrimethoxysilane (MEMO) to ensure hydrophobic characteristics. To reveal the chemical and morphological characteristics of the resultant material, various analyses were conducted. SEM and FTIR analyses were performed to investigate the morphological and chemical structure, whereas TGA analysis was carried out to determine the thermal stability of the silica gels. As a result, the ionic liquid embedded sample was obtained in a monolithic structure with a low density (0.45 g/cm^3) and had a good thermal stability (up to $381 \text{ }^\circ\text{C}$). Contact angle measurement also demonstrated that the desired monolithic sample has a hydrophobic characteristic with a water contact angle value of 113° .

Keywords: Ionic liquid, silica aerogel, APTES, ambient pressure drying, monolithic structure.

Submitted: February 5, 2018. **Accepted:** March 26, 2018.

Cite this: Gizli N, Sert Çok S, Koç F. EFFECT of IONIC LIQUID CONTENT on the MONOLITHIC STRUCTURE of AMINE-MEDIATED SILICA AEROGEL via AMBIENT PRESSURE DRYING. JOTCSA. 2018;5(2):663–78.

DOI: <http://dx.doi.org/10.18596/jotcsa.390372>.

***Corresponding author.** E-mail: nilay.gizli@ege.edu.tr

INTRODUCTION

Silica aerogels are exceptional porous materials with splendid physical properties such as very low density ($0.003\text{-}0.5\text{ g/cm}^3$), notably high surface area ($500\text{-}1200\text{ m}^2/\text{g}$), and high porosity ($80\%\text{-}99.8\%$) (1-4). Due to their outstanding properties aerogels are become a promising candidate in a wide range of applications such as thermal insulation in the construction sector (5), catalysis, chemical sensors (6), drug delivery systems (7), acoustic impedance (8), and space applications (9). They can be produced in various forms (*i.e.* powders, granular, or monolithic) by changing the synthesis conditions. Silica aerogels in monolithic form have wider applications as it allows controlling final shape of the product for any particular applications. Hence, production of silica aerogel as monolithic blocks can promote the commercialization of these materials.

The silica aerogels are mainly synthesized with the traditional sol-gel method. Typical sol-gel chemistry consists of consecutive hydrolysis and condensation reactions of a silicon alkoxide group in a liquid solvent with proper acid and/or base catalysis to form a colloidal solution called "sol". This process is followed by gelation of the sol, aging of the gel, and then drying (10). Several parameters affect the evolution of the microstructural pattern of the aerogel network, such as the type and amount of precursors, catalyst concentration, type of solvent, and reaction temperature and pH of sol (7). Aging is also an important step that allows continuation of condensation reactions of some monomers and unreacted Si-OR and Si-OH groups. Hence, it strengthens the structural gel network. However, drying is the most crucial step to satisfy the desired properties of the final product. The main challenge of drying is to perform it without allowing the collapse of a 3D network of the gel. During drying, development of capillary tension in pore walls causes a shrinkage of the gel body and crack the gel (7). This problem generally can be overcome by CO₂ supercritical drying. Although supercritical drying technique is used to avoid the destruction of the porous structure, it is unable to proceed beyond the small-scale batch type applications as it is both an expensive and risky process due to its high-pressure requirement. Therefore, most of the recent studies mainly focus on producing silica aerogels by ambient pressure drying (5-9). Generally, during the production of silica aerogels under ambient conditions, gel shrinkage arises from organic solvent evaporation during aging period and pore destruction and the collapse of the network occurs during the drying period. So, the resulting product often exhibits a low degree of monolithicity (16). Hence, several modifications can be applied to overcome these circumstances such as:

1. Using co-precursor to accelerate the condensation reaction rate during aging to be able to develop a stable network.
2. Adding target specific agents to control the gel shrinkage within the pores by satisfying a "spring back effect" on the pore walls.

3. Exchanging solvents to eliminate the capillary effect by minimizing surface tension on the liquid and vapor interface.

Gel shrinkage, which is the main obstacle obtaining crack-free monolithic silica aerogel, usually arises from organic solvent evaporation during the aging period. This situation can be prevented by replacing organic solvent with some other solvent that has a lower vapor pressure. Ionic liquids are organic salts with an extremely low vapor pressure over a large temperature range (-96 to 400 °C), therefore they do not evaporate during long aging periods (10). For that reason, using ionic liquids in the sol-gel process may yield a well-ordered pore structure and a stable gel network. They composed of a large organic cation group such as ammonium, phosphonium, pyridinium, imidazolium, *etc.* and inorganic/organic anion group. Due to their wide range of cation-anion combinations, ionic liquids can be produced with tunable properties and applied in diverse applications (17). Zhang *et al.* used various room temperature ionic liquids as templates in the synthesis of mesoporous silica gels and reported that increasing the alkyl chain length on the imidazolium cation can increase the pore size of silica gel and lead to slightly enlarged pores (18). Ivanova *et al.* produced silica ionogels with a one-step sol-gel method dried with supercritical CO₂ by using imidazolium-based ionic liquids with different anionic groups. They stated that each ionic liquid behaved as a co-catalyst during the sol-gel process and reduced the required gelation time (17). Same authors in another study denoted that depending on the functional groups of ILs incorporated in aerogel structure can lead to tailor-made porous materials (19). Karout and Pierre investigated the effect of ionic liquids on silica aerogel produced by partial evaporative drying followed by supercritical drying and stated that shrinkage of xerogels depended largely on the IL volume present in the gel before drying (20). They also investigated the effect of four kinds of ionic liquids on the silica gelation time and indicated that ionic liquids combine a double effect of condensation catalysts of silica and moderator of the condensation rate (21).

Dorcheh and Abbasi reported that acid-catalyzed hydrolysis and condensation lead to weakly branch and microporous structure, whereas basic conditions or two-step acid-base processes increase crosslinking, leading to decrease microporosity and a broader distribution of larger pores in silica gels. However, silica aerogels with larger pores usually have a lower specific surface area (4). In another study, Dourbash *et al.* explained that although ammonium hydroxide is the most used basic catalyst in the preparation of alcogels, it prolongs the gelation time and usually results in a dense structure. Instead of ammonium hydroxide, they recommended the fluoride-based catalysis to reduce the gelation time (22). On the other hand, Yang *et al.* prepared a silica aerogel using a two-step process in which a silica co-precursor containing an amine group 3-aminopropyltriethoxysilane (APTES) was involved to the sol. They reported that amine-rich APTES behaved like a basic catalyst and eliminated the additional requirement for a base catalyst during condensation reactions (15).

In this study, the main purpose is to prepare monolithic silica aerogels mediated with APTES under ambient conditions. It is also aimed to explore the synergistic spring back effect of adding ionic liquid into the sol-gel process on the morphological and chemical structure of the final product. Additionally, the reciprocal influence of ionic liquid and APTES on each other through the synthesis is evaluated with various characterizations for the first time to the best of our knowledge.

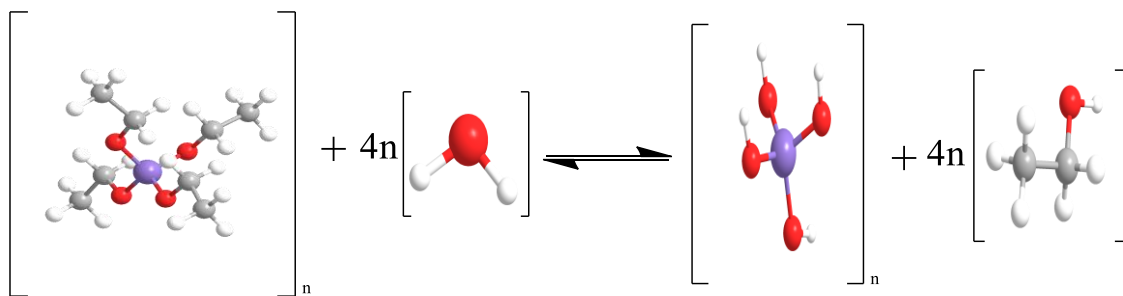
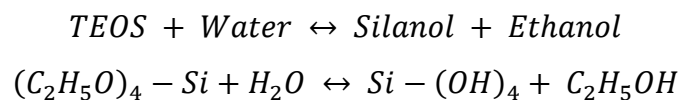
EXPERIMENTAL PROCEDURE

Materials

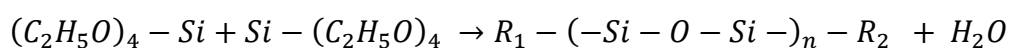
Tetraethylorthosilicate (TEOS) as precursor and 3-aminopropyltriethoxy-silane (APTES) as co-precursor were acquired from Sigma Aldrich. 1-Ethyl-3-methylimidazolium bis(trifluoromethanesulfonyl)imide (EMIMTF2N) was utilized as the short-chain imidazolium-based ionic liquid, and 3-methacryloxypropyltrimethoxysilane (MEMO) as surface modification agent were purchased from Sigma Aldrich. Ethanol (EtOH) and n-hexane were used as solvents and hydrochloric acid (HCl) was used as the acid catalyst.

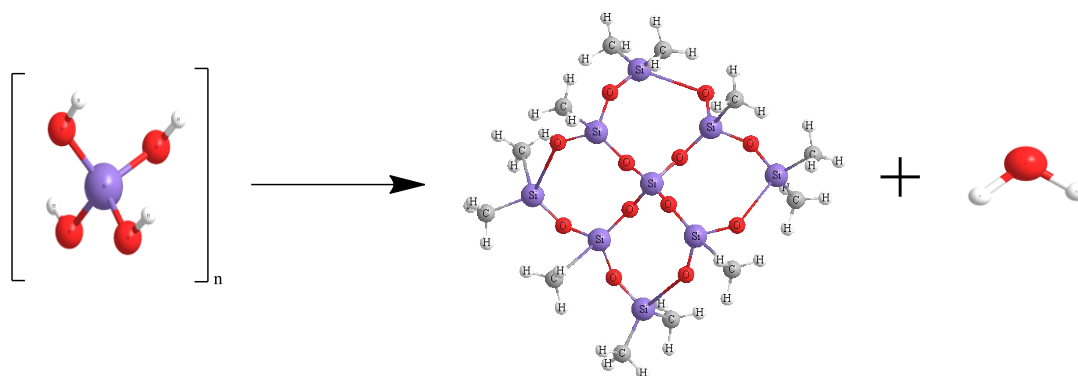
Preparation of silica aerogels

The silica aerogels were prepared by following one-step sol-gel processes with or without ionic liquid. For comparison purposes, silica aerogels were prepared in the absence (SG) or presence (SG-IL) of ionic liquid. During the preparation of the first sample SG-IL, TEOS was hydrolyzed by using 0.01 M HCl for 90 min by stirring at 25 °C. Hydrolysis reaction can take place as follows:

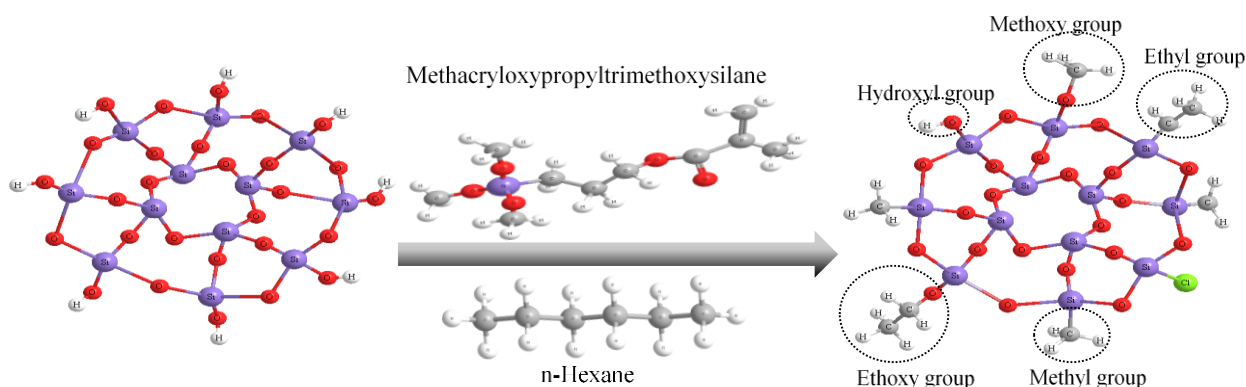


EtOH was used as a solvent whereas imidazolium-based ionic liquid was involved in the sol to serve as target-specific agent. After stirring for 90 minutes, the sol was placed in an ultrasonic media and APTES was added to the sol to start condensation reaction. It can be demonstrated as given below:





The sol component consists of TEOS: APTES: IL: EtOH: HCl with the molar ratios of 1:0.47:0.14:6.3:7.4 $\times 10^{-5}$. After complete gelation, the sample was allowed to age for 24 h in a polypropylene cylindrical mold to further continuation of the condensation reaction. Subsequently, the solvent exchange was carried out by treating the wet gels with fresh n-hexane for 12 h to ensure complete removal of the impurities within the gel. Then, surface modification was conducted by immersing the sample in silylating agent MEMO diluted with n-hexane at a volumetric percent of 50% at room temperature. Surface modification reaction can be shown as follows;



Finally, the sample SG-IL was dried in atmospheric media for two days. During the preparation of the second sample SG, the same procedure was followed with one difference that, unlike SG-IL, sample SG did not include ionic liquid in the sol. The sol components molar ratio for SG was 1:0.47:6.3:7.4 $\times 10^{-5}$ for TEOS: APTES: EtOH: HCl. Figure 1 represents to preparation steps of the samples by following sol-gel method.

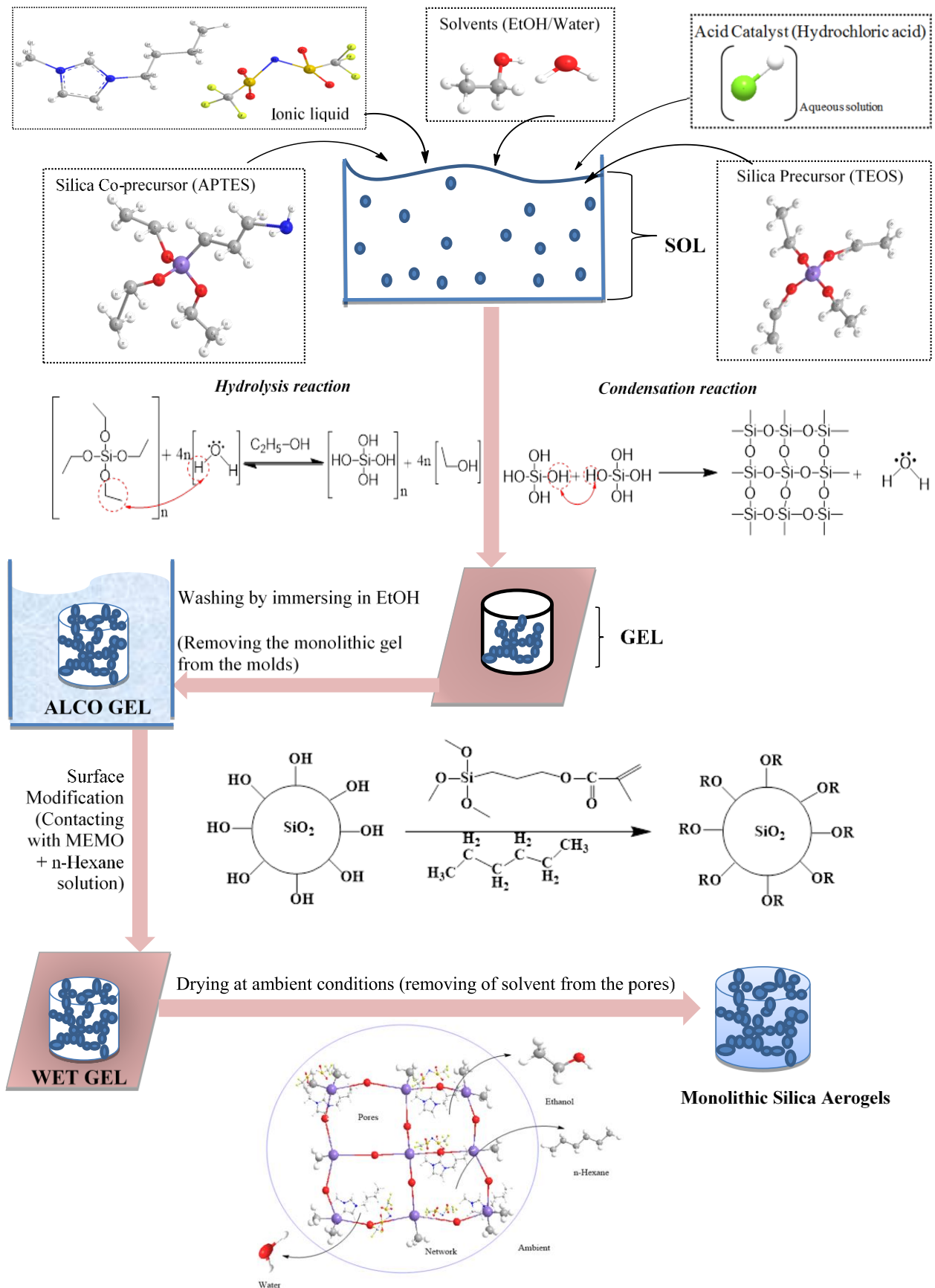


Figure 1 Sol-gel preparation steps.

Characterization

Bulk densities of dried gels were determined from mass to volume ratio (Eq. 1). The percentages of volume shrinkage and porosity of the samples were estimated according to equations below (Eq. 2, Eq. 3):

$$\rho_b \text{ (g/cm}^3\text{)} = m_{bulk} / V_{bulk} \quad (\text{Eq. 1})$$

$$\% \text{Porosity} = (1 - \rho_b / \rho_s) \times 100 \quad (\text{Eq. 2})$$

$$\% \text{Volume shrinkage} = \left(1 - \frac{V_a}{V_g}\right) \times 100 \quad (\text{Eq. 3})$$

where ρ_b is the bulk density of synthesized silica aerogel and ρ_s is the density of solid skeleton. With respect to former studies ρ_s can be assumed as (2.2 g)/cm³ (1). V_a and V_g in the Eq. 3 denote the volumes of the samples after drying and before the solvent exchange, respectively (4, 23).

Fourier Transform Infrared Spectroscopy (FTIR) (PERKIN ELMER Spectrum 100, USA) was used between the wavenumber range of 500 - 4000 cm⁻¹ to identify the chemical compositions of the samples.

The morphology of the samples was observed by using scanning electron microscope (SEM) (PHILIPS, XL 30S FEG) with a magnification rate of 5000.

To investigate the thermal stability of the samples, thermo-gravimetric analysis (TGA) was performed using a TA Instruments SDT Q600 operating at a heating rate of 5 °C/min from room temperature to 600 °C under a nitrogen atmosphere.

Hydrophobicity of the aerogels was examined by measuring the contact angle (θ) of the water droplet with the sample surface.

$$\theta = 2 \tan^{-1} \left(\frac{2h}{w} \right) \quad (4)$$

where h is the height and w is the width of the water droplet touching the aerogel surface. Travelling micropores were used for measuring h and w (24). Figure 2 demonstrates that small values of contact angle (<90°) correspond to high wettability whereas large contact angles represent hydrophobicity.

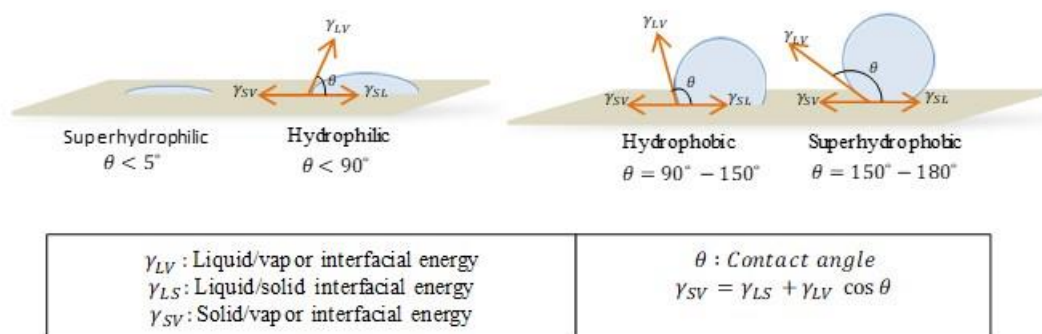


Figure 2: Water drop - surface contact angle.

RESULTS and DISCUSSION

Up to now, many studies have been directed their attention toward the enhancement of aerogel production under ambient conditions for further commercialization of these materials. One of the key issues about ambient pressure drying in aerogel production is to conserve monolithic structure during drying. Hence, removing of entrapped solvents from the wet gel while avoiding shrinkage and maintaining the porous structure become today's prior challenge. Imidazolium-based ionic liquid incorporated into silica aerogel synthesis in this study with the intention of promoting spring-back effect against deterioration of porous structure during ambient drying. On the other hand, an amine-containing silica co-precursor APTES was involved in the preparation of aerogels for the purpose of reducing required time for synthesis. To explore the interaction between ionic liquid and APTES, two different samples were prepared using same components and same procedure with or without ionic liquid and various physical and chemical characterizations were conducted as follows.

Physical Properties

To compute the density values of the samples with standard errors by using Eq.1, the weight and volume of the samples was measured three times. Calculated density, porosity and percentage of volumetric shrinkage of the SG-IL and SG were tabulated in Table 1 with standard deviations. The sample SG-IL had small volume shrinkage and lower density ($\rho_{SG-IL}=0.45 \text{ g/cm}^3$) whether the sample SG could not resist the capillary effect.

Table 1. Observations about the produced silica aerogels.

Sample ID	Density , g/cm^3 (Eq.1)	%Porosity (Eq.2)	%Volume Shrinkage (Eq.3)
SG-IL	0.45 ± 0.01	80 ± 0.012	8.50 ± 0.010
SG	1.23 ± 0.01	4480 ± 0.012	-

It can be stated that the sample prepared without ionic liquid may contain dense regions in the silica network and has large pores. Since ionic liquid controls the solvent evaporation by ensuring elasticity on the pore walls, without ionic liquid as a support, solid skeleton of the silica cluster of sample SG drastically collapse due to the severe capillary tension. Besides, IL-embedded sample SG-IL exhibit high porosity with relatively low density. Also, we can say that it remained stable after drying process as the total volumetric shrinkage has a relatively low value of 8.5%.

Visual observations

Physical appearance

Figure 3 demonstrates the physical form of two samples SG-IL and SG after ambient pressure drying. As seen from the figure, the physical appearance of silica aerogels dried under ambient conditions strongly affected by the addition of ionic liquid through the synthesis. The sample SG-IL appeared in monolithic form without cracks while the sample SG was grounded into pieces because of capillary forces occurred during the solvent evaporation. On the other hand, the low surface tension and lower vapor pressure of ILs make it possible to sustain the physical stability of silica framework after the subsequent solvent exchange and drying steps.

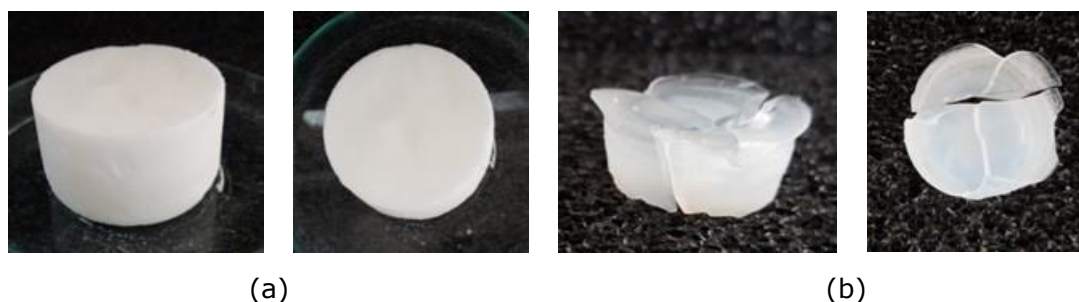


Figure 3. Physical appearances of the samples SG-IL(a) and SG (b).

Gelation time

Reduction the required time for complete gelation became a major interest in recent studies. An appreciable decrease in a total synthesis time of silica aerogels brings about considerable advantages to these materials for practical purposes. It was suggested in the study of Dourbash *et al.* that developing one-step sol-gel process instead of time-consuming two-step processes would be preferable (22). In this study, it was observed that amine-rich APTES used as co-precursor eliminated the need for additional base catalyst in the sol-gel method. Regarding its marvelous ability in catalyzing the condensation reactions, APTES significantly reduced to gelation time. Necessary times for complete gelation in this study are observed as 3 min and 6 min for the samples of SG-IL and SG, respectively which indicates that ionic liquid supports the catalytic activity of APTES in the condensation reactions, synergistically.

Morphological properties

Although the physical appearance of the first sample points out the desired monolithic form under ambient conditions has been achieved, it was not conclusive in visualizing the morphological differences in the porous structures of the samples with or without ionic liquid. The SEM images of the synthesized silica aerogels prepared with/without ionic liquid are demonstrated in Figure 4. Sample SG-IL exhibits a three-dimensional porous network consisting of the spherical silica clusters indicates that typical microstructure pattern of silica aerogels was obtained. Sample SG, however, results in the insufficient porous network. As it is very weak to withstand capillary pressure, it exhibits a rigid structure.

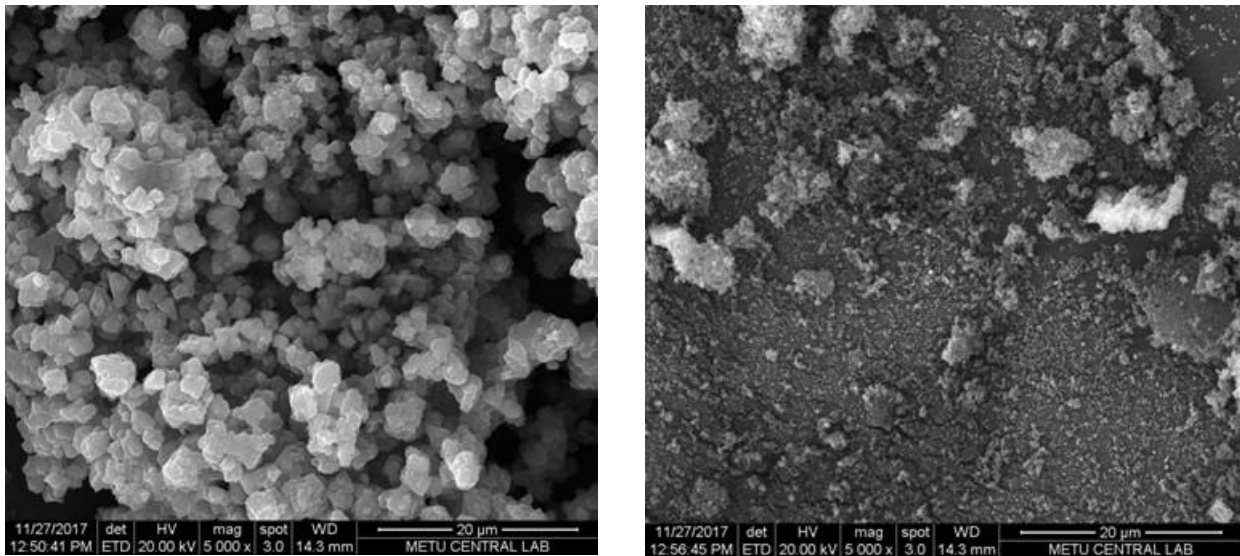


Figure 4. SEM Images of the samples SG-IL and SG with magnification rate is 5000.

FTIR spectra

FTIR analysis was conducted to reveal related chemical bonding in silica aerogel synthesis and shown in Figure 5.

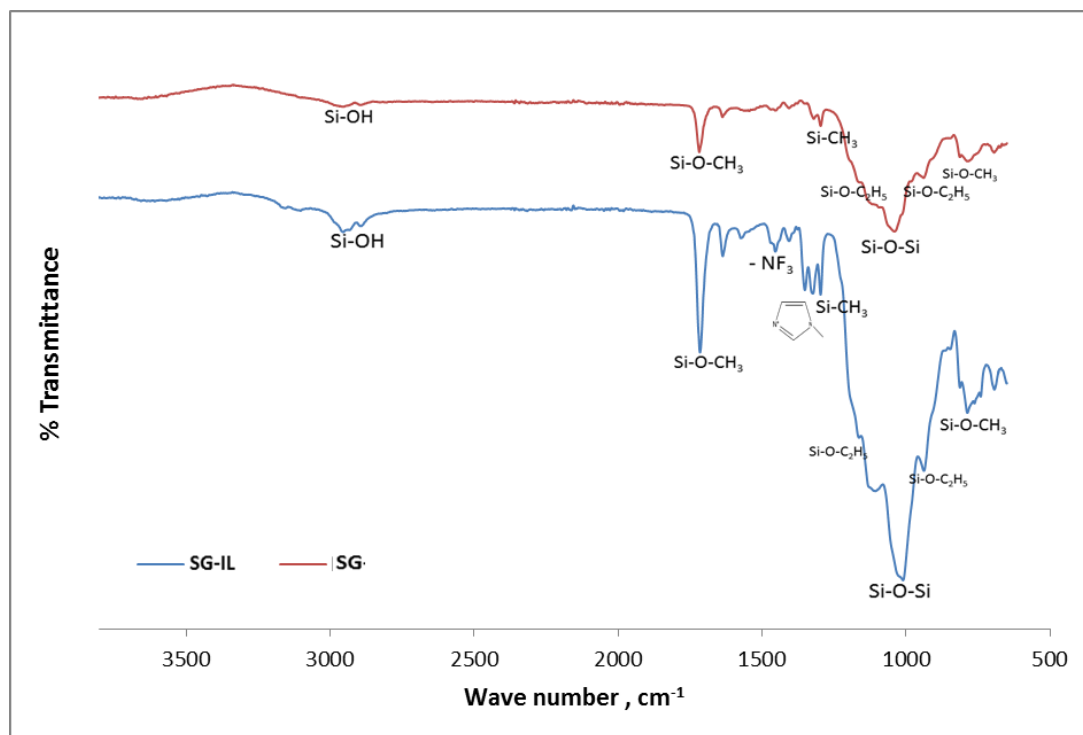


Figure 5. FTIR Spectral results of the samples SG-IL and SG.

The absorption peaks around 1080 cm^{-1} may be attributed to Si-O-Si bonding confirming the development of the silica network. It is obvious from the spectrum that intensity of the Si-O-Si vibrations increases prominently with the addition of ionic liquid to the sample. Hence, it can be affirmed that ionic liquid is incorporated into the structure of silica aerogels and can improve network formation. The peaks observed the around 1352 cm^{-1} and 1471 cm^{-1} may be related to the existence of the imidazolium-based ionic liquid. Distinct Si-CH₃ peaks observed around 785 cm^{-1} and 1350 cm^{-1} verify stronger gel network and attachment of the methyl groups to the gel surface may indicate a successful surface modification with MEMO.

TGA/DTG analysis and thermal stability

Based on the previous characterizations applied through the study, it can be seen that ionic liquids enhanced the formation and conservation of the monolithicity of the samples as well as it served as a catalyst and accelerated the condensation rate in the sol-gel method. TGA analysis was conducted to investigate the effect of the ionic liquid on the thermal stability of the samples. Figure 6 demonstrates the thermal degradation of the Sample SG-IL and Sample SG with respect to temperature. The sample prepared without ionic liquid exhibited a thermal decomposition temperature around $144\text{ }^{\circ}\text{C}$. It lost almost 12% of its total weight up to this temperature. Confinement ionic liquid, however, increased the thermal stability of the sample SG-IL by extending the thermal degradation temperature of the sample up to $381\text{ }^{\circ}\text{C}$.

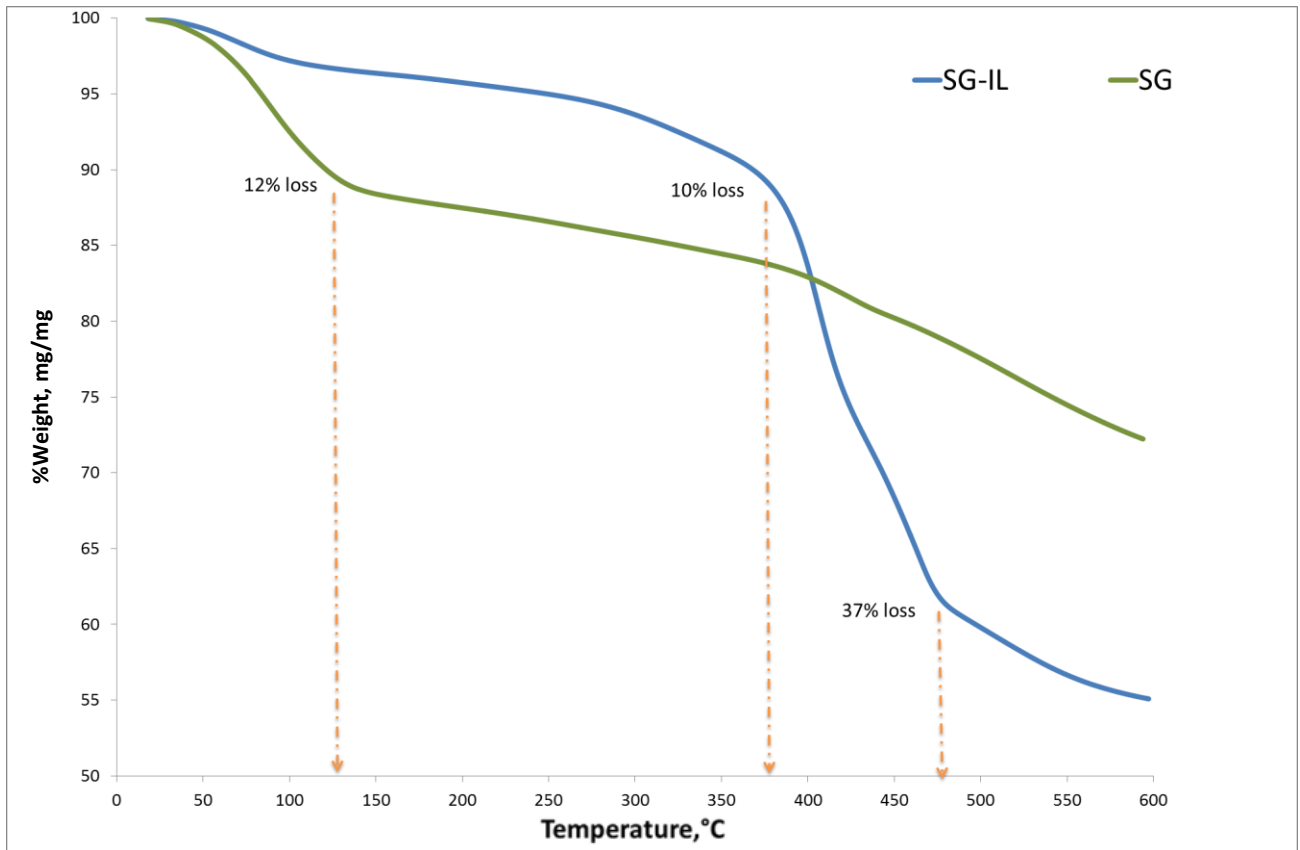


Figure 6. TGA analysis results of the samples SG-IL and SG.

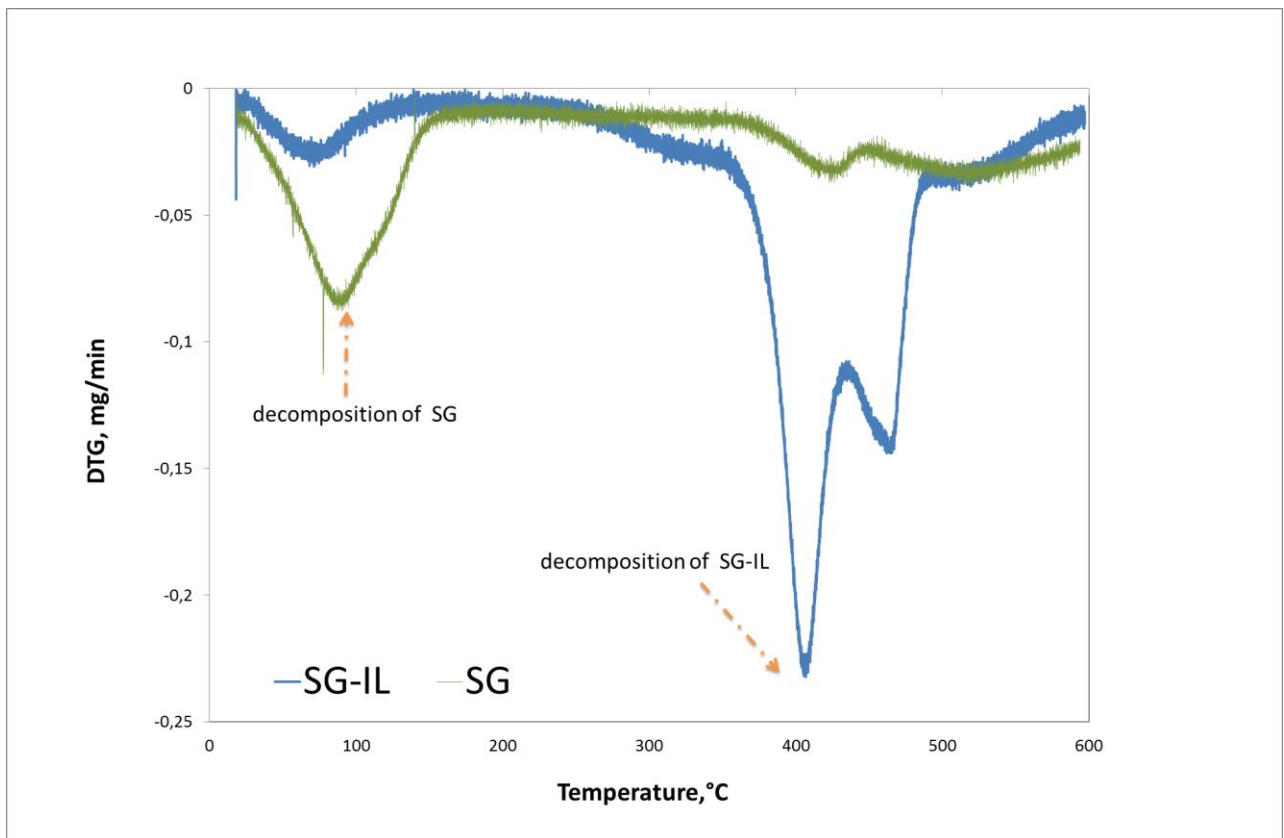


Figure 7. DTG analysis results of the samples SG-IL and SG.

Then, a drastic change in the total weight of the sample of SG-IL after the temperature of 381°C which leads almost two times higher weight loss comparing with the other sample (SG), can be attributed to the degradation of imidazolium based ionic liquid. The results also confirmed with the DTG analysis given in Figure 7. For the ionic liquid embedded samples, having good thermal stability within the temperature range of 0°C- 380°C, can bring the material a valuable characteristic when considering possible target applications such as household thermal insulation material, as catalyst supports or as adsorbents.

Hydrophobicity and contact angle

The surface modification was performed by replacing hydroxyl groups on the surface of the silica gel with the alkyl groups for the purpose of reducing the surface energy of the gel and turns the sample into hydrophobic form. MEMO was selected as silylating agent and the water re-balancing ability of dried sample SG-IL was determined by measuring the contact angle of water droplet on the sample surface and presented in Figure 8. Then again, surface energy of the sample SG-IL was determined 15.47 mN/m by the same measurement. For the sample SG, however, contact angle measurement could not be performed because of its fractural structure.

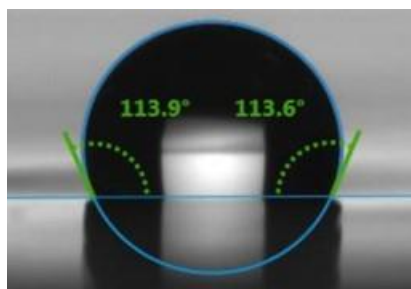


Figure 8. The contact angle value of the sample SG-IL

CONCLUSION

In this study, monolithic silica gels were synthesized by taking advantage of the synergistic effect of imidazolium-based short-chain ionic liquid and amine-rich co-precursor APTES in the sol-gel method. With the help of these agents, required gelation time was reduced down to 3 min. This collective interaction also eliminated the need for the repeated surface modification periods and hydrophobic characteristic of the samples was achieved by applying one-step surface modification only. Ionic liquid also served as a drying control agent during the solvent evaporation of the gel and contributed in retaining solid skeleton network of silica particles with highly homogeneous pore distribution after ambient pressure drying. It was also observed that thermal stability of these samples highly affected by the presence of ionic liquid.

Due to the obtained superior physical properties such as low density and highly porous structure and high thermal stability, the synthesized samples can be promising candidates for a wide range of applications to be used as thermal and acoustic insulators, as adsorbents (especially in the CO₂ capture applications due to the amine containing functional groups of the samples) as

catalyst supports or as energy storage barriers. Synthesizing the samples as monolithic blocks with controlled shape, have also gave them the opportunity to be used more easily for any particular application.

For the further studies, it can be suggested that using ionic liquids along with an amine mediated precursor through the silica aerogel preparation can be an attractive approach.

REFERENCES

1. Li M, Jiang H, Xu D, Hai O, and Zheng W. Low density and hydrophobic silica aerogels dried under ambient pressure using a new co-precursor method. *Journal of Non-Crystalline Solids*. 2016 Nov; 452: 187–193.
2. Li Z, Cheng X, He S, Shi X, Gong L, and Zhang H. "Aramid fibers reinforced silica aerogel composites with low thermal conductivity and improved mechanical performance. *Compos. Part A Appl. Sci. Manuf.* 2016; 84: 316–325.
3. Laskowski J, Milow B, and Ratke L. Aerogel-aerogel composites for normal temperature range thermal insulations. *Journal of Non-Crystalline Solids*. 2016; 441: 42–48.
4. Soleimani Dorcheh A and Abbasi M. H. Silica aerogel; synthesis, properties and characterization. *J. Mater. Process. Technol.* 2008; 199-1:10–26.
5. Parmenter K. E. Mechanical properties of silica aerogels. *Journal of Non-Crystalline Solids*. 1996 Nov; 1: 79–189
6. Amonette J. E, and Matyáš J. Functionalized silica aerogels for gas-phase purification, sensing, and catalysis: A review. *Microporous Mesoporous Materials*. 2017; 250: 100–119.
7. Maleki H, Dur L, and Garc C. A. Synthesis and Biomedical Applications of Aerogels: Possibilities and Challenges Hajar. *Advance Colloid Interface Science*. 2016; 236: 1–27.
8. Buratti C, Merli F, and Moretti E. Aerogel-based materials for building applications: Influence of granule size on thermal and acoustic performance. *Energy Buildings*. 2017; 152: 472–482.
9. Berthon-Fabry S, Hildenbrand C, Ilbizian P, Jones E, and Tavera S. Evaluation of lightweight and flexible insulating aerogel blankets based on Resorcinol-Formaldehyde-Silica for space applications. *Eur. Polym. J.* 2017 May; 93: 403–416.
10. Wu C. M, Lin S. Y, and Chen H. L. Structure of a monolithic silica aerogel prepared from a short-chain ionic liquid. *Microporous Mesoporous Matererials*. 2012; 156: 189-195.
11. Hilonga A, Kim J. K, Sarawade P. B, and Kim H. T. Low-density TEOS-based silica aerogels prepared at ambient pressure using isopropanol as the preparative solvent. *J. Alloys Compd.* 2009; 487: 744–750.
12. Wei T. Y, Chang T. F, Lu S. Y, and Chang Y.C. Preparation of monolithic silica aerogel of low thermal conductivity by ambient pressure drying. *J. Am. Ceram. Soc.* 2007; 90: 2003–2007.
13. Garay Martinez R, Goiti E, Reichenauer G, Zhao S, Koebel M, and Barrio A. Thermal assessment of ambient pressure dried silica aerogel composite boards at laboratory and field scale. *Energy Buildings*. 2016; 128: 111–118.
14. Mazraeh-Shahi Z. T, Shoushtari A. M, Abdouss M, and Bahramian A. R. Relationship analysis of processing parameters with micro and macro structure of silica aerogel dried at ambient pressure. *Journal of Non-Crystalline Solids*. 2013; 376: 30–37.
15. Yang H, Kong X, Zhang Y, Wu C, and Cao E. Mechanical properties of polymer-modified silica aerogels dried under ambient pressure. *Journal of Non-Crystalline Solids*. 2011; 357: 3447–3453.
16. Pons A, Casas L, Estop E, Molins E, Harris K. D. M, and Xu M. A new route to aerogels: Monolithic silica cryogels. *Journal of Non-Crystalline Solids*. 2012; 358: 461–469.

17. Ivanova M, Kareth S, Spielberg E. T, Mudring A. V, and Petermann M. Silica ionogels synthesized with imidazolium based ionic liquids in presence of supercritical CO₂. *J. Supercrit. Fluids*. 2014; 105: 60–65.
18. Zhang J, Ma Y, Shi F, Liu L, and Deng Y. Microporous and Mesoporous Materials Room temperature ionic liquids as templates in the synthesis of mesoporous silica via a sol – gel method. 2009; 119: 97–103.
19. Ivanova M, Kareth S, and Petermann M. Supercritical carbon dioxide and imidazolium based ionic liquids applied during the sol–gel process as suitable candidates for the replacement of classical organic solvents. *J. Supercritical Fluids*. 2017 July; 132: 76–82.
20. Karout A and Pierre A. C. Silica xerogels and aerogels synthesized with ionic liquids. 2007; 353: 2900–2909.
21. Karout A and Pierre A. C. Silica gelation catalysis by ionic liquids. *Catal. Commun.* 2009; 10-4: 359–361.
22. Dourbash A, Motahari S, and Omranpour H. Effect of water content on properties of one-step catalyzed silica aerogels via ambient pressure drying. *Journal of Non-Crystalline Solids*. 2014; 405: 135–140.
23. Li S, Ren H, Zhu J, Bi Y, Xu Y, and Zhang L. Facile fabrication of superhydrophobic, mechanically strong multifunctional silica-based aerogels at benign temperature. *Journal of Non-Crystalline Solids*. 2017; 473: 59–63.
24. Yu H, Liang X, Wang J, Wang M, and Yang S. Preparation and characterization of hydrophobic silica aerogel sphere products by co-precursor method. *Solid State Sci.* 2015; 48: 155–162.



Quinaldinium Chlorochromate(VI), (QnCC) Catalyzed Oxidation of Alcohols with Periodic Acid Under Solvent-Free Conditions and Microwave Irradiation

Melek Canbulat Özdemir^{1*}  

Department of Chemistry, Faculty of Science, Gazi University, Ankara/Turkey.

Abstract: The atom efficient synthesis of quinaldinium chlorochromate(VI), $C_{10}H_9NH[CrO_3Cl]$, (QnCC) was performed by using a 1:1:1 stoichiometric amounts of CrO_3 , HCl (aq) and quinaldine. QnCC was isolated in 99% yield as an orange crystalline solid and characterized with FT-IR, 1H -NMR, and ^{13}C -NMR. An efficient, selective, and environmentally friendly periodic acid (H_5IO_6) oxidation of alcohols catalyzed by QnCC (2 mol%) is described. Oxidation reactions of some primary and secondary alcohols to their corresponding aldehydes and ketones were performed under solvent-free conditions at room temperature and MW irradiation in high to excellent yields.

Keywords: Alcohols, quinaldinium chlorochromate, periodic acid, solvent-free, microwave irradiation.

Submitted: November 24, 2017. **Accepted:** April 09, 2018.

Cite this: Canbulat Özdemir M. Quinaldinium Chlorochromate(VI), (QnCC) Catalyzed Oxidation of Alcohols with Periodic Acid Under Solvent-Free Conditions and Microwave Irradiation. JOTCSA. 2018;5(2):679–90.

DOI: <http://dx.doi.org/10.18596/jotcsa.357452>.

***Corresponding author:** E-mail address: ozmelek@metu.edu.tr; T: +90 312 2102640; F: +90 312 2102646

¹Present Address: Department of Environmental Engineering, Faculty of Engineering, Middle East Technical University, 06800, Ankara, Turkey.

INTRODUCTION

The selective oxidation of alcohols to carbonyl compounds is a foremost functional group conversion in synthetic organic chemistry, due to the key role of this process in the production of valuable compounds for pharmaceutical, dyestuff, and agrochemical industries (1–4). Thus, to date, various oxochromium(VI) amine complexes have been commonly used as stable oxidizing agents for selective oxidation of alcohols with high efficiency. Some of them are pyridinium chlorochromate, pyridinium fluorochromate, pyridinium dichromate, dipyrazinium tris(fluorotrioxochromate), 1-decyl-4-aza-1-azonia-bicyclo[2.2.2]-octane chlorochromate, 3,5-dimethylpyrazolium fluorochromate, and triethylammonium chlorochromate (5–11).

In traditional oxidation processes, volatile organic solvents and stoichiometric amounts of chromium(VI) based reagents have widely been used though these reagents are highly toxic, and environmentally polluting. Therefore, the search for effective catalytic oxidation systems that use clean, inexpensive primary oxidant with high activity and selectivity are still needed (12–18). Recently, several methods have been reported for the catalytic oxidation of various alcohols by using periodic acid (H_5IO_6) as co-oxidant and CrO_3 or oxochromium(VI) reagents as catalysts (19–22). However, these oxidation reactions are generally carried out in a solvent and long reaction times are required. Additionally, microwave-assisted oxidation reactions coupled with solvent-free conditions have gained special attention as environmentally friendly processes in recent years (23–25).

We have described for the first time the quinaldinium fluorochromate (QnFC)-catalyzed periodic acid oxidation of various alcohols under solvent-free conditions (26). Herein, in order to continue to develop environmentally benign synthetic protocols, oxidation of alcohols with periodic acid catalyzed by quinaldinium chlorochromate (QnCC) under solvent-free conditions at room temperature and under microwave irradiation has been investigated.

MATERIAL AND METHODS

All chemicals were supplied by Aldrich, Merck, and Fluka and used without further purification. Thermo Fischer Scientific Nicolet iS10 FT-IR spectrometer was used to obtain an FT-IR spectrum of QnCC. 1H NMR and ^{13}C NMR spectra were recorded on Bruker Avance III- 400 MHz spectrometer (in $DMSO-d_6$). Microwave-assisted oxidation reactions were performed with professional multimode Microsynth-Milestone oven.

Economic synthesis of quinaldinium chlorochromate

Chromium(VI) oxide (5 mmol, 0.5 g) was taken in a beaker and hydrochloric acid (37%, 5 mmol, 0.41 mL) was added dropwise with continuous stirring for 10 min. This was followed by dropwise addition of 1.0 mL of water under stirring over a period of 15 min, leading to a clear orange colored solution. The solution was cooled in an ice-water bath for 15 min and quinaldine (5 mmol, 0.71 mL) was added dropwise to this solution with vigorous stirring. The whole was allowed to stand first in an ice-water bath for 30 min. and then at room temperature for 30 min. The compound was washed twice with hexane, kept under suction until moderately dried. Yield: 99.0%, mp: 139 °C.

FT-IR (ATR, cm^{-1}) ν_{max} = 3292, 3030, 2884, 2610, 1645, 1603, 1546, 1492, 1412, 1382, 1307, 1231, 1150, 1047, 938, 880, 770, 726, 639, 615. $^1\text{H-NMR}$ (400 MHz, DMSO-d_6 , ppm): δ = 2.85 (s, 3H); 7.77-8.15 (m, 6H); 8.78 (s, 1H) . $^{13}\text{C-NMR}$ (100 MHz, DMSO-d_6 , ppm) δ = 22.02; 122.45; 123.25; 126.39; 127.96; 128.60; 132.81; 142.75; 158.19.

General procedure for oxidation of alcohols with QnCC/ H_5IO_6 under solvent-free conditions

A mixture of the corresponding alcohol (1 mmol) and QnCC (2 mol%) was ground in a mortar until it became homogeneous and H_5IO_6 (1.1 mmol) was introduced slowly. The progress of the reaction was monitored by using TLC on silica gel (n-hexane-ethyl acetate: 2:1). Upon completion of the reaction, work up with ether (3x15 mL) and evaporation of the solvent gave the corresponding carbonyl compounds.

General procedure for microwave-assisted oxidation of alcohols with QnCC/ H_5IO_6 under solvent-free conditions

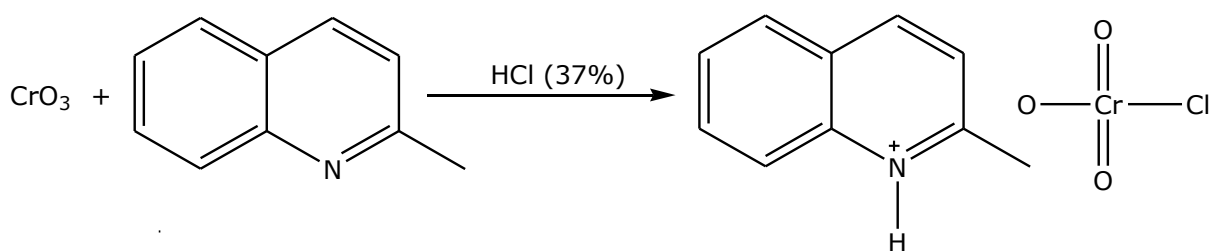
The mixture of the corresponding alcohol (1 mmol), QnCC (2 mol %), and H_5IO_6 (1.1 mmol) was irradiated and heated to 50 °C in the microwave reactor by the time indicated in Table 1. The progress of the reaction was monitored by using TLC on silica gel (n-hexane-ethyl acetate: 2:1). At the end of the exposure to microwaves, the mixture was cooled to room temperature and extracted with ether (3x15 mL) and evaporation of the solvent gave the corresponding carbonyl compounds.

Yields were based on the isolation of the 2,4-dinitrophenylhydrazones (DNPH) (Table 1). Since the carbonyl compounds are all known compounds, the qualitative identification of the

products was made by comparing of the melting points of the 2,4-dinitrophenylhydrazones with those of corresponding DNPH derivatives.

RESULTS AND DISCUSSION

An atom-efficient and environmentally benign procedure for the synthesis of quinaldinium chlorochromate was accomplished by using stoichiometric amounts of hydrochloric acid, chromium trioxide, quinaldine and minimum amount of water. Using a minimum amount of water leads to waste minimization by preventing the loss of QnCC through its solubility. Thereby, quinaldinium chlorochromate(VI) was obtained in 99.0 % isolated yield as an orange-colored crystalline solid (Scheme 1).



Scheme 1: Atom-efficient synthesis of quinaldinium chlorochromate.

The structure of QnCC was confirmed by FT-IR, $^1\text{H-NMR}$, and $^{13}\text{C-NMR}$. The FTIR spectra of QnCC shows the characteristic bands of the quinaldine moiety and chlorochromate anion, where appropriate. In particular, characteristic bands of chlorochromate anion are observed at *ca.* $\nu = 938$, and 880 cm^{-1} corresponding to $\nu_{\text{asym}}(\text{Cr}=\text{O})$, and $\nu_{\text{sym}}(\text{Cr}=\text{O})$, respectively (27). The singlet observed at $\delta 2.85$ at the $^1\text{H-NMR}$ spectra of QnCC proved three aliphatic protons of a methyl group and multiple peak at $\delta 7.77\text{--}8.15$ substantiated the presence of aromatic protons of quinaldinium cation. In addition, singlet at $\delta 8.78$ verified the N-H proton of quinaldinium cation. The obtained $^{13}\text{C-NMR}$ spectral data for QnCC was compatible with its the structure.

Quinaldinium chlorochromate (QnCC) supported on alumina has previously been reported as a powerful oxidant for the oxidation of various alcohols (28). However, the need to use an excess amount of QnCC/alumina (alcohol to oxidant ratio 1:1.5) in CH_2Cl_2 to perform the oxidation is a major drawback, due to toxicity and environmentally polluting effects of chromium based reagents and chlorinated solvents. Therefore, practical and efficient oxidation processes that produce smaller amounts of toxic chromium waste are still in demand.

In the absence of QnCC, benzyl alcohol was oxidized to benzaldehyde by using 1.1 equivalents of H_5IO_6 under solvent-free conditions at room temperature, and under MW irradiation. The yields of the reactions obtained were 15% after 180 min at room temperature, and 22% after 2 min under MW irradiation.

In order to determine the optimum amount of QnCC which maximizes the yield of oxidation reaction, benzyl alcohol was oxidized to benzaldehyde by using 1.1 equivalents of H_5IO_6 and 0.5%, 1.0%, 1.5%, 2.0%, 2.5%, 3.0%, 3.5%, and 4.0% moles of QnCC under solvent-free conditions at room temperature. The use of 2.0 mol% QnCC almost maximized the yield of reaction (Figure 1). To avoid the use of excess amount of chromium compound, 2 mol% of QnCC was used for the oxidation of all the alcohols.

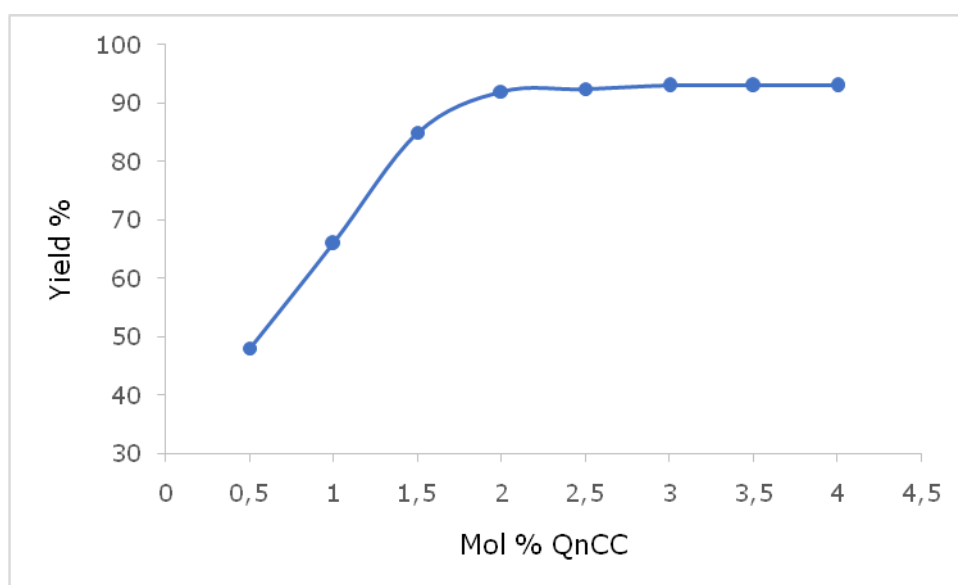


Figure 1: The influence of QnCC amount on the yield of oxidation reaction of benzyl alcohol.

Having determined the optimum QnCC amount which maximizes the yield of reaction, the oxidation reactions of various alcohols were examined. As shown in Table 1, all the primary benzylic alcohols (1-7) were almost quantitatively and selectively oxidized to corresponding aldehydes and all the secondary alcohols (8-11) to ketones with high to excellent yields in very short reaction times with the H_5IO_6 /QnCC system.

In the present procedure the chemoselectivity of the oxidation reactions of some primary benzylic alcohols into the corresponding aldehydes was provided by using 1.1 equivalents of H_5IO_6 and 2% mol of QnCC (Table 1). As a result, no overoxidation to carboxylic acids has been observed. On the other hand, in the oxidation reactions carried out by using with 2.2 equivalents of H_5IO_6 , and catalytic (2% mol) amount of QnCC almost quantitative conversion to carboxylic acids with the yields of 85% (8 min), 91% (5 min), 92% (5 min), and 90%(15

min) has been observed for the oxidation of benzyl alcohol, 4-methylbenzyl alcohol, 4-chlorobenzyl alcohol, and 4-nitrobenzyl alcohol, respectively, at room temperature under solvent-free conditions.

The solvent-free oxidation reactions of all the alcohols with the $H_5IO_6/QnCC$ system were also carried out under MW irradiation at 50 °C. The results are presented in Table 1 in comparison to the results of the reactions performed at room temperature. It is notable that the yields of the products are close to each other, but the reactions which were carried out under MW irradiation occur much faster than the reactions carried out at room temperature.

Table 1: Solvent-free oxidation of alcohols by QnCC/H₅IO₆ at room temperature and under MW irradiation.

Entry	Substrate	Product ^a	QnCC/H ₅ IO ₆ (RT)		QnCC/H ₅ IO ₆ (MW)		Mp(°C) of DNPH	
			Time (min)	Yield (%) ^b	Time (sec)	Yield (%) ^b	Found	Reported (29)
1	Benzyl alcohol	Benzaldehyde	1	92	30	96	237	237
2	4-Methylbenzyl alcohol	4-Methylbenzaldehyde	1.5	100	20	98	232	233
3	4-Chlorobenzyl alcohol	4-Chlorobenzaldehyde	2	95	30	97	265	265
4	4-Methoxybenzyl alcohol	4-Methoxybenzaldehyde	2	98	10	98	254	254
5	4-Nitrobenzyl alcohol	4-Nitrobenzaldehyde	5	85	40	90	319	320
6	3-Chlorobenzyl alcohol	3-Chlorobenzaldehyde	2	100	30	100	247	248
7	3-Nitrobenzyl alcohol	3-Nitrobenzaldehyde	3	83	40	90	291	292
8	4-tert-Butylcyclohexanol	4-tert-Butylcyclohexanone	6	99	30	98	155	156
9	Cyclohexanol	Cyclohexanone	6	89	40	90	162	162
10	Menthol	Menthone	12	86	40	88	146	146
11	Cycloheptanol	Cycloheptanone	3	97	20	92	148	148

^a All the products have already been reported in the literature and were defined by melting points of their 2,4-dinitrophenylhydrazones. ^b Isolated yields based on their corresponding dinitrophenylhydrazones.

The recyclability of QnCC was determined by performing the oxidation reaction of benzyl alcohol to benzaldehyde. Subsequent to the end of the first run of the oxidation reaction, benzaldehyde was separated from QnCC with diethyl ether extraction. Then, the fresh charges of H_5IO_6 (1.1 mmol) and benzyl alcohol (1.0 mmol) were introduced for each subsequent run of the oxidation reactions. The yields thus obtained were 92%, 90%, 89%, 83%, and 70%, respectively. As shown in Figure 2, QnCC is recyclable for 4 runs without a considerable reduction in its catalytic performance.

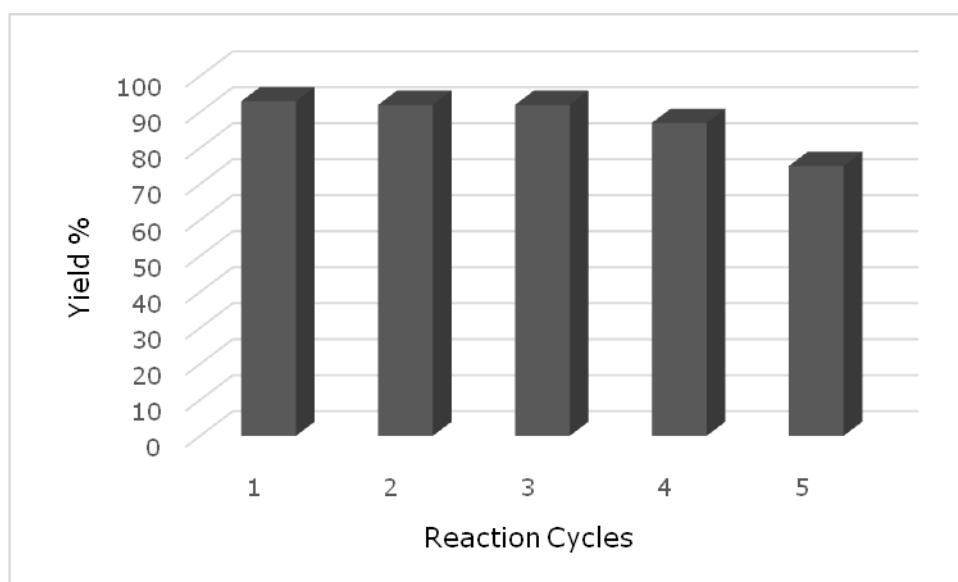
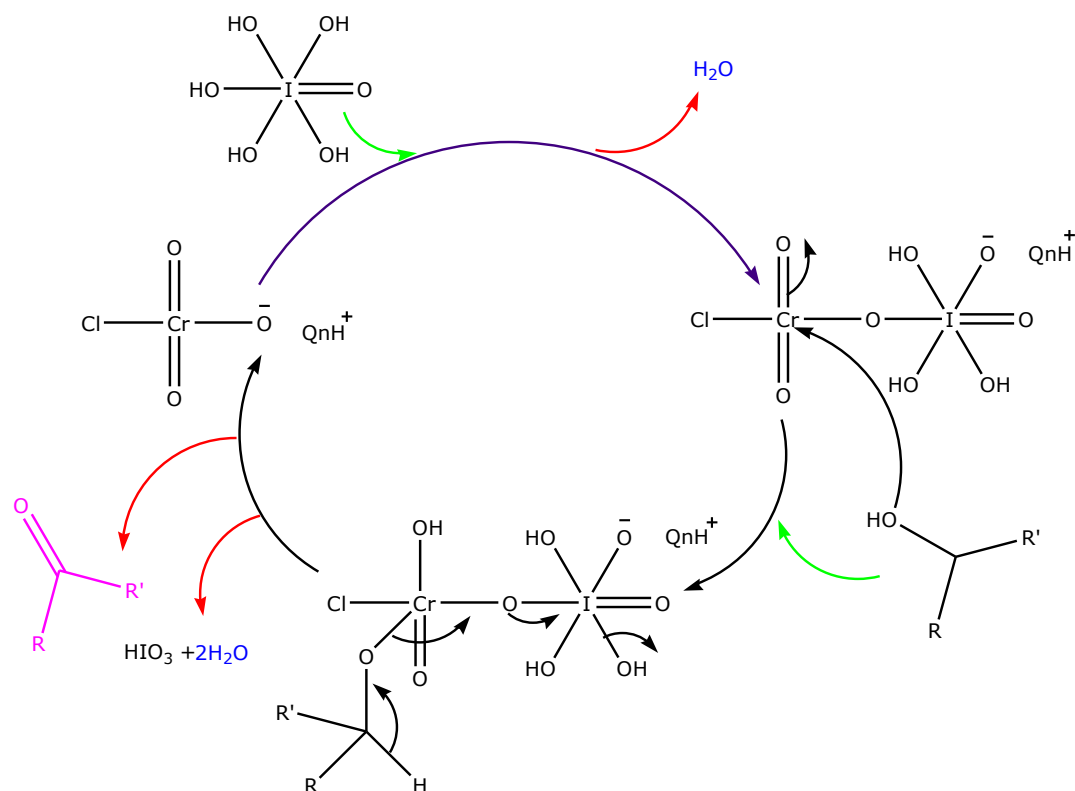


Figure 2: Recyclability of the QnCC for oxidation of benzyl alcohol.

The mechanism of periodic acid oxidation reactions catalyzed by chromium(VI) reagents has not been exactly clarified. However, based on the previously reported mechanism (20,22), it may be presumed that the QnCC/ H_5IO_6 system may form chlorochromateperiodate which is possibly a more efficient oxidant than the chlorochromate (Scheme 2). Besides, Cr(VI) may keep its oxidation state during the reaction until all periodic acid is consumed (30).



Scheme 2: The recommended mechanism for QnCC catalyzed the periodic acid oxidation of alcohols.

To show the catalytic activity of QnCC/H₅IO₆ system, we compared the results of our study with the known data from the literature for the oxidation of benzyl alcohol (Table 2). As shown in Table 2, QnCC-catalyzed periodic acid oxidation has many advantages such as the amount of chromium(VI) compound used, solvent-free conditions, relatively short reaction times, and high to excellent yields of products in comparison with previous reports. Compared to our previous work (26), a catalytic amount of QnCC (2 mol%) required for the oxidation reactions is less than that of QnFC (3 mol%), and the reactions which were carried out under MW were completed in very short reaction times with high yields.

Table 2: Comparison of oxidation of benzyl alcohol with periodic acid catalyzed by chromium(VI) based oxidants.

Catalyst	H ₅ IO ₆ (equiv.)	Catalyst (mol %)	Conditions	Time (min.)	Yield (%)	Ref.
QnCC	1.1	2	Solvent-free, rt	2	92	-
QnCC	1.1	2	Solvent-free, MW	0.5	96	-
QnFC	1.1	3	Solvent-free, rt	2	93	(26)
PCC	1.1	2	CH ₃ CN, 0 °C to rt	120	72	(20)
Cr(acac) ₃	1.5	10	CH ₃ CN, rt	180	93	(31)

CONCLUSION

In conclusion, QnCC effectively catalyzes the selective oxidation of alcohols with periodic acid under solvent-free conditions at room temperature and under MW irradiation. The QnCC/H₅IO₆ system is simple, effective, versatile and selectively oxidizes various alcohols in very short reaction times with high to excellent yields. In addition, this system leads to much less chromium contamination while preserving the all known advantages of chromium(VI) based oxidant. Remarkably, QnCC can be recycled for 4 times without notable loss of its catalytic performance. From the environmental point of view, this new catalytic system can be evaluated as a green protocol for the oxidation of alcohols.

REFERENCES

1. Larock RC. *Comprehensive organic transformations: A guide to functional group preparations*. Wiley-VCH; 1999.
2. Li G, Enache DI, Edwards J, Carley AF, Knight DW, Hutchings GJ. Solvent-free oxidation of benzyl alcohol with oxygen using zeolite-supported Au and Au – Pd catalysts. *Catal Letters*. 2006;110(1–2):7–13.
3. Ren P, Fu X, Zhang Y. Carbon quantum dots-TiO₂ nanocomposites with enhanced catalytic activities for selective liquid phase oxidation of alcohols. *Catal Letters*. 2017;147(7):1679–85.
4. Fardjahromi M, Moghadam M, Tangestaninejad S, Mirkhani V, Mohammadpoor-Baltork I. Manganese (III) salophen supported on nanosilica triazine dendrimer as a selective heterogeneous catalyst for oxidation of alcohols with sodium periodate. *J Iran Chem Soc*. 2017;14(6):1317–23.
5. Corey EJ, Suggs JW. Pyridinium chlorochromate. An efficient reagent for oxidation of primary and secondary alcohols to carbonyl compounds. *Tetrahedron Lett*. 1975;16(31):2647–50.
6. Bhattacharjee MN, Chaudhuri MK, Dasgupta HS, Roy N, Khathing DT. Pyridinium fluorochromate; A new and efficient oxidant for organic substrates. *Synthesis (Stuttg)*. 1982;1982(7):588–90.
7. Corey EJ, Schmidt G. Useful procedures for the oxidation of alcohols involving pyridinium dichromate in aprotic media. *Tetrahedron Lett*. 1979;20(5):399–402.
8. Şendil K, Özgün B. Dipyrazinium tri(fluorotrioxochromate): An efficient oxidant for organic substrates. *Monatshefte für Chemie*. 2006;137(12):1529–33.
9. Hajipour AR, Bagheri HR, Ruoho AE. Oxidation of alcohols with 1-decyl-4-aza-1-azonia-bicyclo[2.2.2]-octane chlorochromate under conventional and solvent-free conditions. *Russ J Org Chem*. 2006;42(6):844–8.
10. Bora U, Chaudhuri MK, Dey D, Kalita D, Kharmawphlang W, Mandal GC. 3,5-Dimethylpyrazolium fluorochromate(VI), C₅H₈N₂H[CrO₃F], (DmpzHFC): A convenient new reagent for oxidation of organic substrates. *Tetrahedron*. 2001;57(12):2445–8.
11. Mansoor SS, Shafi SS. Oxidation of aliphatic alcohols by triethylammonium chlorochromate in non-aqueous medium - A kinetic and mechanistic study. *Arab J Chem*. 2014;7(3):312–8.
12. Bai C, Li A, Yao X, Liu H, Li Y. Efficient and selective aerobic oxidation of alcohols catalysed by MOF-derived Co catalysts. *Green Chem*. 2016;18(4):1061–9.

13. Aryanejad S, Bagherzade G, Farrokhi A. A nanoscale Cu-metal organic framework with Schiff base ligand: Synthesis, characterization and investigation catalytic activity in the oxidation of alcohols. *Inorg Chem Commun.* 2017;81:37-42.
14. Hatefi-Ardakani M, Saeednia S, Pakdin-Parizi Z, Rafeezadeh M. Efficient and selective oxidation of alcohols with tert - BuOOH catalyzed by a dioxomolybdenum (VI) Schiff base complex under organic solvent-free conditions. *Res Chem Intermed.* 2016;42(10):7223-30.
15. Hajian R, Alghour Z. Selective oxidation of alcohols with H₂O₂ catalyzed by zinc polyoxometalate immobilized on multi-wall carbon nanotubes modified with ionic liquid. *Chinese Chem Lett.* 2017;28(5):971-5.
16. Dijkman A, Marino-Gonzalez A, Payeras AM, Arends IWCE, Sheldon RA. Efficient and Selective Aerobic Oxidation of Alcohols into Aldehydes and Ketones Using Ruthenium / TEMPO as the Catalytic System. *J Am Chem Soc.* 2001;123(28):6826-33.
17. Elhamifar D, Yari O, Karimi B. Highly ordered mesoporous organosilica-titania with ionic liquid framework as very efficient nanocatalyst for green oxidation of alcohols. *J Colloid Interface Sci.* 2017;500:212-9.
18. Matsumoto T, Ueno M, Wang N, Kobayashi S. Recent advances in immobilized metal catalysts for environmentally benign oxidation of alcohols. *Chem. Asian J.* 2008;3(2):196-214.
19. Zhao M, Li J, Song Z, Desmond R, Tschäen DM, Grabowski EJJ, et al. A novel chromium trioxide catalyzed oxidation of primary alcohols to the carboxylic acids. *Tetrahedron Lett.* 1998;39(30):5323-6.
20. Hunsen M. Pyridinium chlorochromate catalyzed oxidation of alcohols to aldehydes and ketones with periodic acid. *Tetrahedron Lett.* 2005;46(10):1651-3.
21. Hunsen M. Carboxylic acids from primary alcohols and aldehydes by a pyridinium chlorochromate catalyzed oxidation. *Synthesis (Stuttg).* 2005;15:2487-90.
22. Hunsen M. Fluorochromate-catalyzed periodic acid oxidation of alcohols and aldehydes. *J Fluor Chem.* 2005;126(9-10):1356-60.
23. Martins NMR, Martins LMDRS, Amorim CO, Amaral VS, Pombeiro AJL. Solvent-free microwave-induced oxidation of alcohols catalyzed by ferrite magnetic nanoparticles. *Catalyst.* 2017;7(7):1-18.
24. Şendil K, Özgün H, Üstün E. Two new 1,1,3,3-tetramethylguanidinium halochromates (C₅H₁₄N₃CrO₃X)(X: Cl, F): efficient reagents for oxidation of organic substrates under solvent-free conditions and microwave irradiation. *J Chem.* 2016;2016:1-8.
25. Ghorbani-Vaghei R, Veisi H, Amiri M. Microwave-assisted oxidation of alcohols with N,N,N, N-Tetrabromobenzene-1,3-disulfonamide and poly(N-bromobenzene-1,3-disulfonamide) under solvent-free conditions. *J Chinese Chem.* 2007;54(5):1257-60.
26. Özdemir MC, Özgün HB. Economic synthesis of quinaldinium fluorochromate(VI), (QnFC), and solvent-free periodic acid oxidation of alcohols catalyzed by QnFC. *Turkish J Chem.* 2014;38(1):63-9.
27. Stammreich H, Sala O, Kawai K. Vibrational spectrum and force constants of the monochlorochromate ion. *Spectrochim Acta.* 1961;17(2):226-32.
28. Değirmenbaşı N, Özgün B. Quinaldinium chlorochromate supported on alumina: A new and efficient reagent for the oxidation of alcohols. *Monatshefte für Chemie.* 2003;134(12):1565-9.
29. Furniss BS, Hannaford AJ, Smith PWG, Tatchell AR. Vogel's textbook of practical organic chemistry. John Wiley & Sons, Inc.; 1989.
30. Okumura A, Kitani M, Murata M. Kinetic studies of the catalytic oxygen exchange of chromate ions with water by periodate ions. *Bull Chem Soc Jpn.* 1994;67(6):1522-30.
31. Xu L, Trudell ML. A mild and efficient oxidation of alcohols to aldehydes and ketones with periodic acid catalyzed by chromium (III) acetylacetonate. *Tetrahedron Lett.* 2003;44(12):2553-5.



Removal of Zinc from an Aqueous Solution Using Micellar-Enhanced Ultrafiltration (MEUF) with Surfactants

Deniz ŞAHİN TAŞ 

Gazi University, Faculty of Science, Department of Chemistry, 06500, Ankara, TURKEY

Abstract: In the present study, the optimum conditions have been investigated for the separation of Zn^{2+} ions from aqueous solution by micellar enhanced ultrafiltration (MEUF). For this purpose, the best conditions for the concentration of surface active agent in the feed solution (sodium dodecyl sulfate, SDS), cetyltrimethylammonium bromide (CTAB), triton-X-100 (TX100)), filtering pressure, stirring rate, and for the membrane porosity have been determined. It was found that the filtering pressure has a significant effect on the permeate flux but a relatively insignificant impact on rejection of Zn^{2+} . Permeate flux increased linearly with increasing pressure, ranging from $0.32 \text{ mLmin}^{-1}\text{m}^{-2}$ at 3 bar to $0.72 \text{ mLmin}^{-1}\text{m}^{-2}$ at 4 bar. The results showed that by adding SDS anionic surfactant, the permeate flux and the removal efficiency of zinc increased. Best results in terms of zinc rejection coefficient is 97.5 % at $5.0 \times 10^{-4} \text{ M}$ zinc concentration, $1.0 \times 10^{-2} \text{ M}$ SDS concentration ($\sim 8 \text{ cmc}$), stirring rate 500 rpm and transmembrane pressure 4 bar.

Keywords: Micellar Enhanced Ultrafiltration, SDS, CTAB, TX100, Zinc.

Submitted: January 31, 2017. **Accepted:** February 24, 2018.

Cite this: Şahin Taş D. Removal of Zinc from an Aqueous Solution Using Micellar-Enhanced Ultrafiltration (MEUF) with Surfactants. JOTCSA. 2018;5(2):691–700.

DOI: <http://dx.doi.org/10.18596/jotcsa.288933>.

***Corresponding author. E-mail:** dennoka1k@hotmail.com.

INTRODUCTION

Zinc is a trace element known to be an essential nutrient for life. It plays an important role in biological functions; however, if it is in excess, it has major effects on the human body, including abdominal pain, vomiting, nausea, cramps, cardiac irregularities, and increase the risk for development of an autoimmune disease, between others (1, 2). The heavy metal toxicity effects is highly dependent on the metal's chemical form. Generally, toxicities of aquo-ionic forms of metals are assumed to be more than those of the bound into particles or organic compounds. Zinc is found naturally in water. Industrial wastewaters with dissolved zinc compounds is released from battery production industries, galvanic industries, the fertilizer industry *etc.* Zinc compounds are widely used in industry. Zinc chloride is applied for dry cell batteries and paper-parchment production, zinc oxide used in production of creams, paints and catalysts, and zinc sulfate is especially applied as a fertilizer ingredient. The main source of Zn in the surface waters is from zinc leakages zinc pipes and/or rain pipes, consequential to the circulation of carbon-rich water. Car tires containing zinc and motor oil from zinc tanks which releases zinc compounds on the roads. Other source of zinc into water surface is use of fungicides and insecticides and zinc may be emitted from chemical waste dumps and landfills, or from dredge mortar (3, 4).

Several different techniques have been developed for use in removal of zinc from waters, such as chemical precipitation, ion-exchange, adsorption, coagulation–flocculation, flotation and electrochemical methods (5). These methods present deficiencies such as, quite energy intensive and operating costs. The main inconvenience of chemical precipitation is the formation of hydroxide precipitate and further, necessity of this compound disposal. Ion-exchange and adsorption are preferred methods for the purification of diluted effluents due to limited adsorption/ion exchange capacity. To overcome the aforementioned problems, a micellar enhanced ultrafiltration (MEUF) system was introduced. In this process, small pollutants are bound (for ionic pollutants) or solubilized (for organic pollutants) in large surfactant micelles which can be separated by ultrafiltration membranes with larger pore size. This process was studied for the removal of metal ions from dilute aqueous streams by researchers (6-10). Scamehorn *et al.* (11, 12) proposed that MEUF was very effective in removing multivalent metal ions and toxic organics simultaneously from industrial wastestreams with the use of anionic synthetic surfactants like sodium dodecyl sulfate. They conclude that system performance can be improved by reducing the feed concentration of metal ions, and/or increasing the surfactant concentration, transmembrane pressure, and membrane pore size (up to 5000 MWCO). The permeate concentration decreases with use of surfactant mixtures (non-ionic and anionic surfactants) and increases with addition of monovalent salts such as NaCl. The rejection rate increases with the following metal types: Ca^{2+} Cu^{2+} Zn^{2+} Cd^{2+} . In the removal of copper, zinc, and cadmium, rejection rates of 99+% were observed. Akita used in MEUF to remove zinc ions

from aqueous solutions (up to 0.5 mmol/L) include CPC, PONPE10 and SDS, the Zn²⁺ rejection were near to 0, 8.7, and 84.8% (13).

In this work, MEUF was used to remove zinc from aqueous solutions using the ultrafiltration membrane. The effects of some important parameters on metal percent rejection and permeate flux were investigated. These parameters include filtering pressure, the concentration of surface active agent, stirring rate, and for the membrane porosity. These results can be helpful in achieving the practical application of this process.

MATERIALS AND METHOD

Materials

All the chemicals used were of analytical reagent grade. Deionized water (DI) was used throughout the experiments. The stock solution of Zn (II) (1000 mg L⁻¹) was prepared by dissolving an appropriate amount of Zn(NO₃)₂·6H₂O (Merck) in DI water. SDS (Merck), CTAB (Aldrich), TX100 (Riedel) were used as supplied. The surfactant stock solutions (2%, v/v) were prepared by dissolving 2 mL of concentrated solution in deionized water.

Method

All experiments were carried out in a batch-stirred ultrafiltration cell (Amicon 8050, Millipore, USA; Figure 1). Two organic regenerated cellulose membranes with a molecular weight cut-off (MWCO) 1000 and 5000 Da obtained from Millipore were used for all the MEUF experiments. A new membrane was used for each test except in cases where the permeability of the used membrane could be fully recovered. A 30 mL feed solution was charged into the cell. The ultrafiltration was carried out at room temperature (28±2°C). Pressurized air was used to maintain the transmembrane pressure. The stirred cell was placed on a magnetic stirrer. The stirring speed was measured with a digital tachometer (Optic DT-838).

The first 5 mL of the permeate was discarded. The ultrafiltration was continued until 5 mL of sample remained in the retentate. 20 mL of permeate was collected and analyzed.



Figure 1. UF cell used in the experiments.

Surfactant concentration in the permeate samples $[S]_p$ was determined via surface tension measurements. The plot of surface tension (ordinate) as a function of the logarithm of surfactant concentration (abscissa) was constructed to determine the $[S]_p$.

Concentrations of Zn(II) ions in the feed and permeate were determined by flame atomic absorption spectrometry (VARIAN 240 FS, FAAS). The operating conditions were as follows: wavelength: 213.9 nm, lamp current: 7 mA, bandpass: 1.0 nm and fuel flow rate: 1.2 Lmin⁻¹. Deuterium lamp background correction was used. Determinations were performed in triplicate.

RESULTS and DISCUSSION

Effect of the surfactant concentration and membrane porosity

Penetration of the surfactant through the membranes to permeate flux is one of the main disadvantages of the MEUF process (14). Due to this disadvantage, the retention of the surfactant was investigated without addition of metal ion in the filtrated solution. For this purpose, the filtration of the surfactant solutions was performed. The results of ultrafiltration of aqueous surfactant solutions of different concentrations with regenerated cellulose membranes (1000-5000 Da) are shown in Table 1. The performance of the membranes is indicated in terms of initial surfactant retention and permeation rate during batch ultrafiltration (15). A general increase in surfactant retention with increase in feed concentration $[S]_i$ is observed during ultrafiltration with each membrane.

Concentration below critical micelle concentration (CMC), micelles are not absent so surfactant will be present as monomers. These monomers are able to form complex with the metal ions which can easily pass through the membrane. At smaller concentrations, due to the membrane effect, monomer attracts towards membrane and either adsorbed in pores or amasses on the membrane surface on a gel layers (16). When surfactant concentration increased up to CMC, the micelle formation provides binding sites to metal ions on the surface and the rejection of ions increases (17). On further increase in the concentration of surfactant, the formed micelles break into smaller aggregates of low aggregation size. These aggregates effectively bind the metal ions, after concentration of the metal ion also increase and pass through the membrane towards the permeate side (18, 19). Examination of the literature shows that the concentration of a surfactant in solution increases after the CMC and a second CMC occurs (20). These, undoubtedly, reflect change in size, shape, polydispersity and degree of concentration binding to binding to the micelle and also change rate of hydration (21). A second CMC exists where the aggregates gain positional order due to increased electrical repulsions among the micelles (22). According to Porte *et al* (23), the second CMC arises from a sphere to rod transition of the micelle geometry.

In our preliminary experiments, we determined to find the CMC of surfactants (not shown). CMCs for SDS, CTAB, and TX-100 using surface tension technique (our propositional method) were 8.1×10^{-3} , 1.14×10^{-3} and 3.6×10^{-4} mol L⁻¹, respectively. The permeate surfactant concentration were approximately equal to the CMCs for SDS and CTAB but about 2 times lower than CMC for TX-100. The difference can be explained in terms of the relative size of the TX-100 micelles. The CMC of TX-100 is lower and the aggregation number of micelles is greater (Table 1), so there are larger TX-100 micelles in a lower TX-100 concentration and the concentration in the retentate of TX-100 micelles may increase. The structural difference of used surfactants depends on their hydrophilicity as listed in Table 2, and an increase aggregation number caused by the decrease in hydrophilic chain length (24, 25) results in increasing the number of Zn²⁺ binding sites.

Table 1. Ultrafiltration of surfactant solutions.

[SDS] x10 ²	[CTAB] x10 ³	[TX100] x10 ³	[S] _p x10 ⁴		Permeation Rate (mLxmin ⁻¹)	
			1000 Da	5000 Da	1000 Da	5000 Da
2.00			21.00	29.00	0.361	0.750
5.00			-	33.00	-	0.670
10.00			38.00	43.00	0.273	0.550
20.00			-	52.00	-	0.360
30.00			52.00	60.00	0.070	0.170
	2.00		4.72	4.81	0.300	0.630
	5.00		4.75	4.85	0.294	0.610
	10.00		4.75	4.90	0.285	0.600
	20.00		4.79	4.90	0.280	0.540
	30.00		4.80	4.95	0.275	0.530
		0.50	0.64	0.94	0.350	0.630
		1.25	-	1.03	-	0.620
		2.50	0.67	1.12	0.347	0.600
		5.00	-	1.19	-	0.600
		7.50	0.77	1.30	0.346	0.600

Further increase in the membrane porosity, up to 5000 Da, resulted in a marginal increase in the permeation rate. Therefore, 5000 Da was selected as membrane porosity for further experimental works.

Table 2. Characteristics of selected surfactants.

Name	MW ^a (g/mol)	CMC (mM)	HLB ^b	Aggregation number ^c	MW of micelle ^d (g/mol)	Solubility ^e
SDS	288	8.1	40	80	23040	s
CTAB	364	1.14	-	-	-	s
TX-100	625	0.36	13.5	140	87500	s

^a MW: An average molecular mass, ^b HLB: hydrophilic–lipophilic balance, ^c Aggregation number of the micelle, ^d MW: molecular mass of the micelle, ^e s means readily soluble in water.

Effect of applied pressure

The pressure was varied from 3 to 4 bar, because the maximum operating pressure limit is 4 bar in our laboratory systems. The flow rates in different pressure and constant surfactant concentrations (Table 3) show same behaviors for each surfactant and help choose the most suitable transmembrane pressure force.

Table 3. Concentration of surfactant in the permeate and permeation rate as a function of applied pressure.

[S] _i	1.0x10 ⁻¹ M SDS		1.0x10 ⁻² M CTAB		2.5x10 ⁻³ M TX100	
Transmembrane Pressure (Bar)	3	4	3	4	3	4
[S] _p x10 ⁴	9.53	9.60	8.33	8.40	1.10	1.12
Permeation Rate (mLxmin ⁻¹)	0.32	0.72	0.34	0.75	0.46	0.89

No significant effect was observed on the permeate surfactant concentration if the pressure was increased from 3 to 4 Bar, but the permeation rate increased slightly. The permeate flux increased linearly with applied pressure at a constant surfactant concentration. This may be due to the fact that the operating pressure between retentate and permeate acts as effective driving force for membrane separation process. The increase of this could overcome the osmotic pressure and the resistance, thereby forcing more solution to filter through the membrane and leading to a higher permeate flux (26-28). At CMC, sites for binding of Zn²⁺ increased with increasing concentration of micelles near the membrane surface which may contribute to increase in rejection. The pressure can also vary according to the capacity of membrane to withstand (29, 30).

Effect of filtration speed

In order to determine the optimize sampling rate, the filtration speed was varied between 100 and 500 rpm, maintaining constant other experimental conditions (Table 4).

Table 4. Effect of filtration speed on the permeation rate and permeate surfactant concentration.

[S] _i	2.0x10 ⁻² M SDS	
Stirring Speed (rpm)	100	500
[S] _p x10 ⁴	0.30	0.28
Permeation Rate (mLxmin ⁻¹)	0.625	0.740

With the increase in the flow rate, velocity and turbulence near the membrane surface also increased. This leads to an increase in mass transfer across the membrane surface and hence an increase in the permeate flux. A filtration flow rate of 500 rpm, was the most adequate for the quantitative retention. Permeation rate of 500 rpm was chosen as optimal. Moreover, the maximum permeate flux is achieved by SDS. SDS has higher CMC and lower aggregation number of single SDS micelle than other surfactants as listed in Table 2, so it makes micellization more difficult and deposit fewer micelles in large size surface area of the membrane. Therefore, SDS was selected as surfactant for following experiences.

Ultrafiltration of Zn (II) ions with addition of surfactant (MEUF process)

The optimum conditions obtained during experimentation were; pressure: 4 bar, surfactant: SDS, flow rate: 500 rpm, and membrane porosity: 5000Da and temperature: 25°C, at which >96.0 % of rejection had been observed for the removal of zinc.

The applicability of MEUF method to zinc ions separation was examined by the use of SDS. As observed from the figure the rejection of Zn²⁺ increased from 10.85% to 97.5%, when removing the Zn²⁺ from the feed solution, we used the rejection rate R expressed as:

$$R\% = \left(1 - \frac{C_p}{C_i}\right) \times 100$$

where C_i is the initial concentration of the Zn²⁺ ion in the feed solution and C_p is the Zn²⁺ ion concentration in the permeate.

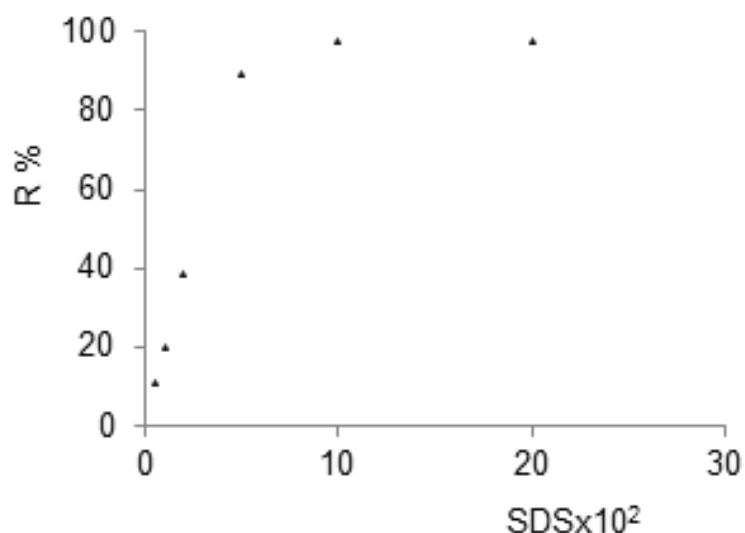


Figure 2. Effect of the initial SDS concentration on the rejection of Zn²⁺.

Figure 2 shows the variation of the Zn²⁺ rejection with the initial SDS concentrations ranging from 5.0×10^{-3} M up to 2.0×10^{-2} M at a constant Zn²⁺ concentration of 5.0×10^{-4} M and a constant pressure of 4 bar. This curve shows an immediate rise in the retention of Zn²⁺ with the increasing feed SDS concentration, which later reaches a plateau at a higher SDS concentration. The rejection may be attributed to the fact that the number of micelles increased with increase in SDS concentration. When the SDS concentration is below its cmc, micelles not found in the bulk solution and no separation of Zn²⁺ is expected in theory. When the SDS concentration reaches cmc level at the concentration polarization layer, many SDS monomers can be present large numbers of big-size micelles at the concentration polarization layer (31).

CONCLUSION

The MEUF process was successfully applied for removal of Zn²⁺ ions from aqueous solutions. A regenerated cellulose membrane was used for filtration process, while SDS was used as the surface active agent. The influence of some important parameters including the feed SDS concentration, membrane porosity, operating pressure, and filtration speed was investigated. The results revealed that the permeate flux increased with increasing, to optimal levels, transmembrane pressure and filtration speed. When the initial SDS concentration was the 6 mM, high Zn²⁺ rejection (97%) was obtained due to concentration polarization phenomena occurring at the membrane/solution interface.

REFERENCES

1. Goldfrank LR, Goldfrank's Toxicologic Emergencies, 8th Edition, McGraw Hill, New York, 2006.
2. Vega M, Augusto M, Talío MC, Fernández LP. Surfactant Enhanced Chemofiltration of Zinc Traces Previous to Their Determination by Solid Surphase Fluorescence American Journal of Analytical Chemistry, 2011 Dec; 2: 902-908.

3. Lenntech, www.lenntech.com/periodic/water/zinc/zinc-and-water.htm
4. Trivunac K, Sekulic Z and Stevanovic S. Zinc removal from wastewater by a complexation–microfiltration process. *J. Serb. Chem. Soc.* 2012; 77(11): 1661-1670.
5. Fu F and Wang Q. Removal of heavy metal ions from wastewaters: A review. *Journal of Environmental Management.* 2011 Mar; 92(3):407-413.
6. Rahmanian B, Pakizeh M and Maskooki A. Micellar-enhanced ultrafiltration of zinc in synthetic wastewater using spiral-wound membrane *Journal of hazardous materials.* 2010 Dec; 184(1-3) : 261-267.
7. Scamehorn J, Dunn Jr, Christian S. Simultaneous removal of dissolved organics and divalent metal cations from water using micellar-enhanced ultrafiltration. *Colloids and Surfaces,* 1989; 35(1): 49-56.
8. Hankins N, Hilal NO, O Ogunbiyi, Azzopardi B. Inverted polarity micellar enhanced ultrafiltration for the treatment of heavy metal polluted wastewater. *Desalination,* 2005; 185(1-3):185–202.
9. Landaburu-Aguirre J, García V, Pongrácz E, Keiski R. The removal of zinc from synthetic wastewaters by micellar-enhanced ultrafiltration: statistical design of experiments. *Desalination.* 2009 May; 240(1-3): 262-269.
10. Landaburu-Aguirre J, Pongrácz E, Perämäki, Keiski R. Micellar-enhanced ultrafiltration for the removal of cadmium and zinc: Use of response surface methodology to improve understanding of process performance and optimisation. *Journal of Hazardous Materials.* 2010 Aug; 180(1): 524–534.
11. Scamehorn, J.F., Ellington, R.T. and Christian, S.D. Removal of Multivalent Metal Cations from Water using Micellar-Enhanced Ultrafiltration, *Recent Separation Techniques-III, AICE symposium Series 250,* p. 48-58 (1986).
12. Scamehorn, J.F, Christian, S.D. and Ellington, R.T. Use of Micellar-Enhanced Ultrafiltration to Remove Multivalent Metal Ions from Aqueous Streams. In: *Surfactant-Based Separation Process,* edited by Scamehorn, J.F. and Harwell, J.H., *Surfactant Science Series, Vol. 33,* p. 29-51, Marcel Dekker, Inc., New York, NY (1989).
13. Akita S, Takeuchi H, Yang L. Micellar-enhanced ultrafiltration of gold(III) with nonionic surfactant. *J. Membr. Sci.* 1997; 133(2): 189-194.
14. Staszak K, Redutko B, Prochaska K. Removal of metal ions from aqueous solutions by micellar enhanced ultrafiltration (MEUF). *Polish Journal of Chemical Technology* 2010; 12(3):62- 65.
15. Shimoda K., In *Colloidal Surfactants (Ed). K. Shinoda, T. Nakagava, B. Tamamushi, and T. Isemura,* 1963 Chap I , Academic Press, N.Y.
16. Karate VD, Marathe KV. Simultaneous Removal of Nickel and Cobalt From Aqueous Stream by Cross Flow Micellar Enhanced Ultrafiltration. *J. Hazard. Mater.* 2008; 157 (2-3):464-471.
17. Bade R, Lee SH, Jo S, Lee HS, Lee SE. Micellar enhanced ultrafiltration (MEUF) and activated carbon fibre (ACF) hybrid processes for chromate removal from wastewater. *Desalination.* 2008; 229(1-3):264-273.
18. Danis U, Keskinler B. Chromate removal from wastewater using micellar enhanced crossflow filtration. *Desalination.* 2009; 249(3):1356-136.
19. Yenphan P, Chanachai A, Jiraratananon R. Experimental study on micellar-enhanced ultrafiltration (MEUF) of aqueous solution and wastewater containing lead ion with mixed surfactants. *Desalination.* 2010; 253:30-37.
20. Roberts, R.T. and Jones, G.P. *Mol. Cryst. Liq. Cryst. Liq.* 17, 281 (1972); Lindman, B. and Brun, B.J. *Colloid Interface Sci.* 42, 388 (1973); Bouaah, K. and Ache. H.J. *ibid.* 85, 2444 (1981); Klason, T. *NMR Studies of Solubilization, hydrocarbon chain motion and the state of water in amphiphile-water systems.* The Royal Institute of Technology Stockholm. (1983).
21. Kubota, Y., Kodama, M. and Miura, Second CMC [critical micelle concentration] of an aqueous solution of sodium dodecyl sulfate. IV. Fluorescence depolarization, *M. Bull. Chem. Soc. Jpn.,* 1973; 46: 100-103.

22. Kale, K. M.; Cussler, E.L. and Evans, Characterization of micellar solutions using surfactant ion electrodes, D.F. J. Phys. Chem., 1980; 84: 593-598.
23. Porte, G., Poggi, Y. Appell, J. and Moret, G. J. Phys. Chem, 1984; 88: 5703-5812.
24. Mackay RA., Solubilization, in: Martin J. Schick (Ed.), Nonionic Surfactants: Physical Chemistry, Surfactant Science Series, M. Dekker Inc., New York, pp. 1987308-314.
25. Mayers D, Surfactants in solution: micelle and related association phenomena, in: Surfactant Science and Technology, VCH Publishers Inc., 2008; 1988:104-106.
26. Zeng GM. et al., Micellar-enhanced ultrafiltration of methylene blue from dye wastewater via a polysulfone hollow fiber membrane. J. Membr. Sci. 2010; 310(1-2):149-160.
27. Park SJ, Yoon HH, Song SK. Solubilization and micellar-enhanced ultrafiltration of o-cresol by sodium dodecyl micelles. Korean J. Chem. Engg. 1997; 14: 233-240.
28. Purkait MK, Gupta SD, De S. Resistance in series model for micellar-enhanced ultrafiltration of eosin dye. J. Colloid Interface Sci. 2004; 270(2):496-506.
29. Chhatre AJ, Marathe KV. Dinamic analysis and optimization of surfactant dosage in micellar enhanced ultrafiltration of nickel from aqueous streams. Sep. Sci. Technol. 2006; 41(12):2755-2770.
30. Aguirre JL, Pongracz E, Keiski RL. Separation of cadmium and copper from phosphorous rich synthetic waters by micellar enhanced ultrafiltration. Sep. Purif. Technol. 2011; 81(1): 41-48.
31. Scamehorn JF, Harwell JH. Surfactant-Based Separation Processes Eds. Marcel Dekker, Inc., 1988 p 46.



Synthesis of Novel Chalcone Substituted Metallophthalocyanines: Electrochemistry, Spectroelectrochemistry, and Catalytic Oxidation of 2-mercaptoethanol

Hüseyin KARACA^{1,*}, Zehranur KURT¹, Serdar SEZER²

¹Department of Chemistry, Sakarya University, 54187 Sakarya, Turkey

²Tübitak Marmara Research Center, Chemistry Institute, 41470 Kocaeli, Turkey

Abstract Novel metallophthalocyanines (M = Zn, Co) carrying four (E)-1-(furan-2-yl)-3-(4-hydroxyphenyl)prop-2-en-1-one (chalcone) at the peripheral positions were synthesized. These complexes have been characterized by a combination of infrared spectroscopy (FT-IR), proton NMR (¹H-NMR), high resolution mass spectroscopy (HRMS), and ultraviolet visible (UV-Vis) spectrophotometry techniques. Also, cyclic voltammograms of these phthalocyanines were recorded and zinc phthalocyanine has one and cobalt phthalocyanine has two reduction reactions. Spectroelectrochemical investigation shows the ring-based reduction of MPcs. **Pc-7** cobalt(II) phthalocyanine was investigated as a catalyst in the catalytic oxidation of 2-mercaptoethanol. Turnover number, initial reaction rate, and the oxygen consumption were found in the catalytic oxidation of 2-mercaptoethanol as 16.6, 0.29, 2.52, respectively.

Keywords: Chalcone, phthalocyanine, UV-Visible spectrophotometry, cyclic voltammetry, 2-mercaptoethanol.

Submitted: November 13, 2017. **Accepted:** April 16, 2018.

Cite this: Karaca H, Kurt Z, Sezer S. Synthesis of Novel Chalcone Substituted Metallophthalocyanines: Electrochemistry, Spectroelectrochemistry, and Catalytic Oxidation of 2-mercaptoethanol. JOTCSA. 2018;5(2):701-18.

DOI: <http://dx.doi.org/10.18596/jotcsa.351559>.

***Corresponding author.** E-mail: karaca@sakarya.edu.tr

INTRODUCTION

Dyes and catalysts (1-4), organic photovoltaic devices (5-10), photodynamic therapy (11-14), and electrochemical applications (15-18) are phthalocyanines' widespread applications stemmed from peripheral functionalization of them. New properties of phthalocyanines arise from their conjugated macrocyclic units. The phthalocyanines should be soluble in water or in organic solvents in order to be used in these applications. Solubility could be improved by deriving on the peripheral or non-peripheral position of the phthalocyanines via substitution with large groups and by changing the metal on the core of the phthalocyanines (19-23).

Chalcones have the following characteristics: Anticancer, anti-inflammatory, antioxidant, cytotoxic, antimicrobial, analgesic and antipyretic (24,25). In recent years, chalcones are investigated as sensors and biological activities. The substituents on the periphery of phthalocyanines effect the physical and chemical properties. In this paper, the chalcone group with furan is directly attached to the phthalonitrile and then newly designed phthalocyanines were obtained (24-30). Chalcone group is electron-rich and has a high absorption property. It is estimated that the electron flow is realized from the chalcone groups located in the peripheral structure towards the phthalocyanine ring. Therefore, this gives usability to these molecules when they are used in dye sensitized solar cells as sensitizer. In addition, it is thought that electron-rich structure of chalcones positively contribute to the catalytic effect of phthalocyanine.

Mercaptans are thiol compounds and have environmental pollutant properties. The removal of mercaptans is not only important in terms of preventing environmental pollution. In addition, the mercaptan eliminates the effects of catalysts added to petroleum products such as petroleum and diesel to improve performance. So the mercaptan oxidation process is used to remove the thiols. Mercaptan oxidation occurs by means of oxygen in the air through catalysts. Both homogeneous and heterogeneous catalysts have been used for the oxidation of thiols (37-40).

In this study, novel MPcs having four chalcone moiety on their peripheral positions were synthesized and characterized by $^1\text{H-NMR}$, $^{13}\text{C-NMR}$, FTIR, MALDI-TOF, and UV/Vis spectra. These phthalocyanines have potential for applications as a multifunctional material in future studies.

EXPERIMENTAL

General

All experimental runs of this work were carried out with a pre-dried glass substrate heated at 150 °C for 1 hour and then cooled under an inert nitrogen atmosphere. Then the reaction solvents are distilled from the specified drying agents: 2-Dimethylaminoethanol, DMAE, N,N-Dimethylformamide, DMF (CaH₂). All fine chemicals were purchased from commercial suppliers and used without further purification. Melting points of the synthesized molecules were obtained on a Barnstead Electrothermal 9200 model melting point apparatus.

The thick-walled glass columns were used for flash column chromatography with flash grade silica (Merck Silica Gel 60). The reaction monitoring was achieved by thin layer chromatography (TLC) using pre-coated silica gel plates (Merck Silica Gel PF-254), visualized under UV-light and polymolybdenum phosphoric acid in ethanol as appropriate. All extracts obtained were dried over anhydrous magnesium sulfate and solvents was evaporated under vacuum by using a rotary evaporator.

Spectroscopy

The NMR spectra, ¹H NMR and ¹³C NMR were taken in deuterio chloroform (CDCl₃) and deuterio DMSO (DMSO-d₆) on a VARIAN Infinity Plus 300 MHz NMR spectrometer. Chemical shifts were expressed in ppm relative to CDCl₃ (δ7.26 and 77.0 for ¹H and ¹³C NMR, respectively) and DMSO-d₆ as the internal standards. For recording of Infrared spectra a Perkin Elmer Spectrum Two FT-IR spectrometer was used. HRMS and MALDI-TOF spectra were taken on Bruker Daltonics flexAnalysis. UV-Visible spectroscopy was measured on a Shimadzu UV 2600 model spectrophotometer.

Catalytic oxidation of 2-mercaptoethanol

A CyberScan DO 300 model dissolved oxygen meter was used to achieve catalytic oxidation of 2-mercaptoethanol. 0.152 micromole (μmol) Co(II) phthalocyanine (Co(II)Pc) (**Pc-7**) was dissolved in 50 mL of THF. The reaction vessel was bubbled with air in order to obtain oxygen saturation in the solution. 7,3 μL (1.52 millimole (mmol)) 2-mercaptoethanol was added. The molar ratio 2-mercaptoethanol as substrate to Co(II)phthalocyanine as catalyst was 10000:1. Then 1 mL of 0.25 wt% aqueous sodium hydroxide solution was added to the reaction vessel. The recording of the oxygen in the reaction mixture was started at the same time. Then time-dependent oxygen consumption was calculated. The catalytic activity of Co(II) phthalocyanine **Pc-7** is characterized by turnover number TON (conversion of mol oxygen per mol phthalocyanine), initial reaction rate (μmol oxygen consumption per second) and the oxygen consumption (μmol/min) (31-33).

Synthesis

Synthesis of (E)-1-(furan-2-yl)-3-(4-hydroxyphenyl)prop-2-en-1-one, (chalcone), 3

KOH solution (16 mL, 10%) and ethanol (32 mL) were mixed in a round-bottomed flask. 2 g of 4-hydroxybenzaldehyde (16.4 mmol) was added into the prepared solution and stirring was continued for 15 minutes. 1.9 g of 1-(furan-2-yl)ethanone **2** (17.2 mmol) was added into the stirring solution. The reaction mixture was continued to stir under nitrogen atmosphere for 24 h. The reaction mixture was poured in a beaker, dilute aqueous HCl solution was added for neutralizing. Solid was filtered over a sintered funnel, recrystallized in ethanol and chromatographed by eluting with ethyl acetate:hexane (ratio is 1:3). Greenish yellow solid (2.99 g, 21.9% chemical yield). Soluble in ethylacetate, acetonitrile and tetrahydrofuran. FT-IR (ATR, cm^{-1}): 3379, 3193, 3174, 3132, 3025, 2971, 2821, 1739, 1643, 1609, 1574, 1508, 1549, 1461, 1379, 1343, 1275, 1225, 1171, 1156, 1086, 1049, 1014, 988, 926, 881, 824, 766, 737. ^1H NMR (300 MHz, DMSO-d_6) δ 8.04 (dd, $J=1.76$, $J=0.59$, 1H), 7.75 (dd, $J=3.51$, $J=0.59$, 2H), 7.73-7.68 (m, 2H), 7.65 (s, 1H), 7.50 (d, $J=15.82$, 1H), 6.86-6.82 (m, 2H), 6.79-6.76 (m, 1H), ^{13}C NMR (75 MHz, DMSO-d_6) δ 177.4, 160.8, 158.1, 153.8, 148.7, 143.9, 131.6, 126.2, 119.5, 119.0 (overlapped 2C signals), 116.5, 113.3. Exact mass: 214.06. HRMS: m/z [M] calcd. For $\text{C}_{13}\text{H}_{10}\text{O}_3$: 214.06; found $[\text{M}+\text{H}]^+$ 215.7 and $[\text{M}+\text{Na}]^+$ 237.6

Synthesis of chalcone-substituted phthalonitrile, 5

Compound **3** (670 mg, 3.1 mmol) and 4-nitrophthalonitrile (540 mg, 3.1 mmol) were dissolved in 12 mL of DMSO in a round-bottomed flask and stirred under nitrogen atmosphere. Potassium carbonate (861 mg, 6.2 mmol) was added and stirring was continued for 24 h. The reaction was monitored by TLC. The mixture was poured into 50 mL cold water. The grey solid obtained was filtered through a sintered funnel, washed with methanol, and dried under vacuum, then separated by column chromatography by eluting with ethyl acetate : hexane (ratio is 1:3, v:v). (421 mg, 39.7% chemical yield). FT-IR (ATR, cm^{-1}): 3146, 3132, 3108, 3073, 3043, 2227, 1661, 1605, 1588, 1561, 1507, 1483, 1465, 1411, 1397, 1341, 1294, 1281, 1248, 1219, 1201, 1181, 1168, 1158, 1117, 1085, 1053, 1016, 983, 954, 930, 894, 884, 870, 854, 831, 826, 816, 764. ^1H NMR (300 MHz, CDCl_3) δ 8.13 (d, $J=8.49$, 1H), 8.07 (s, 1H), 7.98 (d, $J=7.91$, 2H), 7.87 (d, $J=12.59$, 2H), 7.80-7.67 (m, 2H), 7.48 (d, $J=9.08$, 1H), 7.27 (d, $J=8.20$, 2H), 6.80 (s, 1H). ^{13}C NMR (75 MHz, DMSO-d_6) δ 177.9, 161.2, 155.6, 153.8, 147.0, 142.4, 140.0, 135.8, 133.0, 131.1 (overlapped 2C signals), 122.3, 122.1 (overlapped 2C signals), 122.0, 121.1, 118.1 (overlapped 2C signals), 115.5, 113.0, 109.8, Exact mass: 340.08. HRMS: m/z [M] calcd. For $\text{C}_{21}\text{H}_{12}\text{N}_2\text{O}_3$: 340.33; found $[\text{M}+\text{H}]^+$ 341.4 and $[\text{M}+\text{Na}]^+$ 363.5

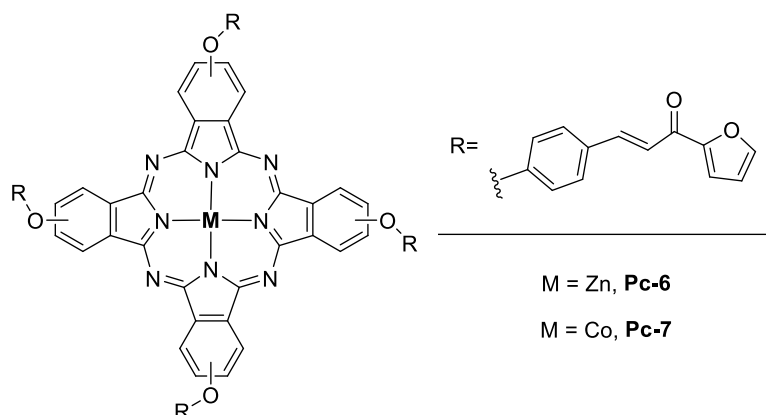
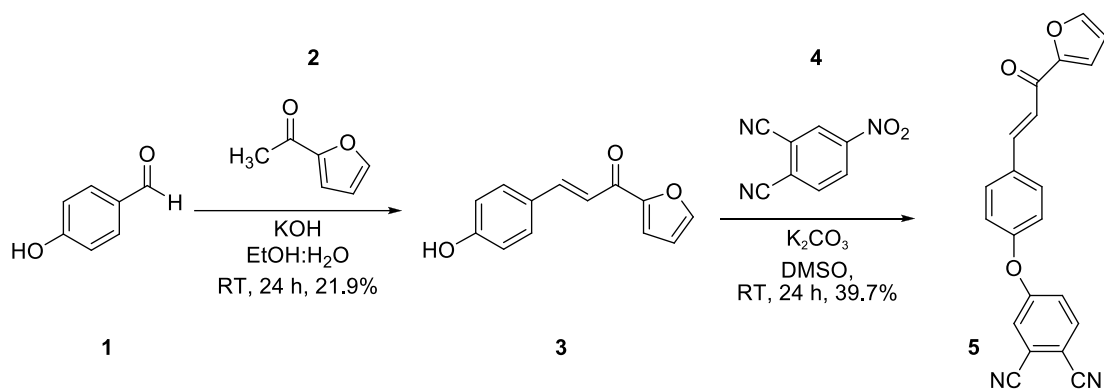
Synthesis of chalcone substituted zinc phthalocyanine, Pc-6

Compound **5** (200 mg, 0.59 mmol) was dissolved in the 6 mL mixture of DMAE/DMF (1:2 v:v). Zinc acetate dihydrate (32.6 mg, 0.15 mmol) was added to this stirring mixture, and then

refluxed under nitrogen atmosphere for 24 h. After finishing the reaction, methanol:water (ratio is 1:1 v:v) was used to stop the reaction and to obtain the precipitate. The obtained dark green solid was centrifuged. The solid was dried in a vacuum incubator and purified by column chromatography (elution with ethyl acetate : hexane (ratio is 1:3)). Dark green solid, mp >300 °C, (162.7 mg, 76.3% chemical yield). FT-IR (ATR, cm^{-1}):3125, 3063, 2924, 2853, 1768, 1713, 1657, 1591, 1504, 1464, 1387, 1358, 1333, 1310, 1292, 1259, 1228, 1165, 1086, 1044, 1013, 986, 943, 923, 883, 830, 759, 746. ^1H NMR (300 MHz, DMSO-d_6) δ 8.11-8.08 (m, 5H), 8.02-7.95 (m, 13H), 7.88-7.83 (m, 8H), 7.78-7.71 (m, 8H), 7.46-7.41 (m, 5H), 7.36-7.33 (m, 3H), 7.28-7.23 (m, 6H), 6.84-6.79 (m 4H). MALDI-TOF MS: m/z $[\text{M}]^+$ calcd. For $\text{C}_{84}\text{H}_{48}\text{N}_8\text{O}_{12}\text{Zn}$: 1422.78; found $[\text{M}+4\text{H}]^+$ 1426.8. Anal. Calc. for C, 70.71; H, 3.39; N, 7.85; O, 13.46; Zn, 4.58, Found: C, 70,7; H, 3.4; N, 7.8 %.

Synthesis of chalcone substituted Cobalt phthalocyanine, Pc-7

Compound **5** (220 mg, 0.65 mmol) was dissolved in a 6 mL mixture of DMAE/DMF (1:2). Cobalt(II) acetate tetrahydrate (41.4 mg, 0.16 mmol) was added to this stirring mixture then refluxed under the nitrogen atmosphere for 24 h. After finishing the reaction, methanol/water mixture (1:1 v:v) was used to stop the reaction and to obtain the precipitate. The obtained dark green solid was centrifuged. The solid was dried in a vacuum incubator and column chromatography was applied by eluting with ethyl acetate : n-hexane (ratio is 1:3 v:v). Dark green solid, mp >300 °C, (163 mg, 71.2% chemical yield). FT-IR (ATR System, cm^{-1}):3124, 2922, 1713, 1657, 1591, 1503, 1463, 1393, 1328, 1290, 1229, 1163, 1117, 1087, 1043, 1011, 955, 922, 882, 824, 751. MALDI-TOF MS: m/z $[\text{M}]^+$ calcd. For $\text{C}_{84}\text{H}_{48}\text{N}_8\text{O}_{12}\text{Co}$: 1424.3; found $[\text{M}-5\text{H}]^+$ 1419.2., Anal. Calc. For C, 71.04; H, 3.41; Co, 4.15; N, 7.89; O, 13.52., Found: C, 71.0; H, 3.4; N, 7.9 %.



Scheme 1. Synthesis of (E)-4-(4-(3-(furan-2-yl)-3-oxoprop-1-enyl)phenoxy)phthalonitrile **5** and target Pc scaffolds.

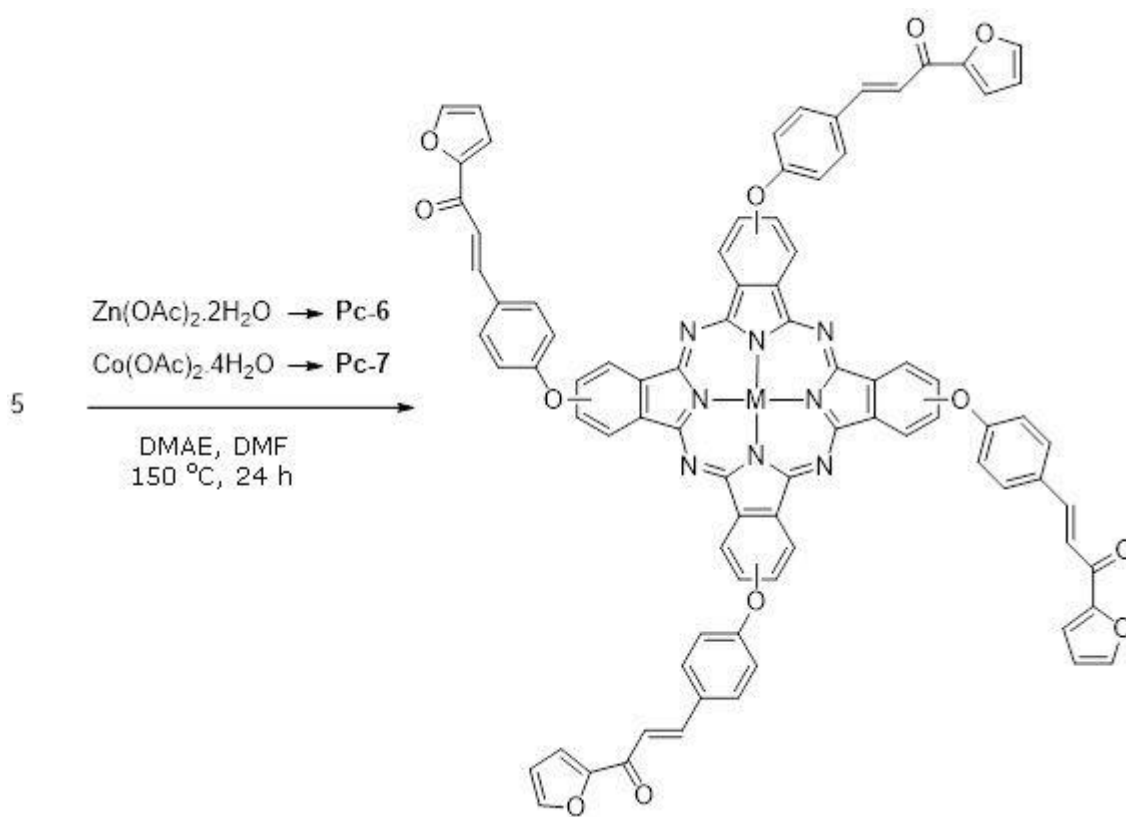
RESULTS AND DISCUSSION

Synthesis

The literature about phthalocyanine shows us that in order to enhance solubility and to prevent aggregation in organic media or water, bulky substituents could be used as peripheral or non-peripheral substituents of phthalocyanines. Furthermore, changing the metal in the phthalocyanine center affects the solubility of the phthalocyanines (1,26). We used chalcone **3** in this research as a bulky substituent synthesized from 4-hydroxybenzaldehyde and 2-acetylfuran in the mixture of ethanol and water by using KOH as the harsh alkaline media. The reaction has given 21.9% yield. Then the novel chalcone-derived phthalonitrile **5** was obtained from the nucleophilic aromatic substitution (**S_NAr**) type substitution reaction between chalcone **3** and 4-nitro-2,6-dicyanobenzonitrile **4**, after the column chromatographic isolation chemical yield was calculated as 39.7% (Scheme 1). Moreover, chalcone-derived phthalocyanines are newly discovered for synthesis and application. Chalcones have metal sensing potential along with biological activity. So, deriving metallo Pcs with chalcones will give solubility and these phthalocyanines will be mentioned in the new researches about biologic activity of Pcs and characteristics for sensing (25-30).

The molecular structures of **3** and **5** are described on the basis of ^1H and ^{13}C NMR spectra and approved by FT-IR spectra. The obtained phthalonitrile **5** was used for the synthesis of metallophthalocyanines **Pc-6** and **Pc-7**. In the synthetic routes of Pcs, $\text{Zn}(\text{OAc})_2 \cdot 2\text{H}_2\text{O}$ and $\text{Co}(\text{OAc})_2 \cdot 4\text{H}_2\text{O}$ salts were used to give center ions to Pcs respectively Zn^{2+} and Co^{2+} in the cyclotetramerization reaction of **5**, using DMEA as the catalyst at high temperature, an isomeric mixture of the desired metallo-Pcs **Pc-6** and **Pc-7** as expected (Scheme 2). The ^1H NMR spectra of **Pc-6** was recorded in DMSO-d_6 .

Pc-6 is soluble in DMSO, so the ^1H NMR spectra for **Pc-6** was carried out in DMSO-d_6 . **Pc-7** is well soluble in both DMSO and DMF. Both phthalocyanines are soluble in the mixture of DMSO-water. The structures of novel Pc compounds **Pc-6** and **Pc-7** were characterized by FTIR, UV-Vis, ^1H and ^{13}C NMR, and MALDI-TOF techniques.



Scheme 2. Synthesis of target phthalocyanines **Pc-6** and **Pc-7**

Structure Elucidation

The FT-IR spectrum of all synthesized species clearly shows that the products desired in all steps are obtained as intended.

The C=O carbonyl bonds stretching vibrations can be attributed to the bands appearing at 1661 cm^{-1} for compound **5**. After the cyclotetramerization of phthalonitrile **5**, this band shifts to 1713 cm^{-1} for both **Pc-6** and **Pc-7**. The band observed at 1605 cm^{-1} for compound **5** was assigned to C=C bonds stretching vibration. After the synthesis of phthalocyanines this band

shifts to 1657 cm^{-1} for both **Pc-6** and **Pc-7**. The FT-IR spectra of **5** gives us the specific information on the synthesis of chalcone-derived phthalonitrile shows the disappearance of the characteristic broad band at 3193 cm^{-1} which can be referred to hydroxyl on the chalcone **3**. Additionally, the strong characteristic single band at 2227 cm^{-1} can be referred to as the CN vibration which was observed clearly. The disappearance of this characteristic signal at 2227 cm^{-1} in the FT-IR spectrum of both **Pc-6** and **Pc-7** have been accepted as a proof of cyclotetramerization of the monomer **5**. The other bands under 2000 cm^{-1} do not have considering changes. Absorption bands at 3125, 3063, 2924, 2853, 1768, 1713, 1657, 1652, 1591, 1504, 1464, 1387, 1358, 1333, 1310, 1292, 1259, 1228, 1165, 1086, 1044, 1013, 986, 943, 923, 883, 830, 759, and 746 cm^{-1} are observed for **Pc-6**; these can be attributed to phthalocyanine's skeletal vibrations (31). **Pc-7** also shows very similar peaks between $751\text{--}3124\text{ cm}^{-1}$. Because of having aromatic structures for **3** and **5**, the NMR spectra of **3** and **5** have peaks in between 6-8 ppm, similar to starting phthalonitriles. The ^1H -NMR spectra of the phthalocyanines show the peaks in the aromatic region with small chemical shift differences (Figure 1).

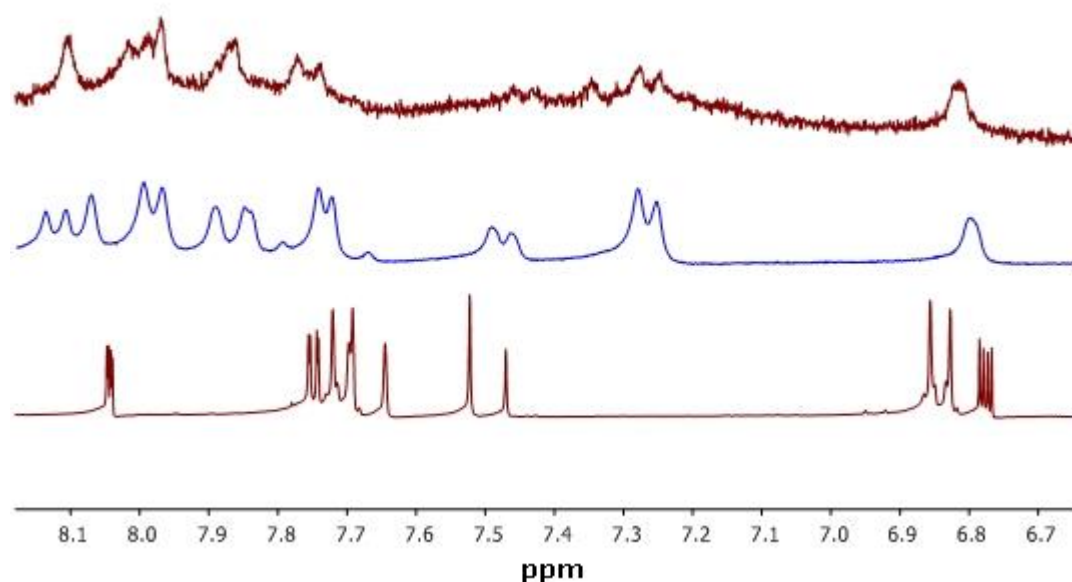


Figure 1. Expanded ^1H NMR spectrum of compounds **3** (bottom), **5** (middle) and **Pc-6** (top).

The mass spectra of phthalocyanines **Pc-6** and **Pc-7** were also acquired. Molecular ion peaks are identified as 1426.8 for $[\text{M}+4\text{H}]^+$ for **Pc-6** and as 1419.2 for $[\text{M}+4\text{H}]^+$ for **Pc-7**.

UV-Vis absorption spectra

The UV-Visible spectra of **Pc-6** and **Pc-7** are recorded in a mixture of DMSO: water (1: 4 ratio, v:v) in DMSO and a wide range of 10^{-6} M and 10^{-5} M . The electronic absorption spectrum in between 300 nm and 750 nm for both solvent systems can be seen in Figures 2 and 3, respectively. All of the absorption spectra show about 330 nm typical Soret band for **Pc-6** and **Pc-7**. Figures 2 and 3 show typical non-aggregated phthalocyanines. Figure 2a shows that **Pc-6** has a strong Q band at 678 nm in DMSO, having a shoulder at 641 nm with a vibronic band

at 611 nm and also a Soret band peaking at 334 nm. Figure 2b, on the other hand, shows that **Pc-6** has a strong Q band at 684 nm in the mixture of DMSO:water (1:4, v:v) with a vibronic band at 637 nm and also a Soret band peaking at 335 nm. Figure 3a shows **Pc-7** gives a weaker but clear Q band at 668 nm, having a shoulder at 617 nm and a Soret band at 332 nm. Figure 3b shows that **Pc-7** has a strong Q band at 679 nm in the mixture of DMSO:water (1:4) having a shoulder at 622 nm and also a Soret band at 329 nm. Non-aggregation behavior of both **Pc-6** and **Pc-7** phthalocyanines can be seen clearly in the insets of Figures 2 and 3. So both Pcs are able to use for water soluble applications.

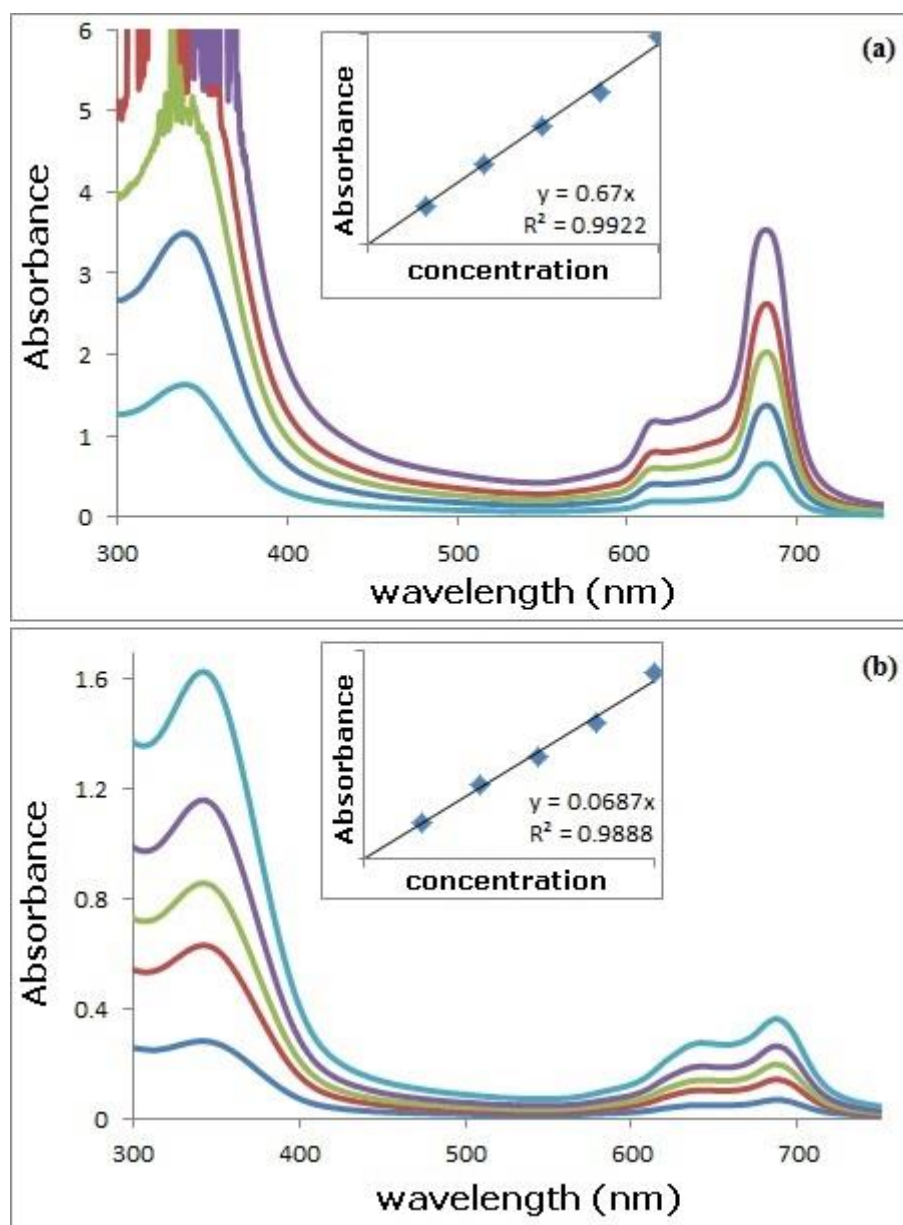


Figure 2. Comparison of the electronic absorption spectra in different concentration (from 10^{-6} M to 10^{-5} M) in the range of 400-750 nm for **Pc-6** (a) in DMSO, (b) in DMSO:water (1:4 ratio).

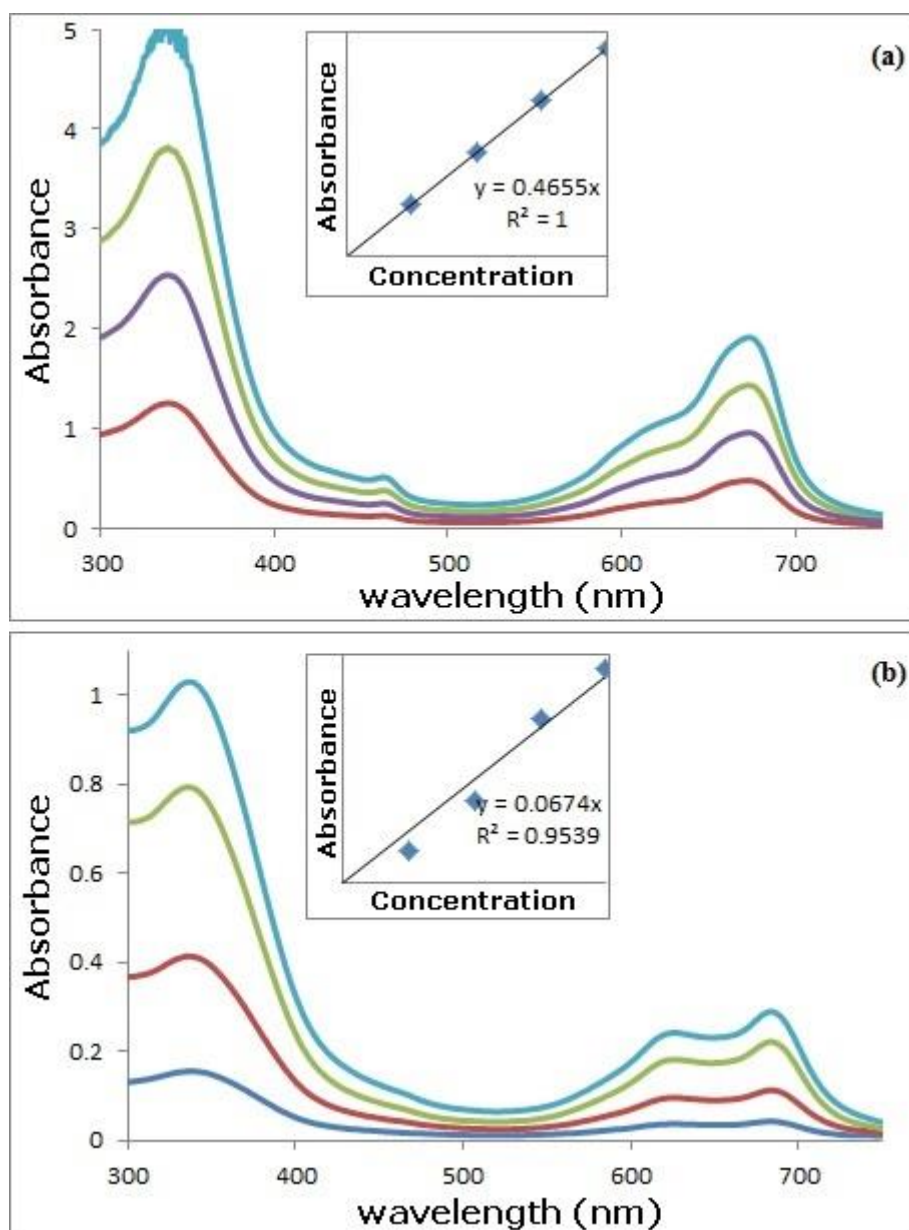


Figure 3. Comparison of the electronic absorption spectra in different concentration (from 10^{-6} M to 10^{-5} M) in the range of 400-750 nm for **Pc-7** and (a) in DMSO (b) in DMSO:water (1:4 ratio)

Cyclic voltammetric measurements

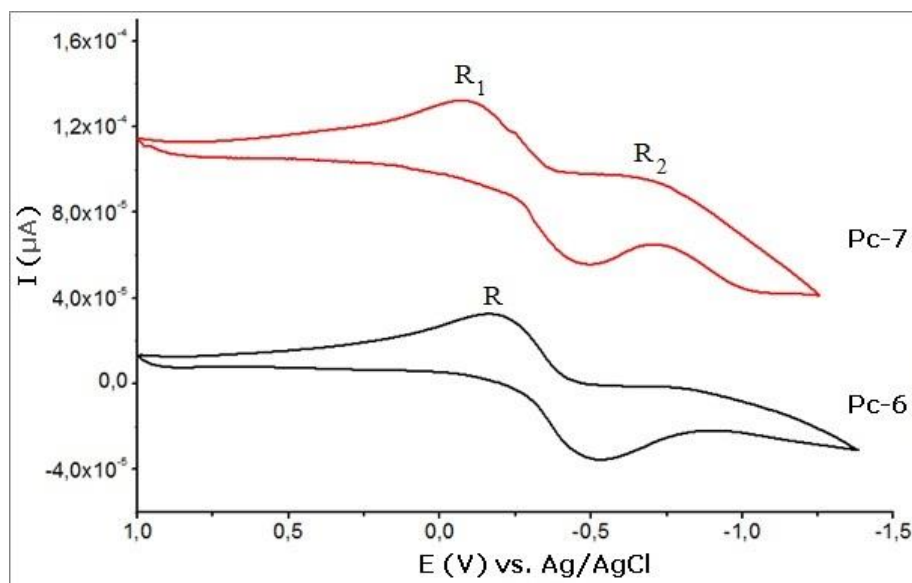


Figure 4. CVs of Zinc phthalocyanine, **Pc-6** and cobalt(II)phthalocyanine, **Pc-7** recorded at 100 mV/s scan rate on a Pt working electrode in DMSO/TBAP for Zinc phthalocyanine, **Pc-6**, DMF/TBAP for cobalt(II)phthalocyanine, **Pc-7**.

Cyclic voltammograms (CVs) were taken with Parstat 2273 potentiostat/galvanostat. A three electrode system having a Pt working electrode, Pt counter electrode, and a Ag/AgCl reference electrode was used. Extra pure dimethylsulfoxide and N,N-dimethylformamide were used to dissolve the phthalocyanines and 0.1 mol/L tetrabutylammonium perchlorate (TBAP) was used as electrolyte.

Figure 4 shows CV responses in DMSO/TBAP for **Pc-6** and DMF/TBAP **Pc-7**. It can be seen clearly from Figure 4 **Pc-6** while zinc phthalocyanine, **Pc-6**, having one reversible reduction, R at -0.22 V, cobalt phthalocyanine, **Pc-7**, has two reversible reductions, R₁ at -0.11 V and R₂ at -0.72 V. The difference that having one and two reduction reaction is coming from metal ions in the cavity of phthalocyanine.

Spectroelectrochemistry

Optically transparent thin-layer electrode cell kit was used cell in order to determine the nature of the redox processes in spectroelectrochemical studies.

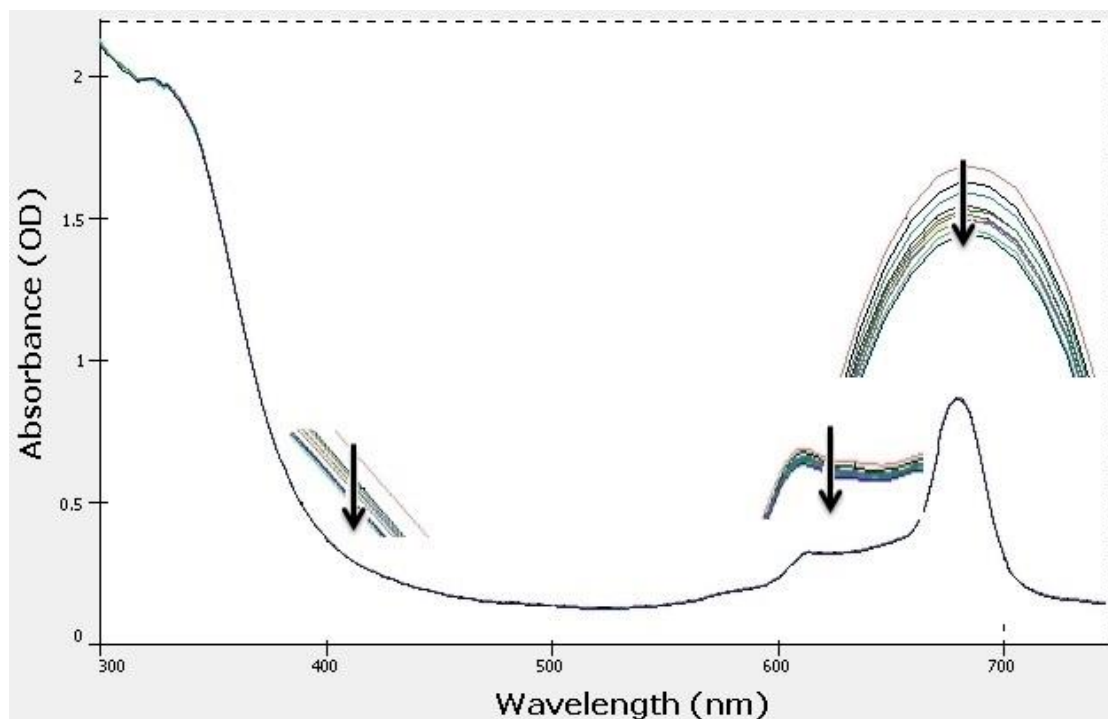


Figure 5. UV-Vis spectral changes of complex **Pc-6** in DMSO containing 0.1 M TBAP observed during application of controlled potential at -0.25 V.

Figure 5 shows UV-Visible spectral changes when the reduction potential at -0.25 V for **Pc-6** with a slight decrease in absorption of whole range and there is no isosbestic point and shift of Q band. It is well known that an isosbestic point occurs when the spectrum collected is overlaid, and it indicates that there is a change from one state to another. The absence of isosbestic point would be interpreted in two ways; the decomposition of the molecule or there is not a change in the structure of the molecule. Decomposition is eliminated because the reduction process is renewable (Fig 4). So the molecule is not decomposing and not undergoing a structural change.

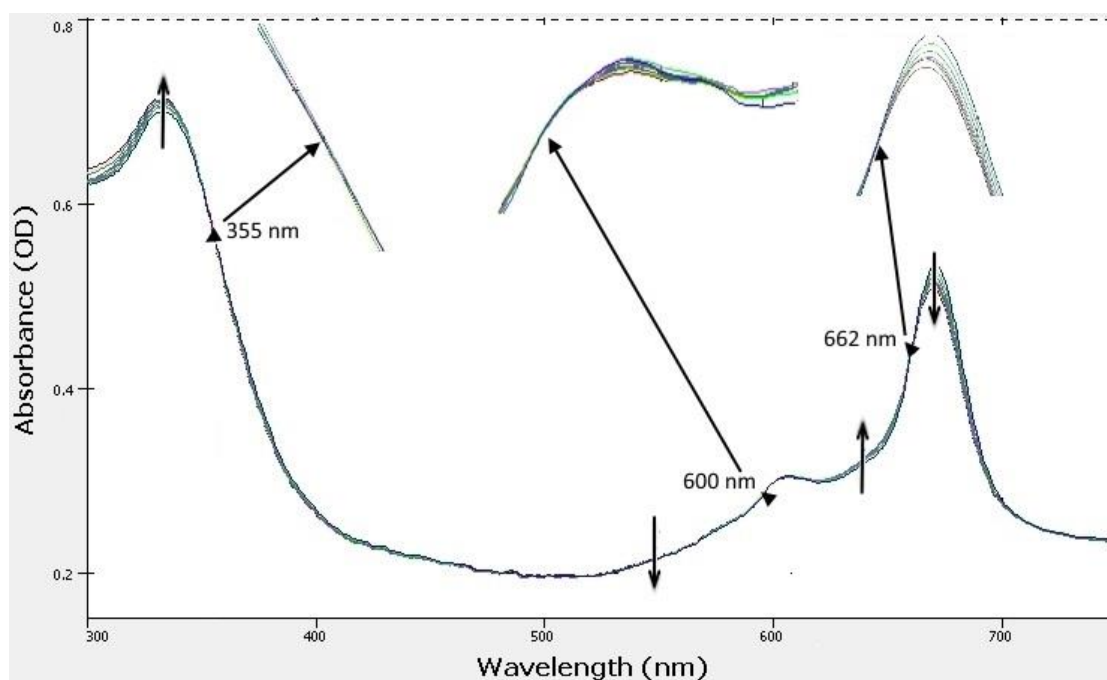
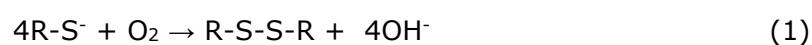


Figure 6. UV-Vis spectral changes of complex **Pc-7** in DMF containing 0.1 M TBAP observed during application of controlled potential at -0.25V.

Figure 6 shows the UV-Visible spectral changes when the reduction potential at -0.25V for **Pc-7**. There is no shift of the Q band. This spectroelectrochemical investigation was done for **Pc-7** R₁ process (Figure 4). It is agreed that there is no change to Co^IPc or Co^{II}Pc from the absence of Q band shift. Isosbestic points were observed at 355 nm, 600 nm and 662 nm. Further reduction at the potential of process R₁ (Figure 4) showed the spectral changes typical of ring-based processes. There is a decrease in the absorbance of Q band with isosbestic points mentioned above. That the Q band is not shifting is due to stabilization of the highest occupied molecular orbital (HOMO) in MPc complexes relative to the lowest unoccupied molecular orbital (LUMO) (35).

Catalytic oxidation of 2-mercaptoethanol

The catalytic activity of Co(II) phthalocyanines on the oxidation of 2-mercaptoethanol is well known application (36-40). **Pc-7** is well soluble and non-aggregated as seen in the sections above. RS⁻ ion generated by NaOH and O₂ coordinate to two axial sides of the central Co(II) in **Pc-7**. Then the electron transfer from the thiolate to oxygen via central Co(II) occurs and disulfide forms. The reaction between 2-mercaptoethanol and oxygen can be seen in equation (1).



The catalytic ratio of 2-mercaptoethanol and phthalocyanine (thiol/catalyst=10000). This reaction needs a basic media. When a small amount of NaOH solution was added to the

reaction mixture, the thiol (RSH) will immediately produce thiolate (RS^-). Then the Co(II)Pc will start to catalyze the oxidation of 2-mercaptoethanol by oxygen. TON (mol oxygen per mol phthalocyanine), initial reaction rate ($\mu\text{mol}/\text{sec}$) and the oxygen consumption ($\mu\text{mol}/\text{min}$) was calculated as 16.6, 0.29, and 2.52 respectively and oxygen consumption over time is seen on Figure 7.

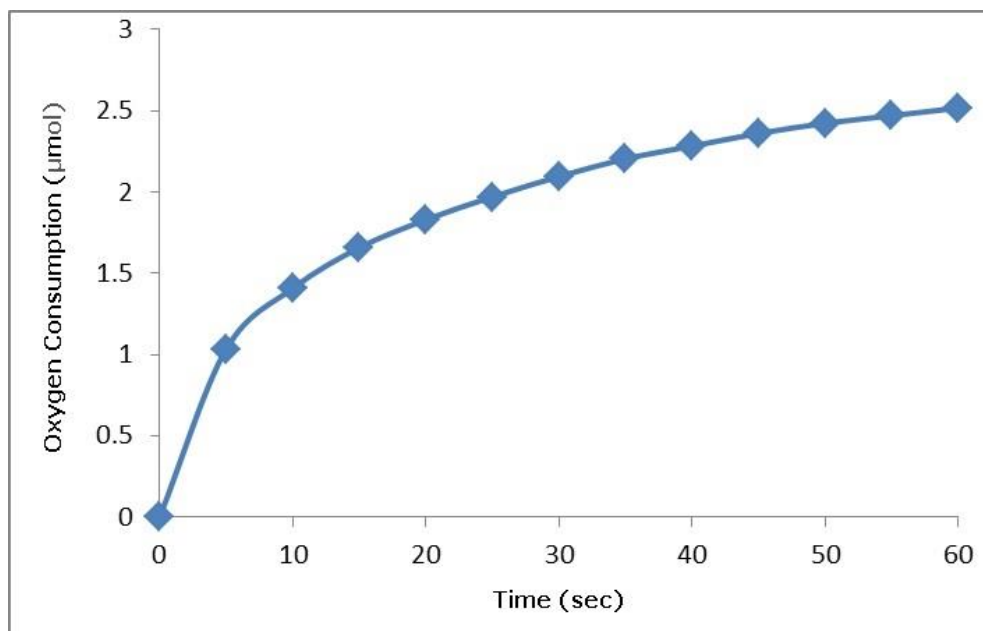


Figure 7. Oxygen consumption in the reaction of catalytic oxidation of 2-mercaptoethanol by Co(II)Pc, **Pc-7**, as catalyst in THF.

CONCLUSION

In conclusion, novel Zn(II) and Co(II) phthalocyanines which are substituted with chalcone bearing furyl moiety have been synthesized and characterized. In our synthetic route, in the presence of KOH as catalyst the chalcone group that is carrying one hydroxyl was synthesized first in the mixture of ethanol and water. Then 4-nitrophthalonitrile was derived with synthesized chalcone group via **SnAr** type substitution reaction. Widespread Pc synthetic approach was used for the direct synthesis of both **Pc-6** and **Pc-7** phthalocyanines. The synthesized chalcone in this study is newly designed and synthesized by our group. The structures of all compounds synthesized have been fully characterized by using FT-IR, ^1H NMR, ^{13}C NMR, MALDI-TOF MS, and UV-Vis spectroscopic techniques. Electronic absorption spectra showed that both Pcs are nonaggregated and also well soluble in DMSO and in the mixture of DMSO : water (1 : 4 ratio). **Pc-7** is also well soluble in DMF. Cyclic voltammograms give one reduction for **Pc-6** and two reduction for **Pc-7**. The spectroelectrochemical investigation shows the ring based reduction potential for MPC's. **Pc-7** cobalt(II) phthalocyanine was investigated as a catalyst in the catalytic oxidation of 2-mercaptoethanol. The catalytic oxidation of 2-mercaptoethanol is a widely studied reaction for the detection of catalytic activity. Turnover

number, initial reaction rate and the oxygen consumption was found in the catalytic oxidation of 2-mercaptoethanol as 16.6, 0.29, 2.52, respectively.

ACKNOWLEDGMENTS

We thank to the research fund of Sakarya University (BAPK: 2015-50-01-041) and (BAPK: 2015-02-04-002)

REFERENCES

1. Leznoff C, Lever A, editors. Phthalocyanines: Properties and applications. Vol. 1. New York: VCH; 1989.
2. Leznoff CC, editor. Phthalocyanines: properties and applications. Vol. 2. New York, NY: VCH; 1993.
3. Leznoff C, Lever A, editors. Phthalocyanines: properties and applications. Vol. 3. Weinheim: Vch; 1993.
4. Leznoff CC, Lever ABP, editors. Phthalocyanines: properties and applications. Volume 4. New York, NY: VCH; 1996.
5. Xue J, Rand BP, Uchida S, Forrest SR. A hybrid planar–mixed molecular heterojunction photovoltaic cell. *Advanced Materials*. 2005;17(1):66–71.
6. Shaheen SE, Ginley DS, Jabbour GE. Organic-based photovoltaics: toward low-cost power generation. *MRS bulletin*. 2005;30(1):10–19.
7. Brumbach M, Placencia D, Armstrong NR. Titanyl phthalocyanine/C60 heterojunctions: Band-edge offsets and photovoltaic device performance. *The Journal of Physical Chemistry C*. 2008;112(8):3142–3151.
8. Thompson BC, Fréchet JM. Polymer–fullerene composite solar cells. *Angewandte chemie international edition*. 2008;47(1):58–77.
9. Szostak J, Jarosz G, Signerski R. Photovoltaic properties of cadmium selenide–titanyl phthalocyanine planar heterojunction devices. *Chemical Physics*. 2015;456:57–60.
10. Zeyada H, El-Nahass M, El-Menyawy E, El-Sawah A. Electrical and photovoltaic characteristics of indium phthalocyanine chloride/p-Si solar cell. *Synthetic Metals*. 2015;207:46–53.
11. Bonnett R. Photosensitizers of the porphyrin and phthalocyanine series for photodynamic therapy. *Chemical Society Reviews*. 1995;24(1):19–33.

12. Bonnett R. Progress with heterocyclic photosensitizers for the photodynamic therapy (PDT) of tumours. *Journal of heterocyclic chemistry*. 2002;39(3):455–470.
13. Chan W-S, Brasseur N, La Madeleine G, Quellet R, Van Lier J. Efficacy and mechanism of aluminium phthalocyanine and its sulphonated derivatives mediated photodynamic therapy on murine tumours. *European Journal of Cancer*. 1997;33(11):1855–1859.
14. Karaca H, Sezer S, Tanyeli C. Synthesis of L-prolinol substituted novel optically active phthalocyanines. *Dyes and Pigments*. 2011;90(2):100–105.
15. Kurt Ö, Koca A, Gül A, Koçak MB. Synthesis, electrochemistry and in situ spectroelectrochemistry of novel hexadeca-substituted phthalocyanines with three different groups. *Synthetic Metals*. 2015;206:72–83.
16. Karaca H, Sezer S, Özalp-Yaman Ş, Tanyeli C. Concise synthesis, electrochemistry and spectroelectrochemistry of phthalocyanines having triazole functionality. *Polyhedron*. 2014;72:147–156.
17. Kobak RZU, Arı MU, Tekin A, Gül A. Aggregation behavior in unsymmetrically substituted metal-free phthalocyanines. *Chemical Physics*. 2015;448:91–97.
18. Nas A, Kahrıman N, Kantekin H, Yaylı N, Durmuş M. The synthesis of novel unmetallated and metallated phthalocyanines including (E)-4-(3-cinnamoylphenoxy) groups at the peripheral positions and photophysicochemical properties of their zinc phthalocyanine derivatives. *Dyes and Pigments*. 2013;99(1):90–98.
19. Rusanova J, Pilkington M, Decurtins S. A novel fully conjugated phenanthroline-appended phthalocyanine: synthesis and characterisation. *Chemical communications*. 2002;(19):2236–2237.
20. Li F, Liu Q, Liang Z, Wang J, Pang M, Huang W, vd. Synthesis and biological evaluation of peptide-conjugated phthalocyanine photosensitizers with highly hydrophilic modifications. *Organic & biomolecular chemistry*. 2016;14(13):3409–3422.
21. Acar İ, Arslan T, Topçu S, Aktaş A, Şen S, Serencam H. Synthesis and electrochemistry of metallophthalocyanines bearing $\text{4-}[(2E)\text{-3-(3, 4, 5-trimethoxyphenyl) prop-2-enoyl}] \text{phenoxy}$ groups. *Journal of Organometallic Chemistry*. 2014;752:25–29.
22. Yildiz SZ, Colak S, Tuna M. Non-ionic peripherally substituted soluble phthalocyanines: Synthesis characterization and investigation of their solution properties. *Journal of Molecular Liquids*. 2014;195:22–29.
23. Ovchenkova EN, Bichan NG, Lomova TN. New soluble octakis-substituted Co (II) phthalocyanines: Synthesis, spectra, supramolecular chemistry. *Dyes and Pigments*. 2016;128:263–270.

24. Ngo D, Kalala M, Hogan V, Manchanayakage R. One-pot synthesis of chalcone epoxides—A green chemistry strategy. *Tetrahedron Letters*. 2014;55(32):4496–4500.
25. Ghouili A, Dusek M, Petricek V, Ayed TB, Hassen RB. Synthesis, crystal structure and spectral characteristics of highly fluorescent chalcone-based coumarin in solution and in polymer matrix. *Journal of Physics and Chemistry of Solids*. 2014;75(2):188–193.
26. Niu C-G, Guan A-L, Zeng G-M, Liu Y-G, Li Z-W. Fluorescence water sensor based on covalent immobilization of chalcone derivative. *Analytica chimica acta*. 2006;577(2):264–270.
27. Shan Y, Liu Z, Cao D, Sun Y, Wang K, Chen H. Nitro substituted chalcone derivatives as quick-response chemosensors for cyanide anions. *Sensors and Actuators B: Chemical*. 2014;198:15–19.
28. Wei Y, Qin G, Wang W, Bian W, Shuang S, Dong C. Development of fluorescent FeIII sensor based on chalcone. *Journal of Luminescence*. 2011;131(8):1672–1676.
29. Sun Y, Chen H, Cao D, Liu Z, Chen H, Deng Y, vd. Chalcone derivatives as fluorescence turn-on chemosensors for cyanide anions. *Journal of Photochemistry and Photobiology A: Chemistry*. 2012;244:65–70.
30. Delavaux-Nicot B, Maynadié J, Lavabre D, Fery-Forgues S. Ca 2+ vs. Ba 2+ electrochemical detection by two disubstituted ferrocenyl chalcone chemosensors. Study of the ligand–metal interactions in CH 3 CN. *Journal of organometallic chemistry*. 2007;692(4):874–886.
31. Gladkov L, Shkirman S, Sushko N, Konstantinova V, Sokolov N, Solovyov K. IR spectra of Zn phthalocyanine and Zn phthalocyanine-d 16 and their interpretation on the basis of normal coordinate analysis. *Spectroscopy letters*. 2001;34(6):709–719.
32. Shinohara H, Tsaryova O, Schnurpfeil G, Wöhrle D. Differently substituted phthalocyanines: Comparison of calculated energy levels, singlet oxygen quantum yields, photo-oxidative stabilities, photocatalytic and catalytic activities. *Journal of Photochemistry and Photobiology A: Chemistry*. 2006;184(1):50–57.
33. Pan Y, Chen W, Lu S, Zhang Y. Novel aqueous soluble cobalt phthalocyanine: synthesis and catalytic activity on oxidation of 2-mercaptoethanol. *Dyes and pigments*. 2005;66(2):115–121.
34. Iliev VI, Ileva AI, Dimitrov LD. Catalytic oxidation of 2-mercaptoethanol by cobalt (II)-phthalocyanine complexes intercalated in layered double hydroxides. *Applied Catalysis A: General*. 1995;126(2):333–340.
35. Karaca H, Çayeğil B, Sezer S. Synthesis characterization and metal sensing applications of novel chalcone substituted phthalocyanines. *Synthetic Metals*. 2016;215:134–141.

36. Nombona N, Nyokong T. The synthesis, cyclic voltammetry and spectroelectrochemical studies of Co (II) phthalocyanines tetra-substituted at the α and β positions with phenylthio groups. *Dyes and Pigments*. 2009;80(1):130–135.
37. Karaca H, Teker M, Gül A. Catalytic Oxidation of 2-Mercaptoethanol by a Water-Soluble Porphyrinatocobalt (II) Complex. *Chem J*. 2016;6(01):55–58.
38. Karaca H, Akcay N, Teker M. PORPHYRAZINE IMMOBILIZATION ON POLYESTER FABRIC AND HETEROGENEOUS CATALYTIC APPLICATION ON OXIDATION OF 2-MERCAPTOETHANOL. *FRESENIUS ENVIRONMENTAL BULLETIN*. 2016;25(5):1714–1718.
39. Karaca H, Tetrapiról Türevlerinin Katalitik Etkilerinin İncelemesi, PhD Thesis, Sakarya University, Institute Of Natural Sciences, 2004.
40. Karaca H. Redox chemistry, spectroelectrochemistry and catalytic activity of novel synthesized phthalocyanines bearing four schiff bases on the periphery. *Journal of Organometallic Chemistry*. 2016;822:39–45.



Synthesis of Chlorotoxin by Native Chemical Ligation

Ulvi KARACA[✉]^{ID}¹, M. Seçkin KESİCİ[✉]^{ID}¹, Salih ÖZÇUBUKÇU[✉]^{ID}^{1*}

¹Middle East Technical University, 06800, Ankara, Turkey

*Corresponding author. Salih ÖZÇUBUKÇU. osalih@metu.edu.tr

Abstract: Chlorotoxin (CLTX) is a neurotoxin found in the venom of the Israeli scorpion, *Leirius quinquestriatus*. It contains 36-amino acids with four disulfide bonds and inhibits low-conductance chloride channels. CLTX also binds to matrix metalloproteinase-2 (MMP-2) selectively. The synthesis of chlorotoxin using solid phase peptide synthesis (SPPS) is very difficult and has a very low yield (<1%) due to high number of amino acid sequence. In this work, to improve the efficiency of the synthesis, native chemical ligation was applied. In this strategy, chlorotoxin sequence was split into two parts having 15 and 21 amino acids. 21-mer peptide was synthesized in its native form based on 9-fluorenylmethyloxycarbonyl (Fmoc) chemistry. 15-mer peptide was synthesized having o-aminoanilide linker on C-terminal. These parts were coupled by native chemical ligation to produce chlorotoxin.

Keywords: Chlorotoxin, solid phase peptide synthesis, native chemical ligation.

Submitted: March 21, 2018. **Accepted:** April 17, 2018.

Cite this: Karaca U, Kesici M, Özçubukçu S. Synthesis of Chlorotoxin by Native Chemical Ligation. JOTCSA. 2018;5(2):719-26.

DOI: <http://dx.doi.org/10.18596/jotcsa.408517>.

*Corresponding author. E-mail: osalih@metu.edu.tr .

INTRODUCTION

Chlorotoxin (CLTX) is a venom peptide that was first isolated from the Israeli scorpion, *Leirius quinquestriatus*. It is a neurotoxic peptide having 36-amino acids and four disulfide bonds. It inhibits low-conductance chloride channels (1). It has also been shown that CLTX is an inhibitor of matrix metalloproteinase-2 (MMP-2) which is a protease that functions in the breakdowns of the extracellular matrix (2). The CLTX is classified as an inhibitor cysteine knot (knottin) due to its "disulfide through disulfide knot" structure. Fluorescent dye conjugated CLTX derivatives were used in the imaging of cancer tissues (3). Iodine radioconjugated CLTX with a trial name TM-601, was in phase II clinical trial for its selective binding to glioma cells without affecting healthy cells (4, 5). Boc-SPPS was used in the chemical synthesis of chlorotoxin and its derivatives (6). There are also examples of one-step Fmoc-based SPPS synthesis of chlorotoxin, however the yields after purification and folding were lower than 1% (7). In general, Fmoc-based SPPS suffers from the low efficiency of coupling reactions after certain length of peptide sequence has been reached due to aggregation of peptide under basic reaction conditions. This results in formation of deletion products and causes difficulties in the purification of peptides (8).

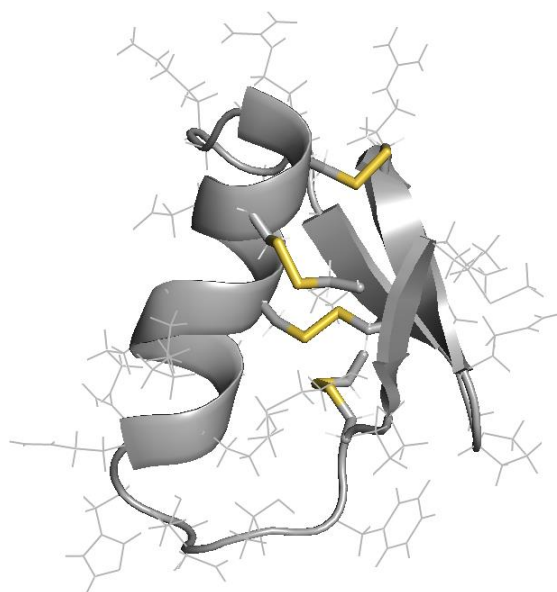


Figure 1. 3D structure of CLTX. Disulfide bridges are shown in yellow (Obtained from Protein Data Bank: 1CHL).

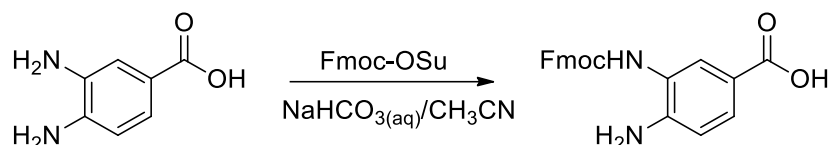
Kent and Dawson developed (8) native chemical ligation (NCL), which is the method commonly used in the synthesis of long peptides from the reaction of two native peptides which are synthesized and purified separately. One peptide has a thioester at its C-terminal and the other peptide has a cysteine at the *N*-terminal of the peptide sequence. Under certain reaction conditions, thiol sidechain in cysteine reacts with thioester moiety selectively and afterwards S-to-N acyl shift that forms an amide bond to form native peptide as ligation product.

NCL method is developed based on Boc-SPPS. The synthesis of thioester moiety at the C-terminal of the peptide is not suitable for Fmoc-based SPPS. But recently, Dawson *et al.* developed a new native chemical ligation method which is suitable for Fmoc-SPPS (10). In this method, *o*-aminoanilides are used as linkers in the synthesis of the peptide and this linker further converted into *N*-acyl urea group at the end of the peptide sequence before cleaving from the resin. The cleaved product is stable under the acidic conditions. However, in neutral conditions, this acyl urea peptide product can undergo rapid thiolysis, and forms thioester peptide to be used in the native chemical ligation.

In this work, chlorotoxin is synthesized by native chemical ligation based on Fmoc-SPPS strategy developed by Dawson *et al.* (9,10).

MATERIALS AND METHODS

Synthesis of 3-((((9H-fluoren-9-yl)methoxy)carbonyl)amino)-4-aminobenzoic acid



Based on the literature procedure (8), to a solution of 3,4-diaminobenzoic acid (1.0 g, 6.6 mmol) in NaHCO₃ (84 mg) water/acetonitrile (1:1, 20 mL) was added *N*-(9-fluorenylmethoxy carbonyloxy) succinimide (Fmoc-OSu) (2.2 g, 6.6 mmol) in small quantities. After stirring overnight at room temperature, acidification with 1 M HCl (aq) formed a precipitate that was filtered, washed with methanol, cold ether and *n*-hexane. The solid was dried under vacuum affording the desired compound as a pale white solid (1.7 g, 70%). ¹H NMR (400 MHz, d₆-DMSO) δ: 4.29-4.40 (m, 3H), 6.72 (d, *J*=8.3 Hz, 1H), 7.33-7.36 (m, 2H), 7.44 (t, *J*=7.4 Hz, 2H), 7.51 (d, *J*=7.8 Hz 1H), 7.72-7.80 (m, 3H), 7.91 (d, *J*=7.4 Hz), 8.78 (s, 1H).

General procedure for solid phase peptide synthesis (8, 10)

Loading the amino acid and coupling with an Fmoc-protected amino acid: 169 mg (0.1 mmol) Rink amide resin was weighed in a reaction vessel. It was washed with DMF (2x) and swollen in 5-6 mL of DMF for 40-45 min. After Fmoc-deprotection of resin, Fmoc-protected amino acid (0.45 mmol, 4.5 eq.) (Fmoc-protected 3,4-diaminobenzoic acid acts like Fmoc-protected amino acid) dissolved in HBTU (0.8 mL, 0.5 M in DMF) then DIEA (140 μL) was added. After addition of DIEA, the solution was mixed and added to the resin in 30 seconds at max. The mixture was allowed to stand for 15 minutes and agitated in every 5 min. Then, the solution was filtered and the resin was washed with DMF. This process repeated one more time. The reaction was monitored by Kaiser test.

Fmoc Deprotection: The Fmoc group was removed by treating the pre-swollen resin with 20% piperidine in dimethylformamide for 2x10 min (2x10 mL). Then the solution is drained and the resin was washed with dimethylformamide several times.

Final Fmoc Deprotection: After deprotection of Fmoc group from the very last amino acid residue, the resin was washed with DMF (4 × 2 mL), DCM (4 × 2 mL) then dried under vacuum. As an alternative way, final Fmoc deprotection can also be done in solution phase, after cleavage. In order to do that, completely dry crude product was dissolved in 20% piperidine in DMF solution. After the mixture was mixed for 10 min. with sonication, it was precipitated with methyl-*tert*-butyl ether. The precipitate was centrifuged and the supernatant was poured off. The process was repeated 3-4 times until the supernatant becomes neutral by checking with pH paper.

Cleavage: 95% TFA, 2.5% decontaminated water and 2.5% TIPS solution (cleavage cocktail) was used to cleave the peptide sequence from resin. This cocktail (for 50 mg peptidyl resin was needed 1 mL of cocktail solution) added to the resin and waited for 2 or 3 hours. Then the solution was collected. The peptide was triturated by addition of ice-cold diethyl ether. The solid was filtered off. The product was dissolved in distilled water and lyophilized.

Conversion of Dbz group into Nbz: After peptide elongation, the resin was washed with dichloromethane and 100 mg *p*-nitrochloroformate in 10 mL dichloromethane was added to the peptide reactor. The resin was bubbled with N₂ for 40 min. This process was repeated one more time. Then, it was washed with dichloromethane and treated with 10 mL 0.5 M DIEA in DMF for 20 min and, finally, it washed with DMF and dichloromethane. The peptidyl-resin was dried under vacuum and the peptide was cleaved by using cleavage cocktail. The final deprotection of Fmoc was not performed.

Native Chemical Ligation: Ligation was performed at room temperature in the following ligation buffer: 6 M guanidine hydrochloride (Gn.HCl), 200 mM potassium phosphate, 200 mM 4-mercaptophenylacetic acid (MPAA), 20 mM tris(2-carboxyethyl) phosphine hydrochloride (TCEP.HCl). Take 2.5 mL of stock solution of 6 M Gn.HCl and 0.2 M K₂HPO₄ and filter using a 0.2 µm syringe-driven filter into a 20 mL scintillation vial containing 14.3 mg TCEP.HCl (0.05 mmol) and 84.1 mg MPAA (0.5 mmol). Buffer was degassed under nitrogen for 15 min before the reaction. And the pH was set to 7.0 with 2 M NaOH.

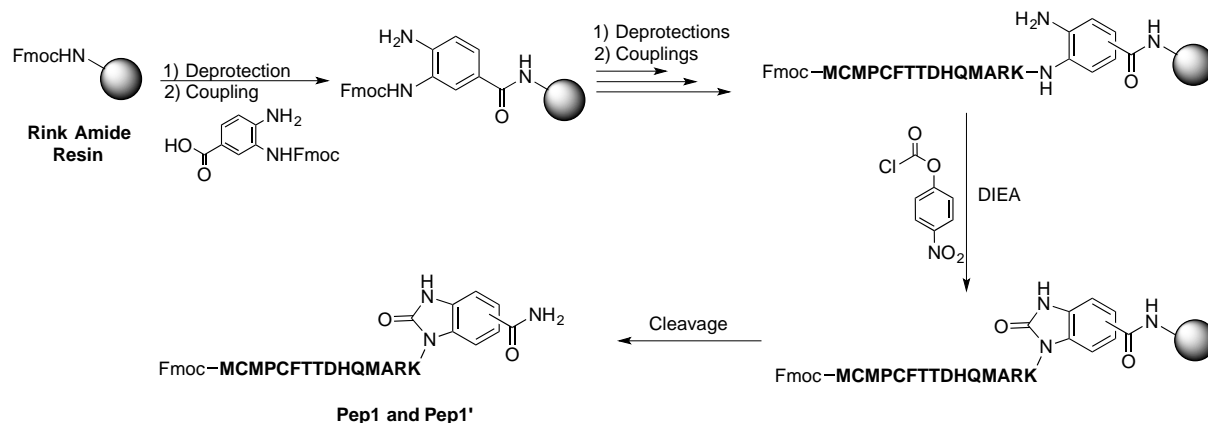
In a 20-mL scintillation vial, the peptide containing Dbz group (1.5x10⁻³ mmol) and linear peptide (1.8x10⁻³ mmol) were dissolved in ligation buffer (0.75 mL) to achieve a final concentration of 2.0 mM with regards to the peptide containing Dbz group. The reaction solution was mixed at room temperature and monitored by HPLC.

RESULTS AND DISCUSSION

The amino acid sequence of chlorotoxin is as follows:



In order to synthesize CLTX by native chemical ligation, the sequence was split into two parts between Lys-15 and Cys-16. 15-mer peptide with methionine on its N-terminal was synthesized having 3,4-diaminobenzamide (Dbz) group on its C-terminal. For this purpose, 3,4-diaminobenzoic acid was selectively protected by Fmoc group by simple treatment with Fmoc-OSu at basic pH values in H₂O/CH₃CN mixture. This benzoic acid derivative was attached to Rink amide resin using standard peptide coupling conditions (HBTU-DIEA). After coupling and deprotection of Fmoc group by 20% piperidine in DMF, amino acids were coupled and Fmoc-MCMPCFTTDHQMARK-Dbz was synthesized. At this stage, the peptide bond could form at the meta- or para-nitrogen atoms on Dbz group. These two structural isomers would not be a problem since both would give the same type of ligation reaction. Before cleaving the peptide from the resin, Dbz group was converted into *N*-acyl-benzimidazolinone (Nbz) by the treatment with *p*-nitrophenyl chloroformate under N₂ atmosphere to give two isomeric form of Fmoc-MCMPCFTTDHQMARK-Nbz (Pep1 and Pep1').

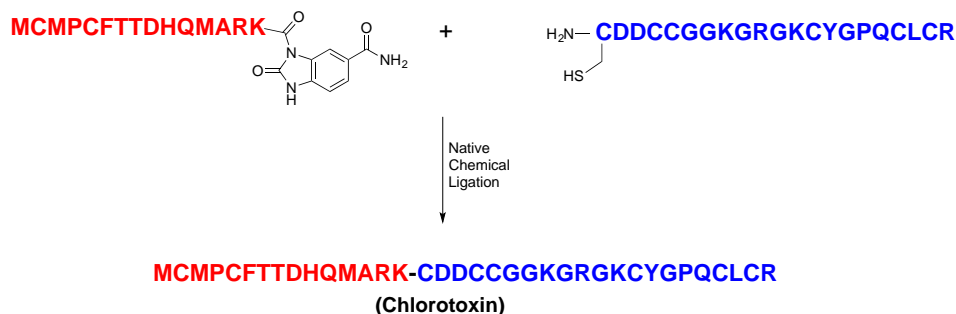


Scheme 1. Synthesis of Pep1-Pep1' starting from Rink amide resin.

Crude Pep1-Pep1' mixture was purified using reverse phase HPLC on a C18 semi-preparative column and characterized by LC-MS (Figure S1).

21-mer peptide (CDDCCGGKGRGKCYGPQCLCR)(Pep2) was synthesized in a native form using standard Fmoc-SPPS conditions on Rink amide resin. After cleaving it from resin, it was purified by reverse phase HPLC C18 semi-preparative column and characterized by LC-MS (Figure S2).

Ligation of Pep1 and Pep2 was performed in ligation buffer which was developed by Kent and Dawson (8, 10). For this purpose, Pep1 and Pep2 were dissolved in ligation buffer with a final concentration of 2 mM. The reaction mixture was stirred at room temperature and monitored by HPLC.



Scheme 2. Synthesis of CLTX via native chemical ligation.

Figure 2A and 2B show the HPLC chromatogram of pure Pep1 and Pep2, respectively. Two isomeric peaks from Pep1 and Pep1' had very separated retention times (10.5 and 23 min.). Figure 2C represents the ligation mixture immediately after mixing (t=0 hour). The peak appeared at 20.3 minutes is 4-mercaptophenylacetic acid (MPAA) that was used in ligation buffer. Between the time after mixing the peptides in ligation buffer and taking an aliquot, it was even possible to see the formation of ligation product (Fmoc-CLTX) as the new peak appeared at 21 minutes. In Figure 2D, it was shown that after 1 hour, the amount of ligation product started to increase and those of Pep1 and Pep2 started to decrease.

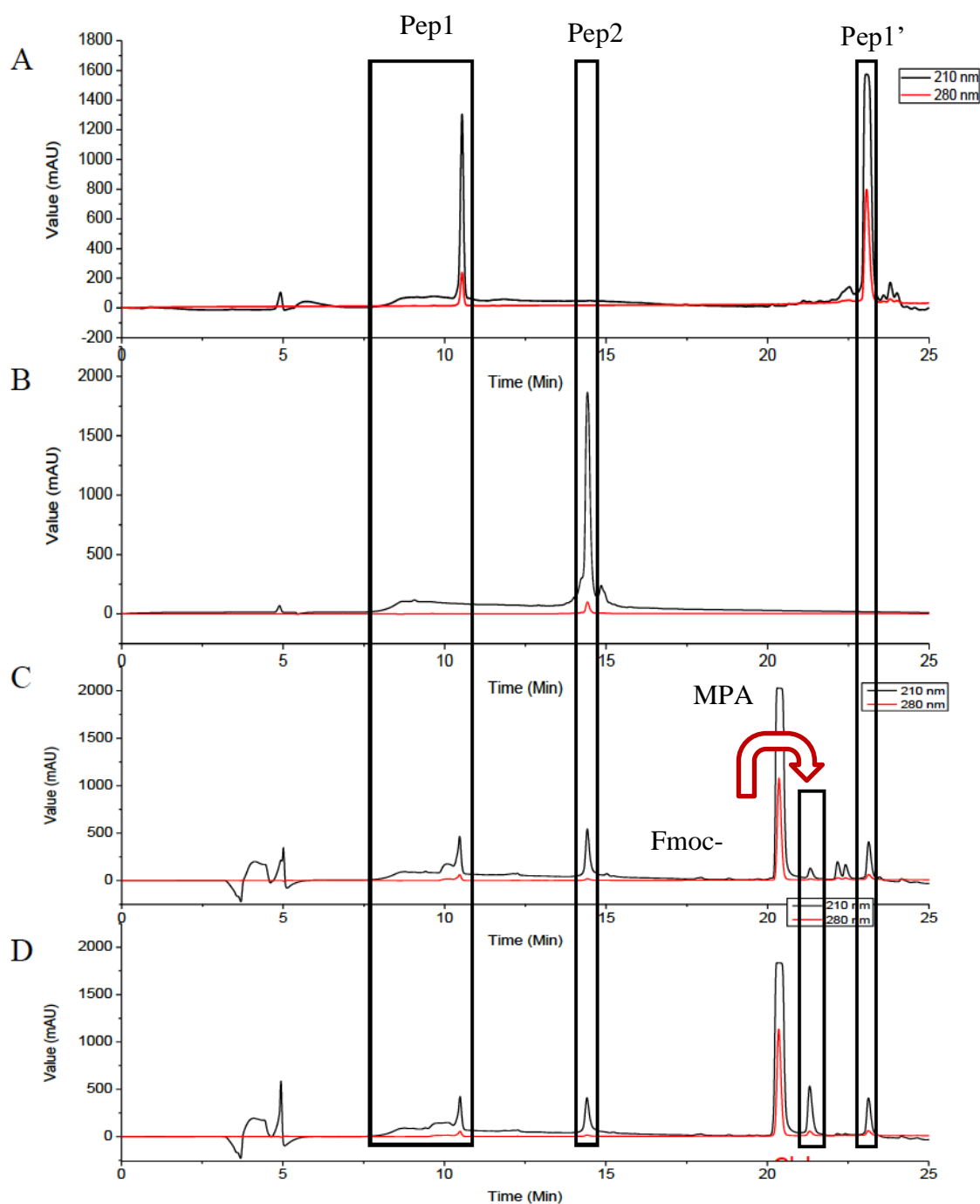


Figure 2. RP-HPLC monitoring of native chemical ligation between Pep1 and Pep2 at 210 and 280 nm using C18 column. **A.** Pure Pep1-Pep1' mixture. **B.** Pure Pep2. **C.** The ligation reaction at t=0 h. **C.** The ligation reaction at t=1 h.

After ligation was over (overnight), the reaction mixture was diluted by water and purified using semi-preparative RP-HPLC C18 column and Fmoc-CLTX was obtained in pure form. It was characterized by LC-MS (Figure S3).

In conclusion, the synthesis of chlorotoxin was successfully completed by native chemical ligation. The overall efficiency of the synthesis was found to be in the range of 5-10%. Ligation

method found to be more efficient and easier in purification compared to the one-step synthesis of chlorotoxin which resulted less than 1% yield and required several purifications (7).

ACKNOWLEDGMENTS

We would like to thank METU-BAP and TUBITAK 214Z083 for financial support.

REFERENCES

1. Debin, JA, Maggio JE, Strichartz, GR. Purification and characterization of chlorotoxin, a chloride channel ligand from the venom of the scorpion. *Am. J. Physiol. Cell Physiol.* 1993; 264(2):C361-C369.
2. Deshane J, Garner CC, Sontheimer H. Chlorotoxin Inhibits Glioma Cell Invasion via Matrix Metalloproteinase-2. *J. Biol. Chem.* 2003; 278(6):4135-4144.
3. Veiseh M, Gabikian P, Bahrami SB, Veiseh O, Zhang M, Hackman RC, Ravanpay AC, Stroud MR, Kusuma Y, Hansen SJ, Kwok D, Munoz NM, Sze RW, Grady WM, Greenberg NM, Ellenbogen RG, Olson JM. Tumor Paint: A Chlorotoxin: Cy5.5 Bioconjugate for Intraoperative Visualization of Cancer Foci. *Cancer Res.* 2007; 67(14):6882-6888.
4. Yang C, Hou VW, Girard EJ, Nelson LY, Siebel EJ. Target-to-Background Enhancement in Multispectral Endoscopy with Background Autofluorescence Mitigation for Quantitative Molecular Imaging. *J. Biomed. Opt.* 2014; 19(7):076014.
5. Kesavan K, Ratliff J, Johnson EW, Dahlberg W, Asara JM, Misra P, Frangioni JV, Jacoby DB. Annexin A2 Is a Molecular Target for TM601, a 51 Peptide with Tumor-Targeting and Anti-Angiogenic Effects. *J. Biol. Chem.* 2010; 285(7):4366-4374.
6. Akcan M, Stroud MR, Hansen SJ, Clark RJ, Daly NL, Craik DJ, Olson JM. Chemical Re-engineering of Chlorotoxin Improves Bioconjugation Properties for Tumor Imaging and Targeted Therapy. *J. Med. Chem.* 2011; 54(3):782-787.
7. Elvheim, I. S. Design, Synthesis and Structural Studies of Relaxin Receptor Modulators. 2011; Master's thesis, Universitetet i Tromsø.
8. Behrendt R, White P, Offer J. Advances in Fmoc Solid-Phase Peptide Synthesis. *J. Pept. Sci.* 2016; 22(1):4-27.
9. Dawson P, Muir T, Clark-Lewis I, Kent S. Synthesis of Proteins by Native Chemical Ligation. *Science* 1994; 266(5186):776-779.
10. Blanco-Canosa JB, Dawson PE. An Efficient Fmoc-SPPS Approach for the Generation of Thioester Peptide Precursors for Use in Native Chemical Ligation. *Angew. Chem. Int. Ed.* 2008; 120(36):6957-6961.
11. Amblard M, Fehrentz J, Martinez J, Subra G. Methods and Protocols of Modern Solid Phase Peptide Synthesis. *Mol. Biotechnol.* 2006; 33:239-254.



Combination of Photoinduced ATRP and Click Processes for the Synthesis of Triblock Copolymers

Gorkem YILMAZ^{1*}

¹Istanbul Technical University, Department of Chemistry, Maslak, Istanbul 34469, Turkey

Abstract: ABA type triblock copolymers possessing polystyrene as middle segment and poly(ϵ -caprolactone) (PCL) and poly(ethylene glycol) (PEG) as side segments were synthesized by combining two photochemical strategies, namely photoinduced atom transfer radical polymerization (ATRP) and click processes. For this purpose, α,ω -diazido functional polystyrene (N_3 -PS- N_3) was synthesized by photoinduced ATRP using a bifunctional initiator, followed by a simple substitution of the chain end halides. Parallel to this, the alkyne-PCL was synthesized by ring opening polymerization of ϵ -caprolactone, employing propargyl alcohol as initiator. For the synthesis of alkyne-PEG, industrially available PEG was functionalized by a simple esterification reaction using 5-pentynoic acid. After the syntheses of these alkyne functional polymers as clickable counterparts, they were reacted with N_3 -PS- N_3 by photoinduced click reactions to prepare the desired triblock copolymers. All polymers were characterized by NMR, FTIR, and GPC analyses.

Keywords: Atom transfer radical polymerization, copper-catalyzed azide-alkyne cycloaddition, photochemistry, block copolymers

Submitted: April 10, 2018. **Accepted:** April 18, 2018.

Cite this: Yılmaz G. Combination of Photoinduced ATRP and Click Processes for the Synthesis of Triblock Copolymers. JOTCSA. 2018;5(2):727–36.

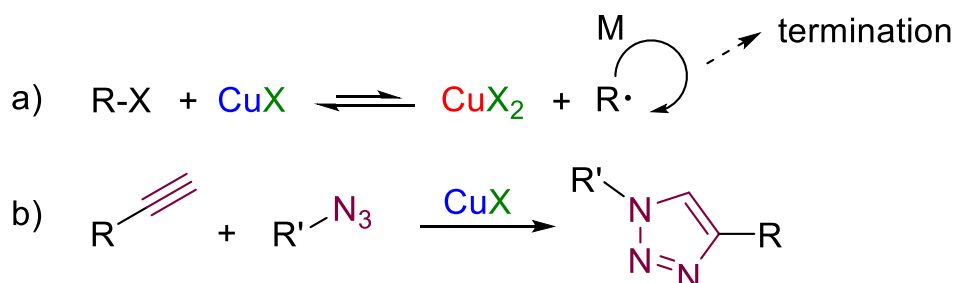
DOI: <http://dx.doi.org/10.18596/jotcsa.414060>.

***Corresponding author.** E-mail: a.gorkemyilmaz@gmail.com.

INTRODUCTION

Development of controlled/living radical polymerization (CLRP) processes has brought a complete breath of fresh air to the synthetic polymer community by providing molecular weight and functional group control over the materials prepared (1-4). Among the most intensively used CLRP techniques, Atom Transfer Radical Polymerization (ATRP) has attracted a great deal of interest, as its applicability to a wide range of monomers and high tolerance to a variety of chemical environments (5-8). In addition, it eventually yields polymers with halogen chain-end functionality, which can be used for further modification processes. Combination of ATRP with highly effective click reactions provides the syntheses of complex macromolecular architectures including telechelic polymers (5), block (9), graft (10, 11), and star copolymers (12, 13), which cannot be synthesized by a single polymerization mechanism. The most favored click reactions by the synthetic polymer scientists are undoubtedly the Diels-Alder (14) and copper-catalyzed azide-alkyne cycloaddition (CuAAC)(14, 15) reactions that can be realized with almost quantitative efficiencies. Specifically, CuAAC reactions, which occur between an alkyne and azido functionality, is the most intensively investigated click reaction due to the possibility of performing these reactions under milder conditions in comparison to Diels-Alder reactions.

Both ATRP and CuAAC require low oxidation state copper (Cu(I)) complexes as catalysts (Scheme 1).

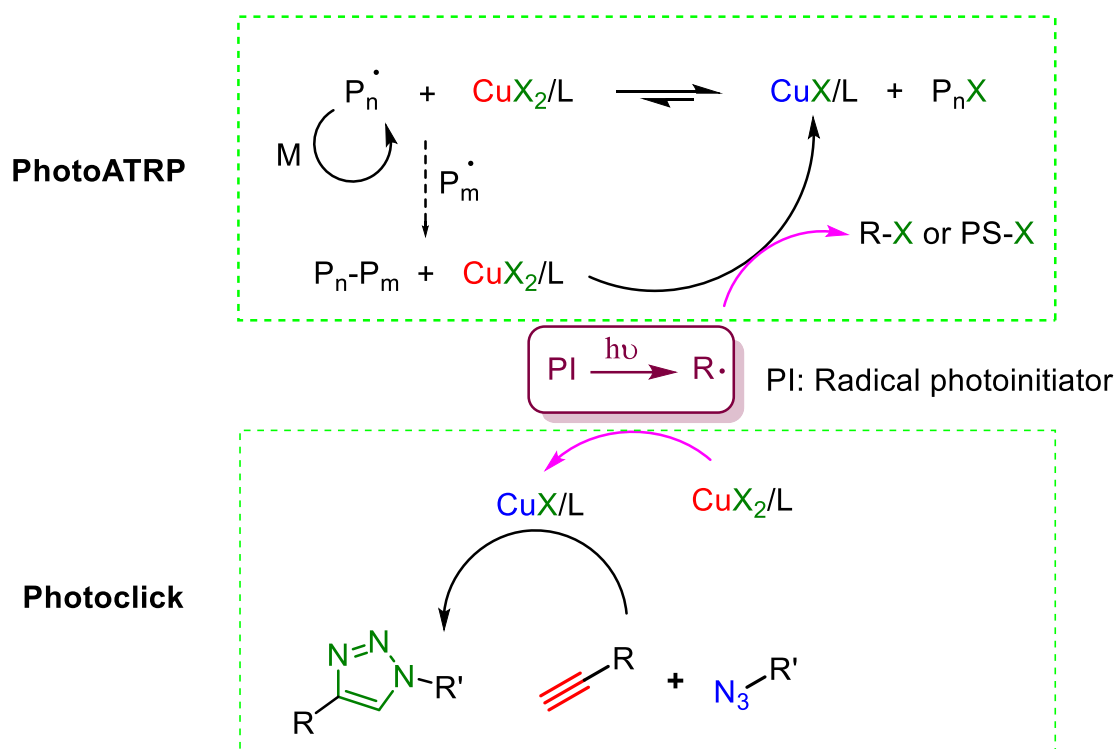


Scheme 1. Conventional ATRP and CuAAC.

Therefore, a major drawback surfaces as Cu(I) complexes may undergo oxidation that alter the rates of reactions. Thus, concurrent generation of Cu(I) catalysts by the reduction of the Cu(II) complexes was proposed to deal with this problem. This is achievable by using the chemical reduction method, which require phenols, ascorbic acid, and hydrazines as reducing agents (16, 17). Alternatively, photochemical reduction processes can also be utilized by employing radicalic photoinitiators or photosensitizers (18-21).

Photochemical approaches have distinctive advantages in comparison to other strategies as they supply 3D-shape control over the materials prepared and temporal control over the reactions. To take such advantages, photochemical processes were utilized to ATRP techniques and CuAAC

(Scheme 2).(9, 22-24) Specifically, decomposition of certain photoinitiators yield radicals, which can efficiently reduce Cu(II) in to Cu(I) catalysts required.



Scheme 2. Photoinduced ATRP and CuAAC reactions.

Herein, a novel strategy for the preparation of triblock copolymers by the combination of two photoinduced processes, namely ATRP and click reactions was described. For this purpose, a bifunctional ATRP initiator was used, which yielded bifunctional polystyrene (Br-PS-Br). Subsequently, the halogen functionalities were substituted to azido groups, which will be used for click reactions (N_3 -PS- N_3). In parallel to this, alkyne functional poly(ϵ -caprolactone) alkyne-PCL and poly(ethylene glycol) (alkyne-PEG) were synthesized as clickable counterparts. Finally, these polymers with antagonist groups were clicked under photoinduced reaction conditions to afford the triblock copolymers. The structures were confirmed by spectral analyses and the molecular weight characteristics were analyzed by chromatographic measurements.

EXPERIMENTAL SECTION

Materials

α,α' -Dibromo-*p*-xylene, sodium azide (97%, Sigma-Aldrich), N, N, N', N'', N''' -pentametyldiethylenetriamine (PMDETA, 99%, Aldrich), copper(II) bromide (98%, Acros), tin(II) chloride, poly(ethylene glycol) methyl ether (Me-PEG, $M_n \sim 550$ g/mol, Aldrich), N, N' -dicyclohexylcarbodiimide (DCC, 99%, Aldrich), bis (2, 4, 6-trimethylbenzoyl)phenylphosphine oxide (BAPO) were used as received. Styrene (99%, Aldrich) and ϵ -Caprolactone (99%, Aldrich) were vacuum-distilled prior to use.

Characterization

^1H NMR of the polymers were recorded at room temperature using a Bruker AC250 (250.133 MHz) instrument. Molecular weight characteristics of the polymers were analyzed by using gel permeation chromatography (GPC) (Agilent 1100 instrument) using polystyrene standards.

Syntheses of Precursor Polymers

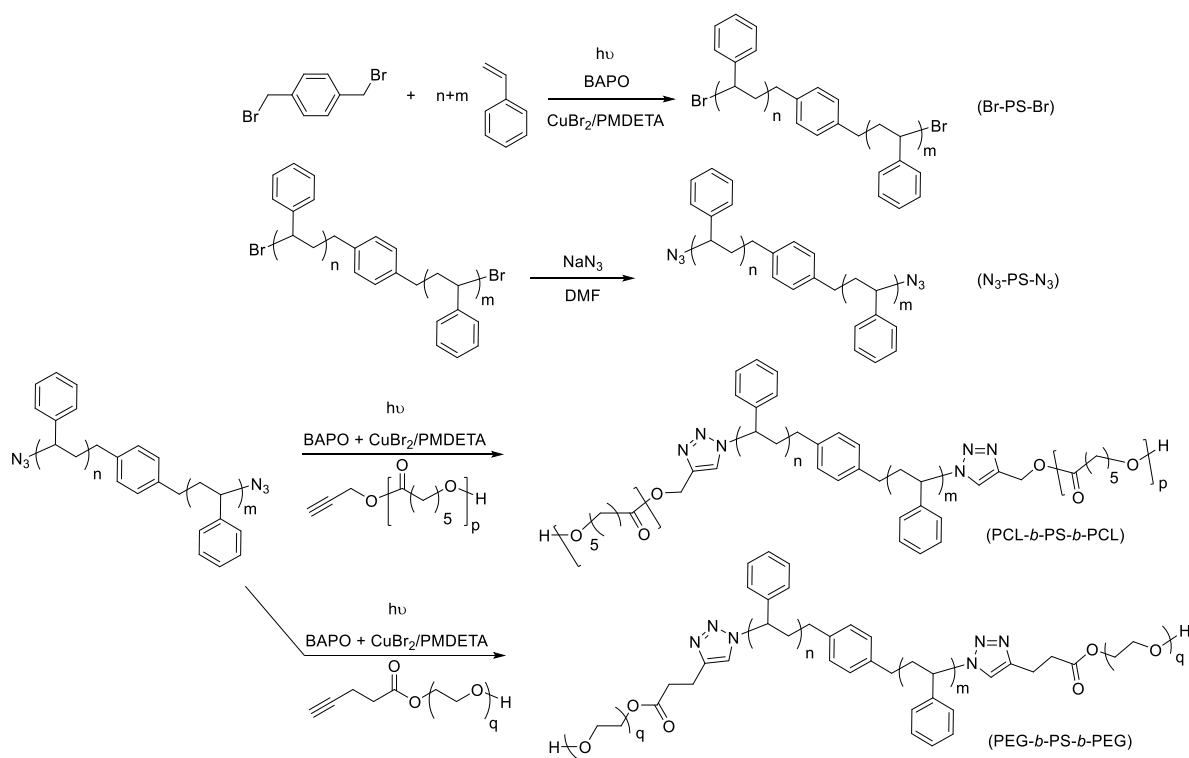
α , ω -Bromo functional polystyrene (Br-PS-Br)(25) ($M_{n,\text{NMR}} = 4800$, $M_{n,\text{GPC}} = 5400$ g/mol, $M_w/M_n = 1.38$), α , ω -azido functional polystyrene (N_3 -PS- N_3)(24) ($M_{n,\text{GPC}} = 5600$ g/mol, $M_w/M_n = 1.37$), α -alkyne functional poly(ϵ -caprolactone) (Alkyne-PCL)(26, 27) ($M_{n,\text{NMR}} = 2100$; $M_{n,\text{GPC}} = 2600$; $M_w/M_n = 1.22$ and ω -alkyne functional poly(ethylene glycol) ($M_{n,\text{GPC}} = 690$; $M_w/M_n = 1.09$) were prepared according to modified literature procedures.

Photoinduced CuAAC reactions

A typical photoinduced CuAAC reaction is carried out as follows: to a Schlenk tube equipped with a magnetic stirrer, N_3 -PS- N_3 (1.0 eq), alkyne-PCL or alkyne-PEG (1.2 eq), ligand (PMDETA, 0.5 eq) and CuCl_2 (0.5 eq) was added and dissolved in dry DMF. The reaction mixture was purged with nitrogen for 5 min and the tube was sealed, which was then exposed to visible light irradiation ($\lambda = 400$ -500 nm) for 24 h. At the end of the irradiation, the reaction mixture was poured into ten-fold excess methanol and the precipitate was filtered off and dried. (PCL-*b*-PS-*b*-PCL: (Yield: 91%, ($M_{n,\text{NMR}} = 8150$ g/mol, $M_{n,\text{GPC}} = 8750$ g/mol, $M_w/M_n = 1.31$); PEG-*b*-PS-*b*-PEG: Yield: 94%, ($M_{n,\text{NMR}} = 5690$ g/mol, $M_{n,\text{GPC}} = 6150$ g/mol, $M_w/M_n = 1.27$).

RESULTS AND DISCUSSION

For the preparation of triblock copolymers, N_3 -PS- N_3 was synthesized as the clickable inner segment by applying photoinduced ATRP, followed by a simple substitution reaction using sodium azide. In parallel to this, alkyne-PCL and alkyne-PEG was synthesized, which were then photochemically clicked with N_3 -PS- N_3 to afford the corresponding PCL-*b*-PS-*b*-PCL and PEG-*b*-PS-*b*-PEG triblock copolymers. In both photoinduced steps, bis(acyl)phosphine oxide (BAPO) was used as the photoreducing agent for the generation of Cu(I) catalyst. The choice of BAPO lies back on the high efficiency of the phosphonyl radicals to reduce Cu(II) salts as reported previously (24, 28, 29). The overall process for the synthesis of triblock copolymers is shown in Scheme 3.



Scheme 3. Syntheses of PCL-*b*-PS-*b*-PCL and PEG-*b*-PS-*b*-PEG by the combination of photoinduced ATRP and CuAAC processes.

The structures of the triblock copolymers were investigated by ^1H NMR spectroscopy (Figure 1). The ^1H NMR spectra of both triblock copolymers show the characteristic protons of the main segments. The triazole proton appeared at 7.9 and 7.6 ppm in the spectra of PCL-*b*-PS-*b*-PCL and PEG-*b*-PS-*b*-PEG, respectively (peak a in Figure 1(a) and (b)), which were used for the calculation of the efficiency of the photoinduced click processes. By comparing the integrated ratios of the triazole peaks with respect to the main PS protons, the click efficiencies were calculated to be 91% and 94% (for PCL-*b*-PS-*b*-PCL and PEG-*b*-PS-*b*-PEG, respectively). In addition, the peaks appeared around 5.1 ppm are attributed to the protons adjacent to the triazole ring (peaks shown as b+c in both cases).

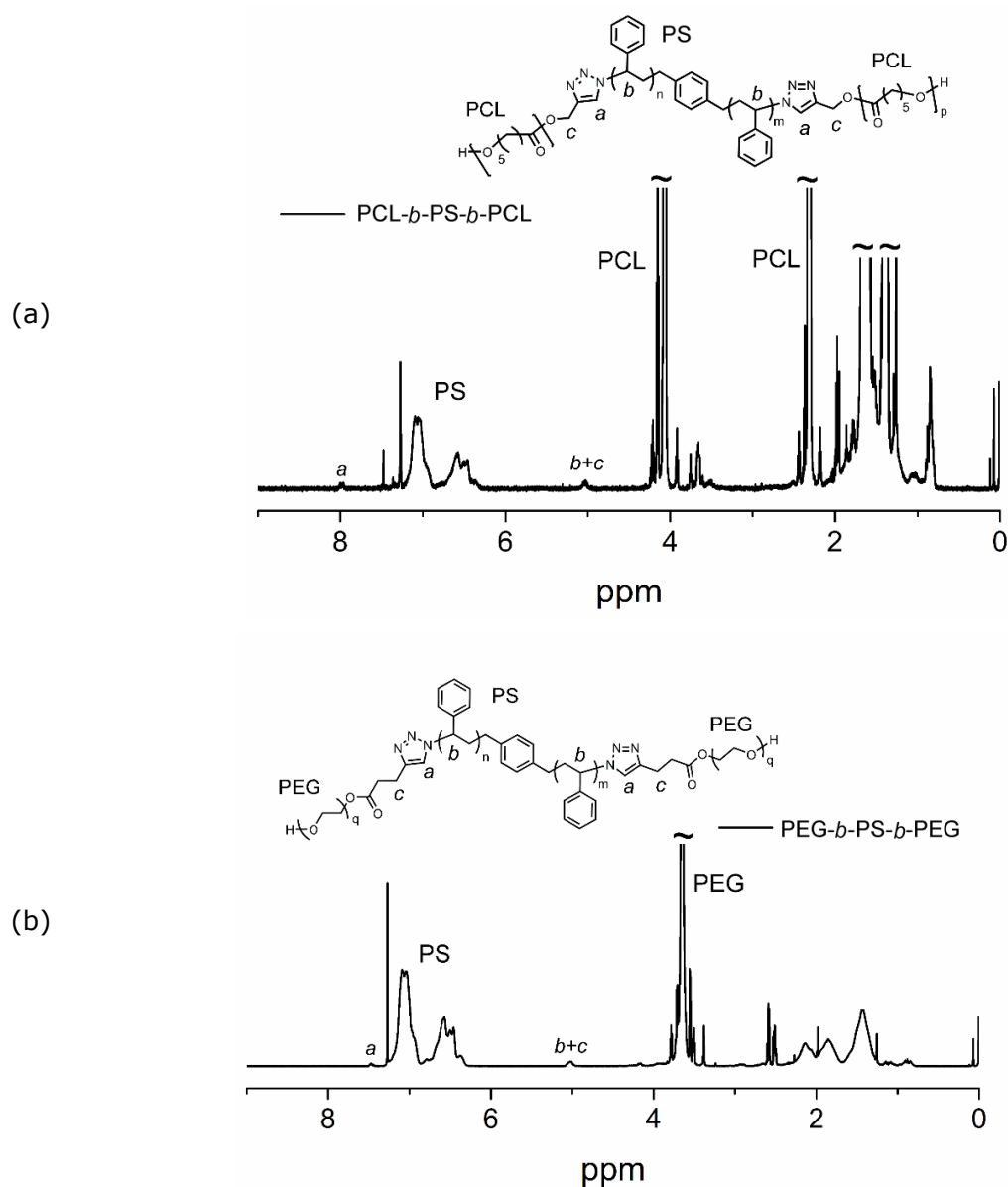


Figure 1. ^1H NMR spectra of PCL-*b*-PS-*b*-PCL (a) and PEG-*b*-PS-*b*-PEG (b). Solvent: CDCl_3 .

The photoinduced click reactions were also followed by FT-IR analyses (Figure 2). In both figures, the black line above shows the FT-IR spectrum of $\text{N}_3\text{-PS-N}_3$, which clearly displays a transition around 2100 cm^{-1} corresponding to the azide functionality. Clearly, after the triblock copolymer formations, the aforementioned peak disappeared and new stretching peaks around 1730 cm^{-1} and 1100 cm^{-1} appeared, which relate to the carbonyl groups of PCL and etheric bonds of PEG segments, correspondingly.

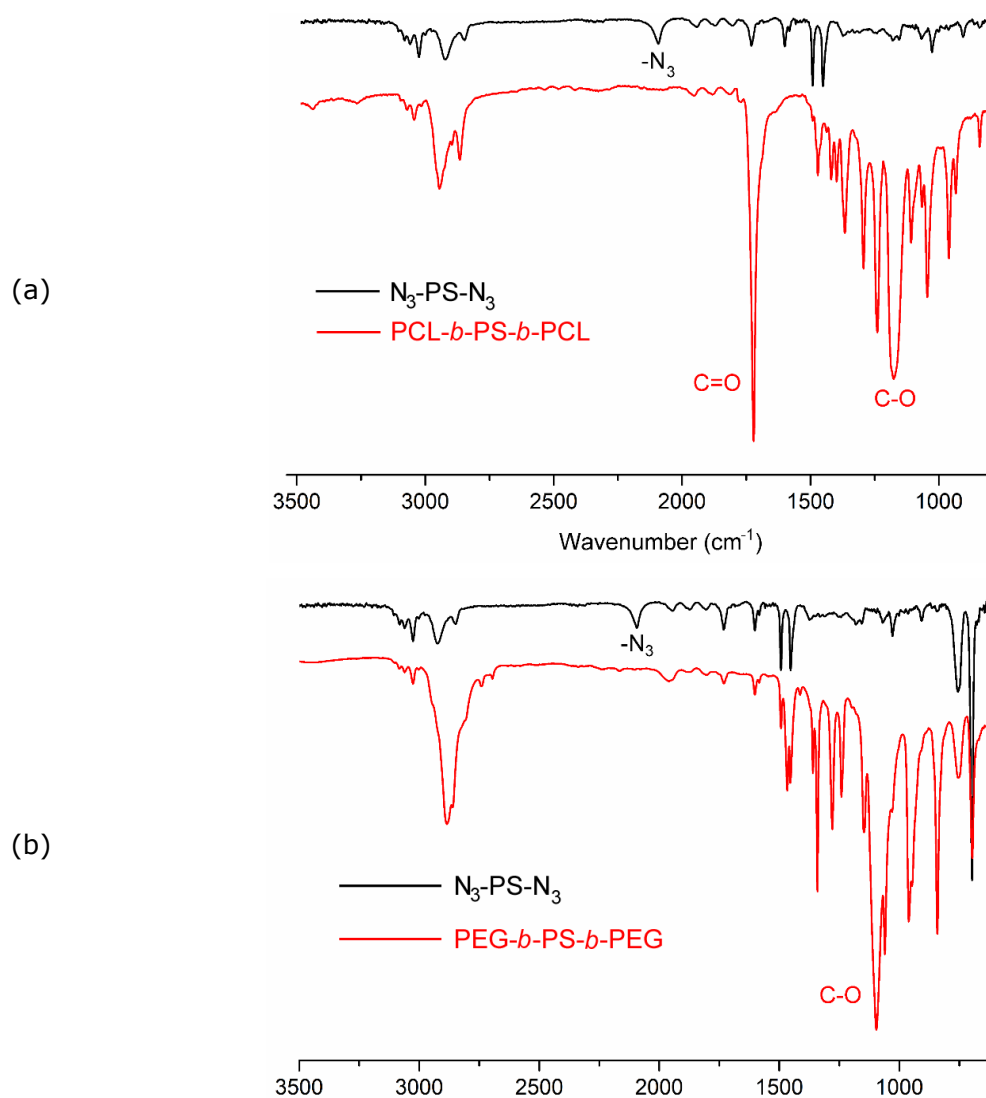


Figure 2. Comparison of the FT-IR spectra of N₃-PS-N₃ with PCL-*b*-PS-*b*-PCL (a) and PEG-*b*-PS-*b*-PEG.

The success of the photoinduced CuAAC reaction was also proved by GPC analyses. As can be seen from Figure 3, there is a clear shift to the high molecular weight region in both cases with respect to the precursor polymers. The unimodal regime of the chromatograms and the absence of shoulder variations confirm that the triblock copolymer formations are efficiently realized without any side reactions.

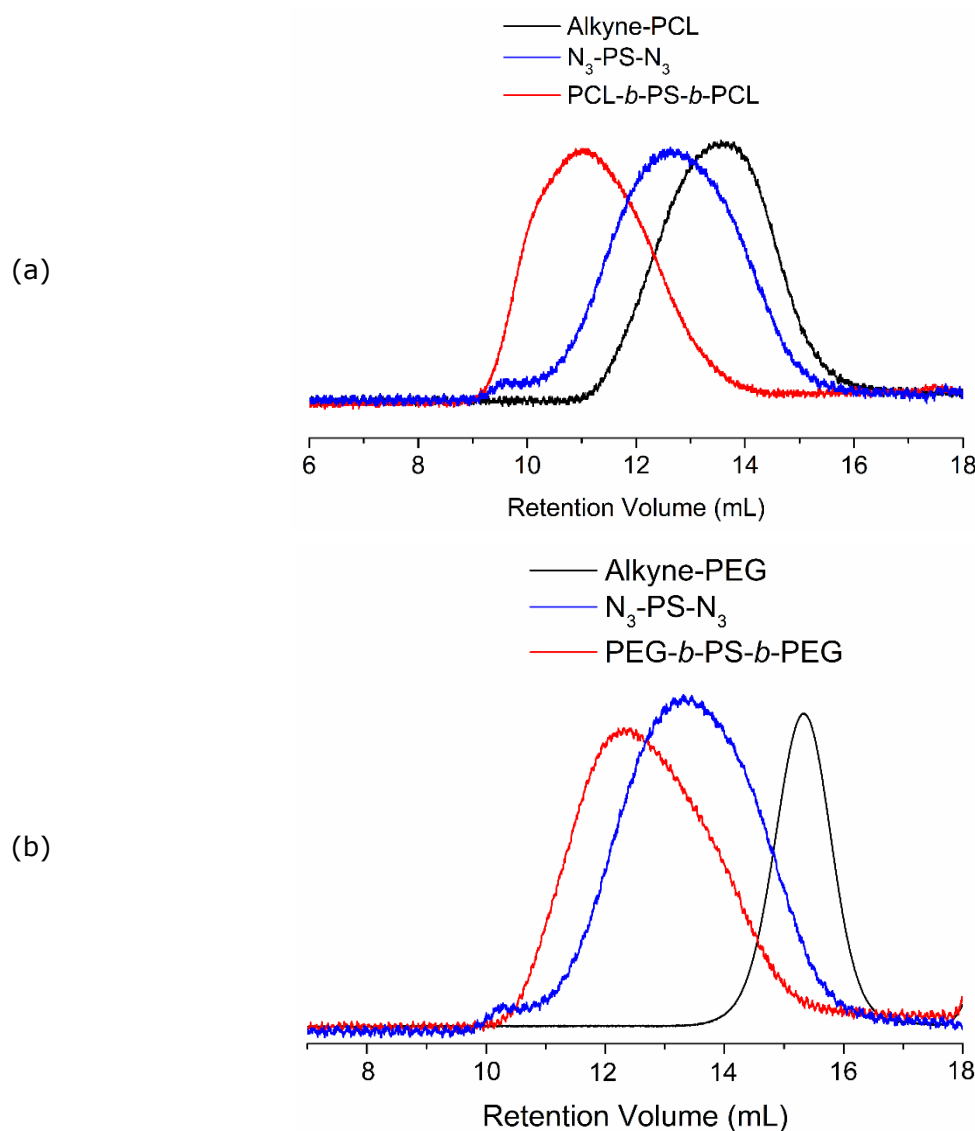


Figure 3. Comparison of the GPC chromatograms of PCL-*b*-PS-*b*-PCL (a) and PEG-*b*-PS-*b*-PEG (b) with respect to their precursor polymers.

CONCLUSION

In conclusion, two photochemical processes, namely photoinduced ATRP and CuAAC, were combined in a sequential fashion for the preparation of triblock copolymers. Given that the antagonist click functionalities are attained at the chain ends of the polymers, the methodology described here was shown to be an efficient and useful strategy for triblock copolymer syntheses. Notably, it provides the preparation of triblock copolymers, which can not be synthesized by a single polymerization technique. Therefore, triblock copolymers with biocompatible segment properties can be synthesized by this strategy as we showed on the case of PCL and PEG. This study is expected to receive interest from the synthetic polymer community and open new pathways for the design and syntheses of various macromolecular architectures.

REFERENCES

1. Matyjaszewski K, Xia JH. Atom transfer radical polymerization. *Chem Rev.* 2001;101(9):2921-90.
2. Chiefari J, Chong YK, Ercole F, Krstina J, Jeffery J, Le TPT, et al. Living free-radical polymerization by reversible addition-fragmentation chain transfer: The RAFT process. *Macromolecules.* 1998;31(16):5559-62.
3. Moad G, Rizzardo E, Thang SH. Living radical polymerization by the RAFT process. *Australian Journal of Chemistry.* 2005;58(6):379-410.
4. Hawker CJ, Bosman AW, Harth E. New polymer synthesis by nitroxide mediated living radical polymerizations. *Chem Rev.* 2001;101(12):3661-88.
5. Coessens V, Pintauer T, Matyjaszewski K. Functional polymers by atom transfer radical polymerization. *Prog Polym Sci.* 2001;26(3):337-77.
6. Matyjaszewski K. Atom Transfer Radical Polymerization (ATRP): Current Status and Future Perspectives. *Macromolecules.* 2012;45(10):4015-39.
7. Pan X, Tasdelen MA, Laun J, Junkers T, Yagci Y, Matyjaszewski K. Photomediated controlled radical polymerization. *Prog Polym Sci.* 2016;62:73-125.
8. Wang JS, Matyjaszewski K. CONTROLLED LIVING RADICAL POLYMERIZATION - HALOGEN ATOM-TRANSFER RADICAL POLYMERIZATION PROMOTED BY A CU(I)CU(II) REDOX PROCESS. *Macromolecules.* 1995;28(23):7901-10.
9. Yilmaz G, Iskin B, Yagci Y. Photoinduced Copper(I)-Catalyzed Click Chemistry by the Electron Transfer Process Using Polynuclear Aromatic Compounds. *Macromol Chem Phys.* 2014;215(7):662-8.
10. Pyun J, Kowalewski T, Matyjaszewski K. Synthesis of polymer brushes using atom transfer radical polymerization. *Macromol Rapid Commun.* 2003;24(18):1043-59.
11. Gacal B, Durmaz H, Tasdelen MA, Hizal G, Tunca U, Yagci Y, et al. Anthracene-maleimide-based Diels-Alder "click chemistry" as a novel route to graft copolymers. *Macromolecules.* 2006;39(16):5330-6.
12. Iskin B, Yilmaz G, Yagci Y. Synthesis of ABC type miktoarm star copolymers by triple click chemistry. *Polym Chem.* 2011;2(12):2865-71.
13. Iskin B, Yilmaz G, Yagci Y. ABC Type Miktoarm Star Copolymers Through Combination of Controlled Polymerization Techniques with Thiol-ene and Azide-Alkyne Click Reactions. *J Polym Sci, Part A: Polym Chem.* 2011;49(11):2417-22.
14. Kolb HC, Finn MG, Sharpless KB. Click chemistry: Diverse chemical function from a few good reactions. *Angewandte Chemie-International Edition.* 2001;40(11):2004-+.
15. Rostovtsev VV, Green LG, Fokin VV, Sharpless KB. A stepwise Huisgen cycloaddition process: Copper(I)-catalyzed regioselective "ligation" of azides and terminal alkynes. *Angewandte Chemie-International Edition.* 2002;41(14):2596-+.
16. Gnanou Y, Hizal G. Effect of phenol and derivatives on atom transfer radical polymerization in the presence of air. *J Polym Sci, Part A: Polym Chem.* 2004;42(2):351-9.
17. Matyjaszewski K, Jakubowski W, Min K, Tang W, Huang J, Braunecker WA, et al. Diminishing catalyst concentration in atom transfer radical polymerization with reducing agents. *Proceedings of the National Academy of Sciences of the United States of America.* 2006;103(42):15309-14.
18. Tasdelen MA, Uygun M, Yagci Y. Photoinduced Controlled Radical Polymerization. *Macromol Rapid Commun.* 2011;32(1):58-62.
19. Konkolewicz D, Schroder K, Buback J, Bernhard S, Matyjaszewski K. Visible Light and Sunlight Photoinduced ATRP with ppm of Cu Catalyst. *Acs Macro Lett.* 2012;1(10):1219-23.

20. Tasdelen MA, Uygun M, Yagci Y. Studies on Photoinduced ATRP in the Presence of Photoinitiator. *Macromol Chem Phys.* 2011;212(18):2036-42.
21. Tasdelen MA, Uygun M, Yagci Y. Photoinduced Controlled Radical Polymerization in Methanol. *Macromol Chem Phys.* 2010;211(21):2271-5.
22. Shanmugam S, Boyer C. Stereo-, Temporal and Chemical Control through Photoactivation of Living Radical Polymerization: Synthesis of Block and Gradient Copolymers. *J Am Chem Soc.* 2015;137(31):9988-99.
23. Shanmugam S, Xu J, Boyer C. Light-Regulated Polymerization under Near-Infrared/Far-Red Irradiation Catalyzed by Bacteriochlorophyll a. *Angew Chem Int Ed Engl.* 2016;55(3):1036-40.
24. Tasdelen MA, Yilmaz G, Iskin B, Yagci Y. Photoinduced Free Radical Promoted Copper(I)-Catalyzed Click Chemistry for Macromolecular Syntheses. *Macromolecules.* 2012;45(1):56-61.
25. Wang J-S, Matyjaszewski K. Controlled/"living" radical polymerization. atom transfer radical polymerization in the presence of transition-metal complexes. *J Am Chem Soc.* 1995;117(20):5614-5.
26. Hoogenboom R, Moore BC, Schubert US. Synthesis of star-shaped poly(ϵ -caprolactone) via 'click' chemistry and 'supramolecular click' chemistry. *Chem Commun.* 2006(38):4010-2.
27. Jerome C, Lecomte P. Recent advances in the synthesis of aliphatic polyesters by ring-opening polymerization. *Advanced drug delivery reviews.* 2008;60(9):1056-76.
28. Dursun C, Degirmenci M, Yagci Y, Jockusch S, Turro NJ. Free radical promoted cationic polymerization by using bisacylphosphine oxide photoinitiators: substituent effect on the reactivity of phosphinoyl radicals. *Polymer.* 2003;44(24):7389-96.
29. Yagci Y, Tasdelen MA, Jockusch S. Reduction of Cu(II) by photochemically generated phosphinoyl radicals to generate Cu(I) as catalyst for atom transfer radical polymerization and azide-alkyne cycloaddition click reactions. *Polymer.* 2014;55(16):3468-74.



Enzyme-Catalyzed Trans-Benzoin Condensation

Gökçil Bilir¹, Ayhan S. Demir¹, Salih Özçubukçu^{1*}

¹Middle East Technical University, 06800, Ankara, Turkey

Abstract: Benzaldehyde lyase (BAL) is an enzyme that is used in the C-C bond cleavage and formation which was isolated first from *Pseudomonas fluorescens* Biovar I. It requires thiamine diphosphate (ThDP) and Mg(II) ions as cofactors. In this work, BAL was used as an enzymatic catalyst for the trans-benzoin condensation reaction between racemic benzoin and benzyloxyacetaldehyde to form unsymmetrical benzoin products with moderate enantiomeric excesses. (*S*)-benzoin derivatives remained unreacted at the end of the reaction. In this enzymatic trans-benzoin condensation, benzyloxyacetaldehyde acted as acceptor and different variety of racemic benzoin derivatives were used as donor and (*R*)-2-hydroxy-1-phenylpropanone derivatives were synthesized up to 66% ee.

Keywords: Benzaldehyde lyase, benzoin condensation, enzymatic asymmetric catalysis.

Note: This article is dedicated to Prof. Dr. Ayhan S. Demir (1950-2012).

Received: April 12, 2018. **Accepted:** April 28, 2018.

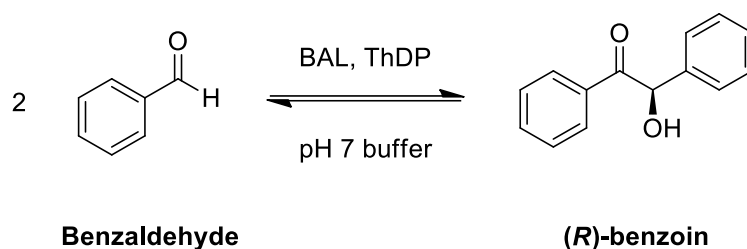
Cite this: Bilir G, Demir A, Özçubukçu S. Enzyme-Catalyzed Trans-Benzoin Condensation. JOTCSA. 2018;5(2):737-50.

DOI: <http://dx.doi.org/10.18596/jotcsa.414603>.

***Corresponding author.** E-mail: osalih@metu.edu.tr.

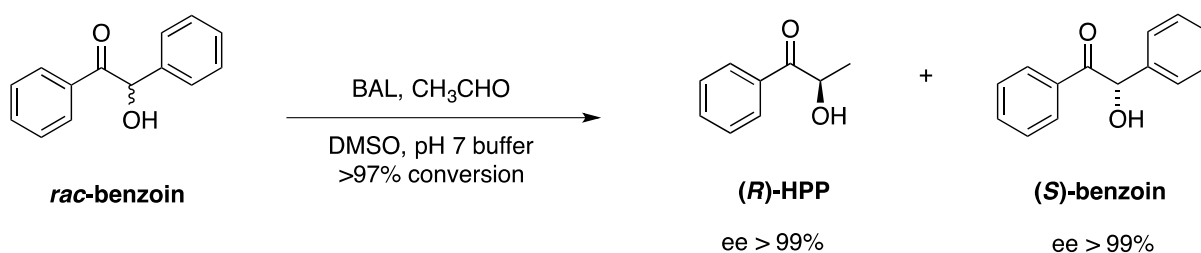
INTRODUCTION

Benzaldehyde lyase was first isolated from *Pseudomonas fluorescens* Biovar I strain which was found in a cellulose factory growing on lignin-degradation products. It was realized that BAL was using a chiral benzoin derivative as an energy source by cleaving the acyloin linkage to give benzaldehyde derivatives (1). BAL can also catalyze the benzoin formation reaction rather than cleavage especially from benzaldehyde to yield (*R*)-benzoin with high chemical yield and enantioselectivity ($ee > 99\%$) (Scheme 1). These high selectivities and yields of BAL-catalyzed benzoin condensation reactions make it very attractive for industrial processes. In benzoin condensation reaction catalyzed by BAL, substituted benzaldehyde derivatives were used as donors. Formaldehyde, acetaldehyde and its derivatives were acted as acceptors (2).



Scheme 1. Benzoin condensation of benzaldehyde catalyzed by BAL to give (*R*)-benzoin.

Demir *et al.* reported various examples of asymmetric benzoin condensation catalyzed by BAL (3, 4). One significant example of BAL-catalyzed reactions was the trans-benzoin condensation where the cleavage of C-C bond and the formation of C-C bond occurred at the same time to give chiral unsymmetrical benzoin derivatives. (*R*)-benzoin was used as a benzaldehyde source and reaction with acetaldehyde in the presence of BAL as a catalyst produced (*R*)-2-hydroxy-1-phenylpropanone, (*R*)-HPP in an optically pure form, quantitatively (5). Furthermore, Demir *et al.* also showed (6) a single example of trans benzoin condensation using *rac*-benzoin as an aromatic aldehyde source to react with acetaldehyde to produce (*R*)-HPP with perfect enantioselectivity (Scheme 2). However, the scope of this reactions remained unexplored.



Scheme 2. Trans-benzoin condensation of *rac*-benzoin with acetaldehyde.

In this work, trans-benzoin condensation of various racemic benzoin derivatives with benzyloxyacetaldehyde catalyzed by BAL to produce unsymmetrical benzoin products were studied. The obtained HPP derivatives are important precursors in the synthesis of asymmetric triol derivatives.

MATERIALS AND METHODS

Production of Benzaldehyde lyase

The cells of *E. coli* SG13009/BALHis that contain the overexpressed enzyme were supplied from Institute of Biotechnology, Research Centre Jülich. Hexahistidine tagged BAL was obtained from recombinant *E. coli* SG13009 cells. Expression of BAL was performed based on the literature (6). The recombinant *E. coli* strains were grown on LB agar that contains 100 µg/mL ampicillin and 35 µg/mL chloroamphenicol incubated in an oven overnight at 37 °C. Firstly, to produce our enzyme, cells were taken from LB agars by sterile loop and transported to a sterile 10 mL LB medium contains 20 µL ampicillin and 20 µL chloroamphenicol. This medium was inoculated for 12 hours at 37 °C. In the precultivation part, growing time range of the bacteria is critical because cells begin to die at some point. In this part, a 500 mL Erlenmeyer flask was used for 100 mL of LB (90 mL distilled water + 10 mL growth cell) medium containing 100 µL ampicillin and chloroamphenicol inoculation ratio 1/1000. It was incubated and grown for 6 hours at 37 °C, then 100 mL transferred to the production medium that contains 1500 mL of LB medium is shaken with 180 rpm. Four hours after the inoculation of the microorganism, production of enzyme was initiated with addition of isopropyl-β-D-thiogalactopyranosid (IPTG). After the induction, enzyme production was started and continued for 12 hours, cell pellets were collected by using centrifugation. In order to break the cell walls to release our enzyme, the cell pellets which are taken from -20 °C were melted to room temperature and sonicated. Finally, removal of water from cells by lyophilization was made with a freeze dryer.

Activity assay

According to the literature (3), one unit (U) of activity is described as the quantity of enzyme that catalyzes the formation of 1 µmol benzoin (1.5 mM) from benzaldehyde in potassium phosphate buffer (50 mM, pH 7) that contains MgSO₄ (2.5 mM), ThDP (0.15 mM) and DMSO (20%, v/v) in 1 minute at 30 °C. To measure the activity of our enzyme, a set of reactions with the same concentration of benzaldehyde was prepared with commercially available benzaldehyde. At appropriate time intervals, samples were withdrawn to measure the amount of benzoin. Then, the standard curve was drawn by using HPLC analysis results to measure the activity of BAL.

For activity experiment, to a set of 2.5 µL benzaldehyde, 0.5 mL DMSO and 1.5 mL phosphate buffer containing ThDP and MgSO₄ was added. The process was initiated with the addition of 5 mg crude enzyme. At 10 minute intervals, one sample was withdrawn by adding chloroform and it was centrifuged. Finally, organic layer was collected and analyzed with HPLC to determine the activity.

General procedure for racemic synthesis of self-benzoin condensation products

The synthesis of racemic benzoin derivatives was done based on the literature procedure (7). A solution of sodium cyanide (2 mmol, 0.098 g) in H₂O (2 mL) was added to a stirred solution of a benzaldehyde derivative (10 mmol) in EtOH (10 mL). The mixture was then refluxed. The progress of reaction was monitored by TLC using hexane/ethyl acetate as eluent. The solvent was then removed by evaporation under reduced pressure. The residue was washed with water and diethyl ether. The product was purified by using flash column chromatography technique.

Synthesis of 3,3'-difluorobenzoin (1)

General procedure stated above starting from 3-fluorobenzaldehyde was applied and the pure product was obtained after crystallization with ethyl acetate and washed with ethyl acetate (48% yield, white solid). TLC: hexane/ethyl acetate = 80:20. R_f = 0.60.

¹H NMR (400 MHz, CDCl₃) δ: 7.67-7.58 (m, 1H), 7.55-7.50 (m, 1H), 7.41-7.29 (m, 2H), 7.08-7.03 (m, 2H), 6.98-6.88 (m, 2H), 5.83 (s, 1H), 4.43 (br s, 1H, OH).

Synthesis of 3,3'-dibromobenzoin (2)

General procedure stated above starting from 3-bromobenzaldehyde was applied and the pure product was obtained after crystallization with ethyl acetate and washed with ethyl acetate (60% yield, yellow oil). TLC: hexane/ethyl acetate = 80:20. R_f = 0.75

¹H NMR (400 MHz, CDCl₃) δ: 8.06 (t, *J* = 1.8 Hz, 1H), 7.78 (t, *J* = 7.5 Hz, 1H), 7.66 (dd, *J* = 8.01, 1.0 Hz, 1H), 7.48 (t, *J* = 1.7 Hz, 1H), 7.42 (d, *J* = 7.7 Hz, 1H), 7.31-7.17 (m, 3H), 5.87 (s, 1H), 4.45 (br s, 1H, OH).

Synthesis of 3,3'-dimethoxybenzoin (3)

The general procedure stated above, starting from 3-methoxybenzaldehyde, was applied and pure product was obtained after crystallization with ethyl acetate and washed with ethyl acetate (45% yield, light yellow solid). TLC: hexane/ethyl acetate = 80:20. R_f = 0.65.

¹H NMR (400 MHz, CDCl₃) δ: 7.50-7.44 (m, 2H), 7.33-7.20 (m, 2H), 7.09-7.02 (m, 1H), 6.92 (d, *J* = 7.6 Hz, 1H), 6.86-6.79 (m, 2H), 5.90 (s, 1H), 4.55 (br s, 1H, OH), 3.79 (s, 3H), 3.76 (s, 3H).

Synthesis of 4,4'-difluorobenzoin (4)

General procedure stated above starting from 4-fluorobenzaldehyde was applied and the pure product was obtained after crystallization with ethyl acetate and washed with ethyl acetate (68% yield, light yellow solid). TLC: hexane/ethyl acetate = 80:20. R_f = 0.63.

^1H NMR (400 MHz, CDCl_3) δ : 8.09-8.03 (m, 1H), 7.89-7.82 (m, 2H), 7.26-7.20 (m, 1H), 7.03-6.89 (m, 4H), 5.83 (s, 1H).

Synthesis of 3,3'-dimethylbenzoin (5)

General procedure stated above starting from *m*-tolualdehyde was applied and the pure product was obtained after crystallization with ethyl acetate and washed with ethyl acetate (42% yield, yellow oil). TLC: hexane/ethyl acetate = 80:20. R_f = 0.62.

^1H NMR (400 MHz, CDCl_3) δ : 7.76 (s, 1H), 7.69 (d, J = 7.6 Hz, 1H), 7.32 (d, J = 7.6 Hz, 1H), 7.21-7.17 (m, 2H), 7.13 (d, J = 5.8 Hz, 2H), 7.06 (t, J = 6.4 Hz, 1H), 5.90 (d, J = 5.5 Hz, 1H), 4.54 (d, J = 6.0 Hz, 1H, OH), 2.34 (s, 3H), 2.29 (s, 3H).

Synthesis of 4,4'-dimethylbenzoin (6)

General procedure stated above starting from *p*-tolualdehyde was applied and the pure product was obtained after crystallization with ethyl acetate and washed with ethyl acetate (55% yield, light yellow oil). TLC: hexane/ethyl acetate = 80:20. R_f = 0.50.

^1H NMR (400 MHz, CDCl_3) δ : 7.70 (d, J = 8.1 Hz, 2H), 7.07 (d, J = 8.0 Hz, 2H), 7.04-6.90 (m, 4H), 5.78 (s, 1H), 2.12 (s, 3H), 2.08 (s, 3H).

General procedure of enzymatic trans-benzoin condensation of benzoin and benzyloxyacetaldehyde

To a mixture of *rac*-benzoin derivative (0.25 mmol) and benzyloxyacetaldehyde (0.25 mmol) in 2.5 mL DMSO (25 vol%) 7.5 mL (75 vol%) MOPS buffer (50 mM, pH 7) that contains 0.15 mM ThDP and 2.5 mM MgSO_4 was transferred. The reaction was initiated with the addition of BAL (0.2 U) at 37 °C (120 rpm). Every 24 hours 0.2 U of BAL was added. The reaction was controlled with TLC and concluded after 72 h. The reaction mixture was extracted with diethyl ether (8 x 40 mL) and the combined organic layers were washed with brine and dried over MgSO_4 , and the solvent was concentrated *in vacuo* to yield the product which was further purified by using flash column chromatography.

Synthesis of (R)-3-(benzyloxy)-2-hydroxy-1-(3-methoxyphenyl)-propan-1-one (8)

General procedure described above starting from *m*-anisoin and benzyloxyacetaldehyde, provided the pure product obtained as white oil (43% yield). TLC: hexane/ethyl acetate = 10:1. R_f = 0.28.

^1H NMR (400 MHz, CDCl_3) δ : 7.40-7.35 (m, 2H), 7.32-7.26 (m, 1H), 7.18-7.12 (m, 3H), 7.10-7.02 (m, 3H), 5.10 (br s, 1H), 4.44 (d, J = 12.3 Hz, 1H), , 4.36 (d, J = 12.3 Hz, 1H), 3.90 (br s, 1H, OH), 3.78 (s, 3H), 3.74 (dd, J = 10.3, 3.8 Hz, 1H), 3.68 (dd, J = 10.3, 4.4 Hz, 1H).

^{13}C NMR (100 MHz, CDCl_3) δ : 199.5, 159.9, 137.6, 135.3, 129.8, 128.3, 127.6, 127.5, 121.0, 120.5, 112.8, 73.9, 73.4, 72.6, 55.5.

IR: 3444, 2959, 2922, 2859, 1684, 1596, 1581, 1452, 1258, 1094, 1014 cm^{-1}

$[\alpha]_D^{22} = +3.22^\circ$ ($c = 0.026$ g/mL, CHCl_3).

HRMS $\text{C}_{17}\text{H}_{18}\text{O}_4$ ($\text{M}+\text{Na}^+$): Calcd. 309.1103, found 309.1104.

Synthesis of (R)-3-(benzyloxy)-2-hydroxy-1-(p-tolyl)-propan-1-one (9)

General procedure described above starting from 4,4'-dimethylbenzoin and benzyloxyacetaldehyde, provided the pure product obtained as yellow oil (44% yield). TLC: hexane/ethyl acetate = 10:1. $R_f = 0.21$.

^1H NMR (400 MHz, CDCl_3) δ : 7.84-7.70 (m, 2H), 7.23-7.14 (m, 5H), 7.07-7.04 (m, 2H), 5.16-5.10 (m, 1H), 4.44 (d, $J = 12.3$ Hz, 1H), 4.38 (d, $J = 12.3$ Hz, 1H), 3.94 (d, $J = 6.6$ Hz, 1H, OH), 3.74 (dd, $J = 10.3, 3.1$ Hz, 1H), 3.66 (dd, $J = 10.3, 4.5$ Hz, 1H), 2.36 (s, 3H).

^{13}C NMR (100 MHz, CDCl_3) δ : 198.0, 144.0, 136.6, 132.9, 130.4, 128.5, 127.7, 127.3, 126.5, 72.6, 72.4, 71.8, 20.7.

IR: 3457, 2957, 2919, 2855, 1680, 1606, 1452, 1258, 1093, 1017 cm^{-1} .

$[\alpha]_D^{22} = +6.80^\circ$ ($c = 1.7 \times 10^{-3}$ g/mL, CHCl_3).

HRMS $\text{C}_{17}\text{H}_{18}\text{O}_3$ ($\text{M}+\text{Na}^+$): Calcd. 293.1154, found 293.1158.

Synthesis of (R)-3-(benzyloxy)-2-hydroxy-1-phenylpropan-1-one (10)

General procedure described above starting from commercially available *rac*-benzoin and benzyloxyacetaldehyde, provided the pure product obtained as white powder (24% yield). TLC: hexane/ethyl acetate = 50:10. $R_f = 0.67$.

^1H NMR (400 MHz, CDCl_3) δ : 7.92-7.88 (d, $J = 7.1$ Hz, 2H), 7.61 (t, $J = 7.5$ Hz, 1H), 7.48 (t, $J = 7.8$ Hz, 2H), 7.25-7.20 (m, 3H), 7.15-7.09 (m, 2H), 5.24-5.18 (m, 1H), 4.52 (d, $J = 12.3$ Hz, 1H), 4.44 (d, $J = 12.3$ Hz, 1H), 3.96 (d, $J = 6.5$ Hz, 1H, OH), 3.82 (dd, $J = 10.3, 3.2$ Hz, 1H), 3.75 (dd, $J = 10.3, 4.4$ Hz, 1H).

^{13}C NMR (100 MHz, CDCl_3) δ : 199.5, 137.6, 134.0, 133.9, 128.8, 128.6, 128.3,

127.6, 127.5, 73.8, 73.4, 72.5.

IR: 3445, 3017, 2926, 1685, 1618, 1559, 1508, 1496, 1214, 1099 cm⁻¹.

$[\alpha]_D^{22} = -0.0264^\circ$ ($c = 1.0 \times 10^{-4}$ g/mL, CHCl₃).

HRMS C₁₆H₁₆O₃ (M+Na⁺): Calcd. 279.0997, found 279.0999.

Synthesis of (R)-3-(benzyloxy)-2-hydroxy-1-(4-methoxyphenyl)-propan-1-one (11)

General procedure described above starting from commercially available *p*-anisoin and benzyloxyacetaldehyde, provided the pure product obtained as white oil (43% yield). TLC: hexane/ethyl acetate = 10:1. R_f = 0.24.

¹H NMR (400 MHz, CDCl₃) δ: 7.83 (d, *J* = 8.9 Hz, 2H), 7.20-7.15 (m, 3H), 7.09 (dd, *J* = 8.3, 5.9 Hz, 2H), 6.89-6.83 (d, *J* = 8.9 Hz, 2H), 5.10 (br s, 1H), 4.45 (d, *J* = 12.3 Hz, 1H), 4.39 (d, *J* = 12.3 Hz, 1H), 3.94 (br s, 1H, OH), 3.81 (s, 3H), 3.73 (dd, *J* = 9.6, 3.4 Hz, 1H), 3.65 (dd, *J* = 9.6, 4.7 Hz, 1H).

¹³C NMR (100 MHz, CDCl₃) δ: 197.7, 164.2, 137.7, 131.0, 129.0, 128.3, 127.5, 126.8, 114.0, 73.4, 73.3, 73.0, 55.6.

IR: 3444, 2923, 2856, 1671, 1598, 1572, 1510, 1454, 1256, 1172, 1101, 1025 cm⁻¹.

$[\alpha]_D^{22} = +19.26^\circ$ ($c = 0.0185$ g/mL, CHCl₃).

HRMS C₁₇H₁₈O₄ (M+Na⁺): Calcd. 309.1103, found 309.1106.

HPLC conditions of chiral α-hydroxy ketones

(*R*)-3-(benzyloxy)-2-hydroxy-1-(3-methoxyphenyl)-propan-1-one (**8**)

Enantiomerically enriched compound **8** was obtained in 36% ee. The enantiomeric excess was verified by using chiral HPLC analysis (AD-H Column, hexane:*i*-PrOH / 90:10, flow rate 0.75 mL/min, λ = 254 nm), t_R = 21.36 min (minor enantiomer), t_R = 26.39 min (major enantiomer).

(*R*)-3-(benzyloxy)-2-hydroxy-1-(*p*-tolyl)-propan-1-one (**9**)

Enantiomerically enriched compound **9** was obtained in 62% ee. The enantiomeric excess was verified by using chiral HPLC analysis (AD-H Column, hexane:*i*-PrOH / 95:5, flow rate 0.75 mL/min, λ = 254 nm), t_R = 31.75 min (minor enantiomer), t_R = 33.46 min (major enantiomer).

(R)-3-(benzyloxy)-2-hydroxy-1-phenylpropan-1-one (10)

Enantiomerically enriched compound **10** was obtained in 36% ee. The enantiomeric excess was verified by using chiral HPLC analysis (AD-H Column, hexane:*i*-PrOH / 90:10, flow rate 0.75 mL/min, $\lambda = 254$ nm) $t_R = 19.49$ min (minor enantiomer), $t_R = 22.75$ min (major enantiomer).

(R)-3-(benzyloxy)-2-hydroxy-1-(4-methoxyphenyl)-propan-1-one (11)

Enantiomerically enriched compound **11** was obtained in 63% ee. The enantiomeric excess was verified by using chiral HPLC analysis (AD-H Column, hexane:*i*-PrOH / 90:10, flow rate 0.75 mL/min, $\lambda = 254$ nm), $t_R = 33.87$ min (minor enantiomer), $t_R = 35.76$ min (major enantiomer).

General procedure for racemic cross benzoin condensation of benzaldehyde derivative and benzyloxyacetaldehyde with thiazolium catalyst (8)

Firstly, to the derivatives of benzaldehyde (0.3 mmol) and benzyloxyacetaldehyde (0.5 mmol), dry THF (1 mL) and 3-ethyl-5-(2-hydroxyethyl)-4-methylthiazol-3-ium bromide was added as a catalyst (0.05 mmol); subsequently Cs_2CO_3 (0.05 mmol) was transferred into the reaction medium. After 20 hours, the reaction mixture was extracted with EtOAc (10 mL x 3), dried over Na_2SO_4 and solvent was removed under reduced pressure. The residue was afforded after flash column chromatography (EtOAc/Hexane = 1:10) as an oil. This procedure was adapted from the literature (8).

Synthesis of racemic-3-(benzyloxy)-2-hydroxy-1-(3-bromophenyl)-propan-1-one (rac-12)

General procedure described above starting from 3-bromobenzaldehyde and benzyloxyacetaldehyde, provided the pure product obtained as yellow powder (21% yield). TLC hexane/ethyl acetate = 90:10. $R_f = 0.67$.

^1H NMR (400 MHz, CDCl_3) δ : 8.18 (t, $J = 1.7$ Hz, 1H), 7.98-7.96 (m, 2H), 7.74- 7.70 (m, 1H), 7.32-7.28 (m, 1H), 7.19-7.16 (m, 4H), 5.07 (t, $J = 3.8$ Hz, 1H), 4.44 (d, $J = 12.3$ Hz, 1H), 4.35 (d, $J = 12.3$ Hz, 1H), 3.71 (dd, $J = 10.3, 3.6$ Hz, 1H), 3.69 (dd, $J = 10.3, 4.1$ Hz, 1H).

Synthesis of racemic-3-(benzyloxy)-2-hydroxy-1-(*m*-tolyl)-propan-1-one (rac-13)

General procedure described above starting from *m*-tolualdehyde and benzyloxyacetaldehyde, provided the pure product obtained as white oil (23% yield). TLC hexane/ethyl acetate = 90:10. $R_f = 0.73$.

^1H NMR (400 MHz, CDCl_3) δ : 7.68-7.59 (m, 3H), 7.35 (d, $J = 7.6$ Hz, 2H), 7.16 (m, 2H), 7.06 (dd, $J = 6.8, 2.5$ Hz, 2H), 5.13 (t, $J = 3.8$ Hz, 1H), 4.44 (d, $J = 12.3$ Hz, 1H), 4.37 (d, $J = 12.3$ Hz, 1H), 3.71 (dd, $J = 10.3, 3.2$ Hz, 1H), 3.67 (dd, $J = 10.3, 4.4$ Hz, 1H), 2.33 (s, 3H).

Synthesis of racemic 3-(benzyloxy)-2-hydroxy-1-(3-fluorophenyl)-propan-1-one (rac-14)

The general procedure described above, starting from 3-fluorobenzaldehyde and benzyloxyacetaldehyde, provided the pure product obtained as a white powder (36% yield). TLC: hexane/ethyl acetate = 90:10. R_f = 0.63.

^1H NMR (400 MHz, CDCl_3) δ : 7.83 (d, J = 7.7 Hz, 1H), 7.59 (d, J = 7.7 Hz, 1H), 7.37 (tt, J = 7.9, 5.5 Hz, 2H), 7.27-7.19 (m, 3H), 7.06 (dd, J = 7.9, 5.1 Hz, 2H), 5.08 (t, J = 3.7 Hz, 1H), 4.45 (d, J = 12.3 Hz, 1H), 4.36 (d, J = 12.3 Hz, 1H), 3.73 (dd, J = 9.8, 3.5 Hz, 1H), 3.69 (dd, J = 10.3, 4.2 Hz, 1H).

RESULTS AND DISCUSSION

BAL was expressed in *E. coli* based on the procedures described before. Crude lysate was used without purification as catalyst after determination of its activity in benzoin condensation reactions based on literature. One unit activity (U) of BAL is defined as the amount of the enzyme that is used for the formation of 1 μmol of benzoin in pH 7 buffer containing 50 mM phosphate, 2.5 mM MgSO_4 , 0.15 mM ThDP and DMSO (20%, v/v) in 1 minute at 30 °C.

For this measurement, a set of reactions with the same concentration of benzaldehyde was treated with BAL and every 10 minutes, a small sample was taken from the reaction mixture. The amount of benzoin that was formed during the reaction was determined by HPLC based on the calibration curve that was drawn by using commercial benzoin samples. The activity of BAL that was used in this work found to be 0.2 U.

For the synthesis of racemic benzoin derivatives, standard benzoin condensation reactions were used by using NaCN as catalyst and water/ethanol mixture as solvent. In Figure 1, the synthesized *rac*-benzoin derivatives are given with their yields. Racemic benzoin and 4,4'-dimethoxybenzoin were commercially available and obtained from Sigma-Aldrich.

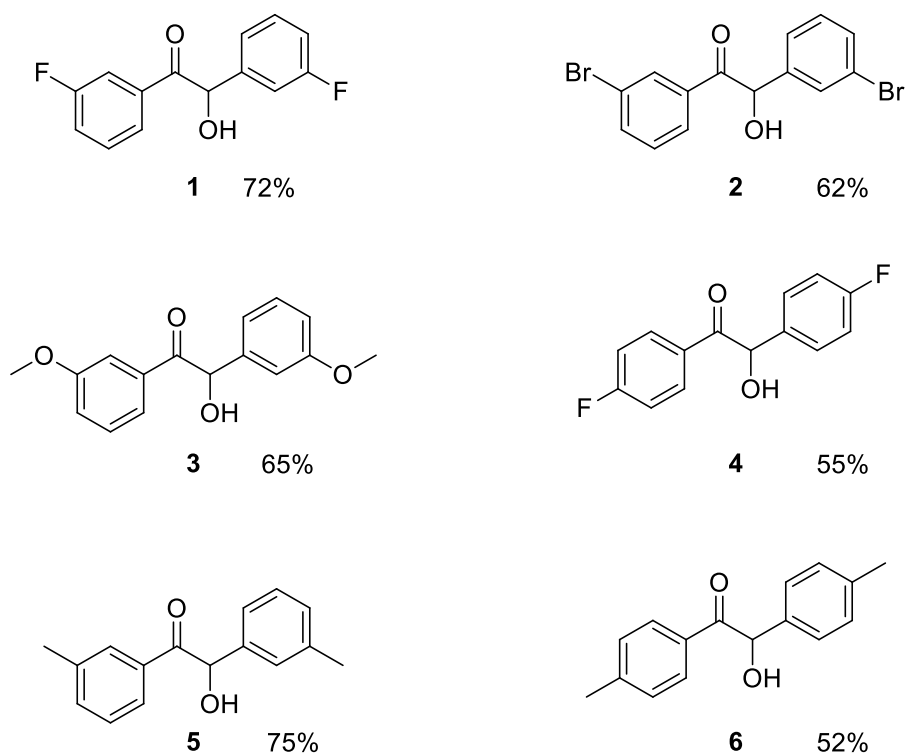
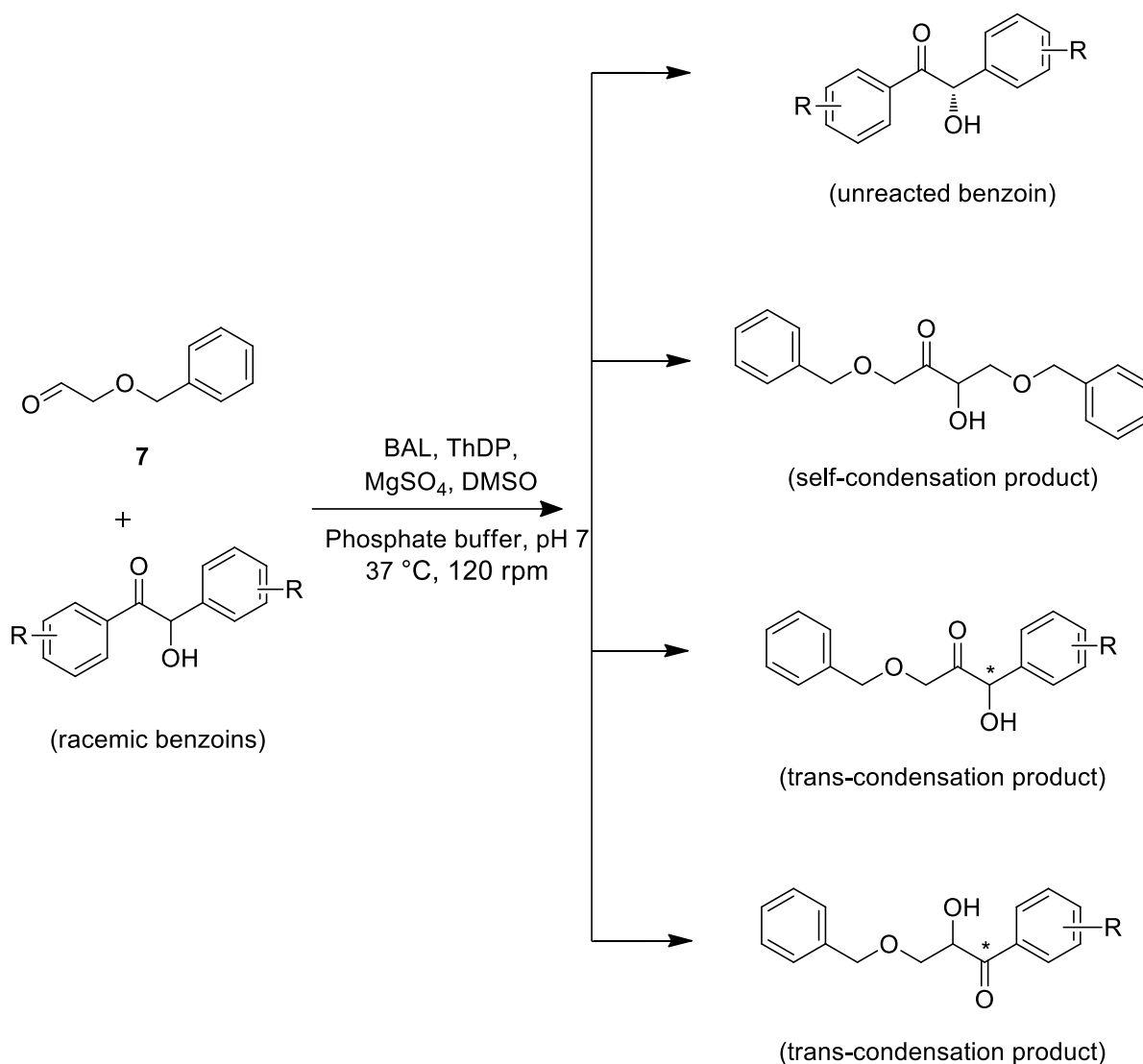


Figure 1. The structure and the yield of the *rac*-benzoin derivatives that were used in trans-benzoin condensation reactions.

These six synthesized and two commercially available *rac*-benzoin derivatives were used in the enzymatic trans-benzoin condensation reactions. For this purpose, each *rac*-benzoin derivative and benzoyloxyacetaldehyde (–) were dissolved in DMSO and then added to pH 7 buffer containing MOPS (50 mM), ThDP and MgSO₄. After the temperature of the reaction mixture was set to 37 °C, BAL was added (0.2 U) and it was shaken with a constant speed at 120 rpm. The reaction was monitored by TLC, and BAL was added daily. After 72 hours, the reaction was stopped and the aqueous phase was extracted by diethyl ether three times. Then, the combined etheric phases were washed with brine and dried over MgSO₄. After removal of the solvent under reduced pressure, the crude product was purified by flash column chromatography using ethyl acetate-hexane solvent mixture as eluent.



Scheme 3. All possible products of enzymatic-trans benzoin condensation reaction.

From the trans-benzoin condensation reaction of *rac*-benzoin and benzyloxyacetaldehyde, theoretically four different products can be formed. One of them is the unreacted (*S*)-benzoin derivative. Two of them are trans-benzoin products where benzyloxyacetaldehyde acts as a donor and acceptor. Another of them is the self-benzoin condensation of benzyloxyacetaldehyde. However, practically only (*S*)-benzoin and one trans-benzoin products, where benzyloxyacetaldehyde acted as an acceptor, was observed (Scheme 3).

Among eight different *rac*-benzoin derivatives, four of them were able to be purified, characterized, and their enantiomeric excess were determined by chiral HPLC (9). 4,4'-dimethoxybenzoin and 4,4'-dimethylbenzoin gave the corresponding trans-benzoin products with the highest enantiomeric excesses (63 and 62% ee, respectively). Benzoin and 3,3'-dimethoxybenzoin resulted trans-benzoin products with relatively low enantiomeric excesses (35 and 36% ee, respectively) (Figure 2).

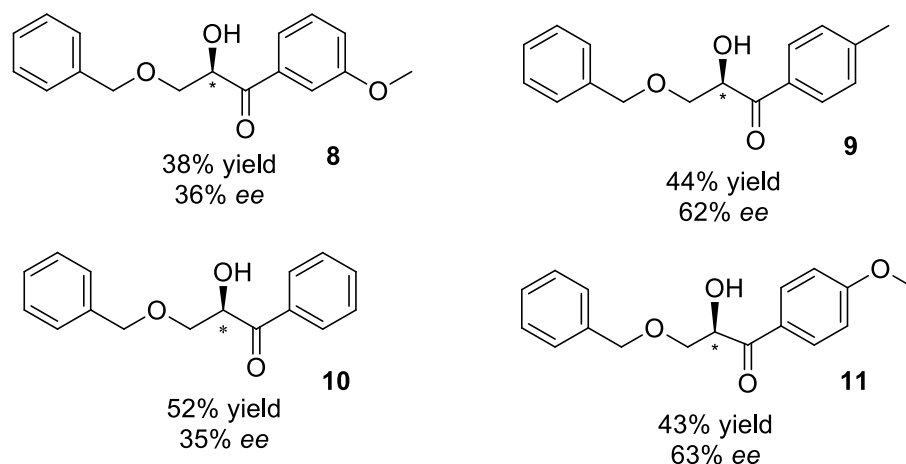


Figure 2. Yield and enantiomeric excess of purified enzymatic trans-benzoin reaction products.

The trans-benzoin products that were formed from 3,3'-difluoro-, 3,3'-dibromo- and 3,3'-dimethylbenzoin derivatives were detected by ^1H NMR spectroscopy in their crude mixture. However, they could not be separated from other benzoin products due to structural similarities. Enantiomeric excesses of these products were able to be determined by chiral HPLC (9) by comparing the retention time of racemic benzoin derivatives (*rac-12*, *rac-13*, *rac-14*) obtained from cross-benzoin condensation reaction of corresponding aldehyde derivatives and benzyloxyacetaldehyde. 4,4'-difluorobenzoin derivative gave a complex mixture of products that were not possible to determine enantiomeric excess of the trans-benzoin product (Figure 3).

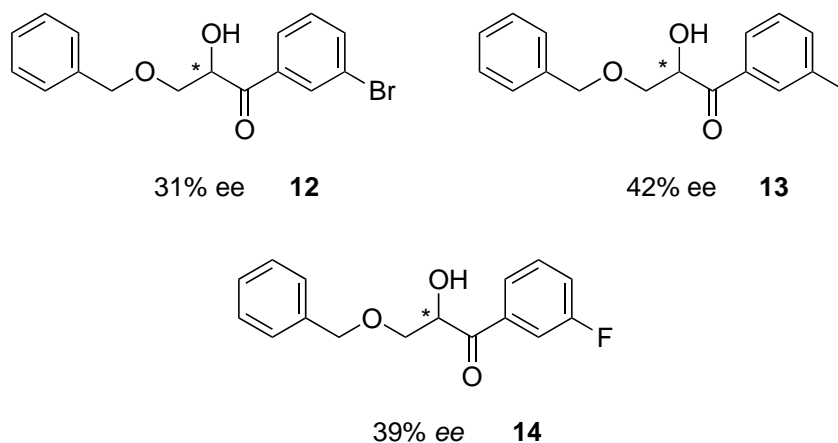


Figure 3. Enantiomeric excesses of crude enzymatic trans-benzoin reaction products.

In conclusion, various racemic benzoin derivatives were reacted with benzyloxyacetaldehyde with BAL as a catalyst to obtain enantiomerically enriched trans-benzoin products. These products are important precursors in the synthesis of chiral polyalcohols. After removal of benzyl

protection and reduction of carbonyl group, they can be converted into corresponding 1,2,3-triols.

ACKNOWLEDGMENTS

We would like to thank METU-BAP for the financial support.

REFERENCES

1. Hinrichsen P, Gomez I, Vicuña R. Cloning and sequencing of the gene encoding benzaldehyde lyase from *Pseudomonas fluorescens* biovar I. *Gene*. 1994 Jun;144(1):137–8.
2. Biotransformations in organic chemistry: a textbook. 1st edition. Vol. 4. New York, NY: Springer Berlin Heidelberg; 1992.
3. Dünkemann P, Kolter-Jung D, Nitsche A, Demir AS, Siegert P, Lingen B, et al. Development of a Donor–Acceptor Concept for Enzymatic Cross-Coupling Reactions of Aldehydes: The First Asymmetric Cross-Benzoin Condensation. *Journal of the American Chemical Society*. 2002 Oct;124(41):12084–5.
4. Demir AS, Ayhan P, Sopaci SB. Thiamine Pyrophosphate Dependent Enzyme Catalyzed Reactions: Stereoselective C–C Bond Formations in Water. *CLEAN – Soil, Air, Water*. 2007 Nov;35(5):406–12.
5. Demir AS, Şeşenoglu Ö, Eren E, Hosrik B, Pohl M, Janzen E, et al. Enantioselective Synthesis of α -Hydroxy Ketones via Benzaldehyde Lyase-Catalyzed C–C Bond Formation Reaction. *Advanced Synthesis & Catalysis*. 2002 Jan;344(1):96.
6. Demir AS, Pohl M, Janzen E, Müller M. Enantioselective synthesis of hydroxy ketones through cleavage and formation of acyloin linkage. Enzymatic kinetic resolution via C–C bond cleavage. *Journal of the Chemical Society, Perkin Transactions 1*. 2001;(7):633–5.
7. Adams R, Marvel C. BENZOIN. *Organic Syntheses*. 1921;1:33.
8. Jin MY, Kim SM, Han H, Ryu DH, Yang JW. Switching Regioselectivity in Crossed Acyloin Condensations between Aromatic Aldehydes and Acetaldehyde by Altering N -Heterocyclic Carbene Catalysts. *Organic Letters*. 2011 Mar 4;13(5):880–3.
9. See supporting information for the HPLC chromatograms used to determine enantiomeric excesses.



Macro and Trace Element Contents of Some Wild Plants Consumed as Vegetable in Manisa District, Turkey

Şerif TARGAN^{1*}, Ersin Gökselel YELBOĞA¹, Mustafa CİTTAN¹

¹ Manisa Celal Bayar University, Faculty of Science and Letters, Department of Chemistry, 45140, Manisa, Turkey

Abstract: In this study, macro elements (Na, Mg, and Ca) and trace elements (Li, Fe, Zn, Mn, Se, Al, V, Cr, Ni, Cu, Pb, As, Co, Cd, and Hg) in wild edible plant samples (*Campanula sp*, *Anethum graveolens*, *Malva sylvestris*, *Onopordum tauricum*, *Cichorium endivia*, *Rumex patientia*, *Urtica dioica*, *Papaver rhaeas*, *Opopanax hispidus*, *Rumex acetosella*, *Eradium sp*, *Petroselinum crispum*, *Metha viridis*, *Eruca sativa*, *Sinapis arvensis*, *Lepidium sativum*, and *Cardaria draba*) purchased from three different markets in Manisa district were analyzed using inductively coupled plasma-mass spectrometry after microwave digestion procedure. Selected plants for analysis are mostly consumed by people throughout the season. The mean concentrations of Na, Mg, Ca, Li, Fe, Zn, Mn, Se, Al, V, Cr, Ni, Cu, Pb, As, Co and Cd were determined as 201 to 15896, 1597 to 4783, 3676 to 13290, 0.27 to 4.37, 144 to 666, 18.0 to 52.0, 21.2 to 86.5, 0.08 to 0.25, 111 to 693, 2.18 to 5.67, 2.62 to 13.4, 1.32 to 6.30, 6.40 to 38.7, 0.12 to 0.78, 1.07 to 3.25, 0.05 to 0.47, 0.08 to 0.50 ($\mu\text{g g}^{-1}$, dry weight), respectively. Hg values for plant samples were well below the detection limit of the method.

Keywords: ICP-MS, macro element, trace element, microwave digestion, wild plant.

Submitted: Dec 06, 2017. **Accepted:** May 02, 2018.

Cite this: Targan Ş, Yelboğa E, Cittan M. Macro and Trace Element Contents of Some Wild Plants Consumed as Vegetable in Manisa District, Turkey. JOTCSA. 2018;5(2):751–62.

DOI: <http://dx.doi.org/10.18596/jotcsa.363151>.

***Corresponding author.** E-mail: serif.targan@cbu.edu.tr.

People living in Aegean region in Turkey consume wild edible plants to provide their nutritional requirements. Wild plants that are not well known in other geographical regions in Turkey constitute the Aegean main cuisine. However, wild plants with leaves have an important role in recent well-balanced diet programs. In dietary programs, the idea of getting less amounts of red meat and more vegetable and fruits becomes more popular (1,2). Due to their high water content, with few exceptions, wild plants are believed to occupy a modest place as a source of trace elements (3).

The trace elements and other essential nutrients are necessary for growth, and maintaining of life. Since the body cannot synthesize them, trace elements must be supplied by food. There is no clear classification of trace vs. macro minerals, but traces are often considered as minerals required by the body in amounts less than 100 mg daily (4). The nutritional and toxicity values have also been studied and extensively discussed (5). Elements, above threshold concentrations, can cause morphological abnormalities, and mutagenic effects in humans (6). Therefore, determination of macro and trace element contents in edible wild plants is important.

Flame and graphite furnace atomic absorption spectrophotometry (7) (FAAS and GFAAS), inductively coupled plasma-optical emission spectrometry (8) (ICP-OES) and inductively coupled plasma-mass spectrometry (9) (ICP-MS) were used in the studies of element concentrations in plant samples. Especially, ICP-MS is considered excellent technique for the analysis of trace and macro elements in plants. MS is, without a doubt, one of the most important and widely used analytical techniques for the detection and determination of element and molecule concentrations. The mass spectrometer is a highly sophisticated instrument that can aid in the measurement of concentrations in the trace and ultra-trace range (10).

Several studies has been carried out to determine the element contents of some plants in different habitats in Turkey (11–13). The aim of present work was to determine the macro (Na, Mg and Ca) and trace (Li, Fe, Zn, Mn, Se, Al, V, Cr, Ni, Cu, Pb, As, Co, Cd and Hg) element content of seventeen wild plants sold in three different markets of Manisa after microwave digestion using ICP-MS.

EXPERIMENTAL

Sampling

Approximately 100 g of each plants were purchased from each of the three markets. Table 1 summarizes botanical features including the scientific name, regional name, family, edible part, and usage.

Table 1: Analysis of characteristics of the plants

Scientific Name	Regional Name	Family	Edible Part	Usage
<i>Campanula sp</i>	Çingirak otu	Campanulaceae	Aerial	Vegetable
<i>Anethum graveolens</i>	Dere Otu	Apiaceae	Aerial	Vegetable, tea
<i>Malva sylvestris</i>	Ebe Gümeçi	Malvaceae	Aerial	Vegetable, tea
<i>Onopordum tauricum</i>	Eşek Helvası	Asteraceae	Aerial	Vegetable
<i>Cichorium endivia</i>	Hindiba	Asteraceae	Aerial	Vegetable
<i>Rumex patientia</i>	Labada	Polygonaceae	Aerial	Vegetable
<i>Urtica dioica</i>	Isırgan Otu	Urticaceae	Aerial	Vegetable, tea
<i>Papaver rhaeas</i>	Kapurcak	Papaveraceae	Aerial	Vegetable
<i>Opopanax hispidus</i>	Kaymak Otu	Apiaceae	Aerial	Vegetable
<i>Rumex acetosella</i>	Kuzu Kulağı	Polygonaceae	Aerial	Vegetable
<i>Eradium sp</i>	Leylek Gagası	Geraniaceae	Aerial	Vegetable
<i>Petroselinum crispum</i>	Maydanoz	Apiaceae	Aerial	Vegetable
<i>Metha viridis</i>	Nane	Lamiaceae	Aerial	Vegetable, tea
<i>Eruca sativa</i>	Roka	Brassicaceae	Aerial	Vegetable
<i>Sinapis arvensis</i>	Tatlı Hardal	Brassicaceae	Aerial	Vegetable
<i>Lepidium sativum</i>	Tere	Brassicaceae	Aerial	Vegetable
<i>Cardaria draba</i>	Toklu Başı	Brassicaceae	Aerial	Vegetable

Sample preparation

Samples were washed with ultra-pure water and 100 g samples from each species were dried in an oven at 80 °C for 24 hours before homogenization. Samples milled in a micro-hammer cutter and sieved through 0.2 mm after homogenization process and placed temporarily in clean self-sealing plastic bags until their analysis for their Na, Mg, Ca, Li, Fe, Zn, Mn, Se, Al, V, Cr, Ni, Cu, Pb, As, Co, Cd and Hg content. An appropriate quantity (1 g) from each 100 g sample was used for analysis. All the samples were analyzed in triplicate and the results were reported as mean values \pm standard deviation.

Instruments

All metal measurements were carried out using a Perkin Elmer, DRC-e; CCD Simultaneous ICP-MS. The ICP-MS operating conditions are listed in Table 2. Microwave MARS 5 closed vessel microwave system (CEM, Matthews, NC, and USA) was used for microwave digestion.

Table 2: The operating parameters of determination of elements by ICP- MS

Plasma conditions	Value
RF power	1.2 kW
Plasma Ar flow rate	15 L min ⁻¹
Auxiliary Ar flow rate	0.89 L min ⁻¹
Carrier Ar flow rate	0.95–1.0 L min ⁻¹
Torch horizontal alignment	(0.5–1.0) mm
Torch vertical alignment	0.2–0.5 mm
Sampling depth	6.0–8.0 mm
Sample uptake rate	0.80 mL min ⁻¹

Reagents and chemicals

Suprapure grade chemicals were employed in the preparation of all solutions. Ultrapure water (Milli-Q Millipore 18.2Ω/cm) was used in all experiments. HCl, HNO₃ and H₂O₂ were of suprapure quality (E. Merck). All the plastic and glassware were cleaned by soaking in dilute nitric acid and were rinsed with distilled water prior to use. The standard solutions of analytes for calibration procedure were produced by diluting individual stock solutions of the investigated element supplied by Sigma.

Digestion procedure

Microwave digestion procedure was applied to the plant samples; microwave digestion (with HNO₃–H₂O₂ in microwave oven). Approximately 1.0 g of sample was digested with 6 mL of HNO₃ and 2 mL of H₂O₂ in microwave digestion system. The temperature program was as follows: 2 min for 400 w, 2 min for 400 w, 6 min for 400 w, 5 min for 400 w, 8 min for 800 w and 8 min for vent. The resulting solutions were cooled and diluted to 10 mL with distilled water. The clear solutions were analyzed by ICP-MS after additional dilution if necessary.

Calibration and detection limits

Calibration standard solutions were prepared by dilution of the stock standard solutions to desired concentration in 1% HNO₃. The ranges of the calibration curves (7 points) were selected to match the expected concentrations (0–30 µg g⁻¹) for all the elements of the sample studied by ICP-MS. The correlation coefficient r^2 obtained for all cases was 0.9999. The detection limits (LOD) were calculated as the concentrations of an element that gave the standard deviation of a series of ten consecutive measurements of microwave digested blank solutions. The LOD values of Na, Mg, Ca, Li, Fe, Zn, Mn, Se, Al, V, Cr, Ni, Cu, Pb, As, Co, Cd and Hg were calculated as; 0.0036, 0.0012, 0.0003, 0.0042, 0.0018, 0.0018, 0.0021, 0.0018, 0.0006, 0.0003, 0.0033, 0.0024, 0.0036, 0.0009, 0.0003, 0.0027, 0.0021 and 0.0009 (µg g⁻¹) respectively.

Statistical analysis

All the samples were analyzed in triplicate and mean values along with standard deviation (\pm) are shown in the Table 3 and 4.

RESULTS AND DISCUSSION

Levels of the macro (Na, Mg and Ca) and the trace (Li, Fe, Zn, Mn, Se, Al, V, Cr, Ni, Cu, Pb, As, Co, Cd and Hg) elements in plant samples are given in Tables 3 and 4, respectively. The mean concentrations of Na, Mg, Ca, Li, Fe, Zn, Mn, Se, Al, V, Cr, Ni, Cu, Pb, As, Co and Cd were found as 201 to 15896, 1597 to 4783, 3676 to 13290, 0.27 to 4.37, 144 to 666, 18.0 to 52.0, 21.2 to 86.5, 0.08 to 0.25, 111 to 693, 2.18 to 5.67, 2.62 to 13.4, 1.32 to 6.30, 6.40 to 38.7, 0.12 to 0.78, 1.07 to 3.25, 0.05 to 0.47, 0.08 to 0.50 $\mu\text{g g}^{-1}$, dry weight in plant samples, respectively (Figures 1, 2, 3 and 4). Hg values for selected plant samples were well below the detection limit of the method.

Table 3: Macro element contents in selected 17 different plants from 3 different markets (51 samples) ($\mu\text{g g}^{-1}$ dry weight) (n=3)

Sample	Na	Mg	Ca
<i>Campanula sp</i>	643 \pm 143	2593 \pm 1925	9012 \pm 1266
<i>Anethum graveolens</i>	13617 \pm 11613	4353 \pm 1624	5851 \pm 155
<i>Malva sylvestris</i>	2919 \pm 1704	2877 \pm 1425	7621 \pm 631
<i>Onopordum tauricum</i>	15896 \pm 10472	2594 \pm 1729	6722 \pm 702
<i>Cichorium endivia</i>	1847 \pm 256	2224 \pm 1275	4417 \pm 103
<i>Rumex patientia</i>	2862 \pm 1847	2433 \pm 3165	3676 \pm 535
<i>Urtica dioica</i>	1185 \pm 133	4783 \pm 3281	13290 \pm 724
<i>Papaver rhaeas</i>	706 \pm 90	2834 \pm 3106	6871 \pm 54
<i>Opopanax hispidus</i>	201 \pm 49	2181 \pm 1443	5381 \pm 717
<i>Rumex acetosella</i>	1442 \pm 1034	3824 \pm 2266	4435 \pm 991
<i>Eradium sp</i>	1494 \pm 1165	1918 \pm 1494	8190 \pm 1138
<i>Petroselinum crispum</i>	1518 \pm 1027	1736 \pm 1238	4757 \pm 656
<i>Metha viridis</i>	391 \pm 60	3224 \pm 1735	5370 \pm 566
<i>Eruca sativa</i>	441 \pm 73	3266 \pm 1382	6926 \pm 487
<i>Sinapis arvensis</i>	1082 \pm 202	1919 \pm 1591	6554 \pm 357
<i>Lepidium sativum</i>	675 \pm 108	1597 \pm 1424	7675 \pm 2179
<i>Cardaria draba</i>	3451 \pm 1644	3364 \pm 1553	6469 \pm 1161
Minimum	201 \pm 48	1597 \pm 1424	3676 \pm 535
Maximum	15896 \pm 10472	4783 \pm 3280	13290 \pm 724
Mean	2962 \pm 1105	2807 \pm 220	6659 \pm 544

Table 4: Trace element contents in selected 17 different plants from 3 different markets (51 samples) ($\mu\text{g g}^{-1}$ dry weight) (n=3)

Sample	Li	Al	V	Cr	Mn	Fe	Co	Ni
<i>Campanula sp</i>	0.93±0.14	327±94.8	2.30±1.32	3.85±0.29	29.2±8.09	364±50.9	0.18±0.17	4.22±1.00
<i>Anethum graveolens</i>	1.00±0.02	287±117	5.17±2.43	5.40±1.75	86.5±28.0	423±142	0.20±0.19	5.10±0.78
<i>Malva sylvestris</i>	1.00±0.19	288±100	2.18±1.60	4.65±1.18	33.4±5.95	334±84.4	0.18±0.09	3.97±0.71
<i>Onopordum tauricum</i>	1.10±0.12	227±81.5	3.95±1.87	4.43±0.60	54.7±5.61	270±71.7	0.08±0.07	6.30±3.57
<i>Cichorium endivia</i>	1.13±0.14	242±64.2	2.48±2.01	3.67±0.76	33.5±3.29	265±54.9	0.17±0.08	2.57±0.45
<i>Rumex patientia</i>	4.37±3.08	420±113	2.63±0.31	5.70±2.17	30.1±0.40	432±124	0.17±0.16	4.02±1.08
<i>Urtica dioica</i>	2.42±0.95	155±49.1	2.83±1.12	2.62±0.20	21.2±0.23	246±34,1	< LOD	2.72±0.23
<i>Papaver rhaeas</i>	1.02±0.27	195±96.5	3.03±2.14	13.4±6.91	45.2±4.28	289±102	0.10±0.09	2.92±0.55
<i>Opopanax hispidus</i>	0.27±0.09	111±35.8	2.22±1.83	5.15±1.08	22.2±0.12	144±26.0	< LOD	1.32±0.16
<i>Rumex acetosella</i>	0.82±0.13	403±155	3.43±2.35	5.52±2.08	53.9±4.74	434±136	0.28±0.16	3.37±0.78
<i>Eradium sp</i>	0.90±0.25	298±43.9	2.18±1.17	6.58±2.52	40.8±4.57	370±41.0	0.13±0.08	3.38±0.97
<i>Petroselinum crispum</i>	1.05±0.27	192±121	3.33±1.34	4.23±1.04	48.9±7.11	262±77.5	0.08±0.07	2.62±0.31
<i>Metha viridis</i>	1.28±0.06	693±60.7	5.67±1.57	7.07±1.43	45.3±6.71	666±75.7	0.47±0.06	5.32±0.75
<i>Eruca sativa</i>	0.60±0.10	163±12.1	2.19±1.28	3.38±0.49	29.5±5.84	243±1.16	< LOD	2.83±0.40
<i>Sinapis arvensis</i>	0.95±0.13	144±15.6	4.95±0.98	11.5±4.78	33.2±3.58	212±8.67	0.05±0.04	2.75±0.40
<i>Lepidium sativum</i>	1.23±0.35	490±103	4.32±1.72	6.95±1.76	61.1±7.57	470±40.5	0.40±0.23	6.30±0.50
<i>Cardaria draba</i>	0.70±0.57	310±88.4	4.30±1.58	4.63±1.10	33.3±5.20	352±91,9	0.22±0.11	3.87±1.64
Minimum	0.27±0.09	111±35.8	2.18±1.17	2.62±0.20	21.2±0.23	144±26.0	0.05±0.04	1.32±0.16
Maximum	4.37±3.07	693±60.7	5.67±1.57	13.4±6.91	86.5±28.0	666±75.7	0.47±0.06	6.30±3.57
Mean	1.22±0.22	291±35.7	3.36±0.28	5.81±0.68	41.29±3.98	340±29.8	0.19±0.03	3.74±0.33

Sample	Cu	Zn	As	Se	Cd	Pb	Hg
<i>Campanula sp</i>	6.40±0.70	33.5±12.3	1.72±1.16	< LOD	< LOD	0.18±0.09	< LOD
<i>Anethum graveolens</i>	18.2±5.50	26.7±3.12	1.53±1.34	< LOD	< LOD	0.32±0.16	< LOD
<i>Malva sylvestris</i>	9.20±0.98	20.7±3.29	1.30±1.11	< LOD	0.13±0.12	0.67±0.48	< LOD
<i>Onopordum tauricum</i>	10.2±0.69	22.1±2.77	2.35±1.18	< LOD	0.08±0.07	0.22±0.11	< LOD
<i>Cichorium endivia</i>	9.60±1.23	21.4±4.51	1.08±0.89	0.25±0.24	< LOD	0.15±0.09	< LOD
<i>Rumex patientia</i>	9.52±1.05	31.3±4.45	1.33±0.16	< LOD	< LOD	0.52±0.13	< LOD
<i>Urtica dioica</i>	38.7±22.3	18.0±0.81	3.25±1.23	< LOD	< LOD	0.12±0.11	< LOD
<i>Papaver rhæas</i>	18.1±6.46	34.9±5.55	1.75±1.38	0.08±0.07	0.27±0.14	0.30±0.03	< LOD
<i>Opopanax hispidus</i>	16.4±9.86	32.3±4.91	1.07±0.92	< LOD	< LOD	0.12±0.11	< LOD
<i>Rumex acetosella</i>	10.2±1.73	22.3±1.27	1.13±0.76	< LOD	< LOD	0.65±0.17	< LOD
<i>Eradium sp</i>	25.4±8.68	21.9±1.97	1.37±1.05	< LOD	< LOD	0.30±0.03	< LOD
<i>Petroselinum crispum</i>	6.68±0.97	19.5±4.05	1.67±0.76	< LOD	< LOD	0.25±0.14	< LOD
<i>Metha viridis</i>	12.9±3.78	31.1±2.43	2.63±0.94	< LOD	< LOD	0.47±0.07	< LOD
<i>Eruca sativa</i>	7.93±0.92	22.6±2.08	1.52±0.83	< LOD	0.12±0.11	0.65±0.30	< LOD
<i>Sinapis arvensis</i>	11.9±1.85	26.9±6.71	2.20±0.82	< LOD	0.50±0.14	0.78±0.27	< LOD
<i>Lepidium sativum</i>	9.78±2.62	52.0±18.6	2.33±1.03	< LOD	0.37±0.20	0.45±0.31	< LOD
<i>Cardaria draba</i>	10.3±2.89	24.3±1.73	2.12±0.84	< LOD	0.10±0.09	0.35±0.08	< LOD
<i>Minimum</i>	6.40±0.70	18.0±0.81	1.07±0.92	0.08±0.08	0.08±0.07	0.12±0.11	< LOD
<i>Maximum</i>	38.7±22.3	52.0±18.6	3.25±1.23	0.25±0.24	0.50±0.14	0.78±0.27	< LOD
<i>Mean</i>	13.6±1.97	27.2±2.01	1.79±0.15	0.17±0.09	0.22±0.06	0.38±0.05	< LOD

The results of macro elements are provided in Table 3. All values are expressed as dry weight in $\mu\text{g g}^{-1}$. In the plants, Na was highest in *Onopordum tauricum* (15896), lowest in *Opopanax hispidus* (201), Mg was highest in *Urtica dioica* (4783), lowest in *Lepidium sativum* (1597), Ca was highest *Urtica dioica* (13290), lowest in *Rumex patientia* (3676).

Trace element results of the plants are presented in Table 4. All values are expressed as dry weight in $\mu\text{g g}^{-1}$. The table shows that Li was highest in *Rumex patientia* (4.37), lowest in *Opopanax hispidus* (0.27), Al was highest *Metha viridis* (693), lowest in *Opopanax hispidus* (111), V was highest in *Metha viridis* (5.67), lowest in *Malva sylvestris* and *Eradium sp* (2.18), Cr was highest in *Papaver rhaeas* (13.4), lowest in *Urtica dioica* (2.62), Mn was highest in *Anethum graveolens* (86.5), lowest in *Urtica dioica* (21.2), Fe was highest in *Metha viridis* (666), lowest in *Opopanax hispidus* (144), Co was highest in *Metha viridis* (0.47), lowest in *Sinapis arvensis* (0.05), Ni was highest in *Onopordum tauricum* (6.30), lowest in *Opopanax hispidus* (1.32), Cu was highest in *Urtica dioica* (38.7), lowest in *Campanula sp* (6.40), Zn was highest in *Lepidium sativum* (52.0), lowest in *Urtica dioica* (18.0), As was highest in *Urtica dioica* (3.25), lowest in *Opopanax hispidus* (1.07), Se was highest in *Cichorium endivia* (0.25), lowest in *Papaver rhaeas* (0.08), Cd was highest in *Sinapis arvensis* (0.50), lowest in *Onopordum tauricum* (0.08), Pb was highest in *Sinapis arvensis* (0.78), lowest in *Urtica dioica* and *Opopanax hispidus* (0.12).

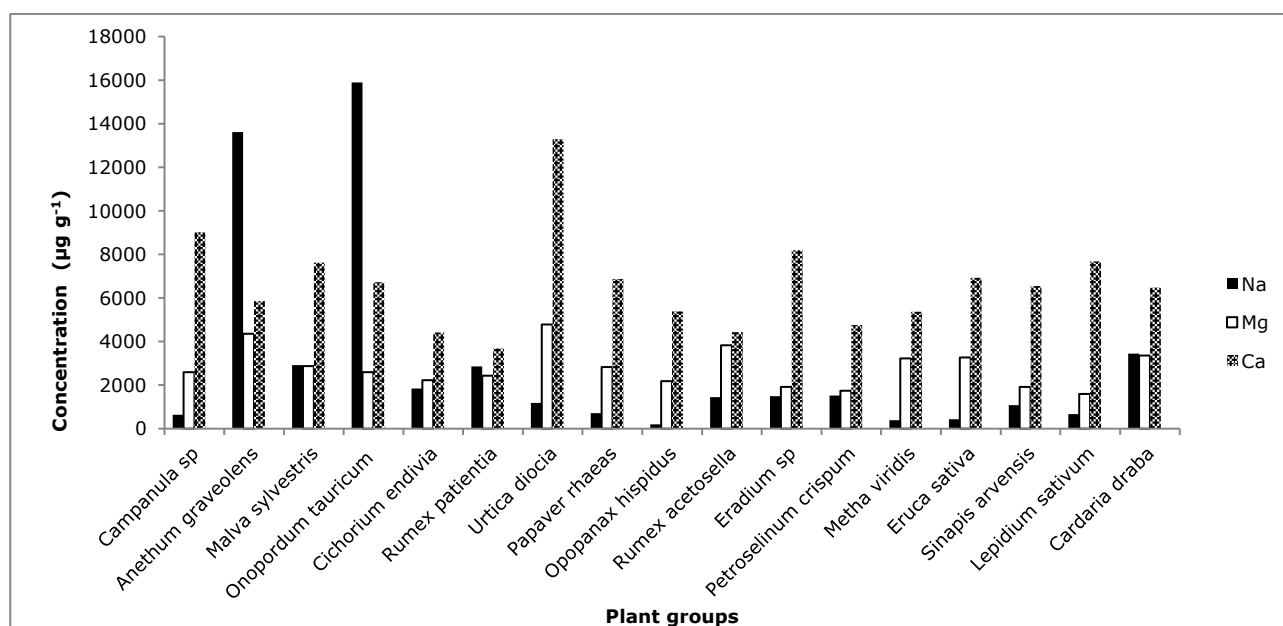


Figure 1: Concentrations of Na, Mg and Ca in selected wild plant samples ($\mu\text{g g}^{-1}$, dry weight).

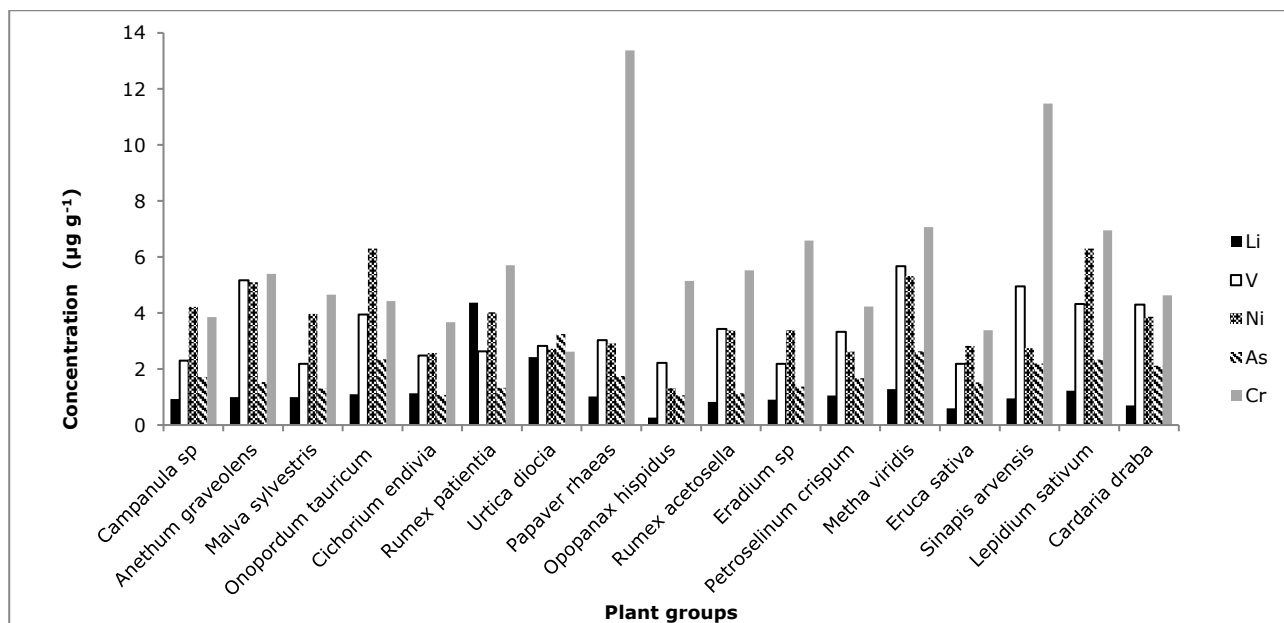


Figure 2: Concentrations of Li, V, Ni, As and Cr in selected wild plant samples ($\mu\text{g g}^{-1}$, dry weight).

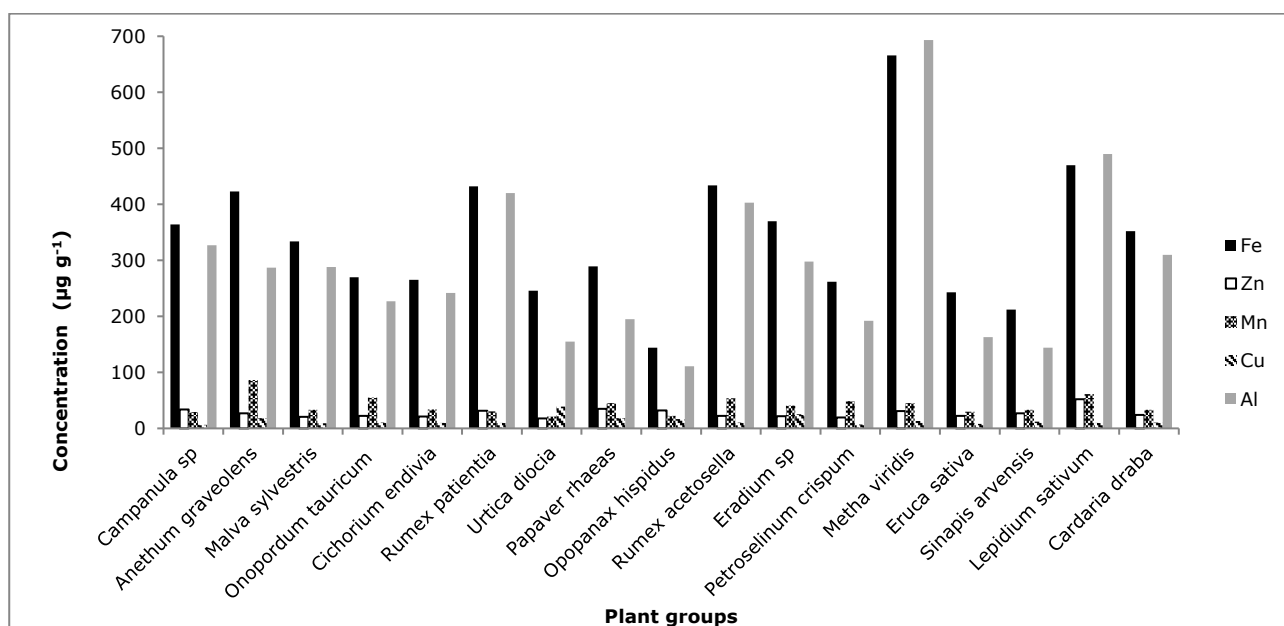


Figure 3: Concentrations of Fe, Zn, Mn, Cu and Al in selected wild plant samples ($\mu\text{g g}^{-1}$, dry weight).

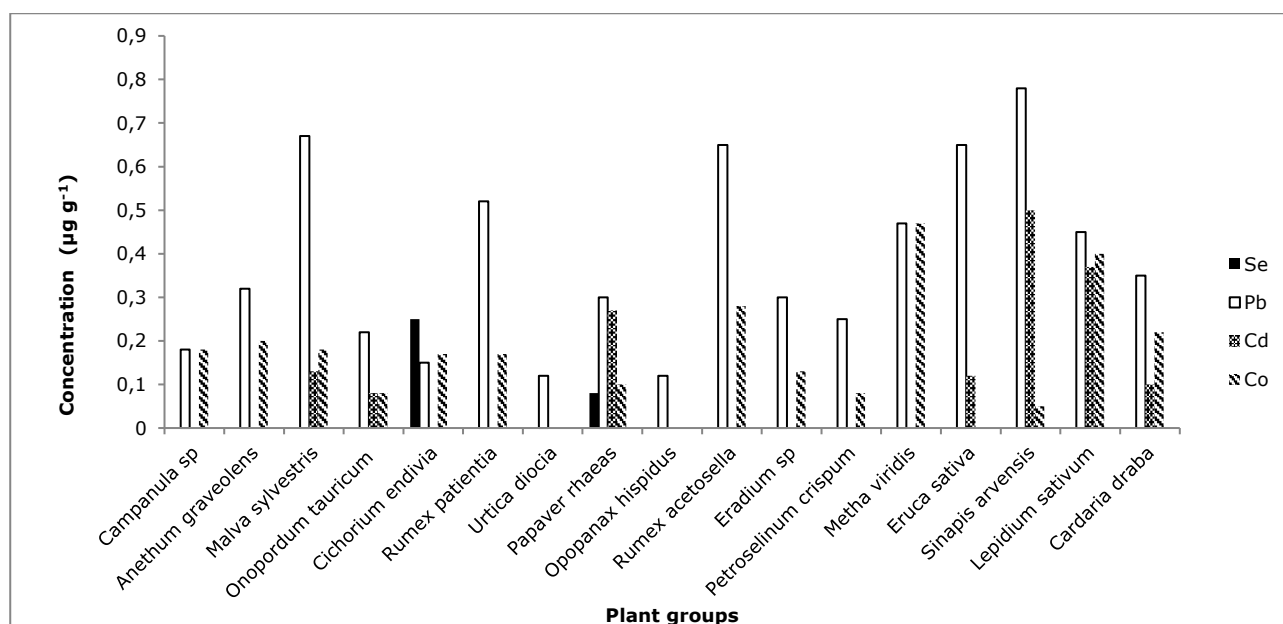


Figure 4: Concentrations of Se, Pb, Cd and Co in selected wild plant samples ($\mu\text{g g}^{-1}$, dry weight).

CONCLUSION

In this study, the concentrations of trace elements: Na, Mg, Ca, Li, Fe, Zn, Mn, Se, Al, V, Cr, Ni, Cu, Pb, As, Co, Cd and Hg in seventeen wild plant samples (*Campanula sp*, *Anethum graveolens*, *Malva sylvestris*, *Onopordum tauricum*, *Cichorium endivia*, *Rumex patientia*, *Urtica dioica*, *Papaver rhaeas*, *Opopanax hispidus*, *Rumex acetosella*, *Eradium sp*, *Petroselinum crispum*, *Metha viridis*, *Eruca sativa*, *Sinapis arvensis*, *Lepidium sativum*, and *Cardaria draba*) purchased from three different markets in Manisa district were analyzed using ICP-MS after microwave digestion procedure. The quantitative results obtained from the study provide significant information about the macro and trace element contents of the wild edible plants that are frequently consumed by the people of the region.

ACKNOWLEDGEMENTS

The authors are grateful to the Academic Dean for College of Science Prof. Dr. Mustafa ERSÖZ and Specialist İlker AKIN at the University of Selçuk for the availability of the ICP-MS instrument.

REFERENCES

1. Kris-Etherton PM, Krummel D, Russell ME, Dreon D, Mackey S, Borchers J, et al. The effect of diet on plasma lipids, lipoproteins, and coronary heart disease. *J Am Diet Assoc.* 1988;88(11):1373–1400.

2. Osler M, Heitmann BL, Gerdes LU, Jørgensen LM, Schroll M. Dietary patterns and mortality in Danish men and women: a prospective observational study. *Br J Nutr.* 2001;85(2):219–225.
3. Gibson RS. Zinc nutrition in developing countries. *Nutr Res Rev.* Cambridge University Press; 1994;7:151–173.
4. Lesniewicz A, Jaworska K, Zyrnicki W. Macro- and micro-nutrients and their bioavailability in polish herbal medicaments. *Food Chem.* 2006;99:670–679.
5. Goldhaber SB. Trace element risk assessment: essentiality vs. toxicity. *Regul Toxicol Pharmacol.* 2003;38:232–242.
6. Falade OS, Adepoju OO, Owoyomi O, Adewusi SR. Chemical composition and toxic trace element composition of some Nigerian edible wild mushrooms. *Int J Food Sci Technol.* 2008;43(1):24–29.
7. Tüzen M. Determination of heavy metals in soil, mushroom and plant samples by atomic absorption spectrometry. *Microchem J.* 2003;74:289–297.
8. Mikula B, Puzio B. Determination of trace metals by ICP-OES in plant materials after preconcentration of 1,10-phenanthroline complexes on activated carbon. *Talanta.* 2007;71:136–140.
9. Krachler M, Mohl C, Emons H, Shotyk W. Analytical procedures for the determination of selected trace elements in peat and plant samples by inductively coupled plasma mass spectrometry. *Spectrochim. Acta Part B At. Spectrosc.* 2002;57:1277–1289.
10. Vogiatzis CG, Zachariadis GA. Tandem mass spectrometry in metallomics and the involving role of ICP-MS detection: A review. *Anal Chim Acta.* 2014;819:1–14.
11. Yilmaz S, Zengin M. Monitoring environmental pollution in Erzurum by chemical analysis of Scots pine (*Pinus sylvestris* L.) needles. *Environ Int.* 2004;29:1041–1047.
12. Yildiz D, Kula I, Ay G, Baslar S, Dogan Y. Determination of trace elements in the plants of Mt. Bozdag, Izmir, Turkey. *Arch Biol Sci.* 2010;62(3):731–738.
13. Ugulu I, Dogan Y, Baslar S, Varol O. Biomonitoring of trace element accumulation in plants growing at Murat Mountain. *Int J Environ Sci Technol.* 2012;9:527–534.



A Facile HPLC-PDA Method for Simultaneous Determination of Paracetamol, Methyl Paraben, Sunset Yellow, and Carmosine in Oral Suspensions

Şule Dinç Zor*, Özlem Aksu Dönmez

*Department of Chemistry, Faculty of Science and Arts, Yıldız Technical University,
34220 Davutpasa-Istanbul, Turkey*

In the present study, a simple, fast, and accurate HPLC-PDA method was developed for the simultaneous determination of paracetamol (PAR), methylparaben (MP), sunset yellow (SSY) and carmoisine (CAR) in oral suspensions. The concentrations of colorants are less than with respect to those of active ingredient and this variation makes process of analysis troublesome. In the developed HPLC method, efficient chromatographic separation was achieved using reversed phase C18 column (4.6 mm x 150 mm x 5 µm particle size) and phosphate buffer solution (pH = 6.5)-acetonitrile mobile phase with a flow rate of 1.6 mL/min in the gradient mode. The eluents were monitored via a PDA detector at 300, 254 and 230 nm. The mean retention times of PAR, MP, SSY and CAR were found to be 2.15, 4.42, 1.58 and 3.81, respectively. The proposed method was validated in accordance with ICH guidelines and it was seen that the method met all requirements in terms of linearity, precision, accuracy, and selectivity. The developed method was successfully applied for simultaneous determination of the studied compounds in two commercial oral suspension samples.

Keywords: Paracetamol, methylparaben, sunset yellow, carmoisine HPLC-PDA, oral suspension.

Submitted: March 09, 2018. **Accepted:** May 03, 2018.

Cite this: Dinç Zor ŞD, Aksu Dönmez Ö. A Facile HPLC-PDA Method for Simultaneous Determination of Paracetamol, Methyl Paraben, Sunset Yellow, and Carmosine in Oral Suspensions. JOTCSA. 2018;5(2):763–74.

DOI: <http://dx.doi.org/10.18596/jotcsa.403497>.

***Corresponding author.** E-mail: sule_dinc@yahoo.com. Tel: +90-2123834156.

INTRODUCTION

Paracetamol (N-acetyl-4-aminophenol) is widely used in pediatric syrup-suspension formulations as a pain-reliever and fever-reducer. It is easily available alone without a prescription or in combination with other drugs. Some preservatives and colorants are commonly used in these pediatric pharmaceutical formulations to prevent microbial growth and to improve appearance and color (1). In general, sodium benzoate, potassium sorbate or parabens such as methyl paraben or propyl paraben are used as a preservative system in the liquid formulations (2). Methyl paraben (methyl 4-hydroxybenzoate) is the most frequently used due to its broad antimicrobial spectrum and the fact that it does not modify the physical properties of the final products like taste, smell or color (3). According to some research reports, parabens exhibit estrogenic activity and their extreme usage could lead to some detrimental effects such as breast cancers and oxidative DNA damage (4-6). Owing to these concerns, many countries have put a ban to limit the use of parabens (7). Hence, determinations of these preservatives in pharmaceuticals are vitally necessary for both quality assurance and consumer safety.

Although the allowable amounts of synthetic colorants which could have toxicity are reduced by human health reasons, many synthetic colorants instead of natural colorants are still widely used due to their low price, high effectiveness, and excellent stability in foods and pharmaceuticals (8-10). Since synthetic colorants could provoke allergic reactions including urticaria, dermatitis, and asthma and may give rise to hyperactive behavior in children, the use of synthetic colorants in many countries is strictly regulated under existing food laws (11,12). Thus, determination of colorants in food samples and pharmaceutical products is important to control the amount of use permitted and to ensure quality control. Also, in order to colorize pharmaceuticals, the mixture of two or three of them is used to create a hue corresponding with selected natural color. So, simultaneous determination of these colorants becomes difficult as the number of components in the mixtures increases (13). Furthermore, since the quantity of active compound is commonly higher than additives, there is a need of accurate, efficient, and fast analytical method for simultaneous quantification of ingredients and excipients (14,15). In this respect, we focused on simultaneous high performance liquid chromatography (HPLC) determination of the single drug, paracetamol, along with colorants, sunset yellow and carmoisine, and preservative, methyl paraben, in pediatric oral suspension samples that belong to the same pharmaceutical company, in this study. Many analytical methods, either for single or combination with other analytes in various matrices, have been described in the literature for determination of paracetamol (16,17), methyl paraben (18,19), sunset yellow (20,21) and carmoisine (22,23) by HPLC in particular. However, no method describes quantification of this drug and color and preservative additives simultaneously. There are some HPLC methods developed in order to quantify different active compounds and additives in association, which are non labor-intensive, without extraction step and with short analysis time (2, 13, 24-27).

This study aims a fast, simple, and sensitive HPLC method for the simultaneous determination of paracetamol, methyl paraben, sunset yellow and carmoisine in pediatric oral suspensions. Validation parameters for the current method were also tested according to the requirements of ICH guidelines.

MATERIALS and METHODS

Chemicals and Reagents

Reference standards of paracetamol (PAR), methyl paraben (MP), sunset yellow (SSY) and carmoisine (CAR) were obtained as gifts from a local pharmaceutical company (all purities \geq 99%). HPLC grade acetonitrile, methanol, orthophosphoric acid (H_3PO_4) and di-potassium hydrogen phosphate (K_2HPO_4) were purchased from Merck Chemicals (Germany). Ultrapure water was produced by a Milli-Q® Elix Water Purification System (Milford, MA, USA).

Instruments and Chromatographic Conditions

The HPLC system was a Shimadzu HPLC system LC-10AT VP equipped with a SIL-20AC autosampler and SPD-M10A VP photodiode array dedector (PDA). The chromatographic separations were performed on an Inertsil C18 column (4.6 mm x 150 mm x 5 μ m particle size, GL Sciences, Japan). The mobile phase was made up of phosphate buffer (0.025 M, pH 6.5) and acetonitrile. Gradient elution conditions are given in Table 1. The flow rate of mobile phase was 1.6 mL/min at room temperature and injection volumes were 20 μ L. The eluents were monitored in the range of 190 to 800 nm via a PDA dedector and the detections were carried out at 300 nm for PAR, at 254 nm for MP, at 230 nm for SSY and CAR. The run time was approximately 5 min and the total peak area was used for the quantification of each analyte.

Table 1. Gradient elution conditions for the separation of analytes.

Mobile Phase A	Mobile Phase B	Gradient Conditions
Acetonitrile	Phosphate buffer (0.025 M, pH 6.5)	87%B 2.0 min, 70%B 3.0 min

Preparation of Standard and Sample Solutions

Stock standard solutions of PAR (5000 μ g/mL) and MP (500 μ g/mL) were prepared in methanol by accurately weighting. Stock standard solutions of SSY and CAR (100 μ g /mL) were prepared in Milli-Q water. All stock solutions were stored at 4 °C and further dilutions to obtain calibration and other validation studies solutions were made in Milli-Q water.

Two kinds of marketed liquid pharmaceutical formulations (suspension) comprising an aqueous solution of paracetamol were purchased from local pharmacy shop in Istanbul, Turkey. 2.5 mL of Suspension I containing 250 mg PAR, 4 mg MP and an unknown amount of SSY in 5 mL was

accurately transferred into an 100 mL measuring flask, sonicated in ultrapure water, and the volume was then made up to the mark with the same solvent. Similarly, 5.0 mL of Suspension II containing 120 mg PAR, 5 mg MP and an unknown amount of CAR in 5 mL was accurately transferred into a 50 mL measuring flask, sonicated and diluted to its volume with ultrapure water. All standard and sample solutions were filtered through 0.45 micron membrane filter.

Method Validation

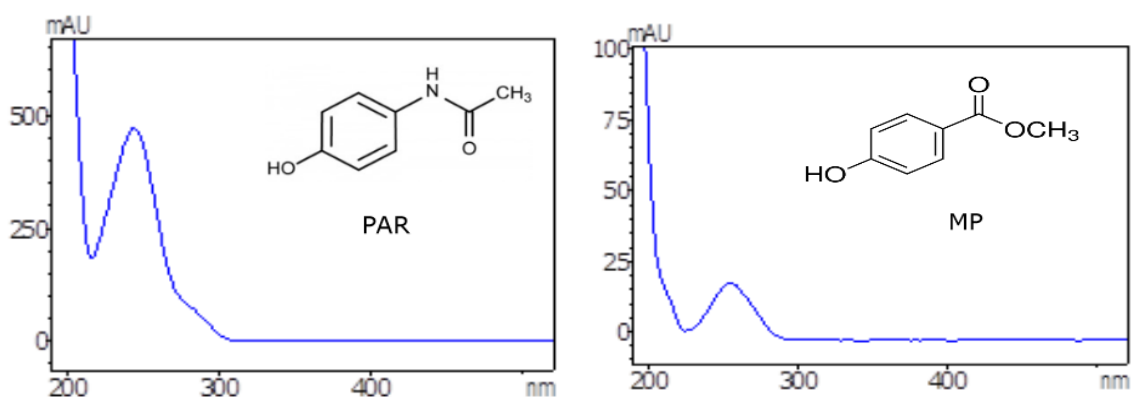
Method validation including selectivity, linearity, limit of detection and limit of quantification, precision and accuracy of the proposed method was performed according to ICH guidelines (28).

RESULTS and DISCUSSION

Method Development

In order to achieve good chromatographic separation of the studied compounds, different solvents (water, acetonitrile and methanol) and buffer solutions (acetic acid/acetate and phosphate), ideal mobile phase proportion, pH and flow rate were duly studied. Satisfactory results were achieved by 87:13% (v:v) of phosphate buffer (0.025 M) pH 6.5 : acetonitrile for first 2.0 min and then 70:30% (v:v) of the same mobile phase for 2.0-5.0 min at flow rate of 1.6 mL/min in the gradient mode.

As the quantity of active ingredient in these pharmaceutical formulations is compared to those of colorants in particular, it is seen that there is an imbalance between the analytes. Generally, the amount of the colorants is less than the active compound and excipients. This variation makes the simultaneous chromatographic analysis of them along with other ingredients difficult. This difficulty can be overcome by choosing the appropriate wavelength for determination. Absorption spectra of the studied compounds can be seen in Figure 1. Detection wavelength was chosen at 300 nm for PAR, at 254 nm for MP, at 230 nm for SSY and CAR, accordingly.



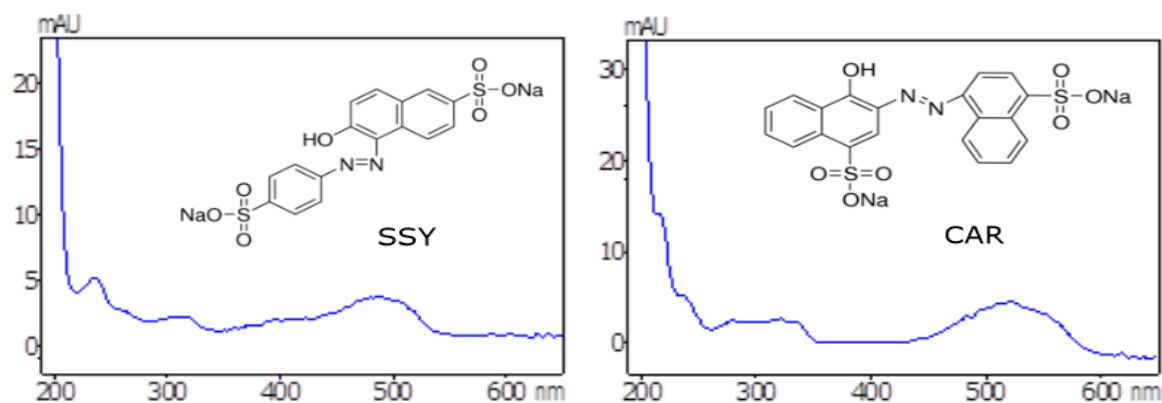
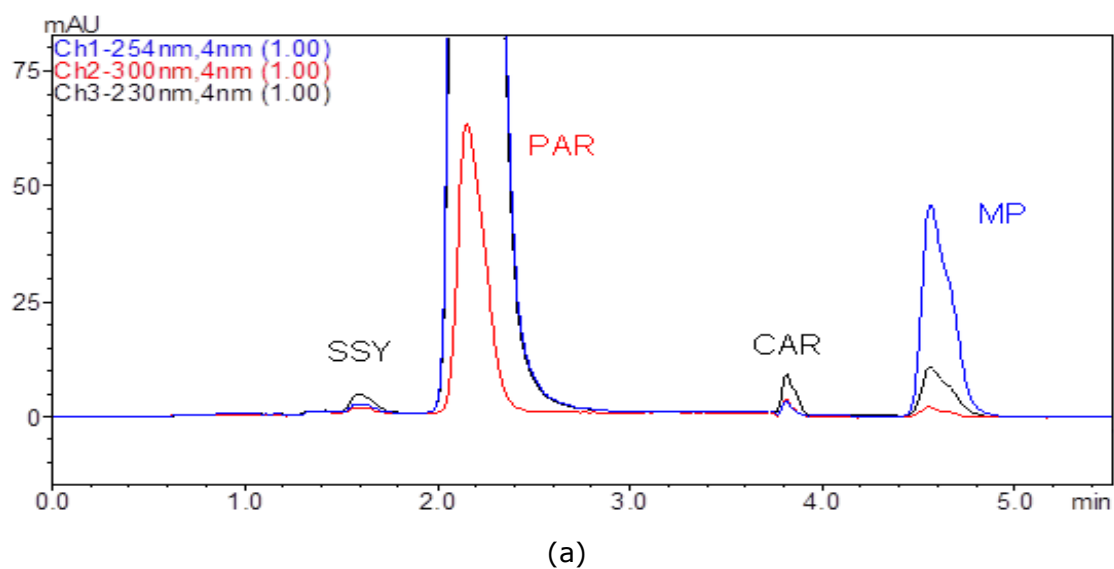
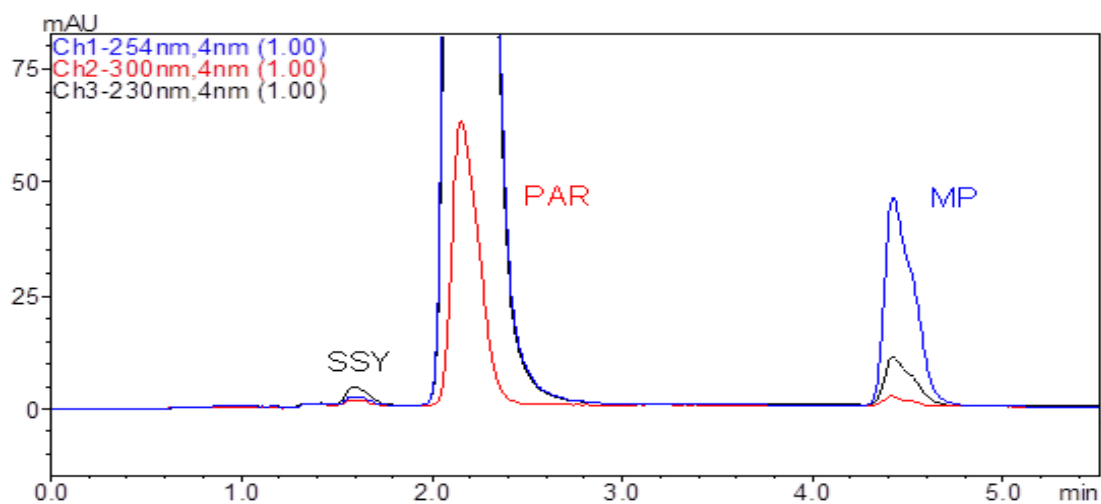


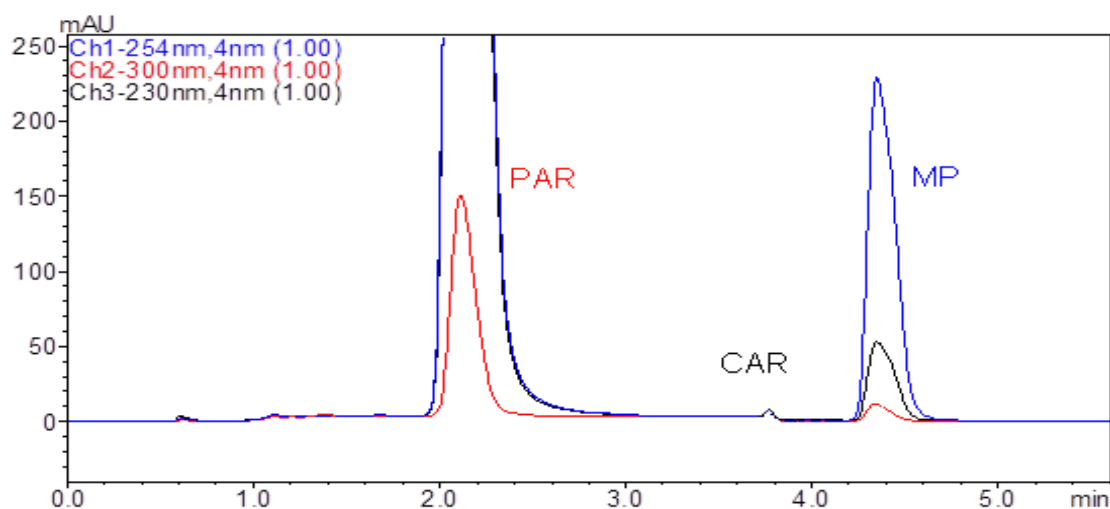
Figure 1. Absorption spectra of paracetamol (PAR), methyl paraben (MP), sunset yellow (SSY) and carmoisine (CAR) by PDA dedector.

Figure 2 shows the chromatogram obtained for the analytes in synthetic mixture and pharmaceutical formulations by the chromatographic conditions described above.





(b)



c)

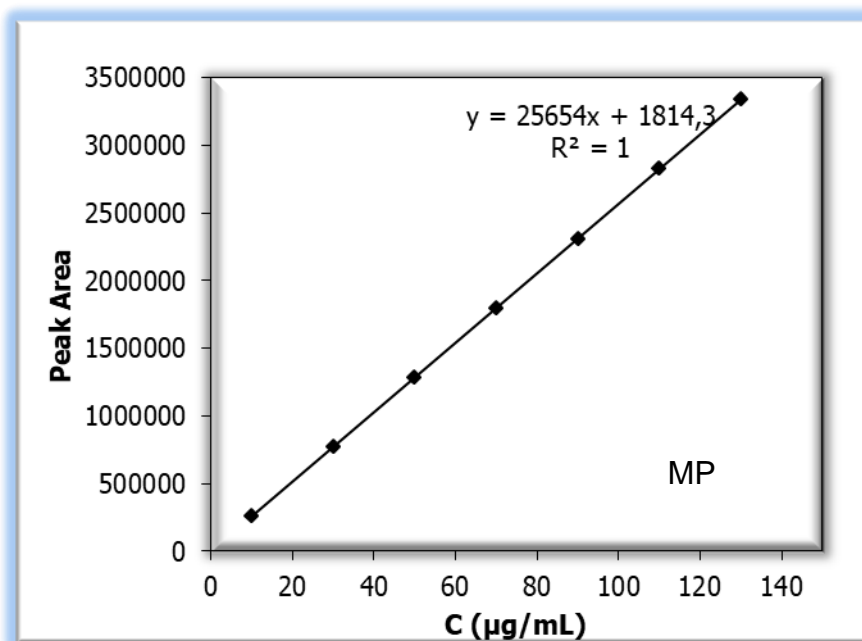
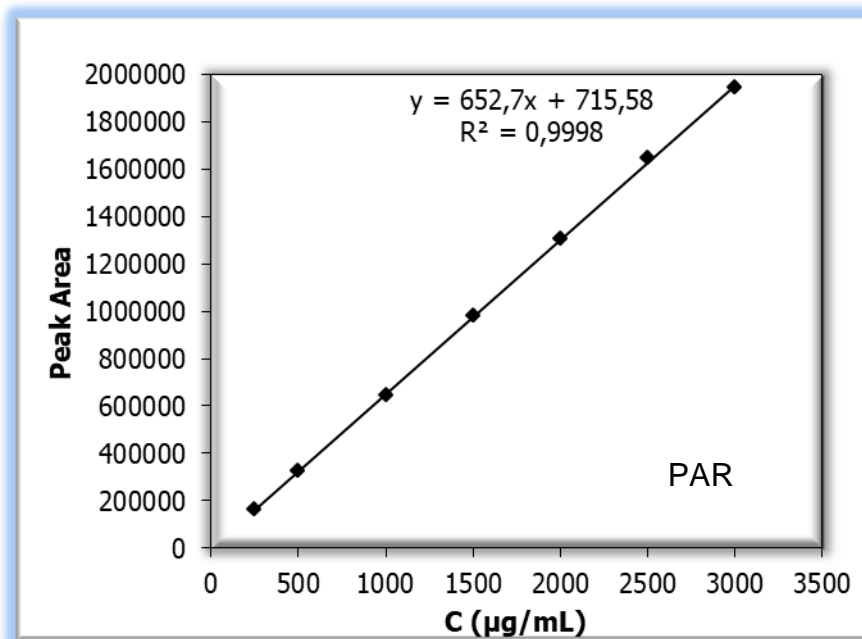
Figure 2. a) Chromatogram of standard mixture solution containing 4 µg/mL SSY, 1000 µg/mL PAR, 2 µg/mL CAR and 20 µg/mL MP. b) Chromatogram of oral Suspension I, c) Chromatogram of oral Suspension II.

Method Validation

Selectivity: Selectivity was evaluated by the peak purity test using PDA detector. According to the results obtained, peak purity values were higher than 0.9990. Also no interferences were detected at retention times of the studied compounds in sample solutions, which shows that the developed method is selective (Figure 2).

Linearity: For linearity, seven different concentrations were chosen taking into account suspension contents. Hence, concentrations of the solutions were PAR 250 to 3000 µg/mL, MP 10 to 110 µg/mL, SSY 1 to 12 µg/mL and CAR 1 to 7 µg/mL. Each concentration of standard solutions was analyzed in triplicate and the mean values of peak areas were calculated and used

for the calibration graph. Calibration curves of the studied compounds obtained by the proposed method can be seen in Figure 3. The linear regression equations for PAR, MP, SSY and CAR were found to be $y = 652.7x - 715.58$, $y = 25654x + 1814.3$, $y = 10558x + 1532.5$ and $y = 15052x + 1742.6$, respectively. The regression coefficients (R^2) were found to be higher than 0.999, which indicates that the method has an acceptable degree of linearity.



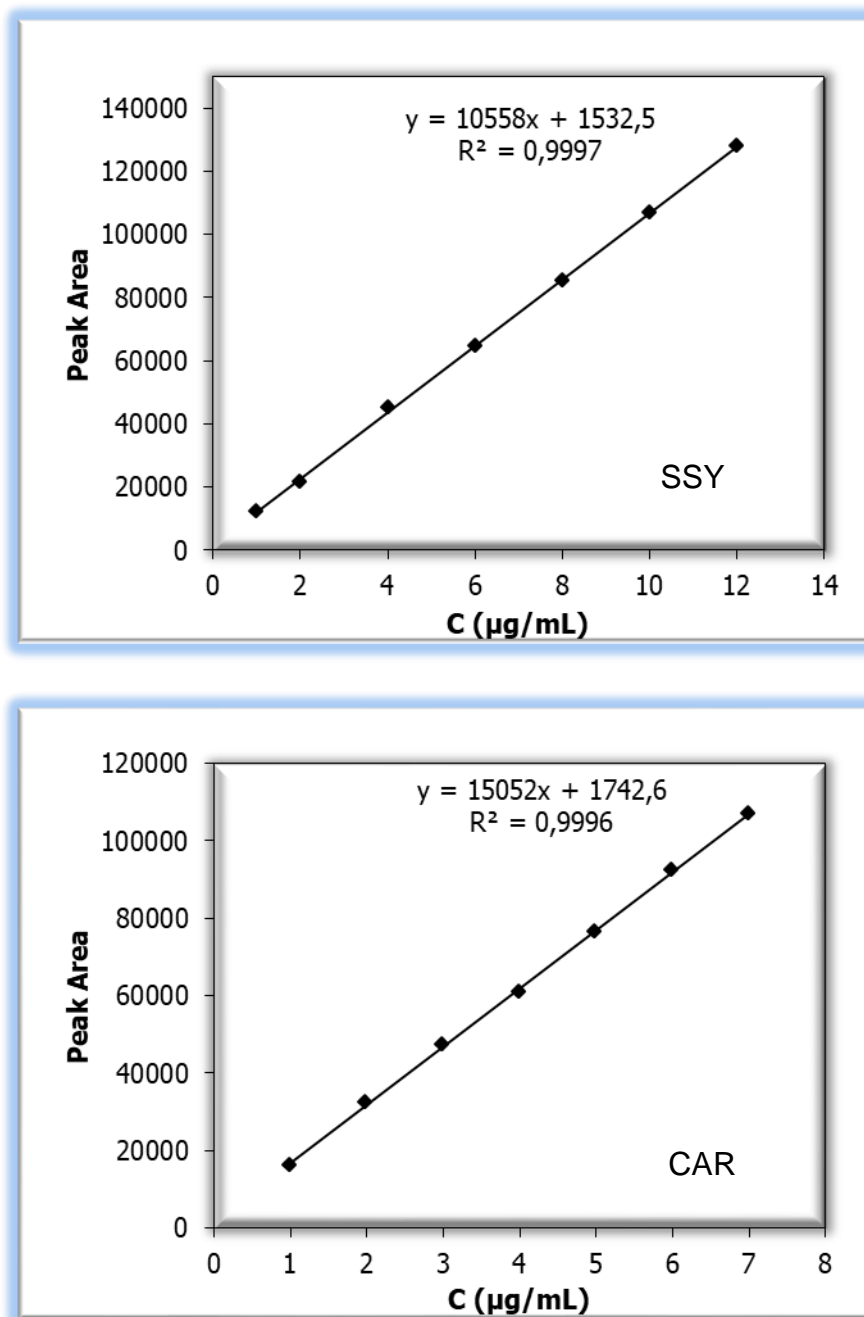


Figure 3. Calibration curves of PAR, MP, SSY and CAR.

Limits of Detection and Quantification (LOD and LOQ): Limits of detection (LOD) were calculated at a signal-to-noise ratio (S/N) of 3. Limits of quantification (LOQ) were calculated at a signal-to-noise ratio (S/N) of 10. The LOD was calculated to be 0.42, 0.20, 0.27 and 0.15 µg/mL and the LOQ was calculated to be 1.35, 0.65, 0.80 and 0.46 µg/mL for PAR, MP, SSY and CAR, respectively.

Precision: Precision of the method is assessed by the estimate of the relative standard deviation (RSD) with respect to both repeatability and intermediate precision. For repeatability, three different concentrations of standard solutions were analyzed in triplicate on the same day.

Intermediate precision (n=4) was performed on three different days. Acceptable RSD% values (<3.38% RSD) as shown in Table 2 were obtained.

Table 2. Repeatability and intermediate precision values of PAR, MP, SSY and CAR.

Compound	Actual Concentration (µg/mL)	Repeatability Mean ± %RSD (n =3) (µg/mL)	Intermediate precision Mean ± %RSD (n=4) (µg/mL)
PAR	1000		993.75 ± 1.49
	1500	990.10 ± 1.52	1487.00 ± 1.66
	2000	1479.33 ± 0.95	1991.75 ± 1.26
		1992.67 ± 1.65	
MP	20		19.19 ± 2.45
	30	20.47 ± 1.97	29.83 ± 1.82
	40	29.5 ± 1.70	40.20 ± 2.96
		39.6 ± 2.91	
SSY	2		1.98 ± 2.80
	4	2.07 ± 3.38	4.08 ± 2.27
	6	3.96 ± 3.26	6.06 ± 2.27
		5.97 ± 1.94	
CAR	1		1.05 ± 2.52
	2	0.98 ± 2.00	1.95 ± 3.05
	3	1.90 ± 2.80	3.15 ± 2.65
		3.10 ± 2.50	

Accuracy

Accuracy of the method was expressed as % recovery obtained by standard addition method at three different levels. Good recovery data for accuracy are displayed in Table 3. The recovery values obtained also imply that there is no matrix effect on the determination of analytes by the proposed method.

Table 3. Accuracy studies of PAR, MP, SSY and CAR.

Analytes	Sample Concentration (µg/mL)	Amount Added (µg/mL)	Amount Found (µg/mL) ± %RSD (n=5)	Mean Recovery (%)
PAR	1250	500	487.0 ± 1.03	97.40
		1000	1002.67 ± 0.75	100.27
		1500	1496 ± 0.68	99.73
MP	20	10	9.98 ± 0.76	99.80
		20	19.80 ± 1.35	99.00
		30	29.12 ± 2.00	97.07
SSY	1.75	2	1.97 ± 2.18	98.50
		4	3.95 ± 2.50	98.75
		6	6.05 ± 2.20	100.83
CAR	1.5	1	1.05 ± 2.44	105.00
		2	1.98 ± 1.96	99.00
		3	3.08 ± 2.15	102.67

Application of the Method to Commercial Oral Suspensions

After method optimization and validation, the developed method was successfully applied for the simultaneous determination of PAR, MP, SSY and CAR in oral suspension samples produced by the same pharmaceutical company. The quantitative results of the analysis are summarized in Table 4. Found values close to 100% demonstrate the applicability of the method for control of the liquid formulations in quality control laboratories. So these formulations containing the studied compounds can be analyzed with the same HPLC method in a short time.

Table 4. Analysis of marketed samples by the HPLC method.

	Ingredients	Labeled amount (mg/5 mL)	Amount found (mg/5 mL)	Recovery (%)
Commercial Oral Suspension I	PAR	250	250.6	100.24
	MP	4	4.05	101.32
	SSY	-	0.35	-
Commercial Oral Suspension II	PAR	120	121.2	101.0
	MP	5	5.11	102.29
	CAR	-	0.075	-

CONCLUSION

A novel, facile, rapid, and efficient reversed phase HPLC-PDA method without any extraction stage was developed for the simultaneous quantification of PAR, MP, SSY and CAR in oral suspensions which the ingredients are present in variable concentrations. The most important advantage of this method is to analyze PAR, MP, SSY and CAR at the same time as there is no method in the literature for simultaneous determination of these compounds. The developed method has a good resolution between all analytes with a short analysis time below 5 min. In addition, according to validation study results, this method is linear, precise, accurate, sensitive, and selective. So the proposed method can be used for routine analysis of these compounds in similar pharmaceutical products.

COMPLIANCE WITH ETHICAL STANDARDS

The authors declare that there is not an unethical situation.

CONFLICT OF INTEREST

The authors declare that they have no conflict of interest.

ACKNOWLEDGEMENTS

Declared none.

REFERENCES

1. Sorouraddin MH, Saadati M, Mirabi F. Simultaneous determination of some common food dyes in commercial products by digital image analysis. *Journal of Food and Drug Analysis*. (2015); 23(3): 447-452.
2. Grosa G, Del Grosso E, Russo R, Allegrone G. Simultaneous, stability indicating, HPLC-DAD determination of guaifenesin and methyl and propyl-parabens in cough syrup. *Journal of Pharmaceutical and Biomedical Analysis*. 2006;41:798-803.
3. Baranowska I, Wojciechowska I, Solarz N, Krutysza E. Determination of preservatives in cosmetics, cleaning agents and pharmaceuticals using fast liquid chromatography. *Journal of Chromatographic Science*. 2013;52:88-94.
4. Yang J, Li Y, Gong W, Wang C, Liu B, Sun C. Simultaneous determination of six parabens in foods by matrix liquid-phase dispersion extraction combined with high-performance liquid chromatography. *Food Analytical Methods*. 2014;7:1693-702.
5. Routledge EJ, Parker J, Odum J, Ashby J, Sumpter JP. Some alkyl hydroxy benzoate preservatives (parabens) are estrogenic. *Toxicology and Applied Pharmacology*. 1998;153: 12-19.
6. Shanmugam G, Ramaswamy BR, Radhakrishnan V, Tao H. GC-MS method for the determination of paraben preservatives in the human breast cancerous tissue, *Microchemical Journal*. 2010; 96: 391-396.
7. Wang W, Wang Y, Zhang J, Chu Q, Ye J. Simultaneous determination of electroactive and non-electroactive food preservatives by novel capillary electrophoresis with amperometric detection. *Analytica Chimica Acta*. 2010; 678:39-43.
8. Pagáčiková D, Lehotay J. Determination of synthetic colors in meat products using high-performance liquid chromatography with photodiode array detector. *Journal of Liquid Chromatography & Related Technologies*. 2015;38:579-583.
9. Martin F, Oberson JM, Meschiari M, Munari C. Determination of 18 water-soluble artificial dyes by LC-MS in selected matrices. *Food Chemistry*. 2016;197:1249-1255.
10. Davletbaeva P, Chocholouš P, Bulatov A, Šatínský D, Solich P. Sub-1 min separation in sequential injection chromatography for determination of synthetic water-soluble dyes in pharmaceutical formulation. *Journal of Pharmaceutical and Biomedical Analysis*. 2017; 143: 123-129.
11. The European Parliament, Regulation (EC) No 1333/2008 of the European Parliament and of The Council of 16 December 2008 on food additives, *Official Journal of the European Union*, No 1333/2008.
12. EFSA (European Food Safety Authority) (2009) *The EFSA Journal* 7: 1328-67.
13. Aksu Dönmez Ö, Aşçı B, Dinç-Zor Ş, Aslan Çakır A. Simultaneous quantitative analysis of ephedrine HCl, guaifenesin, and some synthetic additives in syrups by RP-HPLC using Box-Behnken design. *Latin American Journal of Pharmacy*. 2018; 37: 85-94 (2018).

14. Lokhnauth JK, Snow NH. Determination of parabens in pharmaceutical formulations by solid-phase microextraction-ion mobility spectrometry. *Analytical Chemistry*. 2005;77:5938-5946.
15. Rebbeck C, Hammond R, Wong J, Nair L, Raghavan N, Hepler D, Campbell W, Lynn, R. Solid-phase extraction and HPLC analysis of methylparaben and propylparaben in a concentrated antibiotic suspension. *Drug Development and Industrial Pharmacy*. 2006; 32:1095-1102.
16. Bosch ME, Sánchez AR, Rojas FS, Ojeda CB. Determination of paracetamol: Historical evolution. *Journal of Pharmaceutical and Biomedical Analysis*. 2006;42:291-321.
17. Dinç Ş, Aksu Dönmez Ö, Aşçı B, Bozdoğan AE. Chromatographic and chemometrics-assisted spectrophotometric methods for the simultaneous determination of allobarbitol, adiphenine hydrochloride, and paracetamol in suppository. *Journal of Liquid Chromatography & Related Technologies*. 2014;37:560-571.
18. Tzanavaras P, Karakosta T, Rigas P, Themelis D, Zotou A. Isocratic liquid chromatographic determination of three paraben preservatives in hygiene wipes using a reversed phase core-shell narrow-bore column. *Open Chemistry*. 2012;10:1459-1463.
19. Kumar S, Mathkar S, Romero C, Rustum AM. Development and validation of a single RP-HPLC assay method for analysis of bulk raw material batches of four parabens that are widely used as preservatives in pharmaceutical and cosmetic products. *Journal of Chromatographic Science*. 2011;49: 405-411.
20. Rovina K, Acung LA, Siddiquee S, Akanda JH, Shaarani SM. Extraction and analytical methods for determination of sunset yellow (E110)—a Review. *Food Analytical Methods*. 2017;10:773-787.
21. Rejczak T, Tuzimski T. Application of high-performance liquid chromatography with diode array detector for simultaneous determination of 11 synthetic dyes in selected beverages and foodstuffs. *Food Analytical Methods*. 2017;10: 3572-3588.
22. Khanavi M, Hajimahmoodi M, Ranjbar AM, Oveisi MR, Ardekani MRS, Mogaddam G. Development of a green chromatographic method for simultaneous determination of food colorants. *Food Analytical Methods*. 2012;5:408-415.
23. Yamjala K, Nainar MS, Ramiseti NR. Methods for the analysis of azo dyes employed in food industry—a review. *Food Chemistry*. 2016;192:813-824.
24. Hasan N, Chaiharn M, Toor UA, Mirani ZA, Sajjad G, Sher N, Aziz M, Siddiqui FA. Development, validation and application of RP-HPLC method: Simultaneous determination of antihistamine and preservatives with paracetamol in liquid formulations and human serum. *Open Medicinal Chemistry Journal*, (2016); 10:33-43.
25. Abd El-Hay SS, Mohram MS. Development and validation of new RP-HPLC method for simultaneous determination of methyl and propyl parabens with levetiracetam in pure form and pharmaceutical formulation. *Chromatography Research International*. 2016.
26. Weshahy SAEF, Yaaqob MS, Morcos MN, Hassan DW, Youssef NF. Simultaneous determination of levodropropizine, methylparaben, and propylparaben in oral co-formulated syrup by RP-HPLC method. *Journal of the Chilean Chemical Society*. 2015;60: 2729-2733.
27. Ali MS, Ghori M, Khatri AR. Stability indicating simultaneous determination of domperidone (DP), methylparaben (MP) and propylparaben by high performance liquid chromatography (HPLC). *Journal of Pharmaceutical and Biomedical Analysis*. 2006; 41:358-365.

28. International Conference on Harmonization (ICH) Q2 (R1): Validation of Analytical Procedures-Test and Methodology, Geneva, Switzerland, 2005.



Photophysics, pH Sensing, and Hydrolysis Study of a Novel 1,8-Naphthalimide Derivative

Alparslan ATAHAN^{1*}, Ersin ORHAN²

¹Duzce University, Faculty of Technology, Department of Polymer Engineering, 81620 Duzce, TURKEY

²Duzce University, Faculty of Arts and Sciences, Department of Chemistry, 81620 Duzce, TURKEY

Abstract: In this study, a novel highly emissive compound was synthesized via a two-step synthetic procedure and characterized by ¹H-NMR, ¹³C-NMR and FTIR. Then its photophysical properties, pH sensing behaviors and pH-dependent hydrolysis were systematically investigated by ultraviolet and fluorescence spectroscopy. Photophysics studies were carried out in fourteen common organic solvents and absorption/emission spectra were recorded in Britton Robinson buffers (pH=3-12) to determine pH sensing behaviors. From the photophysical results, it has been shown that the novel compound exhibits strongly solvent polarity dependent emission and has high quantum yield (up to 0.72). Furthermore, at pH=12, absorbance started to decrease while emission was increasing and blue-shifting due to basic hydrolysis after a several minutes. Therefore, time dependent hydrolysis was also investigated at mentioned pH.

Keywords: Naphthalimide, Thiazoline, Photophysical, Fluorescence, pH Sensing, Hydrolysis.

Submitted: April 19, 2018. **Accepted:** May 04, 2018.

Cite this: Atahan A, Orhan E. Photophysics, pH Sensing, and Hydrolysis Study of a Novel 1,8-Naphthalimide Derivative. JOTCSA. 2018;5(2):775-84.

DOI: <http://dx.doi.org/10.18596/jotcsa.414821>.

*Corresponding author. E-mail: alparslanatahan@duzce.edu.tr

INTRODUCTION

Fluorescent molecules are quite important and have been extensively studied due to their usability in optoelectronic area. In the same manner, there are a lot of publications about optical and organic electronics applications of naphthalimide derivatives, and this structure can appear as a different subclass of fluorescent dyes. Especially, donor group containing derivatives at 4-position are generally photo-stable materials and have relatively high fluorescence quantum yield thanks to compact donor-acceptor architecture. Therefore, it is possible to use them as high effective fluorescent materials, fluorescent brightening agents, pH/metal/anion sensors, light harvesting materials, light emitting diodes, and more (1-5).

Light-induced absorption of naphthalimide derivatives occurs by decomposition into charge carriers in the conjugate system. For this reason, the application of naphthalimide derivatives in organic electronic area depends on the relationship between the chemicals. For example, photovoltaic cells require materials with an effective charge separation capability, and therefore high electron mobility is required to increase the probability of electron migration to a charge separation region. Naphthalimide derivatives can be shifted to longer wavelengths by extending the π -conjugation system via structure modification. In addition, the photophysical properties can be changed by modifications on the naphthalimide molecule. With suitable structural arrangements, naphthalimide derivatives can act as energy donor or acceptor in various energy transfer systems (6-10).

pH sensors widely take place in various fields such as chemical process control, environmental analysis, medical diagnostics, and industrial applications (11). Fluorescence-based pH probes have become promising tools due to their high sensitivity, selectivity, and low cost. In order to understand many physiological processes better, the development of effective chemosensors to monitor pH changes has a great deal of precaution (12-15). For example, a proportional pH sensor based on fluorescence resonance energy transfer (FRET) has been recently reported to visualize the stimulus-sensitive changes in intracellular pH values by integrating an amino-naphthalimide pH probe as a FRET acceptor with a pH-insensitive coumarin fluorophore as a FRET donor (16).

In brief, 1,8-naphthalimides are quite suitable candidates for optoelectronic and organic electronics applications and it is essential to synthesize their new derivatives and comprehensively investigate of some properties on photo-physics, pH/metal/anion sensing, and chemical/photo-stability *etc.* to provide development in these areas. In our study, the aim was to combine naphthalimide and thiazoline fragment which might contribute to photophysics and pH sensing behavior of the target compound. For this reason, we synthesized a novel

naphthalimide-thiazoline compound as a fluorophore. Then, comprehensive photophysics, pH sensing and hydrolysis behaviors were also investigated via absorption and emission studies.

EXPERIMENTAL SECTION

DMA-NI (dimethylamino-naphthalimide compound) was synthesized by two steps synthetic method depicted in Scheme 1. The reactions were monitored by Silica Gel TLC plates in CH₂Cl₂/Ethyl acetate mixture (1:1). All the chemicals used in this study were purchased from Merck, Alfa, Sigma, and Fluka. Purification of crude DMA-NI was realized by a silica column chromatography by using dichloromethane and ethyl acetate mixture. Melting point was determined on a Electrothermal IA-9200. FTIR spectra were recorded on a Shimadzu Prestige-21 (200 VCE) spectrometer combined with ATR apparatus. ¹H and ¹³C NMR spectra were measured in CDCl₃ on a Bruker Avance-II spectrometer at 400 and 100 MHz, respectively and TMS (tetramethylsilane) was used as internal standard. The solutions of acetic acid (0.10 M), sodium acetate (0.10 M), KH₂PO₄ (0.10 M), Na₂B₄O₇·10H₂O (0.025 M), hydrochloric acid (0.10 M), sodium hydroxide (0.10 M) and Na₂HPO₄ (0.05 M) were used to prepare Britton Robinson buffer solutions in pH range 3.0 to 12.0. All the photophysical measurements (absorption and emission) were realized by a PG Instruments T80 double beam spectrophotometer and Shimadzu RF 5301PC fluorescence spectrophotometer, respectively, in common organic solvents by a 1 cm path length quartz cells at ~22 °C.

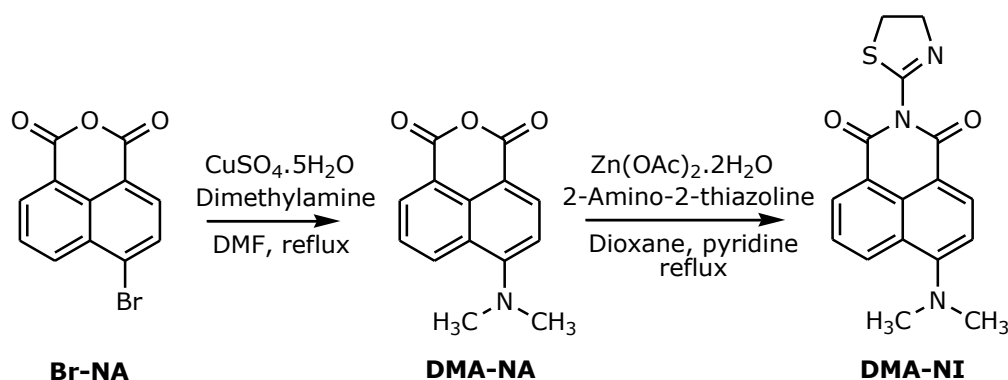
Synthesis

Synthesis of DMA-NA

DMA-NA (dimethylamino-naphthalic anhydride compound) was synthesized and purified according to the known procedure (17). This reaction includes bonding of dimethylamine to 4-bromonaphthalene-1,8-dicarboxylic anhydride in the presence of CuSO₄·5H₂O as catalyst. Spectral data (¹H, ¹³C NMR and FTIR) are fully in accordance with the literature mentioned above.

Synthesis of DMA-NI

0.120 g (0.5 mmol) of DMA-NA, 0.051 (0.5 mmol) 2-amino-2-thiazoline, and 10% mol of zinc acetate dihydrate refluxed in dioxane (5 mL) and pyridine (5 mL) for 2 days. After evaporation of volatiles in the reaction flask, the residue was extracted by adding chloroform and water. Combined organic phases dried over Na₂SO₄, evaporated under vacuum, and the crude product was purified by silica column chromatography by using CH₂Cl₂ and ethyl acetate as eluent. Yield: 75%; melting point: 198-201 °C; FTIR: 2918, 2873, 1699, 1654, 1581, 1354, 1012, 769, 758; ¹H NMR (400 MHz, CDCl₃): 8.52 (dd, *j*= 6.0 Hz, 1.2 Hz, 1H), 8.43-8.40 (m, 2H), 7.60 (dd, *j*= 6.8 Hz, 5.6 Hz, 1H), 7.05 (d, *j*= 6.4 Hz, 1H), 4.44 (t, *j*= 6.8 Hz, 2H), 3.71 (t, *j*= 6.8 Hz, 2H) 3.07 (s, 6H); ¹³C NMR (100 MHz, CDCl₃): 163.0, 162.3, 157.6, 157.6, 133.3, 132.1, 131.7, 130.9, 125.3, 124.9, 122.5, 114.0, 113.3, 61.5, 44.8 (2C), 36.40.



Scheme 1: Synthesis of the target compound.

Photophysics

All the absorption and emission measurements were performed at 10^{-5} M concentration. Quantum yields (Φ) of DMA-NI in common organic solvents were determined by comparing with a perylene reference solution. For this, the following equation has been used to calculate relative quantum yields (18).

$$\Phi_{\text{samp}} = \Phi_{\text{ref}} \frac{\eta^2}{\eta_{\text{ref}}^2} \frac{I}{I_{\text{ref}}} \frac{A_{\text{ref}}}{A} \quad (1)$$

Where η and η_{ref} are the refractive indices of sample and reference solvents, I and I_{ref} are the integrated areas of the emission signal for the sample and reference, respectively. A and A_{ref} are the absorbance values for the sample and reference at the excitation wavelength, respectively. Perylene solution in toluene used as reference and this compound has a known fluorescence quantum yield of 0.75 under these conditions (19).

pH Sensing

pH sensing studies were performed based on absorption and emission of DMA-NI solution (10^{-4} M) in the pH range of 3.0–12.0 at room temperature with slight modification of previous study (20). For this, firstly, 16.2 mg of DMA-NI dissolved in 100 mL acetonitrile to prepare the 5.0×10^{-4} M solution. Britton Robinson buffers in the pH range of 3.0–12.0 have been prepared by following a published method (21). Then 0.5 mL of DMA-NI and 2.0 mL buffer solution were mixed and absorption/emission spectra were recorded. This recording was repeated for each integer of pH between 3 and 12.

Hydrolysis

Hydrolysis of DMA-NI was monitored via adaptation to the literature (20). For this, firstly, 0.5 mL of 5.0×10^{-4} M DMA-NI solution in acetonitrile and 2.0 mL of Britton Robinson buffer (pH=12) were mixed in a 1 cm path length quartz UV cuvette to get 1.0×10^{-4} M concentration and absorption spectrum has been recorded immediately for $t=0$. Then, emission spectrum of same mixture was displayed without losing time. Absorption and emission recordings were repeated for $t=3, 10, 30, 90$ and 180 minutes.

RESULTS AND DISCUSSION

Synthesis

Anhydride compound (DMA-NA) was synthesized and purified according to the known procedure (17) and NMR results verified its structure and purity. Synthesis of its imide derivative (DMA-NI) containing aminothiazoline fragment was accomplished by adaptation of literature method (22). This method contains 10% mol $Zn(OAc)_2$ catalyst under dioxane and pyridine refluxing during 2 days. At the end of this reaction time, it has been shown that a tiny amount of starting compound could be separated from the target compound with column chromatography. 1H NMR spectrum is fully in accordance with proposed structure. Five different signal groups at aromatic region, roughly four doublets (two doublets overlap) and a triplet, verifies the structure. Also two different aliphatic triplets and a singlet having 2, 2 and 6 integration values clearly shows the presence of two $-CH_2-$ and $N(CH_3)_2$ groups, respectively. In the ^{13}C NMR spectrum of DMA-NI, four downfield carbon signals are shown corresponding to two carbonyl carbon, dimethylamino group attached carbon and imine carbon of thiazoline fragment. In aromatic region, nine carbon signals can be seen which concerns naphthalene skeleton except of dimethylamino attached carbon. Also, three aliphatic signals are ascribed to methylene carbons and dimethylamino carbons. Lastly, FTIR spectrum verifies the structure with these specific signals at 2918 (aliphatic C-H), 1699 (C=O), 1654 (C=O), 1581 (C=N) and 1354 (C-N amine) cm^{-1} .

Photophysics

Normalized emission spectra of DMA-NI are shown in Figure 1 and all photophysical results were summarized in Table 1. Absorption values of DMA-NI are affected from solvent polarity as expected and they change between 396-438 nm (Table 1). These changes are directly affected from solvent polarity and increasing of solvent polarity causes bathochromic shift. Fluorescence λ_{max} values are shown between 460-537 nm. These results are also affected from solvent polarity like absorption values. Stokes' shift values are not polarity-related and change between 62-105 nm. The fluorescence quantum yield (Φ_F) varies over a wide range and roughly decreases with increasing solvent polarity.

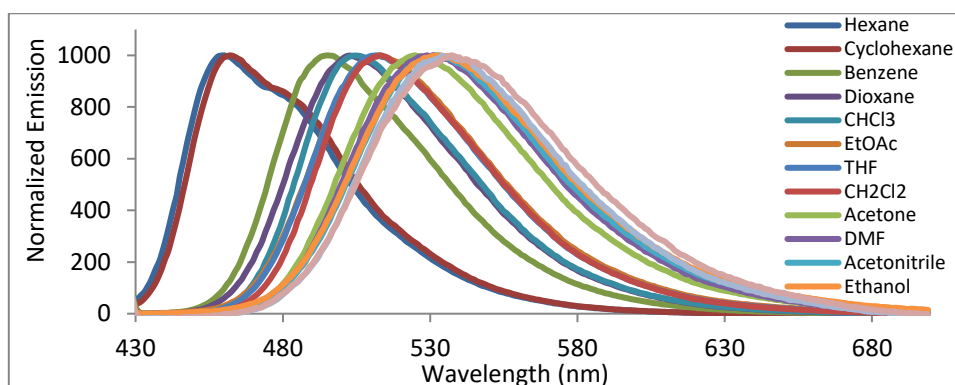


Figure 1: Normalized emission spectra of DMA-NI in common organic solvents.

Table 1: Photophysical results for DMA-NI.

Solvent	$\lambda_{\max}(\text{abs})$	$\lambda_{\max}(\text{ems})$	Stokes' shift	Φ_F
Hexane	396	460	64	0.451
Cyclohexane	400	462	62	0.464
Benzene	410	495	85	0.551
Dioxane	410	503	93	0.282
CHCl_3	412	505	93	0.722
EtOAc	412	513	101	0.347
THF	412	512	100	0.372
CH_2Cl_2	412	513	101	0.510
Acetone	432	525	93	0.015
DMF	434	530	96	0.007
Acetonitrile	428	533	105	0.031
Ethanol	432	533	101	0.014
DMSO	438	534	96	0.008
Methanol	434	537	103	0.006

$\lambda_{\max}(\text{abs})$: maximum absorption wavelength, $\lambda_{\max}(\text{ems})$: maximum emission wavelength, Φ_F : fluorescence quantum yield.

pH Sensing

At first, the aim was to investigate pH sensing behaviors at different pH values based on changing the absorption and emission spectra. For this, 10^{-4} M DMA-NI solutions at known pH was prepared by mixing 5.0×10^{-4} M DMA-NI solution and Robinson Britton buffers in 1:4 volume ratio. After immediately recording absorption and emission spectra, any different spectrum has not been observed at first. However, in a second recording a several minutes later, absorption band started to diminish and $\lambda_{\max}(\text{ems})$ started to blue shifting and enhancing peak area for pH=12. In an hour, the change was clearly observed in absorption and emission spectra (Figure 2). In the literature, it can be shown that a lot of examples about hydrolyzing imide derivatives are present at strong acidic and basic media. For this reason, we think that this change comes from hydrolysis reaction and new spectrum is ascribed to the hydrolysis product of DMA-NI.

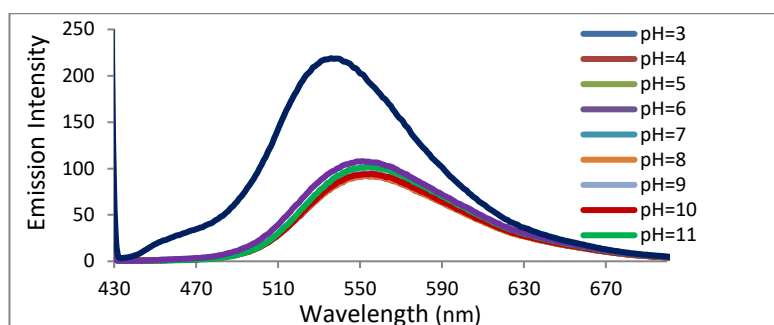


Figure 2: Emission spectra of DMA-NI at different pH values.

Hydrolysis

In order to clarify the special changing in photophysical results, we started to investigate time-dependent hydrolysis of DMA-NI and pH=12 was selected as hydrolysis pH because it has optimal reaction rate value. Investigations have been carried out at 10^{-4} M concentrations and first measurement was made as soon as possible after preparation for $t=0$. At the third minute, it has been shown that the absorbance value started to decrease and following recordings exhibited similar behaviors in absorbance value (Figure 3). From the graphical representation in Figure 4, it can be seen that the decreasing is not linear for selected two different wavelength points and this situation can indicate that the degradation is dependent on DMA-NI and/or OH^- concentrations.

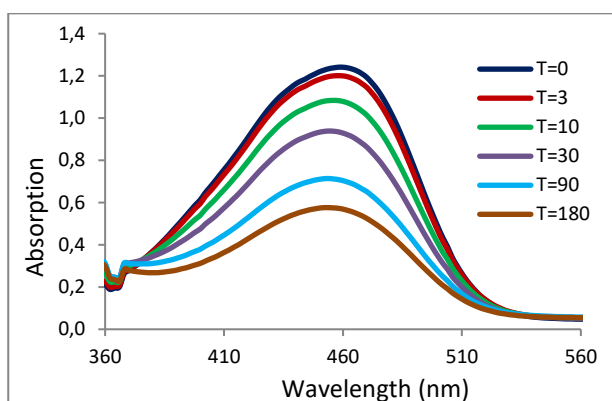


Figure 3: Absorption graphics for DMA-NI hydrolysis at pH=12 ($t=\text{min}$).

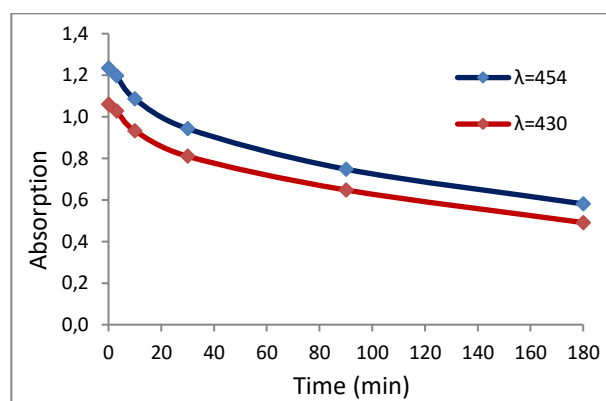


Figure 4: Absorption vs. time graphics of DMA-NI hydrolysis at pH=12.

After a long time, this absorption band completely disappeared because of the completion of hydrolysis reaction. The results have showed a drastic decrease of absorbance with time. Long time experiments under ambient light have been applied to large scale pH values (pH=3-12) and Figure 5 shows the situation of 10^{-4} M solutions of DMA-NI a week later. As seen in Figure 5, at strong basic conditions, the colors of solutions changed from yellow to colourless for pH=10, 11 and 12 and this situation gives an evidence for the significant reactivity of this molecule in alkaline solution. These results show that this compound is quite photo-stable at acidic and neutral pH values.

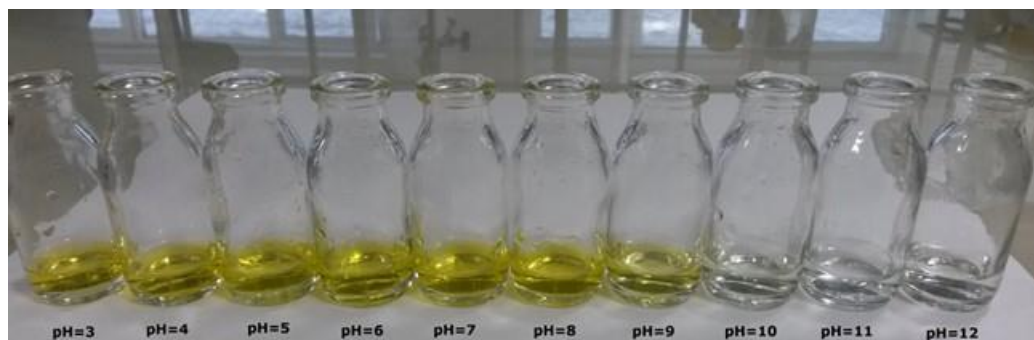


Figure 5: Bleaching of DMA-NI in different pH values a week later.

CONCLUSIONS

In conclusion, we have described the synthesis, photophysics, pH sensing behaviors, and hydrolysis investigation of a new naphthalimide compound (DMA-NI). Herein, the fluorophore was selected as naphthalimide because of its high photo-stability, high fluorescence quantum yield, large Stokes' shift, and simplicity of modification. Samples of DMA-NI were successfully prepared in two steps (amination and imide formation) starting from 4-bromonaphthalic anhydride. The yields were quite high and the procedure was extremely easy and clear. The originality of this structure was the presence of thiazoline fragment which could change the whole characteristics of target compound and we investigated here its effect on the nature of this compound. Then photophysical profile of this compound has been illuminated by absorption and emission studies. DMA-NI compound displayed broadband visible region absorption and emission band, and its emission band is quite broad and featureless due to intramolecular charge transfer of compact donor-acceptor structure. An exception to this generality arises in non-polar solvents, such as n-hexane and cyclohexane, where the emission spectrum is slightly structured. This situation may arise from the relative stability of bipolar resonance structure of excited state in polar solvents. Photophysical calculations based on perylene standard showed that this molecule has the highest quantum yield in chloroform ($\Phi_F=0.72$). In addition, this molecule has high quantum yields in benzene ($\Phi_F=0.55$) and dichloromethane ($\Phi_F=0.51$) as well. For other solvents, quantum yields were less than 0.5. In pH sensing studies and long time pH effect investigations, it has been shown that the compound has similar absorption and emission spectra for all pH values, but differentiated with time. This situation shows no specific pH sensing and stems from hydrolysis of DMA-NI. As a result, the DMA-NI compound is quite photo-stable and resistant to hydrolysis under the neutral and acidic conditions. Therefore, it can be used in optoelectronic and organic electronic devices that need photostability and high fluorescence quantum yield under acidic and neutral pH values. In addition, more effective novel derivatives

of 1,8-naphthalimide can be synthesized and investigated for similar electronic applications in the illumination of this study.

ACKNOWLEDGMENTS

This study was supported by Scientific Research Projects Unit of Duzce University (Project number: 2018.05.03.680).

REFERENCES

1. Atahan A, Durmus S. 1-Amino-2-hydroxy-4-naphthalenesulfonic acid based Schiff bases or naphtho[1,2-d]oxazoles: selective synthesis and photophysical properties. *Spectrochimica Acta A Molecular and Bio-molecular Spectroscopy*. 2015 Jun 5;144:61-7.
2. Orhan E, Gundogdu L, Kose M, Yokoyama Y. Synthesis and photochromic properties of 4,5-bisaryl-3(2H)-pyridazinones. *Journal of Photochemistry and Photobiology A: Chemistry*. 2016;314:164-170.
3. Yoon SA, Lee J, Lee MH. A ratiometric fluorescent probe for Zn²⁺ based on pyrene- appended naphthalimide-dipicolylamine. *Sensors and Actuators B*. 2018;258:50-5.
4. Ulla H, Kiran MR, Garudachari B, Satyanarayan MN, Umesh G, Isloor AM. Blue emitting halogen-phenoxy substituted 1,8-naphthalimides for potential organic light emitting diode applications. *Optical Materials*. 2014;37:311-21.
5. Li ZZ, Niu CG, Zeng GM, Liu YG, Gao PF, Huang GH, Mao YA. A novel fluorescence ratiometric pH sensor based on covalently immobilized piperazinyl-1,8-naphthalimide and benzothioxanthene. *Sensors and Actuators B*. 2006;114:308-15.
6. Simas ER, Gehlen MH, Pinto MFS, Siqueira J, Misoguti L. Intrachain Energy Migration to Weak Charge-Transfer State in Polyfluorene End-Capped with Naphthalimide Derivative. *Journal of Physical Chemistry A*. 2010;114:12384-90.
7. Cao H, Chang V, Hernandez R, and Heagy M D. Matrix Screening of Substituted *N*-Aryl-1,8-naphthalimides Reveals New Dual Fluorescent Dyes and Unusually Bright Pyridine Derivatives. *Journal of Organic Chemistry*. 2005;70:4929-34.
8. Liu J, Qian Y. A novel naphthalimide-rhodamine dye: Intramolecular fluorescence resonance energy transfer and ratiometric chemodosimeter for Hg²⁺ and Fe³⁺. *Dyes and Pigments*. 2017;136:782-90.
9. Singh A, Raj T, Singh N. Highly Selective and Efficient Reduction of Nitroarenes by Imidazolium Salt Stabilized Copper Nanoparticles in Aqueous Medium. *Catalysis Letters* 2015;145:1606-11.
10. Ma Y, Zheng B, Zhao Y, Yuan H, Cai Y, Du C, Xiao D. A sensitive and selective chemosensor for GSSG detection based on the recovered fluorescence of NDPA-Fe₃O₄@SiO₂-Cu(II) nanomaterial. *Biosensors and Bioelectronics*. 2013;48:138-44.
11. Liu X, Zhang S Q, Wei X, Yang T, Chen M L, Wang J H. A novel "modularized" optical sensor for pH monitoring in biological matrixes. *Biosensors and Bioelectronics*. 2018;109:150-5.
12. Niua W, Weia Z, Jia J, Shuang S, Dong C, Yun K. A ratiometric emission NIR-fluorescent probe for sensing and imaging pH changes in live cells. *Dyes and Pigments*. 2018; 152:155-160.
13. Chen Y, Tang T, Chen Y, Xu D. Novel 1,8-naphthalimide dye for multichannel sensing of H⁺ and Cu²⁺. *Research on Chemical Intermediates*. 2018;44:2379-93.

14. Zhang Y, Li S, and Zhao Z. Using Nanoliposomes To Construct a FRET-Based Ratiometric Fluorescent Probe for Sensing Intracellular pH Values. *Analytical Chemistry*. 2016;88:12380-5.
15. Yang L, Li N, Pan W, Yu Z, Tang B. Real-Time Imaging of Mitochondrial Hydrogen Peroxide and pH Fluctuations in Living Cells Using a Fluorescent Nanosensor. *Analytical Chemistry*. 2015;87(7):3678-84.
16. Zhou X, Su F, Lu H, Senechal-Willis P, Tian Y, Johnson R H, Meldrum D R. An FRET-based ratiometric chemosensor for in vitro cellular fluorescence analyses of pH. *Biomaterials*. 2012;33:171-80.
17. Al-Aqar R, Atahan A, Benniston AC, Perks T, Waddell PG, Harriman A. Exciton Migration and Surface Trapping for a Photonic Crystal Displaying Charge-Recombination Fluorescence. *Chemistry: A European Journal*. 2016;22:15420-9.
18. Yang W, He G, Mei S, Zhu J, Zhang W, Chen Q, Zhang G, Guo R. Controllable synthesis of dual emissive Ag:InP/ZnS quantum dots with high fluorescence quantum yield. *Applied Surface Science* 2017;423:686-94.
19. Olmsted J. Calorimetric Determinations of Absolute Fluorescence Quantum Yields. *Journal of Physical Chemistry*. 1979;83:2581-4.
20. Georgiev NI, Dimov SM, Asiri AM, Alamry KA, Obaid AY, Bojinov VB. Synthesis, selective pH-sensing activity and logic behavior of highly water-soluble 1,8-naphthalimide and dihydroimidazo naphthalimide derivatives. *Journal of Luminescence*. 2014;149:325-32.
21. Britton HTS, Robinson RA. Universal buffer solutions and the dissociation constant of veronal *Journal of the Chemical Society*. 1931;0:1456-62.
22. Schab-Balcerzak E, Siwy M, Filapek M, Kula S, Malecki G, Laba K, Lapkowski M, Janeczek H, Domanski M. New core-substituted with electron-donating group 1,8-naphthalimides towards optoelectronic applications. *Journal of Luminescence*. 2015;166:22-39.



Synthesis and characterization of new homo and heteronuclear Schiff base copper(II) complexes

T. Topal^{a*}✉, E. Karapınar^a✉

^aDepartment of Chemistry, Pamukkale University, Kinikli, 20017, Denizli, Turkey,

Abstract: This article describes the synthesis of isonitrosomethyl-p-tolyl ketone [HL] as the starting compound and then we prepared the new oxime ligand from the reactions of the amine materials with 1,2-diaminobenzene [H₂L¹]. (1E, 2E, 1'E, 2'E) - 3,3'-bis [(4-tolyl ketone) - (1,2 phenylene diimine)]. Acetaldehyde dioxime ligand was used to synthesize the metal complexes. The complexes were elucidated by FT-IR, elemental analysis, magnetic moment measurements, molar conductivity, mass spectra, and TGA studies. The free ligand was also described with its ¹³C and ¹H-NMR spectra. For complexes using spectroscopic and stoichiometric data of the complexes showed that metal:ligand ratio of mononuclear copper(II) complex was found to be 1:1 while this ratio was 2:1 in homo- and heterodinuclear copper(II) complex and 3:2 in the trinuclear copper(II) complex. All these data show us that the proposed structure is consistent with the obtained data.

Keywords: Schiff base, heteronuclear, trinuclear, nickel.

Submitted: June 30, 2017. **Accepted:** May 05, 2018.

Cite this: Topal T, Karapınar E. Synthesis and characterization of new homo and heteronuclear Schiff base copper(II) complexes. JOTCSA. 2018;5(2):785–802.

DOI: <http://dx.doi.org/10.18596/jotcsa.324878>.

Corresponding authors. E-mails: tufantopal@hotmail.com, ekarapinar@pau.edu.tr

INTRODUCTION

Heteronuclear and homonuclear complexes especially nickel(II) and copper(II) compounds are of great interest in the last decades years chiefly because of the convenience of bioinorganic chemistry of nickel and copper and molecular magnetism (1-2). Important attention has been devoted to their correlations with the active sites of metalloproteinase including binuclear metalcenters and to the mimicking of the activity of such biomolecules. Important interest has been committed to their relation with the active sites of metalloproteinase and metalloenzymes having homodinuclear and heterodinuclear metalcenters and biomolecules (3-4). Moreover, because copper(II) and nickel(II) complexes especially with tetradentate oxime groups are models of chemical and physical behavior of biological metal system. Recently, biological studies of oxime ligands and metal complexes gained importance. In order to examine the features of DNA cleaving and combining, many studies have been conducted about characterization and developing new compounds modified with organic and inorganic substances for 30 years (5-13).

The importance of nickel and copper compounds is increasing day by day in the preparation and design of new magnetic materials and composites. Nickel- and copper-bridged structures are used for magnetic properties especially in space and medicine industry. (*E, E*)-dioxime-containing unsymmetrical ligands can form square pyramidal, octahedral and square planar complexes with cobalt(II), nickel(II), palladium(II) and copper(II) as central metal atoms (14). The pharmacological properties of the complexes obtained from our study have

been observed but the results of this study have not been reported. Some researchers have synthesized containing *o*-phenylenediamine but the substances we synthesized were not found in the literature. Ligands and complexes were characterized by magnetic susceptibility, elemental analyses, molar conductivity, ¹H- and ¹³C-NMR, FT-IR, LC-MS and TG-DTG studies (15-21). The newly obtained materials provide new contributions especially in the literature and it is aimed to be used as a reference substance for use in various branches of science.

EXPERIMENTAL

IR spectra were performed in the 4000-400 cm⁻¹ on Perkin Elmer FTIR-Spectrometer Spectrum Two Model. Mass spectra were recorded on Agilent Micromass Quattro LC-MS/MS model spectrometer. ¹³C-NMR and ¹H-NMR data of the ligands were recorded from DMSO-d₆ solutions and on a Varian 400 MHz NMR Spectrometer Direct Drive Console Dell Precision 380 Model spectrometer. The molar conductance was measured with WTW Cond 7110. Elemental analyses (C, H and N) were recorded on a Thermo Finnigan Flash EA 1112 Model analyzer. Sherwood Scientific MX1 Model devices used at for Magnetic susceptibility measurements. The TGA thermograms were carried out 900-25 °C on a Perkin-Elmer Diamond TGA System; nitrogen flow and heating rate were 50 mL/min and 10 °C/min⁻¹.

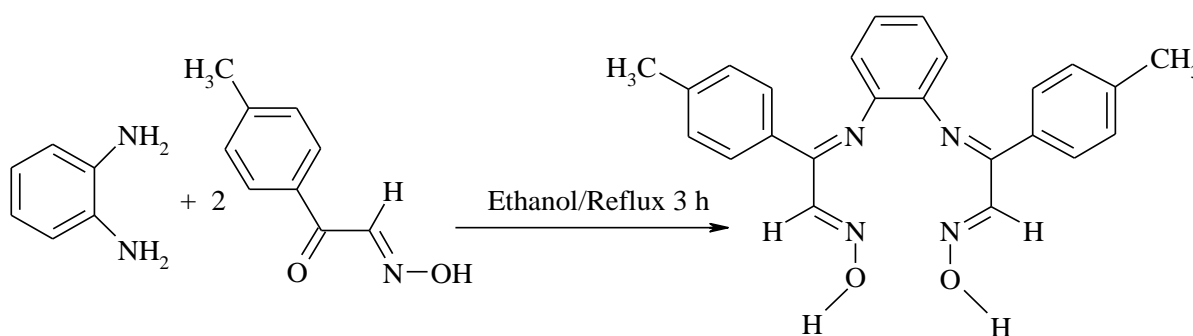
Synthesis of the ligand

The preparation of isonitrosomethyl-*p*-tolyl ketone (HL) was described in the literature (22-24). Coated glass reactors were used in the synthesis of the experiments.

To an ethanolic solution (30 mL) of isonitrosomethyl-p-tolyl ketone (30 mmol, 4.8951 g HL in was added *o*-phenylenediamine (1.622 g, 15 mmol) in ethanol (15 ml) respectively (25-26) (H_2L^1) (**1**). This solution was heated and stirred for 3 h and monitored by thin layer chromatography (TLC) using ethyl acetate/n-hexane (1:5). The precipitates thus formed were filtered off with Et_2O and dried on P_2O_5 .

Light Brown; Yield 81%. m.p.:101 °C. 1H -NMR (400 MHz, $DMSO-d_6$, ppm): δ 9.31 (s, 2H, OH), 8.12 (s, 2H, H-C=N), 8.16-7.37 (m, 12H, Ar-H), 2,46 (s, 6H, Ar- CH_3). ^{13}C -NMR (100 MHz, $DMSO-d_6$, ppm): δ =151.83 (C=N(imine)),

143.26 (C=N(oxime)), 141.38, ($C_{(aromatic)}$) 140.51, ($C_{(aromatic)}$) 133.94 ($C_{(aromatic)}$), 130.21 ($C_{(aromatic)}$), 129.89 ($C_{(aromatic)}$), 129.51 ($C_{(aromatic)}$), 129.31, 129.05, 127.42, ($C_{(aromatic)}$), 21.43 (Ar- CH_3). (MS-ESI): $[M-2]^+ = 398.4$ [$C_{24}H_{22}N_4O_2$, %27.3], 395.2 [$C_{24}H_{21}N_4O_2$, %100], 349.2 [$C_{23}H_{21}N_3O$, %7.8], 255.2 [$C_{15}H_{13}N_3O$, %6.9], 235.1 [$C_{15}H_{14}N_2O$, %31.5], 161.0 [$C_9H_9N_2O$, %2.8]. Elemental analysis: Anal.Calc.for $C_{22}H_{16}Br_2N_4O_2$: C, 72.34; H, 5.57; N, 14.06; Found C, 72.25; H, 5.19; N, 14.67%. IR (KBr) cm^{-1} : 3219 (OH), 1672 (C=N)_{imine}, 1607 (C=N)_{oxime}, 992 (=N-O); Structure of the ligands is given in Scheme 1.



Scheme 1: Synthesis of the H_2L^1 ligand.

Synthesis of the complexes

Caution: All perchlorate salts are potentially explosive so the readers are urged to be careful when using them.

$[Cu(H_2L^1)(H_2O)](ClO_4)_2 \cdot (H_2O)$ (**2**): A solution of $Cu(ClO_4)_2 \cdot 6H_2O$ (370 mg, 1 mmol) dissolved in acetone (10 ml), were added to a stirred solution of ligands (1 mmol) dissolved in 10 mL of acetone, and this mixture was refluxed with stirring for 1 h and monitored by thin layer chromatography (TLC) using ethyl acetate/n-hexane (1:5). The precipitated complexes were filtered off, washed with H_2O and dried over P_4O_{10} . Light green solid; Yield 43%. m.p.:249 °C. μ_{eff} B.M.=1.56. $\Lambda_M^p=325$. (MS-ESI): $[M-[(ClO_4)_2]]^+ = 498.0$

$[C_{24}H_{26}CuN_4O_4$, %19], 379.6 [$C_{24}H_{20}N_4O$, %27], 238.7 [$C_{15}H_{13}N_2O$, %100], 216.8 [$C_{15}H_{13}N_2$, %63]. Elemental analysis: Anal. Calc. for $C_{24}H_{26}Cl_2CuN_4O_{12}$: C, 41.36; H, 3.76; N, 8.04; Cu, 9.12; Found C, 41.46; H, 3.59; N, 8.24; Cu, 9.35%. IR (KBr) cm^{-1} : 3516 (OH or H_2O), 2320 (O \cdots H-H), 1613 (C=N)_{imine}, 1592 (C=N)_{oxime}, 1428 (=N-O), 1091, 1046, 618 (ClO_4), 474 (M-N).

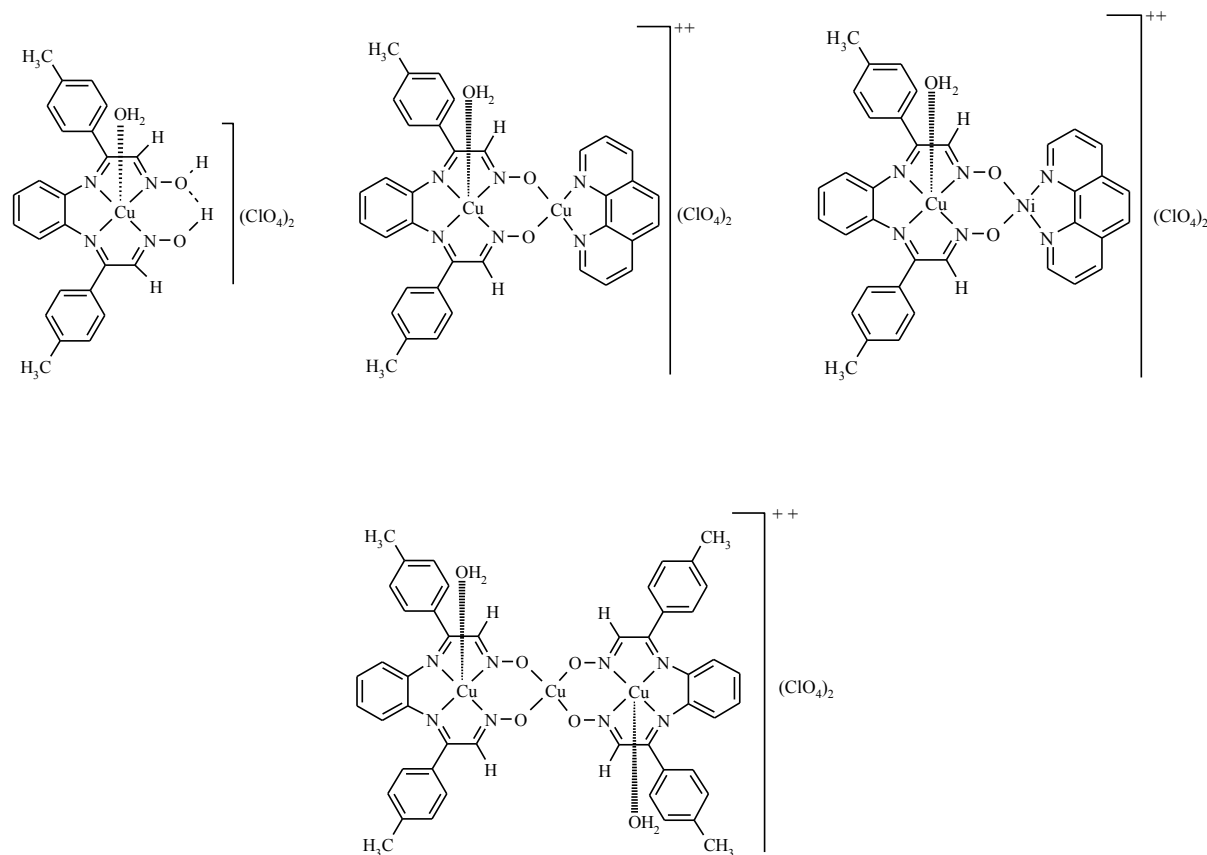
$[Cu(H_2L^1)(H_2O)_2Cu(phen)](ClO_4)_2 \cdot (H_2O)$ (**3**): A mixture of mononuclear copper(II) complex (1 mmol) and Et_3N (101 mg, 1 mmol) in MeOH (20 ml) was refluxed for 0.5 h. The solution of 1,10-phenanthroline monohydrate (198 mg, 1 mmol) in MeOH (10 ml) and $Cu(ClO_4)_2 \cdot 6H_2O$

(370 mg, 1 mmol) in MeOH (10 ml) was added to the resulting mixture, which was refluxed for 3 h and monitored by thin layer chromatography (TLC) using ethyl acetate/n-hexane (1:5). The precipitated complexes were filtered off, washed with H₂O and dried over P₄O₁₀. Dark Brown Solid; Yield 36%. m.p.:217 °C. μ_{eff} B.M.=1.94. $\Lambda_{\text{M}}^{\text{b}}=473$. (MS-ESI): 757.7 [M-[(ClO₄)₂]+2]⁺ = [C₃₆H₃₄Cu₂N₆O₅, %2], 703.7 [C₃₆H₂₈Cu₂N₆O₂, %5], 523.5 [C₂₄H₂₀Cu₂N₄O₂, %100], 398.4 [C₂₄H₂₂N₄O₂, %22]. Elemental analysis: Anal. Calc. for C₃₆H₃₄Cl₂Cu₂N₆O₁₃ C, 45.20; H, 3.58; N, 8.78; Cu, 13.28; Found C, 45.34; H, 3.46; N, 8.59; Cu, 13.41%. IR (KBr) cm⁻¹: 3338 (OH or H₂O), 1610 (C=N)_{imine}, 1589 (C=N)_{oxime}, 1429 (=N-O), 1035, 618 (ClO₄), 557 (M-O), 475 (M-N).

[Cu(H₂L¹)(H₂O)₂Ni(phen)](ClO₄)₂ (**4**) : A mixture of mononuclear copper(II) complex (1 mmol) and Et₃N (101 mg, 1 mmol) in MeOH (20 ml) was refluxed for 0.5 h. The solution of 1,10-phenanthroline monohydrate (198 mg, 1 mmol) in MeOH (10 ml) and Ni(ClO₄)₂.6H₂O (366 mg, 1 mmol) in MeOH (10 ml) was added to the resulting mixture, which was refluxed for 5 h and monitored by thin layer chromatography (TLC) using ethyl acetate/n-hexane (1:5). The precipitated complexes were filtered off washed with H₂O and dried over P₄O₁₀. Dark Yellow Solid; Yield 48%. m.p.:229 °C. μ_{eff} B.M.=2.81. $\Lambda_{\text{M}}^{\text{b}}=369$. (MS-ESI): 734.9 [M-[(ClO₄)₂]+1]⁺ =

[C₃₆H₃₂CuNiN₆O₄, 2%], 698.8 [C₃₆H₂₈CuNiN₆O₂, 18%], 462.0 [C₂₄H₂₂CuN₄O₂ 100%], 253.2 [C₁₅H₁₅N₃O, 56%]. Elemental analysis: Anal. Calc. for C₃₆H₃₂Cl₂CuNiN₆O₁₂ C, 46.30; H, 3.45; N, 9.00; Cu, 6.81; Ni, 6.29; Found C, 46.44; H, 3.39; N, 8.86; Cu, 6.70; Ni, 6.31%. IR (KBr) cm⁻¹: 3538 (OH or H₂O), 1611 (C=N)_{imine}, 1591 (C=N)_{oxime}, 1485 (=N-O), 1089, 1044, 617 (ClO₄), 553 (M-O), 479 (M-N).

[Cu₃(H₂L¹)₂(H₂O)₂](ClO₄)₂ (**5**) : Mononuclear copper complex (2 mmol), Cu(ClO₄)₂.6H₂O (370 mg, 1 mmol) and Et₃N (101 mg, 1 mmol) in MeOH (25 ml) was refluxed for 5 h and monitored by thin layer chromatography (TLC) using ethyl acetate/n-hexane (1:5). The precipitated complexes were filtered off washed with H₂O and dried over P₄O₁₀. Dark Yellow Solid; Yield 42%. m.p.:246 °C. μ_{eff} B.M.=2.13. $\Lambda_{\text{M}}^{\text{b}}=551$. (MS-ESI): 1019.5 [M-[(ClO₄)₂]-4]⁺ = [C₄₈H₄₄Cu₃N₈O₆, 15%], 983.5 [C₄₈H₄₀Cu₃N₈O₄, 28%], 679.6 [C₂₉H₂₈Cu₂N₈O₄ 100%], 557.5 [C₂₄H₂₂Cu₂N₄O₂, 38%], 462.0 [C₂₄H₂₂CuN₄O₂, 37%]. Elemental analysis: Anal. Calc. for C₄₈H₄₄Cl₂Cu₃N₈O₁₄ C, 47.32; H, 3.64; N, 9.20; Cu, 15.65; Found C, 47.21; H, 3.55; N, 9.11; Cu, 15.80%. IR (KBr) cm⁻¹: 3581, 3548, 3510 (OH or H₂O), 1609 (C=N)_{imine}, 1576 (C=N)_{oxime}, 1485 (=N-O), 1101, 1040, 619 (ClO₄), 514 (M-O), 495 (M-N). The materials obtained were based on the studies in the literature.



Scheme 2: Structures for the mono, homo-heterodinuclear copper(II) and homotrimeric copper(II) complexes

RESULTS AND DISCUSSION

In this work, 4'-methylacetophenone was used as the starting substance. Isonitroso-p-methylacetophenone has been isolated through the nitrosation reaction between 4'-methylacetophenone with butylnitrite in sodium ethoxide medium. The new ligand was synthesized as a result of isonitrosoacetophenone derivative reaction with aromatic amine (*o*-phenylenediamine) and four novel complexes were synthesized by the addition of metal salts of nickel(II) and copper(II) to the Schiff-based ligands. Study has shown that the obtained theoretical optimized structural parameters are in coherence with the experimental results.

Condensation of the 4'-methylacetophenone with diamine was coordinated and identified by ^1H and ^{13}C -NMR spectra, elemental analysis, mass spectra, FT-IR and thermal analysis. This newly synthesized oxime ligand and its metal complexes are shown Scheme 2. In addition, ligand and its copper(II) and nickel(II) complexes were verified by elemental analysis, mass spectra, thermal analysis and FT-IR. All the complexes and ligand are durable at room temperature, are soluble in methanol, DMSO and ethanol, insoluble in hexane, diethyl ether and water and slightly soluble in acetone and dichloromethane. Single crystals were not obtained for complexes and the ligand.

The resulting complexes are highly colored, and durable in air. Spectroscopic techniques, elemental analyses, magnetic susceptibility,

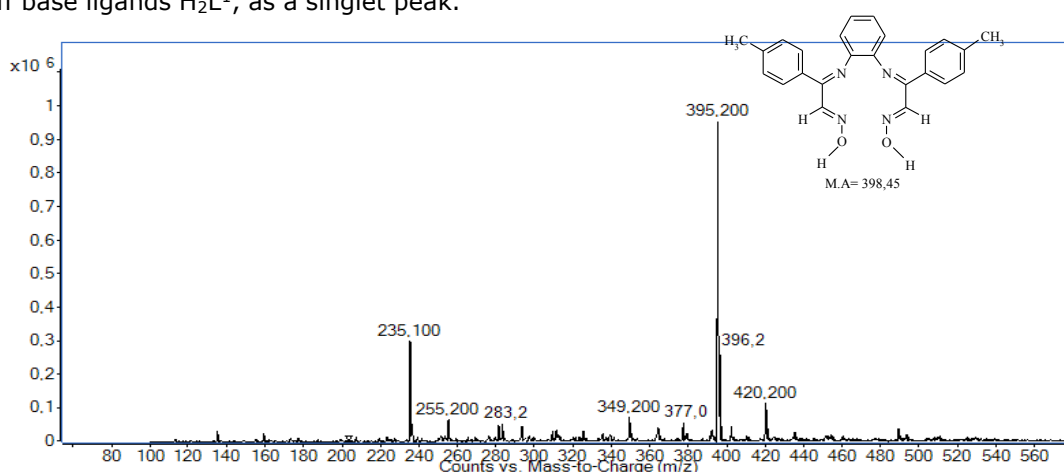
conductivity, and thermal techniques were applied to shed light into the complexes. The ligand and their metal complexes are in good agreement with the previous experimental studies. Mononuclear complexes have square bipyramidal geometric structure while homodinuclear and heterodinuclear complexes have not been stable geometric structure. Because homodinuclear complexes possess two copper(II) ions and heterodinuclear complexes one copper(II) and one nickel(II) ions, and different axial position of metal ions are effected geometrical structure. Homodinuclear and heterodinuclear copper(II) complex were found to have a 2:1 metal:ligand ratio. Due to trinuclear copper(II) complexes have three copper(II) ions and not to say solely one geometrical structure. Homotrinnuclear copper(II) complex were found to have a 3:2 metal:ligand ratio.

NMR spectra

All the $^1\text{H-NMR}$ and $^{13}\text{C-NMR}$ spectra of the tetradentate Schiff base types were recorded in DMSO-d_6 . $^1\text{H-NMR}$ spectrum of the ligand shifts observed at $\delta=9.31$ ppm was observed to the oxime group of the protons (N-OH) of the schiff base ligands H_2L^1 , as a singlet peak.

All the multiplet signals of the ligand 8.16–7.37 ppm range were observed to the protons of the aromatic rings (27). The oxime proton signals (H-C=N) at $\delta=8.12$ ppm disappeared upon deuterium exchange of the H_2L^1 ligand. The spectrum of the H_2L^1 ligand observed at singlets 2.46 (6H) ppm of the aromatic amine of methylene group protons.

$^{13}\text{C-NMR}$ spectrum of H_2L^1 observed a single peak at 151.83 ppm, respectively which showed that the (C=N) imine carbon atoms were equivalent, 143.26 ppm were observed to the (C=N) oxime carbon atoms of the ligands (27). All the signals in the 141.38–127.42 ppm range were assigned to the aromatic carbons of the ligand. In addition, signals were observed in the 21.43 ppm of the aromatic amine of the methylene group carbon (29-30). When the NMR spectra were evaluated, it was determined that they were compatible with previous studies. it is difficult to elucidate the structure solely on the basis of NMR spectroscopy, so the data should be supported by elemental analysis and mass spectral studies.



Scheme 3: The mass spectrum of [(H_2L^1)] ligand

IR spectra

The IR spectra of the metal complexes and ligand were studied in the range 4000–400

cm^{-1} . The oxime peaks in general were determined as $\nu(\text{C}=\text{N})$, $\nu(\text{O}-\text{H})$, and $\nu(\text{N}-\text{O})$ (31). The FT-IR spectrum of the ligand showed $\nu(\text{C}=\text{N})$ imine peak at 1672 cm^{-1} and $\nu(\text{C}=\text{N})$ oxime at 1607 cm^{-1} absence of a $\nu(\text{C}=\text{O})$ at around $1710-1700 \text{ cm}^{-1}$ were observed of oxime ligand condensation. In the IR spectrum of ligand ($-\text{O}-\text{H}$) band of oxime group peak was showed at 3219 cm^{-1} . Coordinated water of the complexes was observed $3581-3338 \text{ cm}^{-1}$ and which exhibit medium intense broad bands. FT-IR data confirmed the presence of coordinated water. $\nu(\text{C}=\text{N})$ imine stretching vibrations for complexes at $1613-1609 \text{ cm}^{-1}$ and $\nu(\text{C}=\text{N})$ oxime stretching vibrations for complexes at $1592-1576 \text{ cm}^{-1}$. it was found that the $\nu(\text{C}=\text{N})$ imine and $\nu(\text{C}=\text{N})$ oxime bands in the complexes were changed by about $63-59 \text{ cm}^{-1}$, $31-15 \text{ cm}^{-1}$ to the free ligand of H_2L^1 . Azomethine nitrogen also coordinated to the metal ion (38).

Results were supported by shifting $\text{N}-\text{O}$ stretching vibrations to lower or higher frequencies than the ligands (32-35). In the FT-IR spectrum of the complexes ($\text{M}-\text{N}$) imino or oximino nitrogen atoms were observed as a new band $495-474 \text{ cm}^{-1}$ (36) and oxygen atom of oxime and the metal ions of the copper(II) complexes ($\text{M}-\text{O}$) showed a new band at $557-514 \text{ cm}^{-1}$ (37). ($\text{H}-\text{O}\cdots\text{H}$) intramolecular hydrogen bond was observed at 2320 cm^{-1} for mononuclear copper(II) complexes (39). All of the perchlorate salts showed a strong band $1101-1089 \text{ cm}^{-1}$ and $1046-1035 \text{ cm}^{-1}$ (antisymmetric stretch) and sharp band at $619-617 \text{ cm}^{-1}$ (antisymmetric bend), which showed of uncoordinated perchlorate anions (40). Although the general spectroscopic peaks for oximes are $(\text{C}=\text{N})$, $(\text{O}-\text{H})$ and $(\text{N}-\text{O})$, perchlorate, $(\text{C}=\text{O})$ and (OH) ions also play an important role.

Thermal studies

The thermal studies of the ligand, one mononuclear, one homodinuclear, one heterodinuclear, and one trinuclear copper(II) complexes were discussed in this section. The data from the thermogravimetric analyses showed that the fragmentation of the complexes occurs in two or three steps and the ligand proceeds in two steps (41). The thermal behavior of the complexes and ligand are given in Table 1.

The ligand $[\text{C}_{24}\text{H}_{22}\text{N}_4\text{O}_2]$ was thermally decomposed two degradation steps. The first step at range $92-186 \text{ }^\circ\text{C}$ with an estimated mass loss 7.97% (calculated mass loss = 8.53) which indicating the removal of two OH groups. The 2nd decomposition step within the temperature range $186-255 \text{ }^\circ\text{C}$ with an estimated mass loss 92.03% (calculated mass loss = 91.47%), due to the removal of four CN , Ar_{amine} , two 4'-methylacetophenone. At the end of the study there is no product left so total estimated mass loss was 100.00% .

The complex $[\text{C}_{24}\text{H}_{26}\text{Cl}_2\text{CuN}_4\text{O}_{12}]$ showed three steps of decomposition at $35-82 \text{ }^\circ\text{C}$ with an estimated mass loss 2.39% leaving one hydrate H_2O group. (calculated mass loss = 2.58%). The second step within the temperature range $82-193 \text{ }^\circ\text{C}$ with an estimated mass loss 2.30% (calculated mass loss = 2.58%), which leaving coordination H_2O . The third and last step exhibited an estimated mass loss of 81.12% (calculated mass loss = 80.52%) within the temperature range $193-1000 \text{ }^\circ\text{C}$ due to the liberation of four CN , Ar_{amine} , two (ClO_4) , and two 4'-methylacetophenone groups. The mass loss is continues, so final product was not determined.

The thermogram of the dimeric complex $[C_{36}H_{34}Cl_2Cu_2N_6O_{13}]$ showed three steps of decomposition at 22–104 °C leaving one hydrate group. The DTG curve gave a peak at 62 °C. The 2nd decomposition step at within the temperature range 104–186 °C with an estimated mass loss 3.68% (calculated mass loss = 3.76%), ascribable to two hydrate molecules leaving coordination. The 3rd step 186–1000 °C with an estimated mass loss of %78.34 leaving four CN, Ar_{amine}, two (ClO₄), phenanthroline groups, two 4'-methylacetophenone groups. Finally two CuO leaves the residue. (calculated mass loss = 77.74%). Total estimated mass loss was 100.00%.

The thermogram of the heterodinuclear complex $[C_{36}H_{32}Cl_2CuNiN_6O_{12}]$ showed three steps of decomposition at 29–94 °C with an estimated mass loss 0.9% which is reasonably accountable for the loss of moisture. The DTG curve gave a peak at 72 °C. The 2nd decomposition step at within the temperature range 94–196 °C with an estimated mass loss of 3.71% (calculated mass loss = 3.85%),

meaning that two hydrate molecules leaving the coordination. The 3rd step indicates the removal of four CN, Ar_{amine}, two (ClO₄), phenanthroline groups, and two 4'-methylacetophenone groups. The mass loss is in continuation, so the final product was not determined.

The thermogram of the trinuclear complex **(5)** $[C_{48}H_{44}Cl_2Cu_3N_8O_{14}]$ was thermally decomposed in three decomposition steps. The first step at range 42–108 °C with an estimated mass loss of 0.85% which means the leaving of moisture. The 2nd decomposition step at range 108–205 °C with an estimated mass loss of 2.84% (calculated mass loss = 2.95%), which means that two hydrate molecules leaving the coordination. The 3rd step between 205–1000 °C with an estimated mass loss of leaving eight CN, two Ar_{amine}, two (ClO₄), and four 4'-methylacetophenone groups. Finally, three moles of CuO was found as residue. Total estimated mass loss was 100.00%.

Table 1. Thermoanalytical results (TG, DTG) of the ligands and their metal complexes

Comp.	TG range (°C)	DTA max.(°C)	Founded mass loss %	Calc. mass loss %	Assignment	Residue
(1)	92-186	96 (+)	7.97	8.53	Loss of two OH	-
	186-255	253 (+)	92.03	91.47	Loss of four CN, Ar _{amine} , two 4'-methylacetophenone	
(2)	35-82	79(+)	2.39	2.58	Loss of hydrate H ₂ O	Decomposition is in progress
	82-193	154(-)	2.30	2.58	Loss of coordination H ₂ O	
	193-1000	395(-) 625(-)	88.12	80.52	Loss of four CN, Ar _{amine} , two (ClO ₄), two 4'-methylacetophenone	
(3)	22-104	62(+)	1.69	1.88	Loss of hydrate H ₂ O	2 CuO 16.29 (16.62)
	104-186	169(+)	3.68	3.76	Loss of coordination two H ₂ O	
	186-1000	376(-)	78.34	77.74	Loss of four CN, Ar _{amine} , two (ClO ₄), phenanthroline groups, two 4'-methylacetophenone	
(4)	29-94	72(+)	0.9	-	Loss of moisture	Decomposition is in progress
	94-196	156(+)	3.71	3.85	Loss of coordination two H ₂ O	
	196-1000	726(-)	86.68	79.40	Loss of four CN, Ar _{amine} , two (ClO ₄), phenanthroline groups, two 4'-methylacetophenone	
(5)	42-108	86(+)	0.85	-	Loss of moisture	3 CuO 20.19 (21.24)
	108-205	203(-)	2.84	2.95	Loss of coordination two H ₂ O	
	205-1000	670(-)	76.12	75.80	Loss of eight CN, two Ar _{amine} , two (ClO ₄), four 4'-methylacetophenone	

Molar conductance and magnetic susceptibility

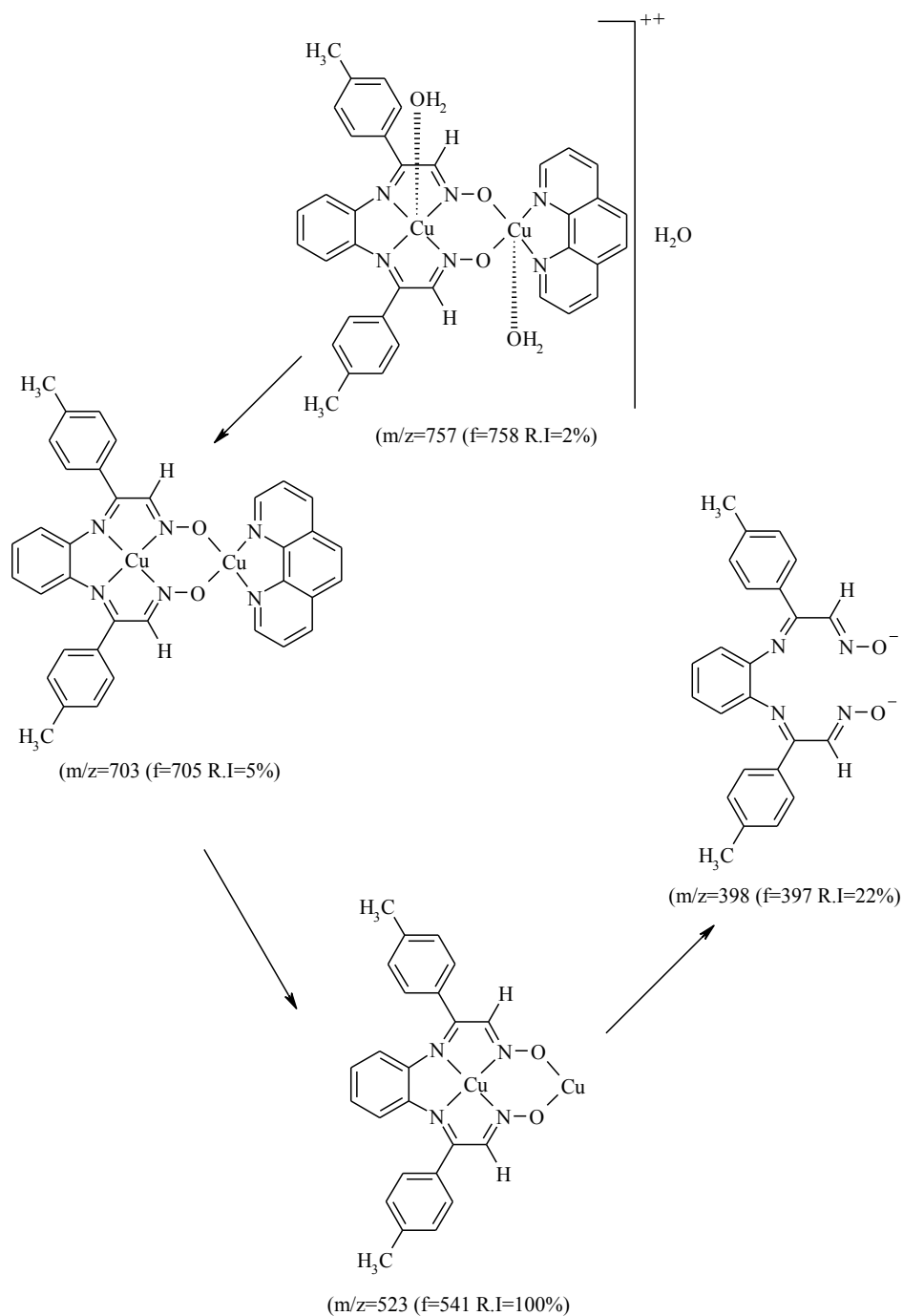
2×10^{-5} mol/dm⁻³ methanolic solutions were used for conductivity measurements at 25 °C. For all the complexes, conductivity measurement data fall within between 325 and 551 Ω^{-1} cm².mol⁻¹ and behaved as 1:2 electrolytes because of the fact that the complex includes perchlorate ions (42).

The magnetic moments measurements showed that complexes were paramagnetic. The magnetic moment data of the mononuclear copper(II) complex (2) 1.56 B.M. corresponding to one unpaired electron. The measured magnetic moments of the trinuclear complex (5) 2.13 B.M., homodinuclear complex (3) have magnetic moments 1.94 B.M., heterodinuclear complex (4) 2.81 B.M., which have strong intramolecular antiferromagnetic effected for the complexes (43-45). It was possible that a distorted tetragonal geometry was responsible for this kind of interaction (46).

Mass spectra

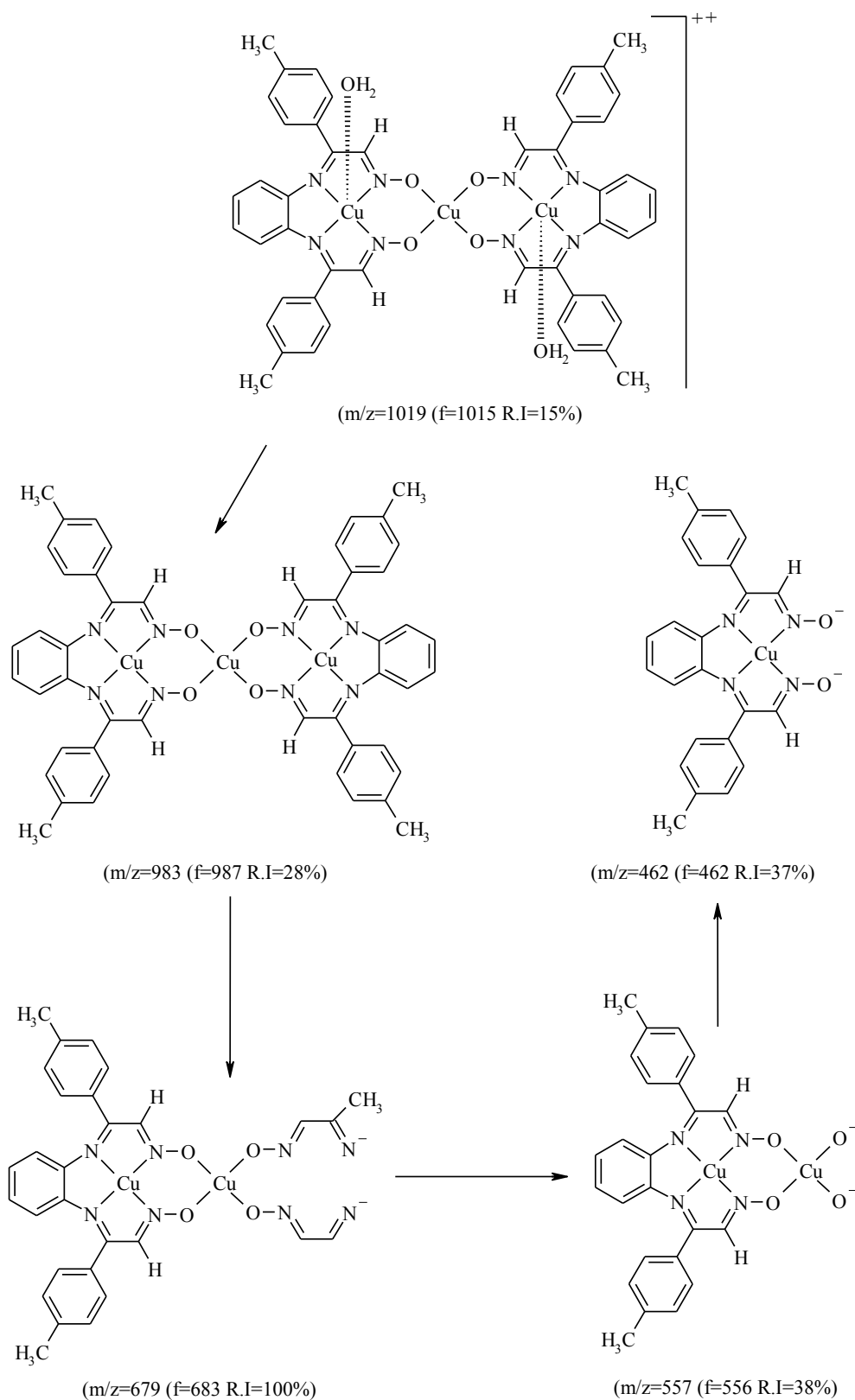
The molecular ion peak of the H₂L¹ ligand was observed at 398.4 [M-2]⁺ (1). The mononuclear copper(II) ion peak appeared at (m/z, ESI) 498.0 [M-[(ClO₄)₂]]⁺ (2), at 757.7 [M-[(ClO₄)₂]+2]⁺ for the homodinuclear copper(II) (3), at 734.9 [M-[(ClO₄)₂]+1]⁺ for

the heterodinuclear copper(II)-nickel(II) (4), at 1019.5 [M-[(ClO₄)₂]-4]⁺ for the homotrinnuclear copper(II) (5) complex. According to the mass spectroscopy values, the proposed structure coincides with the experimental data obtained. Mass spectroscopy shows us the decomposition products of the compounds. There are two figures showing the fragmentation products. In mass spectra of the heterodinuclear Cu(II) complex m/z 734.9 [Cu(H₂L¹)(H₂O)₂Ni(phen)] (Calcd. 734.90 amu) represents the molecular ion of the Cu(II) complex with 2% abundance. The other peaks (698, 462, 253) are attributed to fragmentation. In mass spectra of the mononuclear Cu(II) complex m/z 490.0 [Cu(H₂L¹)(H₂O)](H₂O) Calcd. 490.0 amu) represents the molecular ion of the Cu(II) complex with 19% abundance. The other peaks (379, 238, 216) were attributed to fragmentation. When fragmentation products are carefully evaluated, a cycle is contrary to the synthesized steps. Since mass spectrometer operates in negative mode, all the complexes perchlorate ions was not observed. Schemes 4 and 5 show that the proposed path of decomposition for the investigated homodinuclear and homotrinnuclear Cu(II) complexes (46).



R.I.=relative intensity of the peak, f=found value of m/z , m/z =ratio of mass to charge (calculated);.

Scheme 4. Mass fragmentation pattern of the $[\text{Cu}(\text{H}_2\text{L}^1)(\text{H}_2\text{O})_2\text{Cu}(\text{phen})](\text{H}_2\text{O})$ complex of dioxime.



R.I.=relative intensity of the peak, f=found value of m/z , m/z =ratio of mass to charge (calculated);.

Scheme 5. Mass fragmentation pattern of the $[Cu_3(H_2L^1)_2(H_2O)_2](ClO_4)_2$ complex of dioxime.

CONCLUSION

In this article, a new Schiff base ligand and its metal complexes were designed and synthesized. Spectroscopic and stoichiometric data were shown and discussed above. The metal ion in the mononuclear copper (II) complexes is covalently bound to the nitrogen atom in the oxime and imine groups and a square pyramidal geometric structure is considered. In the homodinuclear and heterodinuclear complexes, the first copper(II) metal atom forms a coordinate covalent bond with the nitrogen atom of the oxime and imine group, while the second metal ion linked with the oxygen atom of the oxime group via the 1,10-phenanthroline nitrogen atom. As there are 2 metal ions in the structure, it is not possible to propose a single geometry. The two mononuclear copper (II) compounds are linked by a coordinated covalent bond to form a homotrimeric compound, and it is not possible to mention any geometrical structure related to this structure. No single crystal analysis of the ligand and complexes could be made, but it was determined that elemental analysis, mass spectroscopy and magnetic moment data yielded the predicted structure and the results were in agreement. The thermal analyses data of ligand and complexes showed that generally thermally decomposed in 2-3 decomposition steps and the correlations between the founded and calculated mass were in good agreement.

ACKNOWLEDGEMENTS

This study has been supported by Pamukkale University (Grant Nos: 2013FBE041 and 2015HZL014)

REFERENCES

1. Kahn O. Dinuclear Complexes with Predictable Magnetic Properties. *Angew. Chem., Int. Ed. Engl.* 1985 October; 24: 834-850.
2. Smith A. G, Tasker P. A and White, D. J. The structures of phenolic oximes and their complexes. *The Coord. Chem. Rev.* 2003; 241: 61-85.
3. Cheng, M. Y, De B, Almstead N. G, Pikul S, Dowty M. E, Dietsch C. R, Dunaway C. M, Gu F, Hsieh L. C, Janusz M. J, Taiwo Y. O, Natchus M. G, Hudlicky T, and Mandel M. Design, synthesis, and biological evaluation of matrix metalloproteinase inhibitors derived from a modified proline scaffold. *J. Med. Chem.* 1999; 42: 5426-5436.
4. Kitajima N. and Moro-oka Y. Copper-Dioxygen Complexes. *Inorganic and Bioinorganic Perspectives. Chem. Rev.* 1994; 94: 737-757.
5. Reddy K. H, Reddy P.S. Nuclease activity of mixed ligand complexes of copper(II) with heteroaromatic derivatives and picoline. *Transition Met. Chem.* 2000; 25: 505-510.
6. Kane S. A, Hecht S.M. Polynucleotide recognition and degradation by bleomycin. *Prog Nucleic Acid Res Mol Biol.* 1994; 49: 313-352.
7. Borah S, Melvin M.S, Lindquist N, Manderville R.A. Copper-mediated nuclease activity of a tambjamine alkaloid. *J Am Chem Soc.* 1998; 120: 4557-4562.
8. Asad S. F, Singh S, Ahmad A, Hadi S.M. Bilirubin- Cu(II) complex degrades DNA. *Biochim. Biophys. Acta.* 1999; 1428: 201-208.
9. Dulger S, Saglam N, Belduz A, Guner S, Karabocek S. Dna Cleavage By Homo- And Heterotetranuclear Cu(II) And Mn(II) Complexes With Tetrathioether-Tetrathiol Moiety. *Biometals.* 2000; 13: 261-265.
10. Athar F, Arjmand F, Tabassum S. New asymmetric N2S2 macrocycles, their metal chelates and the photokinetics of DNA-complex interaction. *Transition Met. Chem.* 2001; 26: 426-429.
11. Saglam N, Colak A, Serbest K, Dulger S, Guner S, Karabocek S, Belduz AO. Oxidative cleavage of DNA by homo- and heteronuclear Cu(II)-Mn(II) complexes of an oxime-type ligand. *Biometals.* 2002; 15: 357-365.
12. Garcia-Raso A, Fiol JJ, Adrover B, Moreno V, Mata I, Espinosa E, Molins E. Synthesis, structure and nuclease properties of several ternary copper(II) peptide

- complexes with 1,10-phenanthroline. *J. Inorg. Biochem.* 2003; 95: 77-86.
13. Gonzalez-Alvarez M, Alzuet G, Borrás J, Macías B, del Olmo M, Liu-Gonzalez M, Sanz F. Nuclease activity of [Cu(sulfathiazolato)(2)(benzimidazole)(2)](2)MeOH. Synthesis, properties and crystal structure. *J. Inorg. Biochem.* 2002; 89: 29-35.
 14. Karapınar N, Karapınar E and Özcan E. Liquid-Liquid Extraction of Transition Metal Cations by Glyoximes and Their Macrocyclic Glyoxime Ether Derivatives. *Journal of Chemistry* 2013; 2013.
 15. Karplus P.A, Pearson M.A. 70 years of crystalline urease: What have we learned?. *Acc. Chem. Res.* 1997; 30: 330-337.
 16. Zhu H.L, Tong Y.X, Chen X.M, Ren C.X. Synthesis, crystal structures and physical properties of two terephthalate-bridged copper(II) and nickel(II) complexes. *Transition Met. Chem.* 2001; 26: 528-531.
 17. Lashanizadegan M, Boghaei D.M. Metal complexes of non-symmetric tetradentate Schiff bases derived from N-(2-hydroxyacetophenone)-1-amino-2-phenyleneimine. *Synth. React. Met.-Org. Chem.* 2000; 30: 89-98.
 18. Lashanizadegan M, Boghaei D.M. Template synthesis and X-ray structure determination of unsymmetrical tetradentate Schiff base complexes of nickel(II) and copper(II). *Synth. React. Met.-Org. Chem.* 2001; 31: 1519-1529.
 19. Boghaei D.M, Mohebi S. Novel unsymmetrical tetradentate Schiff base complexes of cobalt (II) and palladium (II) with N₂O₂ donor sets. *J. Chem. Res. (S)* 2001; 224-226.
 20. Hoyos O.L, Bermejo M.R, Fondo M, Garcia-Daíde A, Gonzalez A.M, Maneiro M.B, Pedrido R. Mn(III) complexes with asymmetrical N₂O₃ Schiff bases. The unusual crystal structure of [Mn(phenglydisal-3-Br,5-Cl)(dmsO)](H(3)phenglydisal=3-aza-N-{2-[1-aza-2-(2-hydroxyphenyl)-vinyl]phenyl}-4-(2-hydroxyphenyl)but-3-enamide), a mononuclear single-stranded helical manganese(III) complex. *J. Chem. Soc., Dalton Trans.* 2000; 3122-3127.
 21. Atkins R, Brewer G, Kokot E, Mockler G.M, Sinn E. Copper(II) and Nickel(II) complexes of unsymmetrical tetradentate schiff-base ligands. *Inorg.Chem.* 1985;24: 127-134.
 22. Karapınar E, Özcan E, Synthesis of N'-[4'-benzo(15-crown-5)]-4-tolylaminoglyoxime and N'-[4'-benzo(15-crown-5)]-4-chlorophenylaminoglyoxime and their complexes with copper (II), nickel (II) and cobalt (II). *Journal of Inclusion Phenomena and Macrocyclic Chemistry.* 2003; 47: 59-63.
 23. Pekacar A.I, Özcan E. The Synthesis of 5 new bis(amino-p-chlorophenyl-glyoximes) and their polymeric complexes with Ni(II), Co(II) and Cu(II). *Journal of Macromolecular science-pure and applied chemistry* 1994; 31: 651-661.
 24. Sevindir H.C, Mirzaoğlu R. Synthesis and complex-formation of 4 new unsymmetrical vic-dioximes. *Synthesis and Reactivity in Inorganic and Metal-Organic Chemistry.* 1992; 22: 851-861.
 25. Dede B, Özmen İ, Karipcin F. Synthesis, characterization, catalase functions and DNA cleavage studies of new homo and heteronuclear Schiff base copper(II) complexes. *Polyhedron* 2009; 28: 3967-3974.
 26. Dede B, Karipcin F, Cengiz M, Novel homo- and hetero-nuclear copper(II) complexes of tetradentate Schiff bases: Synthesis, characterization, solvent-extraction and catalase-like activity studies. *J. of Hazardous Materials* 2009; 163: 1148-1156.
 27. Dede B, Karipcin F, Cengiz M. Synthesis, characterization and extraction studies of N,N''-bis[1-biphenyl-2-hydroxyimino-2-(4-acetylanilino)-1-ethylidene]-diamines and their homo- and heteronuclear copper(II) complexes. *J. Chem. Sci.* 2009; 121: 163-171.
 28. Karabocek S, Karabocek N, Armutcu A. Synthesis and structural studies of 2-(hydroxyimino)-1-methylpropylideneamino-phenyliminobutan-2-one oxime, ligand and its complexes with Cu-(II) and Ni-(II). *Transition Metal Chemistry* 2006; 31: 459-464.
 29. Prushan M.J, Addison A.W, Butcher R.J, Thompson L.K. Copper(II) complexes of tetradentate thioether-oxime ligands. *Inorg. Chim. Acta* 2005; 358: 3449-3456.
 30. Ucan S.Y, Mercimek B. Synthesis and characterization of tetradentate N2O2 Schiff base ligands and their transition metal complexes. *Synth. and React. Inorg. Met.-Org. and Nano-metal Chem.* 2005; 35: 197-201.
 31. Chitrapriya N, Mahalingam V, Zeller M, Lee H, Natarajan K. Synthesis, characterization, DNA binding and cleavage studies of Ru(II) complexes containing oxime ligands. *J. Mol. Struct.* 2010; 984: 30-38.
 32. Serbest K, Karabocek S, Degirmencioglu I, Guner S, Kormali F. Mono-, di- and trinuclear copper(II) dioxime complexes; 3-{2-[2-(2-hydroxyimino-1-methylpropylideneamino)ethylamino]ethyl

- mino}butan-2-one oxime. *Trans. Met. Chem.* 2001; 26: 375-379.
33. Prushan M.J, Addison A.W, Butcher R.J, Thompson L.K, Copper(II) complexes of tetradentate thioether-oxime ligands. *Inorg. Chim. Acta* 2005; 358: 3449-3456.
 34. Karipcin F, Ucan H.I, Karatas I. Binuclear and mononuclear cobalt(II), nickel(II) and copper(II) complexes of 4,4'-bis(alkylaminoisonitrosoacetyl)diphenylmethane derivatives. *Trans. Met. Chem.* 2002; 27: 813-817.
 35. Ferraro J.R. *Low Frequency Vibrations of Inorganic and Coordination Compounds.* Plenum Press, 1971, New York.
 36. David M.A. *Metal-Ligand and Related Vibrations.* Adward Arnold Ltd. 1967, London.
 37. Serbest K, Colak A, Guner S, Karabocek S, Kormali F. Copper(II)-manganese(II) complexes of 3,3'-(1,3-propanediyl-diimine)bis-(3-methyl-2-butanone)dioxime with superoxide dismutase-like activity. *Transition Met. Chem.* 2001; 26: 625-629.
 38. Topal T, Kart H.H, Taşlı T.P and Karapınar E. Synthesis and Structural Study on ((1E,2E,1'E,2'E)-3,3'-Bis[(4-Bromophenyl)-3,3'-(4-Methyl-1,2-Phenylene Diimine)] Acetaldehyde Dioxime: A Combined Experimental and Theoretical Study. 2015; *Optics and Spectroscopy* 118(6):865-881
 39. Bonomo R.P, Conte E, Marchelli R, Santoro A.M, Tabbi G. O-2(-) Scavenger properties of copper(II) complexes with diamino-diamide-type ligands. *J. Inorg. Biochem.* 1994; 53: 127-138.
 40. Karabocek N, Armutcu A, Karabocek S. Synthesis and structural studies of (2E,3E)-3-[(6-[(1E,2E)-2-(hydroxyimino)-1-methylpropylidene]amino}pyridin-2-yl)imino]butan-2-one oxime, ligand and its mono-, di- and trinuclear copper(II) complexes. *Inorg. Chim. Acta*, 2006; 31: 938-942.
 41. Karipcin F, Baskale-Akdogan G. Synthesis and characterization of novel oxime-imine ligands and their heteronuclear ruthenium(III) complexes. *Russian Journal of Coordination Chem.* 2009; 35: 588-596.
 42. Geary W.J. The use of conductivity measurements in organic solvents for the characterisation of coordination compounds. *Coord. Chem. Rev.* 1971; 7: 81-122.
 43. Kulkarni N.D, Bhattacharya P.K. Study of binuclear copper(II) complexes involving bridging schiff bases-I. *Transition Met. Chem.* 1989; 14: 303-305.
 44. Ruiz R, Lloret F, Julve M, Faus J. A study of Exchange interaction through phenolato, oximato and oxamidato bridges in (MnCuII)-Cu-II dimers- Crystal-Structure of [Cu(Salen)Mn(hfa)(2)]. *Inorg. Chim. Acta.* 1993; 213: 261-268.
 45. Luneau D, Oshio H, Okawa H, Koikawa M, Kida S. Synthesis, structure, and magnetism of binuclear Cu(II)Cu(II), Cu(II)Ni(II) and Ni(II)Ni(II) complexes doubly bridged by oximate groups. *Bull. Chem. Soc. of Jpn.* 1990; 63: 2212-2217.
 46. Karabocek S, Karabocek N, Mono- and dinuclear copper(II) complexes of a Schiff base ligand, 4',5'-bis(salicylideneimino)benzo-15-crown-5. *Polyhedron.* 1997; 16: 1771-1774.
 47. Karabocek S, Bayraktar U, Karabocek N, Sahin Z.S, Işık S, Muhsir S. Synthesis of (2E,3E,10E,12E)-3,11-dimethyl-5,9-dioxo-4,10-diazatrideca-3,10-diene-2,12-dione dioxime and its Cu(II), Ni(II), and Co(II) complexes. *Journal of Coordination Chem.* 2012; 65: 1118-1129.



The Photochemical Degradation (PCD) of Nitrobenzene (NB) using UV Light and Fenton Reagent Under Various Conditions

Md. Boshir Ahmed^{1,2*}✉, Ajoy Kumer^{2,3}✉, Muhammad Nazrul Islam^{3,4}✉, Tajmeri S. A. Islam¹✉

¹Department of Chemistry, Faculty of Science, University of Dhaka, Dhaka, Bangladesh, ²Faculty of Science and Engineering, European University of Bangladesh, Dhaka, Bangladesh, ³Department of Chemistry, Faculty of Science, University of Chittagong, Chittagong, Bangladesh, and ⁴Department of Chemistry, Faculty of Science and Arts, Yildiz Technical University, Istanbul, Turkey.

Abstract: Photochemical degradation contributes to the environmental fate of many pesticides, chemicals, and industrial waste in surface waters. Photochemical degradation (PCD) of nitrobenzene (NB) has been studied using a UV light source and Fenton's reagent under different experimental conditions. The effect of concentration on PCD of NB was monitored and recorded in the range 0.5×10^{-4} M to 3.0×10^{-4} M. The concentration of H_2O_2 was performed from 5.0×10^{-4} M to 2.5×10^{-4} M and Fe(II) from 1.0×10^{-4} M to 5.0×10^{-4} M, respectively. In terms of concentration, the absorbance increases with increasing the concentration of the solution of NB, H_2O_2 and Fe(II). The initial rate of PCD was recorded at fixed pH 2.42 of solution. Two optima for pH were found for PCD of nitrobenzene ranging from pH 2.42 to 4.20. The intermediates formed during PCD of NB were identified, by which a mechanism was then suggested that PCD is actually found to follow pseudo-first-order kinetics.

Keywords: Nitrobenzene, Fenton's reagent, Mohr's salt, photo-degradation, UV-Vis spectra, Pseudo-first-order kinetics.

Submitted: December 09, 2017. **Accepted:** May 08, 2018.

Cite this: Boshir Ahmed M, Kumer A, Nazrul Islam M, Islam T. The Photochemical Degradation (PCD) of Nitrobenzene (NB) using UV Light and Fenton Reagent Under Various Conditions. JOTCSA. 2018;5(2):803-18.

DOI: <http://dx.doi.org/10.18596/jotcsa.364152>.

***Corresponding author:** Md. Boshir Ahmed, **E-mail:** boshirahmed069@gmail.com.

INTRODUCTION

In the last decade since 2004, Bangladesh averaged a gross domestic product (GDP) growth of 6.5% that has been largely achieved by its exports ready-made garments, remittances, and the agricultural sector (1,2). Textiles and garments industries are key major export oriented sectors of the country along with other exporting goods like fish, sea-food, jute, and leather. The country also developed self-sufficient industries in pharmaceuticals, steel, and food processing (1-3). Being on the path of a medium developing country, all the structures in any sector are not set-up well. Most of these industries are situated in Dhaka, Chittagong, Khulna, Gazipur, and Narayangong cities which have the Buriganga, the Karnaphuli, the Shitalokkha, and the Poshur rivers, respectively (4,5). These rivers are related, directly or indirectly, to the survival of about fifty million people. More than 60,000 cubic meters of toxic waste, including a majority of textile dying, printing, washing, and pharmaceuticals, are being released into the main water bodies of Dhaka, Chittagong, and Narayangong cities everyday (6,7). The waste water and industrial waste turned into the river water cause river pollution so human health remains under risk from contaminated water (8,9).

Wastewater from manufacturing or chemical processes in industries add to the water pollution (9). Because of being comparatively steady chemical structures of aromatic dyes (10). Most of the commercially available dyestuffs are not favorable to decompose and therefore cause severe contamination to the drinking water and irrigation systems (10-14). Many of the dyestuffs have even been

identified as harmful for human body and environment, and thus severe attention have been raised about it. Industrial waste water usually contains specific and readily identifiable chemical compounds (15). During the last five decades, a large the number of industries in Bangladesh has grown rapidly in both chemical and agricultural fields. The growth of textile (16), pharmaceutical, and garment industries are the highest among all the industries (1,17). Nitrobenzene (NB) is one of the frequently used chemical for aniline manufacturing, solvent in the manufacturing paints, shoe polishes, floor polishes, metal polishes, explosive, rubber making, textile, pesticide, cosmetic, and pharmaceutical purposes (such as acetaminophen) (8,18-23). NB is a highly toxic organic pollutant (24). NBs and their derivatives cause several harmful health effects, for example, nitrobenzene can reduce the ability of blood to carry oxygen because it causes methemoglobinemia (8,19). Repeated exposure to high level of it may cause anemia, development of bluish colour in the skin, headache, nausea, weakness, sleepiness, vomiting, grouchiness, and dizziness (25). Experimental studies in animals showed that 1,3-dinitrobenzene and 1,3,5-trinitrobenzene cause male reproductive damage and may reduce sperm production (25). 4-Chloronitrobenzene has been identified as a potent hemoglobin toxicant, whereas 2-chloronitrobenzine is a potent hepatotoxicant (23). For this reason, it was selected to be the model pollutant in this study. General treatments of such polluted wastewater include adsorption (26), ozonization (27), or biodegradation (20), but water pollution is concentrated within a few sub sectors, mainly in the form of toxic wastes and organic pollutants (24). Out of this, a large portion can be traced to the processing of

industrial chemicals and to the food products industry. In fact, a number of large and medium sized industries in the region are connected to the Buriganga, the Karnaphuli, and the Shitolokha rivers. Action Plan does not have adequate effluent treatment facilities (16). Most of the heavy industries have effluent treatment facilities by effluent treatment plant (ETP). But small and medium scale industries usually are not concern about pollution control and unable to afford huge cost of waste water treatment equipment as their profit margin is very small. They require further treatments and are very prone to cause secondary pollution (16).

In order to remove colour from waste water, it is necessary to find an efficient technique of industrial effluents' treatment (10,28). A number of physical and chemical methods has been reported for the removal of dye compounds, mainly nitrobenzene and its derivatives (27,29) such as adsorption on carbon (26), biodegradation (20), ozonization (27) and advanced oxidation processes (AOPs) (30,31) such as Fenton and photo-Fenton catalytic reactions (32), H₂O₂/UV processes, and semiconductor photo catalysis (13,27,33). Highly reactive species such as hydroxyl radicals ($\cdot\text{OH}$) are produced by advanced oxidation methods. For rapid and non-selective oxidation of organic molecules, hydroxyl radical is a very powerful oxidant that can oxidize organic compounds into carbon dioxide and water, so it is capable to decompose pollutants efficiently. Among the AOPs homogeneous photo-catalytic oxidation using Fenton has been widely studied. H₂O₂ is a very efficient, relatively cheap, commercially available, and chemically stable photo-catalyst (34).

MATERIALS AND METHODS

Used chemicals

Mohr's salt, FeSO₄·(NH₄)₂SO₄·6H₂O (AR.BDH), hydrogen peroxide (BDH), potassium permanganate (AR, BDH), oxalic acid (AR, BDH), buffer solution (ammonium acetate), (MERCK India), nitrobenzene (Analytical grade), sulfuric acid (AR, BDH), sodium hydroxide (AR, BDH) and hydrochloric acid (AR, BDH) were used without further purification. All the aqueous solutions were prepared with deionized water. The stock solution of $1.0 \times 10^{-2} \text{M}$ of nitrobenzene was prepared and kept in the dark (31). Mohr's salt solution (0.01M) was prepared in 0.05M sulfuric acid solution (35). H₂O₂ solutions were freshly prepared before each experiment and titrated against standard KMnO₄ solution.

Experiment of photo-degradation

All the experiments were carried out in a beaker used as the reactor. The source of radiation comprised fluorescent lamps in a wooden box. The top and sides of the box had five (50-watt) fluorescent lamps. The intensity of light at the reactor was measured with a spectro-radiometer (International light, U.S.A., model no IL-588). The intensity was $1.802 \times 10^{-4} \text{Wcm}^{-2}$. The reactor was placed on a magnetically stirred plate and the distance of the solution surface from the lower part of the lamp was fixed. The total system was enclosed in a wooden box, called lamp house. The inner walls of the box were covered with aluminum foil to prevent the absorption of light (31,36,37).

After taking 100 mL of ($0.5 \times 10^{-4} \text{M}$) NB solution in 100 mL volumetric beaker with ($5.0 \times 10^{-3} \text{M}$) H₂O₂ and ($5.0 \times 10^{-4} \text{M}$) Fe(II) solution, the pH of the solution was measured

and recorded at 2.42. The constant pH was controlled by the addition of dilute sulfuric acid and sodium hydroxide before up to the mark. Then absorbance of the solution was measured by UV-visible spectrophotometer at different time intervals in concentration of NB 0.5×10^{-4} M, 1.0×10^{-4} M, 2.0×10^{-4} M, 2.5×10^{-4} M, and 3.0×10^{-4} M respectively. This experiment again was carried on at fixed pH 1.5 and 7.0 and recorded. The effect of H₂O₂ activity in 5.0×10^{-3} M to 0.025 M H₂O₂ solution in fixed pH 2.42 and 4.20 was

$$\% \text{ of degradation} = \left(1 - \frac{A_t}{A_0}\right) \times 100 \dots \dots \dots \text{(Eq. 1)}$$

Here, A_0 = absorbance at time = 0 min, and A_t = Absorbance at t = 30 min.

measured and recorded. Again, the effect of Fe(II) concentration from 1.0×10^{-4} M to 5.0×10^{-4} M were measured and recorded. A peak was recorded at 318 nm at fixed pH at 4.20 in UV-visible spectrophotometer which was confirmed as para-nitrophenol (PNP).

Determination of the percentage (%) degradation by UV-Vis spectra of NB

In each experiment, the % degradation was calculated after 30 minutes using the (Eq. 1)

RESULTS AND DISCUSSION**Determination of the effect of pH in absorbance of photochemical degradation of NB**

Absorbances at different pH's were recorded for the 0.5×10^{-4} M solution of NB with reference water at temperature at 31°C was shown in Figure 1

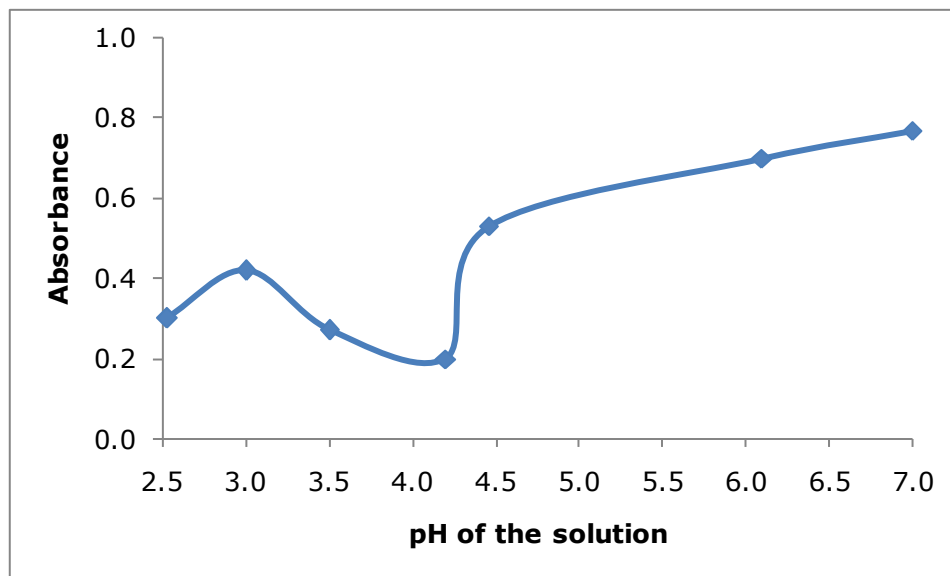


Figure 1. Effect of absorbance of NB solution at different pH.

Effect of different concentration on absorption for nitrobenzene

The solution of nitrobenzene 100 mL of 0.75×10^{-4} M to 2.25×10^{-4} M with 5.00×10^{-4} M [Fe(II)] and 5.0×10^{-3} M $[\text{H}_2\text{O}_2]_0$ was taken for experiment at constant pH at 2.42. The effect

on initial concentration of NBs photodegradation was recorded in Table 1, which shows that with increasing the concentration of NB, the absorbance increases.

Table 1. Absorbance of Nitrobenzene at different concentrations at wavelength 267nm.

Concentration $\times 10^{-4}/\text{M}$	Absorbance at $\lambda_{\text{max}}\text{nm}$
X = 0.75	0.562
1.00	0.729
1.25	0.960
1.50	1.147
1.75	1.328
2.00	1.498
2.25	1.699
2.50	1.880

Effect of time on absorbance and concentration

The effect of time on absorbance and different concentration with 5.00×10^{-4} M [Fe(II)] and 5.0×10^{-3} M $[\text{H}_2\text{O}_2]_0$ was recorded at constant

pH 2.42 and plotted time versus absorbance and concentration (Figure 2). The graph shows that with increasing time, the absorbance

slowly decreases *i.e.*, concentration NB also decrease as with decreasing the concentration of NB, the absorbance decrease (Table 1).

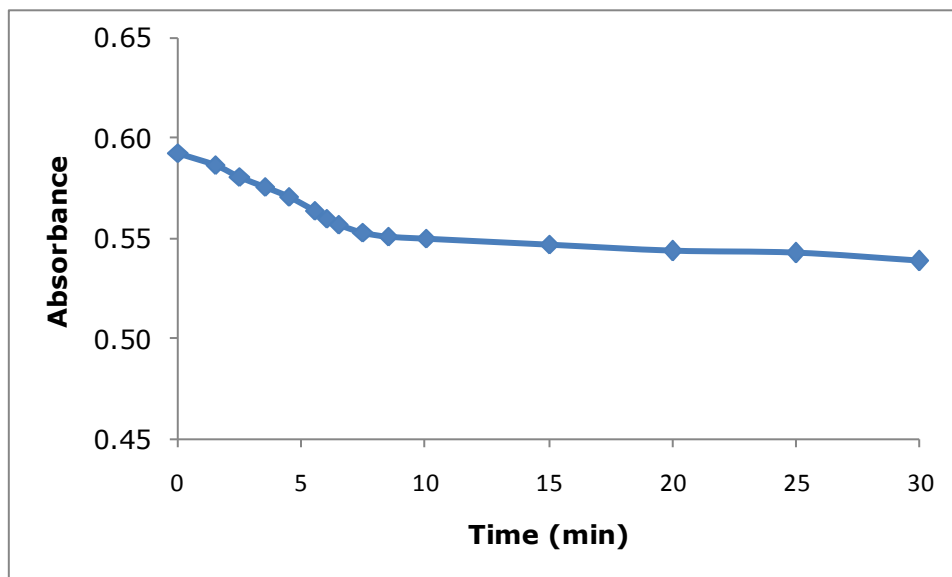
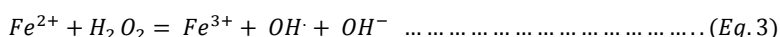
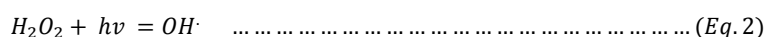


Figure 2. Effect of time on absorbance.

Effect of different concentrations of NB on photodegradation

Solution of nitrobenzene of different concentration with 5.00×10^{-4} M [Fe(II)] and 5.0×10^{-3} M [H₂O₂] was taken for experiment at constant pH 2.42 and at temperature 31.0 °C. The absorption of different concentrations with respect to time were recorded in Table 2, which gives evidence that at high

concentrations the absorption increases. Furthermore, with increasing time both the concentration and absorption decrease. As the concentration of NB increases both the rate constant and the initial rate increase. This might be due to the following reactions taking place. The reactions shown in (Eq. 2) and (Eq. 3) are important to produce OH· Radicals.



These suggest that there were enough OH· radicals during the increasing concentration of NB over the range 0.5×10^{-4} M to 3.0×10^{-4} M.

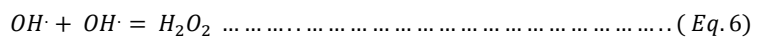
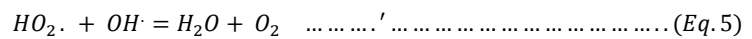
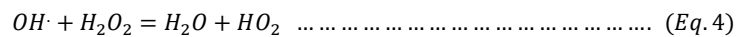
However, the increase of initial rate was influenced by the ratio of H₂O₂ /Fe(II) solution.

Table 2. Effect of different concentration ($\times 10^{-4}$) M of NB on photodegradation in terms of absorbance.

Time (min)	0.5	1.0	2.0	2.5	3.0
0.00	0.593	0.833	1.162	1.476	1.791
1.50	0.587	0.801	1.125	1.418	1.715
2.50	0.581	0.785	1.098	1.369	1.661
3.50	0.576	0.763	1.056	1.321	1.591
4.50	0.571	0.746	1.025	1.287	1.541
5.50	0.564	0.735	1.006	1.234	1.487
6.50	0.557	0.724	0.991	1.189	1.401
7.80	0.553	0.715	0.981	1.141	1.378
8.50	0.551	0.709	0.971	1.118	1.351
10.00	0.550	0.701	0.951	1.069	1.305
12.00	0.543	0.697	0.936	1.045	1.271
14.00	0.547	0.691	0.923	1.031	1.257
16.00	0.539	0.688	0.905	1.023	1.241
18.00	0.531	0.684	0.890	1.011	1.229
20.00	0.523	0.677	0.880	1.005	1.209
25.00	0.516	0.666	0.860	0.987	1.181
30.00	0.508	0.662	0.849	0.971	1.173

When the ratio of $H_2O_2/Fe(II)$ is 10/1, the initial rates observed, during the increasing concentration of NB, when compared with the values obtain using the ratio to be 50/1, it was found that the initial rates were increased at higher rate of $H_2O_2 / Fe(II)$ but the percentage of degradation was found to 35% during 30 minutes in both cases. Although it was

expected that at a higher ratio of $H_2O_2/Fe(II)$ the higher the rate of degradation percentage would be, but practically it did not happen. This might be due to the scavenging effect of $OH\cdot$ radicals at higher concentrations of H_2O_2 . Reactions shown in (Eq. 4), (Eq. 5) and (Eq. 6) might occur under that condition:

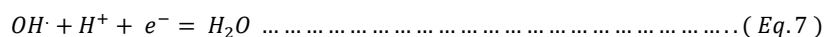


However, it can be concluded that the rate always increased because there was a high concentration of $OH\cdot$ radicals available to degrade NB.

Effect of pH on photo degradation of NB

The effect of pH was studied by varying the pH of the solution from 1.5 to 7.0 keeping the initial concentration of NB, $Fe(II)$ and H_2O_2 constant, the values were 3.0×10^{-4} M, $5.0 \times$

10^{-4} M, and 2.50×10^{-3} M respectively. It was observed that with the increase of pH the initial rate was increased at pH 2.50 but further increases of pH caused the decrease of initial rate of % degradation. Table 4 suggests 2.50 to be the optimal pH. At this pH 75% degradation was observed in less than 2 hours. The low removal rate at pH values 2.50 might be due to the following reaction (Eq. 7) taking place:



100 mL (3.0×10^{-4} M) NB solution was taken in 100 mL volumetric flasks and desired pH was controlled by the addition of hydrochloric acid or sodium hydroxide solution. Absorbance

of each of the solutions at different pH was recorded in Table 3, where the concentration of nitrobenzene is 3.0×10^{-4} M and reference was water at temperature 31 °C.

Table 3. Absorbance in different pH at λ_{\max} 267 (nm).

pH of the solution	Absorbance
2.53	0.30
3.00	0.42
3.50	0.27
4.20	0.20
4.46	0.53
6.10	0.70
7.00	0.77

Effect of concentration of NB by different pH for the photo degradation of NB

The percentage (%) degradation in different pH after 110 min time [NB]= 3.0×10^{-4} M, [H₂O₂] = 0.025 M, [Fe(II)] = 5.0×10^{-4} M was

recorded in Table 4. In acidic solution, this reaction predominates causing the decrease of concentration of OH[·] which in turn decreases the degradation of NB.

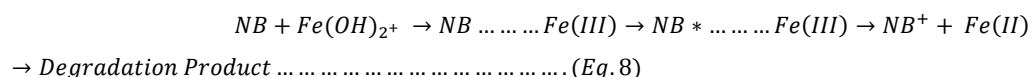
Table 4. Degradation of NB in different pH

pH	1.5	1.75	2	2.25	2.5	2.75	3	3.5	4	4.2	4.5	5	5.5	6	6.5	7
% of NB Deg.	60	61	63	67	72	65	62	78	88	92	85	80	70	60	49	38

The decrease of the degradation rate beyond pH 2.5 might be due to the coagulation of Fe³⁺ complex formed in the reaction which reduces the amount of Fe²⁺ for catalysis. When the concentration was changed to one third of the earlier value, the optimum pH was shifted to 4.2, Table 4 shows that, % degradation was

above 90. S. H. Lin *et al.* (38) has also studied the effect of pH for treatment of wastewater by Fenton process and reported 3.0 as optimum pH.

At higher pH values, there might be the possibility of direct reaction between NB and Fe(III) complexes.



This might be the reason for a higher degradation rate at pH 4.2

Effect of H₂O₂ concentration on photo degradation of NB

The kinetics of photo degradation were studied using the effect of H₂O₂ concentration under

constant values of [NB], and [Fe(II)], which were 3.0×10^{-4} M and 5.0×10^{-4} M respectively, and using optimum pH of 2.42.

From the Figure 3, it is observed that the initial rate increases with the increase of H_2O_2

concentration. In the concentration 0.025 M of Fe(II) solution it shows the high absorbance with low absorbance being shown with concentration of $[\text{H}_2\text{O}_2]_0: 5.0 \times 10^{-4}$ M.

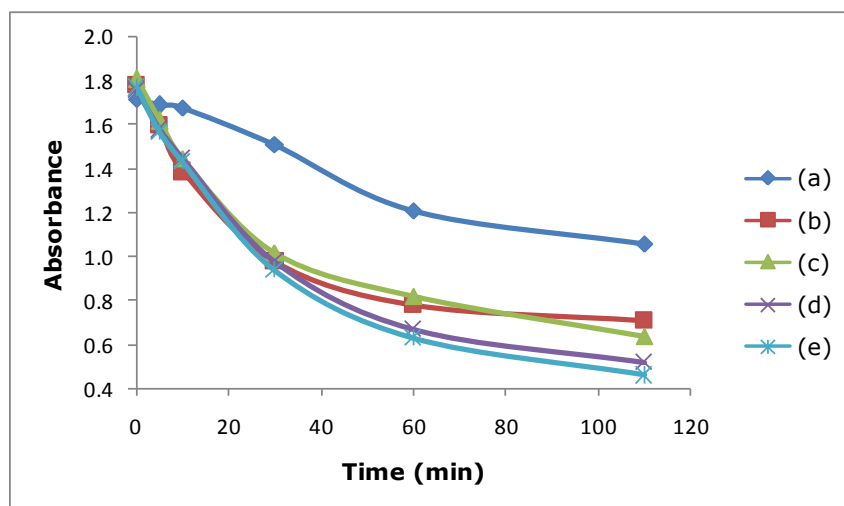


Figure 3. Percentage (%) degradation of NB in presence of Fe(II) at different H_2O_2 concentration (a) conc. 5.0×10^{-4} M (b) conc. 5.0×10^{-3} M (c) conc. 10.0×10^{-4} M (d) conc. 2.0×10^{-2} M and, (e) conc. 2.5×10^{-2} M vs Time in Fenton process [NB]= 3.0×10^{-4} M, [Fe(II)]= 5.0×10^{-4} M, pH 2.42, 4.20, Temp = 31.0 °C.

Effect of Fe(II) ion concentrations on the kinetics of photodegradation of nitrobenzene by Fenton process at pH 2.42

The effect of Fe(II) concentration on the degradation of NB was studied using two optimum pH values of 2.42 and 4.20 and the concentrations of NB and H_2O_2 to be 2.5×10^{-4} M, 0.025 M respectively.

Figure 4 shows at pH 2.42 initial rates increase with the increasing concentration of Fe(II) ions, which is expected because the production of $\cdot\text{OH}$ radicals by reaction 4(b).

The increases of initial rate with the increase of concentration of Fe(II) were observed in case of pH 4.20. This is the major reaction taking place, as supported by the experimental results, that show as the Fe(II) concentration increases, rate of degradation also increases.

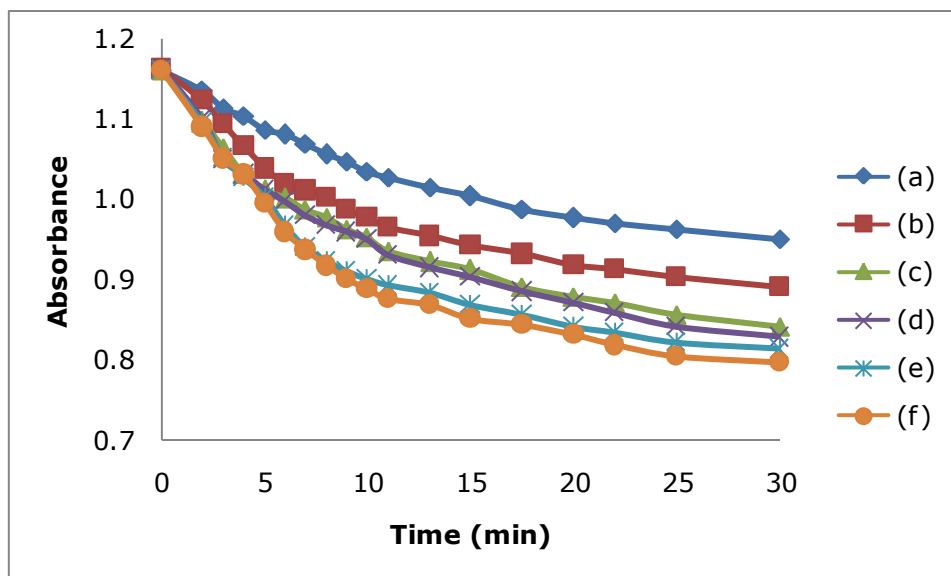


Figure 4. Variation of absorbance of NB with time under different Fe(II) concentrations (a) conc. 1.0×10^{-4} M (b) conc. 2.0×10^{-4} M (c) conc. 3.0×10^{-4} M (d) conc. 4.0×10^{-4} M (e) conc. 4.50×10^{-4} M and, (f) conc. 5.0×10^{-4} M, at pH = 2.42, 4.20 [NB]= 2.5×10^{-4} M, [H₂O₂]=0.025 M, Temp = 31.0 °C.

Estimation of rate constant and reaction kinetics with degradation of NB

Percentage (%) of degradation of NB has been studied at pH 1.5, 2.0, 2.5 and 3.0. over 60 minutes. In all pH studied, degradation of NB follows a nearly similar order. Among them,

percentage (%) of degradation of NB at pH 2.5 is tabulated in Table 5. The results clearly demonstrate that NB significantly decomposed and more than 70% of the initial nitrobenzene disappeared within 60 minutes.

Table 5. Change of c_t/c_0 with degradation time of NB at pH 2.5

Time (min)	% of Degradation	C_0/C_t	$\ln(C_0/C_t)$	Rate constant, k (min ⁻¹)
0	0	1.0000	0.0000	
6.5	15	0.8667	0.1477	
11.5	26	0.7278	0.2626	
31.5	49	0.4844	0.7249	0.0230
46.3	63	0.3444	1.0651	
60.0	72	0.2611	1.3800	

Figure 5 also drawn to present the reaction kinetics that was plotted as $\ln(C_t/C_0)$ versus time where C_t and C_0 are the concentrations of nitrobenzene at a given time t and time zero *i.e.*, initiated concentration of NB, respectively. The linear regression model fits the data very well reflecting that the reduction of nitrobenzene follows pseudo-first-order kinetics (39). Slope of the straight line calculated from equation of the line $y = 0.023x - 0.001$ as 0.0230 that shown in Figure 5. The slope indicates the rate constant of

photodegradation of NB. So the rate constant of disappearance of NB is 0.0230 min⁻¹. Again at higher concentration of H₂O₂, the reaction only depends on the concentration of radical ·OH, which also represents pseudo-first-order reaction. Jun Dong *et al.* (40) have studied degradation of nitrobenzene in groundwater using emulsified nano-zero-valent iron that followed pseudo-first-order reaction and rate constant of nitrobenzene was 0.0942 min⁻¹.

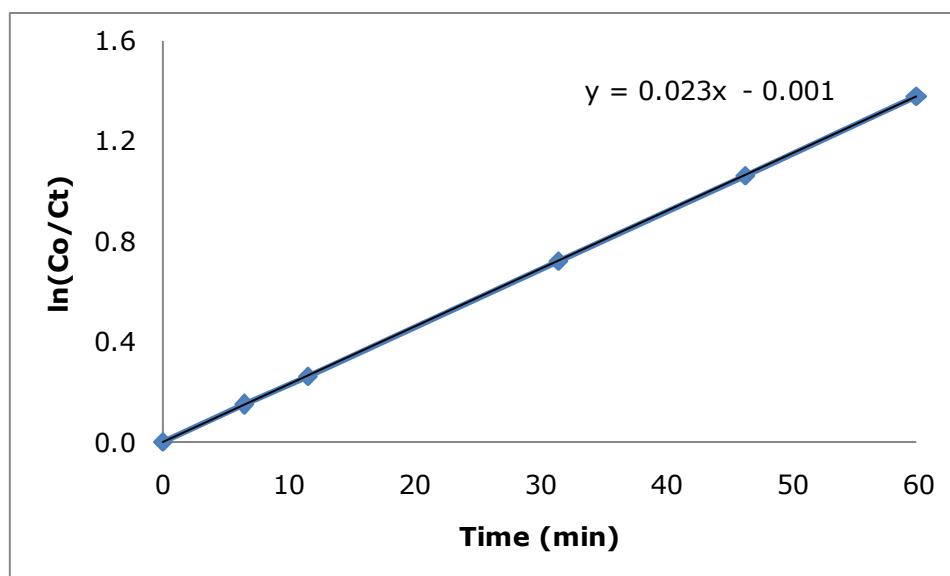
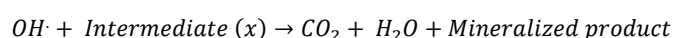
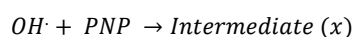
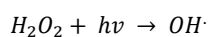


Figure 5. Plot of $\ln(C_0/C_t)$ vs time.

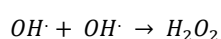
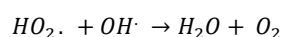
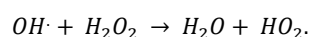
Product analysis

Product analysis (Figure 1) shows that the degradation of NB follows a conjugative state.

The intermediate compound during the experiment was authenticated and found to be PNP. The degradation of NB might follow the following mechanism:



At higher concentrations of H_2O_2 the following reactions might occur:



CONCLUSION

The dependence of percent photodegradation of NB, on initial concentration of NB solution, was studied. The investigation showed that the percentage of photodegradation of NB increases with the increase of initial concentration of NB solution. This is due to the fact that the concentrations of H_2O_2 and Fe (II) were comparable to NB concentration so that enough $\cdot OH$ radicals were produced to oxidize NB throughout the concentrations used.

The effect of concentration of H_2O_2 on photodegradation of NB was studied and it has been observed that the initial rate of photodegradation of NB increases with the increased concentration of H_2O_2 . But the increasing rate was not significant due to some scavenger reactions. Similarly, it was found that the photodegradation of NB increases with the increasing concentration of Fe^{2+} suggesting the product of $\cdot OH$ via reaction of $Fe(II) + H_2O_2$ was important.

The effect of pH on photodegradation of NB solution was studied by varying the pH from 1.0 to 7.0 and it has been deduced that the percent photodegradation was maximum at

the pH 2.42 and pH 4.20. The product analysis suggests that the degradation follows stepwise reactions.

NB → X → Degraded product.

The disappearance of NB follows pseudo-first-order kinetics.

Conclusively, the present method may be used for the destruction of organic compounds discharged from various industries.

REFERENCES

- Sulaiman M, Misha F. Cost benefit analysis of programs for the ultra-poor in Bangladesh. 2016; Available from: http://www.copenhagenconsensus.com/sites/default/files/sulaiman_misha_ultrapoor.pdf
- Khosla N. The ready-made garments industry in Bangladesh: A means to reducing gender-based social exclusion of women? *J Int Womens Stud.* 2009;11(1):289–304.
- Yunus M, Yamagata T. The garment industry in Bangladesh. *Exp Asia and Africa* [Internet]. 2012;1–28. Available from: papers://941fa284-6a3f-4661-b517-cb0b4edbed82/Paper/p1819
- Saha RC. Port Development Opportunities in Bangladesh. 2015;7(7):1–12.
- The World Bank. Bangladesh | Data [Internet]. Bangladesh Data. 2013. Available from: <http://data.worldbank.org/country/bangladesh>
- Enayetullah I, Hashmi QSI. Community Based Solid Waste Management Through Public-Private-Community Partnerships: Experience of Waste Concern in Bangladesh. 2006;1–63. Available from: www.wasteconcern.org
- Alamgir M, Ahsan A. Municipal solid waste and recovery potential: Bangladesh perspective. *Iran J Environ Heal Sci Eng.* 2007;4(2):67–76.
- US EPA. US Environmental Protection Agency. *US Environ Prot Agency.* 2012;1:1–15.
- Harrison RM. *Understanding our Environment: An Introduction to Environmental Chemistry and Pollution.* 3rd ed. Royal Society of Chemistry; 1998. 71-138 p.
- Bizani E, Fytianos K, Poullos I, Tsiroidis V. Photocatalytic decolorization and degradation of dye solutions and wastewaters in the presence of titanium dioxide. *J Hazard Mater.* 2006;136(1 SPEC. ISS.):85–94.
- Cantarella, M.; Sanz, R.; Buccheri, M. A.; Ruffino, F.; Rappazzo, G.; Scalese, S.; Impellizzeri, G.; Romano L. P. Immobilization of nanomaterials in PMMA composites for photocatalytic removal of dyes, phenols and bacteria from water. *J Photochem Photobiol A Chem.* 2016;321:1.
- Zhang J., Zhang X., Dong S., Zhou Xi. DS. N-doped carbon quantum dots/TiO₂ hybrid composites with enhanced visible light driven photocatalytic activity toward dye wastewater degradation and mechanism insight. *J Photochem Photobiol A Chem* [Internet]. 2016;325:104–10. Available from: <https://doi.org/10.1016/j.jphotochem.2016.04.012>
- Reutergardh LB, Iangphasuk M. Photocatalytic decolorization of reactive azo dye: A comparison between TiO₂ and CdS photocatalysis. *Chemosphere.* 1997;35(3):585–96.
- Daneshvar N, Salari D, Khataee AR. Photocatalytic degradation of azo dye acid red 14 in water on ZnO as an alternative catalyst to TiO₂. *J Photochem Photobiol A Chem.* 2004;162(2–3):317–22.
- Chaker H, Chérif-Aouali L, Khaoulani S, Bengueddach A, Fourmentin S. Photocatalytic degradation of methyl orange and real wastewater by silver doped mesoporous TiO₂ catalysts. *J Photochem Photobiol A Chem* [Internet]. 2016;318:142–9. Available from: <http://dx.doi.org/10.1016/j.jphotochem.2015.11.025>
- Robinson T, McMullan G, Marchant R, Nigam P. Remediation of dyes in textile effluent: A critical review on current treatment technologies with a proposed

- alternative. Vol. 77, Bioresource Technology. 2001. p. 247-55.
17. The World Bank. Bangladesh - Poverty Assessment for Bangladesh : Creating Opportunities and Bridging the East-West Divide. IBRD IDA [Internet]. 2008; Available from: <http://hdl.handle.net/10986/7886>
 18. Hayes WJ, Laws ER. Handbook of pesticide toxicology. Classes of pesticides Vol 3. [Internet]. Handbook of pesticide toxicology. 1991. 1576 p. Available from: https://books.google.com.eg/books/about/Handbook_of_Pesticide_Toxicology.html?id=-8bwAAAAMAAJ&redir_esc=y
 19. Gooderham, N. J.; Carmicha PL. Mechanisms of Chemical Carcinogenesis: The Cancer Handbook,. Volume 2. 2007.
 20. Ju K-S, Parales RE. Nitroaromatic Compounds, from Synthesis to Biodegradation. Microbiol Mol Biol Rev [Internet]. 2010;74(2):250-72. Available from: <http://mmlbr.asm.org/cgi/doi/10.1128/MMBR.00006-10>
 21. Agency for Toxic Substances and Disease Registry (ATSDR). US Dep Heal Hum Serv Public Heal Serv Atlanta, Ga, USA. 1990;
 22. Arora PK, Sasikala C, Ramana CV. Degradation of chlorinated nitroaromatic compounds. Vol. 93, Applied Microbiology and Biotechnology. 2012. p. 2265-77.
 23. Matsumoto M, Aiso S, Umeda Y, Arito H. Thirteen-Week Oral Toxicity of Para- and Ortho- Chloronitrobenzene in Rats and Mice. 2006;31(1):9-22.
 24. Serrano B, de Lasa H. Photocatalytic Degradation of Water Organic Pollutants. Kinetic Modeling and Energy Efficiency. Ind Eng Chem Res [Internet]. 1997;36(11):4705-11. Available from: <http://dx.doi.org/10.1021/ie970104r>
 25. Mumtaz MM, George JD. Toxicological profile for polycyclic aromatic hydrocarbons. US Dep Heal Hum Serv. 1996;(August):1-487.
 26. Pan J, Guan B. Adsorption of nitrobenzene from aqueous solution on activated sludge modified by cetyltrimethylammonium bromide. J Hazard Mater. 2010;183(1-3):341-6.
 27. Yang Y, Ma J, Qin Q, Zhai X. Degradation of nitrobenzene by nano-TiO₂ catalyzed ozonation. J Mol Catal A Chem. 2007;267(1-2):41-8.
 28. Wang C, Yao J. Decolorization of methylene blue with TiO₂ sol via UV irradiation photocatalytic degradation. Int J Photoenergy. 2010;2010:1-6.
 29. Rivaton A, Mailhot B, Soulestin J, Varghese H, Gardette JL. Comparison of the photochemical and thermal degradation of bisphenol-A polycarbonate and trimethylcyclohexane-polycarbonate. Polym Degrad Stab. 2002;75(1):17-33.
 30. Nohara K, Hidaka H, Pelizzetti E, Serpone N. Dependence on chemical structure of the production of NH₄⁺ and/or NO₃⁻ ions during the photocatalyzed oxidation of nitrogen-containing substances at the titania/water interface. Catal Letters [Internet]. 1996;36(1-2):115-8. Available from: <http://link.springer.com/10.1007/BF00807215>
 31. Palmisano G, Loddo V, Augugliaro V, Palmisano L, Yurdakal S. Photocatalytic oxidation of nitrobenzene and phenylamine: Pathways and kinetics. AIChE J. 2007;53(4):961-8.
 32. Carlos L, Nichela D, Triszcz JM, Felice JI, García Einschlag FS. Nitration of nitrobenzene in Fenton's processes. Chemosphere. 2010;80(3):340-5.
 33. Piccinini P, Minero C, Vincenti M, Pelizzetti E. Photocatalytic mineralization of nitrogen-containing benzene derivatives. Elsevier Sci BV. 1997;39:187-95.
 34. Stasinakis AS. Use of Selected Advanced Oxidation Processes (AOPs) for Wastewater Treatment – a Mini Review. Glob NEST J. 2008;10(3):376-85.
 35. NN Greenwood AE. Chemistry of the elements [Internet]. Vol. 4, Polyhedron. 1985. 1799-1800 p. Available from: <http://linkinghub.elsevier.com/retrieve/pii/S0277538700841807>
 36. Cottin H, Gazeau M-C, Doussin J-F, Raulin F. An experimental study of the photodegradation of polyoxymethylene at 122, 147 and 193 nm. J Photochem Photobiol A Chem. 2000;135(1):53-64.
 37. Bhatkhande DS, Pangarkar VG, Beenackers A a CM. Photocatalytic

degradation of nitrobenzene using titanium dioxide and concentrated solar radiation: chemical effects and scaleup. *Water Res* [Internet]. 2003;37:1223–30. Available from: <http://www.ncbi.nlm.nih.gov/pubmed/12598186>

38. Lin SH, Lo CC. Fenton process for treatment of desizing wastewater. *Water Res.*

1997;31(8):2050–6.

39. Fu H, Zhu D. Graphene oxide-facilitated reduction of nitrobenzene in sulfide-containing aqueous solutions. *Environ Sci Technol.* 2013;47(9):4204–10.

40. Dong J, Wen C, Liu D, Zhang W, Li J, Jiang H, et al. Study on degradation of nitrobenzene in groundwater using emulsified nano-zero-valent iron. *J Nanoparticle Res.* 2015;17(1).



Synthesis of Aromatic Structured Di-cationic Surfactants Used as Inhibitors Against Corrosion of Carbon Steel in Acidic Medium

Serkan Öztürk*  , Ayhan Yıldırım  

Uludağ University, 16059, Bursa, Turkey

Abstract: In this study, three aromatic-structured di-cationic surfactants of different carbon chain lengths were synthesized and their inhibition efficiencies against metal corrosion in 1.0 M HCl solution were investigated. Corrosion inhibition efficiencies of di-cationic surfactants, the structures of which were elucidated by spectroscopic methods (FT-IR and NMR), were determined in acidic media by gravimetric method based upon weight loss in metal coupons. Corrosion tests resulted in good inhibition efficiencies (90.40% - 96.85%) against metallic corrosion at different concentrations of inhibitors. By using the weight loss values, corrosion rates were also calculated in inhibited and uninhibited medium. Finally, images of metal surfaces were obtained using scanning electron microscopy to give support to the data on the corrosion inhibition effect.

Keywords: Di-cationic surfactants, carbon steel, corrosion inhibitor, acidic medium, SEM.

Submitted: February 27, 2018. **Accepted:** June 04, 2018.

Cite this: Öztürk S, Yıldırım A. Synthesis of Aromatic Structured Di-cationic Surfactants Used as Inhibitors Against Corrosion of Carbon Steel in Acidic Medium. JOTCSA. 2018;5(2):819-28.

DOI: <http://dx.doi.org/10.18596/jotcsa.399297>.

***Corresponding author. E-mail:** serkanozturk@uludag.edu.tr.

INTRODUCTION

Metallic corrosion is the deformation of metals in their environment, which occurs on the surfaces of the metals as a result of chemical and electrochemical attacks (1). The tendency of metals and alloys to turn into stable states of the compound causes metal corrosion leading to serious economic losses. Corrosion in the metals consists of two electrochemical reactions. The metal is oxidized at the anode while the positively charged hydrogen ion from the acidic medium is reduced to H₂ gas at the cathode.

A large number of corrosion types are known in the literature (2). The most common corrosion type occurring in low pH (acidic) environments is called "general corrosion" (3). One of the most commonly used methods to overcome this type of corrosion is the addition of an organic corrosion inhibitor to the corrosive medium. Corrosion inhibitors dissolve or disperse in corrosive media (4) and generally form a protective film layer by adsorbing onto the metal surface. This slows down the corrosion rate by slowing down the

rates of either the anode or cathode reactions or both of them.

In recent years, it has been established that cationic surfactants act as the most effective inhibitors against corrosion occurring on iron and steel materials in acidic environments (5-8). In particular, cationic quaternary ammonium surfactants have been reported to play a significant role in preventing corrosion in iron and steel materials in acidic environments (9-12). Therefore, there has been a growing number of studies on the synthesis of di-cationic surfactants containing more than one positive group and their use as corrosion inhibitors in the acidic medium (15-21).

In this study, three aromatic di-cationic surfactants with different carbon chain lengths were synthesized and their structures were elucidated by FT-IR and NMR techniques. The aim of the study was to determine the corrosion inhibition activities of di-cationic surfactants in the acidic corrosive environment by the gravimetric method based on following the weight loss in metal coupons (in accordance with ASTM

NACE / ASTM G31-12a standard method (22)). For this purpose, corrosion tests were carried out using low carbon steel at room temperature for 24 h at various inhibitor concentrations.

MATERIALS AND METHODS

Materials and Instrumentation

Ethyl-(4-dimethylamino)benzoate, corresponding long-carbon-chain amines, ethanol, and other solvents used in the synthesis part of this work were obtained from Merck and Sigma-Aldrich and used without further purification. FT-IR spectra of the synthesized compounds were recorded using Thermo Nicolet 6700 FT-IR spectrometer. NMR spectra (^1H NMR and ^{13}C NMR) of the compounds were obtained in DMSO (dimethylsulfoxide) solvent with Agilent 600 MHz Premium Compact NMR spectrometer. After the corrosion test, images of the metal surface were taken with a Carl Zeiss EVO 40 model scanning electron microscope. The NUVE EV 018 vacuum oven was used to dry metal coupons to a constant weight in air-free environment. Elemental analyses were performed using a LECO CHNS-932 instrument.

Synthesis of Compounds

Synthesis of 4-(dimethylamino)-N-octylbenzamide (1a): 2.0 g (10.35 mmol) of ethyl-(4-dimethylamino)benzoate and 1.338 g (10.35 mmol) of octylamine reagents were placed in a 50 mL reaction flask. The flask was heated overnight at 150 °C under reflux without solvent. At the end of the reaction, the flask was cooled down to room temperature. A small amount of DMF was added to the cooling reaction mixture, and then cold water to precipitate the crude product. The crude product, after filtering off under vacuum and drying, was crystallized from a mixture of methanol / water (9:1). The yellow solid product was obtained in 82% yield.

Synthesis of 4-(dimethylamino)-N-decylbenzamide (1b): The synthesis of compound **1b** was performed with the same procedure used for **1a**, using 2.0 g (10.35 mmol) of ethyl-(4-dimethylamino)benzoate and 1.628 g (10.35 mmol) of decylamine reagents. The yellow solid product was obtained with a yield of 62%.

Synthesis of 4-(dimethylamino)-N-dodecylbenzamide (1c): The synthesis of compound **1c** was carried out applying the same procedure used for **1a**, using 2.0 g (10.35 mmol) of ethyl-(4-dimethylamino)benzoate and 1.918 g (10.35 mmol) of dodecylamine reagents. The yellow solid product (yield: 69%) was obtained.

Synthesis of N,N,N,N',N'-pentamethyl-N'-[4-(octylcarbamoyl)phenyl]ethane-1,2-diaminium dibromide (2a): 2.0 g (7.23 mmol) of compound **1a**, 1.786 g (7.23 mmol) of (2-bromoethyl)trimethylammonium bromide and 20 mL of ethanol as solvent were placed in a 50 mL reaction flask. The mixture was heated at 100 °C under reflux for 48 h. At the end of the reaction,

ethanol was evaporated under vacuum. The reaction mixture was washed several times with ether and a light brown solid wax was obtained as the product. FT-IR (KBr), vibrational modes, ν/cm^{-1} : 3370 (amide N-H), 3013 (aromatic C-H), 2962, 2904 ve 2871 (aliphatic C-H), 1691 (amide C=O). ^1H NMR data (600 MHz, DMSO- d_6): δ (ppm) = 7.74 (d, 2H, Ar-H), 6.68 (d, 2H, Ar-H), 4.20 (quartet, 2H, $\text{CH}_2\text{-CH}_2\text{-NH-CO}$), 3.31 (t, 2H, Ar-N $^+$ - $\text{CH}_2\text{-CH}_2\text{-N}^+$), 3.24 (t, 2H, Ar-N $^+$ - $\text{CH}_2\text{-CH}_2\text{-N}^+$), 3.10 (s, 6H, $(\text{CH}_3)_2\text{-N}^+\text{-CH}_2\text{-CH}_2\text{-N}^+\text{-(CH}_3)_3$), 2.97 (s, 9H, $\text{CH}_2\text{-N}^+\text{-(CH}_3)_3$), 0.83 (t, 3H, CH_3). ^{13}C NMR data (150 MHz, DMSO- d_6): δ (ppm) = 166.32 (HN-CO), 153.63 (Ar-C), 131.12 (Ar-C), 116.48 (Ar-C), 111.21 (Ar-C), 60.05 (-N $^+$ - $\text{CH}_2\text{-CH}_2\text{-N}^+$), 53.96 (-N $^+$ - $\text{CH}_2\text{-CH}_2\text{-N}^+\text{-(CH}_3)_3$), 53.31 (- $(\text{CH}_3)_2\text{-N}^+\text{-CH}_2\text{-CH}_2\text{-N}^+\text{-(CH}_3)_3$), 39.27 (- $\text{CH}_2\text{-NH-CO}$), 22.51 ($\text{CH}_3\text{-CH}_2\text{-}$), 14.80 ($\text{CH}_3\text{-CH}_2\text{-}$).

Synthesis of N,N,N,N',N'-pentamethyl-N'-[4-(decylcarbamoyl)phenyl]ethane-1,2-diaminium dibromide (2b): The synthesis of compound **2b** was performed with the same procedure used for **2a**, using 1.65 g (5.42 mmol) of compound **1b**, 1.338 g (5.42 mmol) of (2-bromoethyl)trimethylammonium bromide and 20 mL of ethanol as solvent. A light brown solid wax product was obtained. FT-IR (KBr), vibrational modes, ν/cm^{-1} : 3372 (amide N-H), 3015 (aromatic C-H), 2950, 2917 ve 2847 (aliphatic C-H), 1691 (amide C=O). ^1H NMR data (600 MHz, DMSO- d_6): δ (ppm) = 7.74 (d, 2H, Ar-H), 6.69 (d, 2H, Ar-H), 4.20 (quartet, 2H, $\text{CH}_2\text{-CH}_2\text{-NH-CO}$), 3.32 (t, 2H, Ar-N $^+$ - $\text{CH}_2\text{-CH}_2\text{-N}^+$), 3.25 (t, 2H, Ar-N $^+$ - $\text{CH}_2\text{-CH}_2\text{-N}^+$), 3.10 (s, 6H, $(\text{CH}_3)_2\text{-N}^+\text{-CH}_2\text{-CH}_2\text{-N}^+\text{-(CH}_3)_3$), 2.97 (s, 9H, $\text{CH}_2\text{-N}^+\text{-(CH}_3)_3$), 0.83 (t, 3H, CH_3). ^{13}C NMR data (150 MHz, DMSO- d_6): δ (ppm) = 166.32 (HN-CO), 153.64 (Ar-C), 131.11 (Ar-C), 116.48 (Ar-C), 111.21 (Ar-C), 60.04 (-N $^+$ - $\text{CH}_2\text{-CH}_2\text{-N}^+$), 53.95 (-N $^+$ - $\text{CH}_2\text{-CH}_2\text{-N}^+\text{-(CH}_3)_3$), 53.31 (- $(\text{CH}_3)_2\text{-N}^+\text{-CH}_2\text{-CH}_2\text{-N}^+\text{-(CH}_3)_3$), 39.25 (- $\text{CH}_2\text{-NH-CO}$), 22.53 ($\text{CH}_3\text{-CH}_2\text{-}$), 14.80 ($\text{CH}_3\text{-CH}_2\text{-}$).

Synthesis of N,N,N,N',N'-pentamethyl-N'-[4-(dodecylcarbamoyl)phenyl]ethane-1,2-diaminium dibromide (2c): The synthesis of compound **2c** was performed with the same procedure used for **2a**, using 0.30 g (0.90 mmol) of compound **1c**, 0.223 g (0.90 mmol) of (2-bromoethyl)trimethylammonium bromide and 20 mL of ethanol as solvent. FT-IR (KBr), vibrational modes, ν/cm^{-1} : 3411 (amide N-H), 3015 (aromatic C-H), 2950, 2917 ve 2848 (aliphatic C-H), 1691 (amide C=O). ^1H NMR data (600 MHz, DMSO- d_6): δ (ppm) = 7.73 (d, 2H, Ar-H), 6.69 (d, 2H, Ar-H), 4.20 (quartet, 2H, $\text{CH}_2\text{-CH}_2\text{-NH-CO}$), 3.31 (t, 2H, Ar-N $^+$ - $\text{CH}_2\text{-CH}_2\text{-N}^+$), 3.24 (t, 2H, Ar-N $^+$ - $\text{CH}_2\text{-CH}_2\text{-N}^+$), 3.10 (s, 6H, $(\text{CH}_3)_2\text{-N}^+\text{-CH}_2\text{-CH}_2\text{-N}^+\text{-(CH}_3)_3$), 2.97 (s, 9H, $\text{CH}_2\text{-N}^+\text{-(CH}_3)_3$), 0.83 (t, 3H, CH_3). ^{13}C NMR data (150 MHz, DMSO- d_6): δ (ppm) = 166.30 (HN-CO), 153.62 (Ar-C), 131.11 (Ar-C), 116.48 (Ar-C), 111.21 (Ar-C), 60.05 (-N $^+$ - $\text{CH}_2\text{-CH}_2\text{-N}^+$), 53.95 (-N $^+$ - $\text{CH}_2\text{-CH}_2\text{-N}^+\text{-(CH}_3)_3$), 53.32 (- $(\text{CH}_3)_2\text{-N}^+\text{-CH}_2\text{-CH}_2\text{-N}^+\text{-(CH}_3)_3$), 39.25 (- $\text{CH}_2\text{-NH-CO}$), 22.53 ($\text{CH}_3\text{-CH}_2\text{-}$), 14.80 ($\text{CH}_3\text{-CH}_2\text{-}$).

(CH₃)₃), 39.25 (-CH₂-NH-CO), 22.53 (CH₃-CH₂-), 14.80 (CH₃-CH₂-).

Corrosion Test Based on Gravimetric Measurement

Metal and its properties used in corrosion tests: Metal plates used in the corrosion tests in acidic media were prepared from low-carbon cold-rolled steel. The steel material used conforms to the norm of DIN EN 10130 (23) with the content composition of 0.07% (C), 0.35% (Mn), 0.015% (P), 0.015% (S) and the rest is Fe. The metal plates were cut in rectangular shape with the thickness of 0.1 cm, the width of 2.2 cm and the length of 5.0 cm.

Preparation of metal plates before corrosion test: The metal plates of 0.1 cm thickness, 2.2 cm width and 5.0 cm length, were immersed in 15% HCl solution for a short time to clean the rust stains and oxide layer. The plates were then cleaned with distilled water and briefly stored in acetone. Plates removed from acetone were dried in a vacuum oven until constant weight and the mass of the metal plate was recorded before testing.

Corrosion test in acidic environment

Corrosion tests in 1.0 M HCl solution were carried out following the relevant standard method (22). Before testing, 1.0 M HCl solution was freshly prepared. The di-cationic surfactant solutions were prepared in concentrations of 10, 25, 50, 100 and 250 ppm in 100 mL of 1.0 M HCl medium. These solutions were poured into 150-mL sealed glass bottles. The coupons were kept in the solutions without stirring for 24 h at room temperature. Control tests were performed in the same way without the inhibitors. After 24 h test period, metal plates were removed from the corrosive medium and were rinsed with distilled water. The plates were then cleaned with acetone, dried in a vacuum oven and the mass of the metals were measured after testing.

Calculation of percent inhibition efficiencies and corrosion rates: The percent inhibition efficiencies (% IE) of the aromatic structured di-cationic surfactants tested were calculated by the formula given below:

$$IE \% = \frac{W_0 - W}{W_0} \times 100 \quad (\text{Eq. 1})$$

IE % is the percentage inhibition efficiency, W₀ and W represent the weight losses of the coupon in the absence and presence of an inhibitor in the same environment, respectively. However, using the weight loss values, the corrosion rates in the uninhibited and inhibited corrosive media were calculated by the following formula (24, 25):

$$CR = \frac{\Delta W}{A t} \quad (\text{Eq. 2})$$

CR is the corrosion rate; ΔW is the weight loss (mg); A is the surface area of the coupon (cm²) and t is the time of immersion (h).

SEM analysis

The SEM image of the metal surface was taken on the metal coupons that were square-shaped with the thickness of 0.1 cm, the width of 2.0 cm and the length of 2.0 cm. After performing the corrosion tests in the acidic medium, the metal coupons were washed with acetone and then dried in a vacuum oven. Subsequently, the SEM images of the metal surfaces were obtained, using scanning electron microscope under high vacuum at 1000x magnification.

RESULTS AND DISCUSSION

Synthesis of di-cationic surfactants

The synthetic scheme of the aromatic-structured di-cationic surfactants that act as corrosion inhibitors in the acidic environment are shown in Figure 1.

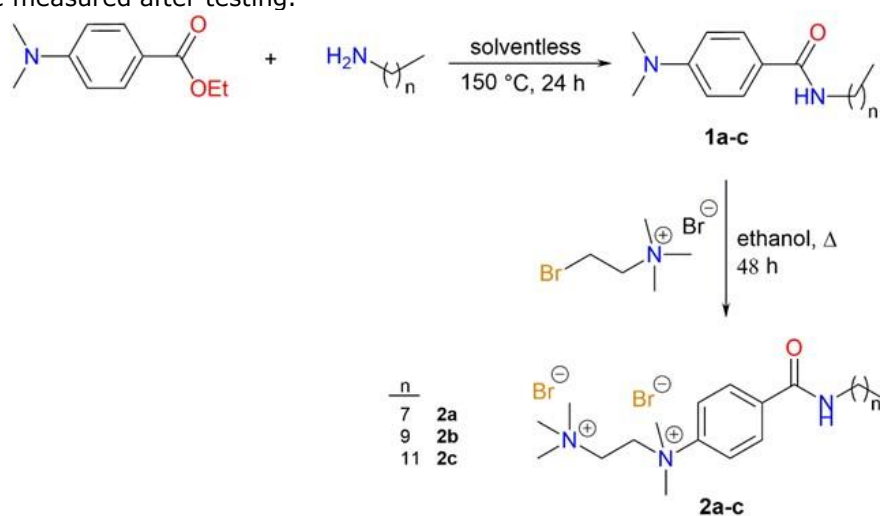


Figure 1. Synthesis scheme of the aromatic di-cationic surfactants.

As can be seen in Figure 1, the synthesis of organic surfactants were carried out in two steps. In the first step, the ethyl-(4-dimethylamino)benzoate compound was reacted with the corresponding long carbon chain amine compound in a solvent-free environment to give compounds **1a-c**. The compounds obtained in the

first step were reacted in ethanol with the (2-bromoethyl)trimethylammonium bromide in the second step to reach the target products **2a-c** di-cationic surfactants. The elemental analysis results of the synthesized **2a-c** compounds and some other physical properties are given in Tables 1 and 2, respectively.

Table 1. Elemental analysis (C, H, N) results of synthesized aromatic structured surfactants.

Compound No	C [%]		H [%]		N [%]	
	Calculated	Found	Calculated	Found	Calculated	Found
2a	50.49	50.60	7.90	7.96	8.03	8.08
2b	52.27	52.38	8.23	8.32	7.62	7.72
2c	53.89	53.75	8.52	8.46	7.25	7.17

Table 2. Some physical properties of the synthesized di-cationic surfactants.

Compound No	Formula	Molecular Weight (g/mol)	Yield (%)	Color
2a	C ₂₂ H ₄₁ N ₃ O . 2Br	523.39	61	Light brown
2b	C ₂₄ H ₄₅ N ₃ O . 2Br	551.45	70	Light brown
2c	C ₂₆ H ₄₉ N ₃ O . 2Br	579.50	85	Light brown

The structures of the synthesized **2a-c** surface active compounds were determined by FT-IR, ¹H NMR, and ¹³C NMR spectroscopic methods. FT-IR

and NMR spectra (¹H and ¹³C NMR) of compound **2b** are given in Figures 2 and 3, respectively.

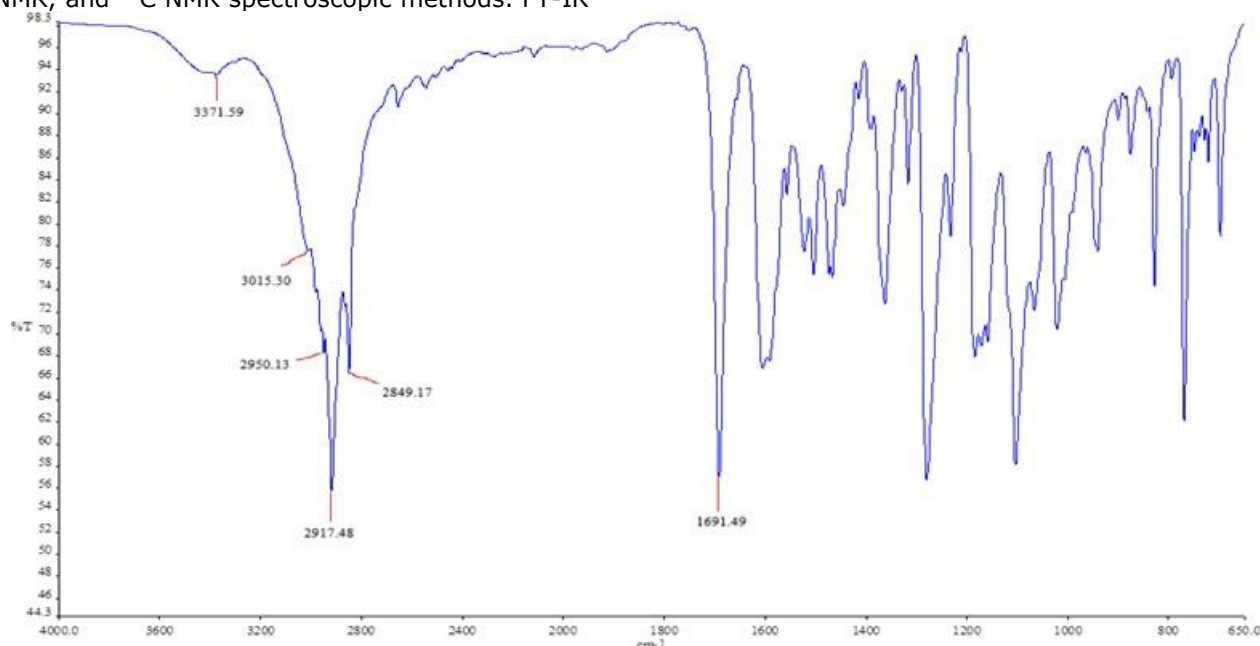


Figure 2. FT-IR spectrum of compound **2b**.

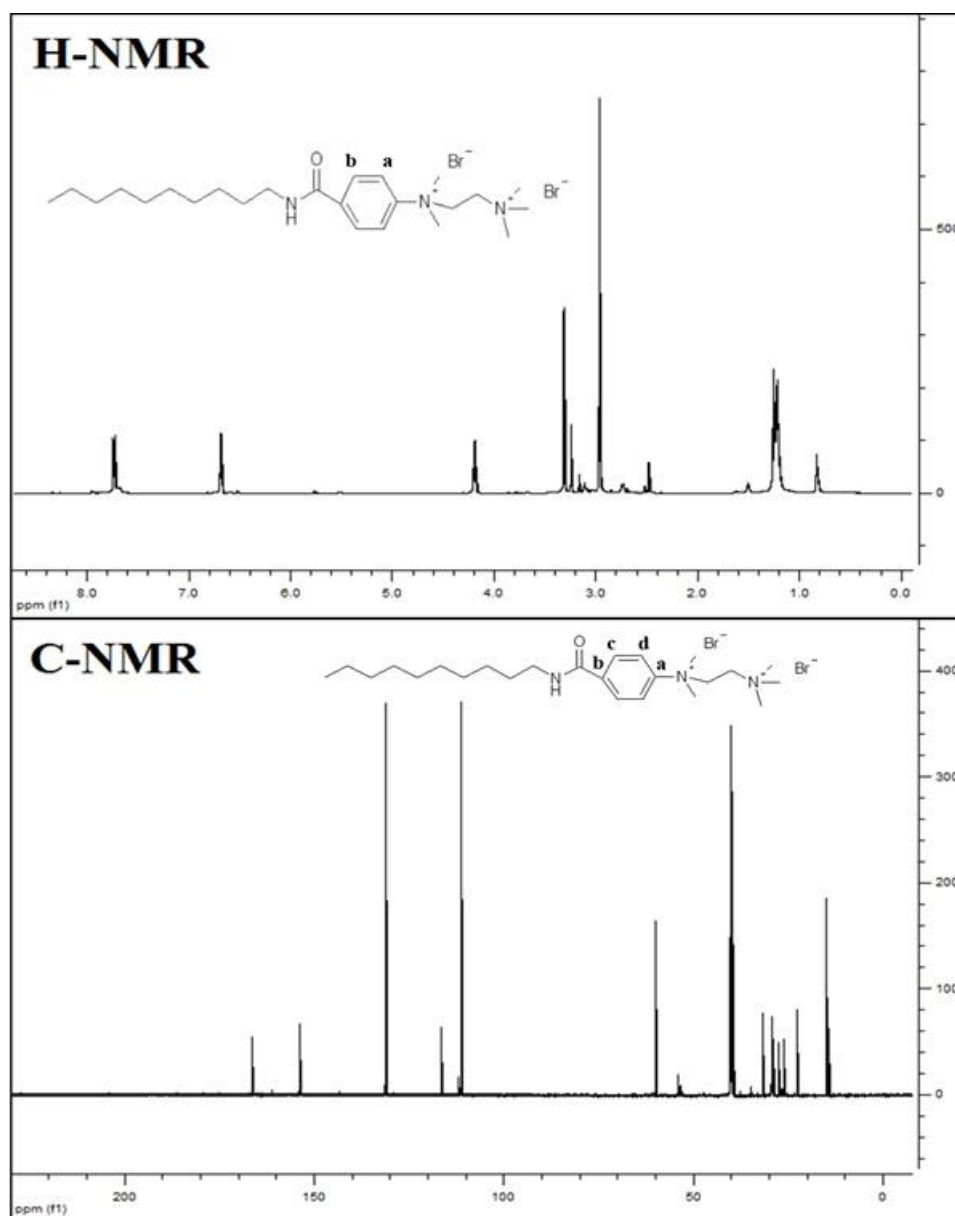


Figure 3. ^1H NMR and ^{13}C NMR spectra of compound **2b**.

The FT-IR spectra of (**2b**) showed absorption bands at 3372 cm^{-1} (amide N-H), at 3015 cm^{-1} (aromatic C-H), at $2950, 2917, 2847\text{ cm}^{-1}$ (aliphatic C-H) and at 1691 cm^{-1} (amide C=O). In the ^1H NMR spectrum of **2b** (Figure 3), there is a doublet peak at 7.74 ppm for the two hydrogen atoms which are connected to aromatic carbon labeled with a, a doublet peak at 6.69 ppm for the two hydrogen atoms of aromatic carbon labeled with b, a triplet peak at 3.32 ppm for the two hydrogen atoms of the $(\text{Ar}-\text{N}^+-\text{CH}_2-\text{CH}_2-\text{N}^+)$ group, a singlet peak at 3.10 ppm originating from the six hydrogen atoms of the $(\text{CH}_3)_2-\text{N}^+-\text{CH}_2-\text{CH}_2-\text{N}^+(\text{CH}_3)_3$ group and a singlet peak at 2.97 ppm ascribed to the nine hydrogen atoms of the $\text{CH}_2-\text{N}^+(\text{CH}_3)_3$. The triplet peak at 3.32 ppm in the spectrum proved that the di-cationic surfactant (**2b**) was successfully synthesized.

Corrosion test results in acidic media

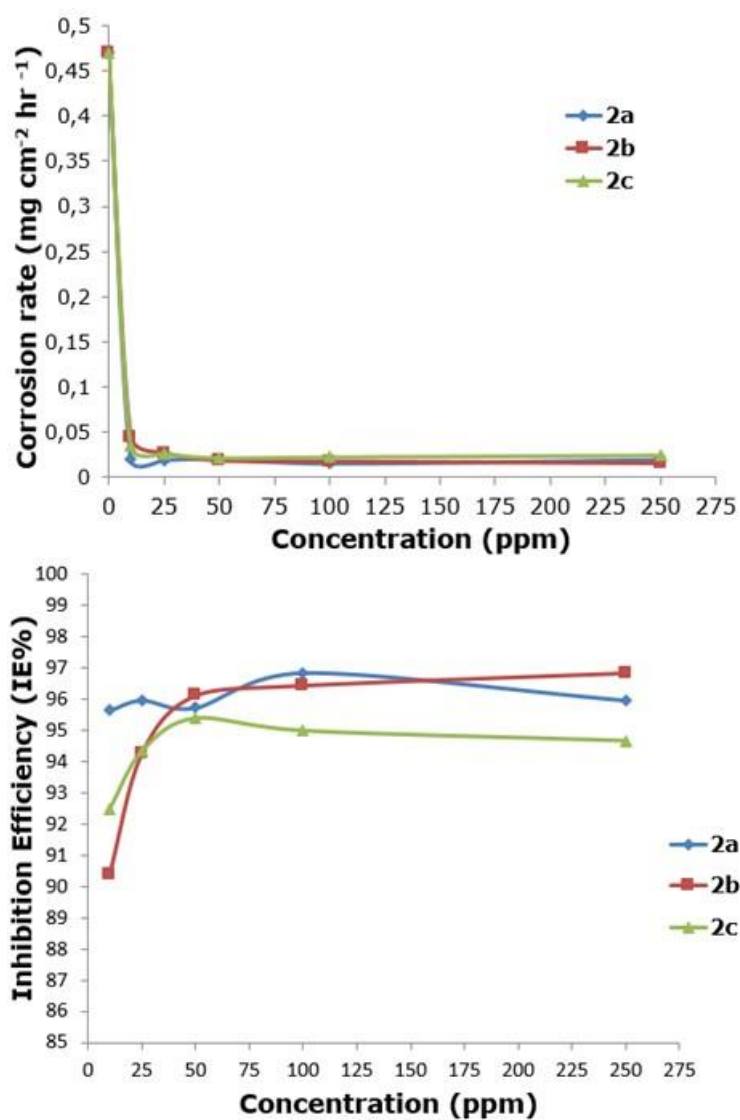
The corrosion test data of the synthesized **2a-c** aromatic structured di-cationic surfactants in 1.0 M HCl are listed in Table 3. The corrosion rate and inhibition efficiency values given here were calculated from the weight loss values determined for the metal coupons after the corrosion tests for 24 h.

It can be seen from Table 3 that the values of weight loss and corrosion rate of the metal coupons in uninhibited medium (0 ppm) are high, while they are quite low in the inhibited medium (10, 25, 50, 100 and 250 ppm). Due to the large differences in weight loss and corrosion rate between inhibited and uninhibited media, the inhibition efficiencies of the synthesized compounds became high. The plots of corrosion rate and inhibition efficiency calculated at different concentrations, versus inhibitor concentration are shown in Figure 4.

Table 3. Weight loss, corrosion rate and corrosion inhibition efficiencies (IE %) calculated for different concentrations of compounds **2a-c** in 1.0 M HCl medium for 24 h at room temperature.

Concentration (ppm)	Weight loss* (mg cm ⁻²)			Corrosion rate (mg cm ⁻² h ⁻¹)			Inhibition efficiency (IE%)		
	2a	2b	2c	2a	2b	2c	2a	2b	2c
0	11.27	11.27	11.27	0.47	0.47	0.47	—	—	—
10	0.49	1.08	0.85	0.020	0.045	0.035	95.64	90.40	92.50
25	0.45	0.65	0.64	0.019	0.027	0.027	95.97	94.27	94.35
50	0.48	0.44	0.52	0.020	0.018	0.022	95.73	96.13	95.40
100	0.35	0.40	0.56	0.015	0.017	0.023	96.85	96.45	95.00
250	0.45	0.35	0.60	0.019	0.015	0.025	95.97	96.85	94.68

* Mean of the two measured values.

**Figure 4.** Plots of corrosion rate and inhibition efficiency against inhibitor concentration from weight loss measurements after immersed in 1.0 M HCl.

SEM analysis results

Surface analysis by scanning electron microscopy is of great importance for observing the morphological changes on metal surfaces. Through examination of these morphological changes, the interactions between the organic molecules and the metal surface can be explained. The 1000x magnified surface images of the metal coupon surfaces immersed to inhibitor-free acid solution and to acid solution with inhibitor for 24 h, are shown in Figure 5.

It may be clearly seen in Figure 5 that the metal surface exposed to acidic environment without inhibitor is exposed to wear and the surface

becomes rough. In this environment containing cationic surfactants **2a**, **2b** and **2c**, there is no wear and roughness on the metal surfaces that have been left for 24 h, and it appears to have a smoother appearance. The scratch marks on the metal surfaces are caused by the sanding process made before the test. This proves that the inhibitor molecules are adsorbed onto the metal surface and protect the metal surface against corrosion. Hence, the SEM images of the metal surface obtained support the high inhibition activity results shown in Table 3.

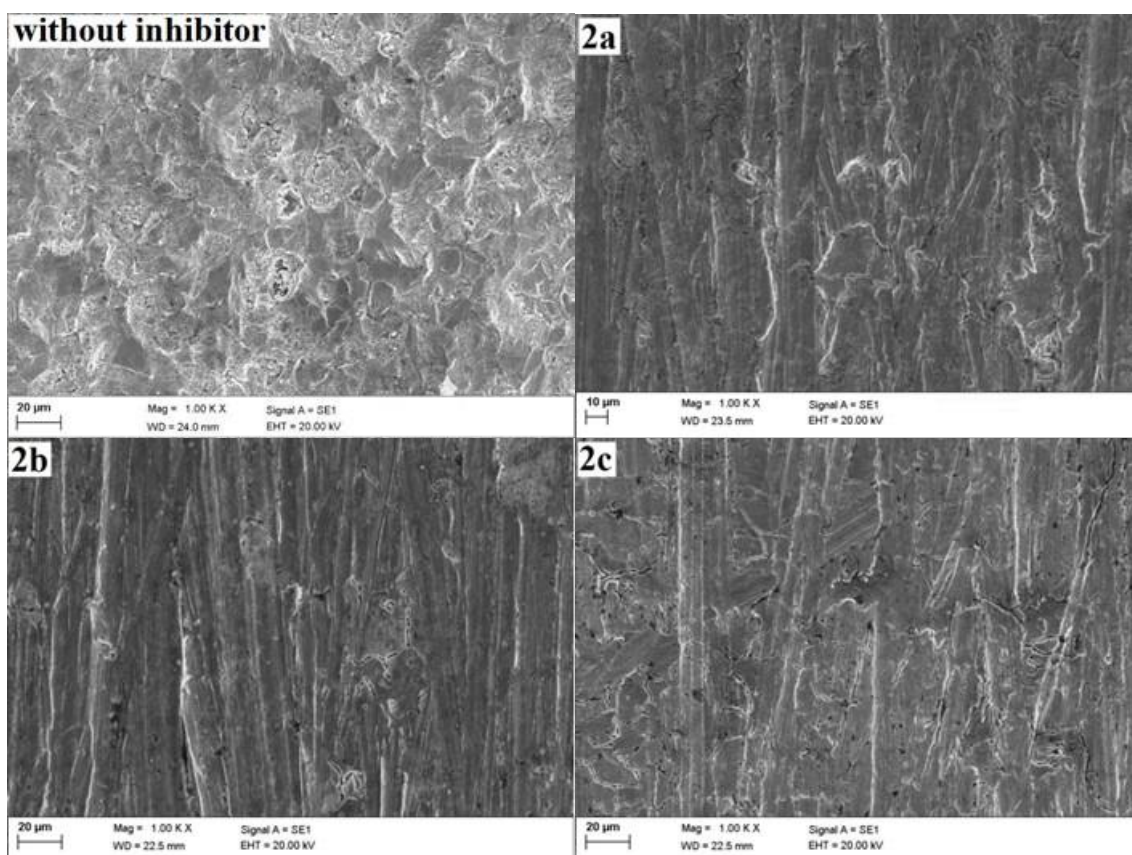


Figure 5. SEM images of the metal coupon surfaces, which were kept in a 1.0 M HCl medium without inhibitor and with 100 ppm inhibitor for 24 h.

The mechanism of corrosion inhibition

The first step in the mechanism of action to retard or prevent corrosion is the adsorption of surfactant molecules onto the metal surface. The adsorption process depends on the nature and surface load of the metal used, the chemical structure of the surface active substance, the nature of both the surface active substance and the corrosive environment (26). In the structure of the synthesized aromatic structured di-cationic surfactants, there are two positively charged nitrogen atoms acting as the hydrophilic group. This hydrophilic group leads both to dissolution of the compounds in the aqueous acid environment and adsorption to the metal surface by electrostatic forces between the positively

charged nitrogen atom and the induced negative charges on the metal surface (27). The induced negative charge on the metal surface is provided by the formation of dipoles on the surface. These dipoles arise as a result of attachment to the positively charged metal surface of negatively charged halogen ions from the acidic medium by electrostatic attraction (13, 14). Due to the dipoles formed on the surface, the aromatic surface-active di-cationic surfactants can be easily attached to the metal surface which becomes negatively charged. Therefore, a protective monomolecular layer is formed against the corrosive nature of the acidic environment on the surface of the carbon steel.

Besides the physisorption process on the metal surface due to the electrostatic attraction force, the chemisorption process also plays an important role on the corrosion inhibition in the acidic environment. Chemisorption occurs via the interaction of the benzene ring and the N and O heteroatoms in the structure of the surface active materials with the iron atoms on the metal surface separately. Non-bonding electrons in the p orbital of the heteroatoms (N and O) and π -electrons in the aromatic benzene ring are involved in chemisorption. Due to the donor-acceptor interactions between these electrons and the free d orbital in the Fe atoms on the metal surface, the surfactant molecules adsorbed onto the metal surface with coordinated covalent bonds (28). The adsorption of the synthesized inhibitors to the metal surface is favoured by these coordinated covalent bonds and provides a stronger protection against corrosion.

The long alkyl chain containing amide functional group of the synthesized aromatic structured di-cationic surfactants constitutes the hydrophobic part of the di-cationic surfactant. This part is oriented perpendicular to the metal surface so as not to bring the water molecules coming from the corrosive environment closer to the surface.

These hydrophobic groups, oriented perpendicular to the metal surface, form non-polar interactions originating from van der Waals attraction forces. Thus, double layered or multilayered protective layers are formed which act as a barrier between the metal surface and the acidic corrosive medium (13). It is known that non-polar interactions between the long alkyl chains in the molecule increase in parallel with the concentration of surfactant (14). Therefore, as the concentration increases, the inhibition efficiency of the surface active compound against corrosion also increases. In Table 3, a slight increase in the inhibition efficiency value with an increase in the concentration of compound **2b** in the 1.0 M HCl medium is a result of this situation. On the other hand, the inhibition efficiencies of the compounds **2a** and **2c**, in particular, does not increase markedly with the increase in the concentration, which means that the di-cationic surfactants reach the critical micelle concentration and are in the form of micelles at the interface of the metal in the working concentrations. The possible orientations and inhibition mechanisms of the compounds **2a**, **2b** and **2c** on the metal surface are shown in Figures 6 and 7, respectively.

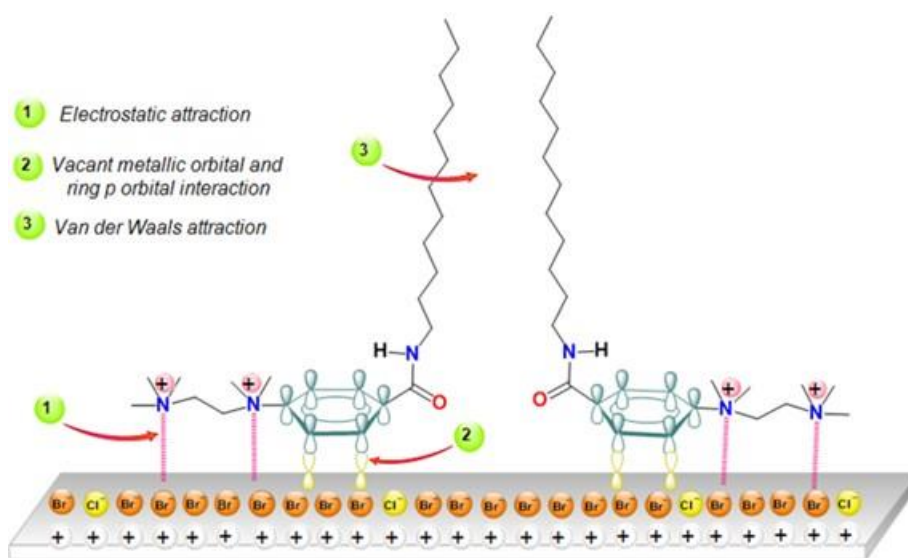


Figure 6. The possible orientations and inhibition mechanism of the compound **2b**.

CONCLUSIONS

Newly synthesized three aromatic di-cationic surfactants having different carbon chain lengths act as inhibitors against corrosion of the carbon steel in 1.0 M HCl solution. In the light of the data obtained in the study, the following conclusions can be drawn:

- (1) All the synthesized aromatic structured di-cationic surfactants exhibited good inhibition activities under working concentrations.
- (2) The inhibitory efficiency of compound **2b** increased with the increasing of the concentration.

(3) The inhibitory efficiencies of the compounds **2a** and **2c** increased slightly up to a certain concentration, and then decreased afterwards.

(4) Physisorption seemed to be more effective than chemisorption on the corrosion behavior of the synthesized aromatic structured di-cationic surfactants.

(5) Corrosion inhibition activities of the synthesized inhibitors in acidic medium were supported by surface imaging technique (SEM).

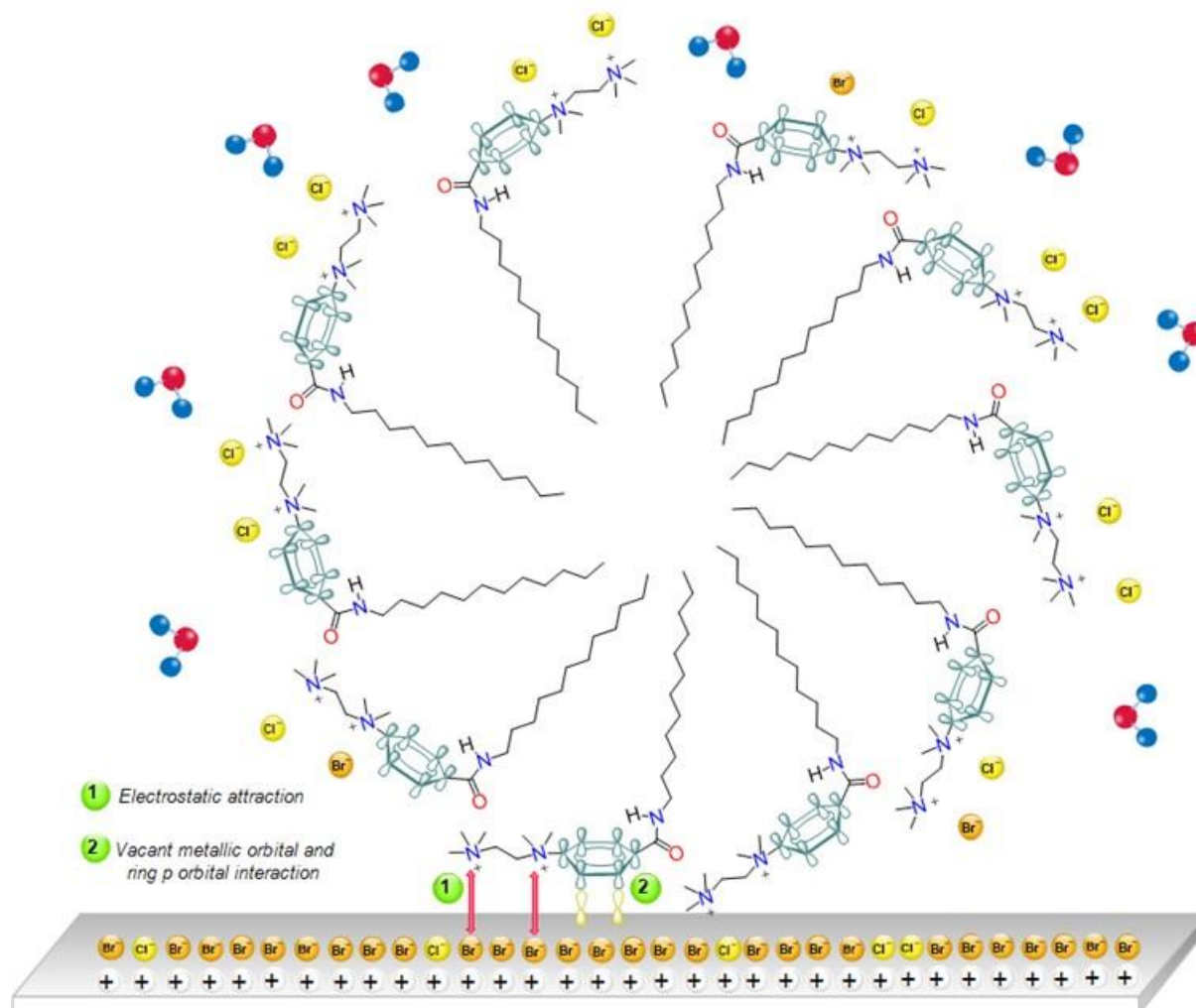


Figure 7. The possible orientations and inhibition mechanism of the compounds **2a** and **2c**.

CONFLICT OF INTEREST

The authors declare no conflict of interest.

REFERENCES

- Gönerler A. Al-Si Matrisli Kompozit Malzemelerin Korozyon Davranışlarının İncelenmesi. Yıldız Technical University, Institute of Science, Master of Science Thesis, 2007 İstanbul.
- Üneri S. Corrosion and Prevention. Corrosion Society, 1998, Ankara, 413 s.
- Öztürk S. Design and Synthesis of Some Amide Compounds as Potential Corrosion Inhibitors. Uludag University, Institute of Science and Technology, PhD Thesis, 2013, Bursa.
- Papavinasam, S. Corrosion Inhibitors. In: Uhlig's Corrosion Handbook, W.R. Revie (Editor), Wiley Interscience, 2000, p.1089-1105.
- Hegazy MA. Novel cationic surfactant based on triazole as a corrosion inhibitor for carbon steel in phosphoric acid produced by dihydrate wet process. J. Mol. Liq. 2015 Aug; 208:227-36.
- Asefi D, Arami M, Sarabi AA, Mahmoodi NM. The chain length influence of cationic surfactant and role of nonionic co-surfactants on controlling the corrosion rate of steel in acidic media. Corros. Sci. 2009 Aug; 51:1817-21.
- El Achouri M, Infante MR, Izquierdo F, Kertit S, Goultaya HM, Nciri B. Synthesis of some cationic gemini surfactants and their inhibitive effect on iron corrosion in hydrochloric acid medium. Corros. Sci. 2001 Jan; 43:19-35.
- Hegazy MA, Abdallah M, Ahmed H. Novel cationic gemini surfactants as corrosion inhibitors for carbon steel pipelines. Corros. Sci. 2010 Sep; 52:2897-2904.
- Likhanova NV, Dominguez-Aguilar MA, Olivares-Xometl O, Nava-Entzana N, Arce E, Dorantes H. The effect of ionic liquids with imidazolium and pyridinium cations on the corrosion inhibition of mild steel in acidic environment. Corros. Sci. 2010 Jun; 52:2088-97.
- Asefi D, Arami M, Mahmoodi NM. Electrochemical effect of cationic gemini surfactant and halide salts on corrosion inhibition of low carbon steel in acid medium. Corros. Sci. 2010 Mar, 52:794-800.

11. Hegazy MA, Badawi AM, Abd El Rehim SS, Kamel WM. Corrosion inhibition of carbon steel using novel N-(2-(2-mercaptoacetoxy)ethyl)-N,N-dimethyl dodecan-1-aminium bromide during acid pickling. *Corros. Sci.* 2013 Apr; 69:110-22.
12. Hegazy MA, El-Tabei AS. Synthesis, surface properties, synergism parameter and inhibitive performance of novel cationic gemini surfactant on carbon steel corrosion in 1 M HCl solution. *J. Surf. Deterg.* 2013 Mar; 16: 221-32.
13. Yıldırım A, Öztürk S, Çetin M. Novel amide-based cationic surfactants as efficient corrosion inhibitors for carbon steel in HCl and H₂SO₄ media. *J. Surf. Deterg.* 2013 Jan; 16:13-23.
14. Öztürk S, Yıldırım A, Çetin M, Tavaslı M. Synthesis of quaternary, long-chain N-alkyl amides and their corrosion inhibition in acidic media. *J. Surfact. Deterg.* 2014 May; 17: 471-81.
15. Hegazy MA, Abd El-Rehim SS, Badr EA, Kamel WM, Youssif AH. Mono-, Di- and Tetra-Cationic Surfactants as Carbon Steel Corrosion Inhibitors, *J. Surfact. Deterg.* 2015 Nov; 18:1033-42.
16. Abd-Elal AA, Shaban SM, Tawfik SM. Three Gemini cationic surfactants based on polyethylene glycol as effective corrosion inhibitor for mild steel in acidic environment. *Journal of the Association of Arab Universities for Basic and Applied Sciences* 2017 Oct; 24:54-65.
17. Heakal F. El-Taib, Deyab MA, Osman MM, Nessim MI, Elkholy AE. Synthesis and assessment of new cationic gemini surfactants as inhibitors for carbon steel corrosion in oilfield water. *RSC Adv.* 2017 Oct; 7:47335-52.
18. Hegazy MA, Azam EMS, Kandil NG, Badawi AM, Sami RM. Corrosion inhibition of carbon steel pipelines by some new amphoteric and di-cationic surfactants in acidic solution by chemical and electrochemical methods. *J. Surfact. Deterg.* 2016 Jul; 19:861-71.
19. Hegazy MA, El-Tabei AS, Bedair AH, Sadeq MA. Synthesis and inhibitive performance of novel cationic and gemini surfactants on carbon steel corrosion in 0.5 M H₂SO₄ solution, *RSC Adv.*, 2015; 5:64633-50.
20. Abd El-Lateef HM, Soliman KA, Tantawy AH. Novel synthesized Schiff Base based cationic gemini surfactants: Electrochemical investigation, theoretical modeling and applicability as biodegradable inhibitors for mild steel against acidic corrosion. *J. Mol. Liq.* 2017 Apr; 232:478-98.
21. Kaczerewska O, Leiva-Garcia R, Akid R, Brycki B, Kowalczyk I, Pospieszny T. Effectiveness of O-bridged cationic gemini surfactants as corrosion inhibitors for stainless steel in 3 M HCl: Experimental and theoretical studies, *J. Mol. Liq.* 2018 Jan; 249:1113-24.
22. ASTM NACE / ASTM G31-12a, Standard Guide for Laboratory Immersion Corrosion Testing of Metals, ASTM International, West Conshohocken, PA, 2012 Oct; p.10 www.astm.org DOI: 10.1520/NACEASTMG0031-12A
23. Anonymous. Cold rolled low carbon steel flat products for cold forming - Technical delivery conditions; German version EN 10130:2006, DIN Deutsches Institut für Normung e. V., 14s., 2007, Berlin, Germany.
24. Abdelrazik H, Mona M, Rehim HA. Surface active hyperbranched polyamide-ester as a corrosion inhibitor for carbon steel in both neutral and acidic media. *Anti-Corros. Method M.* 2015; 62:95-102.
25. Lashgari M, Arshadi MR, Biglar M. Comparative studies of some heterocyclic compounds as corrosion inhibitors of copper in phosphoric acid media. *Chem. Eng. Commun.* 2010; 197:1303-14.
26. Sobhi M, El-sayed R, Abdallah M. The effect of non ionic surfactants containing triazole, thiadiazole and oxadiazole as inhibitors of the corrosion of carbon steel in 1M hydrochloric acid. *J. Surfact. Deterg.* 2013 Nov; 16:937-46.
27. Miller RF, Go TS, Wilson G.R. Method of making corrosion inhibiting polyamine amides, the amides, and use therefor. 1984 Apr; U.S. Patent 4,440,666
28. Emregul KC, Hayvali M. Studies on the effect of a newly synthesized Schiff base compound from phenazone and vanillin on the corrosion of steel in 2 M HCl. *Corros. Sci.* 2006 Apr; 48:797-812.



Decolorization of Reactive Yellow 17 in aqueous solution by ozonation

Kadir Turhan^{1*}  

¹Technical University of Yildiz, Faculty of Arts and Sciences, Department of Chemistry, 34220, İstanbul, Turkey.

Abstract: In this study, factors affecting removal of color by ozonation of synthetic dye solutions containing water-soluble reactive dye [Reactive Yellow 17 (RY17)] were investigated using chemical oxygen demand (COD) measurement method. The research was conducted using a semi-batch bubble column. As a result, the COD of the reactive dye wastewater was reduced by 78.58%, and decolorization was remarkable at pH 12, complete degradation of the dye solution occurs in 12 min, ozone consumption goes on for a further 30 min after which time most degradation reaction is completed. Kinetic study results have shown that direct ozonation of the dye solutions is a pseudo-first-order reaction with respect to dyes. The apparent rate constant increased both with applied ozone dosing and higher pH values, logarithmically decreased with the initial dye concentration.

Keywords: Ozonation, Reactive Yellow 17, Reactive Dye, Decolorization, COD.

Submitted: February 05, 2018. **Accepted:** June 26, 2018.

Cite this: Turhan K. Decolorization of Reactive Yellow 17 in aqueous solution by ozonation. JOTCSA. 2018;5(2):835-44.

DOI: <http://dx.doi.org/10.18596/jotcsa.389062>.

***Corresponding author.** E-mail: kturhan@yildiz.edu.tr.

INTRODUCTION

One of the most important natural resources for living beings and vital water is threatening our world because of the water crisis that will come out with increasing human population, rapid industrialization, living standards, and consumption. One of these threatening factors is the textile industry, which consumes a high volume of wastewater. Textile wastewaters usually consist of many contaminant parameters such as acidic and basic solutions, water-soluble solids, toxic compounds, and coloring materials. Even at low concentrations, the most serious pollutant and textile wastewater are the most serious problems. Disposal of these wastes into the receiving water damages the environment. Removal of dye wastewater from surface waters is due to not only aesthetic reasons and the effect of dyes on plant photosynthesis and fish mortality in water, but also because many of these dyes are toxic and carcinogenic (1-3).

The basis for the classification of the dye according to chemical structures is the chromophore group, which gives absorption to the dye material. Among these classes are the

most known azo dyes. Around 7×10^5 tons of dye are produced annually in the world, and 60-70% of them are azo dyes (4). Most azo dyes, except for some, lead to the formation of aromatic amines that are mutagenic or carcinogenic to human beings. One such class of reactive dyes has complex chemical structures, including organic ring forms with dyed double bonds. A typical case of reactive dyes is the formation of a constant covalent bond between the hydroxyl groups and the dye reactive groups of the cellulose fiber (5). Wastes from reactive dyeing processes require special attention due to their basic properties which relatively low dye fixation ratio, high organic and inorganic substance and high alkalinity (6). It is very difficult to treat wastewater from textile dyeing processes with conventional activated sludge systems. The wastewater color is because the structure of the dyes does not have the biodegradability properties. Physical-chemistry methods such as coagulation/flocculation, clay, perlite and activated carbon adsorption, as well as reverse osmosis systems, have been improved because of removing the color. However, limited success is achieved in these methods and uncompensated costs arise (7). Today, advanced oxidation

processes (AOP's) are present for the treatment of wastewaters, such as electro-oxidation, ozonation, photocatalytic degradation, etc. (8-10).

Among ozone's numerous applications, decolorization of textile wastewater has gained an increasing interest in the over recent years. AOPs, such as treatment with ozone (O₃), ultra-violet and hydrogen peroxide (UV/H₂O₂, UV/O₃/H₂O₂), can prompt to the demolition of the dye-molecule chromophore group, decolorizing thus the textile effluent (11-14).

Ozone is widely used in both drinking and non-drinking water treatment and industrial wastewater treatment. The ozone and its molecular oxygen are the first choice for oxidation or disinfection. Indeed, it is one of the most effective and readily obtainable oxidizing agents that can be produced everywhere. Furthermore, ozone dissociates quickly without leaving any residue, and reactions usually do not produce toxicants.

Ozone reacts, directly or indirectly, with complex organic and inorganic compounds, thereby breaking them into simpler and smaller molecules. The oxidizing action of ozone in aqueous solutions is rather complex since ozone acts by several mechanisms, including the presence of other highly strong oxidizing agents, like atomic oxygen (O), perhydroxyl (HO₂•), or hydroxyl (OH•) free radicals. In fact, oxidation reactions occur both directly and indirectly. However, the reaction is usually dependent on

various factors such as the temperature, pH, and chemical composition of the solution (15-17).

The objective of this study is to demonstrate the ability of ozonation to fully and effectively decolorize aqueous solutions of azo-reactive dye (Reactive Yellow 17 (RY17)). For this purpose, optimum oxidation conditions, e.g. color and Chemical Oxygen Requirement (COD) were removed to determine dye, ozone concentration, pH, and temperature. All of the experiments were applied in the Semi-Batch Bubble Column Reactor (SBBCR).

EXPERIMENTAL

Experimental set-up

The experimental set-up that is shown in Figure 1 consist of oxygen gas, ozone generator, a glass bubble column reactor, reactor, dosimeter, temperature control unit, two peristaltic pumps and two washing bottles. Fischer 502 Model ozone generator was used for the production of ozone from dry oxygen (99.9% purity). All experiments were carried out in a semi-batch bubble column reactor (Diameter: 5 cm, Volume: 2000 mL). Oxygen gas was passed through the ozonizer, where ozone formation takes place. The resulting mixture of O₃ and O₂ was passed through a silicone hose to the bottom of the bubble column in which the dye solution was present. The gas flow rate was controlled by a valve and measured by a flow meter. In all experiments the temperature was kept constant at 20±1 °C.

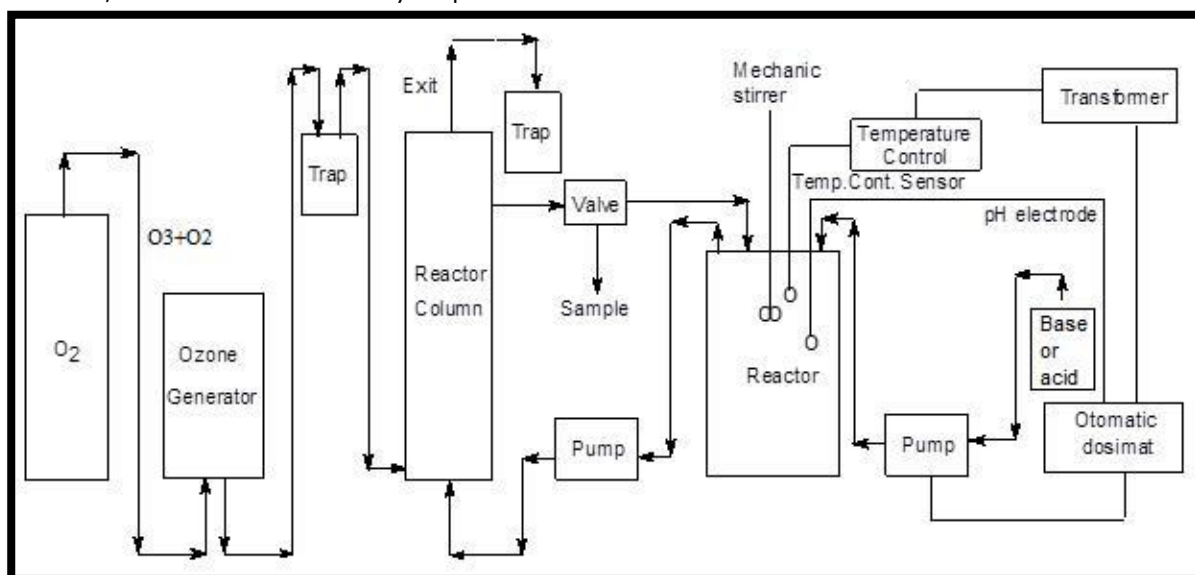
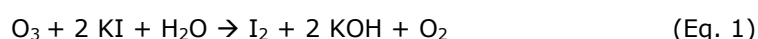


Figure 1. Schematic diagram of the bench-scale reactor system.

Unused ozone was sent to wash bottles containing 2% KI in the bubble column reactor via a silicone hose. The potassium iodide solution was reacted with excess ozone according to the following equation:



The resulting iodine was titrated using standard sodium thiosulfate, in the presence of starch as indicator. The values of unused ozone were determined accordingly. The concentrations of dye solution were

determined by Agilent 8453 model spectrophotometer at its maximum absorption wavelength of 408 nm for RY17.

On the basis of our previous experiences, high ozone-air flow rate and high ozone concentration were required for the effective treatment of the dyestuff wastewater by ozone (18-23). Thus, experiments were performed with ozone-air flow rate at 120 L/h.

Reagents and solutions

Due to its widespread use, C.I. Reactive Yellow 17, chosen as the model dyestuff, was purchased from Alfa Aesar. The characteristics of disperse dyes are displayed in Table 1. Figure 2 shows the general structures of the disperse dyes. Dye solutions at a concentration of 1000 mg/L were prepared from distilled water. The pH of the solutions was adjusted by using NaOH (Merck) or H₂SO₄ (Merck) by dosimeter and was measured by using a pH meter (WTW pH 315i). This stock solution was stirred for 30 min. It was then cooled and stored in the dark. The stock solution was used to prepare the desired concentration (100, 200, 300 and 400 mg/L).

Table 1. The characteristics of the reactive dye.

Reactive Dye	Formula	CAS Number	λ_{max} (nm)	Mw (g/mol)
Reactive Yellow 17	C ₂₀ H ₂₀ K ₂ N ₄ O ₁₂ S ₃	20317-19-5	408.0	682.77

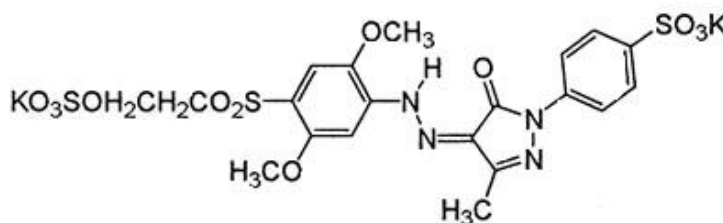


Figure 2. Structures of the Reactive Yellow 17

Equipment

The concentration of each dye solution was determined by an Agilent 8453 model spectrophotometer at maximum absorption wavelength 408.0 nm for RY17. De-ionized water was used throughout the experiments for all solution preparations. The color of dye solutions was measured by an integration method developed COD measurement of Wu *et al.* (1998) and Wu and Wang (2001) (24,25).

This method involved scanning the absorbance of a sample from 200 to 600 nm and integrating the area under the absorbance curve. The integrated area is expressed as the Integrated Absorbance Units (IAU), which is directly proportional to the sample color. The integration method is simpler than the American Dye Manufacturers Institute (ADMI) tristimulus filter method but the two methods have been shown to yield similar results (25,26).

RESULTS AND DISCUSSION

Decolorization kinetics

The reaction mechanisms of ozonation reactions follow two possible pathways of degradation. One of these occurs at basic pH, at which the ozone rapidly forms hydroxyl radical and the other at

acidic pH, where ozone reacts directly with organic substrates as an electrophilic. Because ozone attacks the double bonds associated with the color in the dye, it is often used to decolorizing dye wastewaters.

The decomposition of ozone is also influenced by the presence of inorganic/organic species in the reaction medium.

The decolorization of dyes by ozonation is first order with respect to ozone and the dye, respectively (27). If the amount of ozone is increased, the reaction is pseudo-first order according to dye. When the data obtained in this study were calculated it was found that the pseudo first-order reaction.

$$-\frac{dC_{dye}}{dt} = k_{app} \cdot C_{dye} \quad (\text{Eq. 2})$$

where C_{dye} is dye concentration, and k_{app} is the apparent rate constant.

The representative curve and the corresponding pseudo first-order correlation are shown in Figure 3.

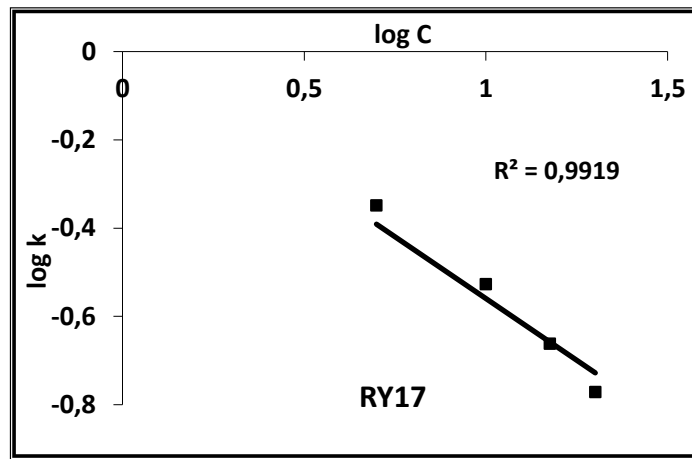


Figure 3. log k = f(log C) plots of RY17.

Also, the apparent rate constant declines logarithmically with the initial dye concentration as follows:

$$k_{app} = 0.8441 \times C_{RY17}^{-0.6955} \quad (\text{Eq. 3})$$

where, k_{app} : apparent rate constant, 1/min; C_{dye} : the initial dye concentration, mg/L.

Initial dye concentrations of 5, 10, 15 and 20 mg/L were taken so that the absorbance of the dye solutions can be measured directly without dilution. As can be seen in Table 2, higher values for rate constant could be obtained in a basic medium. For this reason, the pH environment has been chosen to be high for the duration of the study.

Table 2. Line-fitted values of rate constant k, (1/min).

Reactive dye	pH	k (1/min)			
		C ₀ = 5 mg/L	C ₀ = 10 mg/L	C ₀ = 15 mg/L	C ₀ = 20 mg/L
Reactive Yellow 17	6.0	0.278	0.202	0.145	0.092
	8.0	0.404	0.338	0.246	0.113
	10.0	0.411	0.317	0.208	0.106
	12.0	0.448	0.246	0.187	0.099

The effect of pH of initial solution on COD

At the beginning of the ozonation process, the solution (5 L) of dye that has 300 mg/L concentration was put into the reactor. The experiment was initiated by the formation of ozone gas. Sampling was done at regular intervals to determine dye concentration and COD. The pH of the RY17 wastewater prior to reaction with ozone was determined to be 6.3. The COD of reactive dyestuff wastewaters was reduced from 761 mg/L to 541 mg/L after ozone treatment for 2 hrs. When the pH was adjusted to

12.0, the COD value of the reactive dye solution was reduced to 163 mg/L. With the idea that the difference in the results came from the difference of the pH of samples, ozone treatment experiments were performed with various pH of samples. For this purpose, COD values were measured at selected pH ranges of 2-12 after ozone treatment and the results are shown in Figure 4. The results obtained with RY17 wastewater showed that the COD reduction was significant at pH 12. For this reason, 12 was chosen as the most suitable pH value for subsequent experiments.

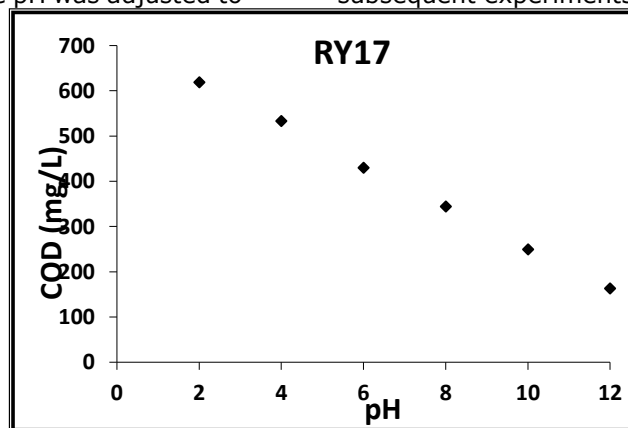


Figure 4. Effect of pH of the initial solution on COD (COD raw reactive dyestuff: 761 mg/L for DY17; Ozone conc.: 24 g/m³; Dye concentration: 300 mg/L; Dye solution: 5 L; Ozone-air flow rate: 120 L/h; Ozonation time: 120 min.).

Spectrophotometric investigation of the process

The decolorization UV-Vis spectra of RY17 is shown in Figure 5. During the course of the 12-minute reaction period, the absorption of RY17 in

solution decreased with the duration of the reaction. In the presence of ozone, the decrease in absorbance at 408.0 nm of the RY17 solution showed that the RY17 structure was reduced or abolished.

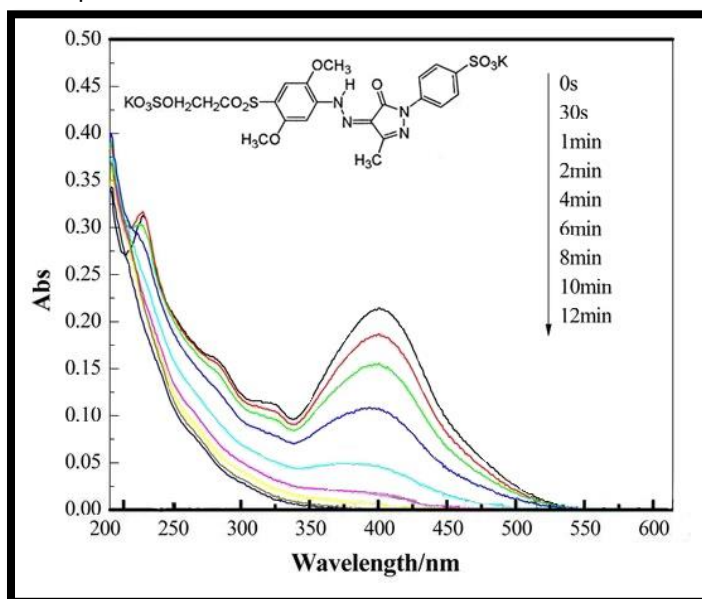


Figure 5. UV-Vis spectral changes of RY17 (300 mg/L) with ozone after different reaction time at initial pH.

Effect of reaction time

COD was also measured during the reaction. As shown in Figure 6, the optimal time for 120 minutes of ozonation was chosen because there

was no reasonable reduction in the COD of the dye solution after 120 minutes of ozonation. Figure 6 shows that COD of dye wastewater decreases 78.58% for RY17 (at pH 12.0) with ozonation.

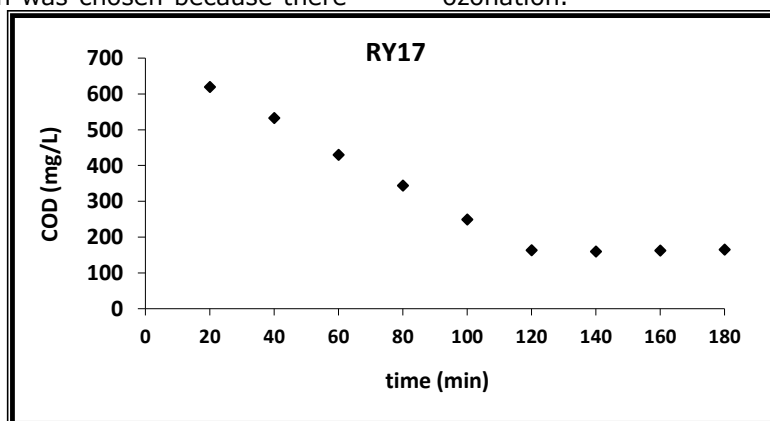


Figure 6. CODs of RY17 with ozone after different reaction time at pH 12. (Ozone conc.: 24 g/m³; Dye concentration: 300 mg/L; Dye solution: 5 L; Ozone-air flow rate: 120 L/h).

Effect of initial dye concentration on rate of dye removal

Figure 7 shows the change in the dye concentration during the ozonation at different

initial concentrations. Based to these results, the removal rate of RY17 is higher at lower initial dye concentrations and lower at higher dye concentrations.

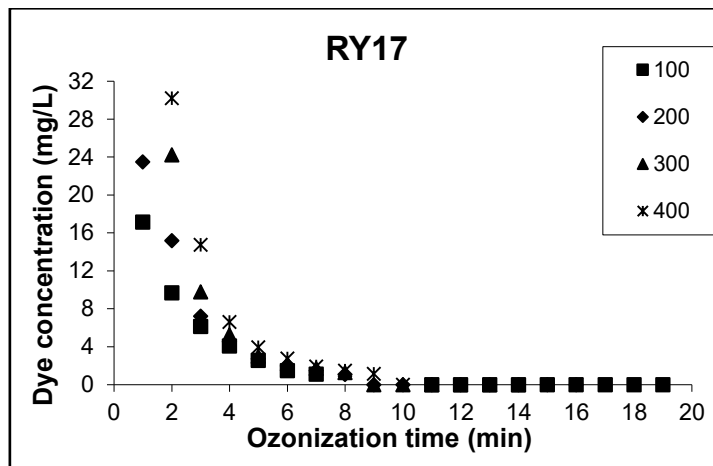


Figure 7. Concentration-time data for different dye concentration treated with ozone (Ozone conc.: 24 g/m³; Dye solution: 5 L; Ozone-air flow rate: 120 L/h; pH:12)

Effect of initial dye concentration on decolorization time

Figure 8 shows the effect of initial dye concentrations (100 to 400 mg/L) on the time required for the decolorization process. According to the results obtained, the color removal time is directly proportional to the initial dye concentration. The data fit equation:

$$t_D = m.c \tag{Eq. 4}$$

where t_D is the dye decolorization time (min), m : a constant, and c : the initial dye concentration (mg/L).

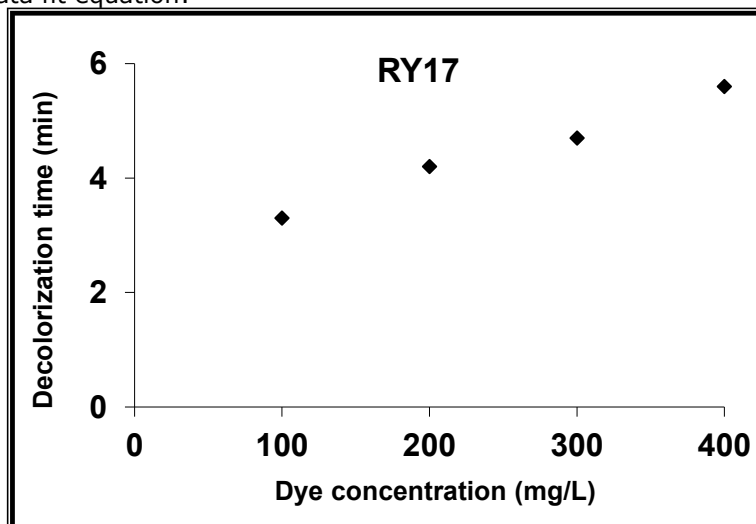


Figure 8. Effect of initial dye concentration on the decolorization time of RY17 or dye treated by ozone (Ozone conc.: 24 g/m³; Dye solution: 5 L; Ozone-air flow rate: 120 L/h; pH: 12).

Effect of ozone concentration on decolorization time

Figure 9 shows the relationship between ozone concentration and the duration of decolorization; with increasing ozone concentration, it is very clear that the duration of color removal decreases linearly. For example, increasing ozone concentration from 4.21 g/m³ to 24.03 g/m³ in

the gas phase reduces the decolorization time of 300 mg/L dye concentration by 73.08%. This result is consistent with mass transfer theory (28). According to this theory, the repulsive force required to transfer the ozone to the dye solution, in other words, increases as the concentration of ozone in the air bubbles (ozone carrier), the rate of dye oxidation increases.

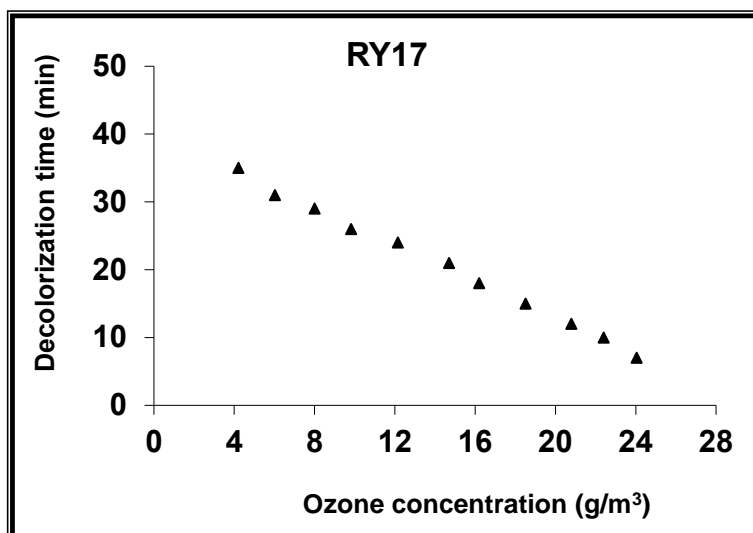


Figure 9. Effect of ozone concentration on dye decolorization time (Dye conc.: 300 mg/L; Dye solution: 5 L; Ozone-air flow rate: 120 L/h; pH: 12).

Effect of pH of initial dye solution on decolorization time

Figure 10 shows the initial dye solution pH versus decolorization time of the dye solution. It appears that the decolorization time decreases with

increasing initial pH of the solution. The rate of decomposition of ozone is directed toward the formation of hydroxyl radicals by increasing pH. This explains the reduction of 67.10% of the dye decolorization time by increasing the pH from 2 to 12.

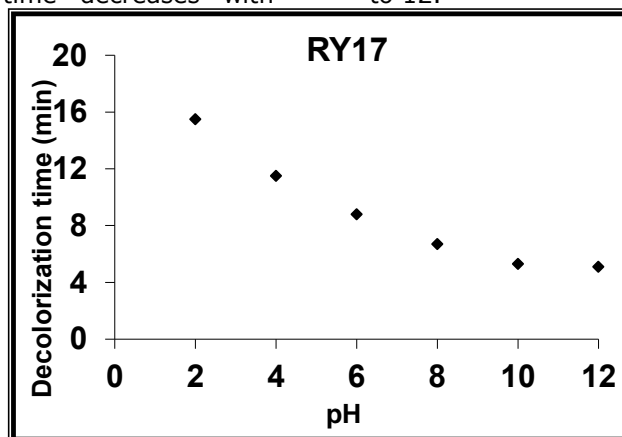


Figure 10. Effect of initial dye solution pH on decolorization time (Dye conc.: 300 mg/L; Dye solution: 5 L; Ozone-air flow rate: 120 L/h; Ozone conc.: 24 g/m³)

CONCLUSIONS

In this study, the aqueous solutions of Reactive Yellow 17, selected as the model textile dye, were ozonated in a semi-batch bubble column reactor. To increase the solubility of the aqueous solutions of the stubborn pollutant at the laboratory scale, an experimental series of experiments was conducted to evaluate the effectiveness of the indirect ozonation of the radical type reactions with the RY17 model. A detailed review of the results provided us with the following results:

After ozone bubbling treatment, the reactive dye wastewater showed a 78.58% reduction in COD. The results obtained with reactive dye (RY17) showed that COD reduction and decolorization were more effective under basic conditions. The

decolorization took place in 12 minutes for RY17, ozone consumption continued for another 30 minutes, after which a large part of the degradation was completed. A large number of bubbly ozone gases at high concentrations have been effective in reducing COD at high inlet gas flow-rates. In all experimental studies, decomposition kinetics for the reaction of the ozone-dye solution were observed as pseudo-first order. The increase in k by the increase of the ozone dose can be explained by the higher ozone dose applied to increase the dissolved ozone concentration. This makes decolorization of the dye solution faster. Higher rate constants were obtained at higher pH values in the experiments. This can be explained by the fact that high pH values promote spontaneous dissociation of ozone in the water.

The knowledge gained in this study is thought to be a guide for future studies. However, it is highly probable that UV-assisted ozonation, which is to be carried out as a continuation of these studies, may have a higher effect. This laboratory-scale work can be used in industrial treatment systems. The industrialists do not prefer ozonation because of its expensiveness, but they should be aware of its benefit for ecosystem. Although they seem cheap, the damage of the systems used as alternatives in the removal and disintegration of the aromatic compounds in particular, must not be ignored. However, it should be remembered that the degradation products in the purification process may be more harmful. For this reason, the continuity of such studies will provide an idea for the plant as well as a pre-feasibility.

ACKNOWLEDGEMENTS

Thanks for Yildiz Technical University Scientific Research Projects Coordination's support in this study. Project No: 2013-01-02-GEP02.

REFERENCES

- Manu B, Chaudhari S. Anaerobic decolourisation of simulated textile wastewater containing azo dyes. *Bioresource Technology* 2002 82(3) 225-231.
- Lourenço ND, Novais JM, Pinheiro HM. Analysis of secondary metabolite fate during anaerobic-aerobic azo dye biodegradation in a sequential batch reactor. *Environmental Technology* 2003 24(6) 679-686.
- Dos Santos AB, Cervantes FJ, van Lier JB. Review paper on current technologies for decolourisation of textile wastewaters perspectives for anaerobic biotechnology. *Bioresource Technology* 2007 98 2369-2385.
- Moosvi S, Kher X, Madamwar D. Isolation, characterization and decolorization of textile dyes by a mixed bacterial consortium. *Water Science and Technology* 2006 36:65-72.
- Gohl EPG, Vilensky LD. *Textile Science Explanation: An Explanation of Fibre Properties (Second Edition)* Published by CBS Publishers & Distributors Pvt. Ltd., 2005.
- Corriea VM. Characterization of textile wastewater - a review. *Environmental and Technology* 1994 15:917-929.
- Slokar YM, Marechal AM. Methods of discoloration of textile waste waters. *Dyes and Pigments* 1998 37:335-356.
- Gutierrez MC, Crespi M. A review of electrochemical treatments for colour elimination. *Journal of the Society of Dyers and Colourists* 1999 115:342-345.
- Lorimer JP, Mason TJ, Plattes M, Phull SS, Walton DJ. Degradation of dye effluent. *Pure and Applied Chemistry* 2001 73:1957-1968.
- Gupta VK, Khamparia S, Tyagi I, Jaspal D, Malviya A. Decolorization of mixture of dyes: A critical review. *Global Journal of Environmental Science and Management* 2015 1(1):71-94.
- Georgiou D, Melidis P, Aivasidis A, Gimouhopoulos K. Degradation of azo reactive dyes by UV radiation in the presence of hydrogen peroxide. *Dyes and Pigments* 2002 52(2):69-78.
- Soares PA, Silva TF, Manenti DR, Souza SM, Boaventura RA, Vilar VJ. Insights into real cotton-textile dyeing wastewater treatment using solar advanced oxidation processes. *Environmental Science and Pollution Research International* 2014 21(2):932-945.
- Asghar A, Raman AAA, Daud WMAW. Advanced oxidation processes for in-situ production of hydrogen peroxide/hydroxyl radical for textile wastewater treatment: a review. *Journal of Cleaner Production* 2015 87:826-838.
- Cardoso JC, Bessegato GG, Zanoni MVB. Efficiency comparison of ozonation, photolysis, photocatalysis and photoelectrocatalysis methods in real textile wastewater decolorization. *Water Research* 2016 98:39-46.
- Gottschalk C, Libra JA, Saupe A. *Ozonation of Water and Waste Water: A Practical Guide to Understanding Ozone and its Applications*, 2nd Edition, WILEY-VCH., 2009.
- Von Gunten U. Ozonation of drinking water: Part I. Oxidation kinetics and product formation. *Water Research* 2003 37(7):1443-1467.
- Von Gunten U. Ozonation of drinking water: Part II. Disinfection and by-product formation in presence of bromide, iodide or chlorine. *Water Research* 2003 37(7):1469-1487.
- Turhan K, Turgut Z. Reducing chemical oxygen demand and decolorization of direct dye from synthetic wastewater by ozonation in a batch bubble column reactor. *Fresenius Environmental Bulletin* 2007 16(7):821-825.

19. Turhan K, Turgut Z. Decolorization of direct dye in textile wastewater by ozonation in a semi-batch bubble column reactor. *Desalination* 2009 242(1-3):256-263.
20. Turhan K, Ozturkcan SA. Decolorization and degradation of reactive dye in aqueous solution by ozonation semi-batch bubble column reactor. *Water, Air and Soil Pollution* 2013 224:1353-1358.
21. Turhan K, Turgut Z. Treatment and degradability of direct dyes in textile wastewater by ozonation: A laboratory investigation. *Desalination and Water Treatment* 2009 11(1-3):184-191.
22. Turhan K, Uzman S. Removal of phenol from water using ozone. *Desalination* 2008 229(1-3):257-263.
23. Turhan K, Durukan I, Ozturkcan SA, Turgut Z. Decolorization of textile basic dye in aqueous solution by ozone. *Dyes and Pigments* 2012 92(3):897-901.
24. Wang C, Yediler A, Lienert D, Wang Z, Kettrup A. Ozonation of an azo dye C.I. Remazol Black 5 and toxicological assessment of oxidation products. *Chemosphere* 2003 52:1225-1232.
25. Wu J, Eiteman MA, Law SE. Evaluation of membrane filtration and ozonation processes for treatment of reactive-dye wastewater. *Journal of Environmental Engineering* 1998 124(3):272-277.
26. American Public Health Association (APHA), American Water Works Association (AWWA), and Water Environment Federation (WEF), Standard methods for the examination of water and wastewater, American Public Health Association Publ., 21th ed., Washington DC, 2005.
27. Langlais B, Reckhow DA, Brink DR, Ozone in water treatment: application and engineering, Boca Raton: Lewis Publishers, 1991:31-54.
28. Raghuvanshi SP, Singh R, Kaushik CP, Raghav AK. Removal of textile basic dye from aqueous solutions using sawdust as bio-adsorbent. *International Journal of Environmental Studies* 2005 62(3):329-339.



Synthesis, spectral studies, XRD, thermal analysis and biological screening of metal complexes derived from (N-(3-methoxyphenyl)-2-[(2E)-3-phenylprop-2-enoyl] hydrazinecarboxamide

T. C. M. Yuvaraj¹, P. Parameshwara Naik^{1*}, T.V. Venkatesh², G. Krishnamurthy¹ and T. Manjuraj¹.

¹Department of Chemistry, S.S.College (Auto), Shivamogga, Karnataka (INDIA).

²Department of Chemistry, Shankaragatta, Kuvempu University, Karnataka (INDIA).

Abstract: Complexes of nickel(II), cobalt(II), copper(II), zinc(II), and manganese(II) are derived from the ligand, (N-(3-methoxyphenyl)-2-[(2E)-3-phenylprop-2-enoyl]hydrazinecarboxamide [MPH] and structurally characterized by various physicochemical and spectral tools such as FTIR, UV-Visible, ¹H NMR, LC-Mass, P-XRD and TGA-DTC. These studies showed that the ligand coordinated to the 3d metal ions in bidentate manner. X-ray diffraction studies indicates that the Ni(II), Cu(II) and Zn(II) complexes are crystalline in nature. Degradation mechanisms, thermodynamic and kinetic parameters of the synthesized metal complexes have been evaluated. The prepared ligand and complexes were evaluated for *in-vitro* antioxidant DPPH assay, in which metal complexes showed excellent activity. The molecular docking analysis by using human antioxidant enzyme *DTT* (*PDB: 3MNG*) have also been evaluated. The ligand and their metal complexes were screened for their antimicrobial activities against different pathogenic bacterial and fungal species.

Keywords: Semicarbazide, Metal complexes, P-XRD, TGA, antioxidant, Molecular docking.

Submitted: December 03, 2017. **Accepted:** June 30, 2018.

Cite this: 1. Yuvaraj T, Parameshwara Naik P, Venkatesh T, Krishnamurthy G, Manjuraj T. Synthesis, spectral studies, XRD, thermal analysis and biological screening of metal complexes derived from (N-(3-methoxyphenyl)-2-[(2E)-3-phenylprop-2-enoyl] hydrazinecarboxamide. JOTCSA. 2018;5(2):845-56.

DOI: <http://dx.doi.org/10.18596/jotcsa.341379>.

***Corresponding author.E-mail:** parashchem@gmail.com.

INTRODUCTION

Semicarbazide and its derivatives are reported to be pharmacologically and physiologically active and find various applications in the treatment of several diseases (1-2). These are biologically active and are nontoxic due to the presence of ureido unit (-NH-CO-NH-NH-), which acts as pseudodipeptide motif. The derivatives of semicarbazone are an important class of ligand containing nitrogen and oxygen as donor atoms. The chemistry of the transition metal complexes of semicarbazone became largely appealing because of their extensive profile of medicinal and pharmacological activity that provides a variety of compounds with diverse applications (3-5). The semicarbazone derivatives and their transition metal complexes

show variable bio-potential activities like antibacterial, antifungal, antiarthritic, antimalarial, antitumor, antiviral, and anti-HIV agents and they have been well documented in the literature (6-7). The above important applications of semicarbazone derivatives and their 3d metal complexes in various fields prompted us to synthesize some derivatives of semicarbazone and their complexes to enhance their activities and test against *mycobacterium tuberculosis* (8-9). Now we report the synthesis, characterization, and biological activities of transition metal complexes containing amide-appended (2E)-3-phenylprop-2-enehydrazide and 1-isocyanato-3-methoxybenzene. This ligand system coordinates with the metal ion in a bidentate manner through the carbonyl oxygen and azomethine nitrogen (10). The aim of the

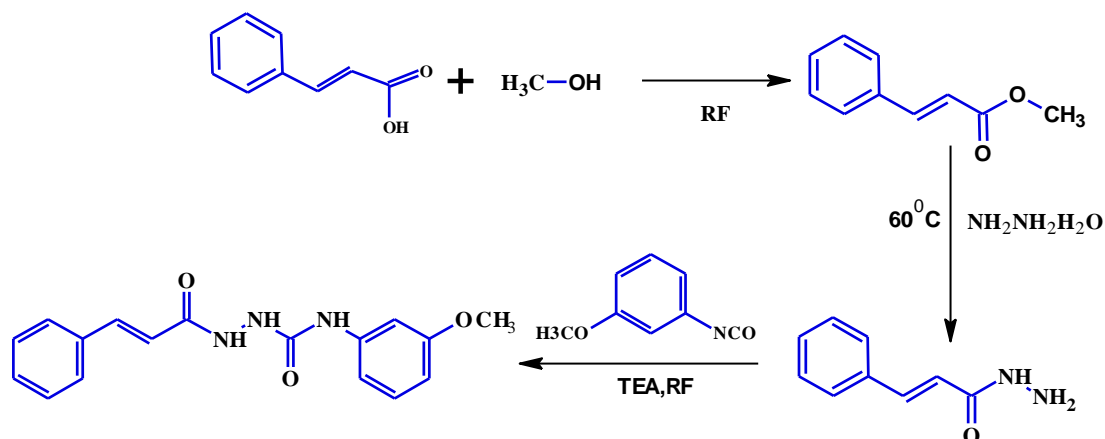
present work deals specifically the coordination properties of *N*-(3-methoxyphenyl)-2-[(*E*)-3-phenylprop-2-enoyl]hydrazinecarboxamide concerning its interactions with Ni(II), Co(II), Cu(II), Zn(II) and Mn(II) complexes, spectral characterization and thermal decomposition studies serve as important tools for the interpretation of structures of molecules and also biological and analytical importance. molecular docking study have been performed to investigate the interaction and binding energies of the complexes with protein enzyme by using HEX 8.2 for antioxidant activity, the compounds were also performed to investigate against the growth of *in-vitro* bacteria and pathogenic fungi.

MATERIALS AND METHODS

The chemicals cinnamic acid, 1-isocyanato-3-methoxybenzene, hydrazine hydrate, and methanol were purchased from Sigma Aldrich, Laboratory chemicals, Bangalore, Karnataka, India. Nickel(II) chloride hexahydrate, cobalt(II) chloride hexahydrate, copper(II) chloride hexahydrate, anhydrous zinc(II) chloride and manganese(II) chloride were purchased from Merck. The metal chlorides were used in their hydrated form. The solvents were distilled and dried by standard method.

Synthesis of *N*-(3-methoxyphenyl)-2-[(*E*)-3-phenylprop-2-enoyl]hydrazinecarboxamide (MPH)

A mixture of cinnamic acid (2.96 g, 0.02 mol) and 5 drops of conc. H₂SO₄ in 30 mL of dry methanol was refluxed for 8 hours. The solvent was evaporated under reduced pressure. The white solid methyl (*E*)-3-phenylprop-2-enoate formed was filtered and recrystallized from a mixture of ethanol and acetone in the ratio 1:2. The mixture of methyl (*E*)-3-phenylprop-2-enoate (3.24 g, 0.02 mol) and hydrazine hydrate (1.10 g, 0.022 mol) in 20 mL of dry methanol was refluxed for 6 hours and the resulting mixture was evaporated under vacuum. The white solid, (*E*)-3-phenylprop-2-enehydrazide formed was filtered off, washed with water, dried and recrystallized from dioxane. Then, the solution of (*E*)-3-phenylprop-2-enehydrazide (3.23 g, 0.02 mol), 1-isocyanato-3-methoxybenzene (2.98 g, 0.02 mol) and triethylamine (0.51 g, 0.005 mol) in 40 mL of dry methanol was added and refluxed for about 10 hours. The reaction mixture was poured into ice-cold water. The cream colored solid of *N*-(3-methoxyphenyl)-2-[(*E*)-3-phenylprop-2-enoyl]hydrazinecarboxamide formed was filtered and recrystallized from ethanol.



Scheme 1: Synthesis of the ligand MPH.

C₁₇H₁₇N₃O₃: Yield: 78%; Color: Cream; M.p: 122-124 °C; Mol.wt: 311.33; Elemental analyses: calculated and found (%): C: 65.58 (65.99), H: 5.50 (5.72), N: 13.50 (13.69), O: 15.42; IR (KBr, cm⁻¹): 3182 (NH⁹), 3243 (NH¹²), 3320 (NH¹³), 2943 (Ar-CH), 1709 (C=O¹⁰), 1665 (C=O¹⁴), 1014 (N-N), 1604 (Ar-OCH₃), 1207 (CH¹⁶=CH¹⁷). ¹H NMR (DMSO-d₆, 400 MHz): δppm 8.24 (s, 1H, NH⁹), 8.84 (s, 1H, NH¹²), 9.99 (s, 1H, NH¹³), 7.16 (s, 1H, Ar-H²), 6.56, 7.25 (d, 2H, Ar-H^{4,6}), 7.13 (t, 1H, Ar-H⁵), 3.71 (s, 3H, OCH₃), 7.62, 7.61 (d, 2H, Ar-H^{19,23}), 7.39-7.45 (t, 3H, Ar-H^{20,21,22}); Mass of the ligand M⁺ at m/z: 312.00.

Synthesis of the metal complexes

A solution of nickel(II) chloride hexahydrate (0.950 g, 0.004 mol), cobalt(II) chloride

hexahydrate (0.951 g, 0.004 mol), copper(II) chloride dihydrate (0.697 g, 0.004 mol), zinc(II) chloride (0.545 g, 0.004 mol) and manganese(II) chloride tetrahydrate (0.692 g, 0.004 mol) in 20 mL of ethanol was added one each time to the solution of *N*-(3-methoxyphenyl)-2-[(*E*)-3-phenylprop-2-enoyl]hydrazinecarboxamide (1.245 g, 0.004 mol) in 20 mL of ethanol. The resulting reaction mixture was refluxed for about 10 hours. The solid product was collected by filtration and washed with 4-5 mL of hot water and dried under vacuum over anhydrous calcium chloride in desiccator.

(i) [Ni(MPH)₂Cl₂].H₂O: C₃₄H₃₂Cl₂N₆NiO₆.H₂O: Yield: 68%; Color: Dark brown; M.p: 280-282 °C; Mol. wt: 768.25; Elemental analyses:

calculated and found (%): C: 54.43 (54.64), H: 4.30 (4.80), N: 11.20 (11.48); IR (KBr, cm^{-1}): 3441 (H_2O), 3168 (NH^9), 3056 (NH^{12}), 1592 ($\text{C}=\text{O}^{10}$), 1504 ($\text{C}=\text{O}^{14}$), 1218 (N-N), 1504 (A-OCH₃), 1218 (CH=CH), 448 (M-O), 422 (M-N); Molar conductance: 15.72 $\text{ohm}^{-1} \text{cm}^2 \text{mol}^{-1}$.

(ii) [Co(MPH)₂Cl₂]: C₃₄H₃₂Cl₂CoN₆O₆: Yield: 62%; Color: Gray; M.p: 253-254 °C; Mol.wt: 750.49; Elemental analyses: calculated and found (%): C: 54.41 (54.61), H: 4.30 (4.44), N: 11.20 (11.32); IR (KBr, cm^{-1}): 3159 (N^9H), 3084 (NH^{12}), 1605 ($\text{C}=\text{O}^{10}$), 1506 ($\text{C}=\text{O}^{14}$), 1221 (N-N), 1508 (Ar-OCH₃), 1221 (CH=CH), 456 (M-O), 424 (M-N); Molar conductance: 14.92 $\text{ohm}^{-1} \text{cm}^2 \text{mol}^{-1}$.

(iii) [Cu(MPH)₂Cl]Cl.H₂O: C₃₄H₃₂Cl₂CuN₆O₆.H₂O: Yield: 74%; Color: Dark green; M.p :290-292 °C; Mol.wt: 773.10; Elemental analyses: calculated and found (%): C: 54.08 (54.68), H: 4.27 (4.63), N: 11.13 (11.34); IR (KBr, cm^{-1}): 3445 (H_2O), 3196 (NH^9), 3056 (NH^{12}), 1592 ($\text{C}=\text{O}^{10}$), 1504 ($\text{C}=\text{O}^{14}$), 1219 (N-N), 1504 (Ar-OCH₃), 1219 (CH=CH), 437 (M-O), 418 (M-N); Molar conductance: 57.40 $\text{ohm}^{-1} \text{cm}^2 \text{mol}^{-1}$.

(iv) [Zn(MPH)₂Cl]Cl.H₂O: C₃₄H₃₂Cl₂N₆O₆Zn: Yield: 66%; Color: White; M.p: 269-272 °C; Mol.wt: 756.97; Elemental analyses: calculated and found (%): C: 53.95 (54.15), H: 4.26 (4.42), N: 11.10 (11.58); IR (KBr, cm^{-1}): 3228 (NH^9), 3068 (NH^{12}), 1594 ($\text{C}=\text{O}^{10}$), 1542 ($\text{C}=\text{O}^{14}$), 1218 (N-N), 1542 (A-OCH₃), 1218 (CH=CH), 456 (M-O), 427 (M-N); Molar conductance: 54.92 $\text{ohm}^{-1} \text{cm}^2 \text{mol}^{-1}$.

(v) [Mn(MPH)₂Cl]Cl: C₃₄H₃₂Cl₂MnN₆O₆: Yield: 71%; Color: light orange; M.p: 281-283 °C; Mol.wt: 746.49; Elemental analyses: calculated and found (%): C: 54.70 (55.10), H: 4.32 (4.72), N: 11.26 (11.48); IR (KBr, cm^{-1}): 3181 (NH^9), 3018 (NH^{12}), 1598 ($\text{C}=\text{O}^{10}$), 1511 ($\text{C}=\text{O}^{14}$), 1242 (N-N), 1541 (A-OCH₃), 1249 (CH=CH), 458 (M-O), 416 (M-N); Molar conductance: 58.62 $\text{ohm}^{-1} \text{cm}^2 \text{mol}^{-1}$.

Biological studies

Antioxidant activity:

The free radical scavenging activity of the ligand MPH and their complexes was measured *in-vitro* by 2, 2-diphenyl-1-picrylhydrazyl (DPPH) assay. The stock solution was prepared by dissolving 24 mg of DPPH with 100 mL of methanol and stored at 20 °C until required. The working solution was obtained by diluting the DPPH solution with methanol to attain an absorbance of about 0.98±0.02 at 517 nm using a spectrophotometer. All the tested samples in various concentrations (50, 75 and 100 µg/mL) were prepared in methanol and the homogeneous solutions were achieved by stirring. An aliquot of test sample (1 mL) was added to 4 mL of 0.004% (w/v) methanolic solution of DPPH and then reaction mixture was vortexed for 1 min and kept at room temperature for 30 min in the dark to complete the reaction. The absorbance was read against blank at 517 nm. The synthetic antioxidant butylated hydroxytoluene (BHT) was used as the positive control (11). The ability of the tested samples at tested concentration to scavenge DPPH radicals was calculated using the equation below.

$$\text{Scavenging ratio (\%)} = [(A_i - A_o) / (A_c - A_o)] \times 100\%$$

Where A_i is the absorbance in the presence of the test compound; A_o is absorbance of the blank in the absence of the test compound and A_c is the absorbance in the absence of the test compound.

Molecular docking studies

Molecular modeling studies were performed by using Hex 8.2 protein-ligand docking in PDB formats. The parameters used for docking include: correlation type-shape only, FFT mode 3D, grid dimension 0.6, receptor range 180, ligand range 180, twist range 360, distance range 40. The starting coordinates of the human antioxidant enzyme in complexes with the competitive inhibitor DTT (PDB: 3MNG) were taken from the Protein Data Bank (<http://www.rcsb.org/pdb>) (12-14). The ligand was docked against the lead competitive inhibitor ligand DTT at the crystal enzyme structure of the target protein and the best energy conformations of receptor ligand was studied and the binding energy was calculated

as the difference between the energy of the MPH, metal complexes and the individual energy of enzyme. In order to interrupt the binding interactions modes of the MPH and metal complexes with human antioxidant enzyme DTT (PDB: 3MNG).

Physical measurements

Elemental analyses (C, H, N) were performed with a Perkin-Elmer 2400 series II analyzer. Molar conductance values (10^{-3}mol/L) of the complexes in DMSO at 28 °C were measured using an EQUIP-TRONICS model-660A instrument. Melting point of the synthesized compounds was recorded by using apparatus model code NAMPA/045. UV-Visible spectra were measured in DMF/DMSO on an Ocean Optics USB 4000USA spectrophotometer, using 1 cm path length cuvette at room temperature. Infrared spectra were recorded using FT-IR 8400s Shimadzu spectrometer with KBr pellets in the range of 400-4000 cm^{-1} . The NMR spectra have been recorded as 400 MHz Varian-AS NMR

spectrometer in DMSO- d_6 using tetramethylsilane (TMS) as the internal standard. Thermal measurements (TGA, DTA, 28–900 °C) were noted on a DTG-50 Shimadzu thermo-gravimetric analyzer at a heating rate of 10 °C/min and nitrogen flow rate of 20 mL/min. Magnetic susceptibilities were recorded with a Sherwood scientific magnetic susceptibility balance at 298 K. Mass spectra was recorded using the instrument Code; SC/AD/10-014.

RESULTS AND DISCUSSION

The molar conductance of 0.1×10^{-2} mol/L solution in DMF was recorded; the synthesized 3d series metal complexes have been confirmed by physico-chemical techniques. The synthesized complexes such as $[\text{Ni}(\text{LMPH})_2\text{Cl}_2]\text{H}_2\text{O}$, $[\text{Co}(\text{LMPH})_2\text{Cl}_2]$, $[\text{Cu}(\text{MPH})_2\text{Cl}]\text{Cl} \cdot \text{H}_2\text{O}$, $[\text{Zn}(\text{MPH})_2\text{Cl}]\text{Cl} \cdot \text{H}_2\text{O}$ and $[\text{Mn}(\text{MPH})_2\text{Cl}]\text{Cl}$ are quite stable in air and soluble in some organic solvents such as DMF and DMSO. The elemental analyses and molar conductivity values were in premising agreement with the suggested structure. The molar conductivity of $[\text{Ni}(\text{LMPH})_2\text{Cl}_2]\text{H}_2\text{O}$ and $[\text{Co}(\text{MPH})_2\text{Cl}_2]$ complexes were 15.72 and 14.92 $\text{ohm}^{-1} \text{cm}^2 \text{mol}^{-1}$ due to non electrolytic nature. Also, the molar conductances of $[\text{Cu}(\text{MPH})_2\text{Cl}]\text{Cl} \cdot \text{H}_2\text{O}$, $[\text{Zn}(\text{MPH})_2\text{Cl}]\text{Cl} \cdot \text{H}_2\text{O}$ and $[\text{Mn}(\text{MPH})_2\text{Cl}]\text{Cl}$ were 57.40, 54.92 and 58.62 $\text{ohm}^{-1} \text{cm}^2 \text{mol}^{-1}$ respectively due to uni-uni valent electrolytic state.

^1H NMR and Mass studies:

The proton NMR spectrum of ligand MPH showed at 8.24, 8.84 and 9.99 ppm (s, 3H, $\text{NH}^9, 12, 13$) are assigned to NH protons of derivative of the semicarbazone group. The aromatic hydrogen resonance observed at 7.16 ppm (s, 1H, Ar- H^2), 6.56, 7.25 ppm (d, 2H, Ar- $\text{H}^4, 6$), 7.13 ppm (t, 1H, Ar- H^5), 3.71 ppm (s, 3H, OCH_3). In addition, the doublets and triplets around 7.62, 7.61 ppm (d, 2H, Ar- $\text{H}^{19, 23}$) and 7.39-7.45 ppm (t, 3H, Ar- $\text{H}^{20, 21, 22}$) are due to aromatic ring protons were represented in Supplementary file S1. The mass spectrum confirms the formula of MPH by giving molecular ion peak (M^+) corresponding to their molecular weight shown in Supplementary file S2.

FT-IR Spectral studies:

Infrared spectrum of the ligand and their metal complexes were taken as KBr pellets. The strong bands appeared at 3182 (NH^9), 3243 (NH^{12}) and 3320 (NH^{13}) cm^{-1} assignable to $\nu(\text{NH})$ of the derivative of semicarbazone group. One band

disappeared out of three in the IR spectra of metal complexes like $[\text{Ni}(\text{MPH})_2\text{Cl}_2]\text{H}_2\text{O}$, $[\text{Co}(\text{MPH})_2\text{Cl}_2]$, $[\text{Cu}(\text{MPH})_2\text{Cl}]\text{Cl} \cdot \text{H}_2\text{O}$, $[\text{Zn}(\text{MPH})_2\text{Cl}]\text{Cl} \cdot \text{H}_2\text{O}$ and $[\text{Mn}(\text{MPH})_2\text{Cl}]\text{Cl}$ which showed the deprotonation of the NH group (12–13). The strong band observed at 1604 cm^{-1} range in the uncoordinated ligand have been assigned to $\nu(\text{N-N})$ stretching vibrations. On complexation, these bands were observed at 1488-1542 cm^{-1} to lower intensity, thus representing the coordination of =N-N= nitrogen to metal ion and appearance of a new bands indicated -N=N- bond formation (14). A sharp bands observed at 1709, 1665 cm^{-1} in derivative of semicarbazone mainly due to $\nu(\text{C=O})$ stretching frequency, a split band is an indicative of *cis* arrangement of both C=O groups. These bands are shifted to lower frequency side at 1605-1542 cm^{-1} which indicates that carbonyl oxygen involves in the coordination with metal ion (15). In the spectra of complexes, the appearance new bands in the region at 437-458 cm^{-1} and 416-427 cm^{-1} showed stretching vibrations of (M-N) and (M-O) respectively.

Electronic absorption spectra and magnetic moment:

Electronic spectrum of gray colored cobalt(II) complex showed three strong bands at 14,598, 16,393 and 16,949 cm^{-1} due to the $^4\text{T}_{1g}(\text{F}) \rightarrow ^4\text{T}_{2g}(\text{F})(\nu_1)$, $^4\text{T}_{1g}(\text{F}) \rightarrow ^4\text{A}_{2g}(\text{F})(\nu_2)$ and $^4\text{T}_{1g}(\text{F}) \rightarrow ^4\text{T}_{1g}(\text{P})(\nu_3)$ transitions, respectively (16). The observed magnetic moment values 3.92 B.M, also support the complex to have octahedral geometry (17). The spectrum of dark brown colored nickel(II) complex showed bands at 14,705, 16,000 and 16,949 cm^{-1} respectively. These bands can be attributed to the transitions $^3\text{A}_{2g}(\text{F}) \rightarrow ^3\text{T}_{2g}(\text{F})(\nu_1)$, $^3\text{A}_{2g}(\text{F}) \rightarrow ^3\text{T}_{1g}(\text{F})(\nu_2)$ and $^3\text{A}_{2g}(\text{F}) \rightarrow ^3\text{T}_{1g}(\text{P})(\nu_3)$ respectively. Three bands exhibited by nickel complex with magnetic moment 2.86 B.M may be due to octahedral geometry. Copper(II) complex showed strong bands at 14,492 and 16,393 cm^{-1} , which can be assigned to the transitions $^2\text{B}_{1g} \rightarrow ^2\text{A}_{1g}(\text{d}_x^2 - \text{y}^2 \leftarrow \text{d}_z^2)(\nu_1)$ and $^2\text{B}_{1g} \rightarrow ^2\text{E}_g(\text{d}_x^2 - \text{y}^2 \leftarrow \text{d}_{xyz})(\nu_1)$. The two bands of dark green colored copper(II) complex showed the magnetic moment value 1.76 B.M evidence for square pyramidal. The manganese(II) complex exhibits a band with weak intensity at 10,309 cm^{-1} and its magnetic moment value 5.95 BM, which can be attributed to $^6\text{A}_{1g} \rightarrow ^4\text{T}_{1g}$ transition in a square pyramidal environment (18). The electronic spectra of the ligand and complexes are presented in Figure 1.

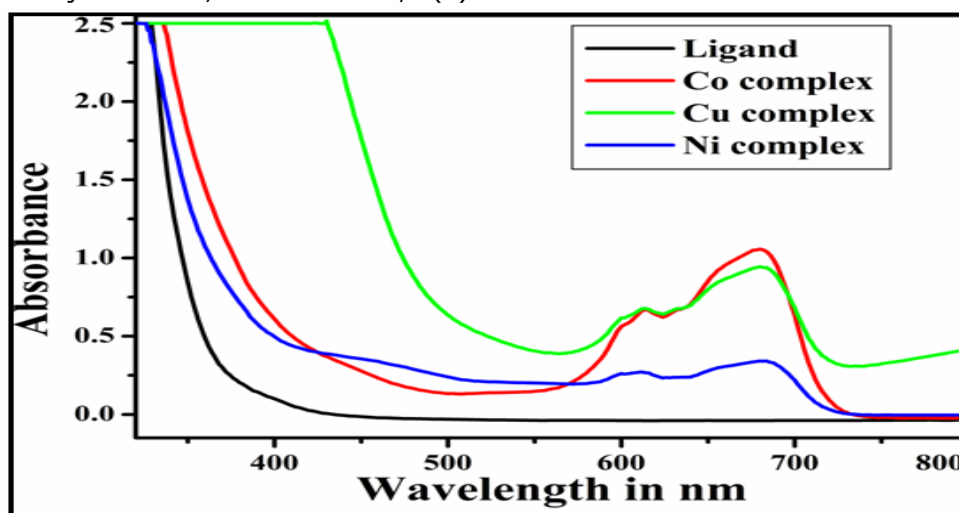


Figure 1: Electronic spectra of ligand and Ni(MPH)₂Cl₂]H₂O, [Co(MPH)₂Cl₂] and [Cu(MPH)₂Cl]Cl.H₂O.

Powder XRD analysis:

Diffraction patterns of Ni(II), Co(II), Cu(II), Zn(II) and Mn(II) complexes have been carried out and recorded at 2θ = 10–80°, among them [Ni(MPH)₂Cl₂]H₂O, [Cu(MPH)₂Cl]Cl.H₂O and

[Zn(MPH)₂Cl]Cl.H₂O complexes exhibited sharp peaks showed crystalline nature. The values of relative intensities, *d*, 2θ and sin2θ values of both observed and calculated are given in Tables 1 and 2.

Table 1. Diffraction pattern of [Cu(L)₂Cl]Cl.H₂O

Peak No	2θ (deg)	θ (deg)	Sinθ	Intensity (cps deg)	d (Å)		FWHM (deg)
					Calcd.	Obs.	
1	15.387	7.693	0.133	359.22	5.752	5.753	0.404
2	18.325	9.162	0.159	425.15	4.836	4.837	0.700
3	21.313	10.656	0.184	344.98	4.164	4.165	1.094
4	22.722	11.361	0.196	329.52	3.969	3.910	0.372
5	23.852	11.926	0.206	58.24	3.726	3.727	0.238
6	24.578	12.289	0.212	195.85	3.617	3.618	0.387
7	25.492	12.746	0.220	366.35	3.490	3.491	0.443
8	26.481	13.740	0.229	470.42	3.362	3.363	0.398
9	27.982	13.991	0.241	51.44	3.185	3.185	0.368
10	28.888	14.444	0.249	62.88	3.092	3.088	0.538

Table 2. Diffraction pattern of [Zn(L)₂Cl]Cl.H₂O

Peak No	2θ (deg)	θ (deg)	Sinθ	Intensity (cps deg)	d (Å)		FWHM (deg)
					Calcd.	Obs.	
1	16.362	8.184	0.142	144.34	5.411	5.413	0.561
2	20.268	10.134	0.176	10109.91	4.372	4.377	9.877
3	22.468	11.234	0.194	319.17	3.952	3.953	0.642
4	23.587	11.793	0.204	408.83	3.768	3.768	0.614
5	26.248	13.124	0.227	878.89	3.315	3.392	0.719
6	27.556	13.778	0.238	126.11	3.233	3.234	0.522
7	30.301	15.150	0.261	119.93	2.946	2.947	0.920
8	46.964	23.484	0.398	245.77	1.932	1.933	6.230

The diffraction patterns were further analyzed by using Debye Scherrer equation $D = K\lambda/\beta\cos\theta$ Where *D* = size of the particle, *K* = dimensionless shape factor, λ = wavelength of the X-ray (1.5406 Å), β = full width half maximum $\times 3.13/180$, θ = Bragg’s diffraction angle, the metal complexes [Ni(MPH)₂Cl₂]H₂O, [Cu(MPH)₂Cl]Cl.H₂O and [Zn(MPH)₂Cl]Cl.H₂O complexes are showing the nano-crystallinity size of 2.445, 11.225 and 20.275 nm respectively, while the other complexes exhibited amorphousness in nature (19). The

unit cell dimension can be calculated by using equation $a = 2r\sqrt{2}$ for Cu(II) and Zn(II) complexes. Where *r* is the atomic radius of corresponding metals. For copper: $a = 4.101\text{Å}$ and zinc: $a = 3.931\text{Å}$.

Thermo gravimetric analysis of metal complexes:

The thermogravimetric analysis was carried out in the temperature range 30–850 °C. Metal complexes of [Ni(MPH)₂Cl₂]H₂O, [Cu(MPH)₂Cl]Cl.H₂O and [Zn(MPH)₂Cl]Cl.H₂O

showed mass loss of calculated: 2.34, 2.32 and 2.31% (found: 2.44, 2.48 and 2.58%) in the temperature range 99-170 °C, 90-160 °C and 99-180 °C, showed the dissociation of water molecules. The second stage of mass loss involves in the temperature range 180-240 °C, 170-220 °C and 180-240 °C, mass loss 9.24, 9.18 and 9.11% (9.11, 10.01 and 9.24%) assigned to dissociation of two chlorine atoms, the next stage involves the dissociation in the temperature range 260-380 °C, 220-310 °C and 240-380 °C respectively, with weight loss 27.62, 27.45 and 27.24% (2.44, 2.48 and 2.58%) which corresponds to the decomposition of methoxy benzene moiety (20-21). The fourth step at 380-600 °C, 310-580 °C and 380-630 °C respectively, with weight loss 51.07, 50.75 and 51.71% (50.01, 49.08 and 51.88%) the removal of phenyl group moiety and the metal residue of NiO, CuO and ZnO with weight loss of 9.72, 10.28 and 9.10% (10.06, 10.30 and 9.18%) from 610-850 °C. Also, the TGA curves of the [Co(MPH)₂Cl₂] and [Mn(MPH)₂Cl]Cl showed three stages of degradation. The first stage from 180-240 °C and 180-230 °C with weight loss 9.46 and 9.51% (10.11 and 10.12%) was attributed to the loss of equivalent mass of two chlorine atoms, the second step with weight loss 28.28 and 28.39% (29.01 and

28.76%) from 220-305 °C and 240-330 °C corresponded to the removal of methoxy benzene moiety. In the third stage from 310-600 °C and 330-600 °C with weight loss 52.36 and 52.10% (51.66 and 50.88%) which involves in the removal of phenyl group moiety. The mass of the final residue, weight loss of 9.91 and 9.96% (10.22, and 10.17%) occur from 620-800 °C as stable metal residue of CoO and MnO. Degradation mechanism and kinetic and thermodynamic parameters of the synthesized complexes has been evaluated by Broido's graphical method for straight-line decomposition portion of the thermodynamic analytical curve (22). Energy of activation (E_a) were calculated by the slope of $\ln(\ln(1/y))$ versus $1/T \times 10^{-3}$. The thermodynamic properties like change in enthalpy (ΔH), entropy change (ΔS), free energy change (ΔG) and frequency factor ($\ln A$) are calculated using the standard equations by employing Broido's relation: $-\ln[\ln(1/y)] = E_a/RT_d - \ln A - \ln(8.314/T_d)$ where y is the fraction of the complex undecomposed, T_d is the decomposition temperature, R is the gas constant and E_a is the activation energy in kJ/mol. The nature of decomposition curve for metal complexes are represented in Figure 2.

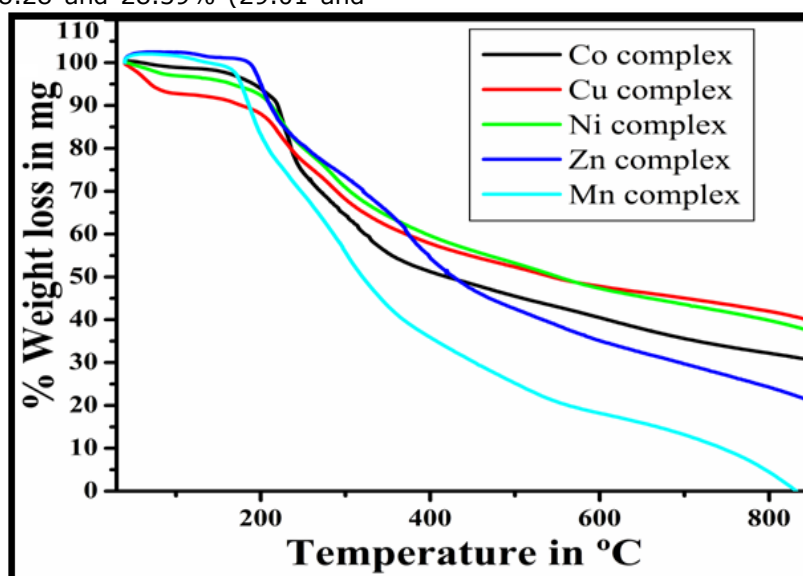


Figure 2: TGA curves of metal complexes.

The major weight loss for all the complexes was found in the temperature range 222.03-294.60 °C. The activation energies of zinc(II) complex (14.381 kJ/mol) and cobalt(II) complex (8.196 kJ/mol) were found to be very high, which accounts for their rapid degradation compared to nickel(II) complex (6.345 kJ/mol), manganese(II) complex (6.343 kJ/mol) and copper(II) complex (5.623 kJ/mol) that exhibit higher thermal stability was in the order of Zn > Mn > Co > Ni > Cu. The negative values of ΔS indicated that the decomposition reactions are slower than normal. The positive sign of ΔG values for the investigated complexes indicated that the free energy of the final residue was

higher than that of the initial compound and all the decomposition stages are non-isothermal processes. The major weight losses for all the complexes were found in the temperature range 222.03-294.60 °C. The activation energies of Zn(II) (14.381 kJ/mol) and Co(II) (8.196 kJ/mol) were found to be very high, which accounts for their rapid degradation compared to Ni(II) (6.345 kJ/mol), Mn(II) (6.343 kJ/mol) and Cu(II) (5.623 kJ/mol) that exhibit higher thermal stability was in the order of Zn > Co > Ni > Mn > Cu. The negative values of ΔS indicated that the decomposition reactions are slower than normal. The positive sign of ΔG values for the investigated complexes indicated

that the free energy of the final residue is higher than that of the initial compound and all the decomposition stages are non-isothermal processes.

Biological evaluation

Antioxidant activity:

The free radical scavenging ability of the synthesized ligand MPH and their metal complexes such as $[\text{Ni}(\text{L})_2\text{Cl}_2]\text{H}_2\text{O}$, $[\text{Co}(\text{L})_2\text{Cl}_2]$, $[\text{Cu}(\text{L})_2\text{Cl}]\text{Cl}\cdot\text{H}_2\text{O}$, $[\text{Zn}(\text{L})_2\text{Cl}]\text{Cl}\cdot\text{H}_2\text{O}$ and

$[\text{Mn}(\text{L})_2\text{Cl}]\text{Cl}$ were evaluated at different concentrations. The metal complexes found to be more potent antioxidant activity as compared to uncoordinated ligand. In which, the Co(II), Cu(II) and Zn(II) complexes assigning more antioxidant result approximately close to the standard butylated hydroxytoluene and Ni(II) and Mn(II) complexes exhibited moderate activity when compared with BHT. The activity is due the chelation of semicarbazone nucleus in the coordinated metal ion with the ligand (23). The results were shown Figure 3.

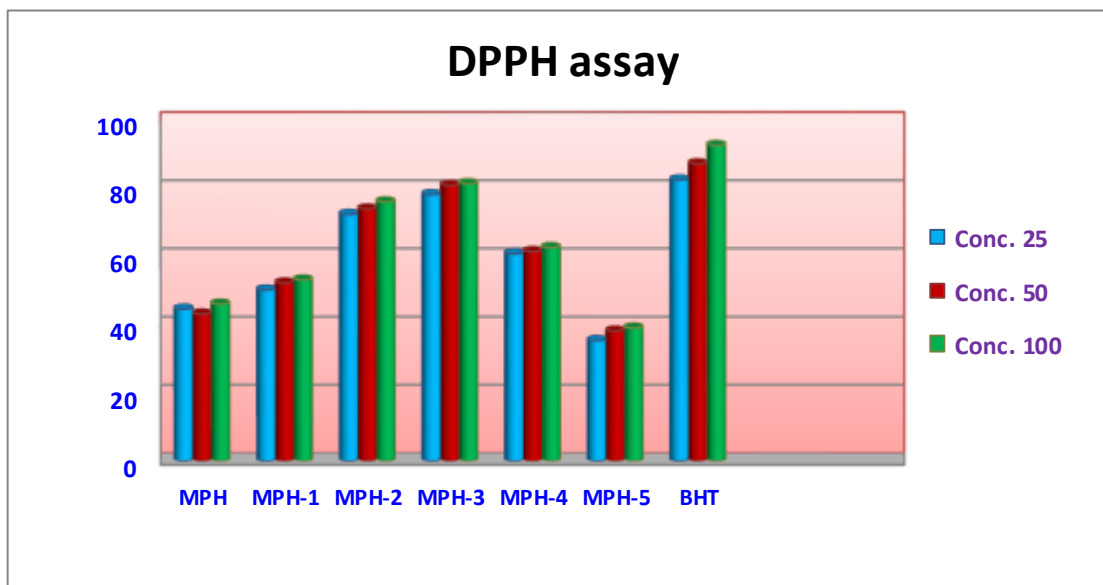


Figure 3: Antioxidant data of the ligand MPH and its metal complexes.

Molecular docking studies:

The docking studies of all the complexes showed prominent binding interactions, Co(II), Cu(II) and Zn(II) complexes offer the highest binding energy of -335.61, -329.54, -330.02 kcal/mol, while Ni(II) complex showed and -318.17 kcal/mol with human antioxidant 3MNG protein receptor by the key of amino acid residues are PHE128, LEU97, VAL39, LEU110, LEU125, GLY38, ARG127, HIS51, PHE37, GLY38, ARG127, HIS51, LEU36, VAL39, LEU125, LEU96, CYS72, LEU97, GLY38, ARG127, PHE37, MET130, LEU36, PHE29, ALA71, LEU97, VAL39, PRO40, LEU125, ARG127, and LEU36 (24). The

binding interaction of ligand with receptors amino acid residues shows conventional hydrogen bond, pi-alkyl and pi-sigma interaction bonds as shown in Figures 4 and 5. The interesting binding sites present in the receptor will favors the binding interaction with ligand, the computational docking studies were done for good docking scored complexes reveals that they showed good antioxidant inhibition activity (25-27). Finally, the results are good comparison for the wet analysis of antioxidant study. These results are shown in Table 3.

Table 3: Docking scores of metal complexes.

Compounds	Receptor PDB code	ΔG (kcal/mol)
MPH	3MNG	-240.51
$[\text{Ni}(\text{MPH})_2\text{Cl}_2]\text{H}_2\text{O}$	3MNG	-318.61
$[\text{Co}(\text{MPH})_2\text{Cl}_2]$	3MNG	-329.54
$[\text{Cu}(\text{MPH})_2\text{Cl}]\text{Cl}\cdot\text{H}_2\text{O}$	3MNG	-330.02
$[\text{Zn}(\text{MPH})_2\text{Cl}]\text{Cl}\cdot\text{H}_2\text{O}$	3MNG	-335.17

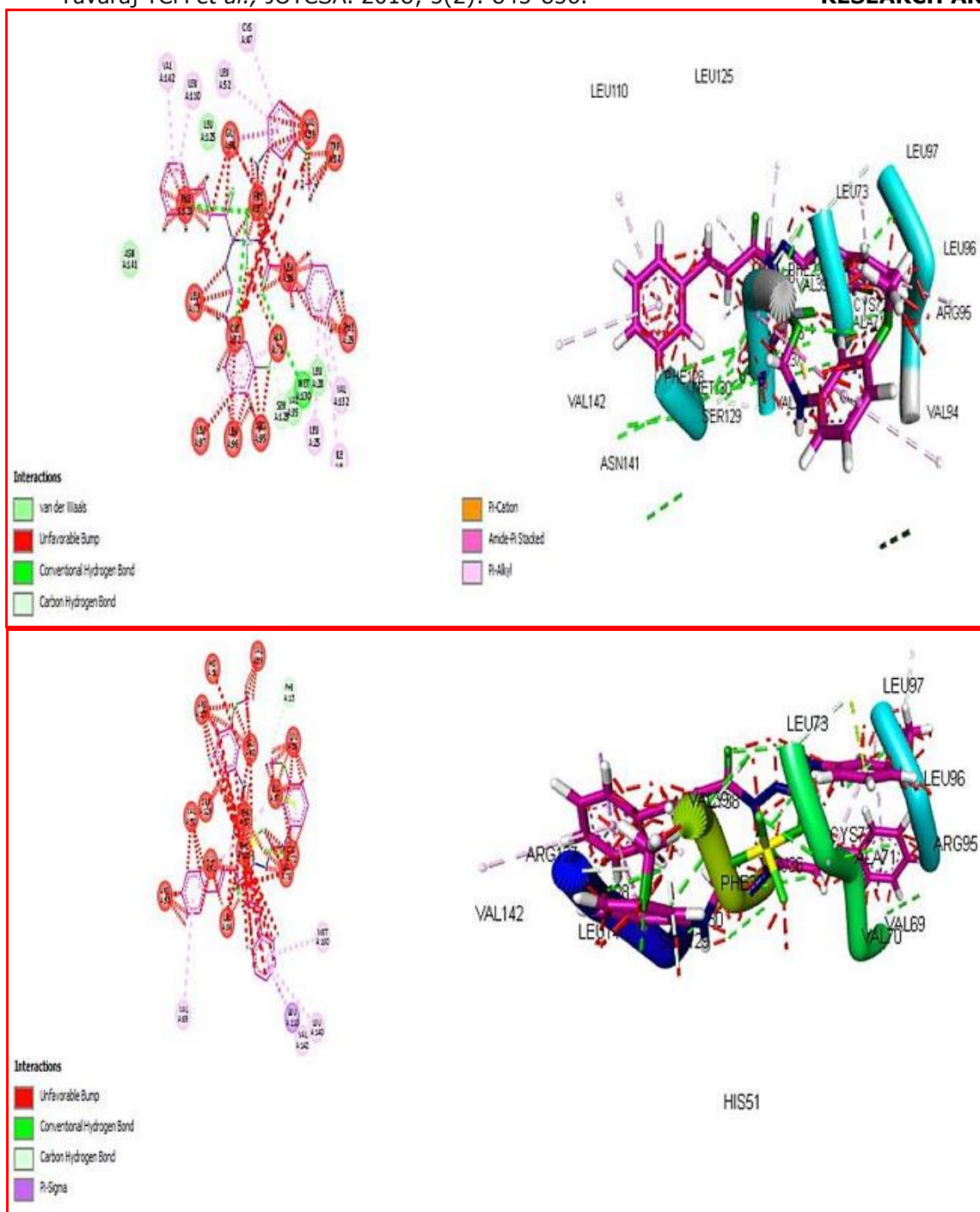


Figure 4: 3D & 2D binding interactions of $[Ni(L)_2Cl_2] \cdot H_2O$ and $[Co(L)_2Cl_2]$

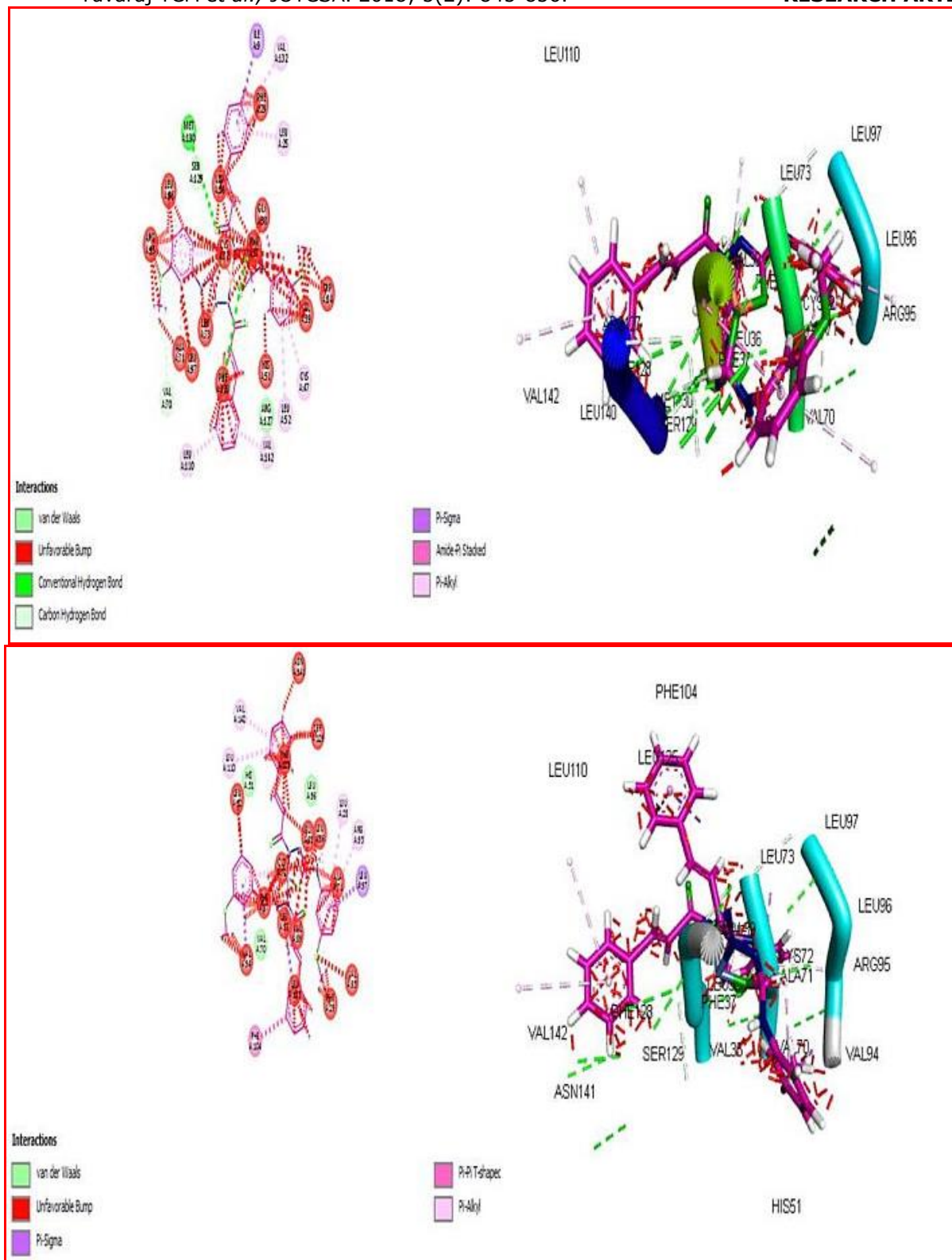


Figure 5: 3D & 2D binding interactions of $[\text{Cu}(\text{L})_2\text{Cl}]\text{Cl}\cdot\text{H}_2\text{O}$ and $[\text{Zn}(\text{L})_2\text{Cl}]\text{Cl}\cdot\text{H}_2\text{O}$

Antimicrobial activity:

The antibacterial and antifungal activity of the ligand and its metal complexes was evaluated against *S.aureus*, *B.subtilis* and *E.coli* bacteria by the agar well diffusion method using nutrient agar medium at $\pm 37^\circ\text{C}$, incubated for 24 hrs and potato dextrose agar (PDA) for fungal strains like *C. neoformans*, *C.albicans* and *A.niger* at $\pm 25^\circ\text{C}$, incubated for 48 to 78 hours.

Compounds were basically dissolved in DMSO and about 100 μL of this compound were filled to pre labelled wells using micropipette (28). DMSO used as negative control and chloramphenicol and fluconazole were used as standards (positive control) for bactericide and fungicide. All the synthesized complexes and the uncoordinated ligand showed inhibition property, among them Cu(II), Zn(II) and Mn(II)

complexes showed excellent activity when compared to standards and represented in Table 4. Our results showed that ligand MPH least activity against *S. aureus* with 03±0.3 mm zone of inhibition, but the complexes MPH₂, MPH₃ and MPH₄ indicated highest activity against *S. aureus* with zone of inhibition 13±0.1 mm. *B. subtilis* showed highest susceptibility against MPH₃, MPH₄ and MPH₅ with zone of inhibition 15±0.1 mm. the complexes MPH₃, MPH₄ and MPH₅

showed a significant antibacterial activity against *E. coli* with zone of inhibition 12±0.3 mm (29). In case of antifungal activity, the highest activity was observed in MPH₂ against *C. neoformans* with 10±0.6 mm zone of inhibition. *C. albicans* showed highest susceptibility against complexes MPH₃, MPH₄ and MPH₅ with zone of inhibition 10±0.1 mm respectively. Also, the complex MPH₂ showed highest activity aligned *A. niger* with 11±0.3 mm zone of inhibition.

Table 4: Zone inhibition of antimicrobial data

Compounds	Antibacterial zone inhibition in mm (mean ± SD)			Antifungal zone inhibition in mm (mean ± SD)		
	<i>S. aureus</i>	<i>B. subtilis</i>	<i>E. coli</i>	<i>C. neoformans</i>	<i>C. albicans</i>	<i>A. niger</i>
	Ligand	03±0.3	05±0.2	05±0.7	04±0.4	03±0.1
MPH₁	06±0.3	-	07±0.3	08±0.2	-	06±0.3
MPH₂	14±0.2	12±0.4	10±0.2	10±0.6	09±0.2	11±0.3
MPH₃	13±0.1	15±0.1	12±0.3	08±0.4	10±0.1	10±0.3
MPH₄	13±0.1	15±0.1	12±0.3	08±0.4	10±0.1	10±0.3
MPH₅	13±0.1	15±0.1	12±0.3	08±0.4	10±0.1	10±0.3
Chloramphenicol	15±0.2	16±0.3	13±0.3	12±0.2	11±0.4	13±0.3
Fluconazole	-	-	-	12±0.2	10±0.1	12±0.3
DMSO	0	0	0	0	0	0

CONCLUSION

In the present work, the ligand and a series of its metal complexes [Ni(MPH)₂Cl₂].H₂O, [Co(MPH)₂Cl₂], [Cu(MPH)₂Cl].Cl.H₂O, [Zn(MPH)₂Cl].Cl.H₂O and [Mn(MPH)₂Cl].Cl have been synthesized by a conventional method. The obtained compounds were analyzed by various spectroscopic techniques. Thermogravimetric analyses curve explains step by step degradation and the results are also supported the stability of metal complexes in the order of Zn(II) > Mn(II) > Co(II) > Ni(II) > Cu(II) complexes. The synthesized ligand is bidentate and coordinates through the nitrogen and carbonyl oxygen atoms of semicarbazone derivative. The two chlorine atoms also occupy the two sites of each metal giving an octahedral geometry for nickel(II) and cobalt(II) complexes. However, copper(II) complex is square pyramidal. The 2D and 3D binding interactions of all metal complexes exhibited highest binding energy scores as compared to ligand with human 3MNG protein receptor. In case of antioxidant activity, the cobalt(II), copper(II), and zinc(II) complexes showed better results than other complexes. The complexes were also screened for antimicrobial and molecular docking studies. The results are suggested that the complexes more prominent when compared to uncoordinated ligand, but

less prominent in comparison with standard drugs.

ACKNOWLEDGEMENT

The authors thank Sahyadri Science College Shivamogga and Manipal Institute of Technology for providing analytical data analysis. Manipal, Karnataka, INDIA.

REFERENCES

1. Asghar SF, Yasin KA, Habib-ur-Rehman, Aziz S. Synthesis and cyclisation of 1,4-disubstituted semicarbazides. Natural Product Research. 2010 Mar 10;24(4):315–25
2. Rajesh-Rane A, Shital-Naphade S, Pavan Kumar, Mahesh Palkar B, Mahamadhanif Shaikh S, Rajshekhkar Karpoomath. Synthesis of novel 4-nitropyrrole-based semicarbazide and thiosemicarbazide hybrids with antimicrobial and anti-tubercular activity. Bioorganic & Medicinal Chemistry Letters. 2014 Jul 24; 10: 3079-3083.
3. Pituchaa M, Karczmarzykb Z, Kosikowska U, and Malm A. Synthesis, Experimental and Theoretical Study on the Structure of Some Semicarbazides with Potential Antibacterial Activity. Zeitschrift für Naturforschung B. 2011 Apr 66;(5) 971-87

4. Rafat-Mohareb M. and Abeer Mohamed A. Uses of 1-Cyanoacetyl-4-Phenyl-3-Thiosemicarbazide in the Synthesis of Antimicrobial and Antifungal Heterocyclic Compounds. *International Research Journal of Pure & Applied Chemistry*. 2012 Jul 2(2): 2012 144-155,
5. Gursoy A, Terzioglu N, Otuk G. Synthesis of some new hydrazide-hydrazones, thiosemicarbazides and thiazolidinones as possible antimicrobials. *European Journal of Medicinal Chemistry*. 1997 Jun 32(9):753-757.
6. Narang KK, Singh VP. Synthesis and characterization of cobalt (II), nickel (II), copper (II) and zinc (II) complexes with acetylacetone bis-benzoyl hydrazone and acetylacetone bis isonicotinoyl hydrazone. *Transition Metal Chemistry*. 1993 Dec 10(18): 287-290.
7. El-Azab AS, El-Tahir KEH. Synthesis and anticonvulsant evaluation of some new 2,3,8-trisubstituted-4(3H)-quinazoline derivatives. *Bioorganic & Medicinal Chemistry Letters*, 2012 Oct 22(1): 327-333.
8. Aly MM, Mohamed YA, El-Bayouki KAM, Basyouni WM, Abbas SY. Synthesis of some new 4(3H)-quinazolinone-2-carboxaldehyde thiosemicarbazones and their metal complexes and a study on their anticonvulsant, analgesic, cytotoxic and antimicrobial activities. *European Journal of Medicinal Chemistry*, 2010 Apr 45(8): 3365- 3373.
9. Azam F, Alkskas IA, Khokra SL, Prakash O. Synthesis of some novel N 4 - (naphtha[1,2-d]thiazol-2-yl) semicarbazides as potential anticonvulsants. *European Journal of Medicinal Chemistry*. 2009 Nov 44(1): 203-211.
10. Shashikumar ND, Krishnamurthy G, Bhojya-Naik HS, Lokesh MR, Jithendra-kumara KS. Synthesis of new biphenyl-substituted quinoline derivatives, preliminary screening and docking studies. *Journal of chemical sciences*. 2014 Jan 126(1): 205-212.
11. Manjuraj T, Krishnamurthy G, Yadav D. Bodke, BhojyaNaik H.S, Metal complexes of quinolin-8-yl [(5-methoxy-1H-benzimidazol-2-yl)sulfanyl]acetate: Spectral, XRD, thermal, cytotoxic, molecular docking and biological evaluation. *Journal of Molecular Structure*, Volume 1148, (15): 2017; 231-237.
12. Nakamoto K, *Infrared and Raman Spectra of Inorganic and Coordination Compounds*. In:Chalmers JM, Griffiths PR, editors. *Handbook of vibrational spectroscopy*, Chichester, UK: John Wiley & Sons, Ltd; 2006.
13. Sangeetha Gowda KR, Bhojya-Naik HS, Vinay-Kumar B, Sudhamani CN, Sudeep HV, Ravikumar-Naik TR, Krishnamurthy G. Synthesis, antimicrobial, DNA-binding and photonuclease studies of Cobalt(III) and Nickel(II) Schiff base complexes. *Spectrochimica Acta Part A: Molecular and Biomolecular Spectroscopy*. 2013 Jun 105(10): 229-237.
14. Emelda AR, Jayachandramani N, Ravichandran S. Synthesis, Characterization and Antimicrobial Study of a New Mannich Base, N-(1-Piperidinobenzyl)benzamide and its Transition Metal(II) Complexes. *Asian Journal of Chemistry*. 2008 Feb 2(20): 2485-2490.
15. Ashraf A, Siddiqui WA, Akbar J, Mustafa G, Krautscheid H, Ullah N. Metal complexes of benzimidazole derived sulfonamide: Synthesis, molecular structures and antimicrobial activity. *Inorganic Chimca Acta*. 2016 Mar (443): 179-85.
16. Lever A.B.P. *Inorganic electronic spectroscopy*. 2nd ed. Amsterdam ; New York: Elsevier; 1984 863.
17. El-Gammal OA, Mostafa MM. Synthesis, characterization, molecular modeling and antioxidant activity of Girard's T thiosemicarbazide and its complexes with some transition metal ions *SpectrochimicaActa Part A: Molecular and Biomolecular Spectroscopy*,2014 Mar(127): 530-42.
18. Rahaman F, Mruthyunjayaswamy BHM. Synthesis, spectral characterization and biological activity studies of transition metal complexes of Schiff base ligand containing indole moiety. *Complex Metals*. (31): (2014); 88-95.
19. Bal M, CEYHAN G, AVAR B, KÖSE M, Kayraldiz A, KURTOĞLU M. Synthesis and X-ray powder diffraction, electrochemical, and genotoxic properties of a new azo-Schiff base and its metal complexes. *Turkish journal of chemistry*. 2014 Apr 17;38(2):222-41.
20. Joseph J, Mehta HB. Synthesis, characterization, and thermal analysis of transition metal complexes of polydentate ONO donor Schiff base ligand. *Russian Journal of Coordination Chemistry*. 2007 Mar 12(33): 124-129.
21. Donia A. M, Al-Ansi T. Y and Othman M. Q., *Journal of Thermal Analysis*. (50) 1997 857.
22. Venugopala Reddy KR, Keshavayya J, Seetharamappa J. Synthesis, spectral, magnetic and thermal studies on symmetrically substituted metal (II) 1,3,8,10,15,17,22,24-octachloro phthalocyanines, *Dyes Pigments*, 2003 Nov (59):237-244.
23. Yapati H, Devineni S.R, Chirumamilla S, Kalluru S. Synthesis, characterization and studies on antioxidant and molecular docking of metal complexes of 1-(benzo[d]thiazol-2-

- Yuvaraj TCM *et al.*, JOTCSA. 2018; 5(2): 845-856.
- yl)thiourea. Journal of Chemical Sciences. 2016 Jan (128): 43-51.
24. Harinath Y, Subbarao D, Suresh C, Sessaiah K. Synthesis, characterization and studies on antioxidant and molecular docking of metal complexes of 1-(benzo[d]thiazol-2-yl)thiourea. Journal of Chemical Sciences. 2016 Jan 128(1): 43-51.
25. Hall Parsonage D, Poole LB, Karplus PA. Structural evidence that peroxiredoxin catalytic power is based on transition-state stabilization. Journal of Molecular Biology. 2010 10; 402(1)194-209.
26. Abdel Nasser MA, Alaghaz-Badr A, El-Sayed A, Ahmed, El-Henawy, Reda, Ammar AA. Synthesis, spectroscopic characterization, potentiometric studies, cytotoxic studies and molecular docking studies of DNA binding of transition metal complexes with 1,1-diaminopropane-Schiff base. Journal of Molecular Structure, 2013 Dec 1035(12): 83-93.
- RESEARCH ARTICLE**
27. Mohammed Shafeeulla R, Ganganai Krishnamurthy, Halehatti S. Bhojyanaik, Manjuraj T. Synthesis, Cytotoxicity, and Molecular Docking Study of Complexes Containing Thiazole Moiety. JOTCSA. 2017 Aug 4(3): 787-810.
28. Bhimagouda-Patil S, Krishnamurthy G, Bhojya-Naik HS, Prashant R. Latthe, Manjunath-Ghate. Synthesis, characterization and antimicrobial studies of 2-(4-methoxy-phenyl)-5-methyl-4-(2-arylsulfanyl-ethyl)-2,4-dihydro-[1,2,4] triazolo-3-ones and their corresponding sulfones. European Journal of Medicinal Chemistry 12(45): 3329-3334.
29. Jayamani A, Sengottuvelan N, Chakkaravarthi G, Synthesis, structural, electrochemical, DNA interaction, antimicrobial and molecular docking studies on dimeric copper(II) complexes involving some potential bidentate ligands. Polyhedron 2014 Feb 81(12): 764-76.



Elemental analysis of henna samples by MP AES

Nil OZBEK ^{1*} 

¹ Department of Chemistry, Science and Letters Faculty, Istanbul Technical University, Istanbul, Turkey.

Abstract : In this study, a new methodology using microwave-induced plasma atomic emission spectrometry (MP AES) after microwave assisted digestion been developed to determine aluminum, boron, cadmium, cobalt, chromium, copper, iron, lead, manganese, molybdenum, nickel, and tin concentrations in 18 commercial henna samples purchased from markets in Turkey. For the elemental determination, 0.100 g henna sample weighed and digested with 10 mL of HNO₃+H₂O₂ (3:1) mixture in a microwave digestion system. The analytes in certified reference material bush branches and the leaves were determined in the uncertainty limits of the certified values as well as the analytes added to the henna sample prior the digestion were recovered quantitatively (95-105 %). Finally found results in henna samples were compared with several regulations from different countries as well as other published results.

Keywords: Microwave Induced Plasma Optical Emission Spectrometry, henna, *Lawsonia inermis*.

Submitted: May 15, 2018. **Accepted:** July 03, 2018.

Cite this: Ozbek N. Elemental analysis of henna samples by MP AES. JOTCSA. 2018; 5(2):857–66.

DOI: <http://dx.doi.org/10.18596/jotcsa.423820>.

Corresponding Author: E-mail: nil.ozbek@itu.edu.tr

INTRODUCTION

Henna is a dye prepared from the *Lawsonia inermis*, plant, which is found in hot climates such as Egypt, India, Africa, and Morocco. Originally, henna was used in Egypt. It is well documented that Cleopatra used henna for cosmetic purposes. It is mainly used for dyeing the skin, hair, and nails, and as a component for some cosmetic products (1). Since it is believed to create healthy and beautiful hair, it is also used as a common hair product, as a natural component for shampoos and

conditioners (2). Henna is also applied as a temporary tattoo on hands and feet for cosmetic purposes. Since it is not permanent and is painless, cheap and carries no risk of HIV or hepatitis infections, it is highly popular among children and young adults (1, 3).

Lawsone, primarily concentrated in the petioles of the leaves of *Lawsonia inermis*, causes staining or dyeing. However, they must be crushed in order to release the lawsone molecules contained within the leaf. Once released, the lawsone gradually binds to the

outer layer of the proteins in the skin or hair, thus staining or dyeing it. Its characteristic staining properties are caused by the compound 2-hydroxy-1,4-naphthoquinone, which is also known as hennotannic acid. Leaves of henna contain this compound up to 5% by weight. Since hennotannic acid does not dissolve in water, henna leaves are mixed with a mild acidic agent (*i.e.* lemon juice, and strong tea, *etc.*) to release it from the plant. In order to enhance the scent of henna paste, various oils and herbs may also be added. One day after mixing, the activation of dye is completed. But after three days, it loses staining capabilities. The lawsone dye does not chemically alter the skin and hair so there is no permanent change. Since the dye molecules, 2-hydroxy-1,4-naphthoquinone, are about the same size as amino acid molecules, they migrate from the outermost layer of the skin or hair.

Natural henna, while being totally organic and natural, is altered by additives such as p-phenyldiamine (PPD), eucalyptus oil, black tea, vinegar, lemon oil, clove oil, mustard oil or coffee powder to obtain different colors in the applications (4, 5). Natural henna is relatively safe but these additions may cause allergic reactions; moreover, heavy metal concentrations of these enhanced types of hennas are reportedly high (6). In a previous study, heavy metals such as chromium, cobalt, nickel and lead were found in black

henna tattoo samples (4). Moreover, as an allergic reaction to cobalt and lead in henna, contact dermatitis were observed in a patient (7).

Some non-essential heavy metals like cadmium, mercury and lead, can damage biological structures and cause health problems even at the lowest concentrations (8). These metals can have toxic effects by ingestion, inhalation, and by skin exposure (9). The Canadian Government determined heavy metal impurity concentrations in cosmetic products as 5 ppm for antimony, 3 ppm for arsenic, 3 ppm for cadmium, 10 ppm for lead and 1 ppm for mercury (10). Heavy metal concentrations in cosmetic products in Germany are also limited to 0.5 ppm for antimony, 0.5 ppm for arsenic, 0.1 ppm for cadmium, 2.0 ppm for lead and 0.1 ppm for mercury (11). U.S. Food and Drug Administration (FDA) limited lead and arsenic content of henna (as a color additive for cosmetic products) as not more than 20 ppm and 3 ppm, respectively (12). In this context, levels of different elements should be determined in henna samples. Till now, potential stripping analysis (PSA) (13), graphite furnace and flame atomic absorption spectrometry (GFAAS and FAAS) (14-17) and inductively coupled plasma atomic emission and mass spectrometry (ICP-AES and ICP-MS) (2, 4, 18) have been used for determination of different elements in henna samples (Table 1).

Table 1: Available methods for determination of different elements in henna samples.

Sample	Method	Elements (Ranges)	Ref
Henna (3 Samples)	PSA	Pb (8.52-19.61 $\mu\text{g g}^{-1}$) Zn (<LOD-490 $\mu\text{g g}^{-1}$)	(13)
Henna (7 Samples)	GFAAS	Pb (2.20-19.9 $\mu\text{g g}^{-1}$)	(16)
Henna (15 samples)	FAAS	Ni (2940-3900 $\mu\text{g g}^{-1}$) Co (2960-3540 $\mu\text{g g}^{-1}$)	(15)
Henna (4 Samples)	ICP-AES	Al (610-3293 $\mu\text{g g}^{-1}$) Cr (33-86 $\mu\text{g g}^{-1}$) Cu (7.0-21 $\mu\text{g g}^{-1}$) Fe (750-2404 $\mu\text{g g}^{-1}$) Mn (65-120 $\mu\text{g g}^{-1}$) Ni (<LOD-8.0 $\mu\text{g g}^{-1}$)	(18)
Henna (20 Samples)	GFAAS	Pb (1.29-16.48 $\mu\text{g g}^{-1}$)	(14)
Henna (12 Samples)	ICP-AES	Pb (2.29-65.98 $\mu\text{g g}^{-1}$)	(2)
Henna (5 Samples)	ICP-MS	Cr (35.0-76.9 $\mu\text{g g}^{-1}$) Co (0.44-3.11 $\mu\text{g g}^{-1}$) Ni (1.13-2.20 $\mu\text{g g}^{-1}$) Pb (1.59-17.7 $\mu\text{g g}^{-1}$)	(4)

Microwave Induced Plasma Atomic Emission Spectrometry (MP AES) is a plasma technique which uses 2.45 GHz microwave magnetic field and nitrogen gas to sustain the plasma (Figure 1). In this technique, since nitrogen generator is used, flammable and toxic gasses are not required. Nitrogen plasma have relatively higher temperature than the flame of AA, which makes possible to determine refractive and carbide forming elements. This technique has recently become commercialized, so the number of papers regarding the applications of MP AES on different samples are relatively low when compared to the AAS and ICP techniques

(19, 20). It was recently used for different elemental determination in various matrices, *i.e.* gasoline and ethanol fuel (21), diesel and biodiesel (22), animal feed and fertilizer (23), steel (24), wine (25), cheese (26), leather and fur (27), maize seed (28), vinegar (29), bread (30) and tarhana (sundried food made of curd, tomato and flour) (31) and geological samples (32). Total dissolved salt (TDS) content limitation of the sample is the only drawback of the method. When TDS of the solution is above 4%, with the aspiration of sample, a critical damage to the torch may occur due to the accumulation of salt residues.

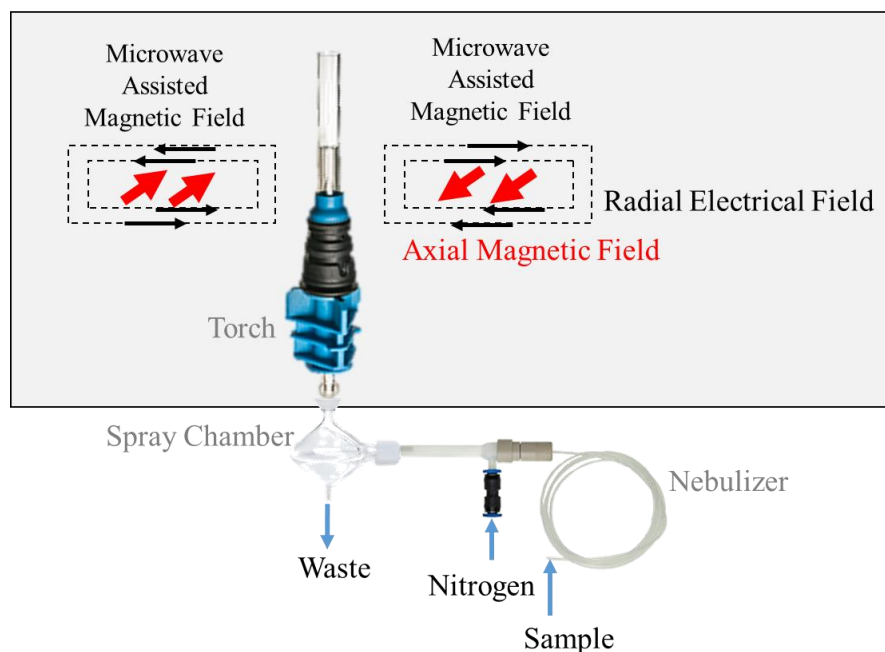


Figure 1: Schematic of Microwave Induced Plasma Atomic Emission Instrument.

In this paper, a novel and easy method were developed for the determination of aluminum, boron, cadmium, chromium, cobalt, copper, iron, manganese, molybdenum, nickel, lead and tin concentrations in 18 commercial henna samples sold in Turkey by MP AES.

MATERIALS AND METHODS

Instrumental

An Agilent 4200 Microwave Induced Plasma Atomic Emission Spectrometer (MP OES) (Agilent Technologies, Melbourne, Australia) equipped with an Inert One Neb nebulizer and a double-pass glass cyclonic spray chamber (Agilent Technologies, Melbourne, Australia) were used throughout this study. Nitrogen was extracted from the air using an F-DGSi, Thyster 8/1 LV, (Innovative Gas System Co., Evry, France), dual flow *nitrogen* generator.

The sample and waste tubings were orange/green and blue/blue solvent resistant, respectively (Agilent Technologies, Melbourne, Australia). Before every sample reading, 10 seconds of uptake time and 20 seconds of torch stabilization time were set, whereas for the emission measurement of each sample, 5 seconds read time with 3 replicates were applied. The torch alignment and wavelength calibration were optimized using a wavelength calibration solution (Agilent Technologies, Melbourne, Australia). The instrumental parameters for MP AES are given in Table 2. Samples were weighed using a Model XR 205SM-DR Precisa 5-digits balance with 0.01 mg readability. For digestion procedure, Topwave microwave-assisted digestion system (Analytik Jena, Berlin, Germany) equipped with pressure controlled Teflon vessels (50 mL) were used.

Table 2: Optimized instrumental parameters and figures of merit for the method.

	Al	B	Cd	Co	Cr	Cu
Wavelength, nm	396.15	249.77	228.80	340.51	425.43	324.75
Ion Type	I	I	I	I	I	I
Viewing Position	0.00	0.00	0.00	0.00	0.00	0.00
Nebulizer Flow, L min ⁻¹	0.85	0.40	0.45	0.65	0.95	0.75
Background Correction	Auto	Auto	Auto	Auto	Auto	Auto
Uptake Time, sec	15.00	15.00	15.00	15.00	15.00	15.00
Stabilization Time, sec	20.00	20.00	20.00	20.00	20.00	20.00
LOD, µg L ⁻¹	1.58	1.14	3.56	4.39	1.19	0.30
LOQ, µg L ⁻¹	5.28	3.79	11.8	14.6	3.98	0.99
Regression Coefficient, r ²	0.999	0.998	0.999	0.999	0.999	0.999
Calibration Curve Equation	44476.694C- 1767.305	17404.721C- 1060.608	23016.624C +86.113	34681.460C+ 144.598	50288.135C +12.838	137723.124C -23.418
Linearity, mg L ⁻¹	LOQ -10	LOQ -10	LOQ -5	LOQ -10	LOQ -10	LOQ -10
	Fe	Mn	Mo	Ni	Pb	Sn
Wavelength, nm	371.99	403.08	379.83	352.45	405.78	317.51
Ion Type	I	I	I	I	I	I
Viewing Position	0.00	0.00	0.00	0.00	0.00	0.00
Nebulizer Flow, L min ⁻¹	0.80	0.75	0.80	0.30	0.65	0.90
Background Correction	Auto	Auto	Auto	Auto	Auto	Auto
Uptake Time, sec	15.00	15.00	15.00	15.00	15.00	15.00
Stabilization Time, sec	20.00	20.00	20.00	20.00	20.00	20.00
LOD, µg L ⁻¹	3.51	0.333	0.987	8.43	2.43	7.71
LOQ, µg L ⁻¹	11.71	1.11	3.29	28.1	8.11	25.7
Regression Coefficient, r ²	0.999	0.999	0.999	0.998	0.999	0.998
Calibration Curve Equation	11874.461C- 9.994	50176.156C+ 17.206	40646.008C- 64.484	7945.255C+8 6.744	8314.895C+ 51.168	3652.684C+ 146.860
Linearity, mg L ⁻¹	LOQ -10	LOQ -10	LOQ -10	LOQ -10	LOQ -10	LOQ -10

*C: concentration, mg L⁻¹.

Reagents and Solutions

For the preparation of the solutions, the water with 18.2 MΩ cm resistivity obtained from a TKA reverse osmosis and a deionizer system (TKA Wasseraufbereitungsstandards, system GmbH, Niederelbert Germany) were used. The calibration standards were prepared from a mixed standard which included 1000 mg L⁻¹ of Al, B, Cd, Co, Cr, Cu, Fe, Mn, Mo, Ni, Pb, and Sn (Carlo Erba, Radona, Italy) daily. For accuracy tests, certified reference material, bush branches and leaves CRM from the China

National Analysis Center for Iron and Steel (Beijing, China) were used.

Procedure

Before starting the experiments, eighteen henna samples were bought from different locations in Istanbul. They and the certified reference materials were stored in polyethylene bags and kept at room temperature. Prior to the analysis, the samples were dried at 50 °C in an air-ventilated oven for 12 h. The samples were allowed to cool over silica gel and stored in

tightly closed folding polyethylene cups. All the samples were ground manually in an agate mortar. A topwave microwave-assisted digestion system (Analytik Jena, Berlin, Germany) equipped with pressure controlled Teflon vessels (50 mL) were used for the sample digestion. Each sample was weighed around 0.1 g with 0.1 mg sensitivity and

underwent microwave-assisted digestion using 10 mL of $\text{HNO}_3+\text{H}_2\text{O}_2$ (3:1) mixture. After the microwave digestion program, the digested samples were allowed to cool down and then completed to 10 mL. The microwave-assisted digestion program is shown in Table 3.

Table 3: The microwave-assisted digestion programme for the digestion of henna samples.

Temperature (°C)	Pressure (bar)	Ramp (min)	Time (min)	Power (%)
180	60	36	5	90
180	60	1	15	90
50	50	10	10	0
50	50	10	10	0
50	50	10	10	0

RESULTS AND DISCUSSION

Instrumental Optimization

The main limitation of this technique is the total dissolved salt (TDS) concentration of the samples. In case of excess salt concentration in the sample, the accumulation of salts may cause blockages of the torch and the nebulizer. For the 4200 MP AES system, the limiting TDS concentration is 4%. This problem can be avoided using diluted solutions. However, while the dilution of the sample reduces the TDS concentration and the risk of damaging the torch and nebulizer, diluting the sample too much may cause the concentration of the analyte falling under LOD. Therefore, selecting the appropriate emission wavelength and optimum dilution factor is an important step for this analysis.

First of all, optimum wavelengths were selected for highest sensitivity and lowest spectral interference. After several experiments 396.15 nm, 249.77 nm, 228.80 nm, 340.51 nm, 425.43 nm, 324.75 nm, 371.99 nm, 405.78 nm, 403.08 nm, 379.83 nm, 352.45 nm, and 317.51 nm were selected

as most appropriate wavelengths for aluminum, boron, cadmium, cobalt, chromium, copper, iron, lead, manganese, molybdenum, nickel, and tin respectively. Then, automatic optimization for nebulizer pressure and viewing position were done by the instrument for the highest sensitivity (Table 1). Finally, the dilution factor was determined. It is important to determine the optimum dilution factor in order to prevent deflections at the torch and stay above LOD for all the analytes. After several tries, it was decided to dilute all samples to 10 mL in order to stay in the linear range of all elements and generally above LOD. Some further dilution were needed for some samples in order to determine aluminum and iron. With this dilution factors, samples did not cause any damage to the torch during the whole study.

Figures of Merit

Limit of detection and quantification (LOD and LOQ) were calculated as figures of merit for the method. The limit of detection (LOD) and the limit of quantification (LOQ) were calculated as 3 and 10 times the standard

deviation (σ) for 10 repetitive aspiration of a blank used for the digestion of samples were divided by the slope of linear calibration graph (3σ and 10σ /slope of calibration graph), respectively. The figures of merit are given in Table 1.

In order to test the accuracy of the method, the analytes in a certified reference material

(CRM) were determined. Since henna CRM could not be found, a plant based CRM, NCS DC 73349-bush branches and leaves were used. As can be seen from Table 4, the accuracy test showed that there were no systematical errors (due to the balance, pipettes, flasks, and impurities of the reagents etc.).

Table 4: Accuracy tests for CRM (NCS DC 73349-bush branches and leaves) (n:4).

	Certified Value ($\mu\text{g g}^{-1}\pm\text{SD}$)	Found Value ($\mu\text{g g}^{-1}\pm\text{SD}$)
Al	2000 \pm 300	1995 \pm 80
B	38 \pm 6	35.2 \pm 8
Cd	(0.38)	0.40 \pm 0.01
Co	0.41 \pm 0.05	0.39 \pm 0.06
Cr	2.6 \pm 0.2	2.8 \pm 0.1
Cu	6.6 \pm 0.8	7.2 \pm 0.1
Fe	1070 \pm 57	999 \pm 32
Mn	61 \pm 5	64 \pm 5
Mo	0.28 \pm 0.05	0.22 \pm 0.5
Ni	1.7 \pm 0.3	2.0 \pm 0.1
Pb	47 \pm 3	43 \pm 3
Sn	(0.27)	0.17 \pm 0.11

*Data enclosed in the brackets show uncertified values, given as reference only in the certificate.

In order to validate the results, recovery tests were conducted also. In order to find out if there is any analyte lost in digestion step, analytes were added to henna samples prior the digestion step. As can be seen from Table 5, added elements were completely recovered. This shows that the sensitivity (emission

intensities) were not influenced from the sample matrix and there is no analyte loss during sample preparation step. The obtained recoveries were between 95 to 105 %, which allows us to use linear calibration technique without needing standard addition technique.

Table 5: Recoveries of analytes added to a henna sample prior to the digestion step.

	Addition	Recovery (%)
Al	0.1 mg g ⁻¹	95.7
B	10 $\mu\text{g g}^{-1}$	97.3
Cr	10 $\mu\text{g g}^{-1}$	96.7
Cu	10 $\mu\text{g g}^{-1}$	98.4
Fe	1 mg g ⁻¹	96.4
Mn	10 $\mu\text{g g}^{-1}$	101.2
Ni	10 $\mu\text{g g}^{-1}$	97.3
Pb	10 $\mu\text{g g}^{-1}$	95.6

Finally, in Table 6, the concentrations of aluminum, boron, cadmium, cobalt, chromium, copper, iron, manganese, molybdenum, nickel, lead, and tin in the henna samples are given. As can be seen from the table, Cd, Co, Mo and Sn concentrations are under their respective LOD values ($0.356 \mu\text{g g}^{-1}$ for Cd, $0.439 \mu\text{g g}^{-1}$ for Co, $0.0333 \mu\text{g g}^{-1}$ for Mo and $0.771 \mu\text{g g}^{-1}$ for Sn). After all the optimizations, there is no accumulation of deposits in the torch during the whole analysis. Repeatability of the results were checked by the RSDs of the emissions, which were below 10% for all the analytes on the same day. In 18 different henna samples bought from Turkey, Fe ($0.26\text{-}3.17 \text{ mg g}^{-1}$) and Al ($0.122\text{-}5.22 \text{ mg g}^{-1}$) were the most abundant elements. On basis of the overall mean levels, the mean heavy metal levels were in the following order Fe ($0.26\text{-}3.17 \text{ mg g}^{-1}$) > Al ($0.122\text{-}5.22 \text{ mg g}^{-1}$) > Mn ($15.5\text{-}188 \mu\text{g g}^{-1}$) > B ($4.5\text{-}71.6 \mu\text{g g}^{-1}$) > Cr ($0.70\text{-}54.4 \mu\text{g g}^{-1}$) > Ni ($6.50\text{-}25.2 \mu\text{g g}^{-1}$) > Cu ($2.70\text{-}67.6 \mu\text{g g}^{-1}$) > Pb ($6.50\text{-}17.4 \mu\text{g g}^{-1}$) which were similar with previous studies. Found concentrations were below the limits regulated by the FDA (12) and Canadian Government (10), except for some lead values for Canadian Government. Lead values also exceeded the limits regulated by Germany (11).

CONCLUSION

In this study, MP AES was used to analyze henna samples after wet digestion procedure. Various elements were determined (aluminum, boron, cadmium, cobalt, chromium, copper, iron, lead, manganese, molybdenum, nickel, and tin) in henna samples. This technique offers multiple benefits over other methods, such as fast sequential determination of multiple elements with lower detection limits when compared to FAAS. Since there is no need to change and optimize lamps, there is no need of a complicated procedure for optimization. Each element was optimized by the software automatically in a few minutes. Sample consumption is also very low when compared to AAS methods (around 2 mL for 10 elements). Moreover, since there is no use of flammable gases and nitrogen is extracted from air by a nitrogen generator, this method is safer and has low running costs when compared to other emission techniques. To conclude, a fast, practical, and environmentally friendly and also a safe procedure was developed. Determined concentration values of 18 henna samples were below regulated limits except lead concentrations. With this study, it is proved that MP AES can be use to determine elemental values in cosmetic industry.

Table 6: Metal concentrations in various kinds of henna samples determined by MP AES (Mean Values±SD, n:4).

Brand	Place of Origin	Color of Henna	Expected Color Effect	Al	B	Cr	Cu	Fe	Mn	Ni	Pb
				mg g ⁻¹	µg g ⁻¹	µg g ⁻¹	µg g ⁻¹	mg g ⁻¹	µg g ⁻¹	µg g ⁻¹	µg g ⁻¹
BRAND 1	Iran	Green	ND	0.122±0.001	<LOD	<LOD	2.70±0.162	0.24±0.015	15.5±0.653	<LOD	<LOD
BRAND 2	Iran	Green	ND	0.743±0.035	14.2±0.712	44.4±1.61	11.8±0.85	1.31±0.079	149±7.46	10.2±0.421	7.82±0.421
BRAND 3	Iran	Green	ND	1.25±0.063	18.2±0.861	0.70±0.042	11.9±0.65	2.61±0.134	188±9.35	11.6±0.543	17.4±0.542
BRAND 4	India	Green	ND	1.22±0.061	18.4±0.744	8.20±0.511	9.50±0.431	2.21±0.143	147±6.54	9.31±0.521	11.5±0.423
BRAND 5	India	Green	ND	1.59±0.081	20.4±0.853	3.70±0.213	9.80±0.588	3.17±0.176	169±7.45	11.3±0.621	6.12±0.352
BRAND 6	India	Brown	Chestnut	0.541±0.027	19.3±0.852	23.6±1.23	6.80±0.421	1.05±0.056	69.6±2.41	10.3±0.554	3.63±0.198
BRAND 6	India	Brown	Brown	0.283±0.015	17.2±0.657	19.2±1.101	6.70±0.561	0.80±0.045	59.8±3.21	10.3±0.345	2.52±0.135
BRAND 7	India	Brown	Burgundy	0.354±0.018	10.1±0.641	34.7±1.53	6.70±0.402	0.75±0.053	101±5.04	9.70±0.521	3.83±0.302
BRAND 7	India	Green	Yellow	0.211±0.010	15.3±0.665	9.70±0.352	4.90±0.321	0.44±0.032	42.5±2.14	25.2±1.32	1.73±0.085
BRAND 8	ND	Green	ND	0.311±0.016	4.50±0.151	2.40±0.151	67.6±3.21	0.26±0.015	29.6±1.54	10.3±0.545	5.14±0.274
BRAND 9	Turkey	Green	ND	1.29±0.065	20.5±1.04	6.30±0.323	10.1±0.511	2.67±0.164	159±6.54	11.0±0.623	13.4±0.713
BRAND 10	Saudi Arabia	Brown	ND	1.11±0.055	15.0±0.644	54.4±2.14	14.0±0.75	2.06±0.123	158±8.53	11.1±0.488	5.11±0.321
BRAND 11	ND	Black	Black	5.22±0.261	6.80±0.457	2.20±0.112	3.60±0.231	1.70±0.321	144±6.54	7.90±0.432	14.5±0.652
BRAND 12	India	Light Brown	Orange	0.721±0.036	71.6±2.89	8.30±0.432	10.9±0.652	1.80±0.234	65.0±3.24	19.7±1.05	5.92±0.213
BRAND 12	India	Light Brown	Burgundy	0.258±0.013	15.1±0.862	2.30±0.112	4.20±0.342	0.74±0.045	28.9±1.54	6.50±0.345	1.62±0.075
BRAND 12	India	Dark Brown	Purple	0.434±0.022	5.20±0.455	3.50±0.164	5.30±0.317	0.86±0.064	63.0±3.15	7.00±0.421	2.14±0.114
BRAND 12	India	Dark Brown	Brown	0.440±0.022	8.90±0.546	2.10±0.142	9.40±0.452	9.59±0.641	87.4±4.24	12.4±0.658	3.63±0.203
BRAND 12	India	Black	Black	0.561±0.028	10.6±0.649	<LOD	6.70±0.328	1.23±0.053	80.6±4.07	9.70±0.521	4.80±0.354

*ND: Not Defined. *Cd, Co, Mo and Sn concentrations are under their respective LOD values.

ACKNOWLEDGMENTS

We are grateful to Agilent Technologies and SEM, Agilent Authorized Distributor in Turkey for providing MP AES 4200 spectrometer. I am very thankful to Hande TINAS for her help during the study.

REFERENCES

1. El Habr C, Mégarbané H. Temporary henna tattoos and hypertrichosis: A case report and review of the literature. *J Dermatol Case Rep.* 2015;9(2):36-8.
2. Jallad KN, Espada-Jallad C. Lead exposure from the use of Lawsonia inermis (Henna) in temporary paint-on-tattooing and hair dyeing. *Sci Total Environ.* 2008;397(1):244-50.
3. Onder M. Temporary holiday "tattoos" may cause lifelong allergic contact dermatitis when henna is mixed with PPD. *J Cosmet Dermatol.* 2003;2(3-4):126-30.
4. Aktas Sukuroglu A, Battal D, Burgaz S. Monitoring of Lawsone, p-phenylenediamine and heavy metals in commercial temporary black henna tattoos sold in Turkey. *Contact Dermatitis.* 2017;76(2):89-95.
5. Neri I, Guareschi E, Savoia F, Patrizi A. Childhood allergic contact dermatitis from henna tattoo. *Pediatr Dermatol.* 2002;19(6):503-5.
6. Ortiz G, Terron M, Bellido J. Contact allergy to henna. *Int Arch Allergy Immunol.* 1997;114(3):298-9.
7. Kang IJ, Lee MH. Quantification of para-phenylenediamine and heavy metals in henna dye. *Contact Dermatitis.* 2006;55(1):26-9.
8. Oymak T, Ulusoy Hİ, Hastaoglu E, Yılmaz V, and Yıldırım Ş. Some Heavy Metal Contents of Various Slaughtered Cattle Tissues in Sivas-Turkey. *JOTCSA* 2017;4(3):721-8.
9. Elaziz MMA, Khalifa MA, Ghariani RA, Mohamed HDA, Ashtewi MAS. Chemical and Physical Investigations of Arabian Eye Kohl Brands as Cosmetic in Libya. *J Turkish Chem Soc Sect A Chem.* 2017;4(1):463-76.
10. Guidance on Heavy Metal Impurities in Cosmetics, (2012).
11. Bund B. Technically avoidable heavy metal contents in cosmetic products. *J Verbrauch Lebensm.* 2017;12(1):51-3.
12. U. S. Food and Drug Administration. FDA's Testing of Cosmetics for Arsenic, Cadmium, Chromium, Cobalt, Lead, Mercury, and Nickel Content 2018 [cited 2018 20.06.2018]. Available from: <https://www.fda.gov/cosmetics/productsingredient/s/potentialcontaminants/ucm452836.htm#S1FP>.
13. Kaličanin B, Velimirović D. A Study of the Possible Harmful Effects of Cosmetic Beauty Products on Human Health. *Biol Trace Elem Res.* 2016;170(2):476-84.
14. Al-Saleh IA, Coate L. Lead exposure in Saudi Arabia from the use of traditional cosmetics and medical remedies. *Environ Geochem Health.* 1995;17(1):29-31.
15. Kang IJ, Lee MH. Quantification of para-phenylenediamine and heavy metals in henna dye. *Contact Dermatitis.* 2006;55(1):26-9.
16. Lekouch N, Sedki A, Nejmeddine A, Gamon S. Lead and traditional Moroccan pharmacopoeia. *Sci Total Environ.* 2001;280(1):39-43.
17. Ozbek N, Akman S. Determination of lead, cadmium and nickel in hennas and other hair dyes sold in Turkey. *Regul Toxicol Pharm.* 2016;79:49-53.
18. Ghanjaoui M, Cervera M, El Rhazi M, de la Guardia M. Assessment Of Trace Elements In Traditional Moroccan Cosmetics By Inductively Coupled Plasma Atomic Emission Spectroscopy. *International Journal of Scientific & Technology Research.* 2014;3(10):104-12.
19. Jankowski KJ, Reszke E. Microwave Induced Plasma Analytical Spectrometry: Royal Society of Chemistry; 2010.
20. Akbıyık D, Özbek N, Akman S. Determination of Ca, Mg, and Mn in Tea Samples with Microwave Plasma Atomic Emission Spectrometry. *J Turkish Chem Soc Sect A Chem.* 2014;1(1):7.
21. Donati GL, Amais RS, Schiavo D, Nobrega JA. Determination of Cr, Ni, Pb and V in gasoline and ethanol fuel by microwave plasma optical emission spectrometry. *J Anal Atom Spec.* 2013;28(5):755-9.
22. Amais RS, Donati GL, Schiavo D, Nóbrega JA. A simple dilute-and-shoot procedure for Si determination in diesel and biodiesel by microwave-induced plasma optical emission spectrometry. *Microchem J.* 2013;106(0):318-22.
23. Li W, Simmons P, Shrader D, Herrman TJ, Dai SY. Microwave plasma-atomic emission spectroscopy as a tool for the determination of copper, iron, manganese and zinc in animal feed and fertilizer. *Talanta.* 2013;112:43-8.
24. Hettipathirana TD. Determination of boron in high-temperature alloy steel using non-linear inter-element correction and microwave plasma-atomic emission spectrometry. *J Anal At Spectrom.* 2013;28(8):1242-6.

25. Ozbek N, Akman S. Determination of boron in Turkish wines by microwave plasma atomic emission spectrometry. *LWT*. 2015;61(2):532-5.
26. Ozbek N, Akman S. Microwave plasma atomic emission spectrometric determination of Ca, K and Mg in various cheese varieties. *Food Chem*. 2016;192:295-8.
27. Zhao Y, Li Z, Ross A, Huang Z, Chang W, Ouyang K, et al. Determination of heavy metals in leather and fur by microwave plasma-atomic emission spectrometry. *Spectrochim Acta B*. 2015;112:6-9.
28. Heredia JZ, Cina M, Savio M, Gil RA, Camiña JM. Ultrasound-assisted pretreatment for multielement determination in maize seed samples by microwave plasma atomic emission spectrometry (MPAES). *Microchem J*. 2016;129:78-82.
29. Ozbek N, Koca M, Akman S. A Practical Method for the Determination of Al, B, Co, Cr, Cu, Fe, Mg, Mn, Pb, and Zn in Different Types of Vinegars by Microwave Induced Plasma Optical Emission Spectrometry. *Food Anal Meth*. 2016:1-5.
30. Ozbek N, Akman S. Method development for the determination of calcium, copper, magnesium, manganese, iron, potassium, phosphorus and zinc in different types of breads by microwave induced plasma-atomic emission spectrometry. *Food Chem*. 2016;200:245-8.
31. Ozbek N, Ozcan M. Elemental Analysis of Tarhana by Microwave Induced Plasma Atomic Emission Spectrometry. *Anal Lett*. 2017;50(13):2139-46.
32. Niedzielski P, Kozak L, Wachelka M, Jakubowski K, Wybieralska J. The microwave induced plasma with optical emission spectrometry (MIP-OES) in 23 elements determination in geological samples. *Talanta*. 2015;132:591-9.



Synthesis of Stable Nano Calcite

Sevgi KILIC 

Department of Chemical Engineering, Izmir Institute of Technology, Urla, Izmir, 35430-Turkey.

Abstract: Synthesis of calcium carbonate (CaCO_3) particles in the presence of a population of carbon dioxide (CO_2) bubbles was investigated in the calcium hydroxide ($\text{Ca}(\text{OH})_2$) solution, which is a natural stabilizer for CaCO_3 . Possible chemical speciation reactions were presented for an inorganic synthesis of hollow nano- CaCO_3 particles. In the progress of CaCO_3 synthesis, some of the particles started to dissolve at their edges and turned into hollow nano- CaCO_3 particles. Some of the pores closed at the end of crystallization as a result of dissolution-recrystallization mechanism. Hollow nano- CaCO_3 particles with sizes of about 300 nm were synthesized with a narrow size distribution. It was concluded that the hollow nano- CaCO_3 particles could be advantageous due to lower weights and higher surface areas.

Keywords: Hollow particles, nanoparticles, CaCO_3 , stability, zeta potential, CO_2 sequestration.

Submitted: December 26, 2017. **Accepted:** July 12, 2018.

Cite this: Kilic S. Synthesis of Stable Nano Calcite. JOTCSA. 2018;5(2):869-80.

DOI: <http://dx.doi.org/10.18596/jotcsa.371374>

***Corresponding author.** e-mail: sevgikilic@iyte.edu.tr; Ph.: +90(232)7506647; Fax: +90(232)7506645

INTRODUCTION

Calcium carbonate (CaCO_3) is one of the cheapest filling materials widely used in paper, cement, and paint industries to decrease the product's cost and to enhance the physical properties of the composite materials. The enhancement in the physical properties of the composite materials is more important when the particles are used in nano sizes (1). However, production of CaCO_3 particles in nano sizes and at narrow size distribution is difficult and rare in the literature (2-4). Therefore, new methods need to be developed to produce monodispersed nano CaCO_3 particles in large scale.

Calcium carbonate from nature was generally supplied to the industry after a series of crushing, grinding, and sieving processes called Ground Calcium Carbonate (GCC) (5). However, nano- CaCO_3 particles cannot be obtained in the GCC process. Furthermore, the produced micron to millimeter sized CaCO_3 are not in desired quality, homogenous size distribution, and purity (5). Nano- CaCO_3 particles therefore need to be

synthesized by recrystallization methods. There are basically two recrystallization methods for the CaCO_3 synthesis. One is chemical method where sodium carbonate (Na_2CO_3) and calcium chloride (CaCl_2) are used as reactants (6). For this case, other ions such as Na^+ and Cl^- play an important role on crystallization and bigger particles are produced with sizes larger than 3 μm (7). The other method is carbonization method and uses carbon dioxide (CO_2) and calcium hydroxide ($\text{Ca}(\text{OH})_2$) as the reactants (8-10). Nano size particles can be produced in carbonization method depending on concentration and temperature of the solution (11). There are different carbonation methods appeared in the literature to synthesize nano- CaCO_3 particles. Examples are reactive crystallization processes (12-15), sono-chemical processes (16, 17), sol-gel processes (18), reverse-microemulsion processes (19, 20), and supercritical chemical processes (16, 21). In reactive crystallization processes, $\text{Ca}(\text{OH})_2$ - CO_2 - H_2O multiphase system is used to produce CaCO_3 nanoparticles. Temperature, concentration of reactants, stirring rates as well as mechanisms of CO_2 transport to the gas-liquid interface were

investigated as the process parameters to obtain nanocrystals (22). In sonochemical process, ultrasonic agitation was employed for a high conversion from $\text{Ca}(\text{OH})_2$ to precipitated CaCO_3 particles. Crystallization usually takes place with the formation of a CaCO_3 layer around the $\text{Ca}(\text{OH})_2$ particles causing a diffusion limitation for Ca^{2+} ions. These limitations could be overcome by the type of stirring and/or increasing the stirring rate. Smaller particles were obtained in short times (16). In sol-gel process, CaCO_3 particles were synthesized by reacting $\text{Ca}(\text{OH})_2$ with CO_2 in the presence of methanol. The resulting product was an aerogel. The aerogel was dried with supercritical carbon dioxide (scCO_2) to produce CaCO_3 aerogel. CaCO_3 aerogel formation was a three-step process; primary CaCO_3 nanoparticles formation (5-20 nm), secondary particles formation by growing primary particles (spherical or fiber-like) and aggregation to the CaCO_3 gel (18). In reverse microemulsion system, CO_2 dissolved in an organic phase and diffused into the reverse micelles containing $\text{Ca}(\text{OH})_2$, where CaCO_3 particles produced at the superstation. The nucleation and growth continued during formation of new CaCO_3 particles in the micelles (19). In supercritical chemical system, accelerated carbonation process was achieved by using scCO_2 with high yield to produce CaCO_3 particles in narrow particle size distribution (16). Among the nano- CaCO_3 production processes, reactive precipitation was the most useful industrial technique because it has low cost and sustainable for a large scale process. However, aggregation is an important problem among the newly formed nano particles and new techniques are needed to overcome the detrimental drawbacks.

Nano particles are naturally unstable due to their unbalanced surface charges, which is generally related to their surface potential (23, 24). It is clear that the CaCO_3 particles aggregate when the zeta potential is between +30 mV and -30 mV (25). A general consensus of about -10 mV of zeta potential value was reported for the CaCO_3 (24). This value shows that the synthesized new CaCO_3 clusters are naturally unstable. However, in one of our recent papers (26), we reported that the zeta potential of CaCO_3 particles are more than +30 mV in $\text{Ca}(\text{OH})_2$ solution and they are stable. We have proved that stable nano- CaCO_3 particles could be produced in "hollow" shapes when CO_2 was injected into the $\text{Ca}(\text{OH})_2$ solution as individual bubbles one after another (27). In this case, however, the CaCO_3 crystallization rate was slower, the conversion took longer time, and the particle size was relatively larger with a particle size of about 450 nm. In our subsequent paper, CO_2 bubbles were injected into the $\text{Ca}(\text{OH})_2$ solution at much higher rates with 420 mL/min and the newly produced particles were forced to be removed from the crystallization region into the

$\text{Ca}(\text{OH})_2$ solution as the stabilization region by a jet-flow (28). In such design, much smaller and "round" shaped nano- CaCO_3 particles of about 300 nm were produced.

In the present study, a population of CO_2 bubbles were injected into the $\text{Ca}(\text{OH})_2$ solution at a slower rate with 80 mL/min and the effect of multiple bubbles next to each other on the formation of "hollow" nano- CaCO_3 synthesis was investigated without a jet flow. It was found that the stirring rate was satisfactory to remove the newly synthesized nano- CaCO_3 particles from the crystallization region into the stabilization region, where rice-like hollow nano- CaCO_3 particles were produced. The chemical speciation reactions were also reviewed for the formation of stable nano- CaCO_3 particles with almost homogenous particle size distribution. It was concluded that hollow nano- CaCO_3 particles can be produced by bubbling the CO_2 into $\text{Ca}(\text{OH})_2$ solution with a concentration of 15 mM without significant aggregation.

MATERIALS AND METHODS

Calcium hydroxide ($\text{Ca}(\text{OH})_2$) was purchased from Merck, Germany, with a purity of about 96%. The impurity contained 3% calcium carbonate (CaCO_3) and 1% other impurities such as 0.05% of Na, K, Fe, Sr; 0.5% of Mg; 0.01% of SO_4^{2-} , and 0.005% of Cl^- . Carbon dioxide (CO_2) gas was purchased from Carbogas, Turkey, and its purity was 99.99%. Ultrapure water was obtained with a MilliQ (Millipore- Elix UV5/ Milli-Q) water purification system with a conductivity of 18.2 $\text{M}\Omega\cdot\text{cm}$ at 25 °C.

Stable Nano CaCO_3 Synthesis

The experimental set up designed to synthesize stable nano- CaCO_3 particles in $\text{Ca}(\text{OH})_2$ solution (26) was shown in Figure 1. Different configurations in the experimental set up was also used in the synthesis of rice-like hollow nano- CaCO_3 particles with a single bubble injection (27) and round shape nano- CaCO_3 particles with a jet flow (28). Briefly, the experimental set up consisted of a coil pipe containing small openings submerged in the $\text{Ca}(\text{OH})_2$ solution at the upper corner of the tank. Therefore, two "crystallization" and "stabilization" regions were created. The diameter of the holes on the coil was about 2 mm for the injection of a population of CO_2 bubbles. 15 mM of $\text{Ca}(\text{OH})_2$ solution was prepared in ultrapure water to a final volume of 7 liters. Dissolution of CO_2 from the atmosphere was measured and found negligible. The mechanical stirring rate was set to 800 rpm to make a homogeneous mixing in the tank containing $\text{Ca}(\text{OH})_2$ solution and later the CaCO_3 slurry. The total CO_2 flow rate was 80 mL/min so that the population of CO_2 bubbles were used to test the effect of CO_2 dissolution on the aggregation of newly synthesized CaCO_3

crystallites and particle growth. pH and conductivity values were monitored during the

crystallization.

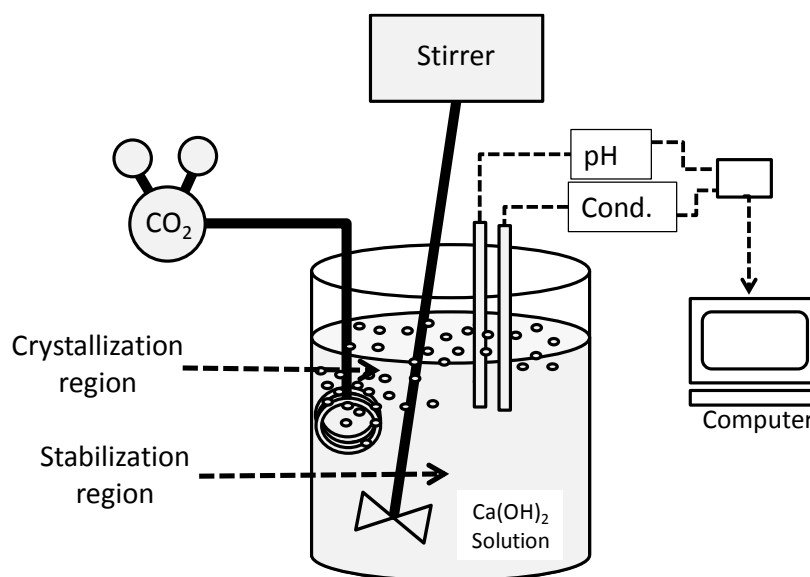


Figure 1: Experimental set up for stable nano- CaCO_3 production.

Sample Preparation and Characterization

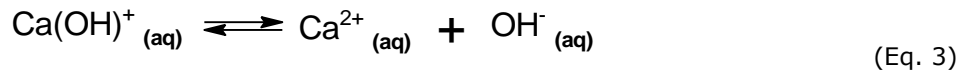
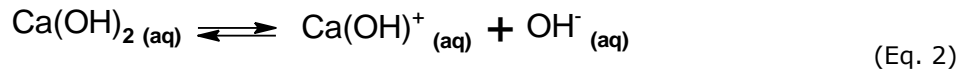
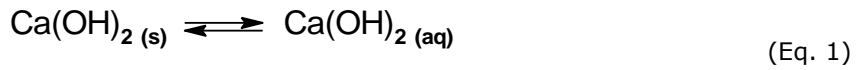
The average size, size distribution, and zeta potential values of the CaCO_3 particles were measured by the dynamic light scattering (DLS) method using particle size analyzer (Malvern nano ZS model). Size distribution was obtained from 1 mL of sample withdrawn from the solution into a UV cuvette and measured by DLS. Zeta potential values were also measured using another 1 mL of sample withdrawn from the solution into a zeta cell and estimated by the DLS. At certain time intervals, precipitates were obtained by centrifugation at 9000 rpm for 20 min. The particles were washed with acetone and dried at 103 °C overnight. The morphologies of the CaCO_3 crystals were determined by the scanning electron microscope (SEM) (Philips XL 30 S FEG). The crystal structure was determined using the X-ray powder diffraction (XRD) measurements.

RESULTS AND DISCUSSION

Crystallization of calcium carbonate is widely studied in the literature because it is a model system for ionic crystallization. The CaCO_3 particles formed in chemical method are generally in micron sizes and CaCO_3 particles synthesized in carbonization method are generally in nano sizes, however, they became usually aggregated (29, 30). In order to synthesize nano sized CaCO_3 particles with a narrow particle size distribution, mass transfer between reactants need to be controlled in a semi-batch bubble reactor. This type of reactor is mostly used in gas-liquid reactive crystallization processes in industry (14).

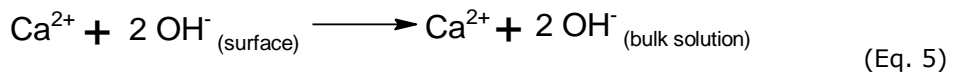
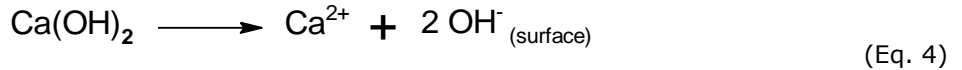
The micron-scale bubble generation also helps micro-mixing. Therefore, the bubble reactor provides to maintain perfect mixing and a rapid mass transfer between reactants in $\text{Ca(OH)}_2\text{-CO}_2\text{-H}_2\text{O-CaCO}_3$ multiphase carbonization system. The size of gas bubbles is the most important parameter for an effective mass transfer and reactive absorption. Decreasing the bubble size causes to increase the gas-liquid interfacial area and the residence time for the bubbles by decreasing the lifting force on bubbles. The CO_2 dissolution at the bubble surface can be increased upon increasing the retention time of the CO_2 bubbles in the solution (15).

The present method was designed to synthesize nano- CaCO_3 particles at narrow size distribution in a bubble crystallizer-reactor. The stability of the particles was achieved by the excess Ca^{2+} ions in the Ca(OH)_2 solution when the surfaces of particles are covered by the Ca^{2+} ions and positively charged (26). Figure 2 shows the measured pH and conductivity values during crystallization in the presence of the CO_2 bubbles. The numbers indicated on the figure show the time at which samples were taken from the crystallization reactor for analysis. As shown in the figure, a sudden increase in pH and conductivity was realized when powdered Ca(OH)_2 was added into the ultrapure water. This was the first step in CaCO_3 crystallization for the dissolution of powder Ca(OH)_2 in water. Ca(OH)_2 was the source for Ca^{2+} , OH^- , and Ca(OH)^+ ions in solution according to the chemical speciation reactions as follows (24):



Reactions (1) to (3) produce a homogeneous solution when the Ca(OH)₂ concentration is less than its solubility limit of 18 mM (26). However, when the Ca(OH)₂ concentration is higher than its solubility limit, part of the powdery Ca(OH)₂ exists

in the solution in solid form and the solution becomes a slurry. In this case, the dissolution from the powder Ca(OH)₂ occurs with a surface diffusion limited process (31).



As shown in the figure, the Ca(OH)₂ dissolution took more than 20 minutes in water, where the

powder Ca(OH)₂ was fully dissolved and converted into Ca²⁺, Ca(OH)⁺, and OH⁻ ions.

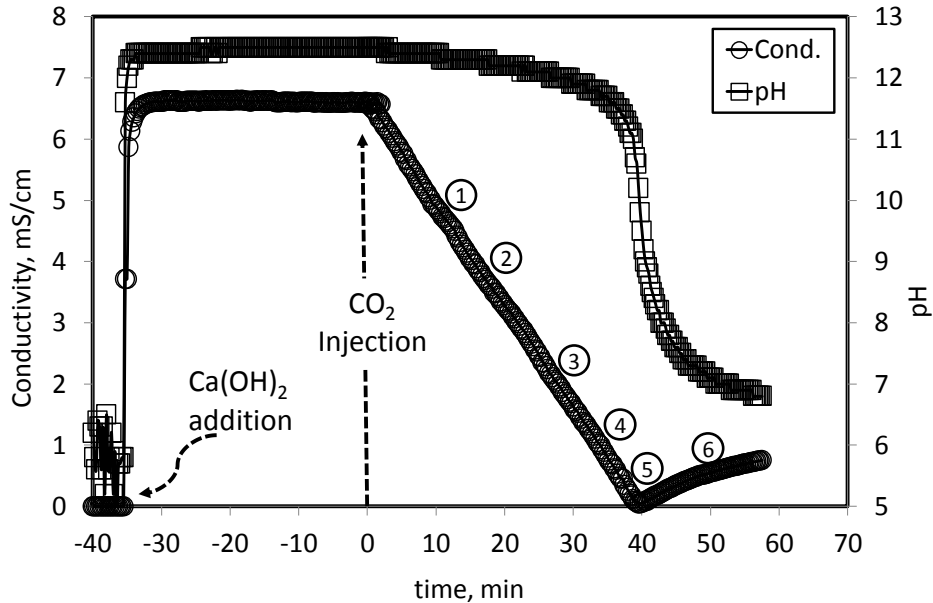
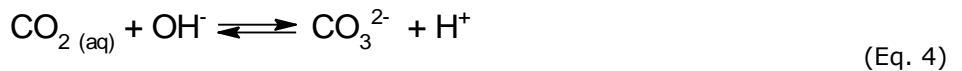


Figure 2: Changes in conductivity and pH during crystallization. Numbers indicate the time intervals where samples were taken.

The time was set to zero when the CO₂ bubbles were injected into the Ca(OH)₂ solution to initiate the CaCO₃ crystallization. Therefore, the second step in CaCO₃ crystallization was the dissolution of CO₂ in Ca(OH)₂ solution. The CO₂ dissolution from the gas phase into the liquid phase is a complicated process. In the two-film theory, the

CO₂ first diffuses from the gas phase to the gas-liquid interphase. Then, it dissolves at the gas-liquid interphase. And finally, it diffuses through the liquid film into the solution (12). When CO₂ was introduced into Ca(OH)₂ solution at pH 12.6, CO₃²⁻ ions were expected to form preferentially (32).



However, when pH was lower, other transformations were expected to occur at the gas-liquid interphase such as dissolution of CO₂ in

aqueous phase (Eq. 5), hydration by water (Eq. 6), followed by quick ionization into HCO₃⁻ and H⁺ ions (Eq. 7) (32).

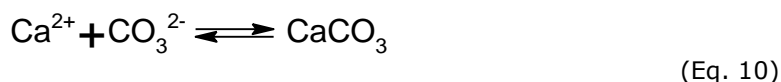
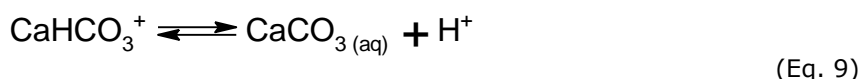
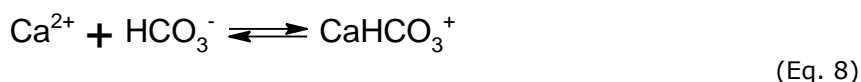




The dissolution of CO₂ in an aqueous solution therefore decreases its pH. It is known that the pK_a of a carbonated water is about 6.4 at atmospheric pressure (26). This value becomes lower when pressure of CO₂ is increased.

The third step in CaCO₃ crystallization was the nucleation and crystalline growth. Newly synthesized nanocrystalline CaCO₃ nuclei forms

from the presence of Ca²⁺, HCO₃⁻ and OH⁻ ions and other ionic species such as CaHCO₃⁺ and CaOH⁺ ions. These latter ions could also participate in nano crystalline CaCO₃ formation, which may initiate new nucleation sites or collide to form growing particles. Here, the solubility of CaCO₃ is about 0.1 mM (26) and all these species were eventually converted into the solid-CaCO₃ particles.



As shown in the figure, at the initial stage of crystallization, the pH and conductivity were higher. A pH value of 11.0 or higher is important for the calcite formation in the solution. When the pH is lower than 11.0, other CaCO₃ polymorphs such as aragonite, vatarite, and its different hydrated species would form during crystallization (33-37). The conductivity started to decrease almost linearly when CO₂ bubbles were injected into the Ca(OH)₂ solution. In the subsequent stages, the decrease in pH was relatively small. The conductivity was related to the Ca²⁺ ion concentration (26). A decrease in conductivity clearly indicated that the Ca²⁺ ions were consumed in the Ca(OH)₂ solution to produce CaCO₃ particles. The near zero conductivity value indicated the consumption of all Ca²⁺ ions in solution. At this late stage, an abrupt decrease in

pH was observed to about 7.0 due to a dissolving of an excess amount of CO₂. In this case, an increase in H⁺ and HCO₃⁻ ion concentrations results in a decrease in pH in the slurry. The low pHs cause the dissolution of some of CaCO₃ particles releasing Ca²⁺ ions back into the slurry. Thus, the released Ca²⁺ ions and its new complexes with OH⁻ and HCO₃⁻ ions to form CaOH⁺ and CaHCO₃⁺ species, respectively, increased the conductivity back again at the end of the crystallization as shown in the figure.

$$\text{Conductivity} = 0.4268 [\text{Ca}(\text{OH})_2] \tag{Eq. 11}$$

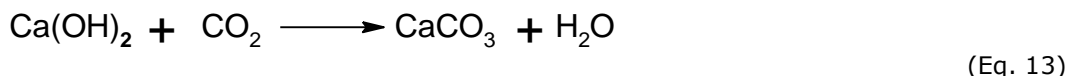
Here, the conductivity is in mS/cm and [Ca(OH)₂] concentration is in mM. Such relationship agreed very well with Burns *et al.* (38). Therefore, the [Ca²⁺] ion concentration was estimated from the

conductivity change during crystallization. The [OH⁻] ion concentration was calculated from Eq. (12), assuming that the OH⁻ ions activity, *a*_{OH⁻}, is about 1.0.

$$[\text{OH}^-] = 10^{-(14-\text{pH})} \tag{Eq. 12}$$

The overall reaction for the crystallization of CaCO₃ is given in Eq. 13, for which the CaCO₃ crystallization rate will be equal to the Ca(OH)₂

consumption rate as well as the CO₂ consumption rate.



Therefore, the CO_2 injection rate, the $\text{Ca}(\text{OH})_2$ consumption rate, and CaCO_3 crystallization rate

Equations (11) and (12) respectively show the calculated $[\text{Ca}^{2+}]$ and $[\text{OH}^-]$ ion concentrations and the results were plotted in Figure 3a. As shown in the figure, Ca^{2+} and OH^- ion concentrations of 15 mM and 30 mM were obtained, respectively, when 15 mM of $\text{Ca}(\text{OH})_2$ was dissolved. As seen in the figure, Ca^{2+} and OH^- ion concentrations both started to decline as the CO_2 bubbles were introduced into the solution. Figure 3b shows the consumption rates for the Ca^{2+} and OH^- ions calculated from the slopes of the Ca^{2+} and OH^- ion concentration curves in Figure 3a, respectively. As shown in the figure, the consumption rates for Ca^{2+} and OH^- were estimated to be about 0.4 ± 0.07 mM/min and 0.8 ± 0.2 mM/min, respectively. Here, the CO_2 consumption rate was calculated in 7 liter of $\text{Ca}(\text{OH})_2$ solution to be

can be estimated from the conductivity measurements for the experiments.

about 0.047 ± 0.012 mmoles/s, which agree very well with the literature (39, 40).

The experimental method can also be used in the estimation of CO_2 dissolution rate and the enzymatic activity of carbonic anhydrase, an enzyme to catalyze the hydration of CO_2 in aqueous media (41). Therefore, a new method was developed for the biocatalytic activity of carbonic anhydrase using CO_2 - $\text{Ca}(\text{OH})_2$ system (41). It was found that free-CA lost its activity in less than 6 mins at pH 12.5 in $\text{Ca}(\text{OH})_2$ solution, however, its activity was retained when the CA was immobilized within polyurethane foam (41). Therefore, the biocatalytic activity of CA could be estimated at alkaline conditions in the aqueous solution of $\text{Ca}(\text{OH})_2$ (41).

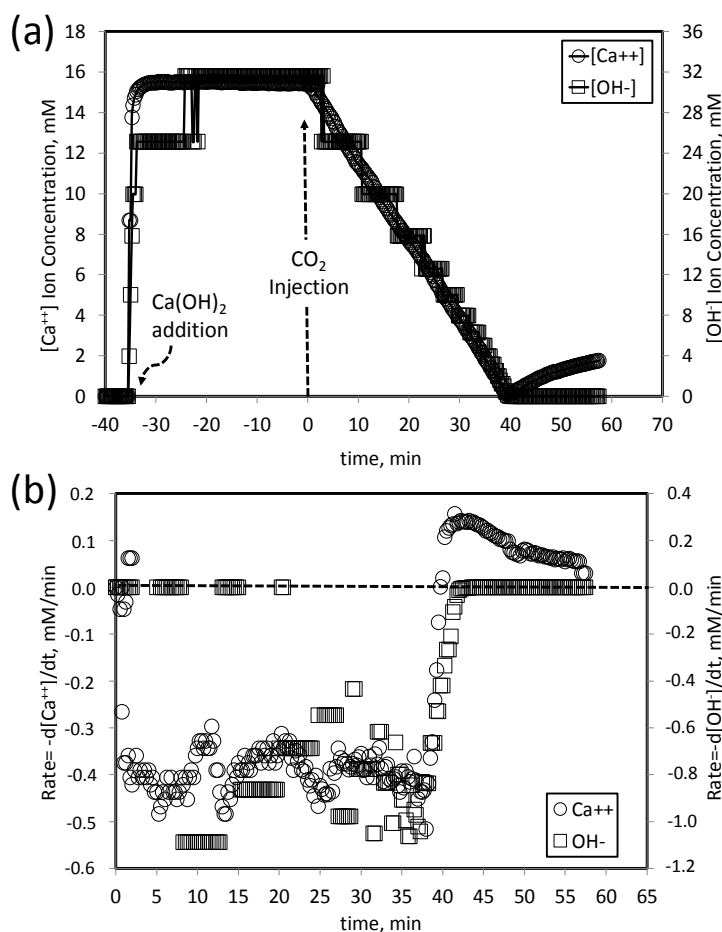


Figure 3. (a) Estimated Ca^{2+} and OH^- concentrations in the stirred reactor during crystallization. (b) Ca^{2+} and OH^- consumption rates calculated from the estimated concentrations.

Figure 4 shows the zeta potential values measured and the average particle sizes for the produced CaCO_3 particles during crystallization. As Figure 4 shows, at the first stage of crystallization, the average size of particles was measured to be ca.

300 nm and the estimated zeta potential value was about +30 mV. The early stage particles were thought to be most probably charged nano CaCO_3 clusters. As CO_2 was injected into the solution, the average particle size was again about 300 nm,

and the zeta potential increased to about +50 mV. The zeta potential is important for the surface charge of the particles. The positive zeta potential higher than +30 mV indicated that the CaCO_3 particles obtained were in a stable form and little or no aggregation was expected to occur (25). As shown in the figure, the removal of particles from the crystallization region in the solution facilitated the formation of nano particles without aggregation and growth to larger particles. At the late stage, where the Ca^{2+} was consumed and pH decreased, the zeta potential value was shown to decrease to about +24 mV for which some

aggregation expected to occur. Therefore, we observed that the average size of particles slightly increased. On the other hand, the measurement in an increase in CaCO_3 particle size could be due to the increase in the population of the particles. When the number of particles increased in the solution, the scattered light to the detectors could be increased due to interactions of these particles in the slurry. Therefore, the figure shows that the increase in particle size towards the end of crystallization could be due to an artifact which can best be visualized from electron microscopic images.

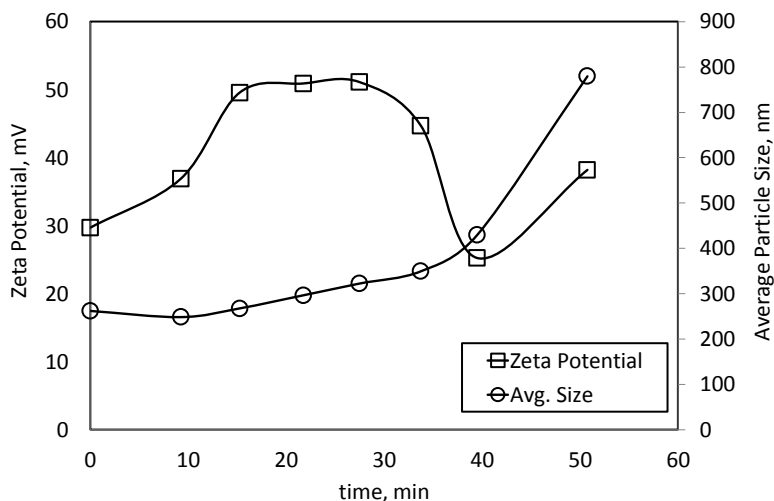


Figure 4. The zeta potential and average particle size for the particles that were obtained in the stirred reactor.

Figure 5 shows the scanning electron microscopy (SEM) images of the CaCO_3 particles obtained at the indicated sampling time intervals of crystallization. The values for the conductivity, pH value, and zeta potential were also provided with the images. As shown in the images, rice-like and chunks of CaCO_3 particles were seen before CO_2 injection. The chunks of cubic CaCO_3 residues were expected to come from the impurities in the $\text{Ca}(\text{OH})_2$ powder. The rice-like particles occurred at lower CO_2 dissolution rates. Or, these rice-like CaCO_3 particles did form initially due to a dissolution-recrystallization mechanism with CaCO_3 particles that are present in the solution as the impurity as defined in the materials section (4, 42-44). When the CO_2 bubbles were introduced in the solution, rice-like nano CaCO_3 particles formed with an average particle size of about 220 nm. Growing the primary CaCO_3 crystals alongside indicating that the edges of the particles are the

most energetic sites. Therefore, the CaCO_3 particles grow much faster at their end-edges. No aggregation was seen due to the stabilization effect of $\text{Ca}(\text{OH})_2$ solution (26), where the zeta potential values were higher than +30 mV (25). During crystallization as pH of the solution started to decrease, some of the particles slightly dissolved at their edges and produced "hollow" CaCO_3 particles. The growth rate and the dissolution rate were both higher at the edges of the CaCO_3 particles. Some of the edges closed as a result of dissolution at low pH values and then recrystallization on the particles (42, 44). The images indicate that negligible aggregations were seen due to their surface potentials indicated from higher zeta potential values. Any aggregation seen in the images, if any, would be probably the effect of drying on particles. The SEM images indicated that nano- CaCO_3 can be produced with almost homogenous size distribution.

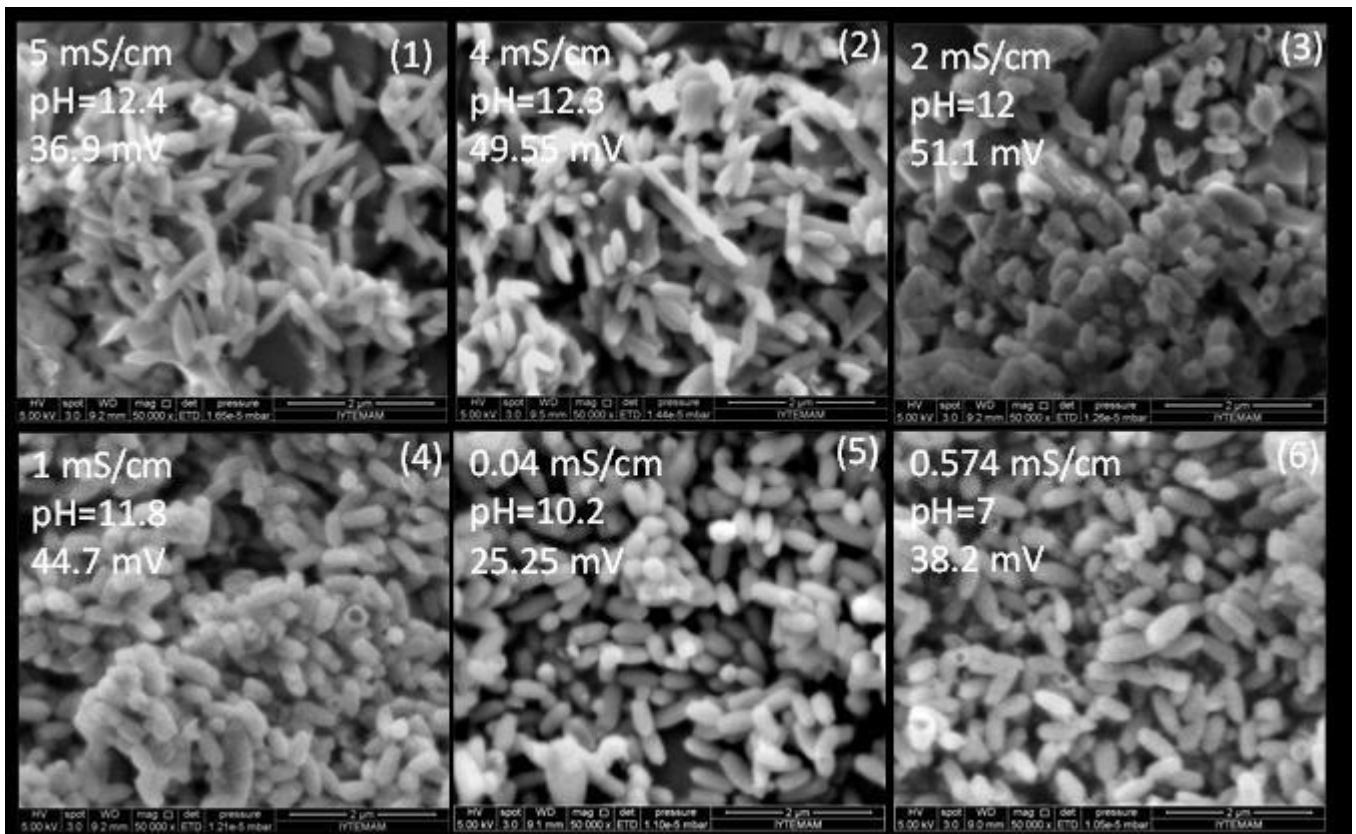


Figure 5. SEM images showing the progress of “hollow” nano CaCO₃ particle production with homogenous size distribution.

XRD patterns for the produced CaCO₃ particles indicated that these particles were all of calcite form as shown in Figure 6. The 2θ value at 29.468° showed the well-characterized calcite form of CaCO₃. The Sheerer equation indicates that the crystallite species on the particles is

about 40 nm. Therefore, it was clear that when the particles were removed from the crystallization region and stabilized in the Ca(OH)₂ solution, hollow nano calcite particles can be produced with a narrow size distribution.

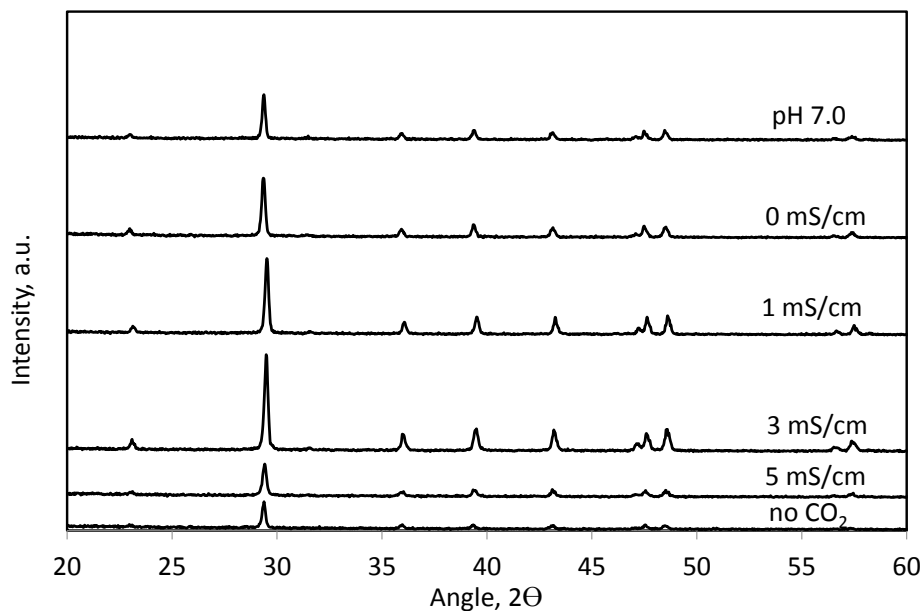


Figure 6. XRD patterns obtained for the CaCO₃ particles in the progress of CaCO₃ crystallization.

CONCLUSIONS

Calcium carbonate particles were synthesized with the carbonization method where a population of CO₂ bubbles were introduced into the Ca(OH)₂ solution. However, the CO₂ bubbling was at the upper left corner of the solution so that the produced particles were separated from the crystallization region into the stabilization region by stirring. In this case, the zeta potential values for the particles were measured to be higher than +30 mV indicating that these particles were stable in Ca(OH)₂ solution. To the end of crystallization, where Ca²⁺ ions were all consumed and pH decreased, some of the CaCO₃ particles were seen to dissolve at their edges. The dissolution at the edges was faster for the rice-like CaCO₃ particles. The dissolution from the edges resulted in an empty space in the CaCO₃ particles. Therefore, "hollow" nano-CaCO₃ particles were produced with homogenous size distribution without aggregation in the Ca(OH)₂ solution. It was concluded that slower CO₂ flow rates needed for the production of nano-CaCO₃ particles at narrow size distribution.

ACKNOWLEDGEMENTS

The Scientific and Technological Research Council of Turkey (TUBITAK) is highly appreciated for the research grant with the project number of 110M104. The author also acknowledges Eda Ulkeryildiz for helping part of the experiments and Ekrem Ozdemir for valuable discussions.

REFERENCES

1. Fu SY, Feng XQ, Lauke B, Mai YW. Effects of particle size, particle/matrix interface adhesion and particle loading on mechanical properties of particulate-polymer composites. *Compos Part B-Eng.* 2008;39(6):933-61.
2. Bots P, Benning LG, Rodriguez-Blanco JD, Roncal-Herrero T, Shaw S. Mechanistic Insights into the Crystallization of Amorphous Calcium Carbonate (ACC). *Cryst Growth Des.* 2012;12(7):3806-14.
3. Lee KB, Park SB, Jang YN, Lee SW. Morphological control of CaCO₃ films with large area: Effect of additives and self-organization under atmospheric conditions. *J Colloid Interf Sci.* 2011;355(1):54-60.
4. Rieger J, Kellermeier M, Nicoleau L. Formation of Nanoparticles and Nanostructures-An Industrial Perspective on CaCO₃, Cement, and Polymers. *Angew Chem Int Edit.* 2014;53(46):12380-96.
5. Sant'Anna SSE, de Souza DA, de Araujo DM, Carvalho CD, Yoshida MI. Physico-chemical

Analysis of Flexible Polyurethane Foams Containing Commercial Calcium Carbonate. *Mater Res-Ibero-Am J.* 2008;11(4):433-8.

6. Andreassen JP. Formation mechanism and morphology in precipitation of vaterite - nano aggregation or crystal growth? *Journal of Crystal Growth.* 2005;274(1-2):256-64.

7. Matahwa H, Ramiah V, Sanderson RD. Calcium carbonate crystallization in the presence of modified polysaccharides and linear polymeric additives. *Journal of Crystal Growth.* 2008;310(21):4561-9.

8. Jung WM, Kang SH, Kim KS, Kim WS, Choi CK. Precipitation of calcium carbonate particles by gas-liquid reaction: Morphology and size distribution of particles in Couette-Taylor and stirred tank reactors. *Journal of Crystal Growth.* 2010;312(22):3331-9.

9. Kakaraniya S, Gupta A, Mehra A. Reactive precipitation in gas-slurry systems: The CO₂Ca(OH)₂-CaCO₃ system. *Ind Eng Chem Res.* 2007;46(10):3170-9.

10. Montes-Hernandez G, Renard F, Geoffroy N, Charlet L, Pironon J. Calcite precipitation from CO₂-H₂O-Ca(OH)₂ slurry under high pressure of CO₂. *Journal of Crystal Growth.* 2007;308(1):228-36.

11. Ukrainczyk M, Kontrec J, Babic-Ivancic V, Brecevic L, Kralj D. Experimental design approach to calcium carbonate precipitation in a semicontinuous process. *Powder Technol.* 2007;171(3):192-9.

12. Chen J-F, Wang Y-H, Guo F, Xin-Ming, Zheng C. <Synthesis of Nanoparticles with Novel Technology: High-Gravity Reactive Precipitation>. *Industrial Engineering Chemical Research.* 2000;39:948-54.

13. Sun B-C, Wang X-M, Chen J-M, Chu G-W, Chen J-F, Shao L. Synthesis of nano-CaCO₃ by simultaneous absorption of CO₂ and NH₃ into CaCl₂ solution in a rotating packed bed. *Chemical Engineering Journal.* 2011;168(2):731-6.

14. Varma S, Chen P-C, Unnikrishnan G. Gas-liquid reactive crystallization for the synthesis of CaCO₃ nanocrystals. *Materials Chemistry and Physics.* 2011;126(1-2):232-6.

15. Matsumoto M, Fukunaga T, Onoe K. Polymorph control of calcium carbonate by reactive crystallization using microbubble technique. *Chemical Engineering Research and Design.* 2010;88(12):1624-30.

16. López-Periago AM, Pacciani R, García-González C, Vega LF, Domingo C. A breakthrough technique for the preparation of high-yield precipitated calcium carbonate. *The Journal of Supercritical Fluids*. 2010;52(3):298-305.
17. Sonawane SH, Shirsath SR, Khanna PK, Pawar S, Mahajan CM, Paithankar V, et al. An innovative method for effective micro-mixing of CO₂ gas during synthesis of nano-calcite crystal using sonochemical carbonization. *Chemical Engineering Journal*. 2008;143(1-3):308-13.
18. Plank J, Hoffmann H, Schölkopf J, Seidl W, Zeitler I, Zhang Z. Preparation and Characterization of a Calcium Carbonate Aerogel. *Research Letters in Materials Science*. 2009;2009:1-3.
19. Tai CY, Chen C-k. Particle morphology, habit, and size control of using reverse microemulsion technique. *Chemical Engineering Science*. 2008;63(14):3632-42.
20. Kang SH, Hirasawa I, Kim WS, Choi CK. Morphological control of calcium carbonate crystallized in reverse micelle system with anionic surfactants SDS and AOT. *J Colloid Interface Sci*. 2005;288(2):496-502.
21. Montes-Hernandez G, Renard F. Co-utilisation of alkaline solid waste and compressed-or-supercritical CO₂ to produce calcite and calcite/SeO red nanocomposite. *The Journal of Supercritical Fluids*. 2011;56(1):48-55.
22. Lin R-y, Zhang J-y, Bai Y-q. Mass transfer of reactive crystallization in synthesizing calcite nanocrystal. *Chemical Engineering Science*. 2006;61(21):7019-28.
23. Chibowski E, Holysz L, Wojcik W. Changes in Zeta-Potential and Surface Free-Energy of Calcium-Carbonate Due to Exposure to Radiofrequency Electric-Field. *Colloid Surface A*. 1994;92(1-2):79-85.
24. Chibowski E, Hotysz L, Szczes A. Time dependent changes in zeta potential of freshly precipitated calcium carbonate. *Colloid Surface A*. 2003;222(1-3):41-54.
25. Kes M. Determination of the particle interactions - rheology- surface roughness relationship for dental ceramics [M.S]. İzmir: İzmir Institute of Technology; 2007.
26. Kilic S, Toprak G, Ozdemir E. Stability of CaCO₃ in Ca(OH)₂ solution. *Int J Miner Process*. 2016;147:1-9.
27. Ulkeryildiz E, Kilic S, Ozdemir E. Rice-like hollow nano-CaCO₃ synthesis. *Journal of Crystal Growth*. 2016;450:174-80.
28. Ulkeryildiz E, Kilic S, Ozdemir E. Nano-CaCO₃ synthesis by jet flow. *Colloid Surface A*. 2017;512:34-40.
29. Carmona JG, Morales JG, Rodriguez-Clemente R. Rhombohedral-scalenohedral calcite transition produced by adjusting the solution electrical conductivity in the system Ca(OH)₂-CO₂-H₂O. *J Colloid Interf Sci*. 2003;261(2):434-40.
30. Carmona JG, Morales JG, Sainz JF, Loste E, Clemente RR. The mechanism of precipitation of chain-like calcite. *Journal of Crystal Growth*. 2004;262(1-4):479-89.
31. Johannsen K, Rademacher S. Modelling the Kinetics of Calcium Hydroxide Dissolution in Water. *Acta Hydrochimica Et Hydrobiologica*. 1999;27(2):72-8.
32. Ozdemir E. Biomimetic CO₂ Sequestration: 1. Immobilization of Carbonic Anhydrase within Polyurethane Foam. *Energ Fuel*. 2009;23:5725-30.
33. Xu AW, Ma YR, Colfen H. Biomimetic mineralization. *J Mater Chem*. 2007;17(5):415-49.
34. Gunasekaran S, Anbalagan G. Spectroscopic study of phase transitions in natural calcite mineral. *Spectrochim Acta A*. 2008;69(4):1246-51.
35. Montes-Hernandez G, Fernández-Martínez A, Charlet L, Tisserand D, Renard F. Textural properties of synthetic nano-calcite produced by hydrothermal carbonation of calcium hydroxide. *Journal of Crystal Growth*. 2008;310(11):2946-53.
36. Carmona JG, Morales JG, Sainz JF, Clemente RR. Morphological characteristics and aggregation of calcite crystals obtained by bubbling CO₂ through a Ca(OH)₂ suspension in the presence of additives. *Powder Technol*. 2003;130(1-3):307-15.
37. Jung WM, Kang SH, Kim W-S, Choi CK. Particle morphology of calcium carbonate precipitated by gas-liquid reaction in a Couette-Taylor reactor. *Chemical Engineering Science*. 2000;55(4):733-47.
38. Burns JR, Jachuck JJ. Monitoring of CaCO₃ production on a spinning disc reactor using conductivity measurements. *Aiche J*. 2005;51(5):1497-507.

39. Lin RY, Zhang JY, Bai YQ. Mass transfer of reactive crystallization in synthesizing calcite nanocrystal. *Chemical Engineering Science*. 2006;61(21):7019-28.

40. Takemura F, Matsumoto Y. Dissolution rate of spherical carbon dioxide bubbles in strong alkaline solutions. *Chemical Engineering Science*. 2000;55(18):3907-17.

41. Molva M, Kilic S, Ozdemir E. Effect of carbonic anhydrase on CaCO₃ crystallization in alkaline solution. *Energ Fuel*. 2016;30(12):10686-95.

42. Rodriguez-Blanco JD, Shaw S, Benning LG. The kinetics and mechanisms of amorphous calcium carbonate (ACC) crystallization to calcite, via vaterite. *Nanoscale*. 2011;3(1):265-71.

43. Rodriguez-Blanco JD, Shaw S, Bots P, Roncal-Herrero T, Benning LG. The role of pH and Mg on the stability and crystallization of amorphous calcium carbonate. *J Alloy Compd*. 2012;536:S477-S9.

44. Tai CY, Chen FB. Polymorphism of CaCO₃ precipitated in a constant-composition environment. *Aiche J*. 1998;44(8):1790-8.

1. Fu SY, Feng XQ, Lauke B, Mai YW. Effects of particle size, particle/matrix interface adhesion and particle loading on mechanical properties of particulate-polymer composites. *Compos Part B-Eng.* 2008;39(6):933-61.
2. Bots P, Benning LG, Rodriguez-Blanco JD, Roncal-Herrero T, Shaw S. Mechanistic Insights into the Crystallization of Amorphous Calcium Carbonate (ACC). *Cryst Growth Des.* 2012;12(7):3806-14.
3. Lee KB, Park SB, Jang YN, Lee SW. Morphological control of CaCO₃ films with large area: Effect of additives and self-organization under atmospheric conditions. *J Colloid Interf Sci.* 2011;355(1):54-60.
4. Rieger J, Kellermeier M, Nicoleau L. Formation of Nanoparticles and Nanostructures-An Industrial Perspective on CaCO₃, Cement, and Polymers. *Angew Chem Int Edit.* 2014;53(46):12380-96.
5. Sant'Anna SSE, de Souza DA, de Araujo DM, Carvalho CD, Yoshida MI. Physico-chemical Analysis of Flexible Polyurethane Foams Containing Commercial Calcium Carbonate. *Mater Res-Ibero-Am J.* 2008;11(4):433-8.
6. Andreassen JP. Formation mechanism and morphology in precipitation of vaterite - nano aggregation or crystal growth? *Journal of Crystal Growth.* 2005;274(1-2):256-64.
7. Matahwa H, Ramiah V, Sanderson RD. Calcium carbonate crystallization in the presence of modified polysaccharides and linear polymeric additives. *Journal of Crystal Growth.* 2008;310(21):4561-9.
8. Jung WM, Kang SH, Kim KS, Kim WS, Choi CK. Precipitation of calcium carbonate particles by gas-liquid reaction: Morphology and size distribution of particles in Couette-Taylor and stirred tank reactors. *Journal of Crystal Growth.* 2010;312(22):3331-9.
9. Kakaraniya S, Gupta A, Mehra A. Reactive precipitation in gas-slurry systems: The CO₂Ca(OH)₂-CaCO₃ system. *Ind Eng Chem Res.* 2007;46(10):3170-9.
10. Montes-Hernandez G, Renard F, Geoffroy N, Charlet L, Pironon J. Calcite precipitation from CO₂-H₂O-Ca(OH)₂ slurry under high pressure of CO₂. *Journal of Crystal Growth.* 2007;308(1):228-36.
11. Ukrainczyk M, Kontrec J, Babic-Ivancic V, Brecevic L, Kralj D. Experimental design approach to calcium carbonate precipitation in a semicontinuous process. *Powder Technol.* 2007;171(3):192-9.
12. Chen J-F, Wang Y-H, Guo F, Xin-Ming, Zheng C. <Synthesis of Nanoparticles with Novel Technology: High-Gravity Reactive Precipitation>. *Industrial Engineering Chemical Research.* 2000;39:948-54.
13. Sun B-C, Wang X-M, Chen J-M, Chu G-W, Chen J-F, Shao L. Synthesis of nano-CaCO₃ by simultaneous absorption of CO₂ and NH₃ into CaCl₂ solution in a rotating packed bed. *Chemical Engineering Journal.* 2011;168(2):731-6.
14. Varma S, Chen P-C, Unnikrishnan G. Gas-liquid reactive crystallization for the synthesis of CaCO₃ nanocrystals. *Materials Chemistry and Physics.* 2011;126(1-2):232-6.
15. Matsumoto M, Fukunaga T, Onoe K. Polymorph control of calcium carbonate by reactive crystallization using microbubble technique. *Chemical Engineering Research and Design.* 2010;88(12):1624-30.
16. López-Periago AM, Pacciani R, García-González C, Vega LF, Domingo C. A breakthrough technique for the preparation of high-yield precipitated calcium carbonate. *The Journal of Supercritical Fluids.* 2010;52(3):298-305.
17. Sonawane SH, Shirsath SR, Khanna PK, Pawar S, Mahajan CM, Paithankar V, et al. An innovative method for effective micro-mixing of CO₂ gas during synthesis of nano-calcite crystal using sonochemical carbonization. *Chemical Engineering Journal.* 2008;143(1-3):308-13.
18. Plank J, Hoffmann H, Schölkopf J, Seidl W, Zeitler I, Zhang Z. Preparation and Characterization of a Calcium Carbonate

Aerogel. *Research Letters in Materials Science*. 2009;2009:1-3.

19. Tai CY, Chen C-k. Particle morphology, habit, and size control of using reverse microemulsion technique. *Chemical Engineering Science*. 2008;63(14):3632-42.

20. Kang SH, Hirasawa I, Kim WS, Choi CK. Morphological control of calcium carbonate crystallized in reverse micelle system with anionic surfactants SDS and AOT. *J Colloid Interface Sci*. 2005;288(2):496-502.

21. Montes-Hernandez G, Renard F. Co-utilisation of alkaline solid waste and compressed-or-supercritical CO₂ to produce calcite and calcite/SeO red nanocomposite. *The Journal of Supercritical Fluids*. 2011;56(1):48-55.

22. Lin R-y, Zhang J-y, Bai Y-q. Mass transfer of reactive crystallization in synthesizing calcite nanocrystal. *Chemical Engineering Science*. 2006;61(21):7019-28.

23. Chibowski E, Holysz L, Wojcik W. Changes in Zeta-Potential and Surface Free-Energy of Calcium-Carbonate Due to Exposure to Radiofrequency Electric-Field. *Colloid Surface A*. 1994;92(1-2):79-85.

24. Chibowski E, Hotysz L, Szczes A. Time dependent changes in zeta potential of freshly precipitated calcium carbonate. *Colloid Surface A*. 2003;222(1-3):41-54.

25. Kes M. Determination of the particle interactions - rheology- surface roughness relationship for dental ceramics [M.S]. İzmir: İzmir Institute of Technology; 2007.

26. Kilic S, Toprak G, Ozdemir E. Stability of CaCO₃ in Ca(OH)₂ solution. *Int J Miner Process*. 2016;147:1-9.

27. Ulkeryildiz E, Kilic S, Ozdemir E. Rice-like hollow nano-CaCO₃ synthesis. *Journal of Crystal Growth*. 2016;450:174-80.

28. Ulkeryildiz E, Kilic S, Ozdemir E. Nano-CaCO₃ synthesis by jet flow. *Colloid Surface A*. 2017;512:34-40.

29. Carmona JG, Morales JG, Rodriguez-Clemente R. Rhombohedral-scalenohedral calcite transition produced by adjusting the solution electrical conductivity in the system Ca(OH)₂-CO₂-H₂O. *J Colloid Interf Sci*. 2003;261(2):434-40.

30. Carmona JG, Morales JG, Sainz JF, Loste E, Clemente RR. The mechanism of precipitation of chain-like calcite. *Journal of Crystal Growth*. 2004;262(1-4):479-89.

31. Johannsen K, Rademacher S. Modelling the Kinetics of Calcium Hydroxide Dissolution in Water. *Acta Hydrochimica Et Hydrobiologica*. 1999;27(2):72-8.

32. Ozdemir E. Biomimetic CO₂ Sequestration: 1. Immobilization of Carbonic Anhydrase within Polyurethane Foam. *Energ Fuel*. 2009;23:5725-30.

33. Xu AW, Ma YR, Colfen H. Biomimetic mineralization. *J Mater Chem*. 2007;17(5):415-49.

34. Gunasekaran S, Anbalagan G. Spectroscopic study of phase transitions in natural calcite mineral. *Spectrochim Acta A*. 2008;69(4):1246-51.

35. Montes-Hernandez G, Fernández-Martínez A, Charlet L, Tisserand D, Renard F. Textural properties of synthetic nano-calcite produced by hydrothermal carbonation of calcium hydroxide. *Journal of Crystal Growth*. 2008;310(11):2946-53.

36. Carmona JG, Morales JG, Sainz JF, Clemente RR. Morphological characteristics and aggregation of calcite crystals obtained by bubbling CO₂ through a Ca(OH)₂ suspension in the presence of additives. *Powder Technol*. 2003;130(1-3):307-15.

37. Jung WM, Kang SH, Kim W-S, Choi CK. Particle morphology of calcium carbonate precipitated by gas-liquid reaction in a Couette-Taylor reactor. *Chemical Engineering Science*. 2000;55(4):733-47.

38. Burns JR, Jachuck JJ. Monitoring of CaCO₃ production on a spinning disc reactor using conductivity measurements. *Aiche J*. 2005;51(5):1497-507.

39. Lin RY, Zhang JY, Bai YQ. Mass transfer of reactive crystallization in synthesizing calcite nanocrystal. *Chemical Engineering Science*. 2006;61(21):7019-28.

40. Takemura F, Matsumoto Y. Dissolution rate of spherical carbon dioxide bubbles in strong alkaline solutions. *Chemical Engineering Science*. 2000;55(18):3907-17.

41. Molva M, Kilic S, Ozdemir E. Effect of carbonic anhydrase on CaCO_3 crystallization in alkaline solution. *Energ Fuel*. 2016;30(12):10686-95.
42. Rodriguez-Blanco JD, Shaw S, Benning LG. The kinetics and mechanisms of amorphous calcium carbonate (ACC) crystallization to calcite, via vaterite. *Nanoscale*. 2011;3(1):265-71.
43. Rodriguez-Blanco JD, Shaw S, Bots P, Roncal-Herrero T, Benning LG. The role of pH and Mg on the stability and crystallization of amorphous calcium carbonate. *J Alloy Compd*. 2012;536:S477-S9.
44. Tai CY, Chen FB. Polymorphism of CaCO_3 precipitated in a constant-composition environment. *Aiche J*. 1998;44(8):1790-8.



(This article was produced from 6th National Congress of Inorganic Chemistry and was sent to the JOTCSA editorial board for publication)

CrVMoO₇: MICROWAVE SYNTHESIS AND STRUCTURAL CHARACTERIZATION

Gülşah Çelik Gül ¹ 

¹University of Balıkesir, 10145, Balıkesir, Turkey

Abstract: In this study, microwave synthesis method was operated to obtain CrVMoO₇. Structural characterization of the compound was realized by powder X-ray diffraction (XRD) and Fourier transform infrared spectrometry (FTIR). Morphological property and elemental composition were determined via scanning electron microscopy (SEM) and energy dispersive X-ray analysis (EDS). Thermal nature of the sample was identified by thermogravimetric analyzer (TGA).

Keywords: CrVMoO₇; X-ray diffraction; Rietveld refinement method; Microwave synthesis.

Submitted: May 22, 2017. **Accepted:** July 16, 2018.

Cite this: Çelik Gül G. CrVMoO₇: MICROWAVE SYNTHESIS AND STRUCTURAL CHARACTERIZATION. JOTCSA. 2018;5(2):881-4.

DOI: <http://dx.doi.org/10.18596/jotcsa.315212>.

***Corresponding author.** E-mail: gulsahcelik9@gmail.com, Tel.: +90 266 612 1067/2012.

INTRODUCTION

Catalysis for most industrial processes has significance due to saving time, energy, and money. The catalysts used in these processes are generally transition metal oxides which are applied either alone or mixtures. The basic mixtures contain V₂O₅ and MoO₃/WO₃/Fe₂O₃/Cr₂O₃. Among them, Cr₂O₃-V₂O₅-MoO₃ three-component system has been studied in early times by many researchers (1-4). The formula CrVMoO₇ as unknown phase has occurred by the reaction of Cr₂O₃-V₂O₅-MoO₃ system in the solid-state form (5-7). The properties of this phase have been limitedly known, except melting point at 820 °C to form solid Cr₂O₃ (2). According to the other investigations, the related phase has been formed via incorporation of MoO₃ into the Cr₂V₄O₁₃ lattice (6, 7). It has not been examined in previous reports what the nature of CrVMoO₇ is and how the structure occurs (3, 8, 9). There are only a few documents about crystallographic morphology and thermal properties of CrVMoO₇. The prominent one is about indexing of powder X-ray diffraction pattern and calculation of unit cell parameters of CrVMoO₇ resulting a=5.53346 Å, b=6.58901 Å and c=7.86551 Å in triclinic system

(8). The infrared spectrum of the compound point out that VO₄, MoO₄ and CrO₆ subgroups exist in the structure (10, 11). As a result of these, to the best of our knowledge, microwave synthesis, crystallographic, morphologic and thermal properties of CrVMoO₇ have been studied for the first time with this paper which has not been reported previously.

MATERIALS AND METHODS

Cr₂O₃, V₂O₅ and MoO₃ compounds have been used as analytical grade and supplied by Merck. Oxide types starting materials have been weighed in 0.5:0.5:1 molar ratio and ground in an agate mortar followed by microwave treatment in a domestic microwave oven (2.45 GHz, 850 W power) for 20 min. The final sample has been washed three times with hot pure water and ethanol. The washed material has been treated at 400 °C for 2 hours to get the best crystals.

The powder X-ray diffraction (XRD) measurement has been completed by Panalytical X'Pert Pro Diffractometer and CuK_α radiation (λ=1.54056 Å, 40 mA, 50 kV) with a scan rate of 1°/min with a step size 0.02°. The Rietveld analysis of the sample has been calculated by using powder

diffraction data via High Score Plus (HS+) Program (License number: 92000029). Fourier transform infrared spectrum (FTIR) has been formed on a Perkin Elmer Spectrum 100 FTIR Spectrometer from 4000 to 650 cm^{-1} . Scanning electron microscopy/energy dispersive X-ray analysis has been achieved in SEM JEOL 6390-LV/EDX. Thermal property of the sample has been checked by Perkin Elmer thermogravimetric analyzer TGA. A Siemens V12 domestic microwave oven has been used as the microwave source.

RESULTS AND DISCUSSION

Figure 1 displays the XRD pattern of the synthesized material. The XRD pattern of the sample corresponds to CrVMoO_7 with the ICSD card number 008-5712 (Fig. 2). The unit cell parameters of the observed diffraction data has been calculated by Rietveld Refinement Program. The findings are completely in accordance with database given in Table 1. There is no other phase as an impurity or starting material.

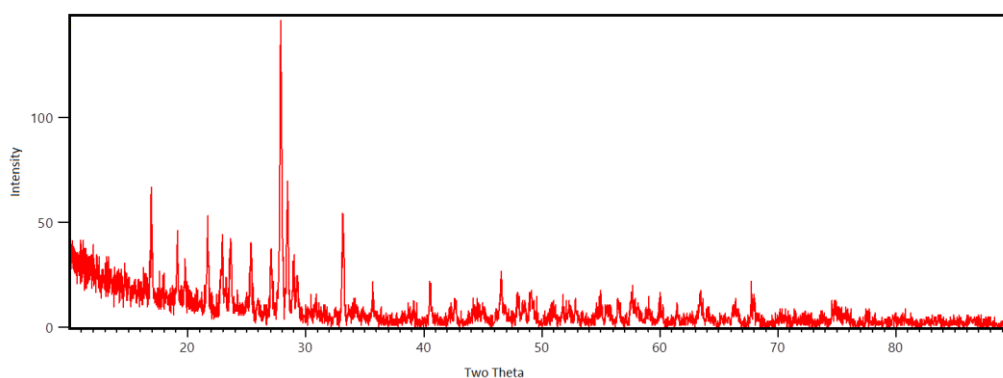


Figure 1. The XRD pattern of CrVMoO_7 .

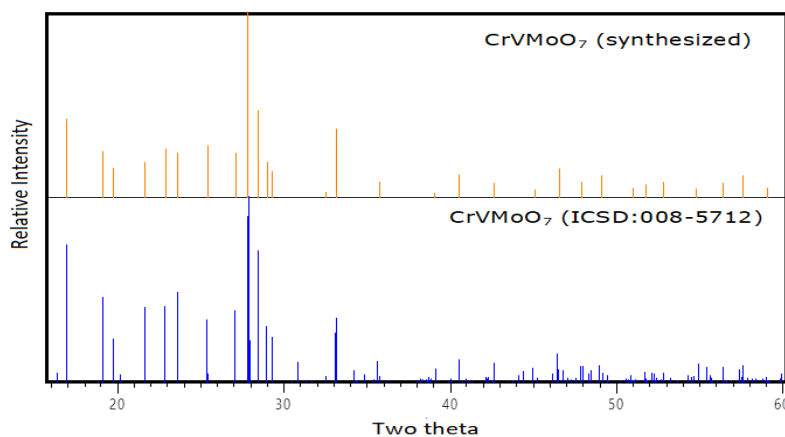


Figure 2. The comparison of powder XRD pattern between CrVMoO_7 (ICSD:008-5712) and CrVMoO_7 (synthesized).

Table 1. The comparison of unit cell parameters calculated and database values.

Compound	Unit cell parameters		
	a (Å)	b (Å)	c (Å)
CrVMoO_7 (ICSD:008-5712)	5.5310	6.5850	7.8640
CrVMoO_7 (synthesized)	5.5253	6.5792	7.8532

Figure 3 shows FTIR spectrum of CrVMoO_7 . The four wavenumbers in the range of 600-1000 cm^{-1}

¹ correspond to vibrations of M-M and Mo-O bonds (12-14).

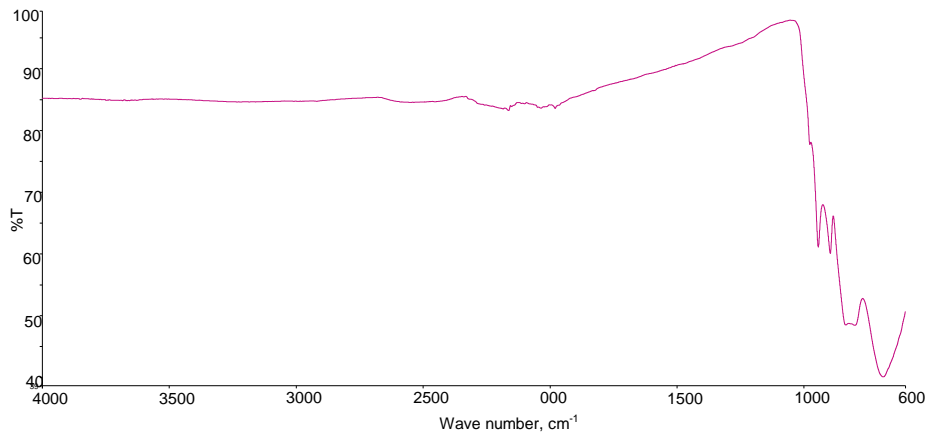


Figure 3. The FTIR spectrum of CrVMoO₇.

formation of chromium vanadium molybdate. The particle size distribution of CrVMoO₇ is in 2-5 μm.

Figure 4 exhibits the SEM micrograph of CrVMoO₇. The homogeneous view of the sample confirm the

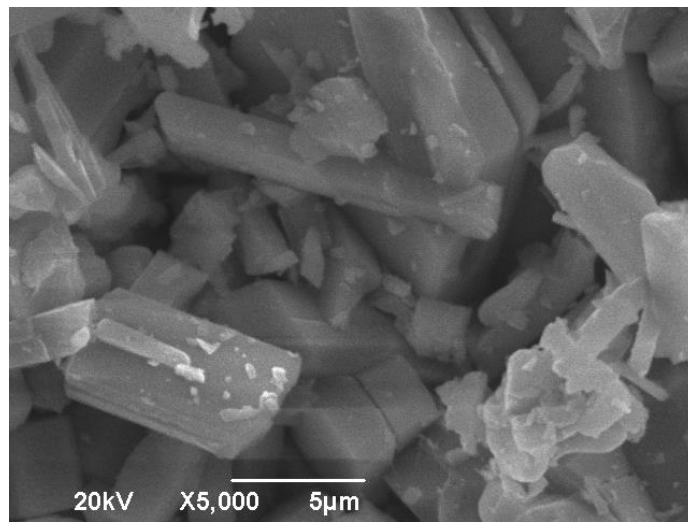


Figure 4. The SEM image of CrVMoO₇.

The EDS graph of CrVMoO₇ is given in Figure 5. The elemental composition of the compounds has been calculated as 3:3:3.2:6.8 by EDS results

which are in accordance with the molecular formula.

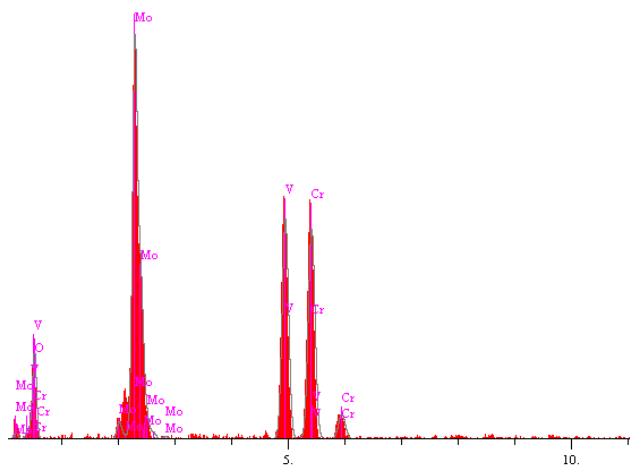


Figure 5. The EDS graph of CrVMoO₇.

The graph of thermogravimetric analysis is represented in Figure 6. The first smaller thermal loss starts nearly at 700 °C, and the other is in

the range of 1050–1200 °C. The material lost totally 40% of its mass.

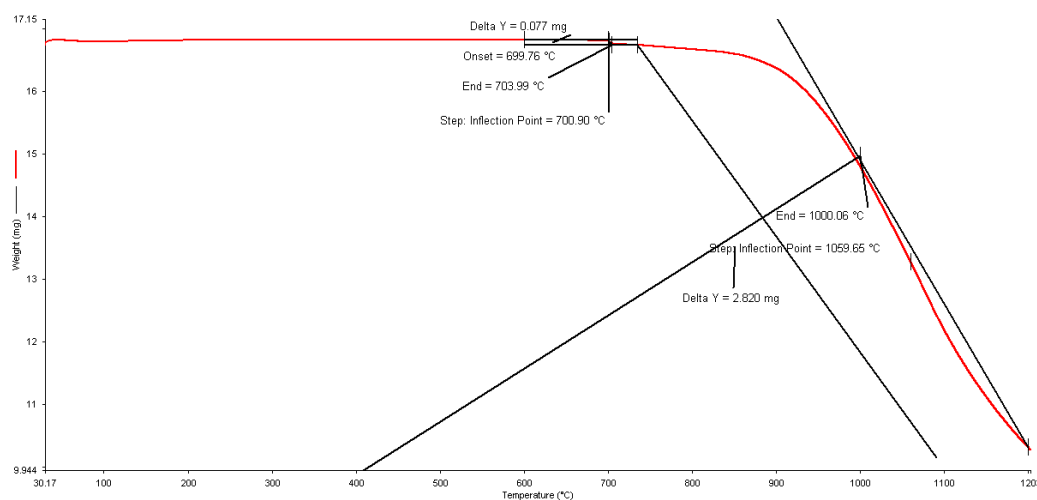


Figure 6. TGA thermograph of CrVMoO₇.

As a conclusion, CrVMoO₇ has been synthesized for the first time with microwave method at 850 W power for 20 minutes. The unit cell parameters of the compound have been calculated by Rietveld Refinement Program benefiting from XRD data. The homogeneous morphology and similar elemental composition have been confirmed via SEM and EDS results. High thermal stability of the compound has been determined from TGA.

ACKNOWLEDGMENTS

We want to thank The Scientific and Technological Research Council of Turkey and Scientific Research Project Fund of Balikesir University for financial supports and Dr. Sevim Demirözü Şenol for scientific support.

REFERENCES

1. Walczak J, Filipek E. In Sofia, Bulgaria: IUPAC; 1987. p. 171.
2. Walczak J, Filipek E. The CrVO₄-MoO₃ system. *Thermochimica Acta*. 1989 Sep;150(1):125–31.
3. Walczak J, Filipek E. Phase equilibria in the Cr₂V₄O₁₃-CrVMoO₇ system. *Thermochimica Acta*. 1990 May;161(2):239–45.
4. Walczak J, Filipek E. Studies on the V₂O₅-CrVMoO₇ system. *Thermochimica Acta*. 1990 Dec;173:235–40.
5. Walczak J, Filipek E. *Zeszyty Naukowe Politechniki Slaskiej. Seria: Chemia*. 1988;119(958):380.
6. Walczak J, Filipek E. Reactivity of MoO₃ towards Cr₂V₄O₁₃. *Thermochimica Acta*. 1988 Oct;133:67–72.
7. Kuriata J, Sadłowski L, Walczak J, Filipek E. Temperature Dependence of the EPR Linewidth of CrVO₄. *physica status solidi (b)*. 1987 Jul 1;142(1):K73–7.
8. Walczak J, Filipek E, Tabero P. CrVMoO₇ and phase equilibria in the V₉Mo₆O₄₀-CrVMoO₇ system. *Thermochimica Acta*. 1992 Sep;206:279–84.
9. Walczak J, Filipek E. Studies on the CrVMoO₇-Cr₂(MoO₄)₃ system. *Thermochimica Acta*. 1993 Nov;228:127–30.
10. Walczak J, Rychiowska-Himmel I, Tabero P. Iron(III) tungstate and its modifications. *Journal of Materials Science*. 1992;27(13):3680–4.
11. Plasova L, Kefeli L. *Inorganic Materials*. Vol. 3. 1967. 906 p.
12. Baykal A, Kizilyalli M, Kniep R. X-ray powder diffraction and IR study of NaMg (H₂O)₂ [BP2O8]·H₂O and NH₄Mg (H₂O)₂ [BP2O8]·H₂O. *Journal of materials science*. 2000;35(18):4621–4626.
13. Gözel G, Kizilyalli M, Kniep R. Characterization of a new calcium ultraphosphate, Ca₃ (P₅O₁₄)₂. *Journal of Solid State Chemistry*. 1997;129(2):196–199.
14. Gözel G, Baykal A, Kizilyalli M, Kniep R. Solid-State Synthesis, X-ray Powder Investigation and IR Study of α-Mg₃[BPO₇]. *Journal of the European Ceramic Society*. 1998 Dec;18(14):2241–6.



Synthesis and Characterization of Jeffamine Core PAMAM Dendrimer-Silver Nanocomposites (Ag JCPDNCs) and Their Evaluation in the Reduction of 4-Nitrophenol

Mustafa Ulvi Gürbüz¹✉, Ali Serol Ertürk^{2*}✉

¹Yıldız Technical University, Faculty of Arts and Sciences, Department of Chemistry, 34210, Esenler, İstanbul, Turkey.

²Adıyaman University, Faculty of Pharmacy, Department of Analytical Chemistry, 02040, Adıyaman, Turkey.

Abstract: This paper presents the synthesis, characterization, and catalytic evaluation of Jeffamine core PAMAM dendrimer-silver nanocomposites (Ag JCPDNCs). Generation-4 polymeric Jeffamine cored PAMAM dendrimer (JCPD or P4.NH₂) was used as the stabilizing and templating agent for the synthesis of Ag-JCPDNCs. Characterization of the synthesized Ag JCPDNC was performed by UV-visible (UV-Vis) spectroscopy and high resolution transmission electron microscopy (HRTEM). The catalytic activity of dendrimer nanocomposite (DNC) was assessed on the reduction of 4-nitrophenol (4-NP) to 4-aminophenol (4-AMP) in the presence of sodium borohydride (NaBH₄) as reducing agent by monitoring the conversion at $\lambda = 400$ nm. The prepared Ag JCPDNCs displayed a good catalytic activity ($K = 0.12 \times 10^{-2} \text{ s}^{-1}$) for the model reduction reaction of 4-NP with the particle size distribution of 4.72 ± 0.81 nm, which offer a mixed type (interior and exterior) of DNC formation. The Ag JCPDNCs can be a valid complete alternative to their existing candidates in the literature with their different polymeric organics components and be great potential for the future studies as new materials.

Keywords: Poly (amidoamine) Dendrimers (PAMAMs), Dendrimer Nanocomposite (DNC), Jeffamine, 4-nitrophenol, Kinetics.

Submitted: May 30, 2018. **Accepted:** July 16, 2018.

Cite this: Gürbüz M, Ertürk A. Synthesis and Characterization of Jeffamine Core PAMAM Dendrimer-Silver Nanocomposites (Ag JCPDNCs) and Their Evaluation in the Reduction of 4-Nitrophenol. JOTCSA. 2018;5(2):885-94.

DOI: <http://dx.doi.org/10.18596/jotcsa.428572>.

***Corresponding author.** E-mail: aserturk@gmail.com; Phone: +90-416-2233800/2808; fax: +90 (416) 223 3809.

INTRODUCTION

Over the last decades, due to their unique structural properties, metal nanoparticles (NPs) have received greater attraction in various applications compared to their bulk counterparts (1, 2). Although NPs have been applied in several applications (3-7), their use as catalysts has attracted great interest (8-10). In case of their prone-to-agglomerate in solution, stabilization of NPs is of great deal. Among various stabilizers such as surfactants (11), ligands, micelles and polymers (12, 13), dendrimers are promising templates to synthesize numerous transition

metal NPs such as Ag (14-16), Au (14, 17), Cu (18, 19), Ni (20), and Ru (21) with well-regulated size, position, and composition depending on their three-dimensional, monodisperse, unique architectures preventing them from nanoparticle growth, assembly, aggregation, and damage (22, 23). Thus, the size and shape of the resulting dendrimer nanocomposites (DNCs) or dendrimer-encapsulated metal nanoparticles (DENs), can remain steady so that a constant desired activity can be reached. These characteristics of DNCs make them useful and attractive in various applications involving optoelectronics (24), semiconductor, noble metals, magnetic DNC,

environmental cleanup, and especially in catalysis (25-27). In particular, DNCs can be potentially used in homogeneous and heterogeneous catalysis owing to their size and the ability to design catalytic active sites (28).

In recent years, DNCs have been intensively prepared and characterized by using commercially available ethylene diamine core poly(amido amine) (PAMAM) cored dendrimers, and their catalytic properties were investigated (22). Results of these studies revealed that generation number and surface functional group has a crucial role on effect on the catalytic activity of DNCs. However, no one to the best of our knowledge has studied to the preparation of DNCs by using a polymeric cored PAMAM dendrimer and a little attention has been paid for the preparation DNCs from PAMAMs having a different core than traditional ones (ethylene diamine) and investigation of their catalytic activities.

Nitrophenols are regarded to be one of the most common sources of organic pollutants from industrial and agricultural activities. This case also involves the companies which area manufacturing explosives, dyestuffs, insecticides, and other products (29-31). In particular, United States Environmental Protection Agency (USEPA) considers nitrophenols as the leading toxic pollutants (19). Interestingly, 4-aminophenol (4-AMP) is an important commercial intermediate for the production of analgesic and antipyretic drugs, one of which is paracetamol (32). Thus, the direct catalytic reduction of 4-nitrophenol (4-NP) to the 4-AMP is a significant and urgent request by many industries as it could be an environmentally friendly process (33).

In one of our recent studies (34), we have reported the microwave assisted fast, facile and one pot synthesis of polymeric cored Jeffamine core PAMAM dendrimers (JCPDs) up to generation-4 (G4). Here, we introduce for the first time the synthesis and characterization of Jeffamine core PAMAM dendrimer-silver nanocomposites (Ag-JCPDNCs) with the use G4 JCPD and later applied these DNCs in the catalytic conversion of 4-NP to 4-AMP by using sodium borohydride (NaBH_4).

MATERIALS AND METHODS

Chemicals and Materials

Jeffamine® T-403 cored and amine terminated P4.NH₂ PAMAM dendrimers were synthesized by using microwave technology according to the

procedure which was reported in our recent study (34). All the other chemicals were of analytical grade and obtained from Merck and Sigma chemical companies, and used without any further purifications. All the experiments were conducted using ultrapure water (18.2 mΩ cm) from a Millipore Milli-Q system.

Instrumentation

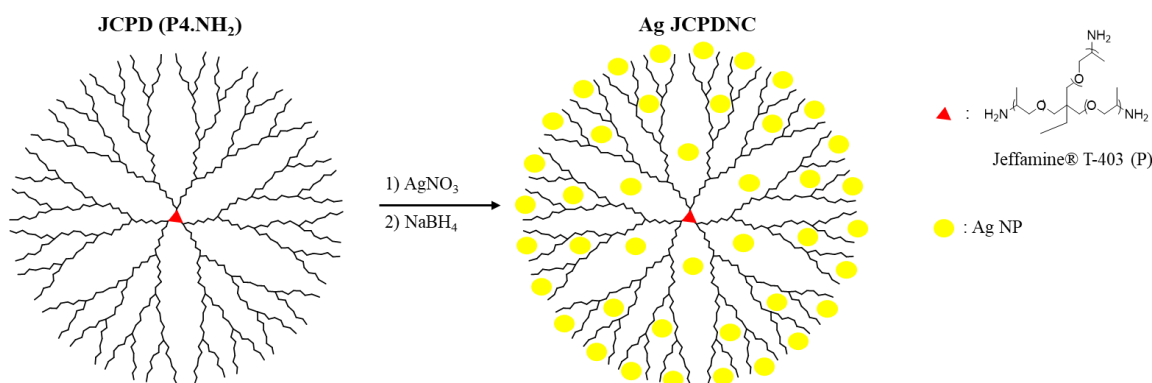
pH measurements were performed with Mettler Toledo five easy pH meter. Calibration of the pH meter was performed by using pH solutions at 4.01, 7.00 and 10.01 standard solutions (Merck Millipore, USA).

Ultraviolet-visible (UV-Vis) absorption spectra were recorded with Cary 60 UV-Vis spectrophotometer (Agilent, USA) with 1-cm quartz cells. The morphology and the sizes of the Ag JCDNCs were characterized using a Tecnai G2 Spirit BioTwin high resolution transmission electron microscope (HRTEM, FEI, USA) at 80 kV accelerating voltage. The microscope was equipped with a charge couple device (CCD) digital camera and samples were prepared by using 200 mesh carbon-coated copper grid.

Microwave-irradiated reactions were carried out with a microwave reactor (Discover SP, CEM, Matthews, NC, USA), with a continuous microwave power delivery system with operator selectable power output from 0 to 300 W (± 30 W) programmable at 1-watt increments, infrared temperature control system programmable from 25 to 250 °C, pressure controlled and 5 to 125 mL vessel capacity was used as microwave reactor.

Preparation of Ag-JCPDNCs

The synthetic method used in the preparation of Ag JCPDNCs was adapted from the literature with slight modifications (35). Briefly, the pH of the P4.NH₂ 2 mM dendrimer solution (0.2 mmol, 10 mL in water) was adjusted approximately to 2.0 by using 0.1 N HNO₃ solution. Then, aqueous 8.75 mM AgNO₃ solution (2 mmol, 228 μL) was added to the dendrimer solution. The mixture was stirred for 4 h by purging nitrogen to allow Ag⁺ ions to coordinate with the tertiary amine groups of the dendrimer. This was followed by the dropwise addition of 10-fold excess of 0.1 M NaBH₄ aqueous solution (20 mmol, 200 μL) to reduce the Ag⁺ ions to Ag⁰ in P4.NH₂/Ag⁺ salt complex. The colorless solutions turned immediately to yellow. The reaction was stirred for 1 h at room temperature and the UV-Vis measurements were performed (Scheme 1).



Scheme 1. Schematic illustration of the preparation of P4.NH₂ dendrimer-encapsulated silver nanoparticles (Ag JCPDNCs).

Catalytic Activity Assay

The catalytic activity of Ag JCPDNCs was investigated in the reduction of 4-NP to 4-AMP. In a typical catalysis assay, Ag JCPDNC (100 μ L, 0.02 mM), 0.1 M NaBH₄ (35 mmol, 350 μ L), deionized water (2.5 mL) and 12.75 mM 4-NP (0.38 mmol, 30 μ L) were mixed together in a 10 mm path-length glass cuvette. The change in the absorbance of 4-NP as a function of time was monitored by UV-Vis spectrophotometry in the wavelength range of 250-500 nm immediately. The yellow solution turned to colorless gradually in the presence of dendrimer nanocomposites.

RESULTS AND DISCUSSION

Characterization of Ag JCPDNCs

The preparation of Ag JCPDNCs using JCPDs as

templates were monitored by UV-Vis spectra (Figure 1). Investigation of Figure 1 showed that neat aqueous JCPD solution displayed an absorption band approximately at λ 284 nm in accordance well correlated with the literature (34). The sudden appearance of a new absorption band at around λ 300 nm, indicating the occurrence of (Ag⁺)₁₀ JCPD complex between the tertiary amine groups of PAMAMs and Ag⁺ ions (36), was seen by the addition of the AgNO₃ solution. After reduction by NaBH₄, an intense plasmon peak at λ 400 nm were formed. This clear UV-Vis band was the proof the formation of Ag JCPDNCs and all these spectral changes were in good alignment with the literature where PAMAMs are used as templates for Ag NP preparation (35, 37, 38).

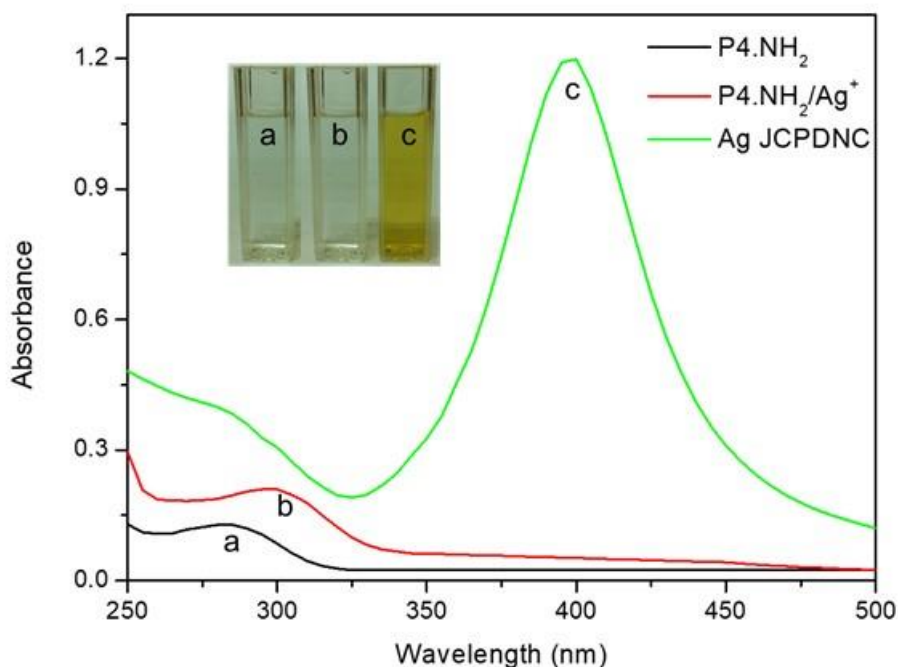


Figure 1. UV-Vis spectra of (a) JCPD or P4.NH₂, aqueous solution, (b) P4.NH₂/Ag⁺ complex and (c) Ag JCPDNC.

Unlike conventional NPs, which are usually in the structure of microcrystalline and their surface are passivated against further crystallization leading to secondary clustering by stabilizers, DNCs are

soft hybrid materials composed of inorganic domains embedded inside or dispersed on the surface of dendrimers and covalent branches behaving like separators (39). Such kind of their

unique structures enable them to be often as amorphous in different types of single nanocomposite structures in which the metal NPs are generated or stabilized as internal "I" (intra type DENs), external "E" (inter type DENs) or mixed "M". Former studies revealed that metallodendrimers, having average particle size between 1 to 4 nm, are supposed to be intra type DENs while those of greater than 5 nm are called as inter type DENs (39, 40).

In order to provoke the small sized Ag NP formation, we have kept the pH~2 and the time long by keeping to metal to dendrimer ratio (10) almost approximate the one fifth of the tertiary amine number (45) of JCPD P4.NH₂ so as to promote the formation of interior type DNCs. The morphology and the average NP size distribution were analyzed using HRTEM. The resultant micrograph and particle size distribution histogram are shown in Figure 2. In general, the

shape of Ag DENs exhibited spherical morphology. HRTEM characterization showed 83.06% distribution with the Ag DEN size of 4.71 ± 0.845 nm. It is noteworthy that the Ag DENs with the polydispersity index of 17.94%. These HRTEM results indicated and it could be concluded that mixed "M" type DNCs, where the NPs are stabilized in both interior and exterior of dendrimer, were formed in all cases when the JCPDs are used as the templating agent for the preparation of DNCs since the average NP size obtained in this study were above 4 nm but not greater than 5 nm (39, 40). Indeed, the smallest Ag DEN can be reasonably attributed to "I" type nanocomposite formation while biggest particles can be evidenced to "E" type formations. This could be attributed to use of G4 JCPD as the templating agent for the preparation of Ag DENs as being different from the existing literature where the conventional ethylene diamine monomer used as the core (35, 37, 38).

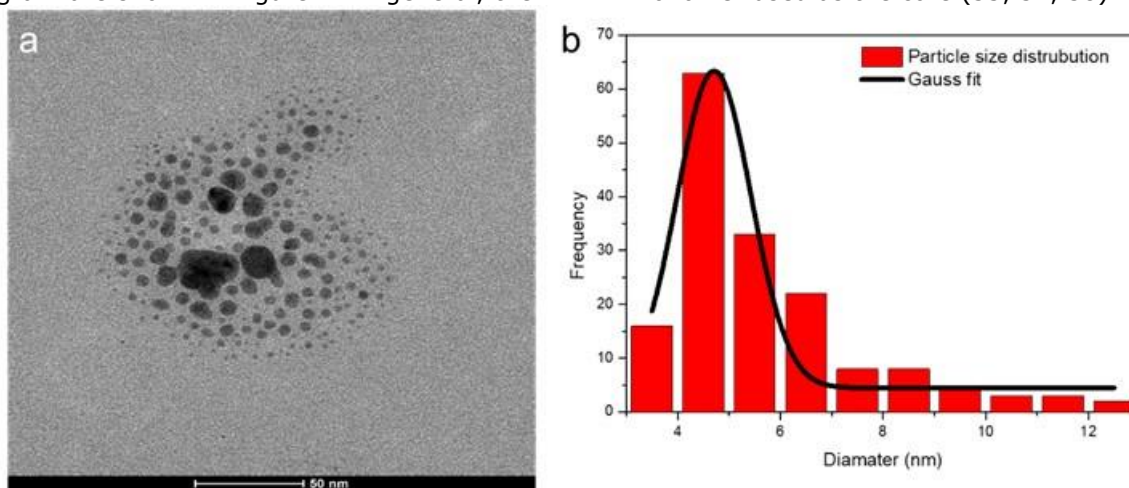


Figure 2. HRTEM image (a) and particle size distribution histogram of Ag JCPDNC (b).

Catalytic activity and UV measurements

The model reduction reaction of 4-NP to 4-AMP with NaBH₄ as the hydrogen source was chosen to estimate the catalytic activity of the synthesized Ag-JCPDNCs (35). This reaction has a unique feature of exhibiting maximum absorbance band at λ 317 nm in water whereas it has a maximum at λ 400 nm because of its conversion to p-nitrophenolate and can be pursued easily by observing the alteration in the UV-Vis spectrum at λ 300 and 400 nm (41). Before investigating the catalytic activity of DNCs, NaBH₄ was added to the 4-NP solution without the nanocatalyst to prove that the NaBH₄ compound used during the reduction only as the proton source. After 24 h, UV-Vis measurement of the prepared solution was taken again and an insignificant decrease in the adsorption band of 4-NP, which is indicating a non-proceeding of the reduction reaction even with the use of large

amount of NaBH₄, was remarked (Figure 3). In the presence of a catalyst, the addition of NaBH₄ arose a gradual drop in the absorption band λ 400 nm while a new characteristic absorption band occurrence and increase at around 295 nm, which is the characteristic peak of 4-AMP and signal of the successful reduction of the 4-NP to 4-AMP, was observed. (42, 43) (Figure 4). It is noteworthy that the UV-Vis spectra are useful tools to identify the species in the solution; however, it fails while getting information about the intermediated on the particle surfaces. All in all, the isosbestic point at λ ~325 nm proves the complete transformation of 4-NP to 4-AMP without side reactions (44). Therefore, it could be inferred that the reactant molecules establish a direct contact with the Ag DENs by transferring electrons from the donor BH₄⁻ to the acceptor 4-NP by adsorption through the dendrimer nanocomposites (42).

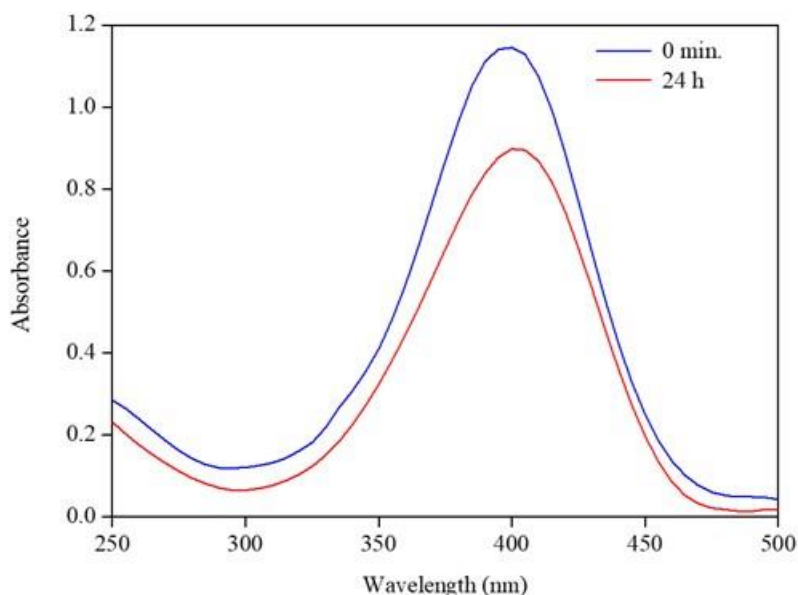


Figure 3. UV-Vis spectra of 4-NP in the presence of NaBH₄ without Ag JCPDNC.

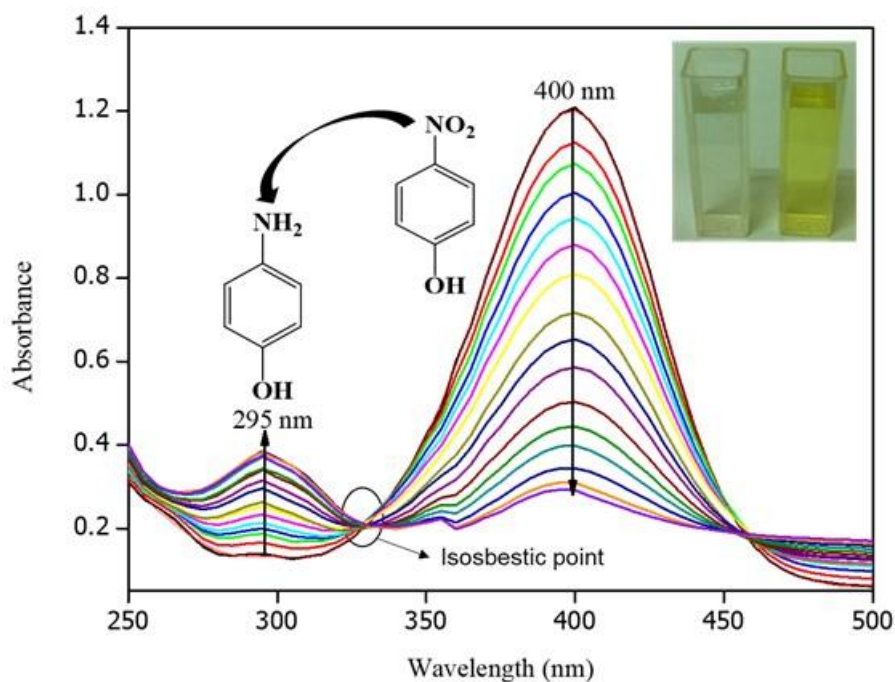


Figure 4. Time based variation in the UV-Vis spectra for the 4-NP reduction reaction in the presence of Ag JCPDNC ([4-NP] = 0.38 mmol; [NaBH₄] = 35 mmol; [Ag JCPDNC] = 0.02 mM; 25 °C)

In the reduction experiments, the reaction media was purged with nitrogen to avoid oxygen. Nevertheless, an induction time was observed in all cases up to 200 sec (Figure 5). This case is a typical one and is related with the activation time of the catalyst at heterogeneous catalytic processes (41). As the concentration of the all used NaBH₄ was in considerable excess in contrast to 4-NP, the reduction process guarantees pseudo-first-order reaction conditions as demonstrated in Figure 5. Investigation of Figure 5 reveals that there occurs and intercept

point at the absorbance variation scatter plots at λ 295 and 400 nm bands in time. This is the point where the solution color decolorized from yellow to colorless and the reaction ended (776.47 sec). The inset of Figure 5 displays the first order kinetic plots for the Ag JCPNCs. As it can be seen clearly, the linear fitting plot of $\ln(A/A_0)$ versus time obeys the first order kinetics and the apparent first-order rate constant (K) were calculated as 0.0012 s⁻¹ from the slope of this curve ($R^2 = 0.9982$).

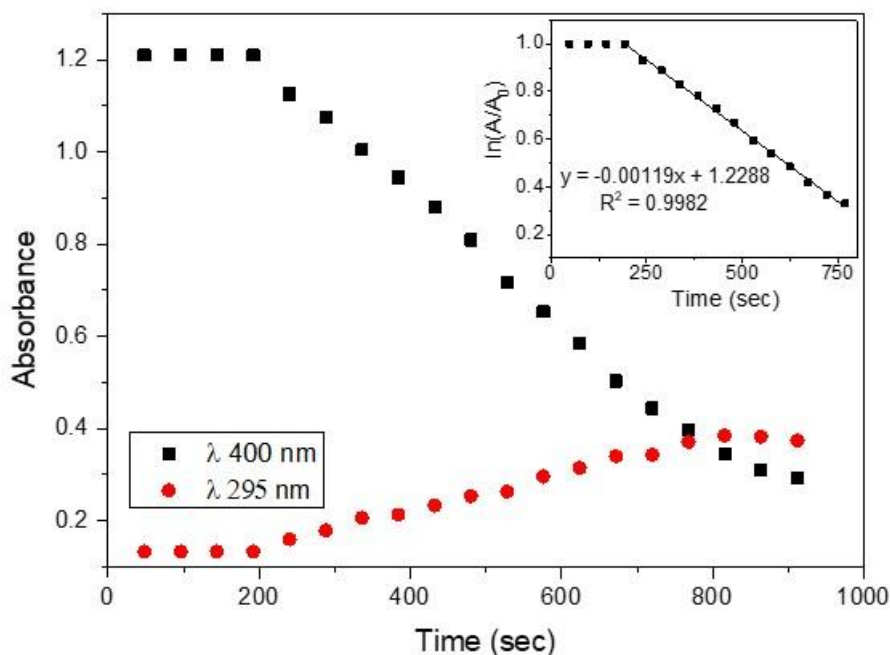


Figure 5. Time dependence of the adsorption of 4-NP ions at λ 295 and 400 nm. The inset demonstrates the linear fit for the first order kinetics at λ 400 nm ($[4\text{-NP}] = 0.38$ mmol; $[\text{NaBH}_4] = 35$ mmol; $[\text{Ag JCPDNC}] = 0.02$ mM; 25°C)

Table 1 shows the catalytic results obtained from different works for the reduction of 4-NP in the presence of Ag DNCs with different structures, where the Ag DENs involved and prepared by ethylene diamine cored conventional G4 amine-terminated PAMAMs as templates (15, 16, 35). As can be seen from Table 1, the rate constant obtained here for Ag JCPDNCs was considerable higher than DNCs having possible exterior type DNC structure while approximate to ones with interior type DNC structures. Notably, it could be clearly seen from Table 1 that a small decrease in the size of Ag DENs are resulted in observable enhance at the rate constant. This could be attributed to size and shape dependence of the synthesized Ag DENs to the type and variation of architecture of the used dendrimer template in the aqueous media as well as the synthesis conditions. Several factors such as generation size, type of core and repeating branches, density of functional groups and voids in the inner cavities can affect the conformation of dendrimers in aqueous media (45). Among these factors, pH is the one of the most important factors. Previous studies have shown that upon lowering the pH, amine-terminated PAMAMs display extended configuration owing to the electrostatic repulsions stemming from the protonated tertiary amine groups in the interior and primary amine groups at the periphery so that dendrimer branches apart (46, 47). On the contrary, at high pHs over 9, shrinking or back-folding happens on account of

the hydrogen bonding between the tertiary amine and surface primary amine groups leading a densely packed structure to dendrimer (47, 48). Considering these results, the common property of the procedures presented in Table 1 except for exterior type possible DNC structure formation is the use of acidic media, $\text{pH} \sim 2$, in the preparation of Ag DENs with a well-defined metal dendrimer ratio for G4 amine-terminated PAMAMs. Thus, the extended structure of the dendrimer templates should be favored to formation of inner type DENs with particles sizes lower than 4 nm. For our study, mixed type DNC structure have been observed. This could be attributed to pH-dependent conformational change and nature of the charged groups on the polymeric Jeffamine core P4.NH₂ PAMAM template due to their extent of protonation, and therefore, stabilization properties while preparing Ag DNCs. In particular, it might be difficult for the substrate to contact the active metallic site on Ag JCPDNCs due to its different pH dependent conformation that may lead to increase in sterically branches emanating from three arms in contrast to two for conventional PAMAMs. Thus, this could be also attributed differences in particle sizes and negligible catalytic activity decrease for Ag JCPDNCs. Overall, the proposed Ag JCPDNCs in here can be complete and good alternative to other Ag DENs present in the literature with mixed type possible structures and good catalytic behaviors.

Table 1. Comparison of the rate constants of Ag DNCs with the literature.

Catalyst	Dendrimer core	Possible DNC structure	D (nm)	K (s ⁻¹)	Reference
Ag ₁₂ DEN	EDA	Interior	3.1 ± 0.6	0.7 × 10 ⁻²	(35)
Ag ₁₃ DEN	EDA ^a	Interior	1.17 ± 0.13	1.1 × 10 ⁻²	(15)
Ag DEN	EDA	Exterior	6.5 ± 1.9	5.9 × 10 ⁻⁴	(16)
Ag ₁₀ DEN	Jeffamine	Mixed ^b	4.72 ± 0.81	0.12 × 10 ⁻²	This work

^a EDA: Ethylene diamine

^b Mixed: Interior and exterior

CONCLUSIONS

In this paper, G4 JCPDs which has a polymeric Jeffamine core were evaluated for the first time for the preparation of Ag JCPDNCs. The average particle size was found to be 4.72 ± 0.81 nm, which offers a mixed type of possible DNC structure. The prepared Ag JCPDNCs were found as catalytically active in the model reduction of 4-NP to 4-AMP by demonstrating first-order kinetics with a rate constant of 0.12 × 10⁻² s⁻¹, which offers a satisfactory and pleasurable performance compared with the existing literature with its different size distributions and structures. In particular, the synthesized Ag JCPDNCs can be a valid complete alternative and great potential to their existing candidates in the literature with their different polymeric organics components for the future studies.

ACKNOWLEDGMENT

This research has been supported by Adıyaman University Scientific Research Projects Coordination Department. Project Number: MÜFMAP/2015-0004.

REFERENCES

- Daniel MC, Astruc D. Gold Nanoparticles: Assembly, Supramolecular Chemistry, Quantum-Size-Related Properties, and Applications Toward Biology, Catalysis, and Nanotechnology. *Chem Rev.* 2004;104(1):293-346.
- Lkhagvajav N, Yaşa I, Çelik E, Koizhaiganova M, Sari O. Antimicrobial activity of colloidal silver nanoparticles prepared by sol-gel method. *Dig J Nanomat Biostr.* 2011;6(1):149-54.
- Ertürk AS, Elmacı G. PAMAM Dendrimer Functionalized Manganese Ferrite Magnetic Nanoparticles: Microwave-Assisted Synthesis and Characterization. *J Inorg Organomet Polym Mater.* 2018.
- Colvin VL, Schlamp MC, Alivisatos AP. Light-emitting diodes made from cadmium selenide nanocrystals and a semiconducting polymer. *Nature.* 1994;370(6488):354-7.
- Elghanian R, Storhoff JJ, Mucic RC, Letsinger RL, Mirkin CA. Selective colorimetric detection of polynucleotides based on the distance-dependent optical properties of gold

nanoparticles. *Science.* 1997;277(5329):1078-81.

6. Reetz MT, Winter M. Fabrication of metallic and bimetallic nanostructures by electron beam induced metallization of surfactant stabilized Pd and Pd/Pt clusters. *J Am Chem Soc.* 1997;119(19):4539-40.

7. Schön G, Simon U. A fascinating new field in colloid science: small ligand-stabilized metal clusters and their possible application in microelectronics - Part II: Future directions. *Colloid Polym Sci.* 1995;273(3):202-18.

8. Chen HC, Liu YC. Creating functional water by treating excited gold nanoparticles for the applications of green chemistry, energy and medicine: A review. *J Ind Eng Chem.* 2018;60:9-18.

9. Patnaik S, Sahoo DP, Parida K. An overview on Ag modified g-C₃N₄ based nanostructured materials for energy and environmental applications. *Renewable Sustainable Energy Rev.* 2018;82:1297-312.

10. Xiao W, Lei W, Gong M, Xin HL, Wang D. Recent Advances of Structurally Ordered Intermetallic Nanoparticles for Electrocatalysis. *ACS Catal.* 2018;8(4):3237-56.

11. Goikolea E, Insausti M, Lezama L, Gil de Muro I, Garitaonandia JS. Magnetic and structural characterization of silver-iron oxide nanoparticles obtained by the microemulsion technique. *J Non-Cryst Solids.* 2008;354(47-51):5216-8.

12. Manesh KM, Gopalan AI, Lee KP, Komathi S. Silver nanoparticles distributed into polyaniline bridged silica network: A functional nanocatalyst having synergistic influence for catalysis. *Catal Commun.* 2010;11(10):913-8.

13. Harish S, Mathiyarasu J, Phani KLN, Yegnaraman V. Synthesis of conducting polymer supported Pd nanoparticles in aqueous medium and catalytic activity towards 4-nitrophenol reduction. *Catal Lett.* 2009;128(1-2):197-202.

14. Nemanashi M, Meijboom R. Synthesis and characterization of Cu, Ag and Au dendrimer-encapsulated nanoparticles and their application in the reduction of 4-nitrophenol to 4-

- aminophenol. *J Colloid Interface Sci.* 2013;389(1):260-7.
15. Bingwa N, Meijboom R. Evaluation of catalytic activity of Ag and Au dendrimer-encapsulated nanoparticles in the reduction of 4-nitrophenol. *J Mol Catal A: Chem.* 2015;396:1-7.
16. Esumi K, Isono R, Yoshimura T. Preparation of PAMAM- and PPI-Metal (Silver, Platinum, and Palladium) Nanocomposites and Their Catalytic Activities for Reduction of 4-Nitrophenol. *Langmuir.* 2004;20(1):237-43.
17. Wu H, Liu Z, Wang X, Zhao B, Zhang J, Li C. Preparation of hollow capsule-stabilized gold nanoparticles through the encapsulation of the dendrimer. *J Colloid Interface Sci.* 2006;302(1):142-8.
18. Ertürk AS, Gürbüz MU, Tülü M, Bozdoğan AE. Preparation of Cu nanocomposites from EDA, DETA, and Jeffamine cored PAMAM dendrimers with TRIS and carboxyl surface functional groups. *Acta Chim Slov.* 2016;63(4):763-71.
19. Feng ZV, Lyon JL, Croley JS, Crooks RM, Vanden Bout DA, Stevenson KJ. Synthesis and Catalytic Evaluation of Dendrimer-Encapsulated Cu Nanoparticles. An Undergraduate Experiment Exploring Catalytic Nanomaterials. *J Chem Educ.* 2009;86(3):368.
20. Ma Z, Wu R, Han Q, Chen R, Gu Z. Preparation of well-dispersed and anti-oxidized Ni nanoparticles using polyaminoamine dendrimers as templates and their catalytic activity in the hydrogenation of p-nitrophenol to p-aminophenol. *Korean J Chem Eng.* 2011;28(3):717-22.
21. Antonels NC, Meijboom R. Preparation of well-defined dendrimer encapsulated ruthenium nanoparticles and their evaluation in the reduction of 4-nitrophenol according to the langmuir-hinshelwood approach. *Langmuir.* 2013;29(44):13433-42.
22. Tang YH, Huang AYT, Chen PY, Chen HT, Kao CL. Metallo-dendrimers and dendrimer nanocomposites. *Catal Commun.* 2011;17(22):2308-30.
23. Lesniak W, Blelinska AU, Sun K, Janczak KW, Shi X, Baker Jr JR, et al. Silver/dendrimer nanocomposites as biomarkers: Fabrication, characterization, in vitro toxicity, and intracellular detection. *Nano Lett.* 2005;5(11):2123-30.
24. Alivisatos AP. Semiconductor Clusters, Nanocrystals, and Quantum Dots. *Science.* 1996;271(5251):933-7.
25. Knapen JWJ, van dMAW, de WJC, van LPWNM, Wijkens P, Grove DM, et al. Homogeneous catalysts based on silane dendrimers functionalized with arylnickel(II) complexes. *Nature* 1994;372(6507):659-63.
26. Tomalia DA, Dvornic PR. What promise for dendrimers? *Nature.* 1994;372(6507):617-8.
27. Balogh L, Tomalia DA. Poly(Amidoamine) Dendrimer-Templated Nanocomposites. 1. Synthesis of Zerovalent Copper Nanoclusters. *J Am Chem Soc.* 1998;120(29):7355-6.
28. Van HR, Kamer PCJ, Van LPWNM, Reek JNH. Dendrimers as Support for Recoverable Catalysts and Reagents. *Chem Rev* 2002;102(10):3717-56.
29. Iinuma Y, Brueggemann E, Gnauk T, Mueller K, Andreae MO, Helas G, et al. Source characterization of biomass burning particles: the combustion of selected European conifers, African hardwood, savanna grass, and German and Indonesian peat. *J Geophys Res.* 2007;112(D8):D08209/1-D/26.
30. Mori T, Watanuki T, Kashiwagura T. Diesel exhaust particles disturb gene expression in mouse testis. *Environ Toxicol.* 2007;22(1):58-63.
31. Li C, Taneda S, Suzuki AK, Furuta C, Watanabe G, Taya K. Estrogenic and anti-androgenic activities of 4-nitrophenol in diesel exhaust particles. *Toxicol Appl Pharmacol.* 2006;217(1):1-6.
32. Rode CV, Vaidya MJ, Jaganathan R, Chaudhari RV. Hydrogenation of nitrobenzene to p-aminophenol in a four-phase reactor: Reaction kinetics and mass transfer effects. *Chem Eng Sci.* 2001;56(4):1299-304.
33. Chen R, Wang Q, Du Y, Xing W, Xu N. Effect of initial solution apparent pH on nano-sized nickel catalysts in p-nitrophenol hydrogenation. *Chem Eng J.* 2009;145(3):371-6.
34. Ertürk AS, Tülü M, Bozdoğan AE, Parali T. Microwave assisted synthesis of Jeffamine cored PAMAM dendrimers. *Eur Polym J.* 2014;52:218-26.
35. Nemanashi M, Meijboom R. Synthesis and characterization of Cu, Ag and Au dendrimer-encapsulated nanoparticles and their application in the reduction of 4-nitrophenol to 4-aminophenol. *Journal of Colloid and Interface Science.* 2013;389(1):260-7.
36. Subhas G, Sangeeta Y, Nadarajah V, Gabriela S. A study of antimicrobial property of textile fabric treated with modified dendrimers. *J Appl Polym Sci.* 2010;115(2):716-22.

37. Manna A, Imae T, Aoi K, Okada M, Yogo T. Synthesis of dendrimer-passivated noble metal nanoparticles in a polar medium: Comparison of size between silver and gold particles. *Chem Mater*. 2001;13(5):1674-81.
38. Esumi K, Suzuki A, Yamahira A, Torigoe K. Role of poly (amidoamine) dendrimers for preparing nanoparticles of gold, platinum, and silver. *Langmuir*. 2000;16(6):2604-8.
39. Balogh L, Valluzzi R, Laverdure KS, Gido SP, Hagnauer GL, Tomalia DA. Formation of Silver and Gold Dendrimer Nanocomposites. *J Nanopart Res*. 1999;1(3):353-68.
40. Manniledam K, R. PM, Edamana P, C. V, C. DP. Generation of Ag Nanoparticles by PAMAM Dendrimers and their Size Dependence on the Aggregation Behavior of Dendrimers. *Macromol Chem Phys*. 2009;210(16):1310-8.
41. Santos KdO, Elias WC, Signori AM, Giacomelli FC, Yang H, Domingos JB. Synthesis and Catalytic Properties of Silver Nanoparticle-Linear Polyethylene Imine Colloidal Systems. *J Phys Chem C*. 2012;116(7):4594-604.
42. Kurtan U, Baykal A. Fabrication and characterization of Fe₃O₄@APTES@PAMAM-Ag highly active and recyclable magnetic nanocatalyst: Catalytic reduction of 4-nitrophenol. *Mater Res Bull*. 2014;60:79-87.
43. Pradhan N, Pal A, Pal T. Catalytic reduction of aromatic nitro compounds by coinage metal nanoparticles. *Langmuir*. 2001;17(5):1800-2.
44. Corma A, Concepción P, Serna P. A different reaction pathway for the reduction of aromatic nitro compounds on gold catalysts. *Angew Chem*. 2007;46(38):7266-9.
45. Martinho N, Florindo H, Silva L, Brocchini S, Zloh M, Barata T. Molecular Modeling to Study Dendrimers for Biomedical Applications. *Molecules (Basel, Switzerland)*. 2014;19(12):20424-67.
46. Lee I, Athey BD, Wetzel AW, Meixner W, Baker Jr JR. Structural molecular dynamics studies on polyamidoamine dendrimers for a therapeutic application: Effects of pH and generation. *Macromolecules*. 2002;35(11):4510-20.

47. Maiti PK, Çağın T, Lin S-T, Goddard WA. Effect of Solvent and pH on the Structure of PAMAM Dendrimers. *Macromolecules*. 2005;38(3):979-91.

48. Chen W, Tomalia DA, Thomas JL. Unusual pH-dependent polarity changes in PAMAM dendrimers: evidence for pH-responsive conformational changes. *Macromolecules*. 2000;33(25):9169-72.



Palladium(II) Complexes of Monodentate Phosphine Ligands and Their Application as Catalyst in Suzuki-Miyaura C-C Coupling Reaction at Room Temperature

Mustafa Kemal Yılmaz^a, Simay İnce^b

^aMersin University, Faculty of Arts and Sciences, Department of Chemistry, 33343 Mersin, Turkey.

^bOsmaniye Korkut Ata University, Faculty of Arts and Sciences, Department of Chemistry, 80000 Osmaniye, Turkey.

Abstract: A series of palladium(II) complexes from monodentate phosphine ligands (**1a-4a**) were successfully prepared and characterized with ¹H, ³¹P, ¹³C NMR, and HRMS techniques. These pre-catalysts were applied for the Suzuki-Miyaura C-C coupling reaction of phenylboronic acid with bromobenzene and the influence of the base and solvent on the performance of the pre-catalysts was investigated. Sterically hindered and electronically deactivated aryl bromides as well as activated ones gave the corresponding coupling products in good to excellent yields at room temperature.

Keywords: Palladium, catalyst, phosphine, Suzuki-Miyaura C-C coupling.

Submitted: June 20, 2018. **Accepted:** July 17, 2018.

Cite this: Yılmaz M, İnce S. Palladium(II) Complexes of Monodentate Phosphine Ligands and Their Application as Catalyst in Suzuki-Miyaura C-C Coupling Reaction at Room Temperature. JOTCSA. 2018;5(2):895-902.

DOI: <http://dx.doi.org/10.18596/jotcsa.435122>.

***Corresponding author.** E-mail: mkyilmaz@mersin.edu.tr. Tel.: +90 324 361 00 01; fax: 90 324 361 00 73.

INTRODUCTION

Suzuki-Miyaura carbon-carbon (SM) coupling reactions generally catalyzed by palladium complexes have been most widely studied for the construction of new carbon-carbon bonds, since they allow the formation of highly complex molecules from relatively simple precursor (1-3). In the SM coupling reaction carbon-carbon bond formation takes place between phenylboronic acid and aryl or vinyl halides. In many cases, the reaction is homogeneously catalyzed by Pd(II) or Pd(0) complexes which were generally formed with phosphine, N-heterocyclic carbene (NHC) or salen type ligands, in good conversions and high yields. Especially, monodentate or bidentate phosphine ligands have been successfully applied for palladium-catalyzed C-C coupling reactions such as SM coupling because of their high reactivity, high turnover numbers and milder reaction conditions (4). Although extremely high catalytic activities can sometimes be achieved by using phosphine-free palladium catalysts such as Pd(OAc)₂, [(η³-C₃H₅)PdCl]₂, and [Pd₂(dba)₃], in some cases the formation of inactive palladium black during the catalytic cycle reveals the necessity of increasing the stability of the palladium center. So, sterically hindered tertiary phosphine ligands are generally used which has often circumvented catalyst deactivation by inhibiting the formation of palladium black (5,6).

So far, many types of monodentate phosphine ligands and their metal catalysts have been prepared and applied for various catalytic transformations such as hydrogenation, hydroformylation or several carbon-carbon coupling reactions etc., (7-9) but triphenylphosphine-based palladium(II) pre-catalysts were not examined for SM coupling reactions. Here we focused on the synthesis and characterization a series of Pd(II) complexes which have monodentate tertiary phosphine ligands and optimization studies of these pre-catalysts for SM coupling reactions. These pre-catalysts were also applied for SM coupling reactions using a wide range of substituted substrates, bearing electron releasing or withdrawing groups at different positions.

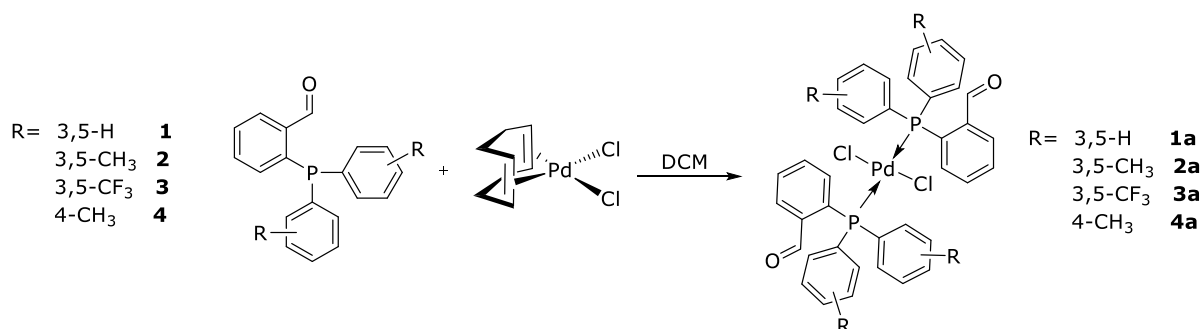
MATERIALS AND METHODS

General

All of the reagents were purchased from commercial sources (Aldrich or ABCR) and used as received, unless otherwise indicated. The solvents were dried, deoxygenated, and purified according to standard methods in the literature (10). 2-(Diphenylphosphino)benzaldehyde (**1**), 2-(bis(3,5-dimethylphenyl)phosphino)benzaldehyde (**2**), 2-(bis(3,5-bis(trifluoromethyl)phenyl)phosphino)benzaldehyde (**3**) and 2-(bis(4-tolyl)phosphino)benzaldehyde (**4**) and their Pd(II) complexes were prepared according to the published procedures (11-14). Pd(II) complexes were characterized by NMR analyses on a Bruker Ultrashield Plus Biospin Avance III 400 spectrometer NaNoBay FT-NMR operating at 400.2 MHz (¹H NMR), 162.0 MHz (³¹P{¹H} NMR) and 100.2 MHz (¹³C NMR) using acetone-d₆ or chloroform-d as the solvent. High resolution mass spectroscopy analyses were provided with a Waters series mass spectrometer (SYNAPT G1 MS model). Melting points were obtained with a Thermo scientific electrothermal digital programmable melting point apparatus system and are uncorrected. GCMS analyses were reported on an Agilent 7890A GC and 5975C MSD system equipped with Rxi-5ms capillary column (5% diphenyl/95% polysiloxane). Flash chromatography was applied on silica gel (230-400 mesh).

Synthesis of [PdCl₂(**1-4**)₂] pre-catalysts (**1a-4a**)

The synthesis of monodentate phosphine based Pd(II) complexes is shown in Scheme 1. The complexes [PdCl₂(**1-4**)₂] were prepared by the reaction of Pd(cod)Cl₂ (**15**) with the corresponding 2-(diaryl)phosphinobenzaldehyde (**1-4**) in dichloromethane according to the literature (16,17). To a solution of 2-(diaryl)phosphinobenzaldehyde (**1-4**) in CH₂Cl₂ (10 mL) was added Pd(cod)Cl₂ in CH₂Cl₂ (10 mL). Reaction mixture was stirred for 2 hours at 25 °C. The solvents were then evaporated and remaining precipitate was washed with diethyl ether to give the title Pd(II) complexes as an orange powder.



Scheme 1. Synthesis of Pd(II) Complexes.

Synthesis of [PdCl₂(1**)₂], (**1a**).** **1a** was prepared using 2-

(diphenylphosphino)benzaldehyde (10.4 mmol, 3.01 g) and Pd(cod)Cl₂ (5.07 mmol, 1.44 g)

according to the procedure given above. Yield 3.06 g (80%). **Melting point:** 219 °C. **¹H NMR (400.2 MHz, CDCl₃):** δ (ppm) 10.39 (s, -C(H)O, 2H), 7.92 (dd, *J* = 7.6, 1.5 Hz, ArH, 2H), 7.74 (dt, *J* = 12.7, 3.5 Hz, ArH, 9H), 7.50 (t, *J* = 7.4 Hz, ArH, 2H), 7.38 (d, *J* = 7.1 Hz, ArH, 6H), 7.33 (d, *J* = 7.5 Hz, ArH, 7H), 6.96 (dd, *J* = 12.4, 5.5 Hz, ArH, 2H). **³¹P NMR (162.0 MHz, CDCl₃):** δ (ppm) 20.28. **¹³C NMR (100.6 MHz, CDCl₃):** δ (ppm) 189.07 (s), 134.58 (t, *J*_{PC} = 6.4 Hz), 132.61 (t, *J*_{PC} = 2.5 Hz), 131.85 (t, *J*_{PC} = 4.0 Hz), 130.28 (t, *J*_{PC} = 3.5 Hz), 129.82 (s), 129.56 (s), 128.52 (s), 128.27 (s), 128.02 (s), 127.32 (t, *J*_{PC} = 5.4 Hz). **HRMS (ESI):** calcd. for [M+2H]²⁺: C₃₈H₃₀Cl₂O₂P₂Pd 758.0289; found [M+2H]²⁺: 758.0131.

Synthesis of [PdCl₂(2)₂], (2a). **2a** was prepared using 2-(bis(3,5-dimethylphenyl)phosphino)benzaldehyde (**2**) (11.6 mmol, 4.02 g) and Pd(cod)Cl₂ (5.6 mmol, 1.61 g) according to the procedure given above. Yield 3.83 g (78%). **Melting point:** 215-216°C. **¹H NMR (400.2 MHz, CDCl₃):** δ (ppm) 10.51 (s, -C(H)O, 2H), 7.91 (dd, *J* = 7.6, 1.4 Hz, ArH, 2H), 7.45 (t, *J* = 7.4 Hz, ArH, 2H), 7.35 (t, *J* = 5.7 Hz, ArH, 10H), 7.18 (s, ArH, 4H), 6.92 (dd, *J* = 12.6, 5.7 Hz, ArH, 2H), 2.22 (s, ArCH₃, 24H). **³¹P NMR (162.0 MHz, CDCl₃):** δ (ppm) 20.11. **¹³C NMR (100.6 MHz, CDCl₃):** δ (ppm) 189.80 (t, *J*_{PC} = 4.5 Hz), 138.30 (t, *J*_{PC} = 3.3 Hz), 137.85 (t, *J*_{PC} = 5.7 Hz), 133.52 (t, *J*_{PC} = 2.5 Hz), 133.26 (t, *J*_{PC} = 6.4 Hz), 132.82 (s), 130.34 (s), 129.87 (t, *J*_{PC} = 3.3 Hz), 129.04 (s), 128.80 (s), 128.55 (s), 21.45 (s). **HRMS (ESI):** calcd. for [M+2H]²⁺: C₄₆H₄₆Cl₂O₂P₂Pd 870.1541; found [M+2H]²⁺: 870.1385.

Synthesis of [PdCl₂(3)₂], (3a). **3a** was prepared using 2-(bis(3,5-bis(trifluoromethyl)phenyl)phosphino)benzaldehyde (**3**) (6.8 mmol, 3.82 g) and Pd(cod)Cl₂ (3.3 mmol, 0.94 g) according to the procedure given above. Yield 3.62 g (84%). **Melting point:** 225°C. **¹H NMR (400.2 MHz, (CD₃)₂CO):** δ (ppm) 9.87 (s, -C(H)O, 2H), 8.32 (t, *J* = 4.7 Hz, ArH, 8H), 8.17 (d, *J* = 1.5 Hz, ArH, 2H), 8.14 (s, ArH, 4H), 7.78 (t, *J* = 7.5 Hz, ArH, 2H), 7.63 (td, *J* = 7.6, 0.9 Hz, ArH, 2H), 7.29 (dd, *J* = 13.1, 5.7 Hz, ArH, 2H). **³¹P NMR (162.0 MHz, CDCl₃):** δ (ppm) 22.72. **¹³C NMR (100.6 MHz, (CD₃)₂CO):** δ (ppm) 192.95 (s), 140.18 (t, *J*_{PC} = 4.1 Hz), 136.36 (d, *J*_{PC} = 3.5 Hz), 136.01 (t, *J*_{PC} = 4.1 Hz), 135.45 (t, *J*_{PC} = 2.0 Hz), 135.00 (t, *J*_{PC} = 4.4 Hz), 133.88 (s), 133.64 (s), 133.39 (s), 132.28 (t, *J*_{PC} = 5.2 Hz), 131.95 (t, *J*_{PC} = 5.2 Hz), 127.63 (t, *J*_{PC} = 23.2 Hz), 126.01 (s), 124.03 (q, *J*_{PC} = 272.5 Hz). **HRMS (ESI):** calcd. for [M+2H]²⁺: C₄₆H₂₂Cl₂F₂₄O₂P₂Pd 1301.9280; found [M+2H]²⁺: 1301.9125.

Synthesis of [PdCl₂(4)₂], (4a). **4a** was prepared using 2-(bis(4-tolyl)phosphino)benzaldehyde (**4**) (9.54 mmol, 3.03 g) and Pd(cod)Cl₂ (4.6 mmol, 1.32 g) according to the procedure given above. Yield

3.09 g (82%). **Melting point:** 226°C. **¹H NMR (400.2 MHz, CDCl₃):** δ (ppm) 10.58 (s, -C(H)O, 2H), 8.02 (dd, *J* = 7.6, 1.4 Hz, ArH, 2H), 7.73 (dt, *J* = 7.6, 5.6 Hz, ArH, 8H), 7.57 (t, *J* = 7.5 Hz, ArH, 2H), 7.45 (t, *J* = 7.5 Hz, ArH, 2H), 7.23 (d, *J* = 7.9 Hz, ArH, 8H), 7.06 (dd, *J* = 12.9, 5.6 Hz, ArH, 2H), 2.40 (s, ArCH₃, 12H). **³¹P NMR (162.0 MHz, CDCl₃):** δ (ppm) 18.92. **¹³C NMR (100.6 MHz, CDCl₃):** δ (ppm) 190.08 (t, *J*_{PC} = 4.2 Hz), 141.20 (s), 138.29 (t, *J*_{PC} = 3.6 Hz), 135.54 (t, *J*_{PC} = 6.6 Hz), 133.47 (t, *J*_{PC} = 2.4 Hz), 133.20 (s), 133.00 (s), 132.76 (t, *J*_{PC} = 3.9 Hz), 130.59 (t, *J*_{PC} = 3.6 Hz), 130.40 (s), 129.19 (t, *J*_{PC} = 5.5 Hz), 126.14 (s), 125.89 (s), 125.63 (s), 21.49 (s). **HRMS (ESI):** calcd. for [M+2H]²⁺: C₄₂H₃₈Cl₂O₂P₂Pd 814.0915; found [M+2H]²⁺: 814.0758.

Procedure for the SM coupling reaction

Aryl halide (1.0 mmol), phenylboronic acid (1.2 mmol), base (1.2 mmol), catalyst (0.01 mmol) and 4.0 mL of solvent (organic solvent/water:2.0 mL/2.0 mL) was added in a sealed tube and the mixture was stirred for 5 hours at room temperature. Next, the mixture was washed with saturated ammonium chloride solution and extracted with chloroform. The organic phase was dried and then chromatographed on silica gel. Conversions and yields were determined by GCMS analyses.

RESULTS AND DISCUSSION

Characterization

All the palladium(II) complexes **1a-4a** are air- and moisture-stable and they are soluble in a wide range of polar solvents such as CHCl₃, MeOH and DCM, but insoluble in low-polar solvents or non-polar solvents. The NMR (¹H, ¹³C and ³¹P) spectra of the complexes were carried out in order to contribute to the characterization of the synthesized compounds. The Pd(II) complexes were further characterized by high resolution mass spectroscopy (HRMS) analyses and the results are in agreement with the proposed structures. Based on ³¹P NMR analysis, displacement of the phosphorus singlet peaks from up field in non-coordinated ligands (**1**: -11.96; **2**: -12.51; **3**: -6.49; **4**: -13.71 ppm) to the down field in the Pd(II) complexes (**1a**: 20.28; **2a**: 20.11; **3a**: 22.72; **4a**: 18.92 ppm) suggest the coordination of desired Pd(II) complexes (9, 16, 17). Also, the appearance of only one singlet indicates the formation of only one product. Meanwhile, the disappearance of the characteristic doublet (due to the coupling with the lone pair of phosphorus atom) of the aldehyde proton in the free ligands (**1**: 9.04 ppm (*J*_{PH} = 5.1 Hz); **2**: 8.94 ppm (*J*_{PH} = 5.3 Hz); **3**: 8.57 ppm (*J*_{PH} = 3.2 Hz); **4**: 10.58 ppm (*J*_{PH} = 5.5 Hz)) and formation of a singlet for the Pd(II) complexes (**1a**: 10.39; **2a**: 10.51; **3a**: 9.87; **4a**: 10.58 ppm) further confirmed the formation of the desired monodentate complexes (16-20). Otherwise, the signal of the methyl protons in **2a** and **4a** appeared at 2.22 and 2.40 ppm as singlet,

respectively. The signals for the aromatic protons of the complexes appear in the region 6.96-8.48 ppm as expected. In the ^{13}C NMR spectrum of the complexes, the signals of the aldehyde carbon are found at 189.07 (**1a**), 189.80 (**2a**), 192.95 (**3a**) and 190,08 (**4a**) ppm as singlet and triplet (probably carbon-carbon interaction has become more active due to the increasing electron density of the methyl carbon by methyl protons), respectively. Besides that, the signals of the methyl carbon, for the **2a** and **4a** complexes, were observed at 21.45 and 21.49 ppm, respectively (19, 21). Also, ^{13}C NMR spectrum of the complex **3a** showed the characteristic signal of $-\text{CF}_3$ bonded-carbon ($\text{CF}_3\text{-ArC}$) as a quartet at 124.03 ppm ($J_{\text{FC}}=272.5$ Hz) due to the fluorine-carbon coupling (13). These results and high resolution mass spectroscopy data which showed $[\text{M}+2\text{H}]^{2+}$ as the highest molecular weight fragment together support and are in agreement for our suggested structures of the monodentate phosphine-palladium(II) pre-catalysts shown in Scheme 1 (see supporting information).

SM coupling reactions

Initially, we performed optimization studies using various bases (K_2CO_3 , NaOAc , NaOH , and Et_3N) and polar aprotic solvents (1,4-dioxane and DMF) to determine how solvents and bases affect the SM coupling reaction between phenylboronic acid and bromobenzene in the presence of catalyst **1a** (substrate/catalyst:100/1) at room temperature (Figure 1). Among the bases examined, Et_3N afforded none or very little of the biphenyl in both DMF and 1,4-dioxane. We found better

conversion for K_2CO_3 in both solvent when compared to the Na_2CO_3 , it appears that the cation plays a key role and this is known as "potassium effect" which has been previously reported (22-24). Otherwise, when NaOH was used as the base, good to excellent yields (73% and 98% for 1,4-dioxane and DMF, respectively) were obtained for this catalytic system. These results showed strong base has a great effect to neutralize acidic condition and to generate the active species in the catalytic system for facilities the transmetalation step compared to the weak bases such as K_2CO_3 , Na_2CO_3 and Et_3N in SM coupling reaction (25). On the other hand, in all cases, DMF gave better coupling product when comparing the results obtained from 1,4-dioxane. It's known polar aprotic solvents are generally preferred for the SM coupling reactions since they allow the higher solubility of the catalyst and substrates used (26,27). It can also be said DMF is more likely to coordinate to the Pd(II) center since the nitrogen donor in DMF is a softer base than oxygen donor in 1,4-dioxane (6).

It's noted that reaction temperature also plays an important role for the SM coupling reaction. We did not investigate the higher reaction temperatures since we achieved almost complete conversion with a combination of DMF-KOH solvent-base system in the preliminary experiment here reported. Nevertheless, it clearly appears from the optimization studies that the best catalytic activity was obtained in DMF in the presence of NaOH at room temperature.

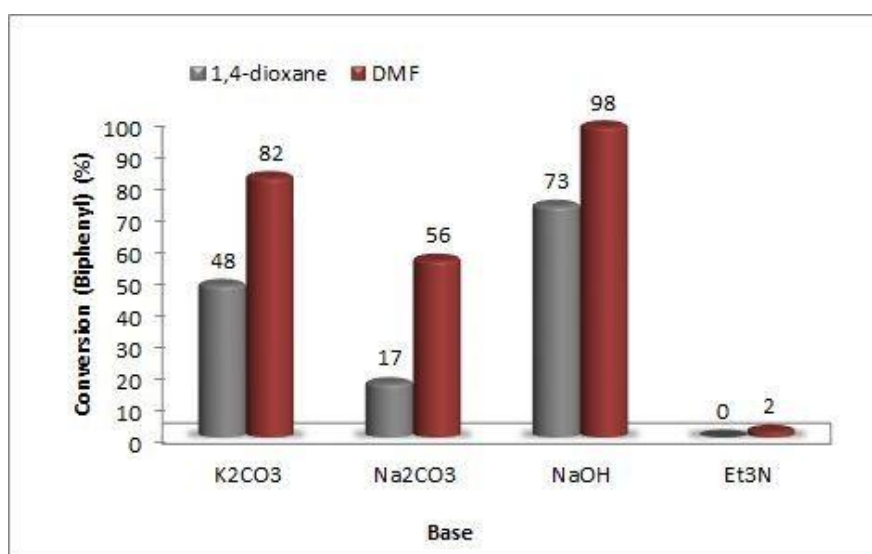


Figure 1: The effect of base and solvent on SM coupling reaction between bromobenzene and phenylboronic acid. Reaction conditions: PhBr (1.0 mmol), PhB(OH)_2 (1.2 mmol), base (1.2 mmol), cat. (**1a**) (0.01 mmol), solvent (2 mL), H_2O (2 mL), temperature: 25°C , time: 5h. Yields were analyzed by GC-MS.

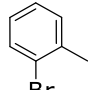
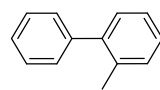
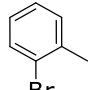
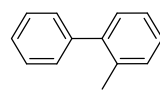
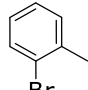
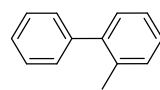
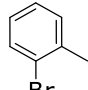
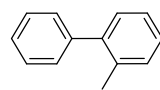
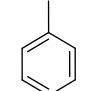
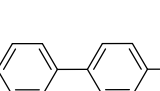
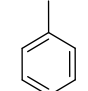
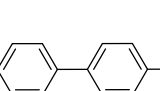
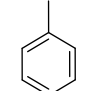
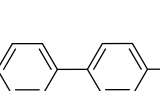
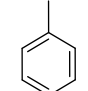
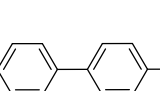
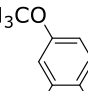
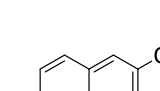
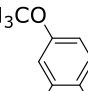
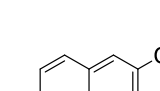
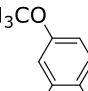
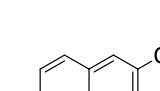
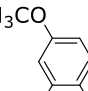
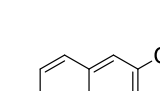
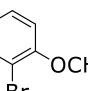
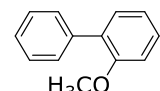
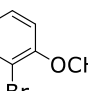
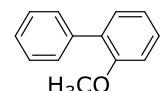
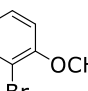
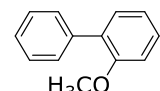
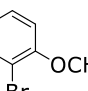
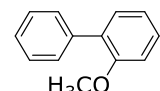
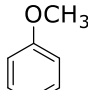
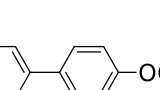
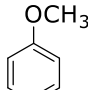
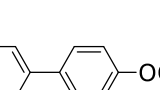
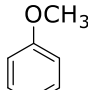
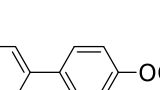
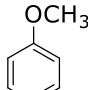
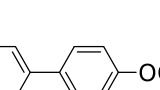
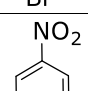
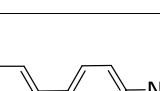
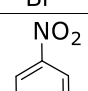
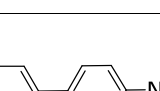
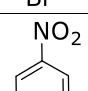
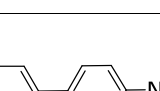
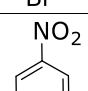
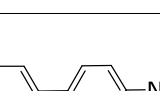
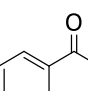
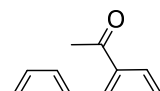
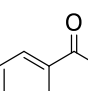
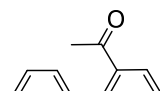
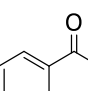
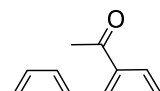
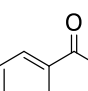
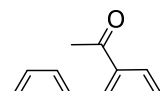
After the optimization of the reaction conditions, we examined a range of substituted aryl bromides in the SM coupling reaction with phenylboronic acid. The results were given in Table 1. We have discovered that, for activated, sterically hindered, and deactivated aryl bromides, our catalyst

systems can serve as an effective catalyst. For example, the reaction of 1-bromo-4-nitrobenzene containing electron-withdrawing group at para position, which could accelerate the rate determining oxidative addition step in the catalytic cycle due to the reduced electron density

of C-Br bond, gave 4-nitrobiphenyl as the principal product in excellent yields (87-99%) with all catalysts (entry 21-24) (6, 28). Our catalysts are also effective towards the coupling of 2-bromoanisole, 2-bromotoluene and 2-bromoacetophenone, which have bulky -methoxy, -ethyl and -aceto group at ortho position respectively, giving corresponding biaryls as major product up to 68% conversion (entry 1-4, 13-16, and 25-28) and steric effect of these substituents on the C-Br bond were well tolerated. In general, the reaction rate slows down in the presence of the electronically deactivated aryl halides, which have electron-releasing groups such as -methoxy and -methyl

group on the phenyl ring for the SM coupling reactions (14, 29). However, the coupling of these deactivated aryl bromides with phenylboronic acid gave desired coupling product moderate to good yields by all catalysts. Also, the catalytic efficiency of the palladium(II) pre-catalysts **1a-3a** were investigated for the coupling of 2-bromo-6-methoxynaphthalene with phenylboronic acid and moderate coupling product was obtained (58-70%, entries 9-12). These results showed that our monodentate phosphine based Pd(II) complexes were capable of effectively catalyzing the coupling of bromobenzene and phenylboronic acid at room temperature.

Table 1. SM coupling reactions with monodentate phosphine based Pd(II) pre-catalysts (**1a-4a**)^a

Entry	Aryl bromide	Product	Catalyst	Conversion (%) ^b	Yield (%) ^b	TOF (h ⁻¹) ^c
1			1a	53	49	11
2			2a	51	48	10
3			3a	37	31	7
4			4a	48	43	10
5			1a	68	65	14
6			2a	80	77	16
7			3a	84	80	17
8			4a	65	60	13
9			1a	58	55	12
10			2a	63	58	13
11			3a	76	75	15
12			4a	70	61	14
13			1a	45	43	9
14			2a	61	58	12
15			3a	68	65	14
16			4a	56	55	11
17			1a	64	56	13
18			2a	70	64	14
19			3a	83	78	17
20			4a	67	65	13
21			1a	99	96	20
22			2a	99	97	20
23			3a	99	87	20
24			4a	87	85	17
25			1a	40	38	8
26			2a	39	37	8
27			3a	55	53	11
28			4a	40	37	8

^aConditions: Aryl bromide (1.0 mmol), PhB(OH)₂ (1.2 mmol), KOH (1.2 mmol), cat. (0.01 mmol), DMF (5 mL), 25°C, time: 5 h.

^bConversions and yields were analyzed by GCMS.

^cTurnover frequency = (mole of product/mole of catalyst)/time(h).

CONCLUSION

We have synthesized and fully characterized a series of monodentate triaryl phosphine based

Pd(II) complexes. These complexes are insensitive to oxygen and moisture. Catalytic activity of these pre-catalysts were tested for SM coupling reaction between phenylboronic acid and bromobenzene and an extensive study on the scope of these complexes was performed. The results showed that, moderate to excellent yields were obtained for these pre-catalysts at room temperature and sterically hindered and deactivated aryl bromides were well tolerated.

ACKNOWLEDGMENTS

We are grateful to the Mersin University for supporting this research.

REFERENCES

- Dounay AB, Overman LE. The Asymmetric Intramolecular Heck Reaction in Natural Product Total Synthesis. *Chem. Rev.* 2003; 103:2945-63.
- Tsuiji J. *Palladium Reagents and Catalysts*; Wiley: New York, 2004; Chapter 3:105.
- Yin L, Liebscher J. Carbon-Carbon Coupling Reactions Catalyzed by Heterogeneous Palladium Catalysts. *Chem. Rev.* 2007; 107:133-73.
- Polshettiwar V, Decottignies A, Len C, Fihri A. Suzuki-Miyaura Cross-Coupling Reactions in Aqueous Media: Green and Sustainable Syntheses of Biaryls. *ChemSusChem.* 2010; 3:502-22.
- Suzuki A. Cross-Coupling Reactions of Organoboranes: An Easy Way To Construct C-C Bonds (Nobel Lecture). *Angew. Chem. Int. Ed.* 2011; 50:6723-37.
- Mahamo T, Mogorosi MM, Moss JR, Mapolie SF, Slootweg JC, Lammertsma K, and Smith GS. Neutral palladium(II) complexes with P,N Schiff-base ligands: Synthesis, characterization and application as Suzuki Miyaura coupling catalysts. *J. Organomet. Chem.* 2012; 703:34-42.
- Zhao F, Xin L, Zhang Y, Jia X. Monodentate phosphorus-coordinated palladium(II) complexes as new catalyst for Mizoroki-Heck reaction of aryl halides with electron-deficient olefins. *Chinese Chemical Letters.* 2018; 29; 493-96.
- Sabouncheia SJ, Hosseinzadeha M, Jevinani MZ. Monodentate palladium(0)-[60]fullerene complexes of diphosphine ligands as efficient and sustainable nanocatalysts for Mizoroki-Heck coupling reaction of aryl chlorides. *New J. Chem.* 2017; 41: 9701-09
- Huang P, Hong FE. Amination and Suzuki coupling reactions catalyzed by palladium complexes coordinated by cobalt-containing monodentate phosphine ligands with bis-trifluoromethyl substituents on bridged arylolefinyl: Observation of some unusual metal-containing compounds. *J. of Org. Chem.* 2009; 694:113-21.
- Armarego WLE, and Chai CLL. *Purification of Laboratory Chemicals*; Oxford: Pergamon Press. 2003; Chapter 5.
- Laue S, Greiner L, Wöltinger J, Liese A. Continuous Application of Chemzymes in a Membrane Reactor: Asymmetric Transfer Hydrogenation of Acetophenone. *Adv. Synt. Catal.* 2001; 343: 711-20.
- Ros A, Estepa B, Bermejo A, Álvarez E, Fernández R, Lassaletta JM. Phosphino hydrazones as suitable ligands in the asymmetric Suzuki-Miyaura cross-coupling. *J Org Chem.* 2012; 77(10): 4740-50.
- Yılmaz MK. Palladium(II) complexes with new bidentate phosphine-imine ligands for the Suzuki C-C coupling reactions in supercritical carbon dioxide. *J. of Supercritical Fluids.* 2018; 138: 221-27.
- Yılmaz MK, Güzel B. Iminophosphine palladium(II) complexes: synthesis, characterization, and application in Heck cross-coupling reaction of aryl bromides. *Appl. Organometal. Chem.* 2014; 28:529-36.
- Drew D, Doyle JR, and Shaver AG. Cyclic Diolefin Complexes of Platinum and Palladium. *Inorganic Syntheses.* 2007; 28:348-49.
- Mahalakshmi H, Phadnis PP, Jain VK, Tiekinkh ERT. Synthesis, spectroscopy and structures. 2004;43(November):2287-93.
- Watkins SE, Craig DC, Colbran SB. A palladium(II) complex of a new iminophosphine ligand derived from diethylenetriamine and 2-(diphenylphosphino)benzaldehyde. 2000; 307: 134-38.
- Hong FE, Ho YJ, Chang YC, Huang YL. Synthesis of cobalt-containing monodentate phosphine ligand and application toward Suzuki cross-coupling reactions. *J. of Org. Chem.* 2005; 690:1249-57.
- Dodds DL, Boele MDK, Strijdonck GPF, Vries JG, Leeuwen PWNM, and Kamer PCJ. Design, Testing and Kinetic Analysis of Bulky Monodentate Phosphorus Ligands in the Mizoroki-Heck Reaction. *Eur. J. Inorg. Chem.* 2012; 1660-71.
- Yılmaz MK, Keleş M. The catalytic activity of Palladium(II) complexes containing PN ligands in the Heck and Suzuki C-C coupling reactions. *JOTCSA.* 2018;5(1):133-48.

21. Cheng YH, Weng CM, Hong FE. Preparation of monodentate phosphinite ligands: their applications in palladium catalyzed Suzuki reactions. *Tetrahedron*. 2007; 63:12277–85.
22. Bedford RB, Hazelwood SL, Horton PN, Hursthouse MB. Orthopalladated phosphinite complexes as high-activity catalysts for the Suzuki reaction. *Dalton Trans*. 2003; 4164-4174.
23. Bedford RB, Hazelwood SL, Limmert ME, Albisson DA, Draper SM, Scully PN, Coles SJ, Hursthouse MB. Orthopalladated and -platinated Bulky Triarylphosphite Complexes: Synthesis, Reactivity and Application as High-Activity Catalysts for Suzuki and Stille Coupling Reactions. *Chem. Eur. J*. 2003; 9:3216-27.
24. So CM, Yeung CC, Lau CP, Kwong FYJ. A New Family of Tunable Indolylphosphine Ligands by One-Pot Assembly and Their Applications in Suzuki-Miyaura Coupling of Aryl Chlorides. *Org. Chem*. 2008; 73:7803-06.
25. Mondal M, Begum T, Gogoi PK, Bora U. Gallic Acid Derived Palladium(0) Nanoparticles: An In Situ Formed "Green and Recyclable" Catalyst for Suzuki-Miyaura Coupling in Water. *Chemistry Select*. 2016; 1: 4645-51.
26. Billingsley K, Buchwald SL. Highly Efficient Monophosphine-Based Catalyst for the Palladium-Catalyzed Suzuki-Miyaura Reaction of Heteroaryl Halides and Heteroaryl Boronic Acids and Esters. *J. Am. Chem. Soc*. 2007; 129: 3358-66.
27. Zapf A, Beller M. Palladium Catalyst Systems for Cross-Coupling Reactions of Aryl Chlorides and Olefins. *Chem. Eur. J*. 2001; 7: 2908-15.
28. Nobre SM, Monteiro AL. Pd complexes of iminophosphine ligands: A homogeneous molecular catalyst for Suzuki-Miyaura cross-coupling reactions under mild conditions. *J. Mol. Cat. A: Chem*. 2009; 313:65-73.
29. Scrivanti A, Bertoldini M, Matteoli U, Beghetto V, Antonaroli S, Marini A, Crociani B. Highly efficient Heck olefin arylation in the presence of iminophosphine-palladium(0) complexes. *Journal of Molecular Catalysis A: Chemical*. 2005; 235:12-16.



Ferulic Acid Substituted Zn(II) Phthalocyanine: Synthesis, Characterization and Investigation of Photophysical and Photochemical Properties

Semih Gorduk  

Yildiz Technical University, Faculty of Arts and Science, Department of Chemistry, 34210, Istanbul, Turkey.

Abstract: In this study, novel peripherally ferulic acid tetra-substituted Zn(II) phthalocyanine was synthesized for the first time. The synthesized phthalocyanine was characterized by elemental analysis, infrared spectroscopy, UV-Vis spectrophotometry, ¹H-NMR spectroscopy, and MALDI-TOF MS techniques. The photophysical, photochemical and aggregation properties of this phthalocyanine were also investigated in DMSO and DMF solvents. The aggregation studies showed that the synthesized Zn(II) phthalocyanine does not aggregate in DMSO and DMF. Fluorescence quantum yield (Φ_F : 0.23 in DMSO and 0.17 in DMF), singlet oxygen quantum yield (Φ_Δ : 0.57 in DMSO and 0.45 in DMF) and photodegradation quantum yield (Φ_d : 1.08×10^{-5} in DMSO and 4.44×10^{-5} in DMF) were also determined. These results show that the synthesized phthalocyanine has potential use in photodynamic therapy.

Keywords: Ferulic acid, Phthalocyanine, Photochemical, Photophysical, Zinc

Submitted: June 28, 2018. **Accepted:** July 18, 2018.

Cite this: Gördük S. Ferulic Acid Substituted Zn(II) Phthalocyanine: Synthesis, Characterization and Investigation of Photophysical and Photochemical Properties. JOTCSA. 2018;5(2):903-18.

DOI: <http://dx.doi.org/10.18596/jotcsa.438111>.

***Corresponding author. E-mail:** semih_grdk@hotmail.com, sgorduk@yildiz.edu.tr, **Tel:** +90 212 383 41 29.

INTRODUCTION

In the recent years, phthalocyanines (Pcs) have been comprehensively studied by scientists due to their unique chemical, physical, optical and structural properties such as aromatic 18- π conjugated electron systems, very versatile and stable aromatic macrocyclic ring, strong and long-wavelength absorption, high thermal stability, chemical resistance, photoconductivity, and catalytic activity (1-3). Because of these properties, Pcs have been used in many applications. For example, catalysis (4), liquid crystals (5), chemical sensors (6), semiconductor materials (7), photovoltaics (8), electrochemistry (9, 10), photodynamic therapy (PDT) (11) are important areas in which Pcs are used. In particular, metallo Pcs can absorb at high wavelength lights near the red region of light. With this feature, they are used in photodynamic therapy as photosensitizers suitable for cancer treatment studies (12).

Photodynamic therapy (PDT) is a process in which compounds called as photosensitizers absorb light in a specific wavelength, lower energy triplet into a high energy singlet and thus causing the destruction of the cancerous cells in the area where the photosensitizers are located (13). Pcs exhibit photosensitizer properties (14). Pcs containing diamagnetic metal ions (Zn, Ga, In, Si) are photoactive and are usually utilized in PDT due to their high efficiency of cytotoxic singlet oxygen photogeneration and long triplet lifetimes (15, 16). However, Pcs have disadvantage such as insolubility in common organic solvents. The use of Pcs is limited due to this disadvantage. Alkyl, alkoxy/alkylthio, sulfonyl, carboxyl and quaternized ammonium groups may be used in peripheral and non-peripheral positions to overcome this disadvantage (17-19). Especially, carboxylic acid groups are particularly useful to acquire solubility in common organic solvents and water (20-22). There are many studies in the literature that include carboxylic acid groups to increase solubility and prevent aggregation (23).

For example, ZnPc bearing 16-carboxylic acid groups was reported by M. Liu *et al.* (2005) to diminish aggregation for utilize as a potential photosensitizer for PDT (24). M.-R. Ke *et al.* (2009) synthesized non-peripherally and peripherally tetra-substituted with carboxylic acid zinc(II) Pcs as photosensitizers (25). Beta and alpha tetra-[4-oxy-3-methoxybenzoic acid]-substituted Zn(II), Co(II) and Cu(II) Pcs were reported by G. Özgül *et al.* (2015) for comparative electrochemistry studies (26).

Herein, we reported synthesis and characterization of ferulic acid functionalized peripherally tetra-substituted Zn(II) phthalocyanine. Zinc(II) Pcs have a high singlet oxygen quantum yield and thus they were studied as photosensitizers for PDT. For this reason, we investigated the aggregation, photophysical and photochemical properties of the Zn(II) phthalocyanine synthesized here. Fluorescence quantum yield, singlet oxygen quantum yield and photodegradation quantum yield indicate that this compound is a potential photosensitizer in the PDT.

MATERIALS AND METHODS

Chemical and Reagents

Trans-ferulic acid (trans-4-hydroxy-3-methoxycinnamic acid), 4-nitrophthalonitrile, zinc(II) acetate, 1,3-diphenylisobenzofuran (DPBF), potassium carbonate (K₂CO₃), and 1,8-diazabicyclo[5.4.0]undec-7-ene (DBU) were purchased from Sigma-Aldrich and TCI chemical companies. All chemicals and solvents were acquired with high purity from commercial suppliers. All solvents were dried and stored over molecular sieves.

Equipments

Melting points of the substances were determined using an Electrothermal Gallenkamp device. The IR spectra were recorded using a Perkin Elmer spectrometer with ATR sampling accessory. The UV-Vis spectra were recorded on an Agilent 8453 UV/Vis spectrophotometer. Elemental analysis was carried out by a LECO CHNS 932 instrument. A Varian Unity Inova 500 MHz spectrometer was used for ¹H-NMR and ¹³C-NMR spectra. MALDI-TOF mass spectrum was performed using a Bruker Microflex LT MALDI-TOF-MS. The LC-MS spectrum was obtained on a Shimadzu LCMS-8030 Plus. Fluorescence spectra were measured using a Varian Eclipse spectrofluorometer using 1 cm path length cuvettes at room temperature. In photochemical measurements, UV-Vis spectra were recorded on a Shimadzu UV-2001 UV-Vis spectrophotometer.

Photoirradiation studies were performed using a General Electric quartz line lamp (300 W). A 600 nm glass cut off filter (Schott) and a water filter were used to filter off ultraviolet and infrared radiations, respectively. An interference filter (Intor, 670 nm with a band width of 40 nm) was additionally placed in the light path before the sample. Light intensities were measured with a POWER MAX5100 (Molelectron detector incorporated) power meter.

Photophysical and Photochemical Parameters

Fluorescence quantum yield determination

Fluorescence quantum yields (Φ_F) were calculated by the comparative method (Eq. 1) (27, 28) using unsubstituted Zn(II) phthalocyanine as the reference. Φ_F values of unsubstituted Zn(II) phthalocyanine are 0.20 in DMSO and is 0.17 in DMF (29, 30).

$$\Phi_F = \Phi_F(\text{Std}) \frac{F \cdot A_{\text{Std}} \cdot n^2}{F_{\text{Std}} \cdot A \cdot n_{\text{Std}}^2} \quad (\text{Eq. 1})$$

Where F and F_{Std} are the areas under the fluorescence emission curves of the sample (The synthesized phthalocyanine) and the standard, respectively. A and A_{Std} are the respective absorbances of the sample and standard at the excitation wavelengths. n and n_{Std} are the refractive indices of solvents used for the samples and standard, respectively.

Singlet oxygen quantum yield determination

Singlet oxygen quantum yield (Φ_Δ) determinations were carried out using the experimental setup described in the literature

(22, 30, 31) with standard unsubstituted Zn(II) phthalocyanine (in DMSO and DMF) as the reference. Typically, a 2 mL portion of the zinc(II) phthalocyanine solution (C = 1.0 × 10⁻⁵ M) that contained the singlet oxygen scavenger was irradiated in the Q-band region with the photoirradiation setup described in the literature. The Φ_Δ values were determined in air using the relative method with DPBF as a singlet oxygen chemical scavenger in DMSO and DMF using Eq. 2.

$$\Phi_{\Delta} = \Phi_{\Delta}^{\text{Std}} \frac{R \cdot I_{\text{abs}}^{\text{Std}}}{R^{\text{Std}} \cdot I_{\text{abs}}} \quad (\text{Eq. 2})$$

$\Phi_{\Delta}^{\text{Std}}$ is the singlet oxygen quantum yield for the standard unsubstituted Zn(II) phthalocyanine ($\Phi_{\Delta}^{\text{Std}} = 0.67$ in DMSO and 0.56 in DMF) (32) (27). R and R_{Std} are the DPBF photobleaching rates in the presence of the respective sample zinc(II) phthalocyanine and standard Zn(II) phthalocyanine, respectively. I_{abs} and $I_{\text{abs}}^{\text{Std}}$ are the rates of light absorption by the sample zinc(II) phthalocyanine and standard unsubstituted zinc(II) phthalocyanine, respectively. To avoid chain reactions induced by DPBF in the presence of singlet oxygen (33), the concentration of quenchers (DPBF) was lowered to $\sim 3 \times 10^{-5}$ M.

$$\Phi_d = \frac{(C_0 - C_t) \cdot V \cdot N_A}{I_{\text{abs}} \cdot S \cdot t} \quad (\text{Eq. 3})$$

Where C_0 and C_t are the sample concentration before and after irradiation respectively. V is the reaction volume. N_A is the Avogadro's constant. S is the irradiated cell area. t is the irradiation time and I_{abs} is the overlap integral of the radiation source light intensity and the absorption of the sample. A light intensity of 7.05×10^{15} photons. $\text{s}^{-1} \cdot \text{cm}^{-2}$ was employed for Φ_d determinations.

Synthesis of Compounds

Synthesis of (E)-3-(4-(3,4-dicyanophenoxy)-3-methoxyphenyl)acrylic acid (compound 1): Firstly, *trans*-4-hydroxy-3-methoxycinnamic acid (ferulic acid) (2.89 mmol, 0.56 g) was dissolved in dry DMF (50 mL) and then 4-nitrophthalonitrile (2.89 mmol, 0.5 g) was added into the solution. The solution was mixed for 15 min to obtain a homogenous mixture. Then, anhydrous K_2CO_3 (11.56 mmol, 1.59 g) was added into the solution during 2 hours. The system was heated during 72 hours under nitrogen atmosphere at 45-50 °C. The system was cooled to the room temperature at the end of the reaction and diluted HCl was added to set the pH to 2. The solid particles were obtained in one hour. The particles were filtered and then washed with water, n-hexane, and diethyl ether. After drying process, light brown particles were recrystallized in MeOH. The final product was soluble in many solvents such as MeOH, EtOH, acetone, chloroform, and THF. Yield: 0.832 g (90.1%), M.p.: 225-226 °C, Anal. Calc. for $\text{C}_{18}\text{H}_{12}\text{N}_2\text{O}_4$ (MA: 320.30 g/mol): C, 67.50; H, 3.78; N, 8.75. Found: C, 67.30; H, 3.70; N, 8.65%. FT-IR (KBr), $\nu_{\text{max}}/(\text{cm}^{-1})$: 3073-3047 (Ar-CH), 3300-2500 (broad peak, carboxylic acid-COOH), 2981-2844 (aliphatic-CH, -CH₃), 2231 (-C≡N), 1688 (C=O), 1589-1487 (C=C), 1246 (Ar-O-Ar). ¹H-NMR (MeOD₃, 500 MHz, δ :ppm): 12.45 (s, 1H, -OH), 7.85-7.83 (d, 1H, Ar-H), 7.69-7.65 (d, 1H, Ar-H), 7.41-7.39 (dd, 1H Ar-H), 7.29 (s, 1H Ar-CH=C), 7.27 (d, 1H, Ar-H), 7.21 (d, 1H, Ar-H), 7.19-7.18 (d, 1H, Ar-H), 6.53-6.50 (d, 1H, =CH-COO), 3.78 (s, 3H, O-CH₃). ¹³C-NMR (MeOD₃, 500 MHz, δ :ppm): 170.23 (-COOH), 163.09, 153.27, 145.24, 144.50 (Ar-C=C), 137.00, 135.57, 124.15,

Solutions of the photosensitizer containing DPBF were prepared in the dark and irradiated in the Q-band region using the setup described in equipment part. DPBF degradation at 417 nm was monitored. The light intensity of 2.20×10^{16} photons. $\text{s}^{-1} \cdot \text{cm}^{-2}$ was used for Φ_{Δ} determinations.

Photodegradation quantum yield determination

Photodegradation quantum yield (Φ_d) determinations were carried out using the experimental set-up described in the literature (34-36). Photodegradation quantum yields of the sample (The synthesized phthalocyanine) were determined using Eq. 3.

123.14, 122.12, 121.75, 120.47, 118.56 (=C-COOH), 116.65 (-C≡N), 116.39 (-C≡N), 113.78, 109.76, 56.56 (O-CH₃). MS (LC-MS) m/z. Calculated: 320.30 Found: 359.31 [M+K]⁺.

Synthesis of (E)-3-(2,9,16,23-tetrakis-(4-oxy-3-methoxyphenyl)acrylic acid) phthalocyaninato zinc(II) (compound 2): Compound 1 was dissolved in n-pentanol (3 mL). Anhydrous $\text{Zn}(\text{CH}_3\text{COO})_2$ (0.156 mmol, 0.041 g) was added into the solution and the reaction tube was heated to 80 °C under nitrogen atmosphere. Five drops of DBU were added to the solution and kept at 150-160 °C for 24 hours. While the temperature was increasing, the color of solution changed from dark brown to dark green. Then, the solution was cooled to room temperature and diluted HCl was added to arrange of pH as 2-3. Green precipitates were filtered and washed with water, n-hexane, hot acetone, hot dichloromethane, hot acetonitrile, hot chloroform, hot ethyl acetate, and hot diethyl ether. The dried product was soluble in MeOH, EtOH, THF, DMSO and DMF. Yield: 0.064 g (30%). M.p. >300 °C. Anal. Calc. for $\text{C}_{72}\text{H}_{48}\text{ZnN}_8\text{O}_{16}$ (MA: 1346.58 g/mol): C, 64.22; H, 3.59; N, 8.32. Found: C, 64.52; H, 3.45; N, 8.12%. FT-IR (KBr), $\nu_{\text{max}}/(\text{cm}^{-1})$: 3300-2500 (broad peak, carboxylic acid-COOH), 3070 (Ar-CH), 2930-2870 (aliphatic-CH, -CH₃), 1686 (C=O), 1592-1467 (C=C), 1259 (Ar-O-Ar). ¹H-NMR (500 MHz, d-DMSO) δ ppm: 12.30 (s, 4H, -OH), 8.05-7.55 (m, 12H, Pc-Ar-H), 7.29-7.16 (m, 12H, subs-Ar-H) 7.45-7.39 (m, 4H, Ar-HC=C), 6.52 (m, 4H, -C=CH-COO) 3.35 (s, 12H Ar-O-CH₃). UV-vis (DMSO, 1×10^{-5} M): $\lambda_{\text{max}}/\text{nm}$ (log ϵ): 682 (5.03), 614 (4.36), 349 (4.76). UV-vis (DMF, 1×10^{-5} M): $\lambda_{\text{max}}/\text{nm}$ (log ϵ): 680 (4.99), 611 (4.30), 352 (4.71). UV-vis (THF, 1×10^{-5} M): $\lambda_{\text{max}}/\text{nm}$ (log ϵ): 678 (4.98), 610 (4.30), 348 (4.70). MALDI TOF MS (m/z): Calculated: 1346.58, Found: 1346.48 [M]⁺, 1416.49 [M+2CI]⁺, 1485.84 [M+4CI]⁺.

RESULT AND DISCUSSION

Synthesis and Characterization of Compounds

Scheme 1 shows the general synthesis of the compounds. In the first step of synthesis, *trans*-4-hydroxy-3-methoxycinnamic acid and 4-nitrophthalonitrile were dissolved in DMF and anhydrous K₂CO₃ was added into the solution. The solution was heated under nitrogen atmosphere for 72 hours at 45-50 °C. Then, the solution was cooled and diluted HCl was added in the solution to obtain precipitates. The formed precipitate was washed with ultra-pure water for neutralization, the precipitate was then washed with n-hexane and diethyl ether and dried under vacuum. The structure of compound **1** was proved by elemental analysis, FT-IR, ¹H-NMR, ¹³C-NMR and LC-MS techniques.

In the FT-IR spectrum of compound **1**, there is no peak around 1365 cm⁻¹ corresponding -NO₂ groups indicating the full reaction of 4-nitrophthalonitrile. Besides, obtained peaks at around 2231 cm⁻¹, 1688 cm⁻¹ and a broad peak between 2500-3300 cm⁻¹ on the structure of compound **1** support the (-C≡N), carbonyl (C=O) and carboxyl groups (COOH), respectively. Indeed, no peaks at around 3380 cm⁻¹ (-OH) supporting the reaction of *trans*-4-hydroxy-3-methoxycinnamic acid to form of compound **1**. Aliphatic -CH and -CH₃ peaks at around 2981-2844 cm⁻¹ and Ar-O-Ar etheric peak at 1246 cm⁻¹ support the formation of compound **1**.

¹H-NMR analysis of compound **1** also proves the formation of expected structure of this compound. Chemical shifts at around 7.85-7.83, 7.69-7.65 and 7.41-7.39 ppm correspond to aromatic protons to which the nitrile groups are attached. Other aromatic protons were determined in 7.27, 7.21 and 7.19-7.18 ppm as total of three protons. The chemical shifts at around 7.29, 6.53-6.50 and 3.78 ppm were related with Ar-CH=C for one proton bonded aromatic ring, C=CH-COO for one proton and -OCH₃ for three protons, respectively. The signal at 12.45 ppm was related with -OH group (22). ¹H-NMR spectrum supports the formation of compound **1** with total of 12 protons. ¹³C-NMR analysis of compound **1** also supports the formation of proposed structure of this compound. The carbon peaks bonded with nitrile groups were determined at 116.65 and 116.39 ppm. The -OCH₃ bonded carbon peak was also observed at around of 56.56 ppm. ¹³C-NMR spectrum also demonstrates the formation of compound **1** with total of 18 peaks for the carbon atom.

The observed peak at 359.31 [M+K]⁺ in the mass spectrum also confirms structure of compound **1**. Finally, the results of experimental elemental analysis data are consistent with the theoretical data of compound **1** and are satisfactory for the formation of this compound.

Compound **2** was synthesized by cyclotetramerization of compound **1** in presence of Zn(OAc)₂ and DBU in dry n-pentanol at 150-160 °C (**Scheme 1**). Upon addition of diluted HCl to solution of the mixture until pH 2-3, carboxylic acid group bearing compound **2** were obtained. The obtained product was washed many times different solvents and was dried under vacuum. In the synthesis of tetra-substituted zinc(II) phthalocyanine, a mixture of four possible structural isomers occurs. These isomers can be explained by their molecular symmetry as C_s, C_{2v}, C_{4h} and D_{2h}. Herein, the synthesized compound **2** is formed as isomer mixtures as expected. No attempt was made for separating the isomers of compound **2**. The structure of compound **2** was verified by FT-IR, elemental analysis, UV-Vis, ¹H-NMR, and MALDI-TOF MS techniques. The results are consistent with the expected structure.

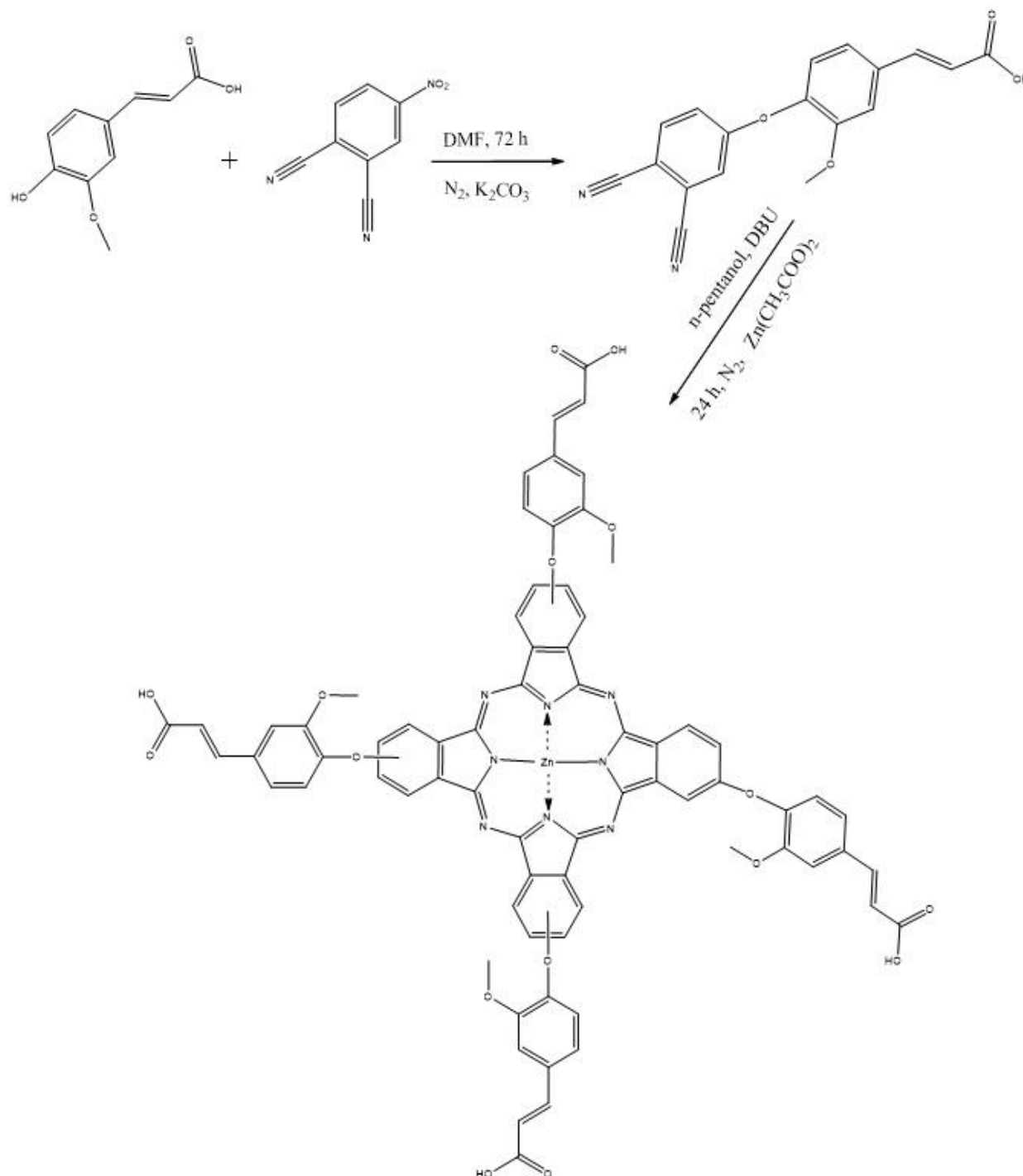
In the FT-IR spectrum of compound **2**, the any peak was observed at around 2231 cm⁻¹ supported formation of compound **2** by cyclotetramerization reaction. Besides, the peaks at around 1686 cm⁻¹ and 2500-3300 cm⁻¹ on the structure of compound **2** belong to the carboxyl group (-C=O) and carboxylic acid group, respectively. The peaks at 1259 cm⁻¹ and 2930-2870 cm⁻¹ are related with Ar-O-Ar ether and aliphatic -CH and -CH₃ supporting the formation of compound **2**.

The ¹H NMR spectrum of compound **2** exhibits quite broad signals when compared with that of starting compound **1** derivative. The OH protons were observed with a total of 4 protons at 12.30 ppm. The Pc ring protons were detected between 8.05 and 7.55 ppm integrating for a total of 12 protons. Aromatic functional group protons were observed with a total of 12 protons at 7.16 ppm. The protons with a total number of 8 at 7.45-7.39 and 6.52 ppm belong to Ar-CH=C- and -C=CH-COO- groups, respectively. Finally, the protons with a total number of 12 were observed at around 3.35 ppm as singlet for the -O-CH₃ groups.

UV-Vis spectrophotometry plays an important role to clarify the structure of metallo-Pcs. Pcs are colored substances and give specific absorption peaks in the visible and ultraviolet regions. Pcs show typical UV-Vis spectra with two characteristic absorption bands, one in the UV region at about 300-400 nm is the B band and the other one in the visible region at 600-700 nm is the Q band, both are based on π-π* transitions (37). The Q band is also a characteristic peak for differentiating metallo and metal-free Pcs. While the metal-free Pcs give two equal bands at 600-700 nm, the metallo Pcs give a single band. UV-Vis spectra of compound **2** were recorded in THF, DMF, and DMSO solvents and can be seen in Figure 1. These spectra show monomeric behavior evidenced by a single (narrow) Q band (at around 678-682 nm) in THF, DMF, and DMSO. The Q band and its shoulder of compound **2** were

determined as a single band at 682 and 614 nm in DMSO, 680 and 611 in DMF, and 678 and 609 nm in THF, respectively and B band of compound **2** was also observed at 349 nm in DMSO, 352 nm in DMF, and 348 nm in THF, respectively supported

the formation of compound **2**. The obtained compound **2** exhibits a single Q band, indicating that it contains the metal ion in the macrocyclic cavity.



Scheme 1: General synthesis procedure of compounds **1** and **2**.

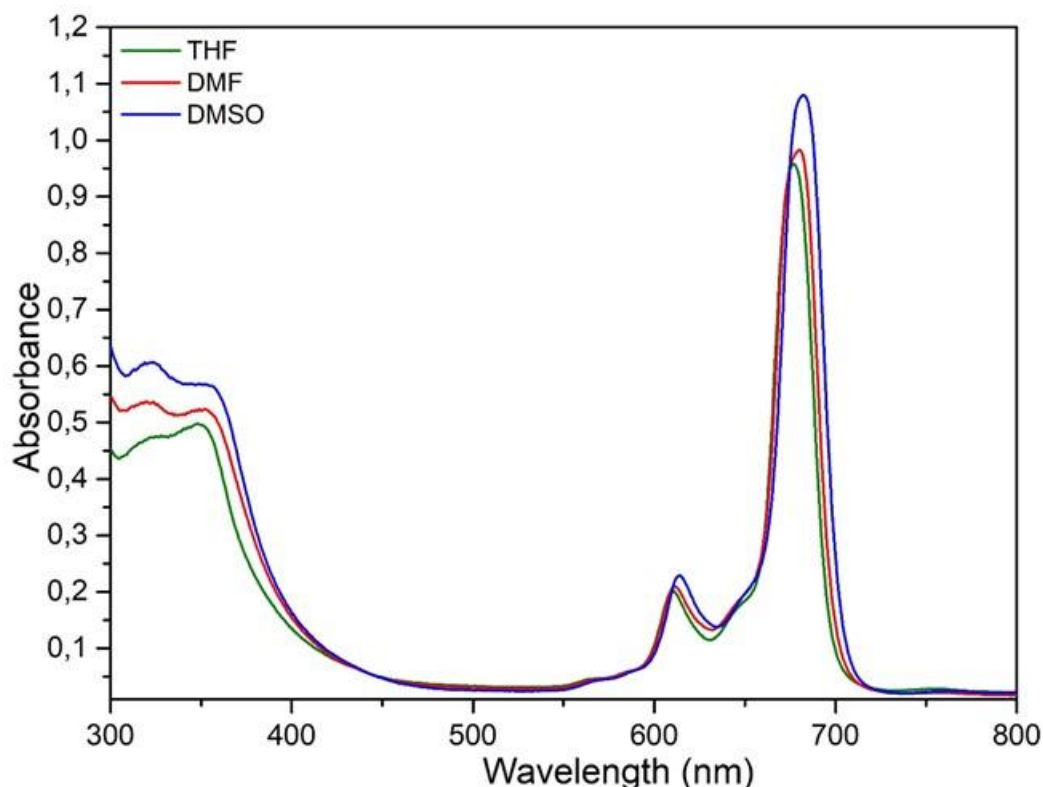


Figure 1: UV-vis spectra of compound **2** in different solvents.

The obtained $[M]^+$ m/z :1346.48, $[M+2Cl]^+$ m/z :1416.49, $[M+4Cl]^+$ m/z :1485.84 peaks in MALDI TOF MS spectrum also support the formation of compound **2** (Figure 2). Finally, the

results of experimental elemental analysis data are consistent with the theoretical data of compound **2** and are satisfactory for the formation of this compound.

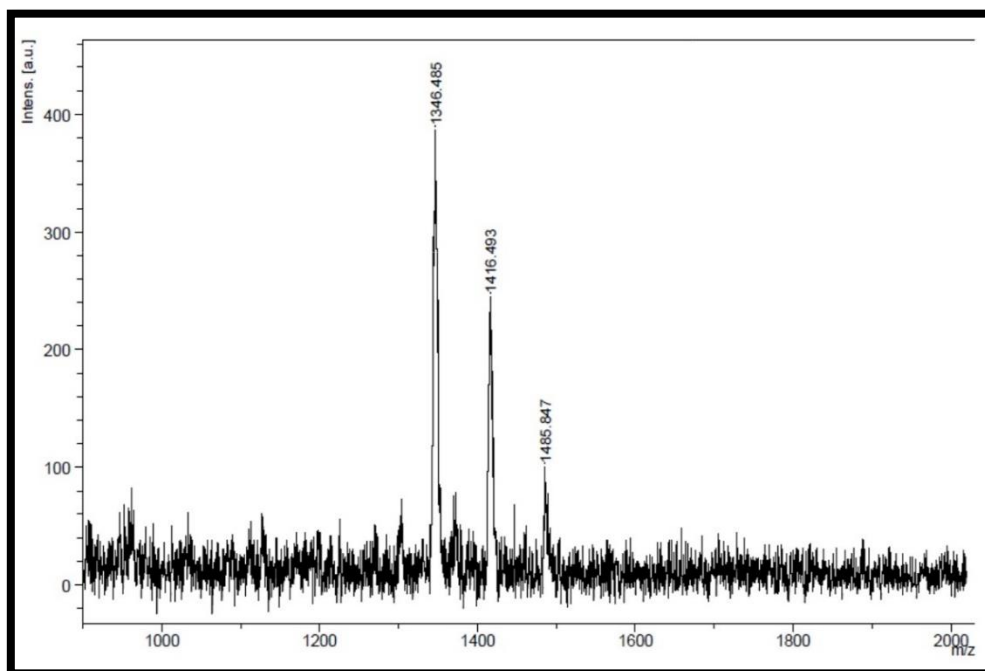


Figure 2: MALDI-TOF MS spectrum of compound **2**.

Aggregation properties of compound **2**

The aggregation properties of Pcs have been known since the discovery of these substances (38, 39). Generally, aggregation is a common association of molecules in solution, which is the overlaying of two or more macro-ring structures

due to intermolecular attraction forces. A coplanar relation of macrocyclic rings and progresses through the assembly of monomers to dimers and higher-order aggregates are effective on aggregation behavior. With aggregation, the structure of compound can change from

monomer to dimeric, trimeric, or oligomeric structure. The structure of the Pcs (neutral, metal, cationic, etc.), size, position of the substituent group, substituents in the peripheral position, solvent and temperature are very effective on aggregation. In the case of Pcs aggregation, the interactions between the electronic molecules change the physical and chemical properties. Aggregation is the most important factor affecting the photochemical and photophysical behavior of Pcs. The resolution of Pcs is reduced due to aggregation and this is an unwanted situation in applications such as PDT (40, 41). In particular, in water and other polar solvents, the macrocyclic Pc becomes an aggregate due to its hydrophobic nature. For this reason, DMSO and DMF solvents which are dipolar aprotic solvents, have similar physical properties and which do not cause aggregation have been chosen. Water, DMSO and DMF are used in many similar applications. Aggregation not only leads to a decrease in solubility, but also decreases the quantum efficiency of fluorescence and singlet oxygen. This means that the sensitivity to light for Pc is reduced (42). To reduce these limiting factors and maintain effective photoactivity, Pc

may be substituted with various ligands, such as carboxylic acid groups at the peripherally position (24). In this study, the purpose of the aggregation assay is to examine whether compound **2** conforms to the Lambert-Beer law in DMSO and DMF solvents at specific concentrations and to determine if they have undergone aggregation. To make these measurements, the solutions of compound **2** in DMSO and DMF were separately prepared. The UV-vis spectra for compound **2** were examined in both DMSO and DMF under different concentrations ranging from 12×10^{-6} M to 2×10^{-6} M. UV-Vis spectra in Figures 3 and 4 show the aggregation behavior of compound **2** in DMSO and DMF, respectively. At the end of this investigation, it was found that the compound **2** conformed to the Lambert-Beer law and there was no aggregation in DMF and DMSO. When Figures 3 and 4 are examined, it is seen that due to the increase in concentration, the Q-band rises but there are no new bands (normally blue-shifted) due to aggregation. The linear variation in the absorbance of the Q band with increasing concentration confirms that there is no tendency to aggregation.

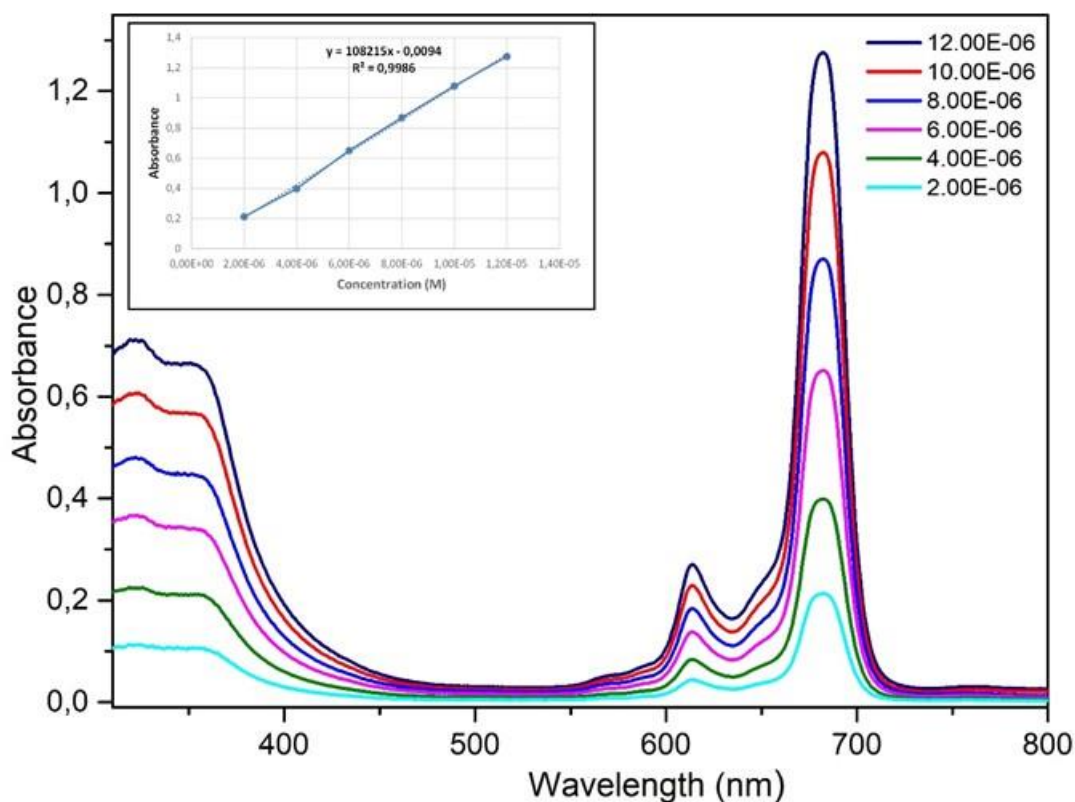


Figure 3: Aggregation behavior of compound **2** in DMSO at different concentrations (Inset: Absorbances versus concentrations).

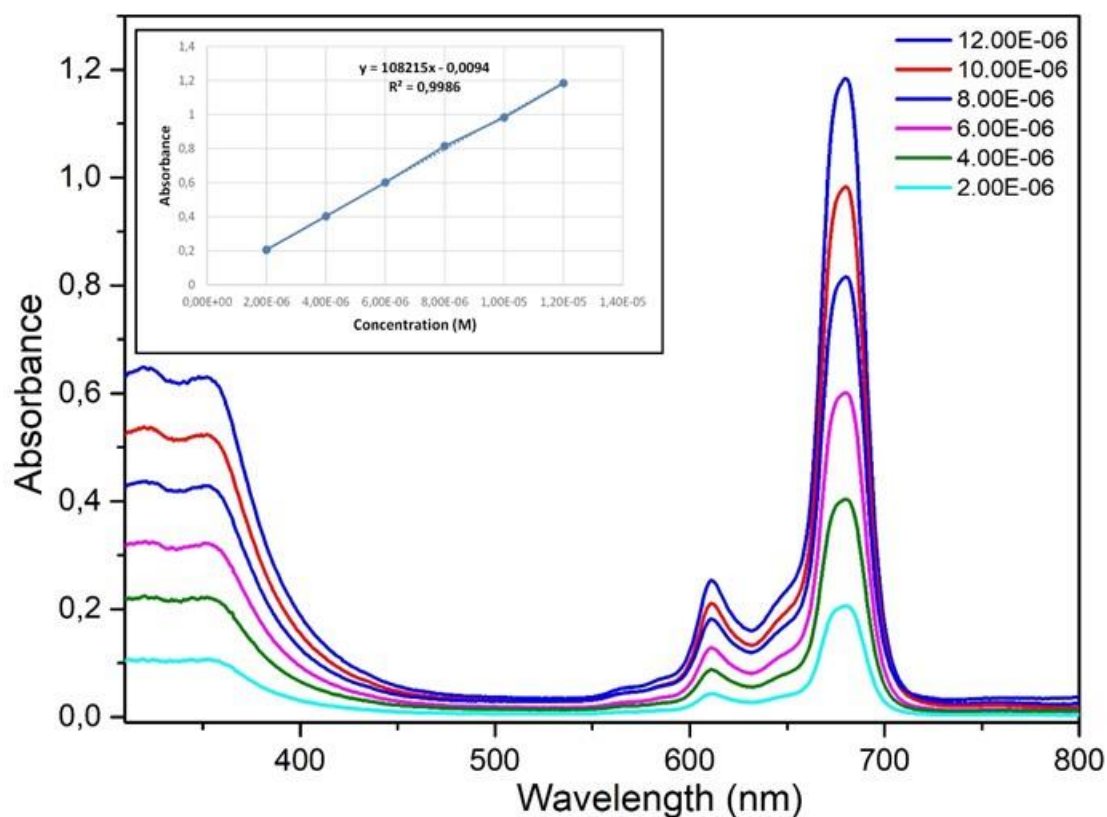


Figure 4: Aggregation behavior of compound **2** in DMF at different concentrations (Inset: Absorbances versus concentrations).

Photophysical properties of compound **2**

The fluorescence excitation, emission, and absorption spectra of compound **2** in DMSO and DMF are depicted in Figures 5 and 6, respectively. Table 1 also shows fluorescence emission, excitation, absorption peaks and Stokes shift values of compound **2**. Stokes shift values have been found in the observed region. The observed Stokes shifts for compound **2** are 12 in DMSO and are 10 in DMF. The obtained Stokes shifts of the compound have been found to be compatible with unsubstituted zinc(II) phthalocyanine (43). The compound exhibits similar fluorescence behavior in both solvents, excitation and absorption spectra are similar and they appear to be mirror

images in both solvents. The wavelengths of the Q band of absorption and the Q band of excitation is proximity and this situation assumes that the nuclear configurations of the ground and excited states are similar and they are not affected by excitation (44). One of the important problems affecting fluorescent behavior of Pcs is aggregation. The reason for this is that the compounds of agglomerated phthalocyanine do not have fluorescence in the solution medium. Compound **2** obtained in this work did not exhibit any aggregation in DMSO and DMF. For this reason, the compound **2** exhibits fluorescence behavior in both solvents.

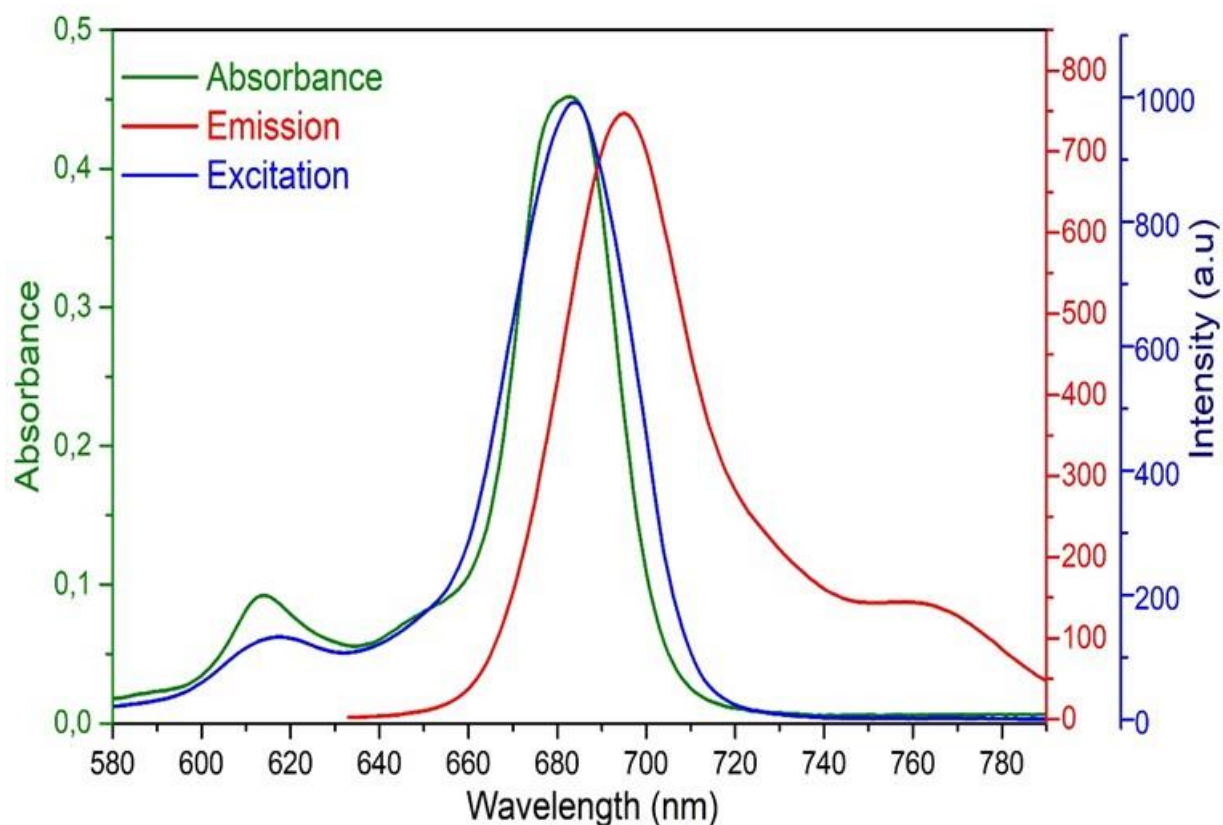


Figure 5: Absorption, emission and excitation spectra for compound **2** in DMSO.

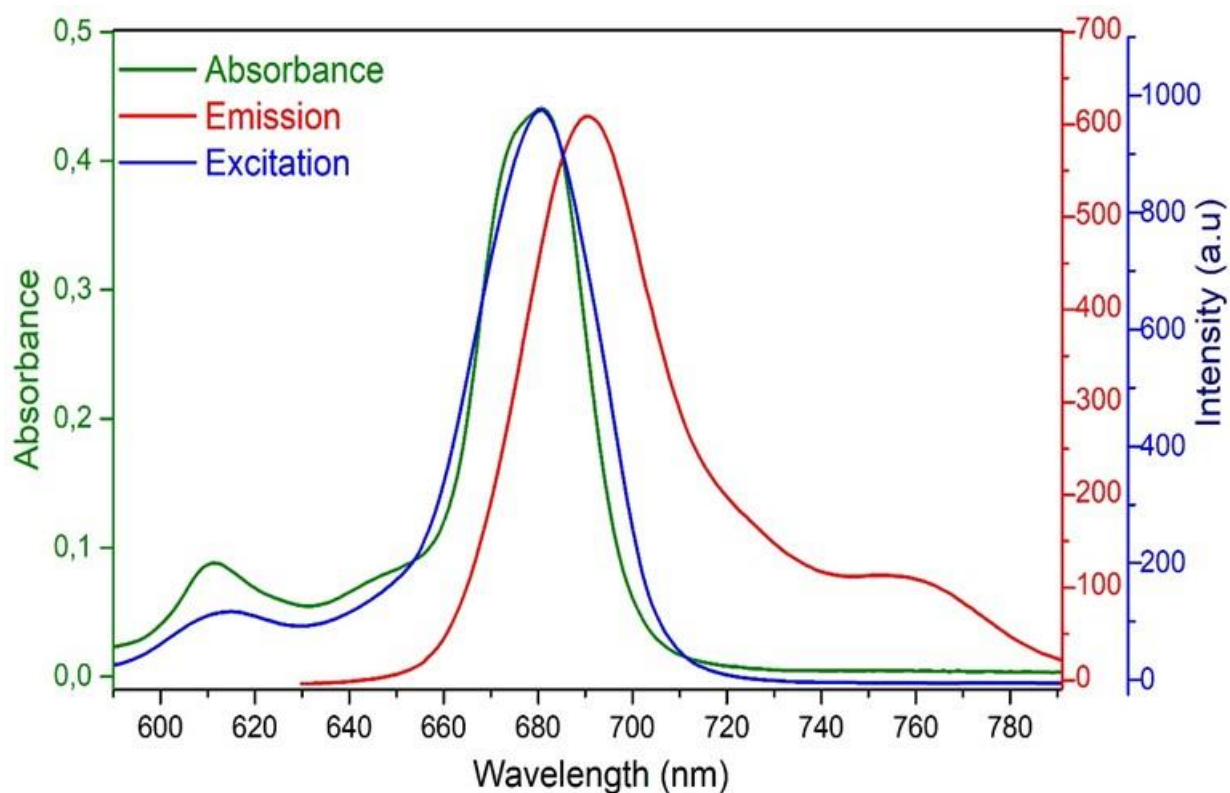


Figure 6: Absorption, emission and excitation spectra for compound **2** in DMF.

Table 1: Absorption, excitation and emission spectral data for compound **2** in DMSO and DMF.

Compound name	Solvent	Q band λ_{\max} (nm)	Log ϵ	Excitation λ_{Ex} (nm)	Emission λ_{Em} (nm)	Stokes shift Δ_{Stokes} (nm)
2	DMSO	682	5.03	683	695	12
2	DMF	680	4.99	681	691	10

The photophysical properties such as fluorescence quantum yield of photosensitizers are highly significant parameters in PDT applications because of the imaging necessity of the photosensitizer in the human body. The fluorescence quantum yields (Φ_F) for compound **2** in both DMSO and DMF are given in Table 2. The Φ_F values for compound **2** in both solvents are compatible with typical zinc(II) Pcs (29) and are

found similar with Φ_F values of unsubstituted standard zinc(II) phthalocyanine in DMSO and DMF (29). These values reveal that the substitution groups of compound **2** are not have important effect on the fluorescence behavior. But the solvent may have little effect (45). Therefore, the compound **2** has showed slightly higher Φ_F values in DMSO (0.23) compared to DMF (0.17).

Table 2: Photophysical and photochemical data for compound **2** in DMSO and DMF.

Solvent	Φ_F	$\Phi_d(10^{-5})$	Φ_Δ
DMSO	0.23	1.08	0.57
DMF	0.17	4.44	0.45

Photochemical properties of compound **2**

The photochemical properties include values such as singlet oxygen quantum yields and photodegradation quantum yields. Pcs act as photosensitizers in PDT of some cancers. The photosensitizer, which is activated by a certain light, is excited and molecular oxygen is converted into a reactive oxygen species such as singlet oxygen. This singlet oxygen helps to destroy the cancerous cells. Because singlet oxygen is highly reactive, it can normally damage healthy cells. But it is unstable, it exists very briefly and its effective area is short. Therefore, healthy cells can be minimally damaged (12). The calculation of the singlet oxygen quantum yield is important in PDT. In this study, for singlet oxygen quantum yield measurements; the solutions of compound **2** in both DMSO and DMF at 1×10^{-5} M concentration were prepared and then 1,3-difenilisobenzofuran (DPBF) (quencher) which prepared at 3×10^{-5} concentration was added into these solutions. The mixtures were exposed to light of 2.20×10^{16} photon/(s.cm²) intensity at a certain time and UV-Vis spectra of these mixture were separately taken. The change in absorption at 417 nm of the DPBF compound was

investigated and singlet oxygen quantum yields were calculated using Eq. 2. The same procedure was made for std-ZnPc in DMSO and DMF for comparative purposes. Figures 7 and 8 show the UV-Vis spectral changes during the measurement of singlet oxygen quantum yield of the compound **2** in DMSO and DMF. The figures show that the concentration of DPBF decreases over time with light irradiation. The Q band intensity of compound **2** does not show a significant change as a result of exposure to light, indicating that the compound is not degraded during singlet oxygen measurements (Figures 7 and 8). The calculated data are given in Table 2. The results show that the calculated Φ_Δ values in DMSO and DMF are slightly lower than the std-ZnPc (29). Substituted groups in the peripheral locations may cause in a slightly lower Φ_Δ value. It is known in the literature that Pcs containing substituted groups in peripheral positions reduce singlet oxygen generation (46). Although compound **2** has slightly low Φ_Δ , it has enough singlet oxygen generation as photosensitizers for PDT application area. The obtained values of singlet oxygen quantum yields for compound **2** in DMSO and DMF are typical for metal Pcs (47, 48).

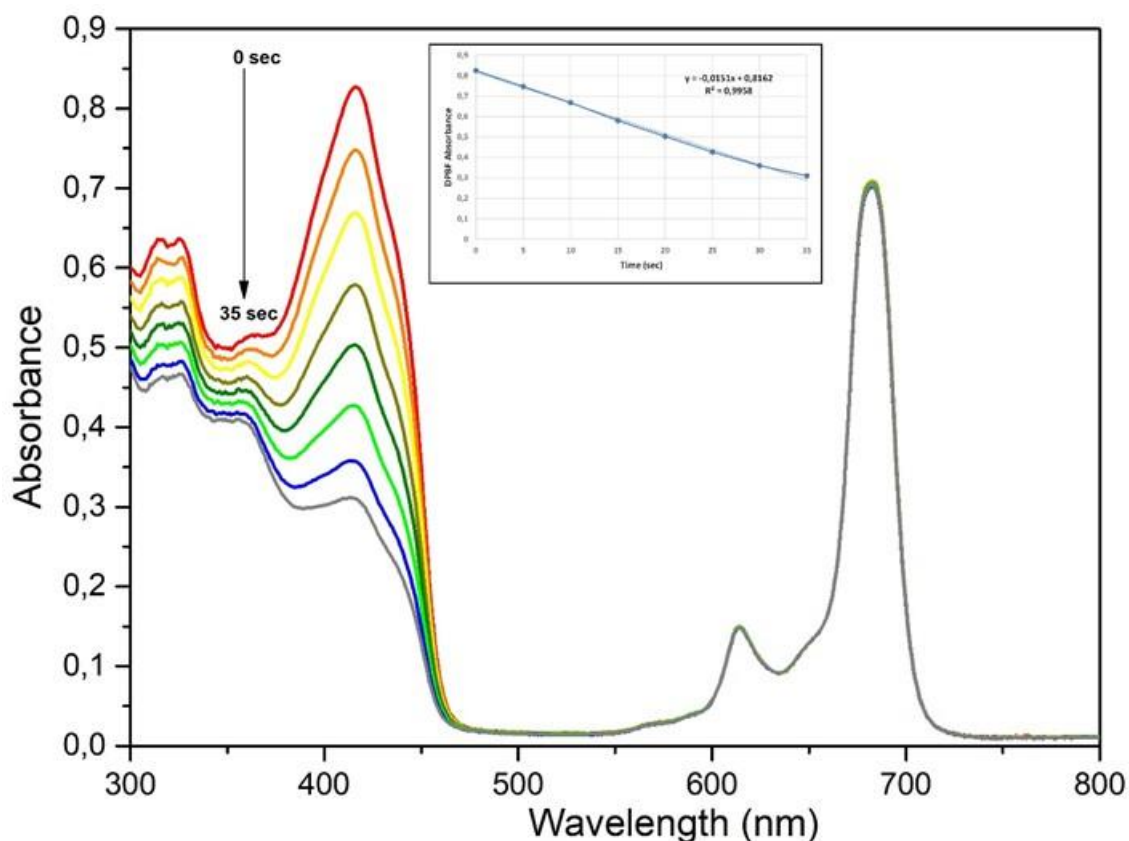


Figure 7: A typical spectrum for the compound **2** during the determination of singlet oxygen quantum yield in DMSO (Inset: Plot of DPBF absorbance versus time).

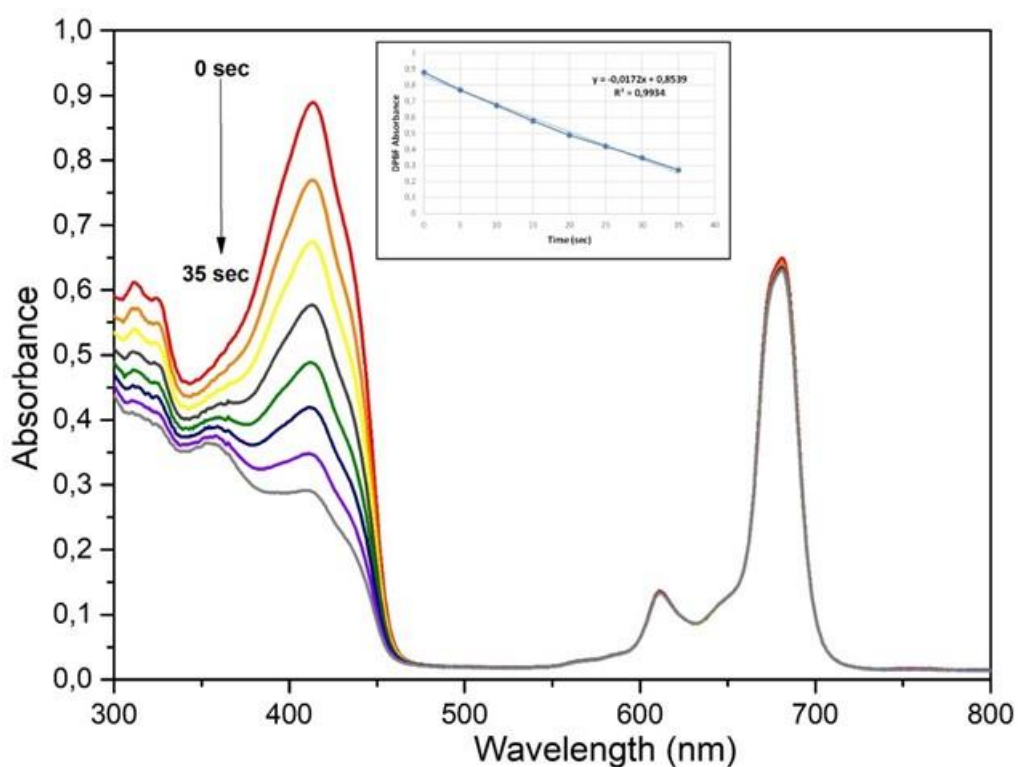


Figure 8: A typical spectrum for the compound **2** during the determination of singlet oxygen quantum yield in DMF (Inset: Plot of DPBF absorbance versus time).

When Pcs are exposed to light irradiation during measurement, they may be degraded. This process is an important parameter for the use of Pcs as photosensitizers. Photodegradation quantum yield (Φ_d) is durability of a molecule

against light. Φ_d can be calculated by examining the change in the absorption spectrum of compound during the light irradiation. Photodegradation in Pcs is observed with a decrease in the Q band. The photodegradation

quantum yields are calculated through Eq. 3 using the slopes of the calibration graphs generated at specific time intervals. In this study, the sensitivity of the compound to light was measured. For these measurements, firstly, the solutions of the compound **2** in both DMSO and DMF solvents were separately prepared and then the mixtures were exposed to light of 7.05×10^{15} photon. $s^{-1}.cm^{-2}$ intensity at a certain time and UV-Vis spectra of these mixtures were separately taken and the change in the Q band of compound **2** was investigated. Figure 9 for DMSO solution and Figure 10 for DMF solution show absorbance change during photodegradation quantum yield measurements of compound **2** showing the decreasing of the Q and B bands. As it can be seen from figures, there are no significant decrease in

Q band of compound **2** in both solvents. The Φ_d values of compound **2** in DMSO and DMF were found the order of 10^{-5} (Table 2). Ordinary values for stable Pcs are of the order of 10^{-6} , but these values for unstable Pcs are of the order of 10^{-3} (49). The Φ_d value of compound **2** is 1.08×10^{-5} in DMSO and is 4.44×10^{-5} in DMF. These values are typical for zinc Pcs bearing different substituents on the periphery as described in the literature (50, 52). The Φ_d value in DMSO is slightly lower than unsubstituted zinc(II) phthalocyanine ($\Phi_d: 2.61 \times 10^{-5}$). But the Φ_d value in DMF is slightly higher than unsubstituted zinc(II) phthalocyanine ($\Phi_d: 2.30 \times 10^{-5}$). According to the data obtained, compound **2** in DMSO is slightly stable than compound **2** in DMF due to having lower Φ_d value.

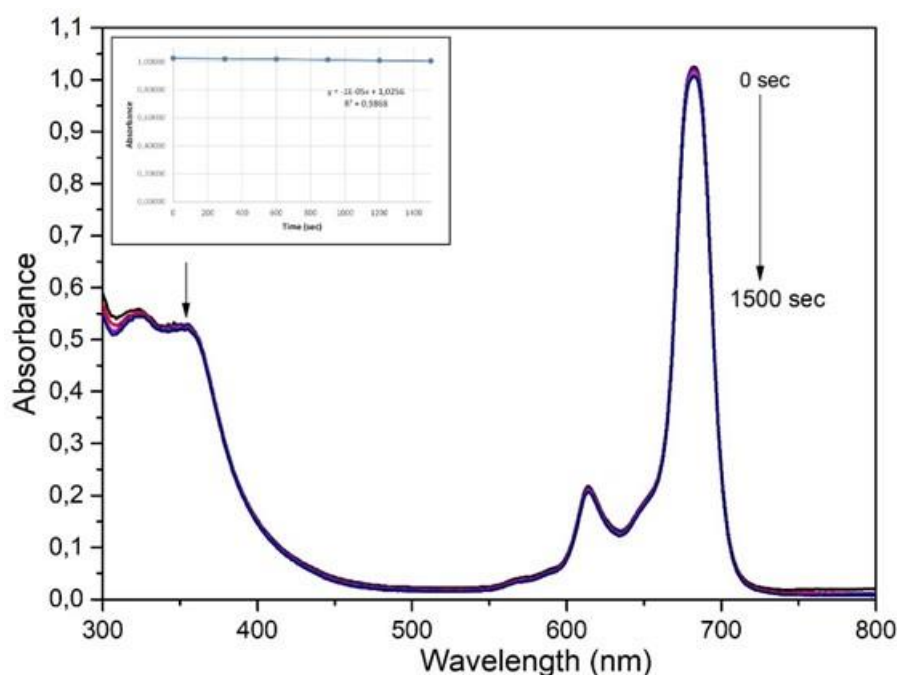


Figure 9: Absorbance changes during the photodegradation study of compound **2** in DMSO (Inset: plot of Q band absorbance versus time).

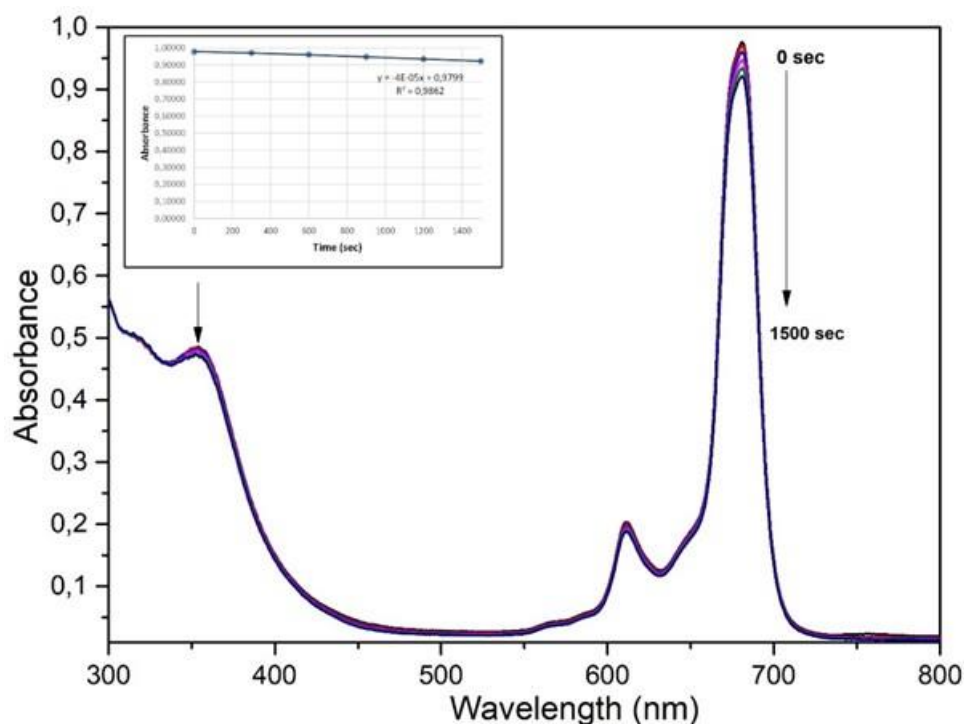


Figure 10: Absorbance changes during the photodegradation study of compound **2** in DMF (Inset: plot of Q band absorbance versus time).

CONCLUSION

In summary, this study reports synthesis, characterization and photochemical and photophysical properties of ferulic acid substituted zinc(II) phthalocyanine for the first time. The synthesized phthalocyanine has solubility in many solvents such as THF, DMSO and DMF and it does not exhibit any aggregation in the mentioned solvents. Fluorescence quantum yield, singlet oxygen quantum yield and photodegradation quantum yield of this phthalocyanine were also determined in DMSO and DMF solvent to reveal their potential in PDT applications. This phthalocyanine gives good results as photosensitizers for PDT treatment.

ACKNOWLEDGEMENTS

Thanks to Prof. Dr. Ayşe Gül Gürek and Mohamad Albakour from Gebze Technical University for their contributions.

Conflict of interest: The authors declare that they have no conflict of interest.

REFERENCES

1. Leznoff CC, Lever ABP, Stuzhin P, Khelevina O, Berezin B. Phthalocyanines: properties and applications: VCH publishers; 1996.
2. Gorduk S, Avciata O, Avciata U. Photocatalytic degradation of methylene blue under visible light irradiation by non-peripherally tetra substituted phthalocyanine-TiO₂ nanocomposites. *Inorg Chim Acta*. 2018;471:137-47.
3. Gottfried JM. Surface chemistry of porphyrins and phthalocyanines. *Surf Sci Rep*. 2015;70(3):259-379.
4. Aktaş A, Acar I, Bıyıklıoğlu Z, Saka ET, Kantekin H. Synthesis, electrochemistry of metal-free, copper, titanium phthalocyanines and investigation of catalytic activity of cobalt, iron phthalocyanines on benzyl alcohol oxidation bearing 4-{2-[3-trifluoromethyl) phenoxy] ethoxy} groups. *Synth Met*. 2014;198:212-20.
5. Durmuş M, Lebrun C, Ahsen V. Synthesis and characterization of novel liquid and liquid crystalline phthalocyanines. *J Porphyrins Phthalocyanines*. 2004;8(10):1175-86.
6. Guillaud G, Simon J, Germain J. Metallophthalocyanines: Gas sensors, resistors and field effect transistors. *Coord Chem Rev*. 1998;178:1433-84.
7. Bouvet M. Radical phthalocyanines and intrinsic semiconduction. *The Porphyrin Handbook*: Elsevier; 2003. p. 37-103.
8. Walter MG, Rudine AB, Wamser CC. Porphyrins and phthalocyanines in solar photovoltaic cells. *J Porphyrins Phthalocyanines*. 2010;14(09):759-92.
9. Koyun Ö, Gördük S, Keskin B, Çetinkaya A, Koca A, Avciata U. Microwave-assisted synthesis, electrochemistry and spectroelectrochemistry of phthalocyanines bearing tetra terminal-alkynyl functionalities and click approach. *Polyhedron*. 2016;113:35-49.

10. Karaca H, Kurt Z, Sezer S. Synthesis of Novel Chalcone Substituted Metallophthalocyanines: Electrochemistry, Spectroelectrochemistry, and Catalytic Oxidation of 2-mercaptoethanol. *JOTCSA*. 2018;5(2):701-18.
11. Oluwole DO, Sarı FA, Prinsloo E, Dube E, Yuzer A, Nyokong T, İnce M. Photophysicochemical properties and photodynamic therapy activity of highly water-soluble Zn(II) phthalocyanines. *Spectrochimica Acta, Part A : Molecular and Biomolecular Spectroscopy*. 2018;203:236-243.
12. Bonnett R. Photosensitizers of the porphyrin and phthalocyanine series for photodynamic therapy. *Chem Soc Rev*. 1995;24(1):19-33.
13. Dolmans DE, Fukumura D, Jain RK. Photodynamic therapy for cancer. *Nature reviews cancer*. 2003;3(5):380.
14. Nas A, Dilber G, Durmuş M, Kantekin H. The influence of the various central metals on photophysical and photochemical properties of benzothiazole-substituted phthalocyanines. *Spectrochimica Acta Part A: Molecular and Biomolecular Spectroscopy*. 2015;135:55-62.
15. Macdonald IJ, Dougherty TJ. Basic principles of photodynamic therapy. *J Porphyrins Phthalocyanines*. 2001;5(02):105-29.
16. Günsel A. Comparative Studies of Photophysicochemical Properties of Non-Peripherally Anisole/Thioanisole-Tetrasubstituted Gallium (III) Phthalocyanines Containing Oxygen/Sulfur Bridge. *JOTCSA*. 2017;5(1):269-82.
17. Dumoulin F, Durmuş M, Ahsen V, Nyokong T. Synthetic pathways to water-soluble phthalocyanines and close analogs. *Coord Chem Rev*. 2010;254(23-24):2792-847.
18. Makhseed S, Machacek M, Alfadly W, Tuhl A, Vinodh M, Simunek T, et al. Water-soluble non-aggregating zinc phthalocyanine and in vitro studies for photodynamic therapy. *Chem Commun*. 2013;49(95):11149-51.
19. Kliesch H, Weitemeyer A, Müller S, Wöhrle D. Synthesis of phthalocyanines with one sulfonic acid, carboxylic acid, or amino group. *Liebigs Annalen*. 1995;1995(7):1269-73.
20. Opris DM, Nuesch F, Löwe C, Molberg M, Nagel M. Synthesis, characterization, and dielectric properties of phthalocyanines with ester and carboxylic acid functionalities. *Chem Mater*. 2008;20(21):6889-96.
21. Sevim AM, Arıkan S, Koca A, Gül A. Synthesis and spectroelectrochemistry of new phthalocyanines with ester functionalities. *Dyes and Pigments*. 2012;92(3):1114-21.
22. Tekdaş DA, Gürek AG, Ahsen V. Asymmetric zinc phthalocyanines substituted with a single carboxyl and triethylenesulfonyl groups: synthesis, characterization and validation for photodynamic therapy. *J Porphyrins Phthalocyanines*. 2014;18(10-11):899-908.
23. Verdree VT, Pakhomov S, Su G, Allen MW, Countryman AC, Hammer RP, et al. Water soluble metallo-phthalocyanines: the role of the functional groups on the spectral and photophysical properties. *J Fluoresc*. 2007;17(5):547-63.
24. Liu W, Jensen TJ, Fronczek FR, Hammer RP, Smith KM, Vicente MGH. Synthesis and cellular studies of nonaggregated water-soluble phthalocyanines. *J Med Chem*. 2005;48(4):1033-41.
25. Ke M-R, Huang J-D, Weng S-M. Comparison between non-peripherally and peripherally tetra-substituted zinc(II) phthalocyanines as photosensitizers: Synthesis, spectroscopic, photochemical and photobiological properties. *J Photochem Photobiol A*. 2009;201(1):23-31.
26. Özgül G, Taştemel A, Özkaya AR, Bulut M. Synthesis, characterization and comparative electrochemistry of beta and alpha tetra-[4-oxy-3-methoxybenzoic acid]-substituted Zn(II), Co(II) and Cu(II) phthalocyanines. *Polyhedron*. 2015;85:181-89.
27. Fery-Forgues S, Lavabre D. Are fluorescence quantum yields so tricky to measure? A demonstration using familiar stationery products. *J Chem Educ*. 1999;76(9):1260.
28. Maree MD, Nyokong T, Suhling K, Phillips D. Effects of axial ligands on the photophysical properties of silicon octaphenoxypthalocyanine. *J Porphyrins Phthalocyanines*. 2002;6(06):373-76.
29. Ogunsipe A, Chen J-Y, Nyokong T. Photophysical and photochemical studies of zinc(II) phthalocyanine derivatives—effects of substituents and solvents. *New J Chem*. 2004;28(7):822-27.
30. Gürol I, Durmuş M, Ahsen V, Nyokong T. Synthesis, photophysical and photochemical properties of substituted zinc phthalocyanines. *Dalton Transactions*. 2007(34):3782-91.
31. Ogunsipe A, Nyokong T. Effects of substituents and solvents on the photochemical properties of zinc phthalocyanine complexes and their protonated derivatives. *J Mol Struct*. 2004;689(1-2):89-97.
32. Perrin DD, Armarego W, Perrin DR. Purification of Laboratory Chemicals, by DD

Perrin. WLF Armarego and Dawn R. Perrin: Pergamon Press; 1966.

33. Spiller W, Kliesch H, Wöhrle D, Hackbarth S, Röder B, Schnurpfeil G. Singlet oxygen quantum yields of different photosensitizers in polar solvents and micellar solutions. *J Porphyrins Phthalocyanines*. 1998;2(2):145-58.

34. Brannon JH, Magde D. Picosecond laser photophysics. Group 3A phthalocyanines. *JACS*. 1980;102(1):62-65.

35. Ogunsipe A, Nyokong T. Photophysical and photochemical studies of sulphonated non-transition metal phthalocyanines in aqueous and non-aqueous media. *J Photochem Photobiol A*. 2005;173(2):211-20.

36. Seotsanyana-Mokhosi I, Kuznetsova N, Nyokong T. Photochemical studies of tetra-2, 3-pyridinoporphyrazines. *J Photochem Photobiol A*. 2001;140(3):215-22.

37. Gorduk S, Koyun O, Avciata O, Altindal A, Avciata U. Synthesis of Peripherally Tetrasubstituted Phthalocyanines and Their Applications in Schottky Barrier Diodes. *Journal of Chemistry*. 2017;2017.

38. Kadish KM, Smith KM, Guillard LR. *The Porphyrin Handbook: Phthalocyanines: Properties and Materials*. 2003. Academic Press.

39. Jeong J, Kumar RS, Mergu N, Son Y-A. Photophysical, electrochemical, thermal and aggregation properties of new metal phthalocyanines. *J Mol Struct*. 2017;1147:469-79.

40. Engelkamp H, Nolte RJ. Molecular materials based on crown ether functionalized phthalocyanines. *J Porphyrins Phthalocyanines*. 2000;4(05):454-59.

41. Dominguez D, Snow A, Shirk J, Pong R. Polyethyleneoxide-capped phthalocyanines: limiting phthalocyanine aggregation to dimer formation. *J Porphyrins Phthalocyanines*. 2001;5(07):582-92.

42. Sibrian-Vazquez M, Ortiz J, Nesterova IV, Fernández-Lázaro F, Sastre-Santos A, Soper SA, et al. Synthesis and properties of cell-targeted Zn(II)-phthalocyanine-peptide conjugates. *Bioconjugate Chem*. 2007;18(2):410-20.

43. Ogunsipe A, Durmuş M, Atilla D, Gürek AG, Ahsen V, Nyokong T. Synthesis, photophysical and photochemical studies on long chain zinc phthalocyanine derivatives. *Synth Met*. 2008;158(21-24):839-47.

44. Durmuş M, Nyokong T. The synthesis, fluorescence behaviour and singlet oxygen studies of new water-soluble cationic gallium (III) phthalocyanines. *Inorg Chem Commun*. 2007;10(3):332-38.

45. Forster T, Hoffmann G. Viscosity dependence of fluorescent quantum yields of some dye systems. *Zeitschrift Fur Physikalische Chemie-Frankfurt*. 1971;75(1-2):63-&.

46. Çakır V, Çakır D, Pişkin M, Durmuş M, Bıyıklıoğlu Z. New peripherally and non-peripherally tetra-substituted water soluble zinc phthalocyanines: synthesis, photophysics and photochemistry. *J Organomet Chem*. 2015;783:120-29.

47. Durmuş M, Nyokong T. Synthesis and solvent effects on the electronic absorption and fluorescence spectral properties of substituted zinc phthalocyanines. *Polyhedron*. 2007;26(12):2767-76.

48. Ogunsipe A, Maree D, Nyokong T. Solvent effects on the photochemical and fluorescence properties of zinc phthalocyanine derivatives. *J Mol Struct*. 2003;650(1-3):131-40.

49. Maree SE, Nyokong T. Syntheses and photochemical properties of octasubstituted phthalocyaninato zinc complexes. *J Porphyrins Phthalocyanines*. 2001;5(11):782-92.

50. Nyokong T, Antunes E. Photochemical and photophysical properties of metallophthalocyanines. *Handbook of Porphyrin Science (Volume 7) With Applications to Chemistry, Physics, Materials Science, Engineering, Biology and Medicine: World Scientific; 2010. p. 247-357.*

51. Durmuş M. Photochemical and photophysical characterization. *Photosensitizers in medicine, environment, and security: Springer; 2011. p. 135-266.*

52. Albakour M, Tunç G, Akyol B, Kostakoğlu S T, Berber S, Bekaroğlu Ö, Gürek A G. Synthesis, characterization, photophysicochemical properties and theoretical study of novel zinc phthalocyanine containing four tetrathia macrocycles. *J Porphyrins Phthalocyanines*. 2018; 22(01n03): 77-87.



Synthesis, Characterization and Optimum Reaction Conditions of Oligo-N-Salicylidenephenylhydrazone via Oxidative Polymerization

Feyza Kolcu 

Çanakkale Onsekiz Mart University, Lapseki Vocational School, Department of Chemistry and Chemical Processing Technologies, Çanakkale, Turkey

Abstract: The oxidative polycondensation conditions and optimum parameters of N-salicylidenephenylhydrazone (SPH) were determined using air, H₂O₂ and NaOCl as oxidants at a temperature range between 50 °C and 95 °C in an aqueous alkaline medium. The molecular structures of the obtained monomer and oligomer were confirmed by FT-IR, UV-Vis, ¹H-NMR and elemental analyses. The molecular weight distributions of oligo-N-salicylidenephenylhydrazone were determined (OSPH) by SEC measurement. Thermal behavior (TG-DTA) of OSPH was examined using thermogravimetric techniques. The conversion of N-salicylidenephenylhydrazone into its oligomeric form was performed using air, H₂O₂ and NaOCl as oxidants in an aqueous alkaline medium. According to SEC analysis, the number-average molecular weight (M_n), weight-average molecular weight (M_w) and polydispersity index (PDI) values of OSPH obtained using NaOCl oxidant were found to be 1436 g mol⁻¹, 1631 g mol⁻¹ and 1.14, respectively. The conversion yield of N-salicylidenephenylhydrazone into oligo-N-salicylidenephenylhydrazone was 100% at optimum reaction conditions such as [SPH]₀ = [KOH]₀ = [H₂O₂]₀ = 0.06 mol/L and at 90 °C for 10 h. Also, according to TG-DTA analysis, oligo-N-salicylidenephenylhydrazone was shown to be thermally stable and resistant to thermo-oxidative decomposition. The weight loss of OSPH was found to be 20, 50 and 92.56% at 275°, 597° and 1000 °C, respectively.

Keywords: oligo-N-salicylidenephenylhydrazone, oxidative polycondensation, reaction conditions, thermo-oxidative decomposition.

Submitted: January 3, 2018. **Accepted:** July 23, 2018.

Cite this: Kolcu F. Synthesis, Characterization and Optimum Reaction Conditions of Oligo-N-Salicylidenephenylhydrazone via Oxidative Polymerization. JOTCSA. 2018;5(2):919–30.

DOI:

***Corresponding author.** E mail: feyzakolcu@comu.edu.tr, Fax: +90-286-522 61 01

INTRODUCTION

The oligo-phenols and their Schiff base derivatives including –OH and –CH=N groups have been used in various fields. They have useful properties such as paramagnetism, semi conductivity, employed in electrochemical cells and they resist to high energy (1-4). Polymer-metal complex compounds can be prepared with the reaction of metal salts and polymers containing electron donor groups such as –OH and –CH=N (5). Antimicrobial properties of

oligophenols with Schiff base substitute and their oligomer-metal complex compounds were investigated by Kaya *et al* (6,7). Oligophenols may be used in cleaning poisonous heavy metals in the industrial wastewaters. Also, Schiff base compounds have been used to determine the transition metals in some natural food samples (8). Therefore, the syntheses of oligomer and oligomer-metal complexes are very important for analytical, environmental and food chemistry.

All azomethine polymers show a remarkable thermal stability. Non-conjugated polymers are white or cream colored and have thermal stabilities at about 300 °C in N₂ and 250 °C in air atmosphere. The color of aromatic azomethine polymers changes from yellow-orange to red-brown or black products, with thermal stabilities up to 500-550 °C in N₂ and 430-480 °C in air atmosphere. They are also resistant to radiation and their stability is found to be independent of dose rate and nature of the ionizing radiation (9).

In this study, we have investigated the effects of different parameters such as temperature, initial concentrations of NaOCl, H₂O₂ and KOH for the polymerization of N-salicylidene phenylhydrazone. The molecular structures of the obtained monomer and oligomer were confirmed by using FT-IR, UV-Vis, ¹H-NMR, elemental analyses. Additionally, OSPH was characterized by TG-DTA, SEC, and solubility tests.

MATERIALS AND METHODS

Materials

Phenylhydrazine, salicylaldehyde (SA), 1,4-dioxane, ethanol, methanol, benzene, acetone, ethyl acetate, n-heptane, tetrahydrofuran (THF), dimethylsulfoxide (DMSO), N,N'-dimethylformamide (DMF), H₂SO₄, toluene, pyridine, n-hexane, hydrochloric acid (HCl) (37%) and H₂O₂ (35% solution in water) were supplied from Merck Chemical Co. (Germany) and they were used as received. Sodium hypochlorite (NaOCl), (30% solution in water) was supplied from Paksoy Chem. Co. (Turkey).

Preparation of N-salicylidene phenylhydrazone (SPH)

N-salicylidene phenylhydrazone (SPH) was prepared by the condensation of salicylaldehyde (0.025 mol) and phenylhydrazine (0.025 mol) in 25-mL methanol under reflux for 3 h (Scheme 1). The precipitated N-salicylidene phenylhydrazone (SPH) was filtered and recrystallized from methanol and dried in a vacuum desiccator (m.p.: 125 °C, yield, 90%).

Anal. calcd. for SPH: C, 73.59; H, 5.66; N, 13.21. Found: C, 73.35; H, 5.52; N, 13.12. UV-Vis (λ_{max}): 220, 236, 280 and 340 nm. FT-IR (KBr, cm⁻¹): ν (O-H) 3470 s, ν (C-H aryl) 3030 m, ν (C=N) 1615 s, ν (N-H) 3300 s, ν (C=C) 1580, 1455, 1450 s, ν (Ar-O) 1280 s. ¹H-NMR (DMSO): δ ppm, 10.15 (s, 1H, OH); 8.30 (s, 1H, CH=N); 5.60 (s, 1H, NH); 7.48 (d, 1H, Ar-Ha), 6.85 (t, 1H, Ar-Hb), 7.25 (t, 1H, Ar-Hc), 6.70 (d, 1H, Ar-Hd) 7.00 (d, 2H,

Ar-Hee') 7.15 (t, 2H, Ar-Hff') 6.70 (t, 1H, Ar-Hg).

Synthesis of Oligo-N-salicylidene phenylhydrazone with air

SPH (4.24 g, 0.02 mol) was dissolved in an aqueous solution of KOH (10%) (1.12 g, 0.02 mol) and placed into a 100 mL three-necked round-bottomed flask. It was fitted with a condenser, thermometer, stirrer and a glass tube was placed over condenser for air to pass through. The reaction mixture was heated at various temperatures and times. Air was passed through an aqueous solution of KOH (20%) before being sent to the reaction tube to eliminate CO₂ in the air. It was cooled to room temperature and then, 0.02 mol of HCl (37%) was added to the reaction mixture. Unreacted monomer was separated from the reaction products by washing with n-heptane. The mixture was filtered and washed with hot water for separating it from mineral salts and dried in the oven at 110 °C

Anal. calcd. for OSPH : C, 74.29; H, 4.76; N, 13.33. Found: C, 73.75; H, 4.62; N, 13.00. UV-Vis (λ_{max}): 221, 241, 291 and 346 nm. FT-IR (KBr, cm⁻¹): ν (O-H) 3500 s, ν (C-H aryl) 3030 m, ν (C=N) 1600 s, ν (N-H) 3280 s, ν (C=C) 1500, 1470 s, ν (Ar-O) 1270 s. ¹H-NMR (DMSO): δ ppm, 10.40 (s, 1H, OH); 9.20 (s, 1H, CH=N); 6.55 (s, 1H, NH); 7.30 (s, 1H, Ar-Ha), 6.80 (s, 1H, Ar-Hc), 6.50 (d, 2H, Ar-Hdd') 7.00 (t, 2H, Ar-Hee') 6.70 (t, 1H, Ar-Hf).

Synthesis of Oligo-N-salicylidene phenylhydrazone with NaOCl

OSPH was synthesized through oxidative polycondensation of SPH using NaOCl (30%) as the oxidant. SPH (4.24 g, 0.02 mol) was placed into a 50-mL three-necked round-bottomed flask and dissolved in an aqueous solution of KOH (10%, 1.12 g, 0.02 mol). The flask was connected to a condenser, a thermometer, a magnetic stirrer, and an additional funnel containing NaOCl. After heating at 60 °C, NaOCl (30%) was added drop wise within 20 min. The reaction mixture was heated at various temperatures and times. The mixture was neutralized by HCl (37%, 0.02 mol) at room temperature. Unreacted monomer was separated from the reaction products by washing with cold n-heptane. The mixture was filtered and washed with hot water for separating from mineral salts and dried in the oven at 110 °C.

Synthesis of Oligo-N-salicylidene phenylhydrazone with H₂O₂

OSPH was synthesized through oxidative polycondensation in an aqueous alkaline medium using H₂O₂ (35%) as the oxidant. Polymerization was performed in a 50 mL

three-necked round-bottomed flask connected to a condenser, a thermometer and a magnetic stirrer, and an addition to funnel containing H_2O_2 . SPH (4.24 g, 0.02 mol) was dissolved in an aqueous solution of KOH (10%, 1.12 g, 0.02 mol). After heating at 40 °C, H_2O_2 was added drop wise within 20 min. The reaction mixture was heated at various temperature and time. The mixture was neutralized by HCl (37%, 0.02 mol) at room temperature. Unreacted monomer was separated from the reaction products using n-heptane. The mixture was filtered and washed with hot water for separating from mineral salts and dried in the oven at 110 °C.

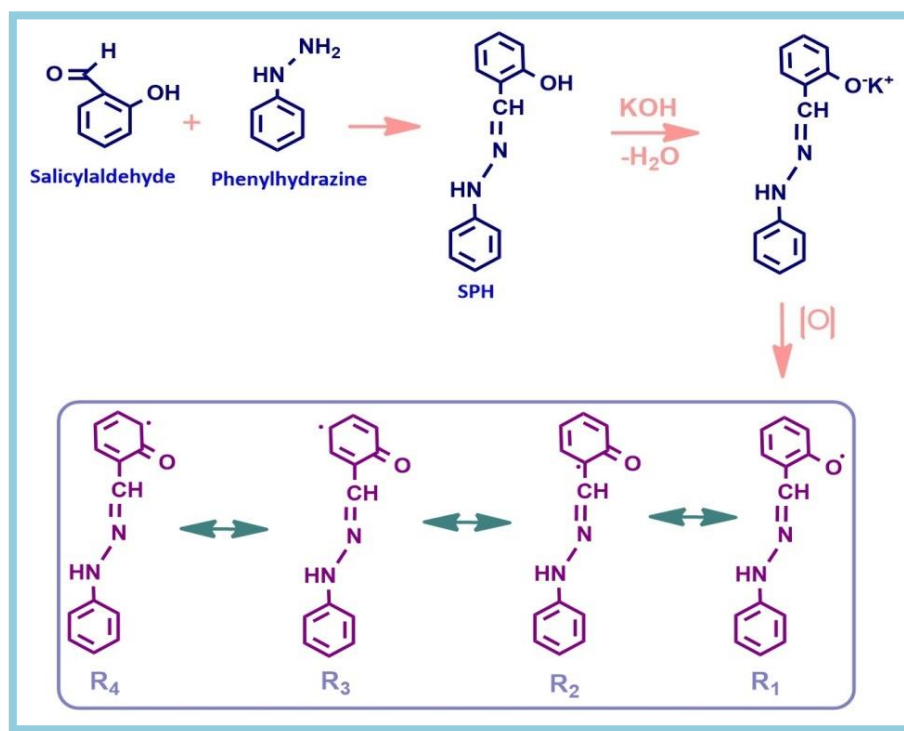
Characterization Techniques

FT-IR and UV-Vis spectra were recorded by Mattson FT-IR 8010 and UV-160 (Shimadzu), respectively. The FT-IR spectra were recorded using KBr disc (4000-400 cm^{-1}). UV-Vis spectra of SPH and OSPH were determined using THF. Elemental analysis was carried out by a Carlo Erba 1106. OSPH was characterized by $^1\text{H-NMR}$ spectra (Bruker AC FT-NMR 400 MHz spectrometer) and the spectra were recorded at 25 °C using deuterated DMSO as solvent. Tetramethylsilane (TMS) was used as internal standard. Thermal data were obtained

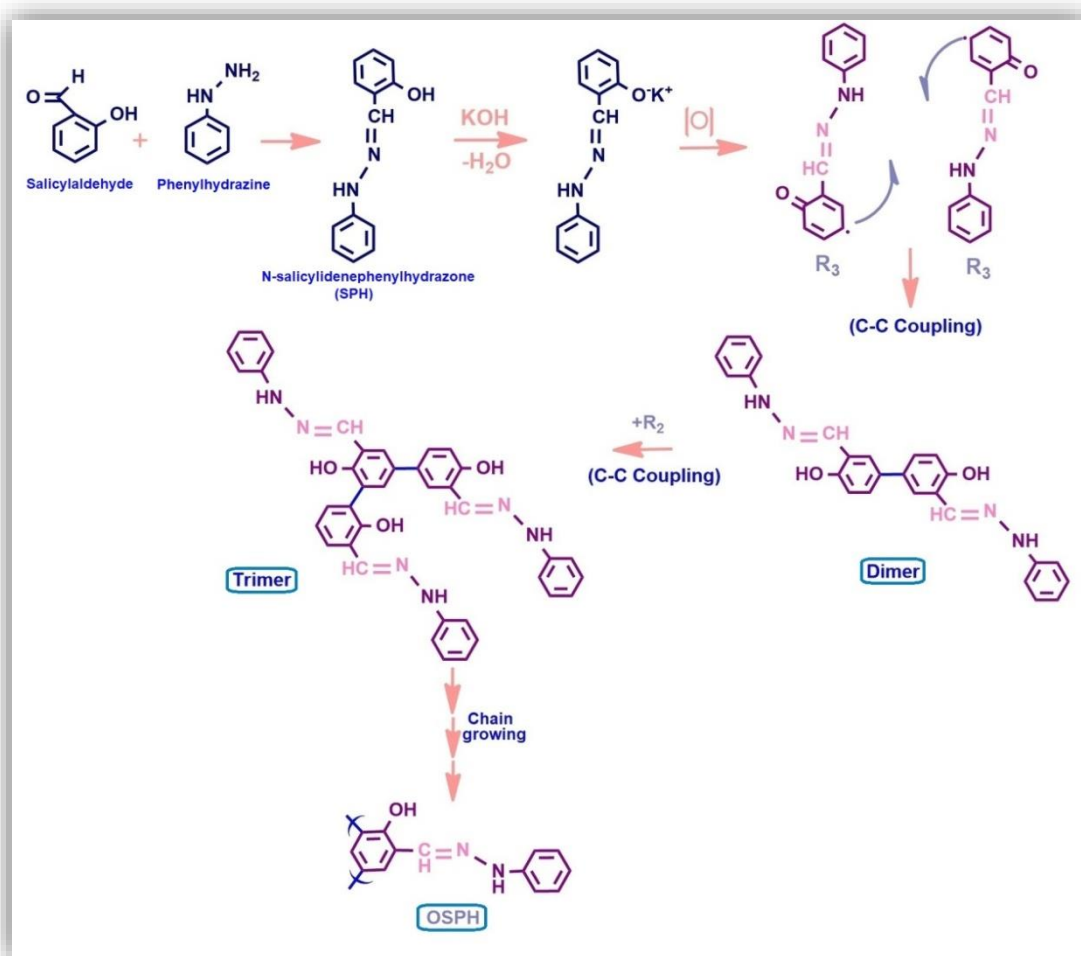
by STA 409C NETZSCH-Geratebau GmbH Thermal Analysis. TG-DTA measurements were performed between 20 and 1000 °C (in air, rate 10°C/min). SEC analyses were used to investigate both size and polydispersity of the synthesized polymers that is, the ability to be able to find the molecular range distribution of the polymer molecules (PDI), as well as the number-average molecular weight (M_n) and the average molecular weight (M_w), by using a mixture of polystyrene standards (Polymer Laboratories; the peak molecular weights, M_p , between 162 and 19880 g mol^{-1}) for calibration of the instrument SEC (Shimadzu 10AVp series HPLC-SEC system), and a SGX (100 Å and 7.7 nm diameter loading material) 3.3 mm i.d. x 300 mm column. DMF as eluent at a flow rate of 0.4 mL/min was used in SEC analyses. A refractive index detector (at 25°C) was used to analyze the product.

RESULTS AND DISCUSSION

Possible four main coupling modes for the polymerization of N-salicylidenehydrazones (SPH) and the general synthetic route for the synthesis of oligo-N-salicylidenehydrazones (OSPH) and were identified and given in Schemes 1 and 2 respectively.



Scheme 1. Synthetic route of N-salicylidenehydrazone (SPH) and possible resonance and coupling modes of SPH.



Scheme 2. Synthetic pathway of OSPH.

Specifying the optimal reaction conditions and solubility of OSPH

Oxidative polymerization of SPH was observed to be affected to different reaction parameters. To specify the optimum polycondensation conditions, polymerization of SPH was carried out using various oxidants

such as NaOCl, H₂O₂ and air in aqueous KOH solution by tuning the temperature in the range between 40 and 95 °C at constant SPH, KOH and oxidant concentration (Figure 1(a)). Additionally, the polymerization was carried out at different reaction time to assign the optimum reaction time (Figure 1(b)).

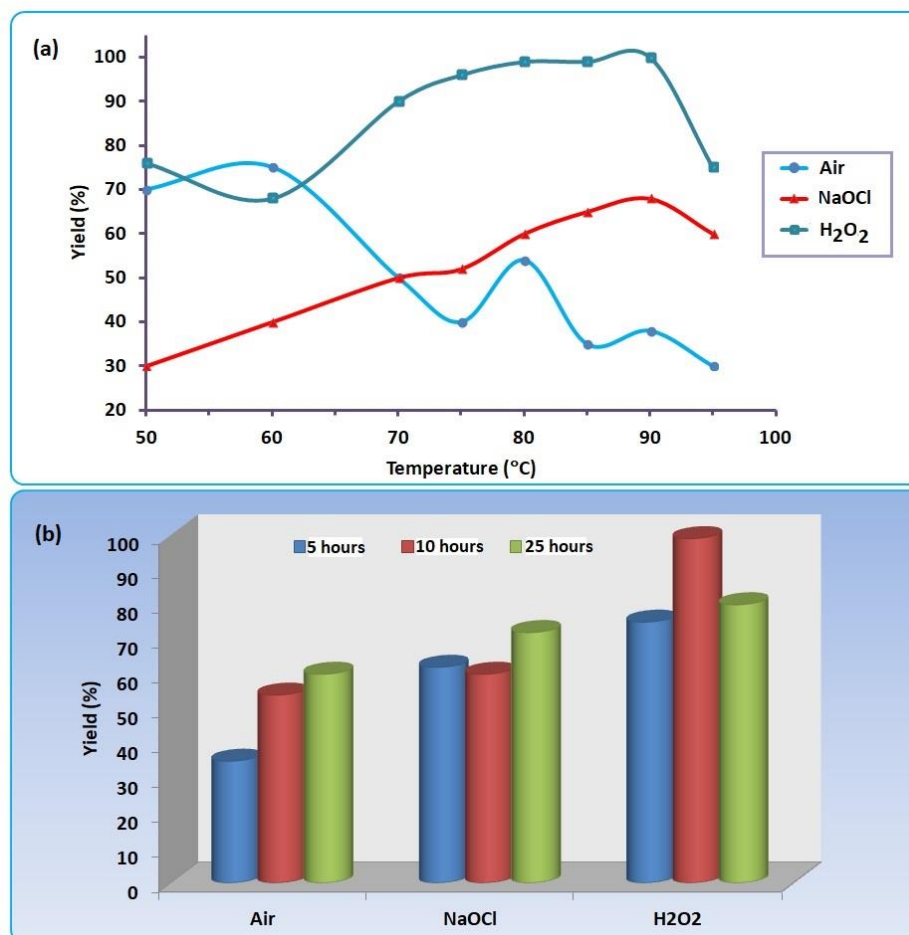


Figure 1. Reaction yields of OSPH at various temperature (a) and time (b) (Conditions: $[\text{SPH}] = 0.06 \text{ mol L}^{-1}$, $[\text{KOH}] = 0.06 \text{ mol L}^{-1}$, $[\text{NaOCl}] = 0.06 \text{ mol L}^{-1}$, $[\text{H}_2\text{O}_2] = 0.06 \text{ mol L}^{-1}$ and air = 8.5 L h^{-1}).

The oxidative polycondensation conditions of SPH with air as oxidant in aqueous alkaline medium are given in Table 1. The oxidative polycondensation of SPH was not observed in THF and acetic acid medium at various temperature and time. SPH was soluble in aqueous KOH but no reaction was observed when it was heated for 3 h at 80 °C. However, the oxidative polycondensation of SPH took place in an aqueous alkaline solution and the

color turned into brown by adding oxidants such as NaOCl, H₂O₂ and air. With $[\text{SPH}]_0 = [\text{KOH}]_0 = 0.06 \text{ mol/L}$, the yield of OSPH was 75% by air oxidant for 5h at 50 °C (Table 1). While the yield of OSPH was 80% for 5 h at 60 °C, the polymerization yield was found to be 35% for 5 h at 80°C. The reason may be the disruption of the polymer into monomers at high temperatures.

Table 1. The optimum oxidative polycondensation conditions of SPH in the aqueous alkaline medium with air oxidant.

Run	[SPH] ₀ (mol/L)	[KOH] ₀ (mol/L)	Air (L/h)	Temp. (°C)	Time (h)	Yield of SPH (%)
1	0.06	0.06	8.5	50	5	75
2	0.06	0.06	8.5	60	5	80
3	0.06	0.06	8.5	80	25	60
4	0.06	0.06	8.5	80	3	20
5	0.06	0.12	8.5	80	5	35
6	0.06	0.06	8.5	70	10	50
7	0.06	0.06	8.5	75	10	40
8	0.06	0.06	8.5	80	10	54
9	0.06	0.06	8.5	85	10	35
10	0.06	0.06	8.5	90	10	38
11	0.06	0.06	8.5	95	10	30

As seen in Table 1, the yield of oligomer depends on temperature and time variables. For air as the oxidant, the maximum yield of OSPH was observed as 80% at optimum conditions, such as [SPH]₀ = [KOH]₀ = 0.06 mol/L for 5 h at 60 °C (Table 1).

The oxidative polycondensation conditions of SPH with 30% NaOCl solution in aqueous

alkaline medium are given in Table 2. The yield of OSPH was 77% at optimum conditions such as [SPH]₀ = [KOH]₀ = [NaOCl]₀ = 0.06 mol/L for 3 h at 80 °C. The yield of OSPH was 73% at the reaction conditions such as [SPH]₀ = [KOH]₀ = 0.06 mol/L and [NaOCl]₀ = 0.12 mol/L for 10 h at 90 °C. The various conditions of OSPH are given for NaOCl in Table 2.

Table 2. The optimum oxidative polycondensation conditions of SPH in the aqueous alkaline medium with NaOCl as the oxidant.

Run	[SPH] ₀ (mol/L)	[KOH] ₀ (mol/L)	[NaOCl] ₀ , (mol/L)	Temp. (°C)	Time (h)	Yield of SPH (%)
1	0.06	0.06	0.06	70	10	50
2	0.06	0.06	0.06	70	5	58
3	0.06	0.06	0.06	80	10	60
4	0.06	0.06	0.06	80	5	62
5	0.06	0.06	0.06	90	10	68
6	0.06	0.06	0.06	90	5	65
7	0.06	0.06	0.06	95	10	60
8	0.06	0.06	0.06	95	5	55
9	0.06	0.06	0.06	70	2	40
10	0.06	0.06	0.06	80	3	77
11	0.06	0.06	0.06	90	25	73
12	0.06	0.06	0.12	90	10	73
13	0.06	0.12	0.06	90	10	68

The oxidative polycondensation conditions of SPH with 35% H₂O₂ solution in aqueous alkaline medium are given in Table 3. The yield of OSPH was 100% at optimum conditions such as [SPH]₀ = [KOH]₀ = [H₂O₂]₀ = 0.06 mol/L for 10 h at 90 °C. The polymerization of SPH was 64% at the reaction conditions such

as [SPH]₀ = [KOH]₀ = 0.06 mol/L and [NaOCl]₀ = 0.12 mol/L for 10 h at 95 °C. While the polymerization of SPH was 100% and 75% for 10 h at 90 °C and for 10 h at 95 °C, respectively. The reason may be the disruption of the polymer into monomers at high temperatures.

Table 3. The optimum oxidative polycondensation conditions of SPH in the aqueous alkaline medium with H₂O₂ as the oxidant.

Run	[SPH] ₀ (mol/L)	[KOH] ₀ (mol/L)	[H ₂ O ₂] ₀ (mol/L)	Temp. (°C)	Time (h)	Yield of SPH (%)
1	0.06	0.06	0.06	50	10	76
2	0.06	0.06	0.06	60	10	68
3	0.06	0.06	0.06	70	10	90
4	0.06	0.06	0.06	75	10	96
5	0.06	0.06	0.06	80	10	99
6	0.06	0.06	0.06	85	10	99
7	0.06	0.06	0.06	90	10	100
8	0.06	0.06	0.06	95	10	75
9	0.06	0.06	0.06	95	2	60
10	0.06	0.06	0.06	95	25	46
11	0.06	0.06	0.12	95	10	64
12	0.06	0.06	0.06	75	5	70

Since the growing macromolecular chain come out of solution during the polycondensation at low polymerization degrees, high molecular weight polymers can not be obtained. Oxidatively polymerized products of OSPH synthesized by air, H₂O₂ and NaOCl in aqueous alkaline medium were brown solid powders. OSPH was soluble in common organic solvents such as CHCl₃, DMSO, concentrated H₂SO₄ and aqueous KOH, DMF, benzene, toluene, acetone, THF, ethyl acetate, 1,4-dioxane, ethanol, methanol and pyridine, but it was insoluble in n-hexane and n-heptane.

Characterization of SPH and OSPH

Based on the SEC chromatograms of OSPH, the calculated number-average molecular weight (M_n), weight average molecular weight (M_w), and polydispersity index (PDI) values were organized in Table 4. According to SEC analyses, M_n , M_w and PDI values of OSPH were

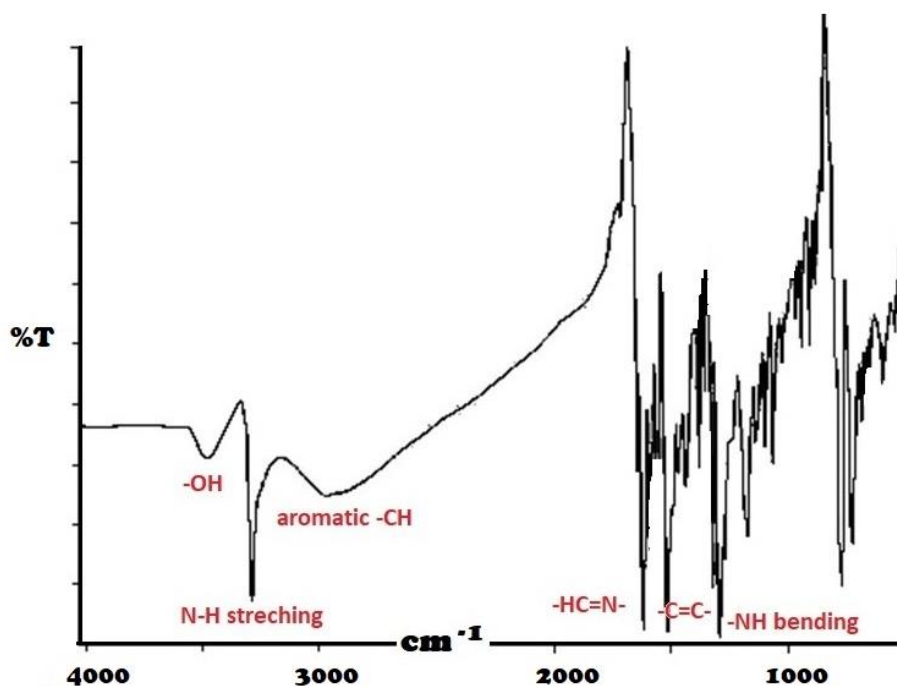
found to be 1436 g mol⁻¹, 1631 g mol⁻¹ and 1.14, respectively, for NaOCl oxidant. Total values delineated that M_n , M_w and PDI values of OSPH were found to be 850 g mol⁻¹, 1155 g mol⁻¹ and 1.36, respectively, for air as the oxidant. At the molecular weight distribution of OSPH, two fractions were observed with 93% of OSPH for the low molecular weight (for the first fraction: M_n , 1418 g mol⁻¹; M_w , 1650 g mol⁻¹; PDI, 1.16), but 7% of its weight for the high molecular weight (for the second fraction: M_n , 37632 g mol⁻¹; M_w , 40217 g mol⁻¹; PDI, 1.07). M_n , M_w and PDI values of OSPH were found to be 825 g mol⁻¹, 1660 g mol⁻¹ and 2.01, respectively, for H₂O₂ oxidant. Two peaks were observed with 92% of OSPH for the low molecular weight (for the first fraction: M_n , 1635 g mol⁻¹; M_w , 2157 g mol⁻¹; PDI, 1.32), but 8 % of its weight for the high molecular weight (for the second fraction: M_n , 8736 g mol⁻¹; M_w , 10123 g mol⁻¹; PDI, 1.16).

Table 4. SEC analyses data of the synthesized compounds.

Compounds	Total			Fraction I				Fraction II			
	M _n	M _w	PDI	M _n	M _w	PDI	%	M _n	M _w	PDI	%
OSPH (air)	850	1155	1.36	1418	1650	1.16	93	37632	40217	1.07	7
OSPH(NaOCl) (na(NaOCl) OSPH (H ₂ O ₂))	1436	1631	1.14 4	1436	1631	1.14 4	100	-	-	-	-
OSPH (H ₂ O ₂)	825	1660	2.01	1635	2157	1.32	92	8736	10123	1.16	8

The electronic spectra of SPH and OSPH were recorded in THF. UV-Vis spectrum of SPH was observed with the bands at 220, 240, 287, 315 and 342 nm. K band belongs to -OH and azomethine groups of SPH observed at 240 and 315 nm, respectively. B and R bands for SPH were observed at 287 and 342 nm, respectively. R band for -CH=N group of SPH was observed at 342 nm. UV-Vis spectrum of OSPH was observed with the same bands at 221, 241, 291 and 346 nm. K bands for -OH and azomethine groups of OSPH were observed at 241 and 291 nm, respectively. R band for -CH=N group of OSPH was seen at 346 nm.

FT-IR spectrum of SPH (Figure 2) shows the characteristic peaks of the functional groups for SPH. Phenolic O-H stretching and secondary N-H stretching frequencies were observed at 3470 cm⁻¹ and 3300 cm⁻¹, respectively. The peak at 2980 cm⁻¹ was attributed to the aromatic -C-H stretching frequency. The peak for imine (-HC=N-) group was observed at 1615 cm⁻¹. Aromatic -C=C stretching and the sharp peak attributed to the N-H bending in the molecular structure of SPH were observed at 1580 cm⁻¹ and 1380 cm⁻¹, respectively. The results confirm the structure of Schiff base containing an imine (-HC=N-) bond in the structure of SPH.

**Figure 2.** FT-IR spectrum of N-salicylidenehydrazone (SPH).

In the FT-IR spectrum of OSPH (Figure 3), the stretching frequencies of -OH and -CH=N groups were observed at 3500 and 1600 cm⁻¹,

respectively. The characteristic peaks clearly show the binding of functional groups of the synthesized products (10,11).

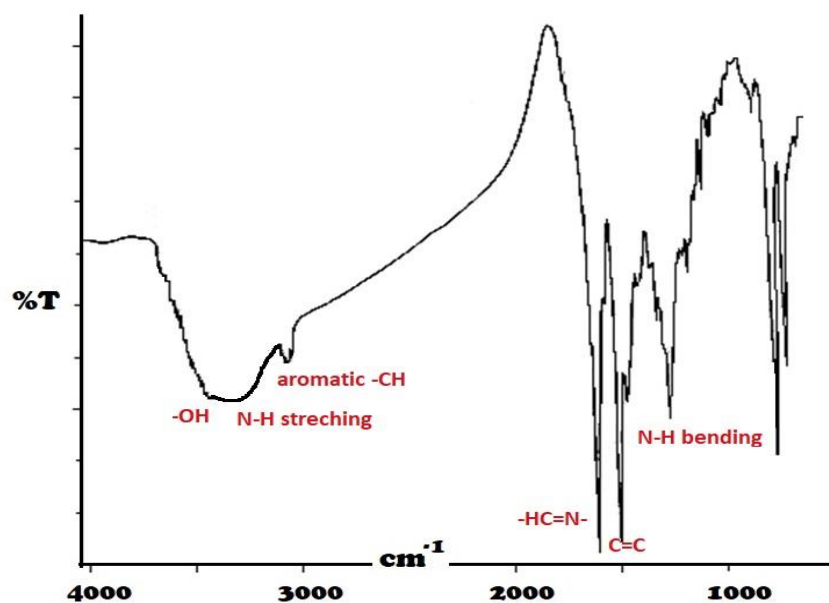


Figure 3. FT-IR spectrum of oligo-N-Salicylidenehydrazone (OSPH).

According to the spectral results and SEC analyses, OSPH's molecular structure is given as in Scheme 3. In order to identify the structures of Schiff base (SPH) and its oligomer (OSPH), $^1\text{H-NMR}$ spectra were recorded in DMSO-d_6 . At the $^1\text{H-NMR}$ spectrum of SPH, the characteristic peaks of the functional groups were observed. Phenyl-OH group at 10.15 ppm, azomethine ($-\text{CH}=\text{N}$) group at 8.30 ppm and secondary amine ($-\text{NH}$) group at 5.60 ppm. The $^1\text{H-NMR}$ and FT-IR results showed the formation of oligomeric macromolecules from SPH unit by the

oxidative polymerization through the carbons which are *ortho* and *para* positioned to hydroxyl group. At the $^1\text{H-NMR}$ spectrum of OSPH, the characteristic peaks of the functional groups were observed. Phenyl-OH group at 10.40 ppm, azomethine ($-\text{CH}=\text{N}$) group at 9.20 ppm and secondary amine ($-\text{NH}$) group at 6.55 ppm (Scheme 3). The FT-IR spectral data and the results of $^1\text{H-NMR}$ spectra of OSPH confirm the formation of the synthesized molecules. The spectral results are given below the synthesis part of the compounds.

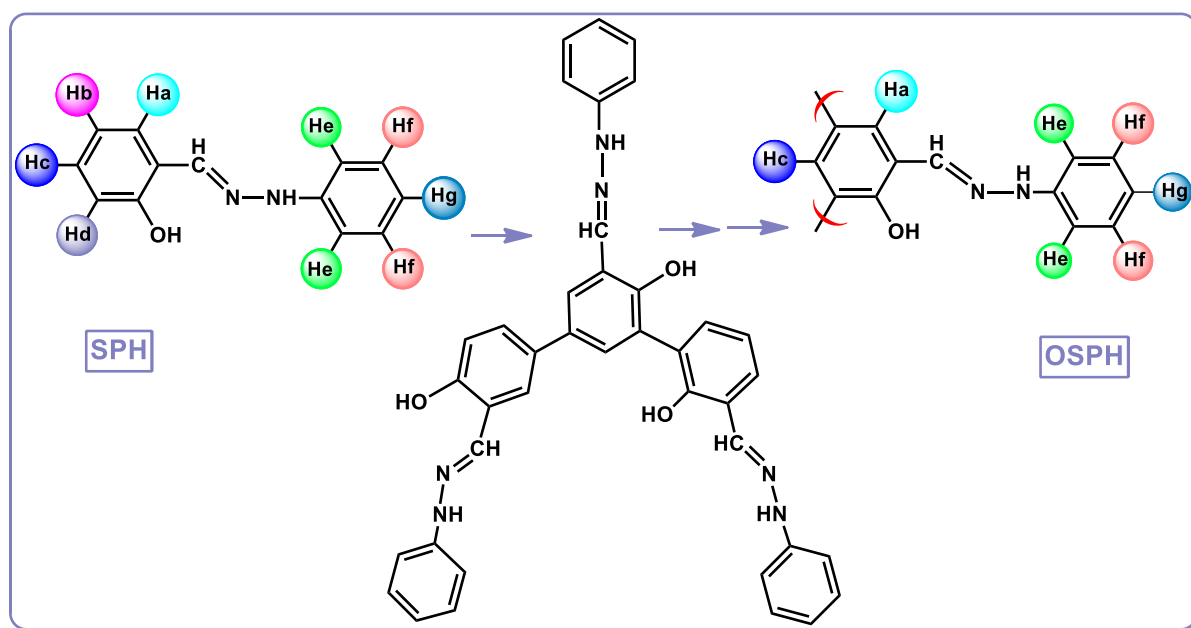


Figure 4. The structures of SPH and OSPH.

Thermal analysis of OSPH

The TG-DTA measurements of OSPH were performed under air atmosphere in the temperature range from 20 °C to 1000 °C in order to investigate its thermal stability. Figure 4 shows the TG-DTA curves for OSPH which was oxidatively polymerized of SPH in the aqueous alkaline medium by air as the oxidant. According to TG curves, OSPH started to degrade at 190 °C. OSPH thermo-oxidatively degraded in three steps. According

to TG curve of OSPH, T_{max} values were observed at 506, 625 and 820 °C. 20% and 50% weight losses of OSPH were found to be at 275 °C and 597 °C, respectively. The weight loss of OSPH was 92.56% at 1000 °C. 5% weight loss in the range of 50-150 °C assigned to water removal was also seen on TG curve of OSPH. TG-DTA analyses showed that OSPH was found to be thermally stable and resistant to thermo-oxidative decomposition.

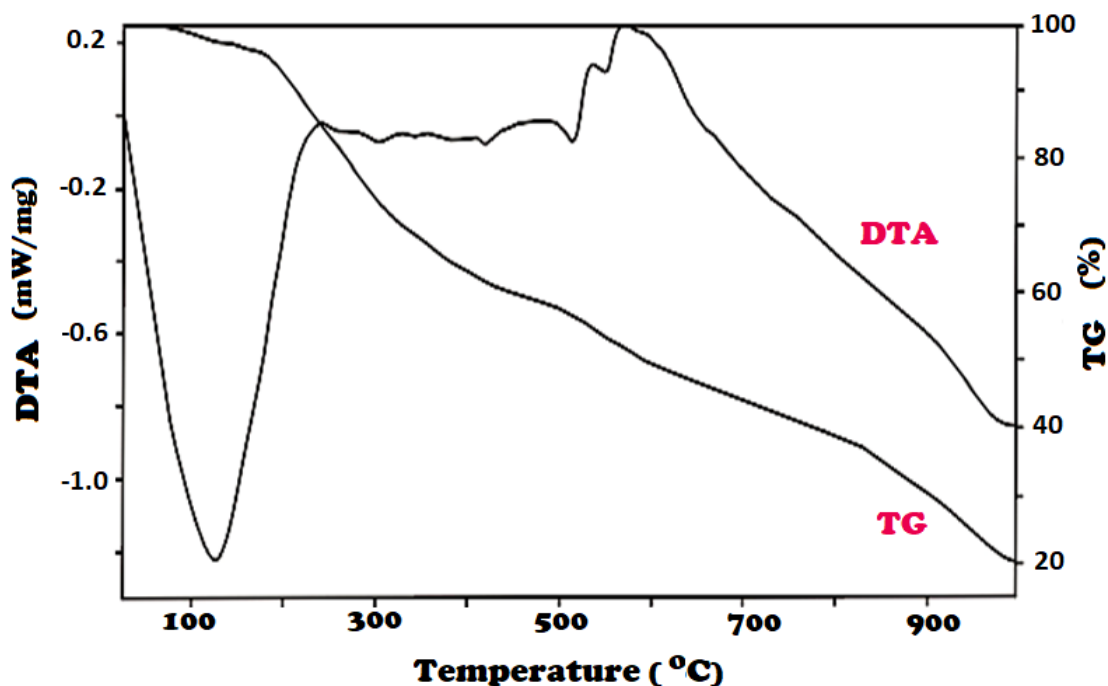


Figure 5. TG/DTA curves of oligo-N-Salicylidenehydrazone (OSPH).

CONCLUSIONS

In this study, the synthesized Schiff base (SPH) was transformed into oligo-N-salicylidenephenylhydrazone (OSPH) using air, H_2O_2 and NaOCl as oxidants in an aqueous alkaline medium. According to spectral analyses, the synthesized oligo-N-salicylidenephenylhydrazone oligomer was confirmed by bonding units through *ortho* and *para* carbons to hydroxyl group of N-salicylidenephenylhydrazone. M_n , M_w and PDI values of OSPH were found to be 1436 g mol⁻¹, 1631 g mol⁻¹ and 1.14; 850 g mol⁻¹, 1155 g mol⁻¹ and 1.36; 825 g mol⁻¹, 1660 g mol⁻¹ and 2.01, respectively, for NaOCl, air and H_2O_2 oxidants. Based on TG analysis OSPH in the aqueous alkaline medium with air oxidant, carbonaceous residue value of OSPH was found to be 7.44% at 1000 °C.

ACKNOWLEDGMENTS

The author thanks Prof. Dr. İsmet Kaya for his valuable comments on instrumental analyses results.

REFERENCES

1. Katon JE, editor. Organic Semiconducting Polymers. Marcel Dekker: New York, NY, USA, 1968.
2. El-Shekeil AG, Al-Yusufy FA, Saknidy S. Synthesis and characterization of some soluble conducting polyazomethine polymers. Polym. Int. 1997;44:78-82.
3. Diaz FR, Moreno J, Tagle LH, East GA. Radic, D. Synthesis, characterization and electrical properties of polyimines derived from selenophene. Synthetic Met. 1999;100:187-193.
4. Ragimov AV, Mamedov BA, Yasamova SY. New efficient dielectric and antistatic materials

based on oligoaminophenols. *Polymer* 1997;43:343-347.

5. Kaliyappan T, Kannan P. Co-ordination polymers. *Prog. Polymer Sci.* 2000;25:343-370.

6b Kaya İ, Demir HÖ, Vilayetoğlu AR. The synthesis and characterization of planar oligophenol with Schiff base substituent. *Synthetic Met.* 2002;126:183-191.

7. Kaya İ, Cihangiroğlu N. Synthesis, characterization and anti-microbial activity of oligo-N-2-aminopyridinylsalicylaldimine and some oligomer-metal complexes. *J. Poly. Res.* 2004;11:37-42.

8. Fakhari AR, Khorrami AR, Naeimi H. Synthesis and analytical application of a novel tetradentate N_2O_2 Schiff base as a chromogenic reagent for determination of nickel in some natural food samples. *Talanta* 2005;66:813-817.

9. Grigoras M, Catanescu CO. Imine oligomers and polymers. *J. Macromol. Sci-Pol R* 2004;C44:131-173.

10. Ayyagari MS, Marx KA, Tripathy SK, Akara JA, Kaplan DL. Controlled free-radical polymerization of phenol derivatives by enzyme-catalyzed reactions in organic solvents. *Macromolecules* 1995;28:5192-5197.

11. Kaya İ, Gökpınar M, Kamacı M. Reaction Conditions, Photophysical, Electrochemical, Conductivity, and Thermal Properties of Polyazomethines. *Macromol. Res.* 2017;25:739-748.



Syntheses and characterization of new dithiophosphinato zinc complexes

Ertuğrul Gazi Sağlam¹   and Nurcan Acar^{2*}  

¹ Department of Chemistry, Bozok University, 66900, Yozgat, Turkey,

² Department of Chemistry, Ankara University, 06100 Tandoğan, Ankara, Turkey

Abstract : Four known dithiophosphinic acids, DTPA, were synthesized and their zinc complexes were newly prepared. The complexes have been proven to have the structures $[\text{Zn}(\mu\text{-DTPA}^n)_2(\text{DTPA}^n)_2]$, ($[\text{DTPA}^n] = \text{R}^n(\text{R})\text{P}(\text{S})\text{H}$, $\text{R} = 4\text{-CH}_3\text{O-C}_6\text{H}_4\text{-}$; $\text{R}^1 = \textit{iso}$ -amyl-, DTPA^1 ; $\text{R}^2 = \textit{iso}$ -butyl-, DTPA^2 ; $\text{R}^3 = \textit{sec}$ -butyl-, DTPA^3 ; $\text{R}^4 = \textit{iso}$ -propyl-, DTPA^4). The DTPAs were prepared by the reaction of the Lawesson reagent, [2,4-bis(4-methoxyphenyl)-1,3,2,4-dithiodiphosphetane-2,4-disulfide] (LR), with the corresponding Grignard compounds. The acids formed are viscous liquids difficult to purify and so they were converted to ammonium salts, $[\text{DTPA}^n][\text{NH}_4]$, which are easy to obtain as pure crystals. The complexes were identified to have dimeric structures on the basis of mass spectroscopic data.

Keywords: Dithiophosphinic Acid, Dithiophosphinate, Phosphinodithioic Acid, Dithiophosphinato Zinc Complex, Lawesson's Reagent.

Submitted: May 25, 2018. **Accepted:** July 30, 2018

Cite this: Sağlam E, Acar N. Syntheses and characterization of new dithiophosphinato zinc complexes. JOTCSA. 2018;5(2):931-40.

DOI: <http://dx.doi.org/10.18596/jotcsa.427192>.

***Corresponding author. E-mail:** nurcanacar97@gmail.com

INTRODUCTION

Acidic organodithiophosphorus compounds like dithiophosphoric, dithiophosphonic and dithiophosphinic acids (Figure 1) and the coordination compounds thereof have some industrial interest because of their use as a

rubber vulcanizing agent (1,2), lubricating oil additives (3-5), metal flotation mediators (6-8), and pesticides (9-11). Potential uses as chemotherapeutic agents (12), clinical imaging aids (13) and antibiotic synergists are also investigated (14).

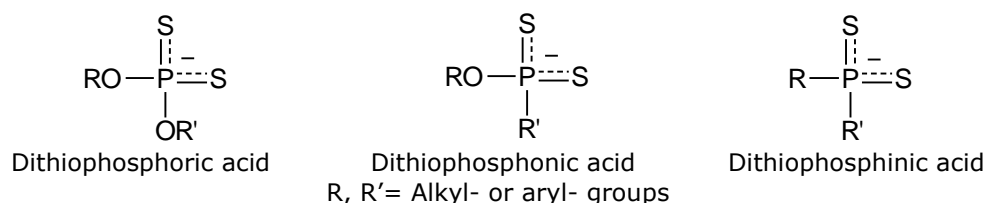


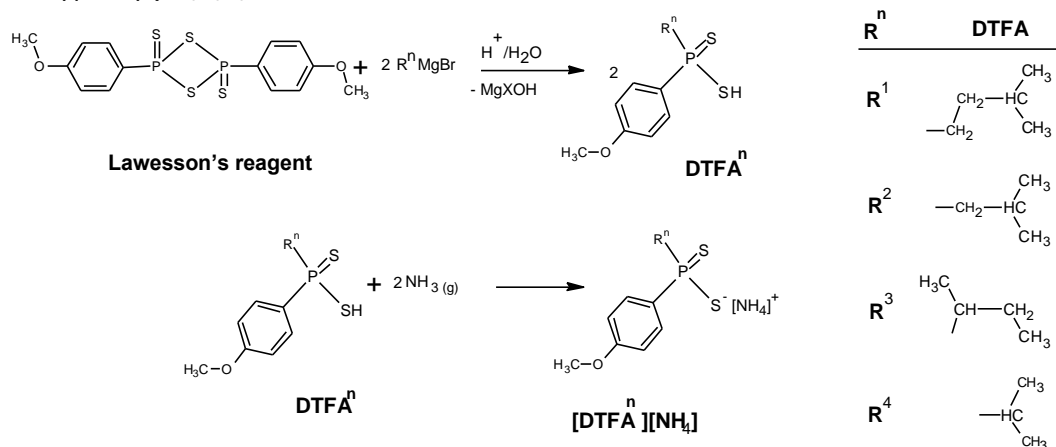
Figure 1. Different types of organodithiophosphorus compounds

DTPA metal complexes are mostly classified as four-coordination number. The nickel(II)-DTPA complexes are mono-nucleic and as a square-planar (15), on the other hand Zn(II)- or Cd(II)-DTPA complexes are shown to be four coordinated, dimeric structures (16,17). Here,

we present the preparation and characterization of the zinc complexes of four different dithiophosphinic acids, $[\text{DTPA}^n]$, 4-methoxyphenyl(3-methylbutyl) dithiophosphinic acid, $[\text{DTPA}^1]$; 4-methoxyphenyl(2-methylpropyl) dithiophosphinic acid, $[\text{DTPA}^2]$;

4-methoxyphenyl(1-methylpropyl) dithiophosphinic acid, [DTPA³]; 4-methoxyphenyl(1-methylpropyl) dithiophosphinic acid, [DTPA⁴]. The synthesis of the dithiophosphinato ligand was described elsewhere (18-20). As it is general for the related compounds the Lawesson reagent, 2,4-bis(4-methoxyphenyl)-1,3,2,4-

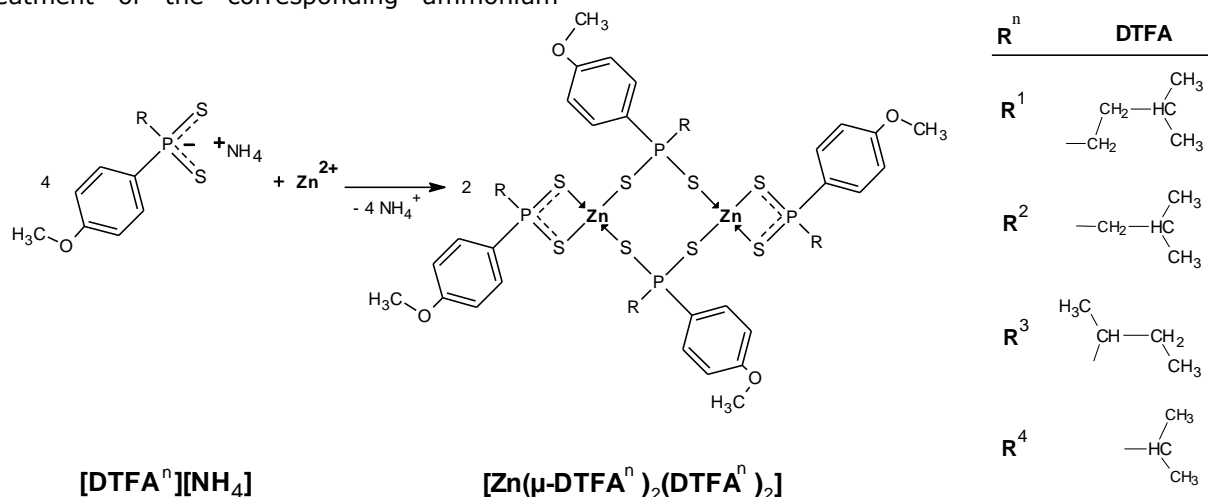
dithiadiphosphetane-2,4-disulfide (LR) was reacted with the appropriate Grignard reagent to obtain the corresponding dithiophosphinic acid and the product was neutralized with dry ammonia to yield a crystallizable ammonium salt for purification, [DTPAⁿ][NH₄]. The reactions and the products are summarized in Scheme 1.



Scheme 1. Synthesis of [DTPAⁿ] and [DTPAⁿ][NH₄].

Zinc complexes of the four dithiophosphinic acids described above were obtained by the treatment of the corresponding ammonium-

ligand salt with zinc(II)chloride in ethanolic medium, [Zn(μ-DTPAⁿ)₂(DTPAⁿ)₂], (Scheme 2).



Scheme 2. Synthesis of [Zn(μ-DTPAⁿ)₂(DTPAⁿ)₂].

EXPERIMENTAL

General

Analytical-grade LR, *iso*-amyl bromide, *iso*-butyl bromide, *sec*-butyl bromide and *iso*-propyl bromide were purchased from Merck and used directly without further purification. Benzene, chloroform, ethanol, diethyl ether and ZnCl₂ were purchased from Merck. Benzene and diethyl ether were distilled and dried before use. [DTPA¹][NH₄], [DTPA²][NH₄], [DTPA³][NH₄] and [DTPA⁴][NH₄] were prepared according to the literature (21).

The LC/MS system was supplied by Waters with a C-18 HPLC column and a Waters Micromass ZQ connected to an ESI ionizer. Melting point

determinations were performed on a Gallenkamp apparatus with a glass capillary. ¹H, proton-coupled ¹³C and ³¹P NMR spectra were recorded on a Varian Mercury (Agilent) 400 MHz FT spectrometer. CDCl₃ was the solvent of preferences for zinc complexes. Internal standards were SiMe₄ for the ¹H-, ¹³C-NMR and 85% H₃PO₄ for ³¹P-NMR. IR spectra were recorded on a Perkin Elmer Spectrum 400 FTIR instrument (200–4000 cm⁻¹) with wavenumbers in cm⁻¹ units. Elemental analyses were performed on a LECO CHNS-932 C instrument.

General procedure for the zinc complexes

To pure ethyl alcoholic solution of 2 mmol (0.04 g) of ZnCl₂ in a beaker (40-50 mL) were added 4 mmoles of the ligand of interest (0.34 g of

[DTFA¹][NH₄]; 0.31 g of [DTFA²][NH₄]; 0.31 g of [DTFA³][NH₄] and 0.28 g of [DTFA⁴][NH₄];). After mixing the cation with the ligand, the colorless complex was formed. Upon waiting for 2 days, fine crystals of the complex were formed at the bottom. These crystals were filtered and recrystallized from ethanol or chloroform.

Bis-{bis-[4-methoxyphenyl(3-methylbutyl)dithiophosphinato]zinc(II)} [Zn(μ-DTPA¹)₂(DTPA¹)₂]. Yield: 1.83 g, 74%. Colorless. M.P. 221-222°C. ¹H NMR (δ:ppm, CDCl₃): δ= 0.85 (dd, ³J_{HH}= 6.51 Hz, 24H, -CH-(CH₃)₂), 1.47 (m, 8H, -CH-), 1.55 (m, 4H, -CH₂-CH), 2.28 (m, 8H, -CH₂-CH₂), 3.84 (s, 12H, OCH₃), 6.95 (A-part of AA'MM'X, ⁴J_{PH}= 2.30 Hz (J_{AX}), N= 8.70 Hz, 8H, *m*-H), 7.86 M-part of AA'MM'X, ³J_{PH}= 13.36 Hz (J_{MX}), N= 8.70 Hz, 8H, *o*-H). ¹³C-NMR (CDCl₃): δ= 22.1 (s, -(CH₃)₂), 32.0 (d, ³J_{P-C}= 4.4 Hz, -CH-(CH₃)₂), 28.6 (d, ²J_{P-C}= 17.5 Hz, -CH₂-CH), 40.2 (d, ³J_{P-C}= 50.9 Hz, P-CH₂-), 55.4 (s, CH₃O-), 113.3 (d, ³J_{P-C}= 14.2 Hz, Ar-C_{meta}), 126.5 (d, ³J_{P-C}= 88.9 Hz, P-C_{arom}) 132.3 (d, ²J_{P-C}= 11.9 Hz, Ar-C_{ortho}), 162.1 (s, CH₃O-C). ³¹P-NMR (CdCl₃): δ= 68.1. LC/MS: *m/z* 647.3 ([M/2+CH₃CN]⁺, 100%), 1222.9 ([M]⁺, 4%), 883.3 ([M-DTPA¹]⁺, 4%), 614.3 ([M/2-H]⁺, 6%). Anal. Calcd. for C₄₈H₇₂Zn₂O₄P₄S₈ (1224.3 g.mol⁻¹): C, 47.1; H, 5.9; S, 21.0. Found: C, 47.2; H, 5.7; S, 20.8%.

Bis-{bis-[4-methoxyphenyl(2-methylpropyl)dithiophosphinato]zinc(II)} [Zn(μ-DTPA²)₂(DTPA²)₂]. Yield: 2.54 g, 85%. Colorless. M.P. 167-168°C. ¹H NMR (CDCl₃): δ= 0.88 (t, ³J_{HH}= 6.67 Hz, 24H, -CH₂-CH₃), 2.11 (m, 4H, -CH-CH₃), 2.28 (m, 8H, ²J_{PH}= 11.90 Hz, ³J_{PH}= 6.10 Hz P-CH₂), 3.84 (s, 12H, OCH₃), 6.92 (A-part of AA'MM'X, ⁴J_{PH}= 2.46 Hz (J_{AX}), N= 8.50 Hz, 8H, *m*-H), 7.91 M-part of AA'MM'X, ³J_{PH}= 13.44 Hz (J_{MX}), N= 8.50 Hz, 8H, *o*-H). ¹³C-NMR (CDCl₃): δ= 25.5 (d, ³J_{P-C}= 3.9 Hz, -(CH₃)₂), 24.3 (d, ²J_{P-C}= 10.0 Hz, -CH-(CH₃)₂), 42.9 (d, ³J_{P-C}= 51.4 Hz, P-CH₂-), 55.4 (s, CH₃O-), 113.7 (d, ³J_{P-C}= 14.1 Hz, Ar-C_{meta}), 127.8 (d, ³J_{P-C}= 80.3 Hz, P-C_{arom}) 132.6 (d, ²J_{P-C}= 13.1 Hz, Ar-C_{ortho}), 161.9 (d, ⁴J_{P-C}= 3.0 Hz, CH₃O-C). ³¹P-NMR (CDCl₃): δ= 60,7. LC/MS: *m/z* 1190.3 ([M+Na]⁺, 2%), 845.2 ([M-(Zn(DTPA²))]⁺, 4%), 619.3 ([M/2+CH₃CN]⁺, 92%), 607.2 ([M/2+Na]⁺, 35%). Anal. Calcd. for C₄₄H₆₄Zn₂O₄P₄S₈ (1168.2 g mol⁻¹): C,45.2; H, 5.5; S, 22.0. Found: C, 45.4; H, 5.5; S, 22.2%.

Bis-{bis-[4-methoxyphenyl(1-methylpropyl)dithiophosphinato]zinc(II)} [Zn(μ-DTPA³)₂(DTPA³)₂]. Yield: 2.33 g, 78%. Colorless. M.P. 187-188°C. ¹H NMR (CDCl₃): δ= 0.92 (t, ³J_{HH}= 7.30 Hz, 12H, -CH₂-CH₃), 1.98 (m, 8H, -CH₂-CH₃), 1.16 (m, -CH₃-CH- adjacent with -CH₃-CH-, 16H), 1.16 (dd, -CH₃-CH- ve -CH₃-CH- adjacent, ²J_{PH}= 21.94 Hz, ³J_{PH}= 6.86

Hz, 16H), 3.84 (s, 12H, OCH₃), 6.95 (A-part of AA'MM'X, ⁴J_{PH}= 2.32 Hz (J_{AX}), N= 8.80 Hz, 8H, *m*-H), 7.83 M-part of AA'MM'X, ³J_{PH}= 12.95 Hz (J_{MX}), N= 8.80 Hz, 4H, *o*-H). ¹³C-NMR (ppm, CDCl₃): δ =16.26 (d, ²J_{P-C}= 1.0 Hz, -(CH₃)₂), 38.19 (d, ³J_{P-C}= 49.6 Hz, P-CH-), 55.37 (s, CH₃O-), 113.6 (d, ³J_{P-C}= 13.9 Hz, Ar-C_{meta}), δ= 124.85 (d, ³J_{P-C}= 78.1 Hz, P-C_{arom}) 132.97 (d, ²J_{P-C}= 12.5 Hz, Ar-C_{ortho}), 162.05 (d, ⁴J_{P-C}= 2.8 Hz, CH₃O-C). ³¹P-NMR (ppm, CDCl₃): δ = 82.9. LC/MS: *m/z* 1191.1 ([M+Na]⁺, 31.2 %); 909.1 ([M-(Zn(DTPA³))]⁺, 89.0 %); 583.2 ([M/2-H]⁺, 78,5 %). Anal. Calcd. for C₄₄H₆₄Zn₂O₄P₄S₈ (1168.2 g mol⁻¹): C,45.2; H, 5.5; S, 22.0. Found: C, 45.6; H, 5.8; S, 22.6%.

Bis-{bis-[4-methoxyphenyl(2-propyl)dithiophosphinato]zinc(II)} [Zn(μ-DTFA⁴)₂(DTFA⁴)₂]. Yield: 2.00 g (81 %). Colorless. M.P. 209-210°C. ¹H NMR (CDCl₃): δ =1.16 (dd, ³J_{PH}= 21.5 Hz, ³J_{HH}= 6.9 Hz, 12H, -CH-(CH₃)₂), 2.3 (m, 4H, -CH-), 3.84 (s, 6H, OCH₃), 6.94 (A-part of AA'MM'X, ⁴J_{PH}= 2.35 Hz (J_{AX}), N= 8.80 Hz, 4H, *m*-H), 7.83 M-part of AA'MM'X, ³J_{PH}= 12.95 Hz (J_{MX}), N= 8.80 Hz, 4H, *o*-H). ¹³C-NMR (ppm, CDCl₃): δ =16.26 (d, ²J_{P-C}= 1.0 Hz, -(CH₃)₂), 38.19 (d, ³J_{P-C}= 49.6 Hz, P-CH-), 55.37 (s, CH₃O-), 113.6 (d, ³J_{P-C}= 13.9 Hz, Ar-C_{meta}), δ= 124.85 (d, ³J_{P-C}= 78.1 Hz, P-C_{arom}) 132.97 (d, ²J_{P-C}= 12.5 Hz, Ar-C_{ortho}), 162.05 (d, ⁴J_{P-C}= 2.8 Hz, CH₃O-C). ³¹P-NMR (ppm, CDCl₃): δ = 82.9. LC/MS: *m/z* 1133.8 ([M+Na]⁺, 31.2 %); 864.9 ([M-(Zn(DTFA⁴))]⁺, 100.0 %); 576.9 ([M/2]⁺+Na]⁺, 78,5 %); 308.8 ([Zn(DTFA⁴)⁺, 12,3 %). Anal. Calcd. for C₄₀H₅₆Zn₂O₄P₄S₈ (1112.1 g mol⁻¹): C,43.2; H, 5.1; S, 23.1. Found: C, 43.2; H, 4.9; S, 23.3%.

RESULT AND DISCUSSION

The data relating to the percent yields, physical appearance, and elemental analyses of the complexes as well as IR-, mass- and NMR (¹H-, ¹³C-, ³¹P-) spectra are given in the section "Experimental". The major spectroscopic features are as follows:

IR Spectra

The prominent IR bands of the complexes, [Zn(μ-DTPA¹)₂(DTPA¹)₂], [Zn(μ-DTPA²)₂(DTPA²)₂], [Zn(μ-DTPA³)₂(DTPA³)₂] and [Zn(μ-DTPA⁴)₂(DTFA⁴)₂], are summarized in Table 1. The asymmetrical and symmetrical PS stretching vibrations, *v*_{asym} and *v*_{sym}, show up in the ranges 610–588 cm⁻¹ and 492–549 cm⁻¹, respectively. The bands in the range 282–311 cm⁻¹ were assigned to Zn-S stretching bands, *v*_{Zn-S}. These values agree well with those reported in the literature for analogous compounds (22-24).

Table 1: Selected FTIR (R) data (cm⁻¹) assignment of significant bands for [Zn(μ-DTPAⁿ)₂(DTPAⁿ)₂]

Compounds	v _{Zn-S}	v _{asym (PS)}	v _{sym (PS)}
	IR	IR	IR
[Zn(μ-DTFA ¹) ₂ (DTFA ¹) ₂]	308	610;599	518;534
[Zn(μ-DTFA ²) ₂ (DTFA ²) ₂]	282	589	517;542
[Zn(μ-DTFA ³) ₂ (DTFA ³) ₂]	297	588	492
[Zn(μ-DTFA ⁴) ₂ (DTFA ⁴) ₂]	311	611	523; 550

Mass Spectra

The mass signals of the complexes reflect the isotopical multitudes of zinc and sulfur. Some of the mass peaks indicate the attachment of an CH₃CN or a Na⁺ cation to the species responsible for the signal. CH₃CN or Na⁺ ions are likely to be originated from the buffer solution used in the ionization chamber and similar cases were reported in the literature (25). The disintegration pattern of the complexes are also comparable to the literature data reported for analogous structures (26-29). Molecular peaks corresponding to the dimeric structures of the complexes are discernable for all the compounds, but [Zn(μ-DTPA¹)₂(DTPA¹)₂]. The complexes display Mass-peaks corresponding to the mono-nuclear [Zn(DTPAⁿ)₂] moieties. In the Mass spectrum of all the [Zn(μ-DTPAⁿ)₂(DTPAⁿ)₂] complexes display peaks indicating removal of a DTPAⁿ leaving back a sort of the formula [Zn₂(DTPAⁿ)₃].

¹H-NMR Spectra

¹H-NMR data are summarized in Table 2. For all the structures investigated the four anisole-ring protons and the phosphorus atom constitute an AA'MM'X system. The AA'MM' part display practically an AMX pattern (30). This is obviously because J_{AM'} and J_{A'M} are virtually zero. The aromatic protons were assigned on the basis of the magnitudes of the coupling constants to phosphorus. In all the compounds, the protons in *ortho*- position to phosphorus display a ³J_{PH} of ~13 Hz and those *meta*- to phosphorus a ⁴J_{PH} of ~2.3 Hz.

The peak area integrals of all the signals confirm the assignments of the peaks. Chemical shift and coupling data are in compliance with the literature (31,32).

¹³C-NMR Spectra

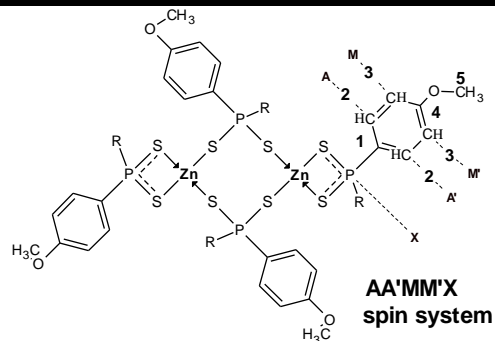
¹³C-NMR data are given in Table 3. The contact ³¹P-¹³C coupling of the *ipso*- carbons varies between 76.3 Hz and 88.8 Hz whereas the one-bond coupling for the aliphatic carbons, C6, lies in the range 48.1 Hz-51.4 Hz. The δ and J values are in agreement with those given in the literature (33-35).

³¹P-NMR Spectra

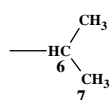
Proton-decoupled ³¹P-NMR signals of the compounds, [Zn(μ-DTPA¹)₂(DTPA¹)₂], [Zn(μ-DTPA²)₂(DTPA²)₂], [Zn(μ-DTPA³)₂(DTPA³)₂] and [Zn(μ-DTPA⁴)₂(DTPA⁴)₂], appear at 68.1, 60.1, 79.4 and 82.9 ppm, respectively. The fact that each compound displays only one singlet indicate that the phosphorus atoms are in an equivalent environment within the molecule except for [Zn(μ-DTPA²)₂(DTPA²)₂]. These data comply with those reported in the literature (31).

CONCLUSION

In this work four new dithiophosphinato zinc complexes were synthesized and characterized. The characteristic ν_{N-H} stretching bands of the ligands appear at ~3000-3100 cm⁻¹ on IR (18-20). These bands disappear on the IR spectra of the complexes proving the substitution of the ammonium group by metal cations. All the complexes are of dimeric structures. The one-bond ¹³C-³¹P coupling constants for the aromatic *ipso*- carbons were found to be 30-40 Hz greater than that of the aliphatic carbons (76.3-88.8 Hz and 48.1-51.4 Hz, respectively). Due to the equivalent chemical environment of the phosphorus in the complexes except for [Zn(μ-DTPA²)₂(DTPA²)₂], a single peak appeared in the ³¹P-NMR spectrum. The structures of the complexes were elucidated on the basis of elemental analysis as well as mas-, FTIR- and NMR- spectra.

Table 2: ¹H NMR spectral data of complexes.

[Zn(μ-DTFA¹)₂(DTFA¹)₂] R¹= <i>iso</i>-amyl-	AA'MM'X spin system, (N = J_{AM} + J_{AM'})		-OCH₃	-C6-H	-C7-H	-C8-H	-C9-H
	δ = 7.86 (dd, 8H) ³ J _{P-H} = 13.36, (J _{MX}) N = 8.70	δ = 6.95 (dd, 8H) ⁴ J _{P-H} = 2.30, (J _{AX}) N = 8.70	δ = 3.84 (s, 12H)	δ = 2.28 (m, 8H)	δ = 1.55 (m, 8H)	δ = 1.47 (m, 4H)	δ = 0.85 (d, 24H) ³ J _{HH} = 6.51
[Zn(μ-DTFA²)₂(DTFA²)₂] R²= <i>iso</i>-butyl-	δ = 7.91 (dd, 8H) ³ J _{P-H} = 13.44, (J _{MX}) N = 8.50	δ = 6.92 (dd 8H) ⁴ J _{P-H} = 2.46, (J _{AX}) N = 8.50	δ = 3.84 (s, 12H)	δ = 2.28 (dd, 8H) ² J _{P-H} = 11.90 ³ J _{HH} = 6.10	δ = 2.11 (m, 24H)	δ = 0.88 (d, 24H) ³ J _{HH} = 6.67	-
[Zn(μ-DTFA³)₂(DTFA³)₂] R³= <i>sec</i>-butyl-	δ = 7.83 (dd, 8H) ³ J _{P-H} = 12.94, (J _{MX}) N = 8.80	δ = 6.92 (dd 8H) ⁴ J _{P-H} = 2.32, (J _{AX}) N = 8.80	δ = 3.84 (s, 12H)	δ = 1.16 (dd, C6-H and C7-H adjacent, 16H) ² J _{P-H} = 21.94 ³ J _{HH} = 6.86	δ = 1.16 (m, C6-H and C7-H adjacent, 16H)	δ = 1.98 (m, 8H)	δ = 0.92 (t, 12H) ³ J _{HH} = 7.30
[Zn(μ-DTFA⁴)₂(DTFA⁴)₂] R⁴= <i>iso</i>-propyl-							



$\delta = 7.83$, (dd, 8H)
 $^3J_{P-H} = 12.95$, (J_{MX})
 $N = 8.80$

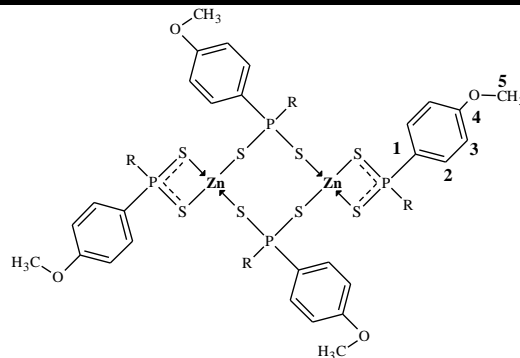
$\delta = 6.94$
 (dd 8H)
 $^4J_{P-H} = 2.35$,
 (J_{AX})
 $N = 8.80$

$\delta = 3.84$
 (s, 12H)

$\delta = 2.28$
 (m, 4H)

$\delta = 1.16$
 (dd 12H)
 $^3J_{P-H} = 21.5$
 $^3J_{HH} = 6.9$

Table 3: ^{13}C -NMR spectral data of complexes.



	-C4	Ar-C _{ortho}	-C1	Ar-C _{meta}	-OCH ₃	-C6	-C7	-C8	-C9
[Zn(μ-DTFA¹)₂(DTFA¹)₂]	R¹ = iso-amyl- $\delta = 162.1$ (s) $^4J_{P-C} = 11.9$	$\delta = 132.3$ (d) $^2J_{P-C} = 11.9$	$\delta = 126.5$ (d) $J_{P-C} = 88.9$	$\delta = 113.3$ (d) $^3J_{P-C} = 14.2$	$\delta = 55.4$ (s)	$\delta = 40.2$ (d) $J_{P-C} = 50.9$	$\delta = 28.6$ (d) $^2J_{P-C} = 17.5$	$\delta = 32.0$ (d) $^3J_{P-C} = 4.4$	$\delta = 22.1$ (s)
[Zn(μ-DTFA²)₂(DTFA²)₂]	R² = iso-butyl- $\delta = 161.9$ (d) $^4J_{P-C} = 3.0$	$\delta = 132.6$ (d) $^2J_{P-C} = 13.1$	$\delta = 127.8$ (d) $J_{P-C} = 80.3$	$\delta = 113.7$ (d) $^3J_{P-C} = 14.1$	$\delta = 55.4$ (s)	$\delta = 42.9$ (d) $J_{P-C} = 51.4$	$\delta = 24.3$ (d) $^2J_{P-C} = 10.0$	$\delta = 25.5$ (d) $^3J_{P-C} = 3.9$	-
[Zn(μ-DTFA³)₂(DTFA³)₂]	R³ = sec-butyl- $\delta = 162.0$ (d) $^4J_{P-C} = 2.9$	$\delta = 132.9$ (d) $^2J_{P-C} = 12.1$	$\delta = 125.1$ (d) $J_{P-C} = 76.3$	$\delta = 113.6$ (d) $^3J_{P-C} = 13.9$	$\delta = 55.4$ (s)	$\delta = 45.6$ (d) $J_{P-C} = 48.1$	$\delta = 12.4$ (d) $^2J_{P-C} = 16.8$	$\delta = 22.8$ (s)	$\delta = 12.4$ (s)
[Zn(μ-DTFA⁴)₂(DTFA⁴)₂]	R⁴ = iso-propyl- $\delta = 162.1$ (d) $^4J_{P-C} = 2.8$	$\delta = 133.0$ (d) $^2J_{P-C} = 12.5$	$\delta = 125.9$ (d) $J_{P-C} = 78.1$	$\delta = 113.6$ (d) $^3J_{P-C} = 13.9$	$\delta = 55.4$ (s)	$\delta = 38.9$ (d) $J_{P-C} = 49.6$	$\delta = 16.3$ (d) $^2J_{P-C} = 1.0$	-	-

Chemical shifts (δ) are reported in ppm. J values are reported in Hz. s: singlet; d: doublet; t: triplet; dd: doublet of doublets; m: multiplet.

ACKNOWLEDGEMENTS

We gratefully acknowledge the financial assistance of Project Coordination Application and Research Center of Bozok University (Project No: 2013 BAP FEF/A049).

REFERENCES

1. Mc.Cleverty J A, Rick S Z, Kowalski N, Bailey A, Mulvaney R, O'Cleirigh D A. Aspects of the Inorganic Chemistry of Rubber Vulcanisation. Part 4.1 Dialkyl- and Diaryl-dithiophosphate and -dithiophosphinate Complexes of Zinc: Phosphorus-31 Nuclear Magnetic Resonance Spectral Studies and Structures of $[\text{NMe}_4][\text{Zn}\{\text{S}_2\text{P}(\text{OC}_6\text{H}_4\text{Me-p})_2\}_3]$ and $[\text{Et}_4][\text{Zn}(\text{S}_2\text{PPh}_2)_3]$. *J. Chem. Soc. Dalton Trans.* 1983; 627-34. DOI 10.1039/DT9830000627.
2. Satake Y, Kashiwadata K, Iizuka Y, Kouyama T, Katto T, Shiiki Z. Poly(arylene thioether-ketone) compositions improved in both melt stability and crystallinity. 1989; may 2; US 4,826,906.
3. Pradip K G, Deba P P, Neeiotpal S. Di(2-methyl- 5-chlorophenyl) dithiophosphinate and its copper(II) derivative as antioxidant lubricating oil additive. *Indian J. Chem. Technol.* 1995; 2(1): 46-8. <http://nopr.niscair.res.in/handle/123456789/31090>.
4. Ziyatdinova G K, Budnikov G K, Samigullin A I, Gabdullina G T, Sofronov A V, Al'metkina, L. A., Nizamov, I. S., Cherkasov, R. A.: Electrochemical determination of synthetic antioxidants of bisdithiophosphonic acids. *J. Anal. Chem.* 2010; 65: 1273-1279. DOI: 10.1134/S1061934810120129.
5. Yagishita K, Konishi S. Lubricating oil additive and lubricating oil composition. 2013; US 8,481,467.
6. Grigorieva N A, Pashkov G L, Fleitlikh I Yu, Nikiforova L K, Pleshkov M A. Nickel extraction from sulfate media with Cyanex 301 in the presence of electron donor additives. *Hydrometallurgy* 2010; 105: 82-8. DOI 10.1016/hydromet.2010.08.001.
7. Xihong H, Guoxin T, Jing C, Linfeng R, Characterization of the extracted complexes of trivalent lanthanides with purified cyanex 301 in comparison with trivalent actinide complexes. *Dalton Trans.* 2014; 43: 17352-17357. DOI:10.1039/C4DT02553A.
8. Jing C, Meng W, Xuegang L, Jianchen W. Back-end of nuclear fuel cycle in China. *Progr. in Nucl. Energy*, 2012; 54: 46-8, DOI:10.1016/j.pnucene.2011.09.003
9. Artem'ev A V, Malysheva S F, Gusarova N K, Belogorlova N A, Fedorov S V, Timokhin B V, Smirnov V I, Trofimov B A. Novel Quinine, Lupinine, And Anabasine Derivatives Containing Dithiophosphinate Groups. *Chem. Heterocycl. Compd.* 2012 Jun; 48(3): 448-52. DOI:10.1007/s10593-012-1013-3.
10. Michalski J, Potrzebowski M, Lopusinski A. Preparation of S-brom-dithiophosphoric, dithiophosphonic and dithiophosphinic acid derivatives, 1984; US 4,470,933.
11. Kabra V, Mitharwal S, Singh S. Synthesis and Insecticidal Activity of Novel Dithiophosphonates. Phosphorus, Sulfur Silicon Relat. Elem. 2009;184: 2431-42. DOI: 10.1080/10426500802487748
12. Bara A C, Silvestru C, Haiduc I. Antitumor organometallics. I. Activity of some diphenyltin(IV) and diphenylantimony(III) derivatives on in vitro and in vivo Ehrlich ascites tumor. *Anticancer Res.* 11, 1651-1656, 1991.
13. Bellande E, Comazzi V, Laine J, Lecayon M, Pasqualini R, Duatti A, Hoffschir D, Synthesis and Biodistribution of Nitrido Technetium-99m Radiopharmaceuticals with Dithiophosphinate Ligands: a Class of Brain Imaging Agents. *Nucl. Med. and Biol.* 1995; 22(3):315-20. DOI: 10.1016/0969-8051(94)00107-U.
14. Durckheimer W, Bormann D, Ehlers E, Schrinner E, Heymes R. Cephem Derivates. 1988; US 4758556.
15. Yordanov, N D, Gochev G, Angelova O, Macicek J. EPR Investigations on bis(dithiophosphinato)copper(II) complexes magnetically diluted in the corresponding nickel(II) single crystals and X-ray crystal structure of bis(di-n-propyldithiophosphinato)nickel(II). *Polyhedron* 1990; 9: 2597-2602. [https://doi.org/10.1016/S0277-5387\(00\)86834-5](https://doi.org/10.1016/S0277-5387(00)86834-5).
16. Byrom C, Malik M A, O'Brien P, White A J P, Williams D J. Synthesis and X-ray single crystal structures of bis(diisobutyldithiophosphinato)cadmium(II) or zinc(II): Potential single-source precursors for II/VI materials. *Polyhedron*, 2000; 19: 211-15. [https://doi.org/10.1016/S0277-5387\(99\)00352-6](https://doi.org/10.1016/S0277-5387(99)00352-6).
17. Calligaris M, Nardin G, Ripamonti A. Crystal and Molecular Structure of Zinc(II) and Cobalt(II) Diethyldithiophosphinates, J.

Chem. Soc. A, 714-22, 1970. DOI: 10.1039/J19700000714.

18. Sağlam E G, Çelik Ö, Yılmaz H, İde S. Synthesis, spectroscopic characterization and X-ray single crystal structures of *trans*-Bis [4-methoxyphenyl (3-methylbutyl) dithiophosphinato]nickel(II) and Bis[4-methoxyphenyl(3-methylbutyl)dithiophosphinato]cobalt(II) complexes. *Transition Met. Chem.* 2010; 35: 399-405. DOI:10.1007/s11243-010-9341-6.

19. Sağlam E G, Yılmaz H, Dal H, Hökelek T, Synthesis and Spectroscopic Characterizations of Novel Ni(II) and Co(II) Dithiophosphinate Complexes, and X-Ray Studies on the Ni(II) Complex Phosphorus, Sulfur Silicon Relat. Elem. 2012; (2)187: 213-24. DOI: 10.1080/10426507.2011.601239.

20. Hoffmann H, Schumacher G, Umsetzungen mit p-methoxyphenyl-dithiophosphonsäure-anhydrid, *Tetrahedron Lett.* 1967; 31:2963-6. DOI:10.1016/50040-4039(00)90895-5.

21. Diemert K, Kuchen W. "Zur Kenntnis der Organophosphorverbindungen XVII, Dithiophosphinsäuren RR'P(S)SH, Ihre Synthese, Derivate und Metallkomplexe", Phosphorus, Sulfur Silicon Relat. Elem. 1977; (2): 131-6. DOI: 10.1080/03086647708077702.

22. Casas J S, García-Tasende M S, Sánchez A, Sordo J, Castellano E E, Zukerman-Schpector J. Synthesis, crystal structure and spectroscopic properties of bis (diphenyldithiophosphinato)cadmium(II). *Inorg. Chim. Acta* 1994; 219: 115-9. DOI:10.1016/0020-1693(94)03822-8.

23. Sunder S, Hanlan L, Bernstein J. Resonance Raman Spectra of Metal Complexes of Substituted Dithiophosphinic Acids., *J. Inorg. Chem.* 1975;14: 2012-3, DOI: 10.1021/ic50150a058.

24. Czernuszewicz R, Maslowsky E, Jr Nakamoto K, Infrared and Raman Spectra of Bis(imidotetraphenyldithiodiphosphino-S,S') Complexes with Cu(II), Co(II) and Fe(II), *Inorg. Chim. Acta*, 1980; 40: 199-202. DOI: 10.1016/S0020-1693(00)92004-8.

25. Chakravarty M, Pailloux S, Ouizem S, Smith K A, Duesler E N, Paine R T, Williams N J, Hancock R D. Synthesis and metal coordination chemistry of (phenyl)(pyridin-2-ylmethyl)phosphinodithioic acid, [2-C₅H₄N]CH₂P(S)(SH)(Ph). 2012; 33: 327-35. DOI:10.1016/j.poly.2011.11.041.

26. Keck H, Kuchen W. Massenspektrometrische Untersuchungen An Organophosphorverbindungen IV. Über den massenspektrometrischen Zerfall von Dithiophosphinsäuren, Phosphorus, Sulfur Silicon Relat. Elem., 1983; 14: 225-8. DOI:10.1080/03086648308075944.

27. Heinz S, Keck H, Kuchen W. Mass spectrometric studies of dithiophosphinato metal complexes. *Org. Mass Spectrom.* 1984; 19: 82-6. DOI:10.1002/oms.120190207.

28. Christoph D, Keck H, Kuchen W, Mathow J, Wunderlich H. Synthesis, properties and structure of bis(dialkyldithiophosphinato)manganese(II) complexes. *Inorg. Chim. Acta* 1987; 132: 213-5. DOI:10.1016/S0020-1693(00)81744-2.

29. Mohan P N, Keck H, Kuchen W, Haegele G. Metal complexes of phosphinic acids—XII: Praseodymium(III), neodymium(III) and europium(III) complexes of dimethyldithiophosphinic acid. *J. Inorg. & Nuclear Chem.* 1977; 39: 833-5. DOI:10.1016/0022-1902(77)80164-4.

30. Sağlam E G, Nurcan A, Berline M-S, Hakan D, Tuncer H. Syntheses and Structural Characterizations of a New Benzyl(4-Methoxyphenyl)Dithiophosphinic Acid and Its Ni(II), Co(II), Zn(II), Cd(II) and Ni-Pyridino Complexes. Phosphorus, Sulfur Silicon Relat. Elem. 2016; 191(1): 22-9. DOI:10.1080/10426507.2015.1067206.

31. Karakuş M, Yılmaz H, Bulak E, Lonneck, P. Bis{μ-[O-cyclopentyl(4-methoxyphenyl) dithiophosphonato]1κ: S,2κ: S-[O-cyclopentyl (4-methoxyphenyl) dithiophosphonato] 1κ2S,S } dizinc (II). *Appl. Organometal. Chem.* 2005; 19: 396-7. DOI:10.1002/aoc.850.

32. Karakuş M, Yılmaz H, Özcan Y, S İde. Appl. Crystallographic report: Bis{μ-[O-cyclopentyl (4-methoxyphenyl) dithiophosphonato] 1κ:S,2κ: S-[O-cyclopentyl(4-methoxyphenyl) dithiophosphonato]-1κ2S,S'}dicadmium(II). *Organometal. Chem.* 2004; 18: 141-142. DOI: 10.1002/aoc.588.

33. Ramirez R G, Toscano R A, Silverstu C, Haiduc I. Studies on inorganic tin diphenyldithiophosphinates. Crystal and molecular structure of CIS-dichlorobis(diphenyldithiophosphinato)tin(IV). *Polyhedron* 1996; 15(21): 3857-67. DOI:10.1016/0277-5387(96)00100-3.

34. Karakuş M, Yılmaz H. Synthesis and Characterization of Ni(II), Zn(II), and Cd(II) Complexes with Dithiophosphonate Derivatives. Rus. J. Coord Chem 2006; 32(6): 437-43. DOI: 10.1134/S1070328406060078.

35. Przychodzen W. New Products of Reaction of Lawesson's Reagent With Diols. Phosphorus, Sulfur Silicon Relat. Elem. 2004; 179: 1621-33. DOI:10.1080/10426500490466175.



Nicotinamide-Modified poly(HEMA-GMA)-Nic Cryogels for Removal of Pesticides

Kazım Köse¹, Gönül Arslan Akveran¹, Kadir Erol², Dursun Ali Köse³

¹Hitit University, Alaca Avni Çelik Vocational School, Department of Food Processing, Alaca, TURKEY

²Hitit University, Osmançık Derindere Vocational School, Department of Property Protection and Safety, Osmançık, TURKEY

³Hitit University, Faculty of Science and Arts, Department Chemistry, Çorum, TURKEY

Abstract: Chlordane is only one of the persistent pesticides used in some countries despite the ban. Removal of chlordane, a severe threat to all living things, was performed using nicotinamide-modified poly(2-hydroxyethyl methacrylate-glycidyl methacrylate), poly(HEMA-GMA)-Nic, polymeric cryogels in this study. Poly(HEMA-GMA) polymeric cryogels were synthesized based on previously reported literature procedures and were subsequently modified by nicotinamide moieties. Removal of chlordane in alcoholic medium has been accomplished exploiting the alcho-phobic interaction, which was the first indication in our previous study. Structural analysis of poly(HEMA-GMA)-Nic was performed using Fourier transform infrared spectroscopy (FT-IR) and elemental analysis methods. Scanning electron microscopy (SEM) was used to understand the surface morphology of cryogels. Surface area and cavity volume calculations were determined by applying N₂ adsorption method and swelling test. The interaction time and maximum adsorption capacity were identified as 5 minutes and 64.61 mg chlordane/g cryogel for 300 mg/L chlordane concentration and 108.818 mg chlordane/g cryogel for 800 mg/L chlordane concentration during the adsorption experiments. Cyclohexane, toluene, chloroform, dichloromethane, acetone, and acetonitrile were used as solvents to observe the solvent effect on adsorption of chlordane onto the polymeric material. As expected, the removal of chlordane was performed with the highest adsorption performance in cyclohexane with the lowest dielectric constant.

Keywords: Chlordane, Pesticide, Alcho-phobic, Cryogel, Nicotinamide.

Submitted: February 14, 2018. **Accepted:** August 02, 2018.

Cite this: Köse K, Arslan Akveran G, Erol K, Köse D. Nicotinamide-Modified poly(HEMA-GMA)-Nic Cryogels for Removal of Pesticides. JOTCSA. 2018;5(2):941-52.

DOI: <http://dx.doi.org/10.18596/jotcsa.394592>.

***Corresponding author. E-mail:** kazimkose@hitit.edu.tr.

INTRODUCTION

The technical chlordane, which is a mixture of approximately 150 different chemicals, mainly contains three chlordane compounds, cis-chlordane (CC), trans-chlordane (TC), and trans-nonachlor (1, 2). Chlordane was at the forefront of 12 prohibited pesticides in the UNER Stockholm Convention, which was signed on persistent organic pollutants in 2001 (3). As a broad-spectrum pesticide used against insects and pests in many vegetable and fruit cultures, chlordane, which has been used for many years in the United

States of America (after the 1940s) and Japan (1980s), is almost insoluble in water, like other pesticides (4-7). Chlordane, which is considered to be one of the most harmful members of pesticides, is profoundly harmful to health, and a severe endocrine disruptor (8-11). Results of exposure to low doses of chlordane may be the symptoms such as a headache, vomiting, loss of consciousness while exposure to high doses can result in death (12, 13). Also, it has been revealed that chlordane is linked to diabetes in the recent researches (14).

Monitoring, removal and degradation studies have been performed up to date to deal with the persistent organic pollutants resistant to degradation (7, 15-23). These methods have disadvantages such as the need for experienced users, harmful chemicals, long-term experimental procedure. Therefore, it is necessary to find new ways to be able to remove unwanted compounds in a short process efficiently.

Polymeric cryogels have been used extensively in many studies over the last 20 years and continue to be used due to the advantages such as easy synthesis, adequate performance, and low cost (24-27). In particular, the micro- and macroporous structure of cryogels overcome the disadvantages in conventional techniques. The primary downside of cryogels over micro- and nano-adsorbents is that they seem to have a low surface area, but they also eliminate many problems coming from these adsorbents such as agglomeration, low yield, and the need for high-performance devices such as centrifuges (28-32). Polymeric cryogels have interconnected flow-channels providing the diffusion of the target molecule to the cavities of the cryogels, therefore, this provides a healthy interaction between the ligands on the surface of cryogels and the target molecules residing on the cavities for a while (33).

We have applied the modification of a polymeric structure used in affinity techniques. Nicotinamide was added as a ligand to the poly (HEMA-GMA) polymeric structure, which was previously used in some studies (34). As an adsorbent, poly (HEMA-GMA) polymeric cryogels have been modified using nicotinamide. The modification of poly(HEMA-GMA) with nicotinamide is quite rare in the literature. Ethanol was used instead of water as a solvent. The main reason for using ethanol is that chlordane does not dissolve in water as mentioned before. Also, various organic solvents were also used to measure the chlordane adsorption performance of the synthesized polymeric material in different solutions.

MATERIALS AND METHODS

Materials

2-Hydroxyethyl methacrylate (HEMA), ethylene glycol di-methacrylate (EGDMA), glycidyl methacrylate (GMA), nicotinamide (Nic), ammonium persulfate (APS), sodium dodecyl sulfate (SDS) and N,N,N',N'-tetramethyl ethylenediamine (TEMED) and chlordane

(C₁₀H₆Cl₈, analytical standard, PN: 442449) were obtained from Sigma-Aldrich (St. Louis, MO, USA). All experiments were conducted using freshly prepared deionized (DI, (18 MΩ.cm)) water.

Synthesis and Characterization

The mixture of GMA (500 µL), HEMA (5000 µL) and distilled water (6500 µL) was prepared as the monomer phase. The dispersing phase was prepared using 1 g of sodium lauryl sulfate (SLS), 25.60 mL of distilled water, and 2.4 mL of EGDMA. The two phases were then mixed. They were kept in ice cubes for 10-15 minutes. 20 mg of APS and 100 µL of TEMED were added to start the polymerization. The polymerization mixture was poured in between two glass plates to have a polymeric plate. The polymeric mixture in between the glass plates was kept at -20 °C for 24 hours. At the end of this period, the glass plates were removed, and the polymeric plate was cut in the shape of a disk. The polymeric cryogel discs were washed with distilled water many times to remove unwanted chemicals. All cryogel disks were kept at +4 °C until use.

Some cryogel membranes (20 cryogel discs) were mixed with 1 M NaOH (10 mL) for 2 hours. Membranes washed several times with distilled water were incubated with 50 mg/mL nicotinamide solution (10 mL) for 24 hours. The aim of this process is to provide oxygen bonding of the epoxy groups of the GMA monomer of the amine groups in the nicotinamide molecules. Proof of Nic decoration can be observed by the color change from white to yellow.

For structural characterization of poly(HEMA-GMA)-Nic cryogels, Fourier transform infrared spectroscopy (FT-IR, Nicolet™ is™10 FTIR spectrometer, USA) and elemental analysis (CHNS-932, Leco, USA) methods were used. Surface morphology of the polymeric structure was observed in the course of the physical characterization. For this purpose, a scanning electron microscope (SEM, Carl Zeiss AG - EVO® 50 Series, Germany) was used. Also, surface area estimation of the cryogels was crucial for the successful interaction process. Surface area calculations were performed using the BET equations using the AUTOSORPI 6B (Quantachrome Instruments, USA) N₂-adsorption method. At last, swelling test, the water holding capacity of the polymeric material, was calculated using Equation 1 given below. The water holding capacity is informative about analyte diffusion.

$$\text{Water uptake \%} = \left[\frac{W_{\text{swollen}} - W_{\text{dry}}}{W_{\text{dry}}} \right] \quad (\text{Eq. 1})$$

W_{swollen} : weight in grams of water-retained
 W_{dry} : weight in grams of dry cryogels.

The polymeric material that will serve as solid support has been given functional properties by adding nicotinamide to the synthesized

poly(HEMA-GMA) polymeric structure. The target molecule contains six chlorine atoms and therefore acts as a Lewis base. The need for the adsorbent to be a suitable Lewis acid will be met by the nitrogen molecule around the nicotinamide and the unpaired electrons on the nitrogen atom.

Thus, a substantial electrostatic interaction will take place, and the removal will be successful, as the Lewis acid-base interaction and consequently the dipole-dipole electrostatic interaction between the positively charged amine groups and the polymer-dependent amino acids and chlorine atoms in the chlordane structure. If no nicotinamide were added, the electron cloud on the GMA would push the electron cloud around the chlordane, and there would be no interaction. The quantitative adsorption performance of

poly(HEMA-GMA)-Nic polymeric cryogels was measured using a UV-Visible spectrophotometer (OPTIZEN POP UV/Vis, Mecasys Co., Ltd., Korea).

Adsorption Studies

To determine the amount of adsorbed chlordane on the polymeric material spectroscopically, the wavelength at which chlordane has the highest absorbance was scanned. The highest absorbance of chlordane was observed at 216 cm^{-1} (Figure 1). This result is consistent with the literature (35).

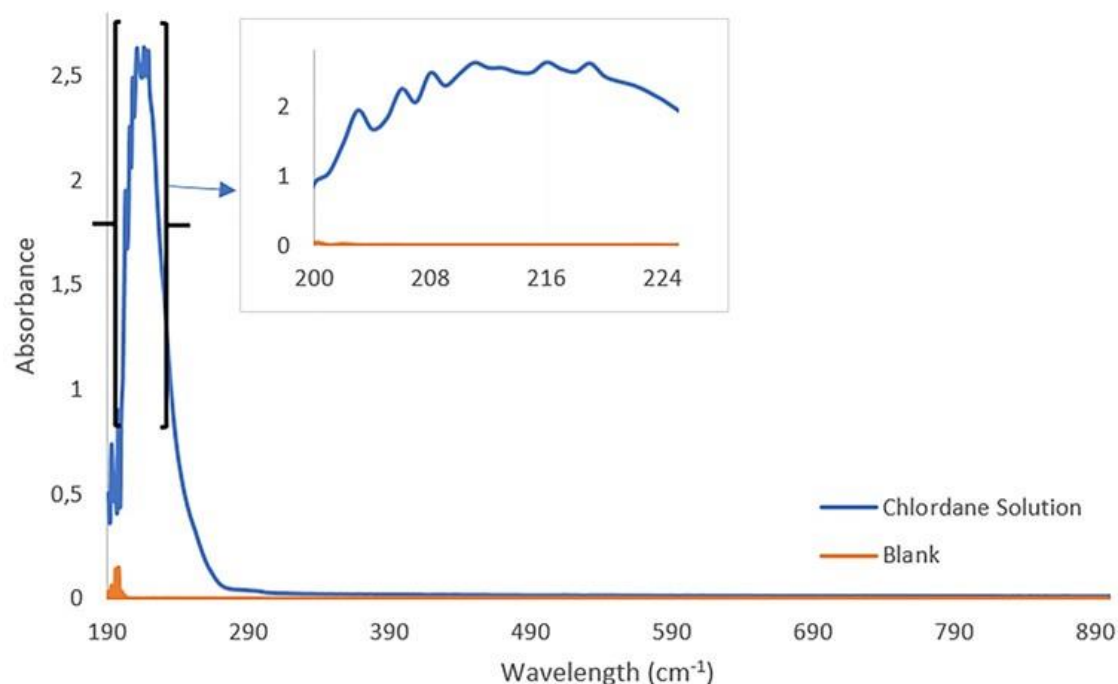


Figure 1. Maximum wavelength survey taken from the UV spectrum.

Adsorption experiments were carried out using 2 mL of chlordane (taken from 500 ppm stock solution)/8 mL of ethanol (98% v/v) in closed test tubes since the solvent is a volatile chemical. Chlordane (2 mL) was added to ethanol and homogenized for 15 minutes to ensure physical equilibrium. The disk-shaped cryogels, which were introduced to the adsorption solution, were then interacted with the chlordane during the optimum period determined by preliminary

experiments. The amount of chlordane adsorbed on the polymeric cryogels was calculated using Equation 2. Chloride solutions with concentrations ranging from 200-1000 mg/L were used to determine the chlordane saturation concentration capacities of the synthesized polymeric cryogels. All solutions were prepared using stock solutions of 500 and 1000 mg of chlordane/L ethanol.

$$q = \frac{(C_i - C_f) \times V}{m} \quad (\text{Eq. 2})$$

q : adsorption capacity in mg/g,

C_i : amount of chlordane before adsorption in mg/L

C_f : amount of chlordane after adsorption in mg/L

V : volume of the adsorption medium in mL

m : absorbance in g.

RESULTS and DISCUSSION

Characterization

The synthetic procedure of the poly (HEMA-GMA)-Nic polymeric cryogels used as adsorbents in this study is shown in Figure 2. As can be seen from the figure, the oxirane ring on the glycidyl methacrylate is opened when the nicotinamide is

attached. A bond was formed in between oxirane ring and amide end of nicotinamide. According to the FT-IR results, the peaks in the region of 1200-1700 cm^{-1} originating from the nitrogen atom on the nicotinamide are the most prominent indicators that nicotinamide is involved in the structure (Figure 3A). The characteristic poly (HEMA-GMA) peaks given by green circles are the peaks at 343.11 (-OH from HEMA), 1733.44 (-C=O from HEMA), 1247.75 and 903.35 cm^{-1} (36, 37). C-H, C = O, N-H, C = N, C-NH₂, C-N stretching and C-N-C bending peaks of the nicotinamide indicated by red circles were observed at 2931.48, 1680.46, 1571.55, 1274.24, 1160.56 and 520.69 cm^{-1} , respectively

(38). As a conclusion, 18.10^{-4} mole of nicotinamide has been successfully incorporated into the poly(HEMA-GMA) polymeric structure.

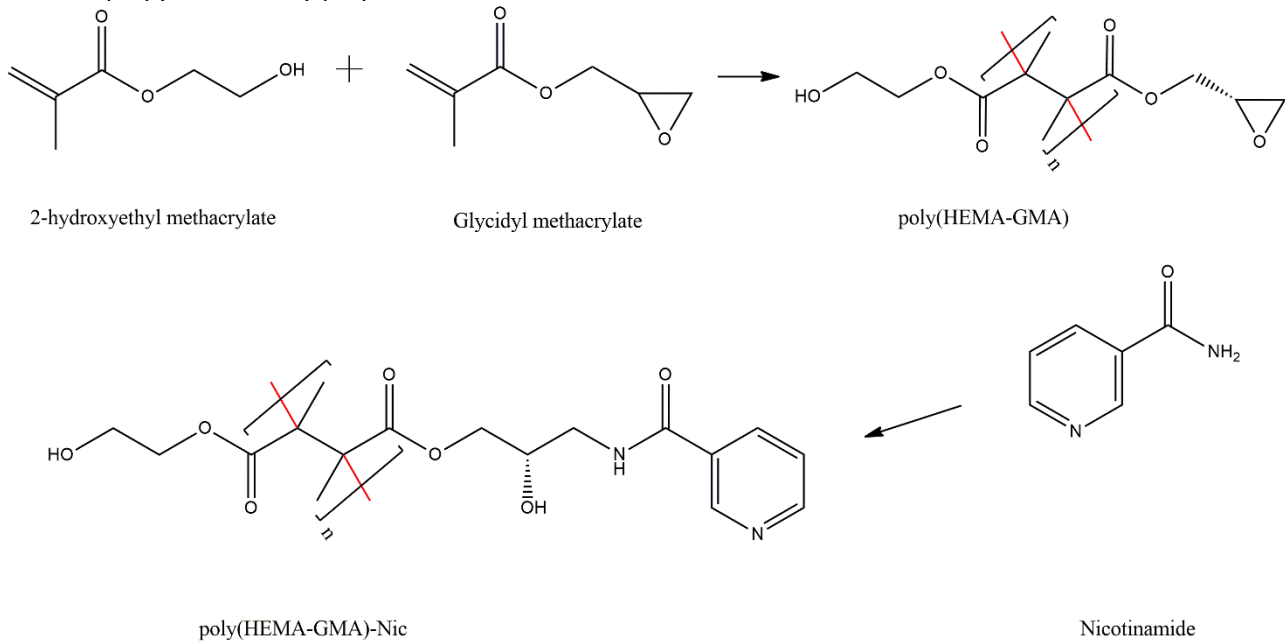


Figure 2. Schematic diagram of Poly(HEMA-GMA)-Nic polymeric cryogels.

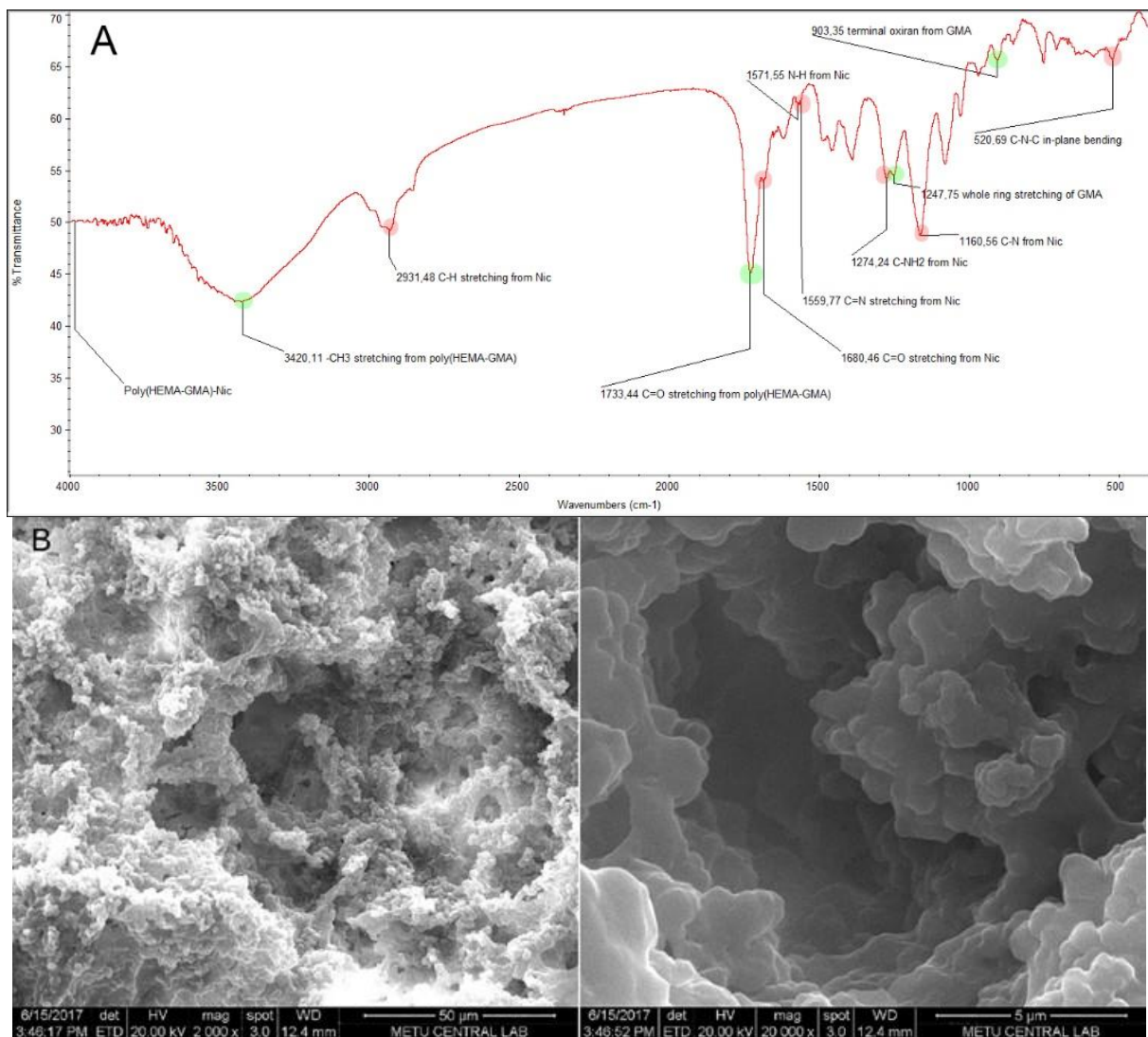


Figure 3. A) FT-IR spectrum and **B)** SEM images of poly(HEMA-GMA)-Nic polymeric cryogels

As can be seen from Figure 3B, the synthesized cryogels have cavities that allow the analyte to diffuse readily. The presence of holes in the porous structure, having a water retention capacity of about ~800%, although having a surface area of ~8.5 m²/g less than microparticles or nanoparticles (28-32, 39), provides the necessary retention time for the analyte to interact with ligand within polymeric structure. Ability to swallow high amount of analytes and the cavities connected with interconnected flow channels are the critical

properties of cryogels providing them to be indispensable absorbents.

To increase the strength of electrostatic attraction, the addition of iron cation with oxidation number 2 caused changes in the morphological structure of polymeric cryogels, such as the disappearance of the cavities and the appearance of needle-like structures (Figure 4). It is thought that the degradation of the surface morphology affects the adsorption kinetics in the negative direction.

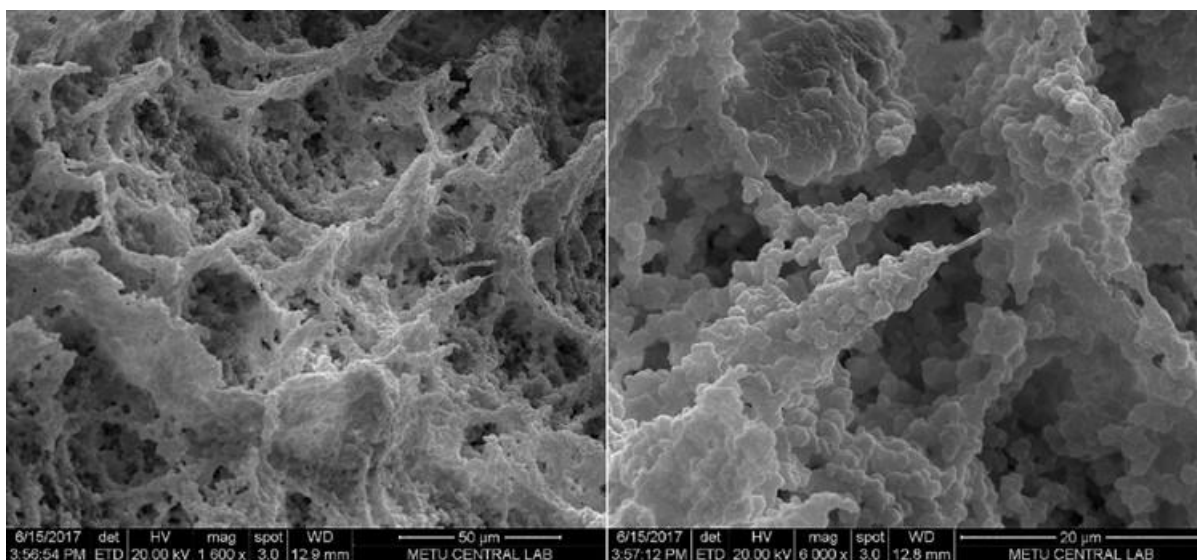


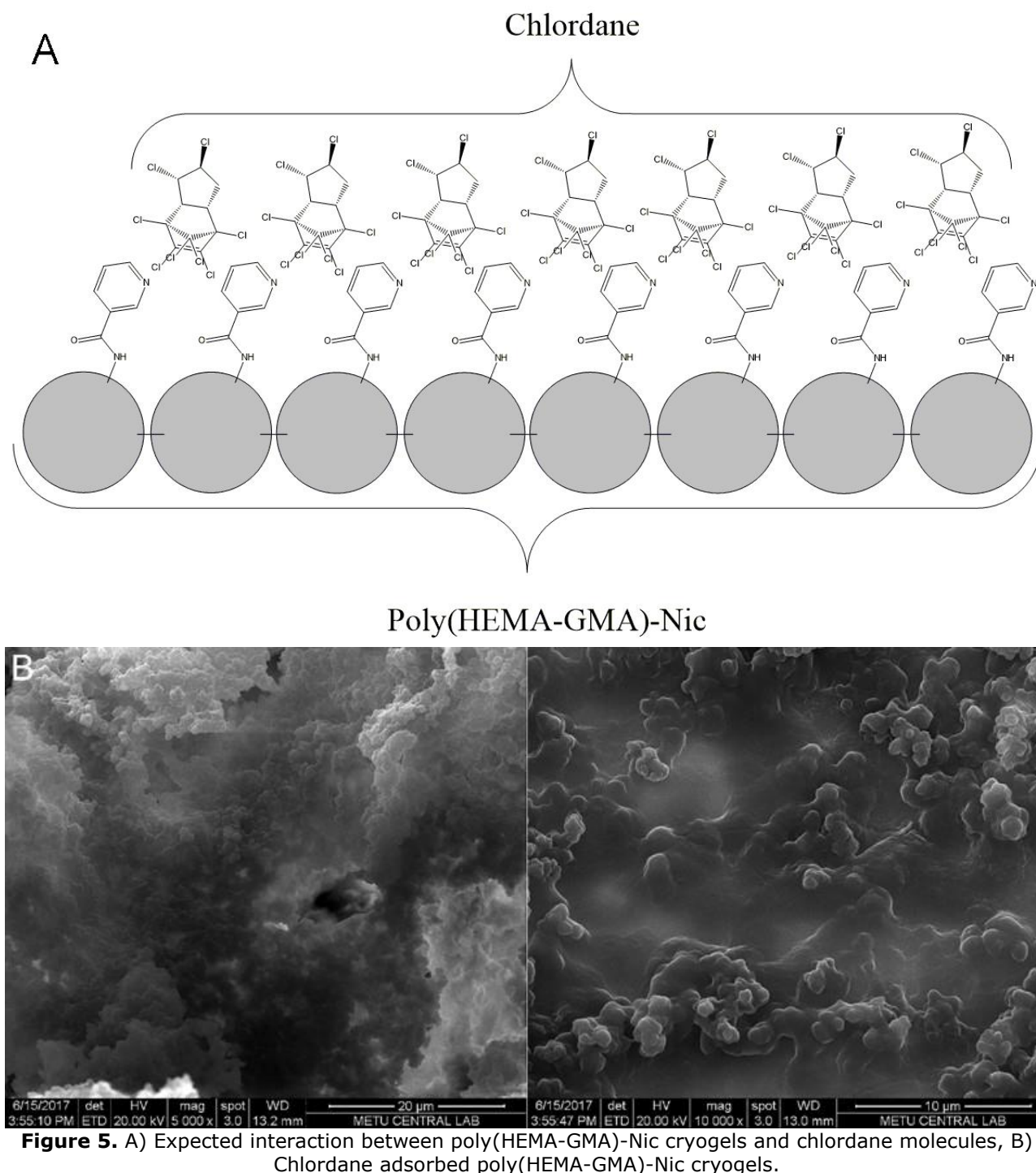
Figure 4. SEM images of Fe²⁺-decorated polymeric cryogels

Adsorption Studies

Since the chlordane is not soluble in water, all experiments were carried out in ethanol (98% v/v) (40). The eight chlorine atoms around the chlordane form a dense electron cloud around the molecule. Therefore, the adsorbent expected to interact with chlordane should have binding sites with positive charges. However, the structure of poly(HEMA-GMA) shows that the electron density is high in the periphery of GMA. To overcome this obstacle, decoration of nicotinamide to the polymeric structure will provide a positive charge, and thus it will act as a Lewis base. Nicotinamide is attached to the polymeric material from the -NH₂ end (Figure 2). Due to the resonance stability of the pyridine ring, the N atom within the ring is partially positively charged. Also, the unpaired electron on the nitrogen atom of the pyridine ring will also contribute to the electrostatic interaction by allowing the molecule to behave like a Lewis base. Fe²⁺ ions were added to the structure to increase the electrostatic attraction force of the structure. However, low adsorption was observed on the contrary to expectation (41). In their work, Köse and Köse, added Ni²⁺, Cu²⁺ and Co²⁺ ions to the structure to increase electrostatic force, but they have observed a decrease in the adsorption of the pesticides to the polymeric adsorbent (42). As a result, poly(HEMA-GMA)-Nic without Fe²⁺ was used in all experiments. The electron cloud around the chlordane molecule causes electrostatic attraction because of the existence

of eight chlorine atoms to create the desired interaction with the Nic molecule linked to the ligand of the polymeric material. The pK_a value of the nicotinamide molecule is 3.35 (43). Thus the partially positively charged N atom and the stable pyridine ring because of resonance phenomenon meet this requirement in the adsorption environment with neutral pH value. However, the carbonyl structure found in the nicotinamide molecule repels the -OH moieties and thus the partially positively charged N-atom in the pyridine ring does the -CH₂-CH₃ moieties of the ethanol molecules. In the same way, chlordane will cause ethanol to move away due to its massive structure, dense electron cloud, and its 3-dimensional structure. The ethanol will be withdrawn from between interacting groups, the alcohol-phobic interaction, resulting in a substantial electrostatic interaction between chlordane and poly(HEMA-GMA)@Nic polymeric cryogels (40) (Figure 5A). The adsorption of chlordane on the surface of cryogels can be seen clearly in Figure 5B, the surface morphology of poly(HEMA-GMA)-Nic cryogels was changed. In the meantime, decorating the Nic molecules causes an increase in the route of the electrons traveling on around of the Nic molecule itself. Therefore, the time for the presence of the partially positive charge clouds on the Nic was increased. Thus, the interaction between Nic and the chlordane will be stronger. It is significantly important that because the ethanol does not have

ionization ability, it meets the requirement as a solvent for an ideal electrostatic interaction.

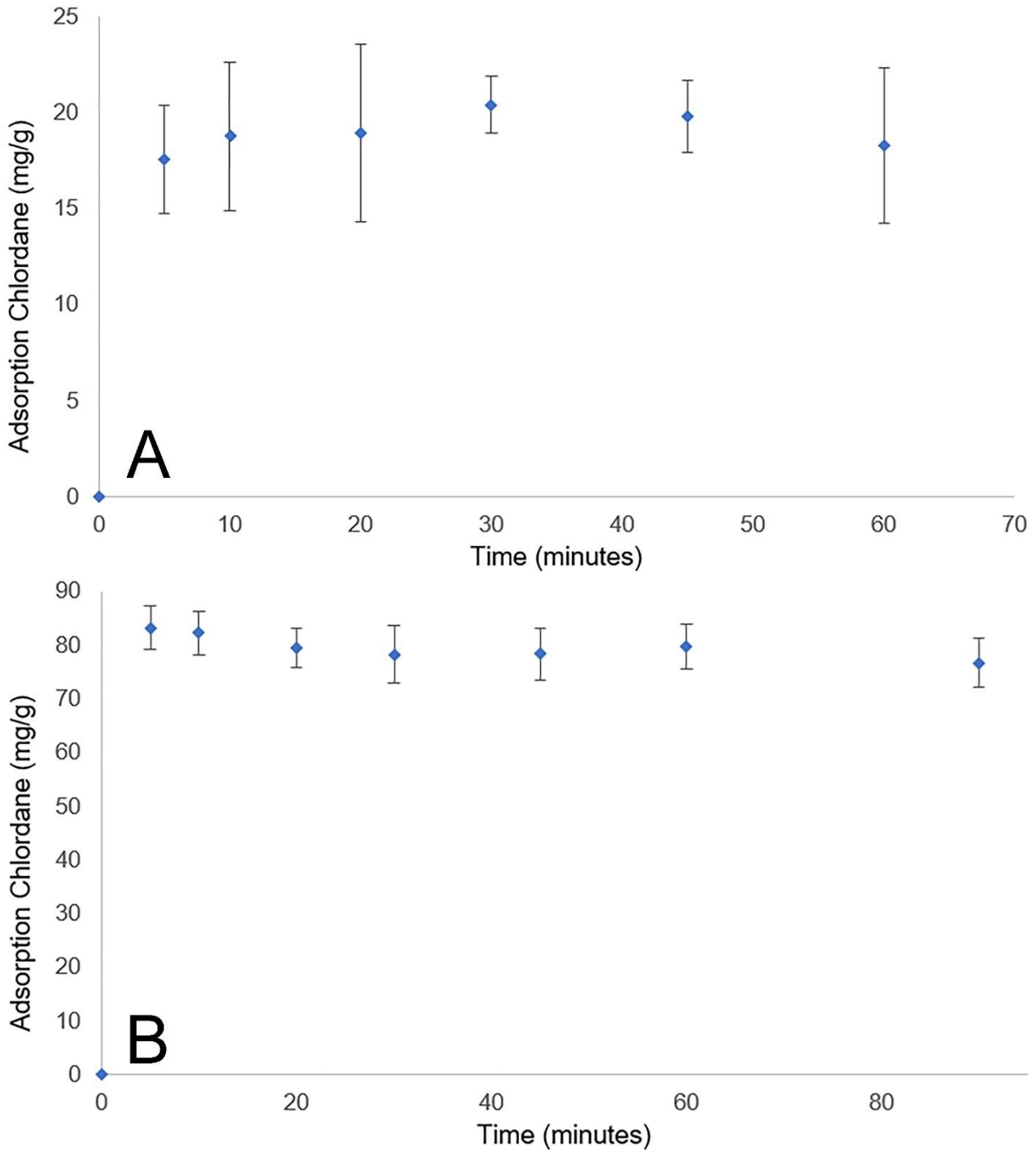


As can be seen from Figure 6, the chlordane adsorption performance of poly(HEMA-GMA)-Nic cryogels was investigated at varying time intervals for different chlordane concentrations. Moreover, the effect of initial chlordane concentration on the adsorption performance of the polymeric material was determined. All experiments were repeated three times, and standard deviations were calculated. Adsorption experiments were carried out at concentrations of 100, 200 and 300 mg chlordane/ethanol to determine the effect of concentration on the optimum adsorption time. As expected, the

increased concentration of chlordane increased the amount of adsorption but no significant change in the time of interaction was observed. The interaction was completed within the first 5 minutes (Figure 6a-b-c). A plateau was observed in all plots after five minutes, which is attributed to the fact that all binding sites of the polymeric cryogels were saturated by the chlordane. Likewise, Figure 6d shows how the increased chlordane initial concentration affects the adsorption performance of polymeric cryogels. As can be seen, adsorption process increased up to 800 mg chlordane/L ethanol concentration, after

which a plateau was observed in the graph. This value is critical regarding the adsorption amount of 108.818 mg of chlordane/L ethanol for a short period of 5 minutes for each same-sized cryogel disk. This value achieved by the removal of chlordane is quite comparable to similar studies in the literature (17, 44, 45). At the same time,

as mentioned above, all of the binding sites of a cryogel disk were engaged with the target molecules, chlordane. It can be concluded that the poly(HEMA-GMA)-Nic cryogels can be a good candidate for every concentration of pesticides, i.e., very low and very high amount of pesticide.



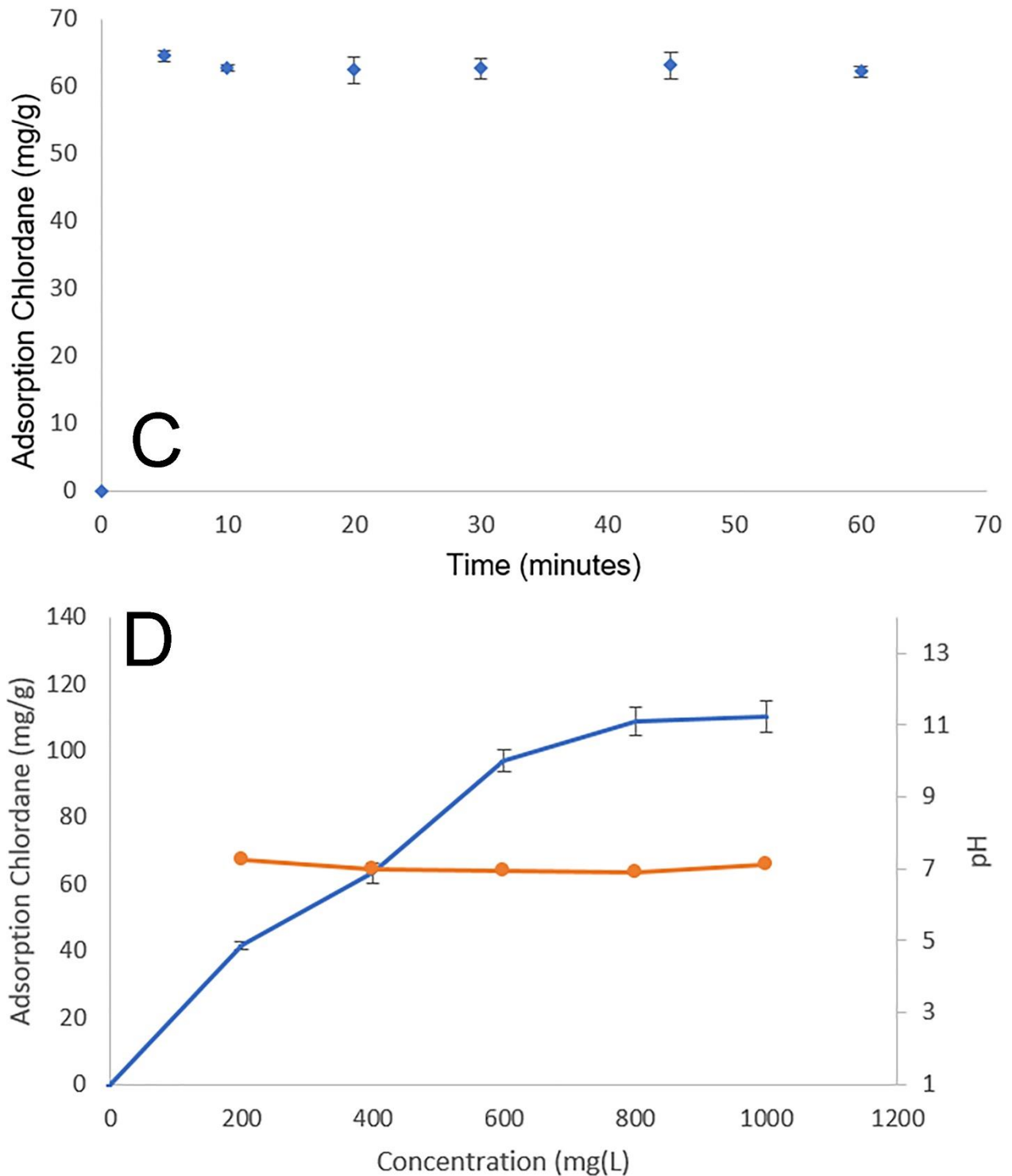


Figure 6. Parameters for chlordane adsorption process: A) $t_{\text{interaction}}$; $C_{\text{chlordane}}$: 100 mg/L, pH: 7.0 (ethanol medium), T: 25°C, B) $t_{\text{interaction}}$; $C_{\text{chlordane}}$: 200 mg/L, pH: 7.0 (ethanol medium), T: 25°C, C) $t_{\text{interaction}}$; $C_{\text{chlordane}}$: 300 mg/L, pH: 7.0 (ethanol medium), T: 25°C, D) $C_{i,\text{chlordane}}$; pH: 7.0 (ethanol medium), $t_{\text{Adsorption}}$: 10 min, T: 25°C.

Like other pesticides, chlordane is highly soluble in organic solvents (46, 47). The adsorption performances in the solutions containing chlordane molecules and solvents such as cyclohexane, toluene, chloroform, dichloromethane, acetone and acetonitrile solvents were compared with that in ethanol to observe how the chemical structures of the solvents affected the interaction between the

polymeric cryogels and the chlordane in this study (Figure 7). Since the dielectric coefficients of organic solvents mentioned are different (48), the solubility of chlordane and therefore the electrostatic interaction in between will be different. At the end of the adsorption experiments, a correlation was observed between the dielectric coefficients and the adsorption performance. The solvent with a relatively high

dielectric constant will separate the opposing charges better which is the primary requirement for stronger electrostatic interaction. Therefore, electron cloud formation will occur smoothly and so thus proton clustering (49). As seen in Figure 7, the solubility of the chlordane in cyclohexane and hence its adsorption on the polymeric material is the highest. All works were performed in ethanol although the performances in other organic solvents were higher than that in ethanol.

The most important reasons for this are the toxicity (50) and cost of these organic solvents. Moreover, polymeric materials have been gone deformation during adsorption in acetone and acetonitrile. Therefore, it is more feasible to use the least harmful chemical in the adsorption process. Also, studies performed in ethanol have been carried out, and very positive results have been obtained in the literature (40).

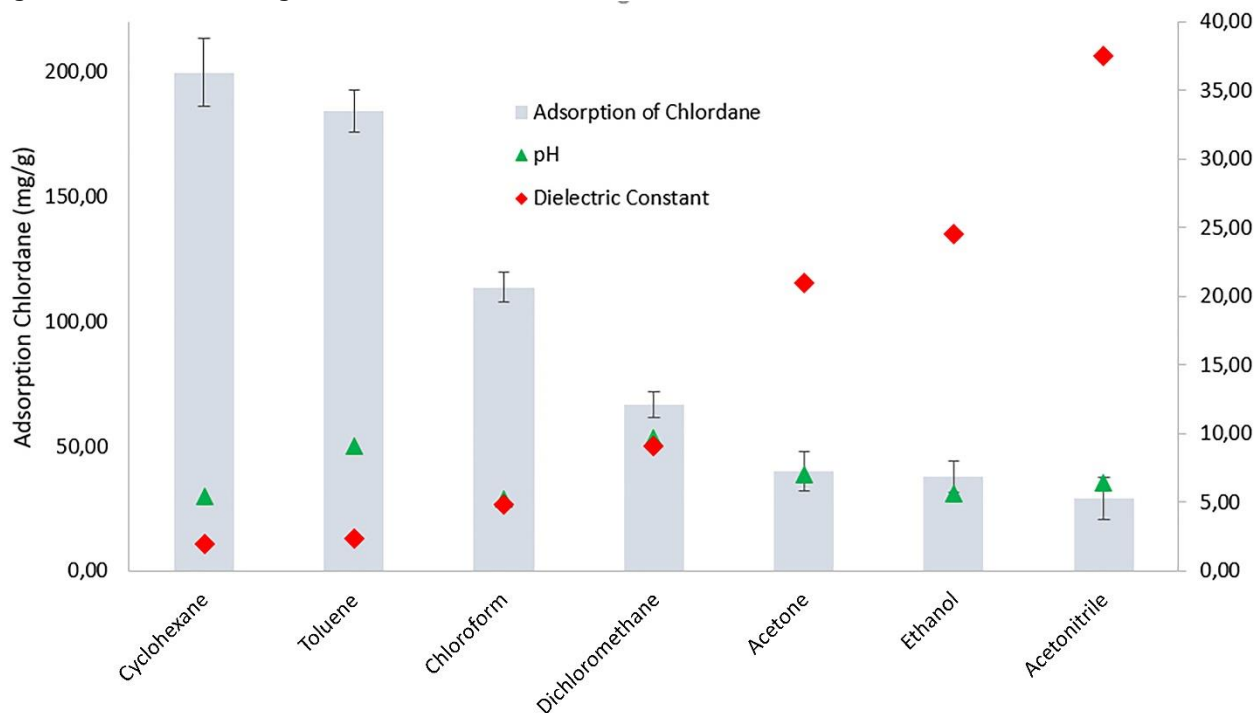


Figure 7. Solvent effect on the chlordane adsorption.

Mathematical calculations performed to characterize the interaction between the polymeric material and chlordane indicate that the adsorption is chemically controlled and homogeneous. The chemical character of the interaction is determined by pseudo-first and -second-order kinetic models and results are given in Table 1. As can be seen, the correlation coefficient (R^2) obtained with the pseudo-second-order kinetic model is very close to unity. Moreover, the theoretically calculated adsorption amount of chlordane is almost similar to that obtained experimentally. The polymeric cryogels acted virtually like a chemical adhesive throughout the adsorption.

The degree of homogeneity and non-specific interactions are determined by Langmuir and Freundlich adsorption isotherm calculations. According to the values given in Table 2, the correlation constant obtained for the Langmuir adsorption model is closer to 1 than the value obtained in the Freundlich model calculations. Furthermore, the fact that the b value is close to 0 and the experimental and theoretical Q values are nearly the same indicates that the interaction in this study is more appropriate for the Langmuir adsorption model. The interaction was homogeneous in a single layer and resulted in no interaction between neighboring regions.

Table 1. Chemical kinetic parameters for the chlordane-poly(HEMA-GMA)-Nic interaction.

Chemical Kin.		Pseudo-First Order			Pseudo-Second Order		
In. Conc. (mg/L)	Q _{exp.} (mg/g)	Q _{calc.} (mg/g)	k ₁ (1/min.)	R ²	Q _{calc.} (mg/g)	k ₂ (g/mg.min)	R ²
100	20.41	2.89	-0.35	0.9467	20.33	0.06	0.9986
200	46.82	0.71	0.04	0.6670	43.48	0.05	0.9999
300	64.61	1.45	0.00	0.0570	62.89	0.63	0.9999

Table 2. Adsorption isotherm parameters for the chlordane-poly(HEMA-GMA)-Nic interaction.

Adsorption Isotherms	Langmuir Adsorption Isotherm				Freundlich Adsorption Isotherm		
Equations	$\frac{1}{Q_{eq}} = \left[\frac{1}{Q_{max} \cdot b} \right] \left[\frac{1}{C_{eq}} \right] + \left[\frac{1}{Q_{max}} \right]$				$\ln Q_{eq} = \ln K_F + \frac{1}{n} \ln C_{eq}$		
Linear Equation	$y = 1.1208x + 0.0066$				$y = 0.4961x + 1.7118$		
Cryogel / Parameters	Q _{exp}	Q _{max} (mg/g)	b (L/mg)	R ²	K _F	1/n	R ²
Poly(HEMA-GMA)-Nic	110.19	151,51	0,0058	0.9946	5,5389	2,0157	0.9714

CONCLUSION

In this study, the previously synthesized poly(HEMA-GMA) polymeric material was modified with Nic, and chlordane removal performance in ethanol was investigated. As a first step of the study, poly(HEMA-GMA) polymeric material was synthesized and modified with nicotinamide monomer.

Successful Nic-decoration on the poly(HEMA-GMA) cryogels was confirmed with the presence of bending and stretching of N containing bonds in the FT-IR plot. The porous and 3-dimensional structure of polymeric cryogel were approved SEM images. Changes in the surface morphology given by SEM images also is also a proof of chlordane adsorption. Chlordane molecules were adsorbed on the poly(HEMA-GMA)-Nic quite fast. The highest chlordane adsorption capacity was achieved at the chlordane concentration of 800 mg/L as 108.818 mg/g. According to the experimental results, Nic-decoration enhances the Lewis acid-base interaction between polarized chlordane shell and poly(HEMA-GMA) polymeric solid support. This polarization causes the inductive polarization of Nic decorated on the polymeric material. As mentioned in the text, Nic decoration increases the pathway of an electron on the Nic along the whole polymeric structure, so thus the time of being positively charged. As a conclusion, poly(HEMA-GMA)-Nic cryogels can be used efficiently for the removal of pesticides from alcohol matrix. Therefore, it is the main advantages of this method over the traditional removal methods with some difficulties. It is claimed by this study that formation of alcohol-phobic interaction enables adsorption of chlordane in ethanol.

ACKNOWLEDGEMENTS

The authors of this research were very indebted to the Hitit University, Alaca Avni Çelik Vocational School for the laboratory facilities. The authors of this study, which was supported by the Hitit University Scientific Research Projects Coordination Unit with a grant number as FEF19002.17, thank the Hitit University Research Funds.

REFERENCES

- Xiao P, Mori T, Kondo R. Biotransformation of the organochlorine pesticide trans-chlordane by wood-rot fungi. *New biotechnology*. 2011;29(1):107-15.
- Dearth MA, Hites RA. Highly chlorinated dimethanofluorenes in technical chlordane and in human adipose tissue. *Journal of the American Society for Mass Spectrometry*. 1990;1(1):99-103.
- Hirano T, Ishida T, Oh K, Sudo R. Biodegradation of chlordane and hexachlorobenzenes in river sediment. *Chemosphere*. 2007;67(3):428-34.
- Eitzer BD, Mattina MI, Iannucci-Berger W. Compositional and chiral profiles of weathered chlordane residues in soil. *Environmental toxicology and chemistry*. 2001;20(10):2198-204.
- Ouyang Y, Ou L-T, Sigua G. Characterization of the pesticide chlordane in estuarine river sediments. *Journal of environmental quality*. 2005;34(2):544-51.
- Taguchi S, Yakushiji T. Influence of termite treatment in the home on the chlordane concentration in human milk. *Arch Environ Con Tox*. 1988;17(1):65-71.

7. Janouskova E, Krbuskova M, Rehurkova I, Klimova M, Prokes L, Ruprich J. Determination of chlordane in foods by gas chromatography. *Food chemistry*. 2005;93(1):161-9.
8. Council NR. An assessment of the health risks of seven pesticides used for termite control. 1982.
9. Combarous Y. Endocrine Disruptor Compounds (EDCs) and agriculture: The case of pesticides. *Comptes Rendus Biologies*. 2017;340(9):406-9.
10. Yadav IC, Devi NL, Li J, Zhang G, Breivik K. Possible emissions of POPs in plain and hilly areas of Nepal: implications for source apportionment and health risk assessment. *Environmental pollution*. 2017;220:1289-300.
11. Goldner WS, Sandler DP, Yu F, Hoppin JA, Kamel F, LeVan TD. Pesticide use and thyroid disease among women in the Agricultural Health Study. *American journal of epidemiology*. 2010;171(4):455-64.
12. Shindell S, Ulrich S. Mortality of workers employed in the manufacture of chlordane: an update. *Journal of occupational medicine: official publication of the Industrial Medical Association*. 1986;28(7):497-501.
13. MacMahon B, Monson RR, Wang HH, Zheng T. A second follow-up of mortality in a cohort of pesticide applicators. *Journal of occupational medicine: official publication of the Industrial Medical Association*. 1988;30(5):429-32.
14. Everett CJ, Matheson EM. Biomarkers of pesticide exposure and diabetes in the 1999–2004 National Health and Nutrition Examination Survey. *Environment international*. 2010;36(4):398-401.
15. Wu X, Lam JC, Xia C, Kang H, Xie Z, Lam PK. Atmospheric concentrations of DDTs and chlordanes measured from Shanghai, China to the Arctic Ocean during the Third China Arctic Research Expedition in 2008. *Atmospheric environment*. 2011;45(22):3750-7.
16. Vorkamp K, Møller S, Falk K, Rigét FF, Thomsen M, Sørensen PB. Levels and trends of toxaphene and chlordane-related pesticides in peregrine falcon eggs from South Greenland. *Science of the Total Environment*. 2014;468:614-21.
17. Fuentes MS, Raimondo EE, Amoroso MJ, Benimeli CS. Removal of a mixture of pesticides by a *Streptomyces* consortium: Influence of different soil systems. *Chemosphere*. 2017;173:359-67.
18. Man YB, Chow KL, Cheng Z, Kang Y, Wong MH. Profiles and removal efficiency of organochlorine pesticides with emphasis on DDTs and HCHs by two different sewage treatment works. *Environmental Technology & Innovation*. 2017.
19. Kida M, Ziembowicz S, Koszelnik P. Removal of organochlorine pesticides (OCPs) from aqueous solutions using hydrogen peroxide, ultrasonic waves, and a hybrid process. *Separation and Purification Technology*. 2018;192:457-64.
20. Kim S, Chu KH, Al-Hamadani YA, Park CM, Jang M, Kim D-H, et al. Removal of contaminants of emerging concern by membranes in water and wastewater: A review. *Chemical Engineering Journal*. 2017.
21. Yamada S, Naito Y, Funakawa M, Nakai S, Hosomi M. Photodegradation fates of cis-chlordane, trans-chlordane, and heptachlor in ethanol. *Chemosphere*. 2008;70(9):1669-75.
22. Cuozzo SA, Fuentes MS, Bourguignon N, Benimeli CS, Amoroso MJ. Chlordane biodegradation under aerobic conditions by indigenous *Streptomyces* strains. *Int Biodeter Biodegr*. 2012;66(1):19-24.
23. Fang Y, Nie Z, Die Q, Tian Y, Liu F, He J, et al. Organochlorine pesticides in soil, air, and vegetation at and around a contaminated site in southwestern China: Concentration, transmission, and risk evaluation. *Chemosphere*. 2017;178:340-9.
24. Gun'ko VM, Savina IN, Mikhalovsky SV. Cryogels: Morphological, structural and adsorption characterisation. *Advances in Colloid and Interface Science*. 2013;187-188:1-46.
25. Erol K. The Adsorption of Calmoduline via Nicotinamide Immobilized Poly (HEMA-GMA) Cryogels. *Journal of the Turkish Chemical Society, Section A: Chemistry*. 2017;4(1):133-48.
26. Erol K. Polychelated cryogels: hemoglobin adsorption from human blood. *Artificial cells, nanomedicine, and biotechnology*. 2017;45(1):31-8.
27. Erol K, Uzun L. Two-step polymerization approach for synthesis of macroporous surface ion-imprinted cryogels. *Journal of Macromolecular Science, Part A*. 2017;54(11):867-75.
28. Kose K, Denizli A. Poly(hydroxyethyl methacrylate) based magnetic nanoparticles for lysozyme purification from chicken egg white. *Artif Cells Nanomed Biotechnol*. 2013;41(1):13-20.

29. Yilmaz F, Kose K, Sari MM, Demirel G, Uzun L, Denizli A. Bioinspired surface modification of poly(2-hydroxyethyl methacrylate) based microbeads via oxidative polymerization of dopamine. *Colloid Surface B*. 2013;109:176-82.
30. Kose K, Erol K, Emniyet AA, Kose DA, Avci GA, Uzun L. Fe(II)-Co(II) Double Salt Incorporated Magnetic Hydrophobic Microparticles for Invertase Adsorption. *Appl Biochem Biotechnol*. 2015;177(5):1025-39.
31. Kose K. Nucleotide incorporated magnetic microparticles for isolation of DNA. *Process Biochem*. 2016;51(10):1644-9.
32. Kose K. Characterization of Magnetic Polymeric Microparticles. *Journal of the Turkish Chemical Society, Section A: Chemistry*. 2016;3(3):185-204.
33. Lozinsky VI, Galaev IY, Plieva FM, Savina IN, Jungvid H, Mattiasson B. Polymeric cryogels as promising materials of biotechnological interest. *Trends Biotechnol*. 2003;21(10):445-51.
34. Bayramoğlu G, Yalçın E, Arıca MY. Characterization of polyethylenimine grafted and Cibacron Blue F3GA immobilized poly(hydroxyethylmethacrylate-co-glycidylmethacrylate) membranes and application to bilirubin removal from human serum. *Colloids and Surfaces A: Physicochemical and Engineering Aspects*. 2005;264(1-3):195-202.
35. Gore RC, Hannah RW, Pattacini SC, Porro TJ. Infrared and ultraviolet spectra of seventy-six pesticides. *Journal of the Association of Official Analytical Chemists*. 1971;54(5):1040-82.
36. Doğan A, Özkara S, Sarı MM, Uzun L, Denizli A. Evaluation of human interferon adsorption performance of Cibacron Blue F3GA attached cryogels and interferon purification by using FPLC system. *J Chromatogr B*. 2012;893-894(Supplement C):69-76.
37. Akduman B, Uygun M, Uygun DA, Akgöl S, Denizli A. Purification of yeast alcohol dehydrogenase by using immobilized metal affinity cryogels. *Materials Science and Engineering: C*. 2013;33(8):4842-8.
38. Ramalingam S, Periandy S, Govindarajan M, Mohan S. FT-IR and FT-Raman vibrational spectra and molecular structure investigation of nicotinamide: A combined experimental and theoretical study. *Spectrochimica Acta Part A: Molecular and Biomolecular Spectroscopy*. 2010;75(5):1552-8.
39. Erol K, Kose K, Kose DA, Sizer U, Satir IT, Uzun L. Adsorption of Victoria Blue R (VBR) dye on magnetic microparticles containing Fe(II)-Co(II) double salt. *Desalin Water Treat*. 2016;57(20):9307-17.
40. Köse K, Köse DA. Removal of DDE by exploiting the alcohol-phobic interactions. *Environmental Science and Pollution Research*. 2017;24(10):9187-93.
41. Lalah JO, Njogu S, Wandiga S. The effects of Mn²⁺, Ni²⁺, Cu²⁺, Co²⁺ and Zn²⁺ ions on pesticide adsorption and mobility in a tropical soil. *Bulletin of environmental contamination and toxicology*. 2009;83(3):352-8.
42. Kose K, Kose DA. Removal of DDE by exploiting the alcohol-phobic interactions. *Environ Sci Pollut Res Int*. 2017;24(10):9187-93.
43. Perrin DD. Ionisation constants of inorganic acids and bases in aqueous solution: Elsevier; 2016.
44. Dobbs RA, Cohen JM. Carbon adsorption isotherms for toxic organics: Municipal Environmental Research Laboratory, Office of Research and Development, US Environmental Protection Agency; 1980.
45. Murray R, Phillips P, Bender J. Degradation of pesticides applied to banana farm soil: comparison of indigenous bacteria and a microbial mat. *Environmental toxicology and chemistry*. 1997;16(1):84-90.
46. Tomlin C. The e-Pesticide manual: a world compendium, 11th edn., Version 1.1, Farnham. British Crop Protection Council. 1999.
47. Worthing CR, Walker SB, Flores G, Hilje L, Mora G, Carballo M. The Pesticide Manual, A World Compendium. The British Crop Protection Council. Londres (RU). 1987.
48. Maryott AA, Smith ER. Table of dielectric constants of pure liquids. National Bureau of Standards Gaithersburg MD; 1951.
49. Paruta AN, Sciarrone BJ, Lordi NG. Correlation between solubility parameters and dielectric constants. *Journal of pharmaceutical sciences*. 1962;51(7):704-5.
50. Lvet A, Bordes C, Clément Y, Mignon P, Chermette H, Marote P, et al. Quantitative structure-activity relationship to predict acute fish toxicity of organic solvents. *Chemosphere*. 2013;93(6):1094-103.



Novel Coordination Compounds Based on 2-Methylimidazole and 2,2'-Dimethylglutarate: Synthesis and Characterization

Pelin Köse Yaman^{1*}  , Hakan Erer²  

¹Dokuz Eylül University, Faculty of Sciences, Department of Chemistry, 35390, İzmir, Turkey

²Eskişehir Osmangazi University, Faculty of Arts and Sciences, Department of Chemistry, 26480, Eskişehir, Turkey

Abstract: Two novel complexes, $[\text{Cu}_2(\mu\text{-dmg})_2(2\text{-meim})_4]\cdot 5\text{H}_2\text{O}$ (**1**) and $\{[\text{Cd}(\mu\text{-dmg})(2\text{-meim})_2]\cdot \text{H}_2\text{O}\}_n$ (**2**), with 2-methylimidazole (2-meim) and 2,2'-dimethylglutarate (dmg) as ligands, have been systematically prepared by a conventional method. As a result, organic-inorganic crystalline solids were obtained. Their solid-state structures have been solved with elemental analysis, fourier transform infrared spectroscopy (FTIR) Powder X-ray diffraction (PXRD) and single-crystal X-ray diffraction (XRD). The Cu(II) ions displayed a distorted square planar geometry (CuO_2N_2), while Cd(II) ions showed a distorted octahedral geometry (CdO_4N_2). Complex **1** formed a dimeric structure, in which the Cu(II) ions were bridged by dmg. These dimeric units were extended to the 3D supramolecular structure with hydrogen bonding and π -bonding interactions. Complex **2** formed a 1D polymeric structure, where the Cd(II) ions were linked by dmg ligand to form 1D zig-zag polymer layers which were further extended in 3D supramolecular structure through molecular interactions as complex **1**. Moreover, the thermal properties of the complexes were reported.

Keywords: 2-methylimidazole ligand; Cu(II) complex, Cd(II) complex, Coordination polymers, Supramolecular.

Submitted: May 02, 2018. **Accepted:** August 25, 2018.

Cite this: Köse Yaman P, Erer H. Novel Coordination Compounds Based on 2-Methylimidazole and 2,2'-Dimethylglutarate: Synthesis and Characterization. JOTCSA. 2018;5(2):953-62.

DOI: <http://dx.doi.org/10.18596/jotcsa.420361>.

***Corresponding author.** E-mail: (pelin.kose@deu.edu.tr), Tel: (+902323017913)

INTRODUCTION

Supramolecular systems and coordination polymers are quite remarkable in coordination chemistry due to their new topologies and different potentials applications like a luminescence, adsorption, catalysis, gas storage, and magnetism, etc. (1-4). In many cases, it is very difficult to establish an interaction between the synthesis conditions and the structural properties (5-7). In determining the chemical properties of the coordination polymer, selected metal ions and organic ligands play the key role (8,9). Molecular interactions such as strong hydrogen bonds and weaker non-covalent interactions such as, $\pi\cdots\pi$, C-H $\cdots\pi$, C-H, van der Waals force in the stability of inorganic

complexes have shown to be very significant (10,11). Organic molecules containing carboxylic acid have been used as building blocks in crystal solids (12). When heterocyclic rings containing N-donor atoms such as imidazole, triazole, etc., are used as ligands, they determine the size and structure of the inorganic network (13-15). Complexes of 2-methylimidazole (2-meim) with transition metal ions have attracted great importance because of their biological and pharmaceutical activities (13,16). In the past, our group studied various N-donor molecules which are a member of the potentially interesting imidazole ligands (11,17). In this work, new dimeric Cu(II) and polymeric Cd(II) complexes,

$[\text{Cu}_2(\mu\text{-dmg})_2(2\text{-meim})_4]\cdot 5\text{H}_2\text{O}$ (**1**) and $\{[\text{Cd}(\mu\text{-dmg})(2\text{-meim})_2]\cdot \text{H}_2\text{O}\}_n$ (**2**) were synthesized with dmg and 2-meim ligands. These complexes were characterized with FTIR, XRD, elemental analysis, PXRD and thermal analysis techniques (TG/DTA) (Scheme 1).

EXPERIMENTAL SECTION

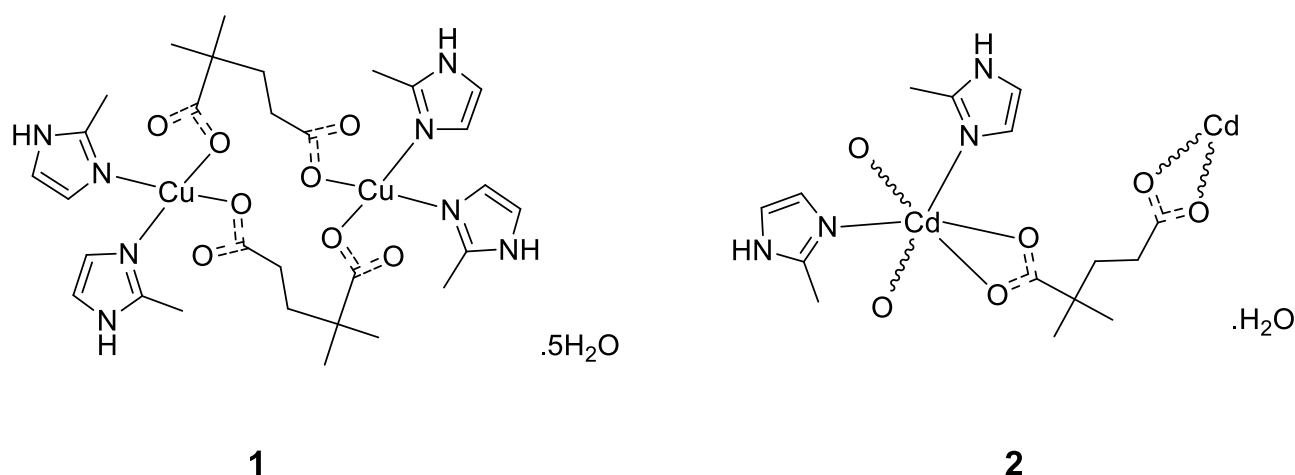
Materials and methods

All chemicals were received and used without any further purification. Elemental analyses (C, H, and N) were performed on a Perkin Elmer 2400C Elemental Analyzer. Powder X-ray diffraction (PXRD) patterns were collected by a Panalytical Empyrian X-ray diffractometer with Cu-K α radiation ($\lambda = 1.5406$ nm). FTIR spectra of the complexes were carried out at room temperature by a Perkin-Elmer FTIR 100 spectrometer in the region of 4000–400 cm^{-1} . The resolution was set up to 4 cm^{-1} , signal/noise ratio was established by 16 scans with Attenuated Total Reflection (ATR). A Perkin Elmer Diamond TG/DTA thermal analyzer was used to record simultaneous TG, DTG and DTA curves in a static air atmosphere at

a heating rate of 10 $^\circ\text{C min}^{-1}$ in the temperature range 30–1000 $^\circ\text{C}$ using platinum crucibles.

Crystallographic analyses

Suitable crystals of **1** and **2** were selected for data collection which was performed on a Bruker D8 QUEST diffractometer equipped with a graphite-monochromatic Mo-K α radiation at 296 K. The structures were solved by SHELXT and refined by full-matrix least-squares on all F^2 data using SHELXL in conjunction with the OLEX2 graphical user interface (18,19). For all complexes, the anisotropic thermal parameters were refined for non-hydrogen atoms and hydrogen atoms were calculated and refined with a riding model. Molecular drawings were obtained by Mercury and OLEX2 programs (20). The details of data collection and crystal structure determinations are given in Table 1. The crystallographic information file was deposited with the Cambridge Crystallographic Data Centre (CCDC) with the reference number 1826900 for **1** and 1826901 for **2**.



Scheme 1: Molecular structures and coordination modes of dmg and 2-meim ligands in complexes **1** and **2**

Synthesis of complexes 1-2

A solution of 2,2'-dimethylglutaric acid (0.80 g, 5 mmol) in water (50 mL) was added dropwise with stirring at 80 $^\circ\text{C}$ to a solution of $\text{Cu}(\text{CH}_3\text{COO})_2\cdot\text{H}_2\text{O}$ (0.99 g, 5 mmol) (**1**) or $\text{Cd}(\text{CH}_3\text{COO})_2\cdot 2\text{H}_2\text{O}$ (1.33 g, 5 mmol) (**2**) in distilled water (25 mL). The solutions immediately became suspensions and were stirred for 10 h at 60 $^\circ\text{C}$. Then 2-methylimidazole (2-meim) (1.65 g, 20 mmol) in water (10 mL) was added dropwise to these suspensions. The clear solutions that formed were stirred for 2 h at 60 $^\circ\text{C}$ and then cooled to room temperature. The blue (**1**) and colorless (**2**) crystals that formed were filtered and washed with 10 mL of water and dried in air. Anal. Calc. for complex **1** $\text{C}_{30}\text{H}_{54}\text{Cu}_2\text{N}_8\text{O}_{13}$: C, 41.81; H, 6.32; N, 13.00. Found: C, 41.01; H, 6.26; N, 13.53%. Anal. Calc.

for complex **2** $\text{C}_{15}\text{H}_{24}\text{N}_4\text{O}_5\text{Cd}$: C, 39.79; H, 5.34; N, 12.37. Found: C, 39.94; H, 5.88; N, 12.96%.

RESULTS AND DISCUSSION

Synthesis and characterization

IR spectroscopy was used to elucidate the structures of the synthesized coordination polymers and to identify functional groups. IR spectra showed frequencies in the range 2934–2852 cm^{-1} which are due to $\nu(\text{C-H})$ stretching vibrations. $\nu(\text{N-H})$ stretching vibrations appear in the range 3152–3263 cm^{-1} for **1** and 3157–3249 cm^{-1} for **2**. The new complexes display a very strong and slightly broad band about at 1500 cm^{-1} due to the combination of C-O and C-C stretches (15). The broad absorption bands of $\nu(\text{OH})$ vibrations of water in complexes are

detected 3411 and 3433 cm^{-1} , respectively for **1** and **2**. The strong and broad bands corresponding to the asymmetric ($\nu_{\text{as}}\text{COO}^-$) and symmetric ($\nu_{\text{s}}\text{COO}^-$) stretching vibrations of carboxylate groups of free dmg ligand approximately at 1694 and 1414 cm^{-1} (21). In the

resulting new complexes, these bands are seen at about 1526-1572 cm^{-1} and 1414-1401 cm^{-1} regions respectively.

Description of the crystal structure

Table 1 indicates the crystal data and structural refinement parameters for complexes **1** and **2**.

Table 1. Crystal data and structural refinement parameters for complexes **1** and **2**.

	1	2
Empirical formula	$\text{C}_{30}\text{H}_{54}\text{Cu}_2\text{N}_8\text{O}_1$	$\text{C}_{15}\text{H}_{24}\text{CdN}_4\text{O}_5$
Formula weight (g/mol)	861.89	452.78
Crystal system	Orthorhombic	Monoclinic
Space group	Pbca	P21/n
a (Å)	14.3309 (11)	14.020 (5)
b (Å)	14.1050 (14)	10.644 (4)
c (Å)	40.693 (4)	14.659 (6)
α (°)	90	90
β (°)	90	117.492 (11)
γ (°)	90	90
V (Å³)	8225.6 (13)	1940.6 (13)
Z	8	4
Dc (g cm⁻³)	1.392	1.550
μ (mm⁻¹)	1.10	1.16
Measured refls.	89930	20572
Independent refls.	8351	3880
Rint	0.086	0.085
R [I > 2σ(I)]	0.077	0.070
wR [I > 2σ(I)]	0.166	0.181
S	1.27	1.20

[Cu₂(μ -dmg)₂(2-meim)₄]-5H₂O (1). The molecular structure of complex **1** consists of dimeric [Cu₂(μ -dmg)₂(2-meim)₄] units (Figure 1). The complex has the orthorhombic crystal system with the *Pbca* space group (Table 1). According to single crystal X-ray structural analysis, the asymmetric unit of the complex **1** contains two copper ions, two bridging dmg ligands, four 2-meim moieties and five uncoordinated water molecules. Each copper metal ion coordinated to two different dmg ligands by means of the

oxygen atoms and two different 2-meim ligands by means of the nitrogen atoms. The geometry of each Cu(II) ion is a distorted square planar geometry (CuO₂N₂). The dmg ligands forms a bridge between the Cu(II) ions by means of the four carboxylate atoms of each dmg to form a 16 membered dimeric [Cu₂(μ -dmg)₂] unit. These dimeric units are extended to 3D supramolecular structure with intra- and intermolecular hydrogen bonds, C-H... π , C-O... π and π ... π interactions (Figure 2).

Table 2: Selected bond distances (Å), angles (°) and hydrogen-bond geometry data for **1**.

Bond Lengths (Å)			
Cu1—O1	2.005 (4)	Cu2—O3	1.967 (4)
Cu1—O5	1.968 (4)	Cu2—O7	1.966 (4)
Cu1—N3	1.992 (4)	Cu2—N7	1.982 (5)
Cu1—N1	1.981 (4)	Cu2—N5	1.983 (5)
Angles (°)			
O5—Cu1—O1	90.98 (16)	O3—Cu2—N7	162.1 (2)
O5—Cu1—N3	92.07 (18)	O3—Cu2—N5	90.4 (2)

O5—Cu1—N1	159.71 (19)	O7—Cu2—O3	90.19 (18)
N3—Cu1—O1	165.27 (17)	O7—Cu2—N7	90.48 (19)
N1—Cu1—O1	89.47 (17)	O7—Cu2—N5	163.3 (2)
N1—Cu1—N3	92.62 (19)	N7—Cu2—N5	94.1 (2)

Hydrogen bond geometry (Å, °)

D—H...A	D—H	H...A	D...A	D—H...A
O11—H11A...O10	0.85	1.91	2.753 (7)	173
O11—H11B...O5	0.85	1.88	2.729 (6)	173
N4—H4...O1 ⁱ	0.86	2.13	2.930 (6)	155
N2—H2...O11 ⁱⁱ	0.86	2.01	2.851 (7)	167
O10—H10C...O9	0.85	1.96	2.807 (8)	174
O10—H10D...O2 ⁱⁱⁱ	0.85	1.96	2.803 (6)	172
N6—H6...O12 ^{iv}	0.86	1.96	2.804 (8)	167
O12—H12D...O4	0.85	2.17	2.890 (7)	142
O12—H12E...O7	0.85	1.91	2.732 (7)	162
N8—H8...O13	0.86	1.96	2.780 (7)	160
O9—H9C...O13 ^v	0.85	2.03	2.881 (8)	174

*Symmetry codes: (i) $x-1/2, y, -z+3/2$; (ii) $x+1/2, y, -z+3/2$; (iii) $-x+1/2, y+1/2, z$; (iv) $x-1/2, -y+3/2, -z+1$; (v) $-x+1, -y+2, -z+1$; (vi) $x+1/2, -y+3/2, -z+1$.

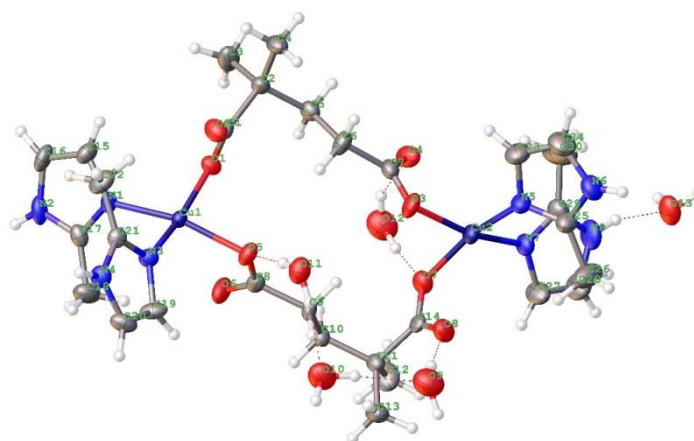


Figure 1. The molecular structure of **1**.

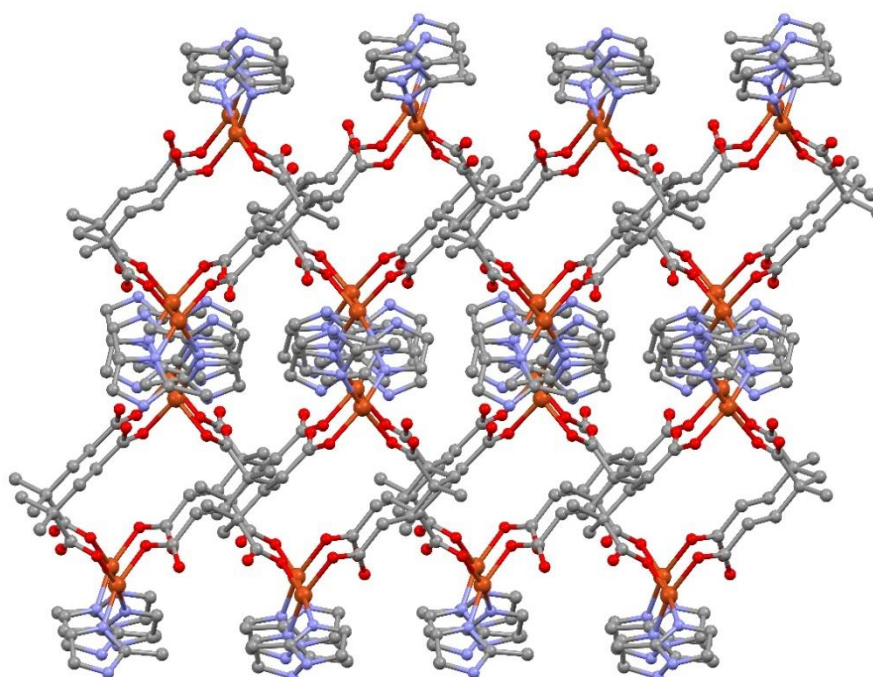


Figure 2: 3D supramolecular structure of complex **1** generated by hydrogen bonds and C–H $\cdots\pi$, C–O $\cdots\pi$ and $\pi\cdots\pi$ interactions.

$\{[\text{Cd}(\mu\text{-dmg})(2\text{-meim})_2]\cdot\text{H}_2\text{O}\}_n$ (2**).** The molecular structure of complex **2** consists of polymeric $[\text{Cd}(\mu\text{-dmg})(2\text{-meim})_2]$ units (Figure 3). The complex has the monoclinic crystal system with the $P21/n$ space group (Table 2.). The asymmetric unit consists of one Cd(II) ion, one dmg ligand, two 2-meim ligands and one water molecule (Scheme 1). As shown in Figure 3, Cd ion has distorted octahedral geometry and linked to four carboxylate oxygens from two different dmg ligands and two nitrogen atoms from 2-meim ligands (CdO_4N_2). The Cd(II) ions in **2** are bound by dmg ligands to form 1D zig-zag chains. The adjacent 1D chains are linked with

the dmg to form the zig-zag-like structure shown in Figure 4. The neighboring 1D chains are expanded into 2D supramolecular layer with hydrogen bonding between carboxylate oxygen atom (O1) of dmg and uncoordinated water molecule (O5) [$\text{O1}\cdots\text{O5} = 2.85 \text{ \AA}$, $\text{O1}\cdots\text{H5D-O5} = 170.06^\circ$] and between the imidazole nitrogen atom (N4) of adjacent 2-meim ligand and water molecule (O5) [$\text{N4}\cdots\text{O5} = 2.69 \text{ \AA}$, $\text{N4-H4}\cdots\text{O5} = 166.89^\circ$] (Figure 5). Furthermore, 2D supramolecular structures form a three dimensional (3D) supramolecular network through C–H $\cdots\pi$ and C–O $\cdots\pi$ interactions. (Figure 6).

Table 3. Selected bond distances (\AA), angles ($^\circ$) and hydrogen-bond geometry data for **2***.

Bond Lengths (\AA)			
Cd1–O1	2.344 (6)	Cd1–N3	2.241 (7)
Cd1–O2	2.415 (7)	Cd1–O3 ⁱ	2.375 (7)
Cd1–N1	2.225 (8)	Cd1–C7 ⁱ	2.714 (9)
Cd1–O4 ⁱ	2.356 (8)	O3–Cd1 ⁱⁱ	2.375 (7)
Angles ($^\circ$)			
O1–Cd1–O2	54.4 (2)	O4 ⁱ –Cd1–O2	87.0 (3)
O1–Cd1–O4 ⁱ	97.2 (3)	O4 ⁱ –Cd1–O3 ⁱ	54.2 (3)
O1–Cd1–O3 ⁱ	147.2 (3)	O4 ⁱ –Cd1–C7 ⁱ	27.1 (3)
O1–Cd1–C7 ⁱ	122.3 (3)	N3–Cd1–O1	108.0 (3)
O2–Cd1–C7 ⁱ	94.2 (3)	N3–Cd1–O2	88.1 (3)
N1–Cd1–O1	97.0 (3)	N3–Cd1–O4 ⁱ	144.7 (3)
N1–Cd1–O2	151.3 (2)	N3–Cd1–O3 ⁱ	93.3 (3)
N1–Cd1–O4 ⁱ	98.5 (3)	N3–Cd1–C7 ⁱ	119.0 (3)

N1—Cd1—N3	102.3 (3)	O3 ⁱ —Cd1—O2	103.4 (3)	
N1—Cd1—O3 ⁱ	102.6 (3)	O3 ⁱ —Cd1—C7 ⁱ	27.2 (3)	
N1—Cd1—C7 ⁱ	103.5 (3)			
Hydrogen bond geometry (Å, °)				
D—H...A	D—H	H...A	D...A	D—H...A
N2—H2...O2 ⁱⁱⁱ	0.86	1.89	2.731 (11)	165
N4—H4...O5	0.86	1.85	2.693 (12)	167
O5—H5C...O3 ^{iv}	0.85	1.86	2.714 (11)	179
O5—H5D...O1 ^v	0.85	2.02	2.857 (11)	170

*Symmetry codes: (iii) $x+1/2, -y+1/2, z+1/2$; (iv) $x+1/2, -y+1/2, z-1/2$; (v) $-x+3/2, y-1/2, -z+1/2$.

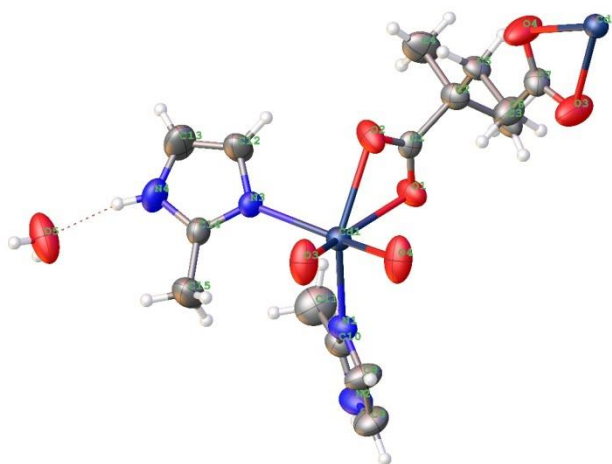


Figure 3: The molecular structure of **2**.

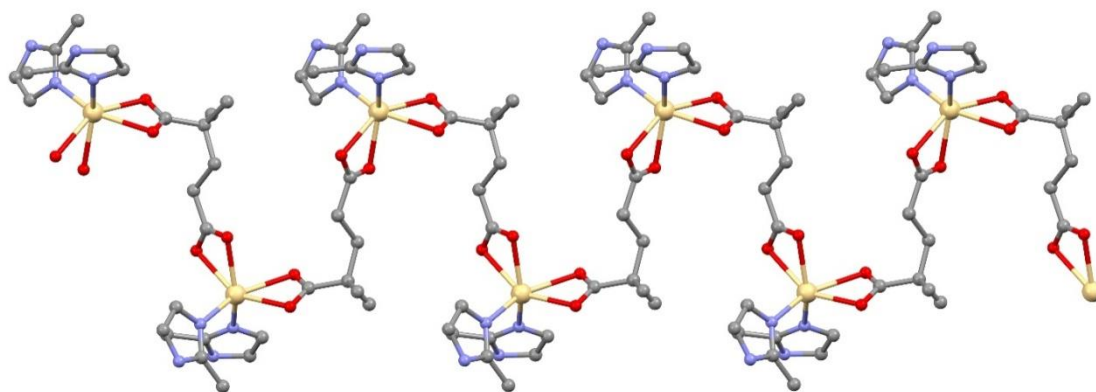


Figure 4: 1D zig-zag polymeric structure of **2**.

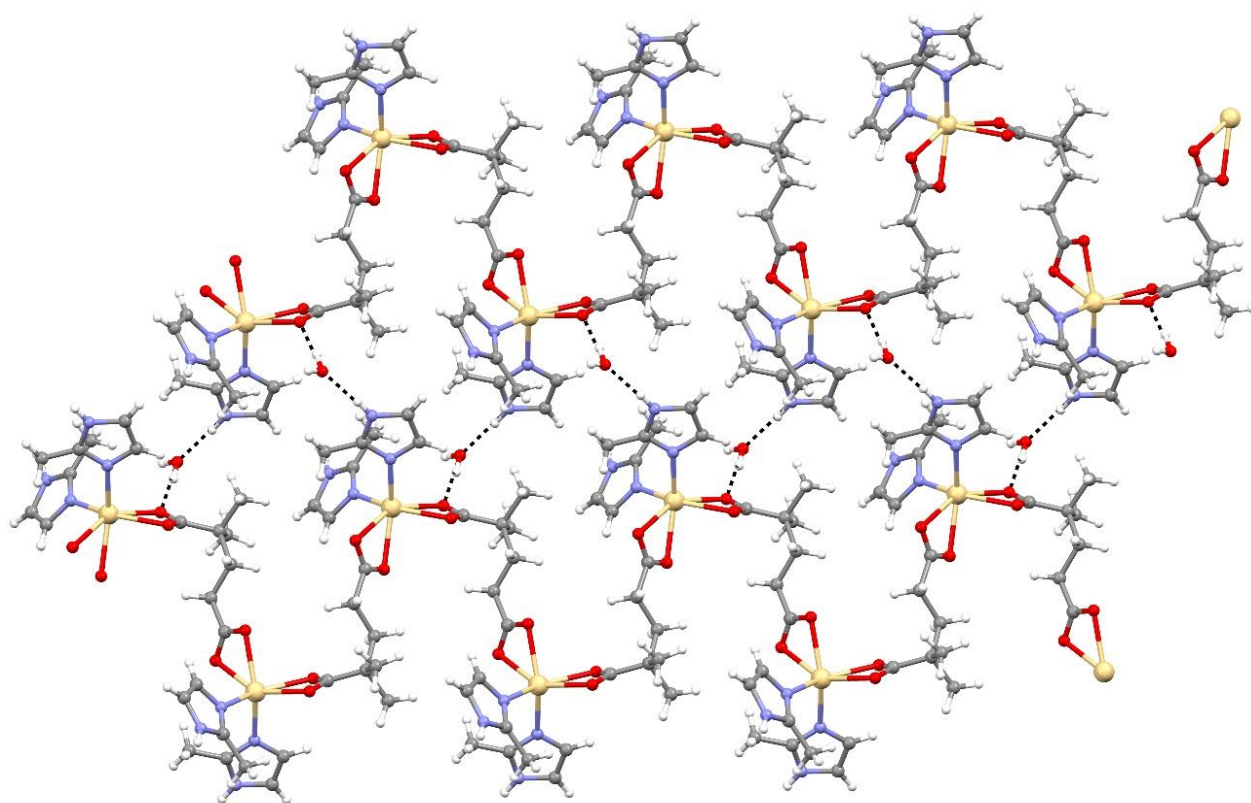


Figure 5: 2D supramolecular layer of complex **2** generated by hydrogen bondings.

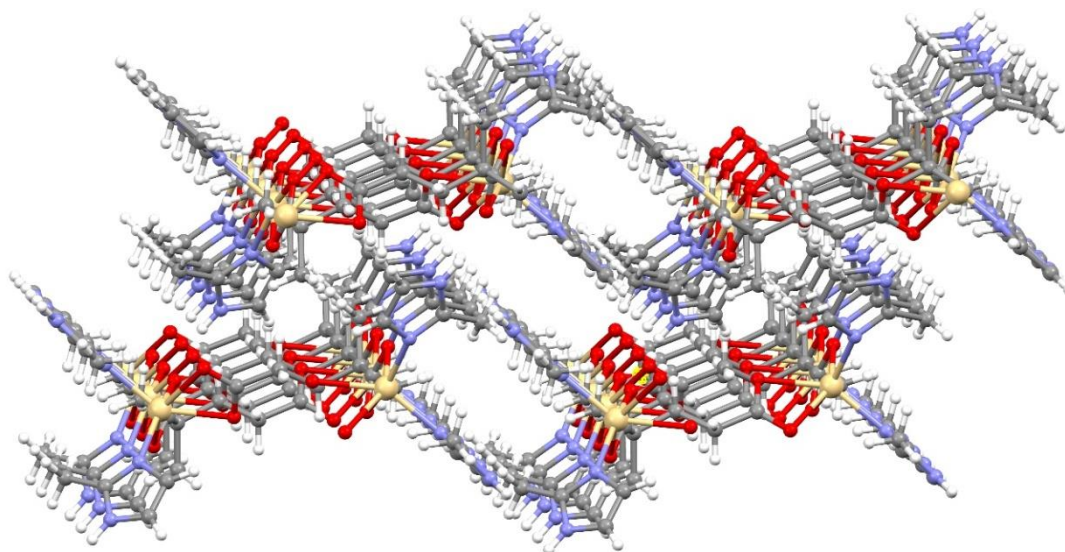


Figure 6: 3D supramolecular structure of complex **2** generated by C–H...N and C–O...N interactions.

Powder X-ray diffraction (PXRD) and Thermal Analyses of complexes 1 and 2

The complexes of the PXRD patterns obtained from the crystal structures are compatible with the simulated patterns obtained from single crystal results; indicating the phase purity of the complexes **1** and **2** (Figure 7 and 8).

TG, DTG and DTA curves for complexes 1 and 2 were obtained in static air atmospheres between 30-1000 °C (Figure 9 and 10). For complex 1, three stage thermal decomposition is observed.

The first stage starts at about 60 °C with the release of the five water molecules and ends at 104 °C (found 10.18%; theoretical value 10.44%). The diversion of water is at low temperature because the water molecule is not coordinated as shown by the crystal structure (Figure 7). The second step occurs between 284 and 334 °C which corresponds to the release of one 2-meim ligand and one dmg ligand (found 57.69%; theoretical value 56.79%). The following stage between 379 and 457 °C involves

the decay of one dmg molecule. Also the highest exothermic mass loss occurs at this step. The final decomposition product is 2 molecules of CuO (found: 17.81%; theoretical value 18.33%). The Cd complex is stable up to 112 °C. The first stage between 112 and 138 °C corresponds to the endothermic removal of uncoordinated water molecule (found 4.10; theoretical value 3.90%). The second weight loss takes place between 226 and 271 °C, corresponding to the decomposition

of one 2-meim ligand (found 8.73%; theoretical value 9.07%). The remaining organic ligands are degradation between 415 and 506 °C (found 52.77%; theoretical value 53.55%) by the most severe exothermic effect ($DTA_{max} = 460$ °C). Total mass loss is 73.22% (theoretical value 71.60%) as a result of the thermal degradation of complex 2 (Figure 8). The final product for the complex 2 is suggested to be CdO.

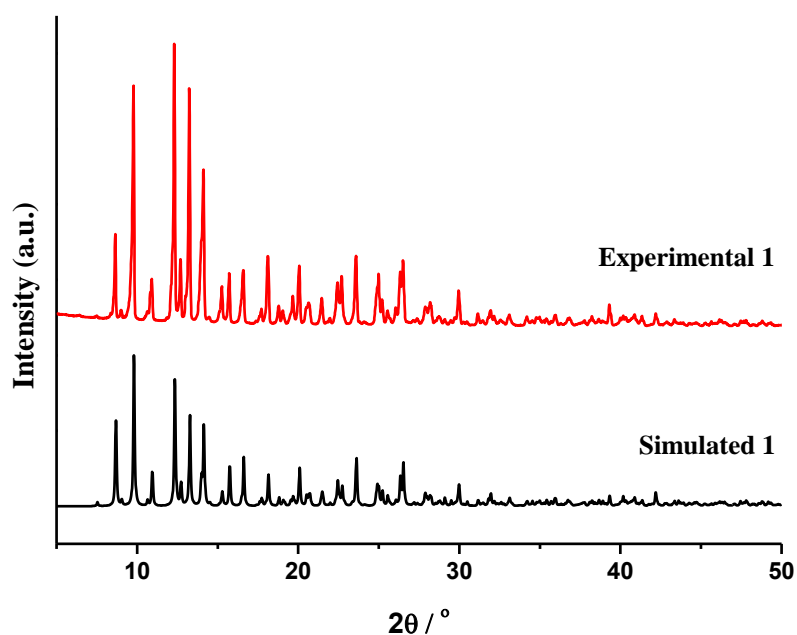


Figure 7 PXRD pattern of $[Cu_2(\mu\text{-dmg})_2(2\text{-meim})_4]_2 \cdot 5H_2O$ (**1**).

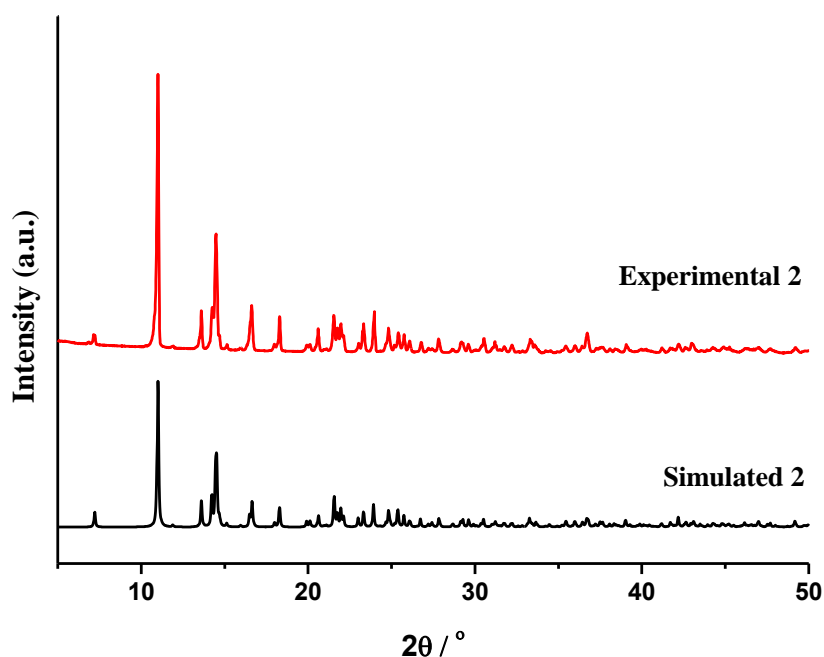


Figure 8 PXRD pattern of $\{[Cd(\mu\text{-dmg})(2\text{-meim})_2] \cdot H_2O\}_n$ (**2**).

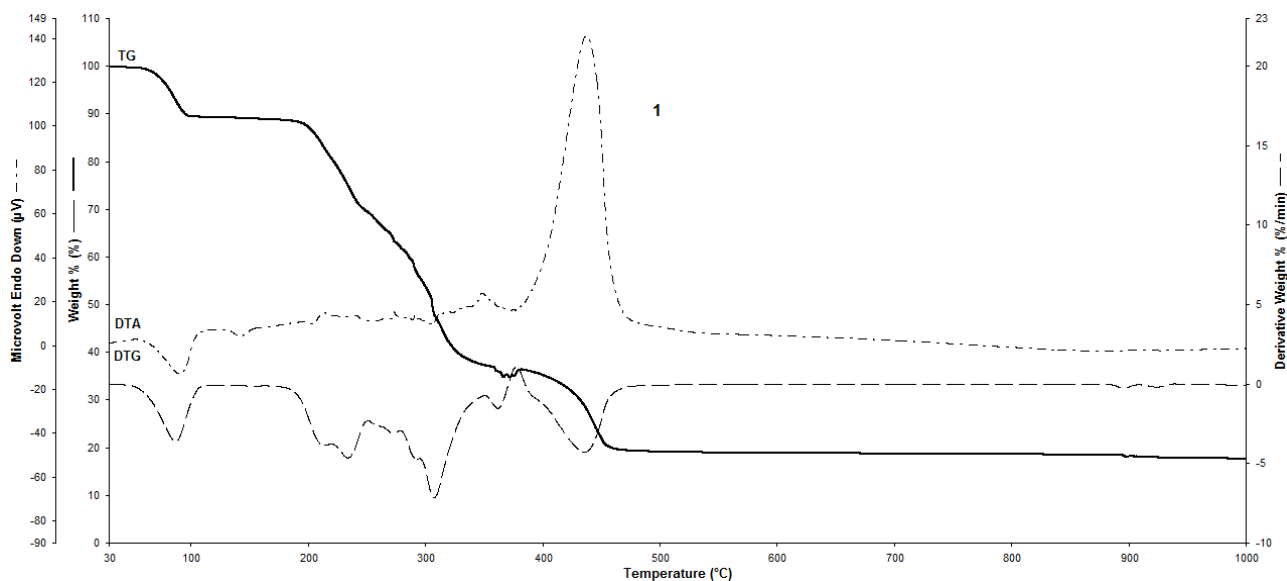


Figure 9. Thermal analysis curves of $[\text{Cu}_2(\mu\text{-dmg})_2(2\text{-meim})_4]_2 \cdot 5\text{H}_2\text{O}$ (**1**).

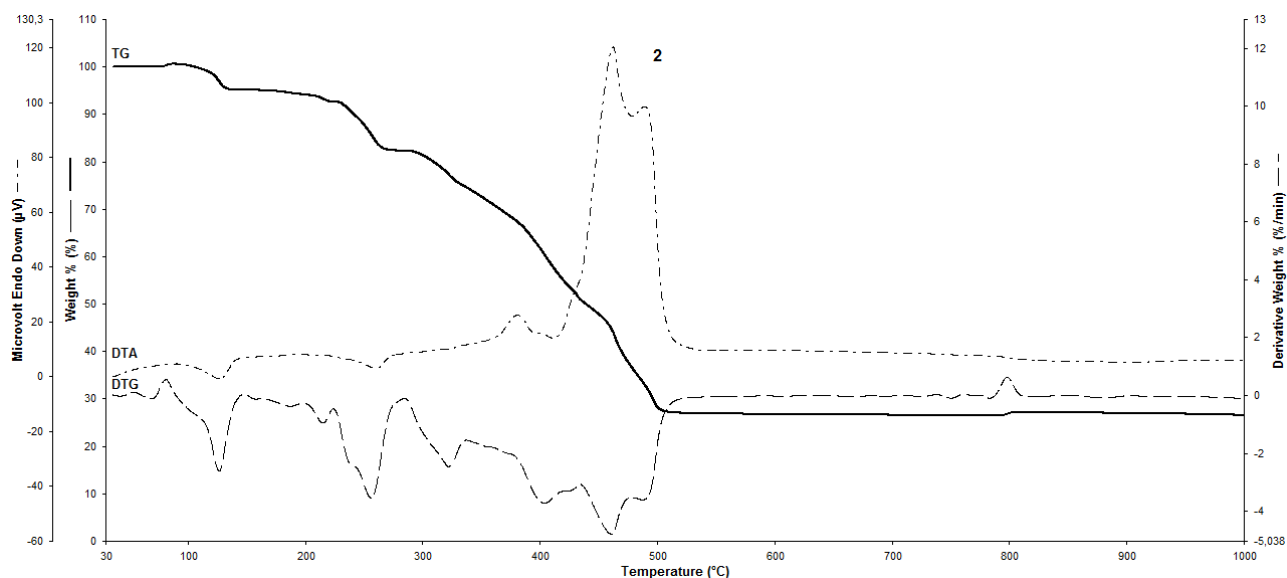


Figure 10. Thermal analysis curves of $\{[\text{Cd}(\mu\text{-dmg})(2\text{-meim})_2] \cdot \text{H}_2\text{O}\}_n$ (**2**).

CONCLUSION

In summary, new dimeric Cu(II) and polymeric Cd(II) coordination compounds with 2-meim and flexible dmg ligands have been successfully synthesized and characterized by spectroscopic and thermal studies. The dmg ligand in all of the complexes coordinated to the metal centers as a bidentate fashion and acted as a bridging ligand between the metal(II) centers to form dimeric $[\text{Cu}_2(\mu\text{-dmg})_2]$ units for complex **1** and 1D zig-zag polymeric structure for complex **2**. The reason for the difference may be due to the radius variations of the metal (II) ions. In addition, the Cd(II) ion may have more coordination ability than the Cu(II) ion. Nevertheless, more studies are necessary to support or disprove such a claim. The compounds

decompose in three main thermal stages. The final decomposition products corresponds to the metal oxides.

ACKNOWLEDGEMENTS

The authors acknowledge Scientific and Technological Research Application and Research Center, Sinop University, Turkey, for the use of the Bruker D8 QUEST diffractometer.

REFERENCES

1. Suezawa H, Yoshida T, Umezawa Y, Tsuboyama S, Nishio M. CH / n Interactions Implicated in the Crystal Structure of Transition Metal Compounds -A Database Study. *Eur J Inorg Chem.* 2002;3148-55.

2. Di Santo A, Osiry H, Reguera E, Alborés P, Carbonio RE, Ben Altabef A, et al. New coordination polymers based on 2-methylimidazole and transition metal nitroprusside containing building blocks: Synthesis, structure and magnetic properties. *New J Chem.* 2018;42(2).
3. Sredojević DN, Tomić ZD, Zarić SD. Evidence of chelate-chelate stacking interactions in crystal structures of transition-metal complexes. *Cryst Growth Des.* 2010;10(9):3901-8.
4. Afkhami FA, Khandar AA, White JM, Guerri A, Ienco A, Bryant JT, et al. Assembly of anion-controlled cadmium(II) coordination polymers from the use of 2-acetyl-pyridyl-isonicotinoylhydrazone. *Inorganica Chim Acta.* 2017;457:150-9.
5. Kitagawa S, Kitaura R, Noro S. Functional Porous Coordination Polymers. *Angew Chemie Int Ed.* 2004;43(18):2334-75.
6. Li M, Li D, O'Keeffe M, Yaghi OM. Topological analysis of metal-organic frameworks with polytopic linkers and/or multiple building units and the minimal transitivity principle. *Chem Rev.* 2014;114(2):1343-70.
7. Tian Z, Lin J, Su Y, Wen L, Liu Y, Zhu H, et al. Flexible ligand, structural, and topological diversity: Isomerism in Zn(NO₃)₂ coordination polymers. *Cryst Growth Des.* 2007;7(9):1863-7.
8. Zhang X-R, Zhang L. Solvent effect on the self-assembly of salt solvates of an antihypertensive drug azilsartan and 2-methylimidazole. *J Mol Struct.* 2017;1137:320-7.
9. Uzun N, Çolak AT, Emen FM, Kismali G, Meral O, Alpay M, et al. The syntheses, crystal structure, thermal analysis, and anticancer activities of novel dipicolinate complexes. *J Coord Chem.* 2015;68(6):949-67.
10. Cui GH, Liu TF, Peng X. Structural and spectroscopic study of Cu(II) pyridine-2,6-dicarboxylate complex with 2-ethylimidazole. *J Chem Crystallogr.* 2011;41(3):322-7.
11. Erer H, Yeşilel OZ, Darcan C, Büyükgüngör O. Synthesis, spectroscopic, thermal Studies, antimicrobial activities and crystal structures of Co(II), Ni(II), Cu(II) and Zn(II)-orotate complexes with 2-methylimidazole. *Polyhedron.* 2009;28(14):3087-93.
12. Semerci F, Yeşilel OZ, Şahin E. Cu(II) and Zn(II)-Pyridine-2,3-Dicarboxylate complexes with 2-Methylimidazole: Syntheses, crystal structures, spectroscopic and thermal analyses. *J Inorg Organomet Polym Mater.* 2010;20(2):334-42.
13. Sharma RP, Saini A, Kumar S, Kumar J, Sathishkumar R, Venugopalan P. Non-covalent interactions in 2-methylimidazolium copper(II) complex (MeImH)₂[Cu(pfbz)₄]: Synthesis, characterization, single crystal X-ray structure and packing analysis. *J Mol Struct.* 2017;1128:135-41.
14. Chakraborty A, Lingampalli SR, Kumari A, Ribas J, Ribas-Arino J, Maji TK. Structural and magnetic diversity based on different imidazolate linkers in Cu(II)-azido coordination compounds. *Inorg Chem.* 2014;53(22):11991-2001.
15. Erer H, Yeşilel OZ, Büyükgüngör O. One-dimensional coordination polymers of Co(II) and Cd(II)-squarate with 2-methylimidazole and 4(5)-methylimidazole ligands. *Polyhedron.* 2010;29(3):1163-7.
16. Salah AM Ben, Naili H, Arczyński M, Fitta M. 0D and 1D copper(II) coordination polymers based on 2-methyl-1H-imidazole: Structural, vibrational and magnetic characterizations. *J Organomet Chem.* 2016;805:42-8.
17. Yeşilel OZ, Ilker I, Büyükgüngör O. Three copper(II) complexes of thiophene-2,5-dicarboxylic acid with dissimilar ligands: Synthesis, IR and UV-Vis spectra, thermal properties and structural characterizations. *Polyhedron.* 2009;28(14):3010-6.
18. Sheldrick GM. SHELXT – Integrated space-group and crystal-structure determination. *Acta Crystallogr Sect A Found Adv.* 2015 Jan 1;71(1):3-8.
19. Sheldrick GM. A short history of SHELX. *Acta Crystallogr Sect A Found Crystallogr.* 2007;64(1):112-22.
20. Dolomanov O V., Bourhis LJ, Gildea RJ, Howard JAK, Puschmann H. OLEX2: A complete structure solution, refinement and analysis program. *J Appl Crystallogr.* 2009;42(2):339-41.
21. Köse Yaman P, Yeşilel OZ. Hydrothermal synthesis and characterization of cobalt(II), nickel(II) and zinc(II) coordination polymers with 2,2'-dimethylglutarate and 1,2-bis(4-pyridyl)ethane. *Polyhedron.* 2018;148:189-94.



Synthesis of Some Mono-, Bis- NH-substituted-1,4-Benzoquinones

Aysecik Kacmaz^{1*} 

¹Istanbul University-Cerrahpasa, Engineering Faculty, Chemistry Department, 34320 Avclar, Istanbul, Turkey

Abstract: The preparation of new mono- and bis- NH-substituted-1,4-benzoquinones, namely 2,5-bis(5,6-dimethylbenzo[d]thiazol-2-ylamino)cyclohexa-2,5-diene-1,4-dione (**3**), 2,5-bis(3-(2-methylpiperidin-1-yl)propylamino)-3-chlorocyclohexa-2,5-diene-1,4-dione (**6**), 2-(4-tert-butylbenzylamino)-3,5,6-trichlorocyclohexa-2,5-diene-1,4-dione (**9**), 2-(4-fluorophenylamino)-6-tert-butylcyclohexa-2,5-diene-1,4-dione (**12**) are reported. The synthesis of new quinone derivatives (**3**, **6**, **9**, **12**) have been carried out from the reactions between quinones (*p*-benzoquinone (**1**), 2,6-dichloro-1,4-benzoquinone (**4**), tetrachloro-1,4-benzoquinone (**7**) or 2-tert-butyl-1,4-benzoquinone (**10**)) and different amines (2-amino-5,6-dimethylbenzothiazole (**2**), N-(3-aminopropyl)-2-pipecoline (**5**), 4-tert-butylbenzylamine (**8**) or 4-fluoroaniline (**11**)). The new compounds were characterized by elemental analysis, mass spectrometry, IR, ¹H-NMR, ¹³C-NMR spectroscopy.

Keywords: Quinones, NH-substituted-benzoquinones, Amines.

Submitted: June 01, 2018. **Accepted:** August 25, 2018.

Cite this: Kaçmaz A. Synthesis of Some Mono-, Bis- NH-substituted-1,4-Benzoquinones. JOTCSA. 2018;5(2):963-70.

DOI: <http://dx.doi.org/10.18596/jotcsa.429197>.

***Corresponding author.** E-mail: kacmaz@istanbul.edu.tr.

INTRODUCTION

Quinones are found in both natural and synthetic products (1-3). And, these compounds are important in many fields including medicinal chemistry, color chemistry, optical data storage, photoconductors, supercapacitors, coordination polymers (4-10). Especially, these compounds are of particular interest because of their biological and chemotherapeutic activities, such as antifungal, antibacterial, anti-tumor, anti-inflammatory, antiplatelet, and antiallergic (11-13). The biological activity of the quinones is related to the redox chemistry of these compounds (14-15).

There are a lot of reports on biological or pharmacological evaluation of amino or thio substituted 1,4-(naphtho/benzo)quinones (16-19). Also, the presence of different substituent (NH, SR, alkyl, halogen, etc.) on

the quinoid structure can impact the quinone's capability to accept electrons and thus its biological activities (12, 20, 21), including antifungal, antibacterial, antitumor, and sometimes the substituents improve these activities. Thus, many researchers have centered their studies on the synthesis, characterization, biological activity and redox properties of quinones. In this respect, many quinones were reacted with amines, thiols, alcohols, to produce amino-, azido, hydroxy-, thio-, halogeno- or alkyl- substituted quinones by using different solvents such as EtOH, MeOH, H₂O, CH₃CN, CH₂Cl₂, at room or reflux temperature (22-26). Recently, in our laboratory, some NH-/SR- substituted quinones were synthesized between the reaction of quinones and amines/thiols, and also the antifungal, antibacterial, antioxidant or anticancer activities of these compounds have been evaluated (27-30).

Among quinones, 2,5-diamino-1,4-benzoquinones are obtained the reaction between 1,4-benzoquinones and primary aliphatic amines, which by the addition, isomerization, and oxidation reactions (31, 32). There are some uses these type of compounds. For example, the quinone-containing conducting additive, 2,5-bis((2-(1H-indol-3-yl)ethyl)amino)cyclohexa-2,5-diene-1,4-dione (HBU), was synthesized and used as an additive for application to electrode material for supercapacitors (8). Another example, Barbosa *et al.* synthesized new 2,5-bis(alkylamino)-1,4-benzoquinones and investigated their cytotoxicity (33). They indicated that the some synthesized 2,5-bis(NH-substituted)-1,4-benzoquinone compounds exhibited activity against HL-60 (leukemia), MDA-MB-435 (melanoma), SF-295 (brain) and HCT-8 (colon) human cancer cell lines (33). In this study, compounds **3** and **6** have 2,5-bis(NH-substituted)-1,4-benzoquinone structure, including not halogen and chlorine, respectively.

MATERIALS AND METHODS

The melting points were obtained on a Buchi B-540 apparatus. The IR spectra were measured using a Jasco FT/IR-4700 instrument. The mass spectra were recorded on a Thermo Finnigan LCQ Advantage MAX system using ion-trap mass analyzer for ESI source. The ^1H and ^{13}C NMR spectra were recorded on a Varian Unity Inova spectrometer (500 and 125 MHz, respectively) using CDCl_3 as solvent and TMS an internal standard. Column chromatography was carried out using silica gel (Kieselgel 60, 70–230 mesh, Merck). Kieselgel 60 F-254 plates (Merck) were used for thin-layer chromatography.

Synthesis of 2,5-bis(5,6-dimethylbenzo[d]thiazol-2-ylamino)cyclohexa-2,5-diene-1,4-dione (**3**):

A solution of *p*-benzoquinone **1** (0.8 g, 4.5 mmol) and 2-amino-5,6-dimethylbenzothiazole **2** (0.5 g, 4.5 mmol) in methanol (20 mL) was stirred at reflux temperature. The progress of the reaction was monitored by thin layer chromatography (TLC) using CH_2Cl_2 as eluent. Upon the completion of the reaction, the reaction mixture was diluted with water (30 mL) and extracted with chloroform (3×15 mL). The combined organic extract was dried over anhydrous Na_2SO_4 , concentrated under vacuum and the residue was subjected to column chromatography using silica gel in dichloromethane/ethyl acetate (1:1) to give the pure product **3**: R_f (MeOH): 0.7. Yield: 16 % (165 mg). Brownish solid. M.p= 180-182 °C. IR (ATR): 3371, 3289, 2912, 1642, 1531, 1454, 1364, 1314, 1272, 1200, 1108, 859. Mass spectrum

(+ESI), m/z $[\text{M}-\text{H}]^+ = 459.3$. ^1H NMR (CDCl_3) δ (ppm): 7.58 (s, CH_{arom} , 1H), 7.52 (s, CH_{arom} , 1H), 7.40 (bs, 2H, NH), 7.27 (s, CH_{arom} , 1H), 7.22 (s, CH_{arom} , 1H), 5.83 (s, 1H, $\text{CH}_{\text{quinone}}$), 5.06 (s, 1H, $\text{CH}_{\text{quinone}}$), 2.27 (s, 3H, CH_3), 2.22 (s, 3H, CH_3), 2.21 (s, 3H, CH_3), 2.20 (s, 3H, CH_3). ^{13}C NMR (CDCl_3) δ (ppm): 182.5 (C=O), 181.7 (C=O), 165.6, 160.9, 157.3, 150.0, 139.7, 135.9, 134.8, 133.9, 132.1, 131.3, 128.6, 127.6, 122.3, 122.3, 121.2, 119.8, 108.0, 103.8, 20.1 (CH_3), 20.1 (CH_3), 20.1 (CH_3), 19.8 (CH_3). $\text{C}_{24}\text{H}_{20}\text{N}_4\text{O}_2\text{S}_2$ calcd. C, 62.59; H, 4.38; N, 12.16; S, 13.92. Found C, 62.60; H, 4.39; N, 12.14; S, 13.90.

Synthesis of 2,5-bis(3-(2-methylpiperidin-1-yl)propylamino)-3-chlorocyclohexa-2,5-diene-1,4-dione (**6**):

A solution of 2,6-dichloro-1,4-benzoquinone **4** (0.75 g, 4.2 mmol) and N-(3-aminopropyl)-2-pipecoline **5** (0.66 g, 4.2 mmol) in dichloromethane (20 mL) was stirred at room temperature. The progress of the reaction was monitored by thin layer chromatography (TLC) using CH_2Cl_2 as eluent. Upon the completion of the reaction, the reaction mixture was diluted with water (30 mL) and extracted with chloroform (3×15 mL). The combined organic extract was dried over anhydrous Na_2SO_4 , concentrated under vacuum and the residue was subjected to column chromatography using silica gel in ethyl acetate to give the pure product **6**: R_f (Ethylacetate): 0.16. Yield: 15% (286 mg). M.p: 126-128 °C. Mass spectrum (+ESI), m/z $[\text{M}+\text{H}]^+ = 451.3$, Mass spectrum (-ESI), m/z $[\text{M}]^- = 449.5$. ^1H NMR (CDCl_3) δ (ppm): 5.19 (s, 1H, $\text{CH}_{\text{quinone}}$), 4.80 (bs, 2H, NH), 3.70-4.0 (m, 2H), 3.08-3.20 (m, 2H), 2.78-2.92 (m, 4H), 2.26-2.46 (m, 4H), 2.06-2.24 (m, 2H), 1.68-1.88 (m, 5H), 1.54-1.64 (m, 7H), 1.38-1.48 (m, 2H), 1.20-1.32 (m, 2H), 1.05 (d, 3H, CH_3 , $^3J = 6.35$ Hz), 1.00 (d, 3H, CH_3 , $^3J = 6.35$ Hz). ^{13}C NMR (CDCl_3) δ (ppm): 176.8 (C=O), 176.3 (C=O), 173.5, 151.0, 146.0, 91.4, 56.7, 52.2, 52.1, 51.8, 51.6, 51.2, 47.5, 43.7, 42.9, 33.6, 33.3, 26.1, 25.3, 25.0, 23.9, 23.8, 23.1, 18.0. $\text{C}_{24}\text{H}_{39}\text{ClN}_4\text{O}_2$ calcd. C, 63.91; H, 8.72; N, 12.42. Found C, 63.90; H, 8.70; N, 12.42.

2-(4-Tert-butylbenzylamino)-3,5,6-trichlorocyclohexa-2,5-diene-1,4-dione (**9**):

A solution of tetrachloro-1,4-benzoquinone **7** (1.5 g, 6.1 mmol) and 4-*tert*-butylbenzylamine **8** (1 g, 6.1 mmol) in dichloromethane (20 mL) and ethanol (20 mL) in the presence of NaHCO_3 was stirred at 45 °C temperature. The progress of the reaction was monitored by thin layer chromatography (TLC) using CH_2Cl_2 as eluent. Upon the completion of the reaction, the reaction mixture was diluted with water (30 mL) and extracted with chloroform (3×15 mL). The combined organic extract was dried over anhydrous Na_2SO_4 ,

concentrated under vacuum and the residue was subjected to column chromatography using silica gel in hexane/chloroform (3:1) to give the pure product **9**: R_f (CH_2Cl_2): 0.66. Dark purple, semi-solid. Yield: 10% (230 mg). IR (ATR): 3299, 2956, 2927, 2861, 1686, 1606, 1572, 1514, 1293, 1085. Mass spectrum (-ESI), m/z $[\text{M}-\text{H}]^- = 370.8$. ^1H NMR (CDCl_3) δ (ppm): 7.33 (dd, 2H, CH_{arom} , $J^3 = 6.35$ Hz, $J^4 = 1.95$ Hz), 7.15 (d, 2H, CH_{arom} , $J^3 = 8.30$ Hz), 5.90-6.0 (bs, 1H, NH), 4.86 (d, 2H, $\text{CH}_{2\text{ethyl}}$, $J^3 = 5.85$ Hz), 1.25 (9H, $3 \times \text{CH}_3$). ^{13}C NMR (CDCl_3) δ (ppm): 188.9, 182.7 (C=O), 164.9, 158.6, 145.6, 138.1, 130.9, 127.6, 126.13, 47.7, 31.3, 29.7. $\text{C}_{17}\text{H}_{16}\text{Cl}_3\text{NO}_2$ calcd. C, 54.79; H, 4.33; N, 3.76. Found C, 54.80; H, 4.31; N, 3.74.

2-(4-Fluorophenylamino)-6-tert-butylcyclohexa-2,5-diene-1,4-dione (**12**)

A solution of 2-*tert*-butyl-1,4-benzoquinone **10** (1.5 g, 9.1 mmol) and 4-fluoroaniline **11** (1.2 g, 9.1 mmol) in dichloromethane (20 mL) was stirred at room temperature. The progress of the reaction was monitored by thin layer chromatography (TLC) using CH_2Cl_2 as eluent. Upon the completion of the reaction, the reaction mixture was diluted with water (30 mL) and extracted with chloroform (3×15 mL). The combined organic extract was dried over anhydrous Na_2SO_4 , concentrated under vacuum and the residue was subjected to column chromatography using silica gel in dichloromethane to give the pure product **12**: Brown solid, M.p = 166-168 °C. Yield: 8 % (200 mg). IR (ATR): 3270 (NH), 2959, 2919, 1666, 1623, 1572, 1496, 1404, 1353, 1210, 908. Mass spectrum (+EI), m/z $[\text{M}]^+ = 273.1$. ^1H NMR (CDCl_3) δ (ppm): 7.08-7.14 (m, 3H, CH_{arom} and NH), 7.03 (t, 2H, $^3J = 8.54$ Hz, CH_{arom}), 6.44 (d, 1H, $\text{CH}_{\text{quinone}}$, $^4J = 2.44$ Hz), 5.88 (d, 1H, $\text{CH}_{\text{quinone}}$, $^4J = 2.44$ Hz), 1.23 (s, 9H, $3 \times \text{CH}_3$). ^{13}C NMR (CDCl_3) δ (ppm): 187.0, 183.3, 161.2, 159.2, 151.7, 144.7, 134.4, 134.4, 133.6, 124.6, 116.5, 99.7, 99.5, 35.0, 29.1, 29.0. ^{19}F NMR (CDCl_3)

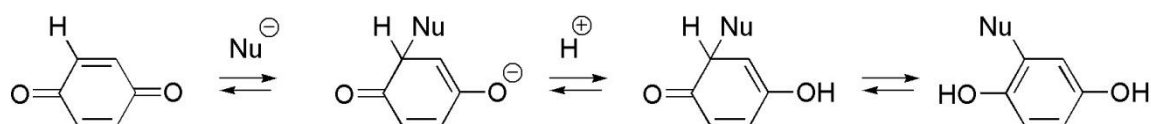
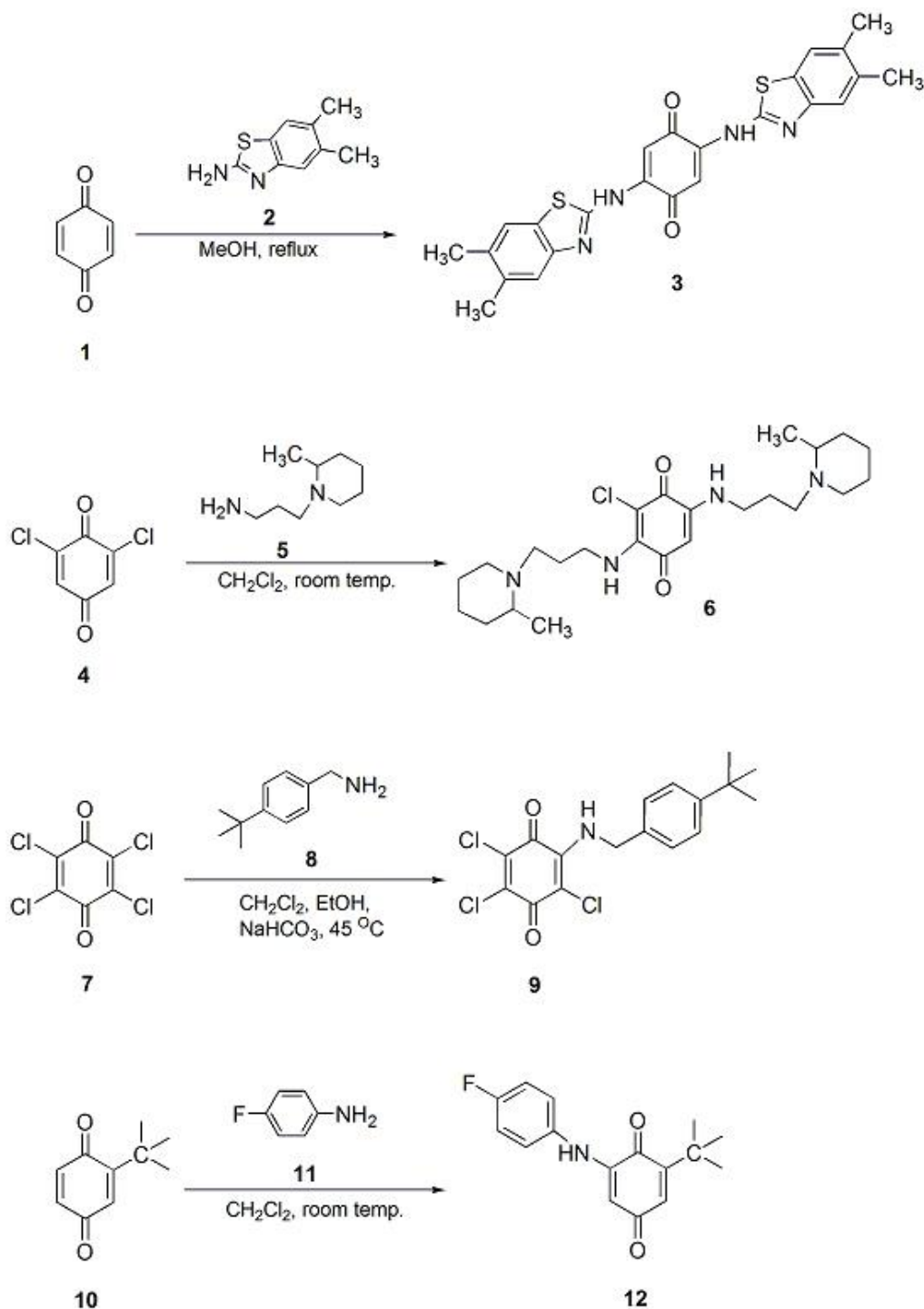
δ (ppm): -115.6. $\text{C}_{16}\text{H}_{16}\text{FNO}_2$ calc. C, 70.31; H, 5.90; N, 5.12. Found C, 70.29; H, 5.87; N, 5.10.

RESULTS AND DISCUSSION

In this study, 1,4-benzoquinone compounds (**1**, **4**, **7** or **10**), respectively, were reacted with primary amines (**2**, **5**, **8** or **11**) to obtain mono-/bis-(NHsubstituted)

1,4,benzoquinones (**3**, **6**, **9**, **12**) as illustrated in Scheme 1. All compounds were purified by column chromatography. The purity was checked by TLC and chemical structures were confirmed using FTIR, ^1H -NMR, ^{13}C -NMR spectroscopies and ESI-MS spectrometry.

Conjugated addition of nucleophiles to *p*-benzoquinone give initially mono-products (**34**). However, depending on the character of the nucleophile (nitrogen, sulfur, oxygen, etc.) may form further nucleophilic reactions to produce bis-, tris- or tetrakis-products. (**34**). For example, *p*-benzoquinone undergoes a nucleophilic attack by primary aliphatic amine to produce 2,5-diamino-1,4-benzoquinones (**31**). Furthermore, monoamino-1,4-benzoquinones were not obtained in this reaction. The result of exclusively 2,5-isomer formation can be explained that attack of two amines to 1,4-benzoquinone require the furthest possible distance due to electrostatic reasons (**35**). According to the explanation of Kuttyrev, the reaction mechanism includes firstly by the addition of an amine to a carbon-carbon double bond (the formation of intermediate), after the intermediate isomerize to aminohydroquinone, which is oxidized to monoaminoquinone, and then the reaction of monoaminoquinone and second amine produce diaminoquinone via intermediate (**31**, **32**). Also, the general scheme of the reaction of 1,4-quinones with nucleophilic compounds was given as Scheme 2 (**31**).



In this study, it was obtained the reaction between *p*-benzoquinone (**1**) and **2** to obtain bis-NH-substituted compound (**3**), in methanol at reflux temperature. The corresponding ¹H NMR spectrum of compound

3, the appearance of CH_{arom} (δ 7.58-7.22 ppm), CH_{quinone} (δ 5.83, 5.06 ppm) and NH- (δ 7.40 ppm) proton signals were a clear evidence for -NHR formation. The stretching vibration of the carbonyl (C=O) group of quinone was

observed at 1642 cm⁻¹, in the IR spectra, whereas the ESI mass spectrum of **3** exhibited the molecular ion peak at m/z 459.3, as expected.

The reaction between 2,6-dichloro-1,4-benzoquinone **4** and N-(3-aminopropyl)-2-pipecoline **5** was obtained at room temperature in dichloromethane to obtain 2,5-(bis-NH)-substituted-3-chloro-1,4-benzoquinone derivative **6**. In ¹H NMR spectra of **6**, the presence of benzoquinone proton was confirmed by one signal at δ 5.19 ppm (s). And, in ¹³C NMR spectrum of **6**, two quinonic carbonyl moieties (C=O) appeared in δ 176.8 and 176.3 ppm, as expected. In the mass spectra (ESI-MS) of this compound (**6**), the protonated [M+H]⁺ molecular ion peak gave m/z= 451.3 in the positive ion mode and molecular ion peak gave m/z [M]⁻=449.5 in the negative ion mode, which were agreement with the molecular formula.

It is known that mono- and bis- NH-substituted-1,4-benzoquinones by the reaction between p-chloranil and primary amines (10, 36, 37). In order to prepare mono(NH-substituted)-trichloro-1,4-benzoquinone derivative (**9**), tetrachloro-1,4-benzoquinone (**7**) was treated with 4-tert-butylbenzylamine (**8**) in dichloromethane and ethanol in the presence of NaHCO₃ at a temperature of 50 °C. Compound **9** displayed signals due to CH_{arom} groups at 7.33 ppm and 7.15 ppm with proper ³J and ⁴J coupling constants. In the mass spectra MS(ESI) of compound **9**, the deprotonated molecular ion peak m/z [M-H]⁻= 370.8 gave the expected molecular weight.

The reaction between 2-tert-butyl-1,4-benzoquinone (**10**) and 4-fluoroaniline (**11**) in equimolar ratio, using dichloromethane as solvent at room temperature, yielded compound **12**. During structural elucidation of compound **12**, the assignment of the location of the -NHR group (C2 or C3) is determined by the splitting pattern (⁴J= 2.44 Hz). In the literature, there are similar situations, including different location of -NHR (38-40). Also, the mass spectrum obtained for **12** and showed a molecular ion peak m/z= 273.1 (C₁₆H₁₆FNO₂, 273.3 g.mol⁻¹). Also, in the corresponding ¹³C NMR spectrum of **12**, the appearance of C=O and C_{tert} carbon signals at δ= 187.0, 183.3 and 35.0 ppm, respectively, and in the corresponding ¹⁹F NMR spectrum of **12**, the presence of signal at δ= -115.6 ppm (belong to F-C₆H₄-) is a clear evidence for -NHR formation.

CONCLUSION

In conclusion, in this study, the synthesis and characterization of mono- or bis- NH-substituted-1,4-benzoquinones (**3**, **6**, **9** and **12**) have been reported. Compounds were prepared by the reaction of *p*-benzoquinone (**1**), 2,6-dichloro-1,4-benzoquinone (**4**), tetrachloro-1,4-benzoquinone (**7**) or 2-tert-butyl-1,4-benzoquinone (**10**), respectively, with amines (2-amino-5,6-dimethylbenzothiazole (**2**), N-(3-aminopropyl)-2-pipecoline (**5**), 4-tert-butylbenzylamine (**8**) or 4-fluoroaniline (**11**) at room temperature to reflux. The new synthesized compounds might have biological activities because of their quinoid skeleton.

ACKNOWLEDGMENTS

This work was supported by Research Fund of the Istanbul University-Cerrahpasa, Istanbul, Turkey. (Project Number: FBA-2017-22046). I am grateful to the Research Fund of Istanbul University-Cerrahpasa for financial support.

REFERENCES

1. Monks TJ, Hanzlik RP, Cohen GM, Ross D, Graham DG. Quinone Chemistry and Toxicity. *Toxicol Appl Pharmacol.* 1992; 112:2-16. [https://doi.org/10.1016/0041-008X\(92\)90273-U](https://doi.org/10.1016/0041-008X(92)90273-U)
2. Tandon VK, Maurya HK, Kumar S, Rashid A, Panda D. Synthesis and evaluation of 2-heteroaryl and 2,3-diheteroaryl-1,4-naphthoquinones that potentially induce apoptosis in cancer cells. *RSC Adv.* 2014;4:12441-12447. DOI: 10.1039/c3ra47720g
3. Satheshkumar A, Ganesh K, Elango KP. Charge transfer facilitated direct electrophilic substitution in phenylaminonaphthoquinones: experimental, theoretical and electrochemical studies. *New J Chem.* 2014;38:993-1003. DOI: 10.1039/c3nj01228j
4. Brun M-P, Braud E, Angotti D, Mondesert O, Quaranta M, Montes M, Miteva M, Gresh N, Ducommun B, Garbay C. Design, synthesis, and biological evaluation of novel naphthoquinone derivatives with CDC25 phosphatase inhibitory activity. *Bioorg Med Chem.* 2005;13:4871-4879. DOI:10.1016/j.bmc.2005.05.005
5. Szymczak AM, Podsiadly R, Podemska K, Sokolowska J. Dyes derived from 1,4-naphthoquinone as initiators for radical and cationic photopolymerisation. *Color Technol.* 2012;128:378-386. DOI: 10.1111/j.1478-4408.2012.00391.x

6. Koroteev NI, Magnitskii SA, Shubin VV, Sokolyuk NT. Photochemical and spectroscopic properties of naphthacenequinones as candidates for 3D optical data storage. *Jpn J Appl Phys. Part 1, No. 1B*, 1997;36:424-425.
7. Ohkura K, Takeshima M, Omokawa S, Hasegawa Y, Kobayashi T. Quinone Compound, electrophotographic photoconductor and electrophotographic apparatus. US Patent 2006/0204874, Sep. 14, 2006.
8. Won JH, Latifatu M, Jang M, Lee HS, Kim B-C, Hamenu L, Park JH, Kim KM, Ko JM. Supercapacitive properties of composite electrode consisting of activated carbon and a quinone-containing conducting additive. *Synth Met.* 2015;203:31–36. <http://dx.doi.org/10.1016/j.synthmet.2015.02.010>
9. Hamenu L, Madzvamuse A, Mohammed L, Hu M, Park J, Ryou M-H, Lee YM, Ko JM. Highly stable 2,3,5,6-tetrachloro-1,4-benzoquinone electrodes for supercapacitors. *Synth Met.* 2017;231:25–33. <http://dx.doi.org/10.1016/j.synthmet.2017.06.006>
10. Singh D, Kushwaha A, Banerjee A, Prasad RL. Synthesis and characterization of multifunctional coordination polymer of the type $[CuxNi_{1-x}(dedb)_2 \cdot 2H_2O]_n$. *Solid State Sciences.* 2015;45:35-45. <http://dx.doi.org/10.1016/j.solidstatesciences.2015.04.004>
11. Gafner S, Wolfender J-L, Nianga M, Stoeckli-Evans H, Hostettmann K. Antifungal and Antibacterial Naphthoquinones from *Newbouldia laevis* Roots. *Phytochemistry.* 1996;42(5):1315-1320.
12. Delarmelina M, Daltoe RD, Cerri MF, Madeira KP, Rangel LBA, Junior VL, Romao W, Taranto AG, Greco SJ. Synthesis, Antitumor Activity and Docking of 2,3-(Substituted)-1,4-Naphthoquinone Derivatives Containing Nitrogen, Oxygen and Sulfur. *J Braz Chem Soc.* 2015;26(9):1804-1816. <http://dx.doi.org/10.5935/0103-5053.20150157>
13. Huang LJ, Chang FC, Lee KH, Wang JP, Tengd CM, Kuo SC. Synthesis and antiplatelet, antiinflammatory, and antiallergic activities of substituted 3-Chloro-5,8-dimethoxy-1,4-naphthoquinone and related compounds. *Bioorg Med Chem.* 1998;6:2261-2269.
14. Ma W, Zhou H, Ying Y-L, Li D-W, Chen G-R, Long Y-T, Chen H-Y. In situ spectroelectrochemistry and cytotoxic activities of natural ubiquinone analogues. *Tetrahedron.* 2011;67:5990-6000. DOI:10.1016/j.tet.2011.06.026
15. Ganesh K, Balraj C, Satheshkumar A, Elango KP. Spectroscopic studies on the formation of molecular complexes of sulfamethoxazole with novel 2,3,5-trichloro-6-alkoxy-1,4-benzoquinones. *J Mol Struct.* 2013;1033:312–320. <http://dx.doi.org/10.1016/j.molstruc.2012.09.062>
16. Kumagai Y, Shinkai Y, Miura T, Cho AK. The chemical biology of naphthoquinones and its environmental implications. *Annu Rev Pharmacol Toxicol.* 2012;52:221-247.
17. Singh VK, Verma SK, Kadu R, Mobin SM. Identification of unusual C-Cl...N contacts in 2-(alkylamino)-3-chloro-1,4-naphthoquinones: effect of N-substituents on crystal packing, fluorescence, redox and anti-microbial properties. *RSC Adv.* 2015;5:43669-43686. DOI: 10.1039/c5ra02295a
18. Tandon VK, Yadav DB, Singh RV, Vaish M, Chaturvedi AK, Shukla PK. Synthesis and biological evaluation of novel 1,4-naphthoquinone derivatives as antibacterial and antiviral agents. *Bioorg Med Chem Lett.* 2005;15:3463–3466. doi:10.1016/j.bmcl.2005.04.075
19. Mori K, Takahashi K, Kishi T, Sayo H. Synthesis and biological activities of 2,3-Dimethyl-1,4-benzoquinones Having alkylthio and arylthio side chains. *Chem Pharm Bull.* 1987;35(3):1270-1274.
20. Tandon VK, Chhor RB, Singh RV, Rai S, Yadav DB. Design, synthesis and evaluation of novel 1,4-naphthoquinone derivatives as antifungal and anticancer agents. *Bioorg Med Chem Lett.* 2004;14:1079–1083. DOI:10.1016/j.bmcl.2004.01.002
21. Tandon VK, Maurya HK, Mishra NN, ShuklaPK. Design, synthesis and biological evaluation of novel nitrogen and sulfur containing hetero-1,4-naphthoquinones as potent antifungal and antibacterial agents. *Eur J Med Chem.* 2009;44:3130–3137. DOI:10.1016/j.ejmech.2009.03.006
22. Zee-Cheng K-Y, Cheng C-C. Preparation and the results of antitumor screening of some substituted amino-, azido-, halogeno- and hydroxy-p-benzoquinones. *J Med Chem.* 1970;13(2):264–268. DOI: 10.1021/jm00296a023

23. Claes P, Jacobs J, Kesteleyn B, Van TN, De Kimpe N. Palladium(II)-Catalyzed Synthesis of 2H,3'H-Spiro[benzofuran-3,2'-naphthoquinones]. *J Org Chem.* 2013;78(17):8330-8339. DOI: 10.1021/jo400852z
24. Jiao M, Ding C, Zhang A. Facile construction of 3-hydroxyphenanthrene-1,4-diones: key intermediates to tanshinone I and its A-ring-modified analogue. *Tetrahedron* 2014;70:2976-2981. <http://dx.doi.org/10.1016/j.tet.2014.03.019>
25. Salunke-Gawali S, Pawar O, Nikalje M, Patil R, Weyhermüller T, Puranik VG, Konkimalla VB. Synthesis, characterization and molecular structures of homologated analogs of 2-bromo-3-(n-alkylamino)-1,4-naphthoquinone. *J Mol Struct.* 2014;1056-1057:97-103. <http://dx.doi.org/10.1016/j.molstruc.2013.10.016>
26. Leyva E, Lopez LI, Loredó-Carrillo SE, Rodríguez-Kessler M, Montes-Rojas A. Synthesis, spectral and electrochemical characterization of novel 2-(fluoroanilino)-1,4-naphthoquinones. *J Fluor Chem.* 2011;132:94-101. DOI:10.1016/j.jfluchem.2010.12.001
27. Yildirim H, Bayrak N, Tuyun AF, Kara Mataracı E, Celik Ozbek B, Gupta Kumar G. 2,3-Disubstituted-1,4-naphthoquinones containing an arylamine with trifluoromethyl group: synthesis, biological evaluation, and computational study. *RSC Adv.* 2017;7(41):25753-25764. DOI: 10.1039/c7ra00868f
28. Deniz NG, Ozyurek M, Tufan AN, Apak R. One-pot synthesis, characterization, and antioxidant capacity of sulfur- and oxygen-substituted 1,4-naphthoquinones and a structural study. *Monatsh Chem.* 2015;146:2117-2126. DOI 10.1007/s00706-015-1517-5
29. Bayrak N, Yıldırım H, Tuyun AF, Kara Mataracı E, Çelik Ozbek B, Kumar Gupta G, Çiftçi IH, Fujita M, Otsuka M, Nasiri RH. Synthesis, Computational Study, and Evaluation of In Vitro Antimicrobial, Antibiofilm, and Anticancer Activities of New Sulfanyl Aminonaphthoquinone Derivatives. *Lett Drug Des Discov.* 2017;14(6):647-661
30. Ibis C, Sahinler Ayla S, Ozkok F, Bahar H. Synthesis of New Piperazinyll and Piperidinolyl Substituted p-Chloranil Derivatives and their Reactions with Thiols. *Phosphorus, Sulfur Silicon Relat. Elem.* 2015;190:2273-2282. DOI: 10.1080/10426507.2015.1071816
31. Kutyrev AA. Nucleophilic reactions of quinones, *Tetrahedron Report Number 298 Tetrahedron* 1991;47(38):8043-8065.
32. Yang J, Cohen Stuart MA, Kamperman M. Jack of all trades : versatile catechol crosslinking mechanisms, *Chem Soc Rev.* 2014;43:8271-8298.
33. Barbosa LCA, Pereira UA, Maltha CRA, Teixeira RR, Valente VMM, Ferreira JRO, Costa-Lotufo LV, Moraes MO, Pessoa C. Synthesis and Biological Evaluation of 2,5-Bis(alkylamino)-1,4-benzoquinones. *Molecules* 2010;15:5629-5643. DOI:10.3390/molecules15085629
34. Katritzky AR, Fedoseyenko D, Mohapatra PP, Steel PJ, Reactions of p-Benzoquinone with Sulfur Nucleophiles, *Synthesis* 2008;5:777-787. DOI: 10.1055/s-2008-1032186
35. Bayen S, Barooah N, Sarma RJ, Kumar Sen T, Karmakar A, Baruah JB. Synthesis, structure and electrochemical properties of 2,5-bis(alkyl/aryl amino)1,4-benzoquinones and 2-aryl amino-1,4-naphthoquinones, *Dyes Pigments.* 2007;75:770-775. DOI:10.1016/j.dyepig.2006.07.033
36. Smith RE, Davis WR. Spectrophotometric determination of amines with p-chloranil, *Anal. Chem.* 1984;56:2345-2349.
37. Tandon VK, Maurya HK. 'On water': unprecedented nucleophilic substitution and addition reactions with 1,4-quinones in aqueous suspension. *Tetrahedron Lett.* 2009; 50:5896-5902. DOI:10.1016/j.tetlet.2009.07.149
38. Martínez-Cifuentes M, Clavijo-Allancan G, Di Vaggio-Conejeros C, Weiss-Lopez B, Araya-Maturana R. On Water Reactivity and Regioselectivity of Quinones in C-N Coupling with Amines: Experimental and Theoretical Study. *Aust. J. Chem.* 2014; 67:217-224.
39. Yogo M, Ito C, Furukawa H. Synthesis of Some Carbazolequinone Alkaloids and Their Analogues. Facile Palladium-Assisted Intramolecular Ring Closure of Arylamino-1,4-benzoquinones to Carbazole-1,4-quinones. *Chem. Pharm. Bull.* 1991;39(2); 328-334.
40. Jeremic M, Pesic M, Dinic J, Bankovic J, Novakovic I, Simple avarone mimetics as selective agents against multidrug resistant cancer cells. *Eur. J. Med. Chem.* 2016; 118; 107-120.



Synthesis of Some New Benzimidazole Derivatives Containing Chlorine and Investigation of Their Antioxidant and Anti-urease Activities

Nesrin Karaali¹

¹Recep Tayyip Erdogan University, Faculty of Arts and Sciences, Department of Chemistry, 53100, Rize, Turkey.

Abstract: In this work, the synthesis of a 2-substituted benzimidazole compound containing chlorine (**1**) was carried out and then converted to the ester (**2**) and hydrazide (**3**) derivatives respectively. In the next steps, the hydrazide compound (**3**) was reacted with the appropriate reagents to give the thiadiazole (**8-10**) and triazole (**11-13**) derivatives. Synthesis of the compound **4** was carried out as a result of the interaction of the ester derivative compound (**2**) with morpholine. The structures of all new synthesized compounds were determined by FT-IR, ¹H NMR, ¹³C NMR and elemental analysis spectroscopic methods. Also, the antioxidant and urease enzyme inhibition properties of these compounds were also investigated.

Keywords: Benzimidazole, triazole, thiadiazole, urease inhibition, antioxidant.

Submitted: July 03, 2018. **Accepted:** August 12, 2018.

Cite this: Karaali N. Synthesis of Some New Benzimidazole Derivatives Containing Chlorine and Investigation of Their Antioxidant and Anti-urease Activities. JOTCSA. 2018;5(2):971-80.

DOI: <http://dx.doi.org/10.18596/jotcsa.440202>.

*Corresponding author. E-mail: nesrin.karaali@erdogan.edu.tr.

INTRODUCTION

Nitrogen-containing heterocycles are unique pharmacophoric units found in bioactive natural products, synthetic medicines, and agrochemicals. Among these heterocyclic compounds, benzimidazole and its derivatives have a significant role due to their wide variety pharmacological properties such as anticancer, antimicrobial, anti-inflammatory, anti-diabetic, anticonvulsant, antibacterial, antihypertensive, anti-cholinesterase, antimalarial, antitumor, antivirals, antiparasite, antioxidant, antiurease, CNS stimulant, and depressant (1-13). And also, literature studies have clearly demonstrated that the attachment of different groups to the benzimidazole core at different positions leads to the increase and differentiation of the activities of this class of compounds (10, 14-17). Especially, it is known that the presence of groups such as triazole, thiadiazole, oxadiazole, morpholine, piperazine, piperidine, etc. increases the bioactivity and biodiversity of the benzimidazole core (12-16).

In this work, we have synthesized a series of new 5,6-dichlorobenzimidazole derivatives containing the 2,4-dichlorobenzyl group at position 2 and

carbothioamide structure, triazole, thiadiazole rings at position 1 of benzimidazole ring. Moreover, we have studied the urease and antioxidant properties of these compounds.

MATERIALS AND METHODS

Chemistry

The chemicals were supplied from Merck, Sigma-Aldrich and Tekkim. Melting points were detected at the SMP30 Stuart melting point device and are uncorrected. The FTIR data were taken on a Perkin-Elmer 100 FTIR spectrometer as ATR (attenuated total reflectance). ¹H and ¹³C NMR spectra were recorded on 400 MHz Varian-Mercury spectrometer in the DMSO-d₆ solvent using TMS as internal standard and the chemical shifts values were given in δ ppm. The reaction times and progress were determined by TLC plates (silicagel 60, F 2.54, 0.2 mm). The elemental compositions were performed on a Carlo Erba 1106 CHN analyzer.

General procedure for the synthesis of compounds 1

2-(2,4-dichlorophenyl)-1-ethoxyethaniminium chloride (**a**) (0.011 mol) synthesized according to the reported method in the literature (18) and

4,5-dichlorobenzene-1,2-diamine (**b**) (0.010 mol) in absolute methanol (30 mL) were stirred for 2 hours at room temperature (monitored by TLC, ethyl acetate : n-hexane, 2:1). Then, plenty of water was added to the mixture to precipitate. The mixture, which was rested for a while, was filtered and washed with plenty of water and purified by recrystallization from a mixture of ethanol:water, v:v 1:1.

5,6-Dichloro-2-(2,4-dichlorobenzyl)-1H-benzimidazole (1). CAS Registry Number: 1632028-81-9. Yield: 3.01 g (87 %). M.P.: 185–187 °C, FTIR (KBr): 3078 (NH), 1628 (CN), 1445, 1097, 864 cm⁻¹. ¹H NMR (400 MHz, DMSO-d₆, δ, ppm): 12.60 (1H, s, NH), 7.77-7.40 (5H, m, Ar-H), 4.30 (2H, s, CH₂).

General procedure for the synthesis of compounds 2

Compound **1** (0.01 mol) and dry K₂CO₃ (0.03 mol) in absolute acetone (30 mL) was stirred at room temperature for 1 hour, followed by addition of ethylbromoacetate (0.01 mol) stirring at room temperature for a further 4 hours (monitored by TLC, ethyl acetate : n-hexane, 2:1). Plenty of water was added to the mixture to dissolve the excess K₂CO₃ and precipitate the expected product. The mixture, which was rested for a while, was filtered and washed with plenty of water and purified by recrystallization from a mixture of ethanol:water, v:v 1:2.

Ethyl [5,6-dichloro-2-(2,4-dichlorobenzyl)-1H-benzimidazol-1-yl]acetate (2). Yield: 3.58 g (83 %). M.P.: 128–130 °C, FTIR (KBr): 1735 (C=O), 1670 (CN), 1228 (C-O) cm⁻¹. ¹H NMR (400 MHz, DMSO-d₆, δ, ppm): 7.96 (1H, s, Ar-H), 7.82 (1H, s, Ar-H), 7.60 (1H, s, Ar-H), 7.40-7.34 (2H, m, Ar-H), 5.28 (2H, s, NCH₂), 4.31 (2H, s, CH₂), 4.10 (2H, q, J=8 Hz, OCH₂), 1.17 (3H, t, J= 8 Hz, CH₃). ¹³C NMR (100 MHz, DMSO-d₆): δ 14.4 (CH₃), 30.9 (CH₂), 45.2 (NCH₂), 61.9 (OCH₂), 112.6 (Ar-CH), 120.3 (Ar-CH), 124.7 (Ar-C), 125.2 (Ar-C), 129.1 (Ar-CH), 132.9 (Ar-C), 133.4 (Ar-CH), 133.6 (Ar-C), 134.9 (Ar-C), 135.7 (Ar-C), 141.9 (Ar-C), 155.7 (NCN), 168.0 (C=O). Elemental analysis: Calculated for C₁₈H₁₄Cl₄N₂O₂: C, 50.03; H, 3.27; N, 6.48. Found: C, 50.09; H, 3.22; N, 6.51.

General procedure for the synthesis of compound 3

A mixture of compound **2** (0.010 mol) and hydrazine monohydrate (0.050 mol) in absolute ethanol (25 mL) was stirred at room temperature for 2 hours (monitored by TLC, ethyl acetate:hexane, 3:1). The mixture was filtered and purified by recrystallization from ethanol.

2-[5,6-Dichloro-2-(2,4-dichlorobenzyl)-1H-benzimidazol-1-yl]acetohydrazide (3). Yield: 2.84 g (68 %). M.P.: 253-254 °C, FTIR (KBr): 3301, 3153 (NH₂+NH), 1650 (CN), 1457, 1092, 868 cm⁻¹. ¹H NMR (400 MHz, DMSO-d₆, δ, ppm): 9.51 (1H, s, NH), 7.86 (1H, s, Ar-H), 7.80 (1H, s, Ar-H), 7.62 (1H, s, Ar-H), 7.41-7.35 (2H, m, Ar-

H), 5.28, 4.92 (2H, s, NCH₂), 4.56, 4.36 (2H, s, NH₂), 4.33, 4.23 (2H, s, CH₂). ¹³C NMR (100 MHz, DMSO-d₆): δ 30.9 (CH₂), 45.2 (NCH₂), 112.6 (Ar-CH), 120.3 (Ar-CH), 124.5 (Ar-C), 124.9 (Ar-C), 127.8 (Ar-CH), 129.1 (Ar-CH), 132.8 (Ar-C), 133.4 (Ar-CH), 133.9 (Ar-C), 134.9 (Ar-C), 135.7 (Ar-C), 142.0 (Ar-C), 155.9 (NCN), 165.9 (C=O). Elemental analysis: Calculated for C₁₆H₁₂Cl₄N₄O: C, 45.96; H, 2.89; N, 13.40. Found: C, 45.94; H, 2.92; N, 13.37.

General procedure for the synthesis of compound 4

A mixture of compound **3** (0.010 mol) and morpholine (0.030 mol) was heated in an oil bath at 130-140 °C reflux temperature for 16 h (monitored by TLC, ethyl acetate:hexane, v:v 2:1). The viscous residue was cooled to room temperature and acetone (10 mL) was added and allowed to cool overnight, a solid appeared. The crude product was recrystallized from a mixture of ethanol:water, 3:1 in order to obtain the desired compound.

5,6-Dichloro-2-(2,4-dichlorobenzyl)-1-(2-morpholin-4-yl-2-oxoethyl)-1H-benzimidazole (4). Yield: 2.45 g (52 %). M.P.: 193-195 °C, FTIR (KBr): 1659 (C=O), 1236 (C-O), 1094, 860, 826 cm⁻¹. ¹H NMR (400 MHz, DMSO-d₆, δ, ppm): 7.91 (1H, s, Ar-H), 7.80 (1H, s, Ar-H), 7.61 (1H, s, Ar-H), 7.34-7.37 (2H, m, Ar-H), 5.33 (2H s, NCH₂), 4.23 (2H s, CH₂), 3.70-3.68 (2H, m, OCH₂), 3.57-3.54 (4H, m, OCH₂, morpholine-NCH₂), 3.41-3.39 (2H, m, morpholine-NCH₂). ¹³C NMR (100 MHz, DMSO-d₆): δ 30.9 (CH₂), 42.2 (morpholine-NCH₂), 42.4 (morpholine-NCH₂), 45.2 (NCH₂), 66.3 (OCH₂), 66.4 (OCH₂), 112.5 (Ar-CH), 120.2 (Ar-CH), 124.3 (Ar-C), 124.8 (Ar-C), 127.8 (Ar-CH), 129.1 (Ar-CH), 132.8 (Ar-C), 133.5 (Ar-CH), 133.8 (Ar-C), 134.8 (Ar-C), 136.1 (Ar-C), 142.1 (Ar-C), 156.3 (NCN), 165.0 (C=O). Elemental analysis: Calculated for C₂₀H₁₇Cl₄N₃O₂: C, 50.77; H, 3.62; N, 8.88. Found: C, 50.81; H, 3.59; N, 8.85.

General procedure for the synthesis of the compounds 5, 6, 7

To a solution of compound **3** (0.010 mol) in absolute ethanol (30 mL), methylisothiocyanate for compound **5**, ethylisothiocyanate for compound **6**, 4-bromophenylisothiocyanate for compound **7** was added and refluxed for 2 hours (monitored by TLC, ethyl acetate:hexane, 2:1). The mixture was cooled to room temperature and water was added. After a while, it was filtered and purified by recrystallization from a mixture of ethanol:water, v:v 3:1.

2-([5,6-Dichloro-2-(2,4-dichlorobenzyl)-1H-benzimidazol-1-yl]acetyl)-N-methylhydrazinecarbothioamide (5). Yield: 4.27 g (87 %). M.P.: 205-206 °C, FTIR (KBr): 3404, 3303, 3152 (NH), 1693 (C=O), 1616, 1554 (CN) cm⁻¹. ¹H NMR (400 MHz, DMSO-d₆, δ, ppm): 10.25, 9.33, 8.08 (3H, s, NH), 7.88 (1H, s, Ar-H), 7.80 (1H, s, Ar-H), 7.63 (1H, s, Ar-H), 7.42-7.35

(2H, m, Ar-H), 5.09, 5.04 (2H, s, NCH₂), 4.31, 4.24 (2H, s, CH₂), 2.90 (3H, s, CH₃). ¹³C NMR (100 MHz, DMSO-d₆): δ 30.9 (CH₂), 31.4 (NCH₃), 45.2 (NCH₂), 112.5 (Ar-CH), 120.3 (Ar-CH), 124.6 (Ar-C), 124.9 (Ar-C), 127.9 (Ar-CH), 129.2 (Ar-CH), 132.9 (Ar-C), 133.4 (Ar-CH), 133.9 (Ar-C), 134.9 (Ar-C), 135.7 (Ar-C), 142.0 (Ar-C), 156.0 (NCN), 166.5 (C=O), 170.3 (CS). Elemental analysis: Calculated for C₁₈H₁₅Cl₄N₅OS: C, 44.01; H, 3.08; N, 14.26. Found: C, 44.05; H, 3.13; N, 14.22.

2-[[5,6-Dichloro-2-(2,4-dichlorobenzyl)-1H-benzimidazol-1-yl]acetyl]-N-ethylhydrazinecarbothioamide (6). Yield: 3.84 g (76 %). M.P.: 214-216 °C, FTIR (KBr): 3382, 3282, 3153 (NH), 1694 (C=O), 1620, 1551 (CN) cm⁻¹. ¹H NMR (400 MHz, DMSO-d₆, δ, ppm): 10.24, 9.26, 8.08 (3H, s, NH), 7.91 (1H, s, Ar-H), 7.81 (1H, s, Ar-H), 7.63 (1H, s, Ar-H), 7.41-7.34 (2H, m, Ar-H), 5.05 (2H, s, NCH₂), 4.24, 4.31 (2H, s, CH₂), 3.45 (2H, q, *J*=8 Hz, OCH₂), 1.06 (3H, t, *J*=8 Hz, CH₃). ¹³C NMR (100 MHz, DMSO-d₆+CH₂): δ 14.8 (CH₃), 30.9 (CH₂), 39.3-40.6 (DMSO-d₆+CH₂), 45.1 (NCH₂), 112.5 (Ar-CH), 120.3 (Ar-CH), 124.6 (Ar-C), 124.9 (Ar-C), 127.9 (Ar-CH), 129.1 (Ar-CH), 132.8 (Ar-C), 133.4 (Ar-CH), 133.9 (Ar-C), 134.9 (Ar-C), 135.7 (Ar-C), 142.1 (Ar-C), 156.1 (NCN), 166.4 (C=O), 172.6 (CS). Elemental analysis: Calculated for C₁₉H₁₇Cl₄N₅OS: C, 45.17; H, 3.39; N, 13.84. Found: C, 45.18; H, 3.34; N, 13.88.

N-(4-bromophenyl)-2-[[5,6-dichloro-2-(2,4-dichlorobenzyl)-1H-benzimidazol-1-yl]acetyl]hydrazinecarbothioamide (7). Yield: 4.23 g (67 %). M.P.: 184-185 °C, FTIR (KBr): 3354, 3296, 3151 (NH), 1691 (C=O), 1590, 1541 (CN) cm⁻¹. ¹H NMR (400 MHz, DMSO-d₆, δ, ppm): 10.53, 9.89, 9.82 (3H, s, NH), 7.94 (1H, s, Ar-H), 7.82 (1H, s, Ar-H), 7.63 (1H, s, Ar-H), 7.57-7.51 (3H, m, Ar-H), 7.42-7.34 (3H, m, Ar-H), 5.19, 5.12 (2H, s, NCH₂), 4.35 (2H, s, CH₂). ¹³C NMR (100 MHz, DMSO-d₆): δ 31.0 (CH₂), 45.3 (NCH₂), 112.6 (Ar-CH), 120.3 (Ar-CH), 124.6 (Ar-C), 124.9 (Ar-C), 127.9 (Ar-CH), 129.2 (Ar-CH), 131.5 (Ar-CH), 132.5 (Ar-C), 132.8 (Ar-C), 133.4 (Ar-CH), 133.5 (Ar-CH), 133.9 (Ar-C), 134.9 (Ar-C), 135.7 (Ar-C), 138.8 (Ar-C), 142.1 (Ar-C), 156.1 (NCN), 166.5 (C=O), 171.9 (CS). Elemental analysis: Calculated for C₂₃H₁₆BrCl₄N₅OS: C, 43.70; H, 2.55; N, 11.08. Found: C, 43.68; H, 2.52; N, 11.13.

General procedure for the synthesis of compounds 8, 9, 10

To the appropriate carbothioamide compound (**5**, **6**, **7**) (0.01 mol) in an ice bath, concentrated cold sulfuric acid (0.064 mol) was added dropwise and the mixture was stirred for 15 minutes. Then, the mixture was stirred at room temperature for an additional 30 minutes. Then the mixture was added to ice-water and adjusted to pH 7-8 with ammonia. The resulting product was filtered, washed with water purified by recrystallization from a mixture of ethanol:water, v:v 3:1.

5-[[5,6-Dichloro-2-(2,4-dichlorobenzyl)-1H-benzimidazol-1-yl]methyl]-N-methyl-1,3,4-thiadiazol-2-amine (8). Yield: 2.64 g (56 %). M.P.: 242-244 °C, FTIR (KBr): 3219 (NH), 1567, 1520, 1501 (CN) cm⁻¹. ¹H NMR (400 MHz, DMSO-d₆, δ, ppm): 8.03 (1H, s, Ar-H), 7.83 (1H, s, Ar-H), 7.68-7.59 (1H, m, Ar-H), 7.32-7.38 (2H, s, Ar-H), 5.80 (2H, s, NCH₂), 4.42 (2H, s, CH₂), 2.81 (3H, s, CH₃). ¹³C NMR (100 MHz, DMSO-d₆): δ 31.2 (CH₂), 31.7 (CH₃), 42.3 (NCH₂), 112.5 (Ar-CH), 120.5 (Ar-CH), 124.9 (Ar-C), 125.2 (Ar-C), 127.8 (Ar-CH), 129.2 (Ar-CH), 132.9 (Ar-C), 133.4 (Ar-CH), 133.7 (Ar-C), 134.9 (2Ar-C), 142.1 (Ar-C), 152.2 (NCN), 155.2 (thiadiazole-C₅), 170.8 (thiadiazole-C₂). Elemental analysis: Calculated for C₁₈H₁₃Cl₄N₅S: C, 45.69; H, 2.77; N, 14.80. Found: C, 45.72; H, 2.73; N, 14.82.

5-[[5,6-Dichloro-2-(2,4-dichlorobenzyl)-1H-benzimidazol-1-yl]methyl]-N-ethyl-1,3,4-thiadiazol-2-amine (9). Yield: 2.28 g (47 %). M.P.: 205-207 °C, FTIR (KBr): 3203 (NH), 1581, 1563, 1516 (CN) cm⁻¹. ¹H NMR (400 MHz, DMSO-d₆, δ, ppm): 8.04 (1H, s, Ar-H), 7.83 (1H, s, Ar-H), 7.73-7.59 (1H, m, Ar-H), 7.38-7.32 (2H, s, Ar-H), 5.79 (2H, s, NCH₂), 4.42 (2H, s, CH₂), 3.20 (2H, q, *J*=8 Hz, CH₂), 2.48 (3H, t, *J*=8 Hz, CH₃). ¹³C NMR (100 MHz, DMSO-d₆): δ 14.6 (CH₃), 31.2 (CH₂), 39.4-40.6 (DMSO-d₆+CH₂), 42.3 (NCH₂), 112.5 (Ar-CH), 120.5 (Ar-CH), 124.9 (Ar-C), 125.2 (Ar-C), 127.8 (Ar-CH), 129.2 (Ar-CH), 132.9 (Ar-C), 133.4 (Ar-CH), 133.7 (Ar-C), 134.9 (Ar-C), 134.9 (Ar-C), 142.1 (Ar-C), 152.0 (NCN), 155.4 (thiadiazole-C₅), 169.8 (thiadiazole-C₂). Elemental analysis: Calculated for C₁₉H₁₅Cl₄N₅S: C, 46.84; H, 3.10; N, 14.37. Found: C, 46.82; H, 3.07; N, 14.39.

N-(4-bromophenyl)-5-[[5,6-dichloro-2-(2,4-dichlorobenzyl)-1H-benzimidazol-1-yl]methyl]-1,3,4-thiadiazol-2-amine (10). Yield: 3.68 g (60 %). M.P.: 263-264 °C, FTIR (KBr): 3188 (NH), 1617, 1556, 1511 (CN) cm⁻¹. ¹H NMR (400 MHz, DMSO-d₆, δ, ppm): 10.48 (1H, brs, NH), 8.09 (1H, s, Ar-H), 7.85 (1H, s, Ar-H), 7.60-7.56 (1H, m, Ar-H), 7.54-7.08 (6H, m, Ar-H), 5.92 (2H, s, NCH₂), 4.45 (2H, s, CH₂). ¹³C NMR (100 MHz, DMSO-d₆): δ 31.2 (CH₂), 42.1 (NCH₂), 112.6 (Ar-CH), 113.8 (Ar-C), 119.8 (Ar-CH), 120.5 (Ar-CH), 125.1 (Ar-C), 125.4 (Ar-C), 127.8 (Ar-CH), 129.2 (Ar-CH), 132.2 (Ar-CH), 132.9 (Ar-C), 133.4 (Ar-CH), 133.6 (Ar-C), 134.9 (Ar-C), 140.0 (Ar-C), 142.0 (Ar-C), 154.8 (NCN), 155.5 (thiadiazole-C₅), 165.3 (thiadiazole-C₂). Elemental analysis: Calculated for C₂₃H₁₄BrCl₄N₅S: C, 44.98; H, 2.30; N, 11.40. Found: C, 44.96; H, 2.32; N, 11.38.

General procedure for the synthesis of the compounds 11, 12, 13

To the appropriate carbothioamide compound (**5**, **6**, **7**) (0.01 mol) in ethanol (15 mL) 2 N 15 mL of NaOH (0.064 mol) is added and the mixture was refluxed for 2 h. Then, the mixture was cooled to room temperature and adjusted to pH 4-5 with 37% HCl. The resulting product was filtered,

washed with water and purified by recrystallization from a mixture of ethanol:water, v:v 2:1.

5-*{[5,6-Dichloro-2-(2,4-dichlorobenzyl)-1H-benzimidazol-1-yl]methyl}*-4-methyl-4H-1,2,4-triazole-3-thiol (**11**). Yield: 3.40 g (72 %). M.P.: 255-256 °C, FTIR (KBr): 2930 (SH), 1598, 1584 (CN) cm^{-1} . ^1H NMR (400 MHz, DMSO- d_6 , δ , ppm): 13.53 (1H, s, SH), 8.03 (1H, s, Ar-H), 7.83 (1H, s, Ar-H), 7.59 (1H, s, Ar-H), 7.40-7.33 (2H, m, Ar-H), 5.73 (2H, s, NCH₂), 4.32 (2H, s, CH₂), 3.50 (3H, s, CH₃). ^{13}C NMR (100 MHz, DMSO- d_6): δ 30.4 (NCH₃), 30.9 (CH₂), 45.2 (NCH₂), 112.7 (Ar-CH), 120.4 (Ar-CH), 124.8 (Ar-C), 125.2 (Ar-C), 127.8 (Ar-CH), 129.1 (Ar-CH), 132.9 (Ar-C), 133.4 (Ar-CH), 133.8 (Ar-C), 134.9 (Ar-C), 135.6 (Ar-C), 142.1 (Ar-C), 148.5 (NCN), 155.9 (triazole-C₅), 168.1 (triazole-C₂). Elemental analysis: Calculated for C₁₈H₁₃Cl₄N₅S: C, 45.69; H, 2.77; N, 14.80. Found: C, 45.71; H, 2.79; N, 14.83.

5-*{[5,6-Dichloro-2-(2,4-dichlorobenzyl)-1H-benzimidazol-1-yl]methyl}*-4-ethyl-4H-1,2,4-triazole-3-thiol (**12**). Yield: 3.31 g (68 %). M.P.: 240-242 °C, FTIR (KBr): 2832 (SH), 1590, 1567 (CN) cm^{-1} . ^1H NMR (400 MHz, DMSO- d_6 , δ , ppm): 13.58 (1H, s, SH), 8.04 (1H, s, Ar-H), 7.84 (1H, s, Ar-H), 7.59 (1H, s, Ar-H), 7.37-7.33 (2H, m, Ar-H), 5.78 (2H, s, NCH₂), 4.34 (2H, s, CH₂), 4.03 (2H, q, $J=8$ Hz, OCH₂), 1.19 (3H, t, $J=8$ Hz, CH₃). ^{13}C NMR (100 MHz, DMSO- d_6): δ 13.5 (CH₃), 30.9 (CH₂), 39.1 (triazole-NCH₂), 45.2 (NCH₂), 112.6 (Ar-CH), 120.4 (Ar-CH), 124.9 (Ar-C), 125.3 (Ar-C), 127.8 (Ar-CH), 129.1 (Ar-CH), 132.9 (Ar-C), 133.4 (Ar-CH), 133.6 (Ar-C), 134.8 (Ar-C), 135.6 (Ar-C), 142.0 (Ar-C), 147.0 (NCN), 155.9 (triazole-C₅), 167.6 (triazole-C₂). Elemental analysis: Calculated for C₁₉H₁₅Cl₄N₅S: C, 46.84; H, 3.10; N, 14.37. Found: C, 46.81; H, 3.14; N, 14.32.

4-(4-Bromophenyl)-5-*{[5,6-dichloro-2-(2,4-dichlorobenzyl)-1H-benzimidazol-1-yl]methyl}*-4H-1,2,4-triazole-3-thiol (**13**). Yield: 3.93 g (64 %). M.P.: 254-255 °C, FTIR (KBr): 2893 (SH), 1587, 1578 (CN) cm^{-1} . ^1H NMR (400 MHz, DMSO- d_6 , δ , ppm): 13.93 (1H, s, SH), 7.96 (1H, s, Ar-H), 7.81 (1H, s, Ar-H), 7.74 (1H, s, Ar-H), 7.66-7.61 (3H, m, Ar-H), 7.40-7.29 (3H, m, Ar-H), 5.50 (2H, s, NCH₂), 4.29 (2H, s, CH₂). ^{13}C NMR (100 MHz, DMSO- d_6): δ 30.8 (CH₂), 45.3 (NCH₂), 112.6 (Ar-CH), 120.2 (Ar-CH), 123.7 (Ar-C), 124.6 (Ar-C), 125.1 (Ar-C), 127.8 (Ar-CH), 129.1 (Ar-CH), 130.7 (Ar-CH), 132.5 (Ar-C), 132.9 (Ar-C), 133.4 (Ar-CH), 133.4 (Ar-CH), 133.7 (Ar-C), 134.8 (Ar-C), 135.7 (Ar-C), 141.9 (Ar-C), 147.5 (NCN), 155.8 (triazole-C₅), 169.5 (triazole-C₂). Elemental analysis: Calculated for C₂₃H₁₄BrCl₄N₅S: C, 44.98; H, 2.30; N, 11.40. Found: C, 45.01; H, 2.27; N, 11.43.

Antioxidant Activity and Radical Scavenging Assays

Antioxidant activities of the synthesized compounds were clarified using various *in vitro* antioxidant assays, including Cupric Reducing Antioxidant Capacity (CUPRAC), ABTS (2,2-azinobis(3-ethylbenzothiazoline-6-sulfonic acid)/Persulfate and DPPH (1,1-diphenyl-2-picrylhydrazyl) assays. Catechin, Trolox® and Ascorbic acid were used as positive antioxidants.

Cupric reducing antioxidant capacity (CUPRAC) assay

In order to determine the cupric ions (Cu²⁺) reducing ability of the synthesized compounds was determined according to the literature (19, 20, 21). The standard curve was linear between 32 mM and 1.25 mM trolox ($r^2=0.9989$). CUPRAC values were expressed as mM Trolox® equivalent of 1 mg synthesized compound.

DPPH-Free radical scavenging assay

The DPPH radical scavenging activity of the synthesized compounds was measured using the method of Brand-Williams (20, 21, 22, 23,). Briefly, 1200 microliter of 0.1 mM DPPH (2,2-diphenyl-1-picrylhydrazyl) solution in methanol was added 300 μL of the synthesized compound's solution in DMSO. Then, the mixture was kept in the dark for 50 minutes, the decrease in absorbance at 517 nm was measured, using a UV-Visible spectrophotometer (1601UV-Shimadzu, Australia). All determinations were carried out in triplicate and the results are expressed as % scavenging of DPPH radical, the percentage scavenging was calculated from the Formula given below:

$$\% \text{ Scavenging} = [(\text{OD}_{\text{control}} - \text{OD}_{\text{test}}) / (\text{OD}_{\text{control}} \times 100)].$$

ABTS^{•+} Radical Cation Decolorization Assay

The ability of the synthesized compounds to scavenge ABTS^{•+} radical was determined according to the literature (20, 21, 24). ABTS [2,2'-azino-bis(3-ethylbenzothiazoline-6-sulfonic acid)] was dissolved in water to a 7 mM concentration and diluted to get an absorbance of 0.700 ± 0.020 at 734 nm before use. After 5 min in the dark at room temperature, the decrease of absorbance of reaction mixture containing 200 μL of compound solution and 1800 μL of the ABTS^{•+} solution was measured. The percentage scavenging was calculated from the formula below:

$$\% \text{ Scavenging} = [(\text{OD}_{\text{control}} - \text{OD}_{\text{test}}) / (\text{OD}_{\text{control}} \times 100)].$$

Urease inhibition assay

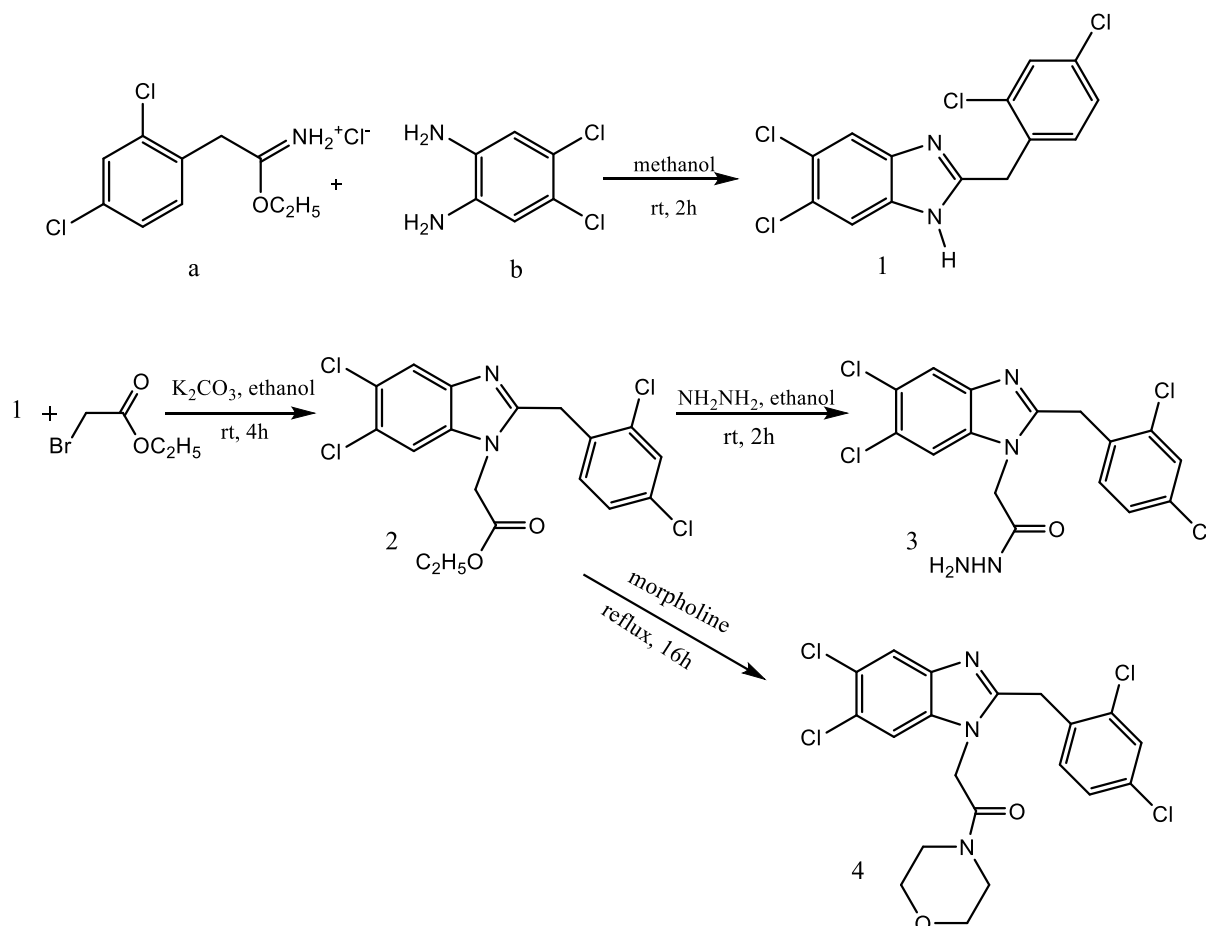
Urease is an enzyme that catalyzes the hydrolysis of urea into carbon dioxide and ammonia. The production of ammonia was measured by indophenol method and used to determine the urease inhibitory activity (25, 26, 27). The percentage remaining activity was calculated from the formula % Remaining Activity = $[(\text{OD}_{\text{test}})/(\text{OD}_{\text{control}}) \times 100]$. Thiourea (S1) and

acetoxyhydroamic acid (S2) were used as standard inhibitors. In order to calculate IC₅₀ values, different concentrations of synthesized compounds and standards were assayed at the same reaction conditions.

RESULTS AND DISCUSSION

In the present study, we reported the synthesis and investigated the biological activities of

antioxidant and urease inhibition of new 2-substituted benzimidazole derivatives containing triazole, thiadiazole, morpholine ring, and carbothioamide moiety. The synthetic procedures for target compounds were depicted in Schemes 1 and 2. The structures of the newly synthesized compounds were elucidated by elemental analysis, ¹H-¹³C (APT) NMR, and FTIR spectral data.

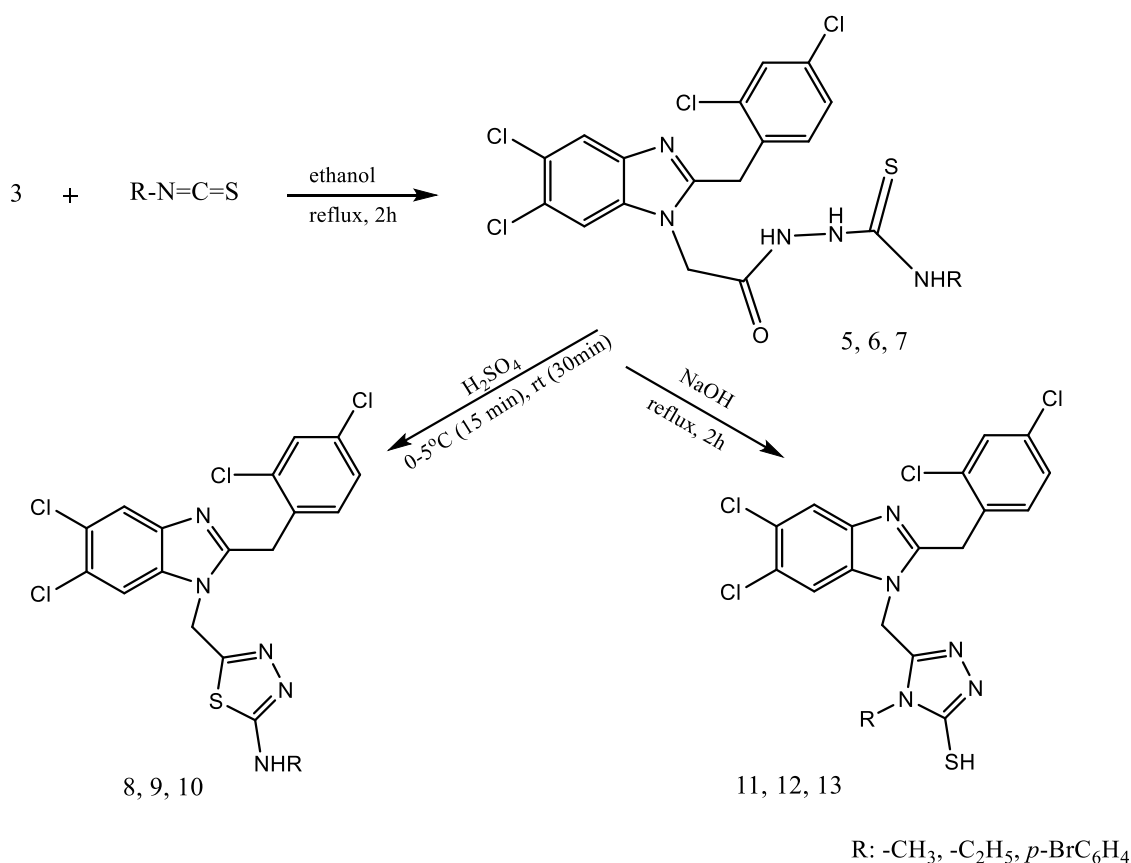


Scheme 1. The synthetic routes for compounds **1-4**.

Imino ester hydrochloride compound (**a**) was synthesized according to the reported method in the literature (18). 5,6-Dichloro-2-(2,4-dichlorobenzyl)-1H-benzimidazole (**1**) was obtained by the nucleophilic attack of 4,5-dichlorobenzene-1,2-diamine to the imine carbon of compound **a** and subsequent removal of the ester group. The compound **1** was treated with ethylbromoacetate in the presence of potassium carbonate at room temperature to give ethyl [5,6-dichloro-2-(2,4-dichlorobenzyl)-1H-benzimidazol-1-yl]acetate (**2**) followed by

nucleophilic substitution with hydrazine monohydrate to obtain 2-[5,6-dichloro-2-(2,4-dichlorobenzyl)-1H-benzimidazol-1-yl]acetohydrazide (**3**).

The nucleophilic addition of morpholine nitrogen to the carbonyl group of compound **2** and followed by elimination of a mole of ethanol afforded 5,6-dichloro-2-(2,4-dichlorobenzyl)-1-(2-morpholin-4-yl-2-oxoethyl)-1H-benzimidazole (**4**). The reaction was carried out in solvent-free at 130-140 °C (reflux temperature).



Scheme 2. The synthetic routes for compounds **5-13**.

The synthesis of carbothioamide compounds (**5**, **6**, **7**) was accomplished by nucleophilic addition of the acetoxyhydrazone compound (**3**) to the alkyl(aryl)isothiocyanates under reflux in ethanol. 1,3,4-Thiadiazole compounds (**8**, **9**, **10**) were obtained by the intramolecular cyclization reaction of carbothioamide compounds (**5**, **6**, **7**) in the presence of concentrated sulfuric acid. On the other hand, the synthesis of 1,2,4-triazole compounds (**11**, **12**, **13**) in the presence of 2 N NaOH was carried out by cyclization of the same compound (**5**, **6**, **7**). These compounds (**11**, **12**, **13**) may be present in the mercapto (-SH) or thioxo (C=S) tautomeric forms. The -SH protons of these compounds (**11**, **12**, **13**) resonate at 13.53, 13.58 and 13.93 ppm in the ¹H NMR, respectively. And also in the FT-IR spectra, the stretching bands of -SH function at 2913, 2832 and 2893 cm⁻¹ and the signals of the triazole-C2 atom at 168.1, 167.6 and 169.5 ppm in ¹³C NMR show us that these compounds are in the mercapto form. The ¹H NMR and ¹³C NMR spectra of the synthesized compounds are in accordance with the structures of the synthesized compounds and the elemental data results of C, H and N atoms are within acceptable limits.

CUPRAC Antioxidant Activity Assay

With CUPRAC analysis, the exemplary compounds were examined for their capacity to reduce Cu²⁺ ions of Cu⁺. And the absorbance of the complex Cu⁺ neocuproin was gauged at 450 nm, increasing the antioxidants with higher activity. The absorbance values for the samples were transformed to Trolox-equivalent antioxidant capacity (TEAC) values using the absorbance calibration graph [Trolox®]. And the TEAC results (mM) were shown in Figure 1. The highest antioxidant capacity was observed for the compound **11** (4.60 mM) in the CUPRAC method (Figure 1.). On the other hand, the compounds **3**, **5**, **6**, **7** and **12** showed good activity, while compounds **1**, **2**, **4**, **8** and **9** showed little activity. The others (**10** and **13**) had moderate TEAC values. Similar to the CUPRAC test results obtained, we have published benzimidazole derivative compounds containing triazole and thiophene groups with TEAC data in the range of 0.400 to 1.476 mM in one of our previous studies (20). Another study reported that a series of new benzimidazole derivative containing the triazole ring compounds with a high inhibitory activity with TEAC values at 4.16-8.67 mM in cuprac assay were synthesized (21).

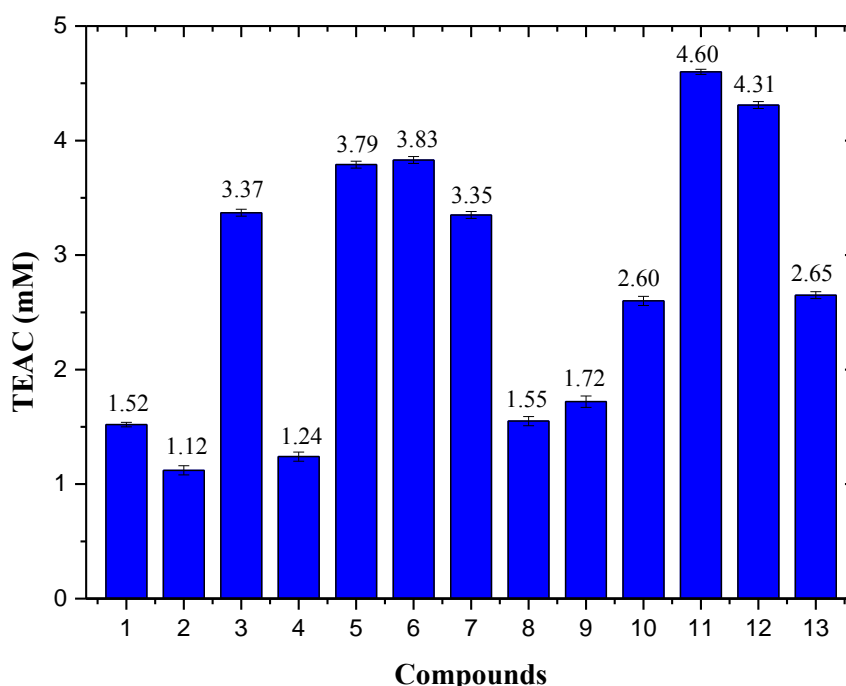


Figure 1. CUPRAC test results of all the synthesized compounds as mM TEAC (Trolox equivalent antioxidant capacity) values obtained from [Trolox]- absorbance calibration graph. TEAC values of compounds are expressed as the mean \pm S.D. in triplicate.

DPPH[•] and ABTS^{•+} Radical Scavenging Activity Results

The total radical scavenging activity of the synthesized compounds was identified using DPPH and ABTS^{•+} radical scavenging assays and compared with catechin, ascorbic acid and Trolox® as standards. DPPH activity results of the synthesized compounds are given in Table 1. The compound **13** showed good DPPH activity at the 240 μ g/mL concentration with 86.43% (Table 1). Beside this reality, it has been found that compounds **7**, **9** and **10** moderate scavenging activity at the same concentration. In the earlier

published study, it has been determined that the SC₅₀ results of the benzimidazole compounds containing the 1,2,4-triazole circle vary from 3.91 to 16.75 μ g / mL according to the DPPH method (28). The benzimidazole compounds containing thiosemicarbazide moiety and 1,3,4-oxadiazole circle, were also effective DPPH radical scavengers, with SC₅₀ results 77.36, 19.34, 13.46 and 13.27 μ g/mL (23). In another study, benzimidazole derivatives containing triazole cycle were reported to be highly active with the SC₅₀ values 7.03-31.27 μ g / mL in the DPPH method (21).

Table 1. DPPH[•] radical scavenging activities of the compounds and standards at various final concentrations were expressed as the mean \pm S.D. in triplicate.

Compounds and Standards	DPPH [•] Method				
	Radical Scavenging (%)				
	240 μ g/mL	120 μ g/mL	60 μ g/mL	30 μ g/mL	15 μ g/mL
1	10.71	10.71	10.71	9.29	8.71
2	9.43	9.43	9.43	9.00	9.00
3	56.71	57.86	58.86	57.43	46.57
4	13.29	8.57	8.29	8.14	7.86
5	50.86	43.00	50.14	50.29	43.14
6	53.14	51.71	51.14	52.14	48.86
7	69.57	67.00	60.57	58.43	45.71
8	16.86	10.43	10.43	10.29	9.71
9	63.29	54.57	34.29	17.00	11.71
10	70.00	35.43	17.29	11.71	10.00
11	45.86	35.00	26.57	20.14	13.29
12	49.86	39.29	26.43	19.57	15.43
13	86.43	74.43	50.00	26.57	17.71
Catechin	90.71	90.71	90.71	90.71	85.57
Ascorbic Acid	90.71	90.71	90.71	90.71	82.29
Trolox®	90.71	90.71	90.71	85.86	80.14

ABTS^{•+} is produced by oxidation of ABTS with K₂S₂O₈ and is reduced in the presence of

hydrogen-donating antioxidants. The compounds **3**, **5**, **6**, **7**, **11**, **12** and **13** showed efficient radical

scavenging activity, at all concentrations (Table 2). According to Radical Scavenging (%) activity results, the compounds can be listed **12 = 7, 11**

= 5, 3 = 6, 13 by decreasing degree at 24 µg/mL concentration (Table 2.).

Table 2. % ABTS^{•+} radical scavenging activities of the compounds and standards at various final concentrations were expressed as the mean ±S.D. in triplicate.

Compounds and Standards	ABTS ^{•+} Method				
	Radical Scavenging (%)				
	24 µg/mL	12 µg/mL	6 µg/mL	3 µg/mL	1.5 µg/mL
1	11.43	11.43	11.29	11.29	11.29
2	8.71	8.57	8.43	8.29	8.14
3	90.43	89.86	75.57	57.29	30.57
4	15.71	12.86	12.71	11.86	11.00
5	91.00	89.57	83.00	49.71	30.43
6	90.43	90.29	76.43	48.14	31.14
7	91.14	91.14	70.14	41.71	27.14
8	13.43	13.43	13.43	12.86	12.00
9	47.00	27.43	20.00	18.00	15.00
10	33.43	23.00	20.86	19.43	18.57
11	91.00	80.14	54.71	40.00	30.71
12	91.14	82.14	54.29	38.00	31.00
13	84.29	57.14	38.57	29.14	24.29
Catechin	91.43	91.43	90.71	85.43	43.43
Ascorbic Acid	91.43	91.43	90.71	75.00	36.43
Trolox®	91.43	91.43	90.71	67.57	45.00

Urease Inhibition Results

In vitro inhibitory activity of all the synthesized compounds against Jack bean urease were investigated. Thiourea (S1) and acetohydroxamic acid (S2), clinically used for the treatment of urinary tract infections, were used as standard inhibitors. Initially, all the synthesized compounds were evaluated at the 60 µg/mL final concentration. Among these compounds, **6** exhibited the best inhibitory effect against urease with IC₅₀ 2.52 µg/mL (Figure 2.). Also, the compounds **1, 2, 3, 4, 5, 7, 8, 9, 11, 12** and **13** had higher inhibitory effect on urease and exhibited the lower IC₅₀ values than

acetohydroxamic acid and thiourea (Figure 2). The compound **10** demonstrated moderately inhibitory effect, according to the others. Baltas *et al.*, reported IC₅₀ values of thiourea, compounds 5b and 5c as 11.91±0.33, 7.41±0.13 and 10.48±0.15 µg/mL, respectively (26). Researchers emphasized **9b** exhibited the best inhibitory effect against urease with IC₅₀ value 28.89±0.11 µM. Compound **9b** inhibited urease activity by 36.07±0.41%, 68.29±0.09% and 98.43±0.28 at concentrations of 10.94, 21.87 and 43.75 µg/mL, respectively (27).

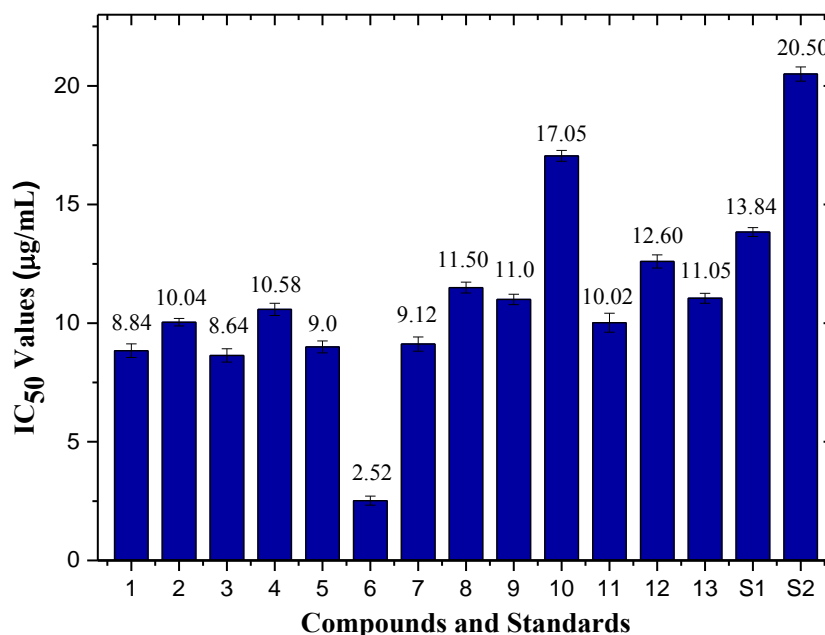


Figure 2. IC₅₀ values of the synthesized compounds and standards against *Jack bean* urease. Thiourea (S1) and acetohydroxamic acid (S2) were used as standard inhibitors.

CONCLUSION

The present work led to the synthesis of novel benzimidazole derivatives containing the hybridization of the 5,6-dichlorobenzimidazole ring with different bioactive groups such as carbothioamide, morpholine, triazole ring and thiadiazole rings. Also, inhibition of antioxidant and urease enzymes of these compounds has been examined in this study. Most of the synthesized compounds showed good and moderate antioxidant activity. Especially **3, 5, 6, 7, 11, 12, 13** compounds showed efficient antioxidant activity in % ABTS•+ radical scavenging capacity tests. It was also found that all synthesized compounds except compound **10** had higher inhibitory effect on urease and exhibited the lower IC₅₀ values (2.52-12.60 µg/mL) than acetohydroxamic acid (20.50 µg/mL) and thiourea (13.84 µg/mL), which are used as standard. The literature and this study show that the differences, location and number of substituents significantly effect the activities of these compounds.

REFERENCES

1. Neelima S, Naim MJ, Alam J, Nawaz F, Shujaiddin A, Alam O. Benzimidazole Scaffold as Anticancer Agent: Synthetic Approaches and Structure-Activity Relationship. *Arch Pharm Chem Life Sci.* 2017;350:1-80.
2. Ozkay Y, Tunai Y, Karaca H, Isikdag I. Antimicrobial activity and a SAR study of some novel benzimidazole derivatives bearing hydrazone moiety. *Eur J Med Chem.* 2010;45: 3293-8.
3. Achar KC, Hosamani KM, Seetharamareddy HR. In-vivo analgesic and anti-inflammatory activities of newly synthesized benzimidazole derivatives. *Eur J Med Chem.* 2010;45:2048-54.
4. Ramya VS, Kallappa MH, Rangappa SK, Mallinath HH. Derivatives of benzimidazole pharmacophore: Synthesis, anticonvulsant, antidiabetic and DNA cleavage studies. *European Journal of Medicinal Chemistry.* 2010;45:1753-9.
5. Ajania O, Olayinka O, Tolu B, Shade JO, Yuxia Z, Damilola VA. Structure-based design of functionalized 2-substituted and 1,2-disubstituted benzimidazole derivatives and their in vitro antibacterial efficacy. *Journal of Advanced Research.* 2017;8(6):703-12.
6. Kumar JR, Jawaharand J, Pathak DP. Synthesis of Benzimidazole Derivatives: As Anti-hypertensive Agents. *E-J Chem.* 2006;3:278-85.
7. Yeong KY, Mohamed AA, Ang CW, Tan SC, Kooi YK, Vikneswaran M, Hasnah O, Vijay HM. Synthesis, characterization, and molecular docking analysis of novel benzimidazole derivatives as cholinesterase inhibitors. *Bioorganic Chemistry.* 2013;49:33-9.
8. Patricia T, Hugo AK, Bruno P, Fernando L, Aurélie P, Christophe B, Rodrigo A. Organometallic benzimidazoles: Synthesis, characterization and antimalarial activity. *Inorganic Chemistry Communications.* 2013;35:126-9.
9. Kahveci B, Yilmaz F, Mentese E, et al. Design, Synthesis, and Biological Evaluation of Coumarin-Triazole Hybrid Molecules as Potential Antitumor and Pancreatic Lipase Agents. *Archiv Der Pharmazie.* 2017;350(8):1-9.
10. Mentese E, Bektas H, Sokmen BB, Emirik M, Cakir D, Kahveci B. Synthesis and molecular docking study of some 5,6-dichloro-2-cyclopropyl-1H-benzimidazole derivatives bearing triazole, oxadiazole, and imine functionalities as potent inhibitors of urease. *Bioorganic & Med Chem Lett.* 2017;27(13):3014-8.
11. Yogita B, Om S. The therapeutic journey of benzimidazoles: A review. *Bioorg & Med Chem.* 2012;20:6208-36.
12. Erb KL, Ravula SB, Yu J, Kord SZ, Moree WJ, Petroski RE, Wen J, Malany S, Hoare S RJ, Madan A, Crowe PD, Beaton G. The discovery and structure-activity relationships of 2-(piperidin-3-yl)-1H-benzimidazoles as selective, CNS penetrating H1-antihistamines for insomnia. *Bioorg Med Chem Lett.* 2010;20:2916- 9.
13. Kus C, Kilcigil GA, Ozbey S, Betu F, Kaynak I, Kaya M, Coban T, Eke BC. Synthesis and antioxidant properties of novel N-methyl-1,3,4-thiadiazol-2-amine and 4-methyl-2H-1,2,4-triazole-3(4H)-thione derivatives of benzimidazole class. *Bioorg Med Chem.* 2008;16, 4294-303.
14. Desai KG, Desai KR. Green route for the heterocyclization of 2-mercaptobenzimidazole into β-lactum segment derivatives containing -CONH-bridge with benzimidazole: Screening in vitro antimicrobial activity with various microorganisms. *Bioorg Med Chem.* 2006;14:8271-9.
15. Mentese E, Karaali N, Yilmaz F, Ulker S, Kahveci K. Microwave-Assisted Synthesis and Biological Evaluation of Some Benzimidazole Derivatives Containing a

- 1,2,4-Triazol Ring. *Archiv der Pharmazie*. 2013;346:556-61.
16. Mentese E, Yilmaz F, Baltaş N, Bekircan O, Kahveci B. Synthesis and antioxidant activities of some new triheterocyclic compounds containing benzimidazole, thiophene, and 1,2,4-triazole rings. *J Enzy Inh and Med Chem*. 2015;30:435-441.
 17. Schulz WG, Islam I, Skibo EB. Pyrrolo[1,2-a]benzimidazole-Based Quinones and Iminoquinones. The Role of the 3-Substituent on Cytotoxicity. *Jour Med Chem*. 1995; 38:109-18.
 18. Pinner A. Die Imidoäther und ihre Derivate, 1. Auflage, R. Oppenheim, Berlin (1892), S. 2.
 19. Apak R, Guclu K, Ozyurek M, Karademir SE. Novel total antioxidant capacity index for dietary polyphenols and vitamins C and E, using their cupric ion reducing capability in the presence of neocuproine: CUPRAC method. *J Agr Food Chem*. 2004;52(26):7970-81.
 20. Mentese E, Yilmaz F, Emirik M, Ulker S, Kahveci B. Synthesis, molecular docking and biological evaluation of some benzimidazole derivatives as potent pancreatic lipase inhibitors. *Bioorg Chem*. 2018;76:478-86.
 21. Yilmaz F, Mentese E, Baltaş N. Synthesis and Antioxidant Evaluation of Some Novel Benzimidazole Derivatives Containing a Triazole Nucleus. *Letters in Drug Design & Discovery*. 2017;14:201-8.
 22. Brandwilliams W, Cuvelier ME, Berset C. Use of a Free-Radical Method to Evaluate Antioxidant Activity. *Food Sci Technol-Leb*. 1995;28(1):25-30.
 23. Usta A, Yilmaz F, Kapucu G, Baltaş N, Mentese E. Synthesis of Some New Benzimidazole Derivatives with their Antioxidant Activities. *Lett Org Chem*. 2015; 12: 227-32.
 24. Re R, Pellegrini N, Proteggente A, Pannala A, Yang M, Rice-Evans C. Antioxidant activity applying an improved ABTS radical cation decolorization assay. *Free Radical Bio Med*. 1999;26(9-10):1231-7.
 25. Weatherburn MW (1967) Phenol-hypochlorite reaction for determination of ammonia. *Anal Chem* 1967, 39(8):971-4.
 26. Baltaş N, Yılmaz F, Mentese E. Synthesis, Antioxidant, Xanthine Oxidase and Urease Inhibitory Activities of Some Chlorine Containing Benzimidazoles. *Hacettepe J Biol & Chem*. 2016;44(3):293-305.
 27. Bekircan O, Baltaş N, Mentese E, Gültekin E. Synthesis of new fluorine-containing 1,2,4-triazole-5-on derivatives with their anti-urease, anti-xanthine oxidase and antioxidant activities. *Revue Roumaine de Chimie*. 2016;61(10):733-46.
 28. Mentese E, Karaali N, Yilmaz F, Ulker S, Kahveci B. Microwave- Assisted Synthesis and Biological Evaluation of Some Benzimidazole Derivatives Containing a 1,2,4-Triazol Ring. *Arch Pharm*. 2013;346:556-61.